

Jiadong Sun
Jingnan Liu
Shiwei Fan
Xiaochun Lu
Editors

China Satellite Navigation Conference (CSNC) 2015 Proceedings: Volume I



Lecture Notes in Electrical Engineering

Volume 340

Board of Series editors

Leopoldo Angrisani, Napoli, Italy
Marco Arteaga, Coyoacán, México
Samarjit Chakraborty, München, Germany
Jiming Chen, Hangzhou, P.R. China
Tan Kay Chen, Singapore, Singapore
Rüdiger Dillmann, Karlsruhe, Germany
Haibin Duan, Beijing, China
Gianluigi Ferrari, Parma, Italy
Manuel Ferre, Madrid, Spain
Sandra Hirche, München, Germany
Faryar Jabbari, Irvine, USA
Janusz Kacprzyk, Warsaw, Poland
Alaa Khamis, New Cairo City, Egypt
Torsten Kroeger, Stanford, USA
Tan Cher Ming, Singapore, Singapore
Wolfgang Minker, Ulm, Germany
Pradeep Misra, Dayton, USA
Sebastian Möller, Berlin, Germany
Subhas Mukhopadhyay, Palmerston, New Zealand
Cun-Zheng Ning, Tempe, USA
Toyoaki Nishida, Sakyo-ku, Japan
Bijaya Ketan Panigrahi, New Delhi, India
Federica Pascucci, Roma, Italy
Tariq Samad, Minneapolis, USA
Gan Woon Seng, Nanyang Avenue, Singapore
Germano Veiga, Porto, Portugal
Haitao Wu, Beijing, China
Junjie James Zhang, Charlotte, USA

About this Series

“Lecture Notes in Electrical Engineering (LNEE)” is a book series which reports the latest research and developments in Electrical Engineering, namely:

- Communication, Networks, and Information Theory
- Computer Engineering
- Signal, Image, Speech and Information Processing
- Circuits and Systems
- Bioengineering

LNEE publishes authored monographs and contributed volumes which present cutting edge research information as well as new perspectives on classical fields, while maintaining Springer’s high standards of academic excellence. Also considered for publication are lecture materials, proceedings, and other related materials of exceptionally high quality and interest. The subject matter should be original and timely, reporting the latest research and developments in all areas of electrical engineering.

The audience for the books in LNEE consists of advanced level students, researchers, and industry professionals working at the forefront of their fields. Much like Springer’s other Lecture Notes series, LNEE will be distributed through Springer’s print and electronic publishing channels.

More information about this series at <http://www.springer.com/series/7818>

Jiadong Sun · Jingnan Liu
Shiwei Fan · Xiaochun Lu
Editors

China Satellite Navigation Conference (CSNC) 2015 Proceedings: Volume I



Editors

Jiadong Sun
China Aerospace Science
and Technology Corporation
Chinese Academy of Sciences
Beijing
China

Jingnan Liu
Wuhan University
Wuhan
China

Shiwei Fan
China Satellite Navigation Office
Beijing
China

Xiaochun Lu
Chinese Academy of Sciences
Beijing
China

ISSN 1876-1100 ISSN 1876-1119 (electronic)
Lecture Notes in Electrical Engineering
ISBN 978-3-662-46637-7 ISBN 978-3-662-46638-4 (eBook)
DOI 10.1007/978-3-662-46638-4

Library of Congress Control Number: 2014937269

Springer Heidelberg New York Dordrecht London
© Springer-Verlag Berlin Heidelberg 2015

This work is subject to copyright. All rights are reserved by the Publisher, whether the whole or part of the material is concerned, specifically the rights of translation, reprinting, reuse of illustrations, recitation, broadcasting, reproduction on microfilms or in any other physical way, and transmission or information storage and retrieval, electronic adaptation, computer software, or by similar or dissimilar methodology now known or hereafter developed.

The use of general descriptive names, registered names, trademarks, service marks, etc. in this publication does not imply, even in the absence of a specific statement, that such names are exempt from the relevant protective laws and regulations and therefore free for general use.

The publisher, the authors and the editors are safe to assume that the advice and information in this book are believed to be true and accurate at the date of publication. Neither the publisher nor the authors or the editors give a warranty, express or implied, with respect to the material contained herein or for any errors or omissions that may have been made.

Printed on acid-free paper

Springer-Verlag GmbH Berlin Heidelberg is part of Springer Science+Business Media
(www.springer.com)

Editorial Board

Topic 1: BDS/GNSS Navigation Applications

Yamin Dang, Chinese Academy of Surveying and Mapping, China

Jianping Cao, Research Institute of Air Force Equipment, China

Jing Li, Communication and Information Center of Ministry of Transport, China

Shuanggen Jin, Shanghai Astronomical Observatory, Chinese Academy of Sciences, China

Yanming Feng, Queensland University of Technology Brisbane, Australia

Topic 2: Satellite Navigation Signal System, Compatibility and Interoperability

Feixue Wang, National University of Defense Technology, China

Xingqun Zhan, Shanghai Jiaotong University, China

Guangxia Li, PLA University of Science and Technology

Baowang Lian, Northwest University

Topic 3: Precise Orbit Determination and Positioning

Qile Zhao, Wuhan University, China

Xiaogong Hu, Shanghai Astronomical Observatory, Chinese Academy of Sciences, China

Geshi Tang, Beijing Aerospace Control Center (BACC), China

Maorong Ge, Geological Research Center in Germany

Chris Rizos, University of New South Wales International Association of Geodesy International GNSS Service, Australia

Topic 4: Atomic Clock Technique and Time-Frequency System

Lianshan Gao, Beijing Institute of Radio Metrology and Measurement, China

Chunhao Han, Beijing Satellite Navigation Center, China

Jinjun Zheng, China Academy of Space Technology (CAST), China

Xiaohui Li, National Time Service Center, Chinese Academy of Sciences, China

Zhiheng Jiang, Time Department Bureau International Des Poids et Mesures, France

Topic 5: Satellite Navigation Augmentation and Integrity Monitoring

Jinping Chen, Beijing Satellite Navigation Center, China

Junlin Zhang, OLinkStar Co., Ltd., China

Jianwen Li, Surveying and Mapping Institute of Zhengzhou, China

Rongzhi Zhang, Xi'an Satellite Control Center, China

Yang Gao, University of Calgary, Canada

Topic 6: BDS/GNSS Test and Assessment Technology

Jun Yang, National University of Defense Technology, China

Henglin Chu, Beijing Satellite Navigation Center, China

Baoguo Yu, The 54th Research Institute of China Electronics Technology Group Corporation, China

Wenxian Yu, Shanghai Jiaotong University, China

Jinling Wang, University of New South Wales, Australia

Topic 7: BDS/GNSS User Terminal Technology

Haibo He, Beijing Satellite Navigation Center, China

Hong Li, Tsinghua University, China

Yongchao Geng, The 20th Research Institute of China Electronics Technology Group Corporation, China

Sam Pullen, Stanford University

Yan Liu, Guangzhou Haige Communications Group Incorporated Company, China

Topic 8: Satellite Navigation Model and Method

Qin Zhang, Chang'an University, China

Luping Xu, Xidian University

Xiaolin Jia, Xi'an Institute of Surveying and Mapping, China

Kefei Zhang, RMIT University, Australia

Shaojun Feng, Imperial College London, England

Topic 9: PNT System and New Technologies of Navigation

Mingquan Lu, Tsinghua University, China

Zhongliang Deng, Beijing University of Posts and Telecommunications, China

Hong Yuan, Navigation Headquarters, Chinese Academy of Sciences, China

Dangwei Wang, The 20th Research Institute of China Electronics Technology Group Corporation, China

Yongbin Zhou, National University of Defense Technology, China

Ping Shuai, China Academy of Space Technology, China

Topic 10: Policies and Regulations, Standard and Intellectual Property

Daiping Zhang, China Defence Science and Technology Information Center, China

Yonggang Wei, China Academy of Aerospace Standardization and Product Assurance, China

Ping Zhang, Peking University, China

Haibo Liu, Institute of Policy and Management, Chinese Academy of Science, China

Preface

BeiDou Navigation Satellite System (BDS) is China's global navigation satellite system which has been developed independently. BDS is similar in principle to the global positioning system (GPS) and compatible with other global satellite navigation systems (GNSS) worldwide. The BDS will provide highly reliable and precise positioning, navigation and timing (PNT) services as well as short-message communication for all users under all-weather, all-time and worldwide conditions.

China Satellite Navigation Conference (CSNC) is an open platform for academic exchanges in the field of satellite navigation. It aims to encourage technological innovation, accelerate GNSS engineering and boost the development of the satellite navigation industry in China and in the world.

The 6th China Satellite Navigation Conference (CSNC 2015) was held during May 13–15, 2015, Xian, China. The theme of CSNC2015 is Opening-up, Connectivity, Win-win, which covers a wide range of activities, including technical seminars, academic exchanges, forums, exhibitions and lectures. The main topics are as follows:

1. BDS/GNSS Navigation Applications
2. Satellite Navigation Signal System, Compatibility and Interoperability
3. Precise Orbit Determination and Positioning
4. Atomic Clock Technique and Time-Frequency System
5. Satellite Navigation Augmentation and Integrity Monitoring
6. BDS/GNSS Test and Assessment Technology
7. BDS/GNSS User Terminal Technology
8. Satellite Navigation Models and Methods
9. PNT System and New Technologies of Navigation
10. Policies and Regulations, Standard and Intellectual Property

The proceedings (Lecture Notes in Electrical Engineering) have 197 papers in ten topics of the conference, which were selected through a strict peer-review process from 513 papers presented at CSNC2015. In addition, another 251 papers were selected as the electronic proceedings of CSNC2015, which are also indexed

by “China Proceedings of Conferences Full-text Database (CPCD)” of CNKI and Wan Fang Data.

We thank the contribution of each author and extend our gratitude to the 215 referees and 49 session chairs who are listed as members of the editorial board. The assistance of the organizing committees of CNSC2015 and the Springer editorial office is highly appreciated.

Jiadong Sun
Chair of CSNC2015

The 6th China Satellite Navigation Conference (CSNC 2015)

Scientific Committee

Chairman

Jiadong Sun, China Aerospace Science and Technology Corporation

Vice-Chairman

Rongjun Shen, China

Jisheng Li, China

Qisheng Sui, China

Zuhong Li, China Academy of Space Technology

Shusen Tan, Beijing Satellite Navigation Center, China

Executive Chairman

Jingnan Liu, Wuhan University

Yuanxi Yang, China National Administration of GNSS and Applications

Shiwei Fan, China

Committee Members: (By Surnames Stroke Order)

Xiancheng Ding, China Electronics Technology Group Corporation

Qingjun Bu, China

Liheng Wang, China Aerospace Science and Technology Corporation

Yuzhu Wang, Shanghai Institute of Optics and Fine Mechanics, Chinese Academy of Sciences

Guoxiang Ai, National Astronomical Observatories, Chinese Academy of Sciences

Shuhua Ye, Shanghai Astronomical Observatories, Chinese Academy of Sciences

Zhaowen Zhuang, National University of Defense Technology
Qifeng Xu, PLA Information Engineering University
Houze Xu, Institute of Geodesy and Geophysics, Chinese Academy of Sciences
Guirong Min, China Academy of Space Technology
Xixiang Zhang, China Electronics Technology Group Corporation
Lvqian Zhang, China Aerospace Science and Technology Corporation
Junyong Chen, National Administration of Surveying, Mapping
and Geoinformation
Benyao Fan, China Academy of Space Technology
Dongjin Luo, China
Guohong Xia, China Aerospace Science and Industry Corporation
Chong Cao, China Research Institute of Radio Wave Propagation (CETC 22)
Faren Qi, China Academy of Space Technology
Sili Liang, China Aerospace Science and Technology Corporation
Shancheng Tu, China Academy of Space Technology
Rongsheng Su, China
Zhipeng Tong, China Electronics Technology Group Corporation
Ziqing Wei, Xi'an Institute of Surveying and mapping

Organizing Committee

Secretary General

Haitao Wu, Navigation Headquarters, Chinese Academy of Sciences

Vice-Secretary General

Wenhai Jiao, China Satellite Navigation Office Engineering Center
Yuehu Hu, The 20th Research Institute of China Electronics Technology Group
Corporation
Weina Hao, Navigation Headquarters, Chinese Academy of Sciences

Committee Members: (By Surnames Stroke Order)

Qun Ding, Xi'an Institute of Navigation Technology
Miao Yu, Beijing Institute of Space Science and Technology Information
Jun Lu, China Satellite Navigation Office Engineering Center
Yintang Yang, Xidian University
Xiuwan Chen, Peking University
Mingquan Lu, Tsinghua University

Xiang'an Zhao, China Defense Science and Technology Information Center
Jing Zhao, Ministry of Science and Technology National Remote Sensing Center
Guangzhou Ouyang, Academy of Opto-Electronics, Chinese Academy of Science
Gang Hu, Beijing Unicore Communications Inc.
Yamin Dang, Chinese Academy of Surveying and Mapping, China
Zhong Dou, National Time Service Center of Chinese Academy of Sciences

Contents

Part I BDS/GNSS Navigation Applications

1 Accuracy Assessment of the Doppler Frequency and Pseudorange Model Based on GPS/LEO Radio Occultation	3
Xian-Sheng Xu, Yan Liu, Ye Li and Xu Xu	
2 Application of BeiDou Navigation Satellite System on Attitude Determination for Chinese Space Station	13
Sihao Zhao, Cai Huang, Xin Qi and Mingquan Lu	
3 Feasibility Analysis of High-Precision Deformation Monitoring Using BeiDou Navigation Satellite System	27
Ruijie Xi, Yugang Xiao, Xingwei Liu and Kaihua Wang	
4 Analysis on Velocity Measurement Precision of High Dynamic GPS Receiver Carrier Tracking Loop	35
Xudong Liu, Guangjun Liu, Qiang Li and Haiying Luo	
5 Theoretical Study of Bare Soil Parameters' Effects on GPS Multipath Observables	45
Xuerui Wu, Shuanggen Jin and Ye Li	
6 Satellite-Ground TT&C United Scheduling Methods of GNSS Constellation Based on Nodes Constraint	55
Li Jing, Zhang Tianjiao and Ye Gangqiang	
7 Realization of Real Time Kinematic Positioning Software Based on Kalman Filter	67
Dangwei Wang and Yi Lai	

8	Analysis of BeiDou Satellite Orbit Prediction Based on ERP Prediction Errors Impact	77
	Xiusong Ye, Hai Guo, Jie Yang, Chao Li and Canyou Liu	
9	The Repeatability Test of BDS Baseline Processing	85
	Yanguo Liu, Jinzhong Bei, Dehai Li, Hu Wang and Xiaying Wang	
10	A System Developed for Monitoring and Analyzing Dynamic Changes of GNSS Precipitable Water Vapor and Its Application	95
	Li Li, Zhimin Yuan, Ping Luo, Jun Shen, Sichun Long, Liya Zhang and Zongli Jiang	
11	Multifunctional Satellite Navigation and Communication Mast Antenna Based on Mobile Platform.	107
	Jia Zhang, Ximing Liang and Haiguang Zhang	
12	Optimal Satellite Selecting Algorithm in GPS/BDS Navigation System and Its Implementation	117
	Zhuoxi Ma, Li Yang, Xiaolin Jia, Dan Zhang and Shuai Liu	
13	An Improved Method to Accelerate the Convergence of PPP-RTK with Sparse CORS Stations' Augmentation	129
	Shoujian Zhang, Jiancheng Li and Lei Zhao	
14	Research on GEO Satellite Global Monitoring and Control Based on BeiDou Navigation Satellite System.	141
	Yue Zhao, Xianqing Yi, Zhenwei Hou and Tao Zhong	
15	The Optimal Distribution Strategy of BeiDou Monitoring Stations for GEO Precise Orbit Determination.	153
	Longping Zhang, Yamin Dang, Shuqiang Xue, Hu Wang, Shouzhou Gu and Chuanyang Wang	
16	Analysis and Comparison of Non-coherent and Differential Acquisition Integration Strategies	163
	Dandan Zeng, Songlin Ou, Jinhai Li, Jinhai Sun, Yuepeng Yan and Haofeng Li	
17	A New Method Based on QSE Processing for Interferometric GNSS-R Ocean Altimetry	177
	Chenghui Yu, Chundi Xiu, Weiqiang Li and Dongkai Yang	

18 Analysis of GNSS Signals with Application to Lunar Navigation 187
 Xiaoliang Wang, Longlong Li, Xingyuan Han, Yansong Meng and Lin Wu

19 Experiment and Result of Precise Kinematic Orbit Determination for LEO Satellite 195
 Rengui Ruan, Laiping Feng and Xianbing Wu

20 A GNSS Anti-spoofing Method Based on the Cooperation of Multiple Techniques 205
 Huiqi Tao, Hong Li and Mingquan Lu

21 Based on Singular Spectrum Analysis in the Study of GPS Time Series Analysis 217
 Ronghai Qiu, Yingyan Cheng, Hu Wang and Xiaoming Wang

22 Initial Performance Assessment of BDS Real-Time Relative Positioning with Triple-Frequency Observations 227
 Min Wang, Hongzhou Cai, Jun Liu and Anmin Zeng

23 Unified Estimation Model of Multi-system Biases Including BDS/GPS/GLONASS/Galileo 241
 Changhui Xu, Hu Wang, Yamin Dang, Hao Chen and Longping Zhang

24 The Study on Ocean Ice Intensity Surveyed by GNSS-R Signal on the Coast 251
 Fuyang Ke, Fangyuan Chen and Yunchang Cao

25 Research on Tracking Technology of High Sensitive BD Signals 261
 Zheng Zhao and Li Li

26 Characteristic Analysis for Regional Traffic Data Using Random Matrix Theory. 273
 Haichun Liu, Changchun Pan, Genke Yang, Chunxia Zhang and Robert C. Qiu

27 Impact Analysis of Differential Code Biases of GPS Satellites on the Kinematic Precise Point Positioning 283
 Shoujian Zhang and Lei Zhao

Part II BDS/GNSS Test and Assessment Technology

28 Performance Improvements of Combined Satellites Navigation System with System Time Offset 293
Longxia Xu, Ye Ren, Xiaohui Li and Dandan Li

29 Modeling and Multi-state Analysis for Availability of a Navigation Monitor Network 305
Zhuopeng Yang, Feng Xue, Jinjing Wang and Heng Zheng

30 A GNSS Multipath Detecting Method Based on Antenna Arrays 319
Min Li, Wei Zhao, Liang Yuan and Qinli Liu

31 Reliability Allocation Method of Satellite Navigation System Based on Dynamic Simulation 331
Heng Zheng, Haisheng Li, Chang Li, En Xue, Zhuopeng Yang and Peipei Gong

32 A Study on Measuring Channel Bias in GNSS Receiver 343
Hailong Chen, Wen Li, Xin Liu and Wenhai Jiao

33 The Development, Test and Application of New Technology on Beidou/GPS Dual-Mode Pseudolites 353
Xingli Gan, Baoguo Yu, Lei Chao and Shi Liu

34 Study on Judgment Method of Signal Correlation Performance Based on Complex Correlation Vector 365
Ying Wang, Zhe Su, Yansong Meng and Xiaoxia Tao

35 The Analysis of GNSS SIS Accuracy 375
Shuai Liu, Xiaolin Jia and Zhuoxi Ma

36 BeiDou Satellite Multipath Characteristics Research-From the “Micro” Parameters Point of View 387
Xin Chen, Xiaoran Fang, Yuze Wang, Yanhong Kou, Le Cai, Peilin Liu and Wenxian Yu

37 Analysis and Evaluation Method of Multiple-Access Interference in Navigation Satellite Communication System 403
Chenglong He and Baoguo Yu

38 Research Progress on TWSTFT Mobile Calibration Station 415
Guoyong Wang, Ya Liu, Xiaohui Li and Chen Shi

39 Analysis of BeiDou Signals on the Accuracy of Common-View Time Transfer 425
 MeiJun Guo, Hua Lu, Yun Xiao, YiJun Mo and XiaoGang Liu

40 Assessment of BDS Signal-in-Space Accuracy and Standard Positioning Performance During 2013 and 2014 437
 Gucang Chen, Zhigang Hu, Guangxing Wang, Guo Chen, Zhaoying Liu and Qile Zhao

41 Design and Implementation of Distributed Simulation Testbed for GNSS Experimentation 455
 Long Yang, Yufei Yang and Jinping Chen

42 High Precision and Difference Measurement of Inter-element Amplitude and Phase Bias Errors Based on Channel Multiplexing 467
 Ke Zhang, Huaming Chen, Xiangwei Zhu and Guangfu Sun

43 A High-Precision and Flexible Array Antenna Signal Simulator Based on VFD Filter 479
 Hai Sha, Han Mu and Hui Zhang

44 New Generation Signal Structure Evaluation System for GNSS 491
 Jianlei Yang, Tian Jin, Zhigang Huang and Honglei Qin

45 Research of Satellite Receiver Anti-replay Attack Techniques 503
 Mengjiang Liu, Zhixin Deng and Li Jun

46 Detect Techniques and Test Analysis on Navigation Signal Code Correlation Peak 517
 Xiaochao Feng, Yongheng Fu, Lei Gong and Jiancheng Liu

47 Research on Time Synchronization Method of Ground-Based Navigation System 529
 Xiye Guo, Yongbin Zhou and Jun Yang

48 BDS/GPS Stochastic Model Refinement and Assessment Using Satellite Elevation Angle and SNR 537
 Yan Li, Huang Dingfa, Li Meng and Zhu Dongwei

Part III BDS/GNSS User Terminal Technology

49 A GLONASS Navigation Data Verification Algorithm Under High Bit-error Rates 553
 Jian Hu, Aishui Rao, Long Zhang and Yimei Sun

50 The Design and Implementation of an Acquisition Scheme for Weak GNSS Signal 563
 Linfeng Zhang, Hairong Guo, Chong Zheng and Haibo He

51 Adaptive Notch Filter Design Based on Krylov Subspace 575
 Zhaoliang Duan, Guangwei Fan and Yi Luo

52 A Novel High Dynamic Carrier Tracking Algorithm Based on the Gaussian Particle Filter 587
 Qize Chen, Gengmin Li and Ao Peng

53 Research on the Mast Antenna System for Communications Compounds Satellite Navigation 599
 Haiguang Zhang, Ximing Liang and Jia Zhang

54 Research on the Satellite Navigation Independent Compound Receiving and Transmitting Array Concept 611
 Ximing Liang, Haiguang Zhang and Jia Zhang

55 A Framework of Mathematic Model and Performance Evaluation for Conjunct GNSS Spoofing Detection. 635
 Dingbo Yuan, Hong Li and Mingquan Lu

56 A Near-Far Effect Mitigation Method of Pseudolites Based on Array Signal 647
 Libin Shen, Lixin Li, Huisheng Zhang and Tao Bao

57 A Fast Positioning Method for Hot Start in GNSS Receiver 657
 Xiaohui Ba, Shidong Luo, Haiyang Liu, Qing Yuan, Yun Wang and Jie Chen

58 A New Iterative Method for Multipath Mitigation 667
 Yan Gao, Wei Li, Jinli Li, Hongliang Qu and Xiang Shi

59 An Improved Practical Anti-jamming Technique for GNSS Receivers Based ADP in Frequency Domain. 677
 Tianqiao Zhang, Yao Wang, Yang Gao and Hongbing Wang

60 A Robust Dynamic Satellite-Searching Algorithm for Multi-constellation GNSS Receivers 695
 Hengwei Zhou, Zheng Yao and Mingquan Lu

61 A High-Dynamic Null-Widen GNSS Anti-jamming Algorithm Based on Reduced-Dimension Space-Time Adaptive Processing 707
 Lu Ge, Dan Lu, Wenyi Wang, Lu Wang, Qiongqiong Jia and Renbiao Wu

62 Interference Suppression with L1-Norm Constraint for Satellite Navigation Systems. 717
 Wenyi Wang, Qingrong Du, Renbiao Wu, Dan Lu, Lu Wang and Qiongqiong Jia

63 A Spoofing Mitigation Algorithm Based on Subspace Projection for GNSS Receiver 727
 Lei Chen, Shuai Han, Weixiao Meng and Zijun Gong

64 A Quick A-BDS Location Method Based on Characteristics of GEO Satellite and Ridge Estimate 739
 Shourang Jing, Wenxiang Liu, Ling Yong and Guangfu Sun

65 Feasibility Analysis of GNSS Multi-constellation Positioning for Lunar Spacecraft 749
 Lei Chen, Yangbo Huang, Wenxiang Liu and Gang Ou

66 Spoofing Interference Suppression for GNSS Based on Estimating Steering Vectors 765
 Yaotian Zhang, Lu Wang, Wenyi Wang, Dan Lu, Qiongqiong Jia and Renbiao Wu

67 Satellite Navigation Anti-jamming Algorithm Based on Extended Array 773
 Fusheng Li, Wenyi Wang, Dan Lu, Lu Wang, Qiongqiong Jia and Renbiao Wu

68 Performance Assessment of Signal Quality Monitoring Based GNSS Spoofing Detection Techniques 783
 Yichen Yang, Hong Li and Mingquan Lu

69 Robust SFAP Anti-jamming Algorithm Based on Generalized Sidelobe Cancellation. 795
 Long Liu, Zhaolin Zhang and Ling Wang

70 Research on the BDS Inter-Satellite-Type Carrier Phase Bias Introduced by Different NH Code Sign Conventions 805
Zuohu Li, Hailing Wu, Liduan Wang and Hui Liu

71 A Position Calibration Algorithm of Antenna Arrays 817
Jiachi Wang and Zhongjun Chen

72 Performance Analysis of a Dual-Frequency Software-Defined BeiDou Receiver with B1 and B2 Signals 827
M. Zahidul H. Bhuiyan, Stefan Söderholm, Sarang Thombre, Laura Ruotsalainen and Heidi Kuusniemi

Part I
BDS/GNSS Navigation Applications

Chapter 1

Accuracy Assessment of the Doppler Frequency and Pseudorange Model Based on GPS/LEO Radio Occultation

Xian-Sheng Xu, Yan Liu, Ye Li and Xu Xu

Abstract The Doppler frequency and pseudorange model are important information for open-loop tracking of GPS/LEO signal. The Doppler frequency model can be predicted through iteration, with the use of a bending angle/refractivity climatology and satellite orbits. The pseudorange model can be obtained by multi-epoch or single-epoch algorithm. About 7279 COSMIC radio occultation soundings, from DOY (day of year) 71 to DOY 73 in 2007, recorded in open-loop mode are processed by above-mentioned algorithms, the calculated Doppler frequency and pseudorange model are compared with corresponding COSMIC observations. The statistical comparisons of the difference between COSMIC Doppler frequency observation and Doppler frequency model show: above 2 km impact height, the mean Doppler frequency shift caused by the Earth's neutral atmospheric condition is less than 3 Hz, the corresponding standard deviation is less than 6 Hz. The mean and standard deviation of the difference between COSMIC phase observation and pseudorange model calculated by multi-epoch algorithm are less than 15 m and 23 m, respectively, above 2 km. Similar results can be found in the single-epoch algorithm. The accuracy of the pseudorange model calculated by single-epoch algorithm is better than that of multi-epoch algorithm. Therefore, the atmospheric Doppler and pseudorange model predicted by the single-epoch algorithm can be used to track the GPS radio occultation signals recorded in the open-loop mode.

X.-S. Xu

Ningbo Institute of Technology, Zhejiang University, Ningbo 31500, China
e-mail: xxsnit@126.com; xuxiansheng666@126.com

Y. Liu (✉)

Numerical Weather Prediction Center, China Meteorology Administration,
Beijing 100081, China
e-mail: liuyan@cma.gov.cn

Y. Li

Space Star Technology Co., Ltd, Beijing 100086, China

X. Xu

Oujiang College, Wenzhou University, Wenzhou 325035, China

© Springer-Verlag Berlin Heidelberg 2015

J. Sun et al. (eds.), *China Satellite Navigation Conference (CSNC) 2015*

Proceedings: Volume I, Lecture Notes in Electrical Engineering 340,

DOI 10.1007/978-3-662-46638-4_1

Keywords GPS/LEO occultation · Open-loop · Closed-loop · The doppler frequency · Pseudorange

1.1 Introduction

Using GPS/LEO radio occultation technique to obtain Earth's atmospheric parameter is an accurate detection method. Open-loop (OL) tracking technology used in GPS receivers overcomes shortcomings of closed-loop technology. Different with closed-loop technology, it uses a fixed phase model for down conversion [1].

Doppler and pseudorange model not only affect signal amplitude decay (20 Hz Doppler error or 100 m pseudo-range error will result in about 20 % of amplitude decline), but also are two important parameters for GPS/LEO occultation open-loop tracking. Sokolovskiy's analysis and simulation indicate that Doppler model's accuracy in neutral atmosphere is about 10–15 Hz (based on receiver's real-time ephemeris data), error in ionosphere is 1–2 Hz, and satellite clock error of GPS and LEO is 0–2 Hz respectively, relativistic effect will also bring an error of less than 1 Hz [2]. So predicting Doppler model accuracy will be able to meet requirements of open-loop tracking technology. For GPS pseudorange, mainly geometric distance and satellite clock error of GPS and LEO, and delay caused in neutral atmosphere and ionosphere are involved. Current real-time satellites orbit and clock of GPS and LEO can be calculated down to within 10 m, pseudorange caused by ionosphere is between tens of meters to a few hundreds of meters, and atmospheric occultation delay in low troposphere can be over 1 km [3].

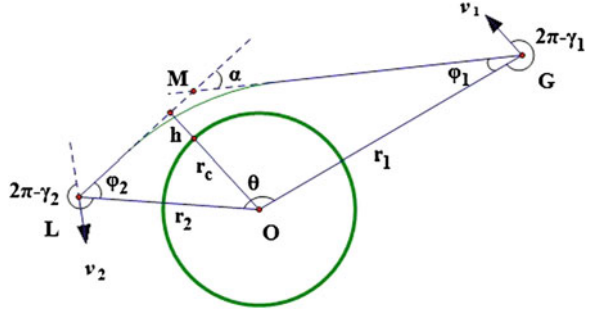
This paper uses satellite orbits and speed data after COSMIC processing and refractive index model to calculate Doppler model, and then obtain neutral atmosphere pseudorange model through integration. Comparison of calculated Doppler model and COSMIC Doppler observation, as well as pseudorange model and COSMIC phase observation help assess accuracy of neutral atmosphere Doppler and pseudorange model.

1.2 Doppler and Pseudorange Algorithm

1.2.1 Doppler Model

With the help of geometrical optics, satellite ephemeris data and bending angle/refractive index model, atmospheric Doppler model can be obtained. As shown in Fig. 1.1, G and L represent GPS and LEO satellite respectively, O is the center of curvature, M is the intersection of LM and GM. Ray zenith angle φ_1 and φ_2 at GPS and LEO can use the following equation set and obtained iteratively [4]:

Fig. 1.1 Diagram of the GPS-LEO radio occultation



$$r_1 \sin \varphi_1 = r_c(\beta) + h \quad (1.1a)$$

$$r_2 \sin \varphi_2 = r_c(\beta) + h \quad (1.1b)$$

$$\varphi_1 + \varphi_2 + \theta - \alpha(h, \beta) - \pi = 0 \quad (1.1c)$$

where r_1 and r_2 are distances between GPS and LEO to the center of curvature **O** respectively, while impact parameter $a = r_c(\beta) + h$. h is impact height, θ is the angle between vector r_1 and r_2 . β is the latitude of occultation, which can be calculated based on satellite coordinate data. r_c is radius of occultation's corresponding reference ellipsoid. In Eqs. (1.1a), (1.1b) and (1.1c), h , φ_1 and φ_2 are unknown.

Initial value of impact height can be obtained under the assumption of straight-line propagation between satellites. After adjusting impact height, bending angle's corresponding center angle θ can be calculated via Eqs. (1.1a), (1.1b) and (1.1c), and center angle θ' via ephemeris data. When their difference $|\theta' - \theta|$ is small enough, stop iterative output of φ_1 and φ_2 . When impact height reaches boundary value (minimum value is h_{\min}), then $h = h_{\min}$.

In Eqs. (1.1a), (1.1b) and (1.1c), bending angle model value $\alpha(h, \beta)$ is from CIRA + Q model that includes temperature and pressure, as well as information of water vapor partial pressure under 15 km [5].

After ray zenith angle φ_1 and φ_2 and satellite speed are known, it is possible to calculate atmospheric Doppler forecast model via the following equation:

$$f_{\text{mod}} = f_{L1} \cdot \left[\frac{c - \mathbf{s}_2 \mathbf{v}'_2}{c - \mathbf{s}_1 \mathbf{v}'_1} - \frac{c - \mathbf{s}_0 \mathbf{v}'_2}{c - \mathbf{s}_0 \mathbf{v}'_1} \right] \quad (1.2)$$

where $f_{L1} = 1575.42$ MHz represents the frequency of GPS at L1 frequency band, $c = 2.997 \times 10^8$ km/s is the speed of light in a vacuum. \mathbf{s}_0 is the unit vector for GPS and LEO from G to L; $\mathbf{s}_{1,2}$ stands for direction vector of GPS and LEO, \mathbf{s}_1 's direction is from G to M, and \mathbf{s}_2 is from M to L. $\mathbf{v}'_{1,2}$ is the projection of GPS and LEO speed on occultation plane.

1.2.2 Pseudorange Model

After atmospheric Doppler model is available, neutral atmospheric delay can be calculated via the following equation [6]:

$$L_{\text{mod}} = 2\pi \int f_{\text{mod}} dt \quad (1.3)$$

Based on this equation and observation data of multiple epochs, pseudorange model of neutral atmosphere can be obtained through integrating Doppler model, and this is called multi-epoch pseudorange algorithm.

Neutral atmosphere's pseudorange model can also be obtained directly through the refractive index model:

$$L_{\text{mod}} = \int n(r) dl \quad (1.4)$$

where dl is the ray arc length differential, and refractive index n is obtained via from CIRA+Q model.

In the spherically symmetric assumption, Eq. (1.4) can be converted to:

$$L_{\text{mod}} = \int_a^{x_{\text{LEO}}} \frac{\left(1 - \frac{xdn}{ndx}\right)x}{\sqrt{x^2 - a^2}} dx + \int_a^{x_{\text{GPS}}} \frac{\left(1 - \frac{xdn}{ndx}\right)x}{\sqrt{x^2 - a^2}} dx \quad (1.5)$$

where x_{GPS} and x_{LEO} are distances of GPS and LEO to the center of earth respectively; a is the impact parameter at occultation point, which can be obtained in advance via iteration of Eqs. (1.1a), (1.1b) and (1.1c). In Eq. (1.5), pseudorange model can be calculated after x_{GPS} , x_{LEO} and a are given. So corresponding pseudorange model can be calculated directly based on single epoch data, and this is referred to as single-epoch pseudorange algorithm.

1.3 Data Analysis and Statistical Comparison

In order to assess the accuracy of atmospheric Doppler prediction and pseudorange model, compare neutral atmosphere Doppler and pseudorange model with COSMIC atmospheric Doppler and atmospheric phase delay observation respectively. Since ionosphere's influence is very limited during occultation observation in neutral atmosphere, its impact on atmospheric Doppler is generally considered to be less than 1 Hz, while satellite clock error can be eliminated with differential technique. So it is reasonable to validate neutral atmosphere Doppler forecast and pseudorange model with measured data of occultation.

1.3.1 Doppler Observation

COSMIC data uses single-difference technique to correct satellite clock error, and then get atmospheric phase delay [7, 8]. After smoothing and filtering of atmospheric phase delay, Doppler observation is obtained via temporal difference:

$$f_{\text{obs}} = \frac{f_{L1}}{c} \frac{d\phi}{dt} \quad (1.6)$$

where, ϕ is the smooth value of COSMIC phase ϕ_{obs} , and t is time variable.

1.3.2 Case Study

On the basis of GPS and LEO ephemeris in atmPhs file of COSMIC, Doppler and pseudorange model can be calculated using multi-epoch algorithm and single-epoch algorithm, and compared with COSMIC Doppler observation and phase observation. Figure 1.2 shows Doppler calculations, in which horizontal axis and vertical axis represent occultation time and Doppler respectively. The red solid line and black dashed line in Fig. 1.2(a) stand for Doppler observation and model respectively. It should be noted that multi-epoch and single-epoch algorithm produced consistent Doppler results. Figure 1.2(b) shows the difference between Doppler observation and model: $f_{\text{obs}} - f_{\text{mod}}$, which is no more than 4 Hz.

Figure 1.3 shows corresponding pseudorange comparison, in which horizontal axis represents occultation time, vertical axis stands for pseudorange. In Fig. 1.3a, the red solid line is COSMIC phase observation, black dashed line is multi-epoch pseudorange model, and blue dotted line is single-epoch pseudorange model. It can be seen from Fig. 1.3(a) that COSMIC phase observation is consistent with

Fig. 1.2 Comparison of COSMIC Doppler observation and the Doppler model

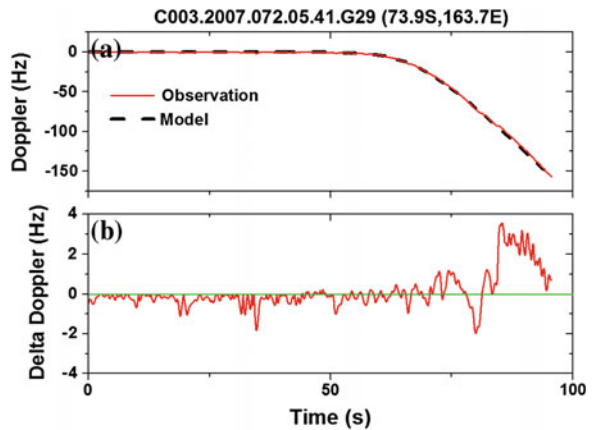
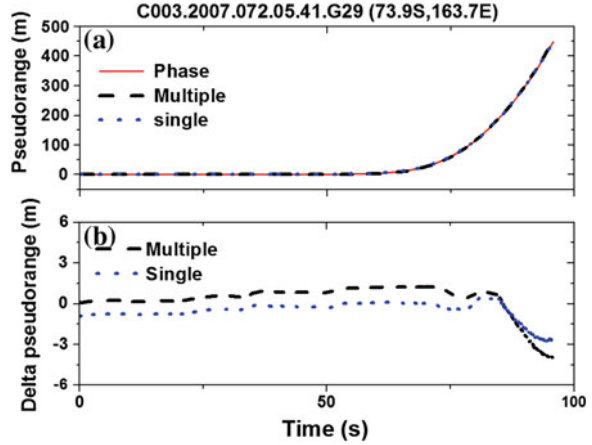


Fig. 1.3 Comparison of COSMIC phase observation and pseudorange models



multi-epoch and single epoch pseudorange model. Figure 1.3b is the difference between COSMIC phase observation and pseudorange model: $\phi_{\text{obs}} - L_{\text{mod}}$, which is no more than 5 m.

Figures 1.4 and 1.5 are large error cases of Doppler and pseudorange. It is obvious in Fig. 1.4a that Doppler observation increased dramatically after 72 s. The difference between Doppler observation and model at occultation time of 76 s, as shown in Fig. 1.4b, reached the peak of 141 Hz.

Figure 1.5 shows the corresponding pseudorange results. Both Figs. 1.5a, b indicate great difference between COSMIC phase observation and pseudorange model. The maximum difference is about -380 m at occultation time of 103 s. Doppler or pseudorange error will affect bending angle, refractive index and other inversion products through inversion process.

Fig. 1.4 Comparison of COSMIC Doppler observation and the Doppler model

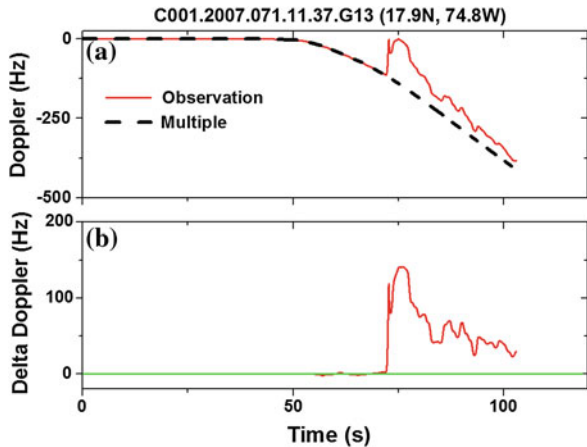
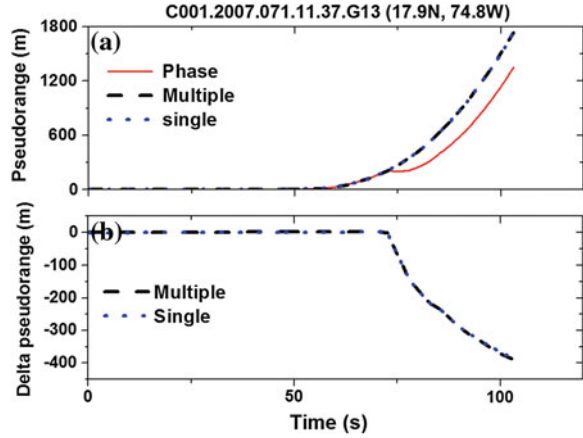


Fig. 1.5 Comparison of COSMIC phase observation and pseudorange models



1.3.3 Statistical Comparison

After processing 7279 COSMIC atmPhs data from DOY 71 to DOY 73 in 2007 with multi-epoch and single-epoch algorithms, 5764 inversion data was successfully obtained. These data were, according to impact height, linear interpolated to equally spaced points. This paper has interpolated Doppler and pseudorange to impact height of 0–30 km, with distance internal of 0.2 km. Main Doppler and Pseudorange statistical comparisons include: (1) Doppler observation and model; (2) COSMIC phase observation and multi-epoch pseudorange model; (3) COSMIC phase observation and single-epoch pseudorange model; (4) multi-epoch pseudorange model and single-epoch pseudorange model.

Figure 1.6 shows Doppler error statistics, where vertical axis represents impact height. In Fig. 1.6a–c, horizontal axis represents the mean difference and standard

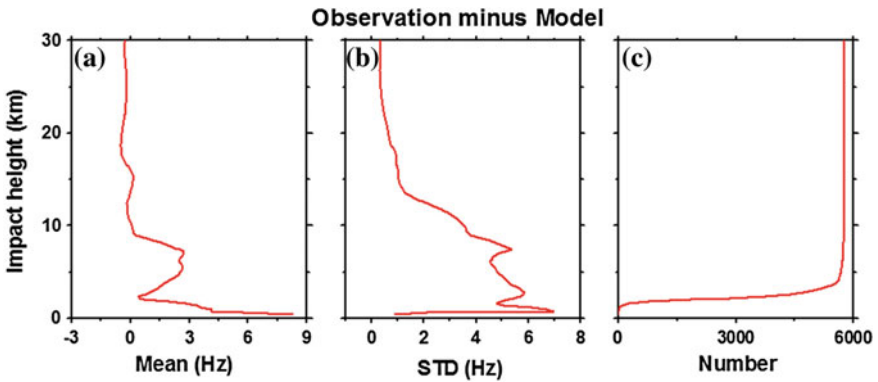


Fig. 1.6 Statistical comparison of the difference between COSMIC Doppler observation and the Doppler model

deviation of Doppler observation and Doppler model, and the number of occultation respectively.

As shown in Fig. 1.6a, if impact height is above 10 km, Doppler mean does not exceed 0.5 Hz; if below 10 km, Doppler mean gradually increases to 8 Hz, and the possible reasons include: more water vapor in lower troposphere which increases signal tracking error, or iterative solution obtained via Eqs. (1.1a), (1.1b) and (1.1c) reached boundary value; Fig. 1.6a shows negative deviation above 10 km, positive deviation below 10 km, and an overall positive deviation trend. So Doppler positive deviation below 10 km may be the main reason that caused refractive index negative deviation in lower troposphere. We can see from Fig. 1.6b that standard deviation of Doppler difference is less than 4 Hz above 10 km, but gradually increase to about 7 Hz when below 10 km. Figure 1.7 shows pseudorange error statistics. Figure 1.7a–c is the difference between COSMIC phase observation and multi-epoch pseudorange, while Fig. 1.7d–f is the difference between COSMIC phase observation and single-epoch pseudorange. Figure 1.7g–i displays the difference between multi-epoch and single-epoch pseudorange. Column 1–3 stands for mean difference, standard deviation and the number of occultation respectively. As seen from Fig. 1.7a, the difference between COSMIC phase observation and multi-epoch pseudorange has a positive deviation of about 2–3 m when above 8 km; when at 2–8 km, there is a negative deviation of -15 m; when below 2 km, the maximum negative deviation reaches -75 m. Figure 1.7b shows standard deviation

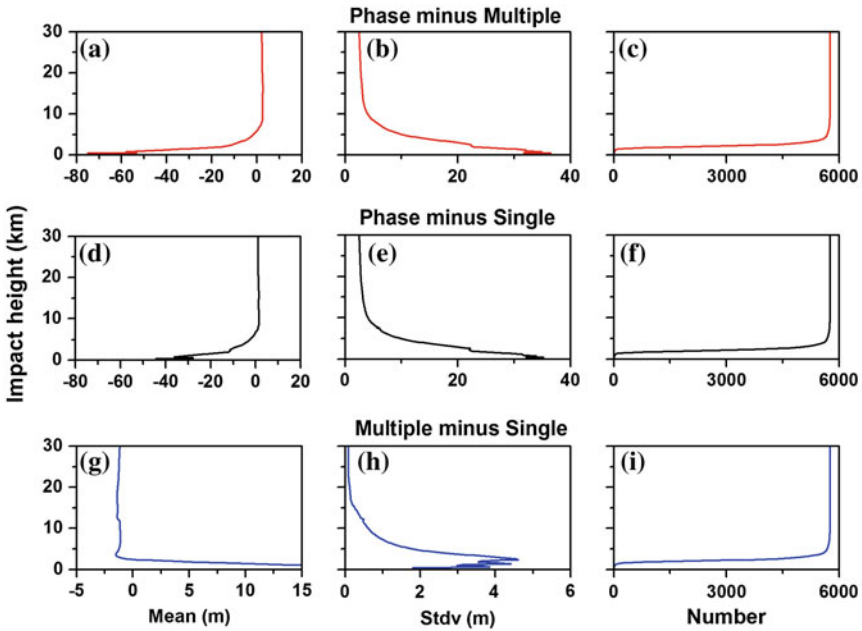


Fig. 1.7 Statistical comparison of the difference between COSMIC phase observation and the pseudorange model

of the difference between phase observation and multi-epoch pseudorange. Figure 1.7b indicates that when above 4 km, standard deviation is less than 15 m, which gradually increases to 36 m from 4 km to the ground. The second line displays the statistical results of difference between COSMIC phase observation and single-epoch pseudorange, which is better than those of multi-epoch algorithm.

1.4 Summaries and Discussion

This paper calculates neutral atmospheric pseudorange model using multi-epoch and single-epoch algorithms. Traditional multi-epoch pseudorange algorithm calculates all Doppler models of an occultation event at each epoch, and then obtains neutral atmospheric pseudorange model through integrating Doppler. While the newly developed single-epoch pseudorange algorithm first gets impact parameters via satellite position and velocity data, and then calculates neutral atmospheric pseudorange model directly through integration, which consequently is more conducive to open-loop satellite signal tracking.

After calculating statistical difference between COSMIC Doppler observation and Doppler model, as well as COSMIC phase observation and pseudorange model, it has been found that mean difference between Doppler observation and Doppler model is less than 0.5 Hz when above 10 km, and their standard deviation is no more than 4 Hz. When above 2 km, their mean difference is no more than 3 Hz and standard deviation is below 6 Hz.

Difference between COSMIC phase observation and multi-epoch pseudorange has a positive deviation of about 2–3 m when above 8 km, and it has shown a growing trend from 8 km. When at 2 km, the deviation is -15 m, which increases to the maximum of -75 m when close to the ground. Standard deviation can be up to 36 m. Negative deviation of pseudorange corresponds with Doppler positive deviation. Results from single-epoch pseudorange algorithm are generally better than multi-epoch ones: system positive deviation is about 1 m when above 8 km, about -12 m at 2 km, and the maximum deviation is about -40 m on the ground, while the standard deviation obtained is less than 35 m. Comparison between multi-epoch and single-epoch pseudorange results shows that their deviation difference is less than 2 m when above 2 km, which increases to 15 m from 2 km to the ground.

Overall, Doppler and pseudorange models based on multi-epoch and single-epoch algorithm have high accuracy. The accuracy of the newly developed single-epoch algorithm is better than that of multi-epoch algorithm, especially when below 2 km, and therefore is able to meet the need of GPS/LEO occultation signal open-loop tracking.

Acknowledgments The authors are grateful to University Corporation for Atmospheric Research (UCAR) for access to COSMIC RO data and ECMWF analysis data. This research is supported by the National Natural Science Foundation of China (11273047, 41305016), the Natural Science Foundation of Zhejiang province (LQ13D050002) and the Natural Science Foundation of Ningbo (2014A610156).

References

1. Sokolovskiy S (2001) Modeling and inverting radio occultation signals in the moist troposphere. *Radio Sci* 36(3):441–458
2. Sokolovskiy S, Rocken C, Schreiner W et al (2010) On the uncertainty of radio occultation inversions in the lower troposphere. *J Geophys Res* 115(D22111). doi: [10.1029/2010JD014058](https://doi.org/10.1029/2010JD014058)
3. Lohmann MS (2007) Analysis of global positioning system (GPS) radio occultation measurement errors based on Satellite de Aplicaciones Cientificas-C (SAC-C) GPS radio occultation data recorded in open-loop and phase-locked-loop mode. *J Geophys Res* 112: D9115. doi:[10.1029/2006JD007764](https://doi.org/10.1029/2006JD007764)
4. Sokolovskiy S (2001) Tracking tropospheric radio occultation signals from low Earth orbit. *Radio Sci* 36(3):483–498
5. Kuo YH, Wee TK, Sokolovskiy S et al (2004) Inversion and error estimation of GPS radio occultation data. *J Meteorol Soc Jpn* 82(1B):507–531
6. Sokolovskiy S, Rocken C, Schreiner WS et al (2009) Postprocessing of L1 GPS radio occultation signals recorded in open-loop mode. *Radio Sci* 44:S2002. doi:[10.1029/2008RS003907](https://doi.org/10.1029/2008RS003907)
7. Schreiner WS, Rocken C, Sokolovskiy S et al (2010) Quality assessment of COSMIC/FORMOSAT-3 GPS radio occultation data derived from single- and double-difference atmospheric excess phase processing. *GPS Solutions* 14:13–22
8. Schreiner WS, Sokolovskiy S, Hunt D et al (2011) Analysis of GPS radio occultation data from the FORMOSAT-3/COSMIC and Metop/GRAS missions at CDAAC. *Atmos Meas Tech* 4:2255–2272. doi:[10.5194/amt-4-2255-2011](https://doi.org/10.5194/amt-4-2255-2011)

Chapter 2

Application of BeiDou Navigation Satellite System on Attitude Determination for Chinese Space Station

Sihao Zhao, Cai Huang, Xin Qi and Mingquan Lu

Abstract BeiDou Navigation Satellite System (BDS) offers service to space-based users. The future Chinese Manned Space Station (CSS) orbits inside the service area of the future global BDS, and can utilize BDS to perform its attitude determination. This contribution first analyzes the constellation situation of the global BDS during the operation phase of the CSS. The results show that the global BDS can provide positioning and attitude determination service to the CSS. Second, the principles of the carrier phase based attitude determination technique are presented and the characteristics of the CSS are discussed, based on which the technical conditions required for BDS-based attitude determination for the CSS are analyzed. An attitude determination scheme which requires three antennas to be installed on the three CSS' component cabins respectively is proposed. Next, simulations and analysis on the roll, pitch and yaw angle measurement errors when the CSS is orbiting are conducted. The results indicate the feasibility of applying BDS on the attitude determination for the CSS, and the root mean square errors of the measured attitude angles can reach about 0.05° for roll and pitch, and 0.04° for yaw respectively, provided the condition of two linearly independent 10 m level base-lines formed by three BDS receiving antennas.

Keywords BeiDou navigation satellite system · Chinese space station · Multi-baseline · Attitude determination · Application

S. Zhao (✉) · M. Lu
Department of Electronic Engineering, Tsinghua University, Beijing, China
e-mail: zsh_thu@tsinghua.edu.cn

C. Huang · X. Qi
Institute of Manned Space System Engineering, China Academy of Space Technology, Beijing, China

2.1 Introduction

BeiDou Navigation Satellite System (BDS) is a Global Navigation Satellite System (GNSS) developed and implemented by China which has achieved its regional service ability covering China and its surrounding areas since the end of 2012 [1] and would form a global constellation comprised of geosynchronous orbit (GEO) and non-geosynchronous orbit satellites by 2020 [2, 3]. The Chinese Space Station (CSS) program has entered its implementation phase, and around 2020, it is planned to complete a large scale manned space station comprised of multiple cabins which will conduct long term on-orbit operation with crew members on it [4]. The operation period of CSS concurs the global service time of BDS. Therefore, it is of theoretical and practical significance to explore the applications of BDS on such influential engineering projects as manned space programs.

GNSSs have been widely adopted by manned spacecraft. For example, the space shuttle determined its position with the Global Positioning System (GPS) operated by USA [5, 6], GPS is adopted as one of the relative measurement methods for spacecraft rendezvous and docking missions [7], and the Chinese manned spacecraft also equips with GNSS devices [8, 9]. It is worth mentioning that the International Space Station (ISS) not only uses GPS for positioning, but also utilizes 4 GPS receiving antennas which form a $1.5 \text{ m} \times 3 \text{ m}$ rectangle to determine its attitude along with gyro data and the post processing precision reaches 0.5° ($3\text{-}\sigma$ root mean square) [10].

BDS has already achieved a regional service ability, however, is still not able to provide a full-orbit coverage for manned spacecraft due to its limited service area. The forthcoming global BDS constellation will be a good complement or/and substitute for GPS and other GNSSs and will offer uninterrupted service to manned space vehicles such as CSS [11]. At present, inertial measurement units, sun sensors, star sensors and etc. are widely adopted for attitude determination by spacecraft while GNSS devices are mainly used to measure the absolute and relative position/velocity of the vehicle as well as support the ground based orbit determination tasks. The CSS requires extremely high safety and reliability during on-orbit operation. With multiple BDS antennas and receivers installed on it, the existing attitude determination methods can be supplemented and augmented. At the same time, BDS can be used for deformation surveillance of the rigid multi-cabin assembly of CSS so as to increase the safety of on-orbit operation.

It is proposed that the CSS will further utilize the service of the BDS to support orbit determination and rendezvous and docking missions [12], which implies that each cabin may be equipped with its own BDS receiver, and consequently, makes it possible to utilize BDS to determine the attitude of the multi-cabin CSS as a whole. It is notable that the CSS will become the largest Chinese earth orbiter ever and one of the largest space vehicles around the world, which enables a superior measurement precision over other spacecraft as a result of the possible longer baselines between antennas.

In this paper, the service ability of the global BDS during the period of the CSS on-orbit operation is firstly simulated and analyzed. Then, the carrier phase double-differencing attitude determination technique is presented based on which the technical conditions required for CSS attitude determination are discussed. An attitude determination scheme using three antennas installed on CSS cabins is proposed. Next, the roll, pitch and yaw angle errors of the CSS measured using the proposed scheme is analyzed based on simulation. The main conclusion and outlook for next-step work are proposed in the final part.

2.2 Analysis on Service Ability of Global BDS for CSS

BDS is comprised of the space constellation, the ground control segment and the user segment, and has achieved its regional coverage. The forthcoming global BDS constellation will consist of 5 GEOs, 3 inclined geosynchronous orbit satellites (IGSO), and 27 medium earth orbit satellites (MEO). The GEOs will locate at 58.75°E, 80°E, 110.5°E, 140°E and 160°E respectively. The 3 IGSOs which will orbit at an altitude of 36,000 km, are distributed evenly on three orbital planes with an identical inclination of 55° and a phase shift of 120°. They share the same 8-shaped ground track which intersects at 118°E. The 27 MEOs will be evenly distributed on 3 orbital planes with an altitude of 21,500 km [2]. The simulated global BDS constellation is shown in Fig. 2.1.

The assumed orbit of CSS is near-circular which has an inclination of 42°–43°, and an altitude of 340–450 km [4]. Table 2.1 lists the orbital elements of Tiangong 1 target vehicle observed from ground [13] which are assumed to be used by CSS, and the ground track of this orbit is shown in Fig. 2.2 [11]. The CSS flight attitude is assumed to be three-axis stable which means that the BDS antenna always points to the zenith as illustrated in Fig. 2.3. The half pitch angle of the antenna field of view is set to 80° which blocks off the BDS signals outside this angle.

A simulation scenario with a total length of 6 days and an epoch step of 1 min is established in Satellite ToolKit (STK) based on the above-mentioned configurations.

The number of visible BDS satellites and their time percentages from the simulation are listed in Table 2.2.

The results indicate that at least 4 BDS satellites can be viewed at any place of the manned space orbit which guarantees an absolute positioning service to CSS [11]. Furthermore, the number of visible satellites for CSS is actually no fewer than 6 which enables a carrier phase differencing technique for high precision relative measurement should more than one BDS receivers/antennas be installed. Therefore, the global BDS is able to provide a full-course coverage for CSS to meet the high precision measurement demand. More specifically, if no fewer than 3 BDS receivers and antennas are installed to form 2 or more linearly independent baselines, attitude determination for CSS can be achieved.

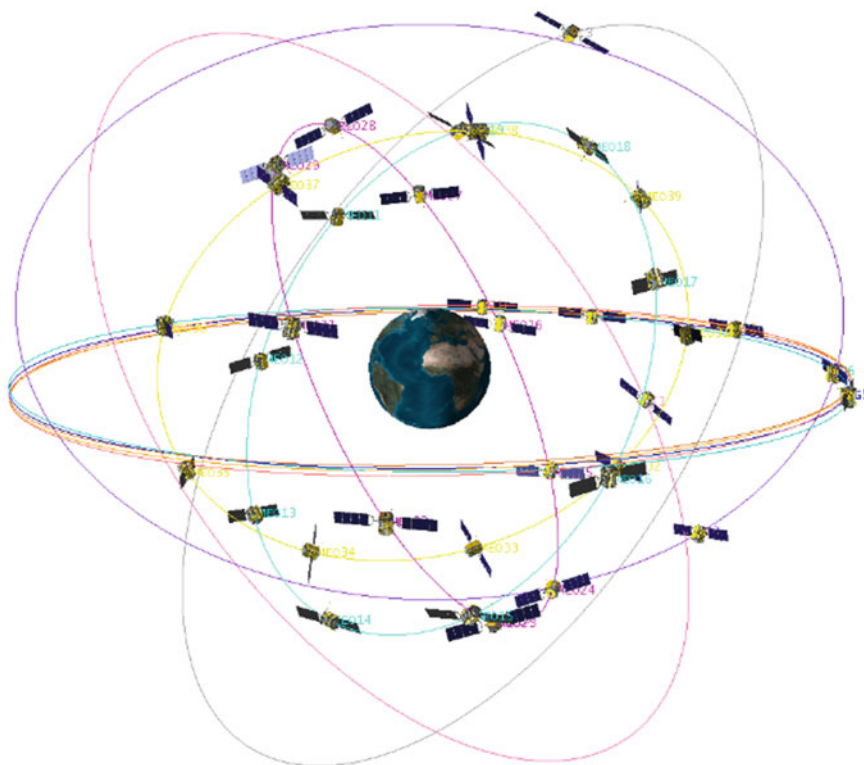


Fig. 2.1 Simulated global BDS constellation

Table 2.1 Orbital parameters of CSS for simulation

Orbital element	Value
Time (UTC)	2014/03/01 12:28:00
Semi-major axis (km)	6753.800
Eccentricity	0.000947
Inclination (°)	42.686
Right ascension of ascending node (°)	241.312
Argument of perigee (°)	20.204
True anomaly (°)	76.347

The validity of BDS for high precision relative positioning is proved by ground tests using carrier phase differencing techniques [14–16], and the root mean square (RMS) error lies within 1 cm under an approximate 10 m baseline condition [15, 17]. In the manned space orbital area, the atmosphere is extremely thin which greatly alleviates the tropospheric delay frequently experienced in a ground application and thus is beneficial to a higher precision. In addition, the fast

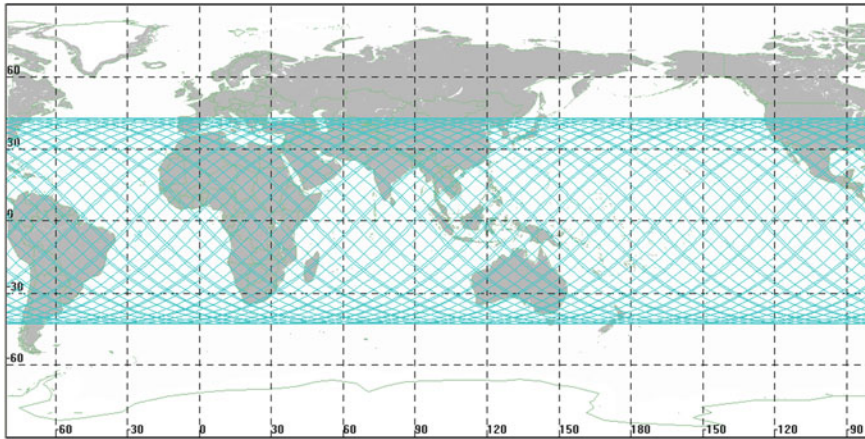


Fig. 2.2 Simulated ground track of CSS

Fig. 2.3 Flight attitude and antenna setup diagram [11]

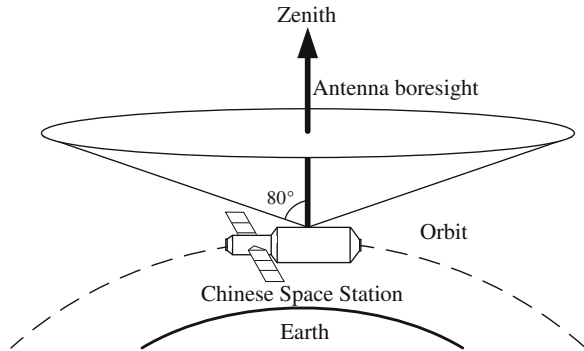


Table 2.2 Statistics of number of visible BDS satellites for CSS

Item	Value
Maximum number	19
Minimum number	6
Average number	10.3
≥9 time percentage (%)	65.1
≥8 time percentage (%)	78.3
≥7 time percentage (%)	90.5
≥6 time percentage (%)	100.0
≥5 time percentage (%)	100.0
≥4 time percentage (%)	100.0

maneuver of the spacecraft is helpful to shorten the convergence time of real-time high precision solutions. From the test and simulation results, we know that BDS has the ability to provide high precision measurement to the CSS.

2.3 Carrier Phase Based Attitude Determination

A vehicle's relative attitude information in a certain coordinate frame can be obtained by measuring the relative relationship between the known baseline vectors and the coordinate frame if there are more than one linearly independent baselines. For example, if \mathbf{C} is denoted as the rotation transformation matrix between the body coordinate frame (b frame) and the navigation coordinate frame (n frame), then \mathbf{C} can be written as the following equation.

$$\mathbf{C} = \begin{bmatrix} \cos p \cos y & \cos r \sin p \cos y - \cos r \sin y & \sin r \sin y + \cos r \sin p \cos y \\ \cos p \sin y & \cos r \cos y + \sin r \sin p \sin y & \cos r \sin p \sin y - \sin r \cos y \\ -\sin p & \sin r \cos p & \cos r \cos p \end{bmatrix} \quad (2.1)$$

where r , p , and y are the roll, pitch and yaw angles respectively.

If \mathbf{v}_{1b} and \mathbf{v}_{2b} are two known vectors in b frame, and their expressions can be defined as \mathbf{v}_{1n} and \mathbf{v}_{2n} in n frame, then

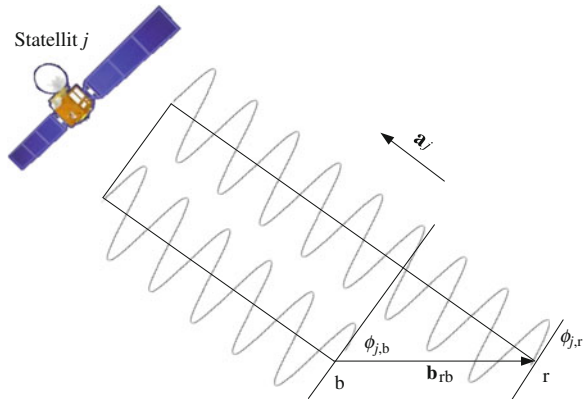
$$\begin{aligned} \mathbf{v}_{1n} &= \mathbf{C}\mathbf{v}_{1b} \\ \mathbf{v}_{2n} &= \mathbf{C}\mathbf{v}_{2b} \end{aligned} \quad (2.2)$$

The values of y , p and r are the solution of this non-linear equation set.

The expressions of the vectors in b frame can be obtained by measuring the vectors directly in b frame. The vectors need to be measured in n frame in order to solve the attitude angles in Eq. (2.2). We use BDS carrier phase based technique to measure the baseline vector in n frame. Figure 2.4 demonstrates the relationship between the carrier phase and the baseline vector.

The two end points of a baseline vector are denoted as b and r respectively, and then the measurement equation of navigation signal carrier phase are given as follows.

Fig. 2.4 Relationship between carrier phase and baseline vector



$$\phi_{j,r} = \lambda^{-1}(d_{j,r} - I_{j,r} + T_{j,r}) + f(\delta t_r - \delta t_{j,r}) + N_{j,r} + \eta_{j,r} \quad (2.3)$$

$$\phi_{j,b} = \lambda^{-1}(d_{j,b} - I_{j,b} + T_{j,b}) + f(\delta t_b - \delta t_{j,b}) + N_{j,b} + \eta_{j,b} \quad (2.4)$$

where ϕ represents the carrier phase (in carrier cycle), λ is the carrier wavelength (in m), d is the true geometrical range between the navigation satellite and the user (in m), T is the troposphere delay (in m), I is the ionosphere delay (in m), f is the carrier frequency (in Hz), δt_r and δt_j are the user and the satellite clock biases respectively (in m), N is the carrier cycle integer ambiguity, ε and η are measurement errors of pseudorange and carrier phase, and the subscript j is the visible satellite number.

The I and T terms can be eliminated via double differencing between r and b and then satellite i and j , provided a short range or baseline between r and b, and Eq. (2.5) is then formed.

$$\phi_{ji,rb} = \lambda^{-1}d_{ji,rb} + N_{ji,rb} + \eta_{ji,rb} \quad (2.5)$$

Equation (2.5) is the carrier phase double-differencing measurement model under the short baseline condition. The baseline vector of interest is buried in the double-differenced range $d_{ji,rb}$ which can be expanded about the estimate positions of b and r with the first order terms remained as shown in Eq. (2.6).

$$d_{ji,rb} = -\lambda^{-1}(\mathbf{a}_{j,r} - \mathbf{a}_{i,r})^T \mathbf{b}_{rb} \quad (2.6)$$

where, $\mathbf{a}_{r,j}$ is the normalized line-of-sight (LOS) vector pointing from the receiver at r to the j th satellite with the assumption that the counterpart LOS vector of b is identical with that of r, i.e. $\mathbf{a}_{r,j}$ equals $\mathbf{a}_{b,j}$, and \mathbf{b}_{rb} is the baseline vector from b to r.

A high precision baseline vector can be obtained if the integer ambiguity N in Eq. (2.5) is solved by some ambiguity resolution method such as LAMBDA [18]. If more than one such linearly independent baselines exist, they can be solved respectively with a high precision based on the carrier phase double-differencing technique. Afterward, the attitude information can be extracted from the two baselines via some calculation such as shown in Eqs. (2.1) and (2.2).

As commonly adopted in ground applications, a joint processing is required for the independent carrier phase measurement outputs from the receivers at r and b. As a consequence, a data communication link or/and a centralized processing device is needed to double-difference the data from r and b as well as solve the attitude angles.

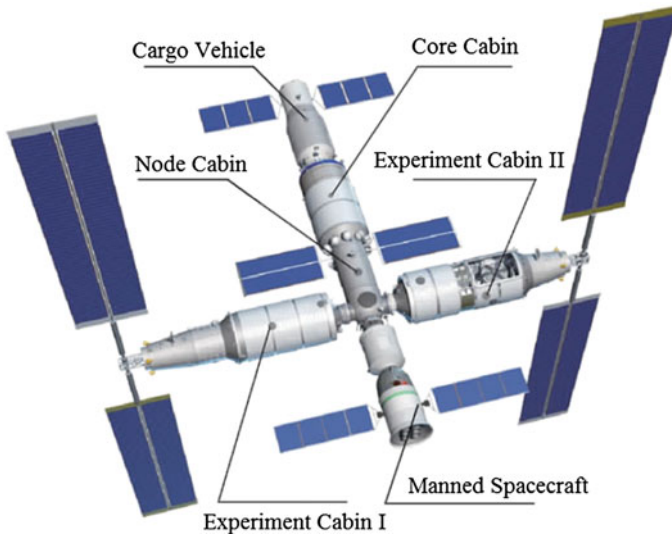


Fig. 2.5 Basic configuration of CSS [4]

2.4 Technical Conditions of BDS Based Attitude Determination for CSS

The CSS is a complex formed by the Core Cabin, the Experiment Cabin I and the Experiment Cabin II and this configuration is illustrated in Fig. 2.5 based on [4].

1. Linearly independent baseline vectors

The Core Cabin, Experiment Cabin I and Experiment Cabin II will form a rigid complex when operating on orbit. Two stable independent baselines as shown in Fig. 2.6 can be formed if there are one BDS receiver and antenna installed on each

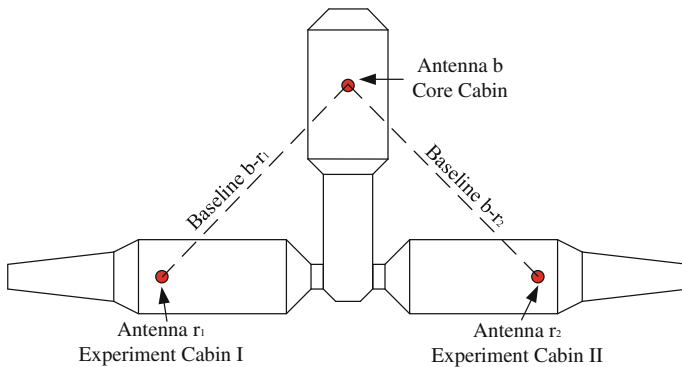


Fig. 2.6 Baselines between BDS antennas on Chinese space station

cabin respectively. We select the antenna b on the Core Cabin as the reference point for the attitude determination system along with which the antennas r_1 and r_2 on Experiment Cabin I and II can establish the two independent baselines.

2. High quality carrier phase measurements

The BDS antennas should be carefully designed so that interference such as multipath effects should be eliminated as far as possible. The receiver should properly handle the spacecraft dynamics and the weak signal reception to guarantee a high quality carrier phase measurement output.

3. Transfer and processing of the measurement data

Besides three sets of antennas and receivers for the three cabins, a module to receive and process the measurement data from the three receivers is required. Therefore a data transfer link and/or a centralized processing device might be needed.

The following 4 preliminary schemes can be considered:

- (1) The Experiment Cabin I and II receivers receive the measurement data from the Core Cabin receiver and solve the baselines $b-r_1$ and $b-r_2$, and then send the results to ground for attitude solution;
- (2) The receivers of the Experiment Cabins send their data to the Core Cabin receiver to solve the attitude angles in a real time manner;
- (3) A specialized device can be installed, for the purpose of receiving and processing the measurements from all the three receivers and real time completing attitude determination on-orbit;
- (4) The three receivers send their own data down to the ground respectively. A ground based device takes the responsibility of calculating the attitude information.

2.5 Error Analysis for BDS Based CSS Attitude Determination

In this section, the attitude measurement errors of the proposed scheme in the previous section are analyzed via simulations. Three antennas are setup based on Fig. 2.6, and their positions in CSS body coordinate frame are set in Table 2.3.

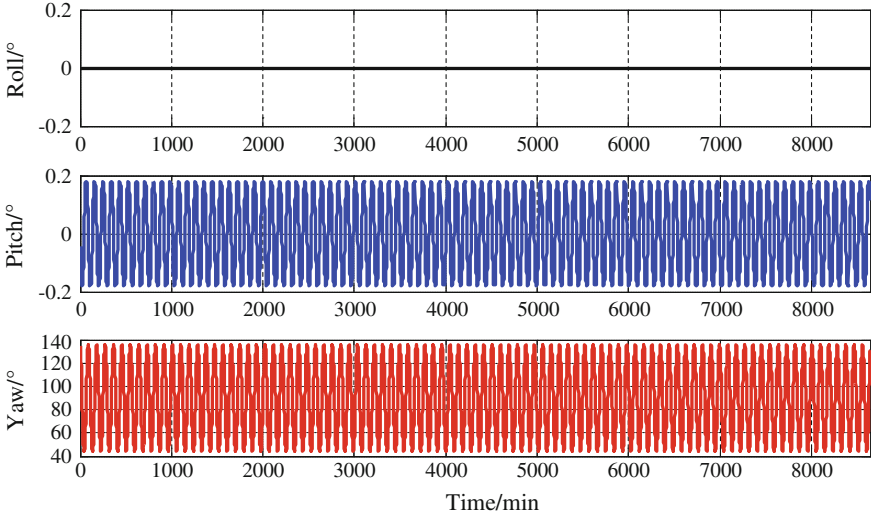
The orbital elements of CSS are identical with Table 2.1. The CSS keeps a three axis stable flight attitude as set in Sect. 2.2. The simulation length is 6 days with 1 min step, and the total number of epochs is 8640. The three dimensional 3D position in earth-centered-earth-fixed (ECEF) frame of b, r_1 and r_2 at every

Table 2.3 Simulated positions for the three antennas in b frame

Position	Antenna b	Antenna r_1	Antenna r_2
X/m	0	-8	8
Y/m	8	0	0
Z/m	0	0	0

Table 2.4 Simulated true position data for the three antennas at one epoch

3D position	Antenna b	Antenna r_1	Antenna r_2
X/m	6061736.78515	6061731.92252	6061737.99753
Y/m	-2884357.11388	-2884367.32930	-2884357.70602
Z/m	-806299.27452	-806299.28819	-806288.04155

**Fig. 2.7** Simulated true attitude angles

simulation epoch are obtained as the truth reference position. Table 2.4 lists the true positions of the antennas at one selected epoch.

We use STK to simulate the flight procedure of the CSS and obtained the true roll, pitch and yaw angles of all epochs in the simulation scenario as plotted in Fig. 2.7.

Random error with a standard deviation of 10 m is added on the true 3D position of the reference point antenna b in ECEF to simulate its positioning results using pseudorange measurements [1]. The standard deviation of the baseline measurement error of $b-r_1$ and $b-r_2$ is set to 1 cm.

The two baseline vector $b-r_1$ and $b-r_2$ are firstly transformed from ECEF frame to the north east down frame (NED) with b as the original point, and then Eqs. (2.1) and (2.2) are adopted to solve the attitude angles. The roll, pitch and yaw angle solutions are compared with the true attitude angles shown in Fig. 2.7 to generate the attitude errors. Figure 2.8 illustrates the attitude errors from one time simulation.

The attitude error in Fig. 2.8 indicates that the measured attitude angles using the proposed scheme are consistent with the true attitude. The RMS errors are 0.0498° , 0.0516° and 0.0357° for roll, pitch and yaw angles respectively. 100 time's Monte

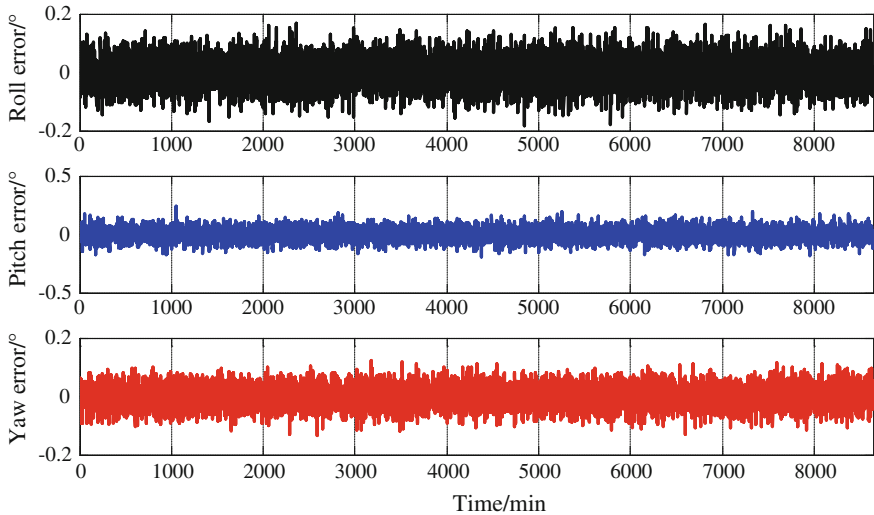


Fig. 2.8 Simulation results of attitude errors

Table 2.5 100 times Monte Carlo simulation results of attitude errors

	Roll	Pitch	Yaw
Average of RMS error/ $^{\circ}$	0.0506	0.0506	0.0359
Average of absolute error/ $^{\circ}$	0.0404	0.0404	0.0286

Carlo simulations are also conducted and the average RMS errors and absolute errors are listed in Table 2.5.

We should note that the above simulation only takes the measurement data of independent single epochs into account without employing any filtering methods to introduce any historical information. The error added to the measurements are also larger than that from the ground tests. As a consequence, the simulation results are more approximate to its lower performance boundary. In other words, an improved attitude determination precision can be expected in the practical operation of CSS, not to mention if other algorithms including filtering methods and constraints are adopted.

Additionally, the space environment of the CSS is expected to be better than the simulation conditions. For example, the manned space orbit is almost outside the atmosphere and the impact of air on the signal propagation is negligible. Apart from that, the BDS antenna for CSS can outperform those on the ground which may offer a higher quality of measurements. For those reasons, the on-orbit baseline measurement error tends to be less than 1 cm and a superior attitude determination performance over the simulated results can thus be expected.

2.6 Conclusion and Outlook

This work analyzes the BDS service ability during the on-orbit operation of CSS, discusses the technical conditions required for applying BDS on CSS attitude determination, and proposes a preliminary attitude determination scheme with a two 10 m linearly independent baselines formed by three BDS antennas distributed on the three cabins. It is feasible to employ BDS to support CSS attitude determination provided that multiple BDS antennas and receivers are installed on distinct cabins and data links and related measurement processing devices are equipped. The analysis and numerical simulation of the proposed scheme demonstrate RMS errors of about 0.05° for roll and pitch angles, and 0.04° for yaw angle which outperforms the existing GPS attitude determination system on ISS. In addition, the real on-orbit environment could be better than the simulation conditions and an improved performance can be expected.

BDS can be applied to offering full-course service to CSS attitude determination using the proposed scheme of multiple BDS devices on different cabins. It is an effective complement and augmentation for existing approaches which can also be used for deformation surveillance on the CSS and can provide better safety protection to the large space vehicle.

To establish a more solid foundation for the application of BDS on CSS attitude determination, the future work includes deeper investigation on constraints such as CSS operation environments, device configuration, and data link availability, further research on fast and reliable attitude determination algorithms with fixed baselines and more thorough analysis, simulation and verification on the performances.

Acknowledgments This work is funded by China Postdoctoral Science Foundation Grant (No. 2014M550732).

References

1. BeiDou Navigation Satellite System Open Service Performance Standard (2013) China Satellite Navigation Office
2. Report on the Development of BeiDou Navigation Satellite System (Version 2.2) (2013) China Satellite Navigation Office, China
3. BeiDou Navigation Satellite System Signal in Space Interface Control Document Open Service Signal (Version 2.0) (2013) China Satellite Navigation Office
4. Zhou J (2012) A review of Tiangong-1/Shenzhou-8 rendezvous and docking mission. *Manned Spaceflight* (1):1–8
5. Goodman JL (2011) Space shuttle guidance, navigation, and rendezvous knowledge capture reports. Revision 1. Lyndon B. Johnson Space Center, Houston, Texas
6. Goodman JL (ed) (2005) Application of GPS navigation to space flight. In: Aerospace conference
7. Chullen C, Blome E, Tetsuya S (2010) H-II transfer vehicle (HTV) and the operations concept for extravehicular activity (EVA) hardware Houston. NASA, Texas

8. Chen X, Gu C, Lv D (2005) The space-borne TT&C telecommunication subsystem of Shenzhou manned spaceship. *Aerosp Shanghai* 5:9–13
9. Zhang Q, Yu X, Zuo L, Li Z (2004) Shenzhou manned spacecraft TT&C and communication system development. *Spacecraft Eng* 13(1):97–103
10. Pendergrass JR, Treder AJ (eds) (2000) GPS-updated attitude determination on ISS despite rich multipath. In: *AIAA guidance, navigation and control conference*, Denver, CO
11. Zhao S, Yao Z, Zhuang X, Lu M (2014) Analysis on coverage ability of BeiDou navigation satellite system for manned spacecraft. *Acta Astronaut* 105(2):487–494
12. Wang Z (2013) Challenges and opportunities facing TT&C and communication systems for China's manned space station program. *J Spacecraft TT&C Technol* 32:281–285
13. <http://www.n2yo.com>. Accessed 2 March 2014
14. Zhao S, Cui X, Guan F, Lu M (2014) Kalman filter-based short baseline RTK algorithm for single-frequency combination of GPS and BDS. *Sensors* 14:15415–15433
15. Odolinski R, Teunissen PJG, Odijk D (2014) First combined COMPASS/BeiDou-2 and GPS positioning results in Australia. Part II: single- and multiple-frequency single-baseline RTK positioning. *J Spat Sci* 59(1):25–46
16. Shi C, Zhao Q, Hu Z, Liu J (2013) Precise relative positioning using real tracking data from COMPASS GEO and IGSO satellites. *GPS Solutions* 17:103–119
17. Wang S, Bei J, Li D, Zhu H (2014) Real-time kinematic positioning algorithm of GPS/BDS. *Geomat Inf Sci Wuhan Univ* 39(5):621–625
18. Teunissen PJG (1995) The least-square ambiguity decorrelation adjustment: a method for fast GPS ambiguity estimation. *J Geodesy* 70(1–2):55–82

Chapter 3

Feasibility Analysis of High-Precision Deformation Monitoring Using BeiDou Navigation Satellite System

Ruijie Xi, Yugang Xiao, Xingwei Liu and Kaihua Wang

Abstract Since the launch of the last GEO satellite on December 27, 2012, BeiDou regional navigation satellite system (BDS) has been announced to provide positioning, navigation, timing (PNT) and short message communication services in the whole Asia-Pacific region, which suggests a new GNSS system could be applied for deformation monitoring in the future. In order to investigate the performance of BDS in high-precision deformation monitoring, an experiment platform was designed where the actual displacements could be defined accurately as the reference and a corresponding BDS data processing software was developed. With the platform, data over 15 days were obtained and were processed every 4 h for evaluating the precision and reliability of deformation monitoring using BDS only. The results show that, for short baselines the repeatability of the horizontal and vertical directions are better than 1 and 2 mm, respectively. In addition, the comparison of deformations calculated from the BDS data and the reference displacements derived by the experiment platform confirms a good agreement, which indicates the potential of BDS for deformation monitoring applications.

Keywords BeiDou navigation satellite system · High-precision · Deformation monitoring · Feasibility

3.1 Introduction

Compared to the traditional deformation monitoring technology, GNSS positioning technology involves considerable advantages such as all-climate working, dispensing with intervisible measuring stations, high degree of automatic and directly access to the 3D coordinates of stations etc. It is reported that the precision of sub-millimeters could be achieved for short baselines in the post-processing mode and

R. Xi (✉) · Y. Xiao · X. Liu · K. Wang
School of Geodesy and Geomatics, Wuhan University, Wuhan, Hubei, China
e-mail: rjxi@whu.edu.cn

could fulfill the demands of most deformation monitoring applications (see [1, 2]). Furthermore, due to the continuously developing and improving of GNSS receivers and corresponding technology, GNSS has been widely utilized in the displacements monitoring for different applications, such as dams safety monitoring, reservoirs and landslide, tectonic movement etc. [2–5]. Whereas, GPS is found to be the dominating GNSS system in current deformation monitoring field.

BeiDou regional navigation satellite system (BDS) which is also called BeiDou-2 has been in full operation since December 27, 2012. It consists of 14 satellites, including 5 satellites in Geostationary Orbit (GEO), 5 satellites in Inclined Geosynchronous Orbit (IGSO), and 4 satellites in Medium Earth Orbit (MEO). Similarly, the BDS also provides precise positioning, navigation, and timing (PNT) services in the Asia-Pacific Region [6–9].

In order to assess the precision and reliability that BDS could achieve for the deformation monitoring, in this paper, a platform was designed where deformations could be simulated and the displacements could be obtained accurately, and a deformation monitoring software was also developed for processing BeiDou data. The results show that BDS could also fulfill the demands of most deformation monitoring applications.

3.2 Experiment Platform and BDS Data Processing

3.2.1 Experiment Platform

To investigate the precision and reliability of BDS in the application of high-precision deformation monitoring, a BDS tracking network with a base station named A001 and three monitor stations named B001, B002 and B003 is employed where the length of baselines range from 115 to 290 m. The stations distribution is shown in Fig. 3.1. At each station, a TRIMBLE NETR9 receiver and a CHOKE RING antenna (TRM59900.00) are installed similarly to the IGS stations. However, a special equipment is installed at station B003, which could be used to move the antenna in both horizontal and vertical directions and the actual displacements could be derived accurately. All stations have a good GNSS satellites tracking condition, no obvious shelters are found above the elevation angle 10° . Observation data during 15 days from August 3rd to 17th (DOY 215–229) are collected for the experiment validation and the sampling interval is 15 s. For comparison, both GPS and BDS data are employed in these experiments.

3.2.2 Data Processing Software

By considering that short baselines are always employed and high precision are always required in deformation monitoring, this paper refined the model of GNSS

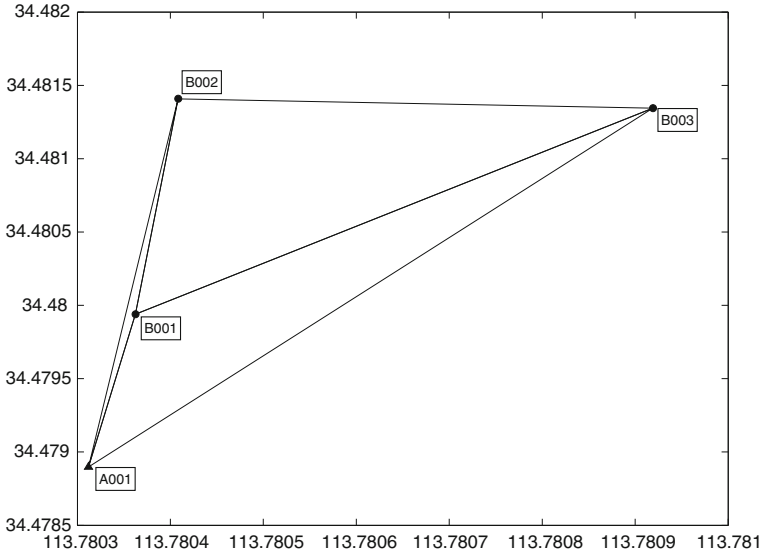


Fig. 3.1 Distribution of experimental tracking stations, where A001 is the reference stations, and other stations are monitor stations

data processing and developed the BDS data processing software. The main data processing model and strategies are as follows:

1. All observations are processed using double-difference (DD) model and every computational arc segment covers 4 h. The cut-off elevation is set to 10° .
2. Broadcast ephemeris are used to compute the position of the satellites. According to [10], satellite orbit will not degrade those baselines less than 1 km. Even in the worst cases, satellites orbits with a bias of 5 m will only result in a bias of 0.05 mm in the final positioning results. Nowadays, the accuracy of broadcast ephemeris could meet the demands of high-precision deformation monitoring [10].
3. Original L1 carrier phase observations are utilized directly to estimate all parameters due to its low noise, L2 observations are only used for detecting cycle slips.
4. The troposphere delay and ionospheric delay effect are considered. According to standard atmospheric model, the effect of tropospheric refraction could be eliminated by Saastamoinen model and the piecewise linear method is adopted to estimate the residual of troposphere delay effect. Ionospheric refraction effect can be eliminated by double difference.
5. The earth tide and ocean tidal correction models are used.
6. The coordinates of base station A001 will be fixed as constants in the parameter estimation.

7. Ambiguity resolution is a key issue in the high-precision GNSS deformation monitoring. In this software, ambiguity resolution followed a sequential strategy:

- (a) An independent set of double-difference phase biases are selected according to the baseline length.
- (b) For each baseline, the satellite with the most observations is selected as reference satellite and form the DD ambiguities.
- (c) Form and solve the normal equation to obtain the float solution.
- (d) All the float ambiguities are sorted by the probability of being fixed to integers and those ambiguities with highest probability are firstly fixed to integers.
- (e) Fix all the fixed ambiguities in (d) and update the normal equation, repeat (c)–(e) until no more ambiguities could be fixed any more.
- (f) A searching criterion based on minimizing the estimated weighted sum of residuals squared (“chi squared”) is employed for searching the remaining float ambiguities.

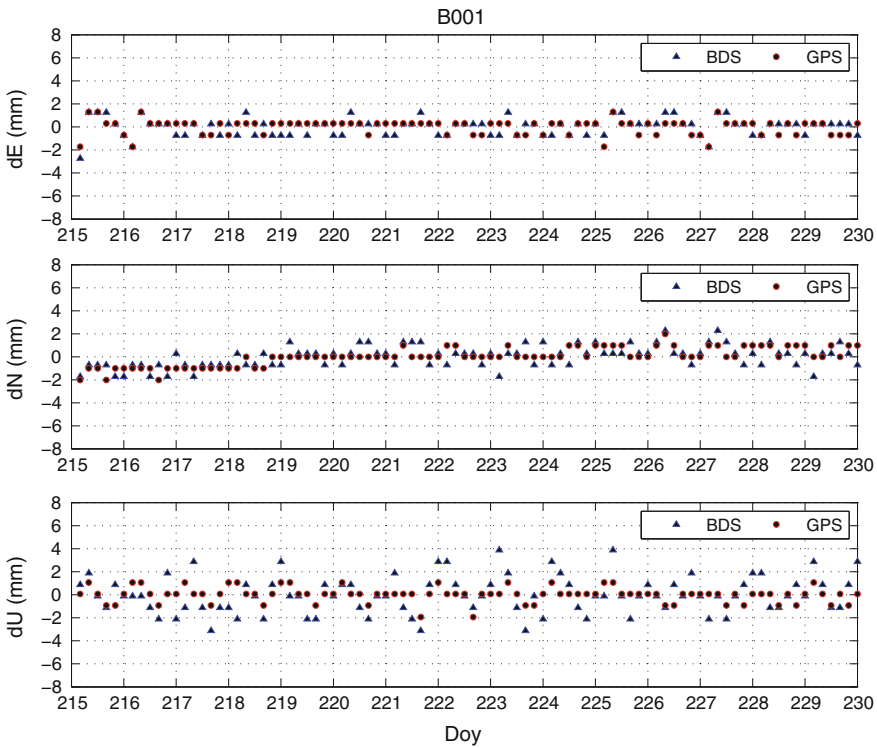


Fig. 3.2 Residual series of B001

3.3 Repeatability Analysis

Because the reference station A001 and monitoring stations B001 and B002 are assumed to be static, the repeatability of the two baselines (A001–B001 and A001–B002) could be used to assess the monitoring precision. In this paper, BDS and GPS data are firstly processed every 4 h independently using the same algorithm, and then the repeatability of baselines is calculated for BDS and GPS separately.

Figures 3.2 and 3.3 show the time series of residual in the north, east and vertical directions after removing the reference value obtained by processing GPS data with GAMIT software.

It can be seen from these figures, for BDS time series, the fluctuations of horizontal components are less than 2 mm, while those of vertical components are less than 4 mm, for GPS time series, the fluctuations seem a little better, especially in the vertical components, which are less than 2 mm. This is because current BDS satellites are always less than GPS satellites and the geometry of BDS is also poorer than GPS satellites at present. However it is believed that with the construction of BDS satellite constellation, the precision will be further improved.

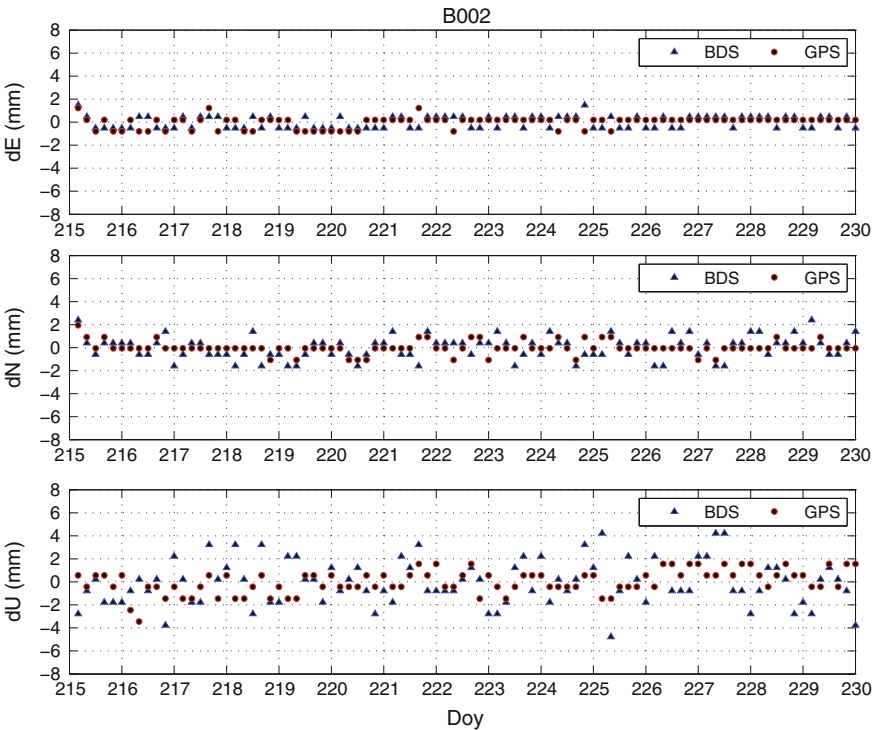


Fig. 3.3 Residual series of B002

Table 3.1 Repeatability of baselines

Baseline name	System	Repeatability of baseline/mm			
		E	N	U	L
A001–B001	BDS	0.8	0.9	1.6	0.9
A001–B001	GPS	0.6	0.8	0.7	0.8
A001–B002	BDS	0.5	1.0	2.0	1.0
A001–B002	GPS	0.5	0.6	1.0	0.5

Table 3.1 shows the repeatability of the baselines. The results suggest the monitoring precision of BDS is 1 mm for the horizontal components and 2 mm for the vertical components, which can meet the demands of most of deformation monitoring applications.

Meanwhile, obvious daily signals were found in all components in the two baseline time series. We have initially identified the source of the daily signals due to the geometric distribution of satellite constellation and thermal expansion of the monument [11, 12].

3.4 Reliability Analysis

As described above, a special equipment was installed at station B003 which could be used to move the antenna freely in both horizontal and vertical directions, and the quantity of displacements could be measured by micrometer precisely. In order to verify the agreements between deformations calculated from BDS data and the actual displacements, as shown in Table 3.2, different displacements were set up at station B003 for day 217–225, and the displacements were recorded as reference.

All data of BDS for baseline A001–B003 were processed every 4 h using the software developed in this paper. And the time series of results in the North, East and Up components are shown in Fig. 3.4. Figure 3.5 shows more details about the Up components. From the Figs. 3.4 and 3.5, diurnal variations are found in each

Table 3.2 Real deformations of the equipment

Day	E/mm	N/mm	U/mm
217	3	4	5
218	1	3	4
219	1	2	3
220	1	3	2
221	0	1	1
222	1	1	45
223	0	0	45
224	0	0	0
225	3	1	0

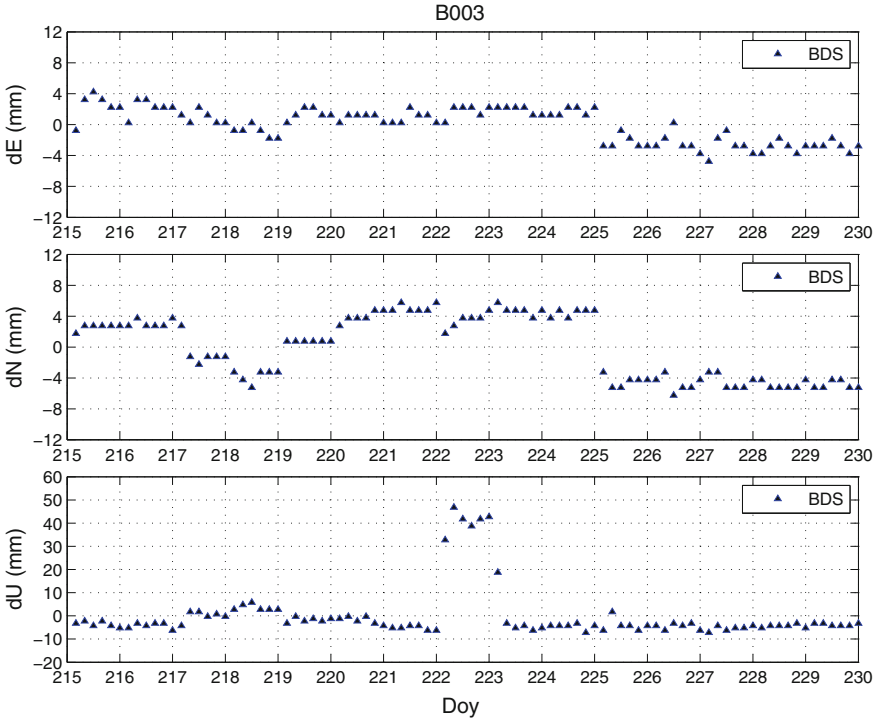


Fig. 3.4 Residual series of B003

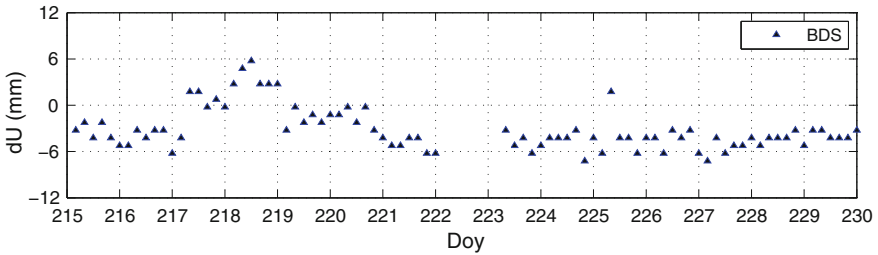


Fig. 3.5 Residual series in the up component of B003

component and the amplitude for horizontal and vertical components are about 1 and 2 mm, respectively. These are likely caused by PDOPs of the satellites and thermal expansion of the monument.

Comparison between the computed deformations and the reference deformations recorded by micrometers confirms a good agreement, which implies a good reliability of BDS in the deformation monitoring.

3.5 Conclusion

This paper designed an experiment platform and developed the corresponding software for assessing the performance of BDS in high-precision deformation monitoring. The results of 4-h solutions show that the repeatability of horizontal and vertical directions for short baselines using BDS are better than 1 and 2 mm, respectively. Additionally, comparison between the computed deformations and the reference deformations recorded by micrometers confirms a good agreement, which implies the potential of BDS for being applied to the deformation monitoring. And from the experiments, it can also be inferred that 4 h might be a reasonable choice for deformations monitoring using BDS.

Acknowledgments This research is supported by the National 863 program of China (2012AA12A209), together with the National Natural Science Foundation of China (41374033).

References

1. Li Z, Zhang X, Zhu Z (2002) A new model of high accuracy deformation monitoring with GPS. *Acta Geodaetica Cartogr Sin* 31(3):206–210
2. Jiang W, Liu H, Liu W et al (2012) CORS development for Xilongchi dam deformation monitoring. *Geomat Inf Sci Wuhan Univ* 37(8):949–952
3. Jiang W, Liu H, Zhou X et al (2012) Analysis of long-term deformation of reservoir using continuous GPS observation. *Acta Geodaetica Cartogr Sin* 41(5):682–689
4. Zhang X, Li Z, Xu S (2001) A new model for high accuracy deformation monitor with GPS. *Geomat Inf Sci Wuhan Univ* 26(5):451–454
5. Dai W, Zhu J, Ding X et al (2007) Single epoch ambiguity resolution in structure monitoring using GPS. *Geomat Inf Sci Wuhan Univ* 32(3):234–237
6. Yang YX, Li JL, Wang AB et al (2014) Preliminary assessment of the navigation and positioning performance of BeiDou regional navigation satellite system. *Sci China Earth Sci* 57:144–152. doi:[10.1007/s11430-013-4769-0](https://doi.org/10.1007/s11430-013-4769-0)
7. Shi C, Zhao QL, Li M et al (2012) Precise orbit determination of BeiDou Satellites with precise positioning. *Sci China Earth Sci* 55:1079–1086. doi:[10.1007/s11430-012-4446-8](https://doi.org/10.1007/s11430-012-4446-8)
8. He H, Li J, Yang Y et al (2013) Performance assessment of single-and dual-frequency BeiDou/GPS single-epoch kinematic positioning. *GPS Solutions* 1–11
9. Deng C, Tang W, Liu J et al (2013) Reliable single-epoch ambiguity resolution for short baselines using combined GPS/BeiDou system. *GPS Solutions* 1–12
10. Jiang W, Liu J, Ye S (2001) The systematical error analysis of baseline processing in GPS network. *Geomat Inf Sci Wuhan Univ* 26(3):196–199
11. King MA, Williams SDP (2009) Apparent stability of GPS monumentation from short baseline time series. *J Geophys Res: Solid Earth* (1978–2012) 114(B10). doi:[10.1029/2009JB006319](https://doi.org/10.1029/2009JB006319)
12. Hill EM, Davis JL, Elósegui P et al (2009) Characterization of site specific GPS errors using a short-baseline network of braced monuments at Yucca Mountain, southern Nevada. *J Geophys Res Solid Earth* (1978–2012) 114(B11). doi:[10.1029/2008JB006027](https://doi.org/10.1029/2008JB006027)

Chapter 4

Analysis on Velocity Measurement Precision of High Dynamic GPS Receiver Carrier Tracking Loop

Xudong Liu, Guangjun Liu, Qiang Li and Haiying Luo

Abstract The dissertation introduced factor that high dynamic condition influence the velocity measurement precision of GPS receiver's carrier tracking loop. Based on analyses on the measurement error and tracking threshold, the adaptability and tracking precision of carrier tracking loop in high dynamic condition were simulated, the measurement error and the finally velocity precision were expressed in different high dynamic condition. The paper has important theoretical significance for comprehending the velocity measurement precision in high dynamic condition and designing tracking loop that is adapted to high dynamic condition.

Keywords High dynamic · Carrier tracking loop · Velocity measurement precision

4.1 Introduction

GPS could provide the information that high precision position, speed and time for global users all-weather. GPS are widely used especially in military field. The basic principle of GPS velocity measurement is the Doppler measurement due to the relative movement between satellite and the user, and calculate the velocity by the least square method or the state estimation method. The basic formula is [1]:

$$\lambda f_d^j = \frac{(r - r_j)(\dot{r} - \dot{r}_j)}{\rho_j} + c\dot{\delta}t_k - c\dot{\delta}t_j + \dot{\delta}\rho_n^j + \dot{\delta}\rho_p^j + \varepsilon_j \quad (4.1)$$

X. Liu (✉) · G. Liu · Q. Li · H. Luo
GNSS TT&C Laboratory, Beijing Institutes of Tracking and Telecommunications
Technology, 5131, Beijing, Haidian, People's Republic of China
e-mail: aokliu@sina.com

λ is a GPS carrier wavelength, f_d^j is the Doppler measurement between the satellite j to receiver, $\dot{\delta}\rho_n^j$ is Time delay variation rate of the ionosphere, $\dot{\delta}\rho_p^j$ is Time delay variation rate of the troposphere, ρ_j is the pseudorange, r is the position vector of receiver, \dot{r} is The velocity vector of receiver, r_j is the position vector of satellite, \dot{r}_j is the velocity vector of satellite, $\dot{\delta}t_k$ is clock rate of receiver, $\dot{\delta}t_j$ is clock rate of the satellite j , ε_j is the observation noise.

The receiver speed measuring precision is influenced by all kinds of error, that mainly including (1) error related to the satellite system, such as satellite orbit error, satellite velocity error, satellite clock error rate error, relativistic effects, etc. (2) the route of transmission, such as changes in the ionosphere and troposphere; (3) the receiver itself, such as the location of the receiver error, receiver clock difference rate of change of error and multipath error rate and receiver noise. Error that is related to the satellite system could be correction through the ephemeris data, error that is related to the propagation path could be correction through the model modification. The impact on the speed measuring precision through correcting the error term could be seen in Table 4.1.

But, the above analysis is based on low dynamic, when carrier move on high dynamically, for example, if the acceleration is 50 g, the acceleration is 30 g/s, speed measuring precision can reach the precision, the problem need further be analysis. Because the clock radio, broadcast ephemeris is space/control section with the actual satellite clock error and the satellite position estimate and load fitting for satellite, the ionosphere, troposphere delay, multipath delay error and the actual space environment, no changes with speed of receiver. So the satellite system and environment section of error sources in high dynamic situations in accordance with low dynamic. Under the high dynamic scene, speed measuring precision mainly affected by receiver noise error source term. The speed measuring precision influence of GPS receiver loop noise on high dynamic station has been analyzed in this paper [2, 3].

Table 4.1 The influence of error term for speed measuring precision

Error term	The influence of error term for speed measuring precision
Satellite orbit changes	Deviation: negligible, Standard deviation: negligible
Satellite clock difference changes	Deviation: mm/s, Standard deviation: mm/s
The troposphere delay	Deviation: negligible, Standard deviation: negligible
Ionospheric delay	Deviation: mm/s, Standard deviation: negligible
The theory of relativity correction	Deviation: mm/s, Standard deviation: mm/s
Positioning accuracy	Deviation: negligible, Standard deviation: negligible
Multipath	Deviation: negligible, Standard deviation: mm/s
The receiver loop noise	Deviation: negligible, Standard deviation: mm/s

4.2 Analysis on Loop Measurement Error and Tracking Threshold

GPS receiver tracking loop includes: code delay locked loop (DLL), carrier frequency locked loop (FLL) and carrier phase lock loop (PLL). As the code loop is rough ring, in the tracking loop more resilient than phase-locked loop, under the condition of the PLL can track, code ring also can guarantee the normal track of signal. Receiver code loop in most of the tracking error is made up of dynamic thermal noise and receiver. For receiver dynamic stress error, because the PLL assisted DLL, can make DLL dynamic stress is reduced to less than 0.1 Hz, so the DLL loop dynamic stress can be ignored. Frequency locked loop to track the frequency of the carrier phase, rather than with high dynamic adaptability, but low tracking precision, are commonly used to assist phase-locked loop. So carrier phase lock loop is the key to realize high precision data receiver decoding [4, 5].

PLL make a copy of the received carrier signal that maintain consistent carrier signal through the numerical control oscillator, and infer the received carrier signal state according to the control parameters. The sources of the measurement error of PLL on signal includes a phase jitter and dynamic stress error, a conservative estimate is a PLL tracking error (3σ) must not exceed 1/4 of PLL discriminator phase traction range, so empirical threshold of 3σ is 45° [6, 7].

$$3\sigma_{PLL} = 3\sigma_i + \theta_e \leq 45^\circ \quad (4.2)$$

σ_i is phase jitter error, θ_e is the dynamic stress error, σ_{PLL} is phase measurement error variance.

(1) Phase jitter error

Sources of error caused by phase jitter mainly jitter oscillation frequency caused by thermal noise, mechanical shock and Allan variance. The phase jitter error σ_i is:

$$\sigma_i = \sqrt{\sigma_{iPLL}^2 + \sigma_v^2 + \sigma_A^2} \quad (4.3)$$

σ_v is oscillator phase jitter induced by the corresponding machinery jitter, $\sigma_v \approx 2^\circ$, σ_A is Alendronate phase jitter mean square error. σ_A is proportional to the PLL pre integration time, if pre integration time is 1 ms, $\sigma_A = 0.57^\circ$.

$$\sigma_{iPLL} = \frac{360}{2\pi} \sqrt{\frac{B_n}{C/N_0} \left(1 + \frac{1}{2T \cdot C/N_0} \right)} \quad (4.4)$$

B_n is Carrier loop bandwidth, C/N_0 is Carrier to noise ratio, T is pre integration time.

The type shows that the thermal noise is independent with the loop order number, the loop order is mainly decided by he dynamic performance.

(2) The dynamic stress error

The dynamic stress error depends on the loop bandwidth and order loop filter, if the response to a step function with overshoot, the maximum dynamic stress error may be slightly larger than the steady-state error, if the filter is designed to have minimal root mean squared error, then the overshoot should not be greater than 7 %, this is typical of the loop filter coefficients the situation.

The dynamic stress error of two order phase locked loop is:

$$\theta_{e2} = \frac{d^2R/dt^2}{\omega_0^2} = \frac{d^2R/dt^2}{\left(\frac{B_n}{0.53}\right)^2} = 0.2809 \frac{d^2R/dt^2}{B_n^2} (\circ) \quad (4.5)$$

d^2R/dt^2 is the minimum sight direction acceleration dynamic ($^\circ/s^2$).

The dynamic stress error of three order phase locked loop is

$$\theta_{e3} = \frac{d^3R/dt^3}{\omega_0^3} = \frac{d^3R/dt^3}{\left(\frac{B_n}{0.53}\right)^3} = 0.4828 \frac{d^3R/dt^3}{B_n^3} (\circ) \quad (4.6)$$

d^3R/dt^3 is the minimum sight direction acceleration dynamic ($^\circ/s^3$).

Because of the two order of carrier tracking loop for speed stress insensitive, oscillator error caused by acceleration can be ignored. For the three order carrier tracking loop, oscillator error caused by acceleration can be ignored, because of the stress of acceleration is not sensitive.

Visible, the receiver in order to adapt to the carrier dynamics of higher, requiring larger loop bandwidth, and the loop the loop bandwidth is larger and would increase the phase jitter error, reduce the tracking precision of PLL carrier, and even cause the receiver to lose lock.

4.3 The Adaptability and Accuracy of PLL on High Dynamic Station

In this paper, the adaptability of the high dynamic environment PLL simulation analysis [8, 9]. As Figs. 4.1 and 4.2 show. PLL can only track the signal to noise ratio of 30 dB_Hz or above, the 8–45 Hz loop bandwidth, and the two order carrier loop is very sensitive to acceleration, three order carrier loop is very sensitive to jerk (Tables 4.2 and 4.3).

Three order GPS receiver carrier loop PLL is used to realize the tracking signal measurement on high dynamic environment. This paper simulated the performance of PLL in this station: $B_n = 18$ Hz, $T_{coh} = 1$ ms, $C/N_0 = 43$ dB_Hz (-161.5 dB W), $a = 50$ g, jerk = 0 g/s, jerk = 10 g/s, jerk = 20 g/s jerk = 30 g/s. When the jerk less than 20 g/s, three order GPS receiver carrier loop could continuous tracking signal, When the jerk more than 30 g/s, PLL would loss the signal. The simulation results

Fig. 4.1 Error curve of second order PLL

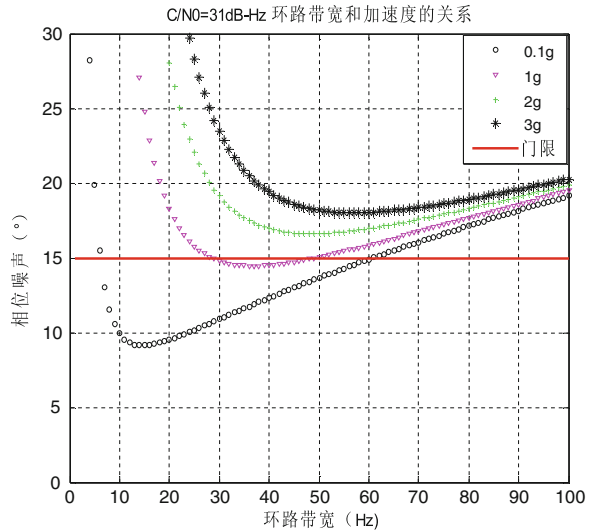
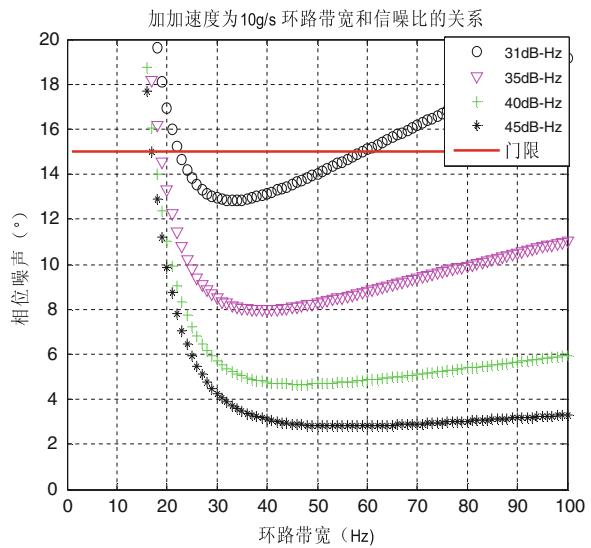


Fig. 4.2 Error curve of three order PLL



are shown in Figs. 4.3, 4.4, 4.5 and 4.6. The statistical results of the PLL tracing error are shown in Table 4.4.

At present, carrier phase tracking loop precision is set for 1 % weeks in the general literature it is 2 mm. Through the simulation when the B_n is 18H, T_{coh} is 1 ms, jerk is 0 g/s, the tracking accuracy of PLL is 0.92 mm, which can better meet the carrier measurement precision is less than 2 mm index, along with the increase of the jerk, when jerk = 5 g/s, the measurement error of this theory has exceeded 2 mm, $j = 30$ g/s loop is at a complete loss of lock state. Error statistics generally

Table 4.2 The loop bandwidth that meeting PLL requirement in different C/N₀ condition

Carrier loop	C/N									
	24		31		35		40		45	
	Min	Optimal	Min	Optimal	Min	Optimal	Min	Optimal	Min	Optimal
Two order carrier loop	Loss	Loss	28	35	20	42	19	43	18	50
Three order carrier loop	Loss	Loss	23	30	18	38	17	41	17	42

Acceleration 1 g, jerk 10 g/s

Table 4.3 The loop bandwidth that meeting PLL requirement in different acceleration or jerk condition

Carrier loop	Acceleration (jerk)							
	0.1 g (10 g/s)		1 g (15 g/s)		2 g (20 g/s)		3 g (30 g/s)	
	Min	Optimal	Min	Optimal	Min	Optimal	Min	Optimal
Two order carrier loop	8	13	28	35	Loss	Loss	Loss	Loss
Three order carrier loop	23	30	26	37	30	40	45	45

C/N₀ = 31 dB_{Hz}

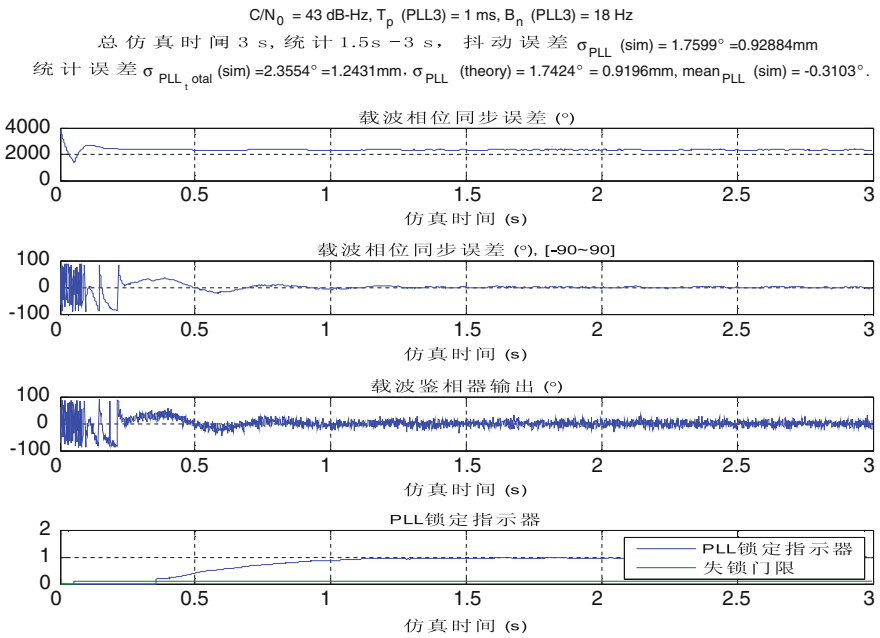


Fig. 4.3 Jerk = 0, the tracking performance of PLL

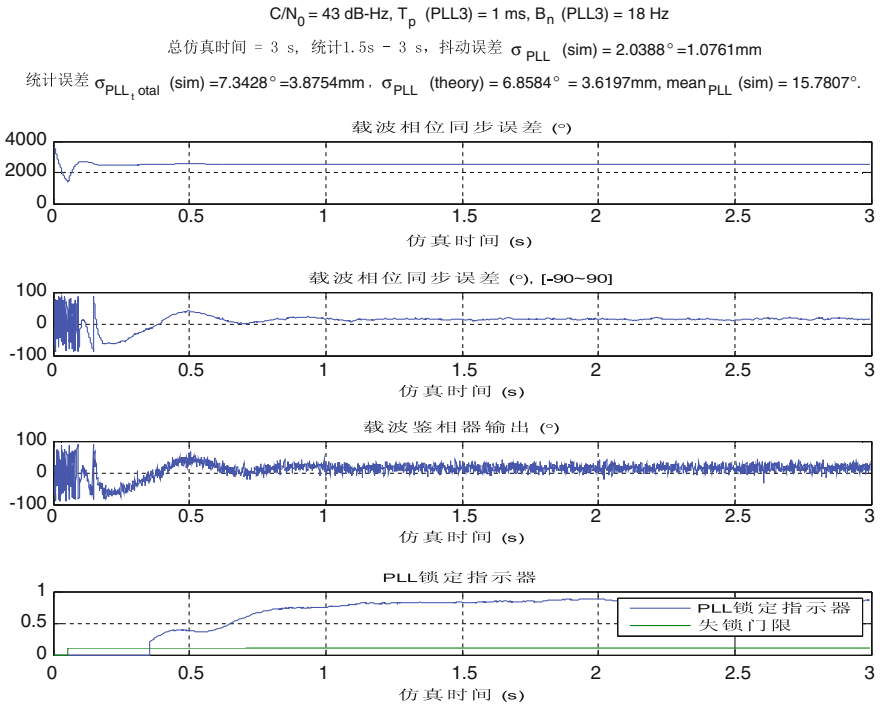


Fig. 4.4 Jerk = 10 g/s, the tracking performance of PLL

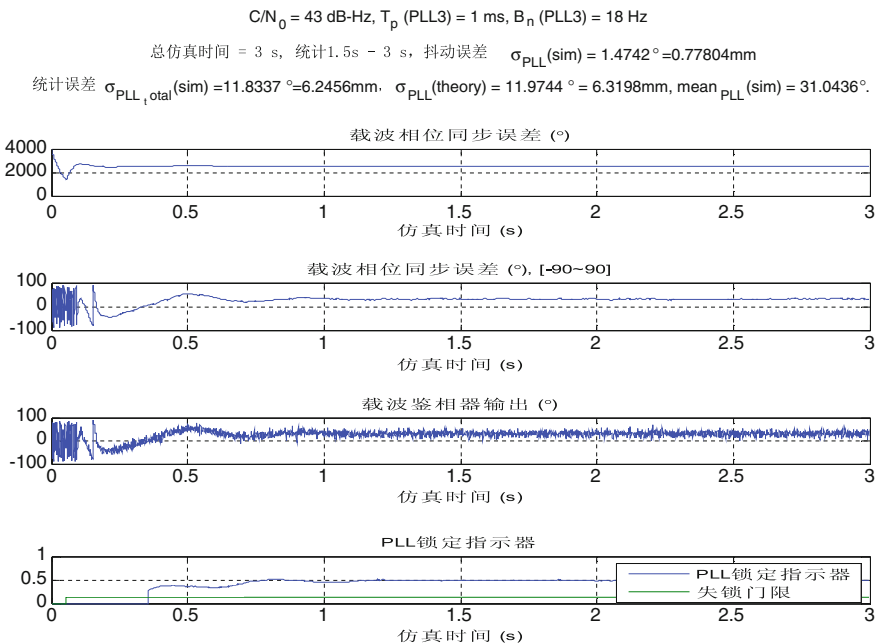


Fig. 4.5 Jerk = 20 g/s, the tracking performance of PLL

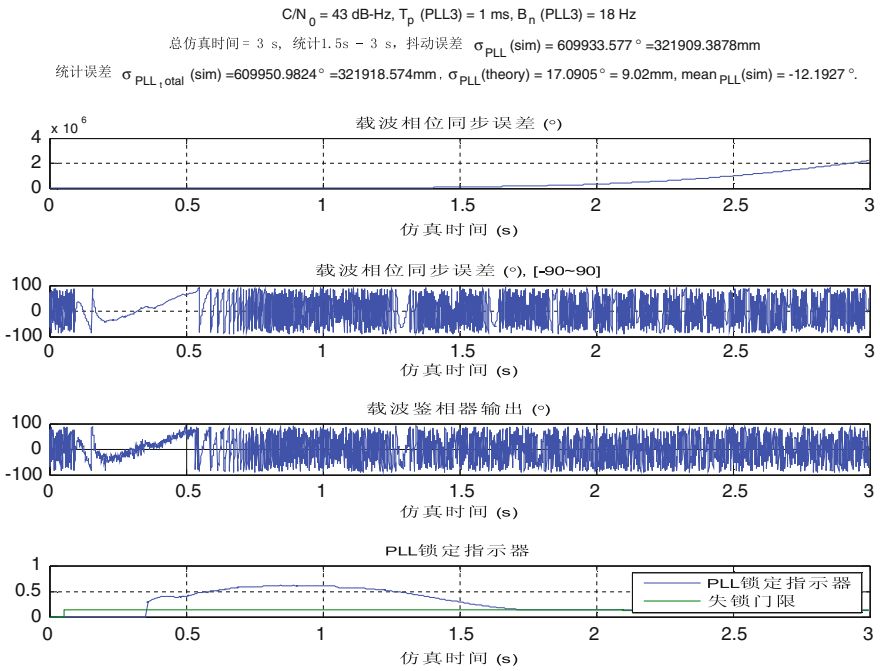


Fig. 4.6 Jerk = 30 g/s, The tracking performance of PLL

Table 4.4 The statistic of simulation

The simulation conditions	The statistical results (mm)	
	Theory value	Statistical integrated error
$a = 50 \text{ g}$, $j = 0 \text{ g/s}$	0.91957	1.2431
$a = 50 \text{ g}$, $j = 2 \text{ g/s}$	1.4596	1.4801
$a = 50 \text{ g}$, $j = 5 \text{ g/s}$	2.2697	2.3087
$a = 50 \text{ g}$, $j = 10 \text{ g/s}$	3.6197	3.8754
$a = 50 \text{ g}$, $j = 15 \text{ g/s}$	4.9698	4.891
$a = 50 \text{ g}$, $j = 20 \text{ g/s}$	6.3198	6.2456

includes thermal noise error, Allan deviation and dynamic stress error caused by acceleration.

The PLL bandwidth of does not exist the case theory the tracking accuracy of PLL is 0.92 mm, which can better meet the carrier measurement precision is less than 2 mm index, along with the increase of the jerk, when jerk = 5 g/s, the measurement error of this theory has exceeded 2 mm, j = 30 g/s loop is at a complete loss of lock state. Error statistics generally includes thermal noise error, Allan deviation caused by acceleration and dynamic stress error.

4.4 Conclusion

In summary, speed measuring precision of GPS receiver tracking loop has the very big relations with carrier dynamic, the jerk is greater, speed measuring precision is worse. As shown as the phase locked loop analysis on measuring error formula and simulation, the measurement error caused by high dynamic, dynamic stress error is one of main part. So the research in some way to eliminate the dynamic stress caused by the carrier tracking loop measurement error, considering only the loop error caused by thermal noise, improve the measurement precision of GPS receiver in high dynamic environment, is the future development direction.

References

1. He H, Yang Y, Sun Z (2002) A comparison of several approaches for velocity determination with GPS. *Acta Geodaetica et Cartographica Sinica* 31:217–221
2. Yang L, Liu Y, Zhou X et al (2007) The precision analysis and application of GPS velocity determination. *Hydrogr Surv Charting* 27(2):23–25
3. Wang P, Zhang X, Huang J (2007) Error analysis and accuracy assessment of GPS absolute velocity determination with SA off. *Geomat Inf Sci Wuhan Univ* 32(6):515–519
4. Lan Y, Jia Y (2008) The study of error distribution for GPS observed values. *Bull Surv Mapp* 4:12–13
5. Dow JM, Neilan RE, Gendt G (2008) The international GPS service (IGS): celebrating the 10th anniversary and looking to the next decade. *Adv Space Res* 36:320–326
6. Chen Y, Yu X, Ye C et al (2008) The precision analysis of static GPS precise point positioning based on experiment. *GNSS World China* 33:35–48
7. Wang J, Zhao J (2011) Convergence analysis and improvement methods in GPS precise point position. *J Spacecr TT&C Technol*
8. Kaplan ED, Hegarty CJ (2005) *Understanding GPS: principles and applications*, 2nd Edition edn. Artech House, Boston
9. Xie G (2009) *Principles of GPS and receiver design*. Electronic Industry Press, Beijing

Chapter 5

Theoretical Study of Bare Soil Parameters' Effects on GPS Multipath Observables

Xuerui Wu, Shuanggen Jin and Ye Li

Abstract In the past two decades, GNSS-R has emerged as a new and attractive remote sensing technique. The geodetic/geophysical GPS receivers are out-of-commercial and their recorded multipath observables have potentials for geophysical parameters detections, e.g. soil moisture, vegetation growth and snow depth. Based on the developed forward GPS multipath model, effects of bare soil parameters on GPS multipath observations are evaluated here. Wave synthesis technique is employed to get the coherent scattering coefficients at VV, HH, RR and LR polarizations, while the bare soil dielectric constant is calculated by a microwave dielectric soil-water mixing model. Effects of three-frequencies GPS modulations (L1 band, L2 band and L5 band) are evaluated: although there are apparent differences for GPS multipath observables, it is not the effects of bare soil but the direct broadcasting signals since soil scattering properties at these frequencies (L band) are the same. Soil texture and surface roughness have almost no effects on GPS observables. As the soil temperature changes from SubZero to above zero, the amplitudes of SNR, phase and code pseudorange increased. Soil moisture also affects GPS observables, as moisture content increases, the amplitudes of GPS observables increase.

Keywords GPS-multipath reflectometry · Triple-frequency · Soil texture · Surface roughness · Soil moisture · Frozen/thawed soil

X. Wu (✉) · S. Jin
Shanghai Astronomical Observatory, Chinese Academy of Sciences,
Shanghai 200030, China
e-mail: xrwu@shao.ac.cn

X. Wu · Y. Li
Space Star Technology CO., Ltd, Beijing 100859, China

5.1 Introduction

In the past two decades, GNSS-R has emerged as an attractive and promising remote sensing technique as complementary to the traditional SAR and radiometer, and its applications have covered from meso-scale ocean remote sensing to land surface such as soil moisture, vegetation growth and snow depth. In order to record the reflected signals once thought to be detrimental, a special GNSS-R receiver should be designed: such as the DMR [1] (Delay Doppler Maps Receiver), SMIGOL [2] (Soil Moisture Interference pattern GNSS Observations at L-band Reflectometer) and SAM receiver [3] used in the ground or airborne experiments. However, it has been shown that the multipath observables record by the ready-made geodetic/geophysical GPS receiver are sensitive to geophysical parameters of bare soil [4, 5], vegetation [6, 7] and snow [8] and have great potentials for the corresponding parameters retrievals. At present, most of the GPS-MR work is based on the experimental data [4–8].

However, in order for the following retrieval applications, theoretical models based on the physical fundamentals should be highly paid attention to. Since the reflected signals are thought to be detrimental for precise positioning and timing applications, most previous forward multipath models focus on the code modulation, adopting arbitrary values or using empirically defined values for the reflected power, phase and delay. Recently, based on the model developed by Zavorotny et al. [9], Nievinski and Larson have developed a fully polarimetric forward multipath model with due considerations of the coherence between the direct and reflected signals [10, 11]. This model takes the right- and left-handed circularly polarized components of the GPS broadcast signal into considerations. The combinations of the antenna and surface responses are also considered.

Changes of the bare soil parameters affect all three GPS interferogram metrics (effective reflector height, phase and amplitude) [12]. Based on Nievinski and Larson's forward multipath model [10, 11], they have tested the relationship of SNR data with near-surface soil moisture using field data [5]: soil moisture in the top 5 cm of the bare soil affects the SNR data apparently. While soil texture's effects can be negligible.

In order for detail description of reflector (vegetation) with GPS broadcasting signals, Wu and Jin had embedded the first-order radiative transfer equation model (bistatic-Michigan Microwave Canopy Scattering Model) into the forward GPS multipath model [13]. Bare soil and vegetation canopy effects on the GPS multipath observables were briefly simulated [13]. Recently, theoretical effects of canopy parameters on GPS SNR data were evaluated in Chew et al. work [14]. Their model was successfully validated with vegetation field data [14].

This work focuses on the explanations of physical fundamentals. As is well known, GPS-MR is a kind of bistatic/multistatic radar. The nature for bare soil remote sensing using GNSS-R is: different soil parameters have their own microwave dielectric behaviors, which result in different surface scattering properties. The GPS receiver gets the combination of direct and reflected GPS signals, which

carry information of reflector. Here a soil-water mixture dielectric model is employed to calculate the dielectric constants [15, 16], which are put into the coherent scattering coefficients proposed by Fung and Eom [17]. In order to get the circular polarization scattering coefficients, wave synthesis technique is used. Then the scattering coefficients of linear and circular polarizations are embedded into the fully polarimetric forward GPS multipath model [10, 11]. Using this theoretical model, relationships between bare soil and three-frequencies (L1, L2 and L5) GPS modulations are simulated. Other bare soil parameters are also evaluated here: soil texture, surface roughness, soil moisture and soil temperature. However, this paper pays more attention to the relationship between microwave dielectric properties and the GPS multipath data (SNR, phase and code pseudorange).

Section 5.2 presents the GPS-MR theory. And then theoretical simulations are given in Sect. 5.3. While the conclusion part is provided in Sect. 5.4.

5.2 GPS-MR Theory

The fundamentals for remote sensing geophysical parameters using GPS-MR are the differences of dielectric constants, which affect the scattering properties of reflector and finally result in the differences of GPS multipath observables.

To carry on theoretical study of bare soil parameters on GPS multipath observables, dielectric constant model is used to get the soil microwave dielectric properties [15, 16], which are put into the coherent scattering model proposed by Fung and Eom [17], and then a fully polarimetric GPS multipath model developed by Nievinski and Larson is used to get the simulations [10, 11]. Theoretical study of the work will backup the phenomena explanation and provide a guidance for geophysical parameters retrieval.

5.3 Theoretical Simulations

5.3.1 *Triple Frequencies GPS Modulations Effects*

The US government raised GPS modernization program in 1999, it includes the addition of civil frequency L5 ($f_5 = 1.17624$ MHz). Linear combination of L5 carrier with L1 carrier ($f_1 = 1.57542$ GHz) and L2 carrier ($f_2 = 1.22760$ GHz) can improve real-time positioning accuracy and civilian navigation security.

The forward multipath model has included the L5-band [10, 11]. Although most previous studies of GPS-MR focus on the GPS L1 and L2 bands, Tabibi et al. have assessed the modernized GPS L5 SNR for ground-based multipath reflectometry applications and concluded that soil moisture at L5 band is equivalent to L2C-derived retrievals [18].

Using the previous mentioned forward GPS multipath model [10, 11], we also simulate triple frequencies GPS modulations effects on GPS multipath simulator as

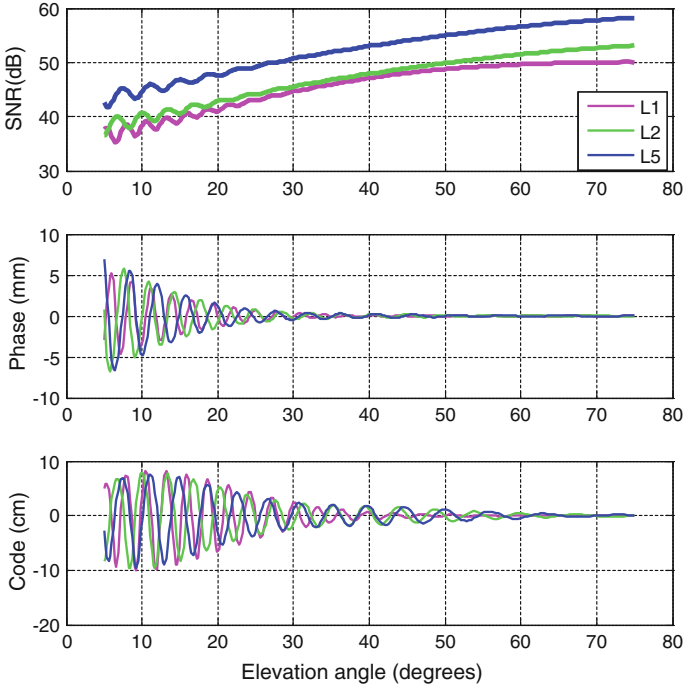


Fig. 5.1 GPS observables for triple frequencies GPS modulations. The *top* of the reflected surface material is air, while the *bottom* is wet soil

shown in Fig. 5.1. We set the top of the surface material as air and set the bottom as fixed wet soil.

Figure 5.1 shows the simulated GPS observables at three different GPS modulations (L1 band, L2 band and L5 band). We can see that although the reflected targets are the same, the oscillation amplitudes of GPS multipath observables are different and there are apparent phase shift for different GPS frequencies.

We use the mixing texture dielectric constant model to calculate dielectric constants of the bare soil [15, 16]. The other parameters of simulated bare soil are: volumetric moisture of soil (vms) is 0.3, buck density is 1.6, soil texture is sandy loam.

Table 5.1 presents the dielectric constants (real part and imagine part) at L1 band, L2 band and L5 band. Table 5.1 also presents the differences of real part and imaginary part between L2 band (L5 band) and L1 band. We can see from

Table 5.1 Bare soil dielectric constants and their differences at triple frequencies GPS modulations

Carrier (GHz)	ϵ'	ϵ''	$\Delta\epsilon'$	$\Delta\epsilon''$
L1 1.575	21.10970	3.54415	–	–
L2 1.227	21.27701	3.49827	0.16731	-0.04588
L5 1.176	21.29776	3.51016	0.18806	-0.03399

Table 5.1 that for different GPS frequencies, the differences of real part are below 0.2, while the differences of imaginary part are below 0.05. Minor differences of dielectric constant for the same soil of different GPS modulations will lead to minor differences of reflectivities at different polarizations, therefore the apparent differences got from GPS observables at different GPS modulations (L1 band, L2 band and L5 band) are not caused by the differences of reflected properties, but due to the differences of GPS direct broadcasting signals. In the following simulations, L2 band is used.

5.3.2 Soil Texture Effects on GPS Multipath Signals

Soil texture affects the microwave transmitting and reflecting properties. For different soil textures, Table 5.2 gives the corresponding dielectric constants. GPS L2 band is used, while the buck density is 1.6, soil temperature is set for 25 °C, vms is 0.3.

We can see that compared to sandy loam and loam, the dielectric constant of silty clay has a little difference. The real part of silty clay is smaller than the one of sandy loam, but the difference is also very little.

Figure 5.2 presents the coherent scattering coefficients of different soil textures (sandy loam, loam, silty clay and silty loam) at linear (VV and HH) and circular polarizations (RR and LR). From the simulations, it can be seen that soil texture has little effects on the soil scattering properties at VV, RR and LR polarizations, although soil texture makes scattering at HH polarization differently at elevation angles larger than 40°, this difference is no larger than 1 dB and it is known that multipath effects are most pronounced at elevation angles lower than 30°.

Soil texture has little effects on bare soil scattering properties; therefore different soil texture has almost no influences on the final GPS multipath observables as shown in Fig. 5.3. In the below simulations, soil texture is set sandy loam for simulations.

5.3.3 Surface Roughness Effects on GPS Multipath Signals

Bare soil surface is randomly rough. To the present, it is thought that a geodetic-quality GPS receiver can only receive the coherent scattering of reflector. There is

Table 5.2 Bare soil dielectric constants for different soil textures

Soil type	Sandy loam	Loam	Silty clay	Silty loam
Sand (%)	51.5	42	5	17.2
Clay (%)	13.5	8.5	47.7	19
Real part	21.97	20.27	16.88	15.71
Image part	1.54	1.38	1.82	3.31

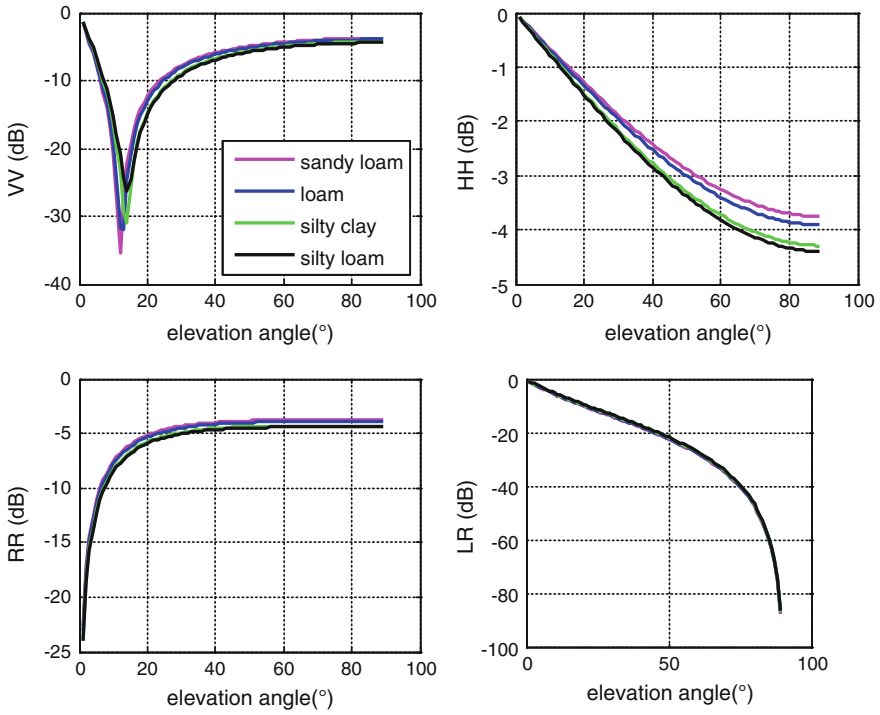


Fig. 5.2 Coherent scattering coefficients of different soil textures (sandy loam, loam, silty clay and silty loam) at linear (VV and HH) and circular polarizations (RR and LR)

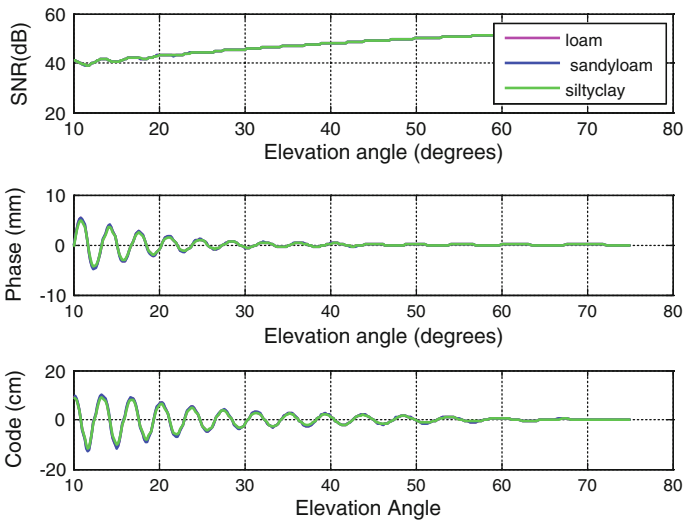


Fig. 5.3 Effects of soil texture on the final GPS multipath observables

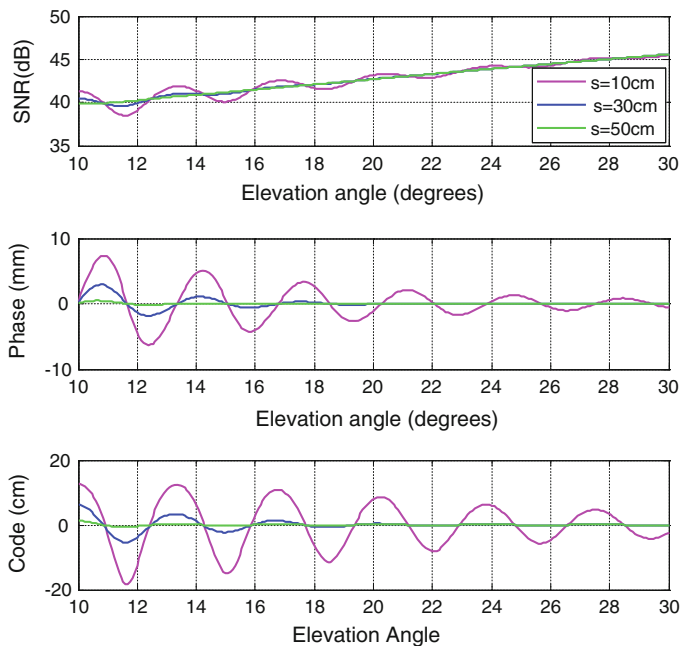


Fig. 5.4 Surface roughness effects on GPS multipath signals

no consideration for non-coherent scattering. In the above-mentioned model, surface roughness is formulated by a roughness factor (F_s) as shown in Eq. 5.1 [17].

$$F_s = e^{(-2k_0s \cos(\theta))^2} \quad (5.1)$$

While k_0 is the wave number, and s is the rms height and θ is the incidence angles. Three kinds of rms heights (s) are set for comparisons: $s_1 = 10$ cm, $s_2 = 30$ cm, $s_3 = 50$ cm.

Surface roughness effects on GPS multipath observables are apparent as shown in Fig. 5.4: as rms heights increase, coherent scattering decrease, which result in smaller amplitudes of GPS multipath observables. It is pointed out that surface roughness of bare soil could be useful for the positioning community since it diminishes the multipath signature [18].

5.3.4 Soil Moisture Effects on GPS Multipath Signals

A wet soil medium is the mixing combinations of soil particles, air voids and liquid water. This part shows water content effects on GPS observables.

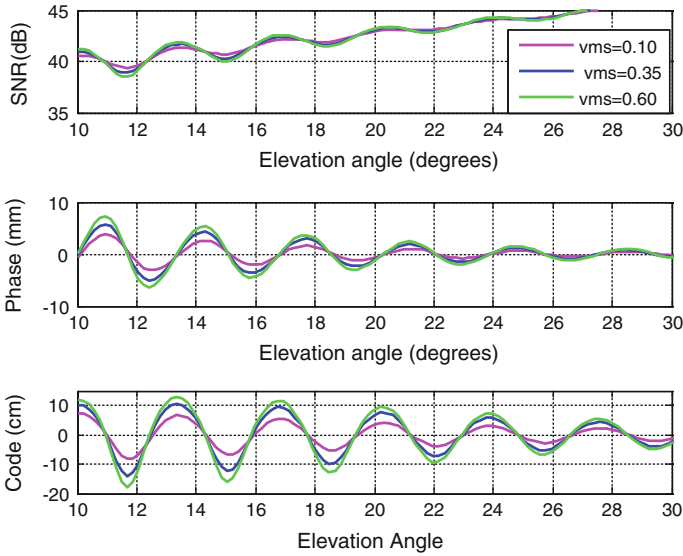


Fig. 5.5 Soil moisture effects on GPS multipath signals

As can be seen from Fig. 5.5, soil moisture contents have apparent effects on GPS multipath observables: larger volumetric soil moisture content corresponds to larger amplitudes of SNR, phase and code pseudorange. The reason is that larger soil moisture corresponds to larger surface reflectivity. This is why we can use geodetic GPS receivers to detect soil moisture. However, it should be pointed out that surface roughness also affects the amplitudes of GPS observables and its effects should be evaluated efficiently as considering for soil moisture retrieval from the Geodetic GPS data.

5.3.5 Soil Temperature on GPS Multipath Signals

Microwave band is suitable for bare soil freeze/thaw detection. It is known that the phase change of soil (frozen to thawed) will lead to large differences of the dielectric constant, and therefore will reduce to apparent changes on GPS multipath observables. As presented in the paper [19], when soil changes from frozen to thawed, the amplitudes of GPS observables increase. GNSS-R (GPS-MR) has the potential for bare soil seasonal frozen/thawed detection [19].

5.4 Conclusions

Dielectric properties of reflector (bare soil) affect the scattering properties and will lead to changes of GPS multipath signatures. Wave synthesis technique is used to get the coherent scattering at linear and circular polarizations.

Bare soil dielectric constants for different soil textures, moisture contents, surface roughnesses and soil temperatures are calculated by the mixing dielectric constant model. Using the forward multipath model opened by Nievinski and Larson, GPS multipath observables are got. GPS L2 band is used for the simulations: although triple frequencies of GPS have different forms of GPS multipath observables, they all work at the same microwave band (L band), therefore the microwave scattering properties are the same. From the simulations, it can be seen that soil texture has almost no effects on the GPS SNR data. While the increase of soil moisture will increase the amplitudes of GPS observables, but as the surface roughness increase, the scattering of coherent component decrease and therefore rougher surfaces have lower amplitudes of GPS observables. When soil temperature changes from SubZero to above zero, there is an apparent increase for the amplitudes of GPS observables, and GNSS-R has the potential for seasonal soil freeze/thaw detections.

Acknowledgments This work is supported by supported by the Open Research Fund of The Academy of Satellite Application under grant NO.2014_CXJJ-DH_05. The Open Research Fund of The Academy of Satellite Application under grant NO.2014_CXJJ-DH_05.

References

1. Masters D, Axelrad P, Katzberg S (2004) Initial results of land-reflected GPS bistatic radar measurements in SMEX02. *Remote Sens Environ* 92(4):507–520
2. Rodriguez-Alvarez N et al (2010) Land geophysical parameters retrieval using the interference pattern GNSS-R technique. *IEEE Trans Geosci Remote Sens* 49(1):71–84
3. Egado A et al (2011) LEiMON land monitoring with navigation signals. ESA/ESTEC, Noordwijk, Netherlands, Final report ESA contract. 22117/08/NL/AF
4. Larson KM et al (2008) Using GPS multipath to measure soil moisture fluctuations: initial results. *GPS Solutions* 12(3):173–177
5. Chew CC et al (2014) Effects of near-surface soil moisture on GPS SNR data: development of a retrieval algorithm for soil moisture. *IEEE Trans Geosci Remote Sens* 52(1):537–543
6. Small EE, Larson KM, Braun JJ (2010) Sensing vegetation growth with reflected GPS signals. *Geophys Res Lett* 37:L12401
7. Chew CC et al (2014) Vegetation sensing using GPS-interferometric reflectometry: theoretical effects of canopy parameters on signal-to-noise ratio data. *IEEE Trans Geosci Remote Sens* 53:2755–2763
8. Larson KM et al (2009) Can we measure snow depth with GPS receivers? *Geophys Res Lett* 36:L17
9. Zavorotny VU et al (2010) A physical model for GPS multipath caused by land reflections: toward bare soil moisture retrievals. *IEEE J Sel Top Appl Earth Obs Remote Sens* 3(1): 100–110

10. Nievinski FG, Larson KM (2014) Forward modeling of GPS multipath for near-surface reflectometry and positioning applications. *GPS Solutions* 18(2):309–322
11. Nievinski FG, Larson KM (2014) An open source GPS multipath simulator in Matlab/Octave. *GPS Solutions* 18(3):1–9
12. Chew CC et al (2013) Effects of near-surface soil moisture on GPS SNR data: development of a retrieval algorithm for soil moisture. *IEEE Trans Geosci Remote Sens* 52:537–543
13. Xuerui W, Shuanggen J (2014) A multipath forward scattering model of GNSS-Reflectometry from bare soil and vegetation. In: 2014 3rd international workshop on earth observation and remote sensing applications (EORSA), pp 5–8
14. Chew CC et al (2014) Vegetation sensing using GPS-interferometric reflectometry: theoretical effects of canopy parameters on signal-to-noise ratio data. *IEEE Trans Geosci Remote Sens* 53:1–10
15. Hallikainen MT et al (1985) Microwave dielectric behavior of wet soil-part 1: empirical models and experimental observations. *IEEE Trans Geosci Remote Sens* GE-23(1):25–34
16. Dobson MC et al (1985) Microwave dielectric behavior of wet soil-part II: dielectric mixing models. *IEEE Trans Geosci Remote Sens* GE-23(1):35–46
17. Fung A, Eom H (1983) Coherent scattering of a spherical wave from an irregular surface. *IEEE Trans Antennas Propag* 31(1):68–72
18. Tabibi S et al (2014) Assessment of modernized GPS L5 SNR for ground-based multipath reflectometry applications. *Adv Space Res* 2014(0). <http://dx.doi.org/10.1016/j.asr.2014.11.019>
19. Wu X, Jin S (2014) Can we monitor the bare soil freeze-thaw process using GNSS-R?: a simulation study. In: SPIE Asia Pacific remote sensing. 2014: international society for optics and photonics

Chapter 6

Satellite-Ground TT&C United Scheduling Methods of GNSS Constellation Based on Nodes Constraint

Li Jing, Zhang Tianjiao and Ye Gangqiang

Abstract In this paper, targeting at the effective management of TT&C and communication system of GNSS constellation, we analyze the constraint demands of TT&C and communication scheduling from the part of autonomous navigation precision, information transmission delay and integrality. Then, the model of node satellite selection is established which satisfy the optimized aims of multi-satellite tracking and exclusive satellite-ground link constraint satisfaction. Furthermore, the improved genetic algorithm is designed, which is used to scheduled satellite-ground resources. The results show that the strategy and algorithm are improved compared with traditional method.

Keywords Inter satellite link · GNSS constellation · Resource scheduling · Satellite-ground united scheduling

6.1 Introduction

GNSS constellation is consisted of multi-satellite satisfied the demands of configuration and coverage. In order to realize autonomous navigation and to solve the problem of continuous management in the situation of scarce resources, the inter satellite links are designed and added in space segment of GNSS constellation. It is become more complex to schedule the TT&C (Tracking, Telemetry and Control) resource after inter satellite links joining. The key problems are included in the parts of nodes satellite selection and the relationship between TT&C resource scheduling and link planning.

L. Jing (✉) · Y. Gangqiang
The State Key Laboratory of Astronautic Dynamics,
Xi'an Satellite Control Center, Xi'an, China
e-mail: carol_lee_0727@sina.com

Z. Tianjiao
Department of Electronics and Engineering, Xi'an Jiaotong University, Xi'an, China

Early in twenty century eighties, IBM cooperated with America AFSCN (Air Force Satellite Control Network) to research the automatic generation method of TT&C (Tracking Telemetry & Commanding) strategy [1]. Doctor Arabi applied hybrid integer programming to solve multi-satellite scheduling problem, the method can be used to schedule the TT&C scenario subter-fifty satellites. Based on above algorithm, Gooley and Schalck combined grading heuristic algorithm with interpolation algorithm to solve multi-satellite scheduling problem [2, 3], the method can be used to schedule three hundred TT&C task everyday, and the scheduling rate reached to 96 %. Furthermore, Pemberton and Greenwald [4], He and Liu [5, 6] used CSP (Constrain Satisfied Problem) method to solve multi-satellite scheduling problem. Marinelli and Nocella who are from ESA (European Space Agency) proposed a kind of heuristic model based on Lagrangian Relax algorithm [7], which is used to solve large scale SRS problem. The TT&C resource scheduling method based on heuristic algorithm also be researched by Chinese experts [8]. In recent years, the scheduling problem of space-based TT&C resource based on TDRSS is researched by world experts [9–11]. Along with application of satellite network, the satellite-ground TT&C united scheduling method is researched by some researchers [12].

During TT&C resource scheduling, the ISLs (Inter Satellite Links) constraint conditions are not considered in above research. In this paper, targeting at the effective management of TT&C and communication system of GNSS constellation, we propose the satellite-ground TT&C united scheduling method of GNSS constellation. In Sect. 6.2, the problem formulation and modeling of multi-satellite network TT&C resource scheduling are discussed. In Sect. 6.3, the realized strategy and steps of improved genetic algorithm are designed in detail. The simulation scenario of multi-satellite network TT&C resource scheduling is established, and the performance of algorithm is evaluated through simulations and analysis in Sect. 6.4. Finally, Sect. 6.5 concludes the paper.

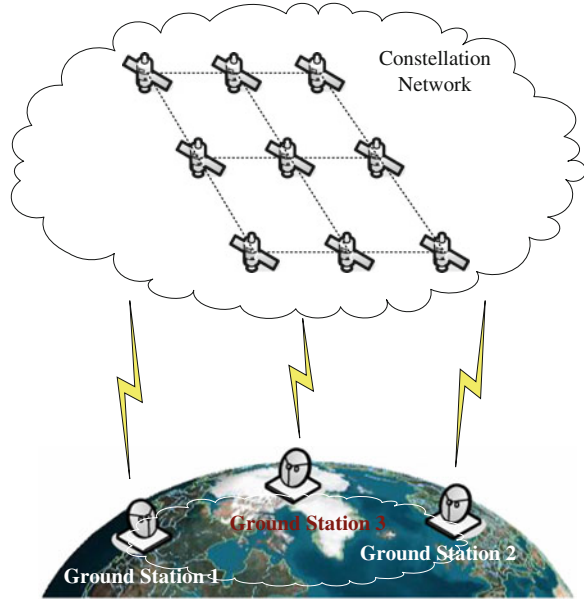
6.2 Problem Formulation and Modeling

6.2.1 TT&C Management Model of Constellation Network

The TT&C management of constellation networks from ground station is depicted in Fig. 6.1. The TT&C management task is consisted of space segment and ground segment.

The task of space segment is to transmit monitoring information of networks working status (telemetry date) and managing commands (telecommand) depend on ISLs. In addition, the application data will be transmitted through space to ground links. The task of ground segment is to scheduling managing resources. A node satellite connect space segment with ground segment.

Fig. 6.1 Management of multi-satellite network from TT&C ground station



The TT&C problem of multi-satellite network can be depicted by the following quintuple

$$M = \langle S, L, N, G, R \rangle \quad (6.1)$$

where,

$S = \{s_1, s_2, \dots\}$ is a satellite set inside constellation networks.

$L = \{l_1, l_2, \dots\}$ is a ISLs set inside constellation networks.

$N = \{n_1, n_2, \dots\}$ is a node satellite set exchanged information with ground TT&C managing resources.

$G = \{g_1, g_2, \dots\}$ is a ground station set dealt with TT&C management.

$R = \{r_1, r_2, \dots\}$ is a routing set connected node satellite with anyone inside constellation.

6.2.2 Model of Links

The process of establishing links includes ISLs establishment and space-ground links establishment. A space-ground link can be established between node satellite and ground TT&C station. A node satellite can established ISLs with multi-satellite in the network simultaneously. Each satellite can transmit TT&C managing data as relay satellite. The integrated linking task based on constellation network and ground TT&C managing network will be expressed as follow

$$L = \{NS - TS, NS - RS, RS - RS, RS - TS, NS - G\} \quad (6.2)$$

where, $NS-TS$ is the link between node satellite and target satellite, $NS-RS$ is the link between node satellite and relay satellite, $RS-RS$ is the link between relay satellite and relay satellite, $RS-TS$ is the link between relay satellite and target satellite, $NS-G$ is the link between node satellite and ground TT&C managing station.

The basic condition of link establishment is expressed as

$$R_L = R_{sat} \cap max_σ_{sat} \cap R_{signal} \quad (6.3)$$

where, R_{sat} is the link member in network satisfied the condition of geometrical vision, $max_σ_{sat}$ is the link member in network satisfied the condition of antenna beam coverage, R_{signal} is the link member in network satisfied the condition of signal reachable.

In the network, the number of ISLs of mono-satellite is depended to number of channels onboard. If the number of channels is expressed as NUM_{sat} , the link establishment condition simultaneous can be expressed as

$$NUM_{ISL} \leq NUM_{sat} \quad (6.4)$$

6.2.3 Model of Node Satellite

6.2.3.1 Nodes Definition

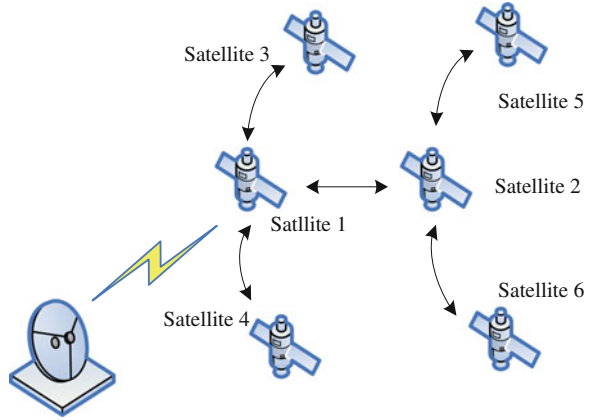
There are three kinds of satellites in each cluster, which is managed by the ground TT&C station. They are called as node satellite, backup node satellite and sub-node satellite, respectively. They are defined as

- Node satellite (N): The satellites can exchange information with ground station directly.
- Backup node satellite (N_b): The satellite can exchange information with node satellites and sub-node satellites. In the next time slot, it may become as the node satellite.
- Sub-node satellite (N_{sub}): The satellite neither belong to node satellites nor backup node satellite.

This three kinds of satellite possess of different functions, they will play the different role during routing maintenance and rerouting. The cluster architecture is depicted in Fig. 6.2. To combine with above definition, we have:

Node satellite: “Satellite 1”. Backup satellite: “Satellite 2”. Sub-node satellites: “Satellite 3”, “Satellite 4”, “Satellite 5” and “Satellite 6”.

Fig. 6.2 Architecture depict of satellite cluster



6.2.3.2 The Principia of Node Satellite Selection

It is close relate with cluster partition and ground managing station distribution when node satellite is chosen. The number of node satellite will be related with the number of cluster, and the selected principia will be related with the cluster members. Let us assume that the number of clusters inside the constellation is represented by $N_{cluster}$. Then, the number of node satellites will be given by

$$N = N_{cluster} \tag{6.5}$$

The set of node satellites is depicted as (6.1). Where, the principia of node satellites selection will be given as

$$n \in \max_l Sat_sight \tag{6.6}$$

$$Sat_sight = \{Sat_sight_1, \dots Sat_sight_l\} \tag{6.7}$$

The meaning of (6.6) and (6.7) can be explained as: the satellite with longest field of vision among all the visible satellite for a ground TT&C managing station will be chosen as node satellite.

6.2.3.3 Principia of Cluster Partition

The principia of cluster partition includes in the number of cluster inside the constellation and the number of satellite in each cluster. The number of satellite in the cluster is related with data transmission bandwidth. Assumption, the data transmission bandwidth of satellite is represented by f_{max}^{GSL} , the data transmission rate of node satellite is represented by R_{node} , the data transmission rate of ISLs is

represented by f_{max}^{ISL} , the total number of satellite inside the constellation is N . Then, the number of satellite in each cluster can be given by

$$N_{member} = \frac{f_{max}^{GSL} - R_{node}}{f_{max}^{ISL}} + 1 \quad (6.8)$$

The number of cluster inside the constellation will be given as

$$N_{cluster} = INT \left[\frac{N_s}{N_{member}} \right] \quad (6.9)$$

6.3 Algorithm Realization

Genetic Algorithms is a kind of multipoint search algorithm, the optimal solution will be chosen from all the calculation results by means of multipoint paralleling optimize. There are some imperfect performances for traditional Genetic Algorithms, which are on the global convergence, population prematurity and convergence rate parts. Therefore, we proposed FAGA (Fine Adaptive Genetic Algorithm).

The input conditions of algorithm realization include the distribution of ground TT&C station G , the orbital characteristics of satellite network S and the technique system of ISLs L .

The satellite-ground united scheduling includes links planning of satellite network and ground TT&C resource scheduling based on node satellite constraint.

Step 1: Analyze and calculation the visibility between satellites and ground stations or inter-satellites. The visible time lengths between satellites and ground stations or inter-satellites are calculated according to above input conditions.

Step 2: Pretreatment of visible time length. The visible time lengths between satellites and ground stations or inter-satellites are normalized as Δt , that means the visible time lengths will be divided into several sets as $ArcS = \{as_1, as_2, \dots, as_{|ArcS|}\}$, the residual part will be discarded. The TT&C task set is $J = \{J_1, J_2, \dots, J_{|ArcS|}\}$, the TT&C task J_i will be scheduled for every as_i . Figure 6.3 is Schematic diagram of visible pass pretreatment [13].

Step 3: Analyze and determine the constraint condition of TT&C resource scheduling. Besides formulae (6.3)–(6.9), the following basic scheduling constraint conditions should be considered.

- TT&C enable

The TT&C links between satellites and ground stations or inter-satellites can be established based on matching of receiving/transmitting frequency, which is expressed as

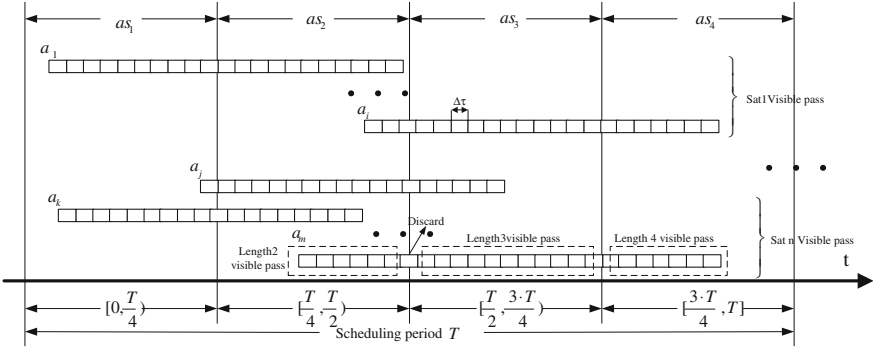


Fig. 6.3 Schematic diagram of visible pass pretreatment

$$C_1 = \{\forall a_i \in A, sF(aS_i) = rF(aR_i)\} \quad (6.10)$$

where, A is the TT&C pass set. sF is the set of TT&C frequency. rF is TT&C resource matched with TT&C frequency.

The switching time is needed between two TT&C task, which is expressed as

$$C_2 = \{\forall a_i, a_j \in A, \forall J_m, J_n \in J, \\ t_n^s - t_m^e \geq \Delta t \text{ or } t_m^s - t_n^e \geq \Delta t \\ \text{if}(x_{im} = 1) \wedge (x_{jn} = 1) \wedge (aR_i = aR_j)\}$$
(6.11)

where, J is the set of task. Δt is switching time between two TT&C task. t_j^s, t_j^e is starting time and ending time of task J_j .

- Exclusive TT&C resource

One TT&C resource can only support one satellite task at one moment, which is given as

$$C_3 = \{\forall a_i, a_j \in A, \forall J_m, J_n \in J, \\ x_{im} + x_{jn} \leq 1, \\ \text{if}(aR_i = aR_j) \wedge ([t_m^s, t_m^e] \cap [t_n^s, t_n^e] \neq \phi)\}$$
(6.12)

- TT&C time requirement

TT&C task should be finished in the TT&C time length, and the durative TT&C time is given as

$$C_4 = \{\forall a_i \in A, \forall J_j \in J, [t_j^s, t_j^e] \subseteq [aW_i^s, aW_i^e], \\ t_j^s - t_j^e \geq JD_j, \text{ if } x_{ij} = 1\}$$
(6.13)

- Elementary requirements

Every TT&C task can be finished only once. That is

$$C_5 = \left\{ \forall a_i \in A, \forall J_j \in J, \sum_{i=1}^{|A|} x_{ij} \leq 1 \right\} \quad (6.14)$$

The least TT&C times of every satellite should be supported during one scheduling period, which is given as

$$C_6 = \left\{ \forall a_i \in A, \forall J_j \in sJ_k, \sum_{j=1}^{|sJ_k|} \sum_{i=1}^{|A|} x_{ij} \geq sN_k \right\} \quad (6.15)$$

Step 4: Establishing hybrid integer programming model of satellite-ground TT&C united scheduling. The scheduling optimization function is depends on the number of successful scheduling, integrated priority and united task profitability. It can be given as

$$\begin{aligned} \max \quad & \sum_{|J|} \sum_{|A|} x_{ij} \cdot (aP_i + JP_j) + \sum_{|Co|} y_k \cdot CP_k \\ \text{s.t.} \quad & X = (x_{11}, x_{12}, \dots, x_{1|J|}, x_{21}, \dots, x_{|A||J|}); \\ & Y = (y_1, y_2, \dots, y_{|Co|}); \\ & x_{ij} \in \{0, 1\}, \forall x_{ij} \in X, \forall a_i \in A, \forall J_j \in J; \\ & y_k \in \{0, 1\}, \forall y_k \in Y; \\ & X \in C_1 \cap C_2 \cap C_3 \cap C_4 \cap C_5 \cap C_6; \end{aligned} \quad (6.16)$$

Figure 6.4 shows the schematic diagram of GA solution.

Step 5: Initialization algorithm parameters. The parameters include the scale of population N , crossover probability Pc , mutation probability Pm , the maximal iterative series Ger and setting iterative counter $k = 0$.

Step 6: To coding TT&C passes as_m , and generating initial population

$$X^m(0) = (X_1^m(0), X_2^m(0), \dots, X_N^m(0)) \in S^N$$

It is given as

$$X^i(k) = \begin{bmatrix} x_{11}^i(k) & x_{12}^i(k) & \dots & x_{1|as_i|}^i(k) \\ x_{21}^i(k) & x_{22}^i(k) & \dots & x_{2|as_i|}^i(k) \\ \dots & \dots & \dots & \dots \\ x_{N1}^i(k) & x_{N2}^i(k) & \dots & x_{N|as_i|}^i(k) \end{bmatrix}_{N \times |as_i|} \quad (6.17)$$

Step 7: The fine management strategy realization. The following expression will be get by means of choosing crossover, mutation and fine parameters.

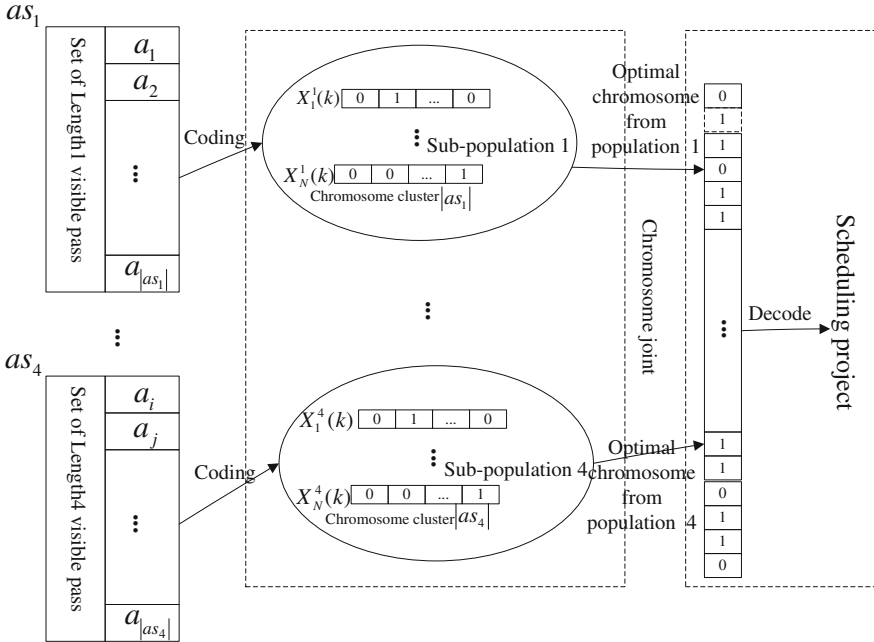


Fig. 6.4 Schematic diagram of algorithm solution

$$\begin{aligned}
 X^{m-new}(k) &= (T_S^i(T_C(T_m(X^m(k))))), i = 1, 2, \dots, N) \\
 &= (X_1^{m-new}(k), X_2^{m-new}(k), \dots, X_N^{m-new}(k))
 \end{aligned}$$

Step 8: To calculating the multiplicity and adaptive of new population and old population respectively: $\lambda(X^m(k))$, $\lambda(X^{m-new}(k))$, $F_S(X^m(k))$, $F_S(X^{m-new}(k))$.

Step 9: To realizing determinant strategy of population multiplicity. The adaptive population will be updated based on the determinant strategy. It is given as $X^m(k + 1)$.

Step 10: The TT&C scheduling project is generated or to set $k = k + 1$ after jointing optimal chromosome and decoding them. Then, the algorithm is backed to step 7.

6.4 Simulation and Results

6.4.1 Scenario Description

6.4.1.1 Space Segment

The space network is consisted of three orbital planes with eight satellites in each plane for a total of 24 MEO satellites. The satellites are in a circular orbit at

an altitude of approximately 20,000 km. The constellation satisfies Walker configuration. Three inter-satellite antennae are installed on each MEO satellite. The satellites of three intra orbital planes are represented by M_{1n} , M_{2n} and M_{3n} respectively.

Each satellite will establish links with two satellites on intra orbital plane and one satellite on inter orbital plane. The constellation is a global connectivity network, and each ISL used is the permanent link.

6.4.1.2 Ground Segment

The ground segment is consisted of four managing station, which is distributed in territory of China. The four ground TT&C stations are named as Northeast station, South station, Northwest station and midstation.

In order to satisfy the need of constellation management, Northeast station and South station are assumed possess of two facilities.

6.4.2 Input Condition

Assumption: the data transmission bandwidth of satellite-ground link is 40 kHz, the telemetry data rate of mono-satellite is about 10 kbps, the data rate of ISLs is about 5 kbps (Where, the telemetry data rate of node satellite is about 1000 bps, the data rate of payload and ISL is about 4000 bps). According to (6.9) and (6.10) and considering margin, we have, $N_{member} \approx 3-6$, $N_{cluster} \approx 5$.

6.4.3 Parameter Setting

Let's population scale $N = 50$, the maximal iterative series $Ger = 2000$, crossover probability $Pc = 0.65$, mutation probability $Pm = 0.08$, fine sample $m = 4$, importance of population multiplicity $\alpha = 1$.

6.4.4 Results Analysis

In order to validate the validity of proposed strategy, three kinds of GA are used to compare the scheduling performance. They are GA1 (traditional GA + essence preserving strategy), GA2 (GA1 + fine choosing strategy) and GA3 (GA2 + adaptive population evolution strategy).

Table 6.1 Scheduling result of ground based TT&C resource

Algorithm	Task period (min)	Task num.	Scheduling rate (%)	Optimization function
GA1	30	672	75.00	72.00
GA2			79.17	76.00
GA3			81.25	78.00

Table 6.2 United scheduling result of satellite-ground resource

Algorithm	Task period (min)	Task num	Scheduling rate (%)	Optimization function
GA1	30	8064	100	80.50
GA2			100	81.70
GA3			100	82.35

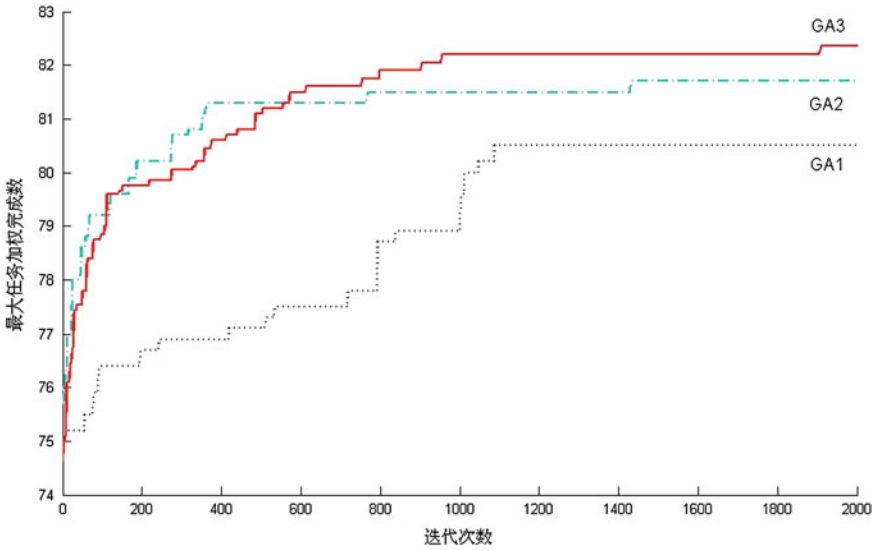


Fig. 6.5 Performance curve of genetic algorithm

Table 6.1 shows the scheduling results used only ground-based resource. Table 6.2 shows the united scheduling results used satellite-ground resource. Figure 6.5 shows the search optimization performance of three algorithm.

To compare Table 6.1 with Table 6.2, we can obtain the results that scheduling rate is improved to 100 % with method of satellite-ground TT&C resource, and the perfect search optimization performance can be obtained with GA3.

6.5 Conclusion

A satellite-ground TT&C united scheduling methods of GNSS constellation based on nodes constraint tion is proposed in this paper. The characteristics of scheduling algorithm are combine satellite network with ground TT&C station to make united scheduling. The typical constellation composed of 24 MEO satellites are considered as a researching object, and the seven days simulation are experimented. The results show that the algorithm can save the ground TT&C resource effectively, and manage the satellite network incessantly.

Acknowledgments The author would like to extend sincere gratitude to iGMAS for the observation data downloaded from its website <http://www.igmas.org>.

References

1. Arbabi M, Garate JA (1985) Interactive real time scheduling and control. In: Proceedings of the 1985 summer simulation conference, Chicago, pp 271–277
2. Gooley TD (1993) Automating the satellite range scheduling process. Master thesis, Air Force Institute of Technology, Ohio
3. Schalck SM (1993) Automating satellite range scheduling. Master thesis, Air Force Institute of Technology, Ohio
4. Pemberton JC, Greenwald LG (2002) On the need for dynamic scheduling of imaging satellites. In: Pecora 15/land satellite information IV/ISRRS commission I/FIEOS 2002 conference proceedings, Denver, 2002
5. He R, Tan Y (2004) Apply constraint satisfaction to optimal allocation of satellite ground station resource. *Comput Eng Appl* 40(18):229–232
6. Liu Y, He R, Tan Y (2004) Modeling the scheduling problem of multi-satellites based on the constraint satisfaction. *Syst Eng Electron* 26(8):1076–1079
7. Marinelli F, Nocella S, Rossi F et al (2005) A Lagrangian heuristic for satellite range scheduling with resource constraints. JPL technical report. <http://www.optimizationonline.org>
8. Huilin W, Dishan Q (2010) Research on electro-magnetic detection satellites scheduling based on greedy preprocessing strategy. In: International conference on electronics and information engineering (ICEIE 2010), pp V449–V453
9. Adinolfi M, Cestari A (1995) Heuristic scheduling of the DRS communication system. *Eng Appl Artif Intell* 8(2):147–156
10. Fang Y, Chen Y (2005) CSP model of the relay satellite scheduling. *J Nat Univ Defense Technol* 27(2):6–10
11. Cui Z (2009) Research on scheduling approach of relay satellites. National University of Defense Technology
12. Zhang T, Li J (2013) An algorithm research of ground-space integrated scheduling TT&C resources of orbit determination of GNSS constellation. In: 4th International conference on intelligent systems design and engineering application, pp 69–73
13. Zhang T (2014) Research on intelligent optimization methods of the ground-space integrated TT&C resource scheduling problem. Xi'an Jiaotong University, Xi'an

Chapter 7

Realization of Real Time Kinematic Positioning Software Based on Kalman Filter

Dangwei Wang and Yi Lai

Abstract As an important optimization estimation theory, Kalman filter is applied to deal with many kinds of dynamic data, especially for GPS data and inertial navigation data. In this paper, the Kalman filter is used to solve the two key problems-integer ambiguity calculation and cycle slip detection and correction, and then a real time kinematic (RTK) positioning technique based on Kalman filter is proposed. The experimental results show that the presented method can obtain the positioning accuracy of RTK up to centimeter for data format in GPS.

Keywords RTK · Kalman filter

7.1 Introduction

Real time kinematic (RTK) is the positioning technique that can provide user real-time position with high precise. RTK have many virtues, such as high precision, real-time and high reliability. Therefore it gets more and more attention. The technology can be widely applied in many fields, e.g. military, agriculture, architecture and engineering measure. For example, this technology can obtain the positioning accuracy up to centimeter when it is applied to measure the position of ownership boundary point and correlative feature points. The basic idea of RTK positioning technique [1, 2]: base station receiver and rover one synchronously observe the common view satellites, and then the ambiguity fast resolution technique is employed to satellite carrier signal to get the initial value of integer ambiguity. Displacement and instantaneous position that rover station produces for holding movement status during the procession of initialization can be calculated by integer ambiguity based on the converse computation technology.

D. Wang (✉) · Y. Lai
The 20th Research Institute of CETC, Xian 710068, China
e-mail: wangdw629@163.com

© Springer-Verlag Berlin Heidelberg 2015
J. Sun et al. (eds.), *China Satellite Navigation Conference (CSNC) 2015 Proceedings: Volume I*, Lecture Notes in Electrical Engineering 340,
DOI 10.1007/978-3-662-46638-4_7

The key problem of RTK positioning technique is to obtain correct carrier phase integer ambiguity quickly. Carrier phase measurement is similar to high precise pseudorange measurement after ambiguity is derived [3]. Cycle slip detection and correction is another important problem of high precise real-time kinematic positioning system. It is necessary that cycle slip should not appear in carrier phase if high precise positioning can be realized based on carrier phase.

Kalman filter is one of filter technologies that appeared at 1960s. As an optimal estimation method, Kalman filter becomes increasingly significant in many application fields, such as communication and global satellite navigation [4]. The main idea of Kalman filter algorithm is to construct one time status equation and another dynamic observation one, and coefficient matrix can be obtained by searching and comparing predictive value and the true one, and then ambiguity can be obtained and fixed after the matrix is substituted into the model.

In this paper, Kalman filter is applied to deal with the key problems of high precise relative position calculation—integer ambiguity resolution and cycle slip detection and correction, and then high precise real-time kinematic positioning algorithm is obtained. Experimental results show that the developed method can obtain the positioning accuracy of RTK up to centimeter for data format in GPS.

7.2 Realization of Real Time Kinematic Positioning Software

7.2.1 Basic Processing Flow

Based on the observation data provided by satellite navigation receivers, the real-time kinematic positioning software based on Kalman filter can obtain the following information, such as position, time, velocity, and length of baseline by four main steps: input data resolution, single point positioning, double stations positioning, and data output. This process can be illustrated in Fig. 7.1. RTK is the main part of the software flowchart, and carrier slip detection and correction, float point

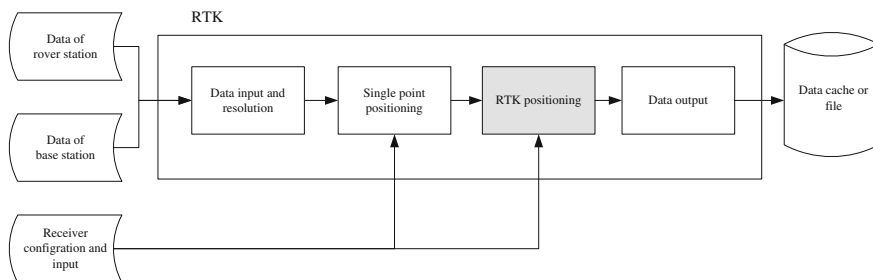


Fig. 7.1 Flow chart of real time kinematic positioning system

solution and integer one can be finished in this part. Input data resolution and data output are the interface between this software and other parts of the discussed system. Single point positioning can provide RTK data input by dealing with cursory coordinate and velocity based on single station observation data.

7.2.2 Software Module

Based on functions of the above described 4 main steps and basic calculation function, the presented software can be divided into 7 modules, as illustrated in Fig. 7.2.

The four modules including data input and resolution, single point position, RTK algorithm and data output correspond to four basic steps of data processing,

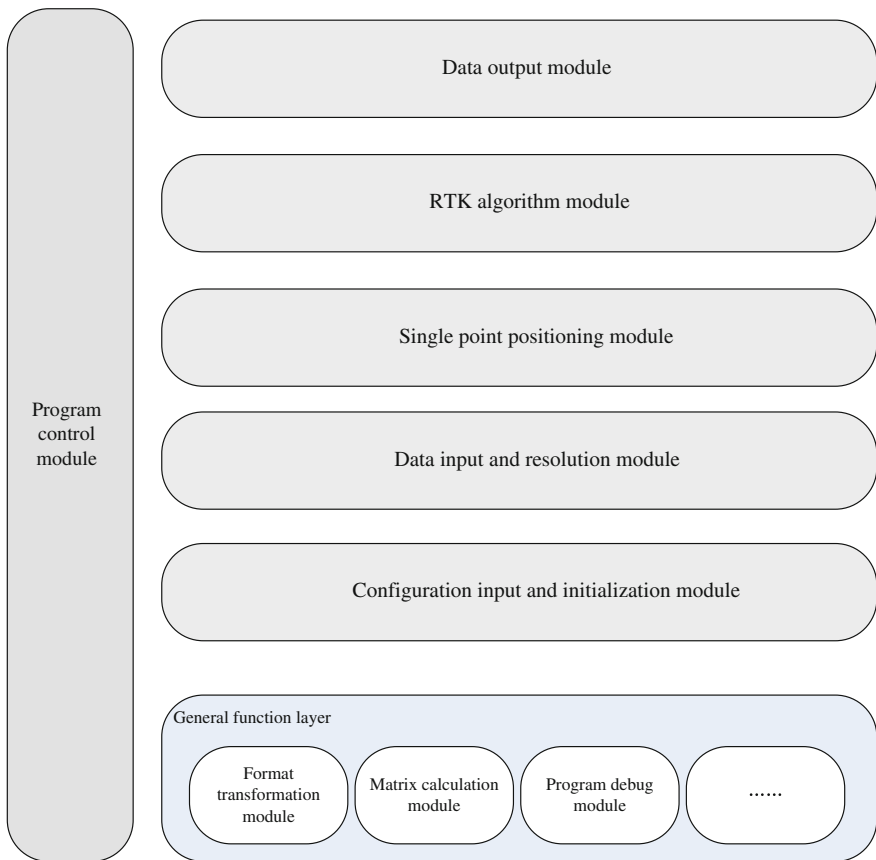


Fig. 7.2 Components of software module

respectively. Configuration input and initialization module can realize initialization for different receiver configuration and input condition (includes position mode). General function module includes matrix calculation function, general model definition and coordinate time transformation function, which are necessary for RTK resolution.

Program flow control module is a main entrance of software and controls the main execution process of the program, and can finish selection and calling for module based on initial configuration.

7.2.2.1 General Function Module

The general function module mainly provides general functions that other modules need and basic functions etc. This module includes several sub-modules, e.g. matrix initialization, matrix inverse, matrix multiplication and matrix transpose etc., these arithmetic functions belongs to matrix calculation function; math functions including least squares and Kalman filter functions; time format conversion and coordinate system format conversion functions; character procession including character read and setting and parity bit calculation function. Besides, this module also includes different data types, e.g. character string, time and integer conversion function; satellite number and navigation system conversion function. Because the software mainly runs on the CMOS chips and running status and results of program is debugged difficultly, debug output module of program mainly includes daily records and intermediate results output that the program produces when it runs. This module has no effect on the whole data resolution flow, but it is the base of other module operation.

7.2.2.2 Configuration Input and Initialization Module

The configuration input and initialization module realizes initialization configuration for multiple kinds of data and data structure that resolution procession needs. The module includes the selected ionosphere and troposphere module, the adopted calculation methods, positioning mode (still, kinematic, rover base station etc.), phase center of antenna, the parameters of ionosphere and troposphere etc.

7.2.2.3 Data Input and Resolution Module

The data input and resolution module is the main interface between the software and the input data. The module has the similar operations for base station to rover station. The module can be divided into the following sub-modules, data input, temporary storage, data head determinant, observation data or ephemeris data analysis, structure assignment, and the optional double station data time calibration etc.

7.2.2.4 Single Point Positioning Module

The single point positioning module can get the cursory result of single point positioning using the iterative weighted least squares estimation methods based on the input base station or rover one observation data and ephemeris data. As shown in Fig. 7.3, this module can be mainly divided into multiple sub-modules, e.g. satellite position calculation, residuals calculation, ionosphere module modification, troposphere module modification, positioning resolution, positioning result verification, RAIM verification etc. The proposed algorithm reads data of each epoch every time, and can get the cursory coordinate (velocity) value of base station or rover one by many times iteration. Different calculation formula and input variable (e.g. status vector, residuals calculation method, and weight matrix selection etc.) can be used in calculation module based on the selected different calculation methods or positioning mode.

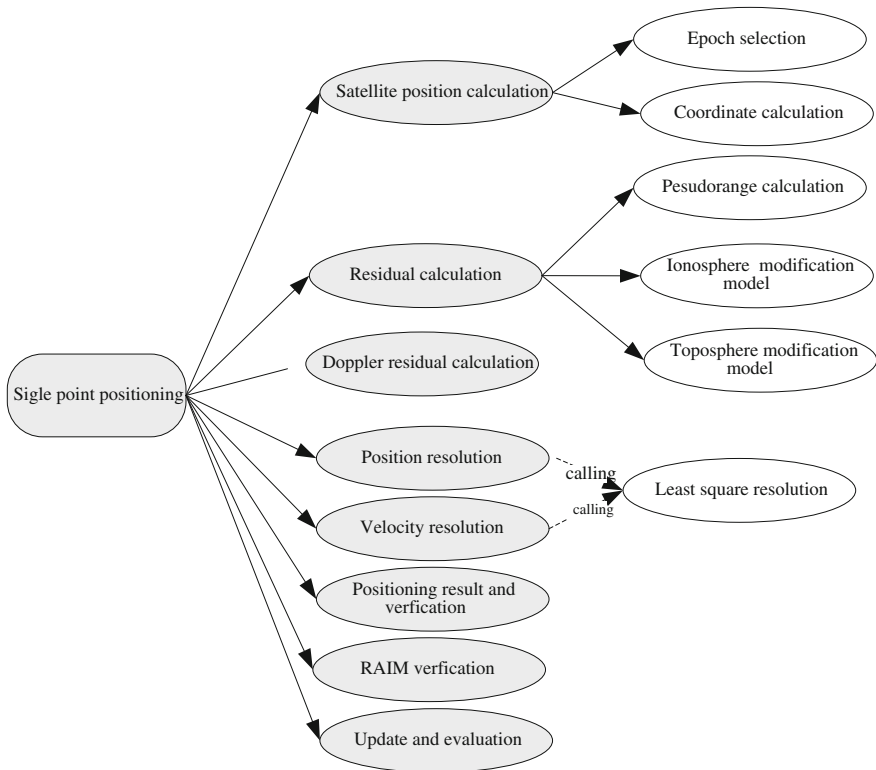


Fig. 7.3 Module of point positioning

7.2.2.5 RTK Module

The RTK Module is a core module of the proposed software. This module mainly includes cycle slip detection and double station data real-time position calculation functions etc. As shown in Fig. 7.4, the module can be divided into multiple modules, including cycle slip detection and determination, common satellite selection, residual calculation, double difference calculation, resolution of float point solution, resolution of integer solution, update of solution status, and verification of positioning results.

The RTK algorithm derives the float point solution and integer one using Kalman filter based on different frequency of input observation data.

This paper achieves N value float point solution of each satellite by Kalman filter, and obtains the corresponding integer solution using LAMBDA [2] algorithm. Because Kalman filter is one of iterative predictive correction methods, the presented algorithm obtains status variables as initial status variable of this epoch using last epoch (or single point positioning). For the addressed RTK algorithm, observation data of each epoch experiences common satellites selection, residual and double difference calculation, float point solution, and integer solution etc. The

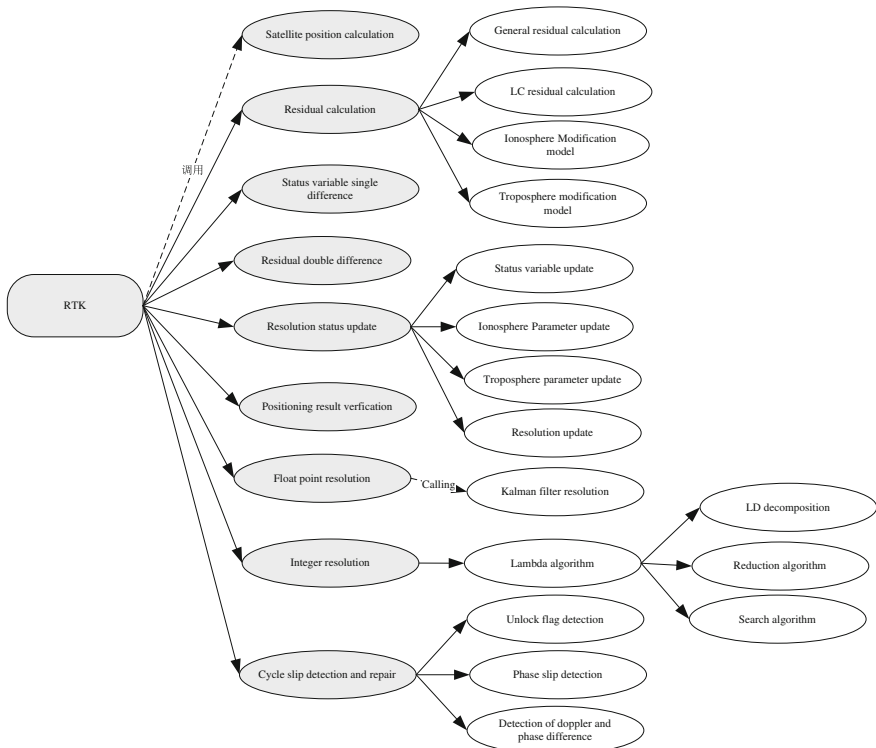


Fig. 7.4 Module of RTK

process of calculation of satellite position and clock difference is similar to single point positioning, but the other steps are complicated.

(1) Status variable initialization and update of solution. The scheme conducts iteration operation using output of last epoch and data of current one in order to get the input of next epoch. Status variables are selected as follows. Status variable $x = \{r, v, N\}$, r denotes position coordinate vector of rover station receiver, v indicates velocity vector of rover station receiver, N represents deviation value of carrier phase of each common satellite at each frequency. For the presented algorithm, N value can be obtained from single difference between base station and rover station. Observation variable $y = \{\phi, p\}$, ϕ denotes double difference of carrier phase at each frequency, p represents pseudorange double difference (double difference between stations and satellites) at each frequency. Definition of status variable of base station is similar to rover station, the difference of them is that vector of base station need not define N vector. Under the circumstance of still base station, position of base station can be obtained from input, and for rover base station, position of base station can be samely obtained from single point positioning.

(2) Residual calculation. In order that the iteration is conducted using Kalman filter, residual between observation variable y and status variable x prediction value should be achieved. Therefore this sub-module can be applied to calculate the residuals v between observation data and status variable prediction data. Calculation process of base station is similar to rover station, but the base station employs different status variable data. After calculation of residuals is finished, the influence of troposphere and satellite clock are removed but the influence of ionosphere and receiver clock are not considered because double difference operation is needed to eliminate partial errors.

(3) Double difference calculation. To eliminate error items, e.g. the influence of ionosphere and receiver clock, double difference operation is needed to do for observation vector. This step mainly includes double difference operation of observation vector residual, operation of control matrix H , R and variation matrix P . under the different positioning mode, compose structure of control matrix and observation vector may be changed.

(4) Resolution of float point solution and integer solution. The integer solution can be calculated using the generated residual matrix, control matrix, status vector, and N vector based on status variables of current epoch calculated by Kalman filter. Before integer solution is derived, the difference operation between satellites should be conducted to get double difference in order to eliminate initial phase value of receiver.

After this step is completed, the step1-update operation of status variable is repeatedly conducted when the next epoch starts.

This method has no demand of number of frequency. Hence, the scheme is applied not only to double frequency data, but also to three frequency data. At the same time, the approach employs carrier phase data and pseudorange data. Therefore, the way can be used to carrier phase difference and code difference

operation. However, the size of matrix used by the algorithm is very large, so LAMBDA approach is needed to do integer solution search operation.

7.2.2.6 Data Output Module

This module mainly outputs partial variables and resolution results which are produced in the resolution process. Therefore its function is simple. The output variables include current epoch time, positioning result mode, and corresponding position, velocity vector (including single point solution, float point solution, and integer solution etc.), N value float point solution, N value integer solution, receiver clock difference, residuals between solution and observation value, elevation angle of satellite, SNR value, and unlock mark etc.

7.3 Experimental Results and Analysis

To verify the performance of the proposed RTK software, the experiments are conducted for the recorded two different classes of GPS data. And then the obtained experimental results are compared with the true value. The time interval of epoch is 1 s, and the threshold of ratio is 3.

In this experiment, two NovAtel receiver boards with double frequency is applied to record test data of GPS. The type of base station receiver is FLEXPAK-OEMV-6, and the type of rover station receiver is OEMV-IDF-RT6. The two receivers employ double frequency antenna which type is GPS-702-GG. To verify the overall performance of the presented algorithm, two classes GPS data are recorded. One is recorded under the circumstance that the length of baseline is 14.575 m for still station to still one, the other is done for still station to rover one.

The experimental results for still station to still one are depicted in Fig. 7.5. The abscissa denotes the number of epoch of resolution the baseline, and the ordinate represents the corresponding difference between of the baseline and the real one. The average length of the obtained baseline is 14.575 m, and the variance is 0.0031 m.

The test results for still station to rover one are depicted in Fig. 7.6. The abscissa denotes the number of epoch of resolution the baseline, and the ordinate represents the length of baseline from the rover station to base one. As shown in Fig. 7.6, the change of coordinates reflects the length of the baseline from base station to rover one.

As illustrated in Figs. 7.5 and 7.6, the experimental results demonstrate the stabilization of the length of baseline is satisfied. The error is about 2 cm, and it can meet the basic measurement requirements. The positioning precise of carrier phase can be high theoretically. However, the flutter of the observation value of carrier phase may result in increasing the positioning error because of the measurement error and the effect of multi path.

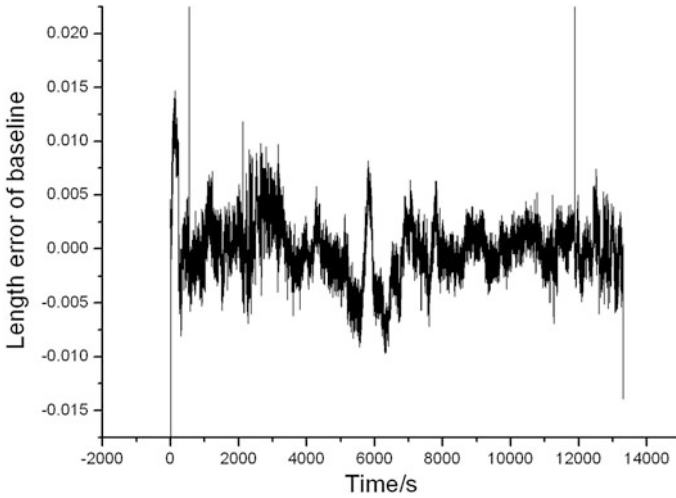


Fig. 7.5 Baseline error for static to static data

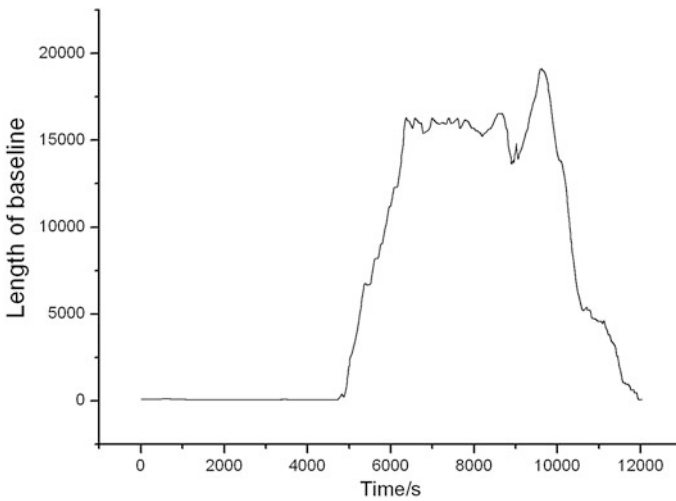


Fig. 7.6 Baseline length for static to kinematic data

7.4 Conclusions

A RTK algorithm process flow is proposed in this paper. The proposed scheme realizes integer ambiguity resolution and cycle slip detection and correction based on the advantage of Kalman filter that is suitable to deal with dynamic data. The experimental results show that the presented method can obtain the positioning

accuracy of RTK up to centimeter for data format in GPS. In the future, the processing procedure of the algorithm should be improved and the reliability of the RTK system should be enhanced.

References

1. Teunissen PJG, de Jonge PJ, iberius CJM (1994) On the spectrum of the GPS DD-ambiguities. In: Proceedings of ION GPS-94, 7th international technical meeting of the satellite, division of the institute of navigation [C], Salt Lake City, UT, pp 115–124
2. Teunissen PJG (1995) The least-squares ambiguity decorrelation adjustment: a method for fast GPS integer ambiguity estimation [J]. *J Geodesy* 70:65–82
3. Xu SQ et al (2001) GPS global position system and its application [M]. Wuhan University of Science and Technology, Wuhan
4. Grewal MS, Andrews AP (2008) Kalman filtering-theory and practice using MATLAB[M]. Wiley, New York, pp 31–120

Chapter 8

Analysis of BeiDou Satellite Orbit Prediction Based on ERP Prediction Errors Impact

Xiusong Ye, Hai Guo, Jie Yang, Chao Li and Canyou Liu

Abstract According to the real-time positioning of BeiDou navigation satellite. Analysis Center (AC) was necessary to develop Earth Rotation Parameters (ERP) products based on autoregressive integrated moving average (ARIMA) mode, then, it necessary to transform the BeiDou navigation satellite ephemeris of Inertial System to the Earth Solid System according to the ERP prediction products. For MEO, IGSO and GEO, the development of ERP products of AC calculated the BeiDou navigation satellite orbit error was less than 50 cm based on the ERP product of Earth Rotation Service System (IERS) forecast for 30 days in the Earth Solid System orbit as a true value, which indicated that the ERP prediction error impacted the Earth Solid System precise ephemeris calculation accuracy, and indicated AC ERP prediction results with IERS products fairly.

Keywords Earth rotation parameters prediction · Auto-regressive moving average model · Beidou navigation · Precise ephemeris · Orbit error

8.1 Introduction

For the BeiDou Satellite navigation, the satellite ephemeris in the Earth Centered Earth Fixed (ECEF) frame are needed in the navigation computation. The extrapolated precise orbit in the inertial frame is accomplished by the master station. Then the orbit in the inertial frame is transformed to that in the ECEF frame. Thus, the satellite ephemeris can be fitted and are then send to be the users. During the transformation between the inertial frame and ECEF frame, the Earth Rotation Parameters (ERP) are critical and its prediction errors has great effects on the transform accuracy and orbit accuracy. This paper focuses on the ERP prediction accuracy of iGMAS (International GNSS Monitoring and Assessment System)

X. Ye (✉) · H. Guo · J. Yang · C. Li · C. Liu
State Key Laboratory of Astronautic Dynamics, Xi'an 710043, China
e-mail: xiusongye@163.com

© Springer-Verlag Berlin Heidelberg 2015
J. Sun et al. (eds.), *China Satellite Navigation Conference (CSNC) 2015 Proceedings: Volume I*, Lecture Notes in Electrical Engineering 340,
DOI 10.1007/978-3-662-46638-4_8

Analysis Center and IERS rapid Bulletin A. Then the effects of ERP prediction errors on the orbit prediction accuracy is analyzed.

8.1.1 ERP Forecast Method

In general, the precession and nutation can be accurately predicted for a long time, such as IAU2000 model with the prediction error less than 0.2 mas. For the GPS satellite, the orbit error is about 2.6 cm without the precession and nutation error. And the orbit error is about 4 cm for the GEO satellite. For the broadcast ephemeris, the predicted orbit error caused by the precession and nutation model error can be acceptable [1]. However, the polar parameters (X_p and Y_p) and LOD (Length of Day) can be hardly predicted accurately for the complexity of Earth rotation. Therefore, this paper puts great efforts on the effects of ERP prediction errors on the BeiDou Satellite orbit prediction accuracy.

The ARIMA (Autoregressive Integrated Moving Average) model is usually utilized in the short-term ERP prediction. First, the periodic and trend components are exacted in the ERP original date sequence to obtain a random process with the normal distribution. Second, the ARIMA-based prediction method see [2, 3] can be effectively implemented as the prediction flow in Fig. 8.1. The historical ERP data sequence issued by the IERS is utilized in the prediction computation. The 30-day ERP prediction results is shown in Fig. 8.2 and Table 8.1. The x -axis polar motion component error is 0.362 mas and 0.264 mas for the y -axis component. The LOD prediction error is about 0.036 ms. The 1-day ERP prediction accuracy computed by Analysis Center, which is compared with IERS bulletin A, is illustrated in Figs. 8.3 and 8.4. The maximum prediction error of polar motion in 1 day is about 0.015 mas and the maximum prediction error of LOD is about 0.01 ms.

8.2 Effects of ERP Prediction Error on Orbit Prediction

The ERP prediction error has no effects on the orbit extrapolation in the inertial frame. The position error is mainly caused by the transform error of the extrapolated orbit from the inertial frame to the ECEF.

The following error test is accomplished. First, the initial ephemeris of GEO, MEO and IGSO satellites in the inertial frame are computed by the XSCC Precise Orbit Determination software. Second, the prediction ephemeris are transformed from the inertial frame to the ECEF by use of the predicted ERP issued respectively by the Analysis Centre and IERS. Third, the orbit prediction error caused by the ERP prediction error can be evaluated as the error between the above two sets of ephemeris in the ECEF.

Firstly, the effects of 1-day ERP prediction error on the MEO orbit prediction accuracy in 1 day is illustrated in Fig. 8.5(a-h). The RMS of total position error is

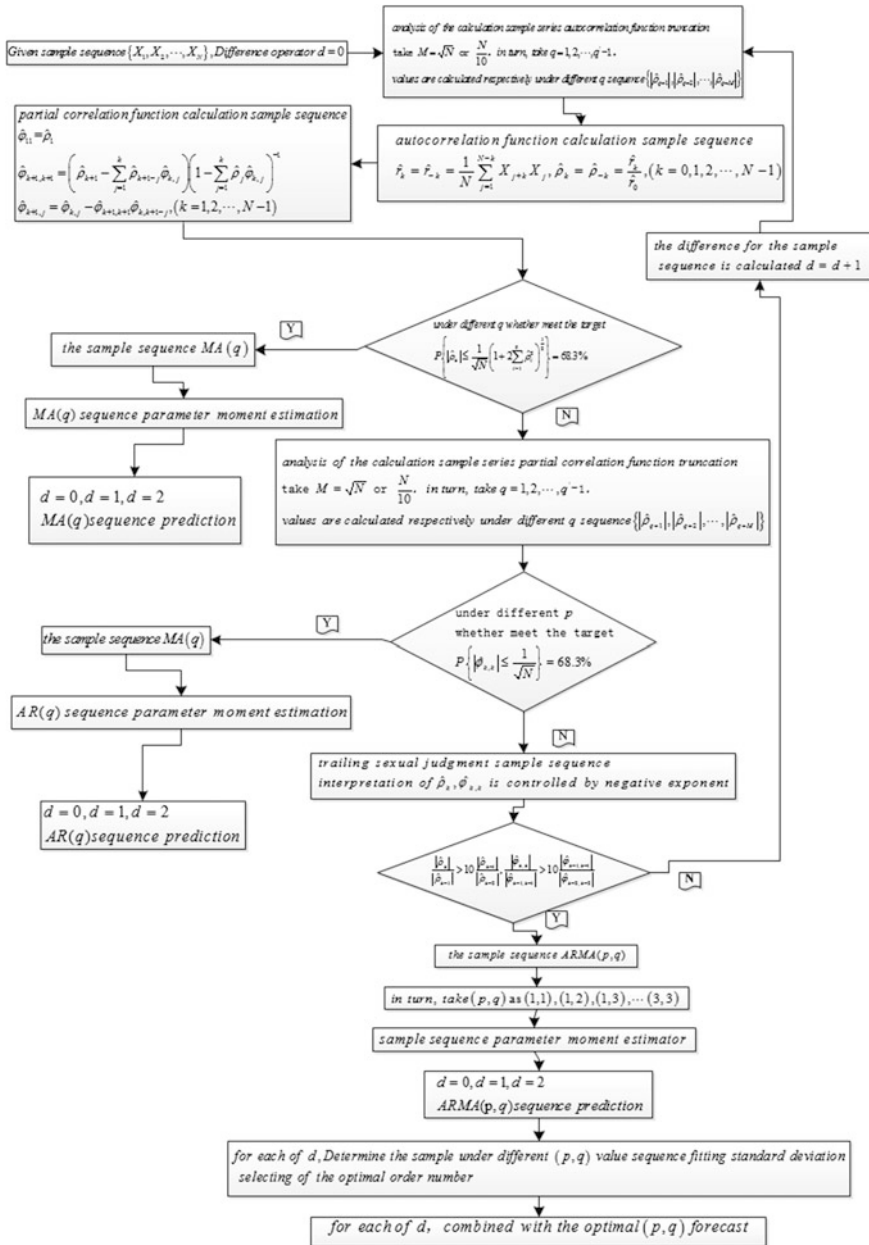


Fig. 8.1 ARIM algorithm process

between 5 and 30 cm and the maximum error is between 10 and 40 cm. The RMS of and x-axis position error is between 3 and 21 cm. The maximum of x-axis position error is between 5 and 40 cm. The RMS of and y-axis position error is

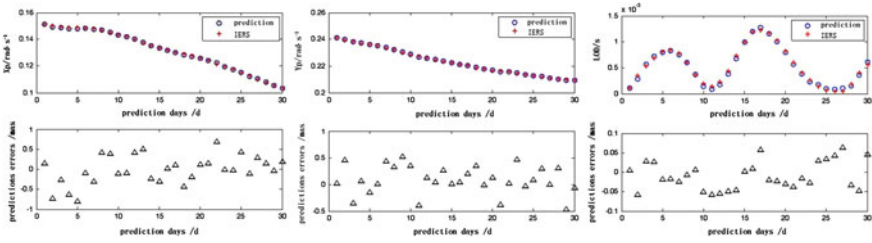


Fig. 8.2 AC 30 day ERP forecast results compared with the IERS

Table 8.1 AC ERP forecast error statistics of 30 day

Statistics	X_p /mas	Y_p /mas	LOD/ms
min	-0.801	-0.464	-0.05719
max	0.697	0.525	0.06481
average	-0.004	0.095	-0.00790
standard deviation	0.362	0.264	0.03623

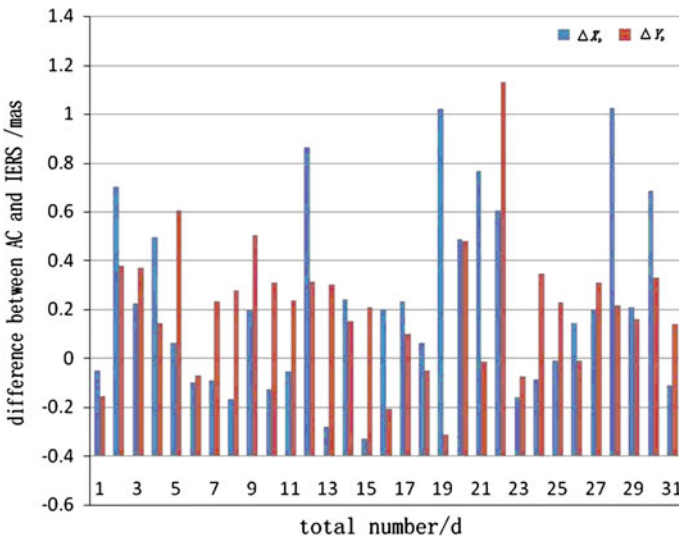


Fig. 8.3 The comparison results of between AC X_p , Y_p parameters forecast the results of 1 day and IERS

between 2 and 20 cm. The maximum of y-axis position error is between 3 and 35 cm. The RMS of and z-axis position error is between 1 and 8 cm. The maximum of z-axis position error is between 1 and 14 cm.

Secondly, the effects of 1-day ERP prediction error on the GEO orbit prediction accuracy in 1 day is illustrated in Table 8.2. The RMS of total position error is between 13 and 35 cm and the maximum error is between 2 and 42 cm. The RMS

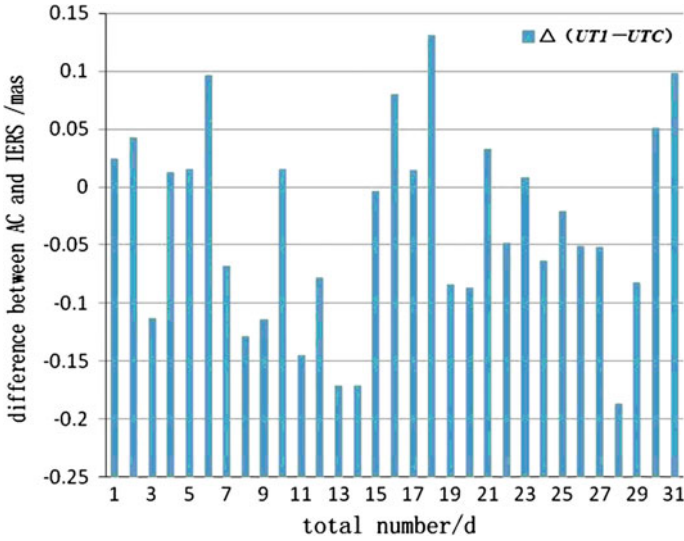


Fig. 8.4 The comparison results of between AC UT1-UTC parameter forecast the results of 1 day and IERS communique released A

of and x -axis position error is between 2 and 25 cm. The maximum of x -axis position error is between 4 and 40 cm. The RMS of and y -axis position error is between 5 and 35 cm. The maximum of y -axis position error is between 7 and 40 cm. The RMS of and z -axis position error is between 1 and 11 cm. The maximum of z -axis position error is between 1 and 20 cm.

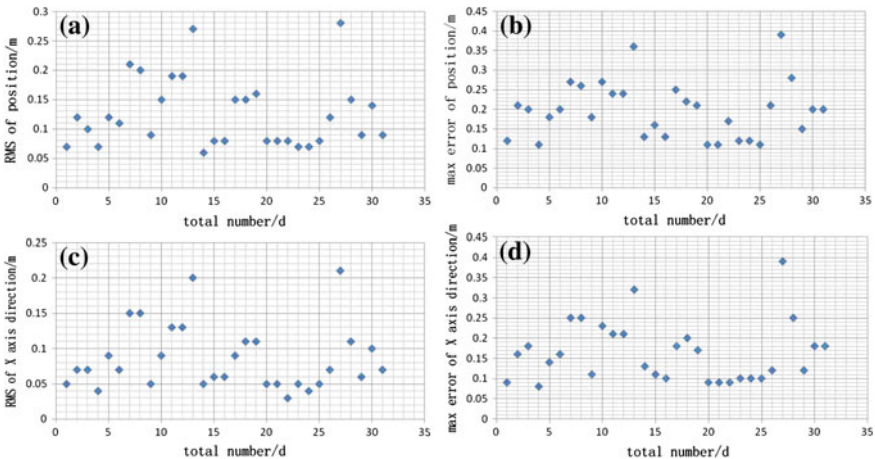


Fig. 8.5 One day the ERP forecast error of MEO satellite orbit forecast the influence of the 1 day. **a** RMS distribution of the position. **b** Max error distribution of the position. **c** RMS distribution of the X axis. **d** Max error distribution of the X axis direction. **e** RMS distribution of the Y axis direction. **f** Max error distribution of the Y axis direction. **g** RMS distribution of the Z axis direction. **h** Max error distribution of the Y axis direction

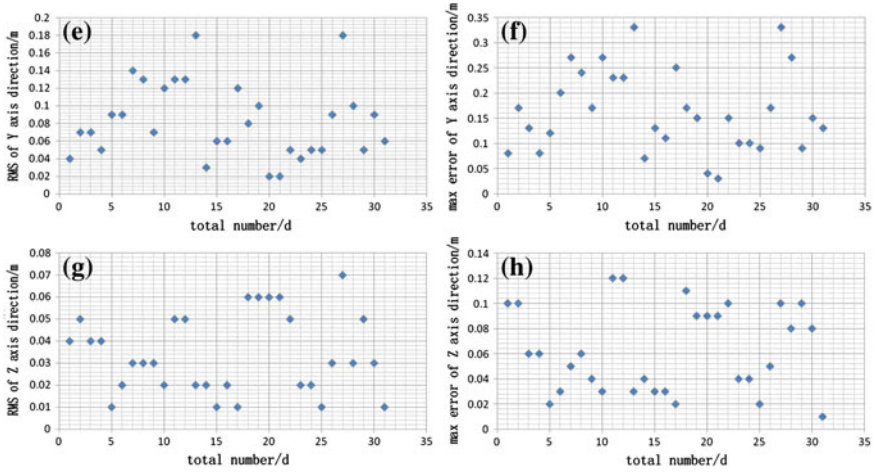


Fig. 8.5 (continued)

Table 8.2 ERP prediction error effect on GEO orbit prediction (10 samples)

Total Position/m		X/m		Y/m		Z/m	
rms	max	rms	max	rms	max	rms	max
0.17	0.29	0.09	0.18	0.11	0.21	0.09	0.11
0.23	0.38	0.15	0.24	0.18	0.29	0.03	0.05
0.25	0.31	0.16	0.20	0.19	0.23	0.08	0.14
0.23	0.42	0.21	0.39	0.08	0.15	0.05	0.05
0.16	0.20	0.14	0.18	0.05	0.07	0.05	0.06
0.34	0.38	0.12	0.13	0.32	0.36	0.05	0.07
0.19	0.35	0.06	0.12	0.18	0.32	0.04	0.07
0.13	0.23	0.02	0.04	0.07	0.12	0.11	0.20
0.24	0.28	0.20	0.24	0.12	0.15	0.03	0.06
0.13	0.23	0.02	0.04	0.07	0.12	0.11	0.20

Table 8.3 ERP prediction error effect on IGSO orbit prediction (5 samples)

Total Position/m		X/m		Y/m		Z/m	
rms	max	rms	max	rms	max	rms	max
0.16	0.22	0.14	0.18	0.09	0.15	0.01	0.02
0.14	0.25	0.12	0.21	0.07	0.15	0.01	0.01
0.17	0.26	0.16	0.26	0.05	0.11	0.04	0.06
0.11	0.17	0.11	0.17	0.02	0.03	0.01	0.02
0.21	0.28	0.19	0.28	0.05	0.09	0.05	0.08

Lastly, the effects of 1-day ERP prediction error on the IGSO orbit prediction accuracy in 1 day is illustrated in Table 8.3. The RMS of total position error is between 2 and 20 cm and the maximum error is between 15 and 30 cm. The RMS of and x -axis position error is between 10 and 20 cm. The maximum of x -axis position error is between 20 and 30 cm. The RMS of and y -axis position error is between 2 and 10 cm. The maximum of y -axis position error is between 3 and 15 cm. The RMS of and z -axis position error is between 1 and 5 cm. The maximum of z -axis position error is between 1 and 10 cm.

8.3 Conclusion

The predicted Earth Rotation Parameters are needed in the transform of GNSS precise orbit from the inertial frame to the ECEF. Thus the ERP prediction error can lead to the transform error and orbit error between two different frames. This paper analyzes the effects of ERP error between the analysis centre and the IERS bulletin A on the orbit prediction accuracy. Then the following conclusions can be yielded.

- (1) For the MEO satellite, the maximum orbit position error in 1 day caused by the 1-day ERP prediction error is between 10 and 40 cm.
- (2) For the GEO satellite, the maximum orbit position error in 1 day caused by the 1-day ERP prediction error is between 2 and 42 cm.
- (3) For the IGSO satellite, the maximum orbit position error in 1 day caused by the 1-day ERP prediction error is between 15 and 30 cm.

The analysis results indicate that the x -axis and y -axis position errors is more obvious than that in the z -axis direction. The prediction errors of Y_p and UT1-UTC are related with the x -axis position error. Similarly, the y -axis position error is caused by the prediction errors of X_p and UT1-UTC. But the z -axis position error is mainly determined by the prediction errors of X_p and Y_p . Thus, the prediction error of UT1-UTC has more great effects on the orbit position accuracy than that of X_p and Y_p . Consequently, the ERP prediction error cannot be omitted in the orbit prediction.

References

1. Wenming L (2009) Track generalized coordinate system conversion of navigation satellite precise orbit determination of impact analysis. National University of Defense Technology, College of Electronic Science and Engineering, Department of Information and Communication Engineering, Changsha, pp 26–32
2. Xiusong Y, Yufan H, Guang Z et al (2014) Using autoregressive moving average model of earth rotation parameters of short-term prediction. *J Navig Position* 2(3):6–9
3. Niedzielski T, Kosek W (2008) Prediction of UT1-UTC, LOD and AAM χ_3 by combination of least-squares and multivariate stochastic methods. *J Geodesy* 82(2):83–92

Chapter 9

The Repeatability Test of BDS Baseline Processing

Yanguo Liu, Jinzhong Bei, Dehai Li, Hu Wang and Xiaying Wang

Abstract BeiDou Navigation System (BDS) has already covered all areas in our country. Getting high precision positioning results becomes hot topic in the research of BDS. This paper calculates parts of BDS baseline observation data from Hebei Province, and the results indicate the BDS system is stable, the external compliance precision of plane is within 1 cm, and the precision of elevation is about 4 cm, meeting the requirements of the precision of the control network of national grade B, the differences of precision for the same baseline results is limited in 5 mm, and the unit weight variance value and RMS error precision indicators also meet the specification requirements.

Keywords BeiDou navigation satellite system (BDS) · Baseline processing · Repeatability test · Precision evaluation

9.1 Introduction

BeiDou Navigation Satellite System is the global Satellite Navigation System developed by China independently. Now, The BDS system has to cover the Asia-pacific region of positioning, navigation, timing as well as the short message communication service ability, and it will cover the global region by 2020 or so [1]. The current method of baseline processing using carrier phase difference method for solving high-precision point coordinates is the most widely used method [2]. Many scholars are researching this topic at present, Yang et al. has assessed the navigation

Y. Liu (✉) · J. Bei · D. Li · H. Wang
China Academy of Surveying and Mapping, Beijing, China
e-mail: liuyanguo0@163.com

X. Wang
Chang'an University, Xi'an, China

© Springer-Verlag Berlin Heidelberg 2015
J. Sun et al. (eds.), *China Satellite Navigation Conference (CSNC) 2015 Proceedings: Volume I*, Lecture Notes in Electrical Engineering 340,
DOI 10.1007/978-3-662-46638-4_9

and positioning ability of BeiDou system, the result shows that the precision of carrier phase differential of BeiDou system is equal to GPS [3]. Tang et al. has proved that the success rate of single epoch ambiguity resolution of short baseline of BeiDou system reaches 80 %, and the preliminary results is close to GPS [4]. It is confirmed that fixed carrier phase difference can obtain higher accuracy by Huang et al. [5]. The study by Chuang Shi on precision orbit determination and positioning of BDS indicates that the current positioning precision of BeiDou system has reached millimeter level [6].

It should make quality analysis after baseline processing. This paper contains the abnormal detecting of baseline vector, the accuracy analysis and the repeatability test of the results by calculating several days' BDS data.

9.2 The Principle of Baseline Processing

BDS observation data including 3 frequency phase and pseudo range measurements, which contains orbit error, clock error, atmospheric delay etc. Usually, the error mentioned above could be offset by the method of double difference between satellites and stations, so it could complete baseline solution and high precision positioning [1]. This section would introduce the model of observation, the detection of cycle slip, ambiguity resolution, error processing method and the inspection indexes of repeatability test etc.

9.2.1 The Model of Observation

The carrier phase measurement observation equation is as follows:

$$\Phi_k^j(t) = \frac{f}{c} \rho_k^j(t) - f[\delta t_k(t) - \delta t^j(t)] - \frac{f}{c} [\Delta_{k,\text{ion}}^j(t) + \Delta_{k,\text{trop}}^j(t)] + N_k^j(t) \quad (9.1)$$

where ' Φ ' stands for carrier phase observation, ' j ' represents satellite number, ' k ' represents receiver number, ' t ' represents epoch time, ' f ' represents carrier frequency, ' c ' represents electromagnetic wave speed, ' ρ ' represents the distance between satellite to receiver, ' δt_k ' represents receiver clock error, ' δt^j ' represents satellite clock error, ' $\Delta_{k,\text{ion}}^j$ ' represents ionospheric delay, ' $\Delta_{k,\text{trop}}^j$ ' represents tropospheric delay, ' N ' represents integer ambiguity.

The model of double difference observation is the most widely used model in the application of measuring. Assume that there are 2 receiving terminals receive k satellites altogether n epochs, the linearized observation equation is as follows:

$$\begin{aligned}
DD_{12}^{ij}(t) = & -\frac{f}{c} [\Delta l_2^i(t), \Delta m_2^i(t), \Delta n_2^i(t)] \begin{bmatrix} \delta x_2 \\ \delta y_2 \\ \delta z_2 \end{bmatrix} - \Delta \Delta N \\
& + \frac{f}{c} [\rho_{20}^i(t) - \rho_1^i(t) - \rho_{20}^j(t) + \rho_1^j(t)]
\end{aligned} \quad (9.2)$$

where ‘ $\rho_{20}^i(t)$ ’ represents the pseudo-range between the second station to satellite i, ‘ $\rho_{20}^j(t)$ ’ represents the pseudo-range between the second station to satellite j, ‘ $\rho_1^i(t)$ ’ represents the geometrical distance between the first station to satellite i, ‘ $\rho_1^j(t)$ ’ represents the geometrical distance between the first station to satellite j, ‘ $\Delta \Delta N$ ’ represents the double difference of integer ambiguity, ‘ $(\delta x_2 \delta y_2 \delta z_2)$ ’ represents the correction of station 2, ‘ $[\Delta l_2^i(t), \Delta m_2^i(t), \Delta n_2^i(t)]$ ’ represents the direction cosine of station 2 to satellite i.

The error equation is as follows:

$$V = AX - L \quad (9.3)$$

where the X is as follows:

$$X = (A^T A^{-1})(A^T L) \quad (9.4)$$

If the station 1 coordinates are known, the coordinates of station 2 could be as follows:

$$\begin{cases} x_2 = x_1 + \delta X \\ y_2 = y_1 + \delta Y \\ z_2 = z_1 + \delta Z \end{cases} \quad (9.5)$$

9.2.2 The Model of Cycle Slip Detection and Ambiguity Resolution

There are a variety of methods detecting and repairing cycle slip, and combining ionosphere residual LC combination with MW combination would be a more effective method to detect cycle slip [7].

The ionosphere residual error equation is as follows:

$$\Delta_{\text{ion}}(t_i) = \left(\frac{\lambda_2}{\lambda_1} \right) (\Phi_2(t_{i+1}) - \Phi_2(t_i) - (\Phi_1(t_{i+1}) - \Phi_1(t_i))) \quad (9.6)$$

where ‘ λ_1 ’ and ‘ λ_2 ’ represent wave length, ‘ t_i ’ and ‘ t_{i+1} ’ represent adjacent epoch. ‘ Φ_1 ’ and ‘ Φ_2 ’ represent carrier phase measurement. If ‘ $\Delta_{\text{ion}}(t_i)$ ’ is greater than $0.28(1 + \text{inerval}/60.0)$, there are cycle slips need to repair.

The MW combination equation is as follows:

$$W_5 = L_5 - \hat{P}_5 \quad (9.7)$$

$$L_5 = \frac{1}{(f_1 - f_2)} (f_1 L_1 - f_2 L_2) \quad (9.8)$$

$$\hat{P}_5 = \frac{1}{(f_1 + f_2)} (f_1 P_1 + f_2 P_2) \quad (9.9)$$

where ‘f1’ and ‘f2’ represent frequency, ‘L1’ and ‘L2’ represent carrier phase measurement, ‘P1’ and ‘P2’ represent pseudo-range. If ‘W5’ is bigger than wave length, there are cycle slips need to repair.

High precision of baseline solution depends on the correct ambiguity value. The essay [8] has discussed the algorithm of damped LAMBDA; the essay [9] tells the theory is as follows: firstly, fixing the ambiguity of wide lane, and then fixing the ambiguity of L1 and L2 based on the linear relationship of L1 and L2. Considering of the advantage of above algorithm, this paper determines the algorithm of ambiguity fixed, according to the superposition of the baseline equation solution algorithm calculating site coordinates and the ambiguity float solution, then using the LAMBDA method fixed integer ambiguity. And outputting the state of ambiguity fixed in result report, the state generally depends on the RATIO value, if RATIO greater than 3, it indicates ambiguity has been fixed correctly [4].

The error of receiver and satellite can be eliminated by double difference model. The ionosphere and troposphere delay need to correct by model. Double-frequency observation model can correct most of the ionosphere delay, as shown in the essay [1]. The model of SAASTAMOINEN 1973 is often used to correct Tropospheric zenith direction atmospheric delay, which could be found in the essay [1].

9.2.3 The Index of Baseline Repeatability Test

Repetitive indicators reflect the discrete degree of observation data [10]. The standard deviation is very sensitive to heavy or small error of a set of measurements, which can effectively reflect the fluctuation range of the measured results [11]. The formula is as follows:

$$\sigma_0 = \sqrt{(x_i - \bar{x})/n} \quad (9.10)$$

where ‘ σ_0 ’ represents the standard deviation, ‘ x_i ’ represents external compliance value, ‘ \bar{x} ’ represents the expectation of external compliance value, ‘n’ represents the number of the baseline. Usually, the three times of mean square error would be as limit error, it is wrong when the result beyond the limit error, the probability of falling within the $(-3\sigma_0, 3\sigma_0)$ would be 99.7 %.

Baseline chord length error, also known as the equivalent distance error [2]. The formula is as follows:

$$\sigma = \sqrt{a^2 + (bd)^2} \tag{9.11}$$

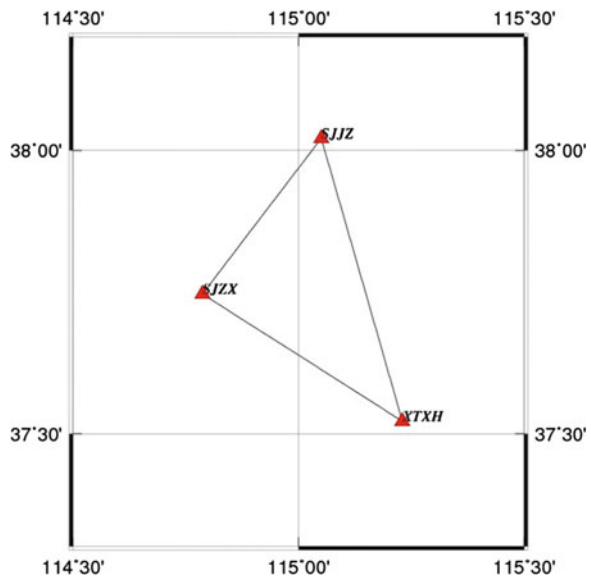
where ‘ σ ’ represents baseline chord length error, ‘ a ’ represents fixed error, ‘ b ’ represents the coefficient of percentage error, which is depend on the Chinese standard, ‘ d ’ represents the length of the baseline. The limit error of each coordinate component is $\sigma_x = \sigma_y = \sigma_z = \sigma/\sqrt{3}$.

9.3 Data Example

The observation data is from Hebei province, April 25–28, 30 and May 1, 2014, the receiver is UR240BDS/GPS dual frequency receiver produced by Unicorecomm Company. There are three baselines, sampling rate for 1 s. The application software of baseline processing is written by FORTRAN language, and this paper analyses the accuracy and repeatability test of each baseline.

The coordinates of CORS station are based on CGCS2000 coordinate frame. The CORS station name are ‘SJZX’, ‘XTXH’, ‘SJJZ’, which distribution is shown as follows (Fig. 9.1).

Fig. 9.1 The plan of CORS site



9.3.1 The External Compliance of Baseline Result

(1) The length of ‘SJZX -> XTXH’ is 46.403 km, the result is as follows:

‘BDS’ represents BeiDou Navigation Satellite system; ‘MIX’ represents double system of BDS and GPS. ‘N’, ‘E’, ‘U’ represent the coordinate’s deviation between the processing result and the true value. The result of BDS, GPS and BDS/GPS dual system all differ in centimeter level, especially the direction of the plane, which deviation within 1 cm. The result of BDS/GPS dual system is superior to the result of the two single system, it is because of the dual system could search more satellites which has a good geometric structure; therefore the result is better than single system.

The index of the control network of national grade B is that ‘8 mm + 1 ppm’, the length of this baseline is 46.403 km, the chord length error is 69 mm; the limit error of each coordinate component is 40 mm. As shown as Fig. 9.2, the accuracy of result meets the requirements of the precision of the control network of national grade B.

(2) The length of ‘SJZX -> SJJZ’ is 98.572 km, the result is as follows:

As shown in the above figure, the deviation of direction of the plane within 1.5 cm, and the deviation of direction of the elevation focus on 2–3 cm. The precision of BDS, GPS and BDS/GPS dual system is equivalent. The chord length error is 99 mm, the limit error of each coordinate component is 57 mm. As shown as Fig. 9.3, the accuracy of result meets the requirements of the precision of the control network of national grade B.

Fig. 9.2 The result of external precision of ‘SJZX -> XTXH’

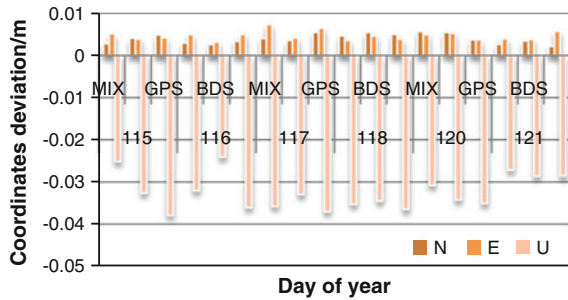


Fig. 9.3 The result of external precision of ‘SJZX -> SJJZ’

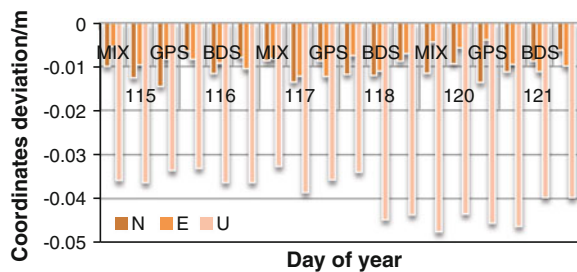
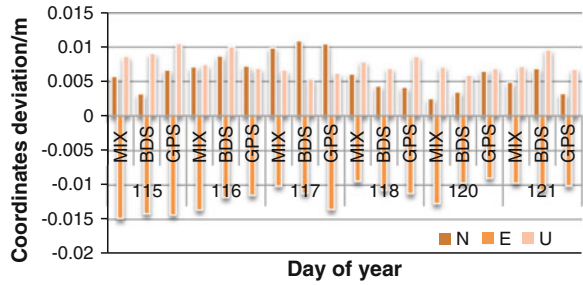


Fig. 9.4 The result of external precision of ‘SJJZ -> XTXH’



(3) The length of ‘SJJZ -> XTXH’ is 38.283 km, the result is as follows:

As shown in the above figure, the deviation of direction of the plane within 1.3 cm, and the deviation of direction of the elevation within 4 cm. The result of BDS/GPS dual system is superior to the result of the two single system. The chord length error is 40 mm, the limit error of each coordinate component is 23 mm. As shown as Fig. 9.4, the accuracy of result meets the requirements of the precision of the control network of national grade B.

9.3.2 The Repeatability Test of Baseline

The error of each coordinate component is shown as follows:

(1) The result of ‘SJZX -> XTXH’ is as follows:

As shown as Fig. 9.5 and Table 9.1, the accuracy of each coordinate component is limited in three times of mean square error, and the repeatability index of the planet is within 2 mm, and the repeatability index of the elevation is within 7 mm.

(2) The result of ‘SJZX -> SJJZ’ is as follows:

As shown as Fig. 9.6 and Table 9.2, the accuracy of each coordinate component is limited in three times of mean square error, and the repeatability index of the planet is within 5 mm, and the repeatability index of the elevation is within 7 mm.

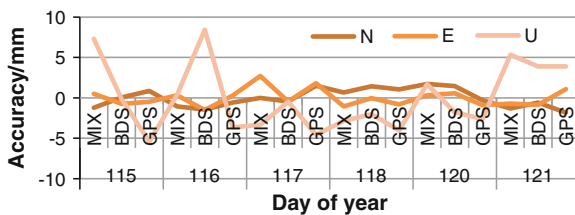


Fig. 9.5 The accuracy of external precision of ‘SJZX -> XTXH’

Table 9.1 The test index of SJZX → XTXH

Index	Distance d/km	The limit error of the mean square error $3*\sigma_0(n)/mm$	The limit error of the mean square error $3*\sigma_0(n)/mm$	The limit error of the mean square error $3*\sigma_0(n)/mm$
Value	46.403	3.4	3.2	12.2

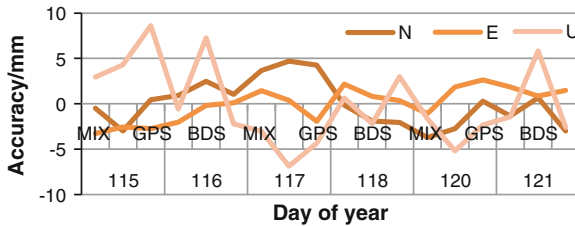
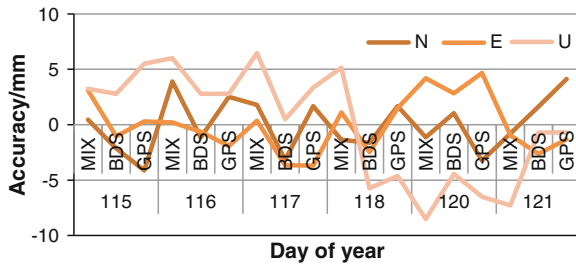


Fig. 9.6 The accuracy of external precision of ‘SJZX -> SJJZ’

Table 9.2 The test index of SJZX → SJJZ

Index	Distance d/km	The limit error of the mean square error $3*\sigma_0(n)/mm$	The limit error of the mean square error $3*\sigma_0(n)/mm$	The limit error of the mean square error $3*\sigma_0(n)/mm$
Value	98.572	7.5	5.4	12.5

Fig. 9.7 The accuracy of external precision of ‘SJJZ -> XTXH’



(3) The result of ‘SJJZ -> XTXH’ is as follows:

As shown as Fig. 9.7 and Table 9.3, the accuracy of each coordinate component is limited in three times of mean square error, and the repeatability index of the planet is within 5 mm, and the repeatability index of the elevation is within 7 mm.

Table 9.3 The test index of SJJZ → XTXH

Index	Distance d/km	The limit error of the mean square error $3 \cdot \sigma_0(n)/\text{mm}$	The limit error of the mean square error $3 \cdot \sigma_0(n)/\text{mm}$	The limit error of the mean square error $3 \cdot \sigma_0(n)/\text{mm}$
Value	38.283	7.1	7.4	14.5

9.3.3 Results Analysis

According to three CORS stations in Hebei province 6 days of baseline data processing results, the comparison of BDS, GPS and BDS/GPS dual system is as follows:

- (1) The external compliance of all baselines differ within centimeter level, the precision of plane within 1 cm, and the precision of elevation is slightly lower than plane, which is focus on 4 cm.
- (2) The precision of BDS is similar to GPS and mixed double system, but in most cases the precision of the blend system is superior to the single system.
- (3) As shown in Figs. 9.5, 9.6 and 9.7, the result of same baseline of different days within 7 mm, which can meet the production requirements completely.
- (4) According to the theory of limit error, the deviations of the coordinates all less than the tolerance in this paper, conforming to the requirements of the theory.
- (5) From the comparison of different length baseline, we could found that the accuracy of 30 and 40 km is better than 100 km long baseline

9.4 Conclusion

According the results above, we can draw the conclusion as follows: the control network of national grade C is suitable for large, medium city basic control network and engineering measurement, the control network of national grade B is suitable for all kinds of precision engineering measurement. The accuracy of result in this paper meets the requirements of the precision of the control network of national grade B and the repetitive inspection result of all baselines differ within 7 mm.

In this paper, all independent baselines does not constitute a baseline network for joint adjustment and overall accuracy assess, and the error of earth tide, relativistic effects, multipath, deviation of antenna phase center have not been corrected yet. The precision of height direction need to improve in the further study.

Acknowledgments This study is funded by the National Natural Science Fund (41404034/41304030) and the International GNSS monitoring and assessment system (GFZX0301040308-06). This work is also supported by the fundamental research funds of Chinese Academy of Surveying and Mapping (7771405/7771416) and the Key Laboratory of Surveying and Mapping Technology on Island and Reef, National Administration of Surveying, Mapping and Geo

information (2013B01). Besides, this paper is also funded by Ministry of Science and Technology Support Program (2012BAB16B01) and Ministry of Science and Technology 863 plan (2013AA122501) and Geospatial Information Engineering Laboratory of National Administration of Surveying, Mapping and Geoinformation project funding (201301).

References

1. Dang YM, Bei JZ, Cheng YY (2007) Principle and application of global navigation satellite system. Surveying and Mapping Press, Beijing
2. Xu SQ, Zhang HH, Yang ZQ, Wang ZM (2011) Principle and application of GPS. Wuhan University Press, Wuhan
3. Yang YX, Li JL, Wang AB et al (2014) Preliminary assessment of the navigation and positioning performance of BeiDou regional navigation satellite system. *Sci China: Earth Sci* 57:144–152
4. Tang WM, Deng CL, Gao LF (2013) Preliminary results of single epoch baseline solution based on BeiDou navigation satellite system. *Geomatics Inf Sci Wuhan Univ* 38(8):897–901
5. Huang LY, Lv ZP, Chen ZS, et al (2013) Research on methodologies of long-baseline BeiDou triple-frequency rapid ambiguity resolution. In: China satellite navigation conference
6. Shi C, Zhao QL, Li M, et al. (2012) High precision orbit determination and positioning research of BeiDou satellite navigation system. *Sci China: Earth Sci*
7. Wang XY, Bei JZ (2013) GPS/BDS static baseline processing method and result analysis. *J Navig Positioning* 1(2):71–73
8. Liu G, Zhu YZ, Han BM (2004) LAMBDA algorithm of GPS single epoch positioning. *Geomatics Inf Sci Wuhan Univ* 29(3):195–197
9. Wei ZQ, Ge MR (1998) The mathematical model of GPS relative positioning. Wuhan Univ Press, Wuhan
10. Huang GW, Wang B, Wang YW (2011) Baseline repeatability test and quality analysis of high-precision GPS control network. *Bull Surveying Mapp* 7:9–11
11. Jiang WP, Liu JN, Ye SR (2001) GPS deformation monitoring network baseline processing system error analysis. *Geomatics Inf Sci Wuhan Univ* 26(3):196–199

Chapter 10

A System Developed for Monitoring and Analyzing Dynamic Changes of GNSS Precipitable Water Vapor and Its Application

Li Li, Zhimin Yuan, Ping Luo, Jun Shen, Sichun Long, Liya Zhang and Zongli Jiang

Abstract Water vapor is an important factor to the formation of small and medium-scale disastrous weather. Its temporal and spatial variation is extremely violent and uneven in the air. Therefore, the development of a real-time monitoring and analysis system for dynamic variations characteristics of spatial and temporal water vapor has great practical significance and application value to short-impending rainstorm forecast. The GNSS/PWV dynamic changes monitoring and analysis system was built on the Matlab platform. Based on the calculated PWV of every CORS reference station, it can be used to demonstrate the time series analysis and planar dynamic changes of various kinds of meteorological elements (PWV, temperature, barometric pressure and relative humidity, etc.). Especially, it can accurately reflect one and two dimensional dynamic trends of the water vapor within the CORS coverage area, track the dynamic changes of atmospheric water vapor content and enhance the monitoring and forecasting capabilities of meteorological departments for small and medium scale disastrous weather.

Keywords Ground-based GNSS · Precipitable water vapor · Dynamic changes · Monitoring system

L. Li (✉) · Z. Yuan · S. Long · L. Zhang · Z. Jiang
Hunan Provincial Key Laboratory of Clean Coal Resources Utilization and Mine Environmental Protection, Hunan University of Science and Technology,
Xiangtan 411201, China
e-mail: gszl.lili@gmail.com

P. Luo
Guangzhou Hi-Target GNSS Navigation Technology Co. Ltd, R&D Center,
Guangzhou 511400, China

J. Shen
The Climate Center of Hunan Province, Changsha 410119, China

10.1 Introduction

The detection of water vapor changes trend is one of the most important tasks in meteorology study [1]. Water vapor is the main driving force to weather changes, and it is also the main participant in the atmospheric circulation. It is easy to form the thunderstorms and other disastrous weather when the water vapor distributions centralize somewhere densely. Therefore, it has important significance on the real-time monitoring and short impending prediction if we can grasp the water vapor variation trend and distribution timely and accurately in the atmosphere [2–6]. There are many limits for the current detection means, such as expensive equipment, limited monitoring range, and low temporal and spatial resolution etc. it is difficult to meet the requirements to detect and analyse water vapor for small and medium scale weather system. The short impending rainstorms generate, develop and disappear fast, so it is harder to detect and predict real-time [1, 7].

With the increasing density of CORS reference network stations and expanding covering range, ground-based GNSS meteorology is developing gradually and getting more attentions [8–10]. Ground-based GNSS meteorology is a new interdisciplinary approach using Precipitable Water Vapor (PWV) for the meteorological service. The PWV can be retrieved from tropospheric delay of reference stations by using GNSS technology, in combination with other meteorological elements (temperature, barometric pressure and relative humidity). It can be used to obtain real-time water vapor distributions maps and their change trends with higher temporal and spatial resolution, which has positive effects for monitoring and forecasting the small and medium scale weather system [11, 12].

In this paper, based on the Matlab software and Zenith Tropospheric Delay (ZTD) information obtained from Precise Point Positioning (PPP) technology, a GNSS/PWV dynamic monitoring and analysis system will be developed. The system can solve GNSS/PWV, and can also be used for time series analysis and graphic dynamic changes demonstration of the ZTD, ZHD, ZWD, PWV and other meteorological parameters (temperature, pressure, and relative humidity). It can accurately reflect the one and two dimensional dynamic change trends of various meteorological elements in CORS coverage region.

10.2 Principle of Water Vapor Detection from Ground-Based GNSS

ZTD can be obtained by un-differenced or network solutions generally in ground-based GNSS meteorology. Un-differential PPP mode will be used to calculate ZTD in this paper [13]. ZTD includes Zenith Wet Delay (ZWD) and Zenith Dry Delay (ZHD). ZHD is induced by non-water vapor in the atmosphere, which has 90 % of ZTD. ZHD has a very good correlation with the ground pressure. It can be modified to millimeters level by using the related model. ZWD is caused by the atmospheric

water vapor and its influence factors are very complicated. Currently, it can only achieve 10–20 % estimated precision by using models. While in GNSS positioning, ZWD can be obtained with millimeter level precision if estimated ZTD minus modeled ZHD [14, 15].

$$\begin{cases} ZHD = [(0.002279 \pm 0.0000024)] \frac{P_c}{f(\varphi_c, H_c)} \\ f(\varphi_c, H_c) = 1 - 0.00266 \cos 2\varphi_c - 0.00028H_c \end{cases} \quad (10.1)$$

Formula (10.1) is a model called Saastamoinen using for ZHD estimation. P_c is the Pressure at station (hPa); φ_c is the station's geographic latitude; H_c is the station altitude (km). The measurement precision of pressure can generally reach 0.5 hPa, so ZHD estimation precision can achieve millimeters level with Saastamoinen model.

$$ZWD = ZTD - ZHD \quad (10.2)$$

PWV is defined as the height of liquid condensed from all the atmospheric water vapor within vertical air column in a unit area. It can be calculated by formula (10.3).

$$\begin{cases} PWV = \frac{\pi}{\rho_w} \cdot ZWD \\ \pi = \frac{10^5}{R[(k/T_m) + k']} \end{cases} \quad (10.3)$$

In formula (10.3), ρ_w is the water density; the unit of ZWD is m; $R = 461 \text{ (Jkg}^{-1}\text{K}^{-1}\text{)}$; $k = (3.776 \pm 0.014) \times 10^5 \text{ K}^2\text{hPa}^{-1}$; $k' = 16.48 \text{ KhPa}^{-1}$; T_m is the weighted average temperature of troposphere:

$$T_m = 106.7 + 0.605T \quad (10.4)$$

Formula (10.4) is also suitable for Hong Kong area [16], T is the ground temperature (K).

10.3 Monitoring and Analysis System for Water Vapor Dynamic Changes

10.3.1 System Operation Procedures and Functions

The monitoring and analysis system for GNSS/PWV dynamic changes mainly consists of three steps. Firstly, importing necessary data (including ZTD, meteorological data and other geographical data such as reference station coordinates and

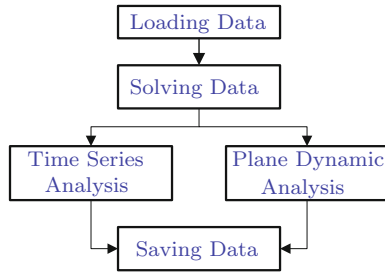


Fig. 10.1 The flow chart of monitoring and analysis system for GNSS/PWV dynamic changes

map boundary) for the calculation of PWV; secondly, PWV will be obtained by using ground-based GNSS water vapor inversion principle mentioned in Sect. 10.2; finally, the time series analysis and plane dynamic changes of PWV and other meteorological parameters (temperature, pressure and relative humidity) can be demonstrated in the system. Figure 10.1 is the flowchart of the system. As can be seen, it includes five functional modules: data loading, data calculation, time series analysis and plane dynamic changes analysis, data and figure storage. Each module consists of a plurality of subroutines.

10.3.1.1 Data Loading Module

This module is used to load the necessary data (including ZTD, meteorological data and other geographic data such as reference station coordinates and map boundary) for PWV calculation. All the data can be open and read line by line. The information extraction subroutine is used to extract corresponding data on set time node, which can be stored in the memory for subsequent calculations.

10.3.1.2 Data Solving Module

The main role of data solving module is to calculate ZHD, ZWD and PWV, based on the water vapor inversion principle of ground-based GNSS in Sect. 10.2. Before the data solving, all the data are needed to match time, making all kinds of previous loaded data matching to the same time node in accordance with the set sampling rate.

10.3.1.3 Time Series Analysis Module

The module is to map out the change trends of one specific parameter within a set time. It can create a new drawing window for each parameter and draw a graph of the parameters over time. PWV, ZHD, ZWD, ZTD and other meteorological

parameters (temperature, barometric pressure and relative humidity) will be analyzed over time.

10.3.1.4 Plane Dynamic Changes Analysis Module

This module is used to analyze the plane dynamic changes of all the meteorological elements (PWV, temperature, barometric pressure and relative humidity etc.) by using four time spline interpolation algorithm within the reference network coverage. It can draw a two-dimensional plane chart of dynamic changes at a specific period. In addition, there is a progress bar under the figure, which can also be used to control the drawing process (start/pause/exit) along with the drawing loop submodule.

10.3.1.5 Results Saving Module

This module can save results of some major meteorological parameter (PWV, ZHD and ZWD) information in text file. The program will create a text file named by the station name. The program can also preserve the single specified figure. All the figures of dynamic changes can also be saved in batches, and even these batches pictures can be synthesized as a separate animated GIF image to facilitate dissemination and presentation.

10.3.2 System Menu Design

Figure 10.2 is the main interface of monitoring and analysis system for GNSS/PWV dynamic changes. The main interface consists of a menu bar and drawing window.

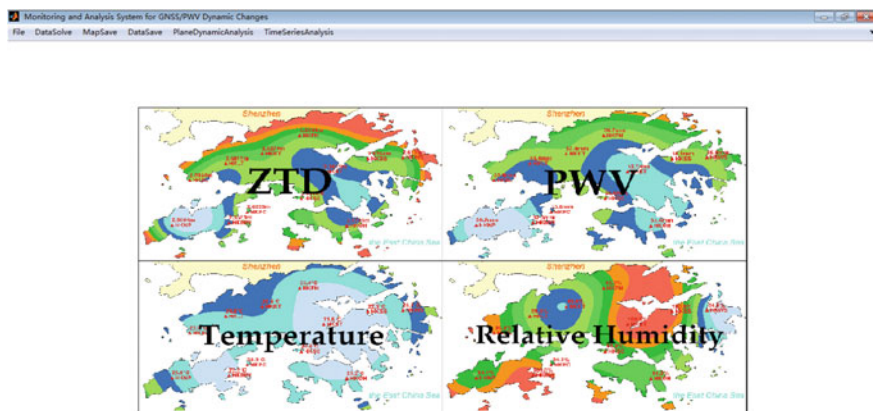


Fig. 10.2 Main interface of monitoring and analysis system for GNSS/PWV dynamic changes

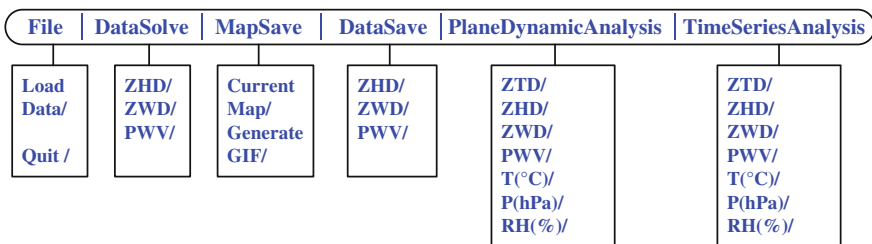


Fig. 10.3 Menu drop-down list of monitoring and analysis system for GNSS/PWV dynamic changes

There are six menus (file, data solving, image saving, data saving, plane dynamic changes and time series analysis), each menu has its corresponding drop-down list as shown in Fig. 10.3.

10.4 Testing Example

The testing data is downloaded from the website of Hong Kong Satellite Positioning Reference Station Network (SatRef), which is established by Hong Kong Lands Department and Marine Department. SatRef has a total of 12 continuously operating reference stations (see Fig. 10.4, <http://www.geodetic.gov.hk/smo/gsi/>)

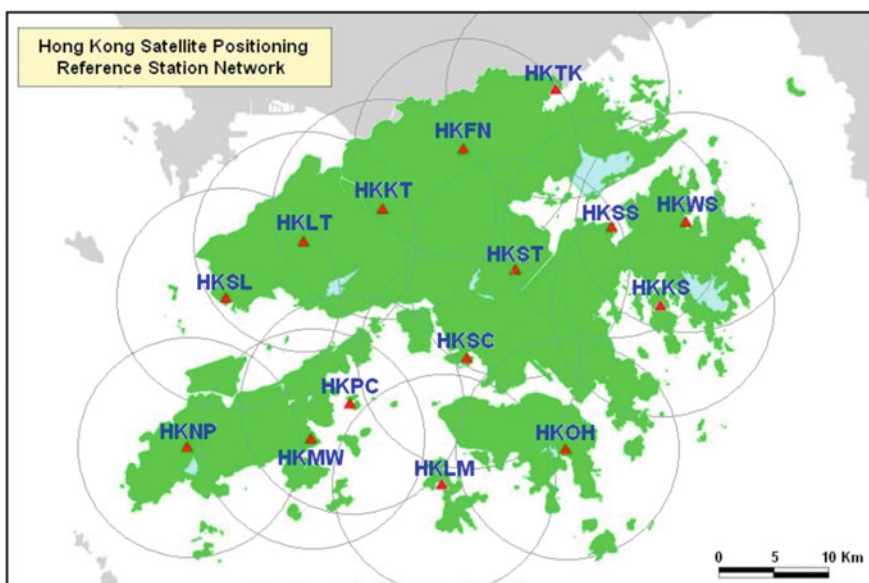


Fig. 10.4 Hong Kong satellite positioning reference network

[programs/en/GSS/satref/satref.htm](#)). The distance between stations is about 7–27 km. The sampling rate of GNSS observation data and meteorological data is 5 s and 1 min respectively. All these data can be downloaded from its website. Before the calculation, we need first to get ZTD, which is necessary to calculate PWV. In this experiment, we first get the ZTD of each reference station by using PPP technique [12]. Figure 10.5 is the final PPP-ZTD results at 5 min interval.

To save space, Fig. 10.6 only shows the time series changes of each parameter (ZTD, ZHD, ZWD, temperature, barometric pressure and relative humidity) at station HKFN on May 16. It can accurately reflect the time series trends of each parameter. As can be seen, it can show the true value and fitted value both.

Figure 10.7 is the distribution maps of plane dynamic changes of the main meteorological parameters at 10:00 on May 16, 2010. Before demonstration, the Hong Kong map (.shp) data will be required to load automatically. Based on the interpolated meteorological parameters value of each station, their contour figures will be drawn on the map. The positions (red triangles), name and meteorological parameter values of all the stations are marked on the map. The GMT time is given on the upper left corner of the figure. The color bar situates on the right side of the figure. Its scale and color change indicate the size of the parameter values. The playback progress bar below the map prompts the playing progress. We can skip some of the time by dragging the progress bar to control the playing progress.

Figure 10.8 is plane maps of 2 h interval PWV on May 16 (00:00-24:00), 2010 in Hong Kong area. These maps are shown from left to right, top to bottom

% TROPOSPHERIC PARAMETER : HKFN : 2010/05/16 00:00:00-2010/05/16 23:55:00 GPST								
% date	time(sec)	ztd(m)	grade(m)	gradn(m)	sdztd(m)	sdge(m)	sdgn(m)	
2010, 05, 16,	0.00,	2.62440,	-0.00089,	-0.00213,	0.00298,	0.00098,	0.00106	
2010, 05, 16,	300.00,	2.62483,	-0.00090,	-0.00223,	0.00310,	0.00098,	0.00107	
2010, 05, 16,	600.00,	2.62423,	-0.00082,	-0.00227,	0.00316,	0.00098,	0.00108	
2010, 05, 16,	900.00,	2.62427,	-0.00085,	-0.00232,	0.00331,	0.00099,	0.00109	
2010, 05, 16,	1200.00,	2.62435,	-0.00087,	-0.00234,	0.00345,	0.00100,	0.00109	
2010, 05, 16,	1500.00,	2.62426,	-0.00081,	-0.00242,	0.00358,	0.00100,	0.00110	
2010, 05, 16,	1800.00,	2.62388,	-0.00086,	-0.00233,	0.00370,	0.00101,	0.00110	
2010, 05, 16,	2100.00,	2.62303,	-0.00082,	-0.00226,	0.00380,	0.00101,	0.00110	
2010, 05, 16,	2400.00,	2.62301,	-0.00080,	-0.00222,	0.00389,	0.00101,	0.00111	
2010, 05, 16,	2700.00,	2.62279,	-0.00076,	-0.00226,	0.00394,	0.00101,	0.00111	
2010, 05, 16,	3000.00,	2.62274,	-0.00074,	-0.00223,	0.00397,	0.00101,	0.00111	
2010, 05, 16,	3300.00,	2.62272,	-0.00074,	-0.00216,	0.00397,	0.00102,	0.00111	
2010, 05, 16,	3600.00,	2.62139,	-0.00074,	-0.00218,	0.00395,	0.00102,	0.00112	
2010, 05, 16,	3900.00,	2.62235,	-0.00102,	-0.00198,	0.00389,	0.00102,	0.00112	
2010, 05, 16,	4200.00,	2.62149,	-0.00136,	-0.00165,	0.00381,	0.00102,	0.00112	
2010, 05, 16,	4500.00,	2.61971,	-0.00125,	-0.00182,	0.00363,	0.00102,	0.00112	
2010, 05, 16,	4800.00,	2.61827,	-0.00121,	-0.00195,	0.00360,	0.00101,	0.00112	
2010, 05, 16,	5100.00,	2.61737,	-0.00127,	-0.00195,	0.00369,	0.00102,	0.00112	
2010, 05, 16,	5400.00,	2.61665,	-0.00130,	-0.00193,	0.00376,	0.00102,	0.00112	
2010, 05, 16,	5700.00,	2.61578,	-0.00132,	-0.00197,	0.00380,	0.00102,	0.00112	
2010, 05, 16,	6000.00,	2.61625,	-0.00129,	-0.00197,	0.00380,	0.00102,	0.00112	
2010, 05, 16,	6300.00,	2.61595,	-0.00132,	-0.00190,	0.00378,	0.00102,	0.00112	
2010, 05, 16,	6600.00,	2.61535,	-0.00130,	-0.00182,	0.00373,	0.00102,	0.00112	
2010, 05, 16,	6900.00,	2.61448,	-0.00124,	-0.00181,	0.00366,	0.00102,	0.00112	
2010, 05, 16,	7200.00,	2.61467,	-0.00117,	-0.00170,	0.00356,	0.00102,	0.00112	
2010, 05, 16,	7500.00,	2.61422,	-0.00110,	-0.00168,	0.00333,	0.00101,	0.00111	

Fig. 10.5 ZTD results calculated by PPP technology

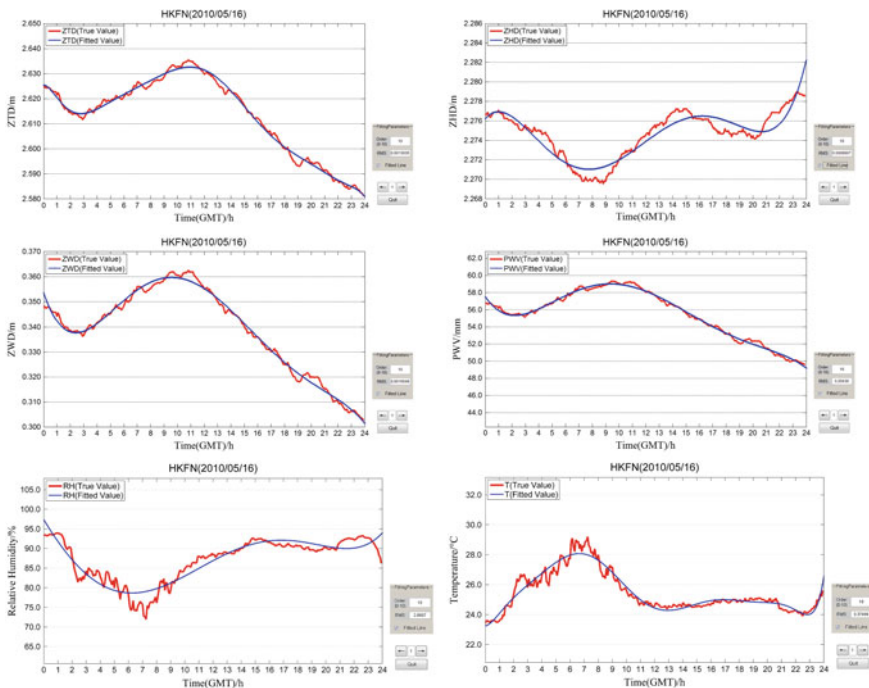


Fig. 10.6 Time series analysis of HKFN meteorological elements

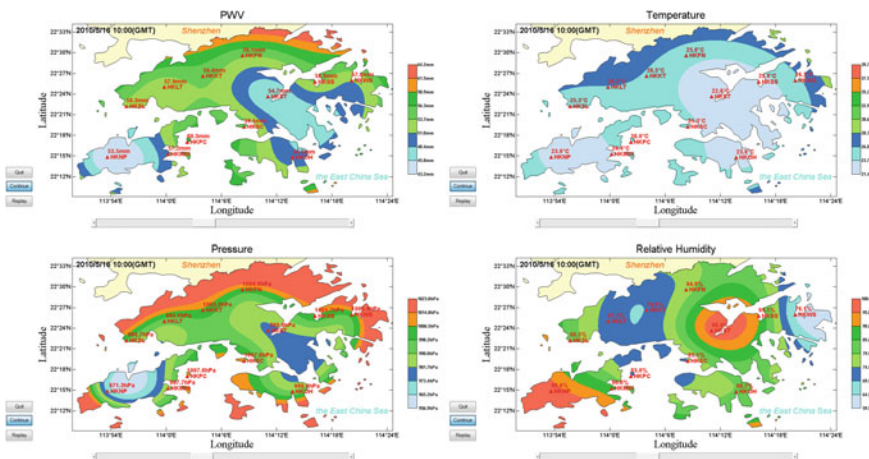


Fig. 10.7 Maps of plane dynamic changes of meteorological parameters (2010/5/16)

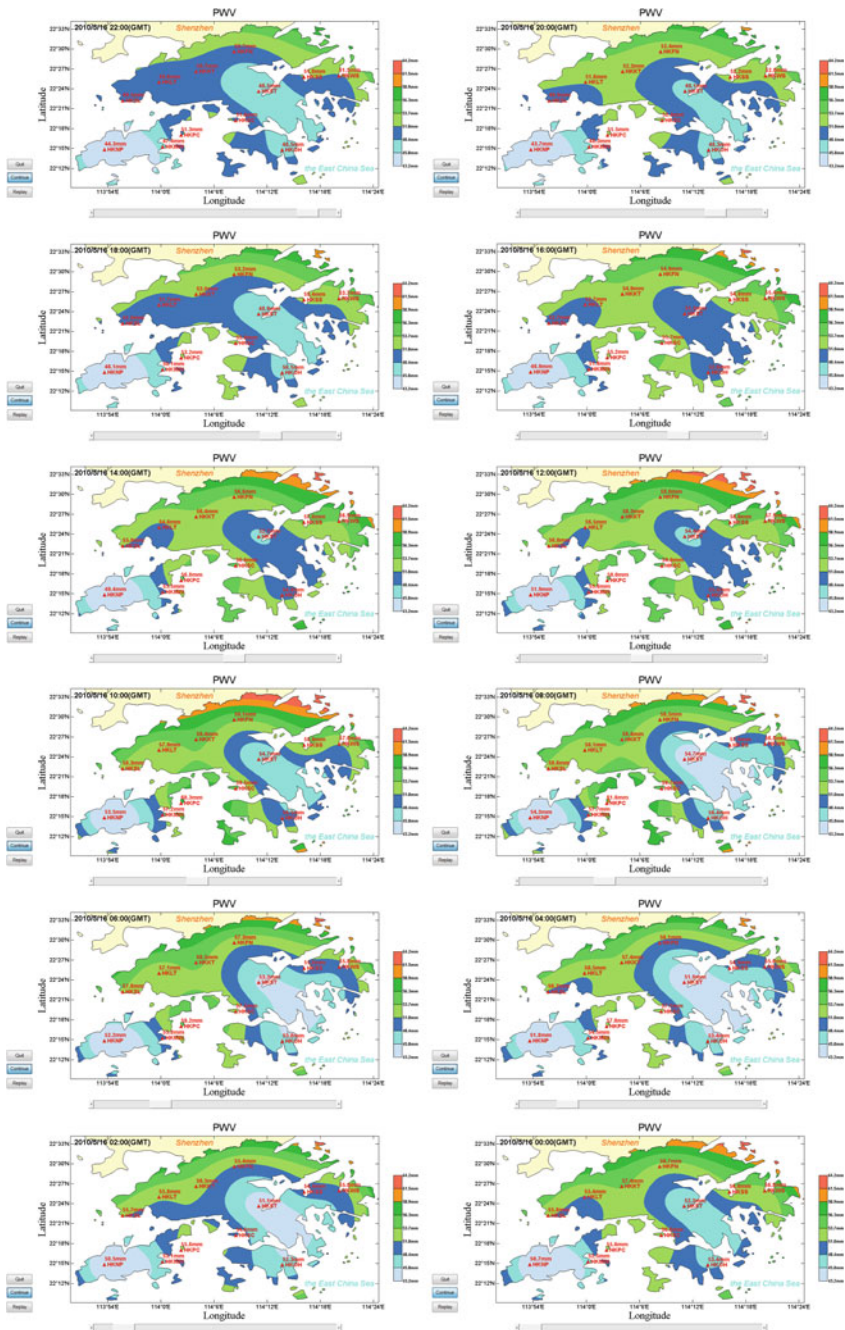


Fig. 10.8 PWV plane dynamic changes maps every 2 h (2010/5/16)

chronologically. Similarly, the system can also demonstrate the dynamic changes maps of temperature, barometric pressure and relative humidity. They are no longer listed due to the limited space.

10.5 Conclusions

In a specific area, the instantaneous dynamic changes of water vapor can be tracked by accurately analyzing its one and two dimensional real-time dynamic trends. It can enhance the meteorological prediction ability of existing forecasting system for small and medium-scale disastrous weather. Therefore, based on the Matlab platform, we developed a system for monitoring and analyzing GNSS/PWV dynamic change, which contains five functional modules including the data loading (temperature, pressure and relative humidity, etc.), data solving (ZHD, ZWD and PWV), time series analysis, plane dynamic change analysis and its demonstration, and data preservation. Each module has a plurality of subroutines. This system has a certain practical value for monitoring temporal and spatial variation of water vapor and forecasting short-impending rainstorm.

Acknowledgments This research are supported by the National Natural Science Foundation of China (NSFC) (No: 41304029; 41204034; 41471067; 41474014).

References

1. Ding J (2009) GPS meteorology and its application. China Meteorological Press, Beijing
2. Li G (2010) Ground-based GPS meteorology. Science Press, Beijing
3. Ding J, Ye Q (2003) The Yangtze river delta region near real time GPS meteorological network. *Meteorology* 29(6):26–30
4. Zhao F, Dai L, Nie Z, et al (2006) Research and application on GPS water vapor auto processing system. *Sci Surveying Mapp* 31(6):63–65
5. Li Y, Li W, Cao Y et al (2014) Design and implementation of data management system for ground based navigation satellite remote sensing of water vapor. *Meteorol Sci Technol* 42(2):273–277
6. Li G (2011) Research of remote sensing technology of atmospheric water vapor by using ground-based GPS and application system of meteorological operations. *Trans Atmos Sci* 34(4):385–392
7. de Haan S, Holleman I, Holtslag AAM (2009) Real-time water vapor maps from a GPS surface network: construction, validation, and applications. *J Appl Meteorol Climatol* 48(7):1302–1316
8. Wang R (2012) Precipitable water vapor retrieval technology research and application of ground-based GPS observations. Nanjing University of Information Science and Technology, Nanjing
9. Fan S (2013) Research on GPS marine water vapor inversion and three dimensional water vapor tomography. Wuhan University, Wuhan
10. Jiang P, Ye S (2013) Technical advances in water vapor detection using ground-based GPS observations. *Chinese J Nature* 35(4): 251–257

11. Hao Wang, Guoping Li (2011) Construction and application about the monitoring system of water vapor derived from ground- based GPS in Chengdu. *Geo-Inf Sci* 13(2):213–218
12. Li L et al (2012) Rainstorm nowcasting based on GPS real-time precise point positioning technology. *Chinese J Geophys* 55(4):1129–1136
13. Li L, Long S, Shen J et al (2014) ZTD high-frequency variation detection based on the kinematic precise point positioning. *Geodesy Geodyn* 34(2):74–78
14. Bevis M, Businger S, Herring TA et al (1992) GPS meteorology: remote sensing of atmospheric water vapor using the global positioning system. *J Geophys Res* 97 (D14):15787–15801
15. Rocken C, Hove TV, Johnson J et al (1995) GPS/STORM-GPS sensing of atmospheric water vapor for meteorology. *J Atmos Oceanic Technol* 12:468–478
16. Chen Y et al (2007) GPS real-time estimation of precipitable water vapor-Hong Kong experiences. *Acta Geodaetica Cartogr Sin* 36(1):9–12

Chapter 11

Multifunctional Satellite Navigation and Communication Mast Antenna Based on Mobile Platform

Jia Zhang, Ximing Liang and Haiguang Zhang

Abstract The paper is mainly about one kind of communication antenna based on civilian vehicles, which can meet the requirement of satellite navigation, communication. The paper focuses on the analysis of the technology of a broadband UHF quadrifilar helix antenna. Also the paper explores the implementation method of broadband quadrifilar helix antennas by theoretical research and electromagnetic model analysis. We achieve the goal that VSWR is less than 3 from f_1 to $2.5f_1$. Experimental results and simulation results match better and we get the expected radiation characteristic. The cascade connection of multi-band frequency and different function antennas has been achieved. The study of the paper has significance for implementation of the technology of civilian communication vehicles and rescue vehicles.

Keywords Satellite navigation · Satellite communication · Quadrifilar helix antenna

11.1 Introduction

Many of our communications and navigation stations, vehicles, boats and even buildings erected on the roof of a lot of BD, GPS, UHF, HF, etc. Antenna and RF network, this forest of antennas resulting complex electromagnetic environment and waste a lot of resources, especially in the mobile this contradiction is more

J. Zhang (✉) · X. Liang · H. Zhang
Xi'an Research Institute of Navigation Technology, Xi'an 710068, China
e-mail: 51800071@qq.com

X. Liang
e-mail: Mysun896@sina.com

H. Zhang
e-mail: zhg54321@163.com

prominent on the platform. In order to improve efficiency, improve the electromagnetic environment, many users expect to receive a variety of antenna systems for effective integration, integrated antenna, integrated RF, thoughts and comprehensive signal processing platform will be integrated antenna integrated design.

In this paper, a satellite navigation through the rod antenna complex satellite communications, the overall structure of the antenna from top to bottom for satellite navigation antenna, satellite communications antenna. Satellite navigation antenna cables through the hollow metal tube through the four-arm spiral antenna, satellite communications center, one of the two antennas integrated from top to bottom, structure, and metal rods can also integrate other functions wearing underneath other bands of different antennas, such as measuring to communicate and detect VHF antenna or an antenna that can meet the satellite navigation, satellite communication, detection and other functions, can be applied to civilian communications vehicles, earthquake rescue vehicles.

In recent years, in civilian areas, satellite navigation and mobile satellite communication has been more widely used, has played an increasingly important role in working life. Such systems require an antenna with a wide beam and circular polarization characteristics, and can maintain a low elevation gain. Quadrifilar helical antenna due to circularly polarized radiation having a wide beam, high gain can be maintained at a lower elevation position, cut and can be formed by selecting the appropriate physical size of the different radiation patterns to meet different space needs of the application.

11.2 Antenna Design

11.2.1 Analysis of the Theory of the Quadrifilar Helix Antenna

J.D. Kraus first antenna helical structure found on the application and development of the helical antenna has made tremendous contributions. A typical helical antenna is cylindrical helical antenna, usually formed by winding a metal, the structure shown in Fig. 11.1. Typically the helical antenna fed by the coaxial line, the inner conductor is connected to an antenna coaxial cable, the outer conductor is connected with the floor.

Kilgus was first proposed in 1968, Resonant four-arm spiral antenna, the structure shown in Fig. 11.2. The antenna comprises four spiral arms and the metal rod, the length of each spiral arm is an integral multiple of one quarter of the operating wavelength. When multiple relationship is odd, spiral arms open termination, when multiple relationship is an even number, the terminal shorted spiral arms. Four spiral arms feeding terminal currents are equal, the phase difference of 90° . By feeding this way can achieve circular polarization [1].

Fig. 11.1 Geometry of quadrifilar helix mast antenna

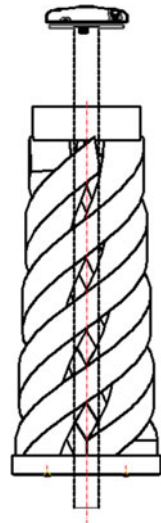
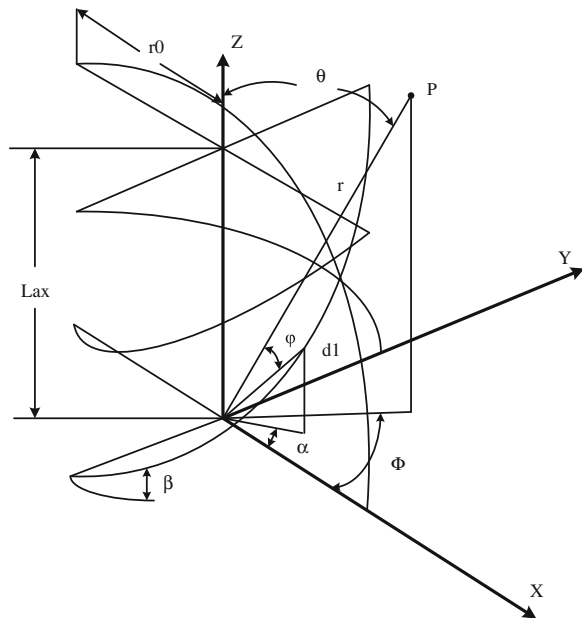


Fig. 11.2 Schematic of quadrifilar helix antenna



Structural parameters of the antenna is determined by the following formula:

$$L_{ax} = N \sqrt{\frac{(L_{ele} - Ar_0)^2}{N^2} - 4\pi^2 r_0^2}$$

$$A = \begin{cases} 1 & \text{Odd} \\ 2 & \text{Even} \end{cases} \quad (11.1)$$

wherein L_{ax} is the axial length of the helix (mm), L_{ele} is the length of the spiral arms (mm), r_0 is the radius of the spiral (mm), N is the number of turns of the spiral.

According to the four-arm spiral antenna structure shown in Fig. 11.2 and the given parameters, to analyze the far-zone radiation field four-arm spiral antenna using equivalent current method [2–4].

According to the current distribution of the spiral arms, respectively, to calculate the field portion and the helical spiral radial portions generated. In general, considered a spiral arm sinusoidal current distribution, and its maximum is located helix start and end points. φ component of total field of the Unit 1 is

$$E_{\varphi 1} = \frac{-j\omega\mu e^{-jkr}}{4\pi r} \int_{l=0}^{l=\lambda/2} \overline{i}_{\varphi} e^{jkr' \cos \psi} dl \quad (11.2)$$

1. The field of the coiled portion:

Suppose A is a variable of integration, we can get,

$$dl = \frac{r_0 d\alpha}{\cos \beta} \quad (11.3)$$

Substitution,

$$E_{\varphi H} = \frac{-j\omega\mu r_0 e^{-jkr}}{4\pi r \cos \beta} \int_{\alpha=0}^{2N\pi} i_{\varphi}(\phi, \alpha) e^{jkr' \cos \psi} d\alpha \quad (11.4)$$

For each cell, the current amplitude,

$$i_{\varphi}(\alpha) = I_0 \cos(kr_0) \cos \frac{\alpha}{2N} \cos \beta \quad (11.5)$$

For elements 1, 2,

$$i_{\varphi}(\varphi, \alpha) = i_{\varphi}(\alpha) \cos(\varphi - \alpha) \quad (11.6)$$

The same, for elements 3 and 4,

$$i_{\varphi}(\varphi, \alpha) = i_{\varphi}(\alpha) \cos(\varphi - \alpha) \quad (11.7)$$

Phase of element 1 is,

$$r' \cos \psi = \frac{\bar{r}\bar{r}}{r} = r_0 \cos \alpha \sin \theta \cos \varphi + r_0 \sin \alpha \sin \theta \sin \varphi + \frac{P\alpha}{2\pi} \cos \theta \quad (11.8)$$

Definite

$$K = \frac{\omega\mu I_0 r_0 \cos(kr_0) e^{-jkr}}{4\pi r} \quad (11.9)$$

Thus, the field of the helical portion is given,

$$E_{\varphi H1} = -jK \int_{\alpha=0}^{2N\pi} \cos\left(\frac{\alpha}{2N}\right) \cos(\varphi - \alpha) \exp[jk(r_0 \cos \alpha \sin \theta \cos \varphi + r_0 \sin \alpha \sin \theta \sin \varphi + \frac{P\alpha}{2\pi} \cos \theta)] d\alpha \quad (11.10)$$

Similarly, the field of element 2 is,

$$E_{\varphi H2} = -jK \int_{\alpha=0}^{2N\pi} \cos\left(\frac{\alpha}{2N}\right) \cos(\varphi - \alpha) \cdot \exp[jk(-r_0 \cos \alpha \sin \theta \cos \varphi - r_0 \sin \alpha \sin \theta \sin \varphi + \frac{P\alpha}{2\pi} \cos \theta)] d\alpha \quad (11.11)$$

Elements 3 and 4 with respect to the elements 1 and 2 are 90° phase difference of the feeder, so the field is,

$$E_{\varphi H3} = K \int_{\alpha=0}^{2N\pi} \cos\left(\frac{\alpha}{2N}\right) \sin(\varphi - \alpha) \cdot \exp[jk(-r_0 \sin \alpha \sin \theta \cos \varphi - r_0 \cos \alpha \sin \theta \sin \varphi + \frac{P\alpha}{2\pi} \cos \theta)] d\alpha \quad (11.12)$$

$$E_{\varphi H4} = K \int_{\alpha=0}^{2N\pi} \cos\left(\frac{\alpha}{2N}\right) \sin(\varphi - \alpha) \cdot \exp[jk(r_0 \sin \alpha \sin \theta \cos \varphi - r_0 \cos \alpha \sin \theta \sin \varphi + \frac{P\alpha}{2\pi} \cos \theta)] d\alpha \quad (11.13)$$

2. The field of spiral radial portion,

Current quadrifilar helical antenna can be approximated that the radial portion is uniformly distributed, the following simplified formula can be obtained,

1/4 turn screw,

$$E_{\varphi R1,2} = \frac{-j\omega\mu e^{-jkr}}{4\pi r} 2r_0 I_0 (\cos \varphi e^{jk \cos \theta P/4} - \sin \varphi) \quad (11.14)$$

$$E_{\varphi R3,4} = \frac{\omega\mu e^{-jkr}}{4\pi r} 2r_0 I_0 (\cos \varphi + \sin \varphi e^{jk \cos \theta P/4}) \quad (11.15)$$

1/2 turn screw,

$$E_{\varphi R1,2} = \frac{-j\omega\mu e^{-jkr}}{4\pi r} 2r_0 I_0 \sin \varphi (e^{jk \cos \theta P/2} - 1) \quad (11.16)$$

$$E_{\varphi R3,4} = \frac{\omega\mu e^{-jkr}}{4\pi r} 2r_0 I_0 \cos \varphi (1 - e^{jk \cos \theta P/2}) \quad (11.17)$$

1 turn screw,

$$E_{\varphi R1,2} = \frac{-j\omega\mu e^{-jkr}}{4\pi r} 2r_0 I_0 \sin \varphi (1 + e^{jkP \cos \theta}) \quad (11.18)$$

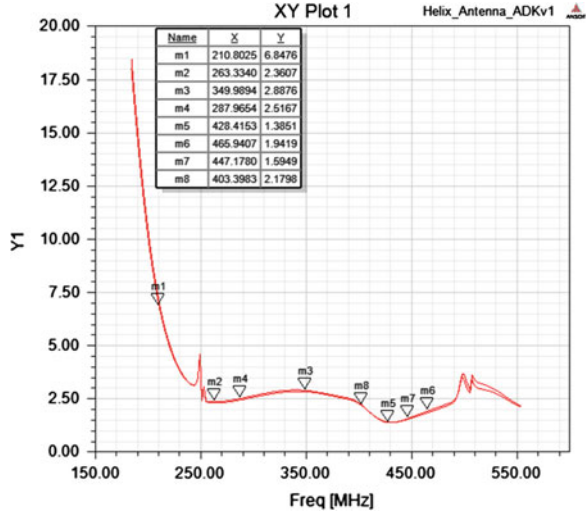
$$E_{\varphi R3,4} = \frac{\omega\mu e^{-jkr}}{4\pi r} 2r_0 I_0 \cos \varphi (1 + e^{jkP \cos \theta}) \quad (11.19)$$

Finally, the principle of superposition field, superimposed on the two far-zone radiation field can be drawn four-arm spiral antenna [5, 6].

11.2.2 The Feed Structure of the Quadrifilar Helix Antenna

Quadrifilar helical antenna is required to produce right-hand circularly polarized, while the traditional 90° toward the network due to the need quarter-wavelength impedance conversion, in the UHF band larger, but this design quadrifilar helical antenna diameter circular floor only 30 cm, so using a 180° phase shifter, and two 90° phase shifter to realize the right-handed circular polarization, high power satellite communications bearer.

Fig. 11.3 Simulated VSWR of the quadrifilar helix antenna



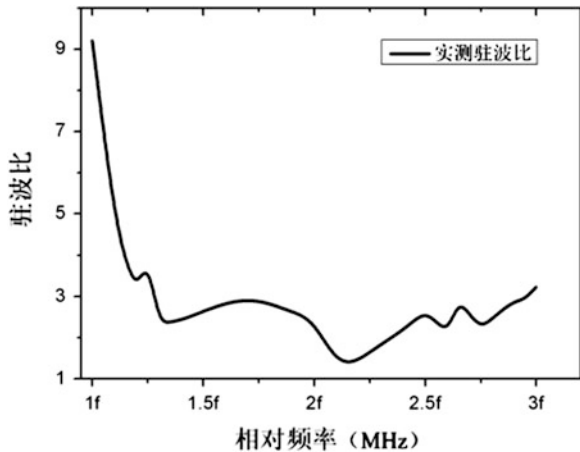
11.3 Simulated and Measured Results

The simulated VSWR results is shown in Fig. 11.3, the top and middle of the antenna were shorted load, VSWR bandwidth of the antenna has been greatly improved in the 250–500 MHz internal antenna VSWR less than 3.

The measured VSWR results of the antenna is shown in Fig. 11.4, the figure shows the measured VSWR bandwidth of the antenna slightly wider than the antenna VSWR bandwidth simulation.

Simulation radiation pattern of the antenna is shown in Fig. 11.5, the antenna pattern is good, when the gain is about 280 MHz 7 dB, but when 430 MHz gain of

Fig. 11.4 Measured VSWR of the quadrifilar helix antenna



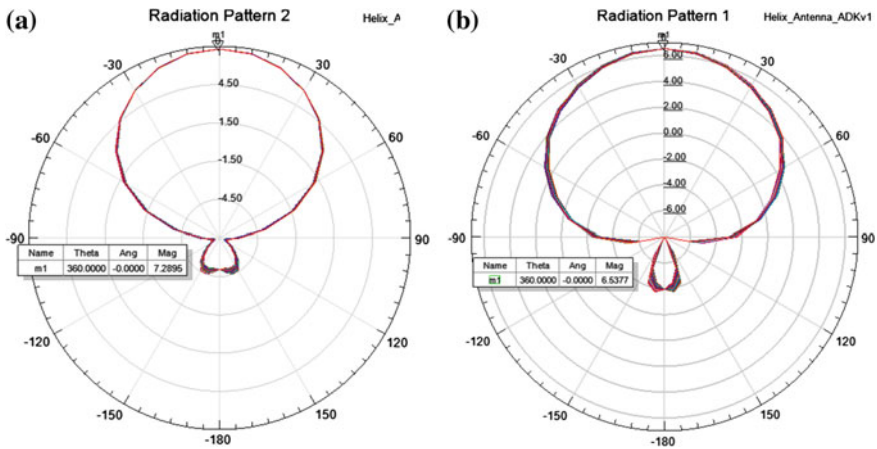


Fig. 11.5 Simulated radiation pattern of the antenna (280 and 430 MHz). a 280 MHz, b 430 MHz

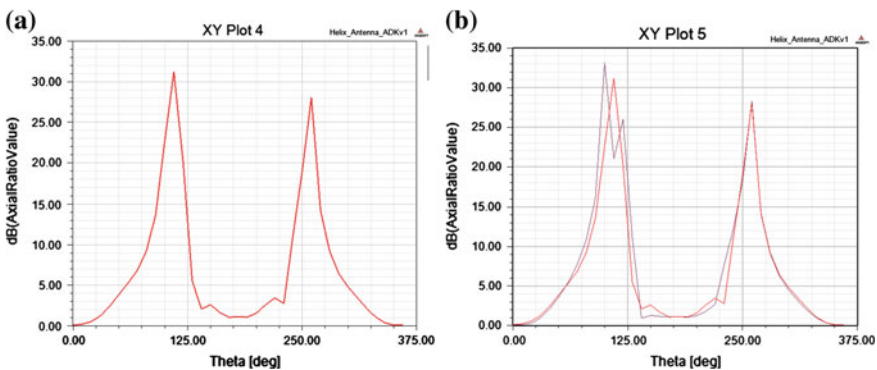


Fig. 11.6 Simulated axial ratio of the antenna (280 MHz). a 280 MHz, b 430 MHz

about 6 dB, half-power beam width is greater than 60° , can be well meet the needs of satellite communication.

Simulation of the axial ratio of the antenna such as shown in Fig. 11.6, the antenna in the elevation angle $180^\circ \pm 50^\circ$ axis is less than 3, the polarization characteristics good.

3D simulation of the antenna pattern shown in Fig. 11.7, visible near the center frequency of the antenna radiation characteristics are very good.

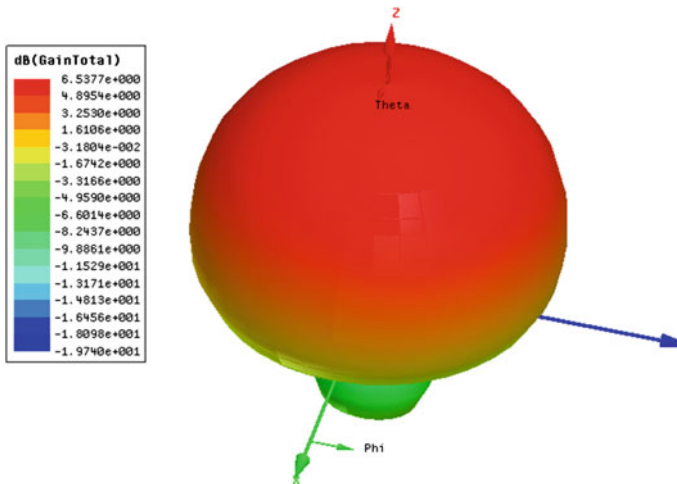


Fig. 11.7 Simulated 3D radiation pattern of the antenna (360 MHz)

11.4 Conclusion

The new article is designed to wear rods used in satellite navigation and satellite communications, four-arm spiral antenna, satellite navigation at the top of the antenna RF cable through the hollow metal tube through the center of the four-arm spiral antenna, antenna VSWR serious deterioration, by adjusting the four load short-circuit the helical antenna at the top and the middle of the arm, the antenna VSWR has been greatly improved, in the UHF band reached two octave, and simple feed structure of the antenna, through a 180° phase shifter 90° and 2° phase shifter, wide beam to achieve a good circular polarization, well adapted to the needs of satellite navigation and mobile satellite communications.

References

1. Kilgus CC (1969) Resonant quadrifilar helix. *IEEE Trans Ap-17*:349–351
2. Takacs A, Fonsca NJG (2009) Miniaturization of quadrifilar helix antenna for VHF band applications. In: *Antennas and propagation conference*, 16–17 Nov 2009, Loughborough, UK
3. Shoaib S, Shah WA (2010) Design and implementation of quadrifilar helix antenna for satellite communication. In: *6th ICET*, 2010
4. Fonseca NJG et al (2009) Antenna of the helix type having radiating strands with a sinusoidal pattern and associated manufacturing process, International Publication WO2009/034125 A1, 19 March 2009
5. Wang J, Wang C, Liang X (2002) Small low-orbit satellite communication application of resonant four-arm spiral antenna. *J Electron* 30(12):1865–1866
6. Zhang C, Fu G, Li M (2007) Research of resonant quadrifilar helix antenna design method. *Electron Technol* (12):39–41

Chapter 12

Optimal Satellite Selecting Algorithm in GPS/BDS Navigation System and Its Implementation

Zhuoxi Ma, Li Yang, Xiaolin Jia, Dan Zhang and Shuai Liu

Abstract As the Global Navigation Satellite System (GNSS) steps into a new era of multiple constellations, multiple constellations bring opportunities for navigation and positioning services. Under the condition of the existence of multiple constellations, the number of observable satellite number will increase sharply in single epoch. Because of the limitation of computing source, too much redundant information brought by redundant satellites can not greatly improve the accuracy of positioning, however, it may actually increase the computational burden of receiver. Therefore, optimizing the satellite selection algorithm is of great significance. Based on the relations of constellation's geometry and the principle of GDOP, this paper proposed a satellite selection algorithm suitable for multiple constellations. Furthermore, a satellite selection strategy applied to 5–7 satellites is considered. The experimental results show that on the premise of positioning accuracy, the improved satellite selection satellite can significantly reduce the calculation time and has good real-time performance and reliability.

Keywords GPS · BDS · Satellite selection algorithm · Dilution of precision

12.1 Introduction

The receiver needs to observe at least four satellite in single epoch to complete the positioning. As the number of satellites which users received more than four, it is significant to optimize the selection of satellites to enhance the precision of positioning. Generally speaking, the index GDOP (Geometry Dilution of Precision) is

Z. Ma (✉) · L. Yang · D. Zhang · S. Liu
College of Navigation and Aerospace Engineering, Information Engineering University,
Zhengzhou 450001, China
e-mail: 523338578@qq.com

X. Jia
Research Institute of Surveying and Mapping, Xi'an 710054, China

used to estimate the geometric distribution of satellites. As the Global Navigation Satellite System (GNSS) steps into a new era of multiple constellations, the number of observable satellite number will increase sharply in single epoch. Because of the limitation of computing source, too much redundant information brought by redundant satellites can not greatly improve the accuracy of positioning. Conversely, it may actually increase the computational burden of receiver.

In single constellation, the commonly used satellite selection algorithms are minimum GDOP algorithm and constellation-tetrahedron selecting algorithm [1, 2, 4, 5]. Zhang uses satellite direction cosine matrix determinant and the the selection of strategy is given in 5 satellites [6]. These two algorithms are simple to implement. But along with the increase of the number of observable satellites, the efficiency of calculation growth in geometric order, thus they have not adapted for the demand of the present development of satellite selection algorithm. At present, the scholars has designed multiple algorithms to reduce the burden of calculation and enhance the efficiency of positioning. These algorithms are convex hull algorithm, algorithm based on elevation and azimuth, etc. But most of these algorithms are designed for single constellation and does not apply to integrated navigation system.

Above all, to design a simple and efficiency satellite selection algorithm and applied to integrated navigation system is of vital significance. It will further reduce the device initialization time and improve the positioning accuracy.

This paper firstly introduces the principle of DOP index and traditional satellite selection algorithm, then aimed at solving the problem that the traditional algorithm is time-consuming, a new selection algorithm suitable for multiple constellations is raised. Finally, the feasibility of the algorithm is analysed combined with experiments. Furthermore, from the perspective of the geometric distribution of satellites, suggestions on satellite selection strategy is put forward.

12.2 Principle of Dilution of Precision

The geometric distribution of satellites can be described by dilution of precision. The spatial coordinates of satellites can be obtained by using broadcast or precise ephemeris products. According to the coordinates of the satellites, the observation equation of n observable satellites reads as formula 12.1:

$$\left\{ \begin{array}{l} \rho_r^1 + (dt^1 - dt_r)c + I_r^1 + T_1^r + T_r^1 + v_1 = \sqrt{(x_1 - X)^2 + (y_1 - Y)^2 + (z_1 - Z)^2} \\ \rho_r^2 + (dt^2 - dt_r)c + I_r^2 + T_r^2 + T_r^2 + v_2 = \sqrt{(x_2 - X)^2 + (y_2 - Y)^2 + (z_2 - Z)^2} \\ \dots \\ \rho_r^p + (dt^n - dt_r)c + I_r^n + T_r^n + T_r^n + v_j = \sqrt{(x_n - X)^2 + (y_n - Y)^2 + (z_n - Z)^2} \end{array} \right. \quad (12.1)$$

where

- ρ_r^p is the observed code pseudorange
 $(dt^p - dt_r)c$ is the range caused by satellite and receive clock correction
 $I_r^p + T_r^p$ is the sum of ionospheric and tropospheric refraction
 (x_p, y_p, z_p) is the spatial coordinates of GNSS satellites

The linearized model of formula 12.1 reads as follows:

$$\begin{cases} v_1 = a_1\Delta X + b_1\Delta Y + c_1\Delta Z + cdt + l_1 \\ v_2 = a_2\Delta X + b_2\Delta Y + c_2\Delta Z + cdt + l_2 \\ \dots \\ v_p = a_p\Delta X + b_p\Delta Y + c_p\Delta Z + cdt + l_p \end{cases} \quad (12.2)$$

where

$$\begin{cases} a_i = \frac{X_t - x_i}{d_{0i}}, b_i = \frac{Y_t - Y_i}{d_{0i}}, c_i = \frac{Z_t - z_i}{d_{0i}} \\ l_p = d_{0P} - \rho_r^p - I_r^p - I_r^T \\ d_{0P} = \sqrt{(X_t - x_P)^2 + (Y_t - x_P)^2 + (Z_t - x_P)^2} \\ a_P = \frac{X_t - x_P}{d_{0P}}, b_i = \frac{Y_t - Y_P}{d_{0P}}, c_i = \frac{Z_t - z_P}{d_{0P}} \end{cases}$$

The observation equation can be simplified by formula 12.3:

$$AX + L = V \quad (12.3)$$

The correlation coefficients matrix reads as:

$$Q = (A^T A)^{-1} = \begin{bmatrix} Q_{XX} & Q_{XY} & Q_{XZ} & Q_{XT} \\ Q_{XY} & Q_{YY} & Q_{YZ} & Q_{YT} \\ Q_{XZ} & Q_{YZ} & Q_{ZZ} & Q_{ZT} \\ Q_{XT} & Q_{YT} & Q_{ZT} & Q_{TT} \end{bmatrix} \quad (12.4)$$

GDOP denotes as formula 12.5:

$$\text{GDOP} = \sqrt{Q_{XX} + Q_{YY} + Q_{ZZ} + Q_{TT}} \quad (12.5)$$

Thus, the smaller the GDOP value, the better the geometric distribution of satellites and the higher the positioning accuracy will get. Therefore, to ensure a relatively high positioning accuracy, it is needed to select the combination of satellites which have relatively small value of GDOP.

12.3 Traditional Satellite Selection Algorithm

12.3.1 Minimum GDOP Algorithm

Take four satellites in single constellation as an example, the core of minimum GDOP algorithm is to iterate all the possible combinations of observable satellite, select the one which has the minimum GDOP value as the optimal result and use this combination to point positioning. For the case that have n satellites, each process needs to calculate for C_n^4 times. The advantage of this algorithm is that it can accurately extract the optimal combination of satellite geometry distribution. But for integrated navigation system, the number of visible satellites is much more than single constellation. Besides, the integrated system may also need to consider the time difference of multiple systems in the process of calculation, which increases the computational complexity of this algorithm to a certain extent. It will seriously affect the effectiveness of the real-time application.

12.3.2 Constellation-Tetrahedron Selecting Algorithm

The principle of GDOP can be expressed as formula 12.6:

$$\text{GDOP} = \frac{\sqrt{\text{trace}(A^T A)^*}}{6V} \quad (12.6)$$

where V denotes the volume of polyhedron formed by satellite to the user receiver unit vectors. It can be obtained through formula 12.6 that GDOP value is inversely proportional to the volume of the polyhedron. The design idea of tetrahedron selecting Algorithm is similar to the former one, namely, the optimal result is extracted by calculating each combination of polyhedron volume and select the one which has the largest volume.

Compared with minimum GDOP algorithm, the constellation-tetrahedron selecting algorithm reduces the computational complexity to some extent, but it is also time-consuming, this algorithm may also need to calculate for C_n^4 times in the situation of four visible satellites.

12.4 Optimal Satellite Selecting Algorithm

According to the related theory of constellation-tetrahedron selecting algorithm, when the selected satellite geometric structure has the largest volume, the satellite structure is the best. Take four satellites as an example, when one satellite in the zenith position, other three satellites locate at the tangent plane of users and they

separate by 120° each other, the volume of the tetrahedron is the largest [3]. The theory for more satellites is the same, when meet two conditions, namely there exist satellites that have high elevation angle and lower satellites have a uniform distribution, the geometric structure is better.

Therefore, the principle of the proposed algorithm can be summarized as two aspects. On the one hand, considering the cutoff elevation angle, the bottom satellite combination is selected based on the selection of most uniform distribution of low elevation satellites. On the other hand to extract the proper number of satellites which have high elevation angle as top satellite combination. Both the top and bottom satellite combination constitute the final combination. We set the cutoff elevation angle to 10° , the range of elevation angle of bottom satellite combination is from 10° to 30° . The specific steps of the algorithm are as follows:

- (1) According to the number of selecting number of satellites n and determine the distribution number of high and low elevation satellites k_1 and k_2 , respectively. For example, if we select seven satellites, the possible values of (k_1, k_2) are: (1, 6), (2, 5), (3, 4).
- (2) Rule out the satellites which have the elevation angle lower than the cutoff elevation angle and select k_1 satellites which have the biggest elevation angle as the top satellite combination.
- (3) Divide visible satellites that meet the range of elevation angle of bottom satellite combination into k_2 groups. According to the principle of uniform distribution, calculate the azimuth difference between each satellites and the ideal value, respectively. If the azimuth angle of the satellite is α , then the difference is $\left| \alpha - j \times \left(\frac{360}{k_2} \right) \right| (j = 1, 2, \dots, k_2)$.
- (4) Calculate the quantitative terms of each satellites that meet the former conditions. Define the satellites with low elevation angle, high precision and small difference with ideal value into bigger quantitative terms. In each group choose the satellite with the largest quantitative value.
- (5) Count all the possible results of (k_1, k_2) combination, calculate the GDOP value of each combinations and select the smallest one as the final combination.

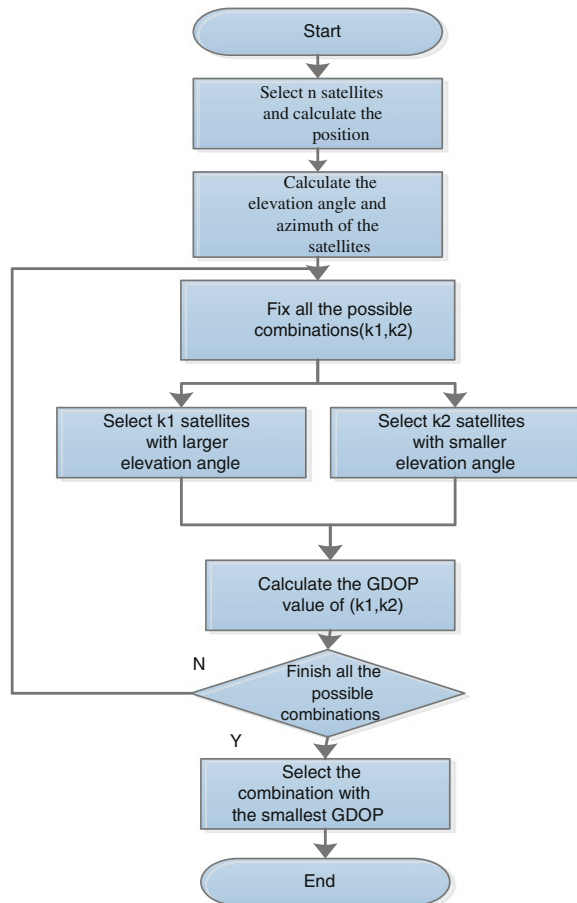
The operation flow chart of the algorithm is shown in Fig. 12.1.

12.5 Results and Discussion

12.5.1 Experiment and Analysis of the Optimization Algorithm

This algorithm can be applied to multi-mode GNSS calculation. The experiment uses the data from GPS and BDS navigation system. In order to verify the feasibility and availability of the algorithm, the selection of a known coordinates of

Fig. 12.1 Flow chart of optimal satellite selecting algorithm



points, with January 7, 2014, 24 h of ephemeris data analysis is selected by the cutoff elevation angle of 10° . The contrast experiment is conducted between the Minimum GDOP algorithm and the Optimization algorithm. We set the number of selection satellite number six, the experimental results are shown in Table 12.1.

According to the results in Table 12.1, due to the optimization algorithm is a kind of subprime selecting algorithm based on the principle of optimal satellite geometric distribution, it can be seen that the results of the optimization algorithm of star is legitimate different from the Results of Minimum GDOP algorithm. But the GDOP value of using the optimal selecting algorithm mostly distributed between 2 and 3, and within the GDOP threshold 5. The more the satellite number selected, the better the result will get. Therefore, it can completely meet the accuracy of requirement.

In terms of processing time, compared with the traditional algorithms. The optimization algorithm only need to compute 2–3 times, thus will greatly save the

Table 12.1 Experiment resulting data of optimal satellite selecting algorithm

Epoch	Results of minimum GDOP algorithm		Results of the optimization algorithm	
	PRN	GDOP	PRN	GDOP
8:0:0	C04 C07 C11 G21 G22 G25	1.91	C04 C06 C07 G16 G22 G27	2.57
10:0:0	C06 C08 G14 G15 G18 G31	1.56	C05 C06 C08 G15 G19 G31	2.36
12:0:0	C05 C08 C09 G13 G15 G28	1.52	C05 C06 C08 G07 G13 G15	2.29
14:0:0	C03 C07 G23 G27 G29 G31	1.63	C03 C06 C07 C08 G07 G29	2.49
16:0:0	C05 C08 C10 G07 G13 G31	2.16	C06 C08 G05 G07 G20 G31	3.20
18:0:0	C08 C10 G01 G08 G16 G32	1.67	C06 C08 C12 G05 G06 G32	2.55
20:0:0	G01 G03 G11 G17 G20 G32	1.39	C06 G03 G05 G11 G20 G32	2.03
22:0:0	C03 C05 G03 G07 G11 G28	1.95	C05 C09 G03 G05 G11 G28	2.56

computation time. Besides, it also will not meet the problem that the calculation burden rises sharply along with the increase of satellite number.

In order to further analyse the computing efficiency of the algorithm, the ratio between the running time of the optimization algorithm and the running time of the Minimum GDOP algorithm is used as an evaluation index. The wuhan station data on January 5–7, 2014 were statistically analyzed. Select the satellite number from 5 to 7, the curve graph reflecting the computational efficiency trend along with the change of observation satellite number as shown in Fig. 12.2.

Fig. 12.2 Curve graph reflecting the computational efficiency trend along with the change of number of satellites

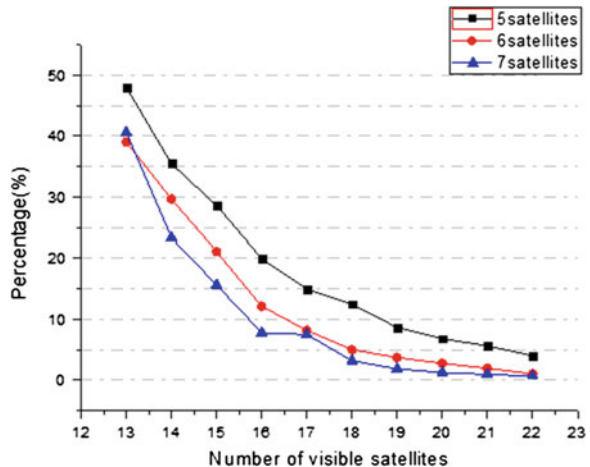


Table 12.2 The relationship between the selecting number and result

Epoch	All sat.	5 sat.	6 sat.	7 sat.
8:0:0	1.76	2.98	2.57	2.03
10:0:0	1.41	2.57	2.36	2.17
12:0:0	1.39	2.45	2.29	2.02
14:0:0	1.45	2.61	2.49	2.30
16:0:0	1.81	5.70	3.20	2.83
18:0:0	1.40	4.32	2.55	2.26
20:0:0	1.26	2.32	2.03	1.92
22:0:0	1.61	2.97	2.56	2.23

Through the data in Fig. 12.2, along with the increase number of observation satellite, the ratio index decreases, the computational efficiency increases; When the number of observation satellite is greater than 19, the optimization algorithm improves the computational efficiency for more than 10 times.

The relationship between the number of selecting satellites and the result is analyzed. Choose the selecting number into 5–7, compare with the GDOP value obtained by using the two different algorithms, the computing results are show in Table 12.2.

According to Table 12.2, in general, along with the increase in the number of selecting satellites, GDOP value decreases. When the choice for more than six satellites, the results are good. When the choice for the satellite number seven, the GDOP values in each epoch is within three, which can provide high positioning accuracy.

In order to further verify the influence of absolute positioning accuracy of the algorithm, this paper selects five different iGMAS monitoring stations locating in different latitude in our country: Beijing station (bjf1), urumqi station (gua2), wuhan station (wuh1), xi'an station (xia1) and kunming station (kun1). The pseudorange positioning program is compiled and we set the number of selected satellite seven, the single point positioning error among using all visible satellites, using Minimum GDOP algorithm and using the optimization algorithm is compared and analysed. The positioning RMS of N, E, U three components is shown from Figs. 12.3, 12.4 and 12.5.

From Figs. 12.3, 12.4 and 12.5, the results shows that the difference between the optimization algorithm and the Minimum GDOP algorithm and the resulting using all satellites are in the m class, which means that it does not cause large precision loss due to loss number of visible satellites after the satellite selection. Therefore, this algorithm can satisfy the demand of real time positioning applications.

12.5.2 Research of the Satellite Optimization Strategy

In order the make a further study on the effect the of satellite geometry distribution on GDOP value, the optimization algorithm is used to compute the value of each

Fig. 12.3 Positioning RMS of N

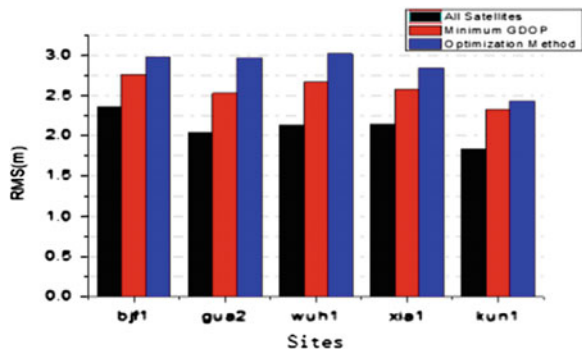


Fig. 12.4 Positioning RMS of E components

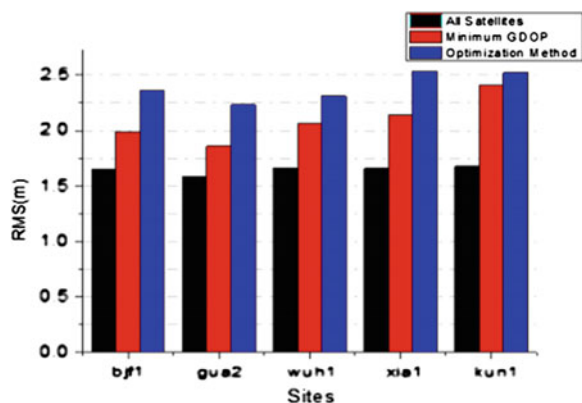
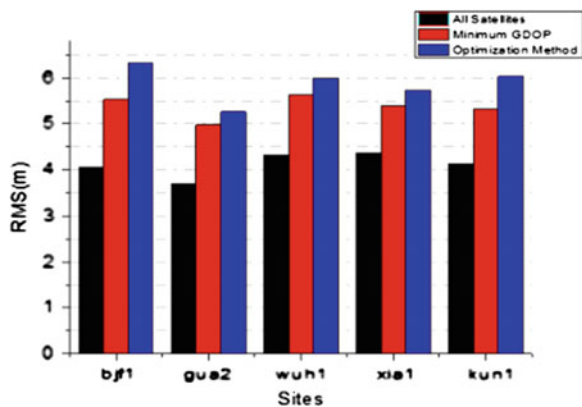


Fig. 12.5 Positioning RMS of U components



epoch every 5 min for 1 day and the results are analysed and isolated by the number of different distribution of high and low elevation angle. We choose the selecting number into 5–7 to analyse and the statistical results are shown from Table 12.3, 12.4 and 12.5.

Through to the data from Table 12.3, 12.4 and 12.5, the conclusion is concluded as follows:

- (1) The value of GDOP overall conform to the principle of optimal in the geometrical structure of satellite. When the satellite geometric structure has large volume, the value of GDOP is relatively small.
- (2) When the selecting satellite number is 5, due to the fewer visible satellites, the percentage of epochs which GDOP value greater than 5 for more than 15 % in multiple combinations of satellite.
- (3) When the selecting satellite number is 6, high and low elevation satellite distribution number (1, 5) is the optimal structure. According to the statistics of the total epoch in 1 day, the percentage of epochs which GDOP value greater than 5 is 5.21 %, which is better than that of (2, 4) and (3, 3) combination.
- (4) When the selecting satellite number is 7, GDOP value has significantly reduced compared with the selecting number is six. When the high and low

Table 12.3 The GDOP value when the selecting number is 5

Number of high elevation satellites (k1)	Number of low elevation satellites (k2)	GDOP >5 %	GDOP <3 %
1	4	17.01	63.88
2	3	19.09	67.36

Table 12.4 The GDOP value when the selecting number is 6

Number of high elevation satellites (k1)	Number of low elevation satellites (k2)	GDOP >5 %	GDOP <3 %
2	4	11.11	70.14
1	5	5.21	81.60
3	3	13.54	74.30

Table 12.5 The GDOP value when the selecting number is 7

Number of high elevation satellites (k1)	Number of low elevation satellites (k2)	GDOP >5 %	GDOP <3 %
3	4	0	74.65
2	5	3.12	80.90
1	6	4.17	80.56

elevation satellite number is 3 and 4, respectively, All epoch of has the GDOP value less than 5, but the percentage which GDOP value less than 3 is 74.65 %, a bit poorer than the combination (2, 5) and (1, 6).

To sum up, it can be advised that the number of high and low elevation satellite can be constraints when the observation satellite quantity is large. It will further achieve the goal of highly efficient satellite selection.

12.6 Conclusions

Based on the principle of optimal satellite geometric distribution, this paper proposed a subprime satellite selection algorithm which uses the satellite elevation angle and azimuth angle to screen the satellites and select the optimal combination. The implementation steps of the algorithm are discussed in detail in this paper. Besides, the related parameters of the actual operation principles of configuration is discussed. The experimental results show that the optimization algorithm overcomes the time-consuming problem of traditional algorithms. It can be effectively applied to real-time navigation and positioning applications. The next step is to further study and optimize the calculation method of quantitative values to meet the different navigation system and different precision of satellites, which meet the requirements of high precision positioning in dynamic environment.

References

1. Duan Y, Wei Z, Liu J (2013) Optimal constellation selecting and pseudo-range positioning algorithm in GPS. *J Chin Inertial, Technol* 21(2):209–213
2. Liu H, Dang Y, Wang Q (2013) A fast sub-optimal satellite selection method in multi-constellation real-time navigation. *J Sci Surv Mapp* 38(1):20–22
3. Li S, Cao K (2009) An improved algorithm of real-time constellation-selecting in GPS locating. *J.Comput Simul* 7:65–68
4. Wu R, Cai T (2009) An satellites selection algorithm based on elevation and azimuth. *J Ship Electron Eng* 29(11):73–75
5. Zhuo N (2009) A new satellite selection algorithm of GPS constellations. *J Astronaut Metrol Measur* 29(2):54–56
6. Zhang Q, Zhang X et al (2007) Satellite selection algorithm for combined satellite receivers. *J Beijing Univ Aeronaut Astronaut* 33(12):1424–1427

Chapter 13

An Improved Method to Accelerate the Convergence of PPP-RTK with Sparse CORS Stations' Augmentation

Shoujian Zhang, Jiancheng Li and Lei Zhao

Abstract Real-time kinematic Precise Point Positioning (PPP-RTK) with dense regional reference stations' augmentation has been proved to be effective for rapid precise positioning. However, with increasing distance between the rover and the reference receivers, the decorrelation of the atmospheric errors will make it more and more difficult to fix the ambiguities quickly. Recent studies show that PPP using the raw observables by estimating the ionospheric and tropospheric delays not only can improve the convergence of PPP but also can overcome the re-initialization of PPP, however the correlations between the atmospheric delays and the ambiguities will cause the wrong fixing of the ambiguities, which will introduce biases in the coordinates. In this contribution, in order to achieve fast precise positioning augmented with sparse continuously operating reference stations (CORS), PPP with raw observables are used as basic observations, the L1/L2 ambiguities are estimated firstly, then the wide-lane and narrow-lane ambiguities are formed, and the wide-lane and narrow-lane ambiguities are fixed recursively. In this new method, the narrow-lane ambiguities are free from ionospheric delays, so the correct fixing can be guaranteed, meanwhile the re-initialization can also be overcome. To evaluate the proposed strategy, four rover stations with average distance of 33 km within a sparse reference network, the average distance of which is about 200 km, are chosen to test the positioning performance. The simulated results show that the wide-lane ambiguities can be fixed immediately, and the narrow-lane ambiguities can be fixed quickly, usually at 3–30 epochs, and after ambiguity fixing, the positioning accuracy can achieve at cm-level.

Keywords PPP · RTK · Ambiguity resolution · Peer-to-peer · GNSS · Positioning

S. Zhang (✉) · J. Li · L. Zhao
School of Geodesy and Geomatics, Wuhan University, Wuhan, China
e-mail: shjzhang@sgg.whu.edu.cn

© Springer-Verlag Berlin Heidelberg 2015
J. Sun et al. (eds.), *China Satellite Navigation Conference (CSNC) 2015 Proceedings: Volume I*, Lecture Notes in Electrical Engineering 340,
DOI 10.1007/978-3-662-46638-4_13

129

13.1 Introduction

Precise Point Positioning, being able to provide mm to cm level positioning accuracy with a single dual-frequency GNSS receiver, has been investigated with great premise for many applications, such as crustal deformation monitoring [1], precise orbit determination (Bock 2012) and ocean tide measuring [2], etc. However, because the typical convergence period is about 30 min under normal conditions, the availability of the solutions needs the continuously uninterrupted tracking of the GNSS satellites. Hence, in real-time service, PPP are only limited in some special applications, e.g. the tsunami monitoring [2].

To accelerate the convergence and improve the positioning accuracy, the integer ambiguity fixing for PPP are exploited and investigated [3] (Collins; Laurichesse 2007). In those approaches, firstly, the Melbourne–Wübbena (MW) combination is implemented to fix the wide-lane ambiguities and then the narrow-lane ambiguities with wavelength about 11 cm are formed and fixed in the ionosphere-free observations. After fixing the undifferenced integer ambiguities, the daily positioning accuracy can be improved by 10 % (Ge et al.) and the hourly one up to 70 % [16]. However, it still cost at least 15–30 min to converge for real-time kinematic PPP, as the slowly moving geometry of the satellites (Laurichesse 2010). To further improve the ambiguity resolution performance, instead of being eliminated using the ionosphere-free combination, the ionospheric delays are estimated with the raw observables. Meanwhile, the time and space ionospheric variations are imposed as constraints to strengthen the solution. Using the raw model with the ionospheric delays consideration, the convergence time can be reduced by 30 %, i.e. from more than 30 min to about 20 min for kinematic solutions [4]. However, this convergence time is still can't be acceptable for the majority of the real-time applications.

As is well known, in the network real-time kinematic (NRTK) positioning, the precise atmospheric delays, in terms of tropospheric delays and ionospheric delays, are computed and represented based on the observations from the dense reference stations, then with the augmentation information, the instantaneous ambiguity resolution can be achieved in the rover end. Therefore, the precise atmospheric representation is the key of fast ambiguity resolution for PPP. To achieve the performance at the level of NRTK, the augmented PPP is developed to provide instantaneously ambiguity resolution for real-time kinematic positioning, in which the atmospheric delays are computed from the observations of the dense reference stations. The results show that the average time of 5 s are needed for reliable ambiguity fixing with the PPP augmentation method.

However, as the distance of the baseline between rover and reference stations increasing, the atmospheric delays errors will increase quickly, and the correlation between the atmospheric delays, especially the ionospheric delays, and the ambiguities will make it difficult to fix the ambiguities correctly. So, how to fix the ambiguities quickly and correctly for PPP-RTK with sparse reference stations' augmentation is a challenge.

In this contribution, firstly, the raw observables which will estimate the ionospheric delays, tropospheric delays along with the ambiguities and coordinates will be treated as the basic model, after the ambiguities on L1 and L2 carrier phases are estimated, the wide-lane ambiguities are formed and fixed firstly, after that, the narrow-lane ambiguities will be fixed. In this new method, the narrow-lane ambiguities are free from the ionospheric delays and can be fixed to correct values easily. So, with the proposed method, the re-initialization problem can be easily resolved by estimating the ionospheric delays in the PPP model, in the same time, the narrow-lane ambiguities which are free from ionospheric delays can be fixed correctly.

13.2 PPP Model with Ionospheric Delay Consideration

In order to estimate the ionospheric delays, the raw undifferenced carrier phase and code observables are used in the PPP data processing [4], which can be expressed as:

$$P_1 = \rho + c(dt_r - dt^s) + b_{r,P_1} - b_{P_1}^s + I_1 + T + \varepsilon_{P_1}, \quad (13.1)$$

$$P_2 = \rho + c(dt_r - dt^s) + b_{r,P_2} - b_{P_2}^s + \gamma I_1 + T + \varepsilon_{P_2}, \quad (13.2)$$

$$L_1 = \rho + c(dt_r - dt^s) + b_{r,L_1} - b_{L_1}^s - I_1 + T - \lambda_1 N_1 + \varepsilon_{L_1}, \quad (13.3)$$

$$L_2 = \rho + c(dt_r - dt^s) + b_{r,L_2} - b_{L_2}^s - \gamma I_1 + T - \lambda_2 N_2 + \varepsilon_{L_2}, \quad (13.4)$$

where P_i and L_i are the code and carrier phase measurement at frequency f_i ($i = 1, 2$); ρ is the geometric distance between the receiver and satellite phase center; c is the vacuum speed of light; dt_r and dt^s are the clock offset of the receiver r and satellite s ; $b_{r,*}$ and b_*^s are the hardware delay for code and phase measurements of the receiver and satellite; I_1 is the slant ionospheric delay on frequency f_1 , and γ is the square of the ratio between frequency f_1 and f_2 ; T is the slant tropospheric delay; λ_i is the carrier phase wavelength on frequency i ; N_i is the integer carrier phase ambiguity on frequency i ; ε_{P_i} and ε_{L_i} are the pseudorange and carrier phase measurement noise. In addition, some other corrections including the satellite antenna offsets, phase wind-up and site displacement correction must be accounted for [5].

In the raw observation equation, the satellite clocks and the hardware delays can't be estimated simultaneously, so the combined satellite clocks are introduced. Then the standard PPP model can be written as:

$$P_1 = \rho + c(dt_{r,c} - dt_c^s) + I_{1,c} + T + \varepsilon_{P_1}, \quad (13.5)$$

$$P_2 = \rho + c(dt_{r,c} - dt_c^s) + \gamma I_{1,c} + T + \varepsilon_{P_2}, \quad (13.6)$$

$$L_1 = \rho + c(dt_{r,c} - dt_c^s) + u_{r,L_1} - u_{L_1}^s - I_{1,c} + T - \hat{\lambda}_1 N_1 + \varepsilon_{L_1}, \quad (13.7)$$

$$L_2 = \rho + c(dt_{r,c} - dt_c^s) + u_{r,L_2} - u_{L_2}^s - \gamma I_{1,c} + T - \hat{\lambda}_2 N_2 + \varepsilon_{L_2}. \quad (13.8)$$

In this model, the combined satellite clock dt_c^s is consistent with the IGS satellite clock product. The symbol $u_{r,*}$ and u_*^s denote as the uncalibrated phase delays (UPD) for receiver and satellite respectively. The new ionospheric delay I_c is the combination of the raw ionospheric delay and the differential code bias (DCB), which can be expressed as:

$$I_{1,c} = I_1 - \frac{f_2^2}{f_1^2 - f_2^2} \text{DCB}. \quad (13.9)$$

For real-time PPP, the real-time GPS orbits, clocks and UPDs must be estimated firstly. Fortunately, under the framework of the IGS Real-Time Pilot Project (<http://www.rtigs.org>), the real-time GPS satellite orbits and clocks can be determined with the real-time GPS measurements from the data stream. Also, the ultra-rapid orbits with a latency of (3 h) can be used for real-time PPP. However, to fix the undifferenced ambiguities in PPP, the real-time UPDs for carrier phase observables must be estimated along with the orbits and clocks. Owing to the correlation between the ionospheric delays and ambiguities, it is difficult to estimate the UPDs on L1 and L2 precisely. However, they can be computed from the wide-lane and narrow-lane UPDs [4]:

$$u_1 = u_{NL} - \frac{f_2}{f_1 - f_2} u_{WL}, \quad (13.10)$$

$$u_2 = u_{NL} - \frac{f_1}{f_1 - f_2} u_{WL}. \quad (13.11)$$

Compared with the traditional ionosphere-free model, the difference is the way to cope with the ionospheric delays. In the ionosphere-free model, the ionospheric delays are eliminated, which means it is treated as white-noise. In the new model based on the raw observables, the ionospheric delays is regarded as unknowns, which will be estimated along with the coordinates, the receiver clock, the tropospheric delays and the ambiguities. In theory, if no constraints are applied on the ionospheric delay parameters, the new model is equivalent with the traditional model. However, many researches have revealed that if proper constraints considering the spatial and temporal correlations are imposed on the ionospheric delays, it will be possible to accelerate the convergence of the solution.

In general, the spatial variations of the ionospheric delays for single stations are modeled as a low-order polynomial of the longitude and latitude [4]. However, considering the complicated variations of the ionospheric delays in global scale, it is

very difficult to model the ionosphere with uniform functional and stochastic models (Feng 2012; Hofman-Wellenhof 2000). Any improper ionospheric constraints will introduce uncertainty biases in the estimated ionospheric delays. So, in order to keep the ionospheric delays unbiased, the a priori ionospheric delays without considering the spatial variations are considered. Moreover, according to the Eq. (13.9), the rover receiver's DCB in the ionospheric delay is unknown and can't be computed from the external ionosphere model. Therefore, the single-difference of the a priori ionospheric delays between satellites is formed as constraint equation to eliminate the receiver's DCB, which can be expressed as:

$$d\tilde{I} = \tilde{I}_{r,IPP}^s(i) - \tilde{I}_{r,IPP}^s(j) = I_r^s(i) - I_r^s(j), \sigma_{d\tilde{I}} \quad (13.12)$$

where the single-difference ionospheric delay $d\tilde{I}$ is the difference between the slant ionospheric delay of satellite i and reference satellite j at the ionospheric pierce point (IPP); $I_r^s(i)$ and $I_r^s(j)$ are the slant ionospheric delay parameters to be estimated, and $\sigma_{d\tilde{I}}$ is the a priori variance.

The time variation of the slant ionospheric delay can be modeled either by piecewise linear functions with the least square adjustment, or by a random-walk process in a Kalman filter. In our study, the Kalman filter is chosen to estimate the parameters, so the temporal constraint for the slant ionospheric delay is formulated as random walk:

$$I_r^s(t) - I_r^s(t-1) = \omega_t, \omega_t \sim N(0, \sigma_{\omega_t}^2) \quad (13.13)$$

where $I_r^s(t)$, $I_r^s(t-1)$ denote the slant ionospheric delay at epoch t and $t-1$ respectively; ω_t is the changes of data the ionospheric delays between successive epochs; $\sigma_{\omega_t}^2$ is the variance of ω_t , which can be obtained based on the empirical analysis of the real and is at cm-level usually.

In the PPP resolution, the correct fixing of the ambiguities is the guarantee of the accuracy of the solution. With the PPP model defined by the Eqs. (13.5)–(13.8), (13.12) and (13.13), the ambiguities on L1 and L2 are estimated, but considering that no spatial constraints are applied on the ionospheric delays, the ambiguities will be biased by the uncertainty of the ionospheric delays. In order to keep the correct ambiguity fixing of PPP for the reference stations, firstly, the wide-lane ambiguities are formed and fixed to integers with the Boot-Strapping method, then, the narrow-lane ambiguities are fixed with the LAMBDA method. To further improve the performance of the ambiguity fixing, the partial ambiguity fixing strategy is introduced in the estimation. The elevation and the variance of the ambiguities are both chosen as the criteria to judge whether the ambiguity should be fixed or not. Based on the criteria, an iteration process is run until no more ambiguities can be fixed. In addition, to avoid the propagation of the wrong fixed ambiguities and keep all the ambiguities freely in the time-update of the Kalman filter, the float ambiguities and their variance-covariance matrix are kept and transferred to the next epoch [6].

Finally, given the real-time precise satellite orbits, clocks, UPDs, and the GIMs, the PPP with integer ambiguity fixing can be performed for the fixed CORS stations. Moreover, if the coordinates are fixed to the known values, it is possible to fix the ambiguities in a few minutes for the reference stations.

13.3 Interpolation of the Atmospheric Delays

If the solution of the reference receiver has converged, the atmospheric delays will be sent to assist the rover stations' solution. Because the atmospheric information has strong correlation with distance, the augmented atmospheric information from different nearby reference stations should be given different weight to interpolate the atmospheric information for the rover.

Let's denote by $g(i)$ one of the atmospheric delays (it could be ionospheric delays or tropospheric delays) received from the i th reference station. Then, the rover station can generate its atmospheric delays by performing a weighted sum of the data from the N aiding reference stations, thus:

$$\bar{g} = \sum_{i=1}^N \alpha(i)g(i), \quad (13.14)$$

where the set of values $\alpha(i)$ are the weights for the quantity $g(i)$.

The selection of these weights will certainly give different interpolated results. In the traditional network RTK applications, several interpolation methods have been investigated, however, it is difficult to say which is better. Considering that the high-correlation of the atmospheric delays with distance. The distance-based linear interpolation method is proposed. If the distance $d(i)$, between the rover and each i th reference station is known, then we can define the weights as inversely proportional to the distance. The weight coefficient will have the following form:

$$\alpha(i) = \frac{1/d(i)}{\sum_{i=1}^N (1/d(i))} \quad (13.15)$$

13.3.1 Rover Solution

Based on the PPP model described above, Firstly, the real-time orbits, clocks and UPDs must be estimated with a local fixed reference stations. Afterwards, the PPP with ambiguity resolution can be performed at the fixed reference stations, and then the atmospheric delays will be transferred to the rovers located in the region. With the local atmospheric delays' augmentation, the PPP-RTK for local rover stations

will be performed epoch by epoch. Owing to the precise atmospheric information, even the interruption of the GNSS tracking is occurred, the re-initialization time will be very short.

13.4 Experiment Results and Analysis

In order to evaluate the performance of the proposed PPP-RTK, a sparse reference network is selected from the National Geodetic Survey (NGS) CORS as shown in Fig. 13.1. Six Stations denoted by the triangles are chosen as the reference stations; and 4 stations denoted by inverted triangles are the simulated rover stations. All the stations are equipped with the same Leica receivers and the dual-frequency phase and code data has been collected over 24 h on 28th November 2013 with 5 s sampling rate. In the data processing, the mask elevation is set to 10° . In PPP processing, all observations are weighted according to their elevation, with a cut-off elevation of 10° .

In order to access the accuracies of the interpolated atmospheric delays for the rover stations, all the rover stations are processed as reference stations in advance. After that, the atmospheric delays between the estimated and the interpolated are compared and evaluated for the rovers.

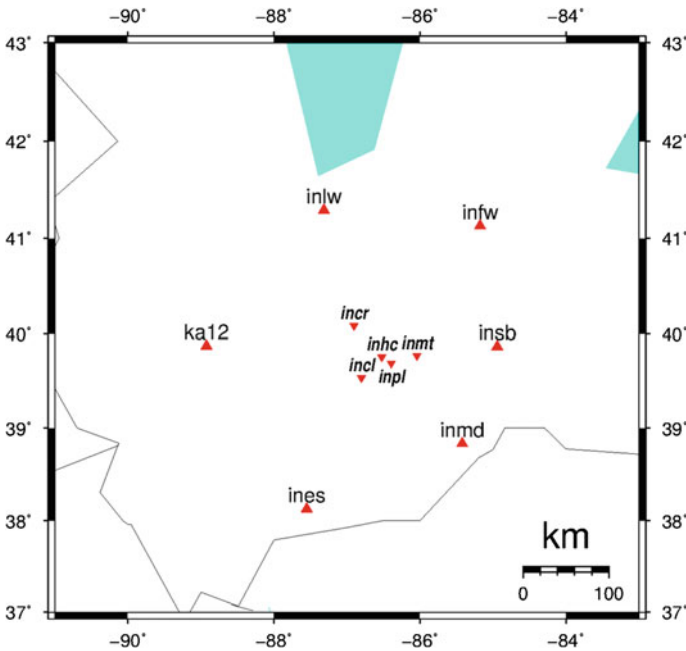


Fig. 13.1 Distribution of the sparse reference network, the *triangles* indicate the reference stations, and the *inverted triangles* denote the selected rover stations

In the experiments, the GPS satellite orbits are from the predicted ultra-rapid orbits, provided by IGS [7], and the real-time satellite clocks are estimated epoch by epoch using Kalman filter. Afterwards, the UPDs of the satellites are computed from 40 regional distributed stations covering the test stations.

In the test, firstly, the 6 static reference stations are processed using PPP with integer ambiguity resolution, and the augmented atmospheric delays will be estimated and delivered to the rovers. After obtaining the atmospheric delays from the reference stations, the augmented PPP is performed for the rovers epoch by epoch.

13.4.1 Accuracy Assessment of the Atmospheric Delays

Before the PPP-RTK positioning, the accuracy of the interpolated atmospheric delays should be assessed firstly. In our test, the atmospheric delays of the rover station INHC are interpolated epoch by epoch with the estimated atmospheric delays from the six augmentation stations denoted as triangles in Fig. 13.1. Then, the interpolated values are compared with the estimated ones to assess the accuracy.

Figure 13.2 shows the differences of the ionospheric delays between the interpolated and estimated values for all the observed GPS satellites. It can be seen that the ionospheric differences are generally smaller than 0.4 m and the RMS is about 0.15 m. If the wide-lane ambiguities are formed, it is possible to fix them in a few epochs.

Additionally, the ionospheric constraints equation should be given a proper weight, which is usually related to the elevation. Figure 13.3 depicts the ionospheric interpolation errors related to the elevation. It can be seen that the ionospheric interpolation errors reduces as the elevation increases, which means the elevation dependent weighting function is reasonable for the ionospheric constraint equation.

Figure 13.4 illustrates the tropospheric interpolation errors, which is better than 1 cm except the last several epochs at the end of the day. Thus, the interpolated tropospheric delay is accurate enough for instantaneous AR.

Fig. 13.2 Ionospheric delay differences between the interpolated and estimated values

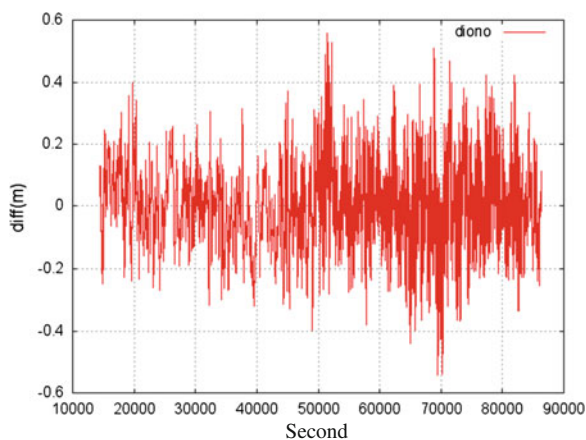


Fig. 13.3 Ionospheric delays differences variations related to the elevation

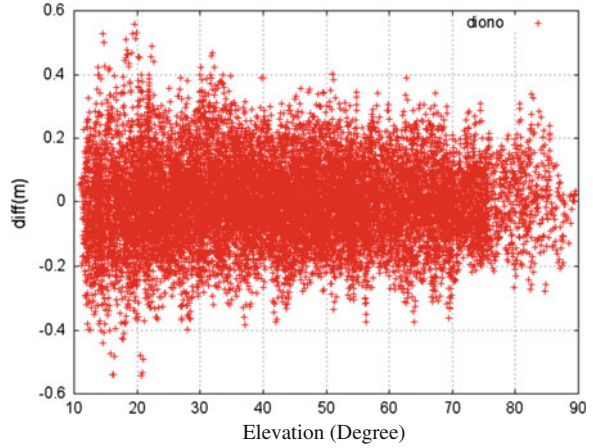
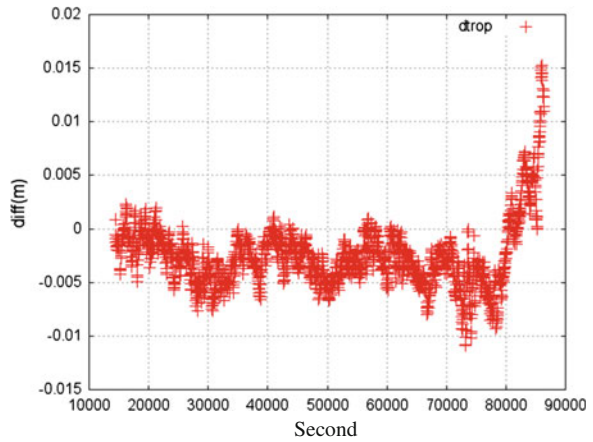


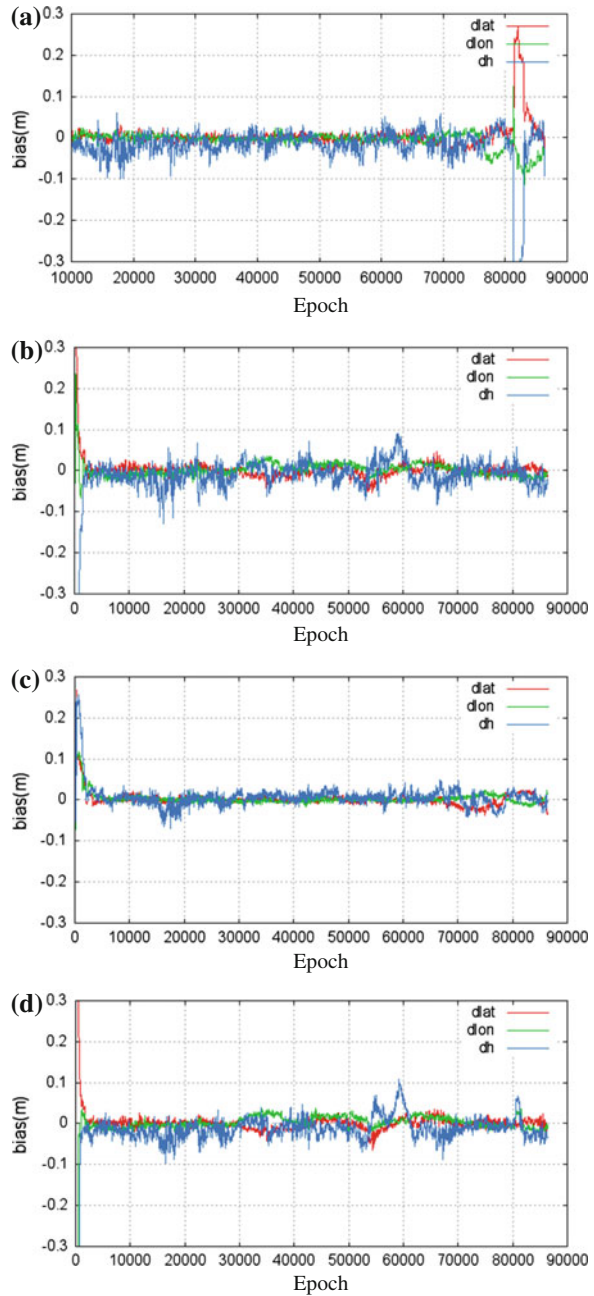
Fig. 13.4 Tropospheric interpolation errors between the interpolated and estimated values



13.4.2 Rover Solution

With the interpolated atmospheric delays, ZD observations of L1, L2 at station incl, inpl, inhc, inmt are corrected. Then, PPP with L1, L2 observations are solved, and then the WL and NL ambiguities are fixed recursively as described in Sect. 13.2. Ambiguity fixing is carried out for the above 4 rover stations epoch by epoch. Figures 13.5 present the position differences of the PPP fixed solution with respect to the static solution. For the 4 stations, the WL ambiguities can be fixed less than 6 epochs, But the NL ambiguities will take longer time to fix. For the INCL, the NL ambiguities can be fixed at 3 epochs, but it will take about 20–30 epoch to fix the NL ambiguities for the INMT, INPL and INHC, the reason the UPD estimation accuracy is the cause of the slow NL ambiguity fixing.

Fig. 13.5 The position errors between the PPP-RTK solution and the fixed solution. **a** INCL, **b** INHC, **c** INPL, **d** INMT



13.5 Conclusion

In this paper, PPP with regional reference network using the raw observables are proposed, and in order to eliminate the correlations between the atmospheric delays and the ambiguities, the WL and NL ambiguities are formed and fixed recursively. Using these derived delays, atmospheric corrections at user stations are interpolated. Then, the atmospheric delay constraint are applied to the PPP model, which then can facilitate the fast ambiguity fixing for the rover stations.

The strategy has been validated experimentally with a regional network of six reference stations and four rover receivers. From the experimental results, the interpolated ionospheric slant corrections have a RMS value of 0.15 m. The tropospheric delays interpolation errors are less than 1 cm. With the interpolated atmospheric corrections, instantaneous ambiguity fixing is available at the user station. The accuracy of the ambiguity fixed positioning solutions is less than 5 cm, and the horizontal positioning solutions is less than 2 cm.

Acknowledgments We would like to thank IGS for providing the precise orbit and clock products, and also thanks to NGS for providing CORS data. This study was supported by National Natural Science Foundation of China (No: 41304027).

References

1. Zumberge JF, Heflin MB, Jefferson DC, Watkins MM, Webb FH (1997) Precise point positioning for the efficient and robust analysis of GPS data from large networks. *J Geophys Res* 102(B3):5005–5017. doi:[10.1029/96JB03860](https://doi.org/10.1029/96JB03860)
2. Bisnath S, Gao Y (2007) Current state of precise point positioning and future prospects and limitations. *Observing our changing earth, international association of geodesy Symposia*. Springer, Berlin, p 133
3. Ge M, Gendt G, Rothacher M, Shi C, Liu J (2008) Resolution of GPS carrier-phase ambiguities in precise point positioning (PPP) with daily observations. *J Geod* 82(7):389–399. doi:[10.1007/s00190-007-0187-4](https://doi.org/10.1007/s00190-007-0187-4)
4. Li X, Ge M, Zhang H, Wickert J (2013) A method for improving uncalibrated phase delay estimation and ambiguity-fixing in real-time precise point positioning. *J Geod* 87(5):405–416. doi:[10.1007/s00190-013-0611-x](https://doi.org/10.1007/s00190-013-0611-x)
5. Kouba J, Héroux P (2001) Precise point positioning using IGS orbit and clock products. *GPS Solution* 5(2):12–28. doi:[10.1007/PL00012883](https://doi.org/10.1007/PL00012883)
6. Collins P, Lahaye F, Héroux P, Bisnath S (2008) Precise point positioning with AR using the decoupled clock model. In: *Proceedings of ION GNSS, USA*, 16–19 Sept 2008
7. Dow JM, Neilan RE, Rizos C (2009) The international GNSS service in a changing landscape of global navigation satellite systems. *J Geod* 83:191–198. doi:[10.1007/s00190-008-0300-3](https://doi.org/10.1007/s00190-008-0300-3)
8. Ge M, Chen J, Gendt G (2009) EPOS-RT: software for real-time GNSS data processing. In: *Geophysical research abstracts*, vol 11. EGU2009-8933, EGU General Assembly, Vienna
9. Banville S, Langley R (2009) Improving real-time kinematic PPP with instantaneous cycle-slip correction. In: *Proceedings of ION GNSS, USA*, 16–19 Sept 2009
10. Boehm J, Niell A, Tregoning P, Schuh H (2005) Global mapping function (GMF): a new empirical mapping function based on numerical weather model data. *Geophys Res Lett* 33: L7304. doi:[10.1029/L025546](https://doi.org/10.1029/L025546)

11. Dai L (2002) Augmentation of GPS with GLONASS and pseudolite signals for carrier phase-based kinematic positioning. School of Surveying and Spatial Information Systems, The University of New South Wales, Sydney
12. Gabor MJ, Nerem RS (1999) GPS carrier phase AR using satellite-satellite single difference. In: Proceedings of 12th international technical meeting, Satellite Division, Institute of Navigation GPS 99, Nashville, 14–17 Sept 1999
13. Gao Y, Li Z, McLellan JF (1997) Carrier phase based regional area differential GPS for decimeter-level positioning and navigation. In: Proceedings of 10th international technical meeting of the Satellite Division of US Institute of Navigation, Kansas City, pp 1305–1313, 16–19 Sept 1997,
14. Gao Y, Shen X (2001) Improving ambiguity convergence in carrier phase-based precise point positioning. In: Proceedings of ION GPS-2001, Salt Lake City, pp 1532–1539, 11–14 Sept 2001
15. Ge M, Zou X, Dick G, Jiang W, Wickert J, Liu J (2010) An alternative network RTK approach based on undifferenced observation corrections. In: ION GNSS 2010, Portland, Oregon
16. Geng J, Meng X, Dodson A, Ge M, Teferle F (2010) Rapid re-convergences to ambiguity-fixed solutions in precise point positioning. *J Geod.* doi:[10.1007/s00190-010-0404-4](https://doi.org/10.1007/s00190-010-0404-4)
17. Han S (1997) Carrier phase-based long-range GPS kinematic positioning. PhD thesis, School of Geomatic Engineering, The University of New South Wales, Sydney
18. Li X, Zhang X (2010) PPP-RTK: real-time precise point positioning with zero-difference ambiguity resolution. In: CPGPS 2010, August, Shanghai
19. Melgard T, Vigen E, Jong K, Lapucha D, Visser H, Oerpen O (2009) G2—the first real-time GPS and GLONASS precise orbit and clock service. In: Proceedings of ION GNSS 2009, Savannah, pp 1885–1891, 22–25 Sept 2009
20. Mireault Y, Tétreault P, Lahaye F, Collins P, Caissy M (2008) Canadian RT/NRT products and services. In: IGS Workshop 2008, Miami Beach, 2–6 June 2008
21. Pérez J, Agrotis L, Fernández J, Garcia C, Dow J (2006) ESA/ESOC real time data processing. IGS Workshop 2006, Darmstadt, 8–11 May 2006
22. Raquet J, Lachapelle G, Fortes L (1998) Use of a covariance analysis technique for predicting performance of regional area differential code and carrier-phase networks. In: 11th international technical meeting of the Satellite Division of the US Institute of Navigation, Nashville, pp 1345–1354, 15–18 Sept 1998
23. Saastamoinen J (1972) Atmospheric correction for the troposphere and stratosphere in radio ranging of satellites. In: Henriksen SW, Mancini A, Chovitz BH (eds) *The use of artificial satellites for Geodesy*. Geophysics Monograph Series, vol 15. AGU, Washington, DC, pp 247–251
24. Teunissen PJG (1995) The least squares ambiguity decorrelation adjustment: a method for fast GPS integer estimation. *J Geod* 70:65–82
25. Wanninger L (1995) Improved AR by regional differential modeling of the ionosphere. In: 8th international technical meeting of the Satellite Division of the US Institute of Navigation, Palm Springs, pp 55–62, 12–15 Sept 1995
26. Wu JT, Wu SC, Hajj GA, Bertiger WI, Lichten SM (1993) Effects of antenna orientation on GPS carrier phase. *Manuscr Geod* 18(2):91–98
27. Wübbena G, Bagge A, Seeber G, Boder V, Hankemeier P (1996) Reducing distance dependent errors for real-time precise DGPS applications by establishing reference station networks. In: 9th international technical meeting of the Satellite Division of the US Institute of Navigation, Kansas City, 17–20 Sept, pp 1845–1852
28. Laurichesse D, Mercier F, Berthias JP, Bijac J (2008) Real time zero- difference ambiguities fixing and absolute RTK. In: Proceedings of ION national technical meeting, San Diego

Chapter 14

Research on GEO Satellite Global Monitoring and Control Based on BeiDou Navigation Satellite System

Yue Zhao, Xianqing Yi, Zhenwei Hou and Tao Zhong

Abstract GEO satellite global monitoring and control refers to the real-time monitoring and control communication for the target satellite in the geostationary orbit through the TT&C system. Due to the presence of invisible arc between the domestic ground station and certain GEO satellite, it's need the help of space-based monitoring and control system or other system with space communication capability to relay forwarding, in order to achieve the real-time communication between the target satellite and the domestic control center. Through the analysis of GEO satellite global mission supporting of current space-based monitoring and control system, it is found that BeiDou Navigation Satellite System (BDS) can be applied to achieve the real-time monitoring and control mission for the domestic control center and overseas GEO satellites. In this paper, the GEO satellite monitoring problem and mission requirements are systematically analyzed combined with the national TT&C network developing status and future plans. According to its composition and mission support capabilities, GEO satellite global monitoring and control communication process is described in support of BDS. Then, the feasible schemes are designed from the geostationary, inclined and medium constellation of BDS. Finally, the recommendation and conclusion of GEO satellite global mission planning based on BDS are given.

Keywords Beidou navigation satellite system · GEO satellite · Monitoring and communication · Application scheme

Y. Zhao (✉) · X. Yi · Z. Hou · T. Zhong
Science and Technology on Information Systems Engineering Laboratory,
National University of Defense Technology, Changsha, China
e-mail: zhaoyue08a@gmail.com

T. Zhong
e-mail: zhongtao09@163.com

14.1 Introduction

Geostationary Earth Orbit (GEO) satellite has characteristics of large orbital radius, wide coverage and geosynchronous cycle, so it is playing an increasingly important role in communications, meteorology, navigation, warning and other civilian and military fields [1]. However, the GEO satellite services are only limited in a fixed area after it is launched in fixed position. For the GEO satellite global mission requirements, there is a need to adjust target GEO satellite to either location or deploy multiple GEO satellites at different locations in orbit. So, we need to study the GEO satellite global monitoring and control problem, whether it considers GEO satellite manager and control, or mission information transmission of GEO satellite.

The ground segment of our space TT&C network is mainly located in the territory with the existence of invisible arc between geostationary orbit satellite and ground station. There are costly and complex management issues with the construction of ground stations across the world to increase the coverage of GEO satellites. Thus, according to the actual development of the space TT&C system, it needs space-based monitoring and control system or other systems with space communications capability to relay forwarding, in order to achieve the real-time monitoring and control of the Control Center for target satellites. Space-based monitoring and control system mainly includes the tracking and data relay satellite system and satellite navigation positioning system. The currently building TDRS system is mainly for data relay terminals of ground and low airborne without planning and construction for the global airborne, while its channel resources is dedicated to the TT&C range without effective coverage for foreign airborne of GEO satellite global monitoring and control missions. On the other hand, it is concluded that BDS can be applied to achieve the global monitoring and control between the control center and target satellite by analyzing the system supporting for GEO satellite global mission.

In this paper, BeiDou Navigation Satellite System (BDS) is applied to support the GEO satellite monitoring and control combined with mission requirements and the national TT&C network developing status and future plans. Then, GEO satellite global monitoring and control feasible schemes are analyzed from the geostationary, inclined and medium constellation of BDS. Finally, it demonstrates the recommendation and conclusion of GEO satellite global mission planning based on BDS.

14.2 Problem Analysis and Mission Supporting of BDS

14.2.1 GEO Satellite Global Monitoring and Control

GEO satellite global monitoring and control refers to the global communication mission between the control center and GEO target satellites through domestic ground stations and relay system.

GEO satellite global monitoring and control communication consists of two sections: one is the direct communication between target satellite and domestic ground station when GEO satellite locates in the directly visual arc segment of geostationary orbit (solid line part in Fig. 14.1); the other is indirect communication between target satellite and ground station via other satellites' relay forwarding, when GEO satellite locates in the directly invisible arc segment of geostationary orbit (dashed portion in Fig. 14.1).

When the target satellite locates in Position A, B of geostationary orbit and it's visible for the domestic station, the control center keeps the real-time monitoring and control for the GEO target satellite via the direct visual link. When the target satellite locates in Position C, D of geostationary orbit and it's invisible for the domestic station, a direct visual link can't be established between the GEO target satellite and ground station, so it needs relay forwarding to achieve not only information transmission but also real-time communication of the control center and the target.

According to the problem analysis of GEO satellite global monitoring and control, the mission is divided into two parts and it's easier to complete missions with the establishment of direct link in the visible area of ground stations, so the key problem is how to build star-ground and inter-satellite link to complete missions with relay system when the GEO satellite is located in the invisible area of ground station. Then, we study mission requirements and supporting abilities of BDS.

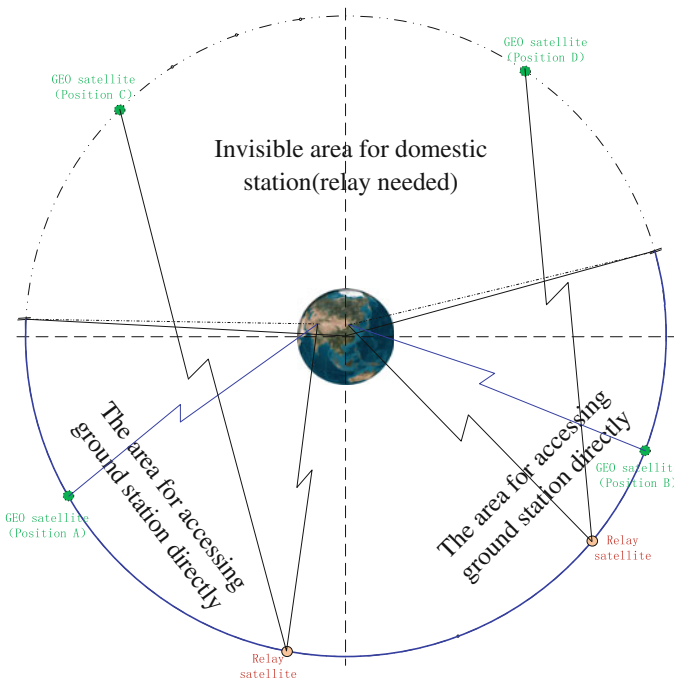


Fig. 14.1 Real-time communication schematic diagram of GEO satellites global mission

14.2.2 Mission Requirements

The space TT&C systems mainly rely on star-ground and inter-satellite links between domestic station and target satellite established by relay satellite to complete the mission of GEO satellite global monitoring and control. Therefore, the following requirements must be satisfied to complete the global mission.

- (1) Reasonable relay satellite of other space system must be chose to meet the requirements of building visible link relaying;
- (2) The star-ground and inter-satellite links must be established as soon as it is required, which has an appropriate mechanism of liaison and link in order to meet the real-time mission requirements;
- (3) The performance indicators of the established star-ground and inter-satellite link must meet GEO target satellite information transfer requirements so that it can be applied for relay forwarding;
- (4) The signal system and protocol specification to meet the mutual compatibility and consistency;
- (5) It can't have too much impact on the existing space system, when the information of GEO target satellite real-time monitoring and control is relayed through the establishment of star-ground and inter-satellite link.

According to the mission requirements, the supporting space system must have the ability to offer relay channel timely to support the global monitoring and control mission, when the target satellite is beyond the visible airborne of domestic station. The relay system must have specific supporting ability: the global visible ability to access the target; the timely and flexible ability to establish link; the ability to have compatible or consistent signal system and protocol specification with the GEO satellite system; the ability to burden additional relaying; the system coordination capacity; the task coordination capacity. The relay supporting system of space TT&C includes TDRS system and satellite navigation and positioning system. The current TDRS system focused on relay forwarding for ground and low airborne to achieve monitoring and control mission [2], so it is difficult to meet required relaying capabilities of the GEO target satellite global mission. On the other hand, it is found that BDS could effectively support GEO satellite global monitoring and control mission through the analysis of GEO satellite global monitoring and control mission and requirement.

14.2.3 Mission Supporting Abilities of BDS

According to the navigation constellation construction requirements of BDS, it has supporting abilities for monitoring and control mission:

- (1) The system has functions for receiving and executing remote command, downloading telemetry parameters;

- (2) The system's communication protocol follows the CCSDS framework, and interface specification is with strong compatibility;
- (3) The system is able to undertake the provisional mission of GEO satellite monitoring and control based on inter-satellite link, satellite ranging, time synchronization, data transfer and extended application capabilities;
- (4) BDS has the ability of in-orbit reconfiguration, constellation independent running, strong anti-interference and environmental monitoring and protection. BDS has a strong mission supporting capability of flexible options according to the specific requirements;
- (5) The GEO satellite has the ability to adjust the orbit position while IGSO and MEO satellites have the ability to adjust the orbit phase. When BDS is applied to the global monitoring and control mission, each constellation can adjust the position and phase for mission requirements to establish flexible visual ISL.

Based on the above analysis, BDS has capabilities to support GEO global monitoring and control mission to meet the proposed requirements of relay system. Therefore, we can apply BDS as relay system to complete GEO satellites global monitoring and control missions. Applying BDS for GEO satellite global monitoring and control communication, it must define space constellation components of BDS, determine the space-based resources to complete the relay mission, and analyze how to apply BDS to support GEO satellite global monitoring and control communication based on mission supporting capabilities of BDS.

14.3 Feasible Scheme Analysis

BDS space constellation contains of 30 satellites in total, including three orbit types of geostationary orbit (GEO), inclined geosynchronous orbit (IGSO) and medium orbit (MEO). Global mission supporting of BDS is analyzed separately from GEO, IGSO and MEO constellations when GEO target satellite is beyond directly visual range of the domestic ground station.

14.3.1 Mission Supporting Process of BDS

BDS space constellation consists of GEO, IGSO and MEO, of which GEO and IGSO are high-orbit constellation in height with GEO target satellite; MEO is medium orbit constellation with the orbit height of 21,528 km [3]. BDS navigation satellite is mainly considered to support GEO global mission when the target is beyond the direct visual range of the ground station. Therefore, we must first determine which domestic ground stations have the largest available direct visual range for target satellites, and the main consideration is for the ground station with the east-west widest range of direct visualization because the target is in

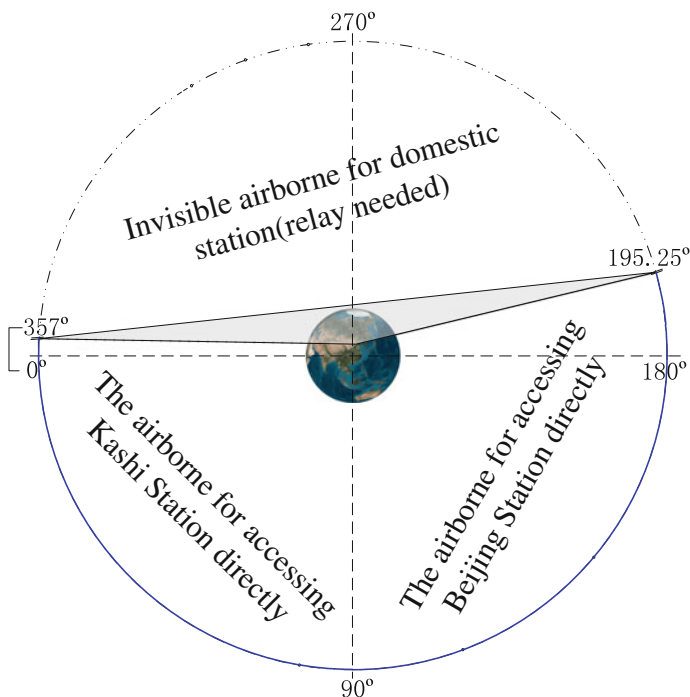


Fig. 14.2 The visible arcs of GEO target satellite

geostationary orbit. Currently, the most typical ground stations with the east-west widest range are Kashi Station and Beijing Station. Therefore, when GEO target is directly visible for domestic station, Beijing Station in the east and Kashi Station in the west are responsible for access task; when GEO target is beyond direct visible range of Beijing Station and Kashi Station, and GEO target is indirectly relayed to access the domestic stations through the BDS navigation satellite.

Build scenario in the STK [4], and Beijing, Kashi and Sanya Station are deployed in the scenario. Adjust the position of the target satellite in geostationary earth orbit, and determine the border of direct visualization between GEO target satellite and ground station according to the access changes, as shown in Fig. 14.2. When the target is located in the ground station's visible geostationary orbit arc (357° – 0° – 90° – 180° – 195.25°), the mission information can be transmitted directly to the ground stations, which then communicate the control center through the Satcom Network or ground network; when the target is located in the ground station's invisible geostationary orbit arc (195.25° – 270° – 357°), GEO target information can't be transmitted directly to the domestic ground station, and it needs the relay forwarding of BDS, then the ground station communicate the control center through the Satcom Network or ground network.

14.3.2 GEO Constellation Supporting Scheme

Both GEO constellation of BDS and GEO target satellite are at geostationary orbit, and GEO1, GEO2 and GEO3 (three current available GEO navigation satellites of BDS) is respectively positioned at 80°E, 110.5°E and 140°E. GEO satellites to support the global monitoring and control can be divided into three combinations: single, binary and triple supporting. By analyzing the positional relationship, it's easy to know, there are certain invisible arcs range (for the earth sheltering) between single GEO satellite and target satellites respectively. Therefore, GEO target global monitoring and control missions can't be supported by a single GEO satellite of BDS.

For binary satellites mission supporting, GEO1/GEO2 (e.g. GEO target at 275.25°) or GEO2/GEO3 (e.g. GEO target at 305.25°) exist invisible arcs with GEO target satellite, as shown in Fig. 14.3, so GEO global mission can't be supported by GEO1/GEO2 or GEO2/GEO3. But when GEO target satellite moves to 290°E (the most unfavorable observation with GEO1 and GEO3 is the angle bisector of which GEO1 and GEO3 is the bottom and the earth center is the top), GEO target can establish direct visible relay link with GEO3 and GEO1

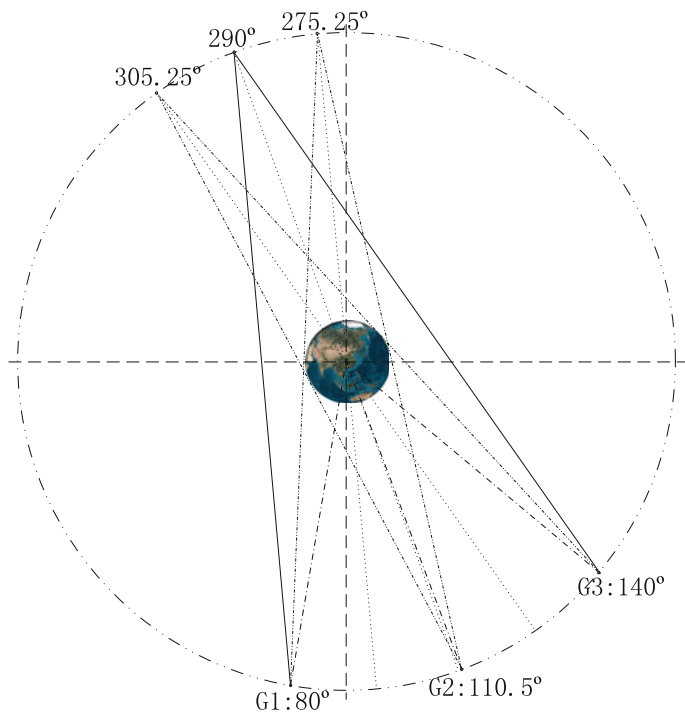


Fig. 14.3 The link analysis of GEO target satellite and GEO1, GEO2 and GEO3 of BDS

simultaneously by access analysis of the STK, so by GEO1 or GEO3 relay forwarding, GEO global mission can be supported by GEO1/GEO3 combination.

Supporting for GEO target global mandate is focused on the specified arc (the arcs in which GEO target satellite can't directly access the station), rather than the entire geostationary orbit. Thus, the entire GEO constellation is to support the global mission by link switching and relay forwarding of GEO1 and GEO3 in GEO constellation; but a single GEO satellite, GEO1 and GEO2 or GEO2 and GEO3 can't realize the supporting of GEO global monitoring and control mission.

14.3.3 IGSO Constellation Supporting Scheme

For the IGSO constellation of BDS, three satellites are located in the orbit of geosynchronous altitude, of which the ascending node longitude is determined as 118° , orbit inclination is 55° , and the phase interval of the star point is 120° . Ground projection is shown in Fig. 14.4.

Because the ascending node longitude of each satellite of IGSO constellation is 118°E , the most unfavorable IGSO satellite observation position for GEO target is 298°E (i.e. $118^\circ + 180^\circ$). When the GEO target moved to 298°E , there exist invisible arcs between the target and each IGSO satellite for building direct visible link, as shown in Fig. 14.5. So GEO global mission can't be supported by a single IGSO satellite, but if completing the switch between three IGSO satellites, the superimposed visual arcs of GEO target and three IGSO satellites will cover the entire period, which can build full-time visible link between GEO target the entire IGSO constellation.

Therefore, it can cover relay global mission for GEO targets beyond the direct visual range of the ground station by IGSO satellite, which explains the whole

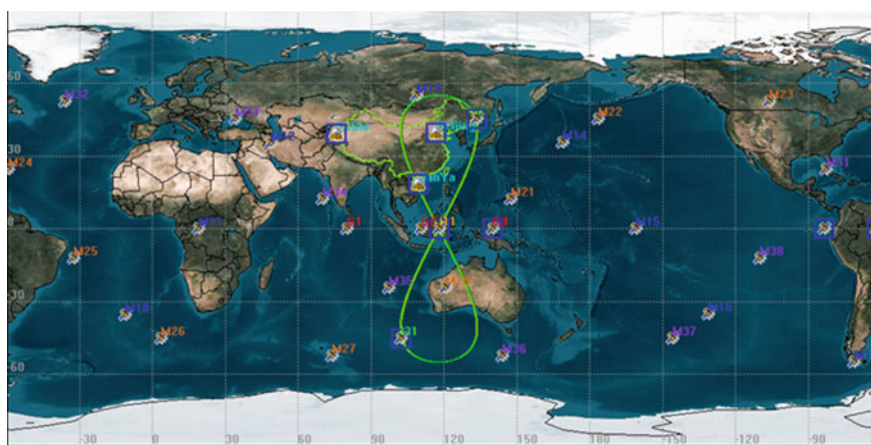


Fig. 14.4 The constellation layout of BDS

Chain-ISL_I1_GMB, ISL_I2_GMB, ISL_I3_GMB: Complete Chain Access Times - 29 Aug 2014 10:38:04

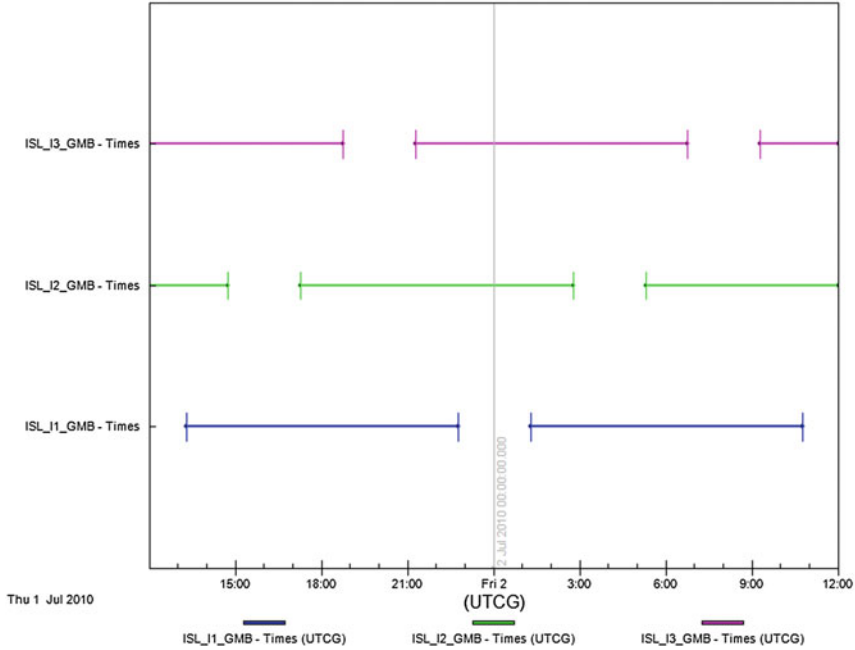


Fig. 14.5 The link connectivity situation of GEO satellites (290°) and IGSO1, IGSO2, IGSO3

IGSO constellation can support the GEO global mission, but a single IGSO satellite can't support.

14.3.4 MEO Constellation Supporting Scheme

MEO constellation of BDS consists of 24 MEO satellites, using Walker 24/3/1 constellation configuration which contains three orbital surfaces with inclination of 55°. Every eight MEO satellites are distributed on each orbital plane with the same phase interval and each side has an MEO backup satellite with orbital height of 21,528 km and satellite orbit return period of 7 days/13 laps.

The same as above GEO or IGSO constellation supporting scheme, the MEO scheme is also aimed at GEO satellites which is located in invisible arcs of 195.25°–357° orbit range for the ground station, only applying MEO constellation as relaying channels for GEO satellites global mission.

According to MEO satellites orbit and operational characteristics, when GEO target satellite is located in the small shaded area in Fig. 14.6 and execute monitoring and control mission (the small shaded area is the domestic station's invisible area for GEO target, while the large shaded area is the domestic station's invisible

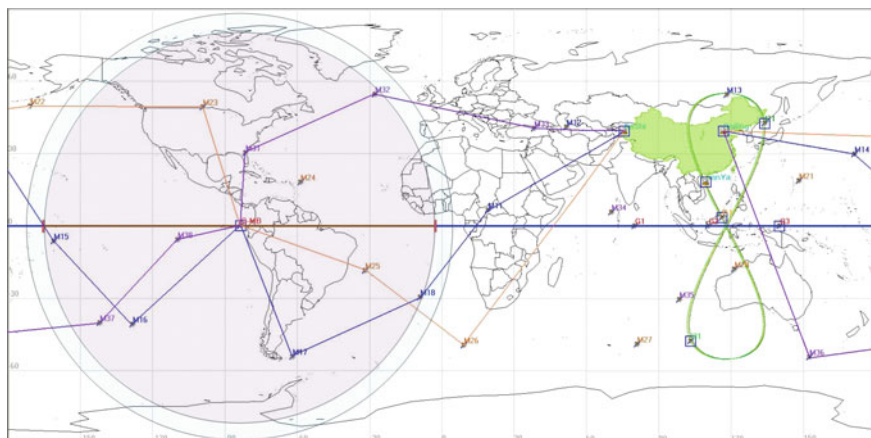


Fig. 14.6 GEO target global mission scheme by MEO constellation relay forwarding

area for MEO satellite), it needs relay forwarding of MEO constellation for GEO target satellite monitoring and control missions. For example, applying the inter-satellite links built for the GEO satellite at orbit position of 276° , the link of MEO31 \rightarrow MEO32 \rightarrow MEO33 \rightarrow Kashi Station or MEO23 \rightarrow MEO22 \rightarrow Beijing Station can be used for relaying communication.

According to MEO constellation composition and operating characteristics, we apply route selection strategies [5] to achieve alternative schemes for supporting GEO target satellite global monitoring and control missions through MEO satellites relay forwarding. There are two signal systems for link construction: double frequency divided in frequency and single frequency divided in time, resulting in route choice being relatively complicated. The relay forwarding of GEO satellites global monitoring and control missions can be achieved through appropriate route selection algorithm to choose the right route, which is relayed by the MEO constellation multi-hop forwards, finally transmitted to the ground station.

The information of MEO satellite constellation can be transferred to the specified ground station through one hop or multi-hop of the inter-satellite link. Therefore, from the view of link topology, GEO global mission can be relayed to ground station by MEO constellation, that is, MEO constellation of BDS supports the GEO target global mandate by one hop or multi-hop relay of MEO satellites.

14.4 Conclusions

This paper studies how to apply BDS to support GEO global monitoring and control. Through a comprehensive analysis of the monitoring and control missions and feasible solutions, the supporting plan is drawn for GEO satellite global monitoring and control missions based on BDS:

- (1) Select GEO constellation of BDS to support GEO satellite global mission. The scheme achieves relay forwarding tasks through the navigation satellite GEO1, GEO3, in which GEO1 is responsible for 290° – 357° arc, GEO3 is responsible for 195.25° – 290° arc and Kashi Station or Beijing Station is directly responsible for other arcs.
- (2) Select IGSO constellation of BDS to support GEO global mission. The scheme achieves GEO global mission relay forwarding through the overlapping switching of any two or three IGSO navigation satellites in the constellation when the visible link is built to GEO target satellite. Through relay forwarding of IGSO constellation, Sanya Station is responsible for receiving mission information.
- (3) Select MEO constellation of BDS to support GEO global mission. The scheme achieves relay tasks through multi-hop relay forwarding of MEO navigation satellites in appropriate place of constellation which chooses the right path by the route selection algorithm, and finally connects the domestic station.

Through comparative analysis, the establishment technology of inter-satellite communication link between the GEO target and GEO navigation satellites is relatively mature, relaying band is more convenient, track alignment and topology is relatively simple, while the establishment of IGSO navigation inter-satellite link is more complicated, and MEO navigation is the most complicated. Therefore, when selecting BDS to support GEO global monitoring and control missions, GEO constellation supporting is the first choice, the follow one is IGSO constellation supporting, and the last is MEO constellation supporting.

References

1. Ren X, Yang L, Zhu Y (2011) Mission planning for multiple GEO satellite proximity inspection. *Flight Dyn* 29(3):76–79
2. NASA (2010) Tracking and data relay satellite system [EB/OL]. <http://www.spacecomm.nasa.gov/spacecomm/tdrss/default1.cfm>. Accessed 26 Aug 2010
3. Yang Y (2010) Progress, contribution and challenges of compass/Beidou satellite navigation system. *Acta Geod et Cartographica Sin* 39(1):1–6
4. Analytical Graphics INC (AGI) (2005) STK user's manual version 4.3 [EB/OL]. <http://www.agi.com/resources/help/help.cfm>. Accessed 01 Aug 2005
5. Yi X, Hou Z, Zhong T, Zhang Y, Sun Z (2014) Research on route strategy of satellite network in GNSS based on topology evolution law. *J Syst Eng Electron* 25(4):596–608

Chapter 15

The Optimal Distribution Strategy of BeiDou Monitoring Stations for GEO Precise Orbit Determination

Longping Zhang, Yamin Dang, Shuqiang Xue, Hu Wang,
Shouzhou Gu and Chuanyang Wang

Abstract The accuracy of BeiDou GEO satellites precise orbit determination is poor. In addition to high altitude and constant position, the monitoring stations distribution is also an important factor of GEO satellites orbit determination. Firstly, the basic principle of geometry orbit determination is introduced and the observation equation is linearized in this paper. Secondly, The GDOP value is parameterized by using orthogonal trigonometric functions. Thirdly, the relationship between stations distribution and the accuracy of precise orbit determination is analyzed according to nested cones. Finally, the simulation experiments are carried out, and a kind of the optimal solution is concluded.

Keywords GEO · Nested cones · GDOP · Monitoring stations distribution

15.1 Introduction

BeiDou navigation satellite system (BDS) is a position and navigation system, which is developed and self-governed by our country. The space segment is designed by mixed constellation which consists of Geostationary Earth Orbit (GEO). Inclined Geosynchronous Satellite Orbit (IGSO) and Medium Earth Orbit (MEO) [1]. In October 2012, the sixteenth BeiDou satellite was launched successfully, which indicated that the area network of China's BeiDou navigation project has completed [2]. Currently, the working satellites include 5 GEO satellites, 5 IGSO satellites, and 4 MEO satellites.

L. Zhang (✉) · C. Wang
Shandong University of Science and Technology, Qingdao, China
e-mail: lpzh1988@163.com

L. Zhang · Y. Dang · S. Xue · H. Wang · S. Gu · C. Wang
Chinese Academy of Surveying and Mapping, Beijing, China

© Springer-Verlag Berlin Heidelberg 2015
J. Sun et al. (eds.), *China Satellite Navigation Conference (CSNC) 2015 Proceedings: Volume I*, Lecture Notes in Electrical Engineering 340,
DOI 10.1007/978-3-662-46638-4_15

In short, there are more than 30 global monitoring stations which can observe GEO satellite, basically meeting the requirements of orbit determination. The stations distribution configuration which is poor has a great influence on GEO satellite orbit determination. Based on the distribution of monitoring stations on the ground, this paper analyzes the impact of the stations configuration on the accuracy of GEO satellites orbit determination.

15.2 The GDOP Optimal Solution of Satellite Orbit Determination

For now, the common methods of GNSS orbit determination include dynamic, geometric, and analytical orbit determination methods, etc. [5]. This chapter illustrates the relationship between the distribution stations and the accuracy of orbit determination with taking geometric orbit determination method for example.

To facilitate the discussion of the problem, the other errors are eliminated. Distance measurements ρ_k are used in observation epoch t_k [6].

$$\rho_k = R_k^j + \Delta + \varepsilon_k \quad (15.1)$$

where the specific expressions of R_{ik}^j is the theoretical distance between the j satellite and the i station as follows:

$$R_{ik}^j = \left[(x_k^j - X_{ik})^2 + (y_k^j - Y_{ik})^2 + (z_k^j - Z_{ik})^2 \right]^{1/2}$$

where (x_k^j, y_k^j, z_k^j) and (X_{ik}, Y_{ik}, Z_{ik}) are the coordinates of satellite and receiver in the terrestrial reference system, respectively; Δ is the equivalent distance measurement of clock offset; ε_k is the observation error with zero mean and variance σ_0^2 [7, 8].

The observation equation is linearized as follows:

$$\Delta\rho_k = H_k\Delta X + \varepsilon_k \quad (15.2)$$

$$H_k = \begin{bmatrix} \frac{x_k^j - X_{ik}}{R_{ik}^j} & \frac{y_k^j - Y_{ik}}{R_{ik}^j} & \frac{z_k^j - Z_{ik}}{R_{ik}^j} & 1 \end{bmatrix}$$

The accuracy of orbit determination is:

$$\sigma_r = \left[\text{tr}(H^T H)^{-1} \right]^{\frac{1}{2}} \cdot \hat{\sigma}_0 \quad (15.3)$$

$$GDOP = \sqrt{\text{tr}(H^T H)^{-1}} = (q_{11} + q_{22} + q_{33} + q_{44})^{\frac{1}{2}} \quad (15.4)$$

where tr is the trace of matrix, $q_{11}, q_{22}, q_{33}, q_{44}$ is the main diagonal elements of weight coefficient matrix; GDOP is used to define the geometric dilution of measuring precision.

The positioning error is proportional to the geometric dilution based on the GNSS positioning theory. Therefore, the lower GDOP value is, the higher accuracy of orbit determination is in the case of the same orbit determination algorithm and observation error. Therefore, the problem of orbit determination accuracy can be converted into solving the GDOP value.

$$H = \begin{bmatrix} e_1^T & e_2^T & \dots & e_i^T \\ 1 & 1 & \dots & 1 \end{bmatrix}^T \tag{15.5}$$

e_i is the direction cosine from the satellite to stations; e_i is the unit direction vector [9, 10] and should follow $\|e_i\|_2 = 1$; the vector e_i is parameterized as follows:

$$e_i = [\sin \theta_i \cos \varphi_i \quad \sin \theta_i \sin \varphi_i \quad \cos \theta_i] \tag{15.6}$$

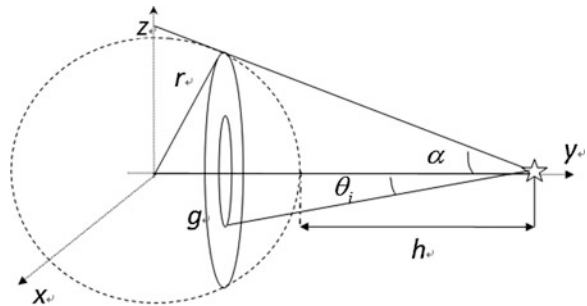
In Fig. 15.2, the asterisk represents one of GEO satellite, α is the angle between the tangent direction of GEO satellite to the Earth and the direction of satellite to the center of the earth; g is the plane of distribution stations; r is the radius of the earth; h is the distance between geocentre and the ground; θ_i is the cone apex angle constructed of the satellite and stations plane.

$$N = H^T H \tag{15.7}$$

GDOP value can get the minimum with the following two conditions by a single cone positioning configuration with minimum GDOP.

$$\sum_{i=1}^n \sin \varphi_i \cos \varphi_i = 0; \quad \sum_{i=1}^n \sin \varphi_i = 0; \quad \sum_{i=1}^n \cos \varphi_i = 0; \tag{15.8}$$

Fig. 15.2 GDOP value with GEO satellites precise orbit determination



$$\sum_{i=1}^n \cos^2 \varphi_i = \sum_{i=1}^n \sin^2 \varphi_i = \frac{n}{2}; \quad (15.9)$$

Some useful equations will be obtained as follows:

$$N_{1,1} = \frac{n}{2} \sin^2 \theta; \quad N_{2,2} = \frac{n}{2} \sin^2 \theta; \quad N_{3,3} = n \cos^2 \theta; \quad N_{4,4} = n; \quad (15.10)$$

$$N_{3,4} = n \cos \theta; \quad N_{4,3} = n \cos \theta; \quad (15.11)$$

$$N_{1,2} = 0; \quad N_{1,3} = 0; \quad N_{2,3} = 0; \quad (15.12)$$

- ① GEO satellites have constant position, so we can think that the configuration of satellites and stations is unchanged;
- ② Additions of multiple such distributions are still the optimal [11].

So the T-layers cones are superimposed and the matrix N can be expressed as:

$$N := H^T H = \begin{bmatrix} \sum_{i=1}^T \frac{n_i}{2} \sin^2 \theta_i & 0 & 0 & 0 \\ 0 & \sum_{i=1}^T \frac{n_i}{2} \sin^2 \theta_i & 0 & 0 \\ 0 & 0 & \sum_{i=1}^T n_i \cos^2 \theta_i & \sum_{i=1}^T n_i \cos \theta_i \\ 0 & 0 & \sum_{i=1}^T n_i \cos \theta_i & \sum_{i=1}^T n_i \end{bmatrix}$$

The inverse of matrix N can be written as:

$$N^{-1} = \begin{bmatrix} \left(\sum_{i=1}^T \frac{n_i}{2} \sin^2 \theta_i \right)^{-1} & 0 & 0 & 0 \\ 0 & \left(\sum_{i=1}^T \frac{n_i}{2} \sin^2 \theta_i \right)^{-1} & 0 & 0 \\ 0 & 0 & k \sum_{i=1}^T n_i & -k \sum_{i=1}^T n_i \cos \theta_i \\ 0 & 0 & -k \sum_{i=1}^T n_i \cos \theta_i & k \sum_{i=1}^T n_i \cos^2 \theta_i \end{bmatrix}$$

The constraint conditions are: $\theta_i \in [0, \alpha]$; $\alpha = \sin \frac{r}{r+h}$, the largest cone angle of GEO is 8.8° .

$k = \frac{1}{\sum_{i=1}^T n_i \cos^2 \theta_i \sum_{i=1}^T n_i - \left(\sum_{i=1}^T n_i \cos \theta_i \right)^2}$; $i = 1, 2, 3, \dots, T$, T is the number of nested cones.

Therefore, the objective function can be established:

$$2\left(\sum_{i=1}^T \frac{n_i}{2} \sin^2 \theta_i\right)^{-1} + \frac{\sum_{i=1}^T n_i + \sum_{i=1}^T n_i \cos^2 \theta_i}{\sum_{i=1}^T n_i \cos^2 \theta_i \sum_{i=1}^T n_i - \left(\sum_{i=1}^T n_i \cos \theta_i\right)^2} = \min \quad (15.13)$$

The minimum GDOP value can be got when the Eq. (15.13) achieves. The highest accuracy of GEO satellites orbit determination will be theoretical obtained with this strategy when the other conditions are agreed.

15.3 The Analysis of Simulation Experiments

Equation (15.13) shows that there are infinitely solutions of nested conical distributions when $T > 1$. Number of different nesting cones and different stations on the same nesting cone will all influence the GDOP value. It is difficult to achieve that the impact of all policies are analysed. Therefore, this paper carries on the simulation analysis as an example of the simple two-layers nested cone and GDOP values are tested with 1 + 7, 2 + 6, 3 + 5, 4 + 4 based on 8 stations.

The first part can be expressed as:

$$M = 2\left(\sum_{i=1}^T \frac{n_i}{2} \sin^2 \theta_i\right)^{-1}$$

The second part can be expressed as:

$$L = \frac{\sum_{i=1}^T n_i + \sum_{i=1}^T n_i \cos^2 \theta_i}{\sum_{i=1}^T n_i \cos^2 \theta_i \sum_{i=1}^T n_i - \left(\sum_{i=1}^T n_i \cos \theta_i\right)^2}$$

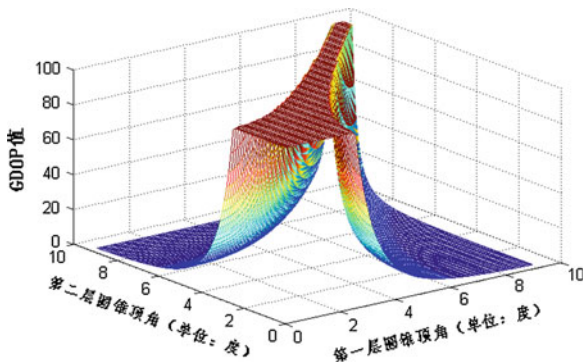
Them show that the objective function will obtain a larger value, when the stations is distributed at a narrow area below of the GEO satellite or similar cones.

So, $T = 2$, $n_1 = n_2 = 4$

$$\frac{1}{\sin^2 \theta_1 + \sin^2 \theta_2} + \frac{2 + \cos^2 \theta_1 + \cos^2 \theta_2}{4(\cos \theta_1 - \cos \theta_2)^2} = \min$$

The extremum of value that eight stations evenly are distributed in two cones is showed in Fig. 15.3 with the plane direction for θ_1, θ_2 and the height direction for the simulation value of GDOP. The minimum value can be achieved as $\theta_1 \approx 0^\circ$
 $\theta_2 \approx 8.8^\circ$.

Fig. 15.3 The simulation of GDOP with 4 + 4



$$T = 2, n_1 = 1, n_2 = 7$$

$$\frac{4}{1 \sin^2 \theta_1 + 7 \sin^2 \theta_2} + \frac{8 + 1 \cos^2 \theta_1 + 7 \cos^2 \theta_2}{8(1 \cos^2 \theta_1 + 7 \cos^2 \theta_2) - (1 \cos \theta_1 + 7 \cos \theta_2)^2} = \min$$

$$T = 2, n_1 = 2, n_2 = 6$$

$$\frac{4}{2 \sin^2 \theta_1 + 6 \sin^2 \theta_2} + \frac{8 + 2 \cos^2 \theta_1 + 6 \cos^2 \theta_2}{8(2 \cos^2 \theta_1 + 6 \cos^2 \theta_2) - (2 \cos \theta_1 + 6 \cos \theta_2)^2} = \min$$

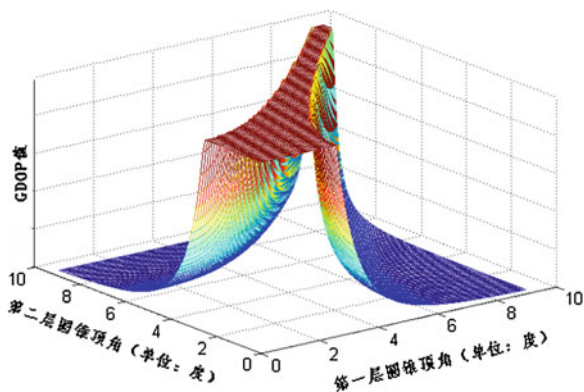
$$T = 2, n_1 = 3, n_2 = 5$$

$$\frac{4}{3 \sin^2 \theta_1 + 5 \sin^2 \theta_2} + \frac{8 + 3 \cos^2 \theta_1 + 5 \cos^2 \theta_2}{8(3 \cos^2 \theta_1 + 5 \cos^2 \theta_2) - (3 \cos \theta_1 + 5 \cos \theta_2)^2} = \min$$

The above three cases of GEO satellites orbit determination simulation experiment with 8 stations is showed in Fig. 15.4. The minimum value can be also

$$\text{achieved as } \begin{matrix} \theta_1 \approx 0^\circ \\ \theta_2 \approx 8.8^\circ \end{matrix}$$

Fig. 15.4 The GDOP simulation of other three cases



This paper respectively carries out simulation experiments of four strategies with eight stations. The trend of results is exactly same. On the one hand, the minimum of GDOP value is achieved as $\theta_1 \approx 0^\circ$, on the other hand, it is the maximum $\theta_2 \approx 8.8^\circ$, when θ_1 is similar or equal with θ_2 . That is to say, we will get the high accuracy when a station is distributed below of the GEO satellite and other are away from it.

15.4 Conclusions

This paper analyses the effect of different stations distribution on GEO satellites orbit determination and obtained a kind of stations distribution of the optimal solution based on the basic principle of satellite orbit determination, using nested cone configuration. The conclusions are as follows:

- (1) Currently, the stations distribution configuration of GEO satellites is poor, which plays an important role on the GEO satellites orbit determination.
- (2) A kind of the optimal solution of GEO can be concluded with the method of nested conical configuration.
- (3) Using two-layers nested cone, the optimal distribution of GEO satellites orbit determination is as follows: a station should be distributed in the down of GEO satellites and other should be wide away from it.
- (4) The greater the number of monitoring stations with different nested cones, the more abundant the configuration of the minimum GDOP value, which can provide a reference for multi-GNSS precise orbit determination.

Acknowledgments This study is funded by the National Natural Science Fund (41404034) and the International GNSS Monitoring and Assessment System (GFZX0301040308-06). This work is also supported by the national science and technology supporting plan (2012BAB16B01), the fundamental research funds of Chinese Academy of Surveying and mapping (7771405/7771416) and the Key Laboratory of Surveying and Mapping Technology on Island and Reef, National Administration of Surveying, Mapping and Geoinformation (2013B01).

References

1. Lou Y, Liu Y, Shi C, et al (2014) Precise orbit determination of BeiDou constellation based on BETS and MGEX network. Scientific Reports
2. [http://www.BeiDou.gov.cn/\[EB/OL\]](http://www.BeiDou.gov.cn/[EB/OL]), (2012)
3. Jiao W (2013) The iGMAS latest progress report. China satellite navigation conference, CSNC
4. Shi C, Zhao QL, Li M et al (2012) Precise orbit determination of BeiDou satellites with precise positioning. Sci China Earth Sci. doi:10.1007/s11430-012-4446-8
5. Liu W (2005). The research on the effect of ground observation stations distribution on the precision of orbit determination. Wuhan University, Wuhan
6. Xu Q (2002) Satellites positioning and navigation. Tsinghua University Press, Beijing

7. Wen Y, Liu Q, Zhu J et al (2007) The effect of TT&C deployment on the regional satellite navigation system. *J Natl Univ Def Technol* 29(1):1–6
8. Zhou Z, Yi J, Zhou Q (2004) *Gps satellite surveying principles and application*. Surveying and Mapping Press, Beijing
9. Xue S, Yang Y, Chen W (2014) A kind of single-point-positioning configuration with minimum GDOP from orthogonal trigonometric functions 39(7):820–825
10. Yang Y (2011) Contribution of the compass satellite navigation system to global PNT users. *Chin Sci Bull*
11. Xue S, Yang Y (2014) Nested cones of single-point-positioning configuration with minimum GDOP. *J Wuhan Univ* 39(11):1369–1374

Chapter 16

Analysis and Comparison of Non-coherent and Differential Acquisition Integration Strategies

Dandan Zeng, Songlin Ou, Jinhai Li, Jinhai Sun, Yuepeng Yan and Haofeng Li

Abstract In the application of global satellite position system, signal adaptive acquisition strategies are required for various environment applications, such as weak signal, emergency moment, so fast and high sensitivity acquisition algorithms are important for the receiver process. This paper presents acquisition algorithms: coherent integration, non-coherent integration, differential coherent and differential non-coherent integration, and the differential integration are analyzed in both standard and pair-wise form, all of which are theoretically compared in their probability distribution with detailed analysis. And testing statics using Monte-Carlo with collected realistic various signal, considering the existence of carrier Doppler frequency and code phase shift in the objectives, give out that in certain probability of detection, differential standard coherent integration is the best detector, non-coherent integration is the second best; and differential pair-wise coherent, differential standard and pair-wise non-coherent integration give out almost the same performance; and the standard algorithm is more tolerable in residual Doppler environment than the pair-wise algorithm; the code phase shift will affect much more in the lower probability of detection; finally, in the theory analysis, the hypothesis of approximated gauss distribution and the IQ data completely independence with each other need to be revised in more accurate model to fit the actual data.

Keywords Non-coherent integration · Differential coherent integration · Differential non-coherent integration · Pair-wise integration · Residual doppler frequency

D. Zeng (✉) · S. Ou · J. Li · J. Sun · Y. Yan · H. Li
Institute of Microelectronics of Chinese Academy of Sciences, IMECAS,
Beijing 100029, China
e-mail: zengdandan@ime.ac.cn

© Springer-Verlag Berlin Heidelberg 2015
J. Sun et al. (eds.), *China Satellite Navigation Conference (CSNC) 2015 Proceedings: Volume I*, Lecture Notes in Electrical Engineering 340,
DOI 10.1007/978-3-662-46638-4_16

16.1 Introduction

In the application of global satellite position system, signal adaptive acquisition strategies are required for various environment applications, such as weak signal, emergency moment, so fast and high sensitivity acquisition algorithms are important for the receiver process. This paper presents acquisition algorithms: coherent integration, non-coherent integration, differential coherent and differential non-coherent integration.

Increasing the coherent integration time is the most effective way to improve the receiver sensitivity, but due to the exits of the navigation data bit modulation and the secondary code, the coherent accumulation effect will be eliminated, and even made no use when encountering the inverted data. Furthermore, the larger coherent integration time will bring out the much bigger number of Doppler frequency bins needed to search, resulting the larger scale of acquisition time. So in the weak signal acquisition application, the combination of the non-coherent or differential integration algorithm will make better use.

Non-coherent integration algorithm can overcome the impact of data bit flipping; but in the cost of squaring loss [1] compared to the original integration gain when increasing the accumulation time. That is why that large integration time is usually required to acquire weak signal if non-coherent integration algorithm is taking. Fortunately, we can get some help from the previous achievements of the excellent intelligent [2, 3], who proposed the differential integration algorithm to solve these problems. In this paper, a non-coherent integration, differential coherent integration and differential non-coherent integration algorithms will be analyzed, and the differential integration algorithm will be presented in the standard form and pair-wise form. And then, a theoretical probability distribution analysis and acquisition probability of these different integration strategies will be simulated. Finally, testing statics using Monte-Carlo with collected realistic various signals, considering the existence of carrier and code phase shift in the objectives, give out the results, which will be described in detail as below.

16.2 Algorithm Analysis

16.2.1 Different Integration Strategies

We usually take the signal envelope or energy to detect if the satellite signal is exist. Here in this paper, we will adopt the signal energy as the detection decision statistic in convenience.

First, the energy decision statistic description of the non-coherent integration detection [1] is in Eq. (16.1)

$$z = \sum_{k=1}^K |I_k + jQ_k|^2 \quad (16.1)$$

Secondly, the energy decision statistic description of the differential non-coherent integration detection [1] is in Eq. (16.2)

$$\begin{aligned} z &= \sum_{k=2}^K |(I_k + jQ_k)(I_{k-1} + jQ_{k-1})^*|^2 \\ &= \sum_{k=2}^K (I_k I_{k-1} + Q_k Q_{k-1})^2 + (Q_k I_{k-1} - I_k Q_{k-1})^2 \end{aligned} \quad (16.2)$$

Using the joint probability distribution, we can derive the conclusion that: the noise variance of the differential processing will be much less than that of non-coherent processing, in the other words, the SNR of the differential processing will be much higher, when the noise is independent to each other [1].

Thirdly, the energy decision statistic description of the differential coherent integration detection [1] is in Eq. (16.3)

$$\begin{aligned} z &= \left| \sum_{k=2}^K (I_k + jQ_k)(I_{k-1} + jQ_{k-1})^* \right|^2 \\ &= \left| \sum_{k=2}^K (I_k I_{k-1} + Q_k Q_{k-1}) + j(Q_k I_{k-1} - I_k Q_{k-1}) \right|^2 \end{aligned} \quad (16.3)$$

Commonly as we know, in the hypothesis that the input signal and the local reference signal being in the perfect synchronization with no code phase shift and no Doppler frequency residual, and the signal being present in the phase I branch, and Q being noise after the coherent integration, also the signal amplitude A being unchanged in the succession data, and the noise average mean being 0, using the $Q_k I_{k-1} - I_k Q_{k-1} \approx 0$, we can get the corresponding simple differential non-coherent detection to replace of Eq. (16.2) in the following Eq. (16.4)

$$z = \sum_{k=2}^K |I_k I_{k-1} + Q_k Q_{k-1}|^2 \quad (16.4)$$

Similarly, we use the Eq. (16.5) to show the simple differential coherent detection.

$$z = \left| \sum_{k=2}^K (I_k I_{k-1} + Q_k Q_{k-1}) \right|^2 \quad (16.5)$$

Currently, most of the processing and analysis of the differential integration algorithm used are based on Eq. (16.4) or (16.5), as it is simple and easy to obtain the probability distribution in the explicit expressions.

But in the actual signal environment, the signal not only exists in the real part of the signal, but also the imaginary part, in the presence of the commonly Doppler residual. As a result, if we take only the real part of signal to detect as the simple expression in Eq. (16.4) or (16.5), we have to confront with the loss of signal energy, and then the worse acquisition performance. Therefore, in this paper we will take the full expression in Eqs. (16.2) and (16.3) to do the corresponding acquisition signal distribution and performance analysis.

In addition, there is a differential pair-wise expression, counterpart to the differential standard expression described above, in a different way to do the detection. So fourthly, the energy decision statistic description of the differential pair-wise non-coherent integration is as follows in Eq. (16.6)

$$z = \sum_{k=1}^{K/2} |(I_{2k} + jQ_{2k})(I_{2k-1} + jQ_{2k-1})^*|^2 \quad (16.6)$$

Similarly in the final, the energy decision statistic description of the differential pair-wise coherent integration is as follows in Eq. (16.7)

$$z = \left| \sum_{k=1}^{K/2} (I_{2k} + jQ_{2k})(I_{2k-1} + jQ_{2k-1}^*) \right|^2 \quad (16.7)$$

To get the performance comparison of the different integration strategies in weak signal application, we focus our interest to the five different integration algorithms: non-coherent integration, differential standard non-coherent integration, differential standard coherent integration, differential pair-wise non-coherent integration and the differential pair-wise coherent integration after one ms coherent integration when figure up the acquisition performance, and then do the verification using the actual collected data.

16.2.2 Probability Distribution and Performance Analysis

The 1 ms coherent integration of the signal can be modeled [1] as Eq. (16.8).

$$r = AD(\Delta\tau)R(\Delta\tau) \exp(j(\Delta\omega_k T_{\text{coh}}/2 + \varphi_k)) \sin c(\Delta\omega_k T_{\text{coh}}/2) + \eta \quad (16.8)$$

where A is the signal amplitude; D is navigation data bits; R() is the auto-correlation function between the input signal and the local code; $\Delta\tau$ is the time shift deviation between the input signal and the local generated code; $\Delta\omega_k$ is the residual

Doppler frequency; T_{coh} is the coherent integration time in ms unit; φ is the residual phase; η is the Gaussian white noise with the zero mean; N_0 is the noise power spectral density and will be normalized to 1 in later description.

Firstly, based on the ideal situation, in the absence of impact from code shift, Doppler frequency residual, and data bit modulation, we can get the detection probability as follows.

When there is no signal present, the non-coherent integration can be described in centered chi-square distribution with $2K$ degree of freedom, as the detection variables are approximately $2K$ independent Gaussian white noises added with the same distribution in zero mean and variance 1; its probability density function can be expressed as Eq. (16.9), where $\Gamma(K)$ is the gamma function.

$$p(z|H_0) = e^{-z/2}y^{K-1}/(2^K\Gamma(K)) \quad (16.9)$$

So the statistic mean and variance of the non-coherent integration in the absence of signal are as Eqs. (16.10) and (16.11)

$$E(z|H_0) = 2K \quad (16.10)$$

$$D(z|H_0) = 4K \quad (16.11)$$

In the same way, we can get the distribution when the signal is present. As the samples preparing for the non-coherent K accumulation are independent to each other, the non-coherent integration detection probability distribution can be regarded as non-central chi-square distribution of $2K$ degree of freedom with the non-central variable in $\lambda = KA^2$; and its probability density function can be expressed as [1]:

$$p(z|H_1) = 1/2\left((z/\lambda)^{K-1/2}\right)e^{-(z+\lambda)/2}I_{K-1}(\sqrt{\lambda z}) \quad (16.12)$$

where $I_{k-1}()$ is the first class modified Bessel function in $K - 1$ order, and $\lambda = KA^2 = 2KT_{\text{coh}}CN_0$, so the statistic mean and variance of the non-coherent integration when the signal is present are as Eqs. (16.13) and (16.14):

$$E(z|H_1) = 2K + \lambda = 2K(1 + T_{\text{coh}}CN_0) \quad (16.13)$$

$$D(z|H_1) = 4K + 4\lambda = 4K(1 + 2T_{\text{coh}}CN_0) \quad (16.14)$$

Secondly, we turn to the differential standard non-coherent integration in Eq. (16.2), which can be re-described in the polar coordination using Eq. (16.15)

$$I_j = r_j \cos\theta_j|_{j=k-1,k} \quad Q_j = r_j \sin\theta_j|_{j=k-1,k} \quad (16.15)$$

So we can get the simplified expression as Eq. (16.16)

$$\begin{aligned}
z &= \sum_{k=2}^K (I_k I_{k-1} + Q_k Q_{k-1})^2 + (Q_k I_{k-1} - I_k Q_{k-1})^2 \\
&= \sum_{k=2}^K (r_k r_{k-1} \cos(\theta_k - \theta_{k-1}))^2 + (r_k r_{k-1} \sin(\theta_k - \theta_{k-1}))^2 = \sum_{k=2}^K (r_k r_{k-1})^2
\end{aligned} \tag{16.16}$$

Then we can get the statistic mean and variance of $z_k = (r_k r_{k-1})^2$ as followed Eqs. (16.17)–(16.20), using the joint probability density function, in the hypothesis descript previously and taking the Gauss distribution approximate.

$$E(z_k | H_0) = 4 \tag{16.17}$$

$$D(z_k | H_0) = 48 \tag{16.18}$$

$$E(z_k | H_1) = A^4 + 4A^2 + 4 \tag{16.19}$$

$$D(z_k | H_1) = 8(A^6 + 5A^4 + 16A^2 + 6) \tag{16.20}$$

We have to note that, to get the precise form fitting the distribution of the differential standard non-coherent integration is so difficult that we have to turn to seek an alternative solution, what is less attractive than one's original objective but can meet requirements. So we pay our attention to the central limit theorem of Gaussian approximation approach. But we should keep in mind that if taking the Gaussian approximation approach in the calculation and the simulation, we should make sure the integration time is large enough, like 20, otherwise, we have to find other accurate model to do the work. In the other words, the calculated probability of detection will be valid only if the integration time is more than 20, and if lower than 20, one have to seek help from Ref. [2], which give some examples to approach the precise model to estimate the probability of detection in fewer hypothesis and closer to the actual environment.

In this paper, we just take the Gaussian approximation approach to do the simulation. So we can get the statistic mean and variance of the differential standard non-coherent integration are as Eqs. (16.21)–(16.24), based on the conclusion of (16.17)–(16.20)

$$E(z | H_0) = 4(K - 1) \tag{16.21}$$

$$D(z | H_0) = 48(K - 1) \tag{16.22}$$

$$E(z | H_1) = (K - 1)(A^4 + 4A^2 + 4) \tag{16.23}$$

$$D(z | H_1) = 8(K - 1)(A^6 + 5A^4 + 16A^2 + 6) \tag{16.24}$$

Similarly, the differential pair-wise non-coherent integration of Eq. (16.4) can be re-descript in Eq. (16.25) under the Gaussian approximation.

$$\begin{aligned} z &= \sum_{k=1}^{K/2} (I_{2k}I_{2k-1} + Q_{2k}Q_{2k-1})^2 + (Q_{2k}I_{2k-1} - I_{2k}Q_{2k-1})^2 \\ &= \sum_{k=1}^{K/2} (r_{2k}r_{2k-1} \cos(\theta_{2k} - \theta_{2k-1}))^2 + (r_{2k}r_{2k-1} \sin(\theta_{2k} - \theta_{2k-1}))^2 = \sum_{k=1}^{K/2} (r_{2k}r_{2k-1})^2 \end{aligned} \quad (16.25)$$

So the mean and variance of the differential pair-wise non-coherent integration can be obtained as (16.26)–(16.29) using the Gaussian approximation.

$$E(z|H_0) = 4(K/2) \quad (16.26)$$

$$D(z|H_0) = 48(K/2) \quad (16.27)$$

$$E(z|H_1) = (K/2)(A^4 + 4A^2 + 4) \quad (16.28)$$

$$D(z_k|H_1) = 8(A^6 + 5A^4 + 16A^2 + 6) \quad (16.29)$$

Now, we can see the differential standard coherent integration in Eq. (16.3) can be rewrite in Eq. (16.30).

$$z = \left| \sum_{k=2}^K (I_k I_{k-1} + Q_k Q_{k-1}) + j(Q_k I_k - I_k Q_{k-1}) \right|^2 = \left| \sum_{k=2}^K A_k + B_k + C_k + D_k \right|^2 \quad (16.30)$$

In Eq. (16.30), we use four parts to calculate the result of differential pair-wise coherent integration, and get the description of each as Eq. (16.31).

$$\begin{aligned} A_k &= A^2 D_k D_{k-1} R(\Delta\tau)^2 \operatorname{sinc}\left(\Delta\omega_k \frac{T_{\text{coh}}}{2}\right) \operatorname{sinc}\left(\Delta\omega_{k-1} \frac{T_{\text{coh}}}{2}\right) \\ &\quad \times \exp\left(j\left((\Delta\omega_k - \Delta\omega_{k-1}) \frac{T_{\text{coh}}}{2} + \Delta\varphi_k\right)\right) \\ B_k &= A D_k R(\Delta\tau) \operatorname{sinc}\left(\Delta\omega_k \frac{T_{\text{coh}}}{2}\right) \exp\left(j\left(\Delta\omega_k \frac{T_{\text{coh}}}{2} + \varphi_k\right)\right) \eta_{k-1}^* \\ C_k &= A D_{k-1} R(\Delta\tau) \operatorname{sinc}\left(\Delta\omega_{k-1} \frac{T_{\text{coh}}}{2}\right) \exp\left(-j\left(\Delta\omega_{k-1} \frac{T_{\text{coh}}}{2} + \varphi_{k-1}\right)\right) \eta_k \\ D_k &= \eta_k \eta_{k-1}^* \end{aligned} \quad (16.31)$$

To get the distribution characteristics of Z in Eq. (16.30), we have to deal with the divided parts.

First we take a look at the noise term D_k , which can be taken as independent Gaussian distribution with zero mean and variance δ^2 , so we can get the joint distribution in Eq. (16.32), according to the joint probability of $\eta_{I,k}$, $\eta_{Q,k}$, where $K_0(\cdot)$ is the modified second class Bessel in zero.

$$f_{\eta_{I,k}, \eta_{Q,k}}(u) = K_0(u/\delta^2)/(\pi\delta^2) \quad (16.32)$$

The noise variance of D_k is in Eq. (16.33)

$$\begin{aligned} \delta_{\sum D_k}^2 &= 4(K-1) \int_{-\infty}^{\infty} u^2 f_{\eta_{I,k}, \eta_{Q,k}}(u) du \\ &= 4(K-1)2 \int_{-\infty}^{\infty} u^2 2K_0(u/\delta^2)/(\pi\delta^2) du = 4(K-1)\Gamma^2(3/2)\delta^4/\pi = (K-1)\delta^4 \end{aligned} \quad (16.33)$$

That is, when signal is absence, the detect statics of z can be fit to the square of zero-mean Gaussian distribution, that is central chi-square distribution with the corresponding probability in Eq. (16.34)

$$p(z|H_0) = 1/\left(\sqrt{D(z|H_0)}2^{1/2}\Gamma\left(\frac{1}{2}\right)\right)z^{-1/2}\exp(-z/2D(z|H_0)) \quad (16.34)$$

So the mean and variance of the noise term D_k are

$$E(z|H_0) = (K-1)\delta^2 = K-1 \quad (16.35)$$

$$D(z|H_0) = \delta_{\sum D_k}^2 = (K-1)\delta^4 = K-1 \quad (16.36)$$

As for B_k and C_k , they can be fit to zero-mean Gaussian distribution, with the condition that the residual Doppler frequency remaining unchanged in the accumulated adjacent data. The variance of B_k and C_k are as followed in Eq. (16.37).

$$\begin{aligned} \delta_{\sum B_k C_k}^2 &= \sum_{k=2}^K \delta_{B_k}^2 + \delta_{C_k}^2 \\ &= A^2 R(\Delta\tau)^2 \delta^2 \left(\sum_{k=2}^K \text{sinc}^2\left(\Delta\omega_k \frac{T_{\text{coh}}}{2}\right) + \text{sinc}^2\left(\Delta\omega_{k-1} \frac{T_{\text{coh}}}{2}\right) \right) \end{aligned} \quad (16.37)$$

Similarly, we can do something to simplify the signal term to get the Eq. (16.38), still assuming the code phase shift, Doppler frequency offset, and data bit reverse do not exist.

$$\sum A_k = (K - 1)A^2 D_k D_{k-1} R(\Delta\tau)^2 \text{sinc}^2\left(\Delta\omega_k \frac{T_{\text{coh}}}{2}\right) = (K - 1)A^2 \quad (16.38)$$

When the signal is present, A_k is non-central chi-square distribution; B_k , C_k , and D_k are the similar central chi-square distribution. In consequence, it is complicated to get the sum of the four terms that we have to appeal to the algorithm of AS155, which can be used to calculate the probability density of the sum of chi-square distribution and non-central chi-square distribution variables. But this work is extremely difficult.

According to the central limit theorem, we can use the Gaussian distribution with non-zero mean to approximate the sum, which is easy and obvious to calculate. So we can get the non-central chi-square distribution of z after the square process to the sum value when signal is present, and the statics probability is as in Eq. (16.39).

$$p(z|H_1) = \frac{1}{\sqrt{2\pi z D(z|H_1)}} \exp(-(z + E(z|H_1))^2 / 2\delta_{D_k}^2) \cosh\left(\frac{\sqrt{z}}{D(z|H_1)} E(z|H_1)\right) \quad (16.39)$$

And the overall mean and variance of the differential standard coherent integration when signal is present are as in Eq. (16.40)

$$E(z|H_1) = \sum A_k = (K - 1)A^2 \quad (16.40)$$

$$D(z|H_1) = \delta_{\sum D_k}^2 + \delta_{\sum B_k C_k}^2 = (K - 1) + 2(K - 1)A^2 \quad (16.41)$$

Much attention should be given to that, in the analysis, we make the hypothesis of the I and Q data branch are completely independent Gaussian distribution, and $I_k I_{k-1}$, $Q_k Q_{k-1}$ are also completely independent to each other, which are not the case in the actual data environment. When the signal is present, $I_k I_{k-1}$ and $Q_k Q_{k-1}$ are practical interrelated. In this paper, we only take the approximate analysis, one can get the detailed description in Refs. [2, 3] if needed.

In the same way, we can get the result just using $K/2$ to replace the K in Eqs. (16.35), (16.36), (16.40) and (16.41) for the differential pair-wise coherent integration.

16.3 Theoretical Simulation and Actual Data Verification

16.3.1 Simulation Results

In the simulation, taking the front RF loss 3 dB, the insertion loss of the transmission line 1 dB, and no impact of code phase shift and Doppler frequency shift and data bit modulation, we give a comparison of the acquisition detection

probability between the non-coherent integration, differential standard non-coherent integration, differential standard coherent integration, differential pair-wise non-coherent integration and differential pair-wise coherent integration, with the false detection probability being $1e-6$ under the Bayes estimation and coherent time being 1 ms.

From Figs. 16.1, 16.2, 16.3 and 16.4, the results can be seen that, differential standard integration is superior to the differential pair-wise integration; the differential coherent integration will promote the detection probability of 5 % relative to the differential non-coherent integration near the detection probability of 90 %; differential standard integration is much more excellent than the non-coherent integration; but differential pair-wise integration performance fairly to the non-coherent integration.

16.3.2 Actual Data Verification

Three sets of actual data will be used to do the verification of the given total integration time, one with average -410 Hz Doppler residual, one in average 847 Hz Doppler residual, and one without Doppler residual; and in the test, 8 different sampling points starting situation (the data sampling rate is 16 MHz, and code half chip rate is 2 MHz, so 8 samples will cover the all code phase shift circumstances) with 1000 times per one sampling point in sequence to give a detection probability; a Doppler residual impact will also be presented.

Note that, the results in the following tables are all the mean probability of detection of the 8 different sampling points starting situation, and in the brackets are the maximum probability of detection with no code phase shift.

Fig. 16.1 Result for $T_{coh} = 1$ ms and $T_{total} = 20$ ms

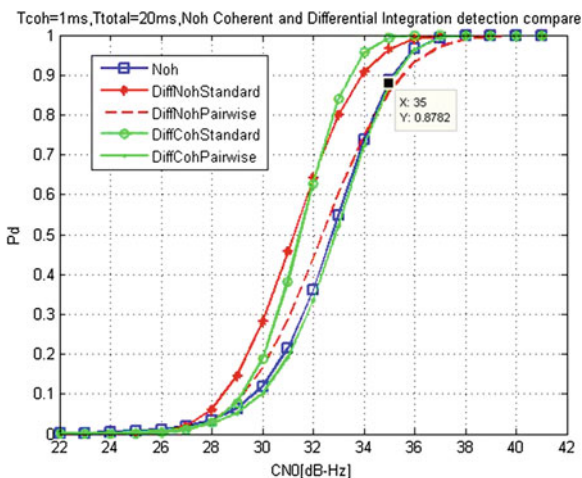


Fig. 16.2 Result for $T_{coh} = 1$ ms and $T_{total} = 40$ ms

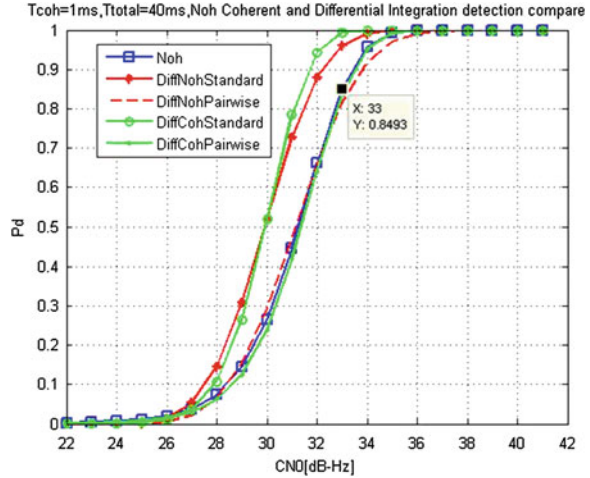
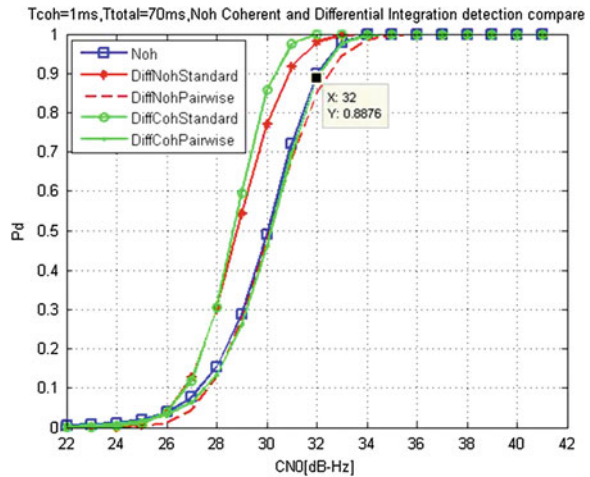


Fig. 16.3 Result for $T_{coh} = 1$ ms and $T_{total} = 70$ ms



In Tables 16.1 and 16.2, we can take the Gaussian distribution to approximate as the test time larger than 20; and in Tables 16.3 and 16.4, the time is less than 20, so the above theoretical analysis can be not supported. From the results, we can get the conclusion as follows:

(1) When the test times >20 , in Tables 16.1 and 16.2, the actual test results are basically consistent with the theoretical analysis; but the differential standard non-coherent integration is out of control, in poor performance, worse than differential pair-wise coherent integration and also the non-coherent integration algorithm

Fig. 16.4 Result for $T_{coh} = 1$ ms and $T_{total} = 100$ ms

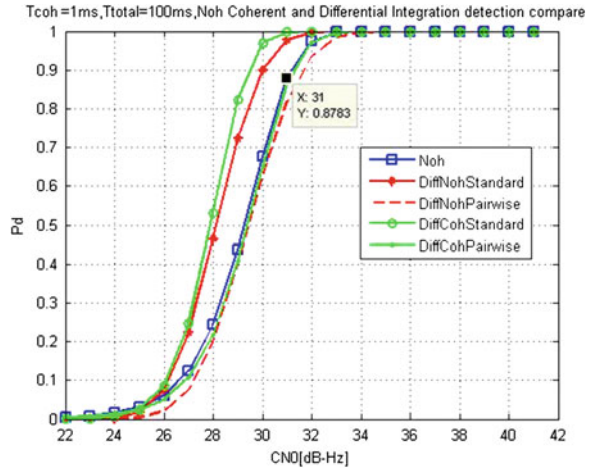


Table 16.1 $T_{coh} = 1$ ms, $T_{total} = 20$ ms, detection of probability result (in %)

Test case		Noh	DiffCSd	DiffCPw	DiffNSd	DiffNPw
33 dB Hz	Doppler residual 0 Hz	93.6 (94.5)	98.5 (99.0)	92.8 (93.6)	93.1 (93.6)	92.4 (93.5)
	Doppler residual -410 Hz	93.8 (94.2)	98.3 (98.5)	92.2 (92.7)	91.9 (93.0)	91.1 (91.6)
	Doppler residual 847 Hz	91.0 (91.6)	97.5 (97.6)	89.7 (91.0)	89.2 (90.1)	88.6 (89.1)
32 dB Hz	Doppler residual 0 Hz	77.4 (78.4)	92.5 (93.7)	78.8 (79.4)	75.7 (77.0)	75.0 (76.5)
	Doppler residual -410 Hz	77.6 (78.5)	91.8 (92.6)	77.8 (79.0)	74.2 (75.8)	73.5 (74.7)
	Doppler residual 847 Hz	71.3 (72.4)	88.5 (89.3)	71.1 (72.2)	69.1 (70.0)	67.0 (68.4)

under the same conditions; and the detection probability basically follow the law: differential standard coherent integration > non-coherent integration > differential pair-wise coherent integration > differential standard non-coherent integration > differential pair-wise non-coherent integration.

The cause of the abnormal performance of differential standard non-coherent integration can be comprehended as the model's un-precise Gaussian approximation uses the central limit theory and the hypothesis of no bias and $I_k I_{k-1}$, $Q_k Q_{k-1}$ being completely independent Gaussian distribution. These actual tests not consistent with the theoretical simulation will be the future research directions in how to get more accurate probability model to fit the signal.

Table 16.2 Tcoh = 1 ms, Ttotal = 40 ms, detection of probability result (in %)

Test case		Noh	DiffCSd	DiffCPw	DiffNSd	DiffNPw
31 dB Hz	Doppler residual 0 Hz	94.1 (94.5)	99.0 (99.5)	92.2 (93.9)	92.6 (94.0)	91.7 (92.6)
	Doppler residual -410 Hz	92.9 (93.4)	98.9 (99.5)	91.2 (92.1)	91.6 (92.4)	90.6 (92.3)
	Doppler residual 847 Hz	89.6 (90.7)	98.1 (98.6)	87.9 (88.6)	87.5 (89.1)	85.9 (87.4)
30 dB Hz	Doppler residual 0 Hz	75.2 (76.3)	90.6 (92.4)	75.5 (76.6)	71.7 (74.3)	70.2 (72.0)
	Doppler residual -410 Hz	73.4 (77.0)	90.5 (92.8)	73.6 (75.4)	69.7 (72.3)	68.3 (69.5)
	Doppler residual 847 Hz	66.2 (67.7)	88.8 (89.2)	64.7 (65.6)	61.8 (63.3)	59.2 (60.3)

Table 16.3 Tcoh = 1 ms, Ttotal = 10 ms, detection of probability result (in %)

Test case		Noh	DiffCSd	DiffCPw	DiffNSd	DiffNPw
35 dB Hz	Doppler residual 0 Hz	93.5 (94.3)	96.2 (96.8)	91.1 (92.3)	92.2 (92.9)	93.0 (93.6)
	Doppler residual -410 Hz	92.5 (93.2)	95.7 (97.0)	90.3 (91.8)	91.1 (92.2)	92.0 (93.1)
	Doppler residual 847 Hz	87.2 (88.8)	93.3 (93.7)	85.9 (87.2)	85.6 (86.8)	86.7 (87.5)
34 dB Hz	Doppler residual 0 Hz	77.6 (79.5)	85.4 (86.3)	77.1 (78.0)	75.7 (76.7)	76.3 (77.8)
	Doppler residual -410 Hz	76.1 (77.1)	84.4 (85.4)	75.6 (76.7)	73.7 (75.5)	74.8 (76.3)
	Doppler residual 847 Hz	70.5 (72.2)	80.7 (82.1)	69.5 (70.6)	68.7 (69.7)	69.3 (70.6)

Table 16.4 Tcoh = 1 ms, Ttotal = 4 ms, detection of probability result (in %)

Test case		Noh	DiffCSd	DiffCPw	DiffNSd	DiffNPw
38 dB Hz	Doppler residual 0 Hz	92.3 (93.2)	93.0 (93.9)	93.4 (94.4)	84.4 (90.0)	86.6 (91.9)
	Doppler residual -410 Hz	87.7 (92.4)	92.5 (93.5)	92.7 (93.4)	84.6 (89.3)	86.5 (90.9)
	Doppler residual 847 Hz	89.0 (89.5)	84.5 (85.3)	83.3 (84.0)	85.8 (87.1)	88.9 (90.1)
37 dB Hz	Doppler residual 0 Hz	75.9 (76.4)	82.4 (83.7)	82.7 (83.9)	64.7 (76.8)	67.6 (79.4)
	Doppler residual -410 Hz	68.6 (76.8)	71.8 (81.4)	71.9 (81.0)	65.7 (74.4)	69.5 (78.7)
	Doppler residual 847 Hz	71.5 (73.4)	75.0 (75.8)	74.8 (76.1)	66.7 (68.2)	72.4 (73.7)

(2) When the signal is strong, in Tables 16.3 and 16.4, as you can see, the differential standard coherent integration is the best choice, and then the non-coherent integration, with the rest giving more or less the same performance.

(3) The impact of Doppler frequency residual will be in the range of 4 % detection probability varied; and the differential standard integration is more tolerant than the differential to the Doppler frequency residual.

(4) The effect of code phase deviation to the detection probability will be within 2 %. And the smaller the impact of the code phase deviation is corresponding to the larger detection probability.

16.4 Summary

The theoretical analysis and actual data verification show that:

- (1) Differential standard coherent integration is optimal and nearly 1 dB performance advantage to the secondary best integration algorithm non-coherent integration in the weak signal environment; but in the strong signal application, they behave quite fair. The remaining algorithms perform almost the same.
- (2) In the Doppler frequency residual and code phase deviation situation, the differential standard integration will be more tolerant than the differential pairwise integration; and the Doppler frequency residual impact much more to the detection probability than the code phase deviation; and in the lower detection probability, the effect of code phase deviation will be distinct, but can be ignored when the detection probability is larger, above 90 %.
- (3) Theoretical analysis can give a clue to the actual test, but cannot fully explain the approximate performance of the analyzed algorithms; they need support from the actual data.

References

1. Dong X, Tang B (2008) Principle and design of satellite navigation software receiver. National Defence Industry Press, Beijing, pp 139–144
2. W Yu (2007) Selected GPS receiver enhancements for weak signal. Master thesis, University of Calgary, Canada
3. O'Driscoll C (2007) Performance analysis of the parallel acquisition of weak GPS signals. Ph. D. thesis, National University of Ireland, Ireland

Chapter 17

A New Method Based on QSE Processing for Interferometric GNSS-R Ocean Altimetry

Chenghui Yu, Chundi Xiu, Weiqiang Li and Dongkai Yang

Abstract Considering that in conventional GNSS-R (Global Navigation Satellite System-Reflection) altimetry, the reflected signals are cross-correlated with a locally generated clean replica of the transmitted signal, interferometric processing consists of the measurement of the complex cross-correlation between the direct and reflected signals. It allows the exploitation of P(Y) code and other civil signals to maximize the height estimation precision. This paper presents a new processing method called QSE (Quadrature Staggered Extracting) which utilizes P(Y) code to explore a further improvement of the altimetry precision. The assessment of the QSE processing procedure illustrates GPS L1 band as an example. In these conditions, this paper analysis the up-looking SNRs obtained by using QSE processing and traditional coherent demodulation respectively. The analysis of the altimetry precision shows that the results obtained by adopting QSE processing improve by a factor about 1.15 as compared to the results obtained by using coherent demodulation.

Keywords GNSS-R · Quadrature staggered extracting · Interferometric processing · Ocean altimetry

17.1 Introduction

From the first proposal of Passive Reflectometry and Interferometry System (PARIS) concept in 1993, global navigation satellite system reflection (GNSS-R) of opportunity signals has stood as a technique with a great potential for remote sensing application such as ocean monitoring (see [1, 2]). Also, it was presented as a complementary technique to the traditional radar remote sensing, but applied to the passive reflectometry signals from the global navigation satellite [3]. Interferometric

C. Yu (✉) · C. Xiu · W. Li · D. Yang
Electronic and Information Engineering Institute, Beihang University, Beijing, China
e-mail: chenghuiyufly@163.com

processing technique is proposed by the Phase-A studies of ESA's Passive Reflectometry and Interferometry System In-Orbit Demonstrator mission [4]. This technique consists of the measurement of the complex cross-correlation between the direct and reflected signals, instead of using a locally generated clean replica of the transmitted signals [5].

In addition, recent theoretical analysis predicts that, for the space-borne scenario, the interferometric processing technique of the P(Y) code could lead to better precision for ocean altimetry and soil moisture monitoring (see [6–8]), which has steeper slope of the power waveforms around the specular point (SP) and the larger bandwidth. Also, for navigation purposes it is known that the tenfold faster chipping rate of the P(Y) code, as compared to the C/A code, leads to a sharper autocorrelation function (ACF), and higher ranging precision (see [9, 10]).

This paper describes a new method called QSE processing to extract P(Y) code for ocean altimetry which has a further improvement of the up-looking chains SNR and altimetry precision.

17.2 Principle

GNSS signals consist of different orthogonal signal components, for example, the L1 frequency of GPS IIA/IIR satellites carries C/A and P(Y) code signals, transmitted in phase quadrature (e.g., [2]). Interferometric processing consists of the measurement of the complex cross-correlation between the L1 band direct signals $w_d(t)$ and reflected signals $w_{GNSS_r}(t)$. Direct signals $w_d(t)$ consist of both in-phase and quadrature components, which was introduced as (17.1):

$$w_d(t) = w_{P(Y)}(t) \cdot \cos(2\pi f_e + \theta_e) + w_{C/A}(t) \cdot \sin(2\pi f_e + \theta_e) + n(t) \quad (17.1)$$

where $w_{P(Y)}(t)$ represents the spreading P(Y) code modulated baseband navigation signals, $w_{C/A}(t)$ represents the spreading C/A code modulated baseband navigation signals, f_e and θ_e is the intermediate frequency and phase of modulated carrier, $n(t)$ is the additive thermal noise which has zero mean.

The QSE processing method could extract P(Y) code as the reference signals as shown in Fig. 17.1. Firstly, $w_d(t)$ is divided into two components, one of them is down converted with in-phase components of the local generated signals, other component needs Hilbert conversion and to be down converted with quadrature components, which is shown as (17.2). Finally, the two processed components are added together to obtain P(Y) code.

$$\begin{aligned} \hat{w}_d(t) = \Xi[w_d(t)] &= w_d(t) \otimes \frac{1}{\pi t} = w_{P(Y)}(t) \cdot \sin(2\pi f_e + \theta_e) \\ &- w_{C/A}(t) \cdot \cos(2\pi f_e + \theta_e) + \hat{n}(t) \end{aligned} \quad (17.2)$$

After that, signal $\hat{w}_d(t)$ is down converted by the quadrature component of the locally generated carrier $\text{Im}[s_{LO}(t)]$ in the same way to extract $\hat{w}_{P(Y)-1}(t)$ as follows (17.5):

$$\hat{w}_{P(Y)-1}(t) = \frac{1}{2} w_{P(Y)}(t) + \hat{n}(t) \cdot \sin\left(2\pi\hat{f}_e t + \hat{\theta}_e\right) \quad (17.5)$$

Finally, both two correlated signals are added by QSE processing to extract P(Y) signals and obtain noise signals $n_1(t)$ simultaneously, as shown in (17.6).

$$\hat{w}_{P(Y)-1}(t) + w_{P(Y)-1}(t) = w_{P(Y)}(t) + n_1(t) \quad (17.6)$$

$$n_1(t) = n(t) \cdot \cos\left(2\pi\hat{f}_e t + \hat{\theta}_e\right) + \hat{n}(t) \cdot \sin\left(2\pi\hat{f}_e t + \hat{\theta}_e\right) \quad (17.7)$$

Complementarily, the traditional coherent demodulation method can extract the required reference signal $w_{P(Y)}(t)$ with in-phase channels, which got noise $n_2(t)$ of chains (e.g., [2]).

$$n_2(t) = 2 \cdot n(t) \cos\left(2\pi\hat{f}_e t + \hat{\theta}_e\right) \quad (17.8)$$

Therefore, by considering that the average SNR at the output of the correlator can be simply related to the SNR of up-looking chains that would be obtained by QSE processing method or traditional coherent demodulation. This paper defines that SNR1 represents the SNR which is calculated by QSE processing technique, and SNR2 is the SNR obtained by traditional coherent demodulation. As shown in (17.9). Where $W_{p(Y)}$ represents the average power of P(Y) code, W_{n1} represents the average power of noise signals $n_1(t)$, W_{n2} represents the average power of noise signals $n_2(t)$.

$$SNR_1 = 10 \times \log\left(\frac{\langle |W_{p(Y)}|^2 \rangle}{\langle |W_{n1}|^2 \rangle}\right), SNR_2 = 10 \times \log\left(\frac{\langle |W_{p(Y)}|^2 \rangle}{\langle |W_{n2}|^2 \rangle}\right) \quad (17.9)$$

Finally, we define the ratio G of SNR1 and SNR2 which is shown as (17.10):

$$G = \frac{SNR_1}{SNR_2} \quad (17.10)$$

17.3 Model of Ocean Height Precision

The model of the sea surface altimetry based on GNSS-R shows in Fig. 17.2. (e.g., [11, 12]) where H_{Rs} represents the distance from geocentric to GNSS receiver, H_{Ts} is the distance from geocentric to GNSS satellite, R_{Earth} represents the radius of the earth, θ_r is the angle between H_{Rs} and R_{Earth} , θ_t is the angle between H_{Ts} and R_{Earth} ,

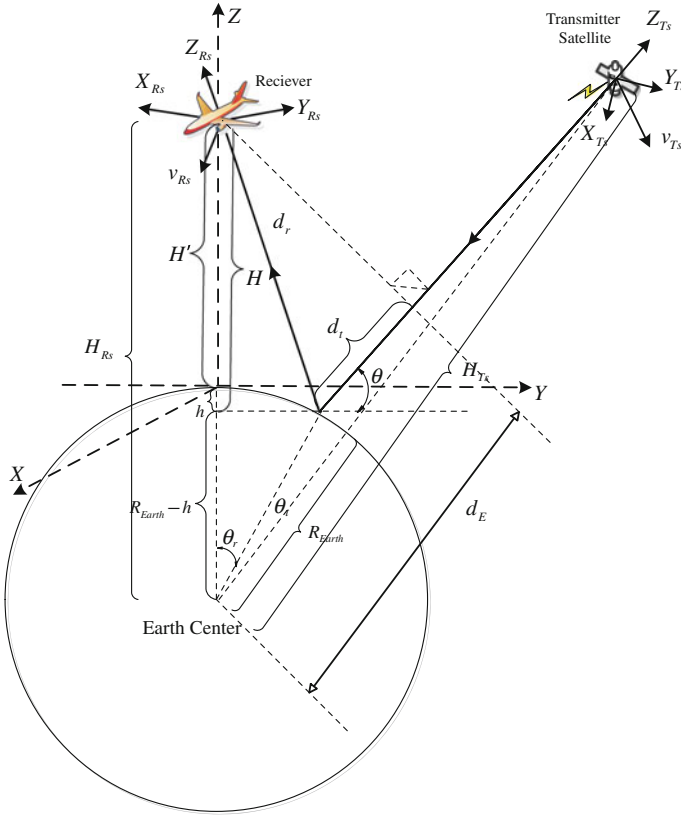


Fig. 17.2 Geometry of altimetry delay model based on GNSS-R

θ_{SP} is the satellite elevation angle in the specular reflection point, d_E is the total delay from direct signals to reflected signal, d_r is the distance from LHCP antenna to specular point. It shown as following:

$$d_E = d_r + d_t \tag{17.11}$$

$$h = R_{Earth} - R_{Earth} \cos \theta_r \tag{17.12}$$

In condition of the shore-based or airborne, if $R_{Earth} \gg h$, the path delay time could be calculated by subtracting the time difference between autocorrelation peak of direct signals and the correlation peaks of the reflected signals, then we can calculate the ocean height based on GNSS-R, as it shown in (17.13) and (17.14), where H is the vertical distance from LHCP antenna to specular point, H' is the actual distance from LHCP antenna to earth surface.

$$H_{Rs} = H + R_{Earth} - h \approx H + R_{Earth} \quad (17.13)$$

$$H' = H_{Rs} - R_{Earth} \approx H = \frac{d_E}{2 \sin \theta} \quad (17.14)$$

Considering with the geometric curvature, the measurement error of the average sea level σ_h is a function of the path delay error σ_{d_E} and the angle θ_{SP} in specular point, which reports the precision of the ocean altimetry, It shown as following (e.g., [13]),

$$\sigma_h = -\frac{\sigma_{d_E}}{2 \sin \theta_{SP}} \quad (17.15)$$

However, the state of the sea is more complex, roughness of the sea surface is changing all the time, which would be affected by the sea clutter. Also, this procedure of continued fluctuations would have an impact on the delay error [14]. It can be measured by the standard deviation of the reflected signals power. Furthermore, the changing of standard deviation would have an influence on the forefront of the relevant power fluctuations. As a result, this affect may reduce the precision of the ocean altimetry.

Moreover, a comprehensive model of the height precision [4] with respect to the different parameters such as the signal-to-noise (SNR), the observation geometry, and the speckle was also introduced in as (17.16)

$$\sigma_h = \frac{c}{2 \sin \theta_{SP}} \times \frac{\overline{P_Z(0)}}{P_Z(0)} \times \frac{1}{\sqrt{N_{inc}}} \times \sqrt{\left(1 + \frac{1}{SNR}\right)^2 + \left(\frac{1}{SNR}\right)^2} \quad (17.16)$$

where c is the speed of light in vacuum, θ_{SP} is the elevation angle at the SP, N_{inc} is the number of incoherently averaged samples, $\overline{P_Z(0)}$ and $P_Z(0)'$ are the averaged power amplitude and the slope of the power waveform at the SP, and SNR is the average signal-to-thermal noise ratio computed at the output of the correlation for the delay of the SP.

17.4 Results and Discussion

17.4.1 QSE Performance Analysis

The aforementioned signal components extracting method, known as QSE processing, could be easily implemented to separate the signal components. In order to intuitively show the performance of the QSE processing technique compared with the traditional coherent demodulation, this paper comprehensively carried out numerical simulations with following parameters: the bandwidth of the receiver was

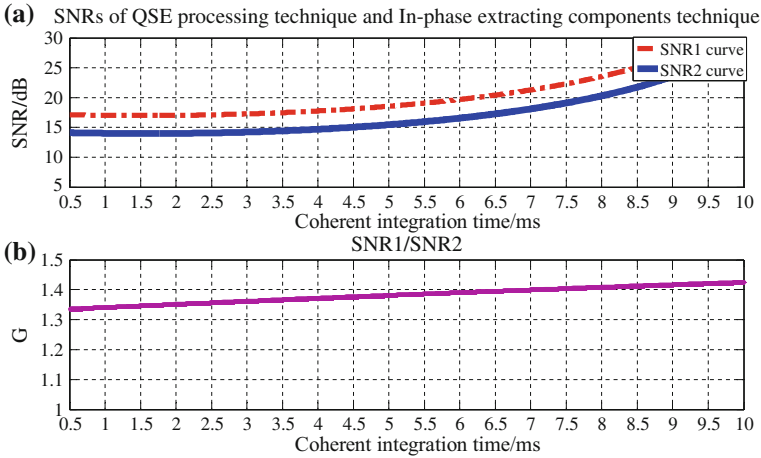


Fig. 17.3 Comparison of the up-looking chains SNR obtained by using different processing method. **a** Red curve presents the SNR which is obtained by QSE technique, and blue curve is the SNR which is obtained by traditional coherent demodulation. **b** The purple curve presents the ratio G of SNR1 and SNR2

45 MHz, gain of up-looking antenna and down-looking antenna were 24 dB, up-looking antenna noise temperature was 45 K, down-looking antenna temperature was 115 K, noise temperature of receiver was 285 K. Figure 17.3 presents the simulations of SNR with increasing in integration time.

As shown in Fig. 17.3a, by considering coherent integration times, SNR1 (see the red curve) obtained by QSE processing technique upgrades about 2.5 dB relative to the SNR2 (see the blue curve) which is obtained by traditional coherent demodulation.

Figure 17.3b presents that SNR obtained by QSE processing method can be increasing by a factor of 1.33 compared with traditional coherent demodulation, which could achieve better height precision.

17.5 Altimetry Performance Analysis

In order to evaluate the altimetry performance of QSE processing, a simulation site is simply adopted which is shown as Fig. 17.4. The elevation angle was from 30° to 33°, and LHCP (Left-Hand Circular Polarization) down-looking antenna has gain of 13 dB [2, 9].

The simulation platform based on GNSS-R includes up-looking antenna which receives direct signals, down-looking antenna which receives reflected signals from sea surface, RF fronts and cross-collection based on QSE processing method. The parameters for simulation are as following, wind speed is about 5 m/s, significant wave height is 1.5 m, and the transmitting power is between 25 and 28 dB W.

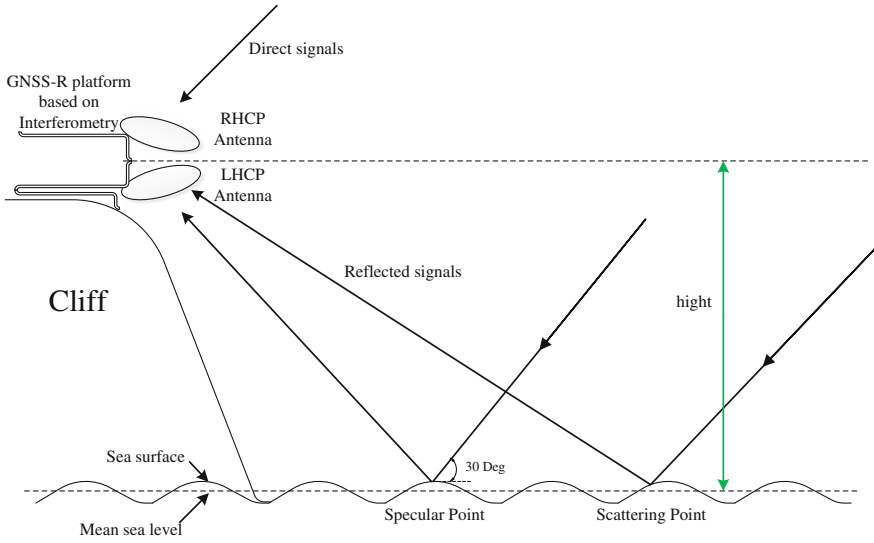


Fig. 17.4 Description of the simulation site based on QSE processing for ocean altimetry

In detail, up-looking antenna and down-looking antenna receive direct signals and reflected signals of both GPS and BD systems separately. RF fronts are used to quantizing above-mentioned signals into digital intermediate frequency signals. Finally, the down-converted and Doppler compensated reflected signals are cross-correlated with the P(Y) code which is extracted by QSE processing method from L1 band direct signals to calculate Delay Doppler Mapping (DDM) for ocean altimetry.

Afterwards, a preliminary analysis of height precision by using QSE processing technique and traditional coherent demodulation has been performed by considering different number of the sampled signals with non-coherent accumulation, as shown in Fig. 17.5. The black curve represents the height precision obtained by

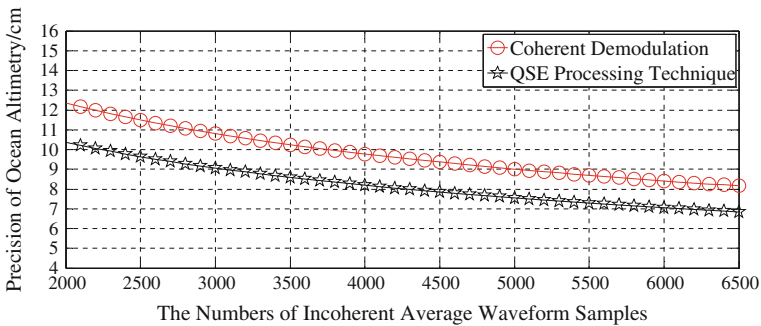


Fig. 17.5 Comparison of the altimetry precision achieved by adopting QSE processing method and coherent demodulation

adopting QSE technique and red curve is obtained by using traditional coherent demodulation. It shows that the altimetry precision under QSE processing method can be better by a factor of 1.15 compared with traditional coherent demodulation, which has certain advantages for ocean altimetry.

17.6 Conclusion

A new method based on QSE processing has been described to extract P(Y) code for interferometric GNSS-R ocean altimetry. This paper illustrated QSE processing and traditional coherent demodulation for GPS L1 band signals. The comparison showed that the QSE processing method could achieve increasing SNR by a factor of 1.33. In these conditions, the improvement factor of the height precision obtained by adopting QSE method as compared to the traditional coherent demodulation, stabilizes about 1.15. By the way, this new method could be used to extracting BD II B2AS and BD III B1A signals.

Future work will include the analysis of other available GNSS systems to employ QSE processing method. More importantly, it's necessary to overcome the effect of high dynamic of specular point onboard and to improve the precision of ocean altimetry, which needed to study deeply in the future [6, 9].

Acknowledgments This study is supported by National High Technology Research and Development Program 863 of China (NO. 2013AA122402, NO. 2011AA120501).

References

1. Martín-Neira M (1993) A passive reflectometry and interferometry system (PARIS)—application to ocean altimetry. *ESA J* 17(4):331–355
2. Li W, Yang D, D'Addio S, Martín-Neira M (2014) Partial interferometric processing of reflected GNSS signals for ocean altimetry. *IEEE Geosci Remote Sens Lett* 11(9):1509–1513
3. H. Li, Q. Xia, C. Yin et al (2013) The current status of research on GNSS-R remote sensing technology in China and future development. *J Radars* 2(4):389–399
4. Martín-Neira M, D'Addio S, Buck C, Flouy N, Prieto-Cerdeira R (2011) The PARIS ocean altimeter in-orbit demonstrator. *IEEE Trans Geosci Remote Sens* 49(6):2209–2237
5. Martín F, Camps A, Park H, D'Addio S, Martín-Neira M, Pascual D (2014) Cross-correlation waveform analysis for conventional and interferometric GNSS-R approaches. *IEEE J Sel Top Appl Earth Observ Remote Sens* 7(5):1560–1572
6. Park H, Valencia E, Camps A, Rius A (2013) Delay tracking in spaceborne GNSS-R ocean altimetry. *IEEE Geosci Remote Sens Lett* 10(1):57–61
7. Alonso Arroyo A, Camps A, Aguasca A (2014) Dual-polarization GNSS-R interference pattern technique for soil moisture mapping. *IEEE J Sel Top Appl Earth Observ Remote Sens* 4(8):1533–1542
8. Mironov VL, Muzalevskiy KV (2012) The new algorithm for retrieval of soil moisture and surface roughness from GNSS reflectometry. In: *IEEE international geoscience and remote sensing symposium (IGASS)*, Munich, Germany, pp 7530–7532, 22–27 July

9. Carreno-Luengo H, Camps A, Ramos-Perez I, Rius A (2014) Experimental evaluation of GNSS-reflectometry altimetric precision using the P(Y) and C/A signals. *IEEE J Sel Top Appl Earth Observ Remote Sens* 7(5):1493–1500
10. Cardellach E, Rius A, Martín-Neira M et al (2013) Consolidating the precision of interferometric GNSS-R ocean altimetry using airborne experimental data. *IEEE Trans Geosci Remote Sens*. doi:[10.1109/TGRS.2013.2286257](https://doi.org/10.1109/TGRS.2013.2286257)
11. Valencia E, Camps A, Park H, Rodriguez-Alvarez N, Ramos-Perez I (2012) Impact of the observation geometry on the GNSS-R direct descriptors used for sea state monitoring. In: *IEEE international geoscience and remote sensing symposium (IGASS)*, Munich, Germany, pp 2825–2828, 22–27 July
12. Park H, Pascual D, Camps A, Martín F, Alonso-Arroyo A, Carreno-Luengo H (2014) Analysis of spaceborne GNSS-R delay-doppler tracking. *IEEE J Sel Top Appl Earth Observ Remote Sens* 7(5):1481–1492
13. Yang D, Zhang Q (2012) *GNSS reflected signal processing: fundamentals and applications*. Publish House of Electronics Industry, Beijing
14. D’Addio S, Martín-Neira M, di Bisceglie M (2014) GNSS-R altimeter based on doppler multi-looking. *IEEE J Sel Top Appl Earth Observ Remote Sens* 7(5):1453–1460

Chapter 18

Analysis of GNSS Signals with Application to Lunar Navigation

Xiaoliang Wang, Longlong Li, Xingyuan Han, Yansong Meng
and Lin Wu

Abstract GNSS-based navigation technology for lunar mission with more than 60,000 km above earth, which is still lack of relevant research and simulation. In this paper, “Chang-E One” lunar mission is used with three stages of orbiting the earth, earth-moon transfer, and around moon. A detailed analysis of feasibility of autonomous navigation using GPS, GALILEO navigation system alone and combination under sidelobe signals is given. The number of visible satellites GNSS receiver to receive, DOP value, receiving signal level and dynamic, etc. are analyzed, and autonomous navigation algorithm design under different observation conditions were also considered. As can be seen from the theoretical analysis and simulation results, the use of GNSS signals fully meet user needs that realize autonomous navigation around earth, earth-moon transfer, and around moon three-stages, which can be considered as the foundation for future engineering applications.

Keywords GNSS signals · Weak signal · Autonomous navigation · Lunar navigation

18.1 Introduction

Lunar navigation can be roughly divided into three stages that around the Earth, Moon transfer and the around lunar phase. At present, basically orbit control is achieved using ground support both in domestic and international lunar exploration missions [1]. With the increase in the number of deep space exploration missions in future, this way will make the ground segment becomes more and more complex,

X. Wang (✉) · L. Li · X. Han · Y. Meng
Institute of Navigation and Intra Satellite Link Technology, Academy of Space Electronic
Information Technology, Xi’an 710100, China
e-mail: xlwang12321@gmail.com

L. Wu
Institute of Space Antenna Technology, Academy of Space Electronic Information
Technology, Xi’an 710100, China

and cannot meet the huge demand for future space development of china. GNSS use space-based radio positioning and timing system. If we can deployment autonomous GNSS receiver in China's future lunar exploration series missions, it will significantly reduce the ground control burden, reduce spacecraft operational and maintenance cost, which has significant engineering value.

This paper takes the China's "Chang'e one" lunar exploration mission as an example, analyzed in detail that the feasibility of the spacecraft autonomous navigation using GPS, GALILEO navigation system downlink sidelobe signal alone and in combination. Analyzed GNSS receiver to visible satellite number, receiving satellite Positional Dilution of Precision (PDOP value), the received signal level and dynamic.

18.2 Navigation Constellation and User Model

18.2.1 Navigation Constellation and Signal

This paper uses the GPS and Galileo constellation model. GPS using Walker 24/4/1 constellation what ephemeris from official IGS web site data [2], Galileo constellation is currently still in progress, here we use the complete stage data which will be 27 satellites in 3 orbit plane. Galileo satellite orbital semimajor axis is 29,600 km, the inclination of 56° , according to the simulation, we can get GPS and Galileo constellation results as follows (2 days of data) (Fig. 18.1):

Generally speaking, the downlink GNSS antenna gain is a function of line of sight angle (bore sight angle), referring to the related literature, the GPS antenna gain data are given below (the relationship between the downlink signals from the EIRP to the line of sight). Here we only use the Block-IIA gain data with main and side lobes. In order to simplify, the Galileo satellite downlink antenna gain data are considered same as GPS since lack of data (Fig. 18.2).

Fig. 18.1 GPS and Galileo constellation (red GPS, blue Galileo)

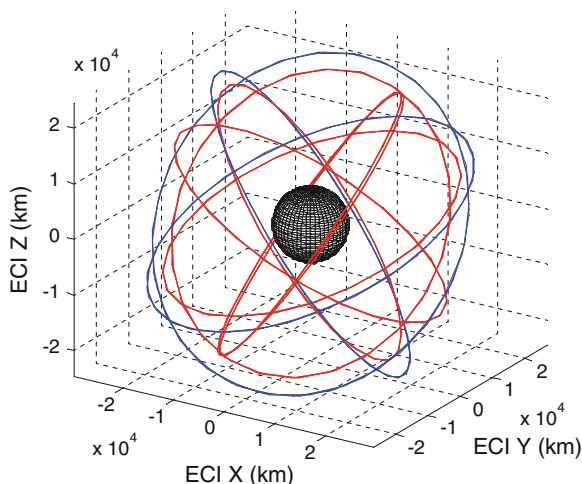


Fig. 18.2 GPS antenna pattern

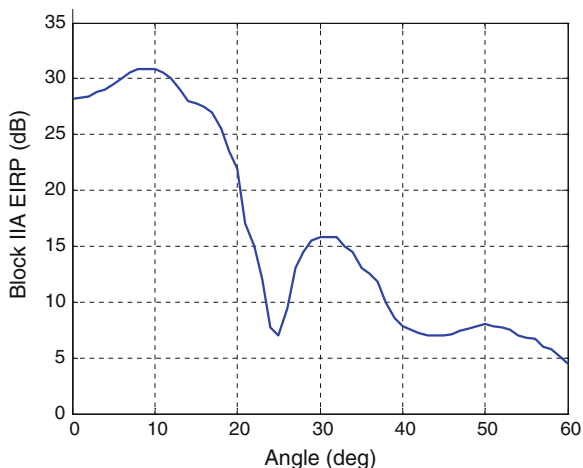


Table 18.1 “Chang-E-One” orbit analysis

	Orbit type	Orbit maneuver
Orbit Earth	2007/10/24 18:00:00 Launch from Xichang	Injection
	Perigee 200 km, apogee 51,000 km with period of 15.8084 h	0.0319 km/s at apogee
	Perigee 600 km, with period of 15.95694 h	0.1541 km/s at perigee
	24 h orbit	0.1691 km/s at perigee
	48 h orbit	–
Earth-Moon transfer	–	0.194 km/s at perigee
	Into cislunar orbit	17 h first correction
	Cislunar orbit	90 h second correction
	Cislunar orbit	–
Orbit Moon	–	–0.3478 km/s break
	Into 12 h elliptical orbit	–0.2630 km/s break
	Into 3.5 h orbit	–0.2112 km/s break
	Into 127.62 min orbit, height of 200 km	–

18.2.2 User Orbit and Receiving Antenna

According to the actual situation of China’s rocket capability, here we use Chang-E-One mission as an example [3]. Lunar exploration task can be roughly divided

Table 18.2 Receiver antenna parameters

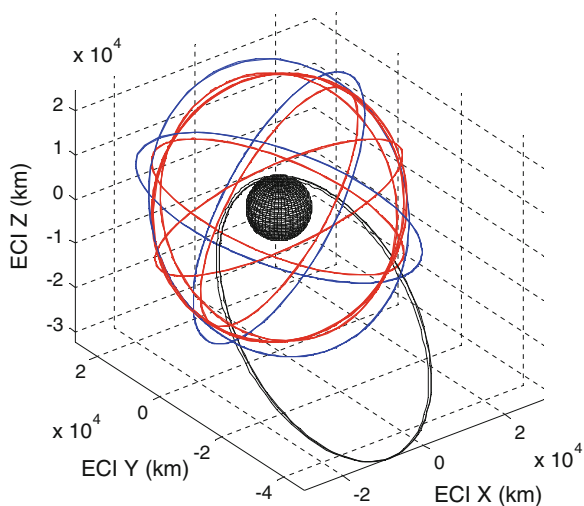
Orbit type	Gain (dB)	Beam width (°)
16 h GTO	3	±35
24 h GTO	4	±25
48 h GTO	5	±15
Cislunar range < 57,400 km	3	±35
57,400 km < cislunar range < 77,482 km	4	±25
77,482 km < cislunar range < 127,106 km	5	±15
127,106 km < cislunar range	10	±7
Orbit Moon	10	±7

into three stages: around the Earth, Moon transfer and the around moon phase, the orbital parameters are provided as in table below (Table 18.1):

The following hypotheses are used for user receiving antenna: two antennas are used according to the receiving function which includes earth pointing and zenith pointing. The zenith pointing antenna is supposed $\pm 8^\circ$ receiving angle with 0 dB gain; the earth pointing antenna is using the following settings (Table 18.2):

18.3 Applications

Based on the GNSS broadcast and receiving parameters introduced above, here we first analysis around earth orbit with 16 h period (super GTO orbit geosynchronous transfer orbit). The rocket firstly carrier probe into the super GTO orbital with perigee height of 200 km and apogee height of 51,000 km, orbital period is

Fig. 18.3 16 h GTO orbit

15.8084 h. After a correction maneuver, the perigee reached 600 km, which is 15.95694 h period orbit. The simulation scene as shown below (Fig. 18.3):

At this stage, the user receiving antenna beam width is $\pm 35^\circ$ with gain of 3 dB. Through the simulation, we can get the user visible number of satellite from different GNSS system as follows (using just earth pointing antenna) (Figs. 18.4 and 18.5):

According to the data above, the satellite visible number for GPS+Galileo system can be more than 8 at orbit apogee using just earth pointing receiving antenna, PDOP value is substantially less than 10, which meet the basic needs of autonomous positioning. However, observation vacuum occurs at orbit perigee, which indicates the supplement of zenith antenna can effectively increase the number of satellite observations and improve PDOP value (Table 18.3).

Fig. 18.4 16 h GTO orbit receiving number

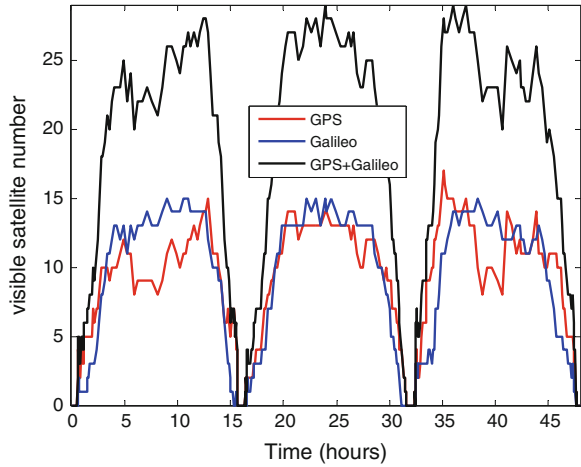


Fig. 18.5 16 h GTO orbit receiving PDOP

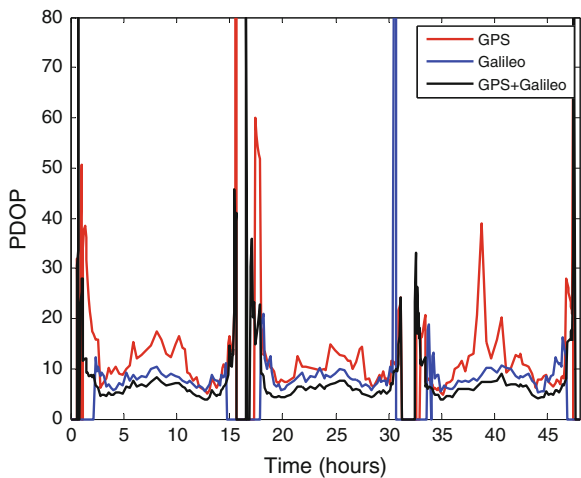


Table 18.3 GNSS receiving parameters

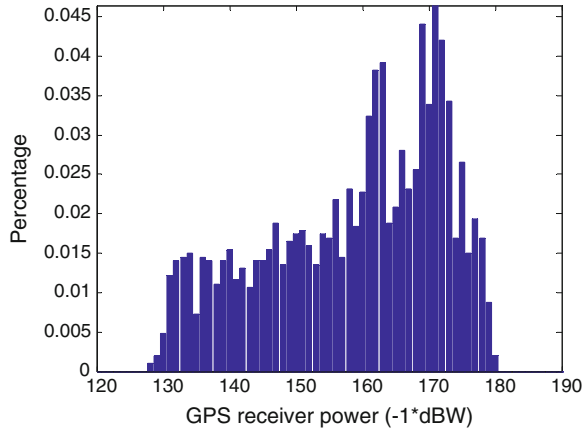
Items	GPS vis. number	GPS receiving PDOP	Receiving power (dBW)	Receiver gain	Beam angle (°)	Dynamic (km/s)	Note	
16 h GTO	Zenith	Max = 30	Max = -55.3	0	±80	GPS	Min = -7.1327	
		Min = 2.5	Min = -167.5				Max = 6.6185	
	Earth pointing	Max = 50	GPS	Min = -179.5182	3	±35	Gal	Min = -5.6406
		Min = 10	Gal	Max = -127.9204				
Use both	Max = 17	Max = 60	Max = -55.3	0/3	±80/± 35		Full work	
		Min = 2	Min = -180.1					
24 h GTO	Zenith	Max = 50	Max = -57.5	0	±80	GPS	Min = -5.9032	
		Min = 2	Min = -165.6				Max = 5.1372	
	Earth pointing	Max = 700	GPS	Min = -180.6675	4	±25	Gal	Min = -5.2322
		Min = 20	Gal	Max = -129.8629				
Use both	Max = 15	Max = 600	Max = -71.9	0/4	±80/±25		Full work	
		Min = 2	Min = -168.7					

(continued)

Table 18.3 (continued)

Items	GPS vis. number	GPS receiving PDPD	Receiving power (dBW)	Receiver gain	Beam angle (°)	Dynamic (km/s)	Note
48 h GTO	Max = 11	Max = 150	Max = -68.4	0	±80	GPS	Min = -4.8309
		Min = 10	Min = -167.4				Max = 4.4988
Earth pointing	Max = 13	Max = 900	Min = -182.5042	5	±15		
		Min = 20	Max = -132.5425				
Use both	Max = 13		Min = -181.4561			Gal	Min = -4.5364
		Max = 800	Max = -133.3016				Max = 4.6730
Earth-Moon transfer	Max = 13	Max = 1800	Max = -72.5	0/5	±80/± 15		Full work
		Min = 10	Min = -166.7				
Earth-Moon transfer	Max = 13	Max = 1800	Min = -187.1696	3	±35	GPS	Min = -2.4824
		Min = 20	Max = -128.4780	4	±25		Max = 6.4307
Orbit Moon	Max = 11	Max = 3800	Min = -186.2450	5	±15	Gal	Min = -2.1540
		Min = 500	Max = -129.3553	10	±7		Max = 5.9688
Orbit Moon	Max = 11	Max = 3800	Min = -186.7627	10	±7	GPS	Min = -5.0905
		Min = 500	Max = -139.2885				Max = 4.8647
Orbit Moon			Min = -186.7144			Gal	Min = -4.9123
			Max = -139.3235				Max = 4.5456

Fig. 18.6 16 h GTO orbit receiving power



Below is the user receives power statistics (antenna entrance level) during 16 h periodic orbits for GPS system, we can see that the received power is greater than -180 dBW all the time, which above the receiver signal acquisition and tracking threshold. The Galileo data is similar to this that not provided here (Fig. 18.6).

After the 16 h GTO orbit, the user satellite has experienced 24, 48 h periodic orbits and Earth-moon transfer/orbit moon phase. Because of its similar analysis method, we no longer provided in detail. Here we just given all the statistical data attached in the end.

18.4 Conclusions

This paper takes the “Chang-E one” lunar exploration mission as an example, detail analyzed the receiving GPS/GALILEO navigation system signal for autonomous navigation. Analyzed the receiving number of visible satellites, Positional Dilution of Precision, receiving signal level and dynamic etc. From the theoretical analysis and simulation results, it can be seen that using GNSS signal and can completely meet the lunar exploration needs.

References

1. Qiao S et al (2009) Application of VLBI in Chang-E One orbit injection monitor. In: 23rd Academy exchange for mapping technology, SanYa
2. <http://igscb.jpl.nasa.gov/components/prods.html>
3. Yang W et al (2007) Orbit design for lunar exploration satellite CE-1. Spacecr Eng 16(6):16–24

Chapter 19

Experiment and Result of Precise Kinematic Orbit Determination for LEO Satellite

Rengui Ruan, Laiping Feng and Xianbing Wu

Abstract Function for LEO kinematic orbit determination was developed and integrated into the SPODS software, which has been designed and developed at Xi'an Research Institute of Surveying and Mapping. This paper presents briefly the principle and method adopted such as observation model, error correction and parameter estimation. Since there are so many epoch-related unknown parameters, the position coordinates and clock offset of onboard receiver, an approach of Least-Square method with parameter pre-eliminating is employed for parameter estimation in data processing. A set of GPS data of GRACE-A/B during Sept. 01–09 2012 was collected and experiments were carried out to evaluate the performance. The result exhibits that, by comparing with the post precise orbit product (GNV1B) from JPL, the accuracy for R component is 0.03–0.05 m, while for T and N components are 0.02–0.04 m.

Keywords GPS · LEO satellite GRACE · Kinematic orbit determination · SPODS

19.1 Introduction

Low Earth Orbiters (LEO), defined as the artificial satellites orbiting the earth in an altitude of 300–1500 km [1], take many missions for science and engineering, such as geodesy, geophysics, oceanography and remote sensing [2]. In order to accomplish these tasks, the orbit position of the LEOs should be accurately determined. Some of the missions, for example gravity recovery and oceanic altimetry, even require the accuracy of the orbit to be on the level of mm–cm.

R. Ruan (✉) · L. Feng · X. Wu
Xi'an Research Institute of Surveying and Mapping, Xi'an 710054, China
e-mail: rrg2002me@163.com

R. Ruan · L. Feng · X. Wu
State Key Laboratory of Geo-information Engineering, Xi'an 710054, China

Therefore, precise orbit determination for the LEOs has become an interesting research field.

Benefiting from the continuous three-dimension positioning capacity of the Global Positioning System (GPS), the accuracy of orbit determination for LEOs has been greatly improved during the past 3 decays. Since the age that GPS was underbuilding, researchers have started to explore the possibility to determine the LEO's orbit with onboard GPS tracking data. This idea was firstly verified as the TOPEX/Poseidon was launched in 1992 and an accuracy better than 3 cm was achieved with the onboard pseudorange and carrier phase data, which exhibits great potential of the precise orbit determination (POD) technique with onboard GPS data [3, 4]. Thereafter, GPS receivers were widely equipped on varied LEO satellites, and the technique of "onboard GPS" became main means for LEO orbit determination, which has played a significance role in the missions of GRACE, CHAMP and GOCE [4–6]. Meanwhile, the method for LEO orbit determination has also enjoyed vigorous development [3, 5, 7], in addition to the traditional dynamical method, reduced dynamical method and kinematic method have been developed and widely employed. A mass of research indicate that the three different approaches can achieve comparable orbit accuracy [3, 5, 7–10]. Among them, the kinematic approach does not require dynamic information and therefore can avoid the influence of dynamical errors and has a special significance for application of gravity recovery and atmosphere model refining [2, 11].

In the past 2 decays, several pieces of software for GPS data (including onboard GNSS data) analysis have been developed and are famous in the geodesy and GNSS community, such as GAMIT, Gipsy, EPOS, NAPEOS, PANDA and Bernese. Be the end of 2013, a package of software named SPODS (Satellite Positioning and Orbit Determination System) [12, 13] has been developed at Xi'an Research Institute of Survey and Mapping, Nowadays the function of kinematic orbit determination for LEO has been fulfilled and integrated. In this paper, we will give a brief introduction on the mathematical principles, including observation model, error corrections and parameter estimation method, adopted by SPODS. And the performance was evaluated with GPS data on board GRACE-A/B.

19.2 Principle and Method

19.2.1 Observation Model

In the SPODS, un-differenced carrier phase and pseudorange are taken as observations. Assuming that an onboard GPS receiver tracks satellite s on the frequency band ($i = 1, 2$), the observation equations for the obtained carrier phase and pseudorange observation can be expressed as [11, 14]:

$$\phi_i^s = \rho^s + c \cdot (\delta t - \delta t^s) - \delta_{ion,i}^s + \lambda_i N_i^s + \varepsilon_i^s \quad (19.1)$$

$$p_i^s = \rho^s + c \cdot (\delta t - \delta t^s) + \delta_{ion,i}^s + \zeta_i^s \quad (19.2)$$

where, ϕ_i^s, p_i^s are observations of carrier phase and pseudorange respectively; ρ_i^s the geometry distance from satellite s to the on board receive; δt and δt^s the clock offset corresponding to GPST of the on board receiver and satellite s respectively; c the speed of light in the vacuum; $\delta_{ion,i}^s$ the ionosphere delay; λ_i the wave length; N_i^s the integer ambiguity of carrier phase; ε_i^s and ζ_i^s the measurement nose of carrier phase and pseudorange respectively. Generally, the orbit of LEOs is higher than 200 km, while the atmosphere layer is below 50 km, therefore the onboard GPS data is free from the influence of atmosphere delay. Although, in the previous equation, terms for antenna phase center correction, equipment delay, effect of phase wind-up and general-relative effect are omitted, they should be carefully considered when data processing [14, 15].

19.2.2 Strategy for Data Processing

It can be concluded from Eqs. (19.1) and (19.2) that there is no distinction between observation models for the GPS observation produced by onboard GPS receivers and ground GPS receivers. On the contrary, the former is simpler than the latter as it does not suffer from the atmosphere delay and the site displacement due to tidal effect. Therefore, for kinematic POD of LEO satellites with onboard GPS data, the data processing procedure is quite similar to the way for kinematic PPP with ground GPS data. Details for kinematic POD with SPODS are described as below:

Data processing starts with a procedure of preprocessing to detect carrier phase cycle slip and bad observations according to the method of TurboEdit [16]. In order to remove the influence of ionosphere delay, the Iono-Free combination of carrier phase and pseudorange are used as observations. Instantaneous mass center of GPS satellite is interpolated from IGS final orbit products with 9-order Lagrange method while the instantaneous satellite clock offset is calculated from IGS final 30-s-sampling clock product with linear polynomial. The antenna phase center offset and variation of GPS satellite are corrected with absolute correction data from `igs08.atx`, while that of onboard GPS receiver is ignored. The periodic clock variation of the theory of relativity, the wind-up effect of carrier-phase, and gravitation delay caused by general relativity are corrected with models. In order to take account of the measurement noise varied with elevation angle, according to the experience from the GNSS data analysis community, the observations are weighted according the elevation angle with weighting function: $P(e) = \sin^2(e)$. A priori sigma for carrier phase and pseudorange are set as 1 cm and 2 m respectively. The method of weighted Least Square with parameter pre-eliminating is adopted to estimate the

unknown parameters which contain the position coordinates and clock offset on every epoch, the ambiguity for every continuous pass. The estimation procedure is conducted in iteration to detect the remained cycle slip and outlier by scanning the posterior residuals and ended till none is detected.

19.2.3 Parameter Estimation

The LEOs orbit the earth in a high speed, for instance, an LEO satellite with an altitude of 500 km can orbit round the earth in 90 min. In an interval of 1 day, the onboard GPS receiver will track a certain GPS satellite several times, so the carrier phase observations will be divided into several continuous passes. Provided that there is no cycle slip in every pass, there will be 1 ambiguity for each pass of each satellite. The number of ambiguities, in a 1-day arc, is about 15 for each GPS satellite and in total 4000–5000 for the whole GPS constellation. It is to be noticed that the position coordinates and clock offset of the onboard receiver should be estimated epoch by epoch. Assuming the sampling interval of the observation is 10 s, totally 8640 epochs, the total number of unknown parameters including ambiguity parameters is about 35,000. When the traditional Least Square method [17] is used for parameter estimation, the dimension of the normal matrix is 35000×35000 , the solution of the normal equation is quite memory and time consuming. In the SPODS, an approach named parameter pre-elimination is applied.

Among all the unknown parameters, the position coordinates and the clock offset are only related to the observations of the current epoch, while a ambiguity parameter are connected to all observations of a continuous pass, so the coordinates and the clock could be pre-eliminated epoch by epoch.

Taking $X_k = [\delta t, x, y, z]_k^T$ as the correction vector of clock offset and coordinates on the k th epoch, and $X_b = [b_1, b_2, \dots, b_m]^T$ the vector containing all the undifferenced IF ambiguities for the whole arc, the observation equation can be written as:

$$L_k = [H_{X_i} H_B] \begin{bmatrix} X_k \\ B \end{bmatrix} + V, P \quad (19.3)$$

where, L_k is the observation vector, V the residual vector, P the weighting matrix. According to the principle of the least square method: $V^T P V = \min$, the normal equation is derived as:

$$\begin{bmatrix} N_{kk} & N_{kb} \\ N_{bk} & N_{bb} \end{bmatrix} \begin{bmatrix} \hat{X}_k \\ \hat{X}_b \end{bmatrix} = \begin{bmatrix} Z_k \\ Z_b \end{bmatrix} \quad (19.4)$$

Which can be divided into two parts:

$$\hat{\mathbf{X}}_k = \hat{\mathbf{X}}'_k - \mathbf{N}'_{kb} \hat{\mathbf{X}}_b \quad (19.5)$$

$$\mathbf{N}'_{bb} \hat{\mathbf{X}}_b = \mathbf{Z}'_b \quad (19.6)$$

where

$$\begin{aligned} \mathbf{X}'_k &= \mathbf{N}^{-1}_{kk} \mathbf{Z}_k \\ \mathbf{N}'_{kb} &= \mathbf{N}^{-1}_{kk} \mathbf{N}_{kb} \\ \mathbf{N}'_{bb} &= \mathbf{N}_{bb} - \mathbf{N}_{bk} \mathbf{N}'_{kb} \\ \mathbf{Z}'_b &= \mathbf{Z}_b - \mathbf{N}_{bk} \mathbf{X}'_k \end{aligned} \quad (19.7)$$

In the procedure of parameter solution, the core information in Eq. (19.5), $\hat{\mathbf{X}}'_k$ and \mathbf{N}'_{kb} , would be saved epoch by epoch for parameter recovery and the Eq. (19.6) of each epoch would be accumulated into a total normal equation:

$$\tilde{\mathbf{N}}_{bb} \hat{\mathbf{X}}_b = \tilde{\mathbf{Z}}_b \quad (19.8)$$

where, $\tilde{\mathbf{N}}_{bb} = \sum \mathbf{N}'_{bb}$, $\tilde{\mathbf{Z}}_b = \sum \mathbf{Z}'_b$. The formation of Eq. (19.8) is carried out recursively. The unknown vector \mathbf{X}_b can be estimated by solving Eq. (19.8):

$$\hat{\mathbf{X}}_b = \tilde{\mathbf{N}}^{-1}_{bb} \tilde{\mathbf{Z}}_b \quad (19.9)$$

Using $\hat{\mathbf{X}}_b$ and the information of $\hat{\mathbf{X}}^1_k$ and \mathbf{N}^1_{kb} saved previously. The unknown vector $\hat{\mathbf{X}}_k$ would be obtained by solving Eq. (19.5) epoch by epoch.

The above approach does not only applicable for kinematic POD of LEOs, but also for GNSS network solution. In practice, one can take full advantage of the sparse feature of the design matrix to improve the efficiency of the algorithm, and some matrix factorization method such as the Cholesky algorithm can be used to improve stability [17].

19.3 Experiment and Analysis

To evaluate the precision of kinematic POD with SPODS, GPS data (GPS1B) of GRACE-A/B during Sept. 1–9 2012 are collected from ISDC of GFZ as well as the post-processed precise orbit (GNV1B) which is of an accuracy of 2–3 cm with a sampling of 5 s. Each daily observation file was processed with SPODS to obtain kinematic orbit result of GRACE-A/B which was compared with the GNV1B orbit and the differences are expressed in RTN coordinate system.

Fig. 19.1 Time series of orbit differences on Sept. 1 2012 expressed in RTN compared with GNV1B

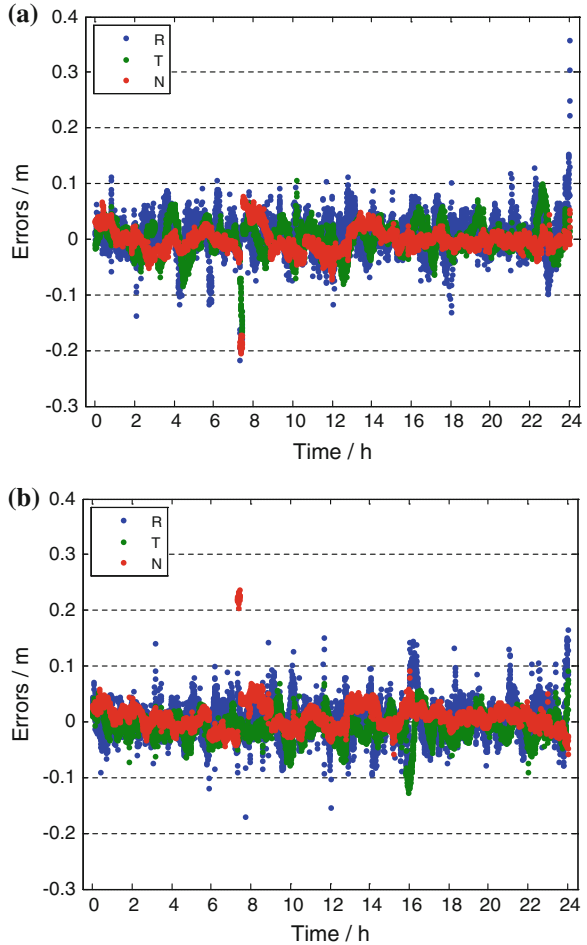


Figure 19.1 shows the time series of orbit differences in RTN on day Sept 1. Obviously, the deviations are largely below 0.1 m, except that a few are bigger but still smaller than 0.4 m. It seems that the error of kinematic orbit is not smooth which exhibit one of the main defects of the kinematic POD approach, This is possible due to the existence of outlier, incorrect satellite attitude model or short observation arc.

The daily mean deviations of orbit for GRACE-A and GRACE-B are listed in Table 19.1. It is apparent that the values are smaller than 1 cm in majority, which indicates that there is no noticeable systematical deviation.

Figure 19.2 illustrates the daily RMS differences of GRACE orbit compared with GNV1B, the RMS values of the three components are all smaller than 0.05 m: in R components are between 0.03–0.05 m, in T and N components are 0.02–0.04 m. So the precision of T and N components are better than that of

Table 19.1 Mean deviations of GRACE orbit compared with GNV1B (unit: cm)

Day	GRACE-A			GRACE-B		
	R	T	N	R	T	N
245	0.83	0.24	-0.12	0.41	-0.92	0.89
246	0.82	0.33	-0.50	0.39	-0.94	0.46
247	0.64	0.36	-0.49	0.49	-0.86	0.68
248	0.64	0.59	-1.23	0.37	-0.43	0.63
249	0.54	0.40	-0.69	0.68	-0.67	0.40
250	0.75	0.32	-0.87	0.22	-1.03	-0.23
251	0.81	0.35	-0.37	0.33	-0.71	1.27
252	0.94	0.41	-1.28	0.60	-0.70	0.04
253	0.62	0.37	-0.48	0.54	-0.77	-0.21

Fig. 19.2 Daily RMS differences of GRACE orbit compared with GNV1B. **a** GRACE-A. **b** GRACE-B.

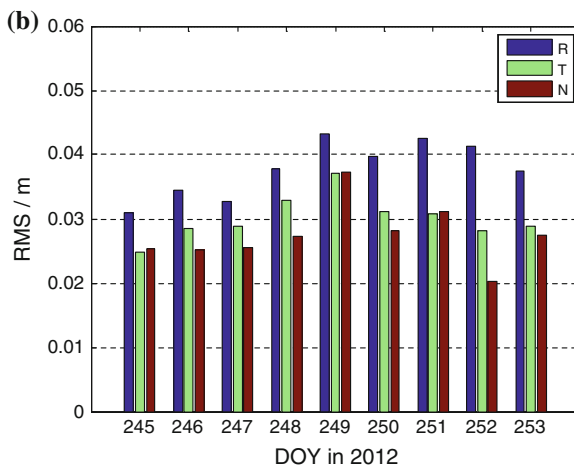
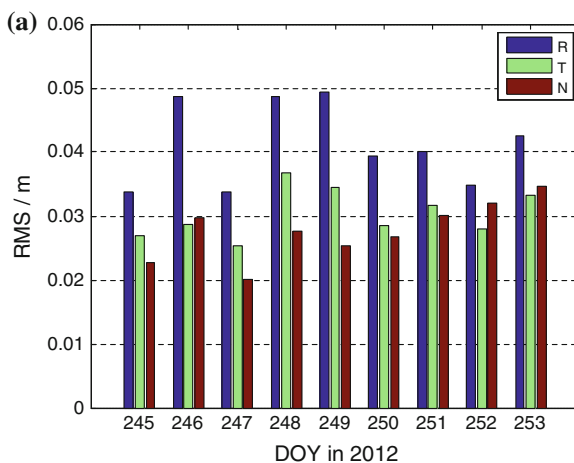
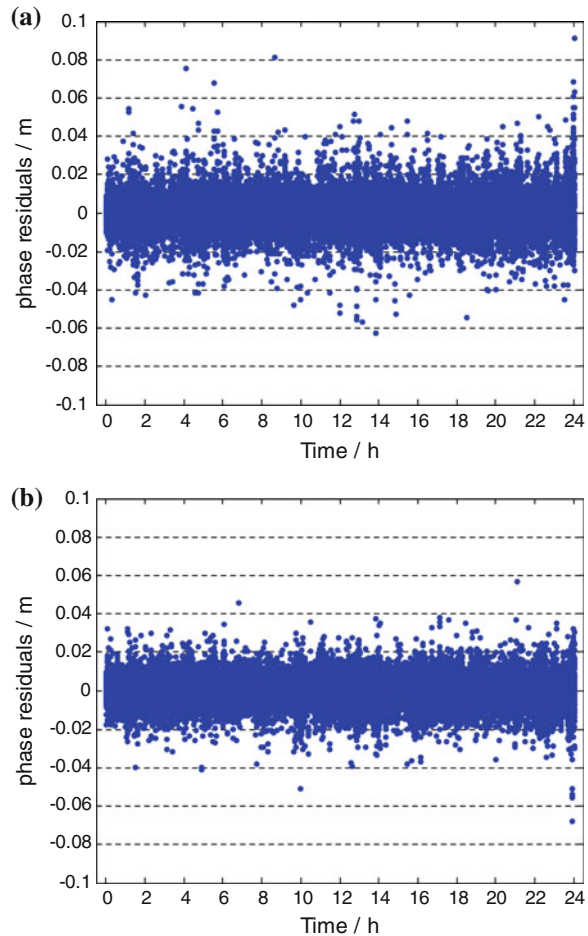


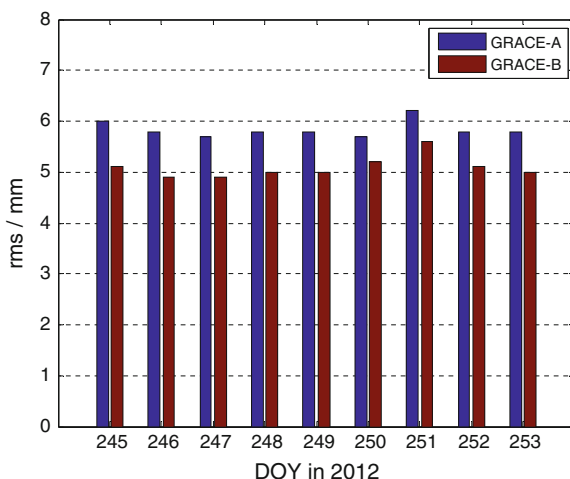
Fig. 19.3 Time series of IF carrier phase residuals on Sept. 1. **a** GRACE-A. **b** GRACE-B.



E component, which is consistent with the result obtained by other researchers. It is easy to compute that the totally mean RMSs for the 9 days, in RTN components, are 0.041, 0.030 and 0.028 m for GRACE-A, while 0.038, 0.030 and 0.028 m for GRACE-B. In a whole, the kinematic orbit precision of GRACE-B is a little better than GRACE-A, which has also been found by many researchers.

The time series of the IF carrier phase residuals are presented in Fig. 19.3. It is obvious that the residuals are majorly smaller than 0.05 m and no systematical bias. Which indicate that models applied in the SPODS is proper and the quality control procedure works. It can also be found that the residual of GRACE-B is a little smaller than CRACE-A, as daily RMS is illustrated in Fig. 19.4 which shows about 6 mm for GRACE-A and 5 mm for GRACE-B.

Fig. 19.4 Daily RMS of IF carrier phase residuals



19.4 Summary

The SPODS developed at Xi'an Research Institute of Surveying and Mapping not only has the function for global GNSS network solution, but also, now, fulfills the capability for kinematic orbit determination for LEO satellites. This paper presents the main principle and method employed and demonstrate the performance with onboard GPS data from GRACE-A/B. the experimental result show an accuracy of 0.03–0.05 m in Radius component and 0.02–0.04 m in Track or Normal components is achievable by kinematic approach with SPODS. This is comparable with the result of other GPS data processing research groups.

References

1. Montenbruck O, Gill E (2001) Satellite orbits models, methods, and applications. Springer, Berlin
2. Li J, Zhang S, Zhou X et al (2009) Precise orbit determination for GRACE with zero-difference kinematic method. *Chin Sci Bull* 64(16):2355–2362
3. Yunck TP, Bertiger WI, Wu SC et al (1994) First assessment of GPS-based reduced dynamic orbit determination on TOPEX/Poseidon. *Geophys Res Lett* 21(7):541–544
4. Qing X (2009) Research on precision orbit determination theory and method of low earth orbiter based on GPS technique. Information Engineering University, Zhengzhou, p 166
5. Svehla D, Rothacher M (2003) Kinematic and reduced-dynamic precise orbit determination of low earth orbiters. *Adv Geosci* 2003(1):47–56
6. Xu T, Jiang N, Sun Z (2013) Research on dynamic orbit smoothing based on kinematic orbit of GOE. *Geomat Sci Eng* 33(1):16–20
7. Schutz BE, Tapley BD, Abusali PAM et al (1994) Dynamic orbit determination using GPS measurements from TOPEX/POSEiDON. *Geophys Res Lett* 21(19):2179–2182

8. Bock H, Jaggi A, Svehla D et al (2007) Precise orbit determination for the GOCE satellite using GPS. *Adv Space Res* 2007(39):1638–1647
9. Svehla D, Rothacher M (2005) Kinematic positioning of LEO and GPS satellites and IGS stations on the ground. *Adv Space Res* 2005(36):376–381
10. Visser PNAM, Ijssel JVD (2003) Aiming at 1-cm orbit for low earth orbiters: reduced-dynamic and kinematic precise orbit determination. *Space Sci Rev* 108:27–36
11. Zhang X, Li P, Zuo X (2013) Kinematic precise orbit determination based ambiguity-fixed PPP. *Geomat Inf Sci Wuhan Univ* 38(9):1009–1013
12. Ruan R, Jia X, Wu X et al (2014) SPODS software and its result of precise orbit determination for GNSS satellites. In: China satellite navigation conference (CSNC) 2014 proceedings, vol III, Nanjing, pp 301–312
13. Wei Z, Ruan R, Jia X et al (2014) Satellite positioning and orbit determination system SPODS: theory and test. *Acta Geodaetica Cartogr Sin* 43(1):1–4
14. Kleusberg A, Teunissen PJG (eds) (1996) GPS for geodesy. Springer, Berlin, p 407
15. Kouba JA (2003) Guide to using international GPS service (IGS) products, p 31. <ftp://igs.cb.jpl.nasa.gov/igs/scb/resource/pubs/GuidetoUsingIGSProducts.pdf>. Accessed 15 Sept 2008
16. Blewitt G (1990) An automatic editing algorithm for GPS data. *Geophys Res Lett* 17(3):199–202
17. Bierman GJ (1977) Factorization methods for discrete sequential estimation. Academic Press, New York, p 241

Chapter 20

A GNSS Anti-spoofing Method Based on the Cooperation of Multiple Techniques

Huiqi Tao, Hong Li and Mingquan Lu

Abstract An anti-spoofing technique based on the cooperation of multiple detections is proposed in this paper. A GNSS receiver could detect more than one correlation peak in one processing channel in acquisition when the spoofing signal exists. Signal quality monitoring (SQM) can detect abnormal changes of the correlation peak when spoofing attack on tracking receiver. Generally, receiver gives up the measurements of the abnormal channel to avoid the risk of tracking fault or spoofing signal. This decreases the number of available signals. Receiver autonomous integrity monitoring (RAIM) is capable of detecting and mitigating single error but lack of dealing with multiple errors. This paper proposes a cooperation method of these three techniques which are complementary. Detailed discussion of the method's procedure and performance are provided in this paper. Simulation results demonstrate that the method is feasible and effective to detect and mitigate multiple spoofing signals.

Keywords Anti-spoofing · Multi-peak detection · SQM · RAIM · Cooperation

20.1 Introduction

Security of GNSS applications has been paid more and more attention with the popularization of positioning and navigation applications. As GNSS signals are vulnerable to interferences and easy to be counterfeited, and there have been relevant reports that devices with low cost had implemented successful spoofing. The experiment taken by Humphreys's team in 2013 has been widely known, they

H. Tao (✉) · H. Li · M. Lu
Department of Electronic Engineering, Tsinghua University, Beijing 100084, China
e-mail: thq12@mails.tsinghua.edu.cn

spoofed a yacht successfully using a GPS spoofing device, and the yacht was tricked onto a parallel track hundreds of meters from its intended one. Therefore, anti-spoofing technique has become a new focus in GNSS studies. There have been many anti-spoofing techniques in different processing levels [1], such as power monitoring in signal processing, consistency check of ephemeris in data bit level, and comparing with other system in position solution level, etc. Some techniques are effective but complex, for instance, spatial processing which uses multi-antenna array is effective to detect medium spoofing that uses only one transmit antenna, but it is too sophisticated to implement in a general GNSS receiver.

Receiver autonomous integrity monitoring (RAIM) is a practical implementation that does not impose extensive hardware modifications to the receiver [2]. RAIM uses the redundant information to detect and exclude the fault signal by checking the consistency of measurements or position solution. In essence, spoofing signals are faults to authentic signals. Therefore, RAIM is a practical anti-spoofing implementation. Typically, RAIM is effective to defense single fault signal or spoofing. For the purpose of improving RAIM's performance, additional information needs to be provided. Some extended RAIM methods take advantage of measurements in other frequencies, constellations, and systems [3, 4], they can detect and mitigate more than one fault signal, but they are too hard to implement in low cost receiver.

Besides, some basic detection may be helpful to RAIM, such as power monitoring, multi-peak detection in acquisition, or signal quality monitoring (SQM) [5] in tracking, etc. These techniques could detect the abnormal changes of receiver's processing channels, such as abnormally sharp or elevated correlation peaks. In fact, any abnormality is likely to indicate the error, especially spoofing signal. It's arbitrary to give up the measurements of these channels and this would decrease the number of available signals. On the other hand, it's difficult to make sure that abnormalities are caused by spoofing. For instance, multipath effects and thermal noise may affect the performance of SQM. However, receiver could take advantage of these techniques to detect the abnormal changes and check them using RAIM. The cooperation of them could exclude more spoofing signals and improve the reliability of PVT solution.

This paper researches the cooperation of these techniques to defense more than one spoofing signal, and the cooperation is medium complexity to implement in general GNSS receivers. The architecture of cooperation is proposed in this work. Some spoofing scenarios are discussed, and the performance of the cooperation solution is simulated as well. The remainder of this paper is organized as follows: Sect. 20.2 analyzes the performance of basic RAIM under multi-spoofing signals and discusses RAIM detection with the aids from acquisition and tracking. Multi-peak detection and SQM which provide the aids are discussed in this section as well. Section 20.3 provides the simulation of the cooperation anti-spoofing method for detecting and mitigating two and three spoofing signals. The finally conclusions are provided in Sect. 20.4.

20.2 The Cooperation of Multiple Techniques

Anti-spoofing techniques could be classified in terms of spoofing detection and spoofing mitigation, authors of [1] provide a brief review of them. Although each technique plays unique role in anti-spoofing architecture, the cooperation of them has not received enough attention. Especially, some detection techniques could find but cannot mitigate the faults, while some mitigating techniques do not have enough ability to deal with multiple faults. Thus, cooperation of multiple detections is necessary to improve the performance of anti-spoofing. This section focuses on three basic techniques and the cooperation of them. They are multi-peak detection in acquisition, SQM in tracking, and RAIM in positioning solution. These three techniques aim at different problems in different steps of signal and information processing, they are complementary and easy to cooperate.

20.2.1 Multi-peak Detection in Acquisition

Compared with other techniques in acquisition such as power monitoring, multi-peak detection does not require complex hardware and is easier to implement. Assuming that an authentic signal and its counterfeit are mixed and received before the victim receiver locks the authentic signal of this satellite, the received signal can be expressed as follow

$$\begin{aligned}
 s^i(t) &= s_A^i(t) + s_S^i(t) \\
 &= \sqrt{P_A}D_A(t)C^i(t) \sin(2\pi ft) + \sqrt{P_S}D_S(t - \tau)C^i(t - \tau) \sin(2\pi f_s(t - \tau))
 \end{aligned}
 \tag{20.1}$$

where the subscripts A and S correspond the authentic signal and spoofing signal. P, D, C, f, and τ are the signal power, navigate data, pseudo-random code, carrier frequency integrated Doppler shift, and code delay, respectively. Although the power of spoofing signal maybe higher than the authentic signal, it's very hard to suppress the authentic signal completely. Unless the spoofer aligns the carrier frequency and phase and code delay to the authentic signal, there would be more than one correlation peak in the process of acquisition in the receiver. If two correlation peaks are detected in acquisition, receiver needs to track both two signals to avoid the risk of tracking the counterfeit signal. The authenticity of two signals can be checked by subsequent detections such as code and phase rate consistency check, RAIM, and so on. This strategy of acquisition and tracking requires additional tracking channels and increases processing complexity. But in some cases, it's not necessary to implement this strategy for all satellites, detailed discussion is provided in subsequent section.

20.2.2 SQM in Tracking

If the spoofing signal attacks the receiver which is tracking the authentic signal, abnormal changes of correlation peak may appear in the process of aligning the spoofing signal to authentic signal. SQM is a basic technique to monitor the correlation peak quality. Two detection tests, delta test and ratio test, are proposed in [5], they are given by (20.2) and (20.3) respectively.

$$\Delta = \frac{I_E - I_L}{2I_P} \quad (20.2)$$

$$R = \frac{I_E + I_L}{2I_P} \quad (20.3)$$

where I_E , I_L , and I_P are the respective in-phase early, late, and prompt accumulations. Delta test is designed to identify asymmetric correlation peaks while ratio test is designed to identify abnormally sharp or elevated correlation peaks. Assuming that signal has been locked by the carrier PLL and the space of correlators is half code chip, the nominal value of delta test is 0 while the nominal value of ratio test is 0.5. The threshold of the test is a key point because the thermal noise or multipath effects may affect the shape of correlation peak. Discussion about threshold can be found in [3] as well.

20.2.3 RAIM Under Multi-spoofing Signals

RAIM is a basic technique to detect and exclude single fault in GNSS receivers. It is based on the assumption that simultaneous multiple-satellite faults occur with an extremely small probability, but this assumption is not true in case of spoofing. Spoofing signals are difficult to distinguish with authentic GNSS signals as the structure of GNSS signal is known publicly. The spoofer would project the false signals with correct signal delay and strength as far as possible for the purpose of misleading or deceiving the victim receiver into pre-specified PVT solution. Thus, more than one spoofing signal is possibly locked by the victim receiver.

RAIM detects the fault signal by comparing test statistic based on pseudorange measurements with the threshold calculated using chi-square method. Least square residual method and parity vector method are two basic RAIM algorithms and they are equivalent [2]. Some improved methods based on them could deal with two faults, such as NIORAIM [6], OWAS [7], and some other extended RAIM algorithms [8]. But they need additional information such as measurements in other frequencies or constellations, they are too complicated to implement in low cost receivers. A detailed theoretical analysis of RAIM under the condition of two errors has been provided in [9], the position error vector and test statistic are given as follows.

$$\begin{aligned}
 E_{ij} &= A[0, \dots, \varepsilon_i, \dots, \varepsilon_j, \dots, 0] \\
 &= [A_{1i}\varepsilon_i + A_{1j}\varepsilon_j, A_{2i}\varepsilon_i + A_{2j}\varepsilon_j, A_{3i}\varepsilon_i \\
 &\quad + A_{3j}\varepsilon_j, A_{4i}\varepsilon_i + A_{4j}\varepsilon_j]^T \\
 &= E_i + E_j
 \end{aligned}
 \tag{20.4}$$

$$\begin{aligned}
 SSE_{ij} &= \sqrt{w^T w} \\
 &= \sqrt{S_{ii}\varepsilon_i^2 + S_{jj}\varepsilon_j^2 + 2S_{ij}\varepsilon_i\varepsilon_j}
 \end{aligned}
 \tag{20.5}$$

Equations (20.4) and (20.5) give the PVT error vector and the test statistic of RAIM under two errors. E_i and E_j denote the PVT errors vector corresponding to measurement errors ε_i and ε_j respectively. E_{ij} is the sum of vectors E_i and E_j . As shown in (20.5), the statistic test is determined by not only the errors but also the geometric distribution of receiver and satellites. It can be concluded that the test statistic is related to the combination of two errors. Some combinations would be easy to be detected and some would be hard. Assuming that one of two errors can be detected and mitigated by RAIM, the other one can be dealt with by RAIM again.

20.2.4 The Cooperation of Three Techniques

Based on the above discussion, three techniques are located in different steps of signal and information processing steps. Multi-peak detection in acquisition and SQM in tracking are capable of finding spoofing signals but they cannot mitigate the spoofing signals, while RAIM in position solution can mitigate the error but it is lack of finding more errors. They are complementary and easy to implement the cooperation. The procedure of cooperation anti-spoofing method based on them is proposed as Fig. 20.1.

As shown in Fig. 20.1, multi-peak detection and SQM classify the measurements into three sets and RAIM check the correctness of them respectively. If more than

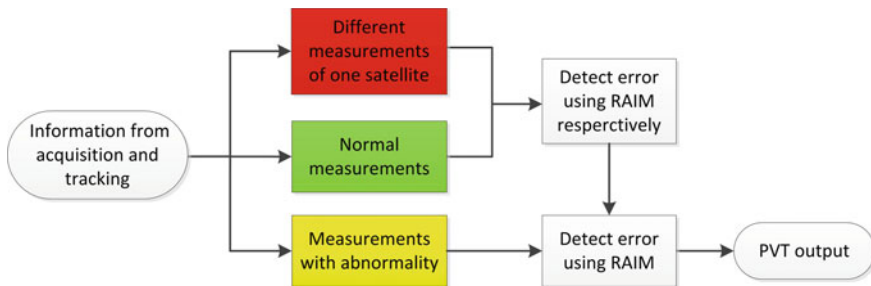


Fig. 20.1 Procedure of cooperation anti-spoofing method

one correlation peak is detected in acquisition, each of them is tracked by receiver and the measurements are classified a set. Besides, SQM can detect abnormalities of channels where spoofing signals attack the authentic, measurements of these channels are classified a set as abnormal. Each measurement of these two sets must be check with normal measurements using RAIM respectively. The correctness of the classification is the key of this method. In theory, every spoofing signal can be detected and mitigated as long as the normal measurements' number is no less than 5, where 5 is the minimum number required by RAIM algorithms.

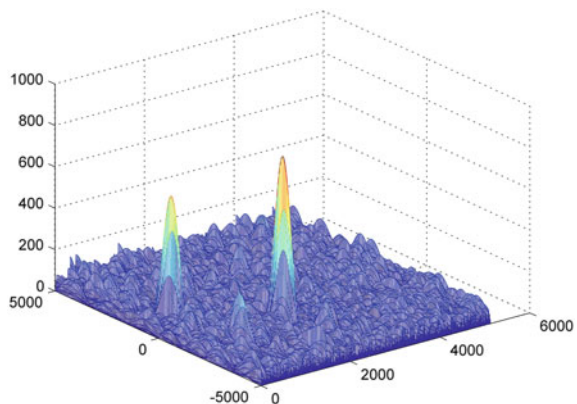
20.3 Simulations

The previous three techniques are simulated respectively in a software-defined GPS receiver. The authentic signal is generated by a GPS signal generator which is capable of generating 10 channels of GPS L1 C/A-code signals simultaneously. Spoofing signals are the delayed sampling of authentic signals and the strength can be falsified. The delays can simulate the pseudorange errors of spoofing signals, especially the retransmit-spoofing signals.

Multi-peak detection in acquisition can be realized in general GPS receivers. Figure 20.2 shows the result of multi-peak detection if an authentic signal and its counterfeit are mixed and acquired together. The amplitude of correlation peak relates to signal's power. Spoofer must project the counterfeit signal with proper strength to skip the detection based on power monitoring. The power of authentic and spoofing signal would be similar and this is propitious to multi-peak detection. As previously mentioned, as long as more than one peak is detected, receiver should set up corresponding channels to track each of them.

The key point of the proposed cooperation method is to track each acquired signal and provide the measurements to PVT solution respectively. SQM in tracking and RAIM in PVT solution are simulated in detail. Figure 20.3 shows the process of spoofing attack on tracking receivers.

Fig. 20.2 The change of correlation peak in the process of spoofing attack on tracking receivers



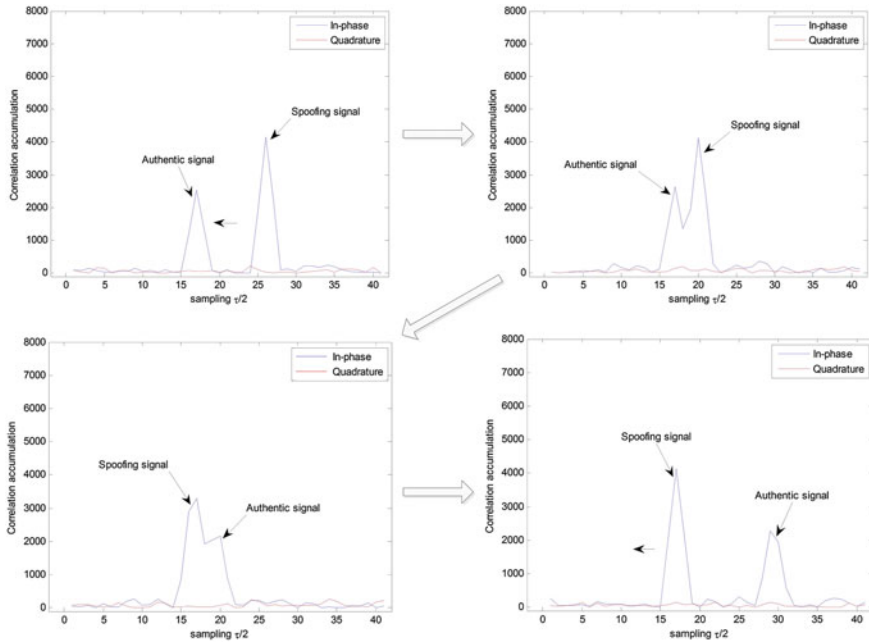


Fig. 20.3 The change of correlation peak in the process of spoofing attack on tracking receivers

As shown in Fig. 20.3, authentic signal is locked by receiver at the start and the spoofing signal is moving toward the authentic with the rate of 4 chips per second. The spoofing signal’s power is 3.5 dB higher than the authentic signal’s power. When the spoofing signal’s code phase aligns the authentic signal, both signals are locked. Then, the receiver locks the signal with higher power, that is, authentic signal is suppressed by the spoofing signal. There is an obvious change on the shape of correlation peak and this change can be reflected from the SQM tests.

Figure 20.4 shows the ratio test and delta test defined as (20.2) and (20.3) in different signal-to-noise ratio (SNR). The value of delta test is no longer equal to 0 and the nominal value of ratio test is no longer equal to 0.5 when the spoofing signal closes to the authentic. The SNR in left figure is -10 dB and the SNR in right figure is -15 dB. Comparing tow figures, it’s obvious that the curves of both tests have different jitter in different SNR. However, these changes of SQM tests are obvious and they indicate the faults. PVT solution can not employ this channel’s measurements as normal. They are treated as distrustful and checked using RAIM respectively in the follow-up process.

As described in Fig. 20.1, abnormalities of acquisition and tracking should be dealt with respectively in PVT solution using RAIM. However, RAIM’s performance without any aids under multi-spoofing is simulated, and this is meaningful to assess the performance of cooperation anti-spoofing. Assuming that one of the two errors can be isolated correctly using RAIM, the remainder measurements still

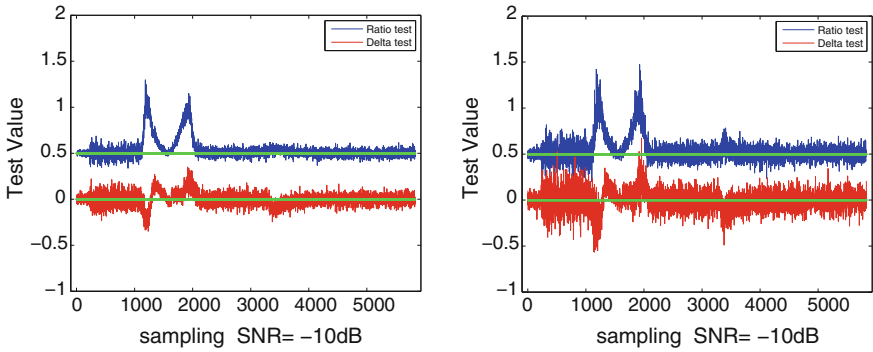


Fig. 20.4 The SQM tests in the process of spoofing attack on tracking receivers

contain one error and this one can be detected and mitigated using RAIM again. The simulation results of repeat RAIM in the case of two errors are provided in detail next.

In this simulation, the signal of 9 satellites is acquired and tracked by the software-defined GPS receiver. The constellation of 9 satellites is shown in Fig. 20.5. Receiver extracts the pseudo-range measurements and falsifies them to simulate the spoofing signals.

Two measurements errors are combined in simulations. The number of two measurements combinations is 36 as the total number of satellites is 9. Table 20.1 shows 8 measurements errors add to the riginal measurements. The errors range from 50 M–100 K. These values cover the most cases of spoofing in practice. Accordingly, there are 64 combinations of two errors with two different satellites.

Fig. 20.5 Constellation of the 9 GPS satellites in simulations

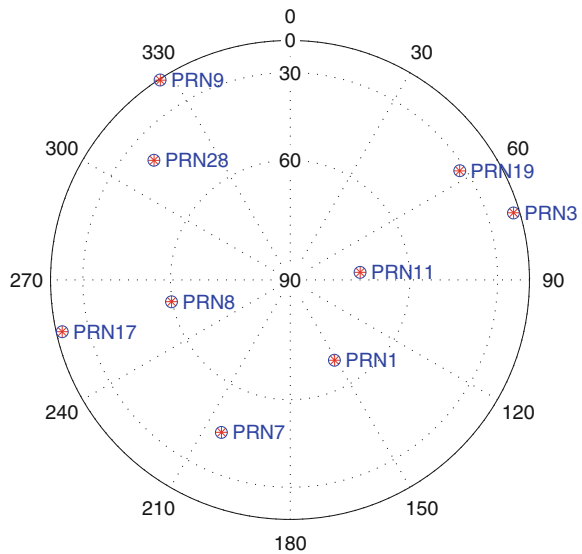


Table 20.1 Numerical value of measurements errors

Errors	Value (m)	Errors	Value (m)
E1	5×10^1	E5	5×10^3
E2	1×10^2	E6	1×10^4
E3	5×10^2	E7	5×10^4
E5	1×10^3	E8	5×10^5

Table 20.2 The statistics of numerical value of successful detection for every pair of measurements of 9 satellites

	E1	E2	E3	E4	E5	E6	E7	E8
E1	36	36	36	36	36	36	36	36
E2	36	36	36	36	36	36	36	36
E3	36	36	29	35	36	36	36	36
E4	36	36	34	29	36	36	36	36
E5	36	36	36	36	29	35	36	36
E6	36	36	36	36	34	29	36	36
E7	36	36	36	36	36	36	29	35
E8	36	36	36	36	36	36	34	29

The simulation results statistics of RAIM in two errors scenarios is shown in Table 20.2. The number in each unit of the table corresponds to the number of successful spoofing detection. For instance, the number in lower right unit is 29, it means that there are 29 successful spoofing detections while 7 detections are failed. A successful detection means both errors are detected correctly and the PVT errors do not exceed the preset limit. Table 20.2 shows that only a few errors combinations can't be detected and mitigated completely. The units with these combinations are colored. It is obvious that the failed detections are concentrated in the diagonal line of the table which represents the combinations that both errors are equal. Figure 20.6 shows the diagonal line numbers' bar graph.

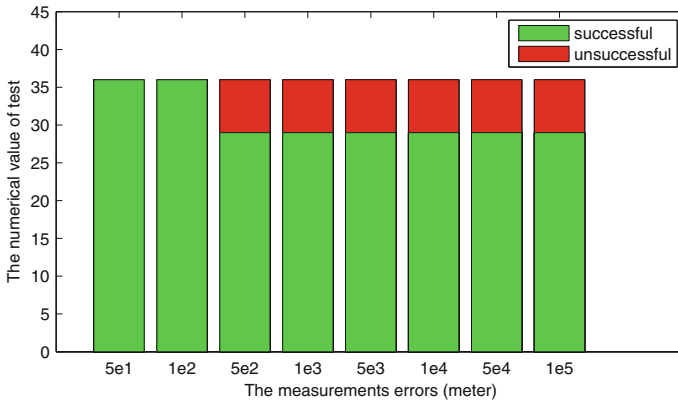


Fig. 20.6 Bar graph of detections with equal errors for every pair of measurements of 10 satellites

The simulation results show that RAIM performs well without any aids in most cases of two errors. It can be concluded that cooperation of RAIM and other spoofing detections would perform better. In fact, most unsuccessful detections are concentrated in a few satellites combinations and a few errors combinations. In other words, just a few combinations are easy to get wrong using RAIM repeatedly. As mentioned previously, it's unnecessary to implement multi-peak detection and tracking each peak strategy for all satellites, for instance, in the case of two spoofing signals, only a few satellites combinations need that strategy, and this is depend on the distribution of satellites and receiver.

Combine the above simulations, it can be concluded that classification of the measurements in Fig. 20.1 determines the performance of the proposed cooperation anti-spoofing method. As long as the number of normal measurements is no less than 5, every spoofing signal can be detected and mitigated. 5 is the minimum number required by RAIM and it ensures the consistency check of the normal measurements. The actual performance of the method can be better than this, because repeat RAIM is capable of dealing with more than one spoofing signal without any aids in some cases. Besides, it can ensure the precision of PVT solution because the number of usable signals does not obviously decrease.

20.4 Conclusions

The cooperation of multiple anti-spoofing techniques is necessary as the insufficient of each technique. This paper proposes a cooperation method of three anti-spoofing techniques. They are multi-peak detection in acquisition, SQM in tracking, and RAIM in position solution. They locate in different steps of signal and information processing steps of receiver and their capabilities of spoofing detection and mitigation are complementary. The cooperation method does not impose extensive hardware modifications to the receiver, it's a feasible and effective way to detect and mitigate more than one spoofing signal. Simulations demonstrate the validity of this method. Nevertheless, there are some problems. As the acquisition and tracking strategy needs more tracking channels, multipath effects and thermal noise may increase the false-alarm probability of SQM, repeat RAIM increases the processing complexity, it's necessary to optimize the architecture and improve the efficiency. Further studies could focus on them.

References

1. Jafarnia-Jahromi A, Broumandan A, Nielsen J, Lachapelle G (2012) GPS vulnerability to spoofing threats and a review of antispoofing techniques. *Int J Navig Obs*, Vol 2012 Article ID 127072, 16 p
2. Kaplan ED, Hegarty CJ (2006) *Understanding GPS-principles and applications*, 2nd edn. Artech House, Boston

3. Brown R (1992) A baseline RAIM scheme and a note on the equivalence of three RAIM methods. In: Proceedings of ION NTM 1992, San Diego, CA, USA, pp 127–137, Jan 1992
4. Hewitson S, Wang J (2010) Extended receiver autonomous integrity monitoring (eRAIM) for GNSS/INS integration. *J Surv Eng* 136(1):13–22
5. Phelts RE (2001) Multicorrelator techniques for robust mitigation of threats to GPS signal quality. Ph.D. thesis, Stanford University, Palo Alto, Calif, USA
6. Hwang P, Brown R (2005) NIORAIM integrity monitoring performance in simultaneous two-fault satellite scenarios. In: Proceedings of ION GNSS 2005, Long Beach, CA, USA, pp 1760–1771, Sept 2005
7. Lee Y, Braff R, Fernow J et al (2005) GPS and Galileo with RAIM or WAAS for vertically guided approaches. In: Proceedings of ION GNSS 2005, Long Beach, CA, USA, pp 1801–1825, Sept 2005
8. Guo J, Lu M, Cui X, Feng Z (2011) A new RAIM algorithm for triple-frequency GNSS receivers. In: Proceedings of ION ITM 2011, San Diego, CA, USA, Jan 2011
9. Liu JX, Lu MQ, Cui XW et al (2007) Theoretical analysis of RAIM in the occurrence of simultaneous two-satellite faults. *IEE Proc Radar Sonar Navig* 1(2):92–97

Chapter 21

Based on Singular Spectrum Analysis in the Study of GPS Time Series Analysis

Ronghai Qiu, Yingyan Cheng, Hu Wang and Xiaoming Wang

Abstract In this paper, using the singular spectrum analysis (SSA) method for analysis of IGS station of ARTU time series was studied. The SSA-IQR (Singular Spectrum Analysis-Inter Quartile Range) is used to detect gross error. Using the method of singular spectrum iteration to fill the gaps of missing datas. This methods can achieve high precision. Singular spectrum analysis method can extract informations effectively to complete the recognition and extraction of trend and cycle item, and it can eliminate noise effectively, to smooth the effect. Experiments show that: ARTU station have trends obviously. Especially the linear trend term. By using the least square fitting the linear trend. Periodic cycle components exist in a variety of parallel.

Keywords Singular spectrum analysis · Trend · Period · Smooth effect · Noise

This research work was supported by the National Natural Science Foundation of China (Grant No. 41374014;41404034;), the National High Technology Research and Development Program of China (Grant No. 2013AA122501), the research foundation of the China Academy of Surveying and Mapping (7771405), the Data analysis center (Grant No. GFZX0301040308-06).

R. Qiu (✉) · Y. Cheng · H. Wang
Chinese Academy of Surveying and Mapping, Beijing, China
e-mail: 154052467@qq.com

Y. Cheng
e-mail: yycheng@casm.ac.cn

H. Wang
e-mail: wanghu@casm.ac.cn

R. Qiu
Institute of Surveying and Mapping Science and Engineering,
Shandong University of Science and Technology, Qingdao, Shandong, China

X. Wang
SPACE Research Centre, School of Mathematical and Geospatial Sciences,
RMIT University, Melbourne 3001 GPO BOX 2476 VIC, Australia

21.1 Introduction

In recent years, the continuous GPS observation plays an important role in many fields. GPS technique has been widely applied [1–2]. Many scholars have adopted different methods to research on the site to reflect the movement characteristics of surface deformation [3, 4, 6–8]. Singular spectrum analysis [5, 9–12] is EOF decomposition that based on the phase space reconstruction. Firstly, it calculates the eigenvector space since the covariance matrix of the original data delay matrix, and then the original data later arrangement were projected onto the orthogonal space. Finally, using principal component analysis of Method to complete the analysis for inner structure of data in reconstruct phase space.

Singular spectrum analysis (referred to as SSA) is the earlier application in digital signal processing field. The method in digital signal processing is also named as the Karhunen-Loeve Biorthogonal Expansion. The first application of SSA in the oceanographic research is Colebrook in 1978. In 1986, Fraedrich have use one dimension time sequence in the delay space to do EOF expansion, and then through significant test to identify a number characteristic components of meaningful, to get climate attractor dimension estimate. This is the first application in meteorology about SSA. This method is currently in the climate variability in the application of gradually increasing. Interpolation theory of singular spectrum analysis is the first proposed by Schoellhamer [10]. The method is change itself delay and covariance matrix and principal components (Principal Components, PCs). In the calculation process, only using existing datas, ignoring the missing datas. It can avoid to dialocate the covariance come from missing data. The singular spectrum analysis method proposed by Shoellhamer applied to the missing data sequence has some enlightening significance, which makes the application of singular spectrum analysis is more flexible. In this paper, the singular spectrum iteration and using the singular spectrum analysis made the following research on time series.

21.2 Data Preprocessing

This paper uses the method of SSA-IQR (Singular Spectrum Analysis-Inter Quartile Range) and singular spectrum iteration to research ARTU station for gross error detection and missing value imputation. The SSA-IQR method can effectively complete rejection of gross errors. Singular spectrum iterated interpolation method has high precision.

21.2.1 The SSA-IQR Method of Gross Error Detection and Elimination

The SSA-IQR method is used for a discrete set of time series analysis. According to the order from small to large, the use of standardized IQR handled to the centralized

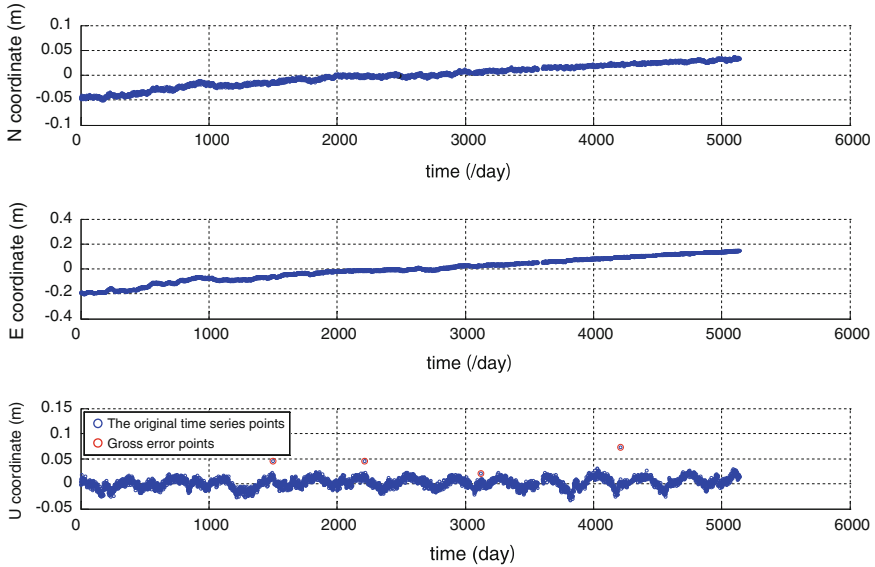


Fig. 21.1 The original time series and gross error detection about ARTU station

datas and dispersed datas. The IQR is the difference between the low four fractile and high four fractile. Lower four point value is nearly to ordered sequence of 1/4. Higher four point value is nearly to ordered sequence at 3/4. The specific calculation formula is as follows:

$$Z = \frac{\hat{v}_i - \text{median}(\hat{v}_{i=w/2, i+w/2})}{\text{IQR}(\hat{v}_{i=w/2, i+w/2})} \tag{21.1}$$

When outlier criteria is $Z \geq 3$, the confidence level is 99 %. That is to say, when $Z \geq 3$, it is considered that the point is the gross error. According to this principle, as shown in Fig. 21.1, that is a time series of coordinate ARTU station including gross error. The horizontal axis is time. A total of 15 years. The discontinuous parts are the lack of datas. Using IQR method to find the gross error. Blue dots are the original time series. The red dots represent gross error. As the Fig. 21.1 to know, the N, E direction without gross error. There are four gross error points in U direction. It must to delete its.

21.2.2 Interpolation Iterative Method Based on the Singular Spectris Analysis

The time series of ARTU station is non continuous. Singular Spectrum Analysis is used to a continuous time series of deletion. Interpolation is one of the main works. In this paper, using the singular spectrum analysis method of interpolation. Many papers have been mentioned. Because of space, not carefully set steps.

Table 21.1 ARTU station interpolation precision

Direction	Mean square error (mm)	Error (mm)
N	4.1	3.2
E	3.3	2.5
U	8.6	6.7

There are a total of 5139 days about ARTU station including 63 interpolation datas, 800 cross validation datas and another datas. The vertical axis represents coordinate under different epochs. The red dots represent the existing data. Greens are interpolation datas by the use of singular spectrum method. As can be seen from Table 21.1, Horizontal interpolation mean square error is less than 5 mm. The height direction is less than 9 mm. The average error of horizontal direction is less than 4 mm. The height direction is less than 7 mm. It can be get a higher interpolation accuracy.

Finally, the complete time series are as shown in Fig. 21.2 below. The red dots represent original time series. Green points represent interpolation results. It can be see that getting a good interpolation effect.

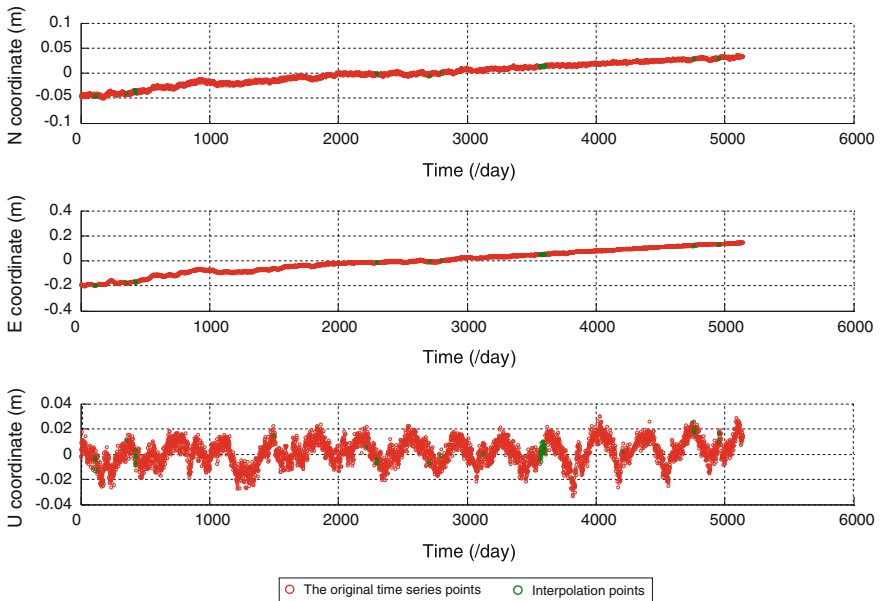


Fig. 21.2 ARTU after the interpolation of time series

21.3 Analysis of Trend and Cycle and Reconstruction Based on SSA

Now, it uses singular spectrum method to analysis completion of interpolated ARTU station time series. The embedded in the window length is 450. Getting three directions forward 10 order Reconstructed components (Reconstructed Components, be called RC for short) with effective information variance contribution amount are shown in Table 21.2.

From the Table 21.2, we can see when the time series in the horizontal direction with a big trend, its energy often account for more than 90 % of singular spectrum energy. There have the periodic components of elevation direction. Firstly, the trend components must be extracted correctly, and then go on SSA decomposition after to remove the trend components. Last but not least, separating the oscillation and noise.

21.3.1 Trend Components Identification and Extraction by Kendall Method

In this paper, it use Kendall test method to identify maximum trend components. According to Vautard, if there exists the trend components in the original sequence, it should appear in the first few time of the main components. It can use Kendall nonparametric test to identify it. Considering the sequence about $Z_i, 1 \leq i \leq n$. If $i < j, Z_i < Z_j$, then figuring out index (I, J) log with K_r . If there exists an upward trend, the K_r is a small. There may be a trend of decline. Methods quantitative inspection is to compute statistics:

$$\tau = \frac{4K_r}{n(n-1)} - 1 \tag{21.2}$$

When the K_r do not exist trend components, the τ means is zero. The mean variance formula is as follows:

$$s = \sqrt{\frac{2(2n+5)}{9n(n-1)}} \tag{21.3}$$

Table 21.2 Effective information variance contribution amount 10 order

Direction	The trend rate of contribution (%)	Periodic contribution rate (%)	The total variance contribution rate (%)
N	91.17	7.88	99.05
E	91.58	7.87	99.45
U	28.56	49.22	77.78

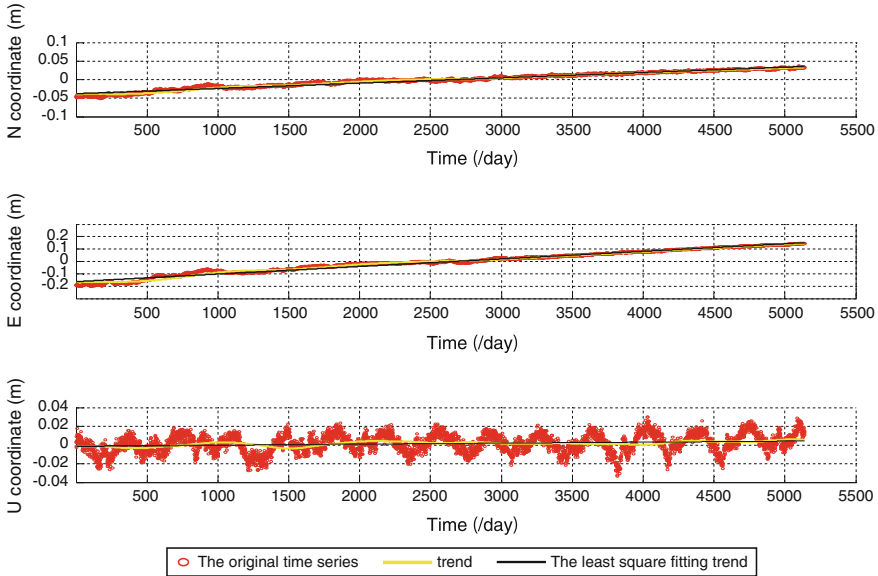


Fig. 21.3 Trend fitting result of ARTU station

So if we take the confidence of α equal 0.05. When the duty falls on $(-1.96, 1.96)$ outside, the null hypothesis is not established. That is to say the time series has the trend components. When $\tau > 1.96$ and < -1.96 respectively correspond to the rising and falling trend. The above test for one by one time principal component. $n = N - M + 1$. The final results are that the first RC component exists obvious trend. After extraction and by using the least square fitting, results are shown in Fig. 21.3

Using the linear rate of least squares fitting are as follows: N direction is 0.0143 mm every day. E direction is 0.0612 mm every day. U direction is 0.0011 mm every day. Error of three directions is as follows, N direction is 2.6 mm. E direction is 10.4 mm. U direction is 1.8 mm. The trend components of N and U direction is linear trend.

21.3.2 Extraction and Analysis of Periodic

Periodicity is an important feature of time series. There are many methods to analysis periodic sequence. The maximum entropy method (MEM) exhibits excellent characteristics to analysis the periodic sequence. It can get the continuous spectral distribution and high precision without any assumptions.

Firstly, this paper have continue a singular spectrum analysis after removal of time series trend. Using MEM to analyze the cycle. If two eigenvalue about Toeplitz matrix have similar relationship, two frequency of the corresponding feature vector must close at the same time. And the two frequency's energy value is large enough. Merging the RC components that they has meet the above characteristics. Founding from the previous description, it can be see that the trend components exist in horizontal direction. Elevation direction has cycle obviously. Figure 21.4 represents the singular spectrum charts of each RC component energy decomposition. If singular spectrum value is greater in the original sequence information, the proportion is the larger. This paper analysis the decomposition of the 9 order RC components of periodic after removing the trend about the ARTU station time series. The U direction of the 9 order RC components analysis results have drawing in this paper. As shown in Fig. 21.5. Each RC components after

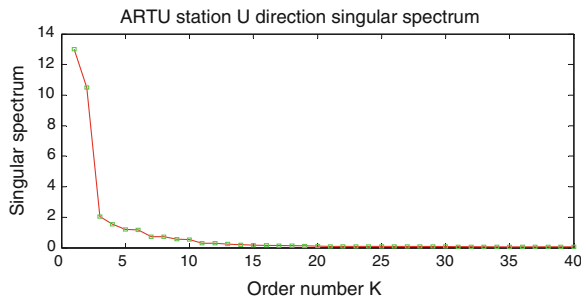


Fig. 21.4 Singular spectrum of U direction

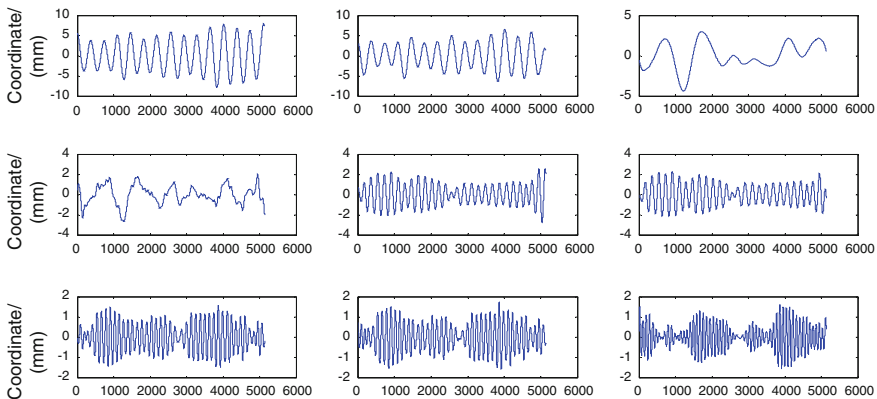


Fig. 21.5 The U direction SSA decomposition results after remove the trend

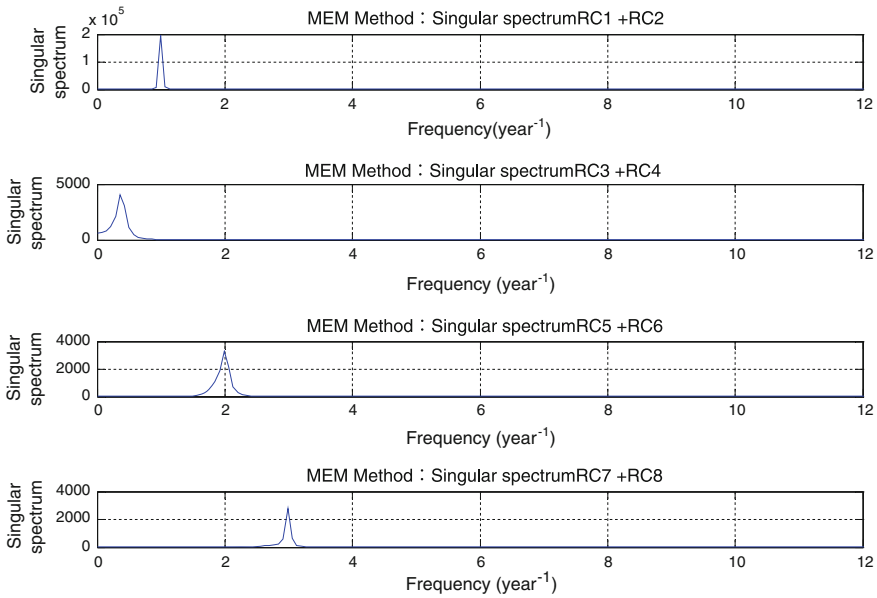


Fig. 21.6 Calculation of spectrum power with MEM method

Table 21.3 The frequency and the cycle of ARTU station

Direction	Frequency	Cycle/days
N	0.284 1.065 1.988	1285 343 184
E	0.284 1.065 1.988	1285 343 184
U	0.994 0.355 1.988 2.983	367 1028 183 122

merged are also given. The frequency and period are be calculated. As shown in Fig. 21.6, It has a multiple periodic components in this time series.

Table 21.3 gives frequency and period information about ARTU station in each direction. There are a multiple periodic in U direction, including the annual cycle, the half year cycle, seasonal cycle and years of periodic components. N and E direction have a same periodic components, including annual cycle, 6 months cycle and years of the periodic components.

The main components of ARTU station can extract correctly. Drawing on the results shown in Fig. 21.7. It calculates the accuracy of residual sequence after removing the trend and oscillation. The results are presented in Table 21.4. It can see that the precision is higher. There are less 5 mm about the average error and the error in three directions.

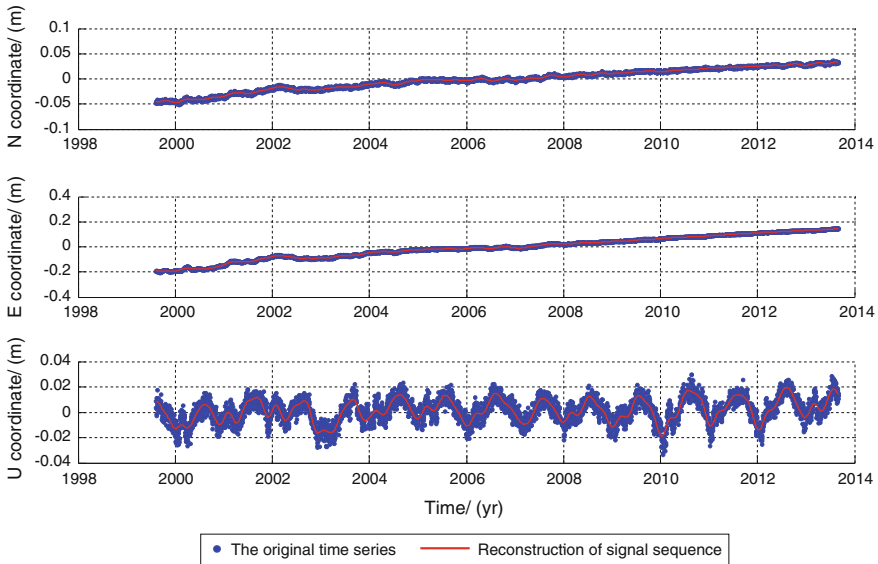


Fig. 21.7 Reconstruction result of ARTU station

Table 21.4 The precision of ARTU residual series

Direction	Average error (mm)	Error (mm)
N	1.2	1.6
E	2.3	3.1
U	3.8	4.8

21.4 Conclusion

SSA-IQR can effectively eliminate the gross error. Singular spectrum interpolation can be better for interpolation of coordinate time series. The interpolation accuracy is higher. The horizontal direction is less than 5 mm, and the height direction is less than 10 mm.

Using Kendall non-parametric to test of trend component. It can be able to identify and extract the trend correctly. The experimental results are as follows: the linear trend plays an important rules on the measured trend component of ARTU station. Using the method of least squares to fit the trend. N direction velocity is 0.0143 mm daily, E direction velocity is 0.0612 mm daily, and U direction is 0.0011 mm.

The cycle of three directions can be extracted correctly. Sometimes RC components have an same cycle, so it must to combine with them. Using the MEM method to analysis periodic. The results show the existence of multiple periodic in the U direction, including the annual cycle, half yearly, seasonal cycle and years of periodic components. N and E owing to the same periodic components, the existence of year cycle, period of 6 months and years of the periodic components

References

1. Dang Y, Bei J, Cheng Y (2007) The principle and application of the global navigation satellite system. Surveying and Mapping Press, Beijing, pp 52–95
2. Zhang X, Li Z (2013) Satellite navigation and positioning of new technology and high precision data processing method. Wuhan university Press, Wuchang, pp 114–137
3. Bei J, Zhang P, Jiang Z et al. (2004) Discussion on the coordinate and velocity precision changed with time transformation rules of GPS base stations. *J Wuhan Univ (Information Science Edition)* 26(9):764–767
4. Gu G, Zhang J (2002) Displacement time series of the crustal movement observation network of chinese reference station of GPS observations. *Geod Geodyn* 76:353–358
5. Wu H (1997) Singular spectrum and multi-channel singular spectrum analysis. *Meteorol Educ Sci Technol* 4:1–7
6. Zhang P, Jiang Z et al (2007) Data processing and the characteristics of time series analysis for GPS tracking station in china. *J Wuhan Univ (Information Science Edition)* 32(3):252–254
7. Huang L, Fu Y (2007) Noise analysis of GPS continuous observation stations. *J Earthq* 29(2):197–202
8. Huang S, Liu J (2002) An effective method to eliminate the noise in GPS deformation monitoring system. *J Surv Mapp* 1:1–25
9. Vautard R (1999) Singular-spectrum analysis:a toolkit for short, noisy chaotic signals. *physica D* 58:95–126
10. Schoellhamer (2001) Singular spectrum analysis for time series with missing data. *Geophys Res Lett* 28(16), 3187–3190
11. Broomhead DS, King GP (1986) Extracting qualitative dynamics from experimental data. *Physica D* 20:217–236
12. Wang H, Zhang R et al (2008) The improved algorithm is applied to the singular spectrum iterative interpolation to recovery the absence of datas. *Appl Math Mech* 29(10):1351–1361

Chapter 22

Initial Performance Assessment of BDS Real-Time Relative Positioning with Triple-Frequency Observations

Min Wang, Hongzhou Cai, Jun Liu and Anmin Zeng

Abstract Corresponding theoretical research has concluded that applying triple-frequency observation could performance of strength of equation system and improve the reliability of positioning result. Currently, BDS transmits navigation signal on three frequencies which enable the performance assessment of BDS using real triple-frequency observation. The characteristic of BDS triple-frequency observation is analyzed in respect of signal strength, multipath level and inter-frequency delay. Moreover, performance of BDS single-epoch relative positioning over different baseline length is assessed with real observation. The experiment results demonstrate that the fixed rate of triple-frequency ambiguity resolution is higher than dual-frequency case. It has also been concluded that application of triple-frequency observations has advantages over dual-frequency solution on reliability of fixed solution and decreased number of incorrectly fixed epoch.

Keywords BDS · Relative positioning · Real-time

22.1 Introduction

Before and after the official launch of regional navigation service, several approaches about the precise positioning algorithms and applications of BDS have been considered in the literatures. He et al. [4] assessed the performance of real-time kinematic (RTK) positioning and concluded that BDS can solely support dual-frequency

M. Wang (✉) · H. Cai
Zhengzhou Institute of Surveying and Mapping, Zhengzhou, China
e-mail: difzibo@163.com

J. Liu
Beijing Space Information Relay and Transmission Technology Research Center,
Beijing, China

A. Zeng
National Key Laboratory of Geographic Information Engineering, Xi'an, China

RTK application over short baseline at centimeter level accuracy. When combining GPS and BDS observation, the success rate of single-epoch ambiguity resolution and positioning accuracy is improved. Especially in case of high cut-off elevation, high success rate of single-epoch ambiguity resolution can be still maintained, which means even under challenging environment, high accuracy relative positioning can be acquired by combining the GPS and BDS observations. Similar conclusions are reported by Deng et al. [2], Shi et al. [9] and Teunissen et al. [12] based on RTK results using real observations collected in China and abroad.

It is an important feature of BDS that the entire constellation broadcast navigation signal in three frequencies, which makes the assessment and study of triple-frequency positioning technique more feasible. Experiment results with real triple-frequency observations of BDS show the success rate of TCAR (Triple-frequency Carrier Ambiguity Resolution) method is higher than dual-frequency case [10]. Li et al. [6] come up a partial ambiguity resolution algorithm for triple-frequency that could effectively decreased the computation time of ambiguity resolution procedure. Ji et al. [5] investigates the influence of different cut-off elevation and troposphere correction strategy on the time required to fix ambiguity for triple observation. Although the test results vary with data set, the averaged initialization time is about 45 min.

The single-epoch ambiguity resolution test is suitable to assess the influence of triple-frequency observation on positioning results. Because the results of single-epoch ambiguity resolution is irrelevant with dynamic state of user station and only depend on the satellite geometry and the accuracy of observation. Therefore, in this paper, we use single-epoch ambiguity resolution test to identify the influence of addition of third frequency on relative positioning result. And the triple-frequency observations are collected with receivers form different manufacturer. The observation characteristic is analyzed in respect of signal strength, multipath level and inter-frequency delay. Moreover, the performance of single-epoch ambiguity resolution and positioning accuracy for dual-frequency and triple-frequency are separately investigated.

22.2 Mathematics Model of Single-Epoch Relative Positioning

For single-epoch relative positioning, pseudorange and phase observations from two stations are involved in data processing. And the two stations are referred as reference station and user station respectively. The coordinates of reference station is fixed to true values and eliminated from observation equation system, and the coordinates of user station are estimated as unknowns. The mathematics model and estimation procedure are introduced as below first.

22.2.1 Observation Model

After linearization process, the double difference phase and pseudorange and observation can be presented as follows:

$$P_{ij}^{kq} = (l_j^q - l_j^k)dx + (m_j^q - m_j^k)dy + (n_j^q - n_j^k)dz \quad (22.1)$$

$$L_{ij}^{kq} = (l_j^q - l_j^k)dx + (m_j^q - m_j^k)dy + (n_j^q - n_j^k)dz + \lambda N_{ij}^{kq} \quad (22.2)$$

where, P and L are the observation minus computation (OMC) terms for pseudorange and phase observation respectively, the superscript k and q denote the satellite, subscript i and j denote the reference station and user station respectively, dx , dy and dz are correction values for user station coordinates, l , m and n are direction cosines of unit vectors pointing from the receiver to the satellites, N is phase ambiguity and λ is corresponding phase wavelength. As for relative positioning over short baseline, troposphere delay and other errors that related to signal broadcast path can be minimized or eliminated.

At one single epoch, observations of several satellites can be modeled as follows in matrix form:

$$\begin{bmatrix} \boldsymbol{\varphi} \\ \mathbf{P} \end{bmatrix} = \begin{bmatrix} \boldsymbol{\Lambda} & \mathbf{A} \\ & \mathbf{A} \end{bmatrix} \begin{bmatrix} \mathbf{a} \\ \mathbf{b} \end{bmatrix} \quad (22.3)$$

where, $\boldsymbol{\varphi}$ and \mathbf{P} are observation vectors for pseudorange and phase respectively, \mathbf{a} and \mathbf{b} are ambiguity vector and user station coordinates vector respectively, \mathbf{A} is coefficient matrix for user station coordinates, $\boldsymbol{\Lambda}$ is coefficient matrix for phase ambiguity state, $\boldsymbol{\Lambda} = \text{diag}[\lambda_1, \dots, \lambda_n] \otimes \mathbf{I}_n$, λ_* is the corresponding wavelength for phase observation, n is the number of phase observation.

22.2.2 Stochastic Model

The covariance matrix of phase and pseudorange observation reads as:

$$D \begin{bmatrix} \boldsymbol{\varphi} \\ \mathbf{P} \end{bmatrix} = \begin{bmatrix} \boldsymbol{Q}_{\varphi\varphi} & \\ & \boldsymbol{Q}_{PP} \end{bmatrix} \quad (22.4)$$

where, \boldsymbol{Q}_{PP} and $\boldsymbol{Q}_{\varphi\varphi}$ are the covariance matrix for pseudorange and phase observation vector respectively and $\boldsymbol{Q}_{PP} = k \cdot \boldsymbol{Q}_{\varphi\varphi}$, k is set as 10^4 in this paper.

Integrating the observation model and stochastic model for single-epoch relative positioning, the float solution of \mathbf{a} and \mathbf{b} and corresponding covariance matrix reads:

$$\begin{bmatrix} \hat{\mathbf{a}} \\ \hat{\mathbf{b}} \end{bmatrix} = \begin{bmatrix} \mathbf{Q}_{\hat{\mathbf{a}}} & \mathbf{Q}_{\hat{\mathbf{a}}\hat{\mathbf{b}}} \\ \mathbf{Q}_{\hat{\mathbf{b}}\hat{\mathbf{a}}} & \mathbf{Q}_{\hat{\mathbf{b}}} \end{bmatrix} \quad (22.5)$$

where, $\hat{\mathbf{a}}$ is the float solution of phase ambiguity (including the original double-difference phase ambiguity on all the frequencies), $\hat{\mathbf{b}}$ is the user coordinates vector.

If the ambiguities are fixed successfully, the fixed solution of user coordinates $\check{\mathbf{b}}$ and its covariance matrix $\check{\mathbf{Q}}_{\check{\mathbf{b}}}$ can be further acquired as follows [11]:

$$\check{\mathbf{b}} = \hat{\mathbf{b}} - \mathbf{Q}_{\hat{\mathbf{b}}\hat{\mathbf{a}}} \mathbf{Q}_{\hat{\mathbf{a}}}^{-1} (\hat{\mathbf{a}} - \check{\mathbf{a}}) \quad (22.6)$$

$$\check{\mathbf{Q}}_{\check{\mathbf{b}}} = \mathbf{Q}_{\hat{\mathbf{b}}} - \mathbf{Q}_{\hat{\mathbf{b}}\hat{\mathbf{a}}} \mathbf{Q}_{\hat{\mathbf{a}}}^{-1} \mathbf{Q}_{\hat{\mathbf{b}}\hat{\mathbf{a}}}^T \quad (22.7)$$

22.2.3 Ambiguity Search and Validation

A modified version of LAMBDA algorithm is applied for ambiguity resolution in this paper Chang et al. [1], which is based on following minimum problem:

$$\check{\mathbf{z}} = \min_{\mathbf{z} \in \mathbb{Z}} (\hat{\mathbf{z}} - \mathbf{z})^T \mathbf{Q}_{\hat{\mathbf{z}}}^{-1} (\hat{\mathbf{z}} - \mathbf{z}) \quad (22.8)$$

where, $\hat{\mathbf{z}} = \mathbf{Z}\hat{\mathbf{a}}$, $\mathbf{Q}_{\hat{\mathbf{z}}} = \mathbf{Z}\mathbf{Q}_{\hat{\mathbf{a}}}\mathbf{Z}^T$, \mathbf{Z} denotes the so-called decorrelation transform matrix, \mathbb{Z} indicates the set of integers. And then the widely applied ratio test is used for ambiguity resolution validation [3]:

$$\text{ratio} = \frac{(\check{\mathbf{a}}_{\text{sec}} - \hat{\mathbf{a}})^T \mathbf{Q}_{\hat{\mathbf{a}}}^{-1} (\check{\mathbf{a}}_{\text{sec}} - \hat{\mathbf{a}})}{(\check{\mathbf{a}}_{\text{min}} - \hat{\mathbf{a}})^T \mathbf{Q}_{\hat{\mathbf{a}}}^{-1} (\check{\mathbf{a}}_{\text{min}} - \hat{\mathbf{a}})} \geq k \quad (22.9)$$

where, $\check{\mathbf{a}}_{\text{min}}$ and $\check{\mathbf{a}}_{\text{sec}}$ are the optimum and second-optimum solution that meets Eq. (22.7), k is a threshold selected according experience and test environment. If Eq. (9) stands, then the optimum solution $\check{\mathbf{a}}_{\text{min}}$ and its corresponding variance matrix $\check{\mathbf{b}}(\check{\mathbf{a}}_{\text{min}})$ are accepted as fixed solution for the unknown states, otherwise, the ambiguity resolution process is given up and the float solution is accepted as final solution for current epoch.

22.3 Triple-Frequency Observation Characteristics of BDS

Two data set are processed and analyzed, including a 4 km short baseline and a 56.6 km long baseline, the details of data set are given in Table 22.1.

22.3.1 Signal Strength

As shown in Fig. 22.1, for station BD, the carrier-to-noise-density ratios (C/N0) of GPS L1 frequency is highest, the lowest is GPS L2 observation and the C/N0 gap between two frequencies is about 20 dB-Hz. The trend of C/N0 variation of BDS signal is more smooth than those of GPS observations. The signal strength of BDS falls between GPS L1 and L2 signal and the C/N0 of three BDS frequencies are close to each other, the C/N0 of BDS signal starts at 40 dB-Hz for low elevation and 50 dB-Hz for high elevation. The B3 signal is the strongest among three BDS frequencies. Besides, the analysis of data from other three stations indicates the same signal strength variation pattern.

Table 22.1 Details of test data

	Data set 1	Data set 2
Baseline length	4 km	56.6 km
Manufacturer	Beijing Beidou Tianhui Ltd	UNI Avionics Science Ltd
Station location	Tianjin, China	Beijing, China
Sample rate	10 s	10 s
Epoch number	1502	1300
User station	F003	HH
Reference station	F001	BD
Date	2013/11/11	2013/11/14

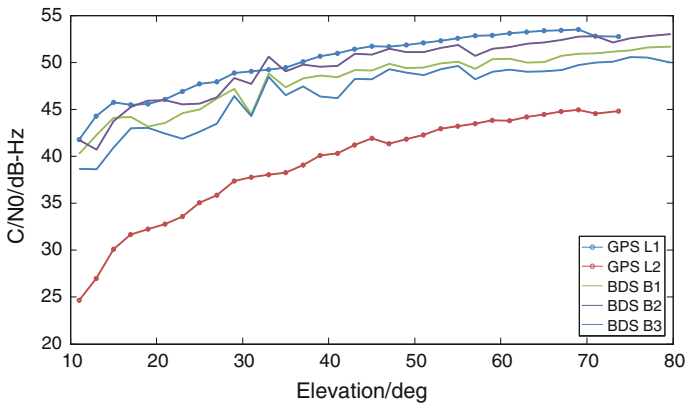


Fig. 22.1 Carrier-to-noise-density ratio (C/N0) for BDS observations at station BD

22.3.2 Multipath Combination

The multipath combination is an indication of multipath level of pseudorange and observation noise. The multipath combination is composed with dual-frequency phase and pseudorange and the multipath delay can be abstracted from pseudorange by eliminating the ionosphere delay and geometry related items with phase observation, which is computed as follows [8]:

$$MP(i, j, k) = P_i + \frac{(\lambda_i^2 + \lambda_k^2)}{(\lambda_k^2 - \lambda_j^2)} L_j + \frac{(\lambda_i^2 + \lambda_j^2)}{(\lambda_k^2 - \lambda_j^2)} L_k \tag{22.10}$$

$MP(i, j, k)$ is the multipath combination of pseudorange on frequency i and phase observation on frequency j and k , P_i and L_i are the pseudorange and phase observation on frequency i , λ_i is the wavelength of frequency i . The ionosphere delay, satellite-receiver distance, satellite and receiver clock offset and troposphere delay are eliminated during the combination process. Because the noise level and multipath Daley of phase is far less than those of pseudorange, the multipath combination mainly includes phase ambiguity, hardware delay, multipath delay and noise of pseudorange. After smoothing the whole arc data, the hardware and phase ambiguity can be further eliminated, only multipath delay and pseudorange noise remained.

The relationship of $MP(1, 1, 2)$ observation and satellite elevation for station F001 is illustrated in Figs. 22.2, 22.3 and 22.4. Because the relative geometry of GEO C01 and receiver is stable, the range of elevation variation is narrow. Low frequency periodical pattern can be found in GEO multipath series, and the RMS of C01 multipath combination of whole arc is 0.830 m. Whereas, multipath combination series of IGSO C07 and MEO C14 are dominated by high frequency variation and the amplitude narrows as the satellite elevation increase, the RMS of multipath

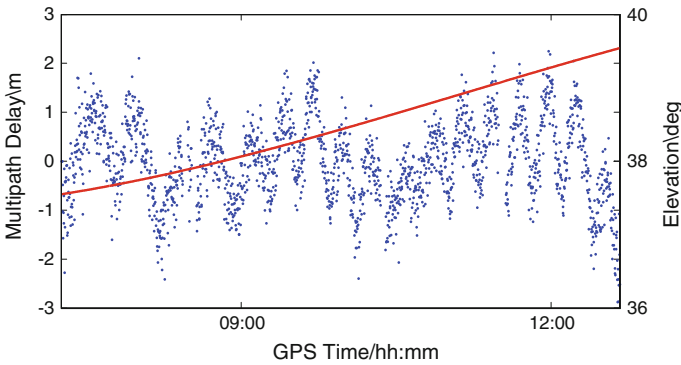


Fig. 22.2 Multipath combination for pseudorange from station F001 on B1 of GEO satellite C01 and its variation with satellite elevation over station F001

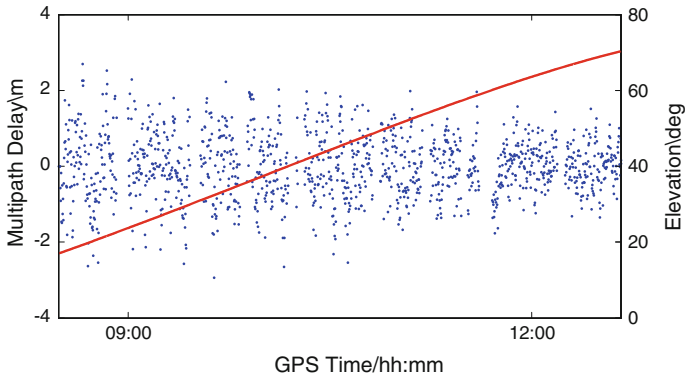


Fig. 22.3 Multipath combination for pseudorange on B1 of IGSO satellite C07 and its variation with satellite elevation over station F001

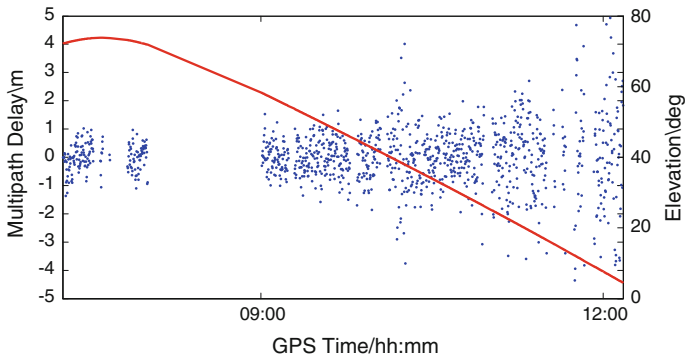


Fig. 22.4 Multipath combination for pseudorange on B1 of MEO satellite C14 and its variation with satellite elevation over station F001

series for C07 and C14 are 0.836 m and 1.086 m respectively. In general, the magnitudes of multipath for three types of BDS satellite are comparable to each other. Contributing to more rapid movement of MEO satellite and more data collected at low elevation, RMS of multipath series for C14 is higher than C01 and C07.

Analyzing the RMS of multipath combination and its variation with satellite elevation (shown in Fig. 22.5), the RMS of GPS L1 is much higher than those of observations on other four frequencies. Among three frequencies of BDS, the multipath level of B1 is the highest and RMS of B2 multipath combination is about 0.2 m lower. It is worthy noticing that the RMS of B3 is significantly lower than other signals, when the satellite elevation rise above 30 , the RMS of B3 multipath combination is less than 0.2 m.

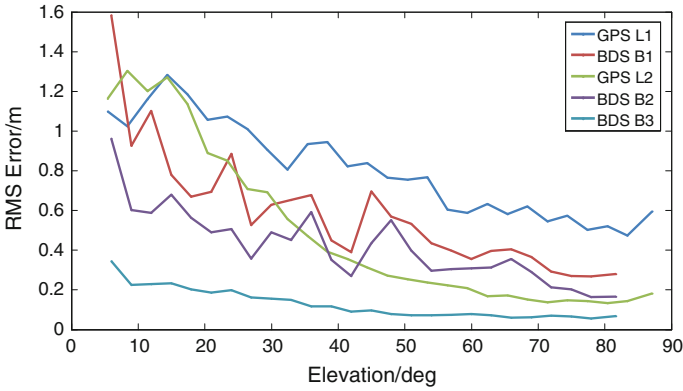


Fig. 22.5 RMS of multipath combination on different frequencies and its variation with elevation for station F001

22.3.3 Inter-Frequency Bias Analysis

An advantage of triple-frequency observation application is the phase geometry-free and ionosphere-free combination (DIF hereinafter) is available for phase bias and multipath analysis. By forming two independent ionosphere-free combination and subtracting the results from each other, the DIF can be presented as follows [7]:

$$DIF = IF(1, 2) - IF(1, 3) = \left(\frac{f_1^2}{f_1^2 - f_2^2} - \frac{f_1^2}{f_1^2 - f_3^2} \right) L_1 \left(\frac{f_2^2}{f_1^2 - f_2^2} \right) L_2 + \left(\frac{f_3^2}{f_1^2 - f_3^2} \right) L_3 \tag{22.11}$$

where, $IF(m, n)$ denotes the ionosphere-free combination formed by phase observation on frequency m and n . The DIF mainly includes the weighted sum of phase noise, multipath and phase ambiguity. Moreover, the DIF reflects the level of thermally-dependent inter-frequency biases and its variation.

Comparing Figs. 22.6 and 22.7, it is noticed that the amplitude of DIF varies with different stations, possible reason maybe different manufacturer of receiver and observation surroundings. The RMS of DIF for C01, C07 and C14 at station BD are 4.5, 4.3 and 3.7 mm respectively and 2.7, 2.1 and 2.2 mm respectively at station F001. There is no obvious systematic difference of DIF found between different types of BDS satellite, which demonstrates the close phase noise level of different BDS satellite type. Furthermore, the series of DIF are dominated by high frequency component and their close to zero mean values indicate a good consistence of triple-frequency phase observation of BDS.

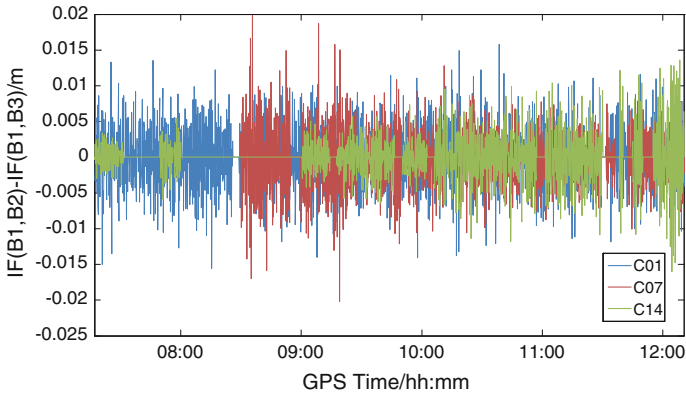


Fig. 22.6 DIF observable series for station F001

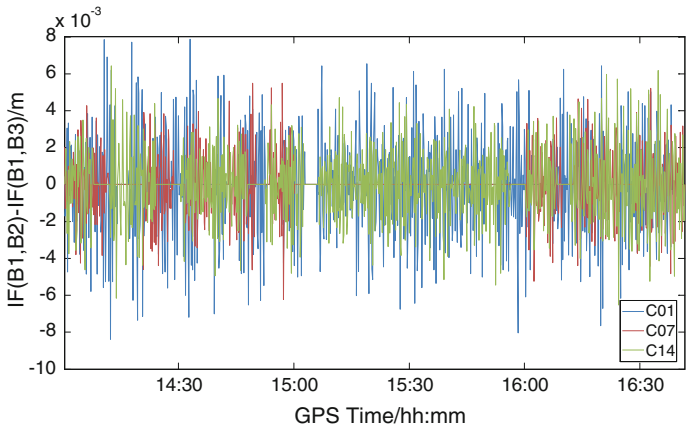


Fig. 22.7 DIF observable series for station BD

22.4 Positioning Results and Analysis

The test data set for single-epoch relative positioning experiment includes a short baseline and a long baseline. The test results are analysis in terms of ambiguity resolution reliability and positioning accuracy and the difference of test results between dual-frequency and triple-frequency is investigated. The true value of station coordinate are estimated with GAMIT v10.4 software based on GPS observation.

22.4.1 Short Baseline Experiment

As shown in Fig. 22.8, the ratio value of ambiguity validation test for triple-frequency is larger than dual-frequency, which indicates that the fixed ambiguity of triple-frequency is more reliable. In, the success rate of ambiguity resolution for is 94.9 and 99.6 % for dual-frequency and triple-frequency case respectively. There is one incorrectly resolution epoch in dual-frequency test. Whereas, all resolved ambiguities for triple-frequency case are correct.

From the comparison of Figs. 22.9 and 22.10, we can see the a incorrectly fixed epoch at 9:44, which makes the solution deviates from zero, whereas, the solution of that epoch is corrected when triple-frequency observations are used. Although influenced by the incorrectly fixed epoch, the difference RMS of dual-frequency test

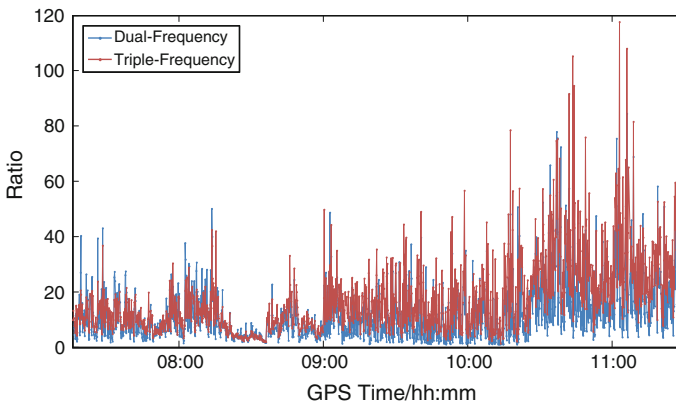


Fig. 22.8 Ratio value series for relative positioning over short baseline

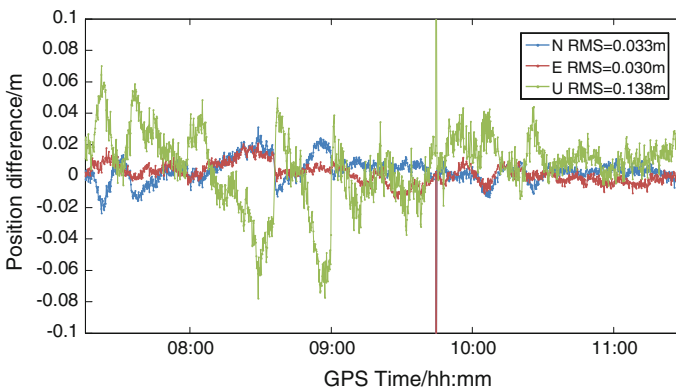


Fig. 22.9 Position difference for dual-frequency BDS single-epoch fixed solution over short baseline

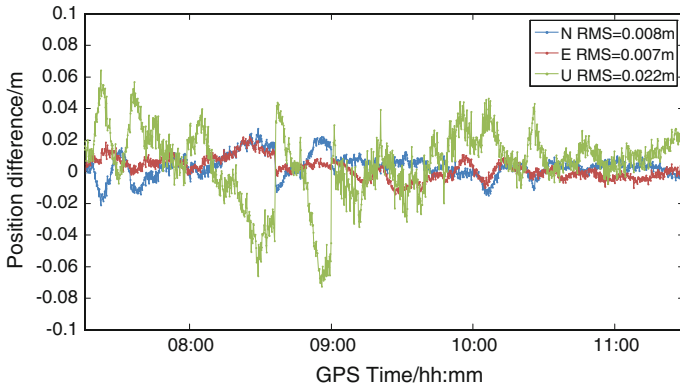


Fig. 22.10 Position difference for triple-frequency BDS single-epoch fixed solution over short baseline

are larger than those for triple-case, there are only slim differences on other epochs between the solution of triple-frequency and dual-frequency observation for other epochs. These results indicate the addition of observation frequency may enhance the reliability of ambiguity resolution, but the positioning accuracy may not be improved.

22.4.2 Long Baseline Experiment

As illustrated in Fig. 22.11, for long baseline test, the ratio values of triple-frequency ambiguity resolution are also higher than dual-frequency. Although the success rate of ambiguity resolution of long baseline decreases, which is contributing to the

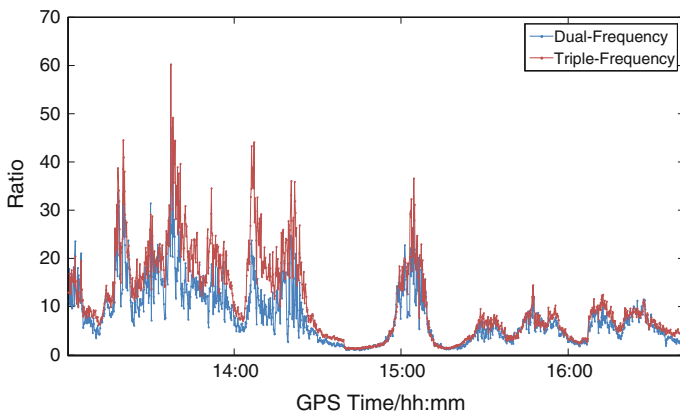


Fig. 22.11 Ratio value series for relative positioning over long baseline

weaker correlation of atmospheric error of reference station and user station as the length of baseline increase, relatively acceptable success rate of ambiguity resolution is obtained. The success rate of triple-frequency ambiguity resolution is 91.2 and 89.2 % for dual-frequency, and the failure number for triple-frequency ambiguity resolution is 12 and 17 for dual-frequency.

Similar with short baseline test, the Figs. 22.12 and 22.13 show the number of successful ambiguity resolution epoch for triple-frequency is more than dual-frequency, but the overall positioning accuracy is not improved greatly. The error RMS of dual-frequency solution in NEU directions are 0.026, 0.019 and 0.032 m respectively and 0.026, 0.020 and 0.033 m for triple-frequency, the accuracy of two solutions is close to each other.

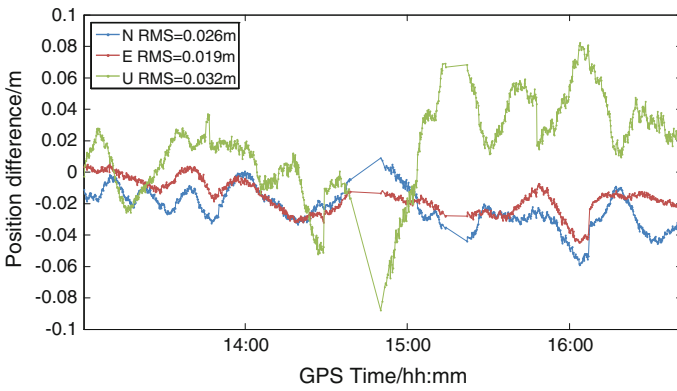


Fig. 22.12 Position difference for dual-frequency BDS single-epoch fixed solution over long baseline

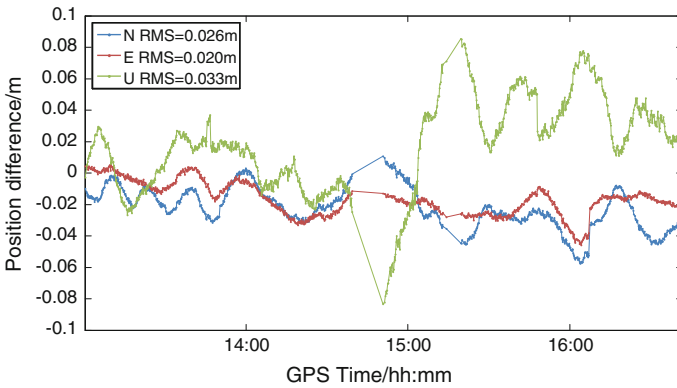


Fig. 22.13 Position difference for triple-frequency BDS single-epoch fixed solution over long baseline

22.5 Conclusions

In this paper, the characteristic of BDS triple-frequency observation are analyzed first in respect to signal strength, multipath level and inter-frequency bias, followed by single-epoch relative positioning test. According to the test results, following conclusions can be drawn:

- (1) The test signal strength of BDS falls between GPS L1 and L2 frequency observation, and the B3 frequency has strongest signal strength over B1 and B2 BDS signal. The BDS pseudorange multipath varies with types of satellite, the multipath variation of GEO satellite is mainly composed with low frequency component whereas the high-frequency fluctuation dominates multipath variation of IGSO and MEO satellite.
- (2) The noise level of phase output by receivers from different manufacturers and surroundings. The zero mean value of DIF indicate a good observation quality and no obvious thermally-dependent inter-frequency bias is noticed.
- (3) The single-epoch relative positioning with only BDS triple-frequency observations is achieved at centimeter level accuracy. By adopting the triple-frequency observation of BDS, the reliability of ambiguity resolution is enhanced, but the improvement of positioning accuracy should not be expected.

Future work will include further collecting observations and investigate the performance of single-epoch relative positioning using BDS/GPS combined observation under different observation environments.

Acknowledgments This work is supported by China National Natural Science Foundation of China (No: 41274045, 41374041,41374042).

References

1. Chang X-W, Yang X, Zhou T (2005) MLAMBDA: a modified LAMBDA method for integer least-squares estimation. *J Geodesy* 79(9):552–565
2. Deng C, Tang W, Liu J, Shi C (2014) Reliable single-epoch ambiguity resolution for short baselines using combined GPS/BeiDou system. *GPS Solutions* 18(3):375–386
3. Euler HJ, Schaffrin B (1991) On a measure for the discernibility between different ambiguity solutions in the static-kinematic GPS-mode. In: Schwarz K-P, Lachapelle G (eds) *Kinematic systems in geodesy, surveying, and remote sensing*, vol 107. International Association of Geodesy Symposia-Springer, New York, pp 285–295
4. He H, Li J, Yang Y, Xu J, Guo H, Wang A (2014) Performance assessment of single- and dual-frequency BeiDou/GPS single-epoch kinematic positioning. *GPS Solutions* 18(3): 393–403
5. Ji S, Wang X, Xu Y, Wang Z, Chen W, Liu H (2014) First preliminary fast static ambiguity resolution results of medium-baseline with triple-frequency beidou wavebands. *J Navig* 67 (06):1109–1119

6. Li J, Yang Y, Xu J, He H, Guo H (2015) GNSS multi-carrier fast partial ambiguity resolution strategy tested with real BDS/GPS dual- and triple-frequency observations. *GPS Solutions* 19(1):5–13
7. Montenbruck O, Hauschild A, Hessels U (2011) Characterization of GPS/GIOVE sensor stations in the CONGO network. *GPS Solutions* 15(3):193–205
8. Schönemann E, Becker M, Springer T (2011) A new approach for GNSS analysis in a multi-GNSS and multi-signal environment. *J Geodetic Sci* 1(3):204–214
9. Shi C, Zhao Q, Hu Z, Liu J (2013) Precise relative positioning using real tracking data from COMPASS GEO and IGSO satellites. *GPS Solutions* 17(1):103–119
10. Tang W, Deng C, Shi C, Liu J (2014) Triple-frequency carrier ambiguity resolution for Beidou navigation satellite system. *GPS Solutions* 18(3):335–344
11. Teunissen PJG (1995) The least-squares ambiguity decorrelation adjustment: a method for fast GPS ambiguity estimation. *J Geodesy* 70(1–2):65–82
12. Teunissen PJG, Odolinski R, Odijk D (2014) Instantaneous BeiDou + GPS RTK positioning with high cut-off elevation angles. *J Geodesy* 88(4):335–350

Chapter 23

Unified Estimation Model of Multi-system Biases Including BDS/GPS/GLONASS/Galileo

Changhui Xu, Hu Wang, Yamin Dang, Hao Chen
and Longping Zhang

Abstract Beidou Navigation Satellite System (BDS) will increase the numbers of available observations to improve the solution accuracy, reliability and availability of precise positioning. Multi-system fusion with BDS is nowadays increasingly paid attention. However, the multi-system fusion focuses only on loose combination model, which means that each system has their reference satellite each other. This model will increase the probability of initialization because the reference satellite can be often changed during the process of positioning. If multi-system fusion has unified time and signal reference, that is, multi-system fusion selects the same satellite as the reference satellite, the problem will be covered. Therefore, the paper proposed an estimation model of multi-system biases for multi-system fusion. The estimation model will investigate differential code bias (DCB) of each system and inter-system biases (ISB) among systems. Multi-system data from IGS, MGEX and iGMAS were collected to analyze the effects of different types of the receivers on various biases, and then a unified multi-system biases estimation model was proposed. The results show that there are some biases of ISBs in GNSS systems and the biases are affected by stations. The variation of GLONASS satellites has a unified tendency and the ISBs of BDS has a fluctuation property, which need to be improved.

Keywords Beidou satellite navigation satellite system · Differential code bias · Inter-frequency bias · Inter-system bias · Bias estimation model

C. Xu · H. Wang (✉) · Y. Dang · L. Zhang
Chinese Academy of Surveying and Mapping, 28 Lianhuachi West Road,
Beijing, China
e-mail: wanghu@casm.ac.cn

C. Xu
e-mail: chxu@casm.ac.cn

H. Chen
College of Resources and Environment, University of Chinese Academy of Sciences,
Beijing, China

23.1 Introduction

Beidou Satellite Navigation System (BDS), with an ability of navigation and positioning in Asia Pacific, has been one of four global navigation satellite systems. The integration of these four systems including BDS, GPS, GLONASS and Galileo, can increase the numbers of available satellites to improve the positioning accuracy, stability and availability and be able to service in a harsh environments, such as urban area. Meanwhile, the integration of multi-systems can speed up the convergence time in Precise Point Positioning (PPP) and increase the distance limitation between the reference station and the rover stations in Real-time Kinematic positioning (RTK) [1, 2].

Each GNSS system has a time system and a coordinate system. The time system and the coordinate system of GPS are GPS Time (GPST) and WGS84, respectively; The time system and the coordinate system of BDS are BDT and China Geodetic Coordinate System 2000 (CGCS2000); The time system and the coordinate system of GLONASS are GLONASS time and PZ90; The time system of Galileo are Galileo system time and the coordinate system of Galileo can be same as the WGS84 because the difference is little [3]. A loose integration method of four systems can be usually used, whose solution model selects a time reference of each system and a satellite reference of each system to deliver receiver hardware delay among systems [4, 5]. Otherwise, there are three types of observation in different receivers including C1/P1/P2, C1/X2 and C1/P2. For example, Rogue and Trimble 4000 receiver can receive the C1/X2 observations, and Leica/Novatel receiver can receive C1/P2 observations [6]. When these observations are used in PPP, Differential Code Bias should be corrected because different code has a bias compared to other codes. The solution precision will be affected if these biases are not considered. A determination method of DCB is given by Song [7].

Tight integration of multi-systems with a same unified time reference and satellite reference should consider not only the effects of DCB between systems, but also the effects of Inter-System Bias (ISB) between different systems and Inter-Frequency Bias (IFB) of GLONASS system. ISB between GPS and Galileo is first estimated with GIOVE combined observation network by Montenbruck [8]. Odijk extracts the characteristics of ISB with GPS/GIOBE model and analyze the its effects on ambiguity resolution [9]. On the base of Odijk's model, Paziewski improves the model to analyze the biases and their effects on PPP [10]. Chen investigates the ISB between GPS and GLONASS and analyzes the effect factors, such as station [11]. With the development of DCB, ISB and IFB, PPP has developing. Multi-system integration will provide more observations to obtain the more stable and reliable solution without the increment of estimation parameters.

A unified estimation model of four systems is proposed. Section one gives the estimation model of multi-system integration. Section two analyzes the difference and factors of different system and the products can be used for PPP and other applications. Section three obtains some conclusions according to the results.

23.2 Unified Estimation Model of Multi-system Bias

Un-difference carrier phase and pseudorange equations of GPS are given by

$$\varphi^G = \rho^G + \delta t_r^G - \delta t_s^G + \delta h_r^G - \delta h_s^G + \lambda^G(\varphi_r^G - \varphi_s^G + N^G) + \delta m^G + \varepsilon^G \quad (23.1)$$

$$P^G = \rho^G + dt_r^G - dt_s^G + dh_r^G - dh_s^G + dm^G + e^G \quad (23.2)$$

where, the superscript G denotes GPS system, φ^G is measurement of GPS un-difference carrier phase, ρ^G is geometric distance between satellite and receiver, δt_r^G and δt_s^G are receiver clock and satellite clock, respectively, δh_r^G and δh_s^G are carrier phase hardware delay of receiver and satellite, respectively, λ^G is wave length of GPS, φ_r^G and φ_s^G are initial phase of receiver and satellite, N^G is ambiguity of GPS carrier phase, δm^G is the sum of other errors including tropospheric delay, ionospheric delay, phase wind, antenna phase center offset and variation of receiver and satellite, relativistic effect, solid earth tide, and so on. ε^G is noise of carrier phase, P^G is pseudorange of GPS un-difference carrier phase.

Un-difference carrier phase and pseudorange measurement equations of BDS are similar as that of GPS, but the integration of GPS and BDS should be under a unified time reference when two systems are combined because GPS uses GPST and BDS uses BDT. There are two methods for unifying time reference. One is to select BDST as an estimation parameter; another is to select the difference between GPST and BDT as an estimation parameter. The integration results of GPS and GLONASS show that the difference as an estimation parameter is better than GLONASS time as an estimation parameter because the difference will eliminate the accumulation of GLONASS time [12]. Un-difference carrier phase and pseudorange measurement of BDS is written as

$$\varphi^C = \rho^C + \delta t_r^C - \delta t_s^C + \delta h_r^C - \delta h_s^C + \lambda^C(\varphi_r^C - \varphi_s^C + N^C) + \delta m^C + \varepsilon^C \quad (23.3)$$

$$P^C = \rho^C + dt_r^C - dt_s^C + dh_r^C - dh_s^C + dm^C + e^C \quad (23.4)$$

where, superscript C denotes BDS, other variable symbols are similar as the measurement equations of GPS, dt^{GC} is the difference between GPST and BDT.

The single difference between GPS satellites selected a GPS satellite as reference satellite can be found in references. The single difference between GPS and BDS can be written as

$$\begin{aligned} \varphi^{GC} = & \rho^{GC} - \delta t_s^{GC} - \delta h_s^{GC} + \lambda^C(\varphi_r^C - \varphi_s^C + N^C) \\ & - \lambda^G(\varphi_r^G - \varphi_s^G + N^G) + \delta m^{GC} + t^{GC} + \varepsilon^{GC} \end{aligned} \quad (23.5)$$

$$P^{GC} = \rho^{GC} - dt_s^{GC} - dh_s^{GC} + dm^{GC} + t^{GC} + e^{GC} \quad (23.6)$$

where, $\delta h_s^{GC} = \delta h_s^C - \delta h_s^G$ is defined as carrier phase ISB of single difference between GPS and BDS, $dh_s^{GC} = dh_s^C - dh_s^G$ is defined as pseudorange ISB of single difference between GPS and BDS. Similarly, symbol E denotes Galileo satellite and be instead of symbol C in un-difference carrier phase and pseudorange measurement of BDS, the single difference equation between Galileo and GPS is obtained by:

$$\begin{aligned} \varphi^{GE} = & \rho^{GE} - \delta t_s^{GE} - \delta h_s^{GE} + \lambda^E (\varphi_r^E - \varphi_s^E + N^E) \\ & - \lambda^G (\varphi_r^G - \varphi_s^G + N^G) + \delta m^{GE} + t^{GE} + \varepsilon^{GE} \end{aligned} \quad (23.7)$$

$$P^{GE} = \rho^{GE} - dt_s^{GE} - dh_s^{GE} + dm^{GE} + t^{GE} + e^{GE} \quad (23.8)$$

GPS, BDS and Galileo satellites use Code Division Multiple Access (CDMA) technique and each system has a same frequency, while GLONASS satellites use Frequency Division Multiple Access (FDMA) technique and each satellite has a unique frequency according to the satellite channel. Satellite frequency can be calculated by $L_1 = 1602 + k * 0.5625$ MHz and $L_2 = 1246 + k * 0.4375$ MHz, where, k denotes the GLONASS satellite channel, which can be found in the website (<http://glonass-iac.ru/en/GLONASS/>). Symbol R is assumed as GLONASS satellite and be instead of symbol C , the single difference equation between GLONASS and GPS is expressed by:

$$\begin{aligned} \varphi^{GR} = & \rho^{GR} - \delta t_s^{GR} - \delta h_s^{GR} + \lambda^R (\varphi_r^R - \varphi_s^R + N^R) \\ & - \lambda^G (\varphi_r^G - \varphi_s^G + N^G) + \delta m^{GR} + t^{GR} + \varepsilon^{GR} \end{aligned} \quad (23.9)$$

$$P^{GE} = \rho^{GE} - dt_s^{GE} - dh_s^{GE} + dm^{GE} + t^{GE} + e^{GE} \quad (23.10)$$

The above equations are combined for ISB estimation of four systems. Least squares or Kalman filtering is employed to estimate parameters through weighting different value because measurements of each system have a different precision.

23.3 Experiments and Results

23.3.1 Data Processing Strategy

The experiment data includes more than one hundred international IGS stations, seventy MGEX stations, tens of iGMAS stations and tens of Wuhan university network stations. These data all come from iGMAS analysis center (CGS)—Chinese Academy of Surveying and Mapping. The data time is from 322nd to 351st, 2014. The station distribution of 322nd as an example is given in Fig. 23.1. The stations including four systems of MGEX and iGMAS will be used according to the global uniform distribution principle. DCB products are estimated through CGS analysis center strategy.

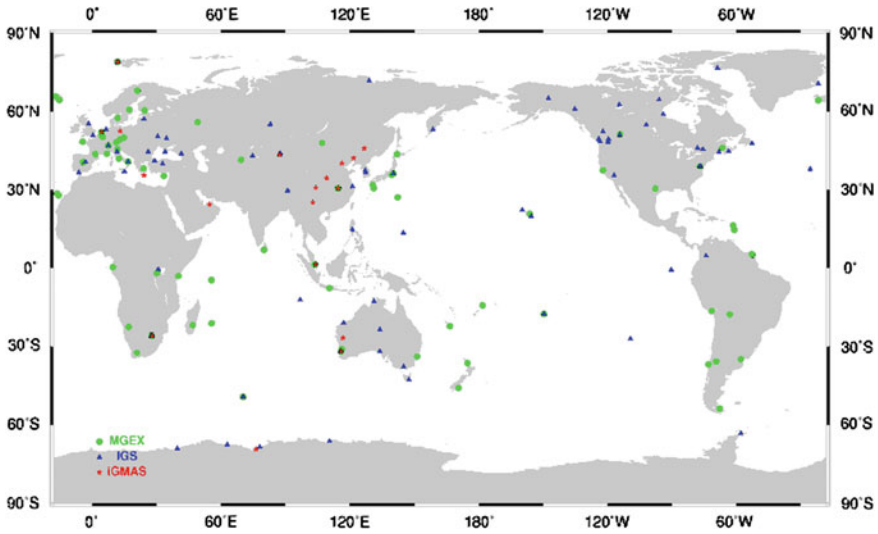


Fig. 23.1 Distribution of solved tracking stations

23.3.2 Differential Code Bias (DCB)

Chinese Academy of Surveying and Mapping analysis center (CGS) provides most IGS products of GPS/GLONASS and related products of BDS. Multi-system DCBs are a part of multi-system biases. CGS has provided DCB of GPS satellite P1C1, P1P2 and P2C2 and DCB of GLONASS satellite P1P2 and P2C2. DCBs from IGS CODE analysis center are selected as the reference, our products compared to these products and the results are shown in Fig. 23.2. The difference between GPS P1C1 and GPS/GLONASS P2C2 are under 0.3 ns. This precision can be satisfied for variable applications.

23.3.3 Inter-system Bias (ISB)

There are ISBs between GPS/BDS, GPS/Galileo and GPS/GLONASS if GPS is selected as a reference system. ISBs usually are in the range of $-30 \sim 30$ m except several more than 100 m. The trend is given in Fig. 23.3. ISBs of one station consist of a constant bias and disturbing term. The disturbing terms are different because the quality of observations is not same as each other. Otherwise, there is also a systematic bias between stations. For example, some stations fluctuate around -6 m and some around 8 m.

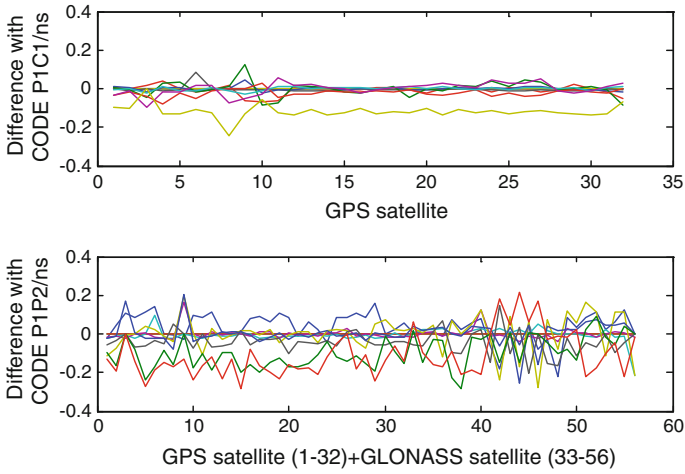


Fig. 23.2 Precision of DCB products of CGS

Fig. 23.3 GPS/BDS ISBs

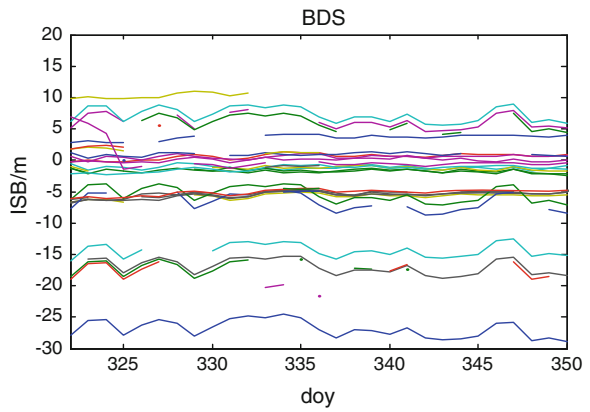
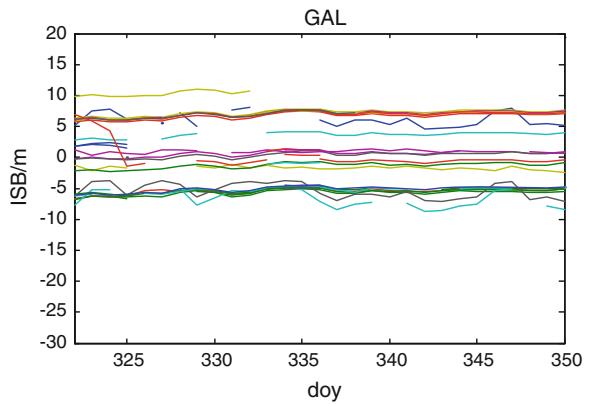


Fig. 23.4 GPS/Galileo ISBs



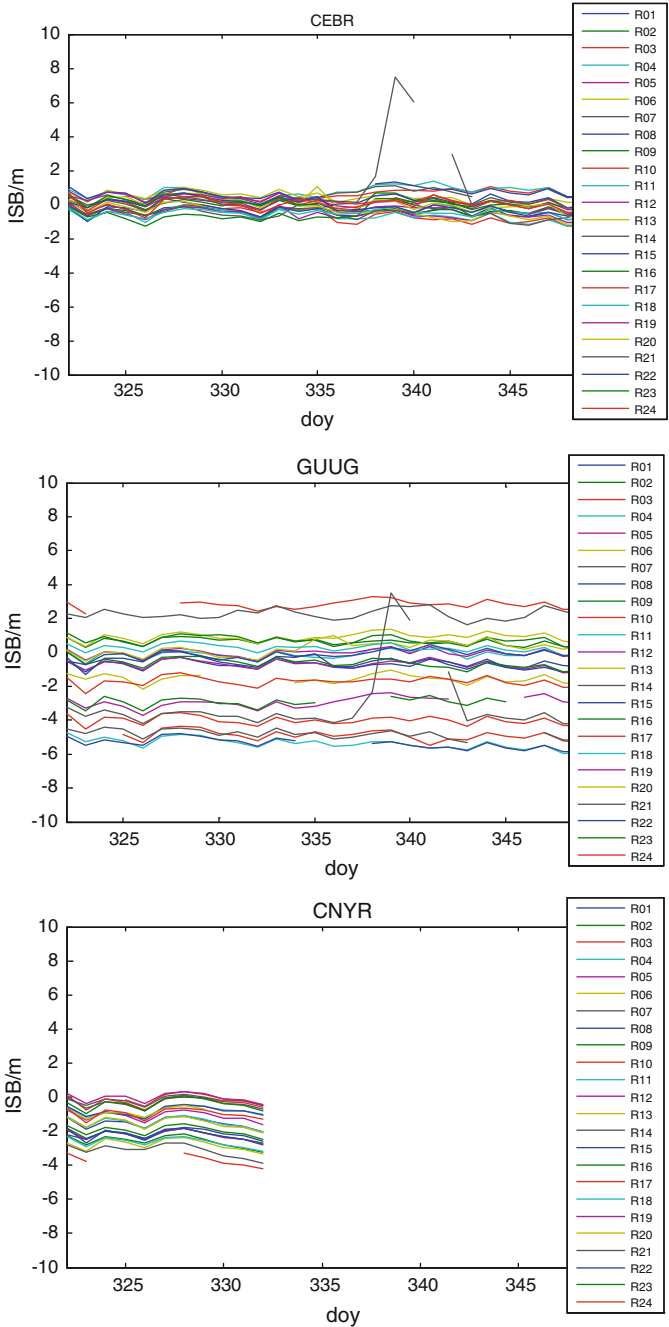


Fig. 23.5 GPS/GLONASS ISBs

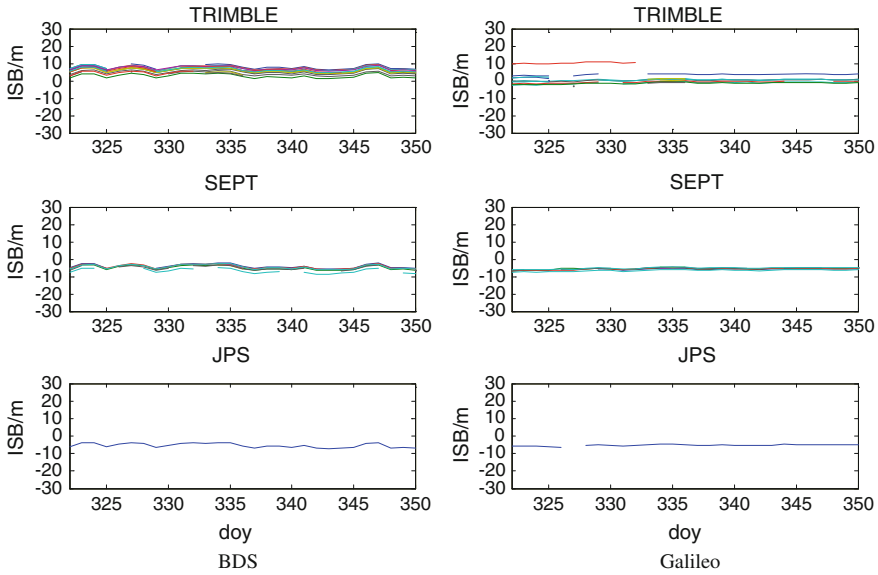


Fig. 23.6 BDS and Galileo ISBs of different receivers

ISBs of GPS/Galileo are given in Fig. 23.4. The ISBs has the same trend with that of GPS/BDS. ISBs of one station has a constant bias and there is a systematic bias between stations.

The signal frequencies of GLONASS satellites are different. Three stations from MGEX, IGS and iGMAS are selected randomly to give the results in the paper, such as CEBR (MGEX), GUUG (IGS) and CNYR (iGMAS). ISB of a GLONASS satellite is stable and the trend of all GLONASS satellites is consistent (Fig. 23.5). ISBs of CEBR station are tight and little, but that of GUUG station are divergent. The reason is that the measurement quality of GUUG station is less than that of CEBR station. However, there is a jump and interruption of a satellite at the same time in both CEBR station and GUUG station because the GLONASS satellite has a fault during the time. Twelve days data of CNYR station is processed because iGMAS is being established and there is no other data. The results show that ISBs of GLONASS satellites are consistent.

GNSS receivers of IGS, MGEX and iGMAS are divided into different types according to manufacturer, such as TRIMBLE, LEICA, JAVAD, ASHTECH, SEPT, TPS and JPS. In these receivers, TRIMBLE, SEPT and JPS can receive BDS signals and Galileo signals. ISBs of BDS and Galileo from three types of receivers are shown in Fig. 23.6. The receivers receiving BDS signals are mainly from TRIMBLE manufacturer. BDS ISBs of all stations fluctuate around a constant. Galileo ISBs is more stable than BDS ISBs. Galileo ISBs of TRIMBLE have almost no constant bias, but SEPT receivers have some constant biases.

23.4 Conclusions

- (1) Satellite DCBs and station DCBs from CGS analysis center meet the requirement and can be used in PPP;
- (2) ISBs of same BDS satellites or Galileo satellites can be divided into a constant bias and a fluctuation around the constant bias if GPS satellite is selected as a reference. The ISBs can be corrected by a model. ISBs of different GLONASS satellites have the same trend and a constant bias.
- (3) Galileo ISBs is more stable than BDS ISBs. Galileo ISBs of TRIMBLE receivers are well modelled, but BDS ISBs is to be improved because BDS is developing;
- (4) ISBs of all systems are not only related with stations, but with receivers and manufacturer.

Acknowledgments This research work was supported by the International GNSS Monitoring and Assessment System (GFZX0301040308-06), the National Natural Science Foundation of China (Grant No.41404034), the research foundation of the china academy of surveying and mapping (7771405) and Jiangsu Key Laboratory of Resources and Environmental Information Engineering China University of Mining and Technology.

References

1. Tiberius C, Pany T, Eissfeller B, Joosten P, Verhagen S (2002) 0.99999999 Confidence ambiguity resolution with GPS and Galileo. *GPS Solutions* 6:96–99
2. Shi C, Zhao Q, Hu Z, Liu J (2013) Precise relative positioning using real tracking data from COMPASS GEO and IGSO satellites. *GPS Solutions* 17(1):103–119
3. Gendt G, Altamimi Z, Dach R, Sohne W, Springer T, Team TGP GGSP (2011) Realization and maintenance of the Galileo terrestrial reference frame. *Adv Space Res* 47(2):174–185
4. Deng C, Tang W, Liu J, Shi C (2013) Reliable single-epoch ambiguity resolution for short baselines using combined GPS/BeiDou system. *GPS Solutions*. doi:[10.1007/s10291-013-0337-5](https://doi.org/10.1007/s10291-013-0337-5)
5. He H, Li J, Yang Y, Xu J, Guo H, Wang A (2014) Performance assessment of single- and dual-frequency BeiDou/GPS single-epoch kinematic positioning. *GPS Solutions*. doi:[10.1007/s10291-013-0339-3](https://doi.org/10.1007/s10291-013-0339-3)
6. Schaer S (2012) Overview of relevant GNSS biases. *Kolloquium Satellite Navigation*, TU Munchen
7. Song XY, Yang ZQ, Jiao WH, Mao Y, Feng LP (2009) Determination of GPS receiver's DCB. *J Geodesy Geodyn* 29(1):127–131
8. Montenbruck O, Hauschild A, Hessels U (2011) Characterization of GPS/GIOVE sensor stations in the CONGO network. *GPS Solutions* 15:193–205
9. Odijk D, Teunissen PJG (2013) Characterization of between receiver GPS-Galileo inter-system biases and their effect on mixed ambiguity resolution. *GPS Solutions* 17(4):521–533
10. Chen JP, Xiao P, Zhang YZ, Wu B (2013) GPS/GLONASS system bias estimation and application in GPS/GLONASS combined positioning. In: *China Satellite Navigation Conference 2013 Proceedings*, pp 323–333

11. Paziewski J, Wielgosz P (2014) Accounting for Galileo-GPS inter-system biases in precise satellite positioning. *J Geodesy*. doi:[10.1007/s00190-014-0763-3](https://doi.org/10.1007/s00190-014-0763-3)
12. Xu CH (2011) Modeling quality control and warning system of high-accuracy GNSS point positioning. China University of Mining and Technology Press, XuZhou

Chapter 24

The Study on Ocean Ice Intensity Surveyed by GNSS-R Signal on the Coast

Fuyang Ke, Fangyuan Chen and Yunchang Cao

Abstract Intensity and thickness of sea ice are the basic parameters of ocean ice disaster monitoring. Compared with other detection methods, GNSS-R with high spatial and temporal resolution, lower cost, abundant sources, etc. has huge potential. Based on electromagnetic theory, the principle of GNSS-R inversion technology of sea ice intensity and thickness will be systematically studied on. Then the experiment of surveying ice thickness and intensity by GNSS-R was performed at Bohai Gulf in Tianjin of China from 17 to 18 in January 2014 in order to study the relation between the polarization ratio (between direct and reflected signal) and ice intensity. The result of the experiment has shown that the relation between polarization ratio and ice intensity is existent.

Keywords GNSS-R · Polarization ratio · Sea ice intensity · Sea ice thickness

24.1 Introduction

At present, it has been a hot spot to obtain the physical information of the cryosphere by the Global Navigation Satellite Positioning System Reflected signal (GNSS-R), which has been an important signal source of remote sensing application in recent years [1]. Therefore in order to verify the feasibility of detection of sea ice information by GNSS-R, the theory and method of detection of sea ice

F. Ke (✉)

GNSS Center, Wuhan University, Wuhan, People's Republic of China
e-mail: kfy_0829@163.com

F. Ke · F. Chen

School of Geography and Remote Sensing, Nanjing University of Information and Science Technology, Nanjing, People's Republic of China

Y. Cao

CMA Meteorological Observation Centre, China Meteorological Administration, Beijing, People's Republic of China

© Springer-Verlag Berlin Heidelberg 2015

J. Sun et al. (eds.), *China Satellite Navigation Conference (CSNC) 2015*

Proceedings: Volume I, Lecture Notes in Electrical Engineering 340,

DOI 10.1007/978-3-662-46638-4_24

information by GNSS-R will be studied on, and the GNSS-R sea ice experiment carried out at the Bohai Bay of China in 2014 year will be introduced as following.

24.2 The Detection Principle of Sea Ice Information by GNSS-R

24.2.1 The Characteristics of Reflected Signal

The principle of GNSS-R remote sensing is to detect the state of the target by GNSS reflected signal from the target, which can be called as L band microwave remote sensing. The amplitude and phase characteristics of GNSS signal from the GNSS satellites through the atmosphere to the earth surface will change, because GNSS signal is effected by the soil moisture, sea water salinity and another environmental factors. Ground based, airborne and space borne (Low orbit satellite) GNSS receiver can respectively receive the direct signal through the atmosphere and the signal reflected by the earth surface, which mainly come from mirror reflection and the first Fresnel Zone Scattering of it. The average dielectric properties of sea ice in the mirror reflection point can be regarded as a smooth surface and meet the Final reflection. The reflected and refraction signal in the particular conditions of the satellite elevation angle, can be used to estimate the atmospheric and surface features of the earth. Under the Finel hypothesis, the reflected signal can be simply expressed as the product of polarization matrix and the incident signal:

$$\begin{bmatrix} E_R^i \\ E_L^s \end{bmatrix} = \begin{bmatrix} U_{RR} & U_{LR} \\ U_{RL} & U_{LL} \end{bmatrix} \quad (24.1)$$

where E is GNSS signal, R and L are respectively the polarization direction of antenna (right and left), i and s are respectively the direct and reflected signal, U is the Fresnel reflection coefficient of smooth surface waves, the polarization matrix composed by them is

$$\begin{bmatrix} U_{RR} & U_{LR} \\ U_{RL} & U_{LL} \end{bmatrix} = \frac{1}{2} \begin{bmatrix} T_V + T_h & T_V - T_h \\ T_V - T_h & T_V + T_h \end{bmatrix} \quad (24.2)$$

where the Finel Coefficients are respectively

$$T_h = \frac{\sin \gamma - \sqrt{\varepsilon_r - \cos^2 \gamma}}{\sin \gamma + \sqrt{\varepsilon_r - \cos^2 \gamma}} \quad (24.3)$$

$$T_V = \frac{\varepsilon_r \sin \gamma - \sqrt{\varepsilon_r - \cos^2 \gamma}}{\varepsilon_r \sin \gamma + \sqrt{\varepsilon_r - \cos^2 \gamma}} \quad (24.4)$$

where γ is glancing angle, ϵ_r is the complex dielectric constant of sea ice, it can be computed by

$$\epsilon_r = \frac{\epsilon}{\epsilon_0} - j60\lambda\sigma \tag{24.5}$$

where ϵ is the dielectric constant of sea ice, σ is the conductivity, ϵ_0 is the dielectric constant in vacuum, λ is the wavelength, i is the imaginary unit of the plural.

The transcendental equations of complex dielectric constant are respectively:

$$\frac{th\mu L_g}{\mu L_g} = \frac{\lambda_g}{j2\pi L_g} \cdot \frac{1 - js \tan\left(\frac{2\pi}{\lambda_g}\right)d'}{s - j \tan\left(\frac{2\pi}{\lambda_g}\right)d'} \tag{24.6}$$

$$\epsilon_r = \lambda_0^2 \left[\frac{1}{4a^2} - \left(\frac{uL_g}{2\pi L_g} \right)^2 \right] \tag{24.7}$$

where $\mu = \beta + j\alpha$ is the transmission coefficient of Full filled dielectric waveguide, L_g is thickness of medium, λ_g is waveguide wavelength, s is the ratio of the standing wave, d' is the distance from the first point of the minimum voltage to the dielectric surface, λ_0 is the wavelength in free space, a is the size of the broadside of waveguide, $\epsilon_r = \epsilon' - j\epsilon'' = E'(1 - j \tan \delta)$, ϵ' is the real part of the complex dielectric constant, $\tan \delta$ is loss tangent.

It can be calculated by formulas (24.6) and (24.7) as following:

$$\epsilon' = \left(\frac{\lambda_0}{2\pi} \right)^2 \left[\left(\frac{\pi}{a} \right)^2 - \beta^2 + \alpha^2 \right] \tag{24.8}$$

$$\tan \delta = \frac{2\alpha\beta}{(\pi/a)^2 - \beta^2 + \alpha^2} \tag{24.9}$$

The complex dielectric constant of sea ice and other medium can be obtained by Newton Iteration by formulas (24.8) and (24.9).

24.2.2 The Correlation Function of Reflected Signal

In a GNSS receiver, the correlation function of the local PRN duplication code at t_0 moment and the receiver antenna output signal $u + n$ at $t_0 + \tau$ is [2]:

$$Y(t_0, \tau, f_c) = \int_0^{T_i} u(t_0 + t' + \tau)a(t_0 + t') \exp[2\pi if_c(t_0 + t')] dt' + n \tag{24.10}$$

where n is additive white Gauss noise, the mean $E[n] = 0$, B is the equivalent noise bandwidth:

$$D[n] = E\left[\left(n - E[n]\right)^2\right] = E[n^2] = KTB \tag{24.11}$$

where T_i is integral time, f_c is the Doppler frequency shift of the compensation received signal, formula (24.10) is the signal expanding process. The navigation and positioning can be carried out by obtaining the distance between transmitter and receiver by the delay time of direct signal. But the scattering signal is more complex, its correlation function can be deduced as following [3–5]:

$$Y(t_0, \tau, f_c) = \exp(2\pi i f_c t_0) T_i A \int D(t_0, r) A[\Delta(t_0, r)] S[\Delta f(t_0, r)] g(t_0 + \tau, r) d^2r + n \tag{24.12}$$

24.2.3 The Relevant Power of Reflected Signal

The relevant power model of reflected signal is [6, 7]:

$$\langle |Y(\tau, f_c)|^2 \rangle = A^2 T_i^2 \iint \frac{D^2(r) \times \Lambda^2[\Delta\tau(r)] \times |S[\Delta f(r)]|^2}{4\pi R_r^2(r) R_r^2(r)} \sigma_0(r) d^2r + n^2 \tag{24.13}$$

where τ is time delay, n^2 is noise power, $\sigma_0(r) = \pi |R(r)|^2 \frac{q_x^4}{q_z} \times p_{pdf}\left(\frac{q_x}{q_z}\right)$. In the formula, the contribution of scattering signal mainly comes from the cross regional of four regions, which are respectively the antenna coverage area, delay area, Doppler district and the irradiated area. They are respectively decided by $D^2(r)$, Λ^2 , $|S|^2$ and P_{pdf} .

The reflectivity of GNSS reflected signal can be calculated by direct power P_i and reflected power P_r as following:

$$r = P_r / P_i \tag{24.14}$$

24.3 GNSS-R Ice Experiment at the Gulf of Bohai

24.3.1 The Introduction of the Experiment

The GNSS-R Ice Experiment was carried out to verify the feasibility of detecting the ice concentration and thickness by GNSS-R at the Dashentang bay in the vicinity of Tianjin Binhai New District from January 17 to January 18 in 2014 [8–10]. In the experiment, the GNSS-R receiver is NewStar210MGPS produced by



Fig. 24.1 Equipment and GNSS receiving data

Beijing OLinkStar Company, which has 4 channels respectively connected with the right-hand circular polarization to receive direct signal and with the left-hand circular, horizontal line, vertical linear polarization antenna to receive the reflected signal. The right-hand circular polarization antenna was set up towards the zenith direction to receive the direct signal of GPS L band. The Left-hand circular polarization antenna was set up inclined towards the sea to receive the reflected signals from the sea. The antenna in the experiment was set up near the sea surface and at the open coast, shown as Fig. 24.1.

24.3.2 The Experiment Data Processing

In the experiment, the GNSS signal was processed and analyzed mainly from January 17 to January 18 in 2014 year. On January 17 in 2014 year, the sea was covered by plenty of sea ice, but the sea was without sea ice cover on January 18 in 2014 year. Because the antenna installation position is more favorable for receiving GNSS signal, the satellites can be used to obtain the GNSS data whose elevation was from 0° to 90° , azimuth was from 75° to 225° . The star diagram of GPS at 15:00 on January 17 in 2014 year was shown as Fig. 24.2. In the period, there were 10 visible GPS satellites, including PRN5, PRN14, PRN15, PRN18, PRN21, PRN22, PRN24, PRN26, PRN27 and PRN28. Based on the time length of visibility, elevation and azimuth, PRN12 was selected to study the sea ice information

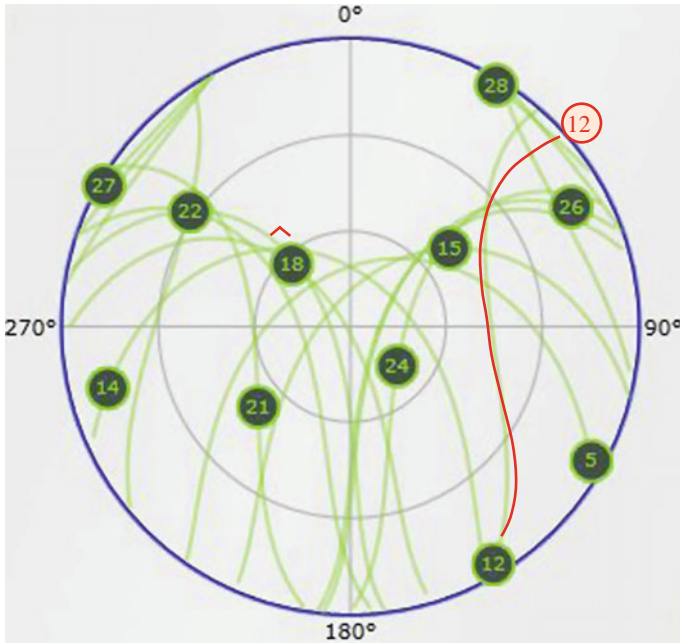


Fig. 24.2 The satellite maps and the traces of PRN12 at 15:00:00 on January 17 in 2014

by GNSS-R method, whose running track was shown as Fig. 24.2. Accordingly, PRN24 was selected on January 18 in 2014 year.

During carrying out the GNSS-R Sea Ice experiment, the cover of sea ice was visually observed at the same time. In the different elevation range, the Fresnel coefficient of left-hand circular reflection of sea water was more than the sea ice. On January 17 in 2014 year, there were a large number of sea ices on the sea surface, shown as the left in Fig. 24.3. But there were almost no sea ice on January 18 in 2014 year, shown as the right in Fig. 24.3. Therefore, the polarization ratio on January 17 in 2014 year was greater than that on January 18 in 2014 in theory.



Fig. 24.3 Sea conditions from January 17–18 in 2014

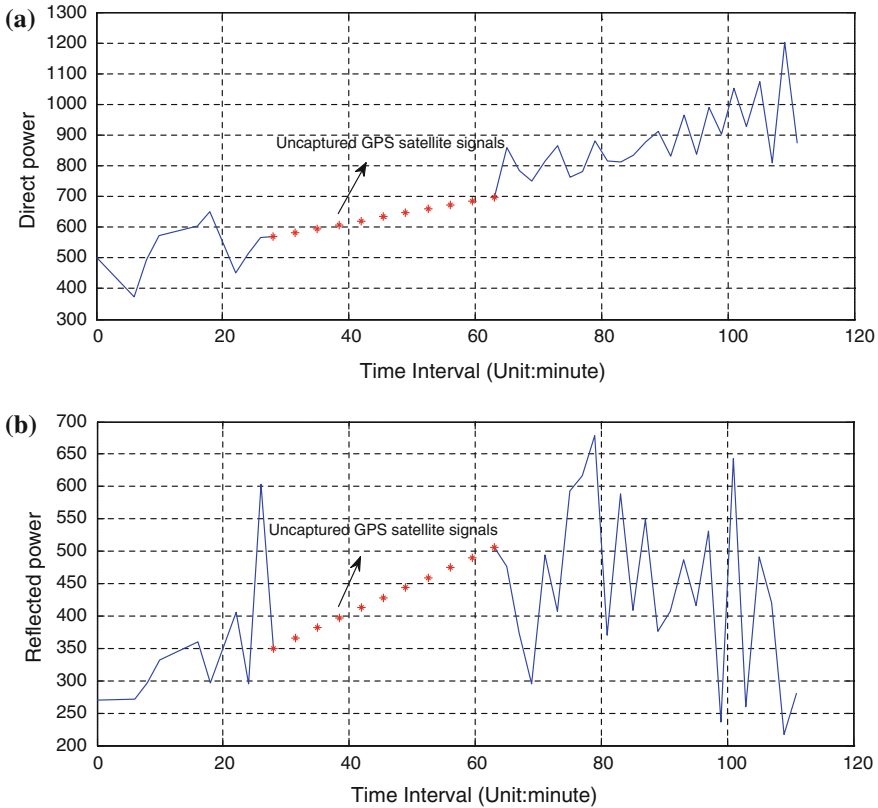


Fig. 24.4 The *left-handed* reflected and *right-handed* direct signal power variation of PRN12 on 17 January 2014. **a** The *right-handed* direct signal. **b** The *left-handed* reflected signal

GNSS-R Receiver started to receive GNSS signal at 2 min interval at 15:00:12 on January 17 in 2014 year, and stopped at 17:08:58. Then the data process software was used to process the GNSS direct signal to obtain the change of the power of the direct and reflected signal, shown as Fig. 24.4. Because of the environment constraints, the quality of some data was low and the jump of some point was greater. But the change trend was obvious.

The polarization ratio of the left-handed circular reflected and right-handed circular direct signal can be used to judge the state information of sea surface. Therefore, the average polarization ratio of PRN12 was 0.560 and the change trend was shown as Fig. 24.5 on January 17 in 2014.

On January 18 in 2014 year, there were almost no sea ices on the sea surface. According to the best conditions, the data of GPS satellite PRN24 was selected to process in order to acquire the power change of left-handed circular reflected signal and right-handed circular direct signal shown as Fig. 24.6 and the polarization ratio change shown as Fig. 24.7.

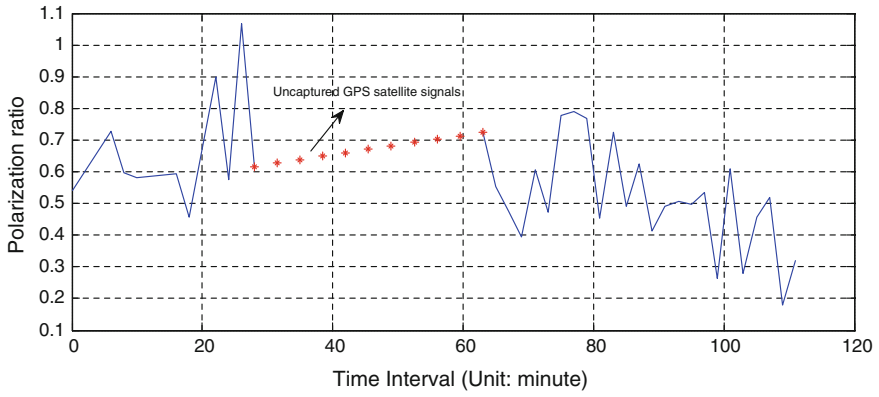


Fig. 24.5 The polarization ratio of PRN12 on 17 January in 2014

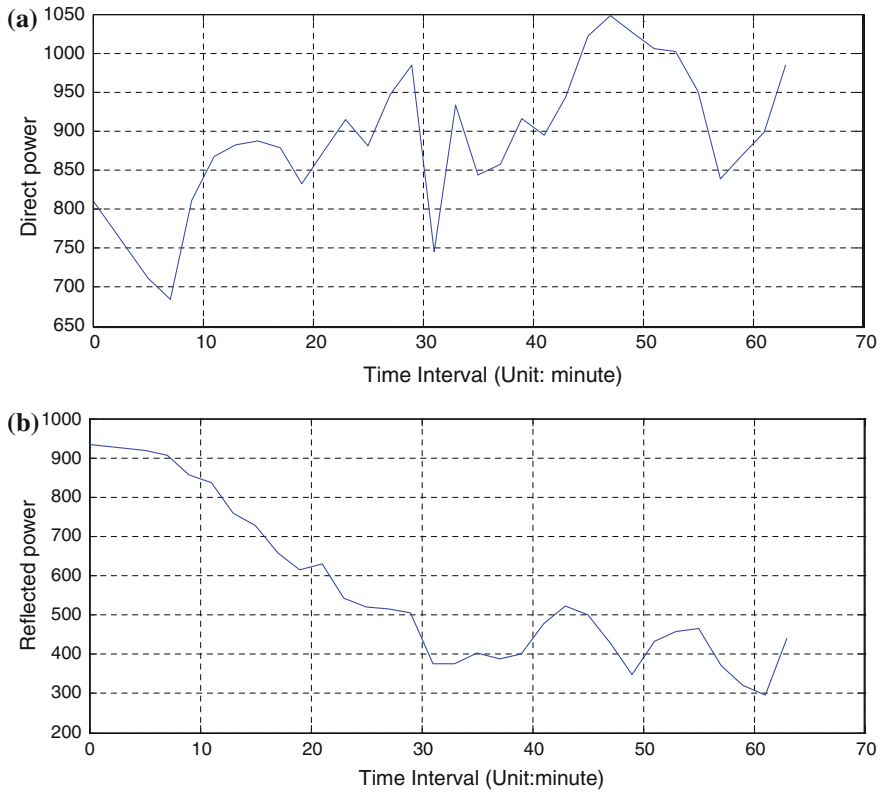


Fig. 24.6 The *left-handed* reflection and *right-handed* direct signal power variation of PRN24 on 18 January 2014. **a** The *right-handed* direct signal. **b** The *left-handed* reflected signal

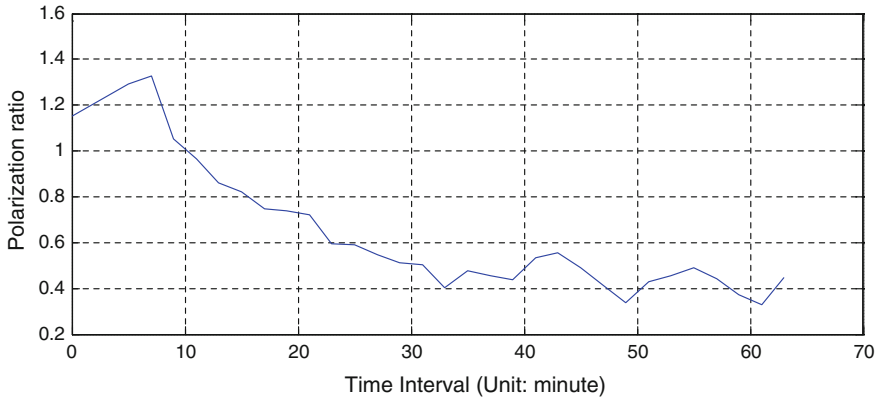


Fig. 24.7 The polarization ratio of PRN24 on 18 January in 2014

The polarization ratio of PRN24 was 0.629 on January 18 in 2014 year. The ratio of the average polarization ratio between January 17 and January 18 in 2014 year was 0.89 to 1. By visual observation, there were no sea ice on the sea surface in January 18, but the concentration of sea ice was about 90 percent on January 17 in 2014 year. Obviously, it has been proved that GNSS-R used to detect the concentration of sea ice is feasible. And the feasibility of detecting sea ice concentration by GNSS-R has been verified.

24.4 Conclusions

Based on the theory of electromagnetic field, the GNSS reflected signal correlation function and power model was studied, and the GNSS-R detecting sea ice information model was set up in theory. At last, the GNSS-R sea ice experiment was carried out at Dashentang of the Gulf of Bohai in China. In the sea ice monitoring activity and sea ice disaster prevention, not only the concentration of sea ice should be acquired, but also the coverage and thickness of sea ice must be determined. Therefore, how to determine coverage and thickness of sea ice by GNSS-R should be further studied on.

Acknowledgments This study is funded by The youth project of National Natural Science Fund in China(41304036) and China postdoctoral fund(2013M540605). Thanks for the help from CMA Meteorological Observation Centre, Tianjin Meteorological Bureau and Shanghai Ocean University.

References

1. Penggen C, Shouzhu Z, Xiaoyong C et al (2014) Application of GNSS-reflection technology to sea-ice retrieval. *Eng Surv Mapp* 23(4):1–5
2. Wei W, Xiuwan C, Guoping L et al (2012) The research progress of GNSS-R remote sensing. *Remote Sens Inf* 27(3):112–119
3. Dongkai Y, Qishan Z (2012) The basis and practice of GNSS-reflection processing. Publishing House of Electronics Industry, Beijing
4. Maurice WL (2001) Radar reflectivity of land and sea. Artech House, Boston
5. Zavorotny VU, Voronovich AG (2000) Scattering of GPS signals from the ocean with wind remote sensing application. *IEEE Trans Geosci Remote Sens* 38(1):951–964
6. Zhaoming Z, Yang F, Zhengang X (2006) Remote sensing of sea surface wind of hurricane michael by GPS reflected signals. *Geomatics Inf Sci Wuhan Univ* 31(11):991–994
7. Cong Y (2011) Application of significant wave height measurement using GNSS-R signals. Nanjing University of Information Science and Technology, Nanjing
8. Yun Z, Jianjing G, Zhonghua H et al (2014) Ground-based reflected GPS for sea ice exploration. *Chin J Polar Res* 26(2):262–267
9. Yun Z, Wanting M, Qiming G et al (2014) Bohai sea ice experiment using GPS reflected signals. *Acta Oceanol Sinica* 36(11):64–73
10. Yang M, Cao Y (2014) The following experiment of sea ice observation using GNSS-R signals. *GNSS Word of China* 39(4):51–54

Chapter 25

Research on Tracking Technology of High Sensitive BD Signals

Zheng Zhao and Li Li

Abstract With the increasingly demanding for navigation and positioning about BD second generation satellite system, many users' applications are in the city, jungle, interior and complex environments, such as the battlefield of human disturbance. Therefore the requirement for receiver becomes more and more high, in order to meet the demand of the application of complex environment, high sensitive receiver has become a hot topic in the current navigation of receiver in the field of technology. In this paper we propose the algorithm of weak signal, the main content include studying on fine acquisition, coherent integral for long time, EKF tracking and a synchronous and related techniques so on.

Keywords Code tracking · Carrier tracking · Coherent integral

25.1 Introduction

When received signal is influenced by the circumstance of serious occlusion and attenuation or interference, signal arriving to the receiver will become very weak, usually only -140 dBm to -160 dm. In this case Navigation receiver has lost the function of positioning.

Signal tracking is the key problem that determining whether the receiver can work normally in the circumstance of very weak signals, it includes carrier tracking and code tracking. By combination with the frequency of the input signal, carrier loop can adjust its local carrier frequency and phase timely, code tracking loop can constantly adjust its initial phase of the local code according to the input BD signal.

This paper first analyzed the basic structure of carrier tracking loop and the code tracking loop and their position in the receiver, combining the characteristic of BD

Z. Zhao (✉) · L. Li

Beidou Shaanxi Hengtong Technology Development Co., Ltd., 4th floor Building C,
No 168, XiDian's Science and Park, KeChuang Road, Xian, Shaanxi, China
e-mail: hr@sxnav.com

signal which modulated from BOC(15,2.5). We proposed the algorithm of carrier tracking and the algorithm of the code tracking, which complete the function of carrier tracking and code tracking in weak signal based on EKF technique.

25.2 Signal Tracking

25.2.1 The Position of Signal Tracking in the Receiver

The procedure baseband signal processing can be divided into acquisition, tracking, bit synchronization, frame synchronization of four stages [1]. Taking one BD signal channel as example, the relationship of block can be showed as follows (Fig. 25.1):

After the acquisition state, the receiver can get the rough Doppler of frequency and code phase, and then send the rough Doppler of frequency and code phase to tracking loop. Basing on the rough Doppler of frequency and code phase generated by acquisition, the tracking loop will constantly adjust its own frequency and phase generated from local carrier NCO, and the code phase and frequency of code NCO according to BD signal, making the modulated signal generated by local and real BD signal to max correlation. The signal output from tracking loop only contain the navigation message while carrier and spreading code is peeled off, The beginning position of each data bit would be find in these signal during the bit synchronization occurred in the next stage, and the beginning of frame can be found in the frame synchronization, then go into the block which is used to decode the navigation message.

25.2.2 The Structure of Tracking Loop

The carrier tracking [2] is to built the frequency tracking loop, thus making the difference between the frequency of local carrier and input signal keep a certain rage. The carrier tracking loop include frequency locked loop and phase locked loop. Take the phase locked loop for example it is made up of composed of five

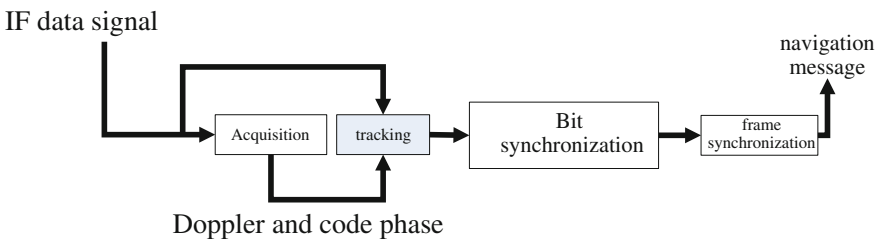


Fig. 25.1 The four stages of signal channel processing

parts: mixer Coherent integrator phase discriminator loop filter numerically controlled oscillator (NCO).

Code tracking loop is used to track the phase changing of spread spectrum code, make the local spread spectrum code and the spread spectrum code become alignment. Code tracking loop is made up of five parts: mixer Coherent integrator code phase discriminator the loop filter of code loop local code generator.

The carrier tracking loop and code tracking loop are usually used together, as shown below:

For the carrier tracking loop, the frequency of input signal is (Fig. 25.2)

$$f_{in} = f_{if} + f_d \tag{25.1}$$

Among them, f_{if} is the representative of mid frequency which does not consider the Doppler. f_d represents Doppler frequency shift, and f_{in} represents frequency of the input signal including Doppler, then

$$y(t) = AC(t)D(t) \cos(2\pi f_{in}t) \tag{25.2}$$

where $D(t)$ is modulation of the navigation message and $C(n)$ is the spread spectrum code of satellite, mixing carrier produced by local carrier generator and the input digital intermediate frequency signal, When the input signal and the local code is aligned, by mixing with I channel carrier $\cos(2\pi f_n + \theta)$, we get the following formula

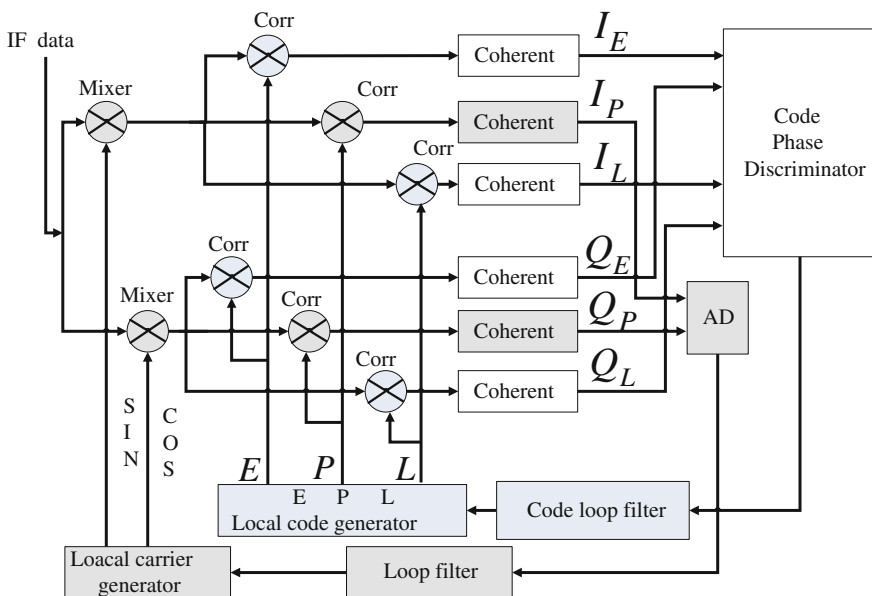


Fig. 25.2 The tracking loop of receiver

$$\begin{aligned}
& AD(t) \cos(2\pi f_i t) * \cos(2\pi f_{in} t + \theta) \\
&= \frac{1}{2} AD(t) \cos(2\pi f_e t + \theta) \\
&\quad + \frac{1}{2} AD(t) \cos(2\pi f_i t + \theta)
\end{aligned} \tag{25.3}$$

Similarly, Q channel can get the following formula:

$$\begin{aligned}
& AD(n) \cos(2\pi f_i t) * \sin(2\pi f_{in} t + \theta) \\
&= \frac{1}{2} AD(n) \sin(2\pi f_e t + \theta) \\
&\quad + \frac{1}{2} AD(n) \sin(2\pi f_i t + \theta)
\end{aligned} \tag{25.4}$$

And then through the coherent integrator, filtering the high frequency component, it gains:

$$I_P = A \sum_{n=0}^{N-1} \frac{1}{2} D(t) \cos(2\pi f_e t + \theta) \tag{25.5}$$

$$Q_P = A \sum_{n=0}^{N-1} \frac{1}{2} D(t) \sin(2\pi f_e t + \theta) \tag{25.6}$$

Then through the phase discriminator, can be gain:

$$\theta_e = \tan^{-1} \left(\frac{Q_P}{I_P} \right) \tag{25.7}$$

When Q_P is minimum and I_P is maximum, θ_e is minimum. When the tracking reach stability after, channel contains the navigation message, since more than one phase discriminator, this paper here only give an example. The loop filter is a low pass filter and is used to smooth the value of θ_e . The results of loop filter are then input to a local carrier generator, to control sine and cosine function of the output of local carrier generator.

For the code tracking loop, local code generator produces three groups of local code of advanced, instant and lag, three sets of initial code phase half a chip or 1/4 chip. Taking advanced code corresponding to the channel for example, the correlative results of correlation output lag after the mixing i_E and q_E can be expressed as

$$i_E = AD(n)R(\tau_E) \cos(2\pi f_e t + \theta) \tag{25.8}$$

$$q_E = AD(n)R(\tau_E) \sin(2\pi f_e / f_s n + \theta) \tag{25.9}$$

After coherent integrator

$$I_E = A \sum_{n=0}^{N-1} D(n)R(\tau_E) \cos(2\pi f_e t + \theta) \quad (25.10)$$

$$Q_E = A \sum_{n=0}^{N-1} D(n)R(\tau_E) \cos(2\pi f_e t + \theta) \quad (25.11)$$

After the code loop phase discriminator, then is obtained

$$\delta_{cp} = \frac{1}{2} ((I_E - I_L)I_P + (Q_E - Q_L)Q_P) \quad (25.12)$$

δ_{cp} represents the difference between the initial phase of local instantaneous code estimated and the initial phase of input signal, and the code loop discriminator are also more than one. δ_{cp} effects on local code generator obtained the results after filtering through the loop filter of the code loop finally.

25.3 Tracking Algorithm of Weak BD Signals by BOC(15,2.5) Mode

For the weak signals of BOC(15,2.5) debug mode, tracking needs to pay attention to two issues: 1. The autocorrelation function produces multi peak phenomenon owing to BOC(15,2.5) debug mode, therefore, if according to the conventional way, tracking loop will not be able to effectively track signal. 2. Weak signal affected by noise is relatively large. The paper will design algorithms according to the above two problems.

25.3.1 The Initial Frequency Selection of Local Carrier NCO

Said $f_0 = 1.023$ MHz to be a fundamental frequency, for BOC(15,2.5) modulated signal, said f_{sc} is subcarrier frequency, f_{ca} is a fundamental frequency, then $f_{sc} = 15f_0$, $f_{ca} = 2.5f_0$. Its frequency is expressed as below (Fig. 25.3).

Its autocorrelation function as shown below (Fig. 25.4).

Visible from above, there are many side lobe In the wave of both sides, assuming Δf is Doppler Captured, if initial frequency of the local carrier $f_l = f_{if} + \Delta f$ which is unable to carry out normal tracking. Effects of subcarriers therefore must be cancelled, and the local carrier frequency must consider the subcarrier frequency, if taking the upper sideband:

Fig. 25.3 The power spectrum of BOC(15,2.5)

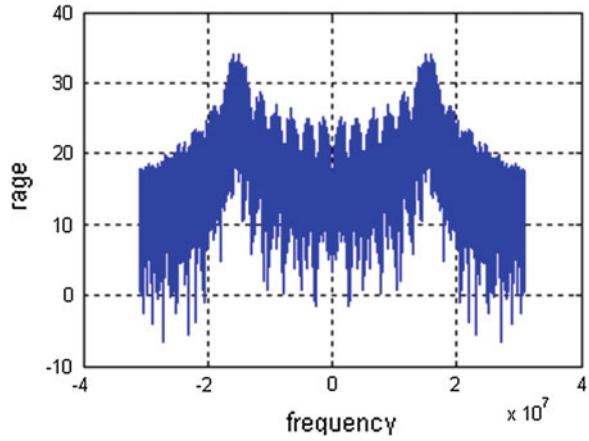
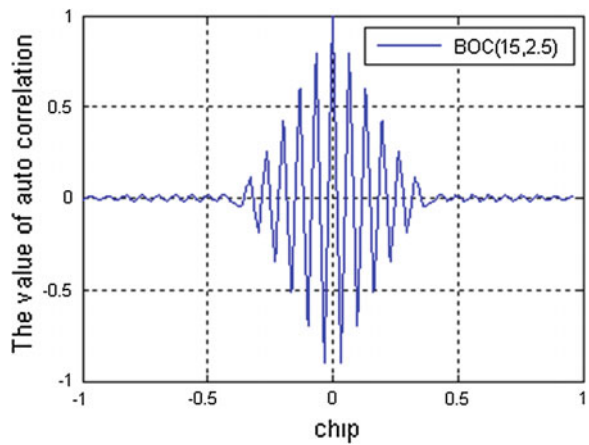


Fig. 25.4 The autocorrelation function of BOC(15,2.5)



$$f_l = f_{if} + \Delta f + f_{sc} \tag{25.13}$$

Taking the lower sideband

$$f_l = f_{if} + \Delta f - f_{sc} \tag{25.14}$$

25.3.2 Tracking Technology Based on EKF

EKF mainly includes the prediction and correction. The output of the coherent integration which

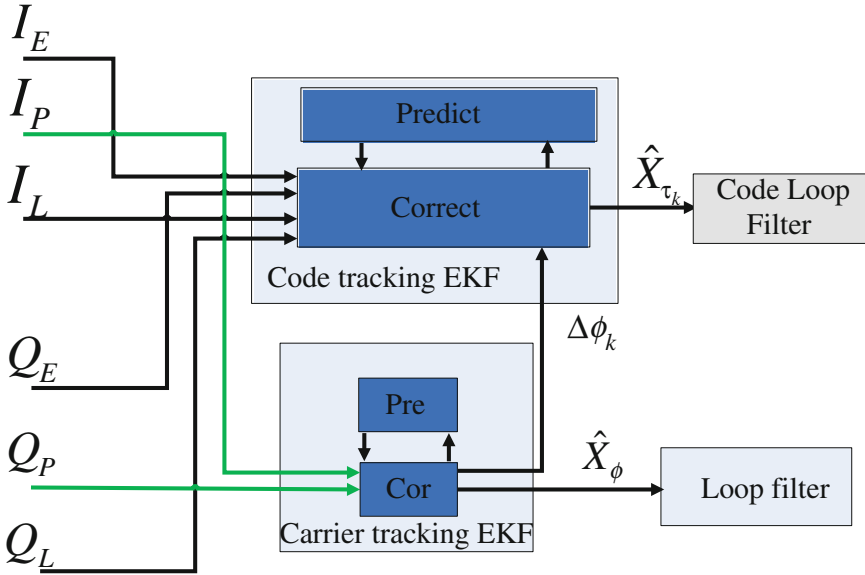


Fig. 25.5 The structure of EKF in tracking loop

I, Q channels corresponding instantaneous code enter the tracking loop based on EKF carrier as the measured value. Four channels which advanced code, delay code corresponding enter the code tracking loop act as the measured value of the correction module either. as shown in Fig. 25.5.

Among them, X_{ϕ} represents the posteriori difference estimation made by the carrier phase of the received signal and the carrier phase of local carrier; \hat{X}_{τ_k} represents the posteriori estimation of delay which comes from code phase.

25.3.2.1 The Carrier Tracking Technology Based on EKF

The carrier phase, magnitude are estimated in carrier tracking loop based on EKF. According to accumulating the correlation value made by input signal and reproducing signal, we can draw:

$$I_k(\delta) = \sum_{i=i_k}^{i_k+N_k} yC_{nco}(t_i + \delta - t_{nco_k}) \cos(2\pi f t + \phi(t_i)) \quad (25.15)$$

$$Q_k(\delta) = \sum_{i=i_k}^{i_k+N_k} yC_{nco}(t_i + \delta - t_{nco_k}) \sin(2\pi f t + \phi(t_i)) \quad (25.16)$$

Among them, $I_k(\delta)$, $Q_k(\delta)$ identify the accumulated value of in-phase signal and the orthogonal signal. N_k represents the number of sampling Every millisecond; $C_{nco}(t_i)$ represents the local repetition code; t_{nco_k} is the starting time for the local spread spectrum code; $\phi_{nco}(t_i)$ is the reproduction value of carrier phase. After coherent integrator module, we can draw:

$$I_k(0) = \frac{1}{2} N_k \bar{A}_k D_k \cos(\Delta\phi_k) R(\Delta t_k) + n_{Ik} \quad (25.17)$$

$$Q_k(0) = \frac{1}{2} N_k \bar{A}_k D_k \sin(\Delta\phi_k) R(\Delta t_k) + n_{Qk} \quad (25.18)$$

In the above formula, \bar{A}_k is the mean value of carrier in the whole cumulative time; D_k is the value of navigation data; Δt_k is the mean value of input signal and reproducing signal in the cumulative time;

Δt_k is the phase difference at the end of cumulative period; $R(\Delta t_k)$ is the auto-correlation function of spread spectrum code; n_{Ik} and n_{Qk} mean the Gauss white noise uncorrelated sequence which is zero mean and its variance is $N_k \sigma_v^2 / 2$.

Taking the Carrier phase difference as the state variables, and the state variables of the system become:

$$X_k = [X_\phi \quad X_\omega \quad X_a \quad A]^T_k$$

Among them, X_ϕ represents the difference between the carrier phase of received signal and the phase of local reproduced carrier; X_ω represents the difference between the carrier frequency of received signal and the frequency of local reproduced carrier; X_a means the Frequency difference rate. A is amplitude of the signal in t_k moment. And the equation of state of carrier tracking loop for EKF can be shown as follow:

$$\begin{aligned} \begin{bmatrix} X_\phi \\ X_\omega \\ X_a \\ A \end{bmatrix}_k &= \begin{bmatrix} 1 & \Delta T & \frac{\Delta T^2}{2} & 0 \\ 0 & 1 & \Delta T & 0 \\ 0 & 0 & 1 & 0 \\ 0 & 0 & 0 & 1 \end{bmatrix} \begin{bmatrix} X_\phi \\ X_\omega \\ X_a \\ A \end{bmatrix}_{k-1} \\ &+ \begin{bmatrix} 1 & 0 & 0 & 0 \\ 0 & 1 & 0 & 0 \\ 0 & 0 & 1 & 0 \\ 0 & 0 & 0 & 1 \end{bmatrix} w_k \end{aligned} \quad (25.19)$$

Among them, the initial value of X_ϕ , X_ω , X_a , A can be provided from fine acquisition algorithm in front of tracking loop.

Taking $I_k(\delta)$ and $Q_k(\delta)$ as the measured value, and code phase error is beyond thinking in carrier tracking, the loop measurement equation [3] can be shown as:

$$\begin{bmatrix} I_k(0) \\ Q_k(0) \end{bmatrix} = \frac{1}{2} N_k A_k D_k \begin{bmatrix} \cos(\Delta\phi_k) \\ \sin(\Delta\phi_k) \end{bmatrix} + \begin{bmatrix} n_{Ik} \\ n_{Qk} \end{bmatrix} \quad (25.20)$$

According to

$$\Delta\phi_k = \begin{bmatrix} 1 & \Delta T & \frac{\Delta T^2}{2} \end{bmatrix} \begin{bmatrix} X_\phi \\ X_\omega \\ X_a \end{bmatrix} + [0 \ 0 \ 0 \ 1] w_k \quad (25.21)$$

$$\bar{A}_k = \frac{A_k + A_{k+1}}{2}$$

Among them, $\Delta\phi_k$ represents the estimated value of phase difference. Mark $Z_k = h[X_k, v_k]$ and Taylor measurement equations can be expanded as:

$$\begin{aligned} Z_k &= h[\hat{X}_k^-, 0] + \left. \frac{\partial h}{\partial v^T} \right|_{\hat{X}_k^-, 0} v_k \\ &+ \left. \frac{\partial h}{\partial X^T} \right|_{\hat{X}_k^-, 0} \bullet (X_k - \hat{X}_k^-, 0) \end{aligned} \quad (25.22)$$

25.3.2.2 The Code Tracking Technology Based on EKF

In this paper we estimate the code delay error in the code tracking model based on EKF. Selecting the code delay error as the state variables and the equation of state is:

$$X_{\tau_k} = \Phi X_{\tau_{k-1}} + w_{\tau_k} \quad (25.23)$$

Among them, X_{τ_k} is code delay error $\Phi = 1$; w_{τ_k} is Gauss white noise.

We select the integral accumulation value which made by received signal and advance code with delay code as observation vector during the code tracking loop. And can be express as follow:

$$Z_k = [I_k(\delta) \quad Q_k(\delta) \quad I_k(-\delta) \quad Q_k(-\delta)]^T \quad (25.24)$$

And then

$$I_k(\delta) = \frac{1}{2}N_k\bar{A}_kD_k \cos(\Delta\phi_k)R(\Delta\tau_k + \delta) + n_{Ik} \quad (25.25)$$

$$Q_k(\delta) = \frac{1}{2}N_k\bar{A}_kD_k \sin(\Delta\phi_k)R(\Delta\tau_k + \delta) + n_{Qk} \quad (25.26)$$

$$I_k(-\delta) = \frac{1}{2}N_k\bar{A}_kD_k \cos(\Delta\phi_k)R(\Delta\tau_k - \delta) + n_{Ik} \quad (25.27)$$

$$Q_k(-\delta) = \frac{1}{2}N_k\bar{A}_kD_k \sin(\Delta\phi_k)R(\Delta\tau_k - \delta) + n_{Qk} \quad (25.28)$$

Characteristic of the spread spectrum code autocorrelation function is

$$R(\tau) = 1 - \frac{|\tau|}{T_{chip}} \quad (25.29)$$

And

$$\frac{\partial R(X_\tau + \delta)}{\partial X_r} = -\frac{1}{T_{chip}} \quad (25.30)$$

$$\frac{\partial R(X_\tau - \delta)}{\partial X_r} = -\frac{1}{T_{chip}} \quad (25.31)$$

Among them, T_{chip} represents the length of a chip.

25.4 The Results of Simulation and Analysis

We generate the B3_C signal modulated by BOC(15,2.5) using Matlab, and set the power of the signal -160 dBm. Doppler is set to 2200 Hz, code phase is set to 500. The simulation of tracking process is for 500 times, and we carry on simulation using the code phase and Doppler of carrier generated by acquisition. In this paper we mainly simulated static and low dynamic condition. The follow picture shows the result of traditional code tracking loop and carrier tracking loop.

The result of the method in this paper is shown as follow:

Judging from Figs. 25.6, 25.7 and 25.8, tracking loop using EKF can make precision of carrier tracking loop greatly improve compared with the traditional method, and make the precision of tracking from 5 Hz of traditional method to 0.5 Hz proposed by our method; And Judging from Figs. 25.7, 25.8 and 25.9, code tracking loop using EKF, we can make precision of code tracking loop greatly

Fig. 25.6 The result of traditional carrier tracking loop

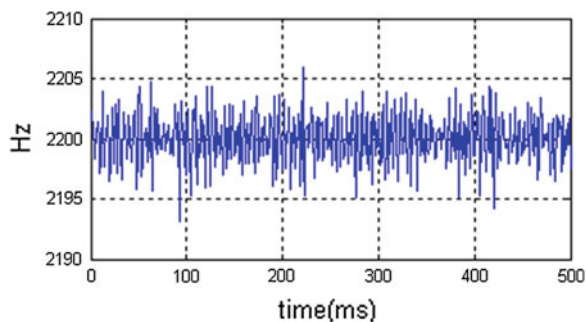


Fig. 25.7 The result of traditional code tracking loop

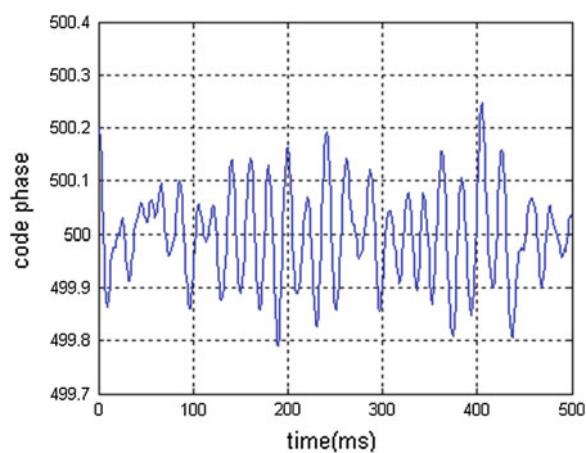


Fig. 25.8 The result of carrier tracking loop in this paper

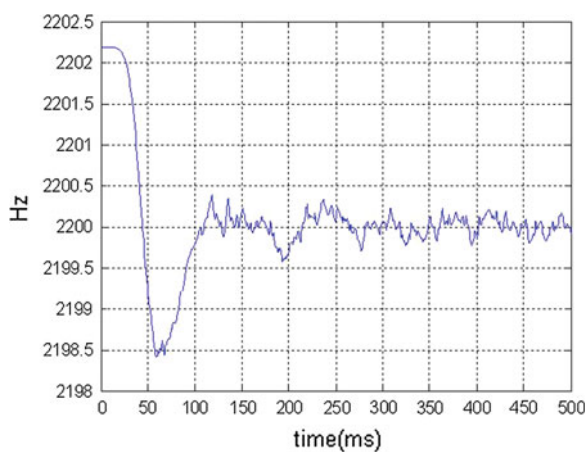
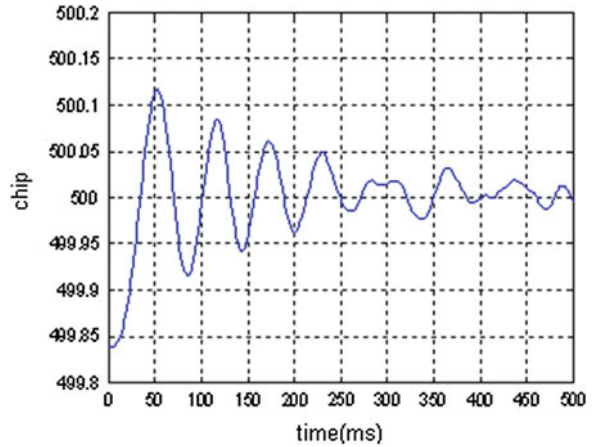


Fig. 25.9 The result of code tracking loop in this paper



improve compared with the traditional method, and make the precision of tracking from 0.25 chip of traditional method to 0.05 proposed by our method.

25.5 Conclusion

As can be seen from the simulation results that though standard DLL/PLL has strong function, because of nonlinear of phase discriminator, the dynamic changes of the signal phase and the increasing of the bit error rate, PLL is easily to lose lock in low carrier to noise ratio. With the time recursive properties, by linearization the expectation and variance, the extended Kalman filter can easily solve the problem of nonlinear phase discriminator and dynamic changing caused by signal phase, and then eventually get better result of tracking.

References

1. Krumvieda K, Cloman C, Olson E, Thomas J, Kober W, Madlhani P, Axelrad P (2001) A complete IF software GPS receiver: a tutorial about the details. ION GPS, Salt Lake City, pp 789–829
2. Kaplan E (2006) Understanding GPS: principles and applications, 2nd edn. Artech House Inc., Boston
3. Zidan NI (2008) The weak signals of global navigation satellite system receiver (translated by Zhang Xin). National Defence Industry Press, Beijing

Chapter 26

Characteristic Analysis for Regional Traffic Data Using Random Matrix Theory

Haichun Liu, Changchun Pan, Genke Yang, Chunxia Zhang
and Robert C. Qiu

Abstract Traffic regional feature analysis of city is an important problem in the study of macro transportation system. The analysis of the current traffic regional feature of the city is mainly through the floating car data, such as velocity's average or variance to characterize the features of different regions. But with the increasing scale of the traffic data in sampling and storage, the average (or variance) velocity as the evaluation of city traffic regional feature such as distinguishing urban and suburb has no significant through our analysis. Therefore, in this paper, we use the Random Matrix Theory (RMT) to analysis traffic data, which is based on floating car position data's distribution of singular value equivalence matrix eigenvalue to distinguish different region such as urban and suburban. By using 1 week's floating car data, we verify the data's eigenvalue of singular value equivalent matrix distribution is better than the velocity's average or variance in indicating the regional feature of city traffic.

Keywords RMT · Big data · Spectral analysis · Data mining

26.1 Introduction

It can give strong support to the intelligent transportation system to looking for the regular pattern of traffic data, the regional traffic feature analysis of city is an important problem in the study of macroscopic transportation system [1]. The main

H. Liu (✉) · C. Pan · G. Yang
Department of Automation, Shanghai Jiao Tong University, Shanghai, China
e-mail: haichunliu@sjtu.edu.cn

C. Zhang
Shanghai Wainmac Information Technology Co. Ltd, Shanghai, China

R.C. Qiu
Department of Electrical and Computer Engineering, Tennessee Technological University,
Knoxville, TN 37996, USA

purpose of traffic data mining is to ease the traffic congestion, optimize traffic road network traffic and promote the healthy and stable development of traffic [2].

Knowing and understanding the city bus movement law is of great significance to improve the comprehensive management ability of city traffic environment and resources, while more and more abundant data collection methods of the moving bus provides more accurate data source for the study of mobile behaviour of city public traffic bus. Floating car technology, also known as the “Rover (Probe Car)”, is one of the advanced technological means to obtain traffic information in the international intelligent transportation system (Intelligent Transport System ITS) in recent years. Floating car generally refers to the buses and taxis which install the GPS bus positioning device and drive in the city on the main road. If there're sufficient number of floating car in the city, and periodically, real-time transmit the position information of these floating car data to the processing centre through the wireless communication system. By the comprehensive process of the information centre, we can obtain the whole city's dynamic, real-time traffic congestion information [3, 4].

The random matrix theory (RMT), based on the random variables as the elements of the matrix, through the comparison of random multidimensional time series statistical properties, can reflect the correlation of real data and the degree of deviation from a random distribution properties, and reveal the behaviour characteristic of the whole actual data. It is a unique angle of view that is different from the traditional methods, RMT is widely applied in the fields of financial, physical, biological statistics, computer science, etc. [5–9]. Based on the RMT, in the study of large radar antenna array signal transmission, it's found that eigenvalue distribution which uses antenna as sensor nodes to construct random matrix, can well describe the correlation between each antenna nodes flow, and can make rapid response to the emergence of abnormal signals in the transmission process [10]. In the financial field, through the analysis, the researchers found the trend of America stock maximum eigenvalue of correlation matrix in 1962–1979 years, analysed American stock character when the market crashed in 1987 [11].

Compared to the taxi, the bus traffic data has the feature of wide coverage and stable travel time, can be used as a reliable source of data to reflect the current situation of the regional feature. So this paper uses random matrix theory to study the bus (floating car) traffic data, and finds the obvious feature of region. Compared to the difference of distribution of the equivalent matrix between floating car data with random data in the singular value spectrum, it's found that floating car's traffic data singular value equivalence matrix eigenvalues deviate significantly from random data's matrix eigenvalue distribution. It points out that this deviation is caused by the correlation between the floating car data, regional traffic feature of city is the embodiment of the correlation between the bus, floating car data matrix eigenvalue distribution can reflect the regional feature of city traffic.

26.2 Floating Car Data and Spectral Analysis of Random Matrix

26.2.1 Data Source and Composition

The data this paper used is provided by the laboratory of intelligent traffic of Shanghai Sciences Academy, from April 1, 2014 to April 7, 2014, all traffic data of buses belongs to Pudong Public Bus Company. The data of the region is shown in Fig. 26.1. Regional scope was located 121.462483-121.717873 east longitude and 31.270335-31.172713 north latitude.

The standard GPS data can be got by analysis of the original data, contains the longitude, latitude, time, license plate number, operation route. Correlation analysis is made according to the matrix of the bus position information in this paper. In the spatial scale, each bus as the sensor node, within the interest region, randomly selected N buses. On a time scale, GPS system collects data once every 10 s, so according to the sampling window size, each car can collect T data. The position information includes the longitude and latitude, taking longitude as the real part, latitude as the imaginary part, storing each coordinate in the form of complex numbers, so as to obtain a matrix of $N \times T$.



Fig. 26.1 Floating car data source's area

26.2.2 Spectral Analysis of Random Matrix

Compared with traditional probability theory, random matrix is defined as a random variable for the elements of the matrix. If the random matrix dimension tends to infinity, it is called Large Random Matrix. Let rectangular matrix $H_{N \times T}$, when $N \rightarrow \infty, T \rightarrow \infty$, and $N/T = c \rightarrow \sigma$, σ is fixed. The large random matrix row and column tends to infinity, but the rank of the ratio is kept constant. Then, the large random matrix empirical spectral distribution (ESD) of this case has many proven characteristics, like Semicircular Law [5], Marčeko-Pastur (M-P) Law [6], and the latest Circle Law [9].

Random matrix theory according to the element distribution characteristics can be divided into: Gauss random matrices, Wishart random matrix, Haar-unitary random matrix. The research method is based on a variety of mathematical theory: the classical limit theory, free probability, mathematical transform, information theory. Several theorems which are given below are more important in RMT, this study is based on the following theorem.

Theorem 26.1 *Let the entries of the $N \times T$ matrix A_n , Then the Stiletjes transform of spectral distribution F_{A_n} of A_n surely to be:*

$$m_{A_n}(z) = \int \frac{1}{x-z} dF_A(x) = \frac{1}{n} \sum_{i=1}^n \frac{1}{\lambda_i - z} = \frac{1}{n} Tr[A_n - zI_n^{-1}] \tag{26.1}$$

wherein x represents a random variable, its distribution is asymptotically ESD of matrix A_n .

Theorem 26.2 *Let the entries of the $N \times T$ matrix X be independent identically distributed entries with zero mean and variance $1/N$. Then the empirical singular value distribution of X converges almost surely to the limit given by.*

$$f(x) = \max(0, 1 - \beta)\delta(x) + \frac{\sqrt{4\beta - (x^2 - 1 - \beta)}}{x\pi} I_{\{\|1-\sqrt{\beta}\|, \|1+\sqrt{\beta}\|\}} \tag{26.2}$$

As $N \rightarrow \infty, T \rightarrow \infty$, and $N/T = c \rightarrow \sigma$, σ is fixed.

Theorem 26.3 *Making a special transformation of random variable $Y = X^2$, gives:*

$$f_{\sqrt{XX^H}}(x) = \frac{1}{2\pi xc\sigma^2} \sqrt{(b-x)(x-a)} (a \leq x \leq b) \tag{26.3}$$

As $a = \sigma^2(1 - \sqrt{c})^2$, $b = \sigma^2(1 + \sqrt{c})^2$, $c = N/T$, which is known as Marčeko-Pastur Law. The covariance matrix of X is calculated as: $A = XX^H$, If the entries of A are i.i.d, A has same approximate limiting distribution as (26.2), within boundaries a and b .

The exact spectrum distribution of A is unknown. To estimate the spectral density of X, a standard non-parametric method popularly known as kernel density estimation is used. Supposing the observations $X_1 \cdots X_n$ are i.i.d random variables with unknown density function $\hat{f}(x)$ and probability distribution $F_n(x)$, the kernel density estimate of $f(x)$ is:

$$\hat{f}_n(x) = \frac{1}{Nh} \sum_{i=1}^N K\left(\frac{x - \gamma_i}{\gamma}\right) \tag{26.4}$$

where $h = n^{-\frac{2}{5}}$ is the bandwidth used to calibrate the smoothing properties.

Theorem 26.4 *Let the entries of the $N \times T$ matrix X be i.i.d with zero mean, variance $1/N$, then the empirical eigenvalue distribution of the singular value equivalent of X converges almost surely to be:*

$$f_{X_u}(z) = \begin{cases} 1/c\pi & \sqrt{1-c} < |z| \leq 1 \\ 0 & \end{cases} \tag{26.5}$$

As $N \rightarrow \infty, T \rightarrow \infty$ and $N/T = c \rightarrow \sigma$, σ is fixed. When ratio of $N/T = c$ is fixed, the radius of the inner circle is $\sqrt{1-c}$. The singular value equivalent matrix of X is defined as X_u :

$$X_u = U\sqrt{XX^H} \tag{26.6}$$

where U is a $N \times N$ Harr-Unitary matrix.

26.2.3 Ring Law for Rectangular Random Matrix

The theorems in Sect. 2.2 meet the conditions: $X_{N \times T}$ and $N \rightarrow \infty, T \rightarrow \infty$. In practical applications, the matrix rows and columns won't satisfy the condition tends to infinity, The following which is proved the results will also approach when N and T is large but not infinity through the simulation.

Let the entries of the $N \times T$ matrix X be independent identically distributed entries with zero mean and variance $1/N$. Given $N = 300, T = 1200$, according to Theorem 26.4, can be obtained:

The theoretical value of inner diameter is $r = \sqrt{1-c} = \sqrt{1-3/4} = 0.866$. As shown in Fig. 26.2 (left), all features are almost uniformly distributed in the ring, in which the minimum eigenvalue of 0.8433, which is very close to the theoretical value of diameter. That in the random matrix X of N and T does not satisfy the conditions tend to infinity, its eigenvalues distribution approximately conform to the theoretical distribution.

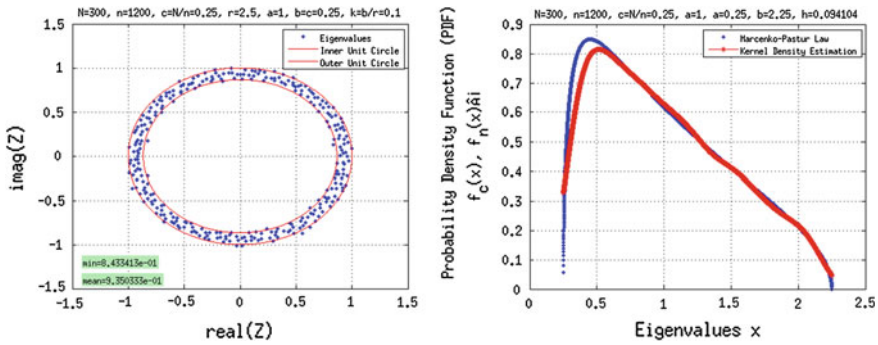


Fig. 26.2 Eigenvalues distribution and empirical eigenvalue density function

Still using the matrix X , according to Theorem 26.3, we can obtain Fig. 26.2 (right). Where the blue curve shows the density distribution function of a random matrix X is obtained by the Marčenko-Pastur law of the eigenvalues of the theoretical value, the red curve represents the eigenvalue probability density function (PDF) of random matrix X which obtained by kernel density method of the value, is also the matrix of the eigenvalue of X actual density distribution. That in the random matrix X of N and T does not satisfy the conditions tend to infinity, its eigenvalue density distribution is approximately the theoretical distribution.

26.3 Regional Feature of City Traffic

26.3.1 Analysis of Low Dimensional Regional Feature

The degree of traffic congestion is the main manifestation of city regional traffic feature, but how to quantify the degree of traffic congestion, the metric of every country in the world is not unified. The bus velocity is used to measure the traffic congestion degree standard in the United States, Japan and China.

Provisions of the Ministry of public security of our country issued “urban traffic management evaluation index system in the 2012 edition”: the average travel velocity of bus on urban trunk road is used to describe the traffic congestion degree, and there’s related quantitative indicators.

However, with the development of computer technology, traffic data which reflects floating car traffic grows massively. With the increase of the statistical sample, the average velocity of each region won’t gradually reflect the differences of every region.

According to the data of Sect. 26.2.1, we selected two block region in the urban and suburban, as Fig. 26.3. The urban contains Lujiazui and Century Avenue, the suburban contains Chuansha and Zhangjiang. Randomly selected 800 buses on each region, randomly selected 2400 GPS data of each bus within a week, and then



Fig. 26.3 Select the regions from urban and suburban areas respectively

calculated the average velocity of these region. As shown in Fig. 26.4 (left), in the urban: the average velocity of Lujiazui and Century Avenue was 16.45 and 9.78 km/h, in the suburbs: the average velocity of ChuanSha and ZhangJiang respectively was 16.08 and 11.88 km/h. It was shown that in such a scale statistical sample space, the difference in average velocity of each region showed a random distribution. Our subjective understanding conditions that urban is more congested than suburb, which can't be reflected in the data, so the average velocity can't be used as an index to distinguish traffic feature of city region. And the velocity variance can't reflect the significant differences, either Fig. 26.4 (right).

26.3.2 High Dimensional Spectral Analysis of Traffic Data

The statistical average velocity of each city region will be different from the actual road situation, sample floating car velocity has large discreteness, and contribution

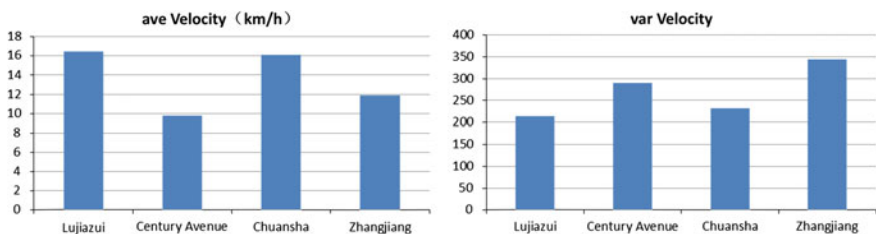
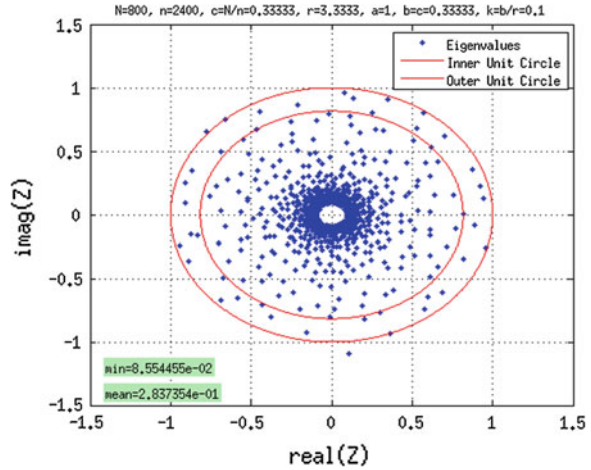


Fig. 26.4 Velocity's average and variance distribution in urban and suburban

Fig. 26.5 Eigenvalues distribution of Lujiazui



degree to the road conditions of every floating car driving behavior on the road is also different, the average or variance of velocity is difficult to be used as the index to reflect difference of city regions. The actual situation of city traffic is the reflection of interaction between buses. The spectral analysis of RMT analyses on the correlation between data. In Sect. 26.3.1, using the Lujiazui regional data as an example, according to Theorem 26.4, it show as Fig. 26.5.

The conditions of Theorem 26.4 is: $N \times T$ matrix X be independent identically distributed entries with zero mean and variance $1/N$. N and T conditions have been discussed, does not tend to infinity, the result of Theorem 26.4 will be infinite approximation. The traffic data discussed in this paper are identically distributed but not completely independent. When all buses are totally static, we can think that the traffic data are independent. Once the buses are in driving state, inevitably there are correlations between them. The performance of the city traffic condition is to understand the correlation among buses, based on spectral analysis of RMT is can discover and quantify this correlation.

Comparing Figs. 26.5 and 26.2, if all buses within the sample space are static, then the traffic data of random matrix eigenvalue distribution will be reflected like Fig. 26.2, it can be understood as the situation of the traffic situation is completely paralyzed. If all buses within the sample space is in the running state, if they are perfectly correlated, then the eigenvalues of the matrix will be concentrated in the center of the circle, this is the extreme state completely smooth traffic conditions. From Fig. 26.5, the correlation between buses was quantified as the distribution of eigenvalues, and which are distributed in the upper and lower bounds. Because the normalized reason, the upper bound is equal to one, then the lower bound to become the main parameters concerned. Therefore, the floating car data random matrix eigenvalue distribution can be a kind of index to describe the regional traffic feature of city.

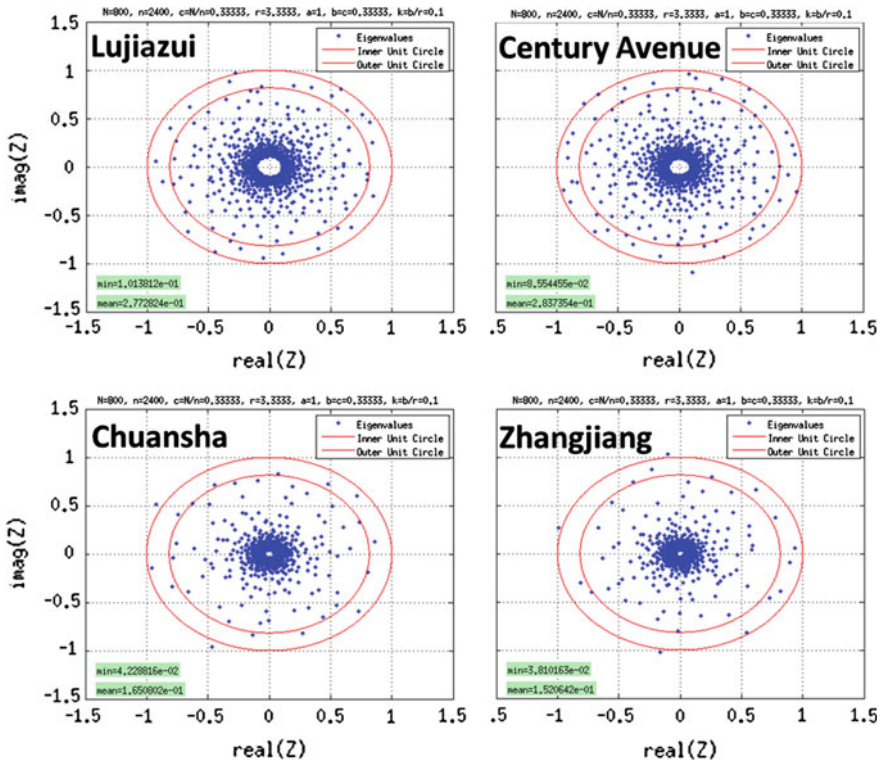


Fig. 26.6 Eigenvalues distribution in urban and suburban

26.3.3 Distribution Pattern of City Regional Feature

In the situation that the average or variance of velocity is unable to determine city regional distribution pattern, based on the above deduction, we use eigenvalue distribution of the traffic data random matrix as the classification index of city regional distribution pattern, respectively carry out spectrum analysis to the data in Sect. 26.3.1.

We should notice that in Fig. 26.6, diameter of eigenvalue distribution in the urban (Lujiazui and Century Avenue) is larger than the suburban (Chuansha and Zhangjiang). According to the objective understanding, urban traffic will be more complex than the suburban, and congestion will be more obvious. The traffic condition is more congested in urban. Its diameter should also be larger in spectrum analysis, this is also in line with the objective reality. At the same time, in the distribution of eigenvalues, the smallest eigenvalue can be uniquely determined, this can provide a clear indicator to the quantitative analysis of the regional division of city traffic.

26.4 Conclusions

Study on random matrix theory has been quietly rising in recent years, many domestic and foreign scholars pay attention to it. With the development of data storage, data needed to be processed is so huge. When traditional method cannot be applied in increasing data gradually, spectrum analysis method based on random matrix theory can transfer data analysis into matrix analysis, carry out data mining through various feature of random matrix.

In this paper, by using random matrix theory, we study the bus (floating car) traffic data, and find the obvious feature of different regions. Compared to the difference of distribution of the equivalent matrix between floating car data with random data in the singular value spectrum, it's found that floating car's traffic data singular value equivalence matrix eigenvalues deviate significantly from random data's matrix eigenvalue distribution. It pointed out that this deviation is caused by the correlation between the floating car data, regional traffic feature of city is the embodiment of the correlation between the buses, floating car data matrix eigenvalue distribution can reflect the regional feature of city traffic. For the distribution difference, this paper tries to give a possible understanding and interpretation.

References

1. Qi L (2008) Research on intelligent transportation system technologies and applications. Workshop on power electronics and intelligent transportation system, pp 529–531
2. Kriegel HP, Renz M, Schubert M, Zuefle A (2008) Statistical density prediction in traffic networks. In: SIAM intelligent conference, pp 692–703
3. Hiribarren G, Herrea JC (2014) Real time traffic states estimation on arterials based on trajectory data. *Transp Res Part B* 69:19–30
4. Jaeyoung L, Mohamed AA, Ximiao J (2014) Development of zone system for macro-level traffic safety analysis. *J Transp Geogr* 38:13–21
5. Wigner EP (1958) On the distribution of the roots of certain symmetric matrices. *Ann Math* 67:325–327
6. Marčenko VA, Pastur LA (1967) Distribution of eigenvalues for some sets of random matrices. *Math USSR-Sb* 1:457–483
7. Debbah M, Muller R (2005) MIMO channel modelling and the principle of maximum entropy. *J Latex Class Files* 1(11):71–77
8. Zhidong B, Silverstein JW (2006) Spectral analysis of large dimensional random matrices. Science Press, Beijing
9. Robert Q, Browning JP (2012) Spectrum sensing in cognitive radio with robust principal component analysis. *IEEE waveform diversity and design conference*, vol 1, p 177
10. Burda Z, Livan G, Swiech A (2013) Commutative law for products of infinitely large isotropic random matrices. *arXiv preprint arXiv 1303.5360*
11. Plerou V, Gopikrishnan P, Rosenow B, Amaral L, Gurrh T (2002) Random matrix approach to cross correlations in financial data. *Phys Rev E* 65:066126

Chapter 27

Impact Analysis of Differential Code Biases of GPS Satellites on the Kinematic Precise Point Positioning

Shoujian Zhang and Lei Zhao

Abstract When the IGS precise orbits and clocks are used to carry on kinematic PPP, it is necessary to make DCB correction according to different types of GPS receivers. Currently, it is well known that DCB has little influence on static PPP, but there is still much work to do about the influence of DCB on kinematic PPP. This paper has a thorough evaluation on that and compares the kinematic results with the P1P2 type receiver by processing observation data from 20 IGS tracking stations. The results show that the accuracy of kinematic PPP of the NONCC receiver reporting C1 and P2 types has improved after DCB correction, but is still lower than that of the NONCC receiver reporting P1 and P2 types, especially in the zenith direction and the difference can reach more than 2 cm. The results indicate that there is a need to improve the accuracy of DCB published by IGS analysis center.

Keywords GPS · Kinematic PPP · DCB

27.1 Introduction

Precise Point Positioning (PPP) by just processing a single station's observation data can achieve high-precision location, which has been widely used in many areas, such as photogrammetry survey [1], crustal deformation monitoring [2] and orbit determination of low-earth-orbiters [3].

S. Zhang (✉) · L. Zhao
School of Geomatics and Geodesy, Wuhan University, 129 Luo Yu Road,
Wuhan 430079, China
e-mail: shjzhang@sgg.whu.edu.cn

L. Zhao
e-mail: zlnmbox@163.com

When carrying on PPP, one will first use the IGS precise orbits and clocks, which are referenced to a P1 and P2 ionosphere-free combination [4]. So it's necessary to make Differential Code Biases (DCB) correction when the pseudorange reported by some types of receivers is not compatible with P1 or P2, otherwise DCB may influence the realization of high-precision location.

Kouba and Heroux [5] (2001, 2009) pointed out that it is indeed necessary to take DCB into consideration on the implementation of PPP. Huang et al. [6] (2010) has studied the impact of DCB on static PPP, and analyzed the positioning difference before and after DCB correction with the use of kinematic data. In spite of the knowledge of the influence of DCB on static positioning, there is still much room to discuss about whether the accuracy of kinematic PPP of the NONCC receiver reporting C1 and P2 types after DCB correction can reach that of the NONCC receiver reporting P1 and P2 types.

This paper compared the accuracy of kinematic PPP between C1P2 type receivers with P1P2 type receivers, both of which belong to non-cross-correlation (NONCC) type receiver and made a qualitative assessment about the influence of DCB correction on kinematic PPP of C1P2 type receivers, which may provide bases and supports for the further improvement of the accuracy of C1P2 type receivers' positioning.

27.2 Mathematic Models

The P1 and P2 based ionosphere-free combination observable equation is as follows:

$$P_3 = \rho + C(dt_r - dt^s) + M \cdot T_{ZTD} + \varepsilon_{P_3} \quad (27.1)$$

where:

P_3 is the ionosphere-free pseudorange measurement;

ρ is the geometric distance between satellite and station;

c is the speed of light;

dt_r is the receiver clock offset;

dt^s is the satellite clock offset;

M is the mapping function;

T_{ZTD} is the zenith troposphere delay;

ε_{P_3} stands for the influence of code multipath and measurement noise;

As one can notice, there are no biases between P1 and P2 being considered in the equation above, because the same observation combination as the one used by IGS to estimate satellite clocks is being used, and the receiver code biases are absorbed by the receiver clock parameter (dt_r in the equation above) [4].

If one is using C1 measurements rather than P1 for positioning, the P1-C1 bias should be considered:

$$P_3 = \rho + c(dt_r - dt^s) + M \cdot T_{ZTD} + \alpha \cdot b_{P_1C_1} + \varepsilon_{P_3} \quad (27.2)$$

where the additional terms:

α can be computed as $\alpha = \frac{f_1^2}{f_1^2 - f_2^2}$;

$b_{P_1C_1}$ is the satellite instrumental bias between P1 code and C1 code;

Current research indicates that the bias between P1 and C1 can reach ± 1 ns (30 cm) [4]. So the magnitude of $\alpha \cdot b_{P_1C_1}$ can be as large as more than 70 cm. It's necessary, therefore, to take P1-C1 bias into consideration if one expects that kinematic PPP can achieve high-precision location.

The pseudorange reported by receiver relies on the inner technique of the receiver itself. At present, GPS receivers can be basically divided into two types; one is cross-correlation (CC) receiver, and the other is non-cross-correlation (NONCC) receiver [7]. CC receiver reports C1 and P2, pseudorange observables, both of which need DCB correction in order to be compatible with IGS standard types. As for NOCC receiver, this kind of receiver generally reports P1 and P2 pseudorange observables, which are the standard observables used by IGS, but it has been recognized that among this kind there are some receivers reporting C1 and P2, which means that DCB correction is needed for C1 pseudorange observable to be compatible with P1.

Given that most of the IGS GPS receivers are the NONCC receiver, this paper concentrated on the influence of DCB on kinematic PPP of NONCC kind receivers reporting C1 and P2 (simply called C1P2 type receiver). The rest of NONCC kind is similarly called P1P2 type receiver here.

27.3 Experiments and Analysis

27.3.1 The Influence of DCB on Kinematic PPP

In order to have a further understanding of DCB's influence on kinematic PPP, this part of experiment randomly chose ten IGS stations all equipped with C1P2 type receiver and simulated kinematic PPP, then analyzed the accuracy difference of kinematic PPP before and after DCB correction. We used a 30 s sampling observation data of this ten stations from DOY (day of year) 300 to DOY 302 in 2013 and developed special software to carry on kinematic PPP analysis. The input products of precise orbits and clocks and DCB are all from CODE analysis center of IGS. The samples of precise clocks are also taken at 30 s to agree with the observation files.

Firstly, we directly used the observation data of the ten stations and implemented simulated kinematic PPP without the consideration of DCB in a forward and back mode of kalman filter. The results RMS in north, east and up direction are as follows. Obviously, the accuracy of the zenith direction of the results is relatively low, which can be as large as 8 cm, and the positioning results are not consistent

among the ten stations, for example, the good one can achieve about 3.5 cm accuracy in zenith direction (Figs. 27.1 and 27.2).

To see the DCB's influence on positioning, we made DCB correction for C1 pseudorange observable of these stations and implemented simulated kinematic PPP again. The results are as follows. Figure 27.3 shows the difference of positioning before and after DCB correction, which makes it clear to see the influence of DCB.

From Fig. 27.3, we can see for most of the stations DCB correction can help improve the accuracy of kinematic PPP, such as TCMS station, the accuracy in zenith direction has improved by 36 %; Whereas for some station, DCB correction seems meaningless, such as MAUI. On the whole, the accuracy of kinematic PPP after DCB correction has obviously improved, except for few stations. Table 27.1

Fig. 27.1 The RMS of PPP for 10 stations with C1P2 receiver

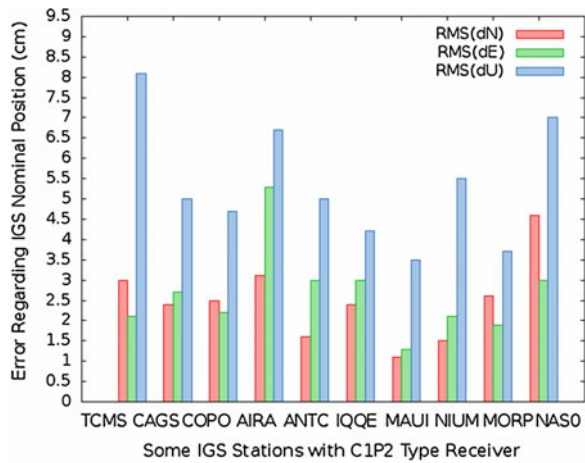


Fig. 27.2 RMS of PPP results for 10 stations with DCB corrections

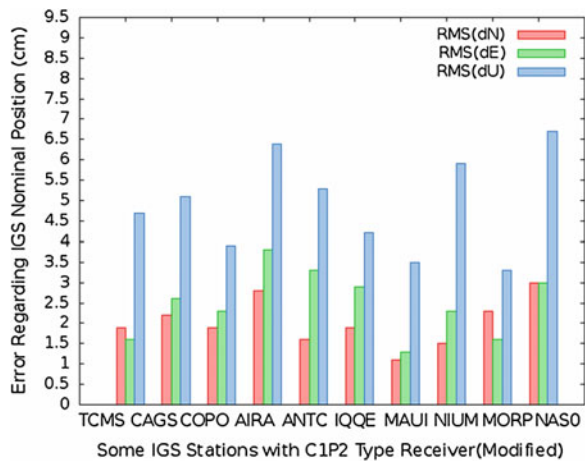


Fig. 27.3 RMS difference of PPP before and after DCB correction

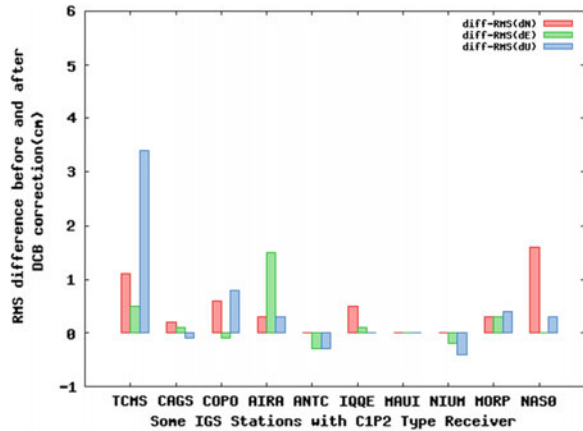


Table 27.1 The improved RMS values of the kinematic PPP after applying the DCB correction

Direction	Max improvement (cm)	Max improvement percent (%)	Average improvement (cm)
N	1.6	36	0.5
E	1.5	28	0.2
U	3.4	42	0.4

lists the improvement percent in N E U direction after DCB correction, which indicates that DCB has more influence on the positioning results in N and U direction.

27.3.2 Comparison of Kinematic PPP Between C1P2 Type and P1P2 Type Receiver

The results based on the experiment above show that the influence of DCB on the accuracy of kinematic PPP varies with stations, which means that for some stations the influence of DCB on kinematic PPP is meaningless while for other stations this impact can not be neglected when kinematic PPP is implemented. Besides, after DCB correction, the results of the kinematic PPP among these stations don't perform in a consistent way. In order to know whether the accuracy and stability of the kinematic PPP of C1P2 type receiver can reach that of P1P2 type receiver, again we chose ten IGS stations equipped with P1P2 type receiver and repeated the procedure above. The results of simulated kinematic PPP are as follows:

Compared Figs. 27.2 and 27.4, we can easily see these two phenomena: (1) the kinematic PPP results of these ten stations with P1P2 type receiver perform in a very consistent way, which indicates high stability of this kind of receiver in

Fig. 27.4 PPP results of 10 GPS tracking stations with P1P2 receiver

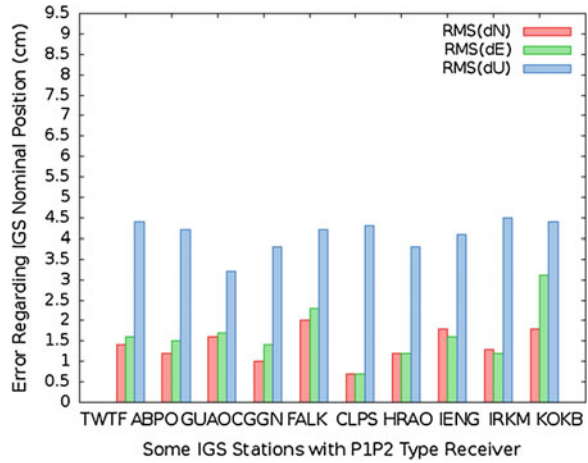


Table 27.2 Comparison of the kinematic PPP between C1P2 receiver after DCB correction and P1P2 type receiver

Receiver type	Average accuracy of kinematic PPP (cm)		
	N	E	U
C1P2	2	2.5	4.9
P1P2	1.4	1.6	4.1

kinematic PPP. (2) in terms of the zenith direction, the accuracy of the results of P1P2 type receiver’s positioning is still higher than that of C1P2 type receiver’s positioning after DCB correction on the whole, and for the numerical example, the disparities are separately 0.6, 0.9 and 0.8 cm in N E U direction. According to the analysis above, we can draw the conclusion that even DCB correction is taken into account, the accuracy of the kinematic PPP results of C1P2 type receiver is still lower than that of P1P2 type receiver, which indicates that there is a need to improve the accuracy of DCB monthly published by CODE (Table 27.2).

27.4 Conclusions

This paper has a thorough analysis of the influence of DCB on kinematic PPP by processing observation data from 20 IGS tracking stations. After taking the DCB monthly published by CODE into consideration, the accuracy of kinematic PPP of C1P2 type receiver is significantly improved and the maximum improvement value can be 3.4 cm in magnitude and 36 % in percent, as for the average improvement of these ten stations equipped with C1P2 type receiver, the values are separately 0.5, 0.2 and 0.4 cm in N E U direction. Besides, this paper finds that even DCB correction is taken into account, the accuracy of the kinematic PPP results of C1P2

type receiver is still lower than that of PIP2 type receiver, especially in the zenith direction, the maximum difference can be 3 cm more and the average differences in N E U direction are separately 0.6, 0.9 and 0.8 cm. Therefore, further improvement of the accuracy of DCB monthly published by CODE is needed, which provides a new direction about improving the kinematic PPP accuracy of C1P2 receiver.

References

1. Zhang B, Wu X, Yu Z, Zhang Z (2009) Precision analysis of GPS-based precise point positioning in aerial photogrammetry. *Sci Surv Mapp* 34(5):5–7
2. Fan S, Liu Y, Zhenjie W (2012) GPS co-seismic and post-seismic response to the 3·11 massive earthquake in Japan. *Geomatics Inf Sci Wuhan Univ* 37(2):191–194
3. Shi C, Zhao QL, Li M, Tang WM, Hu ZG, Lou YD, Zhang HP, Niu XJ, Liu JN (2012) Precise orbit determination of Beidou satellites with precise positioning. *Sci China Earth Sci* 55(7):1079–1086
4. Leandro RF, Langley RB, Santos MC (2007) Estimation of P2-C2 bias by means of precise point positioning. In: *Proceedings of the 63rd annual meeting of the institute of navigation*, pp 225–231
5. Kouba J, Heroux P (2001) Precise point positioning using IGS orbit and clock products. *GPS Solution* 5(2):12–18
6. Huang J, Wang P, Ruan R, Lin Y, Zhang Y (2010) Study on precise point positioning accuracy affected by DCB. *J Geodesy Geodyn* 30(3):110–117
7. Jim R (2014) [IGSMail-3737]: C1/P1 biases for leica and trimble 5700 receivers [EB/OL]. [2002-02-13]. <http://igsch.jpl.nasa.gov/mail/igsmail/2002>. Accessed 20 Mar 2014

Part II
BDS/GNSS Test and Assessment
Technology

Chapter 28

Performance Improvements of Combined Satellites Navigation System with System Time Offset

Longxia Xu, Ye Ren, Xiaohui Li and Dandan Li

Abstract The time offset between different navigation systems are called the system time offset. It can be calculated either at user receiver, monitored by the public institutes or broadcast via the navigation message by navigation system. Currently, the research topic about system time offset is focused on how to accurately obtain its value. However, this paper will pay attention to the application of system time offset in combined navigation systems. The performance improvements of positioning accuracy and availability especially in the case of limited satellite visibility will be analyzed in this paper. According to the distribution of azimuth of visible satellites, ten different circumstances are simulated to implement the following researches. The first aspect is to analyze the improvements on PDOP and positioning accuracy with the application of system time offset. And the second aspect is to study the advancement in the ability of fault detection and exclusion with system time offset. The results indicate that the effects in improving availability and integrity become more obvious with the aggravating of obscured satellite visibility. Besides, the length of time that PDOP is smaller than 6 increases at most 3 h, equivalently 22 % improvements of availability. And the positioning accuracy in East direction enhances 41 %, North direction 61 % and Up direction 46 %. Meanwhile, the MDB of GPS satellites meanly decrease 17 m and coefficient decreases 0.24 in the worst condition with the system time offset.

Keywords System time offset · Accuracy · Availability · Integrity

Funded by the West Ph.D. Program of West Light, CAS (2013BS24) and the State Key Laboratory of Geo-information Engineering, No. SKLGIE2014-M-2-5.

L. Xu (✉) · Y. Ren · X. Li · D. Li
National Time Service Center, CAS, Xi'an 710600, Shaan'xi, China
e-mail: xulongxia@ntsc.ac.cn

L. Xu · Y. Ren · X. Li · D. Li
Key Laboratory of Precision Navigation and Timing Technology, CAS, Xi'an 710600, Shaan'xi, China

L. Xu · Y. Ren · X. Li · D. Li
State Key Laboratory of Geo-information Engineering, Xi'an 710600, Shaan'xi, China

28.1 Introduction

With the development of multiple Global Navigation Satellite Systems, the navigation based on the combination of more than one satellite navigation system will be the important development direction in the future. Users can obtain service of high accuracy, reliability and integrity with combined navigation system. However, since every GNSS has their own time reference system, the time differences between any two navigation systems need to be determined. Currently, it can be obtained through calculating by users or monitoring by the public institutes [1, 2].

The research topic about system time offset is mainly focus on how to acquire it. However, research on how to use the system time offset is rarely. As the time difference of different time scales of navigation system, there is much valuable information contained in it. If can be properly applied, system time offset will become a promising tool for combined navigation systems. Its potential application will impel the development of Beidou navigation system with other GNSS. This paper will analyze the impact of system time offset on availability and integrity of combined navigation systems.

28.2 Analysis of Availability on Combined Navigation System with System Time Offset

28.2.1 Method of Improving Availability with System Time Offset

Availability, measuring the ability of providing service of navigation system in specific area, means the time percentage that providing normal service [3]. The availability of a navigation system contains the availability of SIS and the availability of service [4]. The availability discussed in this paper is the service availability which can be expressed mathematically as:

$$\sigma_p = \text{DOP} \cdot \sigma_{URE} \quad (28.1)$$

Service is considered to be unavailable when the value of PDOP exceeds six [3]. Taking the combined GPS/GLONASS system for example, the direction matrix of users to determine the system time offset between GPS and GLONASS systems is

$$\mathbf{H}_0 = \begin{bmatrix} a_{11} & a_{12} & a_{13} & 1 & 0 \\ \vdots & \vdots & \vdots & \vdots & \vdots \\ & & & 1 & 0 \\ & & & 1 & 1 \\ \vdots & \vdots & \vdots & \vdots & \vdots \\ a_{n1} & a_{n2} & a_{n3} & 1 & 1 \end{bmatrix} \quad (28.2)$$

The solved system time offset is used to deduct the system time offset directly from the pseudo-ranges of different navigation systems and finally synchronizing to a common time reference. Then the four parameters solution is calculated. The corresponding direction matrix is as following [5, 6]:

$$\mathbf{H}_1 = \begin{bmatrix} a_{11} & a_{12} & a_{13} & 1 \\ \vdots & \vdots & \vdots & 1 \\ \vdots & \vdots & \vdots & 1 \\ a_{n1} & a_{n2} & a_{n3} & 1 \end{bmatrix} \quad (28.3)$$

According to Eqs. (28.2) and (28.3), we have Eq. (28.4):

$$\mathbf{H}_0 = [\mathbf{H}_1 \quad h] \quad (28.4)$$

where, $h = [0 \quad \dots \quad 0 \quad 1 \quad \dots \quad 1]^T$ is a column vector. And then

$$\begin{aligned} D_0 &= \text{inv}(\mathbf{H}_0^T * \mathbf{H}_0) \\ &= \text{inv} \begin{pmatrix} \mathbf{H}_1^T * \mathbf{H}_1 & \mathbf{H}_1^T * h \\ h^T * \mathbf{H}_1 & h^T * h \end{pmatrix} \\ &= \text{inv} \begin{pmatrix} \mathbf{A} & \mathbf{D} \\ \mathbf{C} & \mathbf{B} \end{pmatrix} \\ &= \begin{pmatrix} \mathbf{A}^{-1} + \mathbf{A}^{-1} \mathbf{D} \Delta^{-1} \mathbf{C} \mathbf{A}^{-1} & \mathbf{A}^{-1} \mathbf{D} \Delta^{-1} \\ -\Delta^{-1} \mathbf{C} \mathbf{A}^{-1} & \Delta^{-1} \end{pmatrix} \end{aligned} \quad (28.5)$$

Given $\mathbf{A} = \mathbf{H}_1^T * \mathbf{H}_1$, $\mathbf{D} = \mathbf{H}_1^T * h$, $\mathbf{C} = h^T * \mathbf{H}_1$, $\mathbf{B} = h^T * h$, $\Delta = \mathbf{B} - \mathbf{C} \mathbf{A}^{-1} \mathbf{D}$, then:

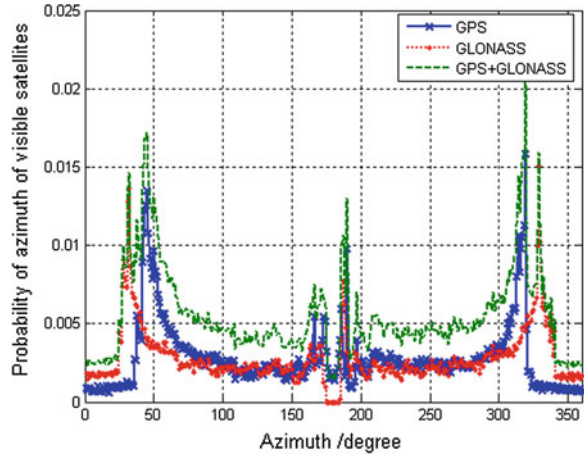
$$PDOP_0^2 - PDOP_1^2 = \text{sum}((\mathbf{A}^{-1} \mathbf{D} \Delta^{-1} \mathbf{C} \mathbf{A}^{-1})(1:3, 1:3)) \quad (28.6)$$

Compared with $PDOP_1$, $PDOP_0$ has a small increment which results to the accretion of PDOP without the system time offset.

28.2.2 Improvements of PDOP with System Time Offset

The positions of satellites that visible for a specific user are usually described with azimuth and elevation in site-centric coordinate system. The probability density of azimuth of visible satellites at a given position is related with the geographical

Fig. 28.1 Distribution of azimuth of GPS/GLONASS satellites that visible in Lin'tong



latitude [7]. Figure 28.1 shows the curve of probability density of GPS and GLONASS satellites that are visible at Lin'tong station under the elevation of 10°.

It can be seen from the figure that the azimuth angle of GPS satellites distributes mainly in the ranges (40°, 60°) and (305°, 320°) and GLONASS satellites in (25°, 40°) and (320°, 340°). Therefore, the azimuth angles mainly lie in (25°, 60°) and (305°, 340°) in the combined GPS/GLONASS systems. Based on the different combination of elevation and azimuth angles, several circumstances are established to simulate the signal blocked by the ground objects which are listed in the left column of Table 28.1.

The analysis is based on the one-day length GPS/GLONASS pseudo-ranges that observed at Lin'tong station. The ionosphere delay is deducted from the pseudo-ranges with the dual-frequency correction method.

Table 28.1 Variation of moments that smaller than 6 with and without the GPS/GLONASS system time offset under the elevation of 30°

Shielded azimuth	Shield area	Before	After	Percentage (%)
–	–	1296	1354	4
(25, 40)	R1	1209	1312	8
(40, 60)	G1	1180	1288	9
(25, 60)	G1 + R1	1051	1205	15
(0, 25)	GR	1205	1276	6
(305, 320)	G2	1171	1272	9
(320, 340)	R2	1215	1271	5
(40, 60) and (305, 320)	G1/2	977	1143	17
(25, 40) and (320, 340)	R1/2	1120	1205	8
(25, 60) and (305, 340)	R1/2 and G1/2	658	800	22

Fig. 28.2 MDBs of GPS/GLONASS in different circumstances without system time offset (Ele = 10°)

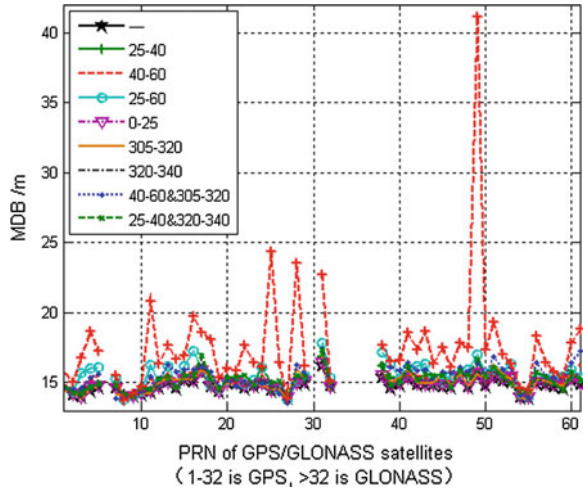


Table 28.1 lists the variation of moments after using the system time offset. It can be seen that the moments that PDOP is smaller than six after applying the system time offset increase at least 1 h, at most 3 h and the service availability maximally enhance 22 %. The denser the azimuth area is shielded the more obvious of the improvements after using system time offset especially the dense range of GPS visible satellites. The PDOP performs the same but un-conspicuous when the elevation is 10°.

28.2.3 Improvements of Positioning Accuracy with System Time Offset

This section intends to analyze the impact of system time offset on positioning accuracy. The positioning results are expressed with the RMS of positioning error in East, North and Up direction. The variation of positioning accuracy with system time offset under the elevation of 10° and 30° is shown in Figs. 28.2 and 28.3. According to the results of Table 28.2, the positioning accuracy in up direction improves meanly four percent and five percent in north direction after with system time offset. However, the improvements in east direction are not obvious.

According to the results of Table 28.3, the positioning accuracy in up direction improves meanly 41, 61 % in north direction and 46 % in up direction with system time offset.

Fig. 28.3 MDBs of GPS/GLONASS in different circumstances without system time offset (Ele = 30°)

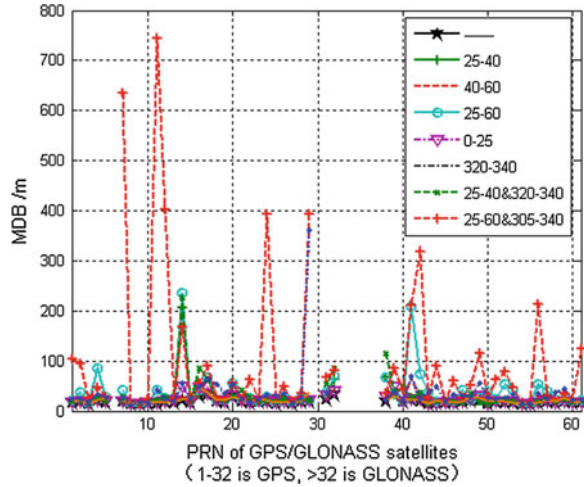


Table 28.2 Positioning accuracy before and after using the system time offset under the elevation of 10°

Shielded azimuth	Positioning error (RMS: m)					
	E (be/af)		N (be/af)		U (be/af)	
–	2.0	2.0	1.2	1.2	1.6	1.5
(25, 40)	2.2	2.2	1.4	1.3	1.7	1.6
(40, 60)	2.4	2.3	1.7	1.6	1.6	1.6
(25, 60)	2.5	2.5	1.9	1.8	1.7	1.7
(0, 25)	2.1	2.1	1.3	1.2	1.6	1.5
(305, 320)	2.3	2.3	1.3	1.3	1.6	1.5
(320, 340)	2.0	2.0	1.3	1.3	1.7	1.6
(40, 60) and (305, 320)	2.7	2.5	1.8	1.7	1.7	1.5
(25, 40) and (320, 340)	2.3	2.3	1.4	1.4	1.9	1.8
(25, 60) and (305, 340)	3.7	3.7	2.1	1.8	1.9	1.9

28.3 Analysis of Integrity on Combined Navigation System with System Time Offset

28.3.1 Method of Improving Integrity with System Time Offset

Currently, there is two ways to improve the integrity of combined navigation system with system time offset. The known system time offset can be used to correct the pseudo-ranges of different navigation systems and then implement the traditional RAIM. The corresponding direction matrix is given by Eq. (28.3). Another way can refer to the paper [8].

Table 28.3 Positioning accuracy before and after using the system time offset under the elevation of 30°

Shielded azimuth	Positioning error (RMS: m)					
	E (be/af)		N (be/af)		U (be/af)	
–	5.3	5.0	4.7	2.5	4.1	3.3
(25, 40)	17.3	6.2	32.2	3.1	20.8	4.9
(40, 60)	6.5	5.5	5.9	2.9	4.4	3.3
(25, 60)	17.4	6.6	32.5	4.3	20.5	3.6
(0, 25)	6.4	5.7	5.3	3.1	4.6	3.8
(305, 320)	9.5	5.4	7.7	2.6	5.2	3.2
(320, 340)	10.1	5.6	6.3	2.8	5.4	3.5
(40, 60) and (305, 320)	13.2	6.0	8.8	3.1	7.8	3.1
(25, 40) and (320, 340)	10.8	6.2	4.4	3.0	4.7	3.7
(25, 60) and (305, 340)	31.7	9.5	18.6	4.7	20.0	4.0

According to the first method, the pseudo-ranges after correction can be expressed as following:

$$\begin{bmatrix} \ell_{G1} \\ \vdots \\ \vdots \\ \ell_{Gn} \end{bmatrix} = \begin{bmatrix} \ell_{G1} \\ \vdots \\ \ell_{Gm} \\ \ell_{Rm+1} \\ \vdots \\ \ell_{Rn} \end{bmatrix} - \begin{bmatrix} 0 \\ \vdots \\ 0 \\ 1 \\ \vdots \\ 1 \end{bmatrix} \ell_T \tag{28.7}$$

ℓ_T is the time offset between GPS and GLONASS system. ℓ_{Gi} represents the GPS pseudo-ranges and ℓ_{Ri} represents that of GLONASS. The left side of this equation is the pseudo-range that correct to the GPST. If \mathbf{v} is position residual, then the test statistic is given as:

$$T = \mathbf{v}^T \mathbf{P}^{-1} \mathbf{v} / \sigma_0^2 \tag{28.8}$$

This statistic is used to test whether there is a bias in the measurements.

28.3.2 Improvements of Fault Detection Ability with System Time Offset

MDB, Minimal Detectable Bias, is the indicator of fault detection ability of integrity for a navigation system. Each satellite correspond a MDB value at each moment which can be obtained with the following equation [9]:

$$MDB_i = \sqrt{\frac{\lambda_0 \sigma_0^2}{(\mathbf{PQ}_V \mathbf{P})_{i,i}}} \tag{28.9}$$

\mathbf{Q}_V and λ_0 can be determined by Eqs. (28.10) and (28.11).

$$\mathbf{Q}_V = \mathbf{P}^{-1} - \mathbf{H}(\mathbf{H}^T \mathbf{P} \mathbf{H})^{-1} \mathbf{H}^T \tag{28.10}$$

$$\chi_{1-P_{FA},f}^2 = \chi_{P_{MD},f,\lambda_0}^2 \tag{28.11}$$

The smaller the computed MDB is, the higher the capability of fault detection. The integrity indexes of non-precision approach are considered. The False Alarm Probability is 1/15,000 and the Miss Detection Probability is 0.001. The UERE of GPS and GLONASS is uniformly taken as 1.4 m.

Figures 28.2 and 28.3 respectively show the MDB curves of GPS/GLONASS satellites when the elevation is 10° and 30° in ten different circumstances without the known system time offsets. The number that is smaller than 33 are GPS satellites and the others are GLOANSS satellites.

Figure 28.4 is the mean curve of MDB difference with and without the system time offset under the elevation of 30°. Figure 28.7 shows the similar results obtained under the elevation of 10°. The results indicate that the difference of MDB without system time offset is relatively greater than that with system time offset.

Figures 28.5 and 28.6 respectively show the MDB curves of GPS/GLONASS satellites when the elevation is 10° and 30° in ten different circumstances with system time offsets. It is obvious that the maximal of MDB reduces with system time offset. And the badly the azimuth are shielded, the notable effect with system time offset.

Fig. 28.4 Mean of difference between MDBs under elevation of 30° and 10° without system time offset

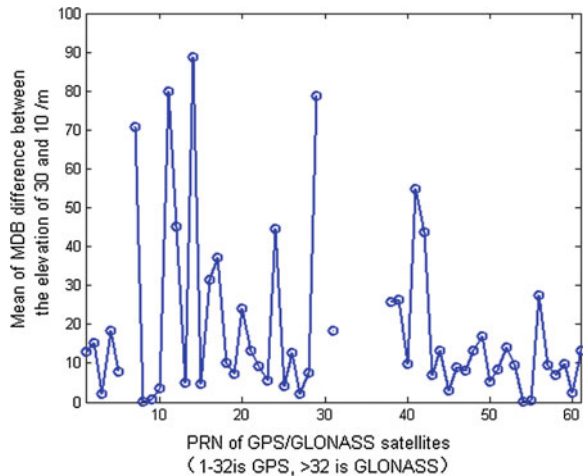


Fig. 28.5 MDBs of GPS/GLONASS in different circumstances with system time offset (Ele = 10°)

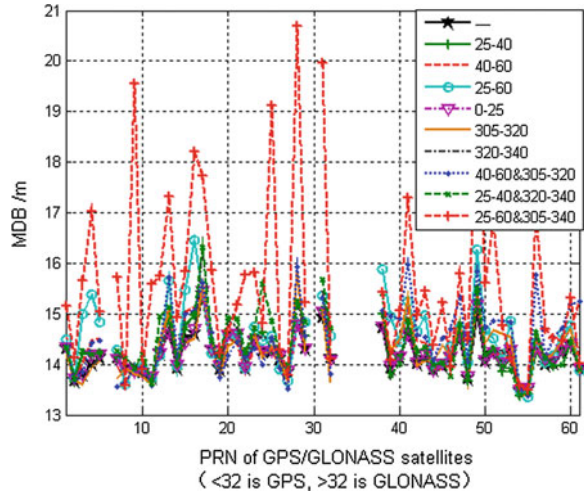
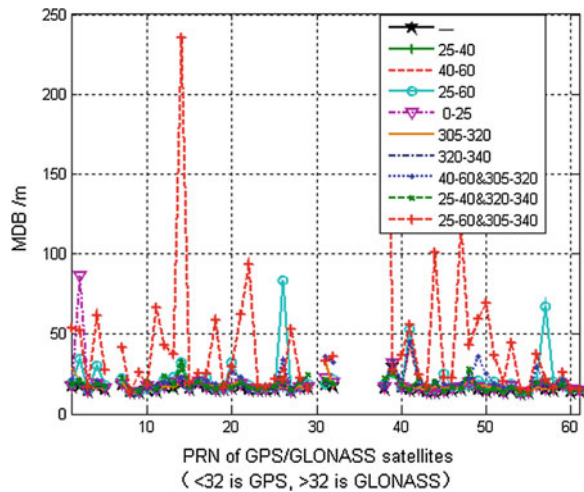
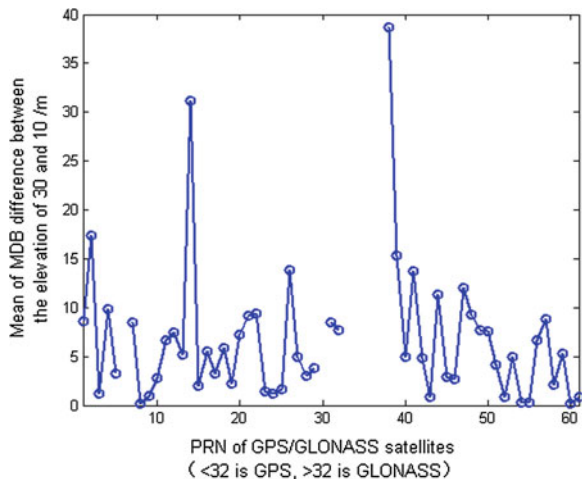


Fig. 28.6 MDBs of GPS/GLONASS in different circumstances with system time offset (Ele = 30°)



All the results show that the use of system time offset indeed improves the capability of fault detection. The application of system time offset mainly reduces the MDBs of GPS satellites by 0.6 m and GLONASS satellites 1.2 m under the elevation of 10°. Besides, the MDBs of GPS satellites mainly decrease 17 m and GLONASS satellites 8.3 m under the elevation of 30° (Fig. 28.7). There is another benefit with the application of system time offset. It reduces the requirement of visible satellites to implement the RAIM.

Fig. 28.7 Mean of difference between MDBs under elevation of 30° and 10° with system time offset



28.3.3 Improvements of Fault Exclusion Ability with System Time Offset

As the only navigation system, one not only can detect fault but also exclude the fault. The coefficients between test statistics reflect the ability of fault exclusion [10, 11]. The coefficient of one-dimension test statistics can be computed as following:

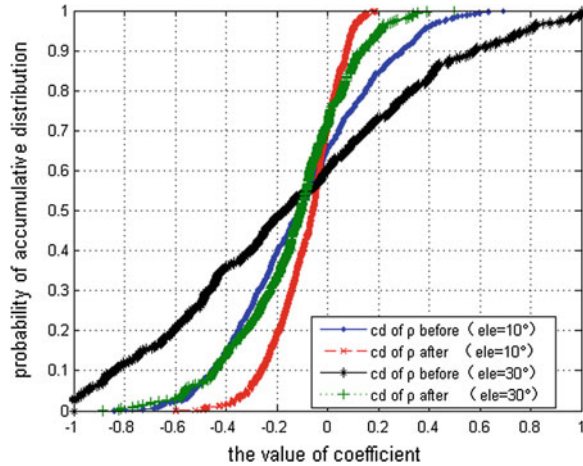
$$\rho_{ij} = \frac{\mathbf{PQ}_V(i,j)\mathbf{P}}{\sqrt{\mathbf{PQ}_V(i,i)\mathbf{P}}\sqrt{\mathbf{PQ}_V(j,j)\mathbf{P}}} \tag{28.12}$$

The smaller the ρ_{ij} is, the weaker the relation between satellites i and j . Therefore, the smaller the ρ_{ij} is, the high ability of fault exclusion.

Figure 28.8 shows the variation of coefficients with and without system time offset in two circumstances. The elevation is 10° and the shielded azimuth is (25, 60) and (305, 340) in the first condition while in the second condition, the elevation is set 30°. The four curves in figure eight demonstrate that the coefficients that nearby zero sharply increase after using the system time offset. This indicate that the use of system time offset improve the distribution of coefficients. The improvements become obvious with the aggravation of the visibility of satellites.

The coefficient meanly decrease 0.13 after the application of system time offset in the first condition and 0.24 in the second condition. Besides, the distribution of coefficients after applying the system time offset is comparative with the coefficient that obtained without the assistant of system time offset.

Fig. 28.8 CDFs of coefficient p before and after using the system time offset in two circumstances



28.4 Conclusions

The paper analyzes the improvements of system time offset on the availability and integrity of combined navigation system. Taken the GPS/GLONASS combined navigation system for example, we have the following conclusions.

Firstly, the application of system time offset can enhance the PDOP value of the combined navigation system. The moments that PDOP is smaller than 6 increases at most 3 h and the service availability enhance maximal 22 % in the worst circumstance.

Secondly, the application of system time offset can improve the positioning accuracy of the combined navigation system. The positioning accuracy in east direction meanly improves 41, 61 % in north direction and 46 % in up direction with the system time offset in the worst condition.

Thirdly, the application of system time offset can advance the ability of fault detection of the combined navigation system. The MDB of GPS satellites averagely reduce 17 m and GLONASS satellites averagely reduce 8.3 m in the setting that elevation is 30° and the azimuth range, (25, 60) and (305, 340), is shielded.

Lastly, the application of system time offset can enhance the ability of fault exclusion of the combined navigation system. The coefficient meanly reduces 0.24 after using the system time offset in the worst circumstance.

All in all, all these conclusions become more rational with the aggravation of limited visibility of satellites. Therefore, it is strongly recommended to apply system time offset in limited visibility of satellites.

References

1. Vanschoenbeek I, Bonhoure B, Boschetti M, Legenne J (2007) CNES, GNSS time offset effects on GPS-Galileo interoperability performance. In: Inside GNSS 60-70, pp 9–10
2. Zhang H, Zhu L, Li X, Zhang X (2013) A method of GNSS system time offset monitoring. In: IEEE international frequency control symposium and European frequency and time forum
3. Kaplan ED, Hegarty CJ (2013) Understanding GPS principles and applications, 2nd edn, vol 3. Publishing House of Electronics Industry, Beijing, p 232
4. Li Z (2012) Research on monitoring and assessment of satellite navigation system performance [D]. University of the PLA Information Engineering (Ch)
5. Knight NL, Wang J (2011) Preciser positioning and timing with the measured time offset. In: International global navigation satellite systems society IGNSS symposium 2011
6. Cai C, Gao Y (2009) A combined GPS/GLONASS navigation algorithm for use with limited satellite visibility. *J Navig* 62:671–685
7. Hu Z (2013) BeiDou navigation satellite system performance assessment theory and Experimental Verification [D]. University of Wuhan (Ch)
8. Xu L, Li X, Xue Y, Cai C, Guo M (2012) System time based RAIM in combined GPS/Beidou navigation system. In: China satellite navigation conference (CSNC) 2012 proceedings LNEE 161, vol 5. Guangzhou, pp 137–144
9. Brown RG, Chin GY (1998) GPS RAIM: calculation of the threshold and protection radius using Chi-Square methods—a geometric approach. In: *Global Positioning System*, vol. 5. The Institute of Navigation, Fairfax, pp 55–178
10. Wang J, Knight NL, Xiaochun L (2011) Impact of the GNSS time offsets on positioning reliability. *J Global Position Syst* 10(2):165–172
11. Hewitson S, Wang J (2006) GNSS receiver autonomous integrity monitoring (RAIM) performance analysis. *GPS Solution* 10(3):155–170

Chapter 29

Modeling and Multi-state Analysis for Availability of a Navigation Monitor Network

Zhuopeng Yang, Feng Xue, Jinjing Wang and Heng Zheng

Abstract For characteristics of reliability, maintainability, supportability and multi-state about a navigation monitor network under real environment, Petri net (PN) and Bayesian network (BN) are applied integrated to availability modeling and analysis of a navigation monitor network in this paper. The relationship of equipments and MTBF, MTTR, MADT, sufficiency, MSRT of spaces are combined for availability modeling of monitor stations by PN. According to normal, degraded and failed states of monitor stations, availability modeling of the monitor network are obtained by BN. By analysis, nominal availability, degraded availability and failed state probability of the monitor network and weakness of monitor stations are confirmed. The multiple schemes are proposed and compared for improving availability. The result shows, improving sufficiency plays a more role in improving availability under real environment, and this method can be used for availability modeling and analysis.

Keywords Availability · Multi-state · Petri net · Bayesian network

29.1 Introduction

The navigation monitor network plays an important role in a satellite navigation system, and its working states have close relationship with user services performance. Availability is a measure of the degree to which a navigation monitor network is in an operable state and can be committed at the start of a mission when

Z. Yang (✉) · J. Wang · H. Zheng
China Academy of Aerospace Standardization and Product Assurance,
Beijing 100071, China
e-mail: yangzhuopeng88@163.com

F. Xue
Beijing Global Information Center of Application and Exploitation,
Beijing 100094, China

the mission is called for at an unknown (random) point in time, and it is a key parameter about working states of the navigation monitor network.

There exist some interesting papers about navigation monitor networks. The history and tendency of monitor stations are introduced in [1]. The function and structure of monitor stations are described in [2, 3] and [4]. The distribution of monitor stations and their failed effects on services performance are analyzed in [5]. But papers considering reliability, maintainability, supportability (RMS), and state probability analysis (normal availability, degraded availability and failed state probability) of navigation monitor networks, have not been presented.

In view of the issues discussed above, Petri net (PN) and Bayesian network (BN) are proposed for availability modeling and analysis of a navigation monitor network in this paper. By analysis, the weakness of monitoring stations is confirmed, and the multiple schemes are put forward and compared for improving availability.

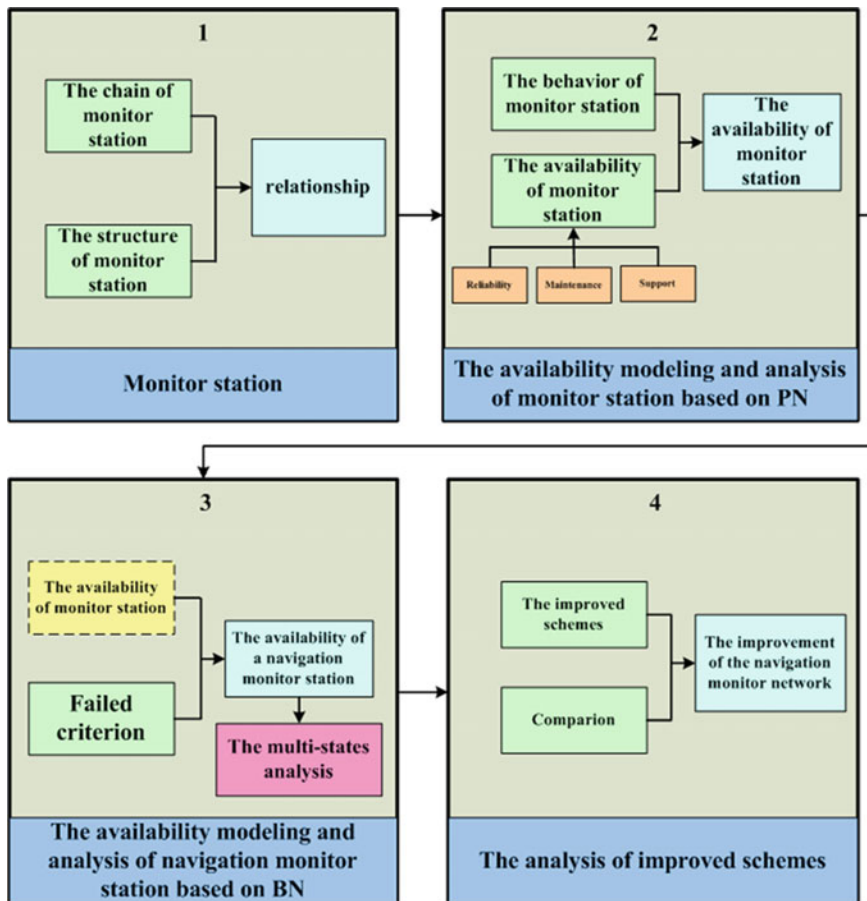


Fig. 29.1 The flow chart of modeling and analysis for a navigation monitor network

29.2 The Organization of Modeling and Analysis

The availability of a navigation monitor network is influenced by RMS of equipments, the working states of monitor stations, the combinations of faults and distribution of monitor stations. There is a complicated network relationship among monitor stations. On the one hand, there is a ‘normal—fault—administrative delay time—waiting spares—restoration’ sequential relationship, which can be described by process definition language, in monitor stations. On the other hand, due to the fault of monitor stations, there is a multi-state and network relationship, which can be modeled by network method, in monitor network.

PN is a typical process definition language for asynchronous and concurrent system, and BN is a method for describing uncertainty relation, multi-state and dependent failure. Therefore, PN and BN are applied respectively to availability model and analysis of monitor stations and the navigation monitor network in this paper. The organization of modeling and analysis is shown in Fig. 29.1.

29.3 Availability Modeling and Analysis of a Navigation Monitor Network

29.3.1 Data Chains of a Monitor Station

According to update frequencies and data paths, the chains of a monitor station can be divided into navigation chain and integrity chain [6, 7]. The navigation chain, which calculates satellite ephemeris and clock error, consists of monitoring receivers, data fusion facilities, receiving and pretreatment facilities, orbit and synchronisation processing facilities. Its update time is 10 min. The integrity chain, which analysis and compares integrity data, includes monitoring receivers, data fusion facilities, message generation facilities, wide area difference and integrity validation facilities. Its update time is 1 s.

29.3.2 Availability Modeling and Analysis of a Monitor Station Based on PN

29.3.2.1 Behavior of a Monitor Station

The working states of a monitor station is decided by state of each chain, without considering a common cause failure due to power supply system, giving time system and inner communications network. The behavior of a monitor station can be divided into system behavior and chain behavior, as shown in Fig. 29.2.

Fig. 29.2 Description of a monitor station

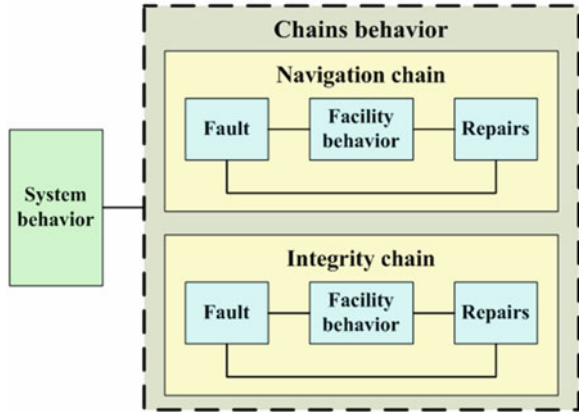
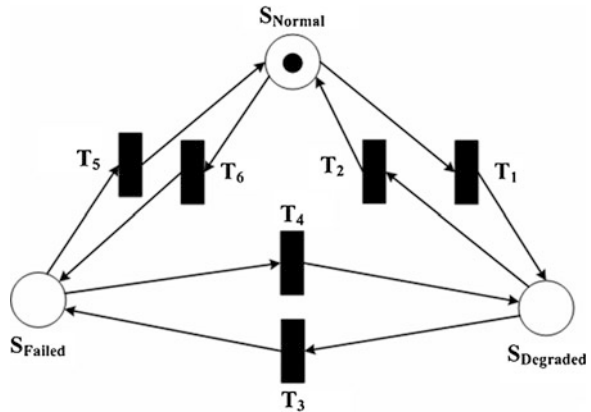


Fig. 29.3 Behavior of a monitor station



Defining the failure criterion of a monitor station:

- Normal state: both chains are in normal
- Degraded state: only one chain is failed
- Failed state: both chains are failed.

The parameters of a monitor station states are classified as: normal availability, degraded availability, and failed states probability. Figure 29.3 shows the transforms about states based on PN. In Fig. 29.3, places S_{Normal} , $S_{Degraded}$ and S_{Failed} (drawn by a circle) model states, token (drawn by a black dot) represents value, and T_n ($n = 1, 2, \dots, 6$), which are triggered by each chain, are immediate transitions.

29.3.2.2 Availability Modeling and Analysis of a Chain

The maintenance and support procession consists of Mean Time To Restoration (MTTR), Mean Logistics Delay Time (MADT), sufficiency and Mean Supply Response Time (MSRT) of spares, as illustrated in Fig. 29.4. In Fig. 29.4, places P_{Normal} and P_{Failed} are states, T_{MADT} is MADT, $T_{SS}(T_{SS} = f)$ is sufficiency of spares, $T_{USS}(T_{USS} = 1 - f)$ is percentage of spares, T_{MSRT} is MSRT, and T_{MTTR} is MTTR.

When the maintenance and support delay rate μ_{Sum} is considered to follow an exponential distribution, it is expressed as follows:

$$\mu_{Sum} = \frac{1}{T_{MADT} + (1 - f) \times T_{MSRT} + T_{MTTR}} \tag{29.1}$$

Taking into account facilities and their data, the availability of a chain is modeled, as shown in Fig. 29.5. In Fig. 29.5, $T_{Sum} = 1/\mu_{sum}$ is maintenance and support delay, and T_{MTBFn} , ($n = 1, 2, 3, 4$) is MTBF of each facility respectively.

When the time-to-failure and time-to-repairs of facility follows an exponential distribution ($T_{MTBFn} = 1/\lambda_n$, $n = 1, 2, 3, 4$), the fault rate and repair rate of a chain can be calculated by the following formula.

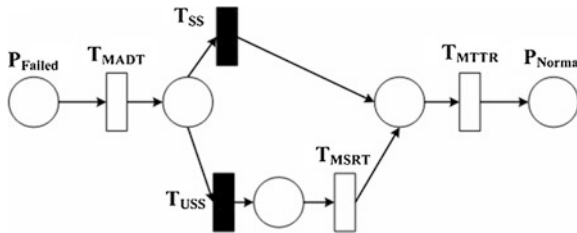
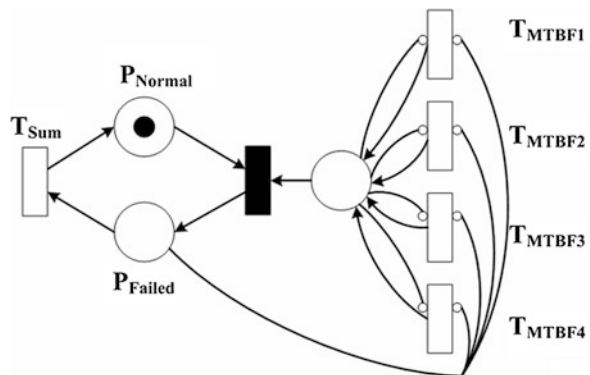


Fig. 29.4 Maintenance and support of a chain

Fig. 29.5 Availability model of a chain based on PN



$$\begin{cases} \lambda_{Total} = \lambda_1 + \lambda_2 + \lambda_3 + \lambda_4 \\ \mu_{Total} = \mu_{Sum} \end{cases} \quad (29.2)$$

The instantaneous availability and steady-state availability can be given.

$$A_{chain}(t) = \frac{\mu_{Total}}{\lambda_{Total} + \mu_{Total}} + \frac{\lambda_{Total}}{\lambda_{Total} + \mu_{Total}} e^{-(\lambda_{Total} + \mu_{Total})t} \quad (29.3)$$

$$A_{chain}(\infty) = \frac{\mu_{Total}}{\lambda_{Total} + \mu_{Total}} \quad (29.4)$$

29.3.2.3 Availability Modeling and Analysis of a Monitor Station

Figure 29.6 shows the availability model of a monitor station. As can be seen from Fig. 29.6, $T_{MTBFij}(i = 1, 2; j = 1, 2, 3, 4)$ is MTBF of each facility.

The initial condition of Petri network, as shown in Fig. 29.6, is:

$$\begin{aligned} &(S_{Normal}, S_{Degraded}, S_{Failed}, S_0, S_1, P_{Normal1}, P_{Failed1}, P_{11}, P_{Normal2}, P_{Failed2}, P_{21}) \\ &= (1, 0, 0, 0, 0, 1, 0, 0, 0, 1, 0, 0) \end{aligned} \quad (29.5)$$

And there is three tokens represent the states of system and chains, thus

$$S_{Normal} + S_{Degraded} + S_{Failed} = 1 \quad (29.6)$$

$$P_{Normal1} + P_{Failed1} = 1 \quad (29.7)$$

$$P_{Normal2} + P_{Failed2} = 1 \quad (29.8)$$

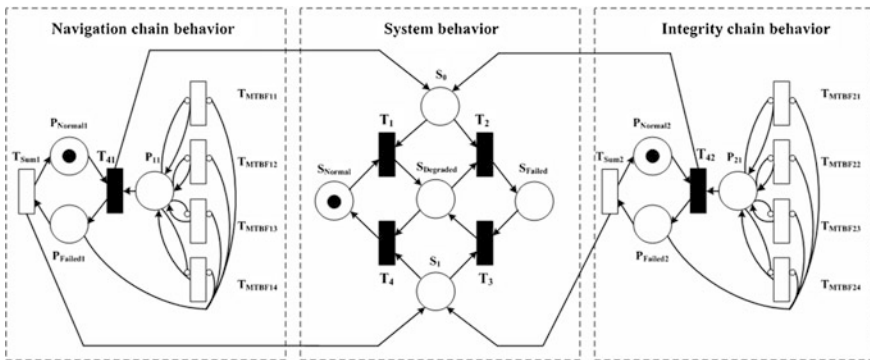


Fig. 29.6 Availability model of a monitoring station based on PN

The normal availability, degraded availability and failed state probability can be expressed.

$$P(M_{Normal}) = P(S_{Normal}) \quad (29.9)$$

$$P(M_{Degraded}) = P(S_{Degraded}) \quad (29.10)$$

$$P(M_{Failed}) = P(S_{Failed}) \quad (29.11)$$

where $P(\cdot)$ is probability, and M_{Normal} , $M_{Degraded}$ and M_{Failed} represent states of a monitor station. Moreover the following relationship can be obtained.

$$P(M_{Normal}) + P(M_{Degraded}) + P(M_{Failed}) = 1 \quad (29.12)$$

29.3.3 Availability Modeling and Analysis of a Navigation Monitor Network Based on BN

29.3.3.1 Failure Criterion and Availability Modeling of a Navigation Monitor Network

The navigation monitor network is composed of several monitor stations, and there is a complicated relationship among them.

Referring to Galileo system, the failure criterion of the navigation monitor network is defined as:

- Normal state: all the monitor stations are in normal, or only one monitor station is on degraded state.
- Degraded state: only one monitor station is failed, or any two monitor stations are degraded simultaneously.
- Failed state: two or more monitor stations are failed simultaneously, or any three or more monitor stations are degraded, or more than one (including) monitor station is failed and more than one (including) monitor station is degraded simultaneously.

The availability model is established based on BN, as shown in Fig. 29.7. The root nodes represent the monitor stations (basic events) which input values are $P(M_{Normal})$, $P(M_{Degraded})$ and $P(M_{Failed})$. The leaf node represents the navigation network, which the input value is from failure criterion of a navigation monitor network. The output value of leaf node is different state values. In this paper, 8 monitor stations are selected and named as M_i , $i = 1, 2, \dots, 8$.

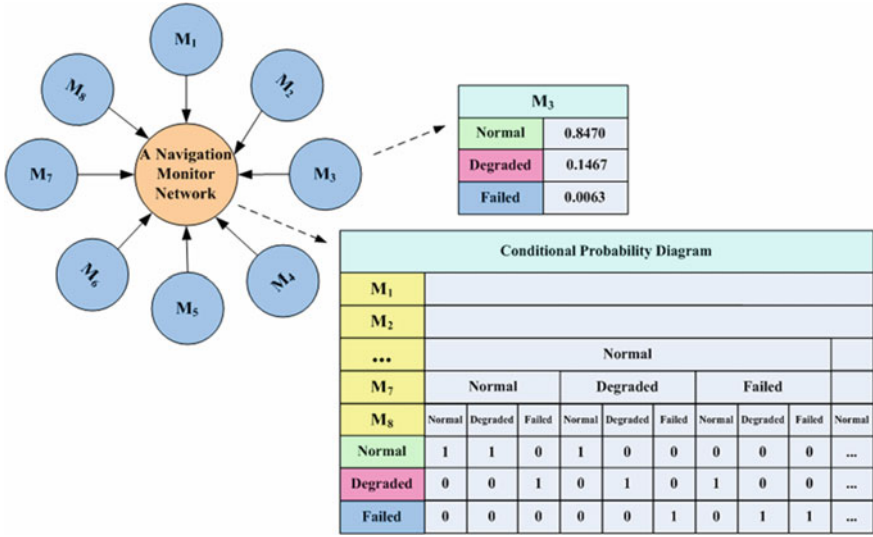


Fig. 29.7 Availability model of a navigation monitor network based on BN

29.3.3.2 Multi-state and Weakness Analysis

According to the rules of BN [8, 9], the state values can be calculated.

$$\begin{aligned}
 &P(N_{Normal}, M_1, M_2, M_3, M_4, M_5, M_6, M_7, M_8) \\
 &= P(N_{Normal} | M_1, M_2, M_3, M_4, M_5, M_6, M_7, M_8,) \quad (29.13) \\
 &\quad \times P(M_1) \cdot P(M_2) \cdot P(M_3) \cdot P(M_4) \cdot P(M_5) \cdot P(M_6) \cdot P(M_7) \cdot P(M_8)
 \end{aligned}$$

$$\begin{aligned}
 &P(N_{Degraded}, M_1, M_2, M_3, M_4, M_5, M_6, M_7, M_8) \\
 &= P(N_{Degraded} | M_1, M_2, M_3, M_4, M_5, M_6, M_7, M_8,) \quad (29.14) \\
 &\quad \times P(M_1) \cdot P(M_2) \cdot P(M_3) \cdot P(M_4) \cdot P(M_5) \cdot P(M_6) \cdot P(M_7) \cdot P(M_8)
 \end{aligned}$$

where N_{Normal} is normal state and $N_{Degraded}$ is degraded state.

Assuming the failed of the navigation monitor network has been observed, the posterior probability of M_i ($i = 1, 2, \dots, 8$) can be calculated by the following formula.

$$P(M_{iDegraded} | N_{Failed}) = \frac{P(N_{Failed} | M_{iDegraded})P(M_{iDegraded})}{P(N_{Failed})} \quad (29.15)$$

$$P(M_{iFailed} | N_{Failed}) = \frac{P(N_{Failed} | M_{iFailed})P(M_{iFailed})}{P(N_{Failed})} \quad (29.16)$$

Table 29.1 Data of M_1

Facility	MTBF (h)	MTTR (h)	MADT (h)	f	MSRT (h)
Monitoring receiver	1500	2	3	0.8	65
Data fusion facility	580	2	3	0.8	65
Orbit and synchronisation processing facility	620	2	3	0.8	65
Wide area difference and integrity validation facility	550	1.5	5	0.8	68
...

Fig. 29.8 Multi-state availability of M_1 , **a** the general drawing, **b** normal state, **C** degraded and failed states

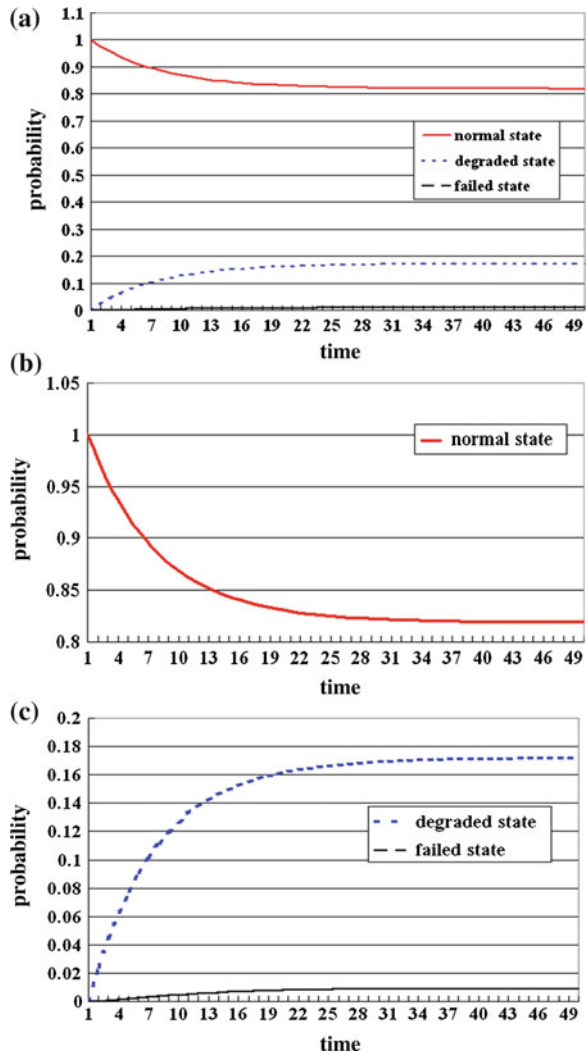


Table 29.2 Multi-state availability of monitor stations

No.	Normal state (%)	Degraded state (%)	Failed state
M ₁	81.91	17.19	0.0090
M ₂	84.36	14.97	0.0067
M ₃	84.70	14.67	0.0063
M ₄	82.87	16.34	0.0079
M ₅	81.51	17.55	0.0094
M ₆	84.76	14.61	0.0063
M ₇	82.61	16.56	0.0083
M ₈	83.23	16.01	0.0076

Table 29.3 Multi-state availability of a navigation monitor network

Time slices	Normal state (%)	Degraded state (%)	Failed state
0	100	0	0
5	88.94	6.39	0.0467
10	75.07	12.44	0.1249
15	67.69	14.90	0.1741
20	64.00	15.94	0.2006
25	62.17	16.40	0.2143
30	61.25	16.62	0.2213
35	60.78	16.73	0.2249
40	60.56	16.78	0.2266
45	60.43	16.81	0.2276
50	60.38	16.82	0.2280

29.3.4 Improvement Schemes

Taking Eqs. (29.1) and (29.2) into (29.4), and defining $\lambda_{Total} = 1/T_{MTBF}$, we get

$$A_{chain}(\infty) = \frac{T_{MTBF}}{T_{MTBF} + T_{MADT} + (1 - f) \times T_{MSRT} + T_{MTTR}} \tag{29.17}$$

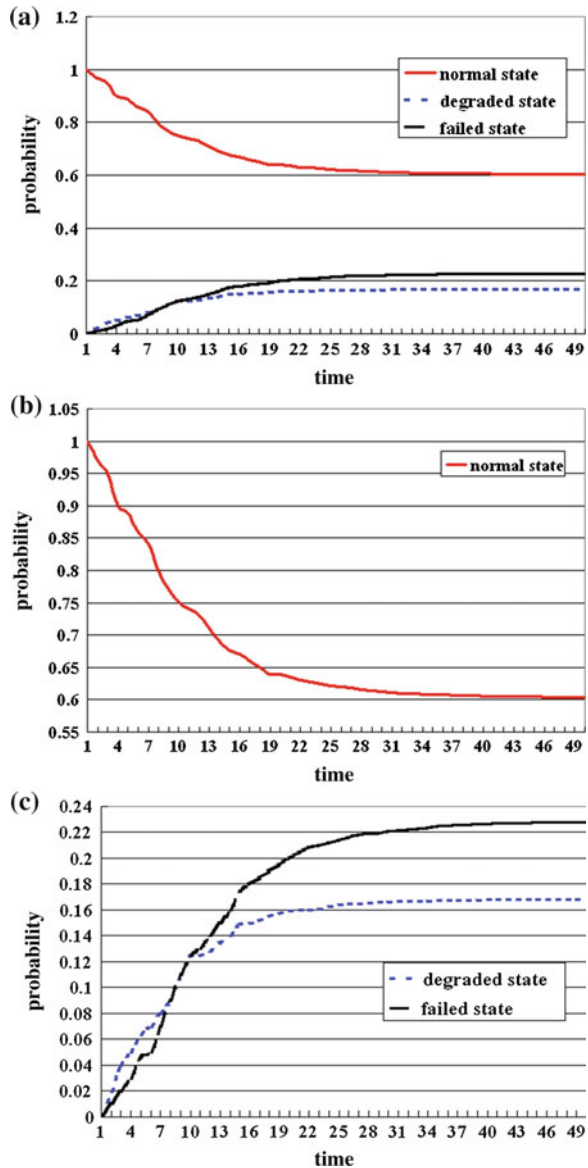
It is shown from Eq. (29.17), T_{MTBF} has little affect on availability due to presenting itself on numerator and denominator simultaneously. Generally, the values of T_{MTTR} and T_{MADT} are small (less than 5 h), and also as T_{MTBF} . T_{MSRT} is related to the transportations of spares, and its value normally big (more than 24 h), thus availability can be improved by f .

29.4 Case Study

According to actual survey and simulation of monitor stations, and supposing sufficiency of spares is same, the data of M_1 are given in Table 29.1.

The availability of a monitor station is modeled through the data of Table 29.1. Figure 29.8 shows the multi-state availability of M_1 during 50 time slices.

Fig. 29.9 Multi-state availability of the navigation monitor network, **a** the general drawing, **b** normal state, **c** degraded and failed states



Similarly, availability of other monitor stations can be calculated. The availability at the 50th time slice is shown in Table 29.2. Table 29.3 shows multi-state availability of the navigation monitor network every 5 time during 50 time slices.

Figure 29.9 shows the multi-state availability of the navigation monitor network during 50 time slices.

Comparing Figs. 29.8 and 29.9, it is shown that availability of any monitor station is more than the navigation monitor network due to rigorous failure criterion. Figure 29.9 shows availability is decreasing with time. The availability is descended observably at beginning and kept smooth which is about 60.4 % at end. Different from the relationship $P(M_{Degraded}) > P(M_{Failed})$ of each monitor station, $P(M_{Degraded}) < P(M_{Failed})$ of the navigation monitor network from the 10th time slice.

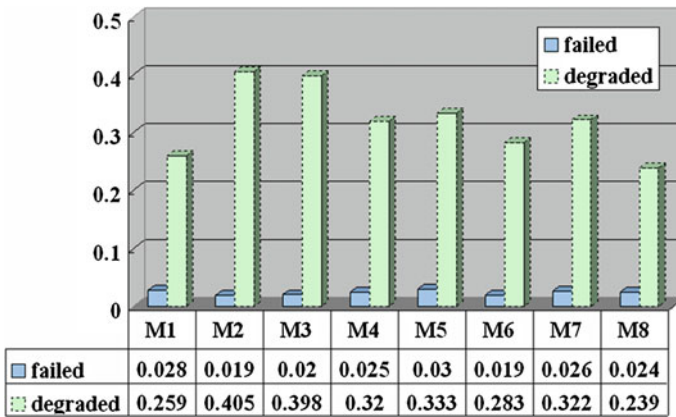


Fig. 29.10 State probability of each monitor station

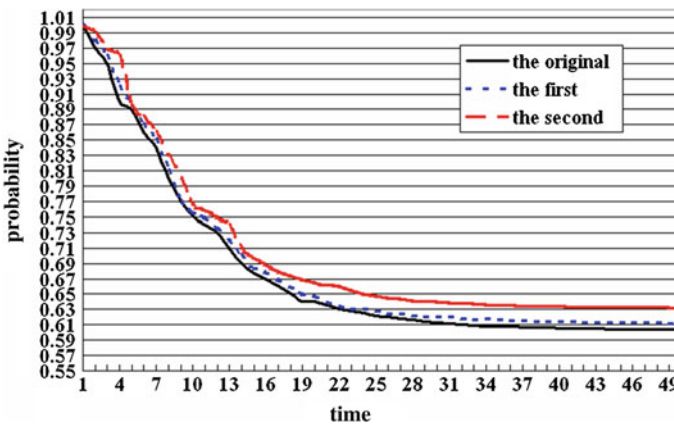
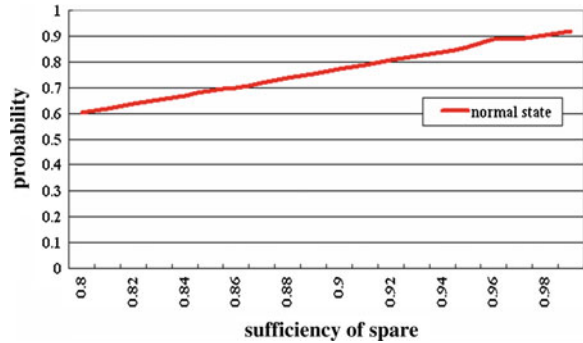


Fig. 29.11 Availability of different schemes

Fig. 29.12 Availability under different spares sufficiency



When there is failed of the navigation monitor network, failed and degraded state probability of each monitor station can be calculated, as is shown in Fig. 29.10.

Figure 29.10 shows, the failed state probability sequence of the first five monitor stations is $M_5 > M_1 > M_7 > M_4 > M_8$, and the degraded state probability sequence is $M_2 > M_3 > M_5 > M_7 > M_4$. Thus, it is determined that M_5 is the weakness of monitor stations.

Two schemes for M_5 are put forward and compared to improve the availability. The first scheme is increasing MTBF of facilities by 5%. Renew computing, the result shows the availability of M_5 raising 3.3%, and the navigation monitor network raising 1.4% at the 50th time slice. The second scheme is increasing sufficiency of spares by 5%. Renew computing, the result shows the availability of M_5 raising 11.8%, and the navigation monitor network raising 4.7% at the 50th time slice. It is known that sufficiency of spare play a more important role than MTBF. Figure 29.11 shows availability of original, the first and the second scheme during 50 time slices.

In this paper, the sufficiency of spare (f) is equal to 0.8, but according to engineering experience, sufficiency of spare is normally between 0.80 and 0.99. Thus, availability of the navigation monitor network can be improved by increasing f , as is shown in Fig. 29.12.

In Fig. 29.12, there exists a directly proportional relationship between sufficiency of spare and availability, when $f \geq 0.92$, then $P(N_{Normal}) \geq 80\%$, when $f \geq 0.98$, then $P(N_{Normal}) \geq 90\%$.

29.5 Conclusions

BN and PN have been applied together to modeling and analysis for availability in this paper.

- (1) Multi-level modeling of availability. Combing reliability, maintainability, and supportability, instantaneous and steady-state availability of a monitor station are calculated based on PN. The availability of the navigation monitor network

is modeled based on BN, and normal, degraded, and failed state probability are obtained.

- (2) Confirming the weakness. By diagnosis, the weakness of monitor stations is confirmed using BN.
- (3) Improving and comparing. Two schemes are approved for improving availability. The result shows: sufficiency of spare plays a more important role than MTBF under the same condition for improving availability.

References

1. Harker RM, Nelson ZK Jr (1999) GPS ground control network modernization. In: ION NTM 1999, San Diego, pp 101–107
2. Lucas R, Hahn JH, Dinwiddy S et al (2000) Galileo space and ground segment definition: system and performance. In: ION GPS 2000, Salt Lake City, UT, pp 19–22
3. Lugert M, Falcone M, Brough M et al (2000) The GalileoSat ground segment architecture concept and operational approach. In: ION GPS 2000, Salt Lake City, UT, pp 19–22
4. Payne C, Toribio S (2005) The Galileo ground control segment: controlling the constellation. In: The European navigation conference GNSS 2005. Munich, Germany, 19–22 July 2005
5. Stanton BJ, Strother R (2007) Analysis of GPS monitor station outages. In: ION GNSS 2007, Fort Worth, TX, pp 176–183, 25–28 Sept 2007
6. Quiles A, Schlarman BK, Ballereau A et al (2009) Development and verification of Galileo ground mission segment (GMS). In: ION 22nd international meeting of the satellite division, Savannah, GA, pp 2980–2989
7. Blomenhofer H, Ehret W, Leonard A (2004) GNSS/Galileo global and regional integrity performance analysis. In: ION 2004
8. Jensen FV (2001) Bayesian networks and decision graphs. Springer, New York, pp 18–28
9. Van der Gaag LC (1996) Bayesian belief networks: odds and ends. *Comput J* 39:97–113

Chapter 30

A GNSS Multipath Detecting Method Based on Antenna Arrays

Min Li, Wei Zhao, Liang Yuan and Qinli Liu

Abstract Although most GNSS monitoring stations located in open and clear places, multipath effects by surrounding environment could not be avoided, which leads to severely degraded observations of GNSS monitoring stations. This paper proposed a multipath detecting method based on antenna arrays, benefiting from different arriving angles of the multipath signal and the satellite signal. This method firstly computes the arriving angle of the satellite signal based on prior information such as satellite ephemeris, the coordinate of the monitoring station, etc. Then the steering vector of the satellite signal is obtained referring to the relative position of the array element. We design the array weights according to the steering vector, so as to minimize the satellite signal power of the array output. Therefore, if there is multipath in the received signal, the correlation peak could be detected in the array output, otherwise could not be detected. So we connect the array output to a GNSS receiver. When the receiver gives out observations such as pseudo-ranges and carrier phases, we predicate multipath to be existed in the received signal. When the receiver is not able to capture the satellite signal, there is no multipath which could affect the observations. Simulations based on software receiver show that the proposed method is able to detect multipath in the received signal quickly and effectively. The results could be used either in evaluating the signal quality of the monitoring stations, or in eliminating the multipath.

Keywords GNSS · Monitoring station · Antenna array · Array weights · Multipath detecting

M. Li (✉) · W. Zhao · L. Yuan · Q. Liu
Beijing Satellite Navigation Center, Beijing 100094, China
e-mail: limin_nudt@126.com

© Springer-Verlag Berlin Heidelberg 2015
J. Sun et al. (eds.), *China Satellite Navigation Conference (CSNC) 2015
Proceedings: Volume I*, Lecture Notes in Electrical Engineering 340,
DOI 10.1007/978-3-662-46638-4_30

319

30.1 Introduction

Although most GNSS monitoring stations located in open and clear places, multipath effects by surrounding environment could not be avoided, which leads to severely degraded observations of GNSS monitoring stations. Multipath detection performed in the monitoring station, which assists GNSS system to determine the quality of observations in the station, has significant meaning in improving the service performance of GNSS systems. For example, GPS system use the observations from multiple stations and ionosphere correcting module, GPS precise orbit calculating module, GPS satellite clock correcting module to determine the integrity of each satellite and differential information. If observations affected by multipath can be effectively detected in GPS monitoring stations and taken into account in the integrity determination process, then the accuracy of integrity determination could be improved obviously.

Currently, the multipath detecting methods could be divided into three categories: The first category operates multiple correlations to obtain a complete correlation function curve [1–3], and multipath signal parameters are determined according to the shape of the correlation function curve; The second category combines multi-frequency pseudoranges or carriers to detect and evaluate the multipath signals [4, 5]; The third category uses multiple antennas (antenna array) to form a directional beam to the satellite signal and suppress the multipath, for example [6] designed a multipath detection and correction system composed by a parabolic antenna, an omnidirectional multipath-suppressing antenna and a 16-element antenna array, and compared the observations of the monitoring station and the correction system to evaluate the multipath environment of the monitoring station.

Considering the multipath signals and the satellite signals reach the receiving antenna from different angles, this paper proposed a new multipath detecting method based on antenna arrays. Different from the conventional method which points the main beam of the antenna array to the satellite signal, this method points the “nulling” of the antenna array to the satellite signal, thereby eliminating satellite signal in the received signal, and then detects the correlation peak of the array output to determine the presence or absence of the multipath signal.

30.2 Multipath Signal Model

30.2.1 Received Signal of Single Antenna

Suppose there's only one receiving antenna in the monitoring station. It receives a signal $r(t)$ composed by the direct signal $s(t)$, the multipath signal $m(t)$, noise and interference. Received signal gets through the antenna, the low noise amplifier and the down-converter, leads to the baseband form which is [7] (noise and interference are ignored here):

$$\begin{aligned}
 r(t) &= s(t) + \sum_{n=1}^N m_n(t) \\
 &= \alpha_0 e^{-j\phi_0} x(t - \tau_0) e^{-j2\pi f_c \tau_0} + \sum_{n=1}^N \alpha_n e^{-j\phi_n} x(t - \tau_n) e^{j2\pi f_n t}
 \end{aligned} \tag{30.1}$$

where,

$x(t)$ is the complex envelope of the navigation signal;

f_c is the carrier frequency;

f_n is the reflected frequency of multipath relative to carrier frequency;

α_0 is the amplitude of the direct signal;

α_n is the amplitude of the n-th multipath signals;

τ_0 is the propagation delay of the direct signal;

τ_n is the propagation delay of the n-th multipath signal;

Φ_0 is the carrier phase of the direct signal;

Φ_n is the carrier phase of the n-th multipath signals

When the relative movement of the satellite, scattering body and the receiver is different from the relative movement between the satellite and the receiver, Doppler shift of the multipath signal is different from the direct signal; however, when the Doppler shift difference is quite large (greater than the reciprocal of the coherent correlating accumulation time), the received multipath signal and the direct signal is substantially uncorrelated, so it is not correlated to local reference signal which is tracking the direct signal. Therefore f_n is often ignored, and the amplitude, delay and carrier phase of the multipath signal are focused.

When the multipath delay is large (for example, BPSK modulated signal, multipath delay is greater than twice of the symbol period), it is easy for the receiver to resolve the multipath. As long as the receiver is tracking the direct signal (always arrives earlier than any multipath), then the multipath is resolvable. However, the arrival time of the multipath may be a little shorter than the direct signal (e.g. tens or hundreds of nanoseconds), then the correlation function of the local signal and the direct signal plus the multipath signal is distorted, and also leads to the distortion of composed phase of the received signal, thus introducing errors in the pseudo-range and carrier phase observations.

30.2.2 Received Signal of Antenna Array

The element spacing of antenna array is usually set to half of the carrier wavelength. For the K-element antenna array, select one of the elements as a reference element. Compared to the signal received by the reference element, the received signal of the k-th element (the k-th signal) arrives just a few tenths of nanoseconds earlier or later, but the carrier phase difference between them could not be ignored. Thus, the

received satellite signal of the antenna array (the direct signal) can be represented by a K-dimension vector:

$$\begin{bmatrix} s(t) \\ s(t)e^{j\theta_2} \\ \vdots \\ s(t)e^{j\theta_K} \end{bmatrix} = \begin{bmatrix} 1 \\ e^{j\theta_2} \\ \vdots \\ e^{j\theta_K} \end{bmatrix} s(t) = \mathbf{a}_0 s(t) \quad (30.2)$$

where, \mathbf{a}_0 is called the steering vector of the direct signal, which could be calculated based on prior information such as the antenna array geometry, the elevation and azimuth of the satellite signal [8].

Similarly, take \mathbf{a}_n as the steering vector of the n-th multipath signal, then the direct signal plus multipath signal received by the antenna array is:

$$\mathbf{r}(t) = \mathbf{a}_0 s(t) + \sum_{n=1}^N \mathbf{a}_n m_n(t) \quad (30.3)$$

In the above formula, the steering vector of the multipath signal \mathbf{a}_n is not calculable, because the arrival direction of the multipath signal is not only related to the complex environment, but also closely related to the satellite motion. When the orientation of the satellite to the antenna of the monitoring station is changed, the number and direction of the multipath signals are very likely to change.

30.3 Multipath Detecting Method Based on Antenna Arrays

The architecture of the antenna array receiver is shown in Fig. 30.1. K received signals of the antenna array get through the RF front end and to an intermediate frequency, then converted by A/D samplers into digital signals.

Within each satellite signal channel, the carriers of the K received signals are simultaneously wiped off, and weighted in baseband. The summation of the weighted signals is formed into the array output signal, which is fed into the correlator acquisition and tracking, then we can measure the pseudo-code phase and carrier phase.

The traditional antenna array adjusts the weights to form a main beam towards the satellite signal. The multipath detecting method proposed by this paper is just the contrary. It forms a “nulling” in the direction of the satellite signal to eliminate the received satellite signal, so as to determine whether there’s multipath in the received signal.

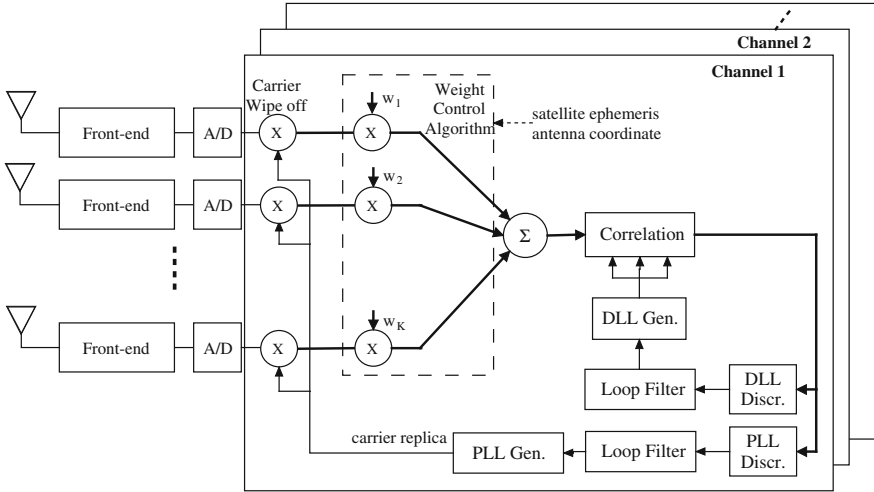


Fig. 30.1 Architecture of antenna array receiver

Assuming the vector of the array weight is \mathbf{w} :

$$\mathbf{w} = [w_1, w_2, \dots, w_K]^T \tag{30.4}$$

Then, based on the above architecture of the antenna array receiver, the output signal after weighted by \mathbf{w} and summed can be expressed as:

$$y(t) = \mathbf{w}^T \mathbf{r}(t) = \mathbf{w}^T \mathbf{a}_0 s(t) + \sum_{n=1}^N \mathbf{w}^T \mathbf{a}_n m_n(t) \tag{30.5}$$

Choose a weighting vector to minimize the power of the satellite signal, which means the array weight \mathbf{w} satisfies:

$$\min_{\mathbf{w}} \mathbf{w}^T E[\mathbf{a}_0 s(t) s^*(t) \mathbf{a}_0^H] \mathbf{w}^* = \min_{\mathbf{w}} \mathbf{w}^T \mathbf{R}_{ss} \mathbf{w}^* \tag{30.6}$$

where \mathbf{R}_{ss} represents the array autocorrelation matrix of the satellite signal.

Then, the main part of the array output $y(t)$ is the multipath. If the receiver is able to capture the satellite signal, it proves the existence of multipath in the current received signal; if the receiver is failed to capture the satellite signal, it proves that multipath does not exist in the current received signal, even if there is multipath, the power of the multipath is too weak to affect the observations of the receiver.

Take dual-element array ($K = 2$) for example. Assume that based on prior information such as satellite ephemeris, antenna coordinate of each element, we calculate the steering vector of the satellite signal:

$$\mathbf{a}_0 = \begin{bmatrix} 1 \\ e^{j\theta_2} \end{bmatrix} \quad (30.7)$$

Take the array weight vector is:

$$\mathbf{w} = \begin{bmatrix} -1 \\ e^{-j\theta_2} \end{bmatrix} \quad (30.8)$$

Substituting formulas (30.7) and (30.8) into formula (30.5), the array output signal can be obtained as follows:

$$\begin{aligned} y(t) &= \mathbf{w}^T \mathbf{a}_0 s(t) + \sum_{n=1}^N \mathbf{w}^T \mathbf{a}_n m_n(t) \\ &= \sum_{n=1}^N \mathbf{w}^T \mathbf{a}_n m_n(t) \end{aligned} \quad (30.9)$$

It can be seen that only the multipath signal $m_n(t)$ is left in the array output signal. When the amount of the multipath signals $N = 1$, one can estimate the strength, delay and phase of the multipath according to CNR, pseudo-range and carrier phase measurements; When the amount of the multipath signals $N > 1$, the parameter of N multipath signals is difficult to estimate, but still very easy to determine the presence of multipath, which means multipath detection is not a problem in any case.

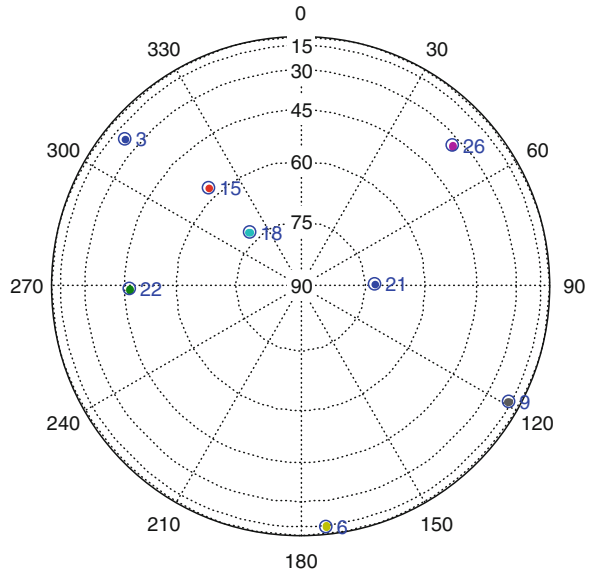
30.4 Simulations

Consider the following typical scenario of navigation signals: There are 8 visible GPS satellites: SVN45, SVN47, SVN15, SVN54, SVN26, SVN36, SVN39 and SVN33. The corresponding pseudo-random sequence numbers (PRN) were 21, 22, 15, 18, 26, 6, 9 and 3. The plot of visible satellites is shown in Fig. 30.2.

Based on the software-defined GPS receiver [9], we verified the multipath detection method proposed in this paper. Receiver IF frequency is 9.548 MHz, A/D sampling frequency is 38.192 Msps, and the number of quantization bits is 4 bits. The antenna array adopts the most simple dual-element antenna array, spacing by half of the carrier wavelength. According to the array signal model in Sect. 30.2.2, regardless of array channel mismatch, the amplitude of the two signals received by the antenna is equal, and there's only carrier phase difference between the two signals.

Based on the above scenario, one multipath signal and N multipath signals ($N > 1$) were added separately for satellite PRN21. We examined the multipath affect on pseudo-range measurements, and the multipath detecting results based on the antenna array.

Fig. 30.2 Plot of visible satellites



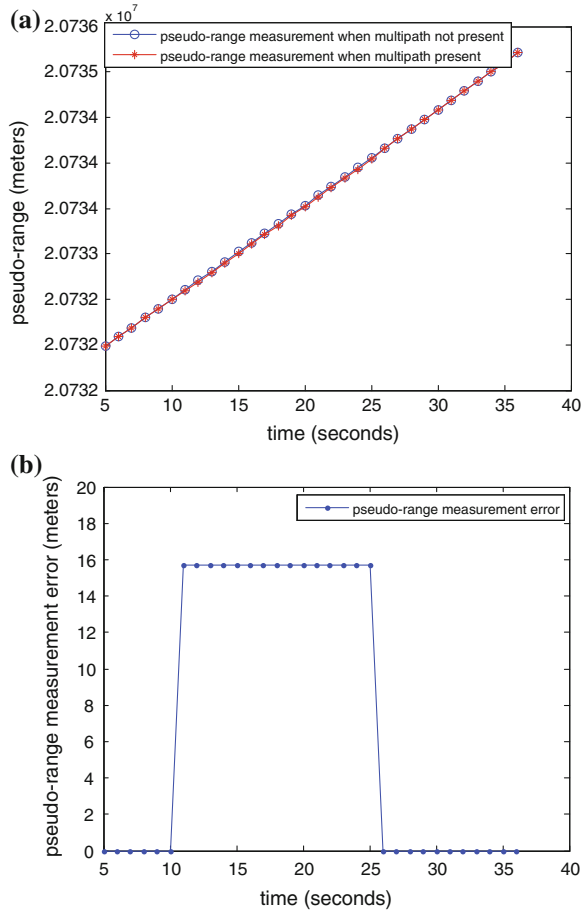
30.4.1 One Multipath Signal

From 10 to 25 s, one multipath signal is added to the basic scenario. Assuming the amplitude of the multipath signal is equal to the direct signal, and the multipath signal arrives 105 ns later than the direct signal, then the propagation distance of multipath signal is 31.4 m more than the direct signal. Simulations are conducted based on software receiver, and pseudo-range measurements when multipath signal is present and not present are shown in Fig. 30.3a, and the difference between the two is shown in Fig. 30.3b.

As shown in Fig. 30.3, for single-antenna receiver, the pseudo-range when multipath is present shows a bias compared to the actual pseudo-range (when there is no multipath). The measurement error is 15.7 m. Understandably, because there's only one multipath, when the multipath signal and the direct signal are added, the position of the correlation peak falls between the pseudo code phase of the direct signal and pseudo code phase of the multipath signal. The amplitude of the direct signal and the amplitude of the multipath signal are equal, therefore the measurement error is just half of the propagation delay (31.4 m), which is 15.7 m.

An antenna array receiver is used to detect the multipath signal. Firstly calculate the steering vector of satellite signal based on prior information such as the satellite ephemeris, element coordinates of the antenna array, then design the array weight according to the steering vector, which aims to null the power of satellite signal at the array output. Multipath detection result of the antenna array receiver is shown in Fig. 30.4a, b.

Fig. 30.3 a Pseudorange observations of single antenna when there's only one multipath signal.
b Pseudorange observation error of single antenna when there's only one multipath signal

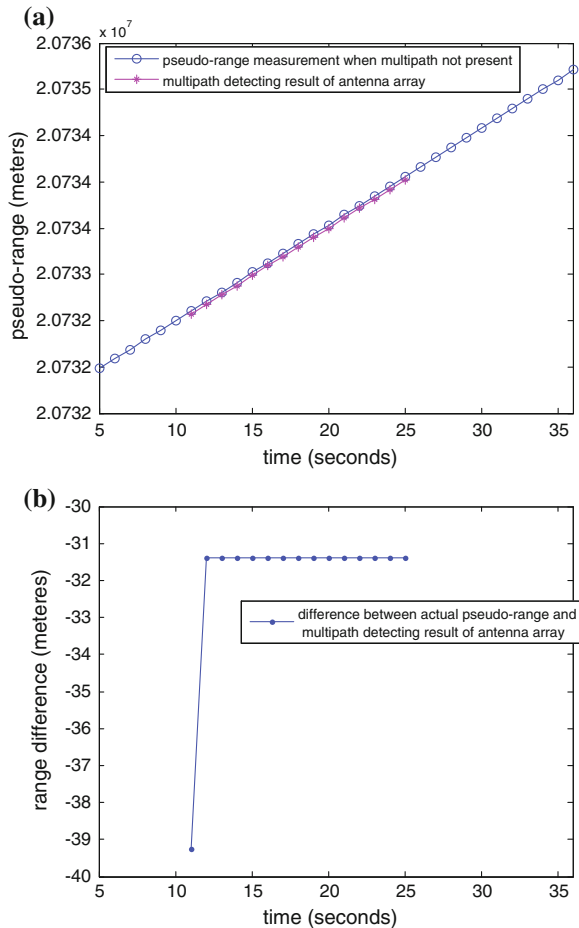


As shown in Fig. 30.4, from 10 to 25 s, the antenna array receiver detects the multipath signal and outputs tracking results of the multipath signal. Except for 11 s the pseudo-code tracking loop has not completely tracked the multipath, multipath detection results of the rest period are coincident to the scenario setup, which has a difference of -31.4 m from the actual pseudo-range. Combined with the amplitude estimate of the antenna array, the detecting result could be directly used in pseudo-range correction.

30.4.2 N Multipath Signals ($N > 1$)

From 12 to 30 s, two multipath signals are added to the basic scenario. Assuming the amplitude of each multipath is equal to the direct signal, the propagation delay of the multipath signals are 105 and 131 ns longer than the direct signal. Then the

Fig. 30.4 **a** Multipath detecting result of antenna array when there's only one multipath signal. **b** Difference between actual pseudorange and multipath detecting result of antenna array when there's only one multipath signal

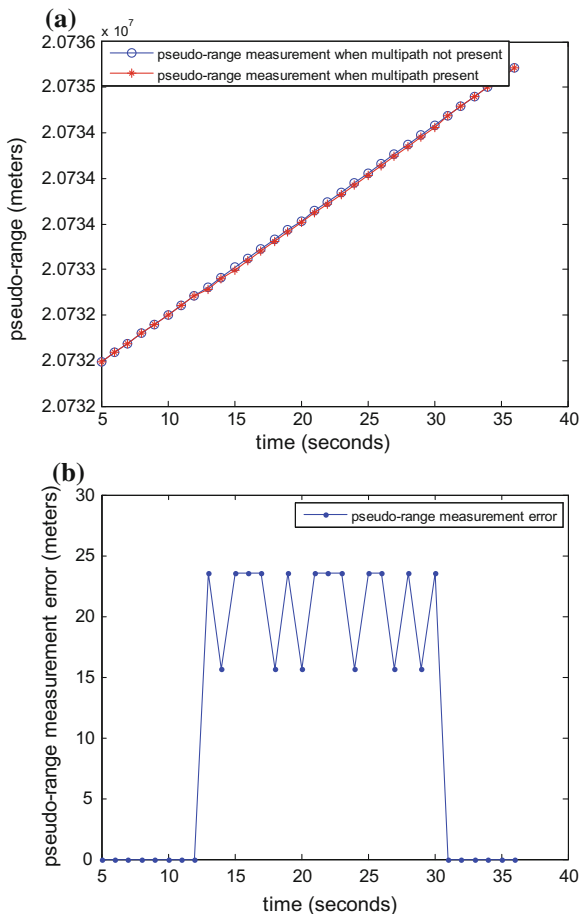


propagation distances of two multipath signals are 31.4 and 39.3 m more than the direct signal separately. Simulations are conducted based on software receiver, and pseudo-range measurements when multipath signals are present and not present are shown in Fig. 30.5a, and the difference between the two is shown in Fig. 30.5b.

As shown in Fig. 30.5, for single-antenna receiver, the pseudo-range when multipath is present shows a bias compared to the actual pseudo-range (when there is no multipath). The measurement error jumps between 15.7 and 23 m. Due to the presence of two multipath signals, when the multipath signal and the direct signal are added, two peaks appear in the correlation curve, so the pseudo-code tracking loop sometimes locks at the front correlation peak, sometimes locks at the back correlation peak, therefore pseudo-range measurement jumps back and forth.

An antenna array receiver is used to detect the multipath signal. Firstly calculate the steering vector of satellite signal based on prior information such as the satellite ephemeris, element coordinates of the antenna array, then design the array weight

Fig. 30.5 **a** Pseudorange observations of single antenna when there are $N = 2$ multipath signals.
b Pseudorange observation error of single antenna when there are $N = 2$ multipath signals

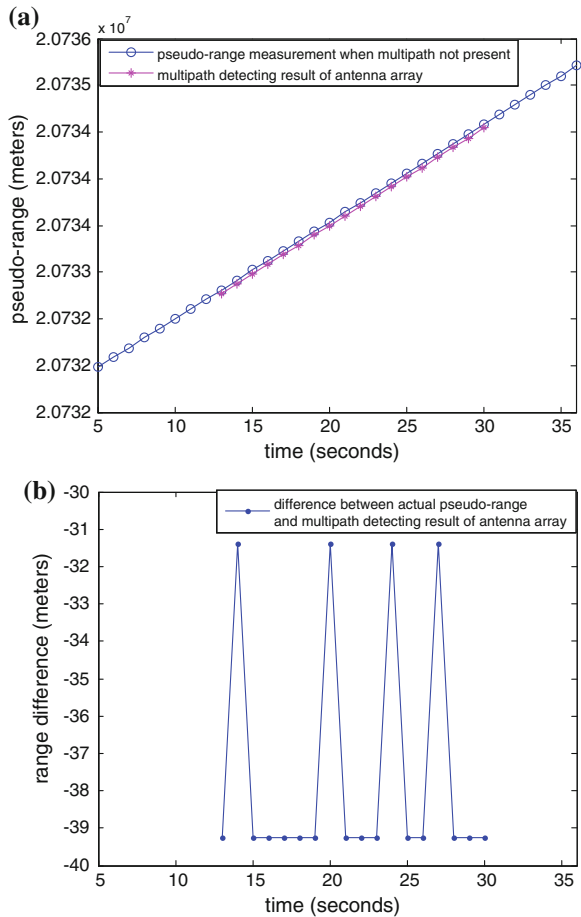


according to the steering vector, which aims to null the power of satellite signal at the array output. Multipath detection result of the antenna array receiver is shown in Fig. 30.6a, b.

As shown in Fig. 30.6, from 12 to 30 s, the antenna array receiver detects the multipath signals and outputs tracking results of the multipath signals. As there are two multipath signals, the pseudo-code tracking loop sometimes locks at one multipath signal, sometimes locks at the other multipath signal, therefore the multipath detecting results jumps between -31.4 and -39.3 m, which is coincident to the scenario setup. Based on this detecting result, pseudo-range measurement can be corrected in the monitoring station. However, since the amount of multipath is big, the amplitude, propagation delay of each multipath signal are likely to change. The process of estimating the parameters of each multipath signal is more complex.

Fig. 30.6 a Multipath detecting result of antenna array when there are $N = 2$ multipath signals.

b Difference between actual pseudorange and multipath detecting result of antenna array when there are $N = 2$ multipath signals



30.5 Conclusion

This paper proposed a multipath detecting method based on the antenna array. Since the arrival angle of the multipath signal is different from the satellite signal, if satellite signal is eliminated in the signal processing of antenna array receiver, then the multipath can be detected according to the output pseudo-range. Theoretical analysis and simulation experiments show that the method could quickly and efficiently detect the multipath signal in the received signals. The elimination of the multipath depends on the specific multipath environment. If only one multi-path signal exists, the multipath detecting result could be directly used to correct pseudo-range measurements in monitoring stations; If there are multiple multipath signals, the process of estimating the parameters such as the amplitude, the propagation delay is complex. Further research will be conducted in this area.

References

1. Chen K, Gui Q-M, Yue L-Q (2012) A multi correlator based GPS multipath estimation method. *J Astronaut* 33(9):1241–1247
2. Xu N-B (2013) A multipath estimation method based on MEDLL improved algorithm. *Radio Commun Technol* 39(4):11–13
3. Gao Y, Li Q (2014) Modified narrow correlator spacing method for mitigation short-delay multipath. *Measur Control Technol* 01:43–46
4. Han L, Kou Y-H (2011) GNSS signal quality assessment based on multi-frequency processing. In: *Proceeding of 2nd China satellite navigation conference*, Shanghai
5. Wang M-L, Wang F-X (2008) An algorithm of multipath error and observation noise weakening in triple-frequency ionospheric delay correction. *Acta Geodaetica Cartogr Sin* 37(4):418–422
6. Gan X-L, Li J (2012) A new multipath detection and calibration method for ground based monitoring station. In: *Proceeding of 3rd China satellite navigation conference*, Guangzhou
7. Kaplan ED, Hegarty CJ (2007) Kou Y-H translated. *understanding GPS: principles and applications*, 2nd edn. Publishing House of Electronics Industry, Beijing
8. Li M, Zeng X-H, Nie J-W, Wang F-X (2011) Analysis on beam pointing error of antenna array receivers in satellite navigation systems. *Aerosp Electron Warfare* 27(5):19–22
9. Borre K, Akos D et al (2006) *A software-defined GPS and Galileo receiver: a single-frequency approach*. Birkhäuser Boston

Chapter 31

Reliability Allocation Method of Satellite Navigation System Based on Dynamic Simulation

Heng Zheng, Haisheng Li, Chang Li, En Xue, Zhuopeng Yang
and Peipei Gong

Abstract A reliability allocation method of satellite navigation system based on dynamic simulation is proposed in this paper. First, Bayesian network is used for allocating the service availability and continuity to a slot. Then, the dynamic colored Petri net is applied to modeling the navigation information flow, which describes the availability and reliability associating the slot with the satellite, control center, mission up-link station and sensor station. Meanwhile, Monte Carlo simulation method is used to determine the availability and reliability index of key functional units. Finally, under conditions of the allocation availability and reliability index, the service availability and continuity is got with the bottom-up approach. Results are consistent with the original allocated values, which verify the validity of the proposed method.

Keywords Availability · Reliability · Simulation allocation · DCPN · Bayesian network

31.1 Introduction

Compared with other global satellite navigation system, the core of BeiDou navigation satellite system with high reliability is to realize the equal level or even better availability, continuity and integrity index. Scientific and rational allocation of reliability index is an important premise for the development of the satellite navigation system. How to convert the top-level reliability index such as service availability, continuity and integrity to each system's reliability and maintainability

H. Zheng (✉) · H. Li · E. Xue · Z. Yang · P. Gong
China Academy of Aerospace Standardization and Product Assurance, Beijing, China
e-mail: bitzheng@163.com

C. Li
Beijing Institute of Tracking and Communication Technology, Beijing, China

index is an important basis for the guidance and constraints of each system reliability work.

For satellite navigation system such typical complex dynamic network, the reliability index allocation technology is very complex. And the traditional reliability allocation methods are difficult to apply, which requires the use of sophisticated modeling and simulation technology. A reliability allocation method of satellite navigation system based on dynamic simulation is proposed in this paper. To highlight the simulation allocation idea, it is focused on the service availability and continuity index allocation process. First, the service availability and continuity index is allocated to slot availability and continuity. Then, the dynamic colored Petri net is applied to modeling the navigation information flow, which describes the availability and reliability associating the slot with the satellite, control center, mission up-link station and sensor station. Meanwhile, Monte Carlo simulation method is used to determine the availability and reliability index of key functional units. Finally, under conditions of the allocation availability and reliability index, the service availability and continuity is got with the bottom-up approach. Results are consistent with the original allocated values, which verify the validity of the proposed method.

31.2 Reliability Allocation Method

31.2.1 Service Availability Allocation to a Slot

31.2.1.1 Service Availability Model

For generality, assuming the constellation as non-uniform configuration, then each state will have a different impact on the service performance. And the service availability can be calculated by the constellation state probability and the constellation value [1]. There is:

$$A = \sum_{k=0}^M \sum_{n=1}^{C_N^k} P_{k,n} \cdot \alpha_{k,n} \quad (31.1)$$

where M is the total number of satellites, C_N^k is the combination number of k failure satellites of N satellites, $P_{k,n}$ is the constellation state probability with k failure satellites in n combination case, $\alpha_{k,n}$ is the constellation value.

According to GPS experience, the constellation value (referred to as CV) is chosen as the objective function to evaluate the constellation performance. CV which reflects the constellation geometry characteristics and continuous visibility is an important manifestation of the constellation performance.

CV is calculated as:

$$CV = \frac{\sum_{t=t_0}^{t_0+\Delta T} \sum_{i=1}^L \text{bool}(DOP_{t,i} \leq DOP_{\max}) \times \text{area}_i}{\Delta T \times \text{Area}} \times 100\% \quad (31.2)$$

where ΔT is the total simulation time, t_0 is the initial time, L is the total number of grid points, $\text{bool}(x)$ is Boolean function, when x is true, $\text{bool}(x) = 1$, when x is false, $\text{bool}(x) = 0$, $DOP_{t,i}$ is the DOP value of the i grid point at time t , Area is the total service area, area_i is the area of the i grid point.

P_k is defined as the constellation state probability of k failure satellites. It determines the availability of each satellite and all combinations, and there must be $\sum P_k = 1$. As the availability of each satellite is different, the constellation state probability with different failure satellite combination is also different. There is:

$$\begin{cases} P_k = \sum_{n=1}^{C_N^k} P_{k,n} \\ P_{k,n} = \left(\prod_{m=1}^{N-k} p_{n,m} \right) \left(\prod_{i=N-k+1}^N (1 - p_{n,i}) \right) \end{cases} \quad (31.3)$$

where C_N^k is the combination number of k satellites in N , $P_{k,n}$ is the constellation state probability of n case with k failure satellites, $p_{n,m}$ is the availability of each satellite of the $(N - k)$ satellites, and $(1 - p_{n,i})$ is the corresponding failure probability.

31.2.1.2 Slot Availability Calculation

Figure 31.1 shows the service availability model by using the Bayesian network [2]. It can be seen that each satellite is a parent node, and the availability of each

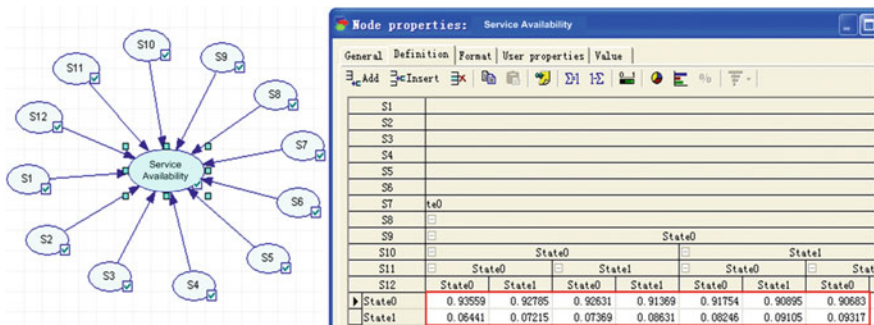


Fig. 31.1 Service availability model based on Bayesian network

satellite is the marginal probability. Every node points to the “service availability” child node, and CPT (conditional probability tables) is the constellation value of different failure satellites.

According to the GPS experience, to describe the constellation performance and hot spare satellites, a slot is used instead of a satellite. Since the slot availability is coupling relationship with other parameters, it is difficult to use analytical methods to get the slot availability; therefore, the simulation technology is required.

Based on the actual availability of operational satellites of BeiDou regional system, Monte Carlo simulation is used to sample spreadsheet. After several rounds of iterative improvement, the best required slot availability index is got.

31.2.2 Service Continuity Allocation to a Slot

Service continuity (C_N) is relevant to the slot continuity, availability, CV, and continuity criterion. On the basis of knowing the slot availability, CV, and continuity criterion, the slot continuity will be calculated. There is:

$$C_N = \sum_{k=m}^N P_k \cdot \left(\sum_{x=0}^k Q_{k,x} \cdot \frac{1}{\binom{k}{x}} \sum_{n=1}^{\binom{k}{x}} bool\{R_n(l, t)\} \right) \tag{31.4}$$

where N is the number of satellites visible to the user, m is the minimum number of satellites required to satisfy the continuity, P_k is the probability of k user-visible satellites that is associated with slot availability p , $Q_{k,x}$ is the conditional probability which another x satellites are interrupted on the basis of k visible satellites,

$\frac{1}{\binom{k}{x}} \sum_{n=1}^{\binom{k}{x}} bool\{R_n(l, t)\}$ is the corresponding availability, $R_n(l, t)$ is the service availability on location l at time t .

Then, $Q_{k,x}$ is represented with the slot continuity c , there is

$$Q_{k,x} = \binom{k}{x} \times c^{k-x}(1 - c)^x \tag{31.5}$$

On the basis of slot availability p , $Q_{k,x}$ can be got from service continuity C_N , thus, slot continuity is obtained.

31.2.3 Slot Availability and Continuity Allocation to Each System

31.2.3.1 Index Allocation Thinking

First, dynamic colored Petri net is applied to modeling the navigation information flow, which describes the availability and reliability associating the slot with the satellite, control center, mission up-link station and sensor station. Meanwhile, Monte Carlo simulation method is used to determine the initial availability and reliability index of key functional units. Then, combined with reliability and maintenance information of engineering operation, and by adjustment and optimization of operating conditions and iterative improvement, the optimal availability and reliability index of critical functional units are determined.

31.2.3.2 Model of Slot Availability and Continuity

1. Introduction to Petri net

Petri net is described with a circular (library), rectangular (changes) and the arrow mark (arc) graphical representation. Arc is located between places and transitions. Library represents a discrete mode or condition, and changes represent transformation behaviour between conditions [3]. When a token (indicated by dots) that resides in the corresponding library, it means conditions satisfied. Petri net can have multiple tokens, indicating mixing conditions. Ordinary and extended Petri nets have many outstanding advantages including graphical representation, etc. So that it is possible in a higher level of observation or simulation of all system components, which is suitable for the dynamic process modeling. In this paper, dynamic colored Petri net (DCPN) is used to modeling analysis; and DCPN has its precise mathematical form definition [4, 5].

2. Information Flow Process Description

Basic navigation service is as the example to describing the navigation data information flow among the satellite, control center, mission up-link station and sensor station. Figure 31.2 shows the information flow process.

3. Top Model of Slot Availability and Continuity

According to the navigation information flow process, the slot availability and continuity is modeled by using the dynamic colored Petri net, which simulates the availability and reliability of functional units affecting to the slot availability and continuity. The information flow varies with the performance of functional units. Information includes availability of signal in space (referred as SIS, available or unavailable) and quality of navigation information (correct, incorrect or unavailable). Figure 31.3 shows the top model of slot availability and continuity.

It can be seen from Fig. 31.3 that the model includes a satellite, control center, mission up-link station and sensor station, which is described by the complex changes. After double-click changes, model can be expanded. And data flow model

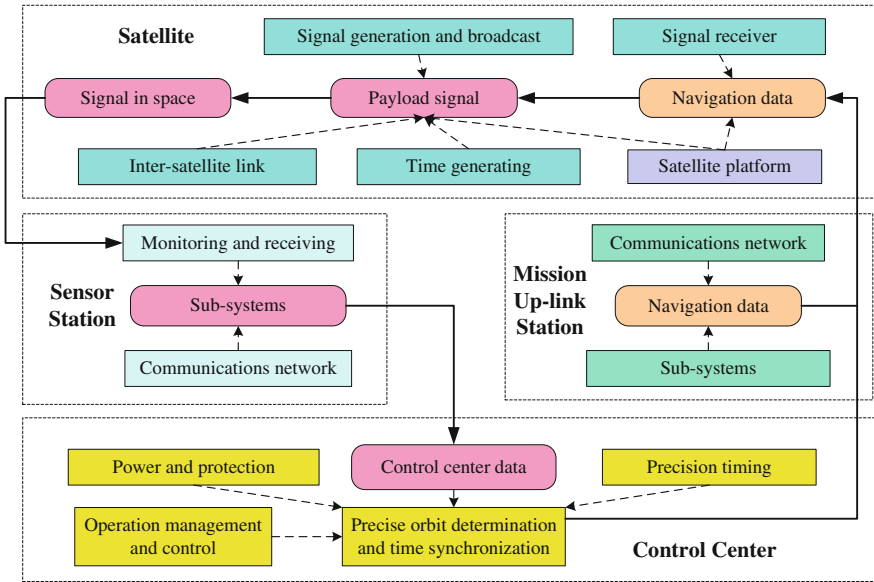


Fig. 31.2 Information flow of satellite navigation

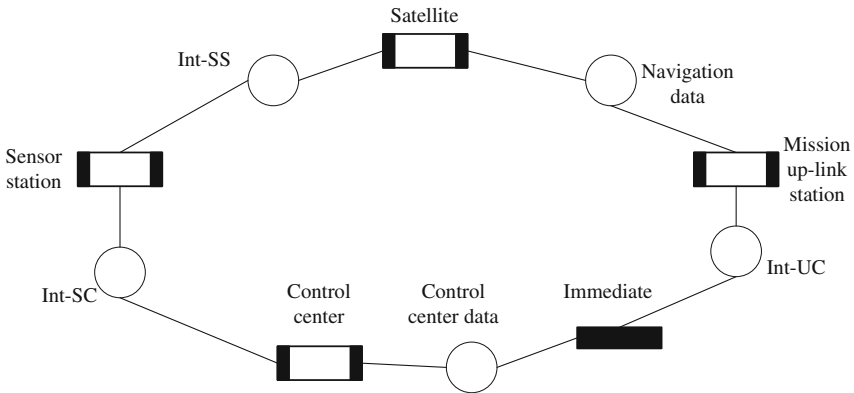


Fig. 31.3 Petri net model of slot availability and continuity

is represented by the circle library. Model assumptions are as follows: (1) Only content related to navigation service is considered; (2) System boundaries are SIS level, not including the user receiver; (3) External environmental events are not considered; (4) Short-term scheme outage is not considered (satellite orbital maneuvering, etc.); (5) Long-term scheme outage is not considered (planned replacement satellite end of life).

4. Petri Net Model of a Satellite (Fig. 31.4)

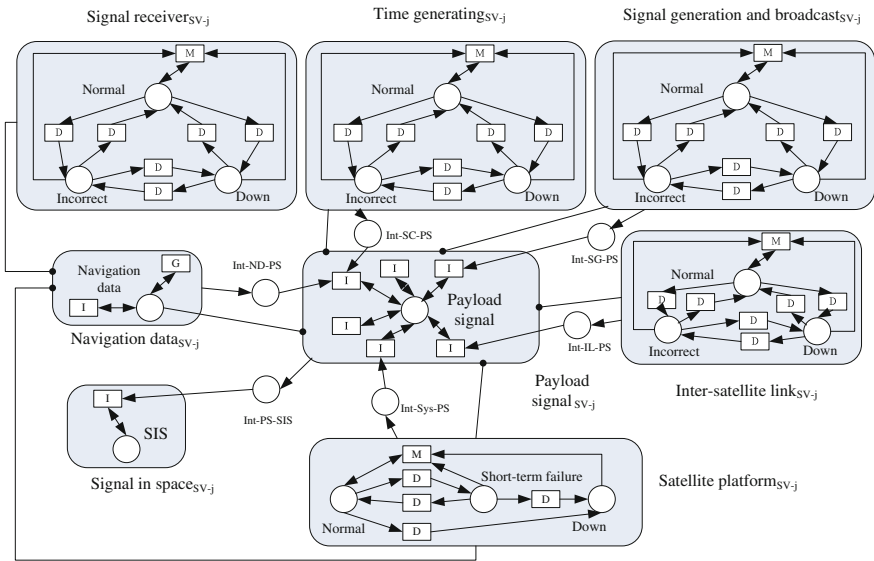


Fig. 31.4 Petri net model of a satellite

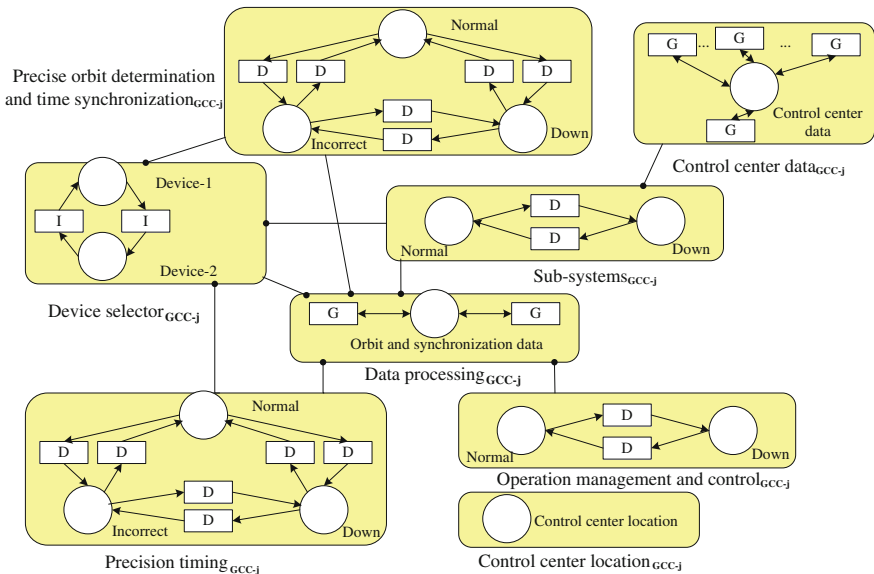


Fig. 31.5 Petri net model of a control center

5. Petri Net Model of a Control Center (Fig. 31.5)
6. Petri Net Model of a Mission Up-link Station (Fig. 31.6)
7. Petri Net Model of a Sensor Station (Fig. 31.7)

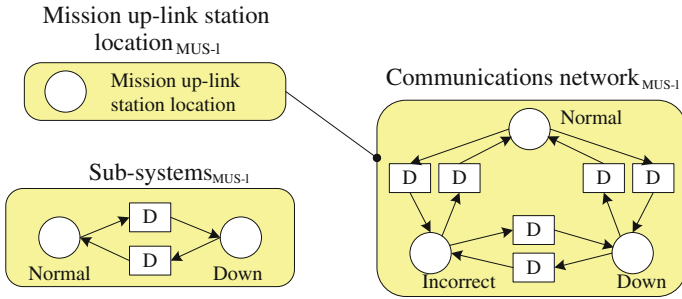


Fig. 31.6 Petri net model of a mission up-link station

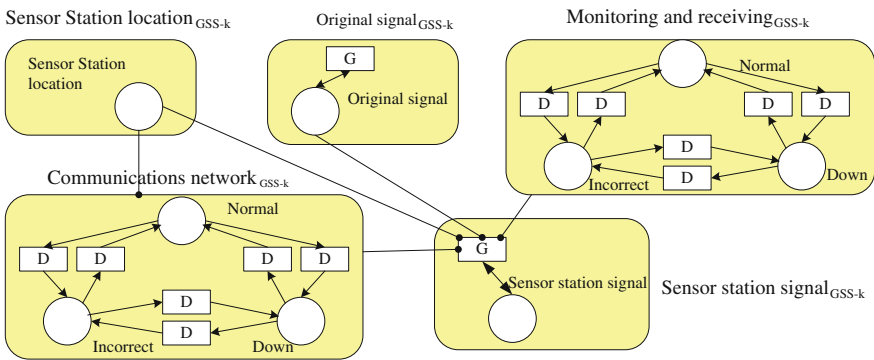


Fig. 31.7 Petri net model of a sensor station

31.3 Simulation Examples

Without loss of generality, the non-uniform constellation is chosen for simulation. Assuming that there are 32 satellites of different orbits (e.g. 20MEO + 6GEO + 6IGSO). Reliability index allocation is based on this constellation in this paper.

31.3.1 Service Availability and Continuity Index Requirements

The basic navigation service availability is assumed to be 0.9, and the service continuity is set to be 0.92, which is as the top index requirements to be carried out the allocation.

31.3.2 Allocation Results of a Slot Availability and Continuity

Considering the large number of satellite constellations, the following processing is made to solve state explosion problem: The three kinds of satellites are each as a node, which is divided into four states 0, 1, 2, 3; where 0 represents no failure satellites, 1 represents a failure satellite, 2 represents two failure satellites, 3 represents other cases. Figure 31.8 shows the model of service availability and continuity. It can be seen that P_{Gk} , P_{Ik} and P_{Mk} ($k = 0, 1, 2, 3$) respectively represents the constellation state probability of GEO, IGSO and MEO satellite nodes under the conditions of k failure satellites.

It also can be seen from Fig. 31.8 that α_k in the conditional probability tables shows the constellation value of three nodes various state combinations. Figure 31.9 shows the constellation state probability of MEO satellites. According to k/n model, the slot availability and continuity can be got.

Based on the above Bayesian network model, the slot avail availability and continuity index is calculated as follows: the slot availability index is 0.93, and the corresponding continuity index is 0.95.

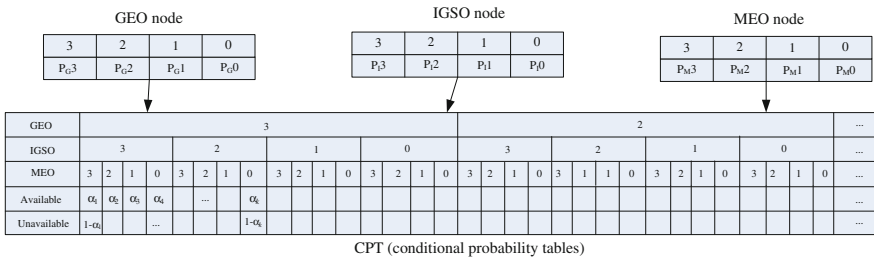
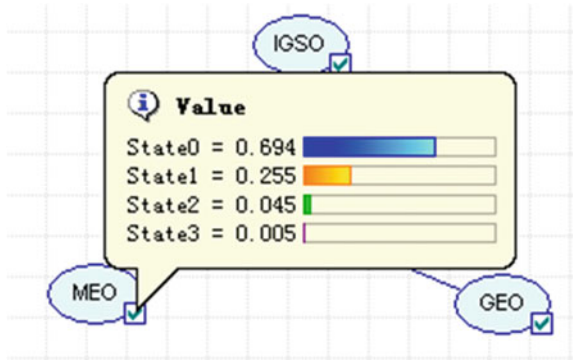


Fig. 31.8 Service availability and continuity model

Fig. 31.9 Constellation state probability of MEO satellites



31.3.3 Allocation Results of Key Functional Units

The availability and reliability allocation results of key functional units of a satellite are shown in Table 31.1. And the corresponding ground station availability and reliability allocation results are shown in Table 31.2.

31.3.4 Reliability Index Simulation Verification

Taking the MTBO and MTTR of functional units of a satellite (as shown in Table 31.1) and a ground segment (as shown in Table 31.2) as input, based on the dynamic colored Petri net information flow model, the slot availability and continuity are calculated to be 0.9327 and 0.9576. Then, combined with the constellation performance simulation results, by using Bayesian network model to obtain the service availability is 0.9118, and the service continuity is 0.9235. That is better than the original planned allocation index: the service availability is 0.9, the service continuity is 0.92. Results show that, the reliability and availability index allocated

Table 31.1 Reliability allocation results of a satellite

No.	Functional units	Mean time between outages (MTBO) (h)	Mean time to repair (MTTR) (h)
1	Signal receiver	2,190	20
2	Time generating	3,285	20
3	Signal generation and broadcast	3,285	20
4	Inter-satellite link	2,190	20

Table 31.2 Reliability allocation results of a ground segment

No.	Ground segment	Functional Units	Mean time between outages (MTBO) (h)	Mean time to repair (MTTR) (h)
1	Control center	Precise orbit determination and time synchronization	4,380	18
2		Precision timing	3,285	18
3		Operation management and control	4,380	18
4		Sub-systems	4,380	18
5	Mission up-link station	Communications network	4,380	18
6		Sub-systems	4,380	18
7	Sensor station	Monitoring and receiving	3,285	18
8		Communications network	4,380	18

to the key functional units of a satellite, control center, mission up-link station and sensor station can meet the requirements of top-level service availability targets.

31.4 Conclusions

Scientific and rational allocation of reliability index is an important premise for the development of the satellite navigation system. For the reliability allocation problem of satellite navigation systems such typical complex dynamic network, this paper presents a reliability allocation method based on dynamic simulation. First, Bayesian network is used for allocating the service availability and continuity to a slot. Then, the dynamic colored Petri net is applied to modeling the navigation information flow, which describes the availability and reliability associating the slot with the satellite, control center, mission up-link station and sensor station. Meanwhile, Monte Carlo simulation method is used to determine the availability and reliability index of key functional units. Finally, under conditions of the allocation reliability index, the service availability and continuity is got with the bottom-up approach. Results are consistent with the original allocated values, which verify the validity of the proposed method. The allocation method for the user-oriented top-level reliability index can be decomposed to key functional units of each engineering system, which can provide an input and guidance to carry out reliability work for them.

References

1. Li H (2013) Research on spare satellites strategy of navigation constellation based on system availability. In: Proceedings of China Satellite Navigation Conference (CSNC), Wuhan, 2013
2. Jensen FV (2001) Bayesian networks and decision graphs. Springer, New York
3. Analysis techniques for dependability—Petri net techniques. IEC 62551. 2012
4. van der Park M (2002) DCPN-based models for dependability assessment. National Aerospace Laboratory NLR
5. Oving BA (2005) Assessment of Galileo key dependability and safety parameters: a simulation-based approach. In: Proceedings of ION national technical meeting, Long Beach, CA, Sept 2005

Chapter 32

A Study on Measuring Channel Bias in GNSS Receiver

Hailong Chen, Wen Li, Xin Liu and Wenhai Jiao

Abstract The Channel Bias of GNSS Receiver affects the precise measurement of navigation signals. It is important to correct the channel bias of GNSS Receiver for precise orbit and clock products in multi-GNSS data analysis. Based on the refined pseudorange observation error mode, the paper proposes a new method of measuring channel bias of GNSS Receiver by using GNSS simulator, which can measure the bias in the same frequency of the same system, between the different frequencies, between the different systems. Finally, this paper uses this method to test three types of iGMAS receivers, the results show that the channel bias in the same frequency is about 0.01 ns, while that in the different frequencies and the different systems is about 0.1 and 20 ns respectively, and all these bias are related with the receiver type.

Keywords GNSS receiver · Channel bias · iGMAS · GNSS simulator

32.1 Introduction

The channel bias in multi-system receiver is not the same for the same frequency, the different frequencies of the same system and the different systems [1], because of the influence of RF front-end filters, pseudo-code generator, correlators and tracking loop performance. The existence of the inter-receiver bias could affect the GNSS receiver observation data application performance in high precision application.

H. Chen (✉) · W. Li · X. Liu
Test and Assessment Research Center of China Satellite Navigation Office,
Beijing, China
e-mail: chen hailong05@163.com

W. Jiao
Beijing Institute of Tracking and Telecommunication Technology, Beijing, China

Numerous studies have been carried out to investigate the influence of L1/L2 channel biases on the ionospheric delay corrections. Gao has made a comprehensive study on this issue. Dual-frequency pseudorange measurements have been used to derive ionospheric delay corrections. The differential delays derived from the L1 and L2 measurements, however, are deteriorated by receiver channel biases. Obtaining accurate absolute ionospheric corrections requires that these bias values be removed from the ionospheric measurement or estimated along with ionosphere parameters [2]. Various research results have indicated that the biases are constant over a relatively long time span such as a month. According to Wilson and Mannucci, the inter-frequency receiver channel biases are constant at the 0.1 ns level [3]. A similar result has also been reported by Schaer [4]. Gao proposed that the receiver channel biases can be estimated through a Least Squares adjustment procedure [2]. Donny uses Kalman filter to measure the inter-frequency receiver channel bias which is applied to data processing of GPS Monitor Station Network [5].

The precise positioning could also be improved by correcting the receiver channel bias. Dhital et al. addresses the problem of receiver channel biases by presenting various biases, such biases could be removed from the measurement, leading to an improvement in the position solution [6].

However these studies are based on a single system receiver. The paper proposes a new method of measuring channel bias of GNSS Receiver by using GNSS simulator, which can measure the bias in the same frequency of the same system, between the different frequencies, between the different systems. This method was used to test the GNSS receivers in the international GNSS Monitoring and Assessment System (iGMAS for short).

32.2 Observation Error Model

The receiver channel bias is caused by path dependent delay of the GNSS signal through hardware, so as to increase the error to observation measurements. Each aspects of the receiver signal processing could be equivalent to some filters. The signal response delay of filters is related to the signal frequency. The bias must be considered in mutli-GNSS data combination analysis. As concluded by Hansen [7], there are two ways to estimate such a bias:

1. By manufacturing a device that could directly measure the bias for each receiver in real time.
2. By fitting a model to separate the bias from the model.

The latter approach will be used in the paper, because it can be implemented in software and is operationally feasible. By assuming that any channel of receiver could be configured to track any signal from any satellite, the range measurements on single frequency n between a receiver and a satellite can be described by the following equations:

$$\begin{aligned}
\rho_{m,n}(j) = & r(j) + c(t_r - t_s(j)) + d_s(j) \\
& + T(j) + I_n(j) \\
& + d_{mult}(j) + d_{r,m,n}(j) \\
& + \varepsilon(\rho_{m,n}(j))
\end{aligned} \tag{32.1}$$

where

- $\rho_{m,n}(j)$ is the measured pseudorange on frequency (n) receiver and the satellite (j) by receiver channel (m).
- $r(j)$ is the geometric range between receiver and the satellite (j).
- c is the speed of light.
- t_r is the receiver clock error in the measured pseudorange.
- $t_s(j)$ is the satellite clock error in the measured pseudorange.
- $d_s(j)$ is the channel delay of the satellite (j).
- $T(j)$ is the tropospheric delay in the measured pseudorange.
- $I_n(j)$ is the ionospheric delay in the measured frequency (n) pseudorange.
- $d_{mult}(j)$ is the multipath effect in the measured pseudorange.
- $d_{r,m,n}(j)$ is the receiver channel (m) delay in the measured frequency (n) pseudorange between receiver and satellite (j).
- $\varepsilon(\rho_{m,n}(j))$ is the measured pseudorange noise.

The above equations have considered all possible error/bias source from signal generation, propagation to reception. The paper's method is based on this observation model.

32.3 A Method to Measure Channel Bias in GNSS Receiver

When GNSS receiver tracks the same signal or signal on the different frequency or signal from the different system by different channel, the channel delay is not the same.

It is difficult to measure the receiver channel bias with actual observation data, because large errors in the measurements make it impossible to measure the much smaller channel bias. This can be done by using a GNSS simulator. Some errors in equations could be set to zero by using a GNSS simulator, such as satellite clock, tropospheric delay, ionospheric delay, multipath error. And the channel bias in GNSS simulator could be corrected. Equation (32.1) can be simplified to:

$$\begin{aligned}
\rho_{m,n}(j) = & r(j) + ct_r + d_{r,m,n}(j) \\
& + \varepsilon(\rho_{m,n}(j))
\end{aligned} \tag{32.2}$$

32.3.1 The Method to Measure the Bias in Same Frequency

Currently, the receiver generally tracks the satellite signal in the dynamic manner, the receiver has not been track the same signal all long by identify channel. The tracking channel will be changed. Because of channel hardware features, the same signal through different channels has different delay. This method is to measure the bias in same frequency by setting all channel of receiver to track the identify signal in the same frequency from the same satellite. The GNSS simulator is set to zero out the satellite error, tropospheric error, ionospheric error, multipath error.

According to Eq. (32.2), differencing the pseudorange measurements in same frequency from any two channel (k , l) of the receiver to eliminate the geometric range $r(j)$ and receiver clock error t_r ,

$$\begin{aligned} \rho_{k,n}(j) - \rho_{l,n}(j) &= d_{r,k,n}(j) - d_{r,l,n}(j) \\ &+ \varepsilon(\rho_{k,n}(j)) - \varepsilon(\rho_{l,n}(j)) \end{aligned} \quad (32.3)$$

Equation (32.3) becomes,

$$\begin{aligned} \delta_{k-l,n}(j) &= d_{r,k,n}(j) - d_{r,l,n}(j) \\ &+ \varepsilon(\rho_{k,n}(j)) - \varepsilon(\rho_{l,n}(j)) \end{aligned} \quad (32.4)$$

Calculate the maximum value of all $\delta_{k-l,n}(j)$

$$\begin{aligned} \delta_n(j) &= \max\{\delta_{k-l,n}(j)\} \\ &= d_{r,p,n}(j) - d_{r,q,n}(j) \\ &+ \varepsilon(\rho_{p,n}(j)) - \varepsilon(\rho_{q,n}(j)) \end{aligned} \quad (32.5)$$

Equation (32.5) only remains the channel bias and pseudorange observation noise. Pseudorange noise could be reduced by time average, because the noise is random noise.

32.3.2 The Method to Measure the Bias in Different Frequency

The receiver channel bias is not the same, when tracking the signal in different frequency from the same satellite, because of the different hardware and filters. The paper proposes a method to measure the bias in the different frequency by setting all channel of receiver to track the signals in the different frequency from the same satellite. The GNSS simulator is set to zero out the satellite error, tropospheric error, ionospheric error, multipath error.

According to Eq. (32.2), differencing the pseudorange measurements in different frequency (w, x) from any two channel (k, l) of the receiver to eliminate the geometric range $r(j)$ and receiver clock error t_r ,

$$\begin{aligned} \rho_{k,w}(j) - \rho_{l,x}(j) &= d_{r,k,w}(j) - d_{r,l,x}(j) \\ &+ \varepsilon(\rho_{k,w}(j)) - \varepsilon(\rho_{l,x}(j)) \end{aligned} \quad (32.6)$$

Equation (32.6) becomes,

$$\begin{aligned} \delta_{k-l,wx}(j) &= d_{r,k,w}(j) - d_{r,l,x}(j) \\ &+ \varepsilon(\rho_{k,w}(j)) - \varepsilon(\rho_{l,x}(j)) \end{aligned} \quad (32.7)$$

Calculate the maximum value of all difference between channel k and l , that is $\delta_{k-l,wx}(j)$,

$$\begin{aligned} \delta_{wx}(j) &= \max\{\delta_{k-l,wx}(j)\} \\ &= d_{r,p,w}(j) - d_{r,q,x}(j) \\ &+ \varepsilon(\rho_{p,w}(j)) - \varepsilon(\rho_{q,x}(j)) \end{aligned} \quad (32.8)$$

Equation (32.8) only remains the channel bias between different frequency (w, x) and pseudorange observation noise. Pseudorange noise could be reduced by an time average, because the noise is random noise.

32.3.3 The Method to Measure the Bias in Different System

When measuring the channel bias between different system, the geometric ranges could be firstly eliminated, because the geometric ranges are different for tracking the different satellite.

The paper proposes a method to measure the bias in the different system by setting some channels of receiver to track the signals from a satellite of certain system, for example GPS, other some channels to track the signals from identify satellite of certain system, for example BDS. The GNSS simulator is set to zero out the satellite error, tropospheric error, ionospheric error, multipath error.

Firstly, the geometric range is subtracting from the measured pseudorange of each system, the value comes from the GNSS simulator, so the Eq. (32.2) becomes,

$$\Delta\rho_{m,n}(j) = ct_r + d_{r,m,n}(j) + \varepsilon(\rho_{m,n}(j)) \quad (32.9)$$

Then, differencing $\Delta\rho_{m,n}(j)$ from any two channel (k, l) of the receiver to tracking two system (w, x) to eliminate receiver clock error t_r ,

$$\begin{aligned} \Delta\rho_{k,w}(j) - \Delta\rho_{l,x}(j) &= t_{wx} + d_{r,k,w}(j) - d_{r,l,x}(j) \\ &+ \varepsilon(\rho_{k,w}(j)) - \varepsilon(\rho_{l,x}(j)) \end{aligned} \quad (32.10)$$

where,

t_{wx} is the system time offset between systems (w, x), this offset could be obtained from satellite ephemeris.

After eliminating the system time offset, the Eq. (32.10) becomes,

$$\begin{aligned} \Delta\delta_{k-l,wx}(j) &= d_{r,k,w}(j) - d_{r,l,x}(j) \\ &+ \varepsilon(\rho_{k,w}(j)) - \varepsilon(\rho_{l,x}(j)) \end{aligned} \quad (32.11)$$

Calculate the maximum value of all difference between channel k and l , that is $\Delta\delta_{k-l,wx}(j)$,

$$\begin{aligned} \Delta\delta_{wx}(j) &= \max\{\delta_{k-l,wx}(j)\} \\ &= d_{r,p,w}(j) - d_{r,q,x}(j) \\ &+ \varepsilon(\rho_{p,w}(j)) - \varepsilon(\rho_{q,x}(j)) \end{aligned} \quad (32.12)$$

Equation (32.12) only remains the channel bias between different system (w, x) and pseudorange observation noise. pseudorange noise could be reduced by an time average, because the noise is random noise.

32.4 The Testing Environment and Results

32.4.1 The Testing Environment

The paper tests the channel bias by using three type receivers from the manufacturers UNICORECOMM, CETC54 and CETC20. Those are quad-system eleven-frequency high precision BDS/GPS/GLONASS receivers and can track fourteen satellites for each frequency at the same time. Details are given in Table 32.1. The quad-system GNSS simulator is produced by National University of Defense Technology [8], and its channel biases have been corrected.

Table 32.1 GNSS receiver equipment

Manufacturer	Model	Available	Note
UNICORE	UR4B0	BDS: B1I, B2I	UNICORECOMM
CE54	GMR-4011	GPS: L1CA, L2Y	CETC54
CE20	gnss-ggr	GLO: G1CA, G2CA GAL:E1B, E5aI, E5bI	CETC20

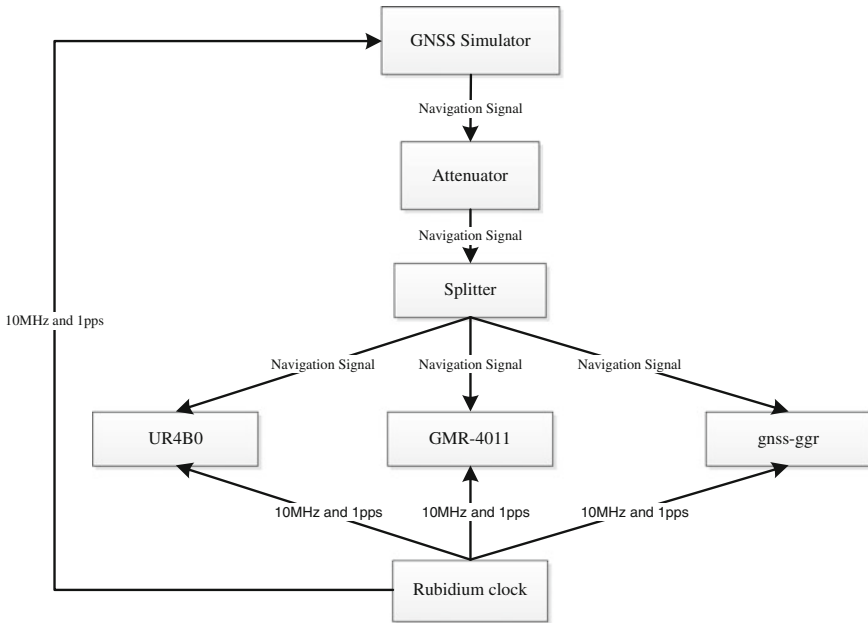


Fig. 32.1 Test configuration

There is Rubidium clock to provide frequency standard to three type receivers and simulator together. The testing configuration is shown in Fig. 32.1

The GNSS simulator is set to dynamic simulation scene mode and is set to zero out the satellite error, tropospheric error, ionospheric error and multipath error. The simulator can output the B1I and B2I of BDS, GPS’s L1 C/A and L2Y, G1CA and G2CA of GLONASS, E1B and E5aI of GALILEO, E5bI. The signal power is attenuated to minimum signal power, which is defined by each system’s Interface Control Document.

The three receivers are set to assign fourteen channels to track each signal in each frequency from each system respectively. For each system, the receivers only track one satellite.

32.4.2 The Testing Results

The paper have tested the channel bias in the same frequency, the different frequencies, and the different systems through using the method introduced in the third section.

The test results of channel bias in same frequency are shown in Table 32.2. This results show that the channel bias is between 0.001 and 0.008 ns. Because UR4B0

Table 32.2 Channel bias in same frequency (*Unit ns*)

System		Frequency		
		B1/L1/G1/E1	B2/L2/G2/E5a	E5b
UR4B0	BDS	0.0017	0.0017	—
	GPS	0.0017	0.0017	—
	GLO	0.0017	0.0017	—
	GAL	0.0017	0.0017	0.0017
GMR-4011	BDS	0.0022	0.0024	—
	GPS	0.0026	0.0069	—
	GLO	0.0016	0.0040	—
	GAL	0.0027	0.0040	0.0010
gnss-ggr	BDS	0.0026	0.0046	—
	GPS	0.0080	0.0074	—
	GLO	0.0062	0.0041	—
	GAL	0.0020	0.0010	0.0020

Table 32.3 Channel bias in different frequency (*Unit ns*)

System		Frequency
		B1-B2, L1-L2 G1-G2, E5a-E5b
UR4B0	BDS	0.0181
	GPS	0.0183
	GLO	0.0185
	GAL	0.0182
GMR-4011	BDS	0.1947
	GPS	0.2036
	GLO	0.1310
	GAL	0.1782
gnss-ggr	BDS	0.1879
	GPS	0.2077
	GLO	0.1647
	GAL	0.1774

receiver adopts a chip architecture, its bias is smaller than that of the GMR-4011 and gnss-ggr. The two type receivers use FPGA plus DSP or ARM architecture.

The test results of channel bias in the different frequency are shown in Table 32.3. This results show that the channel bias is between 0.02 and 0.3 ns.

The test results of channel bias in the different system are shown in Table 32.4. This results show that the channel bias is between 2 and 18 ns. And then this exits difference among receiver by various Manufacturers.

Table 32.4 Channel bias in different system (*Unit ns*)

System	Receiver		
	UR4B0	GMR-4011	gnss-ggr
BDS-GPS	1.96	11.73	13.15
BDS-GLO	7.13	12.56	9.27
BDS-GAL	7.22	8.21	11.16
GPS-GLO	5.25	15.11	13.74
GPS-GAL	4.20	16.73	17.29
GLO-GAL	9.43	10.42	10.09

32.5 Conclusions

The channel bias in GNSS receiver will affect the high precise application and mutli-GNSS data combination analysis. The paper introduced a new method of measuring channel bias of GNSS Receiver by using GNSS simulator, which can measure the bias in the same frequency of the same system, between the different frequencies and between the different systems. Three types of iGMAS receivers are tested using this method. The results show that the channel bias in the same frequency is about 0.01 ns, while the channel bias in the difference frequencies is about 0.1 ns and the channel bias in the different system is about 20 ns. But all these bias are depended on the receiver type. In particular, the bias in the different systems reaches 20 ns if not corrected, and it will affect the accuracy of multi-system data fusion process.

In the future, more researches will be done about how to measure the channel bias in the GNSS receiver with actual observation data and how the channel biases exiting between various receiver influences data processing for those receivers used in the same tracking station network.

Acknowledgments Appreciate for iGMAS’s provision of the testing environment and data in this research.

References

1. Johnson G, Zaugg T (2001) Measuring interchannel bias in GPS receivers. In: Proceeding of ION 57th annual meeting
2. Gao Y, Heroux P, Liao X (1999) GPS instrumental bias between receivers. In: Proceeding of ION GPS-99
3. Wilson BD, Mannucci AJ (1993) Instrumental bias in ionospheric measurements derived from GPS data. In: Proceeding of ION GPS-93
4. Schaer S (1999) Mapping and predicting the earth’s ionosphere using the global positioning system. Ph.D. thesis, Bern Univerity, Switzerland
5. Donny H, Bishop RH, Harris RB, Tolman B (2008) Inter-frequency bias estimation for the GPS monitor station network. In: Proceeding of ION GNSS 2008

6. Dhital A, Morrison A, Lachapelle G (2011) Improvement of GNSS positioning with proper calibration of inter-channel and inter-element bias in receiver front-ends. In: 24th International technical meeting of the satellite division of the institute of navigation
7. Hansen AJ (2002) Tomographic estimation of the ionosphere using terrestrial GPS sensors. PhD. Thesis, Stanford University
8. Zhang X, Mou W, Sun G, Ou G (2012) Multi-level GNSS signal simulator for multi system GNSS receiver developing. In: 25th International technical meeting of the satellite division of the institute of navigation

Chapter 33

The Development, Test and Application of New Technology on Beidou/GPS Dual-Mode Pseudolites

Xingli Gan, Baoguo Yu, Lei Chao and Shi Liu

Abstract Satellite navigation signal was easy to be influenced by urban canyon, highway tunnel, indoor and underground garage. In view of this shading problem, the Beidou/GPS dual-mode pseudolites was developed in China. Firstly, the composition and technical characteristic of pseudolites was introduced. Secondly, Pseudolites compatible with Beidou/GPS signal, navigation message and anti near-far effect was described, then put forward a new high precision time synchronization algorithm between pseudolites and Beidou/GPS. Thirdly, the range stability, navigation chip compatible reception ability, signal coverage and the positioning accuracy was tested in the infield and outfield environment. Test results showed that: by the new time synchronization algorithm, the properties of rubidium clock or crystal oscillator to drive the pseudolites was basically the same, so this pseudolites could use a cheap crystal as the time frequency unit. Under the combined solution between pseudolites and Beidou/GPS, pseudolites could improve the geometric distribution and the positioning accuracy of the navigation system from 10 m up to 5 m. Finally, Verifying the enhanced capabilities of pseudolites in the Mountain valley environment through the practical application data of Jiuzhaigou National Park, the related research results will improve the high availability of China's Beidou satellite navigation system.

Keywords Pseudolites · Beidou · GPS · Time synchronization · Joint positioning

33.1 Introduction

Satellite navigation system was difficult to provide seamless navigation service, due to the environment of shading effect at urban canyon, indoor and valleys, etc. Pseudolite was used to solve the problem [1–4]. In the Galileo project, The EU

X. Gan (✉) · B. Yu · L. Chao · S. Liu
The 54th Research Institute of China Electronics Technology Group Corporation,
Shijiazhuang, China
e-mail: ganxingli@163.com

© Springer-Verlag Berlin Heidelberg 2015
J. Sun et al. (eds.), *China Satellite Navigation Conference (CSNC) 2015 Proceedings: Volume I*, Lecture Notes in Electrical Engineering 340,
DOI 10.1007/978-3-662-46638-4_33

353

(European Union) was putting forward GILT [5], developing indoor and outdoor Galileo pseudolites and Europe communication management committee (ECC) had begun to issue the Galileo pseudolite management framework and the unity standard of the Galileo indoor and outdoor pseudolites [6], which allowed pseudolites to use E1 signal. Japan promoted indoor positioning systems which was called IEMS for GPS. IMES signal interface has been written to QZSS interface control documents and bring [7].

In this paper, Firstly, the function and technical characteristics of Beidou/GPS dual-mode pseudolites system was introduced, Secondly, the pseudolites signal, navigation message, near-far effect, time synchronization algorithm and positioning algorithm were described in detail. Finally, crystal oscillator and rubidium clock had the same performance under the new time synchronization algorithm, so we could use cheap crystal as pseudolites' time-frequency units, and improve geometric distribution, the level of positioning accuracy in the navigation system from 10 up to 5 m.

33.2 Beidou/GPS Dual-Mode Pseudolites System

Under the support of China National science and technology project-“Intelligent navigation search and rescue terminal and region application system” (Item no.: 2011BAH05B00), we had developed the BD/GPS dual-mode pseudollites. The composition of this system was shown in Fig. 33.1, which included the signal transmitters of pseudolites (20 cm × 20 cm × 10 cm), transmitting antenna and receiving antenna. The technical features as follows:

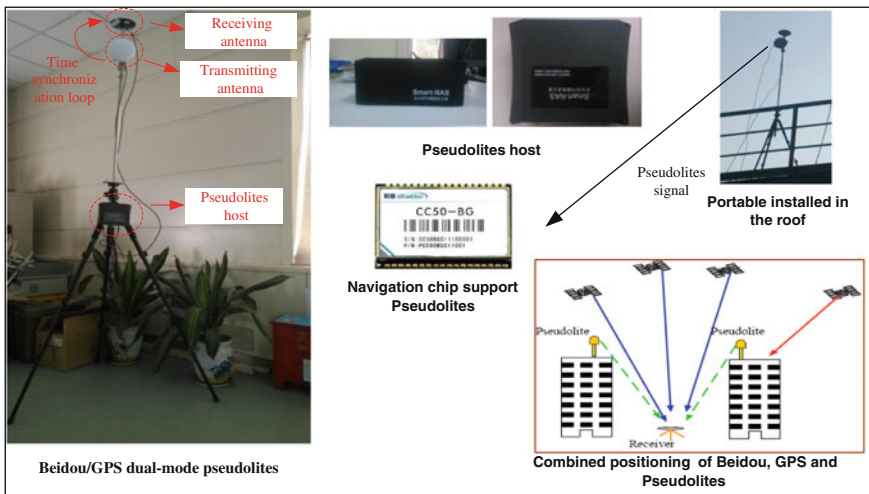


Fig. 33.1 System composition of Beidou/GPS dual-mode pseudolites

- Pseudolites signal and Beidou/GPS signal were highly compatible.
- Using the closed-loop high-precision time synchronization technology.
- Using the crystals drives pseudolites, low cost and miniaturization.
- Pulse signal resistant the near-far effect.
- Positioning accuracy was better than 5 m (95 %), when pseudolites combined with Beidou/GPS.

33.3 Signal and Key Technology of the Beidou/GPS Pseudolites

33.3.1 Beidou/GPS Pseudolites Signal Design

The signal parameters of pseudolites were shown in Table 33.1. It was shown that center frequency, code length and code rate, data rate, modulation mode, polarization mode of pseudolites were the same as GPS and Beidou. The spread spectrum code of pseudolites was using the extension code of Beidou and GPS ICD, it was stated that PRN33-PRN37 of GPS were used for ground transmitter [8].

Navigation message of Beidou/GPS pseudolites was shown in Fig. 33.2. Each pseudolite navigation message frame consists of five subframes, the first subframe was subframe type 1, carrying pseudolite location data. The second to fifth subframes were subframe type 2, supporting pseudorange differential data for six satellites.

33.3.2 Near-Far Effect

The pulse signal modulation of Beidou/GPS pseudolites was an important technology to overcome the near-far effect [9–12]. Pseudolites pulse plan was recommended by RTCM SC-104 committee, it was defined as pulse duration is 1/11 of

Table 33.1 Signal parameters between pseudolites and Beidou/GPS

	GPS	Beidou	Pseudolites	
			GPS L1	Beidou B1
Frequency (MHz)	1575.42	1561.098	1575.42	1561.098
Spread spectrum code	1–32	1–32	33–37	33–37
Code rate (MHz)	1.023	1.023	1.023	1.023
Code length (ms)	1	1	1	1
Data rate (bps)	50	50	50	50
Modulation method	BPSK	BPSK	BPSK	BPSK
Polarization mode	RHCP	RHCP	RHCP	RHCP

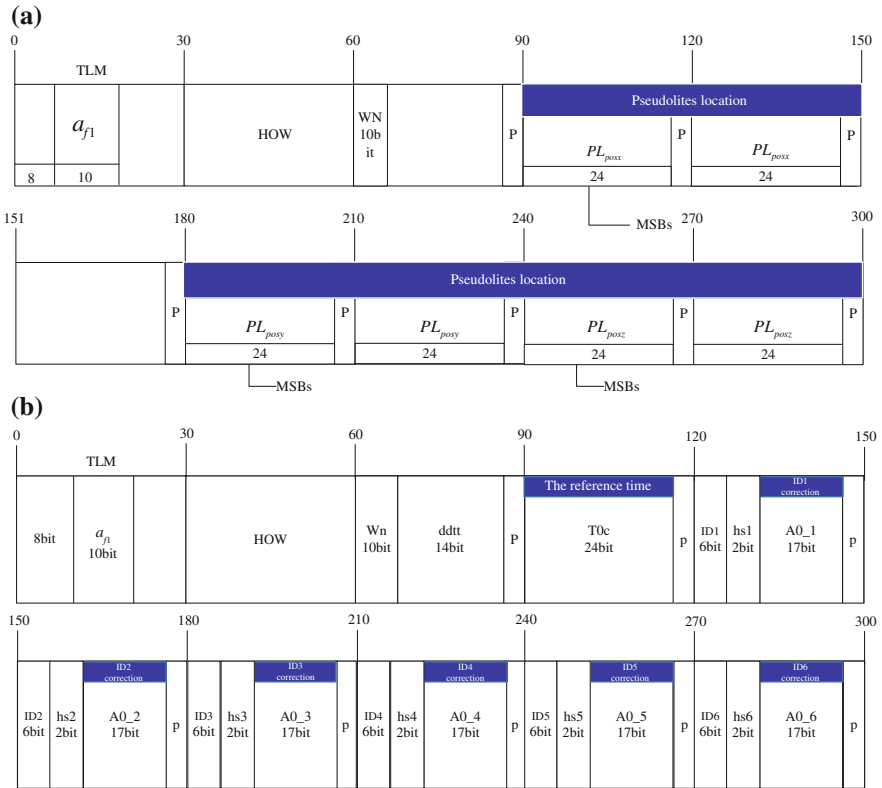


Fig. 33.2 Beidou/GPS dual-mode pseudo satellites' navigation message. **a** The subframe type 1, **b** the subframe type 2

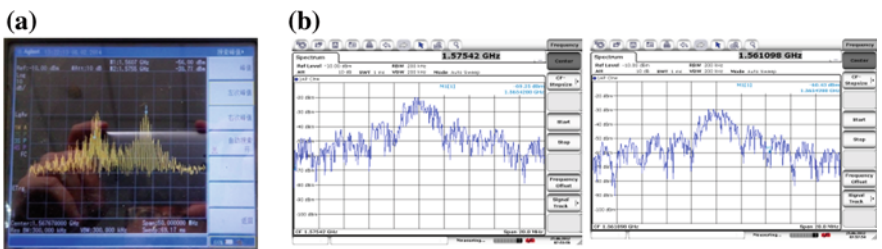


Fig. 33.3 Beidou/GPS dual-mode pseudolites continuous and pulse signal spectrum. **a** Pseudolites pulse signal spectrum. **b** Pseudolites continuous signal spectrum

code cycle. The continuous and pulse signal spectrum of BD/GPS dual-mode pseudolites were showed at Fig. 33.3a was showed pseudolite signal spectrum under the condition of the pulse signal, Fig. 33.3b was showed pseudolite signal

spectrum under the condition of continuous signal. The continuous signal spectrum was more smooth than pulse signal, which was mainly caused by the random distribution of the pulse signal energy.

33.3.3 New Method Of Time Synchronization

In order to realize the combined position of pseudolites and navigation satellites, the technical of high precision time synchronization need to be solved. Figure 33.4 was a diagram of the closed-loop time synchronization. The Beidou/GPS and pseudolites signal was received by a synchronous receiver in pseudolites. The specific methods were introduced:

Building the pseudorange measurement equation between the synchronous receiver and the signal transmitter:

$$\rho_i^m = P_i^m + c \times (dt_i - dt^m) \tag{33.1}$$

Among them, ρ_i^m was the pseudorange between the synchronous receiver to the transmitter; $P_i^m = \sqrt{(x_i - x^m)^2 + (y_i - y^m)^2 + (z_i - z^m)^2}$ was the geometric distance; dt_i was the clock error of synchronous receiver; dt^m was the time deviation of pseudolites; c was the speed of light.

Building the pseudorange measurement equation of the pseudolites synchronous receiver for GPS and Beidou:

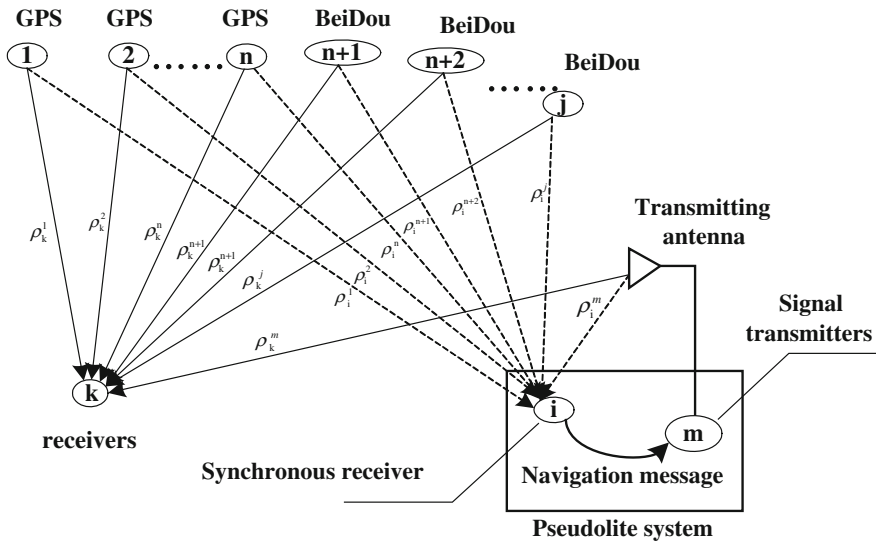


Fig. 33.4 Closed-loop time synchronization technology between Beidou/GPS and pseudolites

$$\rho_i^j = P_i^j + c \times (dt_i - dt^j) + d\rho_R + d\rho_I + d\rho_T + \varepsilon_i^j \quad (33.2)$$

Among them, ρ_i^j was the pseudorange of the synchronous receiver for GPS and Beidou; $P_i^j = \sqrt{(x_i - x^j)^2 + (y_i - y^j)^2 + (z_i - z^j)^2}$ was the geometric distance between synchronized receiver to a navigation satellite; (x^j, y^j, z^j) was the position of satellites; (x_i, y_i, z_i) as the position of the synchronous receiver; $d\rho_R$ was the error of ephemeris; $d\rho_I$ was the ionosphere error; $d\rho_T$ was the troposphere error; dt^j was the time deviation for GPS or Beidou.

We could calculate Beidou or GPS satellite clock correction,

$$M^j = \rho_i^j - P_i^j = c \times (dt_i - dt^j) + d\rho_R + d\rho_I + d\rho_T \quad (33.3)$$

Among them, M^j was the clock correction of GPS or Beidou.

Calculating the clock correction for pseudolites,

$$M^m = \rho_i^m - P_i^m = c \times (dt_i - dt^m) \quad (33.4)$$

Among them, M^m was the clock correction of pseudolites.

The formula (33.3) and (33.4) were used to calculate the clock difference correction as the navigation message parameters, which was sent to the receivers.

33.3.4 Jointing Positioning of Pseudolites/Beidou/GPS

Building the pseudorange measurement equation of Beidou and GPS:

$$\rho_k^j = P_k^j + c \times (dt_k - dt^j) + d\rho_{Rk} + d\rho_{Ik} + d\rho_{Tk} \quad (33.5)$$

Among them, ρ_k^j was the pseudorange values of the user receiver to GPS and Beidou; $P_k^j = \sqrt{(x_k - x^j)^2 + (y_k - y^j)^2 + (z_k - z^j)^2}$ was the geometric distance between the user receiver to GPS and Beidou; (x^j, y^j, z^j) was the position of the navigation satellite; (x_k, y_k, z_k) was the position of the user receiver; $d\rho_{Rk}$ was the ephemeris error; $d\rho_{Ik}$ was the ionosphere error; $d\rho_{Tk}$ was the troposphere error; dt_k was the time deviation of user receiver; dt^j was the time deviation of GPS or Beidou.

Building the pseudorange measurement equation of pseudolites signal transmitter:

$$\rho_k^m = P_k^m + c \times (dt_k - dt^m) \quad (33.6)$$

Among them, ρ_k^m was the pseudorange values of user receiver to the pseudolites; P_k^m was the geometric distance between user receiver to pseudolites; (x^m, y^m, z^m)

was the position of pseudolites; (x_k, y_k, z_k) was the position of the user receiver; dt^m was the pseudolites time deviation.

Pseudorange measurement equation of GPS or Beidou was as follows:

$$\rho_k^j - (\rho_i^j - P_i^j) = P_k^j + c \times (dt_k - dt^j) + d\rho_{Rk} + d\rho_{Ik} + d\rho_{Tk} - c \times (dt_i - dt^j) - d\rho_R - d\rho_I - d\rho_T \tag{33.7}$$

Because $d\rho_{Rk} \approx d\rho_R$, $d\rho_{Ik} \approx d\rho_I$ and $d\rho_{Tk} \approx d\rho_T$, the pseudorange measurement equation of GPS or Beidou was turn into:

$$\rho_k^j = P_k^j + c \times (dt_k - dt_i) + (\rho_i^j - P_i^j) \tag{33.8}$$

Pseudorange measurement equation for pseudolites was as follows:

$$\rho_k^m = P_k^m + c \times (dt_k - dt_i) + (\rho_i^m - P_i^m) \tag{33.9}$$

The measurement equation of Beidou, GPS and pseudolites was combined, which was used to position by the least square method.

$$\begin{cases} \rho_k^1 = P_k^1 + c \times (dt_k - dt_i) + (\rho_i^1 - P_i^1) \\ \rho_k^2 = P_k^2 + c \times (dt_k - dt_i) + (\rho_i^2 - P_i^2) \\ \dots\dots\dots \\ \rho_k^n = P_k^n + c \times (dt_k - dt_i) + (\rho_i^n - P_i^n) \\ \rho_k^m = P_k^m + c \times (dt_k - dt_i) + (\rho_i^m - P_i^m) \end{cases} \tag{33.10}$$

the clock difference of measurement equation $c \times (dt_k - dt_i)$ only matter with the user receiver and the synchronous receiver of pseudolites. Therefore, this digital synchronous method eliminates the navigation satellite clock error, orbit deviation and the influence of the ionosphere and troposphere. Then the Positioning accuracy of pseudolites and GPS/Beidou was improved.

33.4 Key Indicator Test of the Beidou/GPS Dual-Mode Pseudolites

33.4.1 Range Stability Test of Pseudolites Signal

Figure 33.5 were the 10 h test on the range stability of Beidou/GPS pseudolites. the mean value of pseudolites B1I channel was 2979.03 m, the standard deviation was 0.0068 m, the maximum deviation was 0.0267 m, while the mean value of pseudolites L1I channel was 3519.15 m, the standard deviation was 0.0054 m, the maximum deviation was 0.0276 m.

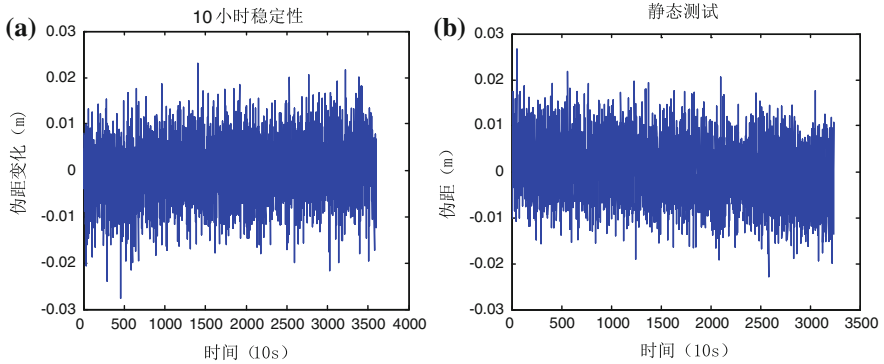


Fig. 33.5 The 24 h test results on the range stability of Beidou/GPS dual-mode pseudolites. **a** L1 C/A channel 10 h stability, **b** B1 C/A channel 10 h stability

33.4.2 Using CC50F—BG Chip to Receive the Pseudolites Signals

Using navigation chip to receive the pseudolites pulse signal was shown at Fig. 33.6. In the indoor environment, pseudolites connects with the adjustable attenuator and, by adjusting attenuation values of the attenuator, CC50F-BG chip was able to receive the pulse signal. It was enough to prove that the design of the high compatibility between the pseudolites signals and navigation chip.

33.4.3 Anti Near-Far Effect Test

Figure 33.7 was pseudolites pulse signal Anti near-far effect test. Test result was as follows: Putting a mobile phone near the pseudolites antenna (about 30 cm), in 5 min, the mobile phone positioning was realized. It was proved that pseudolites' pulse signals could effectively solve the near-far effect, in “near effect zone” did not interfere with the positioning function of Beidou/GPS chip.

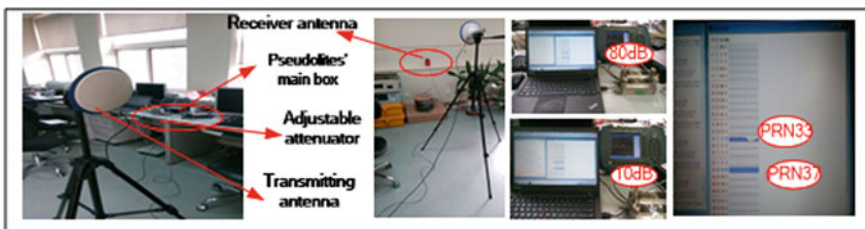


Fig. 33.6 Using CC50F-BG chip receive the pseudolites signals

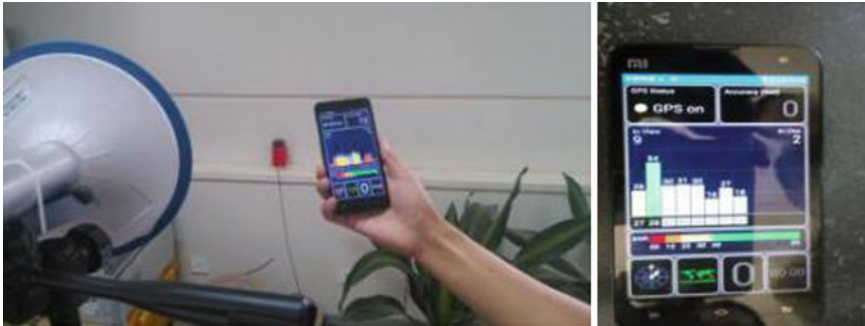


Fig. 33.7 Anti near-far effect test of pseudolites pulse signal

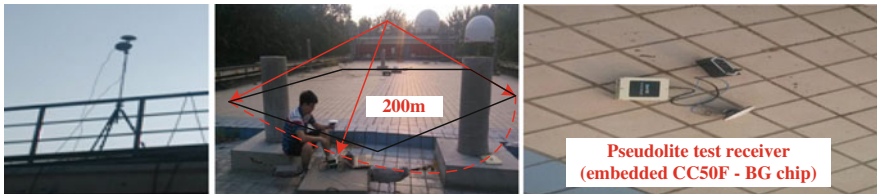


Fig. 33.8 Beidou/GPS pseudolites signals transmitted power and coverage test

Figure 33.8 was the pseudolites signals transmitted power and coverage test environment, the Olinkstar’s CC50F-BG chip was used as a test terminal.

Table 33.2 was the test results of pseudolites signals transmitted power, it could be seen in the table that pseudolites signals made CC50F-BG chip which had been in a saturated state.

33.4.4 Positioning Accuracy Test

Figure 33.9 was the result of pseudolites positioning accuracy by using rubidium standard or crystals, Fig. 33.9a was the result of pseudolites positioning accuracy by rubidium standard, Fig. 33.9b was the result of pseudolites positioning accuracy by

Table 33.2 The test results of pseudolites signals transmitted power

	Distance (m)	GPS (C/N0)	BD (C/N0)
1	15	43	47
2	25	43	47
3	65	43	47
4	200	43	47

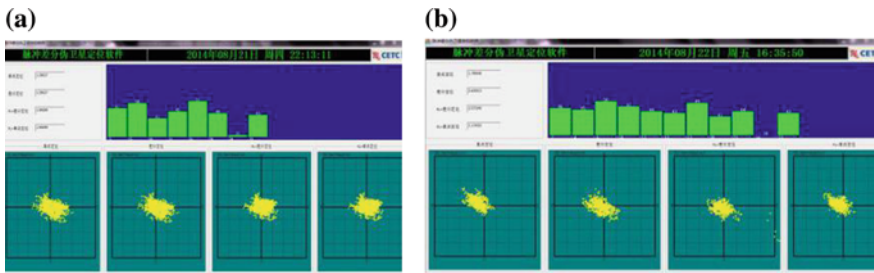


Fig. 33.9 The result of pseudolites positioning accuracy by rubidium standard or crystals. **a** Pseudolites positioning accuracy by rubidium, **b** pseudolites positioning accuracy by crystals

crystals. By the test results could be seen in the graph, Beidou or GPS single point positioning results relative to the coordinate point had some bias, and Horizontal position precision was in line with its nominal value (about 10 m). After joining pseudolites, positioning accuracy was improved (better than 5 m), and Anchor points were concentrated in the known point.

The results expressed in the form, as shown in Table 33.3. It could be seen that: (1) Positioning performance was basically the same between rubidium standard or crystals, therefore, under the support of the new time synchronization algorithm, pseudolites time-frequency units could chosen crystal. (2) Under the combination of pseudolites and Beidou/GPS, HDOP value would be decreased, the advantages of geometric distribution was improved.

33.5 The Applications of the Beidou/GPS Dual-Mode Pseudolites

The pseudolites has been installed Jiuzhaigou national park, as shown in Fig. 33.10. According to the test results, the number of navigation satellite was decreased, and geometric distribution was significantly worse, which made Beidou or GPS positioning precision in 30 m(95 %), had a same direction deviation relative to the known point, then we found that the deviation was mainly due to constellation geometry deformation in canyon area. After by adding the pseudolites signals, positioning accuracy was improved significantly, better than 8 m (95 %).

Table 33.3 The statistics of pseudolites positioning accuracy by rubidium standard or crystals

Positioning mode	HDOP	Rubidium standard	Crystals
Single point positioning	2.37	10 m (95 %)	10 m (95 %)
Pseudolites + Beidou + GPS	1.73	4.78 m (95 %)	4.95 m (95 %)

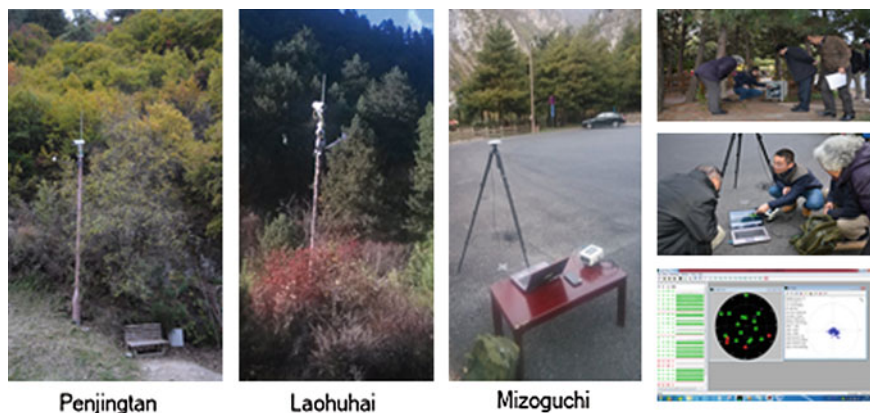


Fig. 33.10 Beidou/GPS dual-mode pseudolites installation and application in Jiuzhaigou

33.6 Conclusion

The algorithm of pseudolites compatible Compass/GPS signals, navigation message and anti near-far effect was described in paper, and proposed the new high precision time synchronization technology. By the infield and outfield test environment, pseudo range stability, navigation chip compatible reception ability, signal coverage and the positioning accuracy was tested. The test results show that: rubidium clock and crystal oscillator to drive the pseudolites had the same performance by using this closed-loop time synchronization algorithm. In the combination of pseudolites/Beidou/GPS, pseudolites could improve the geometric distribution, the positioning accuracy of the navigation system from 10 up to 5 m.

To facilitate the seamless positioning capability of Beidou satellite navigation, the Beidou/GPS pseudolites was developed, which was using a new closed-loop time synchronization and pseudolites/Beidou/GPS combination positioning technology. In the follow-up, we need to strengthen the research of Beidou pseudolites signals and indoor positioning technology [13–17].

References

1. Wang J (2000) Pseudolites applications in positioning and navigation: progress and problems. *J GPS* 1(1):48–56
2. Barnes J (2005) The integration of GPS and pseudolites for bridge monitoring. In: Sanso F (ed) *A window on the future of geodesy, IAG Symposium 2005*, vol 128, pp 83–88
3. Soon BHK (2003) Flight test results of precision approach and landing augmented by airport pseudolites. In: *16th International technical meeting of the satellite division of the U.S. Institute of Navigation, Portland, Oregon, USA*, pp 2318–2325, 9–12 Sept 2003

4. COBB (1997) GPS pseudolites: theory, design, and applications. Stanford. PhD, 1997, pp 39–44
5. GILT Study (2005) Core technology document for pseudolites for enhanced availability. GILT-TRT-DD-15, GALILEO initiative for local technologies. Alenia-Spazio, Thales, Indra
6. E Electronic Communications Committee, Compatibility studies between pseudolites and services in the frequency bands 1164–1215, 1215–1300 and 1559–1610 MHz, ECC report 128. <http://www.cept.org/ecc>
7. Japan Aerospace Exploration Agency. Interface specifications for QZSS™ (IS-QZSS Ver 1.0). <http://www.gnss.co.jp/file/paper/null>
8. GPS. gov, interface specification IS-GPS-200. <http://www.gps.gov/technical/icwg/>
9. Abt T-L, Soualle F (2005) Optimal pulsing schemes for GALILEO pseudolites signals. Paper presented at ION GNSS 2005, Long Beach, CA
10. Kalafus RM, Dierendonck AJ van (1986) Special committee 104 recommendations for differential GPS service. *Navigation* 33(1):26–41
11. Ye H (2010) The analysis and research of pseudolites near-far effect. *J Radio Eng* 40(6):32–34
12. Ye H, Yu B (2008) The optimization research of Galileo pseudolites signal pulse modulation scheme. *J Radio Eng* 37(8):P40–P46
13. Progri IF, Michalson WR (2007) Indoor geolocation using FCDMA pseudolites: signal structure and performance analysis. *Navigation* 54(3):241–256
14. Ford T, Neumann J (1996) HAPPI—a high accuracy pseudolites/GPS positioning integration. In: Proceedings of the 9th international technical meeting of the satellite division of the institute of navigation (ION GPS-96), 17–20 Sept 1996, Kansas City, Missouri, pp 1719–1728
15. Choi IK, Wang J, Han S (2000) Pseudolites: a new tool for surveyors. In: 2nd trans Tasman survey congress, Queenstown, New Zealand, pp 141–149, 20–26 Aug 2000
16. Holden T.(1997) Pseudolites augmented DGPS for land applications, In: 10th International technical meeting of the satellite division of the US institute of navigation GPS ION-97, Kansas City, Missouri, pp 1397–1403, 16–19 Sept 1997
17. Weiser M (1998) Development of a carrier and C/A-code based pseudolites system, In: 11th International technical meeting of the satellite division of the U.S. institute of navigation GPS ION-98, Nashville, Tennessee, pp 1465–1475, 15–18 Sept 1998

Chapter 34

Study on Judgment Method of Signal Correlation Performance Based on Complex Correlation Vector

Ying Wang, Zhe Su, Yansong Meng and Xiaoxia Tao

Abstract For a long time, the satellite navigation signals are performed in a relatively simple BPSK or QPSK modulation of pseudo code and data for loading data information and time information. However, since the USA GPS modernization, the European Galileo satellite navigation system begins to demonstrate, new ideas and new methods for design and receiving signal appear continuously. With the use of AltBOC baseband signal form, we urgent need more complete presentation of a signal related performance. In this paper, the processing of traditional signal and the complex baseband signal was analysed. And the method of complex correlation vector diagram was studied for judgment signal correlation performance. The correlation vector analysis method is given in the process of receiving the actual signal. The method and result provides performance analysis guide for receiving the navigation signals by jointing I and Q branch and receiving full bandwidth AltBOC signal.

Keywords Correlation · Satellite navigation · Navigation signal

34.1 Introduction

GPS played a groundbreaking role in the field of navigation and positioning by using the pseudo code ranging system based on time of arrival measurement. Since then, the satellite navigation signals are performed in a relatively simple BPSK or QPSK modulation of pseudo code and data for loading data information and time information. However, since the USA GPS modernization, and the European Galileo satellite navigation system begins to be deployed, the thought of design for signal and receiving methods are more abundant. Expression of real signal has not accurately represented the signal content. Various methods and new ideas about navigation

Y. Wang (✉) · Z. Su · Y. Meng · X. Tao
China Academy of Space Technology (Xi'an), Xi'an 710100, China
e-mail: eaglesoars@126.com

© Springer-Verlag Berlin Heidelberg 2015
J. Sun et al. (eds.), *China Satellite Navigation Conference (CSNC) 2015 Proceedings: Volume I*, Lecture Notes in Electrical Engineering 340,
DOI 10.1007/978-3-662-46638-4_34

365

signal design and receiving such as AltBOC are constantly appeared. With the use of AltBOC and other complex signal form, a more reliable method is needed to completely demonstrate the navigation signal correlation performance [1–4].

Radio frequency (RF) signals are generally real signals, after receiving by antenna and down conversion, it becomes intermediate frequency (IF) real signals. When the carrier stripped, the distortion such as signal spectrum shape asymmetry makes the baseband signal into complex signal containing I, Q two components. In the present study, the complex correlation vector method was discussed by receiving and analysing of complex signal methods.

34.2 Model Analysis

For general navigation signal received, omitting the intermediate frequency modulation step, the signal can be expressed as

$$s(t) = \text{Re}[c(t)e^{j2\pi ft}] \quad (34.1)$$

where, $c(t)$ is the baseband signal that can be pure real or complex signal. When $c(t)$ is purely real, in the baseband signal vector circle, the clockwise and counterclockwise rotation of two vectors is showed, the synthetic vector is always real vector. When $c(t)$ is a complex signal, it always can be written as

$$c(t) = A(t)\angle\varphi(t) = x(t) + jy(t) \quad (34.2)$$

The signal vector can be clockwise rotation or counterclockwise rotation. There are two kinds of correlation tracking method: One is based on independently tracking x or y; another method is based on the orthogonality of x and y by tracking x (or y) and assisting another. Both methods have the advantages of simple structure, so now a lot of receivers use these methods for tracking signal. For the signal, there is a limit condition: the signal energy must be focused on the I branch. When the receiver stable tracking, the Q branch is mainly the noise component. This treatment is correct and reasonable for ordinary real baseband signal. But for the complex baseband signal, the Q branch has always existed signal energy. It means that this part of the energy will be treated as noise, as a result, it reduced the energy of signal and the relative increased the noise energy, causing greater loss of carrier to noise ratio (C/N0).

When signal becomes complex signal, it has the following circumstances:

1. The Ideal Signal is Real Signal

After modulation, affected by the non-ideal factors of the channel, the real signal amplitude and phase become imbalance. After down conversion, the signal itself becomes complex signal. At this time, the complex signal characteristic shows the influence of the characteristics of channel. The analysis contributes to the understanding of the channel characteristics and improving that.

In addition, the influence caused by the factors such as local clock which makes the carrier removal not clean, and even the introduction of additional dynamic turn this signal into complex signal. The characteristics of the complex signal show the performance of signal and the tracking performance of the receiver.

When the receiver acquisition, usually the square of I and Q integral results is the control variable to eliminate the influence of the interpretation of the results of the acquisition phase. In fact this uses Q branch energy and alleviates the effect of external factors on signal.

In addition, there is another form for (34.2)

$$c(t) = A(t)\angle\varphi(t) = x(t) - jy(t) \quad (34.3)$$

When x or y individually tracked, the signal is exactly the same with the signal (34.2). But for the complex signal receiver jointed x and y, there is a completely different character. According to the correlation operation

$$r_{mm}(l) = \sum_{k=-\infty}^{\infty} m(k)n(k-l), \quad l = 0, \pm 1, \pm 2, \dots \quad (34.4)$$

$$\begin{aligned} r_{c_1c_1}(0) &= \sum_{k=-\infty}^{\infty} c_1(k)c_1^*(k) = \sum_{k=-\infty}^{\infty} (x^2(k) + y^2(k)) \\ &= \sum_{k=-\infty}^{\infty} c_2(k)c_2^*(k) = r_{c_2c_2}(0) \end{aligned} \quad (34.5)$$

where, $c_1(t)$ is $c(t)$ of (34.2), $c_2(t)$ is $c(t)$ of (34.3). The signal cross-correlation

$$\begin{aligned} r_{c_1c_2}(0) &= \sum_{k=-\infty}^{\infty} c_1(k)c_2^*(k) \\ &= \sum_{k=-\infty}^{\infty} (x(k) + jy(k))(x(k) + jy(k)) \\ &= \sum_{k=-\infty}^{\infty} (x^2(k) - y^2(k) + j2x(k)y(k)) \end{aligned} \quad (34.6)$$

The subtraction of x and y component makes correlation peak become lower. While the cross-correlation properties of x and y sequence will make the imaginary part of the accumulated energy is very small. Eventually, the ability of two signals mutual demodulation does not exist. We can also see that when the local signal is only x (or y), namely the signal is real signal, the situation that it cannot be demodulated does not exist in this case.

2. The Ideal Signal Itself is a Complex Signal

The more significance of complex baseband signal design lies in the spectrum shifting. When the center frequency of two signals is far apart, generally,

independent RF channel of frequency conversion, filtering and amplification is deployed. In order to make effective use of equipment on satellite, we can combine the signals which frequencies are closer to each other for sharing RF channel. The AltBOC signal of Galileo satellite navigation system is a typical realization method. At this time, because of the asymmetry of the signal content of both sides of the center frequency, when the baseband signal generated, we must use the complex signal generation method. When signal being received, more common method of receiving is respectively using RF channel, including filtering, down conversion. If the receiver tracking at its real center frequency, this method requires increasing the RF channel number. Another way is to use broadband receiver and complex signal tracking method. With the local signal generated by complex signal method, the receiver can track signal by complex correlation calculation. There are some characteristics such as the larger signal bandwidth, the higher demands on the RF devices, but the main processing volume increased is in the digital domain and easy to control the scale.

The complex correlation vector consists of the vector shape accumulated by two signals. Similar to correlation curves, it can be expected that, complex correlation vector mainly focus concentrated in a few aspects:

- Symmetry.

Today, the satellite navigation signal correlation peaks are symmetrical structure, so the symmetry reflects the distortion degree of correlation peak. In the environment of multipath interference and channel characteristics influence, the symmetry are subject to different degrees of damage. At this time, the complex correlation vector can clearly reflect this kind of influence.

- The sharp characteristics of the peak.

Correlation peak shape reflects the performance of narrow correlation: the shape more smooth, narrow correlator performance worse.

In addition, the complex correlation vector is characterized:

- Carrier phase difference.

It embodies in the rotated relation between complex correlation vector diagram and ideal vector diagram.

- I, Q orthogonality.

For real baseband signal, the area enclosed by complex correlation vector show I, Q orthogonality in a statistical sense. 0 shows a complete orthogonal relation. For the complex baseband signal demodulation, both the symmetry and the graph have influence.

At the same time complex correlation vector graph reflects the gliding movement characteristics of two signals correlation, this motion characteristics can guide the receiver discriminator design.

The key of navigation signals correlation is the estimation of time delay using correlation peak curve, based on the cross correlation function:

$$R_{x_1x_2}(\tau) = E\{x_1(k)x_2(k-l)\} = \alpha R_{ss}(\tau - D) \quad (34.7)$$

where, two independent signals:

$$x_1(t) = s(t) + n_1(t) \quad (34.8)$$

$$x_2(t) = \alpha s(t - D) + n_2(t) \quad (34.9)$$

where, $s(t)$ is the source signal; $n_1(t)$ and $n_2(t)$ are noise; D is the time delay; α is the attenuation coefficient; Time delay estimation becomes the estimation of the maximum position of (34.7). We need τ which makes $R_{ss}(\tau - D)$ maximum.

In band limited conditions, correlation peak becomes smooth, so that reduce the accuracy of estimation of time delay. We can make the peak position convert to zero crossing detection using Hilbert transform, to obtain the exact time delay estimation.

$$\tilde{R}_{ss}(\tau - D) = H[R_{ss}(\tau - D)] = \frac{1}{\pi} \int \frac{R_{ss}(t - D - \xi)}{\xi} d\xi \quad (34.10)$$

where, $H[\]$ is Hilbert operator, defined as

$$\tilde{x}(t) = H[x(t)] = \frac{1}{\pi} \int \frac{x(t - \xi)}{\xi} d\xi \quad (34.11)$$

Hilbert transform will also transform zero for the peak, that can be applied to the use of modulated signals (such as BPSK signal) zero crossing detection delay.

34.3 Complex Demodulation for Real Baseband Signal

After a signal was received, the first thing is to remove carrier

$$s(t)e^{j2\pi f_1 t + j\varphi_1} = \text{Re}[c(t)e^{j2\pi f t + j\varphi}]e^{j2\pi f_1 t + j\varphi_1} \quad (34.12)$$

When the baseband signal for real signals

$$\begin{aligned} s(t)e^{j2\pi f_1 t + j\varphi_1} &= c(t) \cos(2\pi f t + \varphi) e^{j2\pi f_1 t + j\varphi_1} \\ &= \frac{c(t)}{2} \left[e^{j2\pi(f+f_1)t + j(\varphi+\varphi_1)} + e^{j2\pi(-f+f_1)t + j(-\varphi+\varphi_1)} \right] \end{aligned} \quad (34.13)$$

The frequency component of '+' will be removed, and the residual component of frequency and phase difference will be passed on to subsequent demodulation process. From (34.8), when the frequency is constant, the absolute value has nothing to do with the complex component.

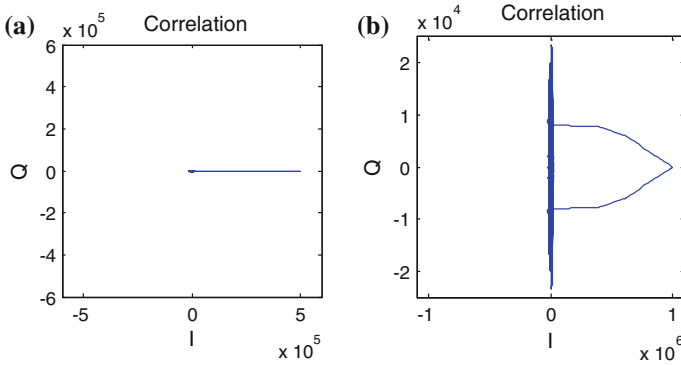


Fig. 34.1 Ideal correlation (a) and its complex correlation vector (b)

Obviously, when the carrier frequency and phase aligned, the complex component will be 1, so

$$s(t)e^{j2\pi f_1 t + j\varphi_1} = \frac{c(t)}{2} e^{j2\pi(-f+f_1)t + j(-\varphi+\varphi_1)} = \frac{c(t)}{2} \tag{34.14}$$

Then correlation operation with local codes

$$\sum s(t)e^{j2\pi f_1 t + j\varphi_1} c_1(t) = \sum \frac{c(t)c_1(t)}{2} \tag{34.15}$$

In Fig. 34.1a, the correlation vector shows the amplitude of I is larger and the amplitude of the Q approximate to 0. It indicated that the imaginary part of correlation function is very small. At this time the absolute value of the vector is the relative peak height.

Adding noise, the signal mobile and its range of complex correlation vector is the representation of the correlation value feature of the real part. In Fig. 34.1b When the signal is the QPSK signal, due to the actual implementation of the process, there may be I, Q modulated quadrature error, which is equivalent to the introduction of the baseband signal I, Q offset.

34.4 AltBOC Signal Complex Correlation Vector

When the baseband signal is complex signal, such as the AltBOC signal of Galileo satellite navigation signal, the baseband signal is a complex expression [2].

The autocorrelation of ideal baseband signal as shown in Fig. 34.2a, and the complex correlation vector as shown in Fig. 34.2b.

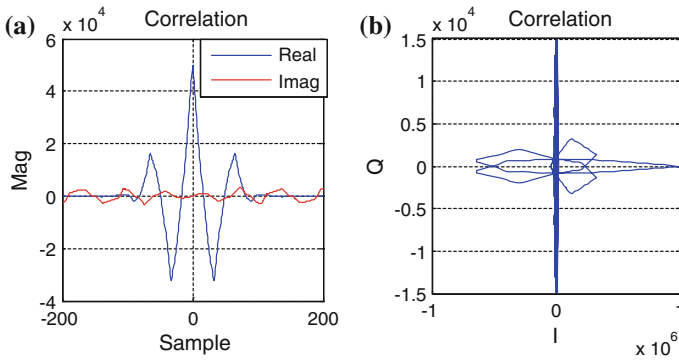


Fig. 34.2 a Correlation; b Complex correlation vector

The conventional autocorrelation is not conducive to the analysis of the relationship. It shows symmetry about $Q = 0$ in the complex correlation vector. In fact, the symmetry is mainly determined by the symmetry properties of real part symmetry and antisymmetric imaginary part. The complex correlation vectors of some signals are shown in Fig. 34.3.

In the vector diagram in Fig. 34.3a, the majority points are concentrated in the vicinity of the origin point; little part is located elsewhere, indicating the existence of correlation peak. The vector approximation on a line of symmetry, the angle of the axis of symmetry and the axis of I, Q coordinates is phase difference. In Fig. 34.3a, the vector diagram presents a more complex rotating pattern, and any rotation are not like Fig. 34.3a that makes I larger (Q less) or Q larger (I smaller). This indicates that the signal itself is a complex signal containing complex sub-carrier. The existence of subcarrier makes the more correlation peaks appear. At this time, the ideal signal autocorrelation actually as Fig. 34.4, and the band limited makes the correlation vector vertex become smooth, changing to Fig. 34.2b. It is

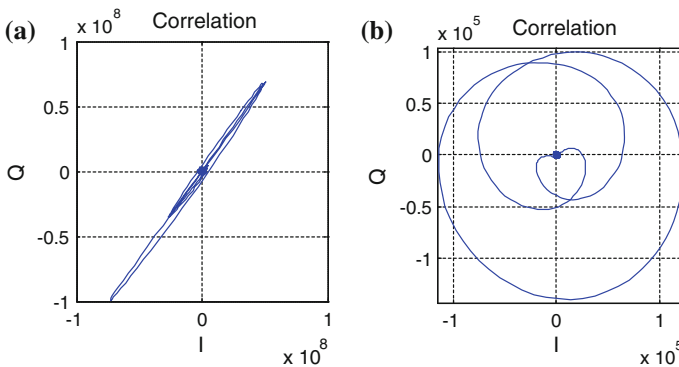
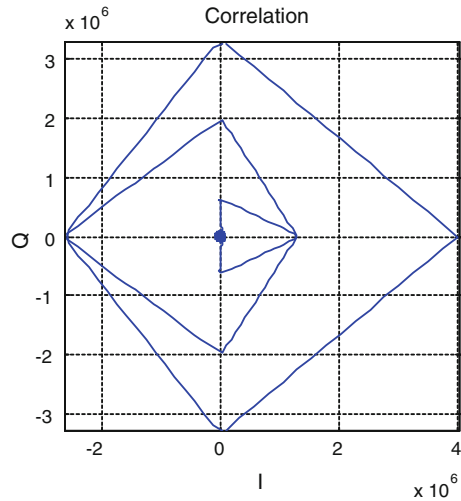


Fig. 34.3 Complex correlation vector

Fig. 34.4 Complex correlation vector (ideal signal)



seen from Figs. 34.3b and 34.4, two paths from the origin, starting along any path, will return to the origin from another path. It shows the process of the two signal slip correlation. The line formed by two path intersection points is a symmetry axis, and the angle with the axis of I, Q is the phase error.

From Fig. 34.4, Complex correlation vector showing the nested polygons, with exact symmetry, the vertex and the intersection point of trajectory have relationship strictly.

Two kinds of signal complex correlation vector pattern measured show in Fig. 34.5a, b. The Fig. 34.5a shows a complex correlation vector in the presence of BPSK modulation in the Q branch. In Fig. 34.5b, the complex correlation vector of signal containing complex subcarrier is shown. At this time the constellation and the spectrum are shown in Fig. 34.6.

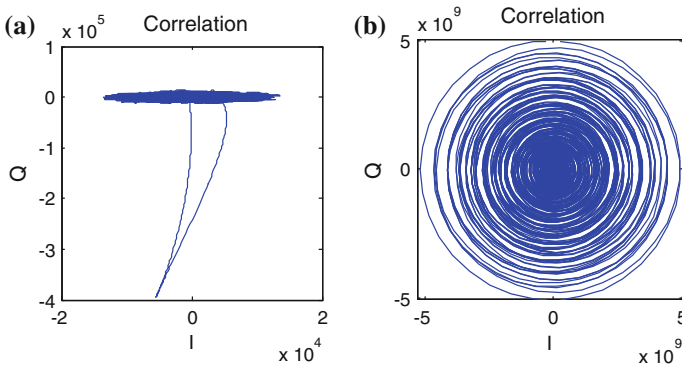
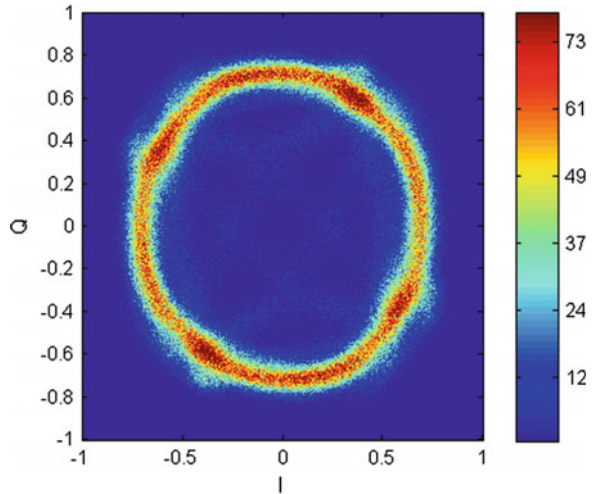


Fig. 34.5 Complex correlation vector. **a** Real signal I. **b** Real signal II

Fig. 34.6 Constellation diagram



Figures 34.5b and 34.6 in fact expressed Galileo E5a signal, receiving and demodulation in the center frequency of 1191.795 MHz. In the actual constellations vaguely we can distinguish QPSK constellation points, but it mainly shows the rotational characteristics of subcarrier.

34.5 Conclusions

Based on the analysis of the demodulation process of satellite navigation signal, the paper points out the deficiency of the traditional correlation method in the analysis of signal correlation performance. Then we put forward the method using complex correlation vector to describe signal component relationship. This method is especially suitable to the complex signals received. Because of the side peaks of AltBOC signal correlation function, which showed more discrepancy with BPSK real signal, and is more suitable for signal analysis using the complex correlation vector analysis method.

References

1. Tan S, Zhou B, Guo S, Liu Z (2010) Design of China global satellite navigation signals. In: CSNC 2010, Beijing
2. Zhou Y, Hu X, Tang Z, Ke T (2011) Tracking performance analysis for BOC signals based on pseudo correlation function method. *J Astronaut* 32(12):128–134
3. Chen H, Wang R, Jia W, Yao M (2012) Combined-correlation-function-based unambiguous tracking method for Cosine-BOC signals. *Syst Eng Electron* 34(6):212–218
4. Li C, Wang F, Guo G (2007) Correlation of PN spread spectrum signal under first-order dynamics. *Acta Electronica Sinica* 35(9):102–109

Chapter 35

The Analysis of GNSS SIS Accuracy

Shuai Liu, Xiaolin Jia and Zhuoxi Ma

Abstract With the rapid development of the global navigation satellite system (GNSS), to build the corresponding GNSS monitoring and evaluation system, has a great realistic significance to the operation condition of the BDS satellite navigation system and various performance indicators for monitoring and evaluation. At present, the International GNSS Monitoring And Assessment Service (iGMAS) launched by China in the world is building in an orderly way. This article direct at GNSS navigation space signal, use the four system's precise ephemeris data and hybrid broadcast ephemeris data from January to October in 2014 to calculate and analysis; Direct at the characteristics of single and mixed constellation, derivation the calculation formula of the SISURE (Signal-in-Space User Range Error); Do statistical analysis and accuracy evaluation to the broadcast ephemeris data based on the four system precise ephemeris data. The calculation results and analysis shows that: the SISURE accuracy of the four systems by broadcast ephemeris is better than 2.5 m.

Keywords GNSS · URE/SISURE · Broadcast ephemeris · Precise ephemeris · Signal-in-Space

35.1 Introductions

At present, the global navigation satellite system (GNSS) has obtained remarkable achievements in worldwide, as the four major global navigation system: GPS, GLONASS, BDS and Galileo comprehensive integration development, as well as a variety of regional system (such as Japanese QZSS, India IRNSS) and enhance the system (such as WAAS and EGNOS, MSAS) is completed. GNSS is entering a new milestone, a multiple, mode and means; High accuracy, high alignment

S. Liu (✉) · X. Jia · Z. Ma
PLA Information Engineering University, Zhengzhou 450000, China
e-mail: liushuai0810@sina.com

© Springer-Verlag Berlin Heidelberg 2015
J. Sun et al. (eds.), *China Satellite Navigation Conference (CSNC) 2015 Proceedings: Volume I*, Lecture Notes in Electrical Engineering 340,
DOI 10.1007/978-3-662-46638-4_35

and fast, efficient combination system are rapidly improve [1–5]. Due to the participation more navigation system, the navigation system compatible with interoperability between the similarities and differences and performance index parameters has become a new research field.

The space of the satellite navigation system signal is connected to the satellites, ground users and the core of the station chain, the analysis of the spatial signal information is a major topic in the field of monitoring and evaluation. Among them, the accuracy of signal-in-space is our service performance evaluation of satellite navigation system is a key index, satellite navigation and positioning accuracy and system integrity monitoring is one of the key factors [6–9]. GNSS Signal-in-Space User Range Error (SISURE) is Space User Range Error Signal, it can be real reaction of navigation information prediction Error, [10, 11] Space inside the GPS SPS PS has GPS Signal User Range Error (URE) for the definition and model of the corresponding deduction, define User Range Error Signal into the Space satellite ephemeris Error and forecast the clock difference of two parts, because of the abbreviations are not clear. In this paper, we use URE show satellite ephemeris Error caused by User Range Error, and use SISURE show satellite ephemeris Error and forecast Space Signal Error together.

In this article, first we introduce some assessment of the commonly used method, spatial signal and precise ephemeris evaluation method, combining with the characteristics of four GNSS system of satellite and deduced the corresponding space information accuracy evaluation model, then using January to October in 2014 single day broadcast ephemeris and precise ephemeris data, the precision of broadcast ephemeris of four system calculation and processing, finally by processing the results of the corresponding space information accuracy evaluation conclusions are given. A large number of measured ephemeris data obtained by <ftp://cddis.gsfs.nasa.gov/>.

35.2 GNSS Space Signal Accuracy Evaluation Method

35.2.1 *Observation with Stars to Distance Comparison Method*

Observation distance comparison method with the stars usually divided into those methods: SLR comparison method, star to two-way time synchronization pseudorange observation and monitoring stations dual-frequency pseudorange observation comparison method. The basic core principle of the method is by observing quantity comparing with star to distance. Among them, the observed quantity need preprocessing, a variety of processes such as error correction; Star distance by the broadcast ephemeris parameters and station coordinates are calculated. The difference between those methods is using the different observation [12–14].

35.2.2 Precise Ephemeris Data Comparison Method

Using the precise ephemeris data broadcast ephemeris precision evaluation method is different from the star to ground observation quantities comparison method, its evaluation is not only the radial direction of the error, but the evaluation of broadcast ephemeris in three dimensional directions: radial (R), tangential (T, or trace), and normal (N), and the URE/SISURE.

Precise ephemeris can be obtained by the international GPS service in the form of post-processing content [15], it contains a fixed time interval on the timing of the satellite three dimensional coordinate parameters, speed and clock error parameters, and can be directly assess the precision of broadcast ephemeris parameters. If the broadcast ephemeris and precise ephemeris do not agree on the time scale, it can be solved through the corresponding difference method and get on the parameter value used in the comparison at the same time. Obtained the broadcast ephemeris and precise ephemeris direction difference in XYZ coordinate, conversion to the RTN coordinate direction and get the radial, tangential, normal and clock offset error, through the URE/SISURE formula to calculate the SIS user range error [16].

This section mentioned four spatial signal accuracy evaluation method, the first three belong to the same type, they used to evaluate the broadcast ephemeris radial error, calculation principle, use different observation, and this has led to the error precision. Precise ephemeris assessment method, can be all the time for all satellite space signal accuracy assessment, although the precise ephemeris has its own error to be the standard, but use this method to do the comprehensive assessment of the three dimensional position error and clock difference has the advantages of the former three methods, thus became the universal applicability method of spatial signal accuracy evaluation method now.

35.3 GNSS Space Signal Accuracy Evaluation Method

In space signal error, have four processing error, we need to consider the RTN three-dimensional direction error and the satellite clock error (the timing error), SPS PS in GPS (DoD US, 2008) is given in the corresponding GPS satellites in SISURE formula (35.1), we get the calculate formula with the four error contribution factor [17]:

$$SISURE = \sqrt{(S_R \times R - C \times \Delta T)^2 + S_{TN}(T^2 + N^2)} \quad (35.1)$$

Regardless of the clock error, only consider orbit error caused by user range error formula:

$$URE = \sqrt{(S_R \times R)^2 + S_{TN}(T^2 + N^2)} \quad (35.2)$$

Among them, C is the speed of light, ΔT is the radio clock error, R is the broadcast ephemeris radial error, T and N is the broadcast ephemeris tangential and normal error, S_R is the contribution of the radial error factor, S_{TN} for the contribution of the tangential and normal error factor, why we need the contribution factor, it is just because of the difference of RTN direction and clock error of spatial signal accuracy range is different. For different types of satellite, because of the different altitude, the contribution of the RTN direction factor is different size. For GPS, GLONASS, and Galileo system, the main components are MEO satellites, so although slight deviation altitude but the size of the contribution factor is almost the same, but BDS is composed of hybrid constellation. BDS not only contains MEO satellite, but also contains GEO/IGSO satellites at high altitude, so the corresponding contribution factor needs to be calculated [18, 19].

As shown in Fig. 35.1, we establish coordinate system as follows, assuming that the earth is an ideal sphere, R_S is the distance from satellite to earth, R_E is the radius of the earth, D is a certain point on the surface of the earth, O is the mass center of the earth, and we connect the earth's center of mass and the mass center of satellite S , to point the positive direction of the satellite orientation (R direction) is to establish the Z axis, with satellite flight direction (T direction) to establish the X axis, according to the right-hand rule to establish the Y axis.

Position of the satellite signal coverage area are assumed to be evenly distributed, known position to density function of the weight function is $\rho(\alpha) \propto \sin \alpha$,

Cover Angle range as follows:

$$(0 \leq \beta \leq 2\pi, 0 \leq \alpha \leq \alpha_{\max} = \cos^{-1}(R_E/R_S))$$

Fig. 35.1 Satellite schematic in space coordinate system

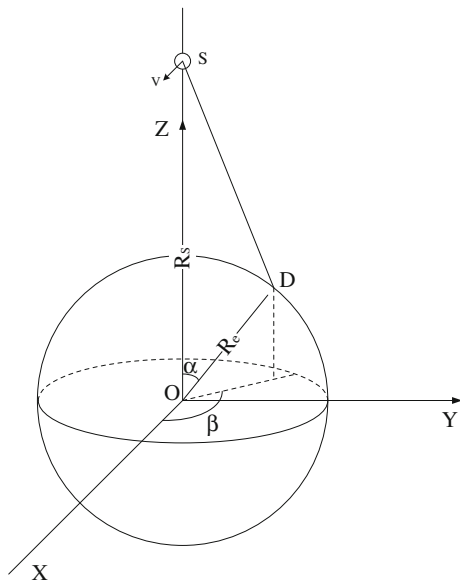


Table 35.1 URE contribution factor of the GNSS four satellite systems

系统	GPS		GLONASS		BDS				Galileo	
High (km)	20200 MEO		19100 MEO		35786 GEO/IGSO		21528 MEO		23222 MEO	
Contribution factor	S_R	S_{TN}	S_R	S_{TN}	S_R	S_{TN}	S_R	S_{TN}	S_R	S_{TN}
Number	0.979	0.143	0.978	0.149	0.992	0.089	0.981	0.136	0.984	0.128

The corresponding precision contribution factor:

$$S_R = \frac{1}{D} \int_0^{\alpha_{max}} \int_0^{2\pi} \frac{R_S - R_E \cos \alpha}{\sqrt{R_E^2 + R_S^2 - 2 R_E R_S \cos \alpha}} \sin \alpha d \beta d \alpha \tag{35.3}$$

$$S_{TN} = \frac{1}{D} \int_0^{\alpha_{max}} \int_0^{2\pi} \frac{R_E^2 \sin^2 \alpha \cos^2 \beta}{R_E^2 + R_S^2 - 2 R_E R_S \cos \alpha} \sin \alpha d \beta d \alpha \tag{35.4}$$

Among them, $D = 2\pi(1 - \cos(\alpha_{max}))$ is the satellite coverage per unit area. Table 35.1 lists the calculation formula of the four systems of URE the contribution factor in numerical [20]. As you can see, when the satellite orbit height is higher, the radial error contribution to URE is greater, tangential and normal error contribution to URE is smaller.

35.4 Broadcast Ephemeris Precision Evaluation and Analysis

Based on the four systems a great deal of broadcast ephemeris and precise ephemeris data from January to October in 2014, independent program is used to calculate the corresponding steps, process considering the problem of eliminate observation gross error; incomplete data extrapolating data deviation to eliminate problem; unhealthy satellites to eliminate problems. About the statistical methods of single satellite URE, generally divided into two categories, one is the 95 % URE statistics, to calculated all sampling time URE according to the absolute value of error from small to large, and get the 95 % points locus corresponding value as the 95 % URE precision statistics; Another is the RMS statistics, is the root mean square error of the mean and the standard deviation, formula is as follows:

$$rms \approx \sqrt{\sigma^2 + \mu^2}$$

In this article, we use the RMS statistical method, this method better reflects the average data and data deviation.

Add clock difference in SISURE error information, due to considering the broadcast ephemeris and precise ephemeris clock error using different time benchmark. So first we calculate the single difference between broadcast ephemeris clock and precision clock for all satellites in the same epoch, then take the average value as the reference value, next make difference between the reference value and the single difference, use this double difference value as ΔT to calculate. This kind of treatment, eliminate the time reference inconsistency problem between the broadcast ephemeris clock error and the precise ephemeris clock error. URE/SISURE statistical methods using all epoch single satellite RMS, the unit is meter, the above treatment methods used in this paper for the four systems, repeat no more in this article.

35.4.1 GPS Broadcast Ephemeris Evaluation Results

GPS systems use the IGS precise ephemeris data in 2014. Because in the unhealthy state, G26 satellite ephemeris information has been dropped.

Figure 35.2 is the result of GPS system, the value can be seen from Table 35.2, after joining difference of clock error of all GPS satellite, SISURE compared with URE the average deviation is about 0.48 m, and different satellites have small change.

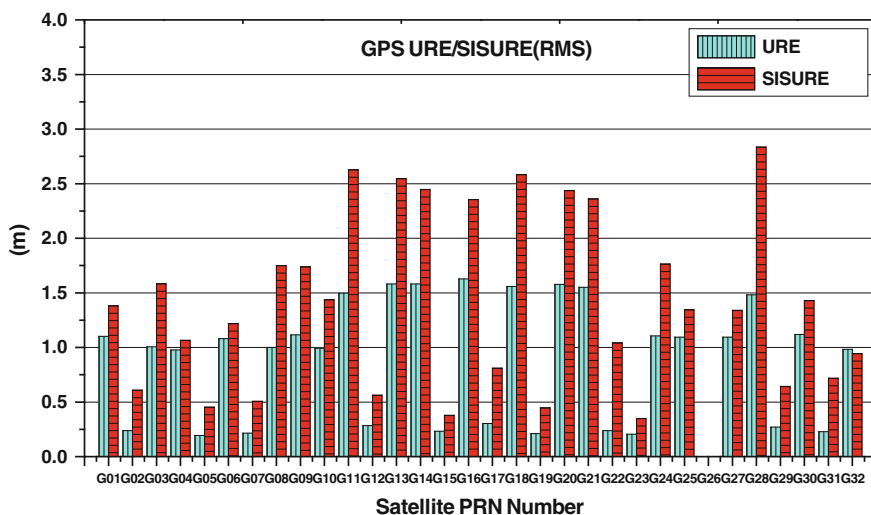


Fig. 35.2 The URE/SISURE accuracy evaluation results of GPS

Table 35.2 The URE/SISURE accuracy of GPS satellites

PRN	G01	G02	G03	G04	G05	G06	G07	G08	G9	G10	G11
URE	1.098	0.236	1.006	0.977	0.192	1.068	0.214	1.000	1.112	0.993	1.495
SISURE	1.366	0.603	1.509	0.978	0.439	1.178	0.484	1.695	1.664	1.389	2.608
G12	G13	G14	G15	G16	G17	G18	G19	G20	G21	G22	G23
0.266	1.581	1.581	0.230	1.627	0.301	1.558	0.210	1.576	1.551	0.235	0.203
0.541	2.531	2.436	0.370	2.354	0.736	2.538	0.430	2.432	2.359	0.972	0.334
G24	G25	G26	G27	G28	G29	G30	G31	G32	平均	–	–
1.104	1.092	–	1.082	1.482	0.268	1.021	0.226	0.985	0.889	–	–
1.727	1.342	–	1.305	2.835	0.702	1.069	0.690	0.908	1.372	–	–

Table 35.3 The URE/SISURE accuracy of BDS satellites

PRN	C01	C02	C03	C04	C05	C06	C07	C08
URE	2.452	1.162	0.799	1.318	0.861	0.615	0.647	0.645
SISURE	2.621	3.488	1.210	1.520	1.417	2.072	1.286	1.127
C9	C10	C11	C12	C13	C14	平均	–	–
0.681	0.672	0.664	0.656	–	0.612	0.657	–	–
1.620	1.080	1.190	1.512	–	1.644	1.409	–	–

35.4.2 BDS Broadcast Ephemeris Evaluation Results

BDS use WUM precise ephemeris data in January to June, use GBM precise ephemeris data in July to October. Because in the unhealthy state, C13 satellite ephemeris information has been dropped (Table 35.3).

Figure 35.3 is the BDS processing result, as we can see in this figure, after joining the clock difference error, the SISURE compared with URE average deviation is about 0.75 m and deviation between different satellite also has big and small.

35.4.3 GLONASS Broadcast Ephemeris Evaluation Results

GLONASS systems use the IGL precise ephemeris data in 2014. The results is shown in Fig. 35.4 (Table 35.4).

The processing result shows that GLONASS satellites joining in the clock error information, SISURE compared with URE change is very small, the average deviation is about 0.036 m. That illustrate GLONASS satellites forecast clock difference error after eliminating system deviation is very small.

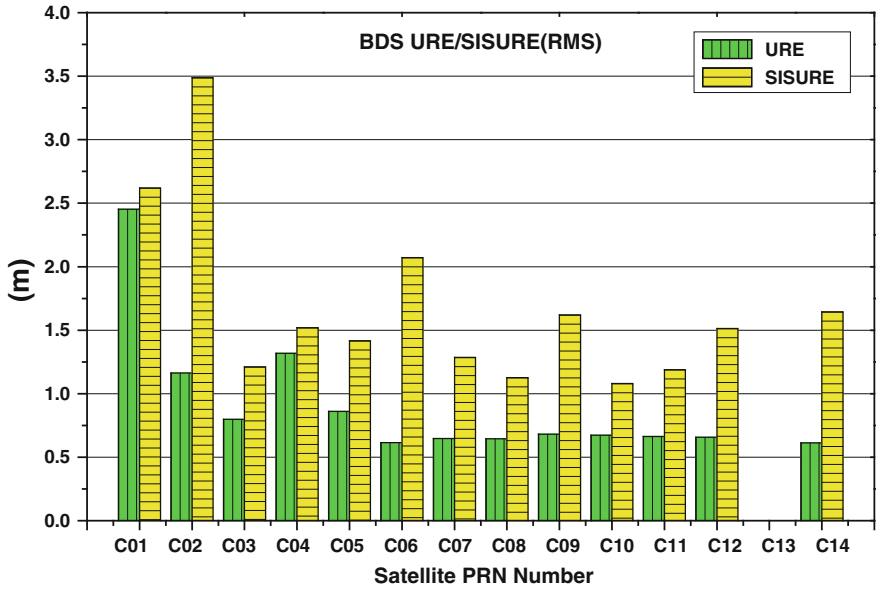


Fig. 35.3 The URE/SISURE accuracy evaluation results of BDS

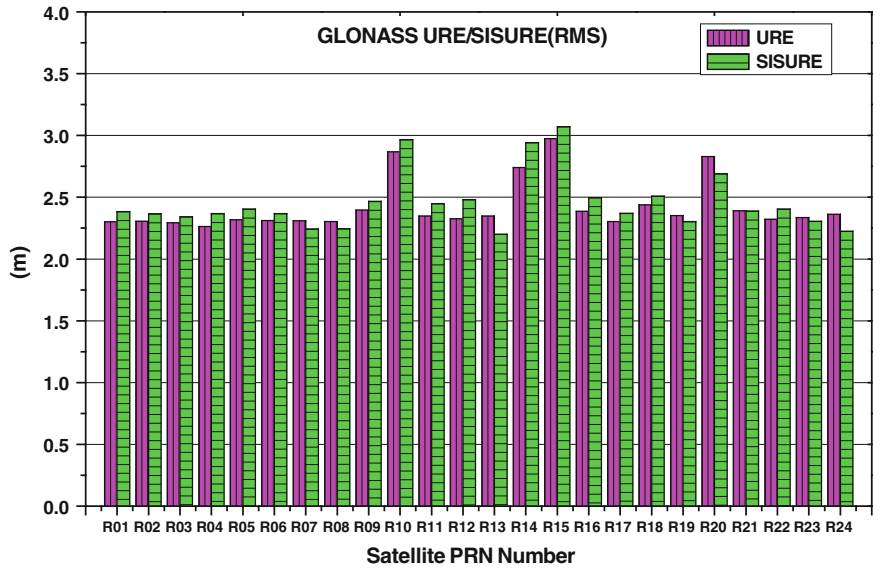
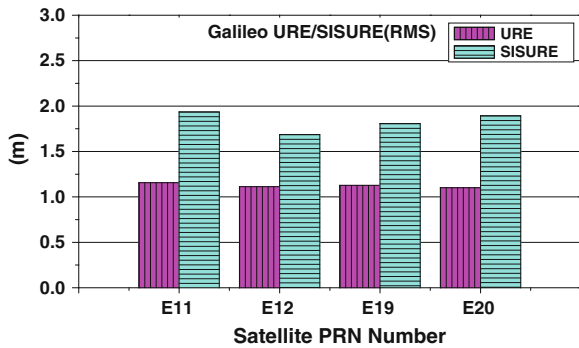


Fig. 35.4 The URE/SISURE accuracy evaluation results of GLONASS

Table 35.4 The URE/SISURE accuracy of GLONASS satellites

PRN	R01	R02	R03	R04	R05	R06	R07	R08
URE	2.300	2.305	2.293	2.264	2.317	2.312	2.310	2.303
SISURE	2.385	2.366	2.341	2.369	2.404	2.367	2.243	2.244
R09	R10	R11	R12	R13	R14	R15	R16	R17
2.397	2.868	2.348	2.325	2.348	2.740	2.975	2.385	2.304
2.466	2.967	2.449	2.480	2.201	2.941	3.071	2.496	2.370
R18	R19	R20	R21	R22	R23	R24	平均	
2.438	2.352	2.829	2.390	2.322	2.335	2.363	2.422	-
2.509	2.303	2.690	2.388	2.403	2.306	2.225	2.458	-

Fig. 35.5 The URE/SISURE accuracy evaluation results of Galileo



35.4.4 Galileo Broadcast Ephemeris Evaluation Results

Galileo systems use the TUM precise ephemeris data in 2014. The results is shown in Fig. 35.5 (Table 35.5).

Galileo satellite navigation system is still in experimental debugging stage now, for the time being only four satellites and often in a state of unhealthy. Looking from the processing results, after joining the clock difference SISURE compared with URE the average deviation is about 0.43 m.

35.4.5 Comprehensive Evaluation Results

Comprehensive the four systems processing data, URE/SISURE statistics in months, the three kinds of BDS satellites statistics respectively. Figure 35.6 is the URE/SISURE statistics for the four systems.

Table 35.5 The URE/SISURE accuracy of Galileo satellites

PRN	E11	E12	E19	E20	平均
URE	1.115	1.094	1.101	1.072	1.095
SISURE	1.680	1.378	1.532	1.509	1.525

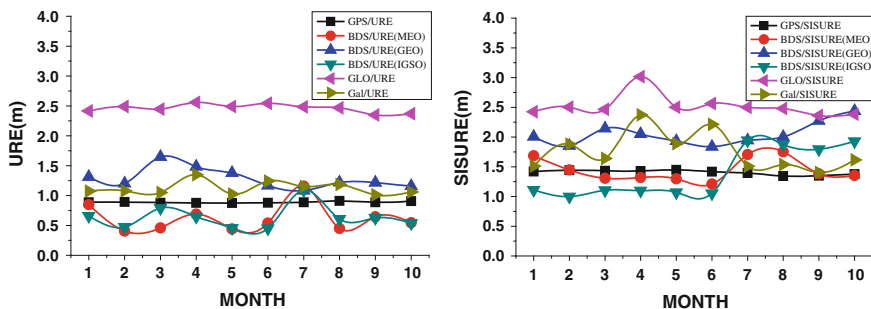


Fig. 35.6 Four systems monthly URE/SISURE accuracy evaluation results

Through the statistics difference of four systems URE/SISURE, we can generally reflect the relative relationship of four system clock error, in order to response four systems difference error of the clock more intuitively. We also use the RMS statistical method to processing clock error ΔT , notice the GBM ephemeris clock difference accuracy is poor, we only use the first 6 months of BDS data. The corresponding four system processing result is shown in Fig. 35.7, the numerical units is ns:

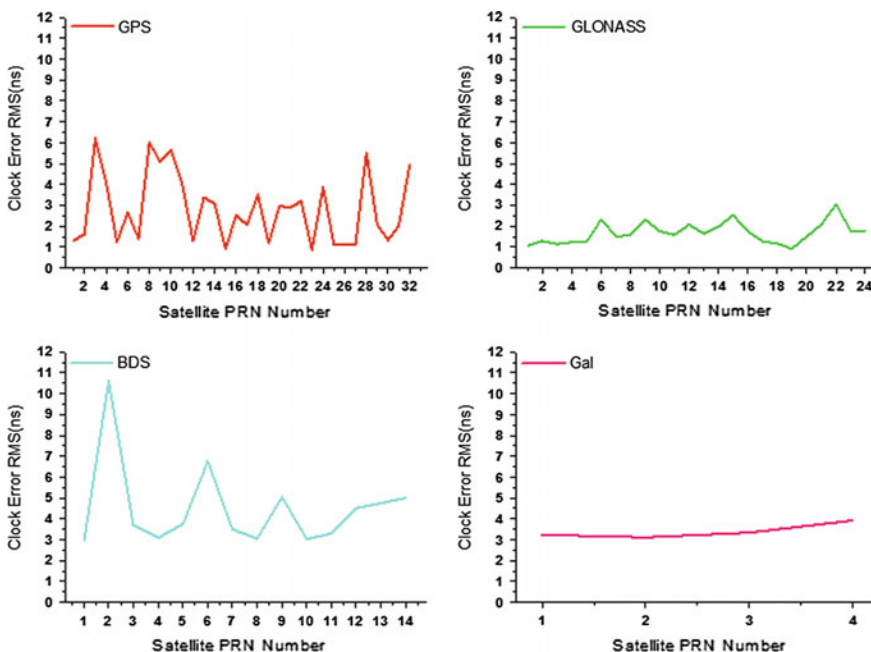


Fig. 35.7 Four systems SIS timing error evaluation results

35.5 Conclusion

1. As we see the GNSS four systems signal in space accuracy in general, URE overall accuracy is better than 2.5 m; GPS URE average accuracy is better than 0.9 m; URE of GLONASS system accuracy is poorer, the average is better than 2.5 m; Galileo system URE average precision is better than that 1.1 m; BDS system GEO/IGSO/MEO satellite URE accuracy is slightly different, GEO satellite URE average precision is better than 1.4 m, IGSO/MEO satellite average precision is better than 0.7 m; The precision of GEO below IGSO/MEO satellite URE precision. Among them, the error of C01 satellite is larger, C04 and C05 two satellites position is deviating from the asia-pacific region, setting station situation is bad, so that together lead to big URE of GEO satellite. Taken together, GNSS URE precision exactly ranking for the four system are: BDS, GPS, Galileo and GLONASS.
2. As we see the GNSS four systems signal in space accuracy in general, SISURE overall accuracy is better than 2.5 m; GPS satellite SISURE precision is better than 1.4 m; GLONASS system SISURE precision is better than 2.5 m; Galileo satellite SISURE reach the precision of better than 1.6 m; By use the first 6 months WUM precise ephemeris produced by wuhan university, BDS's IGSO/MEO satellites SISURE accuracy even better than the accuracy of GPS satellite, the average accuracy is better than 1.3 m, GEO satellite relative accuracy is lower, the average is better than 2 m. When we use the latter 4 months GBM precise ephemeris, the SISURE results is much bigger, this may be due to problems of the foreign setting station and receiver clock difference caused by data is not good. So taken together, GNSS SISURE precision exactly ranking for the four system are: GPS, BDS, Galileo and GLONASS.
3. Timing error processing results with the deviation between SISURE and URE get consistency. GLONASS system timing error is minimum, and overall is better than 1.7 ns on the one hand is due to its satellite clock performance is superior, on the other hand is due to GLONASS ephemeris transmit epoch radio frequency for 30 min, more than 2 h of GPS and BDS for 1 h. GPS timing error is about 3 ns in whole, but the ephemeris transmit time interval is the longest. BDS timing error on average is about 4.5 ns, and large differences among different satellites. Galileo satellite timing error is about 3.5 ns, but its ephemeris transmit frequency is highest at the present stage. Because the four systems' ephemeris transmit frequency is different, so we don't qualitative comparison of the timing error size.

References

1. Yang YX (2010) Review on progress, contribution and challenges of BDS satellite navigation system. *Acta Geodaetica et Cartographica Sinica* 39(1)
2. Zhang Q (2014) The research of GNSS monitoring and evaluation theory and method. Doctoral dissertation, Information Engineering University
3. Yang YX (2014) The progress, contribution and challenge of BDS. *J Surv Mapp* 39:1–6

4. Jiao W (2013) The latest progress of iGMAS. In: CSNC 2013
5. Hofmann W, Lichtenegger H, Walse E (2009) GNSS-global navigation satellite systems GPS, GLONASS, Galileo and more
6. Shuai P, Chen DC, Jiang Y (2014) Errors of GPS broadcast ephemerides and their effects on navigation and positioning accuracy. *J Data Acquis Process* 19(1)
7. Cohenour JC, van Graas F (2009) GPS orbit and clock error distributions. *J Inst Navig*
8. Warren DM (2002) Broadcast vs. precise GPS ephemerides: a historical perspective. Air Force Institute of Technology
9. Cohenour JC, van Graas F (2009) Temporal decor relation distributions of GPS range measurements due to satellite orbit and clock errors. *Navigation* 59(3):77–92
10. CSNO (2012) BeiDou navigation satellite system signal in space interface control document (Open Service Signal B1I (Version 1.0)), ed C.S.N. Office
11. Taylor J, Barnes E (2005) GPS current signal-in-space navigation performance. In: ION NTM 2005, San Diego, CA, pp 385–393
12. Mao Y (2007) Use SLR data to do the precision of broadcast ephemeris assessment. *J Surv Mapp Sci Technol* 27(4):263–266
13. Li ZH (2008) The orbit of GPS broadcast ephemeris error analysis
14. Guo F (2009) GPS satellites broadcast ephemeris orbit and clock difference accuracy analysis. *J Wuhan Univ* 344(4):589–592
15. Guo C (2007) GPS theory, algorithms and applications. Springer, New York, pp 30–31
16. Walter T, Blanch J, Enge P (2010) Evaluation of signal in space error bounds to support aviation integrity. *Navigation* 57:101
17. Global Positioning System Standard Positioning Service Performance Standard, 4th edn. September 2008
18. Walter T, Blanch J, Enge P (2010) Evaluation of signal in space error bounds to support aviation integrity. *Navigation* 57:101
19. Shi C, Zhao Q, Li M, Tang W, Hu Z, Lou Y, Zhang H, Niu X, Liu J (2012) Precise orbit determination of BeiDou satellites with precise positioning. *Sci China Earth Sci* 55:1079–1086
20. Hu ZG (2013) BDS performance evaluation theory and experimental verification

Chapter 36

BeiDou Satellite Multipath Characteristics Research-From the “Micro” Parameters Point of View

Xin Chen, Xiaoran Fang, Yuze Wang, Yanhong Kou, Le Cai,
Peilin Liu and Wenxian Yu

Abstract Multipath is one of the most important factors that affect the positioning accuracy of GNSS receivers. Traditionally, the Code-Minus-Carrier Multipath Observable (CMO) is used to study the characteristics of GPS multipath errors, which takes on period fluctuations. However, BeiDou System comprises of three types of satellite—MEO, IGSO and GEO, the orbits of which differ a lot with each other. The standing multipath observed in GEO multipath causes the fluctuation phenomenon obscure, making the research with CMO technique hard to continue. Up till now, only a few literatures focused on studying the characteristics of multipath ‘micro’ parameters like delay, attenuation, carrier phase and number with real-world signal data. Those parameters indeed reflect the behavior of multipath more straightforward. Therefore, the Code Amplitude Delay Lock Loop (CADLL) technique is used at this paper to decompose the multipath at its signal parameter level. The experiment results reveal that even the GEO multipath can also vary slowly because of the satellite perturbation. The GEO multipath fading period can be a few hours. However, the IGSO and the MEO multipath do not show much distinct difference. The specular multipath fading period of both IGSO and MEO is normally a few minutes, while the diffused multipath parameters take on steady behavior but last very short time. It is found as well that the multipath signal of all kinds of satellites bears the nature of limited existing time. Thus, the concept of multipath life-time is proposed in this paper to describe the statistical distribution of

X. Chen (✉) · X. Fang · Y. Wang · P. Liu · W. Yu
Shanghai Key Laboratory of BeiDou Navigation and Location-Based Service,
School of Electronics, Information and Electrical Engineering,
Shanghai Jiao Tong University, Shanghai 200240, China
e-mail: xin.chen@sjtu.edu.cn

Y. Kou
Department of Electronic and Information Engineering, Beihang University,
Beijing 100191, China

L. Cai
Space Star Technology Co., Ltd, Beijing 100086, China

multipath lasting time as well as the multipath power variation feature during its life-time. Those models are useful for simulator design to emulate more precise multipath scenario.

Keywords Multipath estimation · CADLL · Life time of multipath · Specular multipath · Diffused multipath

36.1 Introduction

Multipath is a major factor that affects the performance of GNSS receiver to be degrading. Since multipath is closely related to application environments, RTK technique cannot remove the positioning errors caused by multipath. Many multipath error mitigation methods have been proposed so far, including choke ring antenna, pseudorange measurement filtering, special code tracking loop design and so on. However, none of them is able to fully resolve the problem. Thus, the research on multipath characteristics of GNSS signal is still an urgent demand.

According to the multipath tap-delay model, a multipath signal can be uniquely expressed by its code phase delay τ , amplitude attenuation α and the changing rate of multipath carrier phase δf . δf is also called multipath error fading frequency since it can caused multipath error to periodically change. At static scenario, multipath error fading frequency depends on the movement of satellite. Literature [1] studied the relationship between multipath error fading and satellite orbits. Traditionally, the Code-Minus-Carrier Multipath Observable (CMO) technique was used to study the features of GPS multipath error [2]. The magnitude of multipath error is able to be measured by manipulating the statistics of CMO [3]. But CMO technique is not so efficient to standing multipath which often appears in WAAS system and SBAS system because the standing multipath error is prone to stay constant. Besides, CMO technique is unable to observe the high frequency part of multipath error [4, 5].

BeiDou system comprises of three types of satellites—GEO, IGSO and MEO, so it has more complex multipath errors. In contrast with CMO, we want to study the multipath characteristics more straightforward from the “micro” parameters point of view, such as multipath delay, power attenuation, carrier phase changing rate, lasting time, etc. Unfortunately, there have only been a few papers so far studying the features of those “micro” parameters of real multipath signal. This is partly due to the complexity of multipath parameter estimation algorithm. But some research entities have designed their multipath estimation methods and been studying the multipath channel of GPS [6].

The authors of this paper proposed a multipath estimation and mitigation algorithm named Coupled Amplitude and Delay Lock Loops (CADLL) in 2011. It is able to detect and estimate multipath with intermediate frequency (IF) sampling data. The parameters of those detected will be continuously tracked and recorded.

In this paper, we used the GNSS Application-defined Software Receiver-multipath mining (GSAR-mm) to process the IF data sampled at two multipath spots, and present the multipath features and models that was found during these experiments.

36.2 Multipath Mathematic Model

36.2.1 Multipath Signal Mathematic Expression

A multipath ray can be uniquely determined by its code phase delay τ , power attenuation α^2 , carrier phase φ and the carrier phase changing rate $\delta f = d\varphi/dt$. All those parameters are measured with respect to direct line-of-sight signal (DLOS). Those signal rays that go into the antenna at multipath scenario are expressed as:

$$s(t) = AD(t) \sum_{n=0}^M \alpha_n c(t - \tau_n) \cos(2\pi ft + \varphi_n) \tag{36.1}$$

where A is the DLOS amplitude, $D(t)$ is the navigation bit, $c(t - \tau_n)$ is the spreading code. $n = 0$ means the DLOS. By default, DLOS has $\alpha_0 = 1$, $\tau_0 = 0$, $\varphi_0 = 0$. The multipath error fading frequency δf is due to the change of delay caused by the relative movement between satellite and receiver. The relationship of multipath, DLOS and the composite signal can be illustrated by the phasor diagram (Fig. 36.1).

The positive multipath ($|\varphi_n| \leq 90^\circ$) will increase the composite signal's power, but the negative multipath ($|\varphi_n| > 90^\circ$) will reduce the composite signal's power. Both of them can affect the accuracy of pseudorange measurement, thus leading to positioning errors.

36.2.2 Multipath Signal Propagation Geometric Model

There are mainly two types of multipath: specular multipath and scattering multipath. Specular multipath is normally produced by the reflection of DLOS on a plain,

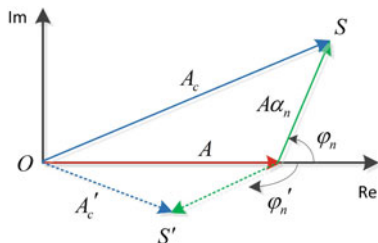


Fig. 36.1 The phasor diagram of multipath signal and DLOS signal

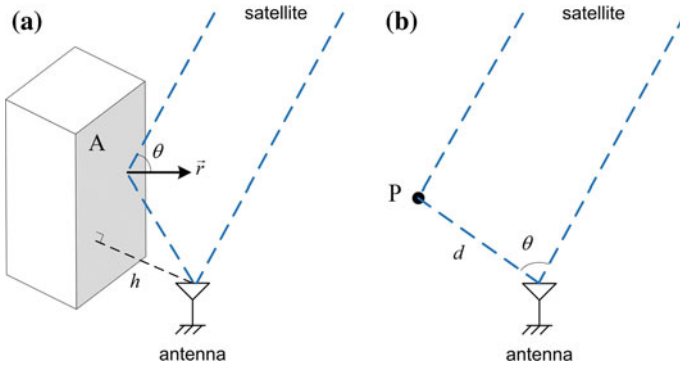


Fig. 36.2 Multipath propagation geometric model. **a** Specular multipath model. **b** Scattering multipath model

which follows the mirror reflection law. Scattering multipath occurs when the DLOS goes incident into an irregular scattering point or the intersection line of two plains. This kind of multipath can be modeled as propagating at a certain direction angle from the scattering point. The propagation models of both specular and scattering multipath are shown in Fig. 36.2:

In Fig. 36.2a, A is the reflection plane; h is the perpendicular distance from antenna to plane A ; \vec{r} is the normal vector of plane A ; θ is the reflection angle. The multipath delay of specular geometric model is:

$$L_{\text{specular}} = 2h \cos \theta \quad (36.2)$$

In Fig. 36.2b, P is the scattering point; d is the distance from antenna to P ; θ is the included angle between multipath and DLOS. The delay of scattering mode is:

$$L_{\text{scatter}} = d(1 - \cos \theta) \quad (36.3)$$

If we denote the carrier wavelength as λ , the multipath carrier phase can be deduced from the delay:

$$\varphi_n = 2\pi L/\lambda + \Delta\varphi \quad (36.4)$$

where $\Delta\varphi$ is the phase abrupt change induced by reflection or scattering. $\Delta\varphi$ is normally constant as long as the material property of the reflection plane or scattering point does not change.

At static scenario, the movement of satellite will cause the change of multipath delay, then leading to the change of multipath carrier phase. Therefore, the multipath error fading frequency can be computed from the derivative of phase:

$$\delta f_n = d\varphi_n/dt/2\pi = dL/dt/\lambda \quad (36.5)$$

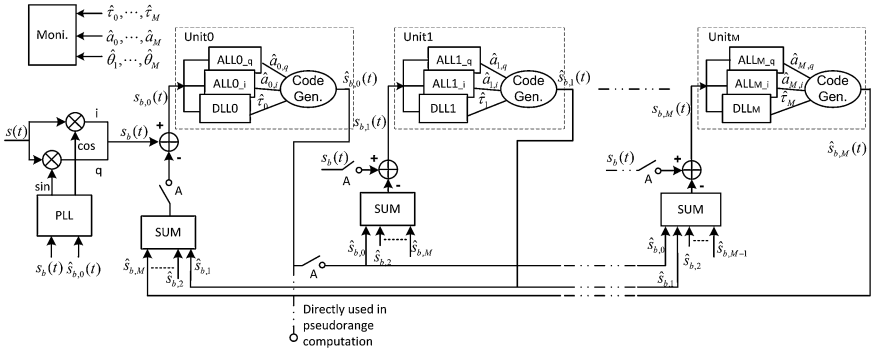


Fig. 36.3 Block structure of CADLL

36.2.3 Coupled Amplitude and Delay Lock Loops

The structure diagram of CADLL algorithm is shown in Fig. 36.3. It is able to detect and estimate multipath with IF sampling data. This architecture exploits the “turbo principle” to separately track the Line Of Sight (LOS) signal and multipath signals in order to mitigate the effects of the multiple reflections. The Delay Lock Loop (DLL) and the Amplitude Lock Loop (ALL) are two basic elements in the structure. DLL is in charge of estimating and tracking the code delay of a specific ray in the incoming signal while ALL is in charge of estimating the corresponding amplitude. A pair of DLL and ALL makes a Unit, devoted to track LOS or a multipath signal. Several Units are incorporated in the CADLL structure, and then able to track the different component rays from the overall incoming signal. The feedback architecture and special working strategy of CADLL boost the performances of the parameter estimation accuracy.

The working procedure of CADLL is also very important. It first uses a conventional tracking loop to lock onto the incoming signal, getting a rough estimation about position of LOS’ code phase; then it activates two units to try to track a multipath signal. If it fails, it means there is no multipath in the incoming signal; if it succeeds, it will continue trying to insert a new unit into this feedback loop to look for a new multipath component. The monitor block is governing the process of searching a new multipath component by checking the tracking results of the new unit. If it is considered that there is no new multipath component, the trial unit will be shut down by the monitor block. The process will not stop until there is no new multipath found or the number of enabled units reaches the maximum number M_M , which is pre-defined according to available resources. Following this specially designed working procedure, CADLL actually has the ability of estimating the number of multipaths and adjusting its structure to match it. The detailed introduction and performance about CADLL can be found in [7, 8].

We used the GNSS signal analyzing receiver GSARx-mm to process the real signals sampled at two representative multipath spots. One is at Shanghai Jiao Tong University (SJTU) and the other is at Beijing Beihang University. The results are shown in the next section.

36.3 Multipath Signal Analyzing Campaign


36.3.1 SJTU Multipath Data Processing Results

The first experiment place is at the patio of Weidianzi Building of SJTU Minghang campus. Two pieces of IF data were sampled at two different time. The specification about the sampling device and the field picture are listed in Table 36.1.

By processing SJTU data1, a multipath was clearly found in the BDS GEO4 signal. This multipath existed about 6805 s in this data. Its delay was about 24.6 m and the carrier phase was mostly staying at -150° , which means a typical standing multipath. However, its power attenuation kept increasing, from the initial -8 dB to the final -16 dB. This explains why the variances of multipath delay and carrier phase estimations kept increasing. The estimation results of the delay, carrier phase, power attenuation and the correlation shapes are shown in Fig. 36.4. From the correlation shape figure, it can be seen that the original signal's correlation shape, which is denoted by the black line was distorted by multipath, while the correlation shape of the restored DLOS signal shows a good symmetry.

In order to figure out how and where the multipath in BDS GEO4 was generated, we surveyed the surrounding buildings of the antenna by using Huace company's high-performance receiver model N71 which can give centimeter level positioning results. The surveyed points for determining the plains of the surrounding buildings are those on the roof of the buildings and with open view of sky, so no multipath interference is in there. In order to determine the plane of the patio, we chose the points at the southeast edge of the patio where is far from other reflection planes and we also checked the signals with GSARx-mm and excluded the possible multipath interference. When all the geometric models about the experiment environment are

Table 36.1 Experiment situations at SJTU

Place	At the patio of Weidianzi Building, SJTU Minghang campus	Time	Data 1: sampled at 3:00 p.m. on Nov. 15th 2014, length of about 2 h
			Data 2: sampled at 21:36 on Nov. 25th 2014, length of about 1 h and 6 min
Sampling parameters	Sampling freq.: 62 MHz	Field picture	
	RF bandwidth: 40 MHz		
	Quantization: 8 bit		
	Sampling mode: Complex sample		

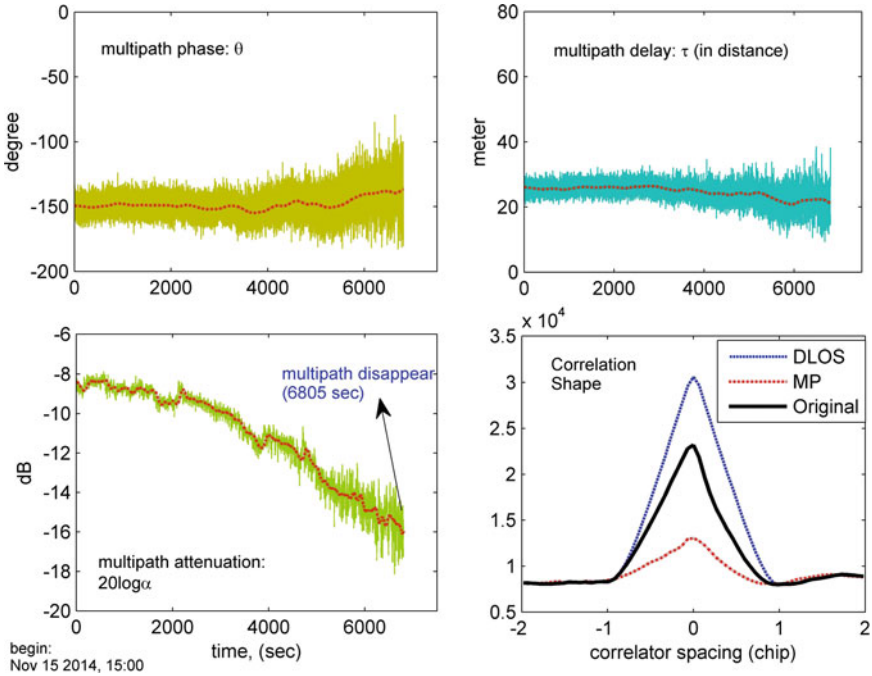


Fig. 36.4 BDS GEO4 B1 multipath signal’s phase degree, delay, attenuation and correlation shape of SJTU data1

established, the geodetic coordinates of the antenna is also able to be obtained by measuring the distance from the antenna point to all other surveyed points. The surveyed geodetic coordinates of the antenna is (31.0250N, 121.4396E, 23.7953H).

It is needed to clarify that although the receiver N71 can give us centimeter level accuracy when determining the relative geometric models of the buildings, the geodetic coordinates of those surveyed points can have consistent biases of even a few meters. This is because the CORS networks we used is not so reliable (built by Huace company itself) and the baseline is comparatively far (>30 km). But these errors will not cause any significant effects on our experiments.

By combining the antenna coordinates, surrounding buildings’ geometric models and the GEO4 satellite orbit information, we constructed a local level coordinate system with the antenna as the origin and computed the possible multipath reflection paths. The results are shown in Fig. 36.5. It is found that Plane N2 does not meet the reflection condition for GEO4 signal. The delays produced by the reflection path of Plane N1 and the reflection path of Plane W1 are 11 and 3.96 m respectively, which is quite different from the estimated delay (24.6 m) shown in Fig. 36.4. It can be concluded that the multipath detected in the data1 is not produced by those one-reflection paths.

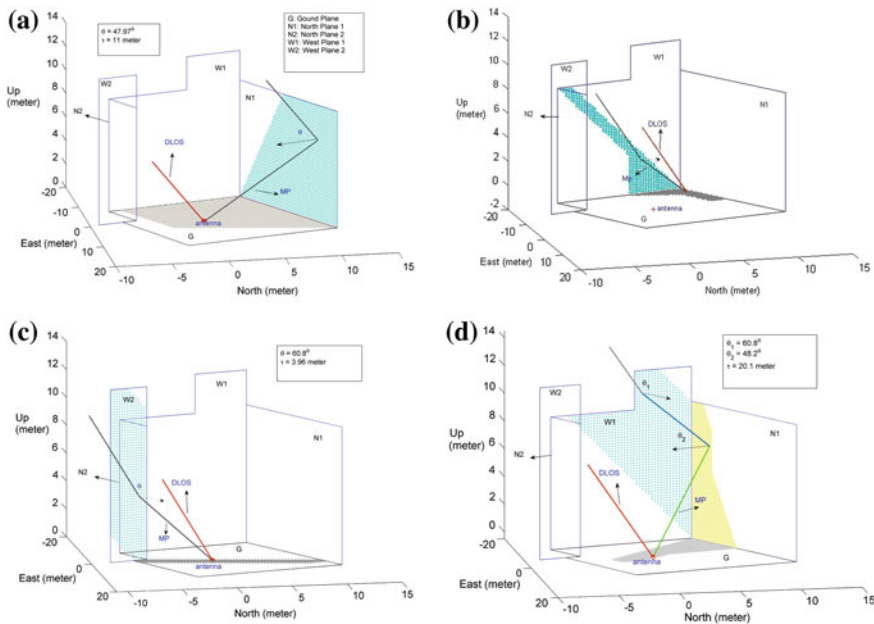


Fig. 36.5 Theoretical reflection paths by the surrounding buildings. **a** Possible reflection path by North1 plane. **b** Possible reflection path by West1 plane. **c** Possible reflection path by West2 plane. **d** Possible double reflection path by West1 and North1 planes

Figure 36.5d shows a double-reflection multipath model, firstly by Plane W1 and then by Plane N1. The delay produced by this path is about 20.1 m. Considering the estimation noise effects and the surveyed errors of the buildings, it can be deduced that this double-reflection model is consistent with the detected one in the experiment. This experiment tells us that under complex multipath scenario the power of one-reflection multipath is even weaker than that of double-reflection multipath. The polarization of one-reflection multipath is normally left-handed, whereas the double-reflection multipath is changed back to right-handed polarization, so this change makes the selectivity of GNSS antenna invalid for it.

The processing results of SJTU data2 are shown in Fig. 36.6. It is found that there is a multipath in MEO12 signal, whose delay is about 25 m. Because of the movement of MEO satellite, the delay takes on an incremental trend. The curve fitting result for the multipath carrier phase shows that its multipath carrier phase change rate is approximately 0.00264 Hz (6.31 min/cycle). So the delay increases by about 6.2 wavelengths during the entire data time length. It is also noted that there are interruptions of the tracking onto this multipath. It is because the materials of the reflection plane are not homogeneous, so it will cause reflection power fading during the satellite’s movement. This phenomenon also appears in the Beihang university experiment data (Table 36.2).

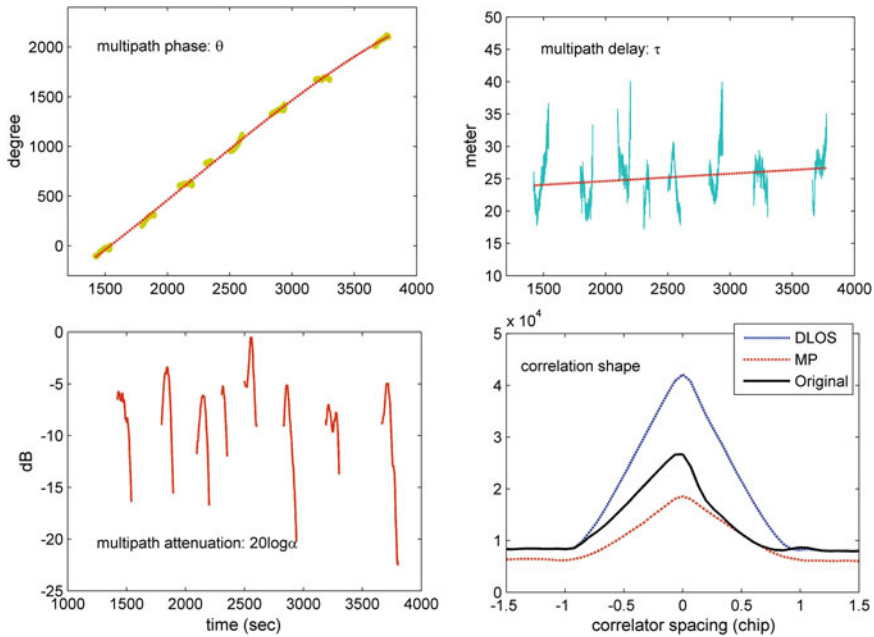



Fig. 36.6 BDS MEO12 B1 multipath signal’s phase degree, delay, attenuation and correlation shape of SJTU data 2

Table 36.2 Experiment situations at Beihang University

Place	On the roof of New Building F Section of Beihang University Campus	Time	Sampled at 9:03 a.m. on Sept. 3rd 2014, length of about 1 h and 20 min
Sampling parameters	Sampling freq.: 100 MHz	Field picture	
	RF bandwidth: 40 MHz		
	Quantization: 12 bit		
	Sampling mode: RF sampling		

36.3.2 Beihang Multipath Data Processing Results

By processing Beihang data, we found that there are multipaths in both GEO5 and IGSO10 signals. Figure 36.7 illustrates the parameter estimation results of the GEO5 multipath. Its delay is about 81 m and has a decreasing trend. Because of the permutation of GEO satellite, the multipath still has a minor fading frequency of $-4.083e-5$ Hz (6.8 h/cycle). Because we did not get the surveyed information about this experiment environment, we could not build the corresponding multipath geometric model, but it is able to speculate from the field picture that the multipath might be produced by the nearby glass wall.

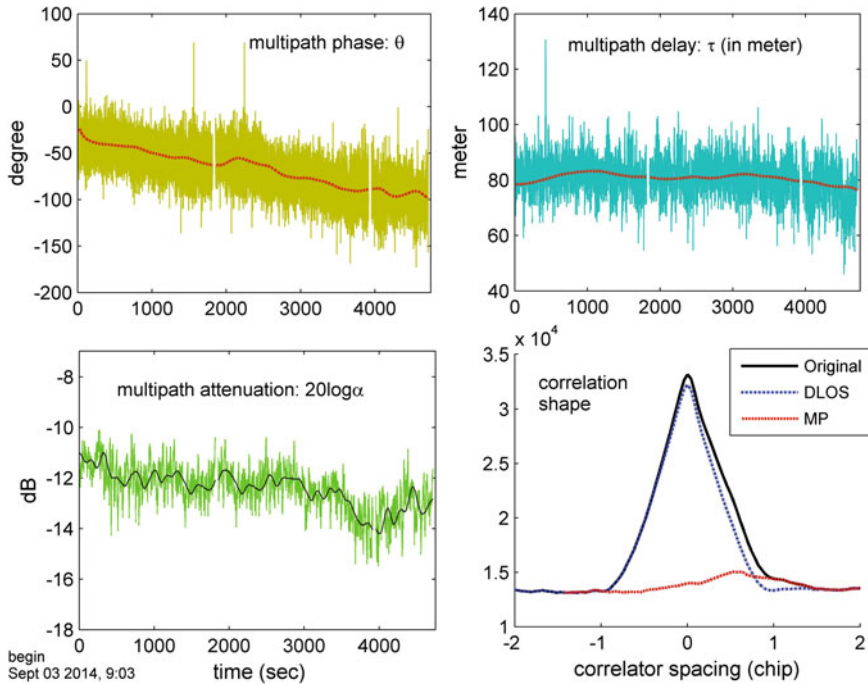


Fig. 36.7 BDS GEO5 B1 multipath signal’s phase degree, delay, attenuation and correlation shape of Beihang data

Apart from GEO5, IGSO10 is detected to have several multipath signals as well. During 0–180 s, there exist tens of detectable multipath pieces, which belong to three groups of reflection sources. Among all the multipath signals in Fig. 36.8, the red one lasts more than 1500 s and its delay is about 85 m. Its carrier phase and delay curve fitting results prove that these detected pieces belong to one multipath signal, but the power attenuation fluctuation causes the tracking interruptions. The fading frequency is -0.0078 Hz (2.14 min/cycle). The green one’s and the yellow one’s delays are about 40.5 and 25 m respectively. They have comparatively short delays, slow multipath fading, and short lasting time, so it can be speculated that they are produced by the nearby small dimensional specular reflection/scattering sources.

In Fig. 36.8, we find the discontinuous multipath tracking phenomenon again. It is caused by the heterogeneous material of the reflection plane. Take the Beihang experiment spot as an example, the reflection plane is composed of glass and coarse bricks. When the satellite is moving, the reflection point for the same multipath is actually moving on the plane as well, according to the multipath propagation model in Fig. 36.2. Therefore, if the reflection point is on the glass wall, the reflection power is strong and it is easier for the software to detect the multipath. However when the reflection point moved to the brick wall, scattering might happen and the attenuation is increased, so it might be too weak for the software to track the multipath.

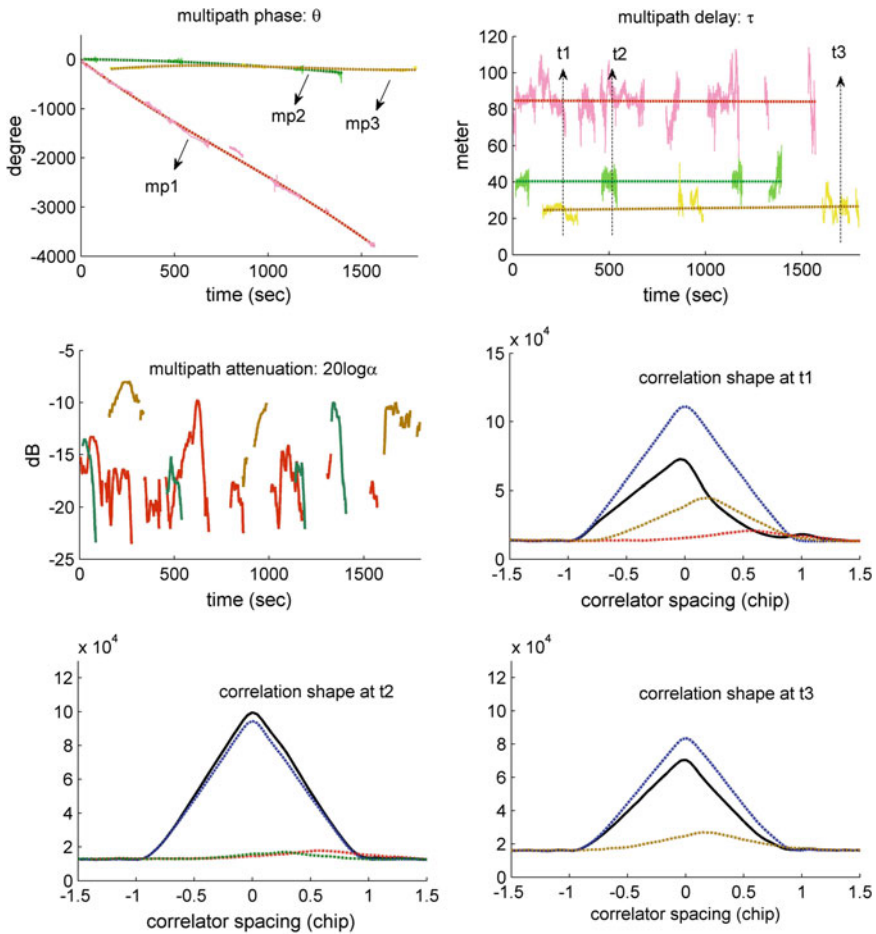


Fig. 36.8 BDS IGSO10 B1 multipath signals' phase degrees, delays, attenuations and correlation shapes of Beihang data

36.3.3 Some Conclusions from the Experiments

Some rules about BDS multipath can be drawn from the above experiment results:

- (1) The perturbation of GEO satellite can make its multipath parameter slowly change as well, even if the antenna is at static. GEO multipath carrier fading period is within a few hours to tens of hours.
- (2) IGSO and MEO multipath exhibits fast carrier phase fading frequency. The fading period is within a few minutes to tens of minutes.
- (3) At complex multipath scenario, the multipath might experience more than once reflection before entering antenna (like the case in Fig. 36.4). Normally

the multipath experiencing one reflection has left-handed polarization, and the one with twice reflections has right-handed polarization again. As a result, such kind of multipath is able to cause much larger errors.

- (4) All kinds of multipath have the feature of limited life time which means that none multipath can last forever even if for GEO. Both the limited dimension of the reflection/scattering source and the movement or perturbation of the satellites could cause the power of multipath decrease or even disappear, making any multipath signal with limited life time. The GEO multipath has the longest life time, normally a few hours. The specular multipath of IGSO and MEO has a life time of tens of minutes to 1 h. The scattering multipath of IGSO and MEO has the shortest life time, often tens of seconds.
- (5) For IGSO or MEO multipath, there might happen multipath tracking interruptions even if during their life time period. This is caused by the heterogeneous property of the reflection material.

36.4 Multipath Life-Time Probability Distribution Model

Since multipath signal is closely related to the surrounding environment, the characteristics of those “micro” parameters of multipath are often described by some probability distribution models. According to the research results in [9], the delay of multipath τ follows an exponential distribution:

$$f(\tau) = \frac{1}{\tau_0} e^{-\frac{\tau}{\tau_0}} \quad (36.6)$$

The multipath power attenuation α^2 follows an exponential function with the delay τ as variable.

$$S(\tau) = S_0 e^{-\delta\tau} \quad (36.7)$$

where τ_0 is the decay factor in the delay model, δ is the decay factor in the power attenuation model, and S_0 is the average multipath attenuation with respect to scenario.

However, none of papers have clearly described the life-time concept about multipath signal so far. At this paper, we propose the multipath life-time parameter which will express the time for a multipath from emerging to extinction. Table 36.3 lists the existing time of all multipath signals detected in the above experiments.

It can be seen from Table 36.3 that at static scenario, the life time of GEO multipath is often greater than 1 h; the life time of IGSO/MEO specular multipath is normally within 1 h; while that of IGSO/MEO scattering multipath is often lying

Table 36.3 Multipath life-time

No	Satellite type	Multipath type	Life-time (s)	Multipath fading frequency (Hz)
1	GEO	Specular	>6800	<1.389e-5
2	GEO	Specular	>4710	-4.083e-5
3	IGSO	Specular	1570	-0.0078
4 ^a	IGSO	Specular	1150	-0.0056
5 ^a	IGSO	Specular	900	-0.0097
6	IGSO	Scattering	180	<1.528e-4
7	IGSO	Scattering	25	-0.005
8	IGSO	Scattering	70	-0.00283
9	IGSO	Scattering	180	<2.78e-6
10	IGSO	Scattering	55	4.028e-4
11 ^a	IGSO	Scattering	75	<3.472e-4
12	MEO	Specular	2360	0.00264

^a Stands for those multipaths without plotted at this paper

between 30 s and 5 min. We construct a modified Gamma probability distribution model to describe the life time of different multipaths:

$$T_{mp} - d \sim Gamma(a, b) = \frac{(T_{mp} - d)^{a-1} e^{-\frac{T_{mp}-d}{b}}}{b^a \Gamma(a)} \tag{36.8}$$

where a is the shape factor, b is the scale factor, and d is the offset factor. Figure 36.9 shows the three kinds of multipath life time distributions with Gamma functions. In Fig. 36.9 the life time of GEO multipath is in units of hour, expressed at the bottom axis; while the life time of IGSO and MEO multipath is in units of minutes expressed at the top axis.

It can be observed from the experiments that multipath power will decrease at the end of its life time. This trend will continue until it is deemed as disappeared. Regarding to this property we construct a logarithm function to model the power variation behavior:

$$S(t)|_{dB} = S(\tau)|_{dB} - 5 \log \left(1 + \varepsilon^2 \left(\frac{t}{T_{mp}} \right)^{2n} \right) \tag{36.9}$$

where $S(\tau)$ is the multipath power attenuation obtained from Eq. (36.7), T_{mp} is the multipath life time obtained from Eq. (36.8), ε and n are the model parameters related to the types of multipath.

Figure 36.10 shows the comparisons between the estimated multipath power attenuations from the data and the model curves from Eq. (36.9) of four representative multipaths selected from Table 36.3. Multipath No1 and No2 are GEO’s. They take on slow changing behavior because of the slow movement of GEO satellites. Multipath No12 and No11 are the MEO specular multipath and the IGSO

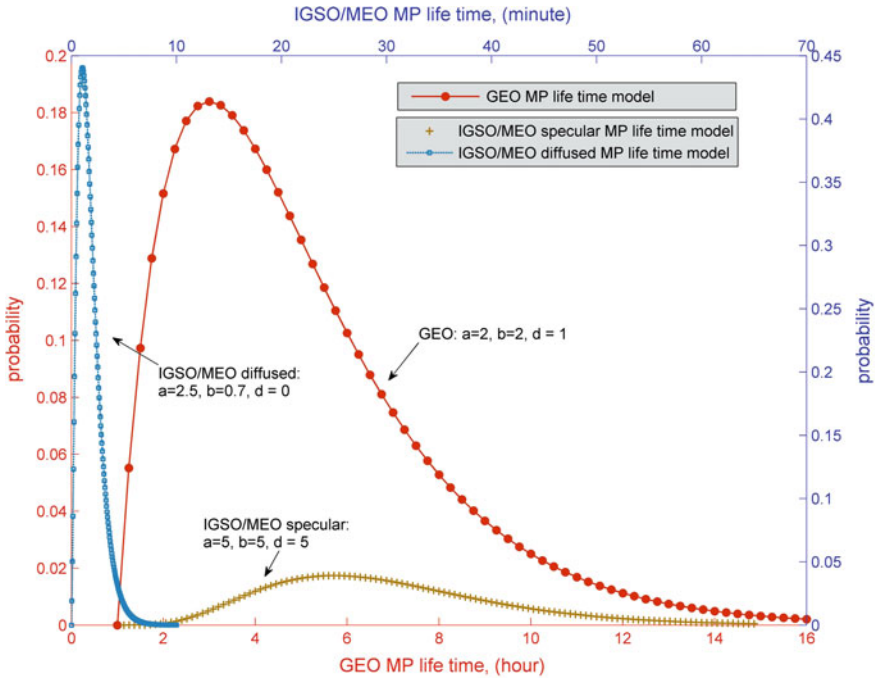


Fig. 36.9 GEO/IGSO/MEO multipath life-time probability distribution models

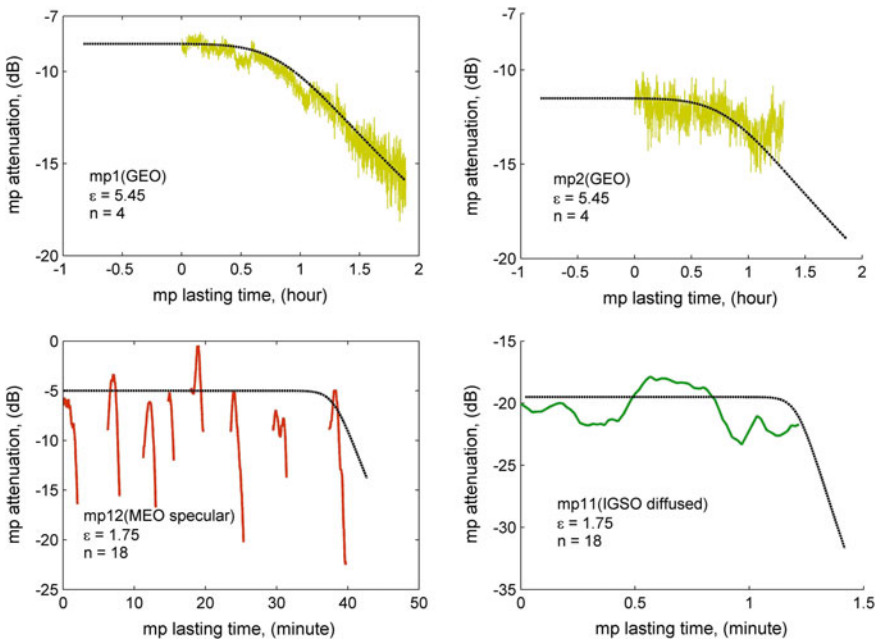


Fig. 36.10 Multipath attenuation evolution in its life time

scattering multipath respectively. So their power curves have much faster decreasing at the end of life time. Comparing the specular multipath and scattering multipath, we can also find that the scattering one have much larger attenuation than the specular reflection one.

Equations (36.6)–(36.9) can be used to design static multipath scenarios for GNSS simulators. It can help the developers to know how the tested receivers will perform under real applications. However, those models proposed at this paper are still needed to be improved because the limited number of multipath samples obtained from the experiments prevents getting more reliable model parameters. Besides, we also need to have more experiments to model the tracking interruption behaviors for the IGSO/MEO specular multipath.

36.5 Conclusions

In this paper, two real multipath signal experiments and analyzing campaigns were conducted respectively at Shanghai and Beijing. Multipaths are observed in GEO, IGSO and MEO signals and include both specular reflection multipath and scattering multipath. By extracting the “micro” parameters, it is found that apart from the delay, attenuation and carrier phase change, multipath also has the property of life time and time-variant power attenuation.

Because of the perturbations, the parameters of GEO multipath have very slowly time-variant changing behavior. Whereas there is not much characteristic difference between IGSO multipath and MEO multipath although these two kinds of satellite are quite different in orbits. Specular reflection multipath and scattering multipath show much distinct difference in power attenuation, carrier phase changing rate and life time. Scattering multipath has more attenuation, shorter life time and slower carrier phase changing rate. In the experiments, the multipath with double reflections is also observed. This kind of multipath has even more effects on receiver because their polarization might become right-handed again.

The multipath life time probability distribution model is proposed in this paper to model the statistical property of multipath existing time. Besides, the time-variant power attenuation function is built to precisely model the multipath power change during its life time. These models will be helpful for the GNSS simulator designs.

The future work about this research will focus on more extensive multipath scenarios' data analyzing to build more accurate models. And the dynamic multipath channel at urban areas will also be studied.

Acknowledgments The research work is funded by National Natural Science Foundation of China (No. 61304225); by the Open Research Fund of The Academy of Satellite Application (grant No. 2014_CXJJ-DH_04); by the Science and Technology Commission of Shanghai Municipality (grand No. 13511501302).

References

1. Yang G, Cui X, Lu M, Li H, Feng Z (2012) The analysis and simulation of multipath error fading characterization in different satellite orbits. In: China satellite navigation conference (CSNC) 2012 proceedings, Guangzhou, China, 15–19 May
2. Misra P, Enge P (2006) Global positioning system—signals, measurements, and performance, 2nd edn. Ganga-Jamuna Press, Lincoln
3. Akos DM, Weiss JP, Murphy T, Pullen S (2004) Airborne multipath investigation via a GPS software receiver. In: Proceedings of ION GPS/GNSS 2004, Long Beach, CA, 21–24 Sept
4. Schempp T (2008) WASS benefits of GEO ranging. In: Proceedings of ION GNSS 2008, Savannah, GA, 16–18 Sept
5. Wanninger L, Wallstab-Freitag S (2007) Combined processing of GPS, GLONASS, and SBAS code phase and carrier phase measurements. In: Proceedings of ION GNSS 2007, Fort Worth, TX, 25–28 Sept
6. Xie P, Petovello MG (2011) Multipath signal assessment in the high sensitivity receivers for vehicular applications. In: ION ITM 2011, Portland OR, USA, 19–23 Sept
7. Chen X, Dovis F, Peng S, Morton Y (2013) Comparative studies of GPS multipath mitigation methods performance. *IEEE Trans Aerosp Electron Syst* 39(3):1555–1568
8. Chen X, Dovis F, Pini M, Mulassano P (2011) Turbo architecture for multipath mitigation in global navigation satellite system receivers. *J IET Radar Sonar Navig* 5:517–527
9. Jahn A, Bischl H, Hein G (1996) Channel characterisation for spread spectrum satellite communications. In: *IEEE 4th international symposium on spread spectrum techniques and applications*, Mainz, Germany, vol 3, pp 1221–1226, 22–25 Sept

Chapter 37

Analysis and Evaluation Method of Multiple-Access Interference in Navigation Satellite Communication System

Chenglong He and Baoguo Yu

Abstract The reliability of monitoring and control directive communication is a crucial factor of GNSS control segment. As several high-speed communication links of CDMA system in a limited bandwidth of navigation satellite, the MAI (Multiple-Access Interference) would serious prejudice the stability and effectiveness of system. Traditional evaluation method simply based on C/N_0 has a large error on BER for the particularity of MAI in limited bandwidth, which could hardly apply in control segment evaluation. To satisfied the need of the system stability and design of communication signal, put forward an accurate modeling and analysis which obtain a result of worst and best signal status of MAI, and put forward a analysis and evaluation method based on signal parameters included of PRN, code phase, polarization phase, cross-correlation distribution estimated parameter and so on. A test system of GNSS limited band communication was established, the test results prove the effectiveness of the method, and achieve the BER in the auxiliary of multi-user detection method of multi-channel high-speed communication system. The research achievements provide the basis for TT&C (telemetry tracking and command) of BeiDou control segment.

Keywords High-speed data transmission · MAI · Signal parameters · Evaluation · Distribution parameter

37.1 Introduction

The control segment of GNSS comprises a ground-based network of several master control stations, data uploading stations and monitor stations which installed over global area for system monitoring, adjusting, data updating and control [1–3]. The reliability of control and monitoring data transfer link of navigation satellites,

C. He (✉) · B. Yu

The 54th Institute of China Electronic Technology Corporation, Shijiazhuang 050081, China
e-mail: hechenglong743@sina.com

© Springer-Verlag Berlin Heidelberg 2015

J. Sun et al. (eds.), *China Satellite Navigation Conference (CSNC) 2015*

Proceedings: Volume I, Lecture Notes in Electrical Engineering 340,

DOI 10.1007/978-3-662-46638-4_37

communication satellites and special Internet is a crucial factor of system stability and its navigation performance. In a limited bandwidth satellite-based CDMA system without time division measurement, a ground station would receive several even tens of high-speed data communication signals which at same or close frequency and have a same modulation pattern, which lead to serious MAI and irreparable loss of communication performance. For the MAI of limited bandwidth link has several characters different from white noise in BER performance, traditional analysis and evaluation method could hardly evaluate the MAI performance accurately. The paper focuses on analysing each parameter's influence pattern, putting forward a targeted evaluate method and proving its reasonableness through hardware test.

37.2 MAI of Satellite-Based Data Transfer Link

The satellite-based link is used for data transfer among ground stations as showed in Fig. 37.1. If consider the satellite transponder and transfer link's influence on signal quality lightly, the received signal from another station could described as

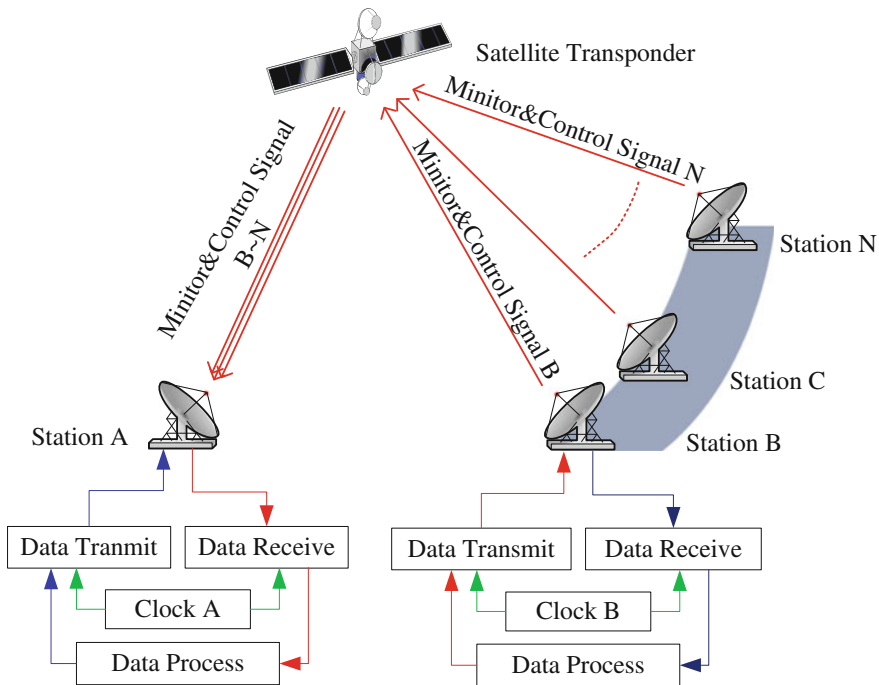


Fig. 37.1 Satellite-based data transmission link

$$s(t) = A_i d_i(t - T_{id}) c_i(t - T_{id}) \cos(2\pi f_i t + \varphi_i) \quad (37.1)$$

In Eq. (37.1), A_i is the amplitude of signal, T_{id} is the signal transfer delay, $d_i(t - T_{id})$ and $c_i(t - T_{id})$ are the data and PRN of signal, f_i is center frequency, and φ_i is the carrier phase shift.

37.2.1 Influence of MAI

If a station received several signals at close frequency from M stations through one satellite link, the received signal could be described as

$$\begin{cases} r(t) = s(t) + J(t) \\ \begin{cases} s(t) = A_1 d_1(t - T_{1d}) c_1(t - T_{1d}) \cos(2\pi f_1 t + \varphi_1) \\ J(t) = \sum_{m=2}^M A_m d_m(t - T_{md}) c_m(t - T_{md}) \cos(2\pi f_m t + \varphi_m) \\ m = 2 \sim M \end{cases} \end{cases} \quad (37.2)$$

If not consider of the loop tracking error, the multi-access signals after receiver code correlation process would become

$$\sum_{m=2}^M A_m E(\varphi) \int_{-\infty}^{\infty} d_1 d_m(\alpha - T_{md}) R_{cmc1}(T_{md} - T_{1d}) h(t - \alpha) d\alpha \quad (37.3)$$

In this equation, $E(\varphi)$ is the mean fading of MAI due to frequency and code phase difference, which could be described as

$$E(\varphi) = \frac{1}{T_c} \int_0^{T_c} \cos[\varphi_1 - \varphi_m + (f_1 - f_m)t] dt \quad (37.4)$$

T_c is the correlation time. If the signals have a same center frequency, it could simply described as $E(\varphi) = \cos(\varphi_1 - \varphi_m)$.

As Eq. (37.3), the MAI is the influence of signals' added cross-correlation value on auto-correlation peak composed of amplitude, phase shift and cross-correlation distribution, and these parameters are determined by PRN, power, code and carrier phase:

- Relative power A_m and carrier phase shift difference $\varphi_1 - \varphi_m$ determine the amplitude gain of MAI;
- Cross-correlation R_{cmc1} determine the cross-correlation peaks and its distribution;
- Code phase shift difference $T_{md} - T_{1d}$ determine the added cross-correlation value.

Due to the signal parameters' influence, MAI affect the signal performance in three ways: the added correlation curve lead to the ranging error; serious MAI lead to the loop loss tracking and mistake acquisition; added value lead to bit error. For high-speed data transfer link, the influence of MAI on system stability and BER are the main factor.

37.2.2 Traditional Evaluation Method and Its Limitation

In Eq. (37.3), if signals relative delay, carrier phase shift difference and data are all independence random variables and have the shape of uniform distribution, the added cross-correlation value $R_{cmc1}(T_{md} - T_{1d})$ satisfied the equation

$$R_{cmc1}(T_{md} - T_{1d}) \sim U[-\max(R_{cmc1}), +\max(R_{cmc1})] \quad (37.5)$$

At same center frequency:

$$\sum_{m=2}^M E^2(\varphi) \approx 0.5 \quad (37.6)$$

The approximate variance of MAI would be frequency (37.7) if all signals have same received power:

$$\text{Var}(MAI) \approx (M - 1)T_c^2/6N \quad (37.7)$$

N is the length of PRN in T_c . As a result, the SNR (Signal to Noise Ratio) of multiple-access channel would be [4, 5]

$$\text{SNR}_{MAI} \approx \left[\frac{M - 1}{3N} + 0.5(E/N_0)^{-1} \right]^{-1/2} \quad (37.8)$$

Equation (37.6) is the traditional evaluation method while it has many applicable conditions: first it need all parameters except the power should be independence uniform distribution shape random variables which is tenable in condition that all signal sources are all in motion separately and independently relative to receiver; and the cross-correlation value should be ideal value which means that used a better PRN such as Gold/Kasami code in channel; MAI have no influence on signal tracking. If satisfied all the conditions the MAI would approach the same intensity of white noise and evaluate the system performance.

The Eq. (37.7) has a satisfied evaluate performance in satellite navigation systems and communication systems, while the limited bandwidth satellite-based link has a certain signals condition, intercepted PRN with bad cross-correlation

distribution so MAI could hardly be evaluated as white noise. On the other hand, the design work should focus on the worst signal conditions to avoid instability signal factors rather than system average performance.

37.3 Evaluation Method of MAI of Limited Bandwidth Link

The limited bandwidth data transfer link means the half-bandwidth to data transfer speed ratio is relative small which means that the signal has a short PRN sequence in each data symbol. In this signal condition the MAI would has different affect pattern.

37.3.1 Worst and Best Signal Conditions of Data Link

According to Eq. (37.3), detailed analysis of signal parameters' influences on MAI are showed as below.

(1) Carrier Phase

Carrier phase shift difference is a main factor of gain of MAI. If phase difference satisfied $\varphi_1 - \varphi_m = 90^\circ/270^\circ$ the channel would have no MAI for signals compose the QPSK modulation. If $\varphi_1 - \varphi_m = 0^\circ/180^\circ$, the gain reach the max value for signals all in same BPSK modulation phase. These are the carrier phase ultimate limit conditions without considering the tracking error.

(2) Code Phase

The code chip width and code phase difference in a chip are described as

$$\begin{cases} T_{code} = T_c/N \\ a = \text{mod}(T_{md} - T_{ld}, T_{code}) \end{cases} \quad (37.9)$$

If the signal condition satisfied $R_{cmc1}(kT_{code}) \neq R_{cmc1}(kT_{code} + T_{code})$, signals used same period PRN sequences and static phase difference (same center frequency), and $R_{cmc1}(kT_{code})R_{cmc1}(kT_{code} + T_{code})$ are positive and negative values, when

$$a = T_c \frac{R_{cmc1}(kT_{code})}{R_{cmc1}(kT_{code}) - R_{cmc1}(kT_{code} + T_{code})} \quad (37.10)$$

the added cross-correlation value would be 0. If the system used non-periodical PRN, there have no condition that the added value is 0, and

$$\begin{aligned}
 E \left\{ R_{cmc1}(kT_{code}) + \frac{a}{T_{code}} [R_{cmc1}(kT_{code} + T_{code}) - R_{cmc1}(kT_{code})] \right\} &= 0 \\
 D \left\{ R_{cmc1}(kT_{code}) + \frac{a}{T_{code}} [R_{cmc1}((k + 1)T_{code}) - R_{cmc1}(kT_{code})] \right\} & \quad (37.11) \\
 \approx \frac{2a^2 - 2aT_{code} + T_{code}^2}{T_{code}} D(R_{cmc1})
 \end{aligned}$$

According to Eq. (37.11), if $a = T_{code}/2$ the variance reach the minimum and symmetry value, while if a is 0 or T_{code} , the variance reach the max value. We could draw a conclusion that the code phase shift couldn't change the mean value of added cross-correlation value obviously but that could reduce the MAI variance for the condition dispersed the cross-correlation peaks.

(3) Doppler

The MAI gain would be statics in the condition that signals have a same center frequency. Doppler shift would lead the code phase and carrier phase become variable:

$$\begin{cases} \Delta T_c(t) = T_c \times (\frac{f_c}{f_m} - \frac{f_c}{f_1}) = \frac{T_c f_c}{f_1 f_m} (f_1 - f_m) \\ \Delta \varphi(t) = T_c \times (f_1 - f_m) \times 2\pi \end{cases} \quad (37.12)$$

f_c is the PRN code speed. The cross-correlation value gains of different PRN length in Doppler condition are showed in Fig. 37.2.

As showed in Fig. 37.2, signal used short PRN length would suffer low Doppler Effect. For limited bandwidth high-speed data transfer link,

$$\frac{f_1 - f_m}{f_1 f_m} \ll 0.1 \quad (37.13)$$

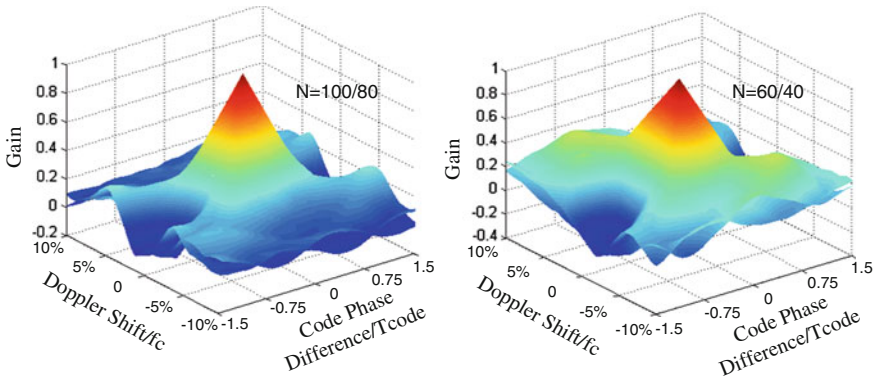


Fig. 37.2 Cross-correlation attenuation of intercepted PRN of N = 100/80/60/40

so the Doppler have a ignorable influence on the code correlation in such a channel, Doppler would mainly affect the MAI by carrier phase.

As a result, the three parameters compose the ultimate limit signal conditions: if all signals have same received power and the carrier and code phase differences are uniform distribution shape, each channel have a similar MAI condition; if all other signals satisfied $\varphi_1 - \varphi_m = 90^\circ/270^\circ$ the expected signal reach the best MAI performance while all signals satisfied $\varphi_1 - \varphi_m = 0^\circ/180^\circ$, $a = 0$ or close to T_{code} , signals would all reach the worst MAI condition and performance.

37.3.2 Cross-Correlation of PRN and Its Influence on MAI

According to Eq. (37.3), PRN with different pattern has different cross-correlation R_{cmc1} value limits and distribution which lead different MAI condition. Usually limited bandwidth high-speed data link used intercepted PRN which have a great lose in correlation performance than integrated PRN sequence for the peak value and its distribution are all increase which increase the MAI variance leading the system suffer worse MAI condition. For example, PRN sequences with different intercepted length from 1023 Gold code have different cross-correlation value distribution showed in Fig. 37.3.

As showed in Fig. 37.3, the intercepted PRN not only lead different distribution but also lead the peak value spread phenomenon which could hardly evaluate the system by Eq. (37.3) and the added correlation value is not the uniform distribution shape, which means the white noise evaluation method is not suitable for the link.

Additionally, the spread phenomenon would lead a higher added correlation value and affect the signals' tracking and acquisition, for example, if $N = 50$ the cross-correlation peak between two signals would approximately reach 0.5, which

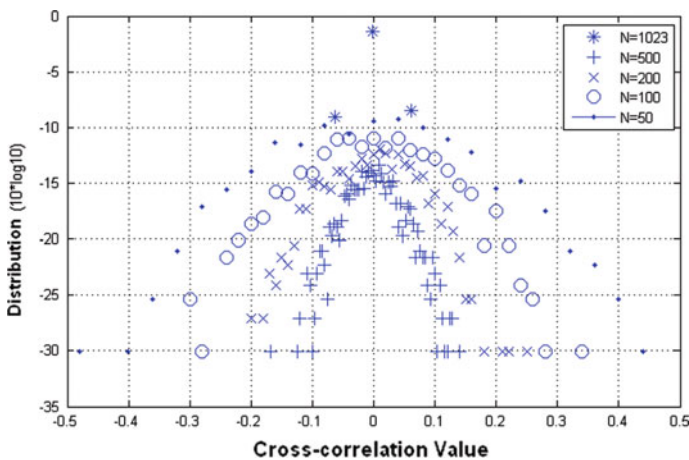


Fig. 37.3 Cross-correlation distribution of intercepted PRN of $N = 1023/500/200/100/50$

means the acquisition mistake or period increase would happen when there exist at least 3 signals and the influence increased by signal number.

37.3.3 MAI Evaluation Method for Limited Bandwidth Link

An evaluation method for satellite-based limited bandwidth high-speed data link is showed as below. The method built a cross-correlation distribution factor ϵ to improve the evaluate performance, the factor is calculated in process showed in Fig. 37.4.

In data fitting process, the logarithmic value of the distribution is approximately close to a quadratic function of correlation value:

$$10 \times \log_{10} P(R_{cmc1}, N) = -f(\epsilon, N)R_{cmc1}^2 + g(\epsilon, N) \tag{37.14}$$

In this equation, $f(\epsilon, N)$ and $g(\epsilon, N)$ are the fitting spread function and mean value function. Using the factor a in Eq. (37.9), fitting factor ϵ and its fitting function, $R_{cmc1}(T_{md} - T_{1d})$ in Eq. (37.3) could change to

$$\begin{aligned} R_{cmc1}(T_{md} - T_{1d}) &= E[P(m, N)m - P(n, N)n] \frac{a}{T_{code}} \\ &= \frac{a}{T_{code}} \int_{-1}^1 \int_{-1}^1 mP(m, N) - nP(n, N) dmdn = \frac{a}{T_{code}} G(\epsilon, N) \end{aligned} \tag{37.15}$$

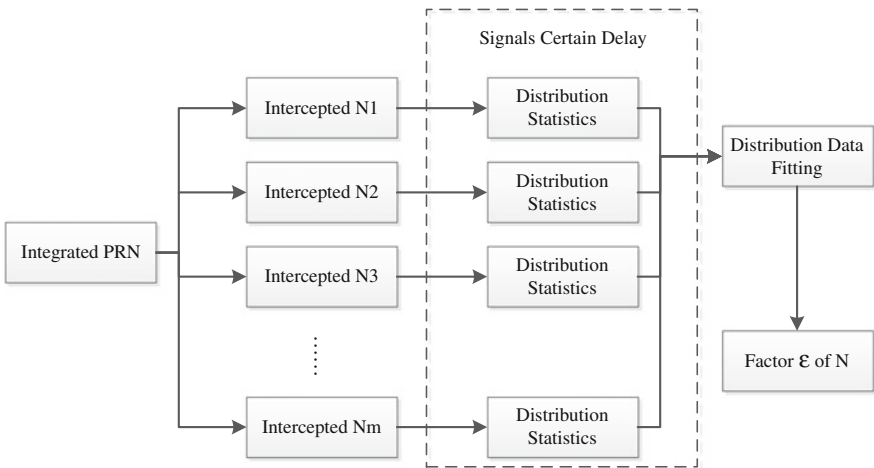


Fig. 37.4 Estimate process of cross-correlation distribution parameter

In Eq. (37.15), $G(\varepsilon, N)$ is the distribution fitting function determined by factor ε and PRN sequence length N . Then we could reach the evaluation results include ultimate limits performance, mean performance, acquisition mistake and period increasing probability.

The ultimate limit performances (worst performance) evaluate equation:

$$\begin{cases} v = \sum_{m=2}^M A_m \int_{-\infty}^{\infty} G(\varepsilon, N) h(t - \alpha) d\alpha \\ SNR_{MAI} \approx [D(v) + 0.5(E/N_0)^{-1}]^{-1/2} \end{cases} \quad (37.16)$$

The mean performances evaluate equation:

$$\begin{cases} v = \sum_{m=2}^M \cos\left(\frac{\pi}{M}\right) \frac{A_m}{M} \int_{-\infty}^{\infty} G(\varepsilon, N) h(t - \alpha) d\alpha \\ SNR_{MAI} \approx [D(v) + 0.5(E/N_0)^{-1}]^{-1/2} \end{cases} \quad (37.17)$$

The acquisition mistake and period increasing probability equation:

$$P_e = P\left(1 - K_c - \sum_{m=2}^M A_m a_m d_m \cos(\varphi_m - \varphi_1), N\right) \prod_{m=2}^M P(a_m, N) \quad (37.18)$$

In Eq. (37.18), K_c is the acquisition threshold of receiver. If there is no need to calculate accurately, the probability could be estimating by Welch limit:

$$P_e = \sum_{i=\frac{1}{2}}^M \frac{1}{2} C_M^i \quad (37.19)$$

In this evaluation method, the evaluate results are in the condition that MAI have no influence on tracking loop and the carrier and code tracking error are all zero, which need the condition that receiver embedded an efficient tracking algorithm in multiple-access data link, pilot assist and frequency synchronization. MAI would lead the tracking loop instable if hardly satisfied the condition, which added extra error in $\varphi_1 - \varphi_m$ and $T_{md} - T_{1d}$ leading the method has a great error in performance evaluation.

37.4 Evaluation Method Testing and Validation

37.4.1 Testing Method and Data Processing

We built a hardware testing and validation platform to proving the exactness of the evaluation method. The component and data processing are showed in Fig. 37.5.

The attenuator was used for analogizing the fade of transfer link and antennas; the noise temperature was measured at first; the signal source could transmit signals in certain ranging and carrier phase shift to reappearance the ultimate limits and mean signal conditions. The test environment is showed in Fig. 37.6.

37.4.2 Testing Result

The test results for targeted link condition are showed below. The results include the multi-user detection algorithms' influence [6, 7]. The evaluate and hardware results haven't include the loop tracking assist algorithm (Table 37.1).

It could be seen that evaluation method have a satisfied evaluate results for the max E_b/N_0 evaluate error is 0.2 dB; the BER evaluate error is better when E_b/N_0 increasing. So the evaluation method is of good suitability for limited bandwidth high-speed data transfer link.

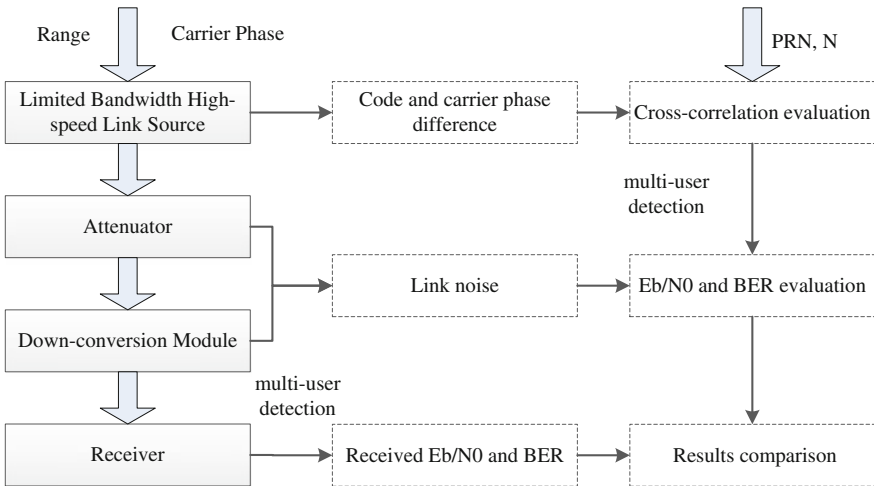


Fig. 37.5 Test system structure and data processing

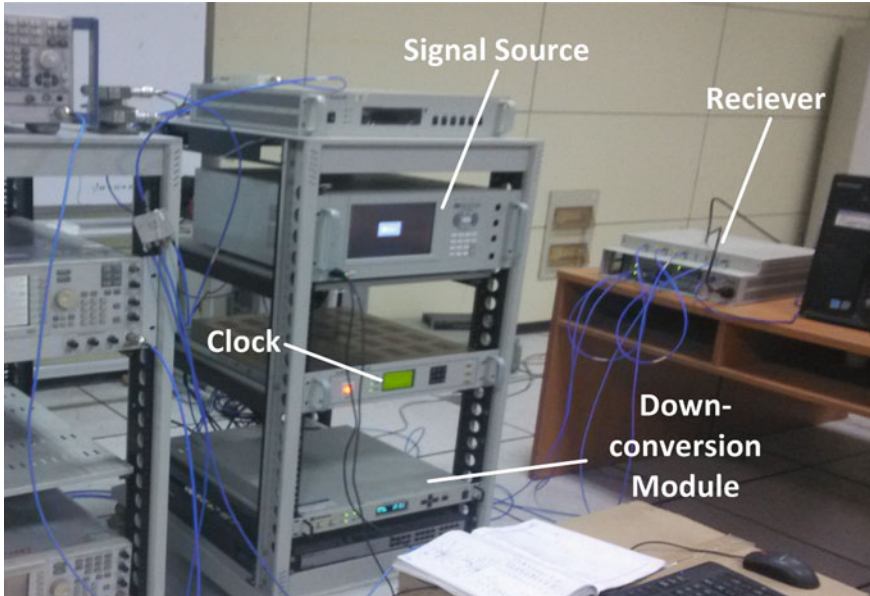


Fig. 37.6 Hardware of the MAI performance test system

Table 37.1 Hardware test results and evaluation results

Output Eb/N0 (dB)	Output BER (log10)	Evaluation Eb/N0 (dB)	Evaluation BER (log10)	Acquisition mistake and period increasing probability (%)
–	–	0.2700	–1.2096	24.1758
1.0	–1.7	1.2016	–2.1305	17.8755
2.2	–6.9	2.3748	–7.2099	12.9670
3.2	–8.5	3.1672	–8.3321	8.1132
3.7	None	3.8588	–10.1013	5.7855
4.8	None	4.7743	<–12	3.8828
6.8	None	6.8157	<–12	0
8.5	None	8.5103	<–12	0
10.9	None	10.8737	<–12	0

37.5 Conclusion

The reliability and stability of satellite-based data transfer links are key factors for satellite navigation system. Ensuring the high-speed data transferring in limited bandwidth link should use accurate evaluation methods to improve the effectiveness of signal structure, tracking algorithm and multi-user detection algorithm [8–12] design. The analysis and evaluation method for limited bandwidth link putted

forward in this paper is added the ultimate limits signal conditions and intercepted PRN fitting algorithm to traditional method to achieve accurate evaluate results in targeted link condition. The results could provide some technical experiences for BeiDou navigation system.

The evaluation method has weakness that it haven't evaluate the MAI influence on code and carrier loop tracking so it could hardly applied in much serious transfer link and receiver conditions. The loop influence and related performance evaluation will be analyzed in future.

References

1. Brown B, Aaron M (2001) The politics of nature. In: Smith J (ed) The rise of modern genomics, 3rd edn. Wiley, New York
2. Dod J (1999) Effective Substances. In: The dictionary of substances and their effects. Royal Society of Chemistry. Available via DIALOG. <http://www.rsc.org/dose/titleofsubordinatedocument>. Accessed 15 Jan 1999
3. Slifka MK, Whitton JL (2000) Clinical implications of dysregulated cytokine production. *J Mol Med*. doi:10.1007/s001090000086
4. Smith J, Jones M Jr, Houghton L et al (1999) Future of health insurance. *N Engl J Med* 341:325–329
5. South J, Blass B (2001) The future of modern genomics. Blackwell, London
6. Xie G (2012) Principles of GPS and receiver design. Publishing House of Electronics Industry, Beijing
7. Misra P, Enge P (2001) Global positioning system—signals, measurement, and performance. Ganga-Jamuna Press, Lincoln
8. Zhou Z, Yi J, Zhou Q (1997) Measuring principle and maintenance of GPS. Surveying and Mapping Press, Beijing
9. Pursley MB (1997) Performance evaluation for phase-coded spread-spectrum multiple-access communication-Part I: system analysis. *IEEE Trans Commun* 45(8):795–799
10. Li Z, Wang X (1997) Relation between sequence correlation and multiple access interference. *J Univ Electron Sci Technol China* 26(2):132–136
11. Hu C (2006) Study of parallel interference cancellation for wideband CDMA. University of Electronic Science and Technology of China
12. Li X, Geng S, Sun G et al (2009) Implementation of a new partial parallel interference cancellation multi-user receiver. *Signal Process* 89(7):1023–1027

Chapter 38

Research Progress on TWSTFT Mobile Calibration Station

Guoyong Wang, Ya Liu, Xiaohui Li and Chen Shi

Abstract To achieve more precision calibration between two any signal system' ground stations of two-way satellite time and frequency transfer (TWSTFT), a new TWSTFT calibration method is proposed based on two TWSTFT mobile stations to calibrate systematic error of time comparison between any two ground stations. Two TWSTFT mobile stations are developed. To measure the systemic error between the two mobile stations, a zero baseline comparison experiment is designed. The standard deviation of equipment delay of two mobile stations are respective 0.102, 0.038 ns. The standard deviation of systematic error of zero baseline comparison is 0.124 ns. To validate function of two mobile stations, a long baseline comparison experiment is designed between two ground stations at Tianjin and Lintong. The result is highly consistent with GPS Common-View comparison between two stations. To farther validate performance of two mobile stations, a long baseline comparison experiment be designed between two ground stations at Changchun and Lintong. The result is shown that the standard deviation of clock difference of two ground stations is 0.347 ns after moving the drift of cesium atomic clock at Changchun. The two TWSTFT mobile stations can implement calibration of systematic error of time comparison between any two ground stations.

Keywords Two-way satellite time and frequency transfer (TWSTFT) · TWSTFT mobile calibration station · Zero baseline · Long baseline

G. Wang (✉) · Y. Liu · X. Li · C. Shi
National Time Service Center, Chinese Academy of Sciences, Xi'an 710600, China
e-mail: wangguoyong321@163.com

G. Wang · C. Shi
University of Chinese Academy of Sciences, Beijing 100190, China

G. Wang · Y. Liu · X. Li · C. Shi
Key Laboratory of Time and Frequency Primary Standard, National Time Service Center,
Chinese Academy of Sciences, Xi'an 710600, China

38.1 Introduction

Two-way satellite time and frequency transfer (TWSTFT) is one of the most accurate means of long-distance time comparison. The time uncertainty of the method is better than 1 ns [1]. Advantages of TWSTFT comparison is that the signal propagation paths are approximate symmetrical, so that additional ionospheric delay, tropospheric refraction delay, geometric path delay, etc. almost is counteracted [2, 3]. TWSTFT ground station equipment delay is the main component of a two-way systematic error, it is essential to accurate calibrate it.

International general method is to use a mobile station to calibrate systematic error between two ground stations. Firstly mobile station and ground station A are measured based on a zero baseline measurement. A equipment delay difference between the two stations is got, then the mobile station and the ground station B to compare for getting the equipment delay difference of two stations. The two ground stations delay difference between A and B is got by subtracting the two equipment delay difference. Combined with TWSTFT formula, the clock difference of two ground stations can be calculated [4–6]. Disadvantages of international general calibration method are: the baseband device of mobile station and the calibrated ground station must be the same, uplink and downlink signal Must correspond to same band in the same satellite transponder.

At present, there are mainly three TWSTFT baseband device, the signals are mainly C-band and Ku-band in China. In accordance with general calibration method using a mobile station, it needs to develop six kinds of mobile stations for each band and baseband devices in order to meet our calibration. If you use multiple devices to calibrate equipment delay, not only cost is too high but also the systematic error among mobile stations is difficult to calibrate. To solve the difficulty of our country TWSTFT calibration, we propose the method that two mobile stations to calibrate the systematic error of time comparison between any two ground stations.

38.2 A Summary of Dual Mobile Stations Calibration Method

Dual mobile stations calibration method is to calibrate two ground stations clock difference using two mobile stations. Specific calibration process is shown in Figs. 38.1 and 38.2. Where M1 is mobile station 1, M2 is mobile station 2, G1 is ground station 1, G2 is ground station 2. The first step two mobile stations are placed at site A to make a zero baseline calibration to obtain the systematic error of two mobile stations (containing mainly equipment delay difference); the second step two mobile stations are respectively placed in site A and B to make a long baseline calibration. By TWSTFT calculation between mobile stations 1 and 2, combined with the result of the first step, the clock difference of two ground stations is got.

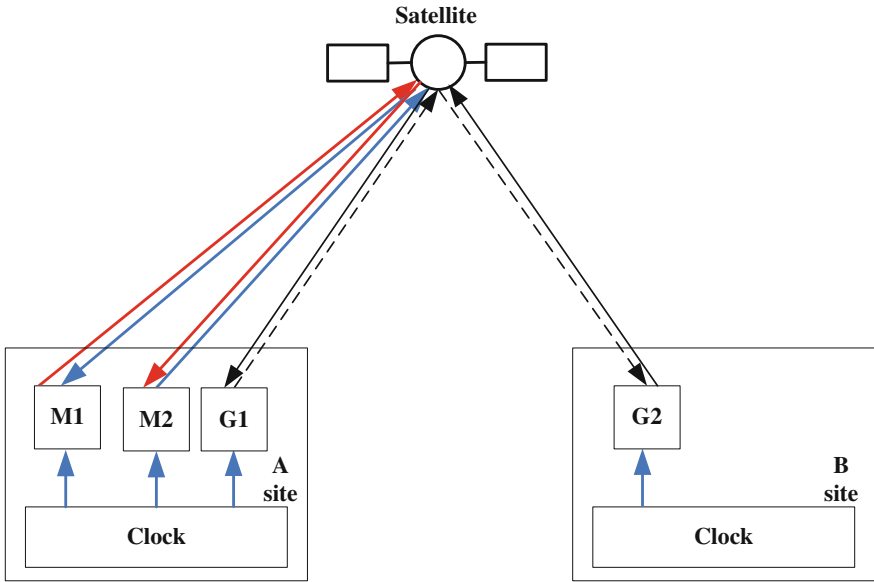


Fig. 38.1 The first step of two mobile stations calibration method

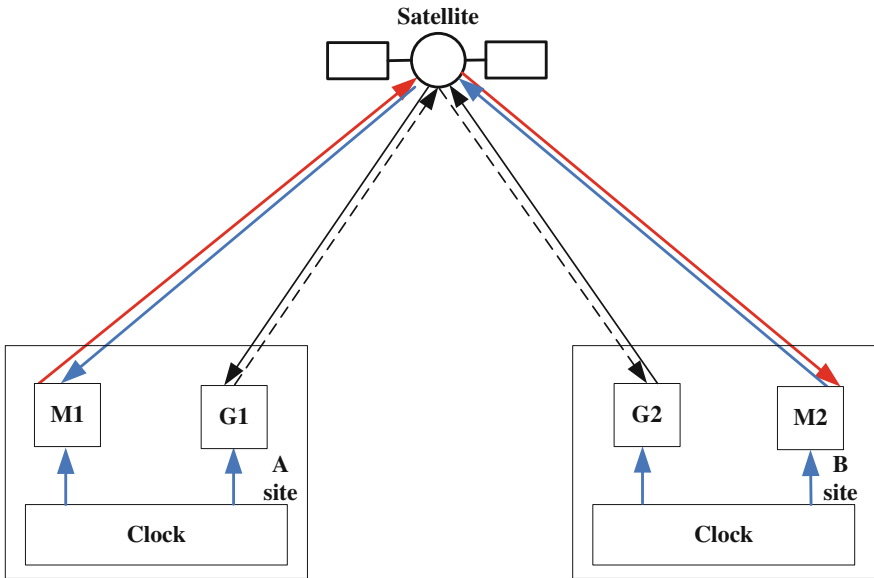


Fig. 38.2 The second step of two mobile stations calibration method

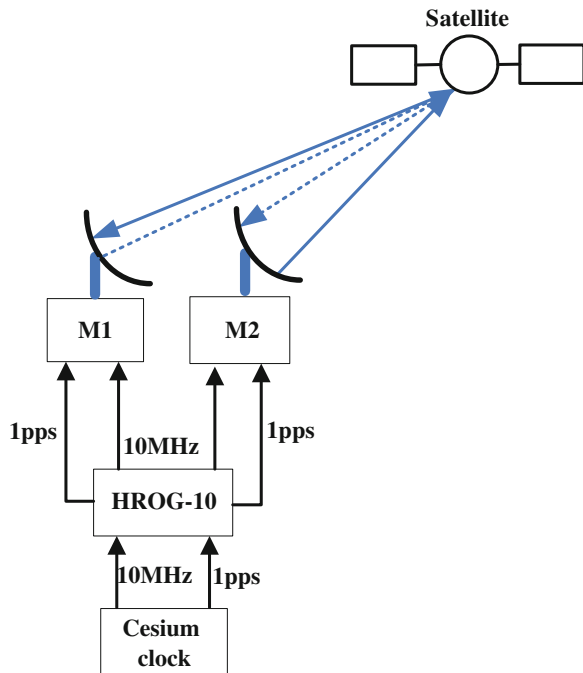
Compared with a single mobile station method, the advantage of dual mobile stations method is that can get rid of the restraint of the ground station signal system, not compare with the ground stations, can calibrate systematic error of any time comparison method between any two ground stations.

38.3 Zero Baseline Test

38.3.1 The Principle of Experiment

In this experiment, a method of common clock based on zero baseline is used, shown in Fig. 38.3. A frequency and phase offset generator HROG-10 is used as a common clock which provides 10 MHz and 1 pps signal for mobile station 1 and mobile station 2. National Time Service Center's master clock provides 10 MHz and 1 pps signal to HROG-10. Systematic error of zero baseline test contains of equipment delay of the two mobile stations, the satellite transponder delay, the signal spatial transmission delay etc. The mainly delay is equipment delay, the other delay can be ignored. Testing time is two days.

Fig. 38.3 The principle of zero baseline comparison experiment



38.3.2 The Results of Experiment

Equipment delay of station 1 is sum of transmitter delay Tx1 and receiver delay Rx1 of station 1. Equipment delay of station 2 is sum of transmitter delay Tx2 and receiver delay Rx2 of station 2. Systematic error means $-(Tx1-Rx1)-(Tx2-Rx2))/2$. From Table 38.1, Figs. 38.4, 38.5 and 38.6, standard deviation of equipment delays of Station 1 and 2 are respectively 0.102, 0.038 ns. Standard deviation of systematic error is 0.124 ns.

Table 38.1 The results of zero baseline comparison experiment

Results	Mean (ns)	Standard deviation (ns)
Equipment delay (station 1)	355.816	0.102
Equipment delay (station 2)	351.611	0.038
Systematic error	0.911	0.124

Fig. 38.4 Equipment delay of mobile station 1

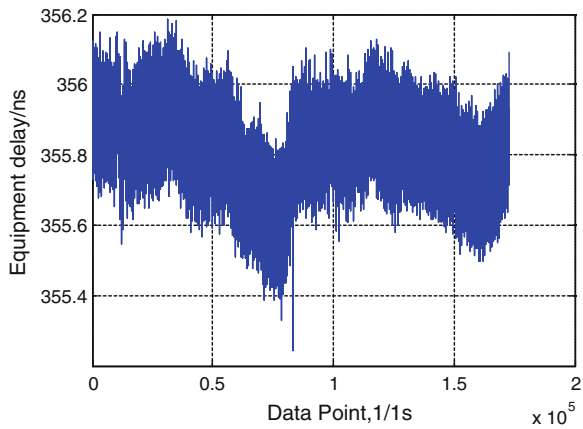


Fig. 38.5 Equipment delay of mobile station 2

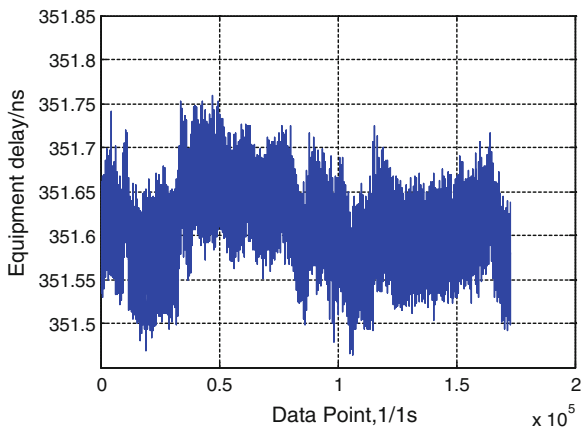
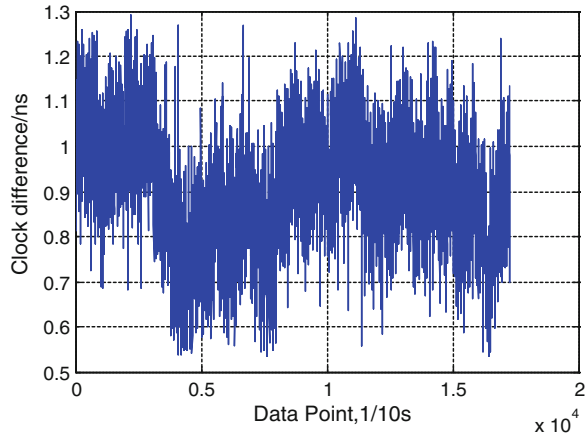


Fig. 38.6 systematic error of zero baseline comparison



38.4 Long Baseline Experiment

38.4.1 Lintong-Tianjin Long Baseline Experiment

38.4.1.1 The Principle of Experiment

The principle of Lintong-Tianjing long baseline comparison test is shown in Fig. 38.7. The mobile station 1 is placed at Lintong. National Time Service Center's master clock provides 10 MHz and 1 pps signal to HROG-10 for mobile station 1. The mobile station 2 is placed at Tianjin. The reference signals of mobile station 2 is provided by rubidium clock' 1 pps and 10 MHz. The rubidium clock is reined by associated control soft and algorithms. So there is no one-way drift. Lintong-Tianjin' baseline length is about 905 km.

38.4.1.2 The Results of Experiment

The red curve represents the results of TWSTFT test, the blue curve represents the results of common view test. As can be seen in Fig. 38.8 and Table 38.2, the results of TWSTFT and common view are highly consistent. It reflects the correctness of TWSTFT results. The limit of Rubidium clock' performance and control method due to poor results of TWSTFT and common view.

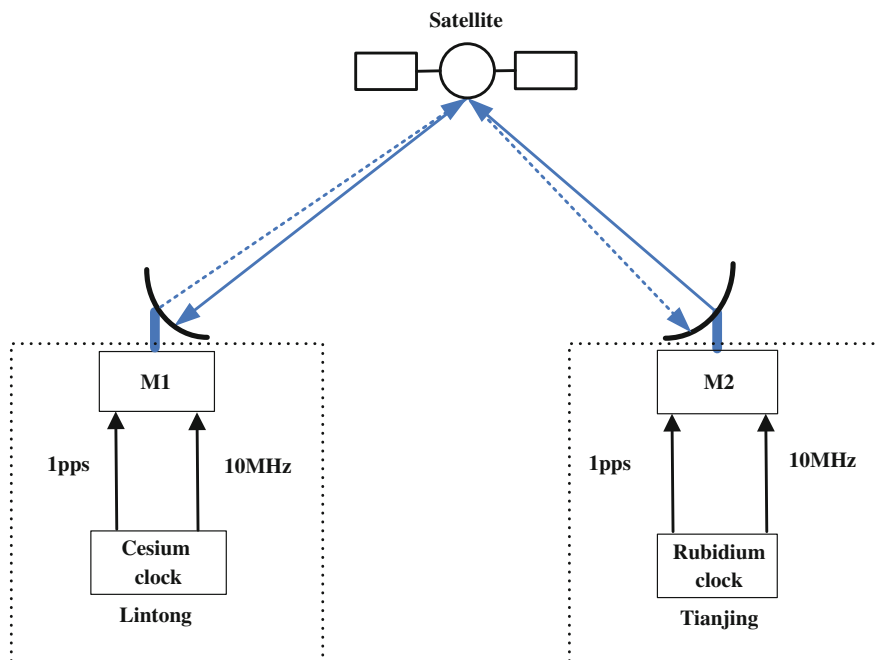


Fig. 38.7 The principle of Lintong-Tianjin long baseline comparison experiment

Fig. 38.8 The comparison of results of TWSTFT and common-view

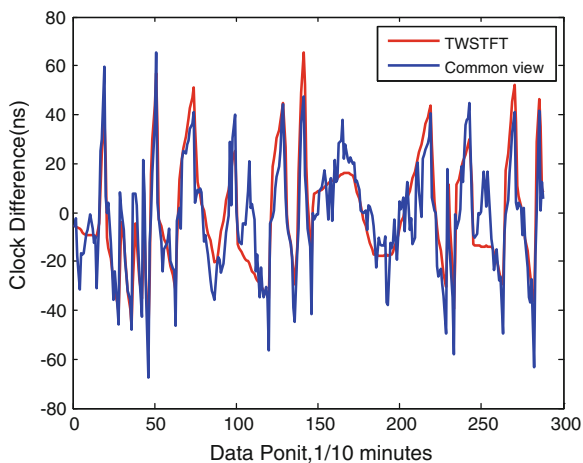


Table 38.2 The results of Lintong-Tianjin long baseline comparison experiment

Results	Mean (ns)	Standard deviation (ns)
TWSTFT	-0.472	22.382
Common view	-2.601	22.325

38.4.2 Lintong-Changchun Long Baseline Experiment

38.4.2.1 The Principle of Experiment

The principle of Lintong-Changchun long baseline comparison test is shown in Fig. 38.9. The mobile station 1 is placed at Lintong. A frequency and phase offset generator HROG-10 is used to provide 10 MHz and 1 pps signal for mobile station 1. National Time Service Center’s master clock provides 10 MHz and 1 pps signal to HROG-10. The mobile station 2 is placed at Changchun. Changchun’s cesium clock output’ 10 MHz and 1 pps to provides a 1 pps and 10 MHz reference signal for mobile station 2. Test data is about 3 h.

38.4.2.2 The Results of Experiment

It can be seen from Fig. 38.10 that Changchun’ OSA3035B cesium clock is run independently, that is to say, the cesium clock is not controlled. Clock difference of two stations has a linear drift. Everyday drift is about 24 ns compared with UTC (NTSC). The result is shown in Fig. 38.11 after removing clock difference linear

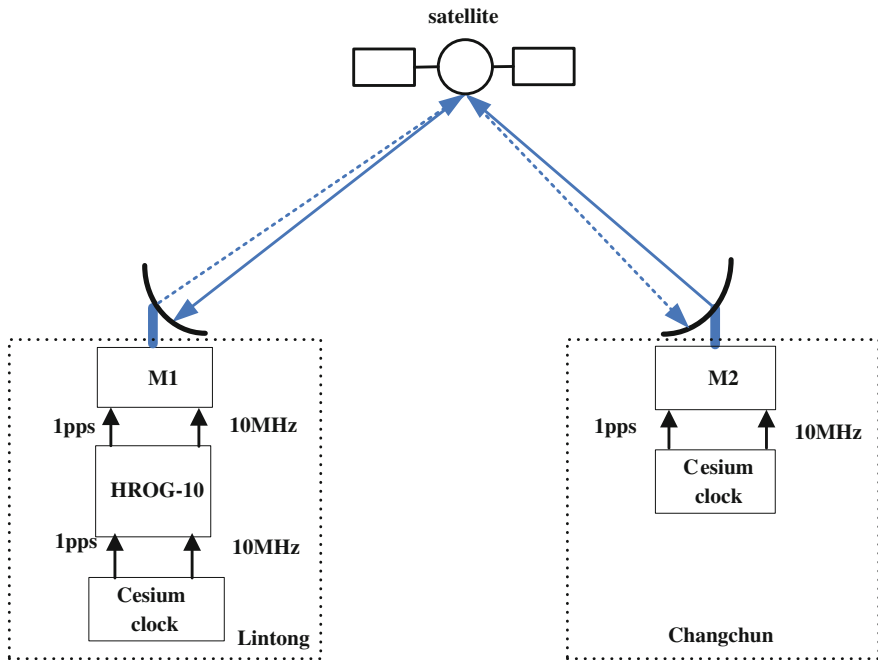


Fig. 38.9 The principle of Lintong-Changchun long baseline comparison experiment

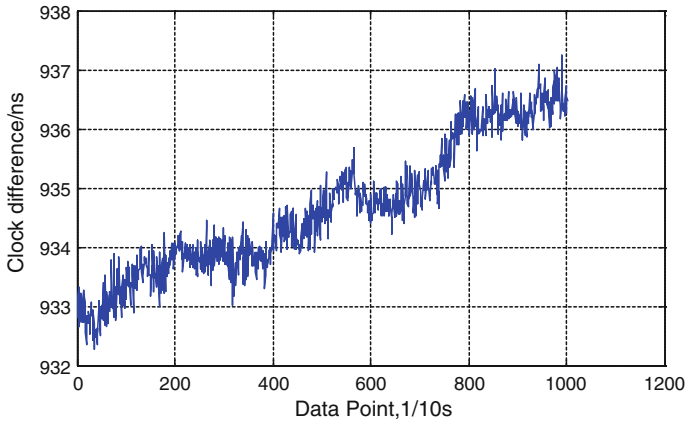


Fig. 38.10 The systematic error of Lintong and Changchun

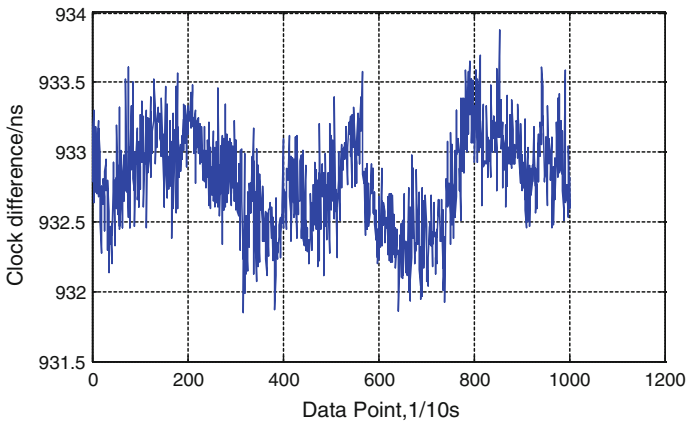


Fig. 38.11 The systematic error of Lintong and Changchun after removing the drift

Table 38.3 The results of Lintong-Changchun long baseline comparison experiment

Measured results	Mean (ns)	Standard deviation (ns)
Result of removing clock difference drift	932.796	0.347

drift. As can be seen from Table 38.3. After removing the clock difference linear drift, the standard deviation of Lintong and Changchun stations' systematic error is about 0.347 ns.

38.5 Conclusions

In this paper, the performance of TWSTFT mobile stations were tested. The results show: When zero baseline calibration, standard deviation of two mobile station equipment delays are respectively 0.102, 0.038 ns, the standard deviation of the systematic error is about 0.124 ns. The results Lintong and Tianjin Station common view and TWSTFT is highly consistent. It reflects the correctness of TWSTFT results. Lintong and Tianjin test results show that after removing the clock difference linear drift, the standard deviation of Lintong and Changchun stations' systematic error is about 0.347 ns. The two-way mobile station can be used to calibrate systematic error of any two TWSTFT sites.

Acknowledgments Thank the National Astronomical Observatory of Changchun Satellite observatory and Wuqing station to support and help for our work. This work was supported by the National Natural Science Foundation of China (No. 61127901).

References

1. Lin H-T, Liao C-S, Chu F-D et al (2011) Full utilization of TWSTFT network data for the short-term stability and uncertainty improvement. *IEEE Trans Instrum Meas* 60(7):2564–2569
2. Liao C-S, Lin H-T, Chu F-D et al (2011) Formation of a real-time time scale with Asia-Pacific TWSTFT network data. *IEEE Trans Instrum Meas* 60(7):2667–2672
3. Wu W, Li Z, Yang X et al (2012) Sagnac effect on two-way satellite time and frequency transfer. *J Astronautics* 33(7):936–941
4. Piester D, Achkar J, Becker J et al (2006) Calibration of six European TWSTFT earth stations using a portable station. In: *Proceedings of the 20th European frequency and time forum*, Braunschweig, Germany, 27–30 Mar 2006, pp 460–467
5. Piester D, Bauch A, Breakiron L et al (2008) Time transfer with nanosecond accuracy for the realization of international atomic time. *Metrologia* 45(2):185–198
6. Piester D, Hlavac' R, Achkar J et al (2005) Calibration of four European TWSTFT earth stations with a portable station through INTELSAT 903. In: *Proceedings of the 19th European frequency and time forum*, Besancon, France, 21–24 Mar 2005, pp 354–359

Chapter 39

Analysis of BeiDou Signals on the Accuracy of Common-View Time Transfer

MeiJun Guo, Hua Lu, Yun Xiao, YiJun Mo and XiaoGang Liu

Abstract The BeiDou navigation satellite system is being in the initial period of providing service. Currently, this system is broadcasting three signals, narrow correlation, wide correlation and anti-multipath, on both I and Q branches of B1, B2 and B3 frequency. One can get the pseudo-range measurements publicly on the civil frequency with a corresponding receiver. This paper firstly analyzed the influence of different satellites types, GEO, MEO and IGSO in BeiDou constellation, on the precision of common view time transfer. The conclusion indicates that the one can achieve the best precision of common view time transfer with GEO satellites among the three different satellites types. Based on this conclusion, this paper further analyzes the impact of different observation types, C/A measurements on any frequency and assembled dual frequency observations of any two frequencies, on the precision of common view time transfer. The results of common view time transfer are evaluated with stability, accuracy and standard deviation of residuals. Except the combination of B2 and B3 and the wide correlation combinations of dual frequency, the results obtained from the other combinations of dual frequency observations perform better than that from any single frequency. The result of B1IA is better than other single frequency, the residual standard deviation is 2.32, the stability of million seconds is $3.18e-13$ and the accuracy is $4.16e-13$. Among the results of all the dual frequency observations, the combination of B1IA and B2IA provides the best precision with the standard deviation of residuals being 1.36, the stability of million seconds being $2.11e-13$ and the accuracy being $5.71e-13$.

Keywords Common view time transfer · BeiDou · Single frequency · Dual frequency

M. Guo (✉) · H. Lu · Y. Mo
Xi'an Aerors Data Technology Lo., Ltd, Xi'an 710054, China
e-mail: guomeijun205@163.com

Y. Xiao · X. Liu
Xi'an Research Institute of Surveying and Mapping, Xi'an 710054, China

39.1 Introduction

Currently, BeiDou navigation satellite system has entered the era of providing service globally. Except the three main functions of high precision timing, positioning, and navigation, it also can provide service of short messages communication which will play an important role in China's economic construction and national security [1–3]. BeiDou navigation system has the unique constellation that consisted of GEO, IGSO and MEO satellites. To guarantee the global coverage, the technique of inter-satellite link is adopted [4, 5]. Currently, BeiDou has launched 5 GEO satellites, 5 IGSO satellites and 4 MEO satellites.

BeiDou signal system adopts the same technique of binary offset carrier modulation as that of GPS system. Currently, BeiDou is broadcasting three types of signals which are the narrow correlation N, wide correlation W and anti-multipath A on B1, B2, and B3 frequency.

At present, GPS common view time transfer is the main way for international time comparison. With the rapid development of BeiDou navigation satellite system, a series of questions need to be answered, such as whether the way of common view time transfer based on GPS satellites is suitable for that of BeiDou satellites? Which kind of satellites types can provide the better precision of time transfer? Whether the errors in the common view time transfer based on BeiDou satellites have any changes? Among the different observations, which kind of observations performs best? This paper intends to answer some of these questions.

Currently, there is no specification for BeiDou common view data processing. Therefore, all the analysis in this paper is based on the raw data of pseudo-ranges with sample rate being one point per second. After the application of error corrections to the raw data, the half-hour common view results are obtained with polynomial fitting.

39.2 Structure of BeiDou Navigation Signal

The navigation signal of BeiDou will adopt the modulation technique of BOC in the third development stage of BeiDou navigation satellites system. Comparing with the techniques of BPSK and QPSK that adopted in the previous stage, this technique has the advantages of multiplexing of signal frequency, reducing signal interference, enhancing the precision of pseudo-range measurements and separating the civil and military signals. Now a days, BeiDou has completed the plan of the second stage and enters the third stage which aiming at providing timing, positioning and navigation service globally until the year of 2020. Table 39.1 list the parameters of signal of the second stage and Fig. 39.1 shows the signal spectrum of the third stage [5, 6].

Table 39.1 BeiDou navigation signal of second stage

Signal	Carrier (MHz)	Code rate (MHz)	Frequency band (MHz)	Modulation type	Service
B1IN	1561.098	2.046	4.092	QPSK	Public
B1QN					Authorized
B1IW					Public
B1QW					Authorized
B1IA					Public
B1QA					Authorized
B2IN	1207.14	2.046	24		Public
B2QN		10.23			Authorized
B2IW		2.046			Public
B2QW		10.23			Authorized
B2IA		2.046			Public
B2QA		10.23			Authorized
B3IN	1268.52	10.23			Public
B3QN					Authorized
B3IW					Public
B3QW					Authorized
B3IA					Public
B3QA					Authorized

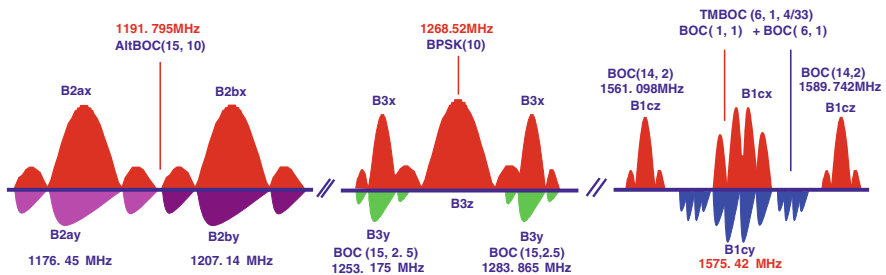


Fig. 39.1 BeiDou navigation signal spectrum of the third stage

39.3 Common View Time Transfer Based on BeiDou Satellites

39.3.1 Principle of BeiDou Common View Time Transfer

The principle of common view time transfer based on BeiDou satellites is the same as that based on the other GNSS satellites. The principle is shown as Fig. 39.2.

Two stations, A and B, simultaneously observe the same BeiDou satellites. We can get the time difference between the local time of station A and the BeiDou navigation

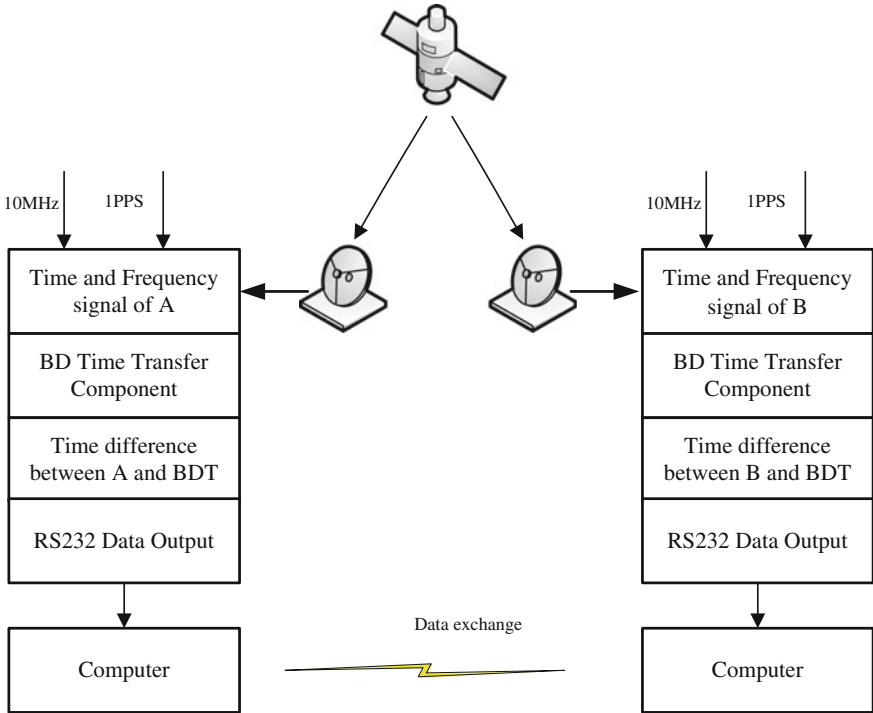


Fig. 39.2 The principle of BeiDou common view time transfer

system time. Similarly, station B can get the time difference between its local time and the BeiDou navigation system time. After the data exchange via network, the time difference between the local time of station A and B are obtained [7].

It is easy to find out that the complete impact of satellites clock instability and part impact of ionosphere delay, troposphere delay and ephemeris error are canceled in the process described above. The time difference between these two stations can be expressed as:

$$\begin{aligned}
 \Delta T_{AB}(T_A) &= \frac{1}{c} [\rho_{SB}(T_B) - \rho_{SA}(T_A)] + [\tau_{SA}(T_A) - \tau_{SB}(T_B)] \\
 &= \frac{1}{c} [\rho_{SB}(T_B) - \rho_{SA}(T_A)] + [\tau_A^R - \tau_B^R] + \frac{1}{c} [\rho_{SA}^{geo}(T_A) - \rho_{SB}^{geo}(T_B)] \\
 &= \frac{1}{2} (\tau_{SA}^{ion} - \tau_{SB}^{ion}) + \frac{1}{2} (\tau_{SA}^{tro} - \tau_{SB}^{tro}) + \frac{1}{2} (\tau_{SA}^{plm} - \tau_{SB}^{plm}) + \frac{1}{2} (\tau_{SA}^{gtide} - \tau_{SB}^{gtide}) \\
 &= \frac{1}{2} (\tau_{SA}^{rel} - \tau_{SB}^{rel}) + \frac{1}{2} (\tau_{SA}^{eccen} - \tau_{SB}^{eccen}) + \frac{1}{2} (\tau_{SA}^{com} - \tau_{SB}^{com}) \tag{39.1}
 \end{aligned}$$

τ_A^R and τ_B^R are respectively the time delay of the station A and B. $\rho_{SA}^{geo}(T_A)$ and $\rho_{SB}^{geo}(T_B)$ are the geometric distance which is from common view satellite to the observation station A and station B. τ_{Si}^{ion} , τ_{Si}^{tro} , τ_{Si}^{plm} , τ_{Si}^{glide} , τ_{Si}^{rel} , τ_{Si}^{eccen} and τ_{Si}^{com} are respectively the ionospheric delay correction, tropospheric delay correction, motion of station correction, earth solid tide correction, relativistic correction, receiver phase center correction and satellite phase center correction.

The correction of the relativistic effect for GEO satellites of BeiDou navigation system is different to that of the IGSO and MEO satellites. For GEO satellites, the effect of the Sagnac can be obtained with formula (39.2) [7],

$$Sagnac = -\frac{\omega}{c^2}R \cos \alpha_A (r + R) \sin(\lambda_S - \lambda_A) \tag{39.2}$$

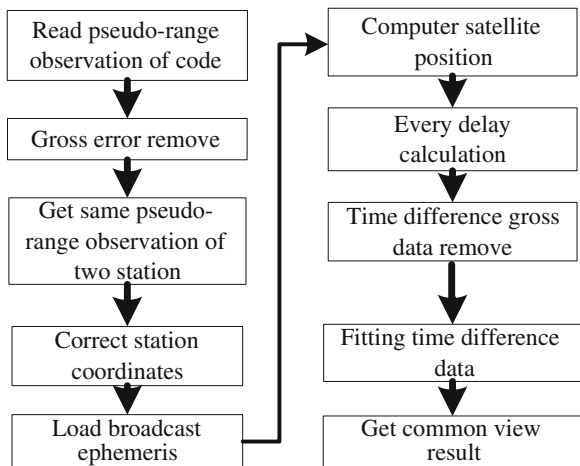
where α_A and λ_A are the latitude and longitude of observation stations and λ_S are the longitude of satellites in WGS84 coordinate system.

39.3.2 Process of BeiDou Common View Data

Figure 39.3 shows the processing diagram of BeiDou common view data. The detailed steps are as following [8].

- Read the original data of the two stations, detect the gross data in the pseudo-range observations, and then remove these data;
- Load the broadcast ephemeris, calculate the satellites positions at the corresponding time of observations with the correlative parameters;

Fig. 39.3 The data process flow of BeiDou common view data



- Calculate all the correction in formula (39.1) and remove them from the raw pseudo-range measurements;
- Find the BD satellites in common view of two stations, match these data of the same time;
- Finally, calculate the time difference between the local time of these two stations.

39.4 Experiment and Results

39.4.1 Experiment

The data from two stations, A and B being apart from about 1200 km, are used to carry out the experiment. With BeiDou receivers setting up at both of these two stations, we can get the raw pseudo-range measurements at three frequencies and further obtain the time difference between the local time of two stations and the BDT.

Basing on the data from two stations, this paper aims to carry out two aspects of researches.

Firstly, the common view results between these two stations based on single and dual frequency observations of MEO, GEO and IGSO satellites are computed.

Secondly, the common view results between these two stations based on I branches of B1, B2 and B3 frequency of GEO satellites are calculated.

Five days data from 1th December, 2013 to 5th of two receivers at two stations are used. The precision of common view results are evaluated with stability, accuracy and standard deviation of the residuals. Stability reflects the stochastic error of the results and the smaller of this index the more stable of the results. And the accuracy characterizes the systematic error of the results. Finally, standard deviation characterizes the fluctuation of the results.

39.4.2 Impact of Satellite Types on the Results

The analysis of this part is based on the data from the five GEO satellites, five IGSO satellites and two MEO satellites that in orbit currently. The common view results respectively based on single frequency of B1, B2 and B3 and combination of dual frequency are computed. The indexes of accuracy, standard deviation and million-second stability are calculated.

Taking the anti-multipath signal for example, Figs. 39.4, 39.5 and 39.6 respectively shows the three indexes of each satellite under three different observation types, B1A, B2A and their combination. According to these results, we can get the following conclusions.

Fig. 39.4 Standard deviation of different types of BeiDou satellites

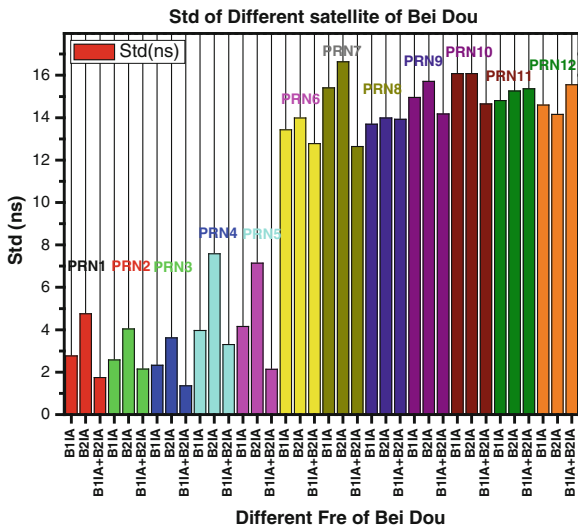
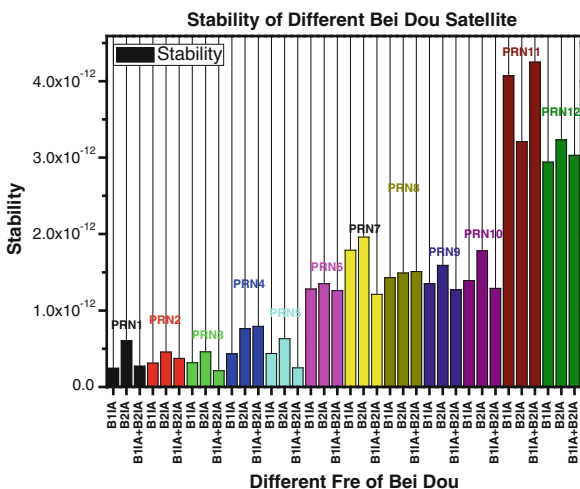


Fig. 39.5 Frequency stability of different types of BeiDou satellites

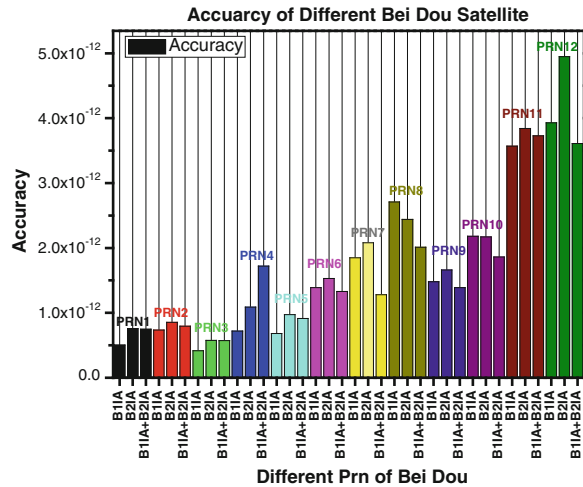


Firstly, it is obvious that all the three indexes of GEO satellites are better than the other two type satellites. And GEO 3 and IGSO 6 have the best results among the same type of satellites.

Secondly, the results of B1 single frequency basically better than that of B2 frequency.

Thirdly, the results based on combination pseudo-ranges of B1 and B2 of GEO and IGSO satellites are better than that based on single frequency of B1 and B2. It is reverse for the MEO satellites.

Fig. 39.6 Accuracy of different types of BeiDou satellites



Lastly, under the combination dual frequency pseudo-ranges of B1IA and B2IA of satellite GEO 3, the standard deviation and million-second stability perform the best, respectively being 1.36 ns and 2.11E-13. And the index of accuracy, being 4.16E-13, achieves the best value with the single B1IA pseudo-range measurements.

39.4.3 Impact of Signal Types of GEO Satellites on the Results

According to the conclusion of the precious section, the results based on measurements of GEO satellites have better results. For the measurements of GEO satellites, this section mainly experiments which kind of signal type performs best. There are, three frequency and 6 different types signals on each frequency, totally 18 kinds of measurements are tested. Figures 39.7, 39.8 and 39.9 gives three indexes of each signal type and Table 39.2 gives the values of each index.

The following conclusions can be summarized. Firstly, the three indexes that evaluating the results based on the observations of B1 I branch superior to that on B2 and B3. Secondly, the results based on the measurements of anti-multipath signal performs superior to other type of signal among the single frequency measurements. Thirdly, the worst results appear under the combination of wide correlation signals on B2 and B3 and the combination anti-multipath signals on B1 and B2 is best among all the dual frequency combinations. When comparing the results of single frequency and dual frequency, results based on the combinations of narrow and wide

Fig. 39.7 The residual standard deviation of different frequency of GEO 3 satellite

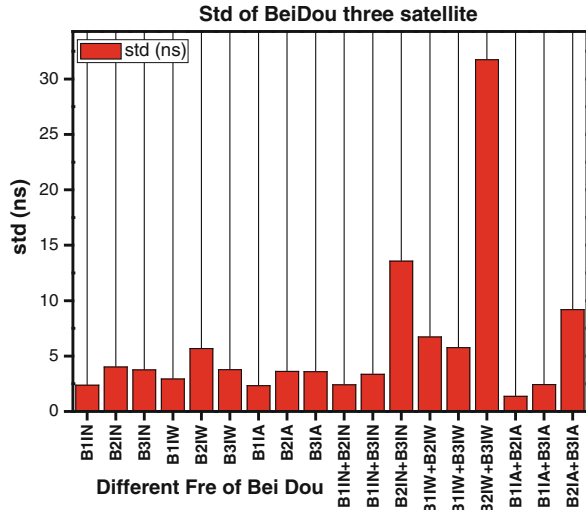
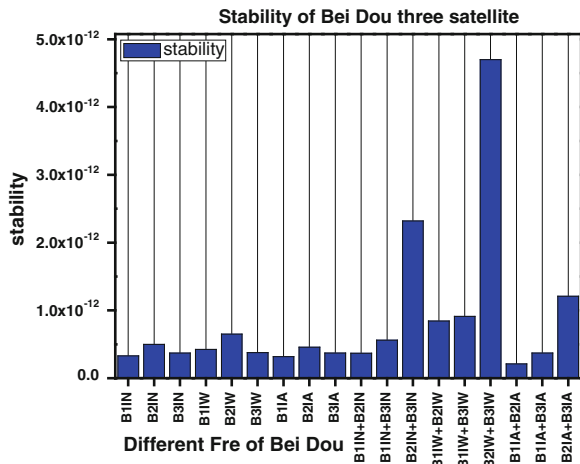


Fig. 39.8 The clock stability of different frequency of GEO 3 satellite



correlation signals are worse than the corresponding observations on the single frequency. However, the results based on the combinations of measurements of anti-multipath signals on B1/B2 and B1/B3 is better than that on single frequency. Lastly, the best results are get under the combination of dual frequency of anti-multipath signals with std deviation being 1.36, million second stability being 2.11e-13.

Fig. 39.9 The clock accuracy of different frequency of GEO 3 satellite

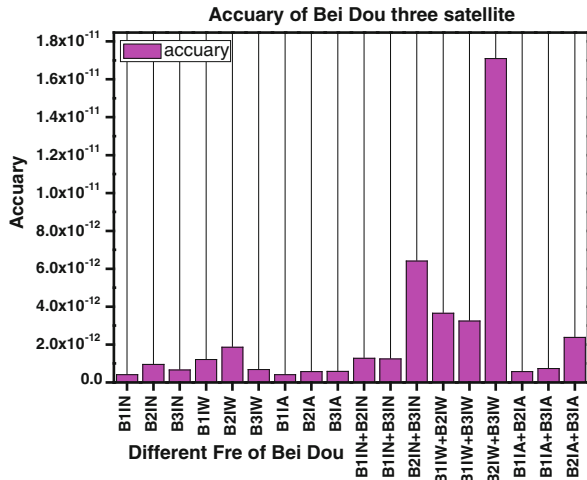


Table 39.2 The value of common view clock base on GEO 3 satellite

PRN	FRE	STD (ns)	Stability	Accuracy
GEO3	B1IN	2.37	3.3E-13	4.16E-13
	B2IN	4.02	4.99E-13	9.56E-13
	B3IN	3.75	3.72E-13	6.54E-13
	B1IW	2.93	4.26E-13	1.21E-12
	B2IW	5.68	6.51E-13	1.86E-12
	B3IW	3.77	3.76E-13	6.83E-13
	B1IA	2.32	3.18E-13	4.16E-13
	B2IA	3.62	4.58E-13	5.77E-13
	B3IA	3.6	3.72E-13	5.87E-13
	B1IN + B2IN	2.4	3.69E-13	1.27E-12
	B1IN + B3IN	3.36	5.6E-13	1.24E-12
	B2IN + B3IN	13.57	2.32E-12	6.41E-12
	B1IW + B2IW	6.72	8.43E-13	3.65E-12
	B1IW + B3IW	5.76	9.12E-13	3.24E-12
	B2IW + B3IW	31.75	4.7E-12	1.71E-11
	B1IA + B2IA	1.36	2.11E-13	5.71E-13
	B1IA + B3IA	2.43	3.71E-13	7.32E-13
	B2IA + B3IA	9.19	1.21E-12	2.38E-12

39.4.4 Analysis of the Results

Now let us analyze the results that obtained in the previous two sections. As far as we known, the orbit altitude of GEO satellites are nearly two times of that of the MEO satellites. And the GEO satellites are almost stationary above the earth

equator. Therefore, stations locating in China can see the BeiDou GEO satellites almost 24 h a day. Although the orbit altitude of IGSO satellites are the same as that of GEO, but its trajectory on the earth likes the character of “8”. The time period that they can be viewed is short. Otherwise, the correlation between ionospheric delays in the paths from common view satellite to two stations becomes weaken when the satellites for common view time transfer is GEO. All these reasons explain the conclusions in Sect. 39.4.2.

As the ionosphere delay is related with the signal frequency and proportional to the inverse of frequency square. So, B1 frequency has the smaller ionosphere delay among the three BeiDou frequencies. This can interpret the results that based on B1 frequency is better than those on the other two frequency.

The combination of measurements on wide correlation signals indeed eliminates the effect of ionosphere delay. However, the noise is also amplified. Taken the combination of B2 and B3 for example, m_2 is the noise on B2 frequency while m_3 is the noise on B3 frequency, and the noise after combination is m [9, 10].

$$\begin{aligned} m &= \sqrt{\frac{f_3^2}{f_3^2 - f_2^2} m_3^2 + \frac{f_2^2}{f_3^2 - f_2^2} m_2^2} \\ &= \sqrt{(10m_3)^2 + (9.6m_2)^2} \end{aligned} \quad (39.3)$$

According to Eq. (39.3), the noise level of the combination is 14 times larger than that of single frequency when the noise level on B2 and B3 are the same. This is why we can get the conclusion in Sect. 39.4.3.

The anti-multipath signal reduces the impact of multipath on the measurements. Therefore, the combination of B1IA and B2IA has better results than other combinations.

39.5 Conclusions

This paper tries to answer some questions about the BeiDou common view time transfer. There are several conclusions. Firstly, the results get from B1IA is the best in terms of time transfer based on measurements of single frequency. The standard deviation is 2.32 ns, million seconds stability is 3.18E-13 and accuracy is 4.16E-13. Secondly, the results based on the combination of B1IA and B2IA is the best in terms of dual frequency combination. The standard deviation is 1.36 ns, million seconds stability is 2.11E-13 and accuracy is 5.71E-13.

These conclusions can provide reference for the selection of satellites type, measuring frequency and signal type for BeiDou common view time transfer.

Acknowledgments Project supported by the National Natural Science Foundation of China (Grant No. 41374083).

References

1. Tan SS (2008) Development and thought of compass navigation satellite system. *J Astronaut* 29(2):391–396
2. Tong K (2003) The progress of Chinese satellite navigation and positioning system. *Int space* 6:1–5
3. Li JJ, Yi XQ (2011) Analysis of property and setup strategies of MEO inter satellite links in COMPASS system. In: CSNC-2011, Shanghai
4. China Satellite Navigation Office (2010) BeiDou (COMPASS) navigation satellite system development, Munich
5. He CY Research on evaluation methods of GNSS signal quality and the influence of GNSS signal on ranging performance. PhD thesis of University of Chinese Academy of Sciences
6. Xu ZG, Li YJ (2011) An overview of the application of the compass navigation satellite system in the marine police force. In: CSNC-2011, Shanghai
7. Yang F High-precision common view time transfer based on BeiDou GEO and IGSO satellites. Master thesis of University of Chinese Academy of Sciences
8. Yuan HB, Guang W Experiment and analysis of BeiDou satellite common-view time transfer. In: CSNC-2011, Shanghai
9. Li ZH, Hang JS (2005) GPS measurement and data processing. Wuhan University Press, Wuhan
10. Wu HT, Lu XC, Li XH, Hua Y, Yang XH The basis of satellite navigation system time. Science Press, Beijing

Chapter 40

Assessment of BDS Signal-in-Space Accuracy and Standard Positioning Performance During 2013 and 2014

Gucang Chen, Zhigang Hu, Guangxing Wang, Guo Chen, Zhaoying Liu and Qile Zhao

Abstract At the end of 2011, BeiDou Satellite Navigation System (BDS) moved into the phase of experimental operation, indicating that BDS, after GPS and GLONASS, became the third satellite system providing free service of PNT. In this paper, the positioning performance of BDS from Jan, 2013 was assessed. The data sources, as well as the generation of precise orbit and clock, were described, and the precisions of broadcast orbit, clock and signal in space for GEO/IGSO/MEO satellites were analyzed. The civil signal B1I of BDS was utilized to assess the accuracy of single point positioning (SPP) with code measurements. It is illustrated that the precision of URE for BDS could reach 1.5–2.0 m, and that the both horizontal and vertical precision of SPP reach 10 m in service area.

Keywords BeiDou · Broadcast ephemeris · Signal-in-space · URE · SPP · Performance assessment

40.1 Introduction

Based on the success of BeiDou I experimental satellite system, the building of Beidou II was kicked off in 2004, and the first medium-earth-orbit (MEO) satellite was launched 3 years later. In 2011, three satellites in the geostationary orbit (GEO)

G. Chen
China Satellite Navigation Office, Beijing 100034, China

Z. Hu (✉) · G. Wang (✉) · G. Chen · Z. Liu · Q. Zhao
GNSS Research Center of Wuhan University, Wuhan 430079, China
e-mail: zhigang.hu@whu.edu.cn

G. Wang
e-mail: gxwang0113@126.com

and four in the inclined geosynchronous orbits (IGSO) were properly deployed, possessing the capacity of regional navigation and positioning. At the end of 2011, the initial operation of BeiDou (BDS) regional satellite system was announced officially. Up to the end of the year 2012, five GEO satellites, five IGSO and four MEO ones had been deployed, and BDS began to formally provide positioning, navigation and timing (PNT) service in Asia-Pacific area. In June, 2014, BDS had been operating for 18 months, and the information of its constellation is shown in Table 40.1.

The performance of signal in space is one of the critical factors in positioning precision and integrity monitoring of GNSS [1]. Signal in space range error (SISRE) or user range error (URE) is the difference between the real position and clock of the satellites and their values in predicted ephemeris, reflecting the precision of ephemeris and finally affecting the positioning accuracy for real-time user. In this paper, the performance of SISRE and positioning of BDS during Jan, 2013 and Jun, 2014 was assessed. Firstly, the method of determining the assessment standards, i.e. the precise orbit and clock products, was described, and SISRE equations tailored to BDS was proposed. The performance of SISRE and PNT service for BDS was then analyzed.

Table 40.1 The components and specifications of satellites for BDS regional constellation

Orbit types	Satellite name (PRN)	Launch date	Altitude (km)	Inclination (°)	Longitude (°)	Status
GEO	G01(C01)	2010.01.17	35,786	<1	140.00E	Normal
	G02	2009.04.14	35,786	–	–	Inactive
	G03(C03)	2010.02.06	35,786	<1	110.50E	Normal
	G04(C04)	2010.11.01	35,786	<1	160.00E	Normal
	G05(C05)	2012.02.24	35,786	<1	58.75E	Normal
	G06(C02)	2012.10.25	35,786	<1	80.00E	Normal
IGSO	I01(C06)	2010.01.08	35,786	55	101–136E	Normal
	I02(C07)	2010.12.18	35,786	55		Normal
	I03(C08)	2011.04.10	35,786	55		Normal
	I04(C09)	2011.07.26	35,786	55	79–112E	Normal
	I05(C10)	2011.12.02	35,786	55		Normal
MEO	M03(C11)	2012.04.29	21,528	55	–180 to 180E	Normal
	M04(C12)	2012.04.29	21,528	55		Normal
	M05(C13)	2012.09.18	21,528	55		Unavailable since Jan, 2014
	M06(C14)	2012.09.18	21,528	55		Normal

40.2 BDS Data Collection and Precision Orbit Determination

According to the development plan, BDS is becoming fledged and the tracking network is expanding. In this paper, the observables were collected from about 20 sites of BeiDou experimental tracking stations (BETS), all of which were equipped with GPS/BDS dual-system and quad-frequency (i.e. GPS L1/L2 and BDS B1I/B2I) Unicore receivers. At present, BDS constellation is composed mainly of GEO and IGSO satellites covering Asia-Pacific area. As is shown in Fig. 40.1, the 14 stations in this area are able to track seven to nine BDS satellites at 95 % of the time.

The prerequisite of the assessment of BDS ephemeris is the precise orbit and clock, which is not officially provided. The upgraded GNSS precision processing software developed by Wuhan University is able to compute precise orbit and conduct positioning [2]. Considering the uneven and sparse distribution of stations, the similar strategy for GIOVE-B [3] precise orbit was employed for precision orbit determination of BDS. Firstly, PPP was conducted using GPS precise orbit and clock to obtain station coordinates, receiver clocks and ZTDs with high precision, which would be fixed in the next step. Slightly different from strategy in [3], the inter-system bias between GPS and BDS were estimated simultaneously [4]. Ionosphere-free observable combination with 30 s sampling interval was processed in batch, and each arc covered 3 days.

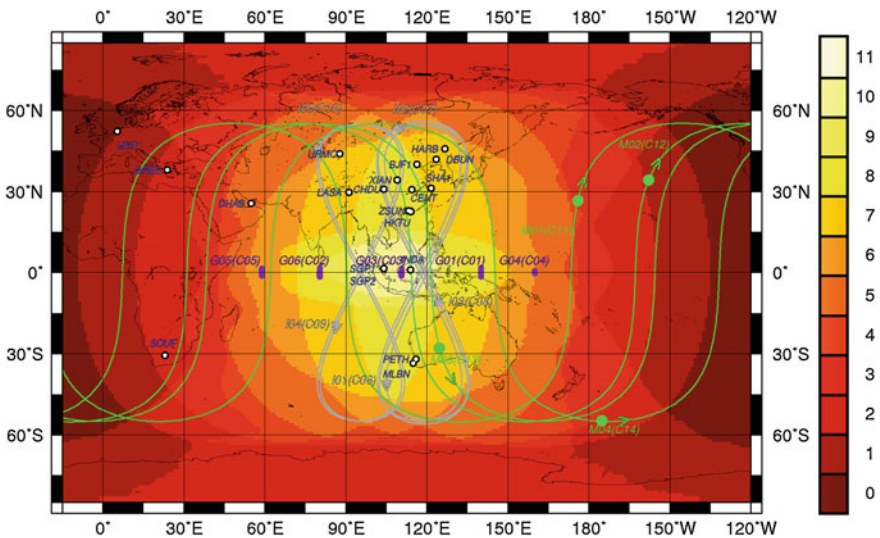


Fig. 40.1 Distribution of satellite coverage strength and the sub-track

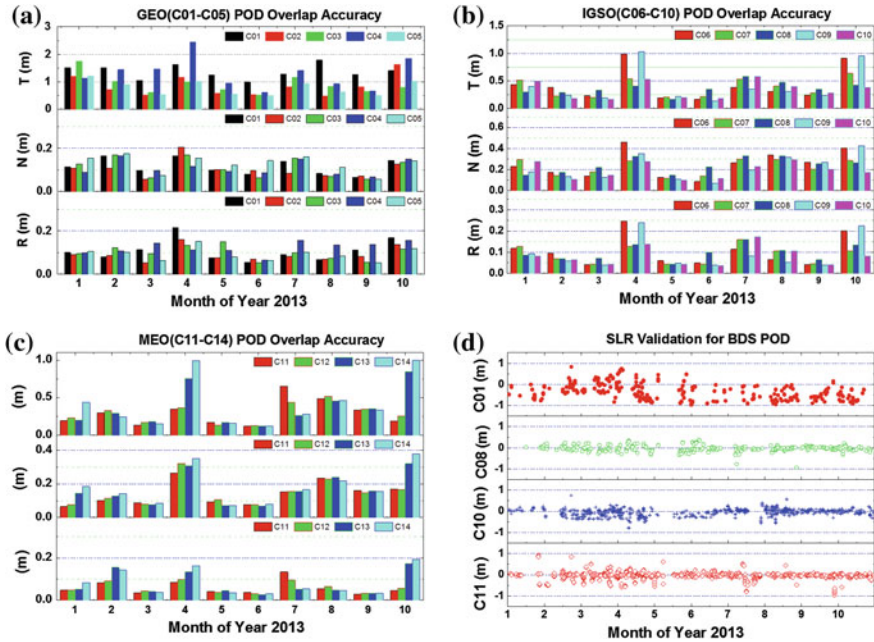


Fig. 40.2 Difference of GEO/IGSO/MEO precise solutions (Jan–Oct, 2013)

In order to assess precision of orbit, the overlap of the first and third arcs of three successive arcs are compared. Shown in Fig. 40.2a–c is the average precision of GEO/IGSO/MEO satellites, respectively, during Jan and Oct in 2013. The precision of GEO satellites in along-track (A), cross-track (C) and radial (R) direction is 1.00, 0.12 and 0.10 m, respectively. Those for IGSO satellites are 0.36, 0.21 and 0.09 m, while MEO 0.33, 0.15 and 0.07 m, respectively. The above results show that the along-track precision of G01 is the worst, which can be explained by its weak geometry and the uneven distribution of stations [4]. It is worth noting that the radial precision, which affects positioning the most, for all three types of satellites are better than 10 cm.

The precision of orbit could also be verified by SLR observables through the external consistency. G01 and I03 and M03 are all equipped with laser reflecting prisms, and the SLR checking results for the three satellites are 0.24, 0.12 and 0.12 m, respectively. Shown in Table 40.2 are the internal and external consistencies for all three satellites.

The above precise orbit with precision better than 10 cm in radial direction, as well as the corresponding clock, is taken as the “real value references”.

Table 40.2 Average precision of BDS precise orbit (Jan–Oct, 2013)

Satellite type	Overlap precision (m)			SLR check (m)
	A	C	R	
GEO	1.00	0.12	0.10	0.24
IGSO	0.36	0.21	0.09	0.12
MEO	0.33	0.15	0.07	0.09

40.3 Method of Assessment

40.3.1 Preprocessing

Station navigation ephemeris files of BETS network are merged into one file which contains all satellites ephemeris information, some error data caused by receiver (e.g. failure decoding) are removed [5]. On the other hand, navigation satellites with orbit maneuver and/or integrity alert information are excluded [6], and the health flag in navigation ephemeris is used to decide whether a satellite is usable or not [7]. Since the master control stations of BDS are in native region, the GEO and IGSO satellites will be tracked in most of the time, the corresponding satellites navigation information can be updated conveniently and in time (every 1 h). The AOD (age of data) of these satellites’ ephemeris is 1 h, shorter than that of GPS. The case is different for MEO satellites, which only can be tracked for a short time in 1 day, so the MEO satellites ephemeris with a relative longer AOD with a not perfect prediction position accuracy. In this paper, only the ephemeris with AOD smaller than 1 h is employed in statistics. Considering that the BDS constellations are still in construction, some satellites are unavailable. Overall, the availability rate of data from GEO and IGSO satellites is over 90 %, while the MEO satellites usable ephemeris is only 70–80 %. Finally, the data with difference between precise orbit and broadcast ephemeris larger than 50 m are excluded in statistics and this assumption is reasonable, considering that 50 m is larger than 30 times of standard deviation for signal in space range error.

40.3.2 Comparison Between Precise and Predicted Orbit

As mentioned above, the precise orbit accuracy of BDS is between 10 and 50 cm, much better than the broadcast ephemeris, so it is taken as reference value and the difference between precise orbit and broadcast ephemeris is considered the broadcast satellites position error. Meanwhile, noting that the precise orbit and broadcast one is not in the same reference frame, the reference frame must be unified before comparison. The computation of BDS precise orbit is under ITRF2008, while the broadcast ephemeris is under CGCS2000 (China Geodetic Coordinate System 2000). Theoretically, position under CGCS2000 should converse to ITRF2008 by seven transformation parameters (three for translation, three

for rotation, and one for scale) [8]. Given that the difference between CGCS2000 and ITRF1997 or ITRF2008 is only several centimeters [9, 10], the transformation between CGCS2000 and ITRF2008 is not considered in this paper.

40.3.3 Comparison Between Precise and Predicted Clocks

When determining the satellite orbit, the satellite relative clock is computed by a selected reference clock, and the selected reference clock can be either a receiver clock or a satellite clock. The different reference clock used has no impact on the user navigation and positioning as the bias existing in the same satellite clock can be absorbed in receiver clock estimation. The BDT is maintained by military time-frequency equipment, while the independent receiver clock is used for orbit determination. Under this condition, a method with second-order differencing is used for broadcast clock assessment instead of first-order differencing. What is more, the predicted clock bias of BDS is based on frequency B3I, so the TGD (group delay timing) correction in broadcast ephemeris between B1I and B3I should be taken into account when assessing the satellite predicted clock bias on B1I. The satellite predicted clock error can be computed by the below formula:

$$\Delta t^i = dt^i - \mu \quad (40.1)$$

where, $dt^i = T^i - t^i$ is the first-order difference between precise satellite clock bias and broadcast clock bias, $\mu = \sum_{i=1}^n dt^i/n$ is the mean of all satellites and used as the datum difference between precise and broadcast satellite clock.

40.3.4 Calculation of URE for BDS

According to ref. [11], if a receiver with known position is synchronized to navigation system time, then the expectation of the difference between pseudo range (the range between satellite position broadcast by satellites and receiver location) and measured range by receiver is IURE (Instantaneous User Range Error). IURE only consists of ephemeris error caused by space and control Segments, ranging error caused by user segment (e.g. troposphere delay, multipath error and noise) is not included in IURE. The main error for IURE comes from prediction satellites position error and satellites clock error. IURE is a function of time and space. In practical statistics, the RMS (root mean square) of IURE is considered the precision of IURE [12]. There are some differences about RMS URE computation between GPS and BDS:

- BDS include three different kinds of satellites, i.e. MEO, IGSO and GEO satellites. Generally, the higher the orbit altitude is, the larger the impact of satellite radial direction position error on user ranging error is [7]. The projection factor for MEO is 0.98 and 0.99 for IGSO/GEO, while the impacts of cross and normal direction position error are much smaller, i.e. 0.0078 and 0.0204 for the cross position projection and the normal position projection, respectively. This means the satellite position error in cross and normal direction is less than 1/11 of radial direction. For MEO satellites, the position error projection factor is 0.98 and 0.0185 in radial direction and cross/normal direction, respectively.
- Noting the property of GEO/IGSO satellites, the coverage region area is different from MEO satellites, so the RMS of IURE for IGSO/GEO is regional other than global level.
- Satellites position error and clock error is correlative [11]. Results from GPS SPS show that the satellite radial direction position error has significant negative correlation and the coefficient is -1.0 . GPS satellites position and clock error are computed by pseudo-range measurements. BDS satellites position is predicted by the same way, while the satellites clock is obtained through time-two-way comparison method. The correlation coefficient is smaller than GPS, RMS of IURE is computed as

$$rms\ URE_{BDS(GEO,IGSO)} = \sqrt{(0.99R)^2 + T^2 + \frac{1}{127}(A^2 + C^2)} \quad (40.2)$$

$$rms\ URE_{BDS(MEO)} = \sqrt{(0.98R)^2 + T^2 + \frac{1}{54}(A^2 + C^2)} \quad (40.3)$$

40.4 Assessment Results and Analysis

With the above-mentioned method, the SISRE, ionosphere model and positioning accuracy of BDS during Jan, 2013 and Jun, 2014 were assessed.

40.4.1 Precision of Broadcast Orbit

Shown in Fig. 40.3a–c are the results for GEO (C01-C05), IGSO (C06-C10) and MEO (C11-C14) satellites, and the “mean” in each panel references the average of all 14 satellites. Comparing among the three types of satellites, it can be found that the radial precision of GEO satellites are marginally higher than the average precisions of GEO/IGSO/MEO satellites and the precisions of GEO satellites are more or less the same. The radial precision for C02 is the best, while the along-track

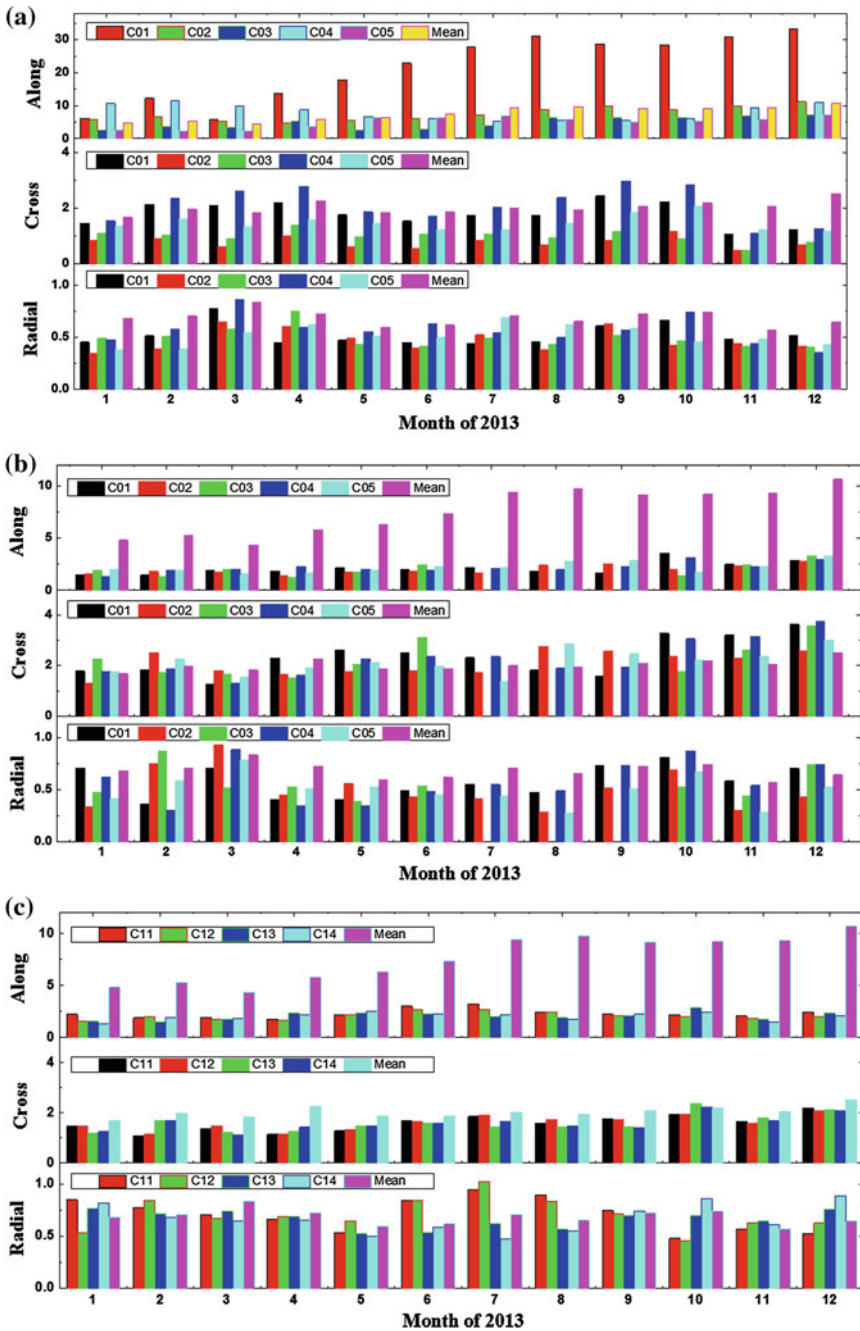


Fig. 40.3 Precision of broadcast orbit for BDS satellites (Jan, 2013–Jun, 2014). **a** Precision of broadcast orbit for GEO satellites (2013). **b** Precision of broadcast orbit for IGSO satellites (2013). **c** Precision of broadcast orbit for MEO satellites (2013). **d** Precision of broadcast orbit for GEO satellites (2014). **e** Precision of broadcast orbit for IGSO satellites (2014). **f** Precision of broadcast orbit for MEO satellites (2014)

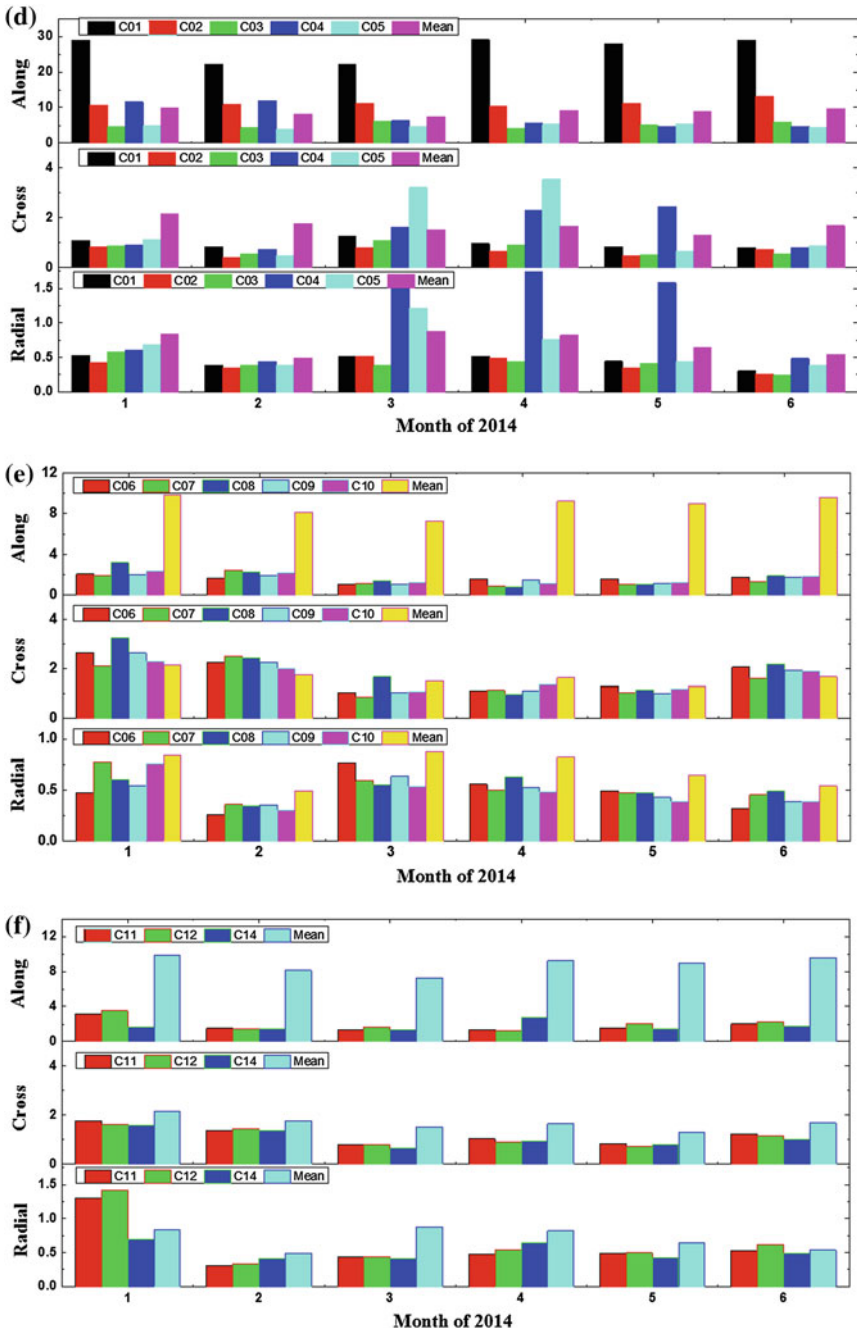


Fig. 40.3 (continued)

precision for C01 the worst. The radial precisions for most satellites could reach 0.5–0.8 m, and the cross-track precisions are better than 2.0 m. The along-track precisions are significantly different from satellite to satellite. Those for most GEO satellites are greater than 5.0 m. The along-track precision for C01 even reaches 10–20 m, while those for IGSO and MEO satellites are about 2.0–3.0 m.

Compared with the year 2013, the BDS broadcast ephemeris in 2014 shows the equivalent precision in along-track direction, but shows better precisions in cross-track and radial direction. The along-track precisions of GEO satellites keep stable in the 2 years, the precisions of IGSO satellites slightly improve in all three directions. The radial precisions of MEO satellites stay at around 0.5 m, and the along-track and cross track 1.5–2.0 m.

40.4.2 Precision of Broadcast Clocks

Normally, the broadcast ephemeris for GEO and IGSO satellites are updated every hour. Frequently updating could help improve the precision of predicted orbit and clocks. Shown in Fig. 40.4a, b are the standard deviations of differences between broadcast and precise clocks for BDS satellites during 2013 and 2014, most of which fall between 2 and 6 ns. In 2013, the clocks of BDS satellites are relatively stable. The precisions of broadcast clocks of GEO satellites are 4–8 ns, slightly worse than those of IGSO and MEO satellites. The precisions for IGSO satellites are around 2–3 ns. Since the ages of assessment data for MEO satellites are longer than 1 h, their precision are around 4 ns, marginally inferior to those of IGSO satellites.

The broadcast clocks of 2014 are around 4 ns, generally consistent with those of 2013. However, the precisions of most GEO and IGSO satellites improve by 1 ns, and they are stable from month to month. The precision of broadcast clocks for MEO satellites are 3–5 ns, consistent with those of 2013.

40.4.3 Signals-in-Space Precision

The calculation of SISRE for BDS satellite is not only different from GPS satellite, but also different for different types of BDS satellites, due to the orbit altitudes. With the tailored equations, the SISREs of BDS satellites during 2013 and 2014 are analyzed, and the results are shown in Fig. 40.5.

Generally speaking, the monthly average UREs of all BDS satellites are relatively stable in 2013, falling between 1.5 and 2.0 m, as shown in Fig. 40.5a. The standard deviation of URE GEO satellites is the greatest, which is mainly caused by the weak geometry and sparse stations. The along-track precision for GEO satellites as C01 and C04 could reach several or even tens of meters, and the precision of clocks are also affected. The precisions of IGSO satellites (C06–C10), with better

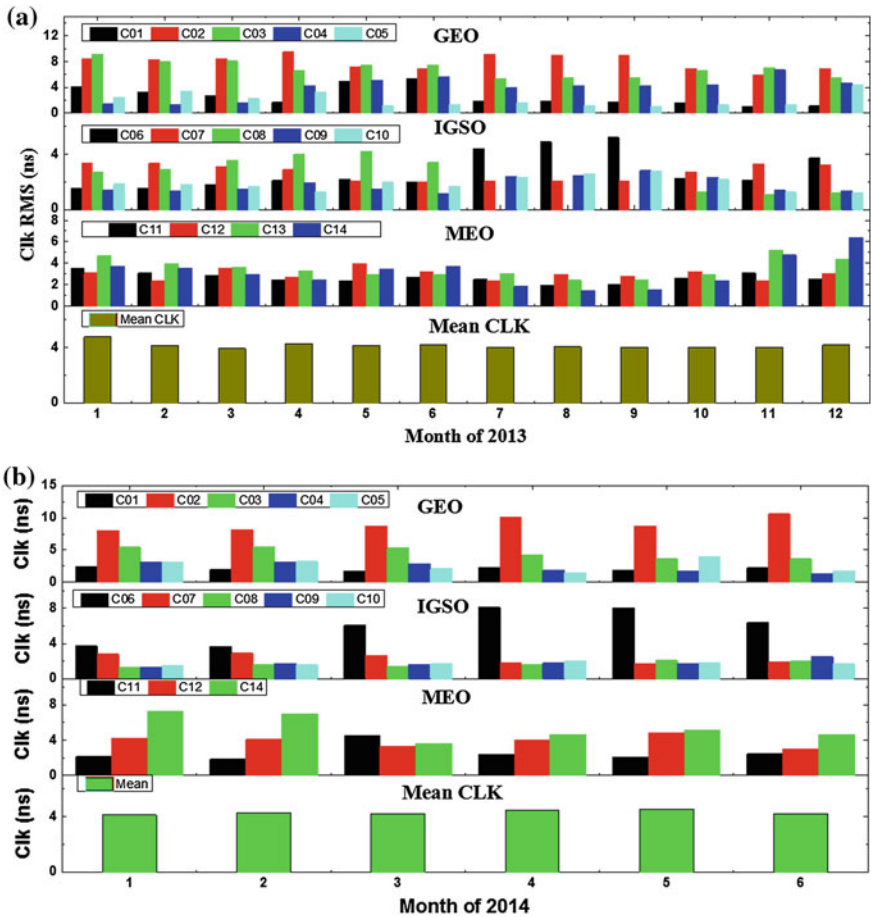


Fig. 40.4 Statistical results of broadcast clocks precisions for BDS satellites (Jan, 2013–Jun, 2014). **a** Broadcast clocks for BDS satellites in 2013. **b** Broadcast clocks for BDS satellites in 2014

geometry, could stay in 2–3 m in along-track and cross track directions, and less than 1 m in radial direction. In addition, the broadcast ephemeris of IGSO satellites update every hour, which helps reduce the extrapolating error and thus improve the URE precision indirectly. However, the MEO satellites are not as fortunate. Although they have equally good or even better observing geometry in Asia-Pacific area, they depend on the extrapolation when wandering outside this region. The longer they are extrapolated, the lower the precision will be. When the abroad part of MEO ephemeris is taken into account, the URE will definitely decrease. This is why the URE of MEO satellite is worse than IGSO satellite in Fig. 40.5. Anyway, the URE precision of MEO satellite, falling in 1.5–1.8 m, is better than GEO satellite.

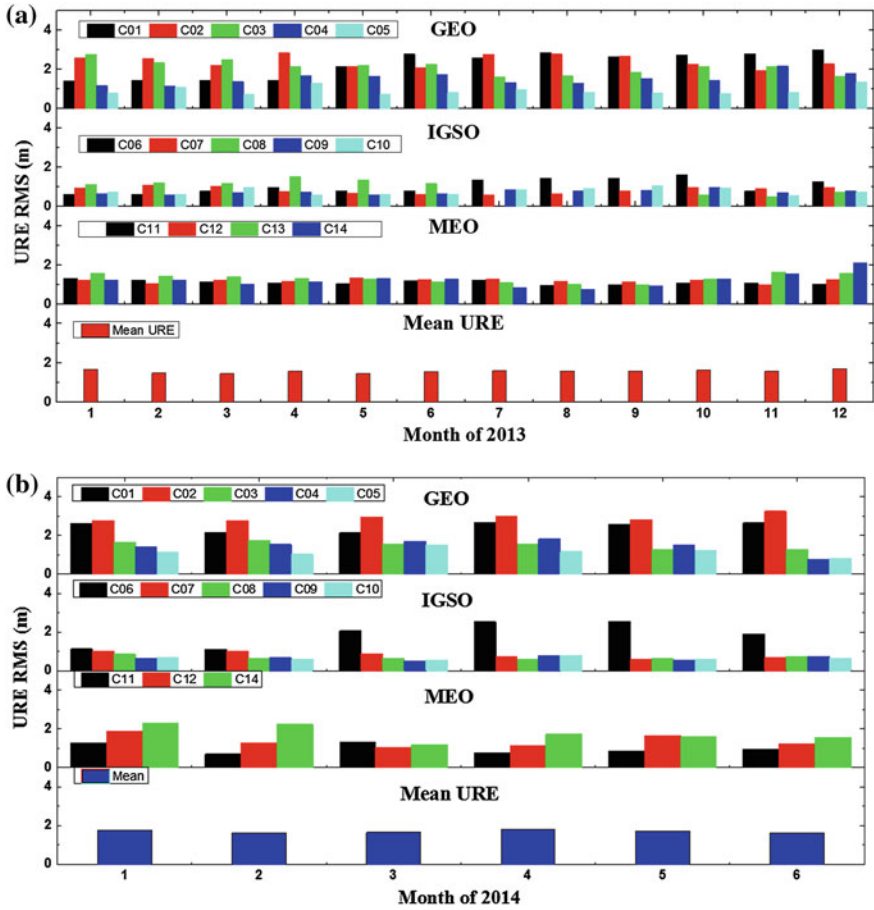


Fig. 40.5 URE precisions for BDS satellites (Jan, 2013–Jun, 2014). **a** URE precision for BDS satellites in 2013. **b** URE precision for BDS satellites in 2014

The general trends of URE in 2014 and 2013 are similar, with an average of 1.8 m. The URE precision of IGSO is the best and GEO the worst. The URE precisions for C02 and C06 are relatively low, due to their bad clocks. Glitches occurred with C13 in 2014, so their UREs are not analyzed here.

40.4.4 Analysis of Positioning Precision with BDS Pseudoranges

To investigate the influence of BDS constellation addition, the time period was divided into three phases, which is shown in Table 40.3. With the number of

Table 40.3 The composition of BDS constellation in different periods

No.	Constellation	Periods
1	3G+4I	2012.01.01–2012.02.06
2	3G+5I	2012.02.07–2012.04.15
3	4G+5I	2012.04.16–2012.06.29
4	4G+5I+2 M	2012.07.01–2012.10.31
5	5G+5I+4 M	2012.11.28–present

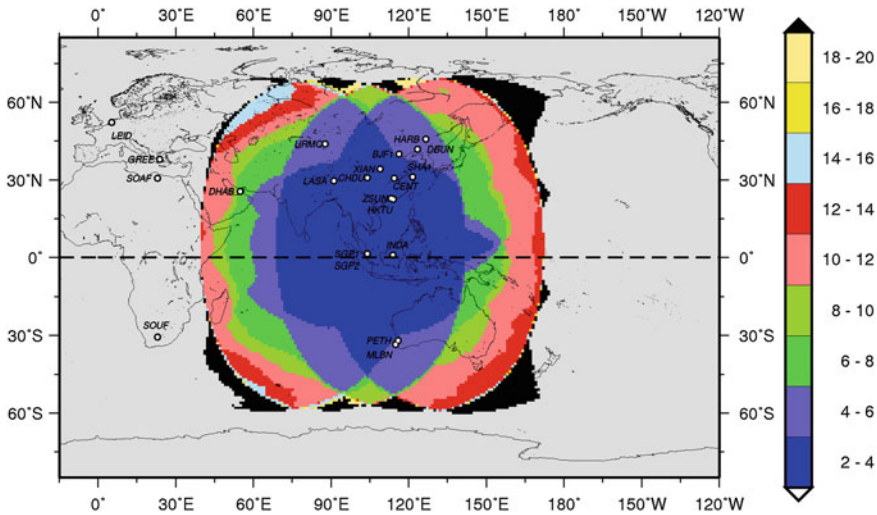


Fig. 40.6 Distribution of PDOP (95 %) for BDS (5GEO+5IGSO+4MEO)

satellites increasing in the year 2011 and 2012, the dilution of precision (DOP) was significantly improved between 75°E and 135°E (see Fig. 40.6), and the PDOP between 30°S and 30°N could reach 2–4 (95 %). When the coverage expanded to the whole Asia-Pacific area, the PDOP is still less than 8. Since the current 14 satellites include GEO, IGSO and MEO ones, the distribution of PDOP in Asia-Pacific area is not even. Three typical stations in the region are selected to analyze the precision of SPP, and the station information is shown in Table 40.4.

Shown in Figs. 40.7, 40.8, 40.9 and 40.10 are the results of SPP with B1I code measurements of BDS. The addition of BDS constellation is of great significance in

Table 40.4 Station information for SPP

Station ID	Observables types	Latitude	Longitude	Receiver types
BJF1	B2I	+40.0	116.3	UNICORE
CHDU	B1I	+30.7	+104.1	UNICORE
SIGP		+1.4	+103.9	UNICORE
PETH		-31.9	+115.8	UNICORE

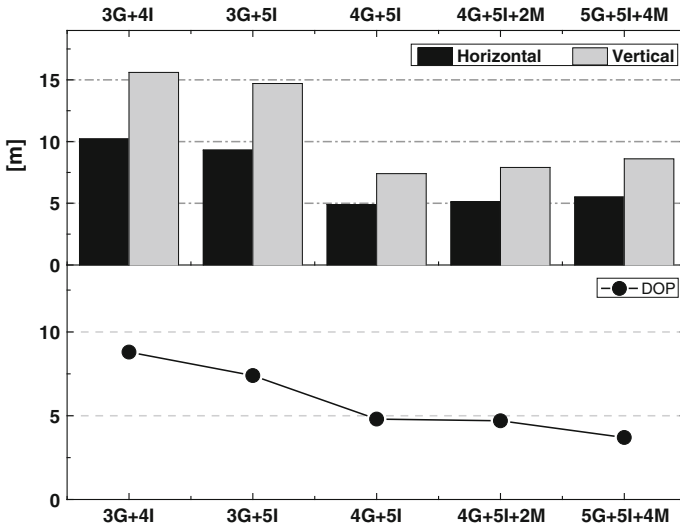


Fig. 40.7 Positioning precision for station BJF1

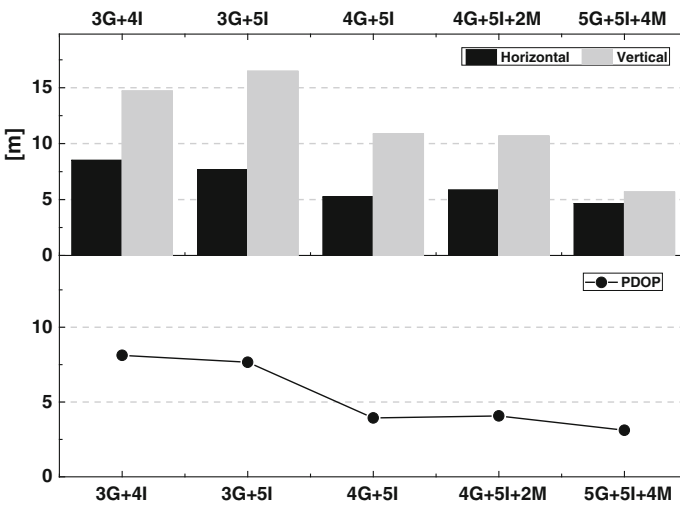


Fig. 40.8 Positioning precision for station CHDU

improving PDOP. When the constellation contained three GEO and five IGSO satellites, the PDOP at the above three stations are greater than 5. The precision of positioning (95 %) with BDS single frequency was about 10 m in horizontal and 15 m in vertical. After the fifth GEO satellite was added, the observing geometry improved significantly. The precision of positioning (95 %) with BDS single frequency was better than 5 m in horizontal and almost 10 m in vertical. When the

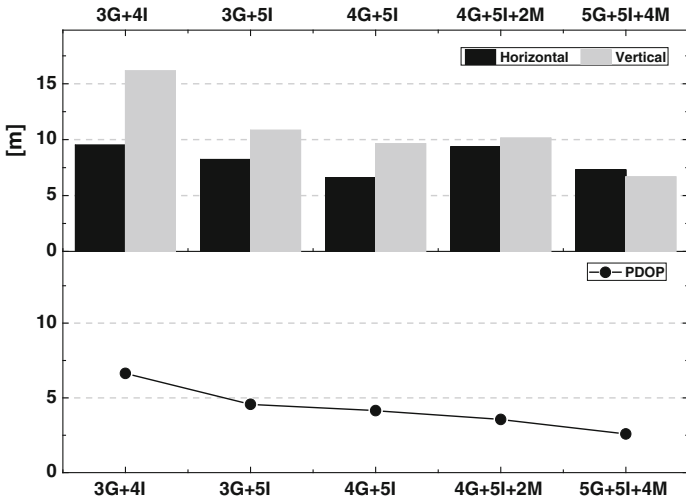


Fig. 40.9 Positioning precision for station SIGP

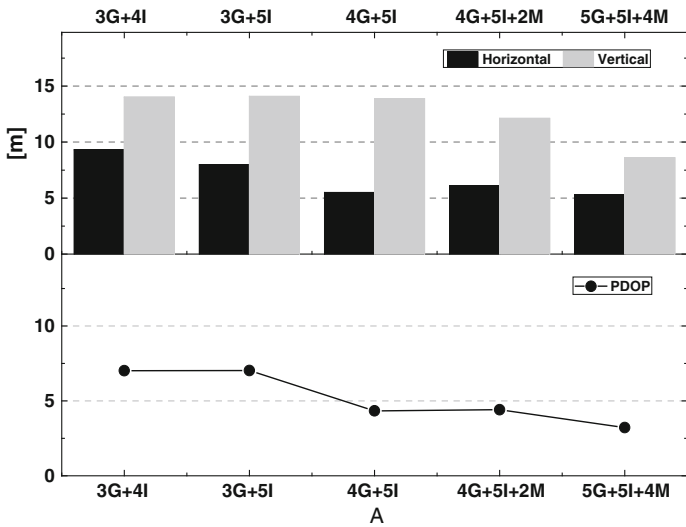


Fig. 40.10 Positioning precision for station PETH

first two MEO satellites were added, no significant improvement was seen in the observing geometry and positioning precision. After another two MEO satellites were added in Nov, 2012, the precision of SPP was improved significantly to better than 6 m (95 %) in horizontal and better than 10 m (95 %) in vertical. According the above results, the precision of SPP with BDS single-frequency measurements can reach 10 m both in horizontal and vertical.

40.5 Conclusions

Some conclusion can be obtained based on the above statistics for the signal in space error and navigation performance on civil frequency B1I:

- (1) There are some small differences among GEO, IGSO and MEO satellites prediction position error. Generally, the position precision is about 0.5–0.8 m for radial direction and better than 2.0 m in normal direction, while for cross direction, the GEO satellites is larger than 5 m in most cases, especially for G01 (the precision is about 10–20 m). The precision of IGSO and MEO satellite orbits is at the same level and the average RMS is about 2.0–3.0 m.
- (2) For BDS satellites broadcast clock error, the mean RMS value of all satellites is about 2–6 ns and the clock performance are stable in 2013. Some differences can be found in three different types of satellites: GEO satellites broadcast clock error is worse than IGSO and MEO satellites, with the RMS about 4–8 ns; it is about 2–3 ns for IGSO satellite; since some MEO broadcast ephemeris AOD are larger than 1 h, the precision of MEO satellites clock is at the level of 4 ns, not as good as IGSO.
- (3) The SISA (signal in space accuracy) of BDS GEO/IGSO/MEO is about 1.5–2.0 m. The same case holds for position and clock precision. The GEO satellites have the worst value, i.e. about 1.5–2.0 m, while it is 1.0 and 1.7 m for IGSO and MEO satellites, respectively.
- (4) With the optimization of BDS constellation structure, i.e. from 3 GEO and 4 IGSO satellites to 5 GEO, 5 IGSO and 4 MEO satellites, BDS navigation performance is improved significantly. The horizontal positioning accuracy (95 %) is improved from 10 to 6 m, and 15–10 m for vertical direction. The navigation results of typical stations in service region show that BDS can provide 10 m navigation service in both horizontal and vertical direction in Asia region.

Acknowledgments This work was partially sponsored by Special Foundation for National Excellent Ph.D Thesis Author (Grant No. 20201162) and partially sponsored by National Natural Science Foundation of China (Grant No. 41304024). The authors would like to thank the editor in chief and the anonymous reviewers for their valuable comments and improvements to this manuscript.

References

1. Heng L, Gao GX, Walter T, Enge P (2010) GPS signal-in-space anomalies in the last decade: data mining of 400,000,000 GPS navigation messages. In: Proceedings of the 23rd international technical meeting of the satellite division of the institute of navigation (ION GNSS 2010), Portland, pp 3115–3122
2. Zhao Q, Guo J, Li M, Qu L, Hu Z, Shi C, Liu J (2013) Initial results of precise orbit and clock determination for COMPASS navigation satellite system. *J Geodesy* 87:478–486. doi:10.1007/s00190-013-0622-7

3. Steigenberger P, Hugentobler U, Montenbruck O, Hauschild A (2011) Precise orbit determination of GIOVE-B based on the CONGO network. *J Geodesy* 85:357–365
4. Zhao Q, Guo J, Li M, Qu L, Hu Z, Shi C, Liu J (2013) Initial results of precise orbit and clock determination for COMPASS navigation satellite system. *J Geodesy* 87:475–486
5. Heng L, Gao GX, Walter T, Enge P (2010) GPS ephemeris error screening and results for 2006–2009. In: Proceedings of the 2010 international technical meeting of the institute of navigation (ION ITM 2010), Jan 2010, pp 1014–1022
6. Warren DLM, Raquet JF (2003) Broadcast versus precise GPS ephemerides: a historical perspective. *GPS Solut* 7:151–156
7. CSNO (China Satellite Navigation Office) (2012) BeiDou navigation satellite system signal In space interface control document (Open service signal BII (Version 1.0)). C.S.N. Office, Beijing
8. Zumbege J, Bertiger W (1996) Ephemeris and clock navigation message accuracy. In: Parkinson B, Spilker J, Axelrad P, Enge P (eds) *Global positioning system: theory and applications*. American Institute of Aeronautics and Astronautics, Washington, DC, pp 585–699
9. Yang Y (2007) National 2000' GPS control network of China. *Prog Nat Sci* 17(8):983–987
10. Yang Y (2009) Chinese geodetic coordinate system 2000. *Prog Nat Sci* 17:983–987
11. US. DoD (2008) *Global positioning system standard positioning service performance standard*. Defense Pentagon, Washington, DC
12. Hu Z (2013) *BeiDou navigation satellite system performance assessment theory and experimental verification*. Wuhan University, Wuhan

Chapter 41

Design and Implementation of Distributed Simulation Testbed for GNSS Experimentation

Long Yang, Yufei Yang and Jinping Chen

Abstract Global navigation satellite system (GNSS) is a complex aeronautic project of great size. There are several steps in the construction process including system design, equipment development and system test procedure. The system design output such as system interface, operation flow and key performance will be validated with simulation experiment in the system design procedure. The real system interface implementation and key performance will be tested in the equipment development and system test procedure. A distributed simulation testbed is provided for the simulation experiment and system test. The simulation testbed structure, key technology, system implementation and applications are described in the paper.

Keywords Global navigation satellite system · Distributed simulation testbed · Simulation experiment · System test

41.1 Introduction

Global navigation satellite system (GNSS) is a complex aeronautic project of great size which consists of satellite constellation, ground segment and user receivers [1]. The satellite constellation generally contains about 30 medium to high orbit satellites which broadcast navigation signal to ground continuously. The ground segment generally contains monitor stations, uploading stations and master control stations. The monitor stations are responsible for receiving the satellite navigation signal, generating pseudorange and carrier phase measurements and sending these measurements to master control stations. The master control station then make data processing based on these measurements, including precise orbit determination, satellite clock error determination, ionosphere delay estimation and integrity

L. Yang (✉) · Y. Yang · J. Chen
Beijing Satellite Navigation Center, Beijing 100094, China
e-mail: 18911286031@189.cn

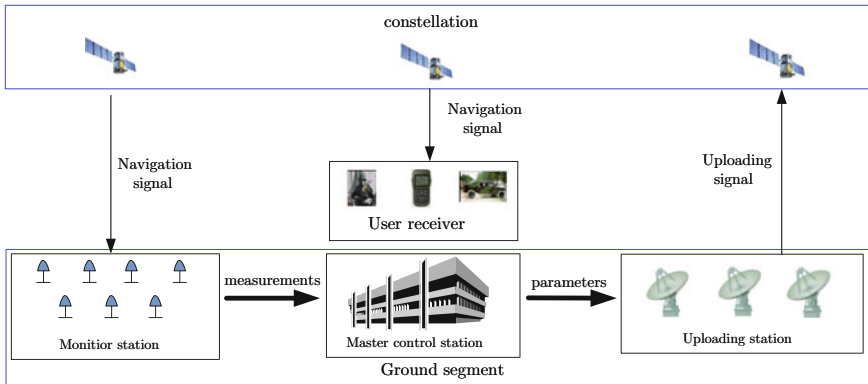


Fig. 41.1 The whole process of GNSS operation

parameter processing. The precise orbit, satellite clock error, ionosphere delay parameters and integrity parameters are then send to the uploading stations via communication network and uploaded to the satellite constellation by means of uploading radio signal. The satellites modulate these parameters on their navigation signal and broadcast to the user receivers. User receivers accomplish the positioning task with these parameters and pseudorange measurements. The whole process of GNSS operation is shown in Fig. 41.1.

From the GPS, GLONASS and Galileo systems experience it can be seen that the construction of satellite navigation system will be a long-term process. There are several stages in the process including system design, equipment development and system test. It usually lasts for decades. In order to ensure the success of the system construction the system design output such as system interface, operation flow and key performance should be validated with simulation experiment in the system design stage. The system interface, operation flow and key performance should also be tested in the equipment development and system test stage with test tools.

A distributed simulation testbed is developed to meet the GNSS simulation experiment and test need. With this platform the GNSS experiment can be accomplished in the system design stage and the system test can also be accomplished in the equipment development and system test stage. It is a technology base for the construction GNSS.

The testbed structure, key technology, implementation and applications of the testbed are provided in the paper. The conclusion is also presented lastly.

41.2 Testbed Structure

The simulation experiment testbed is implemented with software based on the distributed simulation platform. The interface between GNSS components, data stream flow and management control function can be experiment validated and

tested. The key performance of the system can also be experiment validated and tested.

41.2.1 Block Diagram

The testbed block diagram is shown in Fig. 41.2. It consists of the simulators of the GNSS components, the experiment management control subsystem and the test and validation subsystem. The simulators of the GNSS component include constellation simulator, monitor station simulator, uploading station simulator, master control station simulator. Every simulator implements the completed input and output interface and can accomplish the key processing function. The testbed can simulate the operation and processing of the real GNSS system. All the simulator and subsystem run on the same simulation platform.

The experiment management control subsystem include task management module, simulation model management module and simulation data management module. The test and validation subsystem include interface test and validation module and performance test and validation module.

Every simulator subsystem includes input and output module, display and human-computer interaction module. The constellation simulator is also includes satellite orbit generation module, Atmospheric delay simulation module. The monitor station simulator includes measurement generation module. The uploading station simulator includes measurement generation module, uploading simulation module.

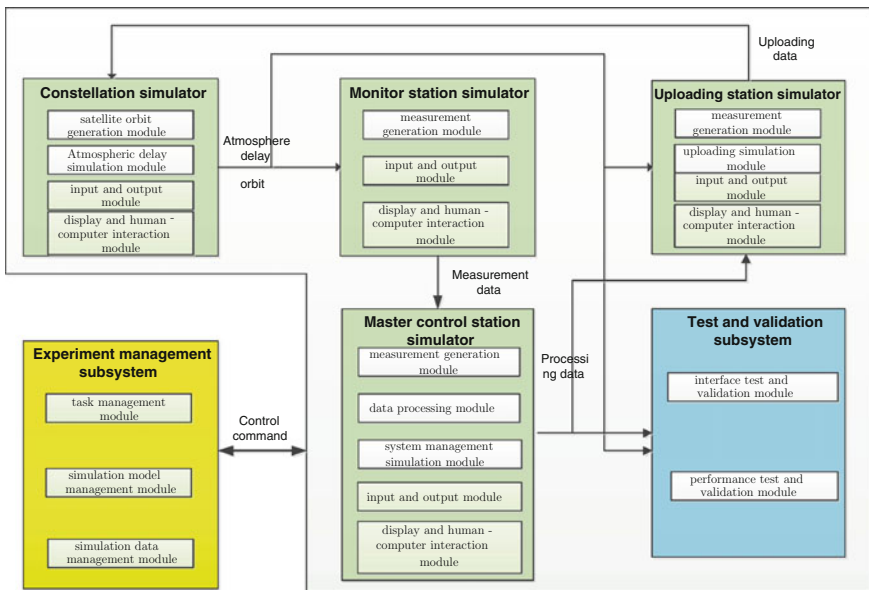


Fig. 41.2 Block diagram of the testbed

module. The master control station simulator includes measurement generation module, data processing module, system management simulation module.

41.2.2 Logical Structure

The testbed employs the layered logical structure which include basic support layer, general service layer and simulate application layer.

The basic support layer is composed of hardware and basic software. The hardware include workstation, network and storage device etc. the basic software include operating software, database software etc. The basic support layer provide the running environment for the testbed.

The general service layer is composed of several dynamic link library including network data transfer software module, time management software module and data formation software module.

The simulate application layer is composed of several executable program and dynamic link library including experiment management control program, simulation calculation library, test and validation program, GNSS component simulator program. And the GNSS component simulator program is built on the simulation calculation library.

The testbed logical structure is shown in Fig. 41.3.

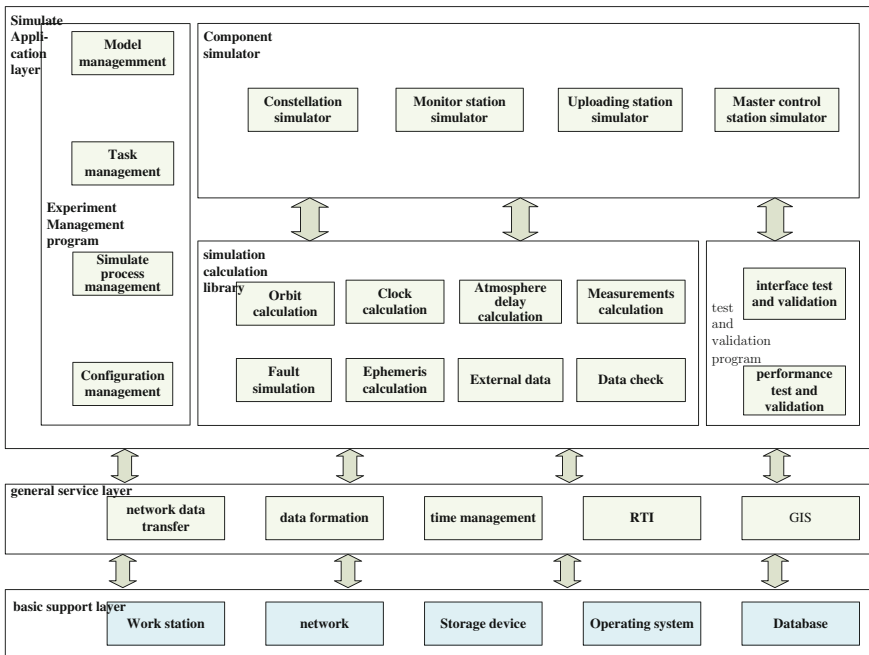


Fig. 41.3 The logical structure of the testbed

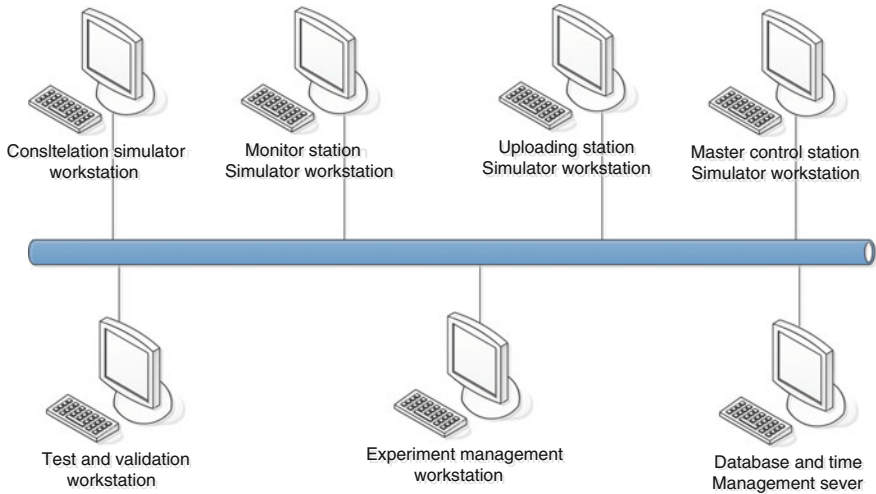


Fig. 41.4 The physical components of the testbed

41.2.3 Physical Components

The testbed physical components are deployed on independent computer which is shown in Fig. 41.4.

The testbed physical equipment is composed of servers, workstations, network and storage device. The software which requires high performance computation is deployed on servers such as database and time management. The GNSS component simulators, experiment management control program and test and validation program are deployed on the workstation. The detailed software deployment scheme is shown in Fig. 41.5.

41.3 Key Technologies

There are many key technologies in the development of the testbed. The navigation satellite orbit modeling and simulation technology, precise global ionosphere delay simulation technology and flexible system interface customization technology is described in the following chapters.

41.3.1 Navigation Satellite Orbit Modelling and Simulation

The navigation satellite orbit modeling and simulation technology is mainly used in the constellation simulator which generates the position, velocity of the navigation satellite.

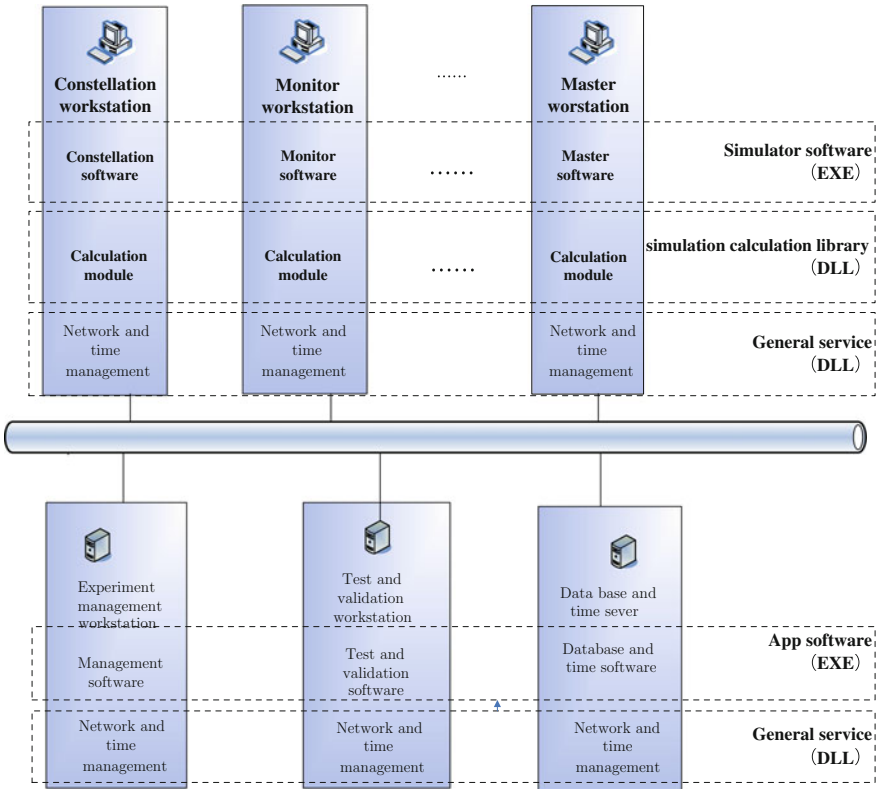


Fig. 41.5 Software deployment of the testbed

Among all the forces acting on the satellite the earth gravity is the main part [2, 3]. If the earth gravity is 1 the other forces are less than 10^{-5} . Among all the perturbations the earth albedo radiation perturbation, the earth rotation deformation perturbation and attitude control force are lesser. Not all the forces acting on the satellite shall be considered in the orbit simulation.

The earth nonspherical perturbation, lunisolar gravitational perturbation, solar radiation perturbation, air drag perturbation, tidal perturbation, relativistic perturbation are calculated for the GEO, IGSO, MEO and LEO satellites. These results are compared to determine which perturbation will be considered in the navigation satellite orbit simulation.

Let $\varepsilon = F_\varepsilon/F_0$, in which F_ε is one of the perturbations and F_0 is the earth gravity. Table 41.1 presents the GEO, IGSO, MEO and LEO satellite perturbations.

If the perturbation less than 10^{-9} will not be considered only the earth non spherical perturbation, lunisolar gravitational perturbation and solar radiation perturbation will be computed in the satellite orbit simulation according to the Table 41.1.

Table 41.1 Perturbations of several typical orbits

Perturbations	GEO	IGSO	MEO
Earth non spherical	3.68×10^{-5}	4.0×10^{-5}	9.27×10^{-5}
Solar gravitation	1.05×10^{-6}	7.42×10^{-6}	2.96×10^{-6}
Lunar gravitation	2.20×10^{-5}	2.10×10^{-5}	5.73×10^{-5}
Solar radiation	4.49×10^{-8}	4.49×10^{-8}	1.93×10^{-8}
Tidal	3.19×10^{-10}	1.69×10^{-10}	4.01×10^{-10}
Relativistic	3.17×10^{-10}	3.17×10^{-10}	4.82×10^{-10}
Air drag	5.04×10^{-21}	5.42×10^{-15}	7.20×10^{-15}

41.3.2 Precise Global Ionosphere Delay Simulation

Currently, there are many global ionospheric models such as the GPS Klobuchar model, Galileo NeQuick model, international IRI model, and the Europe CODE-GIM model. The accuracy of these models is vary [4–6].

The Klobuchar model is firstly presented by American researcher in 1976 and is adopted in GPS. It is assumed that all the electrons are distributed in a thin layer 350 km high above the ground in this model. The characteristic of the day variety of ionosphere delay is expressed as cosine function. The parameters of the model can represent the variety of amplitude and phase. It is mean delay of ionosphere in time.

The NeQuick model is a half experience ionosphere delay model. It is presented by several Europe research institutions. It is a time varied and three dimension model of ionosphere electron density. The total electrons from the satellite to ground station in any time can be computed with this model. A method is presented for describing the ionosphere delay in this model.

The IRI model is the most effective half experience ionosphere delay model. Several atmosphere parameter models are adopted in this model. The solar activity and the monthly average of the geomagnetic direction parameter AP are also considered. The monthly average of electron density and temperature, ion temperature and composition at any point and in any time can be computed with this model.

The CODE-GIM model is expressed as spherical harmonic function. The global TEC grid is generated with the everyday GIM data. The ionosphere delay can be computed with the TEC grid.

A simulation experiment has been done for the Klobuchar model, NeQuick model, IRI model and CODE-GIM model. The accuracy is that Klobuchar 60 %, Nequiuk 70 %, IRI 80 % and CODE-GIM better than 80 %. Table 41.2 presents the detailed results.

41.3.3 Flexible System Interface Customization

The interface between the components of GNSS is very complex and will be upgraded with the system development. The flexible system interface customization

Table 41.2 Accuracy of the ionospheric models

Ionosphere model	Accuracy (%)
Klobuchar	60
Nequiuk	70
IRI	80
CODE-GIM	80

technology can simplify the software upgrade work due to system interface modification [7, 8].

The flexible system interface customization technology adopts the XSD (XML Schema Definition) to describe the interface data format. The interface software will pack or unpack the data stream according to the definition of XSD file. Whenever the data field modification is made only the XSD file is modified. The software remains unchanged. The correctness of the system interface definition can also be validated with the XSD file.

41.4 Implementation and Applications

41.4.1 Implementation

The hardware of the testbed have been constructed and the software have been tested according to the system structure. The constellation simulator, monitor station simulator, uploading station simulator and master control station simulator are shown in Figs. 41.6, 41.7, 41.8 and 41.9.

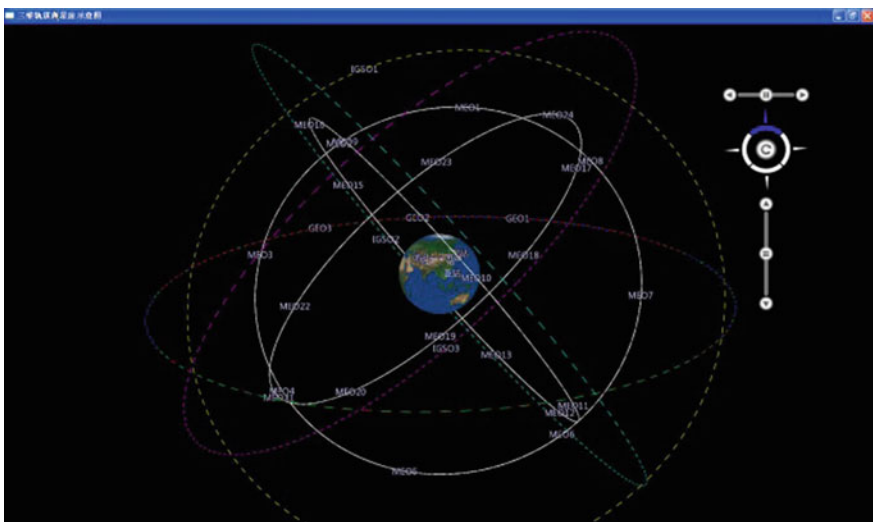


Fig. 41.6 Constellation simulator

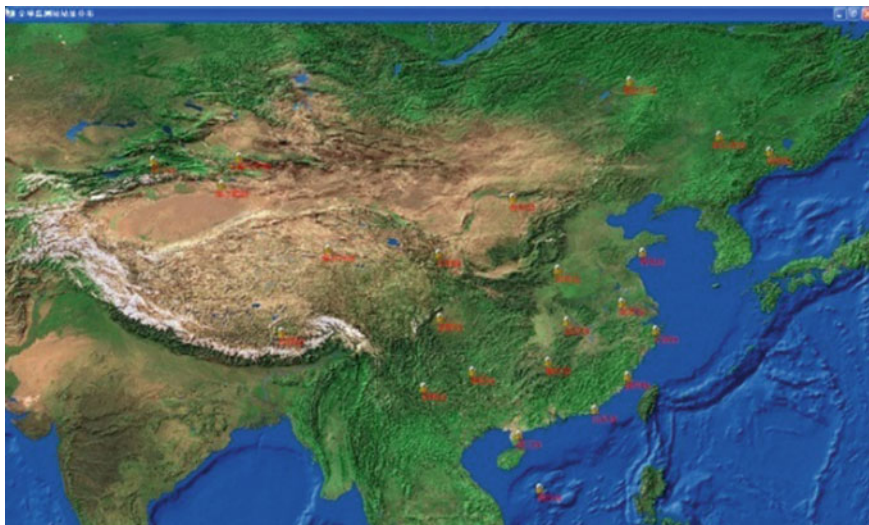


Fig. 41.7 Monitor station simulator

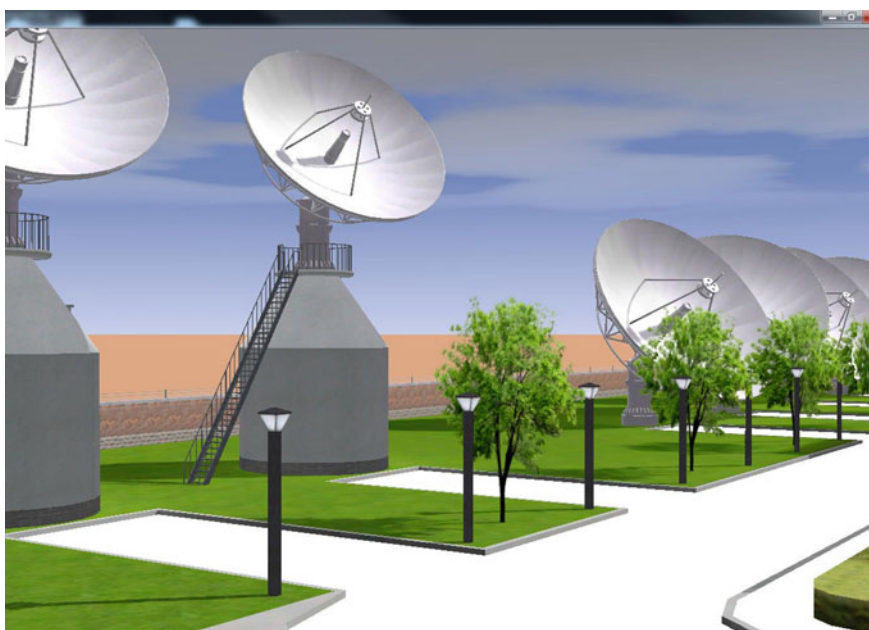


Fig. 41.8 Uploading station simulator

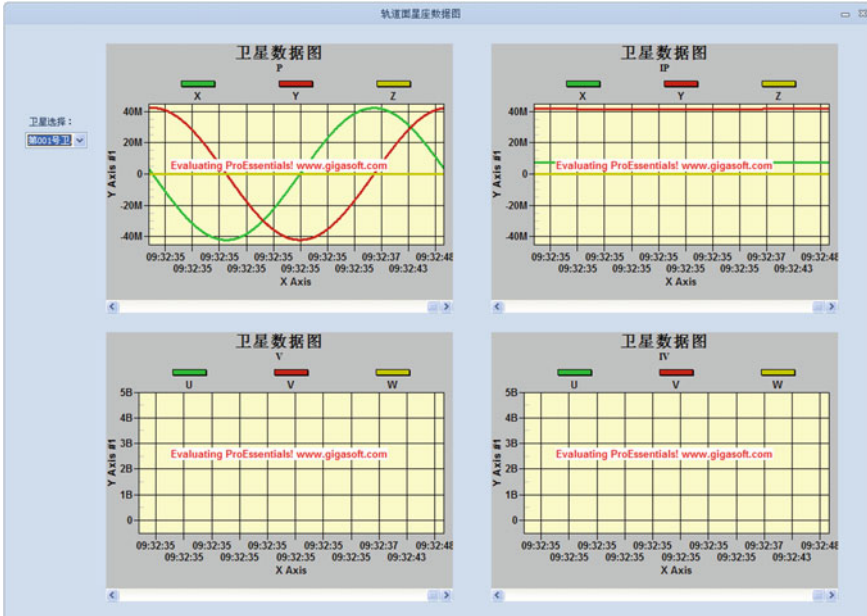


Fig. 41.9 Master control station simulator

41.4.2 Applications

The testbed has a wide application prospect. The validation experiment of constellation design, system interface design, system data stream design and system key performance have been done on this testbed. The test of satellite interface, monitor station interface and performance, uploading station interface and performance, master control station interface and performance have been done with this testbed. The experiment and test results are close to the real system.

41.5 Conclusion

The risk of constructing GNSS is large. A lot of simulation experiment is necessary in the design stage. In order to ensure the quality of the system a full debugging and test process is also necessary in equipment development and installation stage. The testbed presented in this paper can meet the requirements of this two aspects. It can support the development of the GNSS in a long period.

References

1. Tan S (2010) Satellite navigation and position engineering. National Defense Industry Press, Beijing
2. Zhou J (2010) Orbit mechanics. Science Press, Beijing
3. Fang X (2010) Research of satellite orbit model and simulation technology. Ph.D. thesis, University of Electronic Science and Technology, Chengdu, China
4. Zhang H (2011) Establishment and analysis of regional ionosphere model. Ph.D. thesis, The PLA Information Engineering University, Zhengzhou, China
5. Zhang H (2013) The influence of two ionosphere model to satellite navigation precision. *J Navig Position* 1(3):43–47
6. Wu X, Hu X et al (2013) Evaluation of COMPASS ionospheric model in GNSS positioning. *Adv Space Res* 45(3):182–193
7. Su C (2012) The general data interface test tools based on XML. Ordnance Industry Automation, Mianyang
8. Zhu T (2013) The design and implementation of aviation service administration system based on SOA architecture. Ph.D. thesis, Yunnan University, Kunming, China

Chapter 42

High Precision and Difference Measurement of Inter-element Amplitude and Phase Bias Errors Based on Channel Multiplexing

Ke Zhang, Huaming Chen, Xiangwei Zhu and Guangfu Sun

Abstract Modern satellite navigation system receiver use adaptive antenna array to suppress the RF interference and mitigate multipath signals in different directions from signals of interest. The inter-element amplitude and phase bias errors can cause performance degradation in the receiver. This paper presents a measurement with high precision in anechoic chamber, where channel multiplexing, difference measuring is used to decrease bias error caused by too many measuring data. And calibrating equation is put forward based on the three-dimensional rotating turntable, so that inter-element wave-way difference can be removed. Analyses show that the measuring precision can be increased by nearly double with low complexity and high efficiency. Then an automatic measuring system is designed, and data is measured by a multichannel vector network analyzer. A four elements array are measured, comparison between the measuring and simulating results demonstrates that the phase error is less than 8° while the efficiency is improved by nearly 4 times to conventional measurement.

Keywords Antenna array · Amplitude and phase bias error · Difference measuring · Wave-way difference calibration · Channel multiplexing

42.1 Introduction

With the continuous development of modern satellite navigation system, navigation system plays a very important role in the national defense and economic field. However, the navigation receiver often suffer from intentionally or unintentionally RF interference [1]. In order to improve anti-interference ability, adaptive antenna array technology was put forward and even became standard device of

K. Zhang · H. Chen · X. Zhu · G. Sun (✉)
National University of Defense Technology, Deya Road 109, Changsha 410073, China
e-mail: sunguangfu_nnc@163.com

anti-jamming receiver. In recent years, the antenna array also began to emerge in high-precision navigation applications, to be used for monitoring and suppression multipath signals [2].

Adaptive antenna array tend to form a null in direction of interference, while normally receives signal in other direction by the way of pattern control [1]. As the size of receiver is limited, edge effect and mutual coupling between array elements get worse, so that there is amplitude and phase errors between array elements in spatial range. In addition, material and process error of antenna has further exacerbated the errors between the array elements. The literature [3] pointed out that performance of the element position and mutual coupling caused the direction-finding antenna system decreased or even failure; He in [4] analyzed the effect of channel error including antennas on the algorithm for antenna system robustness, convergence speed. Therefore, the high accuracy measurement and calibration of amplitude and phase errors is very important to enhance overall performance of antenna array. So O'Brien and Gupta [5] and Kim et al. [9] had studied the calibration of adaptive antenna array induced bias errors.

Measurement of antenna array can be divided into numerical simulation, outdoor measurement and the anechoic chamber measurements. The literatures [6, 7] had researched into the amplitude and phase pattern based on different kinds of antenna models. Otherwise many microwave simulation software can be used to accomplish this task, such as HFSS and CST. The outdoor measurement required the differential navigation receiver platform with high precision [8, 9], the results also include RF channel errors. Moreover, it is limited by the time synchronization accuracy, the baseline length between antenna array elements and some other factors. Anechoic chamber measurement is stable and all-weather [11]. Reference [10] used anechoic chamber to measure the phase center of the antenna accurately, but only for a single antenna.

Numerical value of Antenna array amplitude and phase error is relative, so it does not require the absolute value of the array element amplitude and phase characteristics by precise measurement. The traditional measurement in anechoic chamber exist more drawbacks like too many error sources and too large the amount of measuring data. This paper presents the application of multiple channels multiplexing method in transmission segment to reduce the error source, and using differential measurement method in the receiving segment to reduce the amount of measuring data. And then the wave path difference between array elements caused by the three-dimensional rotating turntable are eliminate through the calibration equations. Thus, a high-precision measurement of amplitude and phase error of antenna elements was achieved. At last, a fast automatic measurement system based on the presented method are designed.

42.2 Inter-element Amplitude and Phase Bias Errors

Adaptive antenna array technology can be divided into adaptive spatial array and space-time adaptive array. Space-time adaptive array which increased adaptive time domain filter, providing more freedom in signal processing when comparing to spatial array. The block diagram of a space-time adaptive array showed in Fig. 42.1.

The space-time adaptive array consists of M antenna elements. The signals received by each antenna element is down-converted to base band by low noise amplifier, filters, mixers, etc. and then multiplied by a set of P weights. Finally, signals from various taps of all antenna elements are summed to form the adaptive array output.

In Fig. 42.1, ΔT is the inter sample period. Let $H_{ai}(f, \theta, \varphi)$ be the in situ response of the i th antenna element at frequency f and in direction (θ, φ) and $H_i(f)$ be the response of the front end electronics following the i th antenna element. Then the frequency response of the adaptive antenna system in a satellite signal direction (θ, φ) can be written as

$$H(f, \theta, \varphi) = \sum_{i=1}^M H_i(f)H_{ai}(f, \theta, \varphi) \sum_{l=1}^P w_{il}e^{-j2\pi f(n-1)\Delta T} \tag{42.1}$$

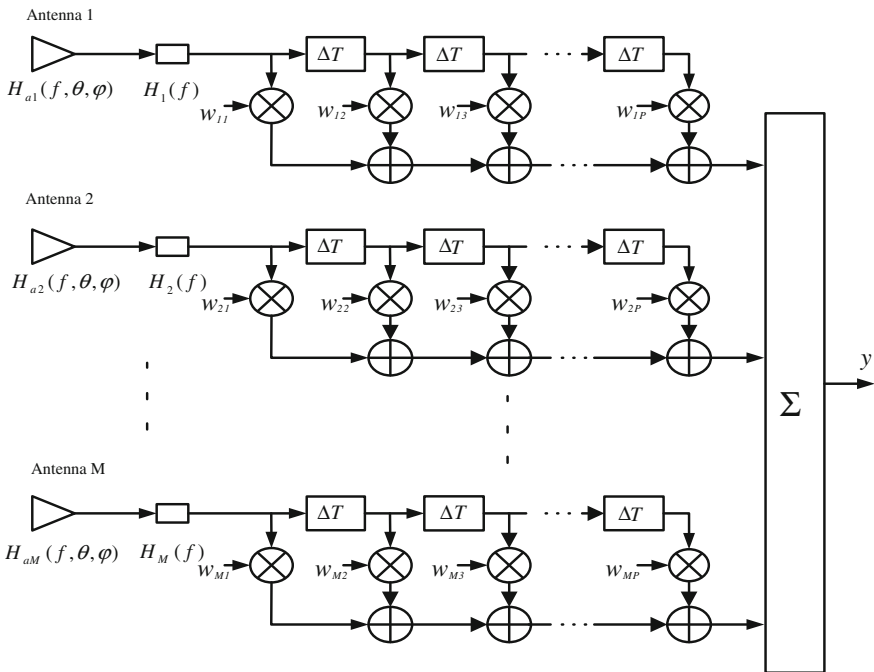


Fig. 42.1 The block diagram of a space-time adaptive array

According to formula (42.1), it can degrade to the expression of adaptive spatial array when $p = 1$. Because wired measurement is mature technology, so that all the channels $H_i(f)$ can be equalized. And the weights depends on different adaptive algorithms. We simplify formula (42.1) as follows:

$$H(f, \theta, \varphi) = H_{a1}(f, \theta, \varphi) \sum_{i=1}^M H_i^*(f) \Delta H_{ai}(f, \theta, \varphi) \quad (42.2)$$

where $H_i^*(f)$ has no relationship with the incoming signal direction. Then define the inter-element amplitude and phase bias errors as the following formula, and assume the first element be the reference.

$$\Delta H_{ai}(f, \theta, \varphi) = \frac{H_{ai}(f, \theta, \varphi)}{H_{a1}(f, \theta, \varphi)}, \quad i = 1, 2, \dots, M \quad (42.3)$$

Obviously, effects of radiation characteristics of the antenna array on null and beam forming direction is mainly cause by the inter-element amplitude and phase bias errors once the adaptive algorithms was chosed. Considering that the inter-element amplitude and phase bias errors is minuteness while the effects is large, it is necessary to improve the measuring precision.

42.3 Principle of High Precision Measurement

42.3.1 Measuring Equation of Antennas Array

When measuring the radiation characteristics of the antenna array in anechoic chamber, each channel is divided into three parts: the transmitting segment, free space segment and the receiving segment. Firstly, in the transmitting segment, a single carrier signal X_s was generated by vector signal generator, transmitted by the RF cable to a transmitting antenna, and transmitting antennas had in situ response denoted by H_s . Free space segment caused a free space loss L_{ci} of signal Thirdly in the receiver, channel included receiving antenna in situ response H_{ai} , receiving RF cable loss L_{ri} and received signal X_{pi} in the receiving device. General measuring equation for the channel is:

$$H_{ai} = X_{pi} - X_{si} - H_{si} + L_{ci} + L_{ri}, \quad i = 1, 2, \dots, M \quad (42.4)$$

Then we enumerate the error sources as follows:

- σ_s transmitting signal precision, comprises transmitting signal precision from the signal generator and transmission cable loss precision;
- σ_c free space loss precision, comprises distance measurement precision, the antenna mounting precision and the turntable rotation precision;

σ_r receiving signal precision, comprises receiving cable loss precision and measuring precision of the receiving device.

While using conventional measurement to measure the inter-element amplitude and phase bias errors, a complete measurement of each antenna in all the radiation direction need to figure out firstly, namely that the need to measure all the data in formula (42.4). Then the results can be get by minus one by another. Because of serial measurements, the precision is $\sqrt{2^*(\sigma_s^2 + \sigma_c^2 + \sigma_r^2)}$. When measuring a single antenna, Zhang in [10] figure out that σ_c was larger than σ_s and σ_r .

42.3.2 Difference Measurement Based on Channel Multiplexing

According to the analysis of formula (42.2), the antenna array pay more attention on bias error measuring precision in one direction, but for different directions measuring precision is loose. In order to reduce the amount of error sources and measuring data, the measuring equation of the antenna array can be optimized as follows:

- Use the channel multiplexing method, the antenna array shared the transmitting signal X_s , the transmitting antenna H_s and free space segment L_c to achieve parallel measurements. Compared to the traditional method, it reduce the two error sources and three sets of measurement data;
- Receiving channel differential measurements to eliminate errors of equal amounts appearing in the measurement process after the channel multiplexing, while reducing the amount of measured intermediate. The residual difference of free space is the wave-way difference relative to the reference array elements, only related to element spacing and the incoming wave directions, and it can be calibrated.

Set the first element to be the reference, the new equation is

$$\begin{bmatrix} \Delta H_{a21} \\ \Delta H_{a31} \\ \vdots \\ \Delta H_{aM1} \end{bmatrix} = \begin{bmatrix} \Delta X_{p21} \\ \Delta X_{p31} \\ \vdots \\ \Delta X_{pM1} \end{bmatrix} - \begin{bmatrix} \Delta L_{c21} \\ \Delta L_{c31} \\ \vdots \\ \Delta L_{cM1} \end{bmatrix} + \begin{bmatrix} L_{r2} \\ L_{r3} \\ \vdots \\ L_{rM} \end{bmatrix} - L_{r1} \begin{bmatrix} 1 \\ 1 \\ \vdots \\ 1 \end{bmatrix} \quad (42.5)$$

In the followed formula, the amplitude and phase bias errors caused by wave-way difference is $\Delta \mathbf{L}_c = [\Delta L_{c21} \quad \Delta L_{c31} \quad \cdots \quad \Delta L_{cM1}]^T$, and the channel differential results by receiving device is $\Delta \mathbf{X}_p = [\Delta X_{p21} \quad \Delta X_{p31} \quad \cdots \quad \Delta X_{pM1}]^T$, then the inter-element amplitude and phase bias errors we have to measure is $\Delta \mathbf{H}_a = [\Delta H_{a21} \quad \Delta H_{a31} \quad \cdots \quad \Delta H_{aM1}]^T$.

According to difference measurement based on channel multiplexing, measuring data only comprises ΔX_p and the receiving cable loss L_r , so the measuring precision is $\sqrt{2\sigma_r^2 + \sigma_c^2}$. When the wave-way difference ΔL_c is calibrated, σ_c can be lower. Assume that $\sigma_c \gg \sigma_r$, the measuring precision can be improved by nearly double when compared to conventional measurement.

42.3.3 Calibrating Inter-element Wave Path Difference Caused by Rotating Turntable

Figure 42.2 showed the relationship between incident wave and measured antenna array plane. When incident wave was not perpendicular to the array plane, the transmission distance of the array element was different which caused inter-element wave path difference between each other. In this study, assume that the phase center of element shared the same bias to the geometric center.

Solving the wave path difference was mainly based on the transformation between coordinates as shown in Fig. 42.3.

The origin O is located in the turntable rotation axis, Z axis was formed by pointing emission antenna geometric center to turntable axis, axis X was vertical to ground and upward, which constitutes the fixed right-handed coordinate XYZ in anechoic chamber. When the turntable rotated around the X axis which namely means that change the elevation angle in the condition of constant azimuth angle, the formation of elevation angle rotation coordinates $X_r^*Y_r^*Z_r^*$ was done, of which the origin and X_r^* axis was the same with the origin and X axis of XYZ coordinate, Z_r^* axis was vertical to the measured antenna array plane. Based on it, when the turntable rotated around Z_r^* axis, the azimuth angle rotating coordinates $X_rY_rZ_r$ was constituted. Both $X_r^*Y_r^*Z_r^*$ and $X_rY_rZ_r$ coordinate were fixed relative to the measured antenna array, and the initial state was superposed to XYZ .

Assumed that the coordinate of antenna array element i in the $X_rY_rZ_r$ coordinate was (x_{ir}, y_{ir}, z_{ir}) , so in XYZ coordinate the coordinate (x_i, y_i, z_i) is

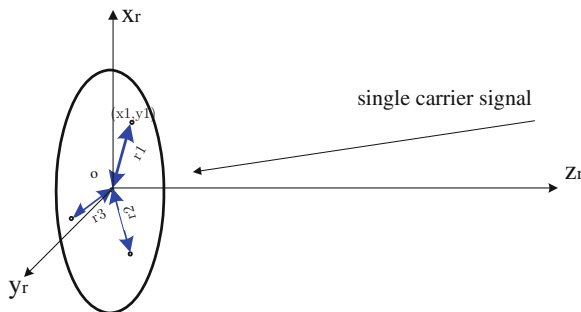


Fig. 42.2 The incoming wave direction relative to measured antenna array

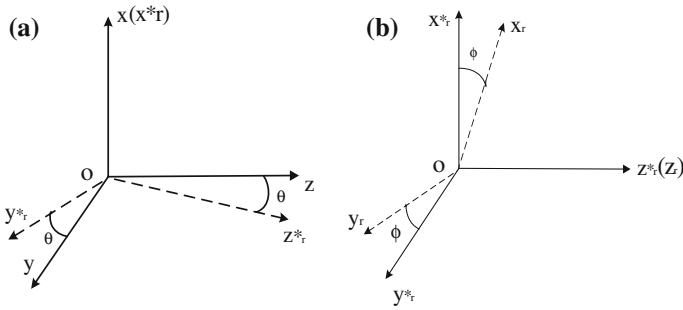


Fig. 42.3 Turntable rotating coordinates. **a** Elevation angle rotation coordinates. **b** Azimuth angle rotating coordinates

$$\begin{aligned}
 x_i &= x_{ir} \cdot \cos \varphi + y_{ir} \cdot \sin \varphi \\
 y_i &= (y_{ir} \cdot \cos \varphi - x_{ir} \cdot \sin \varphi) \cdot \cos \theta + z_{ir} \cdot \sin \theta \\
 z_i &= z_{ir} \cdot \cos \theta - (y_{ir} \cdot \cos \varphi - x_{ir} \cdot \sin \varphi) \cdot \sin \theta
 \end{aligned}
 \tag{42.6}$$

In general measurement, it's defined that the direction of incoming wave is parallel to the Z axis, thereby defining the measured antenna array should remain in the range of quiet zone in anechoic chamber. The projection of element i on the Z axis is coordinate z_i which is wave path difference. When measure phase error, have

$$\Delta L_{ci1}(Phase) = 2\pi \cdot z_i / \lambda
 \tag{42.7}$$

In the process of gain measuring, assume that the distance between transmitting antenna phase center and measured antenna array geometry center is d , and it meets $z_i \ll d$ in the far field test environment. The free space transmitting loss expression can be simplified using Taylor series, and it is:

$$\Delta L_{ci1}(Amplitude) = 20 \cdot z_i / d
 \tag{42.8}$$

42.4 Measurement Application

42.4.1 Automatic Measurement System

The automatic system is showed in Fig. 42.4. Vector signal generator generated a single carrier signal, then signal was radiated by the transmitting antenna, following by the free space propagation, and radiation signal reached the receiver antenna array aperture at last. Signal received by measured antenna array transmit to the multi-channel vector network analyzer through low stable phase coaxial cable for data comparison. Selected a channel as the reference channel and other channels

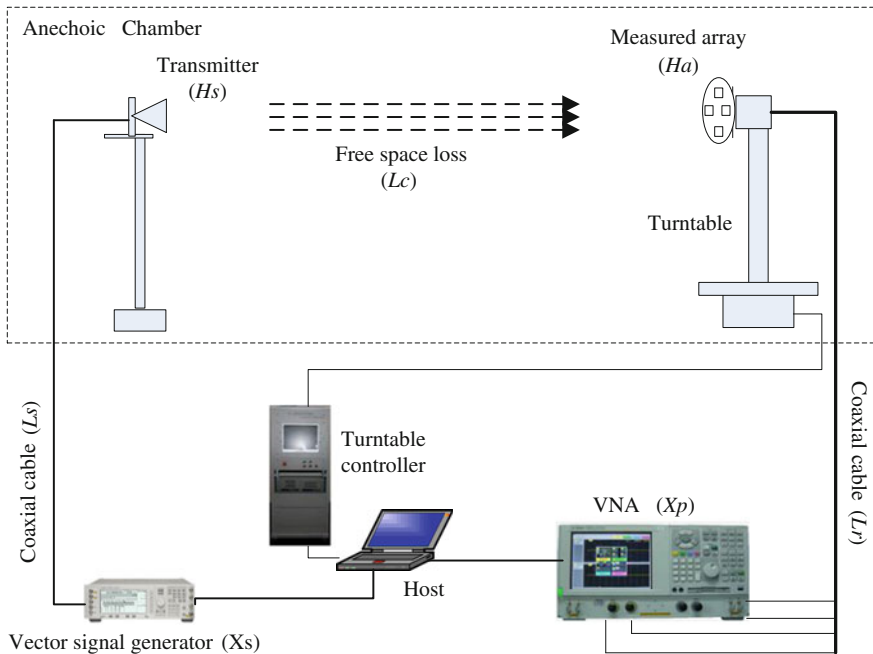


Fig. 42.4 Automatic measurement system

error can be obtained directly. The measured antenna array mounted on turntable, with the computer precision control turntable can meet the traversal in different azimuth angle and elevation angle of the antenna array. The host is set to respectively control vector signal generator, multi-channel vector network analyzer by GPIB, and three-dimensional turntable through the serial port, so to realize automatic measurement. Also, the host has to record the real-time measuring data and then output the measuring results after calibration.

42.4.2 Examples and Results

Experiments are carried out using a B3 antenna array in BD2 satellite navigation system. Right-hand circularly polarized B3 antenna element in orthogonal fed is shown in Fig. 42.5a, and Wilkinson power divider was brought into realize two signals with equal amplitude and 90° phase difference.

Assuming the center element (Ant-A) as the reference element as shown in Fig. 42.5b, the error of other three element relative to the reference element were expressed as B/A, C/A and D/A. Simulating and measuring results of the phase error in different elevation between array elements are shown in Fig. 42.6.

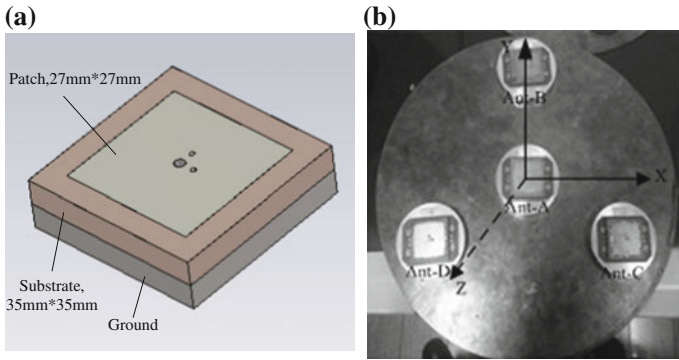


Fig. 42.5 Antenna geometry. **a** Antenna element. **b** Photo of array

Fig. 42.6 Simulating and measuring results of four elements array. **a** Elevation 8°. **b** Elevation 20°

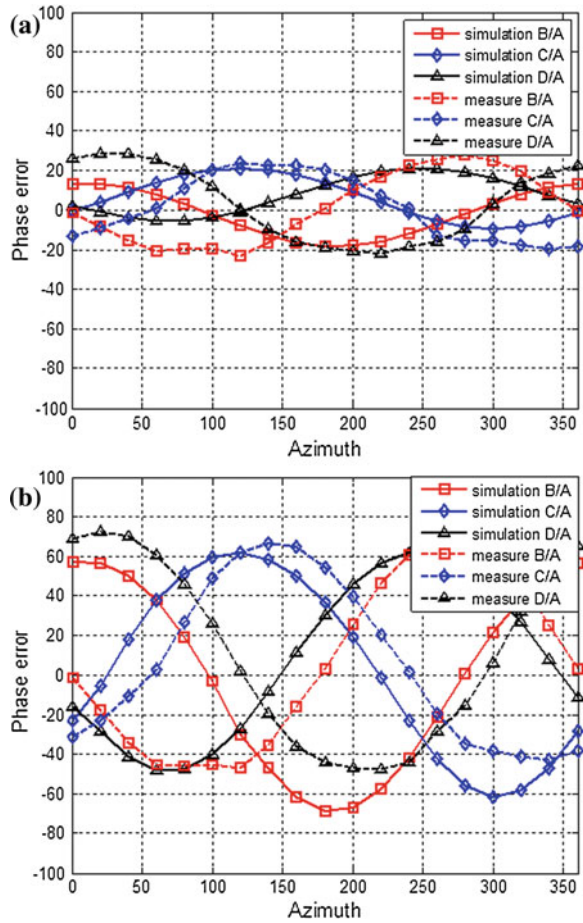


Table 42.1 Comparison of P_o between the simulating and measuring results

P_o (°)		B/A	C/A	D/A
Simulated results	Elevation 8	31.6	30.4	27.1
	Elevation 20	62.9	62.3	55.5
Measured results	Elevation 8	25.6	22.5	25.7
	Elevation 20	57.7	55.0	60.0
Phase error	Elevation 8	-6	-7.9	-1.4
	Elevation 20	5.2	7.3	-4.5

In Fig. 42.6 it can be obtained that variation of array phase error of the simulating results and measuring results agree well in the difference elevation. Assuming that the relationship can be expressed as:

$$Phase = P_o \cdot \sin(\omega \cdot \theta + \phi_o) + \phi_o \quad (42.9)$$

Obviously, value ω of simulation and measured results was equal. ϕ_o had small deviation, and error mainly came from the different azimuth 0° between the turntable and simulation platform. ϕ_o was fixed error, on one hand the transmission line in feed network of antenna element had different lengths, on the other hand it also contained the delayed phase calibration error of channel from antenna to network analyzer. Table 42.1 show the main analysis of P_o in formula (42.9).

Comparing the three sets of data, error of each array element was not equal. Measuring results of D/A was very close to the simulating results, but C/A had the largest error, this difference was mainly due to the difference of the mutual coupling between array elements. In addition, the phase bias error of each channel was less than 8° at all the range of elevation. The error by simulation of array element has only result from the array boundary conditions and mutual coupling, while the actual production of the array including the production process, materials and other factors. Considering the real antenna has kinds of degradation in circular polarization, not roundness, phase center stability, mutual coupling and so on, so the larger error in Table 42.1 is reasonable.

42.5 Conclusion

The high precision and difference measurement of amplitude and phase bias error based on microwave anechoic chamber was studied in this paper. The error sources and the amount of measuring data were reduced by using channel multiplexing and differential measurement method. And then, the wave-way difference between elements can be eliminate by three-dimensional turntable-based calibration equation. The measurement precision is nearly doubled than conventional methods. Design a fast and automatic measuring system based on high-precision measurement, the simulation and measured phase bias error results of a four-element array

are within 8° , while the efficiency is increased nearly four times, so verify that the method has high precision and high efficiency. The high precision differential measurement based on channel multiplexing method is simple, and it can be directly applied on the project for all kinds of small antenna array, so as to provide reliable data to support amplitude and phase calibration for adaptive array. In further study, inner link between physical array and electronic array as well as the effect on adaptive algorithms will be searched based on measuring data.

References

1. Wang Y (2008) Research on anti-jamming antenna arrays in satellite navigation systems. Graduate School of National University of Defense Technology, Changsha
2. Rougerie S, Carrie G, Ries L et al (2011) Multipath mitigation methods based on antenna array. In: ION ITM, San Diego, CA, pp 596–605
3. Viberg M, Lundgren A (2009) Array interpolation based on local polynomial approximation with application to DOA estimation using weighted MUSIC. In: ICASSP, pp 2145–2148
4. He L (2012) Analysis of channel errors on adaptive nulling antenna. *Telecommun Technol* 52 (4):548–552
5. O'Brien AJ, Gupta IJ (2011) Mitigation of adaptive antenna induced bias errors in GNSS. *IEEE Trans Aerosp Electron Syst* 47(1):524–537
6. Krieger JD, Newman EH, Gupta IJ (2006) The single antenna method for the measurement of antenna gain and phase. *IEEE Trans Antennas Propag* 25(14):3562–3565
7. Newell AC, Baird RC, Wacker PF (1973) Accurate measurement of antenna gain and polarization at reduced distances by an extrapolation technique. *IEEE Trans Antennas Propag* 21:418–431
8. O'Brien AJ, Gupta IJ (2011) Precise calibration of adaptive antennas for GNSS receivers on platforms. ION GNSS, Portland, pp 1102–1110
9. Kim US, David SDL et al (2004) Precise phase calibration of a controlled reception pattern GPS antenna for JPALS. In: IEEE PLANS, Monterey, CA, pp 478–485
10. Zhang YH (2006) Research on surveying antenna in satellite navigation systems. Graduate School of National University of Defense Technology, Changsha
11. Mao NH, Ju XD (1987) *The antenna measurement handbook*. National Defence Industry Press, Beijing

Chapter 43

A High-Precision and Flexible Array Antenna Signal Simulator Based on VFD Filter

Hai Sha, Han Mu and Hui Zhang

Abstract An array antenna signal simulator based on VFD filter is presented. To offer the design structure and make delay control more flexible, the VFD filter, which is suitable for changing the delay time, is used to control the delay of different channels. To improve the group delay precision of VFD filter, a design method in group delay minimax sense is proposed, instead of the variable frequency response criterion. The experimental results indicate that, in the DOA simulation, the elevation simulation accuracy of the new designed array simulator is better than 2° , the azimuth simulation accuracy is better than 1° .

Keyword Keywords are separated by half-angle origin

43.1 Introduction

Antenna array has been widely applied in communications, radar, Global Navigation Satellite System (GNSS) receiver, and so on [1–5], due to its excellent anti-interference characteristics. The array anti-interference technology distinguishes the desired signals from interference according to spatial characteristics, and can effectively suppress intentional or unintentional interference coming from different directions of the desired signals [6, 7].

The microwave anechoic chamber is usually the most important testbed for antenna arrays test, but its cost is very expensive, and it is difficult to control the delay accuracy of simulated direction of arrival (DOA). Thereby, the array signal simulators and antenna array test systems are in need. Presently the air force research laboratory [8], Spirent company [9] and CRS company [10, 11] have all

H. Sha (✉) · H. Zhang
Beijing Satellite Navigation Center, Beijing 100094, China
e-mail: sandhai@163.com

H. Mu
61243 Troops, Wulumuqi 830002, China

developed many antenna array test systems. With the concerns of going public, these companies may choose to keep their core technologies confidential as trade secret. In [12], a simulation method based on cable delays was proposed, but this way is low precision and inflexible.

In this paper, a new design method on array antenna simulator was presented, which control the delay of different channel by the variable fractional delay (VFD) digital filter. The VFD filter not only can achieve the high precision fractional sampling delay, but also change the delay flexibility [13, 14]. Meanwhile, the group delay of VFD filter in array simulator plays an important role, but most design methods use variable frequency response criterion to optimize the performance of VFD filters [15–18]. With the group delay smaller, a novel VFD filter design method in group delay minimax sense is also proposed in this paper. In this method, the weighting function is calculated by the absolute error of variable group delay.

The organization of this paper is as follows. The design method of high-precision array simulator is presented in Sect. 43.2. The antenna array model and structure of the array signal simulators are also described in this section. Then, in Sect. 43.3, a novel VFD filter design method in group delay minimax sense is proposed. In Sect. 43.4, the test results of array simulator are presented and discussed.

43.2 Design Method of High-Precision Array Simulator

43.2.1 Antenna Array Model

Four-element square array is typical and commonly used in GNSS antenna arrays anti-interference algorithm research. It is shown in Fig. 43.1, where the element space d (adjacent array element spacing) is half a wavelength λ_0 , i.e. $d = \lambda_0/2$. R is circle radius.

Geometric relationship of four elements in the space is shown in Fig. 43.2, each array element is uniformly distributed on the circumference of the radius R . Element A_1 locates at the x axis, and works as the reference element.

Coordinates of each element on X-Y plane can be expressed as $(x, y, 0)$. θ and φ are the elevation and azimuth of the incident signal respectively. Then the time delay difference of element $(x, y, 0)$ than the origin of coordinates is

$$\tau = -\frac{1}{c}(x \cos \theta \cos \varphi + y \cos \theta \sin \varphi) \quad (43.1)$$

The symbol c is light velocity (3×10^8 m/s). In Fig. 43.2, the time delay differences of each element relative to the origin of coordinates are

Fig. 43.1 Four-element square array diagram

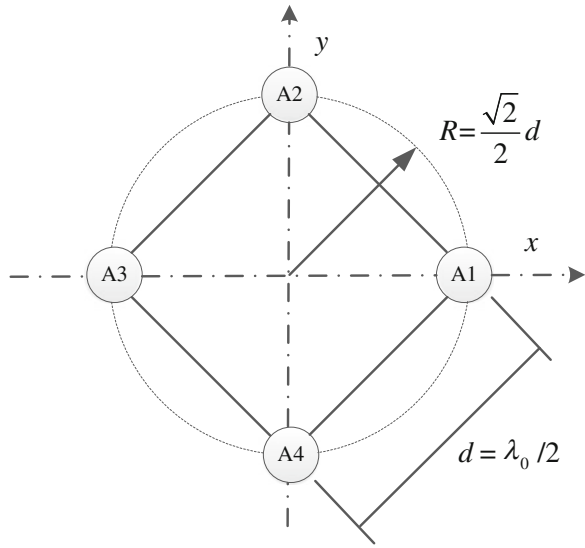
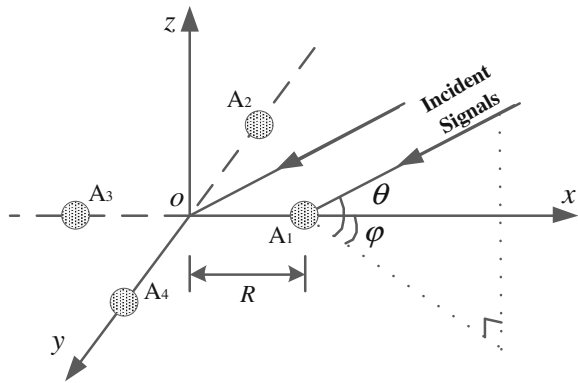


Fig. 43.2 Geometric relationship of four elements in the space



$$\begin{cases} \tau_1 = -\frac{R}{c} \cos \theta \cos \varphi \\ \tau_2 = -\frac{R}{c} \cos \theta \cos \varphi \\ \tau_3 = \frac{R}{c} \cos \theta \cos \varphi \\ \tau_4 = \frac{R}{c} \cos \theta \sin \varphi \end{cases} \quad (43.2)$$

Then the time delay differences of each element relative to the reference element A_1 are

$$\begin{cases} \Delta\tau_1 = 0 \\ \Delta\tau_2 = \tau_2 - \tau_1 = -\frac{R}{c} \cos \theta (\sin \varphi - \cos \varphi) \\ \Delta\tau_3 = \tau_3 - \tau_1 = \frac{2R}{c} \cos \theta \cos \varphi \\ \Delta\tau_4 = \tau_4 - \tau_1 = \frac{R}{c} \cos \theta (\sin \varphi + \cos \varphi) \end{cases} \quad (43.3)$$

where the radius R equals $\lambda_0\sqrt{2}/4$, the Eq. (43.3) also can be further represented by

$$\begin{cases} \Delta\tau_1 = 0 \\ \Delta\tau_2 = -\frac{\sqrt{2}}{4c} \lambda_0 \cos \theta (\sin \varphi - \cos \varphi) \\ \Delta\tau_3 = \frac{\sqrt{2}}{2c} \lambda_0 \cos \theta \cos \varphi \\ \Delta\tau_4 = \frac{\sqrt{2}}{4c} \lambda_0 \cos \theta (\sin \varphi + \cos \varphi) \end{cases} \quad (43.4)$$

The time delay differences of each element relative to the reference element A_1 can be calculated just according to the equations above.

43.2.2 Structure of the Array Signal Simulators

The structure of four-channel array signal simulator is shown in Fig. 43.3. RF signals (or interferences) are fed into the four input ports of array simulator (S_1 , S_2 , S_3 , and S_4). The four input channels of the array receivers are connected with the corresponding four output ports of the array simulator.

In Fig. 43.3, firstly the RF signal is sampled by A/D converter, and then the VFD filter achieves the time delay for the digital signal, at last the delayed digital signals by different VFD filters are combined and dealt with as the input of D/A converter. Thus it can be seen that the VFD filter is the key for the implementation of array signal simulators. The array delay relations between four incident signals and four antenna elements are simulated by 16 VFD filters (V_{11} , V_{12} , V_{13} , V_{14} , V_{21} , V_{22} , V_{23} , V_{24} , V_{31} , V_{32} , V_{33} , V_{34} , V_{41} , V_{42} , V_{43} , and V_{44}).

The VFD filter adopts the Farrow structure [19], which is shown in Fig. 43.4. The group delay of VFD filter is changed by only the fractional delay p . So the time delay $\Delta\tau$ calculated according to Eq. (43.7) is achieved easily and flexibly by VFD filter.

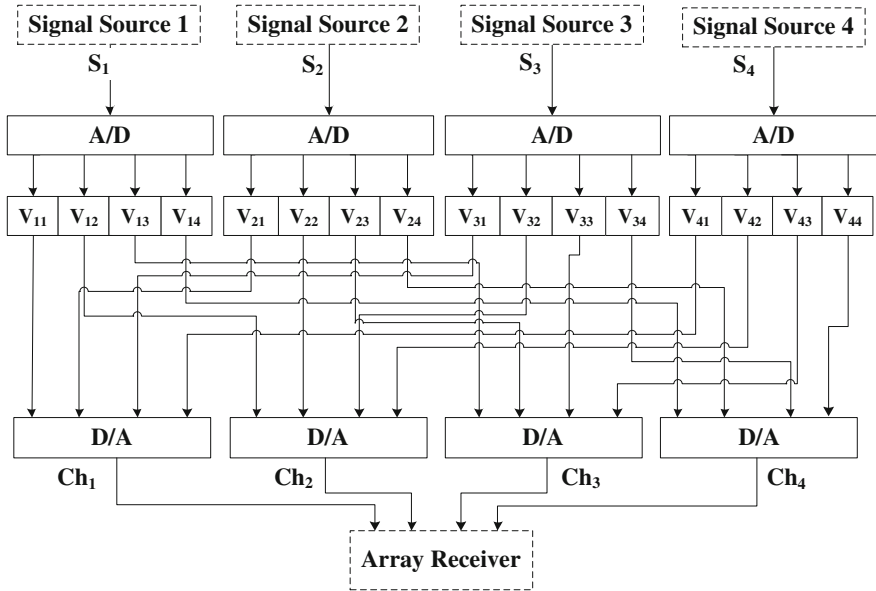


Fig. 43.3 Structure of four-channel array signal simulator

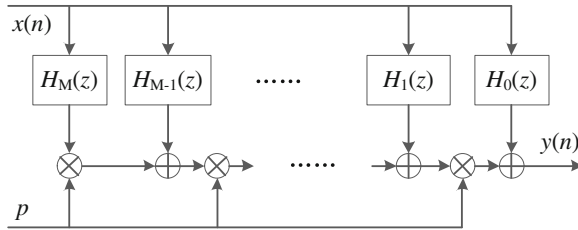


Fig. 43.4 Farrow structure of VFD filter

43.3 A New VFD Filter Design Method

In the array signal simulators, the group delay of VFD filter plays an important role, but most design methods use variable frequency response criterion to optimize the performance of VFD filters, so a novel VFD filter design method in group delay minimax sense is proposed.

43.3.1 Design Method

To design a VFD FIR filter in group delay minimax sense, the iterative method in [15] is modified and applied. The desired variable frequency response of a FIR VFD filter is

$$H_d(\omega, p) = e^{-j(\frac{N}{2}+p)\omega} = e^{-j\frac{N}{2}\omega} [\cos(\omega p) - j \sin(\omega p)] \tag{43.5}$$

where N is the order of the designed FIR digital filter, $p \in [-0.5, 0.5]$ is the VFD parameter, and $\omega \in [-\alpha\pi, \alpha\pi]$ is the normalized angular frequency, the parameter α specifies the passband edge frequency $\alpha\pi$, $0 < \alpha < 1$. Before describing the proposed algorithm, some notations are defines as follows:

$E_\tau(\omega, p)$ the absolute error of variable group delay response defined by

$$E_\tau(\omega, p) = \left| \frac{N}{2} + p - \tau(\omega, p) \right| \tag{43.6}$$

- E_{\max} where $\tau(\omega, p)$ is the actual group delay of $H(e^{j\omega}, p)$;
the maximum of $E_\tau(\omega, p)$;
- p_m the variable p where the maximum of $E_\tau(\omega, p)$ is achieved;
- $\gamma_i(p_m)$ the i th absolute error ripple of $E_\tau(\omega, p_m)$ with ripple interval $(\hat{\omega}_{i-1}, \hat{\omega}_i]$, $0 < i \leq I$, I is the total number of error ripples;

Compared with [15], the absolute error of variable group delay response is used to update the weighting function, and the p_m is found again in every iterative process. The proposed iterative procedure is described as follows:

- Step (1) Initiate the weighting function $W(\omega) = 1, 0 \leq \omega \leq \alpha\pi$, and set iterative counter $k = 0$.
- Step (2) Increase iterative counter k by one, calculate the matrices $\mathbf{A}(k)$ and $\mathbf{B}(k)$, which are defined in [15].
- Step (3) Find $E_{\max}(k), p_m$ for all the iterations, and search for $\gamma_i(p_m)$.
- Step (4) Compute the weighting function

$$\hat{W}(\omega) = W(\omega)\gamma_i^2(p_m) \tag{43.7}$$

and find its maximum value

$$\delta_\omega = \max\{\hat{W}(\omega), 0 \leq \omega \leq \alpha\pi\} \tag{43.8}$$

Then update the weighting function by

$$W(\omega) = \frac{\hat{W}(\omega)}{\delta_\omega}, 0 \leq \omega \leq \alpha\pi \quad (43.9)$$

Step (5) Check whether the k is large enough by $k > K$, K is the maximum iterative counter. If the condition is satisfied, continue the next step; otherwise, go to Step (2).

Step (6) Find the minimum of $E_{\max}(k)$, and output the final coefficient matrices $\mathbf{A}(k)$, $\mathbf{B}(k)$.

43.3.2 Performance Comparison

To evaluate the performance, the maximum absolute error of variable frequency response and the maximum delay error are defined by

$$\varepsilon_m = \max\{|H_d(\omega, p) - H(e^{j\omega}, p)|, 0 \leq \omega \leq \alpha\pi, 0 \leq p \leq 0.5\} \quad (43.10)$$

$$\varepsilon_\tau = \max\left\{\left|\frac{N}{2} + p - \tau(\omega, p)\right|, 0 \leq \omega \leq \alpha\pi, 0 \leq p \leq 0.5\right\} \quad (43.11)$$

For the computation of Eqs. (43.10) and (43.11), the frequency ω and the variable p are uniformly sampled at step sizes $\alpha\pi/200$ and $1/60$, respectively.

An $N = 60$, $M = 9$, $K = 15$ and $\alpha = 0.9$ VFD FIR filter is designed in this example. During all iterations, it is found that the iterative counter k where the minimum of $E_{\max}(k)$ is 7, $\varepsilon_m = 3.613056 \times 10^{-5}$, $\varepsilon_\tau = 9.286823 \times 10^{-4}$. Figure 43.5a, b present the final magnitude and group delay responses, while the absolute errors of variable frequency responses and group delay responses for the seventh iteration are shown in Fig. 43.5c, d, respectively. While the errors in method [15] are $\varepsilon_m = 1.92486931 \times 10^{-5}$, $\varepsilon_\tau = 3.59572 \times 10^{-3}$, the group delay performance of the proposed method is much better than that of the method in [15], but the magnitude is worse, there exists a trade-off relationship between ε_τ and ε_m .

43.4 Test Results of the Array Simulator

43.4.1 The Order of VFD Filter

Assume the sample frequency is 40 MHz, the signal bandwidth is 10 MHz. Typical array time delay range is about 0–0.3 ns, the resolution and accuracy needed for time delay controlling is within 0.001 ns, which is equivalent to 4×10^{-5} sampling

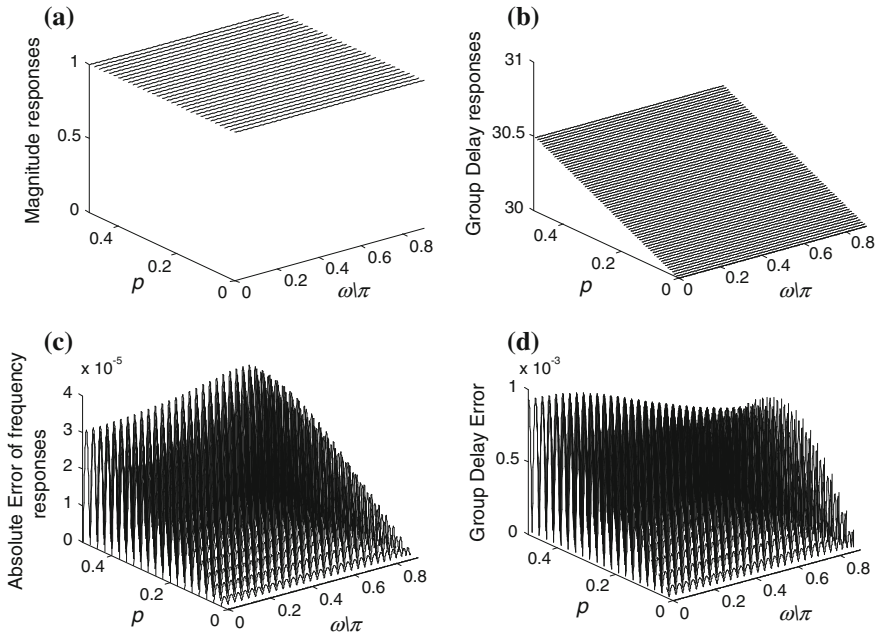


Fig. 43.5 Design of a VFD FIR digital filter with $N = 60$, $M = 9$, and $\alpha = 0.9$: **a** Magnitude response. **b** Variable fractional delay response. **c** Absolute error of variable frequency response. **d** Absolute error of group delay response

Table 43.1 The maximum absolute error of variable frequency response ϵ_m , the maximum absolute group delay error ϵ_τ , for the design of $N = 16$ and $\alpha = 0.5$ VFD FIR filters with different M by the proposed method

M	ϵ_m	ϵ_τ
3	0.004342(-47 dB)	0.008668
4	0.000301(-70 dB)	0.000656
5	0.000029(-90 dB)	0.000086
6	0.000004(-108 dB)	0.000009

delay. Table 43.1 presents the results of the proposed method in Sect. 43.3 for different M when $N = 16$, $\alpha = 0.5$ and $\epsilon_\tau < 4 \times 10^{-5}$.

In Table 43.1, for $M = 6$ the errors in proposed method are $\epsilon_m = 4 \times 10^{-6}$, $\epsilon_\tau = 9 \times 10^{-6}$, the group delay performance is better than the 4×10^{-5} sampling delay. While the absolute errors of variable frequency responses and group delay responses for $M = 6$ are shown in Fig. 43.6.

In conclusion, to satisfy the needs of 4×10^{-5} sampling delay resolution and accuracy, the order of VFD filter is chosen as $N = 16$, $M = 6$.

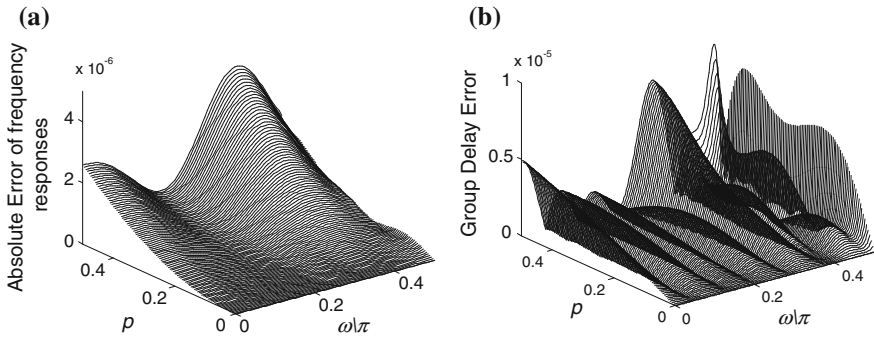


Fig. 43.6 The absolute errors of variable frequency responses and group delay responses for $M = 6$. **a** Absolute error of frequency responses. **b** Group delay error

Table 43.2 Time Delay of VFD filters for Array Simulation

	Desired DOA (θ, φ)	VFD filter No.	Time delays (ps)	Fraction delays p (sampling)
S_1	$(90^\circ, -)$	V_{11}	0	0
		V_{12}	0	0
		V_{13}	0	0
		V_{14}	0	0
S_2	$(15^\circ, 30^\circ)$	V_{21}	0	0
		V_{22}	106.25	0.00425
		V_{23}	502.79	0.02011
		V_{24}	396.54	0.01586

43.4.2 Testing and Data Processing Method

Assume the navigation signal comes from the zenith (i.e. the elevation is 90°), interference comes from elevation 15° and azimuth 120° . RF frequency is 1176.45 MHz (GPS L5), and the corresponding wavelength is 0.2550 m. Each incident signal corresponds to four VFD filters, whose delay time is calculated according to Eq. (43.4); the results are shown in Table 43.2.

Test method of array signal simulators is shown in Fig. 43.7. The GNSS receiver was used to record the pseudorange. Repeat the test and get the pseudoranges at 1 s intervals, and 3600 points average was taken in each channel.

Assume the channel pseudorange test results from GNSS receiver corresponding to each element are r_1, r_2, r_3 and r_4 , then the wavepath differences of each array element relative to the reference point are

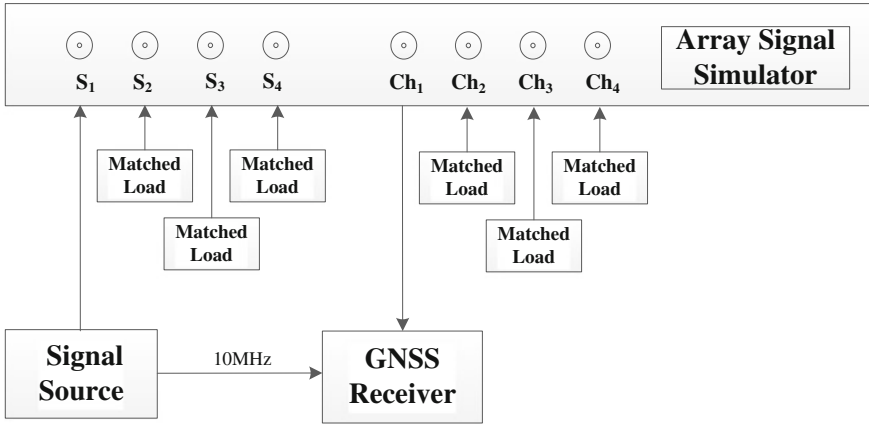


Fig. 43.7 Test equipment connection diagram of array signal simulator

$$\begin{cases} \Delta d_1 = r_1 - r_1 = 0 \\ \Delta d_2 = r_2 - r_1 \\ \Delta d_3 = r_3 - r_1 \\ \Delta d_4 = r_4 - r_1 \end{cases} \quad (43.12)$$

Assume the actual DOA simulation result of (θ, φ) is (θ', φ') , according to Eq. (43.4), the (θ', φ') can be solved out as

$$\begin{cases} \varphi = \left(\frac{\Delta d_3 - 2\Delta d_2}{\Delta d_3} \right) + k\pi, k \in Z \\ \varphi \in [0, 360^\circ] \end{cases} \quad (43.13)$$

$$\begin{cases} \theta = \arccos \left(\frac{\sqrt{2}\Delta d_3}{\lambda_0 \cos \varphi} \right) + 2n\pi, n \in Z \\ \theta \in [0, 90^\circ] \end{cases} \quad (43.14)$$

43.4.3 Testing Results

Calculate wavepath difference according to Eq. (43.12), and then substitute each wavepath differences into Eqs. (43.13) and (43.14) correspondingly. Solve out the actual simulated results.

As shown in Table 43.3, for signal S_1 , the design target of incident elevation is 90° , and the actual tested relative wavepath difference of each channel are 0 m,

Table 43.3 Actual tested results

Source No.	VFD filter No.	Time delay Diff. of each channel relative to Ch1 (ps)	Wavepath Diff. of each channel relative to Ch1 (mm)
S1	V ₁₁	0	0
	V ₁₂	3.25	0.0975
	V ₁₃	-2.58	-0.0744
	V ₁₄	-2.61	-0.0785
S2	V ₂₁	0	0
	V ₂₂	105.17	31.55
	V ₂₃	504.09	151.23
	V ₂₄	398.23	119.47

0.0975 mm, -0.0744 mm, -0.0785 mm respectively. Substitute them into Eq. (43.14), it can be solved out that the actual simulated incident elevation is 90°, which is equal to the design target.

As for signal S₂, the design target of DOA is (15°, 30°), and the actual tested relative wavepath difference of each channel are 0 m, 31.55 mm, 151.23 mm, 119.47 mm respectively. Substitute them into Eq. (43.13), it can be solved out that the actual simulated DOA is (13.896°, 30.232°), which is slightly deviated from the design target.

43.5 Conclusion

In this paper, An array signal simulator based on VFD filter has been presented. Compared with the previous methods, the proposed method can simulate particular DOA accurately and flexibly, which controlled the different channel delays by VFD filter. In this method, the VFD filter is designed by using group delay minimax sense to increase the delay precision farther. Experimental results indicate that in the DOA simulation, the elevation simulation accuracy of the new designed array simulator is better than 2°, the azimuth simulation accuracy is better than 1°. The technique can also be applied to other planar array patterns and conditions with more incident signals.

References

1. Diego C, Maria CV, Toso G, Piero A, Alexander S, Renato C (2013) A hybrid deterministic/metaheuristic synthesis technique for non-uniformly spaced linear printed antenna arrays. *Prog Electromagn Res* 142:107–121
2. Jose MI, Jose MF, Manuel S (2013) Low loss power distribution network in stripline technology for planar array antennas. *Prog Electromagn Res* 143:369–384

3. Yong LR, Jian W, Da CH, Ning Z (2013) Horn-based circular polarized antenna array with a compact feeding for Ka-band monopulse antenna. *Prog Electromagn Res* 142:291–308
4. Liu JZ, Zhao ZQ, Yang K, Liu QH (2014) A hybrid optimization for pattern synthesis of large antenna arrays. *Prog Electromagn Res* 145:81–91
5. Qiu L, Wang SS, Qi HY, Zhao F, Chai SL, Mao JJ (2013) A shaped-beam series-fed aperture-coupled stacked patch array antenna. *Prog Electromagn Res* 141:291–307
6. Chun TF, Zamora A, Lei BJ et al (2011) An interleaved, interelement phase-detecting/phase-shifting retrodirective antenna array for interference reduction. *IEEE Antennas Wirel Propag Lett* 10:919–922
7. Vendik OG, Kozlov DS (2012) Phased antenna array with a sidelobe cancellation for suppression of jamming. *IEEE Antennas Wirel Propag Lett* 11:648–650
8. Dana H, Denice J, Bruce R, Gary G (2000) Virtual flight testing—a versatile approach to evaluate future GPS anti-jam technologies. In: Proceedings of the national technical meeting of the Institute of Navigation, pp 670–678
9. Test solutions for: interference, anti-jam, GPS/inertial, interference mitigation. http://www.spirentfederal.com/gps/documents/MCD00077AAA_Military_Brochure.pdf
10. Multiband GPS wavefront simulator. <http://www.cfrsi.com/pdf/Multiband%20GPS%20Wavefront%20Simulator.pdf>
11. David S, De L (2007) Navigation accuracy and interference rejection for GPS adoptive antenna arrays, Stanford University
12. Han QW, Nie JW, Huo SM, Wang FX (2014) A high-precision and low-cost planar array signal simulator based on cable delays. *IEEE Antennas Wireless Propag Lett* 13:353
13. Laakso TI, Valimaki V, Karjalainen M (1996) Splitting the unit delay: tools for fractional delay filter design. *IEEE Signal Process Mag* 13:30–60
14. Yu YJ, Xu WJ (2013) Investigation on the optimization criteria for the design of variable fractional delay filters. *IEEE Trans Circuits Syst* 60:522–526
15. Soo JJ, Pei SC, Cai CH (2008) Minimax design of variable fractional-delay FIR digital filters by iterative weighted least-squares approach. *IEEE Signal Process Lett* 15:693–696
16. Deng TB, Chivapreecha S, Dejhan K (2012) Bi-minimax design of even-order variable fractional-delay FIR digital filter. *IEEE Trans Circuits Syst* 59:1766–1774
17. Teng CC, Li SL (2011) Efficient design and implementation of variable fractional delay filters using differentiators. *IEEE Trans Circuits Syst I Regul Pap* 58:1311–1322
18. Teng CC, Li SL (2012) Designs of fixed-fractional-delay filters using fractional-derivative constraints. *IEEE Trans Circuits Syst II Express Briefs* 59:683–687
19. Farrow CW (1988) A continuously variable digital delay element. In: IEEE international symposium on circuits and systems

Chapter 44

New Generation Signal Structure Evaluation System for GNSS

Jianlei Yang, Tian Jin, Zhigang Huang and Honglei Qin

Abstract The evaluation of signal structure is an important phase of the signal structure design in the process of GPS modernization, Galileo and BDS construction. The new generation navigation signals of global navigation satellite system (GNSS) have the characteristics of diversification of signal structure, large bandwidth and complicated receiving method. Based on this, a new generation signal structure evaluation system (NGSSES) was proposed. The NGSSES is flexible to configure, and the bandwidth and sampling rate can up to 250 and 150 MHz, respectively. The output signals have the power of resolution of 0.5 dB. The performance of code and carrier tracking accuracy of BOC(14,2) under single channel and channel combining tracking methods, multipath of TMBOC(6,1,4/33) under matching and non-matching methods are evaluated using NGSSES. The anti-jamming performance of BOC(14,2) and AltBOC(15,10), compatibility of BDS B1 BOC(14,2) and GPS L1M BOC(10,5) are also evaluated using NGSSES. The experimental results verified the feasibility and effectiveness of NGSSES.

Keywords GNSS · Signal structure evaluation · Tracking accuracy · Anti-jamming · Multipath · Compatibility

44.1 Introduction

The evaluation of signal structure is an important phase of the global navigation satellite systems (GNSS). In the GPS modernization and Galileo construction process, theoretical analysis, software simulation and hardware verification are adopted to evaluate the signal structure, that guarantee the scientificity and effectiveness of Galileo, modernized GPS signal design.

J. Yang (✉) · T. Jin · Z. Huang · H. Qin
School of Electronic and Information Engineering, BeiHang University, Beijing,
People's Republic of China
e-mail: yangjianlei@buaa.edu.cn

In 1999, MITRE company developed a real-time, RF and full bandwidth transmitter/receiver hardware testbed. The alternative signal of L1 and L2 was tested using this testbed. The testbed had the single sideband and double sideband receiving capability. The testbed provides a powerful support for GPS L1M [1]. In 2002, the Aerospace company developed a hardware simulation platform, and verified independent tracking performance of GPS L2C CM and CL code. The effect of L2C receiving on commercial GPS receiver was also evaluated [2, 3]. In 2006, Aerospace company developed Modernized Aerospace GPS Navigation Evaluation Testbed (MAGNET) to evaluate the GPS L5 [4].

In 2002, the ESA used the Galileo Signal Validation Facility I (GSVF I) to verify and evaluate the signal baseline of 2002 years. The alternative signal of BOC was evaluated using GSVF II in 2007 [5]. In 2003, a Galileo Experimental Test Receiver (GETR) was also developed by Septentrio company to evaluate new Galileo signal [6]. In the same year, Astrium company developed BayNavTech Signal Experimentation Facility (BaySEF) [7]. This device can not only be used for evaluating of navigation signal, but also can be used to monitor the signal quality for satellite ground station and evaluate the performance of satellite payload.

As the GPS and Galileo, some new design ideas of signal structures have been introduced in BDS, such as adopting of BOC, MBOC and AltBOC, broadcasting data and pilot channels simultaneously, etc. [8]. According to the overall planning, the BDS will cover the whole world in 2020 [9]. Liu [10] analysed compatibility of BDS and GPS, Hu [11] researched the evaluation theory in his doctoral dissertation. He [12] analysed the signal quality monitoring and evaluation methods on orbit satellite.

From the analysis above we can see that, there are mature testbed to evaluate the GPS and Galileo signal structures and evaluation theory researched on BDS. The design of signal structures can not achieve a comprehensive optimization result, and it can only a trade-off results of all system performance [13]. Therefore, the establishment of a new generation signal structure evaluation system (NGSSES) is important for the development of new navigation signal design and performance evaluation work.

44.2 The Structure of NGSSES

Compared with GPS L1C and BDS B1I and B2I, the new generation navigation signal have the characteristic of diversification of signal structure, large bandwidth, broadcasting data and pilot channels simultaneously and tiered code, etc. For example, MBOC, BOC, AltBOC and QPSK are adopting by GPS, Galileo and BDS; Galileo E5 and B2 (single sideband receiving), and GPS L5 require more than 20.46 MHz bandwidth; Galileo E5 and B2 require more than 51.15 MHz bandwidth for double sideband receiving; Galileo L1 PRS and BDS B3 require more than 35.805 MHz bandwidth; BDS B1 requires more than 32.736 MHz bandwidth.

Table 44.1 Requirements for NGSSSES

Unit	Requirements for NGSSSES
Signal generation	Flexible configuration. It should be flexible to produce the alternative signal and develop new signal structure; the adjustment of some parameter (such as Doppler, code rate, code phase and navigation message) should be also convenient
Scene simulation	The parameter of scenes (such as power ratio and code phase delay of direct signal and reflected signal, the bandwidth, power and frequency of interference signal) should be adjusted accurately
RF front-end	High sampling rate, more than 102.3 MHz for Galileo E5 and BDS B2 receiver; quantization bit adjustable, 1–16 bit
Receiving method	The development of a variety of tracking and acquisition method flexibly, such as single sideband and double sideband, single channel and channel combining, matching and non-matching methods, etc.; It is flexible to adjust the loop parameters, such as bandwidth, loop order, front-end bandwidth, etc.

However, these new characteristics propose the new requirements for NGSSSES, as shown in Table 44.1.

According to the above table, the structure of the proposed NGSSSES is shown as follows (Fig. 44.1):

An embedded computer is adopted to generate baseband signal. The calculation of signal parameters, including Doppler, code rate, code phase and navigation message, is completed in CPU. The signal modulation is completed in FPGA. The amplitude of the digital signal is produce using 11 bit quantization level, so the gain of digital signal can be adjusted in range of -20 to +20 dB with 0.5 dB resolution. The code NCO bit wide of NGSSSES $N_{code} = 48$, intermediate frequency $f_{IF} = 30$ MHz, thus the corresponding code pseudorange error is

$$\varepsilon_{code} = \frac{1}{f_{IF}} \cdot \frac{2\pi}{2^{N_{code}}} \cdot \frac{1}{2\pi} \cdot 2.99 \times 10^8 = 3.54 \times 10^{-14} \text{ (m)} \quad (44.1)$$

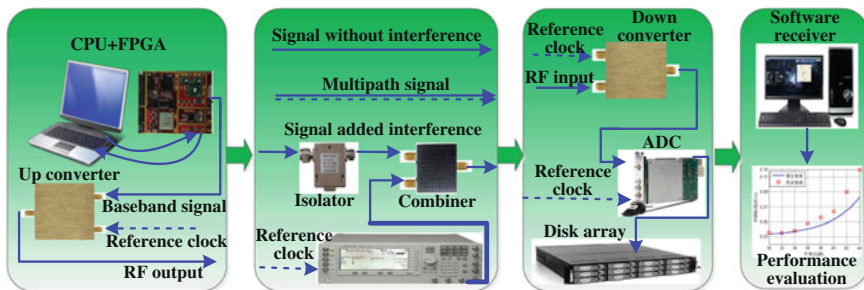


Fig. 44.1 The structure of the NGSSSES

The carrier NCO bitwide of NGSSSES $N_{carrier} = 14$, thus the carrier phase error is

$$\varepsilon_{carrier} = \frac{1}{f_{IF}} \cdot \frac{2\pi}{2^{N_{carrier}}} \cdot \frac{1}{2\pi} \cdot 2.99 \times 10^8 = 6.08 \times 10^{-4} \text{ (m)} \quad (44.2)$$

According to (44.1) and (44.2), it can be seen that $\varepsilon_{carrier}$ is much greater than ε_{code} , so the maximum error of signal generator module is 6.08×10^{-4} m.

Interference signal is produced by vector signal generator Agilent E8267C. It can generate narrowband, broadband, single frequency, frequency sweeping interference signal. The bandwidth, frequency and power can be adjusted flexibly. The adjustable step of power and frequency are 0.01 dBmW and 0.001 Hz, respectively.

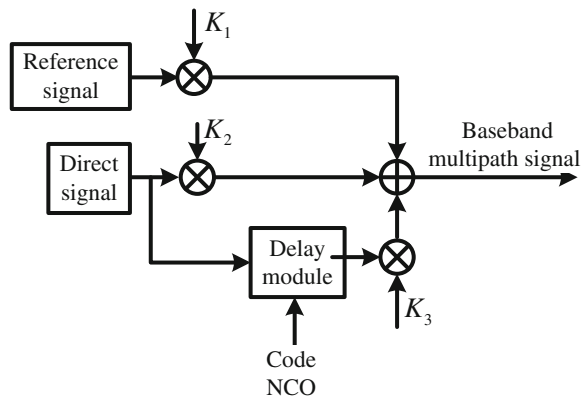
To control of the phase delay and power ratio of reflected signal and direct signal, the generation of multipath signals is completed in the baseband signal generation module, as shown in Fig. 44.2.

In Fig. 44.2, K_1 , K_2 and K_3 are used to control the power of the reference signal, the direct signal and reflected signal, respectively. The delay module is controlled by code NCO, which is 48 bit. The code delay adjusting precision can reached to $1/2^{48}$ chip. Reference signal is designed for anti-multipath performance testing consideration. Software receiver uses two PN code sequences to receive and process the multipath signal respectively at the same time. The code tracking error can be obtained by make subtraction between the two corresponding code phases.

ADC NI PXIe-5622 board, storage devices NI HDD-8265 are used in NGSSSES. The sampling rate, reading and writing speed, quantization bit, and bandwidth can up to 150 MHz, 750 MS/s, 16 bit and 250 MHz, respectively.

To achieve the requested flexibility and configurability, a software receiver appears to be the right technical solution. Compared with hardware receiver, tracking loop parameters can be adjusted more conveniently to testing tracking performance under different loop parameters in software receiver. It is also easier to develop different receiving methods.

Fig. 44.2 The principle of the multipath signal generation



44.3 Evaluation and Analysis of Signal Structure Using NGSSSES

To verify the feasibility and effectiveness of NGSSSES, the code and carrier tracking performance, multipath performance, code tracking performance in the presence of interference and compatibility of BDS B1 BOC(14,2) and GPS L1M BOC(10,5) are tested using NGSSSES. Table 44.2 shows the signal and tracking method used in testing.

The theoretical tracking accuracy expression of channel combining tracking method can be shown as

$$\sigma_{Comb}^2 = \frac{\sigma_{Pilot}^2 \sigma_{Data}^2}{\sigma_{Pilot}^2 + \sigma_{Data}^2} \quad (44.3)$$

where σ_{Pilot}^2 and σ_{Data}^2 is the carrier or code tracking variance of Pilot and Data channels.

44.3.1 Code and Carrier Tracking Jitter

In the testing, the discriminator of Atan and NELP are used, the theoretical tracking performance can be shown as (44.4) [18] and (44.5) [19]. For the testing, early-late spacing $\Delta = 0.06$ chip, loop bandwidth of DLL $B_L = 2$ Hz, loop bandwidth of PLL $B_M = 20$ Hz, coherent integration time $T = 2$ ms, front-end bandwidth $\beta_r = 32.736$ MHz. The normalized power spectral density of BOC can be obtained from the [20].

$$\sigma_{Code, NELP, WhiteNoise}^2 = \frac{B_L(1 - 0.5B_L T) \left(\int_{-\beta_r/2}^{\beta_r/2} G_s(f) \sin^2(\pi f \Delta) df \right)}{(2\pi)^2 \frac{C_s}{N_0} \left(\int_{-\beta_r/2}^{\beta_r/2} f G_s(f) \sin^2(\pi f \Delta) df \right)^2} \times \left(1 + \frac{\int_{-\beta_r/2}^{\beta_r/2} G_s(f) \cos^2(\pi f \Delta) df}{\frac{C_s}{N_0} T \left(\int_{-\beta_r/2}^{\beta_r/2} G_s(f) \cos(\pi f \Delta) df \right)^2} \right) \quad (44.4)$$

$$\sigma_{Carrier}^2 = \frac{360}{2\pi} \sqrt{\frac{B_M}{C_s/N_0} \left(1 + \frac{1}{2TC_s/N_0} \right)} \quad (44.5)$$

Figures 44.3 and 44.4 show the code and carrier tracking performance using single channel and channel combined tracking method.

From Figs. 44.3 and 44.4, we can see that the theoretical and testing results for each method are matched. The channel combining tracking method has 2–3 dB

Table 44.2 The signal and tracking methods adopted in testing

Experiment	Signals	Tracking method	Single or Channel combining tracking [14]
Code and carrier tracking accuracy	BOC(14,2)	Tracking method based on subcarrier tracking [15]	Both of them
Multipath performance	TMBOC(6,1,4/33)	Matching and nonmatching tracking method [16]	Single channel tracking
Code tracking performance in presence of interference	BOC(14,2)	Tracking method based on subcarrier tracking	Single channel tracking
	AltBOC(15,10)	Single sideband tracking method [17]	Channel combining tracking
Compatibility	B1 BOC(14,2) L1M BOC(10,5)	Tracking method based on subcarrier tracking	Both of them

Fig. 44.3 Code tracking accuracy using single channel and channel combining methods

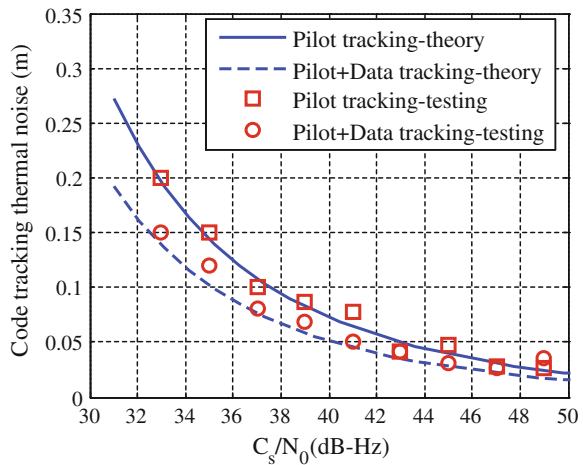
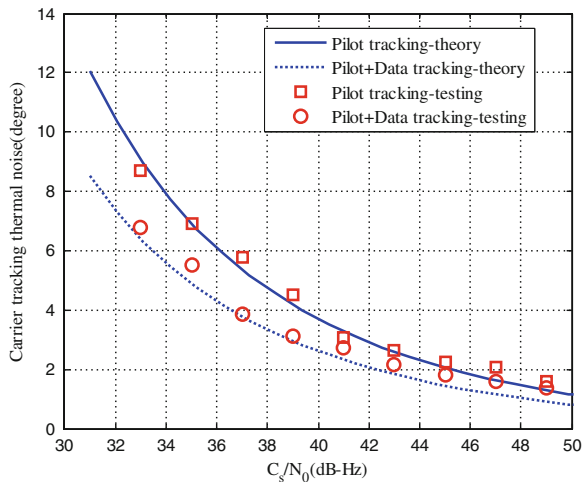


Fig. 44.4 Carrier tracking accuracy using single channel and channel combining methods



improvement compared with single channel tracking method. This is due to the fact that the single channel tracking method only uses the pilot component alone, and half of the signal power is lost.

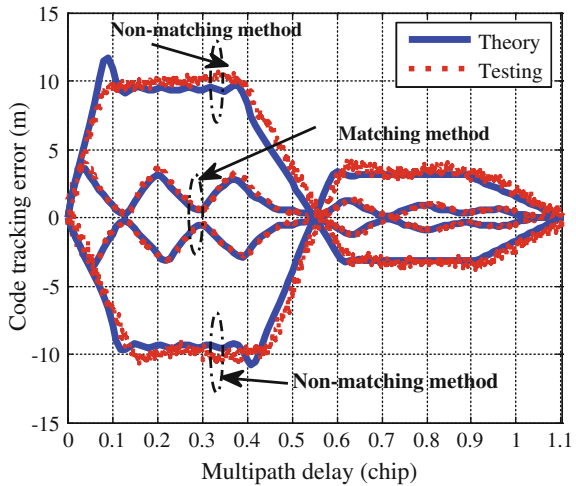
44.3.2 Code Tracking Multipath Error

The multipath performance of TMBOC(6,1,4/33) under matching and non-matching tracking method was analyzed, as shown in Fig. 44.5. The theoretical expression of code tracking multipath error [21] can be shown in (44.6). In the testing process, the power ratio of reflected and the direct signal $\alpha = -10$ dB; relative code phase delay between reflected and the direct signal $\tau = 0-1.1$ chip; early-late spacing under matching and non-matching tracking method Δ is 0.08 chip and 0.2 chip; $G_s(f)$ is the normalized power spectral density of TMBOC, as shown in [22].

$$\varepsilon_\tau = \frac{\pm\sqrt{\alpha} \int_{-\beta_r/2}^{\beta_r/2} G_s(f) \sin(2\pi f\tau) \sin(\pi f\Delta) df}{2\pi \int_{-\beta_r/2}^{\beta_r/2} f G_s(f) \sin(\pi f\Delta) [1 \pm \alpha \cos(2\pi f\tau)] df} \tag{44.6}$$

From Fig. 44.5, we can see that the theoretical and testing results for matching and non-matching strategy are matched. The testing results support the feasibility of multipath signal generation scheme, as shown in Fig. 44.2.

Fig. 44.5 Code tracking multipath error under matching and non-matching tracking methods



44.3.3 Code Tracking Performance in Presence of Interference

The code tracking performance of BOC(14,2) and AltBOC(15,10) are tested in the presence of wideband interference, as shown in Figs. 44.6 and 44.7. The theoretical expression of code tracking multipath error can be shown in (44.7).

$$\sigma_{\text{Code,NELP,Interference}}^2 = \frac{B_L(1 - 0.5B_L T) \left(\int_{-\beta_r/2}^{\beta_r/2} \left[\frac{N_0}{C_s} + \frac{C_i}{C_s} G_i(f) \right] G_s(f) \sin^2(\pi f \Delta) df \right)}{(2\pi)^2 \left(\int_{-\beta_r/2}^{\beta_r/2} f G_s(f) \sin(\pi f \Delta) df \right)^2} \times \left(1 + \frac{\int_{-\beta_r/2}^{\beta_r/2} G_s(f) \cos^2(\pi f \Delta) df}{\frac{C_s}{N_0} T \left(\int_{-\beta_r/2}^{\beta_r/2} G_s(f) \cos(\pi f \Delta) df \right)^2} + \frac{\int_{-\beta_r/2}^{\beta_r/2} G_i(f) \cos^2(\pi f \Delta) df}{\frac{C_i}{C_s} T \left(\int_{-\beta_r/2}^{\beta_r/2} G_s(f) \cos(\pi f \Delta) df \right)^2} \right) \tag{44.7}$$

where $G_i(f)$ is the normalized power spectral density of interference signal; the BPSK signal is adopted as the interference signal, and the corresponding $G_i(f)$ can be obtained from [23]; carrier to noise ratio $C_s/N_0 = 44$ dB-Hz; power ratio of interference and signal $C_i/C_s = 30-44$ dB.

The bandwidth of interference signal for BOC(14,2) and AltBOC(15,10) is 32.736 and 20.46 MHz, respectively. The testing result can be shown as

It can be seen from Figs. 44.6 and 44.7, the theoretical and testing curve have the same change tendency. With the increasing of C_i/C_s , the curve of testing deteriorates faster than theoretical curve. This is because effect carrier to noise ratio $(C_s/N_0)_{\text{effect}}$ decrease as the C_i/C_s increasing, and discriminator range of code discriminator enters the nonlinear region at low $(C_s/N_0)_{\text{effect}}$, which causes the

Fig. 44.6 Code tracking accuracy of BOC(14,2) in presence of wideband interference

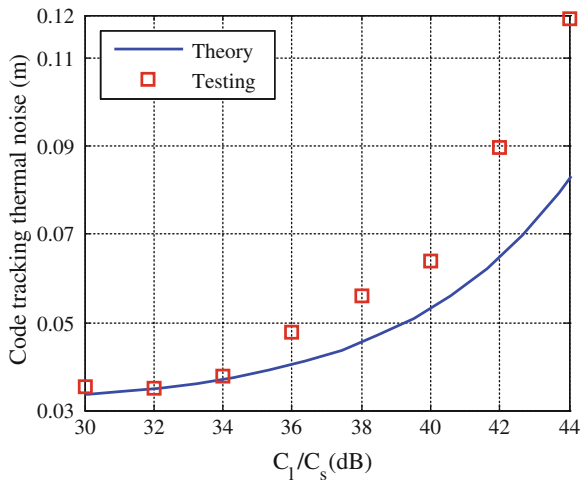
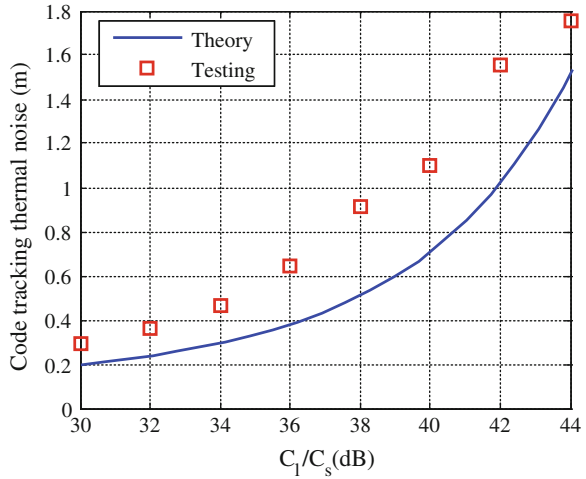


Fig. 44.7 Code tracking accuracy of AltBOC(15,10) in presence of wideband interference



deterioration of the code tracking accuracy. However, the theoretical model (as shown in (44.7)) doesn't consider this factor.

44.3.4 Compatibility

According to [8], the spectrums of BDS B1 BOC (14, 2) and GPS GPS L1M BOC (10,5) are aliasing partly. Consider that, compatibility of these two signals was analyzed. In the testing, considering the interference signals of multiple GPS L1M satellites and $C_1/C_s = 29$ dB, the theoretical effect carrier-to-noise ratio $(C_s/N_0)_{eff}$ [24] is shown as follows

$$(C_s/N_0)_{eff} = \frac{1}{\frac{1}{(C_s/N_0)} + \frac{C_1/C_s}{QR_C}} \tag{44.8}$$

where R_C is signal code rate, Q is said the spread spectrum gain adjustment factor, as shown in (44.9).

$$Q = \frac{\int_{-\infty}^{+\infty} |H_R(f)|^2 G_s(f) df}{R_C \int_{-\infty}^{+\infty} |H_R(f)|^2 G_I(f) G_s(f) df} \tag{44.9}$$

From Table 44.3, we can see that the $(C_s/N_0)_{eff}$ decreased about 1 dB, and code tracking accuracy decreased slightly. By using the channel combining tracking method can improve $(C_s/N_0)_{eff}$ and code tracking accuracy.

Table 44.3 Compatibility testing data of GPS L1M BOC(10,5) and BDS B1 BOC(14,2)

Tracking methods	Test or theoretical value	Before GPS L1M enhanced		After GPS L1M enhanced	
		$(C_s/N_0)_{eff}$ (dB-Hz)	Code tracking accuracy	$(C_s/N_0)_{eff}$ (dB-Hz)	Code tracking accuracy
Single channel tracking	Testing	44.25	0.0717	43.28	0.1028
	Theory	44.25	0.0355	44.10	0.0374
Channel combining tracking	Testing	46.63	0.0524	45.28	0.0789
	Theory	46.63	0.0266	46.37	0.0258

44.4 Conclusion

According to the characteristics of new generation navigation signals of GNSS, NGSSSES was proposed. The NGSSSES are flexible to configure, and the bandwidth and sampling rate can up to 250 and 150 MHz, respectively. The output signals have the level of resolution of 0.5 dB. The NGSSSES can be used to evaluate the performance of tracking accuracy, multipath, anti-jamming and compatibility. The experimental results verified the feasibility and effectiveness of NGSSSES. In addition, the NGSSSES can be also used to evaluate acquisition performance, acquisition algorithm and bit error rate.

Acknowledgments This work was supported by National Science Foundation of China (Grant Nos. 61101076, 41374137, 61471017) and National Basic Research Program of China (973) (Grant No. 2011CB707004).

References

1. Correia JT, Blanchard JJ, Fine PB (2000) A hardware testbed for evaluation of the GPS modernization modulation candidates. In: Proceedings of ION NTM, Anaheim, CA, pp 594–604
2. Dafesh PA, Bow RT, Partridge MD et al (2002) Simulation and hardware demonstration of new L2 civilian GPS ranging codes. In: Proceedings of the ION NTM, San Diego, CA, pp 925–930
3. Dafesh PA, Wong RL, Partridge MD et al (2001) Measurements of GPS receiver compatibility with interplex-modulated M-code signals. In: Proceedings of ION AM, Albuquerque, NM, pp 100–108
4. Hsu J, Choy A, Powell TD et al (2009) Initial on-orbit observations of the L5 demo payload on GPS IIR-20. In: Proceedings of ION GNSS, Savannah, GA, pp 76–85
5. De Gaudenzi R, Hoult N, Batchelor A et al (2001) Galileo signal validation development. In: Proceedings of seventh international workshop on digital signal processing techniques for space communications, Sesimbra, Portugal
6. Simsky A, Sleewaegen JM, De Wilde W et al (2005) Overview of Septentrio's galileo receiver development strategy. In: Proceedings of ION GNSS, Long Beach, CA, pp 1888–1895

7. Soellner M, Briechle C, Hechenblaikner G et al (2007) The BayNavTech™ Signal Experimentation Facility (BaySEF™) is ready for assessing GNSS signal performance. In: Proceeding of the ION GNSS, Fort-Worth, Texas, pp 1065–1072
8. UNOOSA (2010) Current and planned global and regional navigation satellite systems and satellite-based augmentation systems [EB/OL]. http://www.unoosa.org/pdf/publications/icg_ebook.pdf. Accessed 29 June 2010
9. Yang Y (2010) Progress, contribution and challenges of compass/BeiDou satellite navigation system. *Acta Geodaetica Cartogr Sin* 39(1):1–6
10. Liu L, Zhan X, Liu W et al (2011) Assessment of radio frequency compatibility between compass and GPS. *Acta Geodaetica Cartogr Sin* 40(Sup.):11–18
11. Hu Z (2013) BeiDou satellite navigation system performance evaluation theory and experimental verification. Ph.D. thesis, Wuhan University, Wuhan, China
12. He C (2013) Study and analysis of the ranging performance influences the quality of GNSS signal evaluation method. Ph.D. thesis, National Time Service Center, Chinese Academy of Sciences, Xi'an, China
13. Hu X, Tang Z, Zhou H et al (2009) Analysis on design principles of GPS and Galileo signal structure. *Syst Eng Electron* 10:2285–2293
14. Hegarty C (1999) Evaluation of the proposed signal structure for the new civil GPS signal at 1176.45 MHz. MITRE center for Advanced Aviation System Development, Working Note
15. Yang Z, Huang Z, Geng S (2011) Novel tracking loop of BOC signal based on subcarrier tracking. *J Beijing Univ Aeronaut Astronaut* 37(2):245–248
16. Lohan ES (2010) Analytical performance of CBOC-modulated Galileo E1 signal using sine BOC (1, 1) receiver for mass-market applications. In: Proceeding of IEEE/ION PLANS, Indian Wells, CA, USA, pp 245–253
17. Vejražka F, Kovář P, Kačmařík P (2009) Galileo AltBOC E5 signal characteristics for optimal tracking algorithms. *Int J Mar Navig Saf Sea Transp* 4:37–40
18. Betz JW, Kolodziejski KR (2009) Generalized theory of code tracking with an early-late discriminator Part II: noncoherent processing and numerical results. *IEEE Trans Aerosp Electron Syst* 45(4):1557–1564
19. Kaplan ED, Hegarty CJ (2005) Understanding GPS: principles and applications. Artech House, Boston
20. Betz JW (2001) Binary offset carrier modulations for radionavigation. *Navigation* 48(4):227–246
21. Tang Z, Hu X, Huang X (2009) Analysis of multipath rejection performance in GNSS signal design. *J Huazhong Univ Sci Technol (Nat Sci Ed)* 5:1–4
22. Hein GW, Avila-Rodriguez J, Wallner S et al (2006) MBOC: the new optimized spreading modulation recommended for GALILEO L1 OS and GPS L1C. In: Proceedings of IEEE/ION PLANS, pp 884–892
23. Julien O (2005) Design of Galileo L1F receiver tracking loops. Ph.D. thesis, University of Calgary, Department of Geomatics Engineering, Calgary
24. Ross JT, Leva JL, Yoder S (2001) Effect of partial-band interference on receiver estimation of C/N0: measurements. In: Proceedings of ION NTM, Long Beach, CA, pp 829–838

Chapter 45

Research of Satellite Receiver Anti-replay Attack Techniques

Mengjiang Liu, Zhixin Deng and Li Jun

Abstract With the broad application of satellite navigation technique in the society and economy development, the satellite navigation technique has been facing with more and more hidden dangers of being attacked in such key fields as finance, public security, civil aviation and public rescue. In light of the vulnerability of satellite navigation receiver against replay attack in the above fields, this paper proposes several anti-replay attack techniques of low complexity, i.e., inertial positioning test, clock skew test and Doppler shift test. The simulation results show that Doppler shift test can resist replay attack effectively without additional hardware to the receiver. In addition, compared to SNR test, absolute power test and the other techniques, Doppler shift test has the advantages of low implementation difficulty and high adaptability, which can provide technical support for the security applications of satellite navigation technology in the fields of great concern.

Keywords Fields of great concern · Replay attack · Doppler shift test

45.1 Introduction

Along with the advancement of satellite navigation technology, it has been playing more and more important roles in many social and economic fields such as transportation, finance, mobile communication, electric power transmission, civil aviation and public security. However, the civil applications of satellite navigation technology are vulnerable to illegal or even terrorist attacks in such fields as banking finance, public security and civil aviation due to insufficient anti-jamming capability; as a result, the public security and property security are threatened thereby. As one of major security threats to the civil applications of satellite

M. Liu (✉) · Z. Deng · L. Jun
The 54th Research Institute of China Electronic Technology Group Corporation,
Shijiazhuang 050081, Hebei, China
e-mail: 343769896@qq.com

navigation system, replay attack rebroadcasts the received satellite signals after a time delay and amplification, which are very likely to be received and processed by legal satellite receivers, because the rebroadcasted signals are identical with the true satellite signals in structure. Since the rebroadcasted signal is different from the true signal in arrival time, a satellite receiver, once received and processed the rebroadcasted signal, will output a wrong positioning result or even positioning failure. Compared with blanket jamming that disables satellite receiver from positioning by broadcasting high-power signals, replay attack keeps broadcasting the signals of the power similar to or a little higher than that of the true satellite signal, saving much power. Replay attack is undetectable by the civil navigation techniques that have no interference positioning and direction-finding capability because of low power of the jamming signal. In addition, a well-designed replay attack may induce the target satellite receiver to output a desired positioning result for hostile purpose [1]. Therefore, concerning about the serious threats to the civil applications of satellite navigation system, it is of great importance to research satellite receiver anti-replay attack techniques.

45.2 Replay Attack Against Satellite Navigation System

45.2.1 Replay Attack Modes

In the development of modern economic society, large numbers of infrastructures, instruments and facilities depend on GNSS positioning, navigation and time (PNT) service. Because of the vulnerability of GNSS itself however, these infrastructures, instruments and facilities are susceptible to vicious interferences or even controlled. Compared with military navigation signals, civil navigation signals are usually unencrypted. Even if very few civil navigation receivers adopt encryption protocols and assume the private keys are uncrackable [2], it is still possible to interfere with the positioning result of GNSS receivers by rebroadcasting the received satellite signals [3]. The jamming equipments may be divided into three categories [4] in terms of the hardware configuration or the transmission capability of GNSS interference signals.

- (1) One or more jamming signal generators keep broadcasting at a constant power P_i^c and frequency f_i^c .
- (2) One or more jamming signal generators have the capability of automatically changing the transmitting frequency f_i^j with time, where j represents the broadcasting frequency of jamming signal generator.
- (3) More than one jamming signal generators have the transmission capability of changing the above parameters in a self-adaptive manner in addition to rapid communication capability between jamming nodes.

All the above-mentioned three types of interference sources are capable of receiving and recording GNSS signals and navigation messages in a long period of

time. The jamming capability of a jamming signal generator can be characterized by jamming radius R . The jamming signals are receivable within the area defined by the jamming radius, i.e., the attack area. Obviously, the more interference sources are, the higher the jamming power is, the larger the potential effect is and the more satellite receivers are affected.

Before a device equipped with satellite receiver gets into an attack area, the receiver is able to lock the desired GNSS signals and hold for a period of time. The emphases in this paper will not be put on the frequency of receiver entering an attack area or the conditions being attacked, but on the defense performance of different guarding mechanisms against replay attack and expressing the jamming effect with the time when a satellite receiver starts to lock replay attack signal instead of normal navigation signal.

For jammers, it is not practical to take control over a receiver since it is just mounted on equipment. However, it is relatively easy to carry out an attack to a selected position in the running process of the equipment. Here, the said attack against receiver refers to the attack received in the cold start of the receiver or in the searching and acquiring process of GNSS signal after it is initially started [5]. It must be noted that the attack model concerned here is not the worst case.

45.2.2 Replay Attack Against Satellite Navigation Receiver

Replay attack broadcasts jamming signal the same as the true satellite signal and cheats the legal navigation receiver that the received signal is from a visible satellite. The precondition to achieve this target is to force the receiver loss of lock from the true satellite signal, which is achievable by broadcasting jamming signal of power high enough to overwhelm the GNSS signal. This type of interference source is inexpensive and easy to implement, e.g., one jamming signal generator of 1 W transmitting power can overwhelm the GNSS signal within the area of 35 km radius. And then, jamming signal generator can initiate a replay attack against receivers by broadcasting replay signals of the same frequency as the legal GNSS signal but of slightly higher power. The off-the-shelf satellite signal simulator is able to generate more than 10 channels of replay signals carrying navigation data simultaneously. Alternatively, replay attack is achievable simply by receiving and rebroadcasting the true satellite navigation signals. Once a receiver continuously locks the replay signals, its PNT result will surely be affected, which consequently deteriorates the positioning error of the receiver, or even misleads the receiver.

Besides, the navigation blind zone in the coverage area and coverage time might be illegally used for jamming purpose, for a navigation receiver is impossible to lock the navigation signals from more than four visible satellites in the blind zone of GNSS coverage area. This situation usually takes place in an urban area due to topographic effect, e.g., signal blocked by obstacles like road tunnel or high-rise building, which however is not considered in this paper.

The hostile replay attack against receivers usually happens right after a navigation signal is down-converted. A replay signal contains an in-phase component and an orthogonal component.

$$I(t) = a_i C_a(t) M(t) \cos(ft) \quad (45.1)$$

$$Q(t) = a_q C_a(t) M(t) \sin(ft) \quad (45.2)$$

where, C_a represents C/A code, $M(t)$ represents navigation message, coefficients a_i and a_q represent signal attenuation.

The jamming signal generator usually takes the amplification coefficients a_i and a_q so that the received signal power will be greater than the legal GNSS signal and more easier to be locked by navigation receivers [6].

45.2.3 Replay Attack

When a GNSS signal is acquired, the attacker will broadcast it after a time delay $t_{replay} = t_{replay}^{\min} + \tau$, where $\tau \geq 0$ and $t_{replay}^{\min} > 0$, which specifically depends on the configuration and capability of the jamming signal generator.

When received a legal GNSS signal, the interference source usually transfer it to another location within the coverage without any modification [7], which saves the trouble to check if the GNSS signal is encrypted or not. The replay attack capability can be characterized by two features: the capability of receiving, recording and replaying GNSS signal and the time delay t_{replay} between receiving and replay.

The time delay t_{replay} between signal receiving and replay depends on the relevant parameters of the interference source, such as the distance between the hostile receiver and the replay equipment, physical propagation of signal and sometimes the time delay spent on decoding GNSS signal. In t_{replay} , $t_{replay}^{\min} > 0$ is for certain for the attacker, and the additional time delay $\tau > 0$ is up to the attacker; therefore, the total replay time delay is $t_{replay} = t_{replay}^{\min} + \tau$. The schematic diagram of replay attack is given in Fig. 45.1. As shown in the diagram, the navigation information is recorded starting from detection until the navigation signal is received. The lead code 10001011 takes 8 chips plus the decoding time of the first bit, which makes $t_{replay}^{\min} = 2$ ms. Since the bit rate is 50 bit/s, it means the hostile receiver has to take 20 ms to receive the first bit [8].

For different satellite navigation signals, attacker may take different t_{replay} . Even blind transmission that aims at all the navigation signals with the same time delay may achieve good jamming effect. t_{replay} affects the error magnitude of PVT result produced by the attacked receiver.

The influence of replay attack duration to the attack effect is shown in Fig. 45.2.

- (1) Positioning error here refers to the distance error between the real position of a navigation receiver and the output position after being jammed.

Fig. 45.1 Schematic diagram of replay attack

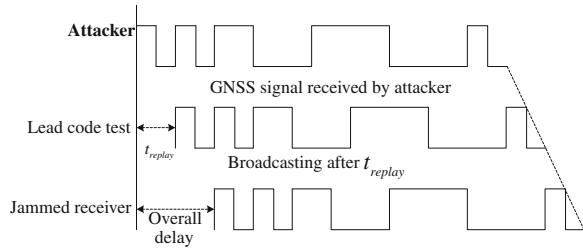
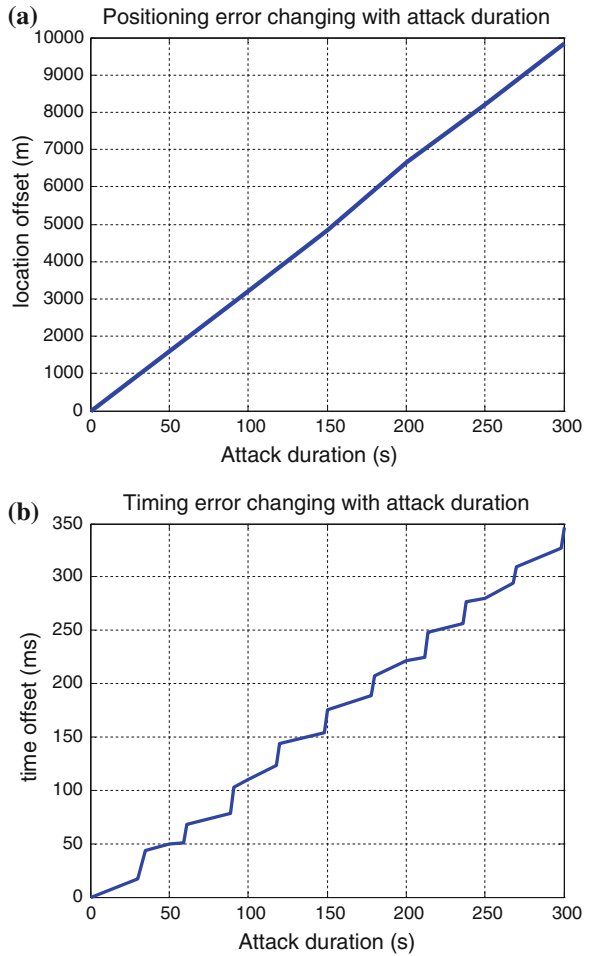


Fig. 45.2 Curve of replay duration and attack effect.
a Positioning error changing with attack duration.
b Timing error changing with attack duration



(2) Timing error refers to the deviation between the true time and the time provided by time service.

For the navigation receiver that locks replay signals, its positioning error grows along with the increase of t_{replay} . Specifically, the pseudo-range error will grow

300 m approximately when t_{replay} increases by 1 ms. The timing error can be taken as an additive effect from hostile jamming effort, which is very easy to be ignored for the magnitude of timing error is generally in millisecond. If t_{replay} is constant, the timing error will accumulate continuously and grow up finally whenever the jammed navigation receiver is resynchronized, especially at the end of the navigation message that lasts about 30 s.

45.3 Defense Mechanisms

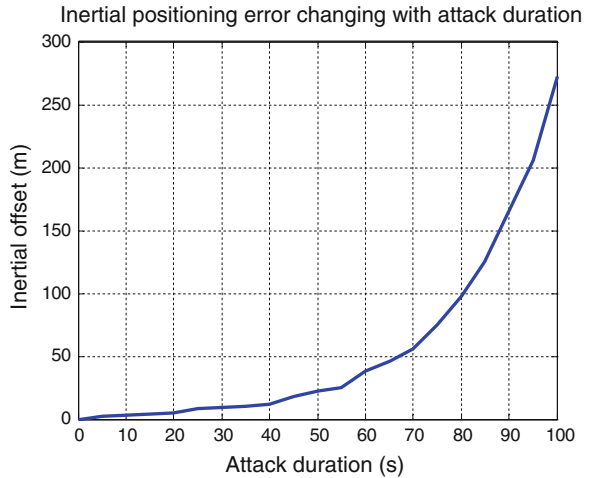
A comparison is made in this paper among the three types of defense mechanisms and effects against replay attack based on a 3-step concept. Firstly, carry out data acquisition about the given parameters in the period of time when a navigation receiver is not considered under attack. This stage is known as normal mode. Secondly, based on the data collected in normal mode, the navigation receiver provides the predicted values about the relevant parameters at next moment. Finally, get into warning mode when a navigation receiver suspects it is under attack. In this mode, the navigation receiver will compare the predicted value with the calculated value from GNSS. If they are different and beyond the threshold defined by the protocol, it can be certain that the navigation receiver is really under attack. In such a case, the navigation receiver will reject all the PVT results in warning mode. If the difference between the calculated value and the predicted value is not beyond the threshold defined by the protocol, it is considered that the PVT result is acceptable and the navigation receiver will go back into normal mode [9].

Concerning the three receiver parameters, i.e., positioning result, timing result and Doppler shift, three replay attack detection mechanisms are proposed accordingly: inertial positioning test, clock error test and Doppler shift test. It must be noted that all these three detection mechanisms are dependent on the prior information acquired in normal mode. To validate the three proposed detection mechanisms, a special receiver was used to collect data and output the observation and navigation data into RINEX format. In addition, the PVT result was input into the Matlab as per the interface protocol of the receiver so as to verify the pseudo-range, Doppler shift and phase measurement results with RINEX data. The 300 s movement of the receiver was simulated with the position updating period set to 1 s.

45.3.1 Inertial Positioning Test

When the receiver is switched into warning mode, it will provide the predicted positioning result in case of replay attack based on the position information in the PVT result. If the predicted positioning result matches the PVT result obtained

Fig. 45.3 Inertial positioning error changing with attack duration



under replay attack, the receiver returns to its normal mode. Here, two approaches are considered for position prediction: inertial transducer and Kalman filtering.

Inertial transducer such as altimeter, velometer or odometer can work out the position of receiver without GNSS; however, the prediction error of inertial transducer will accumulate along with the time going, and consequently degrade the positioning accuracy. The variation curve of inertial positioning error changing with time when the receiver works in warning mode is shown in Fig. 45.3. The jammed receiver has to take the positioning results provided by the inertial transducer as the positioning result under replay attack, though the accuracy of the inertial transducer keeps going down. The positioning errors of inertial transducer are shown in Fig. 45.4, where one curve represents the actual track and the other curve represents the predicted track under replay attack. It is clear that an obvious difference exists between the two curves after a very short period. Conclusively, inertial positioning test can not defend against replay attack satisfactorily. Another more effective approach is to process the positioning information acquired in normal mode with Kalman filtering technique, and the predicted positioning result is obtained with the equation below [10]:

$$S_{k+1} = \Phi_k S_k + W_k \tag{45.3}$$

where, S_k represents the system state, e.g., position (X_k, Y_k, Z_k) and velocity vector (V_{xk}, V_{yk}, V_{zk}), Φ_k represents transform matrix and W_k represents noise. A series of positioning errors for different motion tracks are shown in Fig. 45.5. The positioning error based on Kalman filtering appears linear increase under the condition of no GNSS, different from that based on inertial transducer only.

Generally speaking, the inertial detection mechanism is effective when the attack duration is very short; in other words, it can detect replay attack as long as the error

Fig. 45.4 Inertial transducer positioning track under and without replay attack

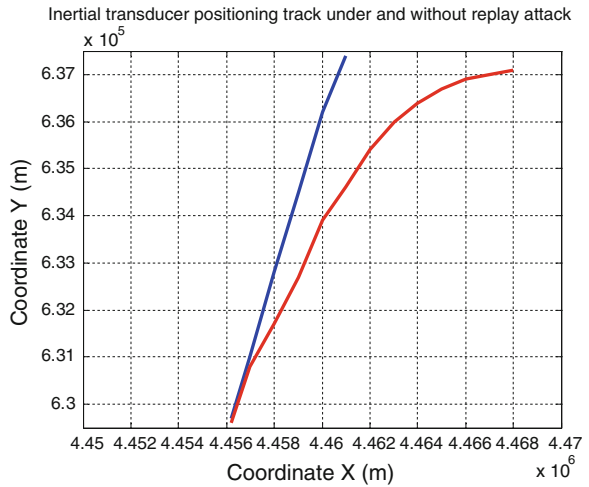
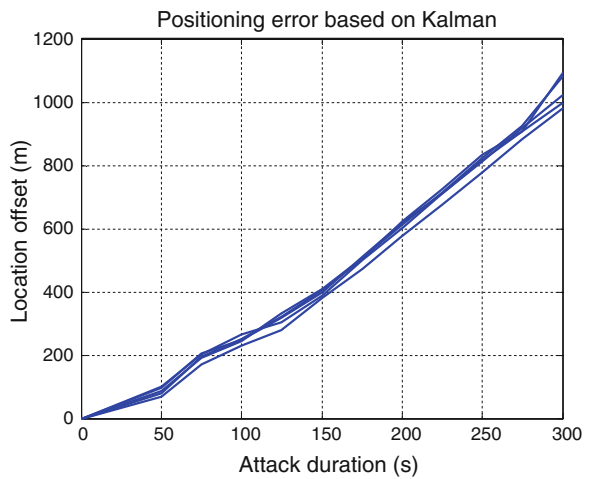


Fig. 45.5 Positioning error based on Kalman filtering changing with attack duration

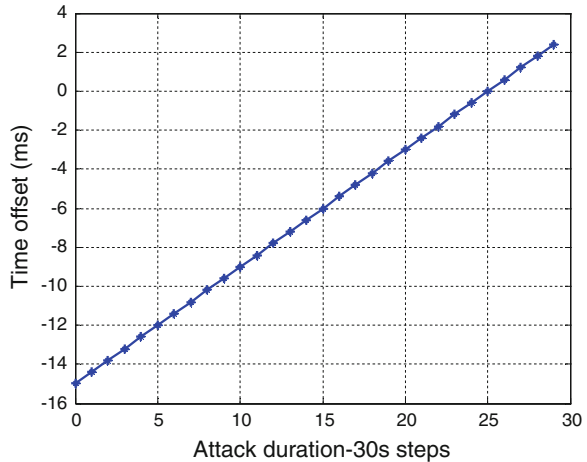


does not increase obviously. However, the detection for replay attack will fail when the error becomes too high.

45.3.2 Clock Error Detection

Generally speaking, every receiver has an inaccurate clock due to the shift of quartz crystal. If the receiving process of GNSS signal is interrupted, the oscillator will be switched from normal mode to hold mode. In hold mode, the timing accuracy is just related to the stability of the local oscillator. The working frequencies of quartz

Fig. 45.6 Timing error based on clock offset changing with attack duration



crystals in different clocks are somewhat different, which will lead to different receiver clock values slowly, i.e., skew error. As per the known research results, a quartz oscillator can maintain synchronization precision in millisecond for several hours, including the error resulting from random error and steady increase. As a matter of fact, in such a case, the hostile replay attack against GNSS signal has to insist several hours, e.g., 10 h, for success. However, the replay attack against receiver would be much easier if no high-stability clock is provided. As for the receiver used in the simulation test, the clock errors are provided at intervals of 30 s in Fig. 45.6. As shown in the graph, within the 900 s simulation period, the receiver is obviously instable and the clock error stays in millisecond. Therefore, the receiver would be misled by replay attack as long as the attack lasts a few minutes till the receiver is forced to get a clock error of 20–32 ms. It must be noted at last that no consideration is made here to synchronizing the receiver with GNSS by other means, e.g., the receiver can acquire precise time if it is linked to a network and supports NTP: however, this exceptional case occurs very seldom; therefore, the best approach against replay attack is still to use high-stability clock.

45.3.3 Doppler Shift Test

If the normal signal transmitting frequency and the Doppler shift of the received GNSS signal are known, the receiver can predict the Doppler shift value at next moment. Once the GNSS signal is locked again, the calculated value will be compared with the predicted value. If they are different and beyond the preset threshold, it can be certain that the navigation receiver is really under attack and the calculated value will be rejected. The best advantage of this detection method is that the Doppler shift changes steadily and stays at very low error for a long period of

time, while the error based on inertial positioning detection will grow with time in exponent form.

It is well known that Doppler shift is generated by the relative motion between a receiver and a satellite, and receiver can work out the satellite velocity using Ephemeris and the orbit model. The signal frequency received by a receiver can be estimated with the equation below:

$$f_r = f_t \cdot \left(1 - \frac{v_r \cdot a}{c}\right) \quad (45.4)$$

where, f_t represents the transmitting frequency, f_r represents the received signal frequency, v_r represents the relative velocity vector between satellite and receiver, c represents the light velocity and the product $v_r \cdot a$ represents the radial component of the relative velocity vector in the LOS direction of satellite. Similarly, If the calculated frequency shift are different from the predicted frequency shift and beyond the preset threshold, it can be certain that what received by the receiver is a jamming signal. The ephemeris contains such satellite information as the rough position (X_{S_i} , Y_{S_i} , Z_{S_i}), time and number of weeks (W_N , t).

Since the carrier frequency is very high and the satellite moves very fast, a large Doppler shift (± 5 kHz) will come up and change very quickly. The receiver oscillator will roughly gain a frequency shift ± 3 kHz, and the resulting frequency shift will go up to ± 9 kHz. When the frequency shift is unknown, the receiver has to search signals within this frequency range. The maximum change rate of Doppler shift resulting from the relative motion between satellite and receiver is about 40 Hz/min. These changes are linear for each satellite. The variation of Doppler shift can be estimated with reference to the receiver motion speed if the receiver is mobile.

By means of simulation, this paper analyzes the Doppler shift of every visible satellite, with the simulation duration of 300 s for the convenience of comparing the simulation result with the ones that use other defense mechanisms. As shown in Fig. 45.7, based on the data collected by the receiver used in the simulation test, the change of Doppler shift is within the range of ± 20 Hz and appears linear variation roughly. It suggests that it is possible to predict the Doppler change rate at next moment and the frequency shift per second as long as the sampling rate is high enough. In practice, the requirement is almost met if sampling keeps going on within 50 s at the sampling rate of once per second. The change rate of frequency shift for each satellite S_i can be worked out with the equation below:

$$r_i = \frac{dD_i(t)}{dt} \quad (45.5)$$

The jamming signal generators are usually still on the ground or in motion at a low speed up to 3 km/s relative to satellite. Therefore, it is impossible for the attacker to get the same Doppler shift as that of the satellite unless the attacker changes the transmitting frequency to make one of the receivers to receive the same Doppler shift as that from satellite signal. If it is this case, it will be relatively easier

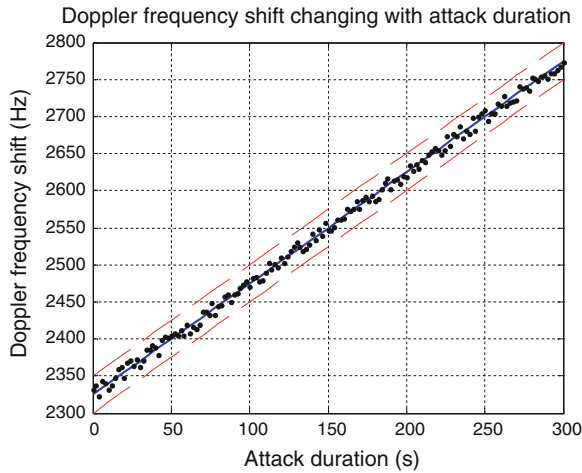


Fig. 45.7 Doppler frequency shift changing with attack duration

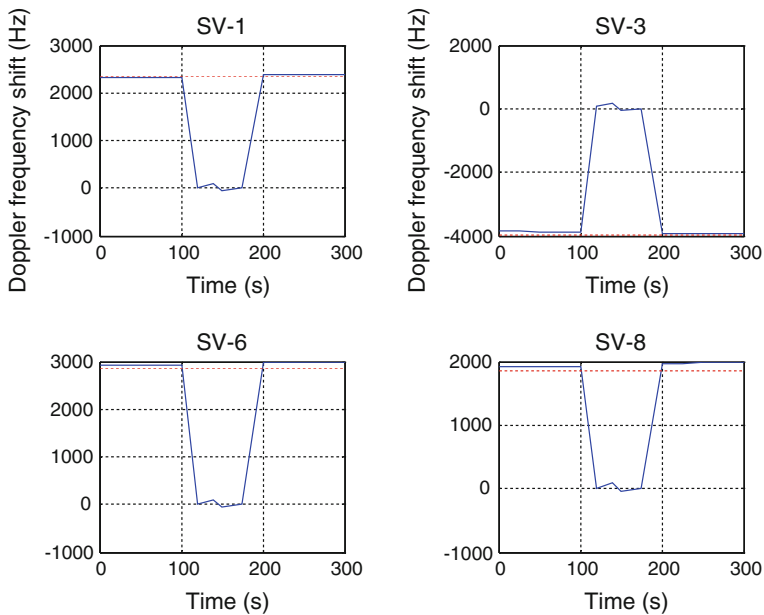


Fig. 45.8 Doppler frequency shift detection against unsophisticated adversary

to detect the interference source that is unsophisticated. Figure 45.8 shows a simulated replay attack against a navigation receiver from a relatively unsophisticated interference source. The red dashed line represents the predicted Doppler shift values and the solid line represents the measured frequency shift values. It can be

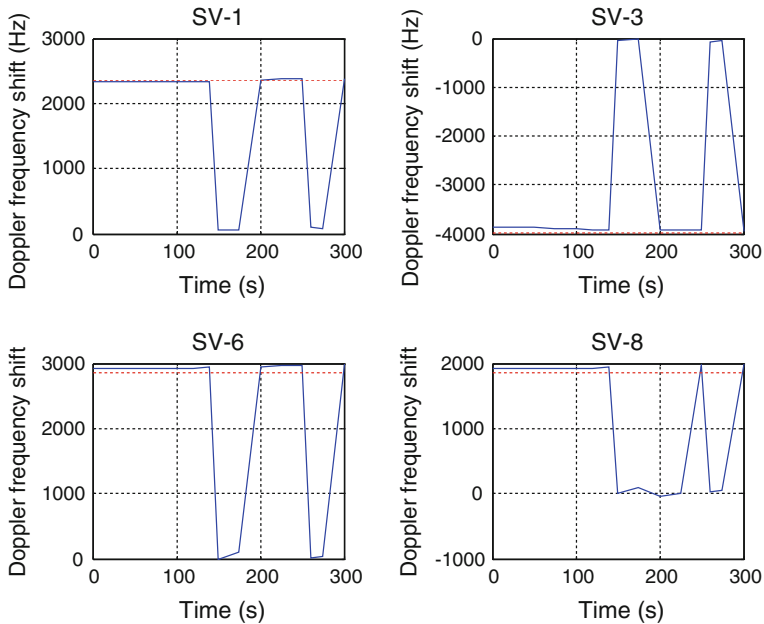


Fig. 45.9 Doppler frequency shift detection against sophisticated adversary

seen that there is obvious difference between the two lines in the period of 120–170 s, by which the hostile jamming is detectable. Figure 45.9 shows a simulated replay attack against a navigation receiver from a sophisticated interference source. The sophisticated interference source is able to predict the Doppler shift of the receiver end and change its transmitting frequency as per the predicted transmitting frequency. If the interference source fails to predict the position and the moving speed of the target receiver accurately, there will be obvious difference between the predicted value and the measured value. As shown in Fig. 45.9, the replay attack is detectable though it starts at 160 s around.

45.3.4 Technical Comparison

The other popular replay attack detection techniques include SNR test and absolute power test. The Table 45.1 provides a comparison among replay attack detection methods in terms of attack feature, implementation difficulty, effect, required capability and adaptability.

As shown in the comparison above, among all the replay attack detection methods, Doppler shift test is characterized by low implementation difficulty, good effect and high adaptability, applicable to detection for replay attack against satellite navigation receiver using low-speed interference source.

Table 45.1 Comparison of replay attack detection techniques

Anti-replay attack techniques	Attack features	Implementation difficulty	Effect	Required capability	Adaptability
SNR test in signal processing layer	Replay attack signals of high SNR	Low	Intermediate	SNR test	Intermediate
Absolute power test	Higher amplitude	Low	Intermediate	Absolute power is calibrated	High
Power change	The closer to the interference source, the faster the power changes	Low	Low	Monitoring SNR dynamically	Low
Dual-frequency power comparison	Attack against one single frequency	Intermediate	Low	Receivable to dual frequency signal	Low
DOA comparison	Attack signal coming from the same direction	High	High	A number of receiving antenna	High
Delay detection	Replay signal having a time delay	Intermediate	Intermediate	Analysis of signal arrival time	Low
Consistence test of code and carriers rate	Mismatch between code and carriers rate of replay signal	Low	Low		Low
AGC gain test	Replay attack signal power greater than noise power	Low	High	AGC gain is calibrated	Intermediate
RN/RD dual mode		Intermediate	High	Dual-mode function	High

45.4 Conclusion

Concerning the existing vulnerability of navigation receiver against replay attack, a quantitative analysis was made to the effect of replay attack to the positioning error and timing error of navigation receiver. On that basis, quantitative and qualitative analyses were given to the performance of three replay attack detection methods, i.e., inertial positioning test, clock error test and Doppler shift test. It is concluded that the Doppler shift test technique is capable of detecting replay attack effectively whether the interference source is unsophisticated or sophisticated. In the future, it is planned to further optimize and universalize the simulation framework in addition

to more consideration to be given to the effects of countermeasures. Besides, an in-depth study will be made to various replay attack detection methods in terms of response time, algorithm as well as software and hardware complexity.

Acknowledgments Supported by National “863 Plan”, No. 2012AA121801.

References

1. Deputy Secretary of Defense Memorandum (2004) Navigation warfare implementation guidance, 17 Nov 2004
2. Wesson K, Rothlisberger M, Humphreys T (2012) Practical cryptographic civil GPS signal authentication. *Navigation* 59(3):177–193
3. DoD Directive 4650.05 (2008) Positioning, navigation, and timing (PNT)
4. Humphreys TE, Ledvina BM, Psiaki ML et al (2008) Assessing the spoofing threat: development of a portable GPS civilian spoofer. In: Proceedings of the ION GNSS international technical meeting of the satellite division, vol 55, p 56
5. Shepard D (2011) Characterization of receiver response to spoofing attacks. University of Texas at Austin, Austin
6. Pozzobon O, Canzian L, Danieletto M et al (2010) Anti-spoofing and open GNSS signal authentication with signal authentication sequences satellite navigation technologies and European workshop on GNSS signals and signal processing (NAVITEC). In: 2010 5th ESA workshop on IEEE, pp 1–6
7. Huang L, Tang X, Wang F (2011) A research of anti-spoofing methods for satellite navigation receiver. *J Wuhan Univ (Information Science Edition)* 36(11):1344–1347
8. Huang L, Lv Z, Wang F (2012) A research of spoofing interference against GNSS Receiver. *Acta Astronaut* 33(7):884–890
9. Montgomery PY, Humphreys TE, Ledvina BM (2009) A multi-antenna defense: receiver-autonomous GPS spoofing detection Inside. *GNSS* 4(2):40–46
10. Wesson K, Shepard D, Humphreys T (2012) Straight talk on anti-spoofing: securing the future of PNT. *GPS World* 23(1)

Chapter 46

Detect Techniques and Test Analysis on Navigation Signal Code Correlation Peak

Xiaochao Feng, Yongheng Fu, Lei Gong and Jiancheng Liu

Abstract The signal quality impacts the precision of the user's Positioning, Navigation and Timing (PNT) provided by the satellite navigation system. The satellite navigation system must monitor the navigation signal quality and gives alarm. During operating of the system, the signal code correlation peak detection is an important work in monitoring, evaluation and control for the navigation signal quality. According to the structure of navigation satellite payload, ICAO (International Civil Aviation Organization) provides the 2OS (2nd-Order Step Threat Model) abnormal signal model, and gives code correlation peak for every abnormal signal. The paper analyses several correlation peak detect techniques based multi-correlator, and gives detection results of the BeiDou system's navigation signal using the especial navigation signal monitoring system of the BeiDou satellite navigation system.

Keywords Navigation signal · Correlation peak · Detecting test · BeiDou satellite navigation system

46.1 Introduction

Satellite navigation systems have been widely used in various fields of national economy, science, social development, and other military operations. Signal quality is directly related to the users' accuracy in various fields available by the satellite navigation systems. the navigation signal quality monitoring and evaluation has become an important work of the satellite navigation system development, building, operation and management, getting attention at home and abroad. Such as: the GNSS Monitoring Stations established by Stanford University GPS laboratory (GPS Lab), the navigation signal monitoring and evaluation observatories established by European Space Technology Centre (ESTEC), the satellite navigation system testing and evaluation

X. Feng (✉) · Y. Fu · L. Gong · J. Liu
BeiJing Satellite Navigation Center, Beijing 100094, China
e-mail: fengxc_bd2@sina.com

center our established by China Aerospace Science and Industry Corporation (CASIC). These institutions monitors and evaluates the space navigation signal quality of the Globe satellite navigation system (GPS, Galileo and Compass) [1].

Correlation peak detection is an important part of the navigation signal quality monitoring. By correlation peak detection can detect anomalies pseudo-code or carrier of navigation signal and provide early warning information for the system.

The paper analyzes several correlation peak detect techniques based on the 2OS abnormal signal model proposed by ICAO, and carries out BeiDou’s space navigation signal correlation peak detect test and analysis.

46.2 Abnormal Signal Model

Nonlinear satellite signal transmission link will cause the chip waveform signal distortion, the most typical example is the GPS SV19 satellite signal anomalies in 1993. In order to explain the anomalies on the SV19 satellite signals, researchers have give three models: a simple model, MEWF (Most Evil Waveform Threat Model) model and 2OS (2nd-Order Step Threat Model). The simple model is that a standard signal is superimposed another signal, not fully reflects all the characteristics of the abnormal signals. MEWF model is defined as a receiver for a particular user will have the maximum differential signal waveform pseudorange errors. Dr. Mitelman and Enge et al. derived in detail the mathematical expression. However, this model is non-causal and difficult to achieve, so the ICAO and Aviation Committee don’t adopt the model. In contrast, 2OS model comprehensively reflects all the satellite circuit failure. General mathematical model of the navigation satellite’s payload shown in Fig. 46.1 [2].

Wherein the signal generating unit generates the navigation baseband signal, the bandwidth of the digital filter for transmitting signals bandwidth; frequency generation and modulation unit to convert digital signals to analog signals, and by the several stages of the signal frequency modulated onto a carrier frequency; High power amplifier to amplify the signal power to complete the work in a saturated state generally are commonly used in traveling wave tube amplifier (TWTA) and solid state power amplifier (SSPA); output multiplexer (OMUX Output

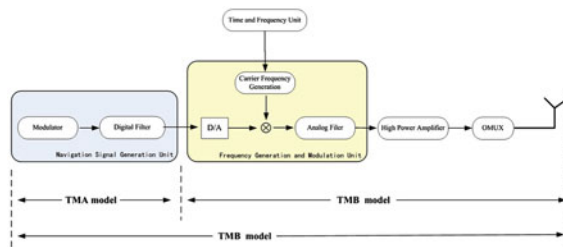


Fig. 46.1 The navigation satellite payload model diagram

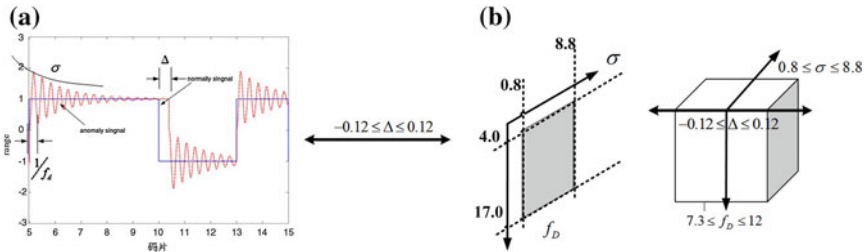


Fig. 46.2 ICAO model parameters. a Meaning, b range

Multiplexer) completed a similar frequency of each navigation signal combiner, coupled to the same antenna output. Each component of the satellite payload abnormality may may cause abnormal signal distortion. According to the various components of the payload, 2OS model divides in reasons the abnormal signal into three categories: digital circuit fault (Threat Model A), an analog circuit fault (Threat Model B), and a combination of both (Threat Model C). The three model is able to cover almost all possible fault signal anomalies. This model is considered to be a standard anomaly signal model by ICAO, also known as the ICAO model. There are three key parameters in the model, namely chips early/late time (chip), damping coefficient (M/Npers/s) and damping oscillation frequency (MHz), the meaning and the range of each parameter are shown in Fig. 46.2a, b.

1. TMA model

TMA model reflects the satellite payload errors generated in a digital circuit, is modeled as a rising or falling edge of the Δ code chip is advanced or delayed chips, and is not affect the analog subsystem. And the time-domain form of the correlation peak shown in Fig. 46.3, the figure gives in the case of delay 0.3 chips. As can be seen, due to the delay of the falling edge of the chip, resulting in a correlation peak appears flattened phenomenon.

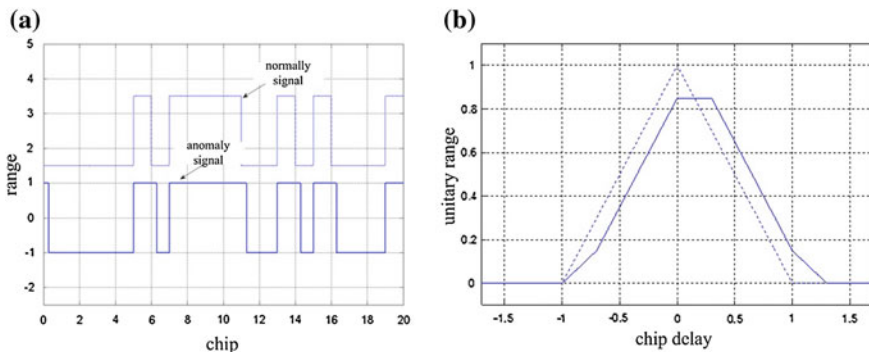


Fig. 46.3 Waveform in time domain and the correlation peak of TMA

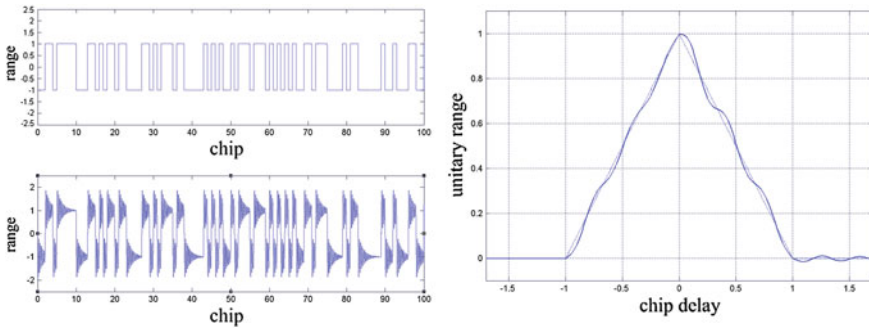


Fig. 46.4 Waveform in time domain and the correlation peak of TMB

2. TMB model

TMB error model can be represented by a second-order system response, the waveform in time domain and correlation peak shown in Fig. 46.4. There can be seen, the damped oscillation chip waveform makes the correlation peaks deformation phenomenon.

3. TMB model

TMC model for the combination of TMA and TMB, the waveform in time domain and the correlation peaks as shown in Fig. 46.5. There can be seen, the damped oscillation chip waveform makes correlation peak of the multi peak phenomenon.

In short, the ICAO model is mainly composed of three parameter. TMA by early/late parameter modeling, change code rising or falling edge of the digital signal is changed chips wide, flat-top can make correlation peak effect; TMB by modeling the resonant frequency f_d and the damping factor σ , with a second-order shocks to mimic analog circuit fault, the two parameters can adjust the peak distortion or error correlation peak; TMC is a combination of both TMA and TMB, by Δ , f_d and σ work together to regulate, as shown in Fig. 46.2.

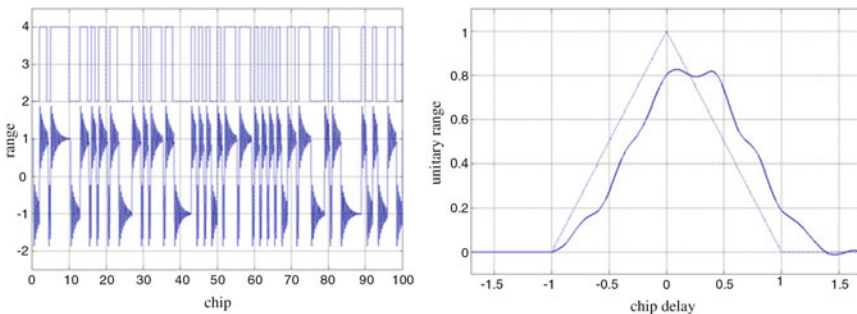


Fig. 46.5 Waveform in time domain and the correlation peak of TMC

46.3 Correlation Peak Detection Techniques

Correlation peak detecting of major multi-correlator technique with increasing multiple groups of correlator in the tracking loop, the method currently used software receiver [3–6]. The monitoring receiver with multi-correlator is associated with N channels, keeping the fixed chip spacing between each channel and real-time channel correlator, as shown in Fig. 46.6. Detection channel can output each channel correlation value of the received signal with the local signal different chip spacing, judging by the correlation peak symmetry and smoothness of the correlation values to determine the composition of the signal is abnormal.

In order to better reproduce the correlation peak of signal, need to join multiple correlator channel, thus greatly increasing the complexity of the receiver, and greatly increases the processing time.

Multiple correlation receiver output a plurality of correlation values of local pseudo-code associated with the received signal spacing, I_{-x} referred to as output to the respective early correlators, I_x referred to as the late output of each correlator, wherein $x = 1, 2, \dots, N$ is the number of the multi-correlator. These correlation values are combined in some criteria to determine whether the signal is abnormal.

Criteria 1: Δ Detection

Δ Detection evaluate the difference between the symmetry of the correlation peak using the early and late correlation for the difference with the reference correlation, which is calculated as

$$\Delta_x = \frac{(I_{-x} - I_x) - (I_{-ref} - I_{ref})}{I_{prompt}} \tag{46.1}$$

wherein I_{-ref} and I_{ref} are respectively output reference branch tracking channel early and late correlation value, I_{prompt} is real-time tracking channels.

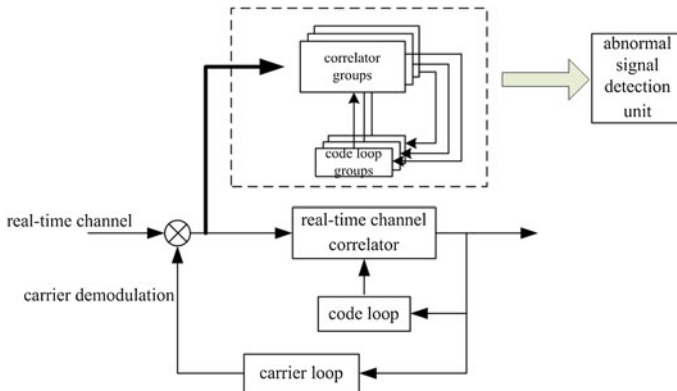


Fig. 46.6 Multi-channel correlation detection

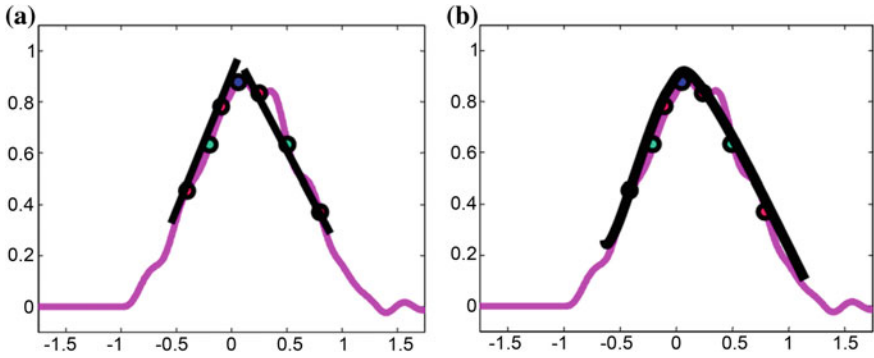


Fig. 46.7 Polynomial curve fitting. **a** First Order, **b** second-order

Criteria 2: Unilateral slope detection

The ratio of unilateral slope detect using early or late correlator output and real-time channel correlator output, which is calculated as

$$S_{-x} = \frac{I_{-x}}{I_{prompt}} \text{ or } S_x = \frac{I_x}{I_{prompt}} \tag{46.2}$$

Criteria 3: Polynomial fitting detection

Polynomial fitting is mainly the use of of the multi-correlator output value fitting, which can effectively attenuate the impact of noise and multipath, and then fitting a curve to determine a correlation peak is abnormal. One-order and second-order curve fitting curve shown in Fig. 46.7.

Setting the order of the curve fit is 2, then, for c_1, c_2, c_0 the curve of the coefficient; if the order is 1, ξ_1 and ξ_0, ξ_3 and ξ_2 for the coefficient curve, these coefficients solving the following formula.

Second-order

$$\begin{bmatrix} d_1 & -d_1 & 1 \\ \vdots & \vdots & \vdots \\ d_N & -d_N & 1 \\ 0 & 0 & 1 \\ d_{-N} & -d_{-N} & 1 \\ \vdots & \vdots & 1 \\ d_{-1} & -d_{-1} & 1 \end{bmatrix} \begin{bmatrix} c_2 \\ c_1 \\ c_0 \end{bmatrix} = \begin{bmatrix} R_{1,p} \\ \vdots \\ R_{N,p} \\ 1 \\ R_{-N,p} \\ \vdots \\ R_{-1,p} \end{bmatrix} \tag{46.3}$$

First Order

$$\begin{bmatrix} d_1 & 1 \\ \vdots & \vdots \\ d_N & 1 \end{bmatrix} \begin{bmatrix} \xi_1 \\ \xi_0 \end{bmatrix} = \begin{bmatrix} R_{1,p} \\ \vdots \\ R_{N,p} \end{bmatrix} \text{ and } \begin{bmatrix} d_{-1} & 1 \\ \vdots & \vdots \\ d_{-N} & 1 \end{bmatrix} \begin{bmatrix} \xi_3 \\ \xi_2 \end{bmatrix} = \begin{bmatrix} R_{-1,p} \\ \vdots \\ R_{-N,p} \end{bmatrix} \quad (46.4)$$

In the formula, $R_{N,p}$ is normalized value based on the real-time channel correlation values. Note that the first-order curve fitting is two lines, one is the early linear fitting correlation values, a linear fitting is late correlation value. By symmetry and smoothness of the curve to determine whether the signal correlation peak is abnormal.

In addition, we can also evaluate the correlation peak anomaly from the correlation loss [1, 7]. The correlation function is an important index to measure navigation performance. The digital signal is received by the removal of Doppler, get the baseband signal component and calculate the ideal code sequence with the local reference signal normalized cross-correlation, the following formula:

$$CCF(\varepsilon) = \frac{\int_0^{T_p} S_{BB-PreProc}(t) \cdot S_{Ref}^*(t - \varepsilon) dt}{\sqrt{\left(\int_0^{T_p} |S_{BB-PreProc}(t)|^2 dt\right) \cdot \left(\int_0^{T_p} |S_{Ref}(t)|^2 dt\right)}} \quad (46.5)$$

In the formula, $S_{BB-PreProc}$ represents the accumulated baseband signal after averaging processing; reference signal S_{Ref} represents the ideal base band local receiver generated replica code signal; integration time T_p generally corresponds to the master key period of the reference signal.

The correlation loss is a very important parameter associated with the navigation performance. The correlation loss refers to the loss of useful signal power relative to the total available power of the received signal in the correlation process.

$$P_{CCF}[dB] = \max_{\text{over all } \varepsilon} (20 \log_{10}(|CCF(\varepsilon)|)) \quad (46.6)$$

$$CL_{Distortion}[dB] = P_{CCF}^{Ideal-input}[dB] - P_{CCF}^{Real-input}[dB] \quad (46.7)$$

There are two main reasons causing the correlation loss, one is multiplexing a plurality of signal components on the same carrier frequency; two is the band limited and distortion caused by channel.

46.4 Correlation Peak Detection Tests

Based on satellite navigation signal quality monitoring equipment of the Beidou ground operation control system, we carried out the correlation peak detection tests of Beidou’s space navigation signals, the composition of the equipment as shown in Fig. 46.8. The test received Space navigation signals broadcasted by Beidou navigation satellite with the system master station 9 m turntable parabolic antenna, while carried out comparative analysis of receiving signal detection results to a standard signal provided by ground transportation control system simulation test system. RF acquisition device can be simultaneously performed on two channels signal acquisition, acquisition bandwidth of 50 MHz/s (I/Q channels). Signal processing and analysis subsystem using high-performance workstations, and devices via Ethernet DAQ devices, data storage playback device is connected, to achieve the digital signal correlation processing and detection analysis of the correlation peak.

In January 18, 2011, we carried out the correlation peak detection test on space navigation signals broadcasted by Beidou’s a satellite in orbit. Test of high gain directional antenna using 9 m turntable parabolic antenna of Beidou system master station, local standard signal generated by the Beidou navigation signal simulator.

In January 18th 19:22 to 19 days of 05:30 on I1 satellite correlation peak continuous monitoring of 10 h, and every 10 min interval time data collection, correlation peak analysis 60 data obtained in the detection curve, Fig. 46.8 shows the B1 navigation signals single and continuous correlation peak detection curve.

According to Δ detection technique of correlation peak analysis results as shown in Fig. 46.9, The left side of the figure for the detection results, right for satellite tracking of carrier to noise ratio curve and Doppler curve. As can be seen from the figure, the existence of a correlation peak asymmetry, and the main peak has additional sub-peak phenomenon, more similar to the TMB model.

Unilateral slope correlation peak detection value as shown in Table 46.1, the detection results show that the correlation peak to the left of the signal is better smoothing to the right with a certain asymmetry, the correlation peak exists, the

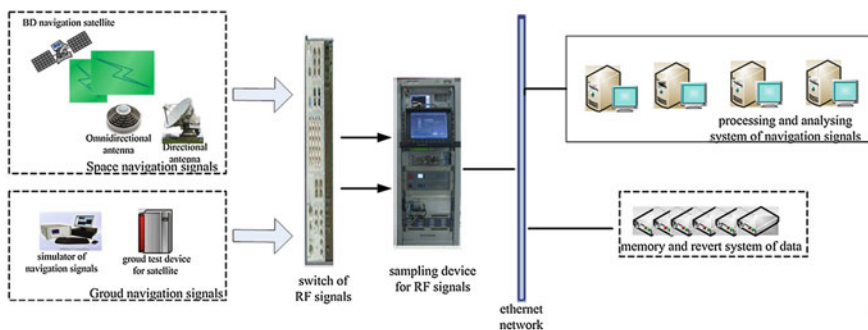


Fig. 46.8 Block diagram of BeiDou signal quality monitoring equipment

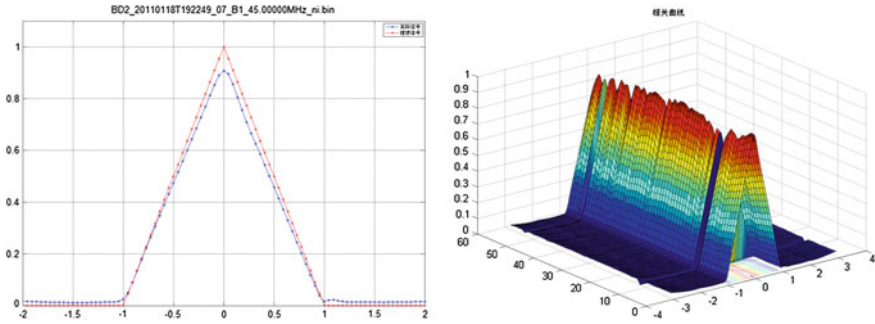


Fig. 46.9 Single and continuous curve correlation peak detection on B1 signal

Table 46.1 Unilateral correlation peak slope detection results

	Left	Right
Mean square error of the slope	0.0263	0.0317

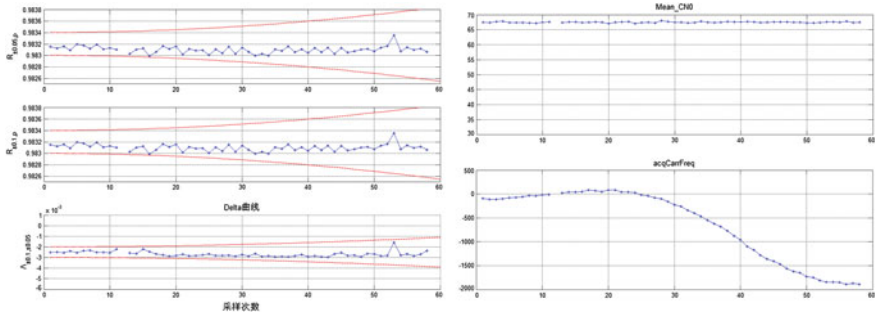


Fig. 46.10 Δ detection results on the correlation peak

right slope is slightly larger than the left slope, is similar with the TMB model (Fig. 46.10).

Polynomial fitting of the signal correlation peaks detection were analyzed using linear. Figure 46.11 shows the results of the data analysis, the left is spaced points early of the correlation fitting error value, the right is the late interval point fitting error value. As can be seen from Fig. 46.11 The late correlation intervals slightly larger than the earlier point fit error associated fitting error point, indicating that changes in the late related point of large fluctuation, the waveform is not smooth.

Figure 46.12 shows the satellite signal power spectrum and the main, sidelobe correlation peak detection results, it can be seen from the figure, the sidelobe power may be the cause of the correlation peak distortion.

The three kinds of detection techniques are demonstrated on the B1 navigation signal detection analysis results, B1 frequency navigation signal of the detected on-

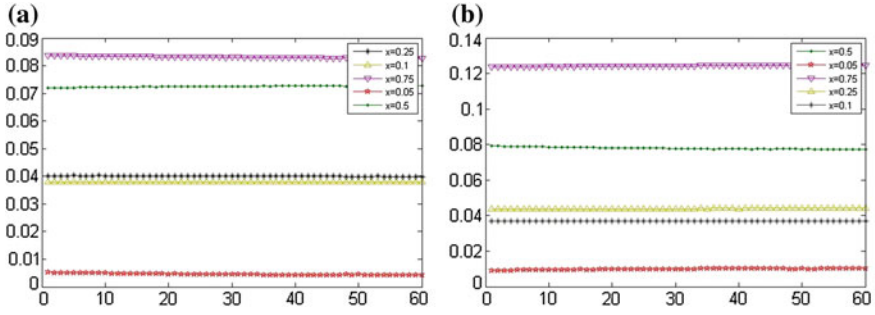


Fig. 46.11 Polynomial fitting error on correlation peak. a Fitting early, b fitting late

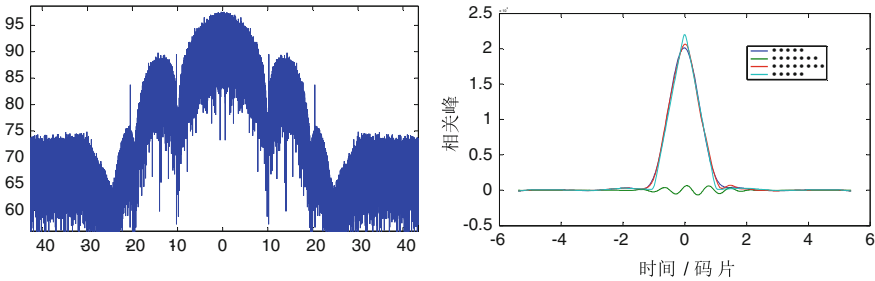


Fig. 46.12 Signal power spectrum and correlation peak detect results

orbit satellite possible correlation peak distortion phenomenon in the test period. at the same time, the signal power spectrum and sidelobe correlation peak detection analysis also indicates that the navigation signal power spectrum may lead to distortion of anomaly correlation peak, is more consistent with the 2OS model TMB model correlation peaks form.

46.5 Conclusion

In the correlation peak detection tests, due to the use of the 9 m turntable parabolic antenna receiving on-orbit satellite navigation signals, large diameter parabolic antenna has a narrow beam, highly directional characteristics, and set up the antenna height from the ground 14.7 m, to ensure that the signal is received and acquisition and processing is not affected by the ground reflected wave and multipath signals and other external factors, improve the accuracy of the results of the correlation peak detection and analysis.

References

1. Lu X, Zhou H (2010) Methods of analysis for GNSS signal quality. *Scientia Sinica Phys Mech Astron* 40(5):528–533
2. Jin G, Wang M, Fan J, Feng X (2012) Image of satellite navigation signal quality monitor. *J Guilin Univ Electr Technol* 32(5):358–363
3. Phelts RE (2001) Multicorrelator techniques for robust mitigation of threats to GPS signal quality. Stanford University, Palo Alto
4. Rooney E, Unwin M, Gatti G et al (2006) Giove A in orbit testing results. In: *Proceedings of ION GNSS-2006*, Fort Worth, Texas, pp 1535–1546, 26–29 Sept 2006
5. R. Eric Phelts, DM. Akos, P Enge (2000) Robust Signal Quality Monitoring and Detection of Evil Waveforms. In: *ION 2000*, pp 1180–1190
6. Jock RIC, Philip BB, John WC (2004) GPS signal quality monitoring system. In: *ION GNSS 17th international technical meeting of the satellite division*. Long Beach, CA, pp 2239–2245
7. Yang Z, Wang W, Meng Y, Geng S et al (2011) Research of GNSS signal quality assessment and measurement methods. In: *CSNC2011*

Chapter 47

Research on Time Synchronization Method of Ground-Based Navigation System

Xiye Guo, Yongbin Zhou and Jun Yang

Abstract In the complex environment, such as in mountainous area, under-ground, urban, in-door situations, the satellite navigation signal will be kept out, which makes the user's receiver unable to receive enough navigation signal to position itself. Ground-Based Navigation System can flexibly deploy ground-based navigation based station according to different environment. It provides navigation signal with high quality to meet the user's needs, so it increases the coverage of the navigation service. With the same principle as satellite navigation system, the user uses the ground-based navigation stations as time and space base to determine its position and time. Comparing with the satellite, the coordinate of ground-based navigation station can be obtained with higher accuracy, which makes the inter-station time synchronization become the very important factor to impact the precision of positioning. To achieve cost-effective and accurate inter-station time synchronization, a time and frequency lock method based on two-way time transfer is proposed in this paper, measurement error model is established, and the synchronization flow is established under the typical ground-based navigation signal framework, i.e. the 'CDMA+TDMA' framework. It not only realizes two-way time difference measurement and navigation signal transmission in the same time, but also tracks time-frequency change through time and frequency lock technology, as a result, the effect of troposphere delay can be reduced and the accuracy of time synchronization can be significantly improved. The simulation and experiment results show that the time synchronization accuracy is better than 1 ns.

Keywords Ground-based navigation · Time synchronization · Two-way time transfer

X. Guo (✉) · Y. Zhou · J. Yang

College of Mechatronics Engineering and Automation, National University of Defense Technology, Changsha, People's Republic of China
e-mail: gxy1_1999@163.com

47.1 Introduction

When applying satellite navigation and positioning system in some complex environment, such as in mountainous areas, urban or indoor, the signal blocking problem exists widely, especially in large cities. Urban canyons will result in decrease of visible stars, making satellite navigation and positioning accuracy greatly reduced. In this case, placing ground-based navigation stations in several known or measurable points and transmitting ground-based navigation signals can enhance and improve the integrity and accuracy of the system. Furthermore, even in the case of satellite signal being fully occluded, ground-based navigation system can become an independent “constellation”, and provide area positioning and navigation services with high precision. Locata is a land-based area navigation and positioning system, which is developed by an Australian GPS manufacturer [1]. It can not only provide service in area in which GPS can't work, but also enhance the GPS performance in some environment with strong electromagnetic interference. Its precision can meet the mine surveying, machine guidance/control and building monitoring. It is also necessary for BeiDou to develop ground-based navigation system.

According to the principles of the ground-based navigation and positioning, the accuracy of time synchronization between the base stations directly affects the positioning and navigation performance. So the time synchronization technology is the key technology of the ground-based navigation system. There are two types of time synchronization technology: wired and wireless as the difference of the signal transmission medium [2]. Wired method such as optical fiber communication is less vulnerable to external impact, which makes it more precise and has better anti-interference performance [3]. But its application is constrained by the topography and so on. Comparing wired communication, wireless method is more suitable for ground-based navigation and positioning which need to be flexible for expanding its application. The satellite system can adjust the frequency of the atomic clock to be synchronized with the system time after determining the clock offset, as the atomic clock' frequency is highly stable [4]. But it is unsuitable to use such an expensive clock widely in a ground-based navigation system.

With the time synchronization technology named as TimeLoc, Locata's receiver can realize time synchronization through only a TCXO (Temperature Compensated Crystal Oscillator). However, if troposphere effects cannot be ignored, Locata time synchronization needs for high-precision model of troposphere [5], which would increase the complexity. To overcome the effect of the troposphere, a time lock method based on two-way time transfer is proposed in this paper.

47.2 Model of the Clock Offset Measurement

The station of the ground-based navigation system consists of receiving and transmitting modules. They share a synthetical baseband signal processing unit. The receiver module consists of ADC, down-conversion channel and receiving antenna.

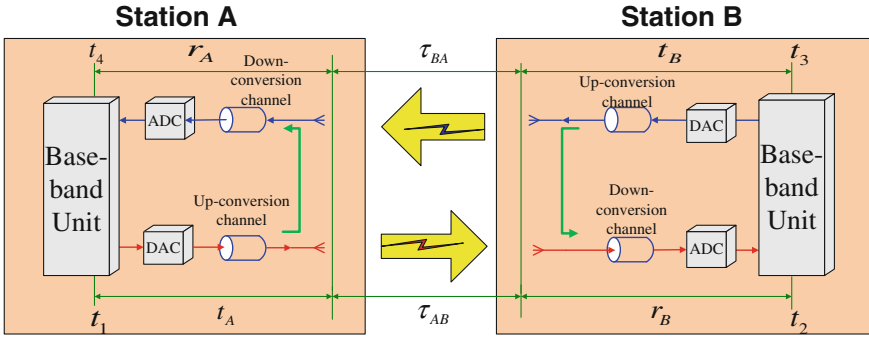


Fig. 47.1 Time delay in inter-station signal propagation

The transmitter one consists of DAC, up-conversion channel and transmitting antenna. Time delay exists in the process of signal propagation. During a transmission from A to B station, there are some kinds of delays as follows: circuit delay t_A of transmitting module in station A, propagation delay τ_{AB} in air and circuit delay r_B of receiving module in station B. During a transmission from B to A station, there are some kinds of delays as follows: circuit delay t_B of transmitting module in station B, propagation delay τ_{BA} in air and circuit delay r_A of receiving module in station A.

Then, we derive the model of the time propagation from A to B. As Fig. 47.1 shows, at t_2 , station B detects the signal transmitted by A which includes time information. Correspondingly the time of A is $t_1 + t_A + \tau_{AB} + r_B$. Due to the existence of clock offset Δt between the two stations, we have

$$t_1 + t_A + \tau_{AB} + r_B + \Delta t = t_2 \tag{47.1}$$

So, clock offset is

$$\Delta t = t_2 - t_1 - t_A - \tau_{AB} - r_B \tag{47.2}$$

By eliminating the inter-station clock offset, several stations can generate navigation signals simultaneously. However, because of the differences of transmitting delay of these stations, it takes different time for signal to reach the user's receiver even when the propagation distances are the same, which can cause the user positioning error. Therefore, time synchronization must be established under the same time point at which signal is transmitted. There, define a new inter-station clock offset $\Delta t'$:

$$\Delta t' = t_B - t_A - \Delta t \tag{47.3}$$

Substituting (47.2) into (47.3), then

$$\Delta t' = t_1 - t_2 + (t_B + r_B) + \tau_{AB} \tag{47.4}$$

After being measured, $\Delta t'$ will be used as the offset quantity to correct time in B, then the inter-station time synchronization is achieved. The synchronization accuracy depends on the measurement error of $\Delta t'$, which includes the error of receiver's tracking and measuring t_1 , the calibration error of the device-related delay ($t_B + r_B$), and the error of the signal propagation time measurement in space, $\sigma(\tau_{AB})$. The related troposphere error is included in $\sigma(\tau_{AB})$. It can be up to meter level in absence of correction using precise troposphere model, which is much higher than the tracking and measuring error and the calibration error of the device-related delay, making it to be the main error source in inter-station time synchronization. Although high precision tropospheric propagation model can be established between satellite and ground station, the mapping model deviation could be large if the elevation angle of the ground-based navigation station is small. To avoid the accuracy degradation of the clock offset measurement, which is caused by the error of troposphere propagation modeling, this paper proposes an inter-station clock offset measurement method using two-way time transfer.

47.3 Time Synchronization Approach

47.3.1 Two-Way Half-Duplex Time Transfer Approach

Two-way time transfer is a high precision clock offset measurement method. Under the assumption that spatial propagation delay is approximately equal in both directions, it can accurately determine the clock offset even if the quantity of the propagation delay is unknown. The station's location is fixed, so the two way propagation delay has short-term stability. Therefore, duplex or half-duplex mode can meet the high demand for precision measurements. To avoid the near-far effect, each station will transmit the navigation signal in different time slots. When using half-duplex mode, the navigation signals transmitted by stations can be used to time synchronization. Figure 47.2 shows the two-way time transfer process in half-duplex mode.

According to the time relations, Eq. (47.2) can be derived when A is transmitter and B is receiver, further Eq. (47.3) can also be derived. In the contrast procession, then

$$\Delta t = t_3 + t_B + \tau_{BA} + r_A - t_4 \quad (47.5)$$

Substituting (47.5) into (47.3), then

$$-\Delta t' = t_3 + (t_A + r_A) + \tau_{BA} - t_4 \quad (47.6)$$

According to Eqs. (47.4) and (47.6), then

$$\Delta t' = \frac{t_4 - t_2 + t_1 - t_3 + (t_B + r_B) - (t_A + r_A) + (\tau_{AB} - \tau_{BA})}{2} \quad (47.7)$$

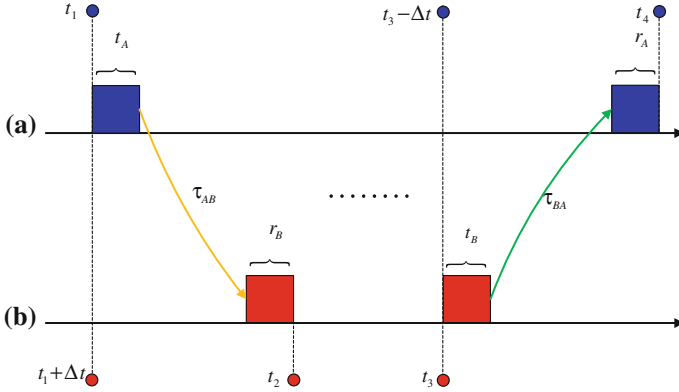


Fig. 47.2 Inter-station two-way time transfer process

Because of the two-way propagation delay is equal in both direction, namely, $\tau_{AB} = \tau_{BA}$, so Eq. (47.7) changes to

$$\Delta t' = \frac{t_4 - t_2 + t_1 - t_3 + (t_B + r_B) - (t_A + r_A)}{2} \tag{47.8}$$

The accuracy of $\Delta t'$ only relates to the tracking and measuring error of the time marker signal t_1 and t_3 , and to the calibration error device-related delay $(t_A + r_A)$ and $(t_B + r_B)$. Station equipment obeys homogeneous design pattern, so the difference between devices, the accuracy of clock offset measurement can be described as follow:

$$\sigma(\Delta t') = \frac{\sqrt{2\sigma_{tran}^2 + 2\sigma_{chan}^2}}{2} \tag{47.9}$$

In Eq. (47.9), σ_{tran} is the standard deviation of time marker signal tracking and measuring process, and σ_{chan} is the standard deviation of device-related delay calibration. When using the same signal system, because of the shorter distance, so $\sigma_{chan} < \sigma_{tran}$, and

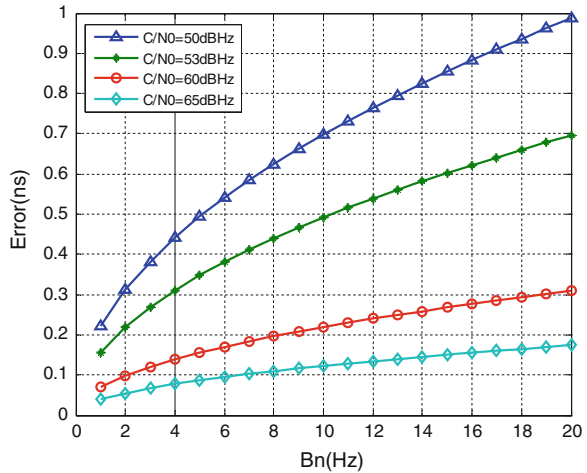
$$\sigma(\Delta t') < \sigma_{tran} \tag{47.10}$$

σ_{tran} can be expressed as Eq. (47.10) when time calibration signal is pseudo-random code:

$$\sigma_{tran} = \sqrt{\frac{B_n}{2C/N_0} D \left(1 + \frac{2}{(2-D)T_{coh} \cdot C/N_0} \right)} \tag{47.11}$$

The B_{n_DLL} is loop noise bandwidth, D is correlator spacing, T_{coh} is coherent-integration time, C/N_0 is CNR, through simulation, we can get the relationship

Fig. 47.3 Deviation curves of tracking and measuring time calibration signal



between PN measurement accuracy and the loop bandwidth in different CNR as Fig. 47.3 shows ($D = 1$, $T_{coh} = 1$ ms):

As shown in Fig. 47.3, when loop bandwidth is below 20 Hz and $C/N_0 > 50$ dBHz, tracking accuracy is better than 1 ns. According to Eq. (47.10), the accuracy of time synchronization is better than that of navigation signal tracking.

47.3.2 Time Synchronization Process

The time synchronization process is the process in which the slave station synchronizes itself to the primary station. It can be decomposed into time and frequency locking and clock offset measurement. Specific procedures are as follows:

- Step1 Slave station tracks and locks the time calibration signal from primary station;
- Step2 After tracking is stable, slave station keeps its frequency equal with the primary station;
- Step3 Determining both pseudo-range between stations and device-related delay in the two-way time transfer process;
- Step4 Collecting measurement results of the primary station;
- Step5 Calculating inter-station clock offset $\Delta t'$ according to Eq. (47.8), then, the slave station adjusts its clock based on $\Delta t'$.

47.4 Wireless Time Synchronization Experiment

Minimum experiment system is constructed in Xi'an experimental field. This system consists of two test stations simulating navigation station, one measurement station simulating user. The station equipments include transceiver and wide-angle

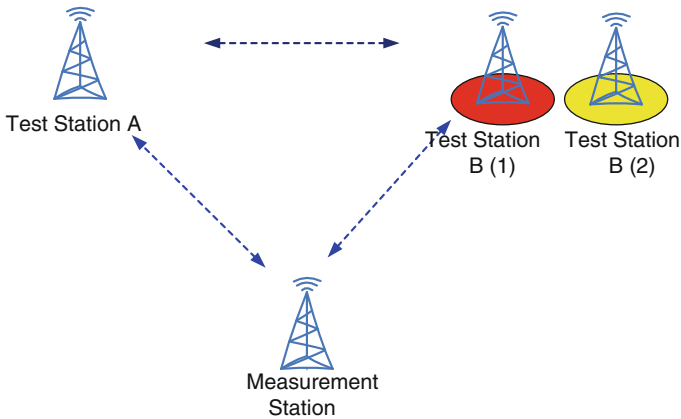


Fig. 47.4 Schematic diagram of the time synchronization experiment scenario

scanning antenna, making it able to transmit and receive navigation signal. All station signals have the same frequency, but the PN code of each station is unique. To reduce the near-far effect, TH (time hopping) is adopted, i.e., each station has the different time slot. The navigation signal which is designed according to the above “CDMA+TDMA” framework can be applied not only in user’s positioning and timing, but also in the inter-station time synchronization.

As Fig. 47.4 shows, test station A and B are 150 m apart during the whole experiment. The measurement station is covered by the signal of the two test stations. At the beginning, test station B synchronizes itself to A during the time synchronization process. Then, the clock offset between A and the test station, Δt_A , offset between B and the test station, Δt_B , is measured sequentially. The difference between the two offset quantities is exactly the clock offset between A and B. To simulate the effect of troposphere changing, the position of B is changed during the experiment. After more than 6 h of data collecting, the result shows that when the CNR of the receiving IF signal is higher than 53 dBHz, the time synchronization accuracy is better than 0.3 ns.

47.5 Conclusion

This paper studies the time synchronization method of ground-based navigation system, establishes its clock offset measurement model, and analyses the factors that affect the measurement accuracy. Above them, the troposphere delay is the main factor. This paper also proposes a highly precise time synchronization method based on Two-way Half-duplex Time Transfer Approach, develops a time synchronization process, and makes a wireless synchronization experiment. The major contributions to this research are as follows:

1. For the user receiver, the reflection of inter-station time being synchronized is that the each station transmitting signal at the same time. According to this feature, inter-station clock offset is redefined using the navigation signal transmitting time;
2. According to the clock offset model, the clock offset measurement accuracy depends on the tracking accuracy, self-calibration accuracy of time delay and the error of troposphere delay correction;
3. Two-way Time Transfer Approach can eliminate the troposphere effect, making the inter-station time synchronization being in the same accuracy level as the receiver's navigation signal tracking process. Analytical and experimental results both show that the time synchronization accuracy is better than 1 ns. Under high CNR condition, the accuracy can be better than 0.3 ns.

References

1. Hui Z, Jin-Ming H, Xiao-Wei S (2014) Locata: a new ground-based navigation system. In: 5th China satellite navigation academic annual meeting proceedings, Nanking
2. Tan S (2006) Two ways pseudo range time synchronization for navigation satellite clock. *Eng Sci* 8(12):P70–P74
3. Gang W, Yin-nian L, Jian-yu W (2007) Study on pseudolite clock synchronization. *Opt Fiber Electr Cable* 2:25–28
4. Fei-jiang H, Xiao-chun L, Hai-tao W (2008) Study on autonomous time synchronization method based on inter-satellite. *Comput Sci* 35(9):123–125
5. Barnes J, Rizos C, Wang J, Small D, Voigt G, Gambale N (2003) Locata: the positioning technology of the future?. In: 6th international symposium on satellite navigation technology including mobile positioning and location services, July 2003

Chapter 48

BDS/GPS Stochastic Model Refinement and Assessment Using Satellite Elevation Angle and SNR

Yan Li, Huang Dingfa, Li Meng and Zhu Dongwei

Abstract Satellite elevation angle and Signal-to-Noise Ratio (SNR) are usually used as measurement quality indicators for global navigation satellite system (GNSS) measurements. The relationship of quality indicators and accuracies of measurements can be expressed as stochastic models. To model the relationship for Beidou navigation satellite system (BDS) and global position system (GPS), five basic stochastic models are presented from satellite elevation angle and SNR. Also, coefficients of these models are refined. It's found that SNR stochastic models with same coefficients can't treat all measurements from BDS and GPS. Moreover, stochastic models with an additive constant could model the relationship better. The performance of the five models are tested, independent and combined, in BDS/GPS precise positioning. The results show that refined stochastic models could improve the success rate of integer ambiguity single-epoch solution 8 % comparing to empirical models. Models with an additive constant could improve the success rate 10 % comparing to models without additive constants. SNR model with an additive constant performs better in performance for integer ambiguity resolution, especially for low elevation satellite or combined system. Using stochastic models with an additive constant, ratios of posteriori and prior variances are closer to 1 in precise positioning. Therefore, for the used receivers, we suggest to choose refined stochastic models with an additive constant, and give priority to SNR model. Here, a refinement and assessment method is proposed to derive proper stochastic models for GNSS data processing, taking into account the differences between navigation satellite systems (e.g. BDS and GPS) and stochastic models.

Y. Li (✉) · H. Dingfa · Z. Dongwei
Faculty of Geosciences and Environmental Engineering, Southwest Jiaotong University,
Chengdu 610031, Sichuan, China
e-mail: yanli20060675@foxmail.com

H. Dingfa
e-mail: dfhuang@home.swjtu.edu.cn

L. Meng
College of Earth Science, Chengdu University of Technology, Chengdu 610059,
Sichuan, China

Keywords BDS · GPS · Satellite elevation angle · SNR · Stochastic model · Integer ambiguity fixed · Precise relative positioning

48.1 Introduction

The stochastic model describes the statistics of GNSS observations, and it is the key to obtain meaningful quality measures as well as improve parameter estimates (i.e. integer ambiguity and position). Very often, satellite elevation angle and receiver's SNR values are regarded as quality indicators to construct stochastic models. Over the past few years, many researchers have studied measurement weighting issues by elevation and SNR. The relationship of satellite elevation, SNR and measurement precision are modeled by a lot of functions, i.e., a sine function [3, 6, 23], an exponential function [16, 25], SIGMA- ε model [5, 7, 14, 24], SIGMA- Δ model [2]. Except for SNR and satellite elevation angle, least-squares residuals as a more realistic quality indicator are used to estimate stochastic models [9, 10, 15, 17]. However, only high-end software may have the option to use post-fitting residuals. Most software packages still use stochastic models based on satellite elevation and SNR. Hereby, we only discuss satellite elevation angle and SNR stochastic models in this contribution.

Many researchers have emphasized the importance of stochastic models conducted from satellite elevation angle and SNR. However, stochastic model is dependent on s not only satellite elevation angle and SNR but also the instruments and measurements [1, 21, 22]. For newly developed BDS/GPS receivers and their measurements, the usually used stochastic models are just satellite elevation stochastic models [4, 11–13, 18, 19]. Models are given as a matter of experience. For some situations, these model can't work properly.

To derive a proper stochastic model, a process of stochastic model refinement and assessment is presented for two same receivers, two frequency bands and two satellite systems (BDS and GPS). The relationship between accuracy, satellite elevation angle and SNR are analyzed for BDS and GPS measurements respectively. Five stochastic models are established to model the relationships. BDS and GPS precise relative positioning as well as both system combined positioning are carried out to evaluate the performance of different stochastic models. The effects of different stochastic models on integer ambiguity fixed and positioning resolution are analyzed and compared. The refinement and assessment results show that refined stochastic models perform better in integer ambiguity resolution than empirical models, refined models with an additive constant are fitter for the used receivers than models without any additive constants, and SNR models could indicate more realistic measurement quality compared with satellite elevation angle models in BDS and GPS combined system.

48.2 Stochastic Model Refinement Using Measured BDS/GPS Data

48.2.1 Stochastic Models Based on Satellite Elevation Angle and SNR

The usually used variances of measurements are approximated as a function of satellite elevation angle and SNR. The elevation function may be an inverse of the sine of the satellite elevation angle [23], an inverse of the square of the sine of the satellite elevation angle [2, 3] or an exponential function [16, 25]. The SNR function can be expressed as SIGMA- ε model [5, 7, 14], SIGMA- ε model with an additive constant [24] and SIGMA- Δ model [2]. Five model functions usually used are listed as the following

$$\sigma_{Li}^2 = \sigma_{0i}^2 / \sin^2 E \quad (48.1)$$

$$\sigma_{Li}^2 = \alpha_i^2 + \beta_i^2 / \sin^2 E \quad (48.2)$$

$$\sigma_{Li} = \kappa_i + \lambda_i \cdot \exp\{-E/\varepsilon_{0i}\} \quad (48.3)$$

$$\sigma_{Li}^2 = C_i \cdot 10^{-\frac{SNR}{10}} \quad (48.4)$$

$$\sigma_{Li}^2 = V_i + C_i \cdot 10^{-\frac{SNR}{10}} \quad (48.5)$$

where σ_L^2 is the observation variance; L is the measurement; E is satellite elevation angle; i indicates receiver/antenna and measurement type index; σ_0 , α , β , κ , λ , ε_0 , V, C are model coefficients. Model (48.1), (48.2) and (48.3) are satellite elevation angle stochastic models. Model (48.4) and (48.5) are SNR models. Model (48.1) and (48.4) have no additive constants, but (48.2), (48.3) and (48.5) all contain an additive constant.

48.2.2 Refining Stochastic Models Using Short Baseline Data

The above model coefficients are dependent on receiver/antenna and measurement types, but empirical values are usually used in BDS/GPS positioning [4, 18]. To come up with a realistic and adequate covariance matrix of BDS and GPS observables, coefficients in BDS and GPS stochastic models will be experimentally determined in case study of one type of receiver. In case study of ZHD V30 receiver, a baseline data set was collected on the roof of a building for a period of 24 h, with an elevation cut-off angle of 0° , four observation types (C1-C2-L1-L2),

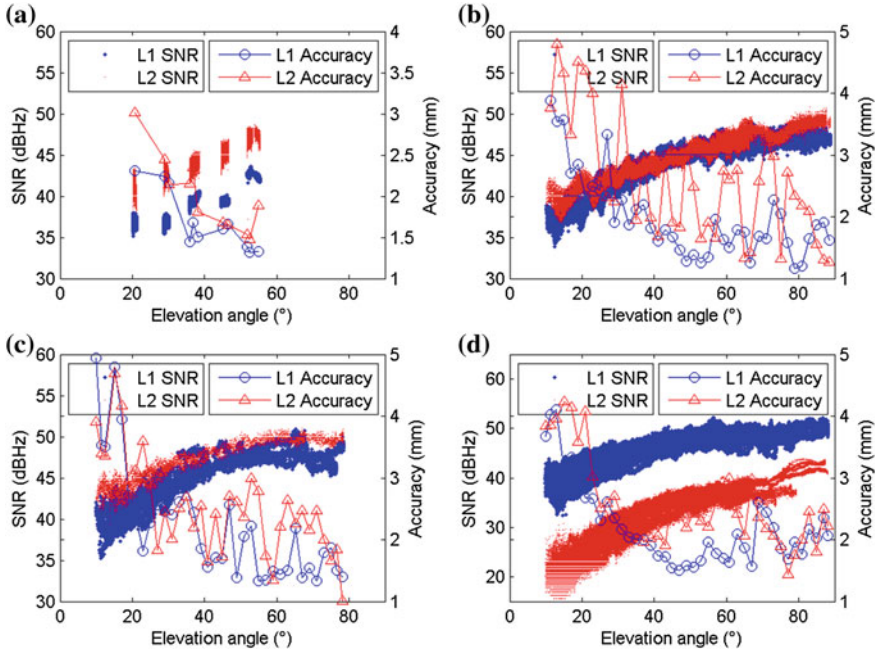


Fig. 48.1 The relationship between accuracies of L1 and L2, SNR and elevation angle for different satellite types. **a** Accuracy, SNR and elevation angle for GEO. **b** Accuracy, SNR and elevation angle for IGSO. **c** Accuracy, SNR and elevation angle for MEO. **d** Accuracy, SNR and elevation angle for GPS

and a recording interval of 1 Hz. The baseline length was approximately 2 m. Short baseline single-differenced (SD) residuals are usually applied to estimate of true errors for each satellite [8, 20]. In precise relative positioning, variances of carrier-phase measurements are mainly discussed. Assuming that the accuracies of measurements are different for different types of satellites, variances of each type of satellite measurements on are derived by law of error propagation. Due to three different satellite orbits in BDS, i.e. geostationary earth orbit (GEO), geosynchronous satellite orbit (IGSO) and medium earth orbit (MEO), GEO, IGSO and MEO satellite measurement accuracies are treated respectively.

Figure 48.1 shows GEO, IGSO, MEO and GPS satellite elevation, SNR and corresponding L1 and L2 accuracy (the positive square root of variance) series. Here, accuracy is a statistical average value within 2° elevation angle range. From Fig. 48.1, it is clearly evident that there are a significant difference in L1 and L2 SNR for BDS and GPS satellites. For BDS satellites, L1 SNR values are smaller than that of L2, and L1 accuracy values are smaller than that of L2. However, for GPS satellites, L1 SNR values are larger than that of L2, but L1 accuracy values are smaller than that of L2. These show that SNR stochastic models with same

coefficients can't precisely model BDS and GPS measurement accuracies. For GEO, IGSO and MEO satellites, there are not significant differences in the relationship between SNR and accuracy values. For all satellites, generally, the lower the satellite elevation, the lower the accuracy of the measurements when satellite elevation are greater than about 40° . Otherwise, accuracy values don't have an obvious change trend.

In order to further investigate the relationship between accuracy, satellite elevation angle and SNR for GEO, IGSO, MEO and GPS satellites, the coefficients of model (48.1), (48.2), (48.3), (48.4) and (48.5) mentioned in 2.1 are fitted and compared. With 95 % confidence bounds, GEO, IGSO, MEO and GPS model coefficients are fitted by least square (LS) method. GEO, IGSO and MEO belong to BDS, BDS model are also estimated with all satellites. All fitting coefficients are described in Table 48.1.

From Table 48.1, for model (48.1) fitting coefficients, we see that the coefficient of L1 is less than that of L2 for all satellite. For model (48.4) fitting coefficients, the coefficient of L1 is less than that of L2 for BDS, but this coefficient on L1 is greater than that on L2 for GPS. For model (48.2), (48.3) and (48.5) with an additive constant respectively, the coefficients are different, but their variety law have not been found.

For all models fitting, the goodness-of-fit statistics is also examined. The degrees of freedom adjusted R-square (DFARS) is generally the best indicator of fit qualities when different numbers of coefficients exist in models. DFARS can take on any value less than or equal to 1, with a value closer to 1 indicating a better fit. Negative values can occur when the model contains terms that do not help to predict the response. DFARS visual comparisons are shown in Fig. 48.2. From the Fig. 48.2, we can see that model (48.2), (48.3) and (48.5) fitting are good for all satellites, and the fit quality of L1 is better than that of L2 on the whole. Model (48.1) and (48.4) fits on L2 have negative DFARS values. It is likely due to the receiver-antenna pattern requiring an additional additive term in these models.

Figures 48.1, Table 48.1 and Fig. 48.2 give a detailed account of how to refine BDS and GPS stochastic models: analyzing the relationship between accuracies of L1 and L2, SNR and elevation angle for different satellite types, fitting stochastic model coefficients and analyzing their fitting efficiency. Considering BDS satellite type dependent observation accuracy, we know that the differences exist between GEO, IGSO and MEO, but the general trend of GEO, IGSO and MEO accuracy, elevation angle and SNR are similar. Then, GEO, IGSO and MEO will not be discussed respectively in following sections. BDS and GPS stochastic models with refined coefficients are used in precise positioning.

Table 48.1 Refined stochastic model coefficients

Model coefficients	Satellite measurements											
	BDS-GEO		BDS-IGSO		BDS-MEO		BDS		GPS			
	L1	L2	L1	L2	L1	L2	L1	L2	L1	L2		
(1) σ_0	0.94	1.14	0.86	1.07	0.85	0.89	0.89	1.01	0.81	0.89		
(2) α	1.09	1.11	1.49	2.09	1.58	2.18	0.95	2.20	1.79	2.24		
β	0.77	1.00	0.74	0.86	0.80	0.64	0.98	0.69	0.67	0.68		
(3) κ	0.90	1.35	1.58	1.94	1.56	1.97	1.65	2.14	1.86	2.15		
λ	3.17	5.25	5.41	4.78	5.65	3.55	14.17	4.20	5.89	4.31		
ε_0	27.61	17.91	13.18	19.01	14.92	18.38	7.83	15.39	10.65	14.84		
(4) C	e+04	e+05	e+04	e+05	e+05	e+05	e+04	e+05	e+05	e+03		
(5) V	42.72	61.74	13.55	18.20	18.38	17.14	20.53	26.36	20.32	49.54		
C	e-02	e-02	e-01	e-01	e-02	e-01	e-01	e-01	e-01	e-01		
	2.06	8.98	5.61	1.40	1.56	2.49	3.99	1.31	8.93	1.63		
	e+04	e+04	e+04	e+05	e+05	e+05	e+04	e+05	e+04	e+03		

The unit of σ_0 , α , β , κ and λ is mm, the unit of ε_0 is degree, the unit of C is mm² Hz, and the unit of V is mm²

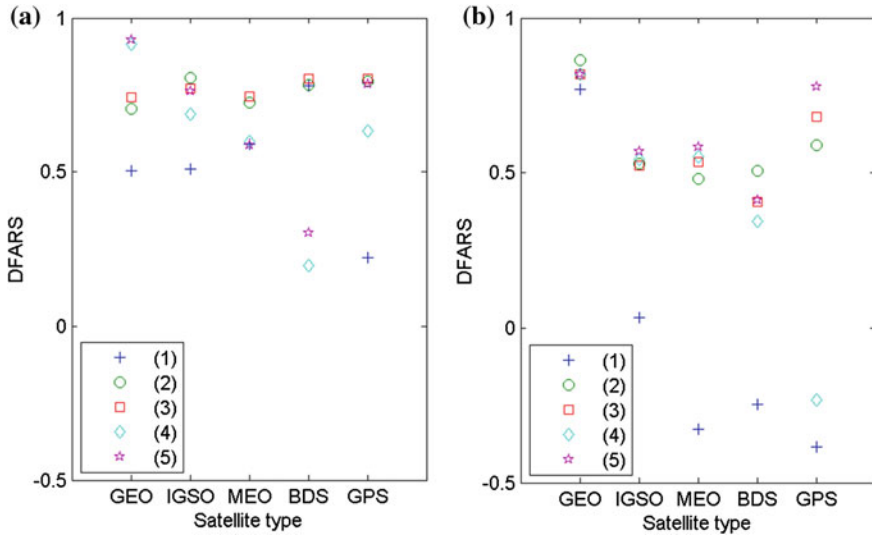


Fig. 48.2 Goodness of stochastic model coefficients fitting. **a** DFARS of L1 accuracy fitting. **b** DFARS of L2 accuracy fitting

48.3 Stochastic Model Assessment in BDS/GPS Precise Relative Positioning

48.3.1 BDS/GPS Precise Relative Positioning Stochastic Models

In order to evaluate the performance of BDS and GPS refined stochastic models, BDS/GPS precise relative positioning experiments are carried out. Three real data sets observing by the same receivers are used in these experiments. The information of test data is listed in Table 48.2.

In precise relative positioning, the commonly used double-differenced (DD) functional model are used since it efficiently cancels many systematic errors existing in the GNSS measurements. For short baselines (<3 km), atmospheric delay can be treated as zero and L1 and L2 measurements treated separately. However, as baseline length increases, the DD atmospheric delays increase, which

Table 48.2 Information of test data

Baseline	Data	Receiver type	Sampling rate (s)	Time (h)	Number of satellites
2 m	2013-8-18	ZHD V30	10	2	13 BDS, 10 GPS
3 km	2013-8-19	ZHD V30	15	1	9 BDS, 7 GPS
7 km	2013-8-20	ZHD V30	15	3	11 BDS, 8 GPS

are not small enough to be neglected. Then, the tropospheric delay is corrected by Saastamoinen model, and LC (ionospheric delay corrected phase) measurement is used to reduce the influence of ionosphere. The variance-covariance of LC measurement is derived by the law of error propagation with L1 and L2 variances. To construct DD stochastic model, the covariance matrix D of zero-differenced carrier phase measurements are formed as

$$D = \text{diag}(\sigma_{\phi_{s1-L1}}^2, \sigma_{\phi_{s1-L2}}^2, \dots, \sigma_{\phi_{sn-L1}}^2, \sigma_{\phi_{sn-L2}}^2) \tag{48.6}$$

where diag denotes a diagonal matrix, $\sigma_{\phi_{s1-L1}}^2, \sigma_{\phi_{s1-L2}}^2, \dots, \sigma_{\phi_{sn-L2}}^2$ are the tridiagonal elements. $\sigma_{\phi_{sn-L2}}$ is the precision of L2 measurements of satellite “sn”. These diagonal elements (variances) of the covariance matrix D describe their statistical quality of measurements. It’s assumed that the covariance (off-diagonal elements) describe the correlation between the measurements are zero in this paper.

The covariance matrix D_{Δ} of single differenced (SD) carrier phase measurements between two stations $k1$ and $k2$ can be formulated as $D_{\Delta} = D_{k1} + D_{k2}$. Then, with DD transformation matrix M , the covariance matrix $D_{\Delta\nabla}$ of double-differenced (DD) measurements can be written as

$$D_{\Delta\nabla} = MD_{\Delta}M^T \tag{48.7}$$

where Δ and $\Delta\nabla$ indicate SD and DD operator, respectively,

$$M = \begin{bmatrix} -1 & 1 & 0 & \dots & 0 \\ -1 & 0 & 1 & \dots & 0 \\ \vdots & \vdots & \vdots & \ddots & \vdots \\ -1 & 0 & 0 & \dots & 1 \end{bmatrix}_{(n-1) \times n}$$

For combined BDS and GPS, the covariance matrix can be expressed as

$$D_{\Delta\nabla} = \begin{bmatrix} D_{\Delta\nabla BD} & \\ & D_{\Delta\nabla GPS} \end{bmatrix} \tag{48.8}$$

48.3.2 Effects of Stochastic Models on Integer Ambiguity Resolution

Pseudo range and carrier phase measurements (C1-C2-L1-L2) are used to derive float ambiguity solutions. The variances of pseudo range measurements are determined as 10,000 of carrier phase variances [22]. After that, integer ambiguities can be estimated by the LAMBDA method, and the critical value for the statistic test is empirically chosen as a tolerant value of 3.0 [4]. Except for refined stochastic models, empirical model (48.1) and (48.2) with $\sigma_0 = 3$ mm, $\alpha = 4$ mm and $\beta = 3$ mm are also used in the ambiguity test.

Success rates of integer ambiguity single-epoch solutions (Fixed epoch/Total epoch) with an elevation mask angle of 10° for BDS and GPS are listed in Tables 48.3 and 48.4, reactively. From Table 48.3, it can be see that refined models are better than empirical models, for example, refined model (48.2) has improved success rate by 8 % compared with empirical model (48.2) for 3 km baseline. Refined models with an additive constant are better than models without an additive constant, for instance, refined model (48.2) and (48.3) improve success rate around 7–10 % compared with model (48.1), also the success rates of model (48.5) are higher than that of (48.4) for 3 and 7 km baseline. In Table 48.4, refined models are also better than empirical models. Refined models (48.2), (48.3) and (48.5) with an additive constant have not improved success rate but they have a slight advantage over the models (48.1) and (48.4) without an additive constant.

Table 48.5 shows the success rate of BD/GPS combined ambiguity single-epoch solution. With cut-off angle of 10°, the success rate of combined system are clearly lower than that of the separate system for 2 m and 3 km baselines. When the cut-off angle is set to 15°, the success rate for 3 km baseline can be improved obviously, particularly for the models dependent on satellite elevation angle. However, even if cut-off elevation angle increases, success rates of combined system are still less than one of both separate systems, which may be affected by satellite geometry or system observation weight. Also it may be affected by the critical value for the statistic test on ambiguity validation. A smaller critical value may be better for combined system. Comparing all kinds of models, it could be drawn that refined models are better than empirical models and refined models with an additive constant are better than models without an additive constant, which is consistent with the conclusions from ambiguity test of separate system. In addition, model (48.5) performs better in performance for combined system integer ambiguity test, which can improve

Table 48.3 Success rate (%) of integer ambiguity single-epoch solution for BDS

Baseline	Refined model					Empirical model	
	(1)	(2)	(3)	(4)	(5)	(1)	(2)
2 m	100	100	100	100	100	100	100
3 km	70.2	78.1	77.6	74.0	75.1	68.7	69.9
7 km	68.1	77.2	78.2	71.7	75.7	67.8	72.9

Table 48.4 Success rate (%) of integer ambiguity single-epoch solution for GPS

Baseline	Refined model					Empirical model	
	(1)	(2)	(3)	(4)	(5)	(1)	(2)
2 m	100	100	100	100	100	100	100
3 km	17.1	18.8	18.4	18.4	18.8	15.1	17.4
7 km	22.4	24.9	24.3	24.4	24.5	22.1	22.3

Table 48.5 Success rate (%) of integer ambiguity single-epoch solution for BDS/GPS combined system

Cut-off angle	Baseline	Refined model					Empirical model	
		(1)	(2)	(3)	(4)	(5)	(1)	(2)
10°	2 m	99.5	99.5	99.5	99.6	99.6	99.5	99.5
	3 km	1.8	2.6	2.6	4.4	14.9	1.7	1.7
	7 km	38.6	40.4	42.9	44.1	51.3	36.4	36.6
15°	2 m	100	100	100	100	100	100	100
	3 km	29.8	30.3	31.6	31.2	33.8	28.8	29.8
	7 km	38.6	40.4	42.9	44.1	51.3	36.4	36.7

success rate by 13 %. With cut-off angle of 10°, the success rate of model (48.5) is obviously higher than that of the other models. While the cut-off angle grows, the superiority of model (48.5) is found to be not insignificant. These signs suggest that model (48.5) can simulate the variance of a low satellite measurement with poor quality better.

48.3.3 Effects of Stochastic Models on BDS/GPS Precise Relative Positioning

With estimated DD integer ambiguity, BDS/GPS precise relative positioning results are derived by using only carrier-phase measurements. Taking 3 km baseline as an example, N, E, U components of baseline are estimated epoch-by-epoch, also Ratio of posterior and prior variance factors are derived by

$$Ratio = \frac{\hat{\sigma}_0}{\sigma_0} = \frac{1}{\sigma_0} \times \frac{v^T D_{\Delta\nabla}^{-1} v}{f} \tag{48.9}$$

where σ_0 is the prior variance factor (1 as its given value while using these fitting model parameters), $\hat{\sigma}_0$ is the posterior variance factor, v is the residuals, f is the degree of freedom. In general, ratio is closer to 1 indicating less discrepancies between the data and the stochastic model [20].

Ratio values from 3 km baseline epoch-by-epoch positioning results are shown in Fig. 48.3. From Fig. 48.3, we see that while using different models ratio values are significant different. For all data processing, Ratio values of model (48.1) are most far from 1, and ratio values of model (48.4) are secondly. For BDS data processing, Ratio values of model (48.5) are most close to 1. For GPS data processing, Ratio values of model (48.3) are most close to 1. The results of (48.2), (48.3) and (48.5) are close, especially for combined system. Ratio values from combined system are lower than that from one system, but higher than that from the

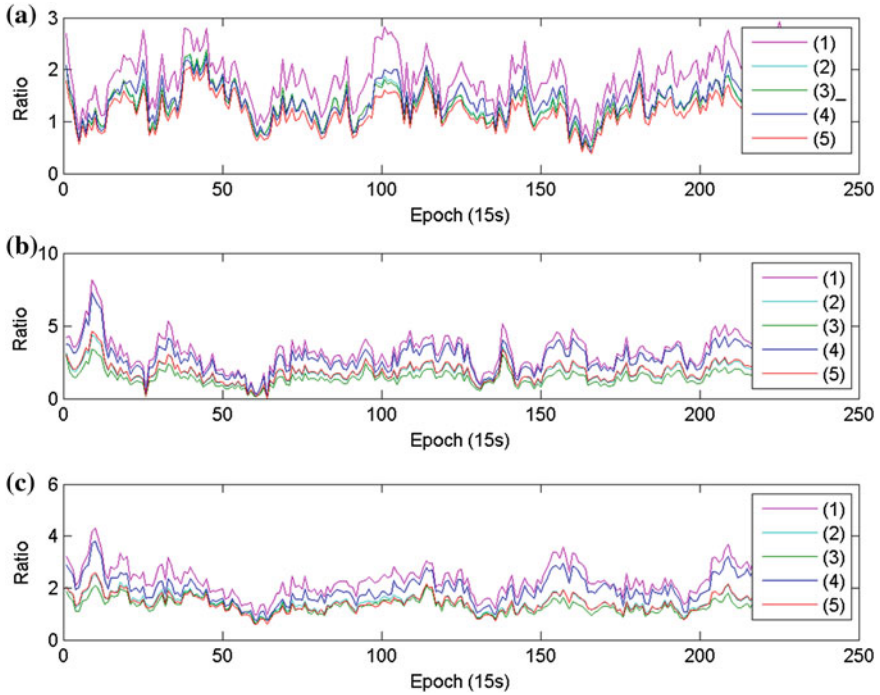


Fig. 48.3 Ratio of posterior and prior variance from BDS/GPS only and combined epoch-by-epoch positioning. **a** Ratio of posterior and prior variance from BDS epoch-by-epoch positioning. **b** Ratio of posterior and prior variance from GPS epoch-by-epoch positioning. **c** Ratio of posterior and prior variance from BDS/GPS epoch-by-epoch positioning

other system, which depends on numbers of satellites from different systems and their data qualities.

48.4 Conclusions

In this paper, it is proved that GNSS stochastic model is dependent on receiver/antenna, measurement types and satellite systems. Thereby we refine stochastic models on used GNSS receivers and satellite systems with real data collected. The process of refining stochastic model are following as: estimating the accuracies of satellite measurements, analyzing the relationship between accuracies of L1 and L2, SNR and elevation angle for different satellite types, fitting stochastic model coefficients and analyzing their fitting efficiency to choose proper stochastic models.

In order to assess the performance of the chosen stochastic models, BDS/GPS only and combined ambiguity single-epoch resolution and precise relative

positioning are carried out using different real data sets observing by the same receivers. Based on the test results, we find that refined stochastic models can perform better in integer ambiguity resolution compared with empirical models, and refined models with an additive constant are better, which has less discrepancies with the measurements.

Acknowledgments This study is supported by 2013 doctoral innovation fund in Southwest Jiao Tong University and the fundamental research funds in Central Universities.

References

1. Brown N, Kealy A et al (2002) Stochastic modelling of GPS phase observations for improved quality estimation. *Cartography* 31(2):143–151
2. Brunner FK, Hartinger H et al (1999) GPS signal diffraction modelling: the stochastic SIGMA- Δ model. *J Geodesy* 73(5):259–267
3. Collins JP, Langley RB (1999) Possible weighting schemes for GPS carrier phase observations in the presence of multipath. Final contract report for the US Army Corps of Engineers Topographic Engineering Center, no. DAAH04-96-C-0086/TCN 98151
4. Deng C, Tang W et al (2013) Reliable single-epoch ambiguity resolution for short baselines using combined GPS/BeiDou system. *GPS Solutions* 18(3):375–386
5. Hartinger H, Brunner FK (1999) Variances of GPS phase observations: the SIGMA- ϵ model. *GPS Solutions* 2(4):35–43
6. Jin S, Wang J et al (2005) An improvement of GPS height estimations-stochastic modeling. *Earth Planets Space* 57(4):253–259
7. Langley RB (1997) GPS receiver system noise. *GPS World* 8(6):40–45
8. Li B, Shen Y et al (2008) Assessment of stochastic models for GPS measurements with different types of receivers. *Chin Sci Bull* 53(20):3219–3225
9. Luo X (2013) *GPS stochastic modelling*. Springer, Berlin
10. Luo X, Mayer M et al (2011) Verification of ARMA identification for modelling temporal correlations of GNSS observations using the ARMASA toolbox. *Stud Geophys Geod* 55(3):537–556
11. Odolinski R, Teunissen PJ et al (2013) Quality analysis of a combined COMPASS/BeiDou-2 and GPS RTK positioning model. *Methodology* 5(1176.45):25.48
12. Odolinski R, Odijk D et al (2014) Combined GPS and BeiDou instantaneous RTK positioning. *Navigation* 61(2):135–148
13. Odolinski R, Teunissen PJG et al (2014) First combined COMPASS/BeiDou-2 and GPS positioning results in Australia. Part II: single- and multiple-frequency single-baseline RTK positioning. *J Spat Sci* 59(1):25–46
14. Ozludemir MT (2004) The stochastic modeling of GPS observations. *Turk J Eng Environ Sci* 28:223–231
15. Satirapod C (2006) Stochastic models used in static GPS relative positioning. *Surv Rev* 38(299):379–386
16. Satirapod C, Wang J (2000) Comparing the quality indicators of GPS carrier phase observations. *Geom Res Australasia* 73:75–92
17. Satirapod C, Wang J et al (2003) Comparing different global positioning system data processing techniques for modeling residual systematic errors. *J Survey Eng* 4(129):129–135
18. Tang W, Deng C et al (2013) Triple-frequency carrier ambiguity resolution for Beidou navigation satellite system. *GPS Solutions* 18(3):335–344

19. Teunissen PJG, Odolinski R et al (2013) Instantaneous BeiDou+GPS RTK positioning with high cut-off elevation angles. *J Geodesy* 88(4):335–350
20. Tiberius CCJM, Kenselaar F (2000) Estimation of the stochastic model for GPS code and phase observables. *Surv Rev* 35(277):441–454
21. Tiberius C, Jonkman N et al (1999) The stochastics of GPS observables. *GPS World* 10(2):49–54
22. Wang J (2001) Modelling and quality control for precise GPS and GLONASS satellite positioning. Curtin University of Technology, Perth
23. Wang J, Stewart MP et al (1998) Stochastic modeling for static GPS baseline data processing. *J Surv Eng* 124(4):171–181
24. Wieser A, Brunner FK (2000) An extended weight model for GPS phase observations. *Earth Planets Space* 52(10):777–782
25. Xin Xiang Jin CDDJ (1996) Relationship between satellite elevation and precision of GPS code observations. *J Navig* 49(2):253–265

Part III
BDS/GNSS User Terminal Technology

Chapter 49

A GLONASS Navigation Data Verification Algorithm Under High Bit-error Rates

Jian Hu, Aishui Rao, Long Zhang and Yimei Sun

Abstract This paper analyzes some GLONASS abnormal data of receiver software processing, and locates the source of the problem in navigation data handling error under high bit-error rates. Through the derivation of the Hamming check method, limitations of the method and mistakes in the interface document were pointed out. This paper proposes a navigation data verification algorithm under high bit-error rates.

Keywords GLONASS · High bit-error rate · Navigation data · Verification algorithm

49.1 Introduction

Navigation data transmitted by the satellites is purposed to provide users with parameters described satellite running state including the system time, ephemeris, almanac, etc. Obtaining the correct navigation data is the precondition of computing receiver's position, velocity and clock-off [1].

This paper analyzes some GLONASS abnormal data of receiver software processing, and locates the source of the problem in navigation data handling error under high bit-error rates. Through the derivation of the Hamming check method, limitations of the method and mistakes in the interface document were pointed out. This paper proposes a navigation data verification algorithm under high bit-error rates.

J. Hu (✉) · A. Rao · L. Zhang · Y. Sun
Satellite Maritime Tracking and Control Department of China, Jiangyin 214431, China
e-mail: mayfan11@163.com

© Springer-Verlag Berlin Heidelberg 2015
J. Sun et al. (eds.), *China Satellite Navigation Conference (CSNC) 2015 Proceedings: Volume I*, Lecture Notes in Electrical Engineering 340,
DOI 10.1007/978-3-662-46638-4_49

553

Table 49.1 Abnormal satellite’s ephemeris parameters (x-axis)

Parameter’s name	Abnormal value	Normal value
X (m)	13847071.777343750	10263071.777343750
X' (m/s)	2711.2836837875166	2711.2836837875166
X'' (m/s ²)	1.86264514924e-006	1.86264514924e-006

Table 49.2 1st string of abnormal satellite’s navigation data

Position of string (bit)	Abnormal value (Hex MSB)	Normal value (Hex MSB)
1–32	0x40b89329	0xb0b89329
33–64	0xab616b15	0xab616b15
65–85	0x00010a32	0x00010a32

49.2 Analysis of Abnormal Data Processing of a Receiver

At a moment the receiver position result computed with GLONASS satellites data became error and returned to correct after some time. Through analyzing the data it’s found that the X-axis position ephemeris parameters of the No. 12 GLONASS satellite are abnormal, such as shown in Table 49.1. Therefore the abnormal parameters caused satellite positioning error in integral calculation. Then the receiver pseudo range positioning equation solver failed.

Each GLONASS navigation data string includes 85 data bits where X-axis position parameters are given in the 9–35th bits of 1st String. Through the observation of navigation data’s source code, it’s found that the navigation data read by receiver software had high bit-error rates which often lead to verification failed at the time. Some navigation data which passed verification are not correct, such as shown in Table 49.2. These undetected wrong navigation data caused the problem.

49.3 Encoding and Verification of GLONASS Navigation Data

GLONASS navigation data encoded and verified using a (85, 77) extend Hamming code. The 77 most significant bits are data chips ($b_{85} \cdots b_9$), and 8 least significant bits are check bits ($\beta_8 \cdots \beta_1$).

The formulas for encoding are as follows [2]:

$$\beta_1 = \left[\sum_i b_i \right]_{\text{mod}2}$$

- $i = 9, 10, 12, 13, 15, 17, 19, 20, 22, 24, 26, 28, 30, 32, 34, 35, 37, 39, 41, 43,$
 $45, 47, 49, 51, 53, 55, 57, 59, 61, 63, 65, 66, 68, 70, 72, 74, 76, 78, 80, 82, 84$

$$\beta_2 = \left[\sum_j b_j \right]_{\text{mod}2}$$

$$j = 9, 11, 12, 14, 15, 18, 19, 21, 22, 25, 26, 29, 30, 33, 34, 36, 37, 40, 41, 44, 45, 48, 49, 52, 53, 56, 57, 60, 61, 64, 65, 67, 68, 71, 72, 75, 76, 79, 80, 83, 84$$

$$\beta_3 = \left[\sum_k b_k \right]_{\text{mod}2}$$

$$k = 10 - 12, 16-19, 23-26, 31-34, 38-41, 46-49, 54-57, 62-65, 69-72, 77-80, 85$$

$$\beta_4 = \left[\sum_q b_q \right]_{\text{mod}2}$$

$$q = 13-19, 27-34, 42-49, 58-65, 73-80$$

$$\beta_5 = \left[\sum_m b_m \right]_{\text{mod}2}$$

$$m = 20-34, 50-65, 81-85$$

$$\beta_6 = \left[\sum_{n=35}^{65} b_n \right]_{\text{mod}2}$$

$$\beta_7 = \left[\sum_{p=66}^{85} b_p \right]_{\text{mod}2}$$

$$\beta_8 = \left[\sum_{n=9}^{85} b_n \right]_{\text{mod}2} \oplus \left[\sum_{m=1}^7 \beta_m \right]_{\text{mod}2}$$

The navigation data could be verified according to the algorithm provided by the GLONASS ICD (Interface Control Document). The algorithm describes the checksum (C1,...,C7 and CΣ) generation formulas and verification rules. The original text of verification rules is as follows:

- (A) A string is considered correct if all checksums (C1,...,C7, and CΣ) are equal to zero, or if only one of the checksums (C1,...,C7) is equal to zero but CΣ = 1;
- (B) If two or more of the checksums (C1,...,C7) are equal to 1 and CΣ = 1, then character b_{icor} is corrected to the opposite character in the following bit position:

$i_{cor} = C7C6C5C4C3C2C1 + 8 - K$, provided that $i_{cor} \leq 85$, where $C7C6C5C4C3C2C1$ is binary number generated from the checksums $(C1, \dots, C7)$ where all binary numbers are written by LSB to the right;

K is ordinal number of most significant checksum not equal to zero;

If a formula for i_{cor} gives $i_{KOP} > 85$ then it indicates that there is odd number of multiple errors. In this case data are not corrected but erased;

(C) If at least one of the checksums $(C1, \dots, C7)$ is equal to 1 and $C\Sigma = 0$, or if all checksums $(C1, \dots, C7)$ are equal to zero but $C\Sigma = 1$, then it indicates that there are multiple errors and data are to be erased.

49.4 The Limitations of the Original Verification Algorithm

49.4.1 The Verification Principle of Hamming Code

Hamming Code was proposed by Richard Hamming in 1950, which is a kind of linear block codes.

A code has k data bits and r check bits. Not only data bits but also check bits could be wrong because of channel noise. Therefore the states that one bit was wrong could be $(k + r)$ kinds. There are all $(k + r + 1)$ kinds considering the state that no error occurred. The code is called Hamming code if there is a linear relationship between the r check bits and $(k + r + 1)$ kinds of states [3]. The relationship meets the following formula:

$$2^r \geq k + r + 1$$

From the foregoing, the 7 check bits $(\beta_7 \cdots \beta_1)$ could correct one bit error for 120 $(2^7 - 1 - 7)$ data bits [4]. To detect two or more bits error the bit (β_8) which could parity check all bits is increased.

Due to the design of even check (modulo 2), the navigation data which has 4 or more even bits error could not be detected. Such as shown in Table 49.2, the 29–32th bits changed to 0100 (0x4) from 1011 (0xb). The navigation data which has 4 bits error also passed the verification algorithm.

49.4.2 Errors of the GLONASS ICD

It is a remarkable fact that the verification rule in the GLONASS ICD is incorrect.

The second criterion of rule A is used for the condition that data bits are correct but check bits are incorrect. The original description of rule A which allows the wrong navigation data to pass verification is confused with rule B.

The correct description of rule A should be:

If all the checksum (C1,...,C7 and C works) is equal to 0, or a checksum (C1,..., C7) equal to 1 and C = 1 works, it is assumed that the string right.

49.5 The Improved Navigation Data Verification Algorithm

49.5.1 Requirements

Because of the particularity design, the processing of the GLONASS navigation data take two risks under high bit-error rates, such as follow:

- (A) The risk of leak detection as is mentioned above. The navigation data which has 4 or more even bits error could not be detected.
- (B) The risk of abnormal framing. Each frame of GLONASS navigation data is composed of 15 strings which don't have flag for frame identification just as IODE and IODC in GPS navigation data [5]. Under high bit-error rates, there are a lot of strings missed or failed in verification. Therefore two frames may be combined into one error frame, just as shown in Fig. 49.1

To prevent error data from navigation data processing, the improved algorithm should identify the two kinds of states above as much as possible.

In addition, the improved algorithm should retain valid data as far as possible. The ephemeris and almanac should be processed separately. Not because of one string missed or failed in verification the other valid data is put away.

49.5.2 The Flow Chart of Algorithm

The main body of the improved navigation data verification algorithm is as shown in Fig. 49.2.

Every received string of GLONASS navigation data must pass verification by the fixed rule A.

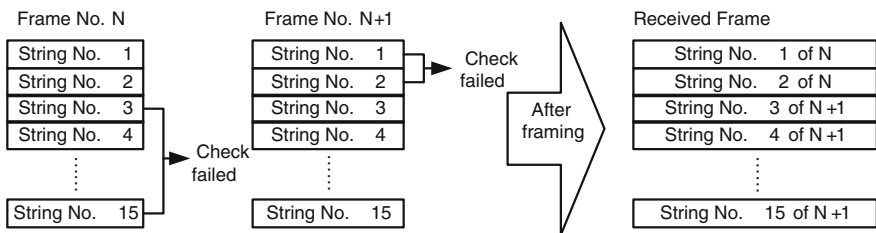
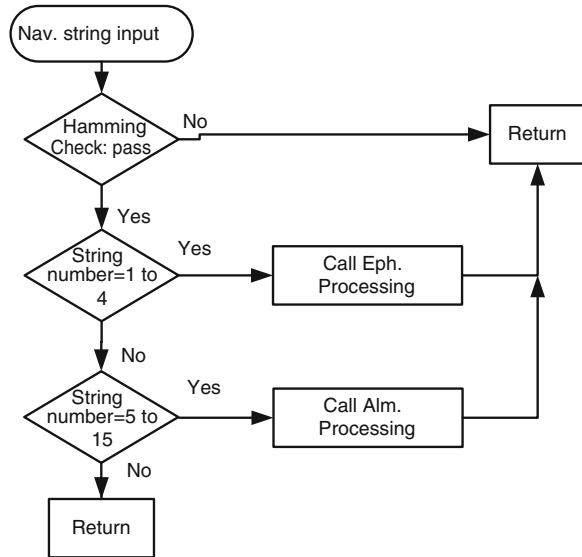


Fig. 49.1 String framing error of GLONASS navigation data

Fig. 49.2 Flow chart: improved verification algorithm body



If it is failed in verification the algorithm returns.

Otherwise there are two branches according to the string number resolved:

- (A) If the string number is 1–4, the string is ephemeris data of the GLONASS satellite. Just call the ephemeris processing algorithm.
- (B) If the string number is 5–15, the string is almanac data of the whole satellite system. Just call the almanac processing algorithm.

The ephemeris processing algorithm is as shown in Fig. 49.3.

For the input string:

- (A) If the string number is 1, all data in ephemeris buffers should be erased. And then the 1st string is stored in buffers. The algorithm returns.
- (B) If the string number is 2–3, the string should be stored in buffers. The algorithm returns.
- (C) If the string number is 4, see if the 1–4 strings are all gathered. If yes, the ephemeris should be calculated. For the positioning parameters which vary slowly such as T_b , position and velocity:
 - (1) These parameters are the same with the last result but different from parameters in the positioning system. The parameters in the positioning system should be updated. The algorithm returns.
 - (2) Otherwise these parameters are saved. The algorithm returns.
- (D) If the string number is other number, the algorithm returns.

The almanac processing algorithm is as shown in Fig. 49.4. It is a remarkable fact that the 14–15 strings of the fifth frame are special.

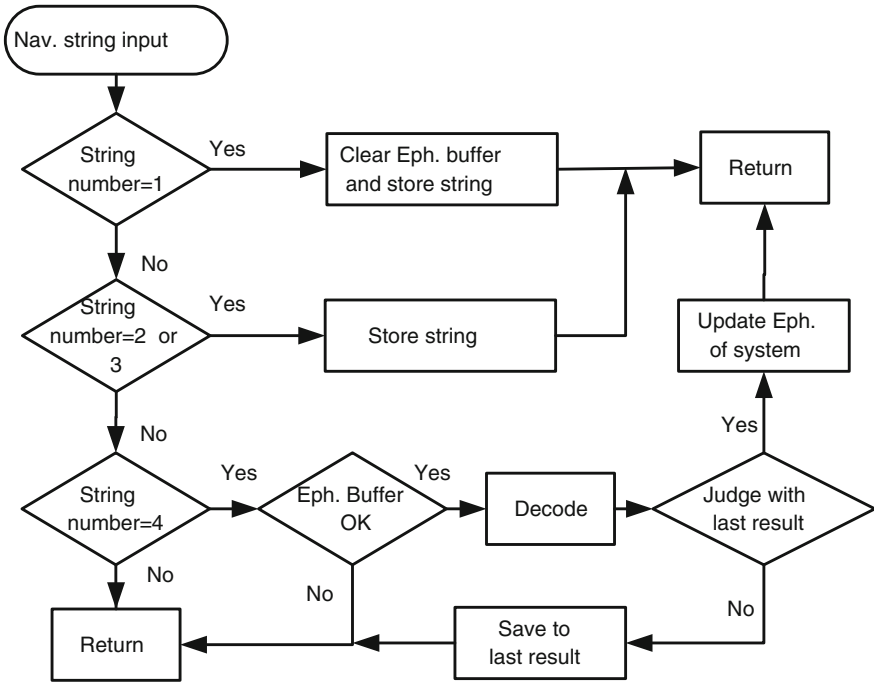


Fig. 49.3 Flow chart: processing ephemeris

For the input string:

- (A) If the string number is 5, the almanac data should be calculated. For the almanac parameters calculated:
 - (1) These parameters are the same with the last result but different from parameters in the positioning system. The parameters in the positioning system should be updated. The algorithm returns.
 - (2) Otherwise these parameters are saved. The algorithm returns.
- (B) If the string number is 6, 8, 10, 12 or 14, all data in almanac buffers should be erased. And then the string is stored in buffers. The algorithm returns.
- (C) If the string number is 7, 9, 11, 13, see if the string number in almanac buffers is equal to current string number minus one. If yes, the almanac should be calculated. For the parameters calculated:
 - (1) These parameters are the same with the last result but different from parameters in the positioning system. The parameters in the positioning system should be updated. The algorithm returns.
 - (2) Otherwise these parameters are saved. The algorithm returns.

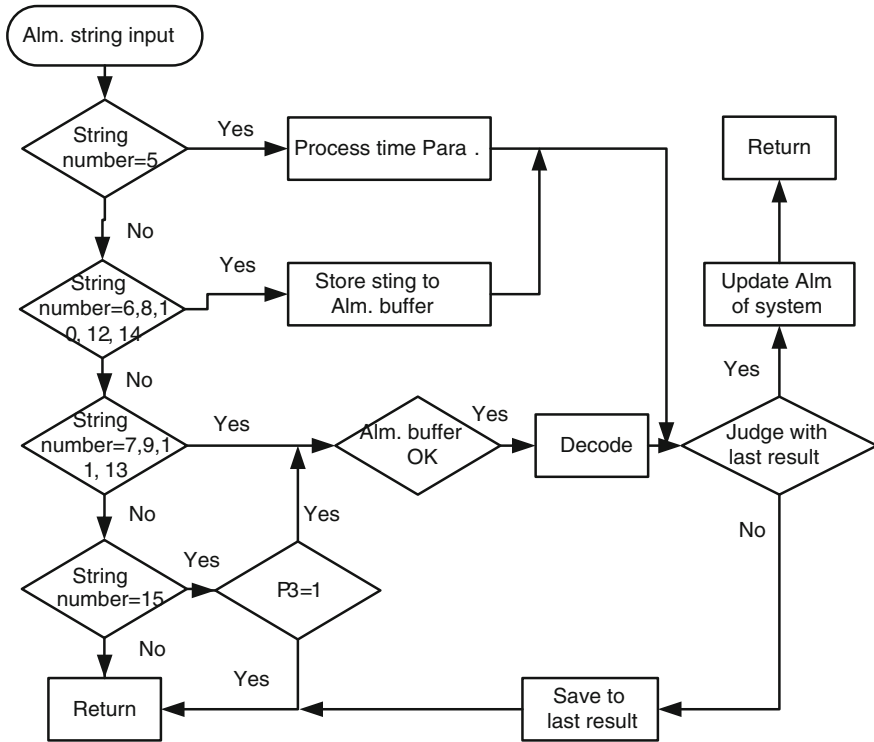


Fig. 49.4 Flow chart: processing almanac

(D) If the string number is 15, see if the P3 parameter of the satellite's ephemeris is equal to zero. If yes, the almanac should be calculated. For the parameters calculated:

- (1) These parameters are the same with the last result but different from parameters in the positioning system. The parameters in the positioning system should be updated. The algorithm returns.
- (2) Otherwise these parameters are saved. The algorithm returns.

49.5.3 Performance Analysis of the Improved Algorithm

Ephemeris in GLONASS navigation data is sent every 30 s. The update cycle of the main ephemeris parameters is above 15 min. Almanac in GLONASS navigation data is sent every 2.5 min each satellite. The more satellites received, the more almanac data is sent. The update cycle of the main almanac parameters is above 1 day.

The improved algorithm pays attention to the difference of the positioning parameters which vary slowly. It reduces the probability of leak detection and abnormal framing by increasing the time delay of first processing.

If there is not any bit-error, the time delay of processing ephemeris is 30 s and the time delay of processing almanac is 2.5 min. Under high bit-error rates, the leak detection would occur only when two same bit-errors occurred in two successive strings. The abnormal framing would occur only when two same abnormal framing occurred in two successive frames.

On the abnormal data recalculation using the improved algorithm, abnormal navigation message has not introduced the positioning computing systems, software localization of normal.

When the abnormal data is calculated using the improved algorithm, the abnormal navigation data is detected and the result of positioning is normal.

49.6 Conclusion

Because of the particularity of GLONASS navigation data, the leak detection and abnormal framing would occur easily under high bit-error rates. This paper proposes an algorithm which reduces the probability of leak detection and abnormal framing by increasing the time delay of first processing. The algorithm can solved the problem of GLONASS navigation data verification under high bit-error rates.

References

1. Tsui JBY et al (2007) Fundamentals of global positioning system receivers a software approach, 2nd edn. Publishing House of Electronics Industry, Beijing
2. Russian Institute of Space Device Engineering (2008) ICD L1, L2 GLONASS, version 5.1
3. Li H et al (2005) Principles of digital communication. Xidian University Press, Xi'an
4. Munro JE (1992) Discrete mathematics for computing. Chapman and Hall, Melbourne
5. Lu Y (2009) GPS global positioning receiver principle and software implement. Publishing House of Electronics Industry, Beijing

Chapter 50

The Design and Implementation of an Acquisition Scheme for Weak GNSS Signal

Linfeng Zhang, Hairong Guo, Chong Zheng and Haibo He

Abstract In order to improve the adaptability of GNSS receivers in weak signal circumstances, this paper designed an acquisition scheme, which could be applied to all GNSS signals, and implemented it on the FPGA platform. Code-phases and carrier frequencies were searched partial-parallel in the scheme, and the searching origin could be configured flexibly. In the phase of pre-detection integration, the signal-noise ratio of detection was enhanced by extending the non-coherent integration time. Since the autocorrelation function of pseudo-code would distort due to the code Doppler while the integration time was extended, two compensation methods were adopted during the procedures of down-sampling and non-coherent integration, respectively. In the phase of detection, a two-stage detector with immediate-rejection was employed, in which a modified location constraint scheme was proposed to suit the lengthened integration time. After an analysis of the detection performance of the acquisition scheme, its implementation principles on FPGA were introduced. In the last part, a hardware test platform was built based on a signal simulator and the acquisition sensitivity of the scheme was tested. The test result showed that the acquisition sensitivity was about -145 dBm when the detection probability was not less than 90 % and the false-alarm probability was not more than $1e-6$.

Keywords GNSS · Weak signal · Acquisition · FPGA

50.1 Introduction

In some rough environment, such as indoor, forest and high space orbit, the GNSS signals are attenuated significantly by obstacles or ultra-long-distance transmission, and conventional GNSS receivers are unable to capture the weak signals.

L. Zhang (✉) · H. Guo · C. Zheng · H. He
Beijing Satellite Navigation Center, Beijing, People's Republic of China
e-mail: zhanglinf04@gmail.com

© Springer-Verlag Berlin Heidelberg 2015
J. Sun et al. (eds.), *China Satellite Navigation Conference (CSNC) 2015 Proceedings: Volume I*, Lecture Notes in Electrical Engineering 340,
DOI 10.1007/978-3-662-46638-4_50

To improve the adaptability of GNSS receivers in weak signal circumstances, the weak signal acquisition techniques have been proposed and become a research hotspot in recent years.

There are two main technologies to improve the acquisition sensitivity [1], the first one is to extend the pre-detection integration time (PIT) and the second one is employing a multiple dwell time detector, both of which are affected by the code Doppler. For the former, the code Doppler results in distortion of code auto-correlation function, which reduces acquisition sensitivity and availability [2]. For the latter, the code Doppler causes the drift of code auto-correlation peak and degrades the detection probability. To solve these problems, the code Doppler need to be compensated. The methods of extending the PIT include extending the coherent integration (CI) time and increasing the number of non-coherent accumulation (NCA). The former is the most effective way, but limited by the width of secondary code chip and navigation data. The CI time should be selected carefully to allow the acquisition program applies to all existing GNSS signals.

This paper analyzed the above issues and designed a weak signal acquisition scheme which can be applied to all existing GNSS signals. The program fixed the CI time at 1 ms and advanced the signal to noise ratio (SNR) by increasing the number of NCA. The code Doppler was compensated at the stages of pre-detection integration and detection. The remainder of this paper describes the design principle of the proposed program, analyzes its detection performance, introduces its implementation on the FPGA platform and gives the test results on a hardware test platform.

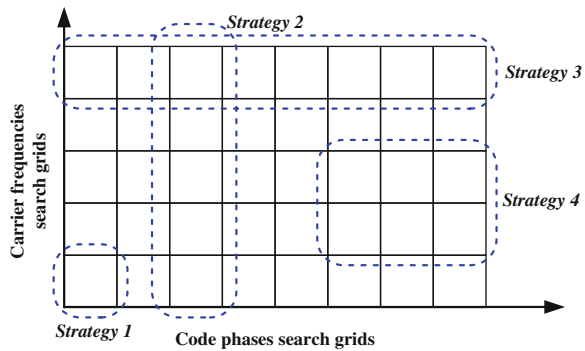
50.2 Program Design

The design of an acquisition program includes three aspects: the search strategy, the pre-detection integration program and the detection method. The following of this chapter describes these three parts of the proposed program.

50.2.1 *The Search Strategy*

Figure 50.1 shows four typical searching strategies of acquisition program [3]. Strategy 1 is the basic serial search strategy and searches only one cell every time; Strategy 2 uses DFT or FFT algorithm and searches all carrier frequency cells at a time; Strategy 3 takes advantage of the character of Fourier transform, which means the circular correlation in time domain is equivalent to the conjugate multiplication in frequency domain, to search the all code phase cells parallelly; Strategy 4 combines the methods of strategy 2 and 3, and searches the code phases and carrier frequencies partial-parallelly [4]. This paper chooses strategy 4 at last because of two main reasons. The first one is that the shape of parallel search area of Strategy 4

Fig. 50.1 Four typical acquisition search strategies



is the closest to the shape of two-dimensional correlation function, which is helpful to find the maximum value of correlation function. The second reason is that strategy 4 can get the maximum search efficiency when the priori information is available. The parallel search area of the proposed program includes 1023 code phases and eight carrier frequencies.

50.2.2 The PIT Program

The pre-detection integration program is consist of CI and NCA. The CI time is limited by the width of secondary code chip and navigation data. Table 50.1 lists the features of pseudo-code and navigation data of all GNSS public signals [5]. As can be seen from the table, a total of nine signals' secondary code chip width is 1 ms [5]. Therefore, in order to make the acquisition program apply to all GNSS signals, this paper fixes the CI time at 1 ms, and extends the integration time by increasing the number of NCA.

To compensate the code Doppler at the stage of integration, this paper uses the method proposed in literature [2]: the code Doppler corresponding to the central carrier frequency among the parallel searched carrier frequencies is compensated at the phase of resampling, and the code Doppler corresponding to other frequencies on the both sides are compensated by shift NCA.

50.2.3 The Detection Method

Another way to improve acquisition sensitivity is employing multi-stages detector. Commonly used multi-stages detector includes immediate-rejection detector, N select M detector and Tong search detector [1]. The first one has variable dwell time on every search cell and is most intolerable for false alarms, the signal is determined not exist as long as detection is not passed at any stage. The dwell time of N select

Table 50.1 Code and navigation data features of civil GNSS signals

System	Civilian signal	Primary code length	Sec'y code width (ms)	Navigation data width
GPS	L1 C/A	1 ms	–	20 ms
	L1C-I	10 ms	–	10 ms
	L1C-Q	10 ms	10	–
	L2 CM	20 ms	–	20 ms
	L2 CL	1.5 s	–	–
	L5-I	1 ms	1	10 ms
	L5-Q	1 ms	1	–
Galileo	E1-B	4 ms	–	4 ms
	E1-C	4 ms	4	–
	E5a-I	1 ms	1	20 ms
	E5a-Q	1 ms	1	–
	E5b-I	1 ms	1	4 ms
	E5b-Q	1 ms	1	–
GLONASS	L1 OF	1 ms	–	10 ms
	L2 OF	1 ms	–	10 ms
BDS	B1-I	1 ms	1	2 ms(GEO) 20 ms(NGEO)
	B2-I	1 ms	1	
	B3-I	1 ms	1	

M detector is fixed to N. It is determined that the signal does not exist when less than M detections pass in all N detections. The dwell time of Tong search detector is also variable. The counter of Tong search detector increases when detection passes and decreases when does not pass. When the counter value is less than certain threshold, signal is determined to be not present, while above another certain threshold, signal is determined to exist. Among the above detectors, an immediate-rejection detector with two stages, which reaches well compromise between improving the capture rate and eliminating false alarm, is employed at last and its probabilities of detection and false alarm is calculated as follows:

$$\begin{cases} P_D = P_{d,1}P_{d,2} \\ P_{FA} = P_{fa,1}P_{fa,2} \end{cases} \quad (50.1)$$

where $P_{d,1}$, $P_{d,2}$, $P_{fa,1}$ and $P_{fa,2}$ are detection probability and false alarm probability of the first and the second stage of detection, respectively.

When a multi-stages detector with a long PIT is employed, the location of correlation peak shifts because of the code Doppler, which may reduce the detection probability in the traditional location constraint scheme [6]. To solve this problem, this paper proposes an improved scheme: according to the location of the correlation peak whose amplitude exceeds the detection threshold in the first stage of

detection, the location of the correlation peak in the second stage of detection can be predicted, we take the prediction error into account the tolerance range. The final location constraint scheme can be described as: only the amplitudes of the first and the second correlation peak both exceed the detection threshold, and the distance between them in the two-dimensional search grids is not more than one cell, the signal is determined present.

50.3 Performance Analysis

The carrier to noise ratio (CNR) of IF signal into the acquisition module is

$$\begin{cases} P_D = P_{d,1}P_{d,2} \\ P_{FA} = P_{fa,1}P_{fa,2} \end{cases} \quad (50.2)$$

where P_R is the signal power arrived at antenna, G_{Ant} is the antenna gain, kT_0 is the noise power spectral density, L_{RF} is CNR loss from the RF front-end. The SNR before CI is $SNR_{IF} = C/(N_0B_{IF})$ where B_{IF} is the IF signal bandwidth. Ideally, the SNR gain of CI is $G_{coh} = 10 \log(B_{IF}T_{coh})$, where T_{coh} is CI time. After considering the processing loss, SNR of CI result is

$$\rho_{c0} = SNR_{IF} + G_{coh} - L_{BB} \quad (50.3)$$

where L_{BB} is SNR loss in the stage of baseband signal processing, and is mainly from estimation error of code phase and carrier frequency.

After NCA, the SNR is

$$\rho_{nc} = \rho_{c0} + 10 \lg(N_{nc}) - L_{sq} \quad (50.4)$$

where N_{nc} is the number of NCA, L_{sq} is the square loss of SNR and its formulas is [7]

$$L_{sq} = 10 \lg[4/\pi - 1] + \rho_{c0} - 20 \lg\left(e^{-\frac{\rho_{c0}}{4}} \left[\left(1 + \frac{\rho_{c0}}{2}\right) I_0\left(\frac{\rho_{c0}}{4}\right) + \frac{\rho_{c0}}{2} I_1\left(\frac{\rho_{c0}}{4}\right) \right] - 1\right) \quad (50.5)$$

where $I_0(\cdot)$ and $I_1(\cdot)$ are the first kind of the zero-order and the first-order modified Bessel function.

The detection probability of single detection is [8]

$$P_{d,1}(V_t) = \int_{V_t}^{+\infty} [1 - P_{fa}(v)]^{H-1} f_A(v) dv \quad (50.6)$$

Table 50.2 Six PIT schemes with sensitivity of -145 dBm

T_{coh} (ms)	N_{nc}	T_{coh} (ms)	N_{nc}	T_{coh} (ms)	N_{nc}
1	1057	4	77	20	6
2	278	10	16	40	3

where V_t is the detection threshold, H is the number of cells in a parallel search, $P_{fa}(\cdot)$ is the false alarm probability in every search cell when signal is absent and its calculation is shown in Eq. (50.7), $f_A(\cdot)$ is the probability density function when signal is present and the calculation is shown in Eq. (50.8).

$$P_{fa} = \exp(-V_t/2) \tag{50.7}$$

$$f_A(v) = \frac{1}{2} \exp\left(-\frac{v + \rho_{nc}}{2}\right) I_0(\sqrt{\rho_{nc}v}) \tag{50.8}$$

The false alarm probability of single detection is

$$P_{fa,1} = 1 - [1 - P_{fa}]^H \tag{50.9}$$

Assuming that the first and the second detection use the same amplitude threshold, the final detection probability and false alarm probability of the proposed acquisition program are

$$P_D = P_{d,1} \times P_{d,2} = P_{d,1}^2 \tag{50.10}$$

$$P_{FA} = P_{fa,1} \times P_{fa,2} = P_{fa,1}^2 \times (K/H) \tag{50.11}$$

where K is the number of cells contained by the tolerance range.

According to the required acquisition sensitivity, detection probability, false alarm probability and other known quantities, a viable PIT scheme can be launched by the inverse process of the above. Take GPS L2P as example, when $P_D = 90\%$, $P_{FA} = 10^{-6}$, $P_R = -145$ dBm, $K = 9$, $H = 8184$, $G_{Ant} = 0$ dBic, $L_{RF} = 1.2$ dB, $L_{BB} = 1.4$ dB and $N_0 = -174$ dBm/Hz, some available PIT schemes are listed in Table 50.2. From the table we can see that, the number of NCA should not be less than 1057 when the CI time is fixed at 1 ms.

50.4 Hardware Implementation

This paper implements the acquisition program proposed above based on the Stratix II EP2S90 FPGA development board. Figure 50.2 shows the modules and interfaces of the FPGA project. As can be seen from the figure, the project has two ADC

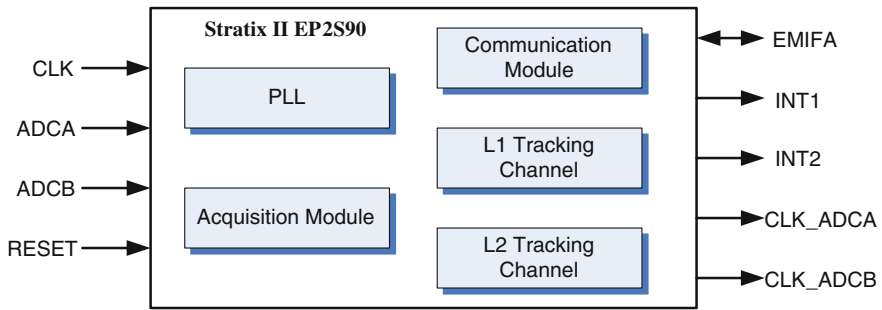


Fig. 50.2 The block program of FPGA project

inputs for GPS L1 and L2 IF signal respectively, acquisition module is responsible for acquisition of L1 C/A and L2P signal, PLL module supplies work clock to other modules, communication module communicates with the host computer, L1 and L2 tracking channels are responsible for tracking the L1 C/A code and L2P signals.

The specific implementation of acquisition module in Fig. 50.2 is shown in Fig. 50.3, from which we can see that the IF signal goes through direct digital converter (DDC) and down-sampler, and then is stored in SAT_RAM. The code Doppler is compensated at the phase of down-sampling for the first time. The local code samples is generated by local code generator and stored in PRN_RAM. The pre-detection integrator completes 1 ms CI and 1057 times NCA, and the code Doppler is compensated at the phase of NCA for the second time. The integration results are sent to the two-stage immediate-rejection detector, which outputs the final acquisition result.

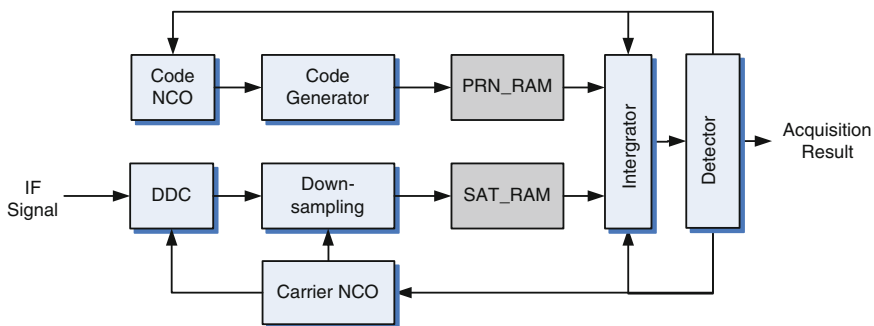


Fig. 50.3 The block program of acquisition module

50.5 Performance Test

In order to test the acquisition performance of proposed program, we build a hardware test platform based on GNSS signal source. Figures 50.4 and 50.5 show the schematic and physical map of the test platform, respectively. As can be seen from the figures, GPS L1 and L2 signals pass through the RF module and LNA and input to the receiver. The receiver is consist of two boards, one is Stratix II EP2S90 FPGA development board and the other is TMS320C6713 DSP development board, both of which communicate via EMIFA bus. The DSP sends commands to FPGA and receives process results reported by FPGA. The PC monitors the entire testing process and analyzes the test results. During every test procedure, the

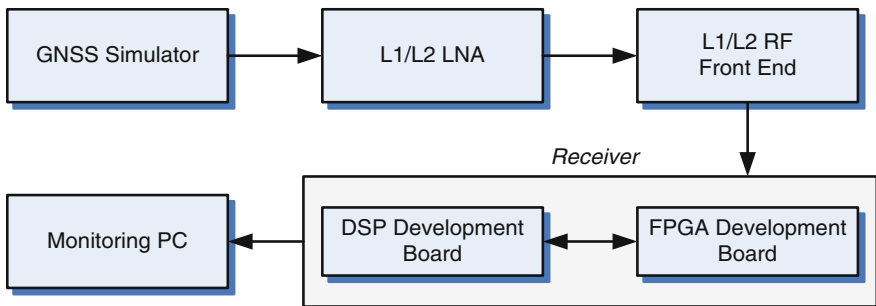


Fig. 50.4 The block program of the test platform

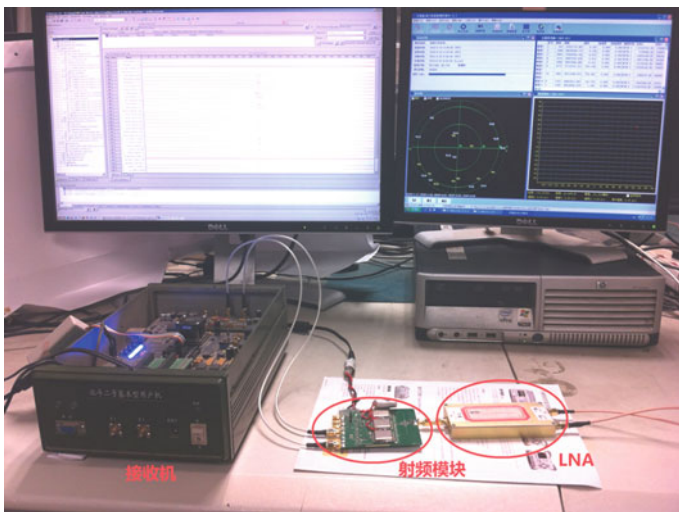


Fig. 50.5 The physical map of the test platform

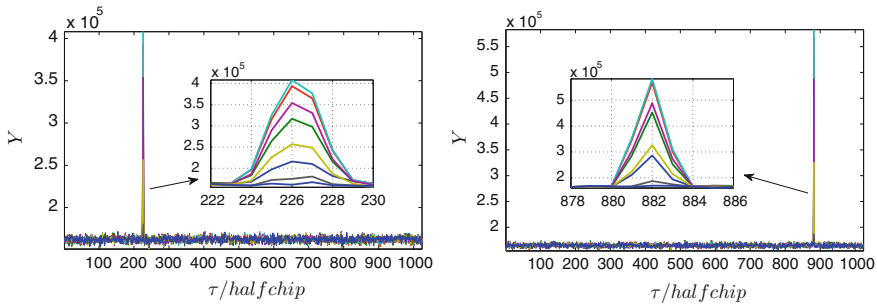


Fig. 50.6 The integration results without (*left*)/with (*right*) compensation of the code Doppler when signal power is -130 dBm

receiver processes L1 C/A signal at first, after obtaining time information from L1 C/A signal, the L2P signal whose power is much more lower than L1 C/A signal is captured. The capture result is used to enable the track loop. By comparing the code phases and carrier frequencies between L1 C/A and L2P track loops at the moment of opening L2p track loop, the validity of acquisition result is determined.

The performance test is divided into two steps. The first step is to test the effectiveness of the code Doppler compensation, the second step is to test detection performance.

Figure 50.6 shows the integration results without and with compensation of the code Doppler when the signal power is -130 dBm, respectively. As can be seen from the figure, the correlation peak width is broadened to 3.5 code chips when the code Doppler is not compensated, meanwhile the peak amplitude is attenuated either. After the compensation, the correlation peak width remains two chips ideally and the amplitude was significantly higher than that before compensation. Figure 50.7 demonstrates the integration results without and with compensation of the code Doppler when the signal power is -145 dBm, respectively. From the figure we can see that, the correlation peak is absent when the code Doppler is not

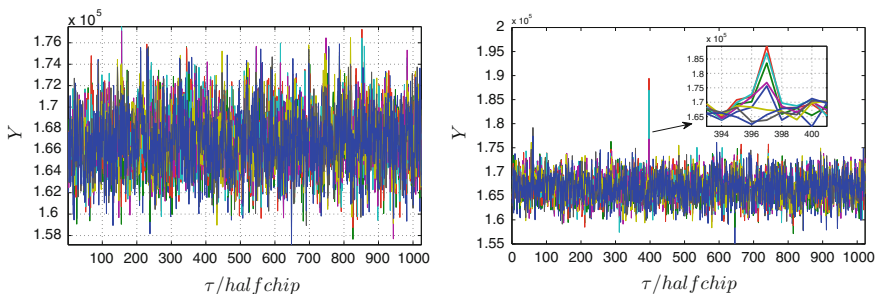


Fig. 50.7 The integration results without (*left*)/with (*right*) compensation of the code Doppler when signal power is -145 dBm

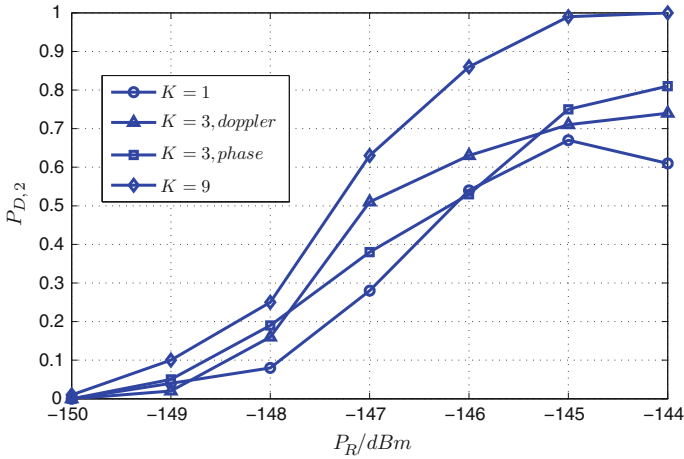


Fig. 50.8 The detection probabilities of different location constraint schemes

compensated, while after compensation, the correlation peak still obvious. The results above indicate that the compensation of the code Doppler is efficient for weak signal.

Figure 50.8 shows the detection performance of different signal power and different location constraint schemes employed in the two-stage immediate-rejection detector. The false alarm probability is set to $1e-6$. As can be seen from the Fig. 50.8, there are four location constraint schemes tested in all and K represents the number of search cells included by the tolerable range of constraint scheme. $K = 1$ corresponds to the traditional location constraint scheme, $K = 3, \text{doppler}$ and $K = 3, \text{phase}$ correspond to the constraint scheme which contains three cells in the domain of carrier Doppler and code phase respectively, $K = 9$ corresponds to the constraint scheme proposed in this paper. The test repeats 100 times in each signal power and each location constraint scheme. According to the test results in Fig. 50.8, the location constraint scheme proposed in this paper has the best detection performance, the other three schemes suffer missing detect in different degrees. If the requirements of detection and false alarm probability are $P_{FA} \leq 10^{-6}$ and $P_D \geq 90\%$, respectively, the acquisition sensitivity of the proposed program reaches -145 dBm, which is in accordance with the theoretical analysis in Chap 3.

50.6 Conclusion

This paper presents a weak signal acquisition program which can be applied to all GNSS signal. In the program, the carrier frequencies and code phases are searched partial-parallel, amplitude threshold and location constraint are both employed in the two-stage immediate-rejection detector, the code Doppler is compensated at

the phases of down-sampling and non-coherent accumulation. The test results indicate that the proposed program compensates the code Doppler efficiently and the acquisition sensitivity reaches -145 dBm.

References

1. Kaplan ED, Hegarty CJ (2006) Understanding GPS: principles and applications, 2nd edn. Artech House Inc., Norwood
2. Zhang LF, Zhang TQ, Li H, Cui XW Lu MQ (2013) Research on the effect of code doppler on acquisition performance and the compensation methods. In: CSNC 2013 Proceedings lecture notes in electronic engineering, vol 243, pp 663–673
3. Xie G (2009) Principles of GPS and receiver design. Publishing House of Electronics Industry, Beijing
4. Lin DM, Tsui JBY, Howell D. (1999) Direct P(Y)-Code acquisition algorithm for software GPS receivers. In: Proceedings of ION GPS 1999, pp 363–368
5. Avila Rodriguez JA (2008) On generalized signal waveform for satellite navigation. Ph.D dissertation, University FAF Munich, Germany
6. Wang J, Li JQ, Wu SL (2011) P code direct acquisition algorithm and its resource optimization method. *J Astronaut*, 32(12):2491–2498
7. van Diggelen F (2009) A-GPS: assisted GPS, GNSS, and SBAS. Artech House Inc, Norwood
8. Borio D (2008) A statistical theory for GNSS signal acquisition. Ph.D dissertation, Politecnico di Torino, Dottorato in Elettronica e delle Comunicazioni-XX ciclo, Italy

Chapter 51

Adaptive Notch Filter Design Based on Krylov Subspace

Zhaoliang Duan, Guangwei Fan and Yi Luo

Abstract Time-domain adaptive filtering as a narrow-band interference suppression technique has great potential and broad prospects in navigation receiver anti-interference applications. In this paper, an adaptive notch filter design method based on Krylov subspace is put forward which achieves adaptive narrow-band interference suppression and optimal output SNR for navigation receivers. The method solves the issue of large computation amount in traditional Wiener filtering algorithm due to matrix inversion. Simulation results show that the algorithm has a simple structure and lower computation than that of the optimal filter. Thus, it is a practical algorithm for narrow-band interference suppression.

Keywords Interference suppression · Adaptive filtering · Krylov subspace · Multistage wiener filtering

51.1 Introduction

Direct spread-spectrum signal system is adopted in Beidou Navigation System, which has favorable spread-spectrum gain in the signal receiving and processing course, but is susceptible to various interferences due to limited satellite transmitting power, high link loss and low power of received signal. In addition, considering the more and more complicated electromagnetic environment and the increasingly serious narrow-band anti-interference issue that BD navigation receivers have to confront, the interference against BD navigation receivers, whether in military field or civil field, is the major factor causing BD navigation receivers' failure to accurately position; therefore, it is requisite to investigate

Z. Duan · G. Fan (✉) · Y. Luo
No 589, Shijiazhuang, Hebei, China
e-mail: fgweihb@163.com

Z. Duan
e-mail: chnav_tec@126.com

narrow-band anti-interference technology, eliminate the effect of narrow-band interferences and improve the service quality and precision of Beidou navigation and positioning [1, 2].

The major interference that the spread-spectrum signal of BD navigation receiver has to deal with is narrow-band interference. At present, popular narrow-band anti-interference techniques include time-domain adaptive filtering technique [3–6] and transform-domain filtering technique [7–9]. The transform-domain filtering technique is not favorable to the miniaturization in receiver due to large computation amount and high resource requirement. The time-domain adaptive filtering technique appears preferable application prospects in navigation receiver because of small computation amount. Certain general criteria are required in the filter design of time-domain adaptive filtering technique. Popular time-domain narrow-band anti-interference filters include optimal Wiener filter, MMSE filter and least-squares filter. To achieve narrow-band interference suppression, time domain filter is implemented by establishing tapped-delay linear prediction filter based on the data collected in the past. In the research of narrow-band anti-interference techniques for Beidou navigation receiver, whatever an algorithm will be used, the guideline that should be taken is to suppress interference signals as many as possible when the negative effect to the received navigation signal is minimized.

With reference to the previous research results and considering the nature of Krylov subspace, this paper proposes a design method of MWF [10–12] closed-loop adaptive notch filter based on Krylov subspace, which shows a higher adjusting speed and better stability in comparison with open-loop filter algorithms like LMS.

51.2 Navigational Narrow-Band Anti-interference Signal Model

The narrow-band anti-interference in a satellite navigation system is achievable in navigation receivers without any change to the hardware of the original configuration. Let's assume the signal received by an interference detection system of satellite navigation is $x(t)$, the received navigation signal is $s(t)$, the system Gaussian noise is $n(t)$ and the interference signal is $j(t)$, then,

$$x(t) = s(t) + j(t) + n(t) \quad (51.1)$$

where, $s(t)$ represents the navigation signal, $j(t)$ represents the interference signal and $n(t)$ represents the system noise. The navigation signal $s(t)$ takes the form of spread-spectrum code, and the navigation signal of each satellite may be expressed as below:

$$s^j(t) = A_C C^j(t) D_C^j(t) \cos(2\pi f t + \varphi_C^j) + A_P P^j(t) D_P^j(t) \sin(2\pi f t + \varphi_P^j) \quad (51.2)$$

where, A_C represents the ranging code amplitude modulated in branch I; A_P represents the ranging code amplitude in branch Q; j represents satellite ID number; f represents the carrier frequency; φ_C represents the initial phase of carrier branch I; φ_P represents the initial phase of carrier branch Q; C represents the ranging code of branch I; P represents the ranging code of branch Q; D_C represents the data code of navigation message modulated with the ranging code of branch I; D_P represents the data code of navigation message modulated with the ranging code of branch Q.

The signal received by a navigation receiver is despread to acquire a high correlation gain, which is defined as follows:

$$G_p = \frac{S_{ic}/N_0}{S_i/N_0} \quad (51.3)$$

where S_i represents the signal power of the i th satellite prior to despreading, S_{ic} represents the signal power of the i th satellite after despreading, N_0 represents the system noise power and G_p represents the despread gain.

$$G_p = 101g \frac{S_{ic}/N_0}{S_i/N_0} \quad (51.4)$$

The navigation receiver has a certain anti-interference capability itself because of the presence of processing gain, however the anti-interference capability is finite, which is defined as follows:

$$J = G_p - [L + G_s] \quad (51.5)$$

where, G_p represents the despread gain of navigation receiver, G_s represents the minimum CNR in normal working condition and L represents the internal system loss. The despread gain G_p is proportional to the signal bandwidth.

Circular polarized antenna is generally used in common navigation receiver, of which the gain is 0 dB approximately. The power of the satellite signal received by such a navigation receiver is typically -160 dB around, 20 dB less than the system noise of the navigation receiver, relatively weak. Although band spread system is adopted in signal design, the anti-interference margin of the navigation receiver is generally 20 dB around. The normal signal receiving of the navigation system is susceptible to even weak interference signals; therefore, a proper anti-interference technique is needed for interference elimination.

51.3 Wiener Filtering Principle

As a type of filter that minimizes the mean square estimation of output filter, Winer filter [13] is applicable to the adaptive interference suppression of navigation receiver.

Let's assume $x(t) = [x_t, x_{t-1}, \dots, x_{t-L+1}]$ represents the vector of the signal received at the moment of t and M represents the order of delay, which may be any integer (Fig. 51.1).

The filter impulse response is defined with the weight coefficient $\omega_0, \omega_1, \dots, \omega_{M-1}$ of M taps, and then the filter output may be expressed as follows:

$$y(n) = \sum_{i=0}^{M-1} \omega_i^* x(n-i) \quad n = 0, 1, \dots \tag{51.6}$$

And Wiener-Hopf equation is simplified as M homogeneous equation:

$$\sum_{i=0}^{M-1} \omega_{opt,i} R_{x,x}(i-k) = R_{u,d}(-k), k = 0, 1, \dots, M-1 \tag{51.7}$$

where, $\omega_{opt,i}$ represents the optimal tap coefficient of transversal filter.

The $M \times 1$ input vector is defined as follows:

$$x(n) = [x(n), x(n-1), \dots, x(n-M+1)]^T \tag{51.8}$$

Then, the autocorrelation matrix is expressed as follows:

$$R = E\{x(n)x^H(n)\} = \begin{bmatrix} R_{x,x}(0) & R_{x,x}(1) & \dots & R_{x,x}(M-1) \\ R_{x,x}^*(1) & R_{x,x}(0) & \dots & R_{x,x}(M-2) \\ \vdots & \vdots & \vdots & \vdots \\ R_{x,x}^*(M-1) & R_{x,x}^*(M-2) & \dots & R_{x,x}(0) \end{bmatrix} \tag{51.9}$$

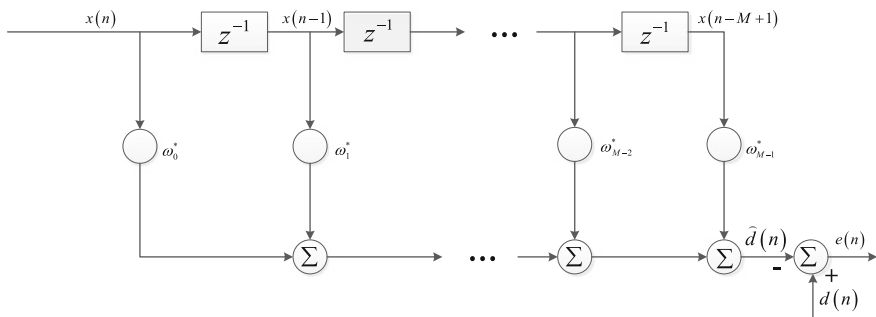


Fig. 51.1 Adaptive filter structure

where, the attribute of auto-correlation function $R_{x,x}(-k) = R_{x,x}^*(k)$ is used. Similarly, input the cross-correlation vector corresponding to the expectation:

$$\begin{aligned} R_{x,d} &= E\{x(n)d^*(n)\} \\ &= [R_{x,d}(0), R_{x,d}(-1), \dots, R_{x,d}(-M+1)] \end{aligned} \quad (51.10)$$

Combine the Eq. (51.9) with the Eq. (51.10) to rewrite the Winer-Hopf equation into a compact matrix form:

$$R_{x,x}\omega_{opt} = R_{x,d} \quad (51.11)$$

where, ω_{opt} represents the $M \times 1$ optimal tap weight vector of transversal filter.

$$\omega_{opt} = [\omega_{opt,0}, \omega_{opt,1}, \dots, \omega_{opt,M-1}] \quad (51.12)$$

Then, the solution of the optimal tap weight vector is

$$\omega_{opt} = R_{x,x}^{-1}R_{x,d} \quad (51.13)$$

The discrete-time transversal filter that satisfies this relation is known as Winer filter, which is the optimal filter under the minimum mean square error criterion. If the value M is too small, the corresponding autocorrelation matrix would have larger distortion and affect the accuracy of SNR estimation; if the M value is too large, the computation amount of the matrix would grow. Therefore, be sure to compromise the two factors when assigning a value to M .

51.4 An Adaptive Interference Suppression Algorithm Based on Krylov Subspace

The multistage Wiener filter uses a nested link composed of scalar Wiener filters, which has very good reduced-rank processing capacity and does not require decomposing the characteristic values of covariance matrix. This feature lowers the computation complexity; therefore, it is an important breakthrough in reduced-rank adaptive filtering technology.

Multistage Wiener filtering technique takes the system as dual input and implement it with multistage decomposition on the basis of regular cross-correlation. If the design filter order is M , then let's assume X_0 represents a matrix formed by a received signal of N long and its $M-1$ time delay signal. Consider $\mathbf{R}_{\mathbf{x}_0} = E(\mathbf{X}_0\mathbf{X}_0^H)$ as a Hermitian matrix and the T_D column vector of rank-reduced matrix forms Krylov subspace; therefore, it is allowed to estimate T_{MWF} using Lanczos iterative algorithm [14] and acquire the analysis and filtering iteration structure using Krylov-MWF method. The observation vector $X_T(k) \in C^D$ of the observation

signal $X_0(k)$, after being processed with the rank-reduced matrix T_D , is expressed as a complex D-dimension space, of which the covariance matrix is a diagonal matrix.

$$R_D = \begin{bmatrix} T_{D-1}^H R_{X_0} & T_{D-1} & \mathbf{0} \\ \mathbf{0}^T & r_{D-1,D}^* & r_{D,D} \end{bmatrix} \quad (51.14)$$

After cross-correlation processing with the desired signal, it is expressed as

$$\mathbf{r}_{X_T d_0}^{(D)} = \mathbf{T}_D^H \mathbf{r}_{X_0 d_0} = \begin{bmatrix} \|\mathbf{r}_{X_0 d_0}\| \\ \mathbf{0} \end{bmatrix} \in C^D \quad (51.15)$$

where, C^D represents the real D-dimension space. The covariance matrix $R_{D-1} = T_{D-1}^H R_{X_0} T_{D-1}$ is already known, then the new term in R_D is $r_{D-1,D} = t_{D-1}^H R_D t_D$. To solve Wiener filter $W_D = R_D^{-1} r_{X_T d_0}^{(D)} \in C^D$ with $r_{D,D} = t_D^H R_D t_D$, considering only the first element in $r_{X_T d_0}^{(D)}$ is not zero, only the first column in $C^{(D)} = R_D^{-1} = [c_1^{(D)}, c_2^{(D)}, \dots, c_D^{(D)}]$ is therefore prerequisite. With reference to the matrix inversion lemma [12] of partitioned matrix, it is possible to use recursion method to work out $C^{(D)}$.

$$C^{(D)} = \begin{bmatrix} C^{(D-1)} & 0 \\ \mathbf{0}^T & 0 \end{bmatrix} + \beta_D^{-1} b^{(D)} b^{(D),H} \quad (51.16)$$

where, $b^{(D)} = \begin{bmatrix} -r_{D-1,D} c_{D-1}^{(D-1)} \\ 1 \end{bmatrix} \in C^D$, $\beta_D = r_{D,D} - |r_{D-1,D}|^2 c_{D-1}^{(D-1)}$ and $c_{D-1}^{(D-1)}$ is the last element in the last column of $C^{(D-1)}$. Therefore, the new first column $c_1^{(D)} \in C^D$ at the Dth step is expressed as:

$$c_1^{(D)} = \begin{bmatrix} c_1^{(D-1)} \\ 0 \end{bmatrix} + \beta_D^{-1} c_{1,D-1}^{(D-1)} \begin{bmatrix} |r_{D-1,D}|^2 c_{D-1}^{(D-1)} \\ -r_{D-1,D} \end{bmatrix} \quad (51.17)$$

where, $c_{1,D-1}^{(D-1)}$ is the first element in the last column $c_{D-1}^{(D-1)}$ of $C^{(D-1)}$. The updating of Wiener filter W_D at the Dth step requires the first column $c_1^{(D-1)}$ at the $D-1$ th step and the two new terms of covariance matrix, i.e., $r_{D-1,D}$ and $r_{D,D}$. The updating of the last matrix column only depends on the last column of the previous matrix and the new term of matrix R_D .

$$c_D^{(D)} = \beta_D^{-1} \begin{bmatrix} -r_{D-1,D} c_{D-1}^{(D-1)} \\ 1 \end{bmatrix} \quad (51.18)$$

Therefore, it is required to update vectors $c_1^{(D)}$ and $c_D^{(D)}$ at every step in a complete iterative process. The MSE of multistage Wiener filter is defined as follows, where D represents the stages:

$$\begin{aligned}
M_{SE}^{(D)} &= \mathbb{E} \left[|e_0(k)|^2 \right] \\
&= \mathbb{E} \left[\left| d_0(k) - W_{MWF}^{(D)} X_0(k) \right|^2 \right]
\end{aligned} \tag{51.19}$$

It is easy to know that $M_{SE}^{(D)}$ may be represented by the first element $c_{1,1}^{(D)}$ of $c_1^{(D)}$.

$$MSE^{(D)} = \sigma_{d_0}^2 - \|r_{x_0, d_0}\|_2^2 c_{1,1}^{(D)} \tag{51.20}$$

The matrix established by t_i that is generated by reduced-rank algorithm at every stage is expressed as follows:

$$T_D = [t_1, t_2, \dots, t_D] \tag{51.21}$$

Thereby, it is possible to obtain the filtering weight coefficient of the adaptive filter:

$$\omega_0^{(D)} = \|r_{x_0, d_0}\|_2 T_D c_{first}^{(D)} \tag{51.22}$$

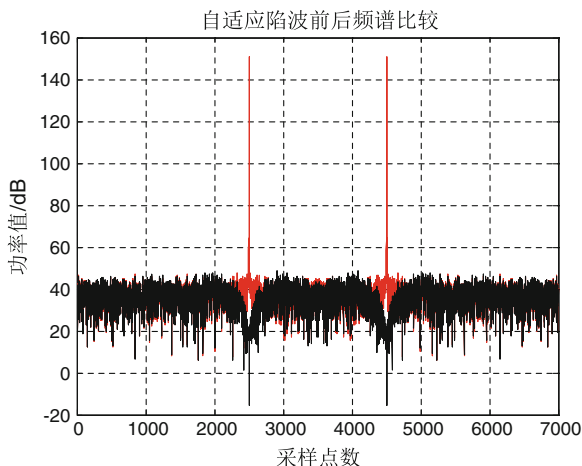
The computation amount of optimal Wiener filtering with matrix inversion algorithm is approximately $O\left((MN)^4 - 2(MN)^3 + 2(MN)^2 - 1\right)$, while that of multistage Wiener filtering based on Krylov subspace is approximately $O\left((MN)^2 + 5(MN)\right)$. Under the condition that the filtering performance is assured, the latter cuts the computation amount effectively comparing with the former.

51.5 Performance Simulation

To validate the performance of the proposed adaptive notch filtering algorithm based on Krylov subspace, a simulation test was conducted to IF baseband signal. Taking B3 signal of Beidou receiving system as example, an analysis was made to the narrow-band anti-interference performance of the algorithm and the effect to navigation receiver.

In the simulation test, the center frequency of the IF navigation signal was 45 MHz, the sampling frequency was 70 MHz, the signal length was 1 pseudo-code period of B3 signal. The Gold code of 2046 bit length was taken as the spread-spectrum code of navigation signal and modulated at B3 frequency point in BPSK mode on the noise background of additive white Gaussian noise. With the code rate of 20.46 MHz/s and the input SNR of -20 dB, chirp signal and single carrier signal of 10 % signal bandwidth were taken to simulate the narrow-band anti-interference performance under different conditions.

Fig. 51.2 Single carrier anti-interference performance



Simulation conditions: assume that single-carrier interference exists at the center frequency of the received signal, with 75 dB SINR and 10 filter order. The signal spectrum diagram before and after interference suppression is as shown in the Fig. 51.2.

The diagram shows that the adaptive notch filter designed with this algorithm has good interference suppression performance. Where the interference took place, a notch was formed where an energy loss occurred to some extent. Where no interference existed, the spectrum distortion is small and hardly appeared any change.

The time-domain spectrums with and without single-carrier interference suppression after correlation despreading are compared in the Fig. 51.3:

As shown in the diagram, there is no correlation peak at all before anti-interference implementation and after correlation integration with the local codes;

Fig. 51.3 Comparison of the correlation functions before and after anti-interference

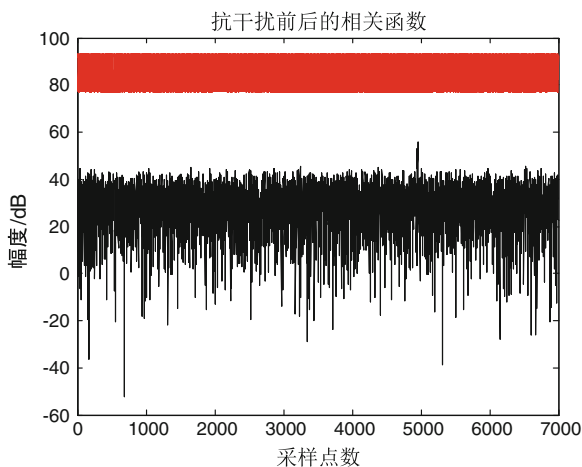
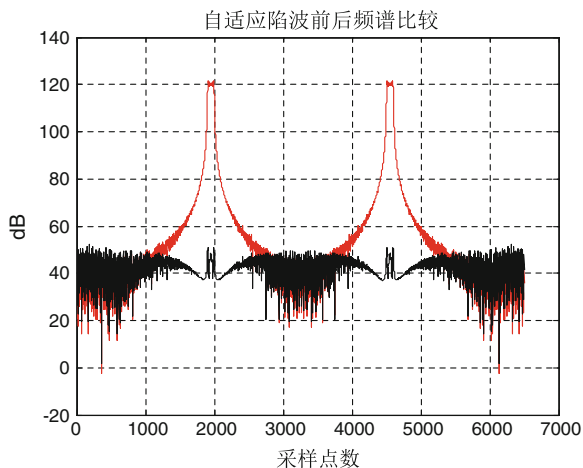


Fig. 51.4 Narrow band anti-interference performance



correlation peak is rather visible after anti-interference implementation. It suggests the anti-interference method reduces the effect resulting from interference and enables the navigation receiver to acquire signals normally.

Simulation conditions: assume that a narrow-band interference of 2.046 MHz bandwidth exists at the center frequency of the received signal, with 75 dB SINR and 10 filter order. The signal spectrum diagrams before and after interference suppression are as shown in the Fig. 51.4

As shown in the diagram, filter can provide favorable suppression to narrow-band interference; however, comparing with the original signal spectrum, the spectrum distortion is relatively large, which might affect the desired signal.

As shown in Fig. 51.5, correlation peak comes up after narrow-band interference suppression, which however is not higher than that after single-carrier suppression

Fig. 51.5 Comparison of the correlation functions before and after narrow band anti-interference

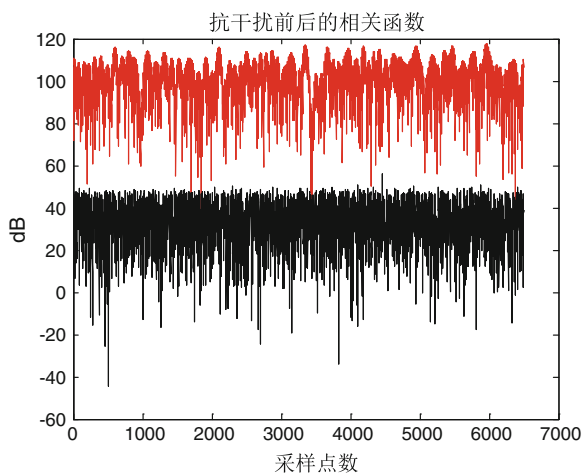


Table 51.1 Loss of signal to noise ratio for different algorithms

Algorithm	Interference		
	No interference (dB)	Single carrier (dB)	10 % bandwidth (dB)
Wiener filtering	0.1	0.9	1.6
Multistage wiener filtering	0.1	1.0	1.8
LMS algorithm	0.2	1.5	2.4

at the same SINR. It means that the performance of interference suppression goes down along with the increase of bandwidth.

For a narrow-band anti-interference algorithm used in navigation receiver, it requires both good anti-interference performance and less effect to the receiving performance of receiver. In other words, the signal CNR should change as little as possible after anti-interference process. Table 51.1 gives a CNR loss comparison with different anti-interference algorithms among Wiener filtering, Wiener filtering based on Krylov subspace and LMS narrow-band anti-interference filtering under different conditions of no interference, single carrier of 50 dB SINR and 10 % signal bandwidth respectively when the filter order is 10.

As shown in the table, all the three algorithms can provide low CNR loss under the condition of no interference, but high CNR loss in case of interference. The comparison among the three algorithms shows that the optimal Wiener filtering algorithm and the Wiener filtering algorithm based on Krylov subspace have no big difference in CNR loss under the same conditions, but the latter reduces the computation amount substantially comparing with the former because it does not require matrix inversion. In comparison with LMS algorithm, the Wiener filtering algorithm based on Krylov subspace can provide much less CNR loss and does not require additional desired signal, which makes it easier to achieve.

51.6 Conclusion

Concerning the weakness of traditional notch filtering algorithms, e.g., the optimal Wiener notch filtering algorithm requires a large amount of computation and the LMS adaptive notch filtering algorithm requires setting of desired signal which is impracticable in engineering applications, an open-loop adaptive notch filtering algorithm based on Krylov subspace is proposed. With quick convergence and excellent narrow-band anti-interference performance, this algorithm is able to further improve the receiving performance in high-precision satellite navigation receiver.

Acknowledgments This research was funded by the 863 Hi-tech Projects Program of the 12th China National Five-Year Plan (2012AA121802.04).

References

1. Kaplan ED (2002) Understanding GPS principles and applications, 2nd edn. Publishing House of Electronics Industry, Beijing
2. Fante RL, Vaccro J (2000) Wideband cancellation of interference in a GPS receive array. *IEEE Trans AES* 36(2):549–564
3. Upadhyay T, Dimos G, Ferzali W (1995) Test results on mitigation of Satcom-induced interference to GPS operation. In: ION GPS
4. Upton DM, Upadhyay TN, Marchese J (1998) Commercial-Off-The-Shelf(COTS) GPS interference canceller and test results. In: ION navigation conference, pp 319–325
5. Pazzani MJ, Billsus D (2007) Content-based recommendation systems. The adaptive web. *Lecturer notes in computer science*, vol 4321. Springer, Berlin, pp 325–341
6. Liu YQ, Hu XL, Ran YH (2011) Study on evaluating the impact of CWI on DLL tracking performance for GNSS Signals. *Acta Electron Sinica* 39(6):1410–1416
7. Du Y, Gao Y, Liu J, Xi X (2013) Frequency-Space domain anti-jamming algorithm assisted with probability statistics. In: International conference on information technology and applications (ITA) 2013, pp 5–8
8. Young JA, Lehnert JS (1998) Analysis of DFT-based frequency excision algorithms for direct spread spectrum communications. *IEEE Trans Commun* 46(8):1076–1087
9. Bai J, Zhang T, Yu X, Wang Y (2011) The estimation of the PN sequence's period of the DSSS signals in narrowband interference environment. In: IEEE international conference on signal processing, communications and computing
10. Joham M, Sun Y, Zoltowski MD, Honig M, Goldstein JS (2001) A new backward recursion for the multistage nested Wiener filter employing Krylov subspace methods. In: IEEE military communications conference, pp 1210–1213
11. Werner S (2007) Matias with, householder multistage wiener filter for space time navigation receivers. *IEEE Trans Aerosp Electron Syst* 43(3):975–988
12. Widrow B, Stearns SD (1985) Adaptive signal processing. Prentice-Hall, Englewood Cliffs
13. Sad Y (1996) Iterative methods for sparse linear systems. PWS—out of print, Boston

Chapter 52

A Novel High Dynamic Carrier Tracking Algorithm Based on the Gaussian Particle Filter

Qize Chen, Gengmin Li and Ao Peng

Abstract The particle filter based tracking algorithms were researched for the GNSS receiver. Traditional GNSS receivers encounter a difficult problem with high Doppler shift and its derivatives in high dynamic scenarios. To track this shift correctly, the bandwidth of tracking loops must increase, which inevitably induces more broadband noise and may lead to a loss-of-lock at low SNR conditions. In this paper, a novel high dynamic carrier tracking algorithm based on the Gaussian particle filter (GPF) is proposed. The GPF approximates the posterior density by estimating parameters of Gaussian densities based on particle approach at each loop update, which avoids the problem of particle degeneracy. To deal with the problem of divergence and to obtain a better robustness, two optimization methods are also proposed: the STF-GPF and the UGPF. Extensive evaluations on the proposed model and algorithms are conducted with different levels of signal-to-noise ratios (SNRs). The numerical simulation results show that the proposed GPF tracking loop and consistently outperform the conventional approaches, as well as achieving lower SNR sensitivity in comparison with EKF and UKF. Both optimization methods improve tracking accuracy than GPF.

Keywords High dynamic · Carrier tracking · Gaussian particle filter

52.1 Introduction

In high dynamic applications, GNSS receiver always uses wide bandwidth in tracking loops to accommodate rapid Doppler changing, which inevitably induces deterioration of SNR [1]. The nonlinear effect of the discriminator under high

Q. Chen (✉) · G. Li · A. Peng
School of Information Science and Engineering, Xiamen University, Fujian, China
e-mail: chcqz@stu.xmu.edu.cn

G. Li
e-mail: lgm@xmu.edu.cn

dynamic conditions is also an important factor of performance limiting conditions. However, the tracking loops based on signal parameter estimation theory, which avoid the usage of discriminator, has been applied to enhance the capability of anti-noise and anti-nonlinearity.

The computational complexity of MLE algorithms is relatively high, and the Kalman filter-based approaches are suboptimal for nonlinear systems and don't easily provide sufficient accuracy. The particle filter (PF), which can be used to acquire better tracking performance, was proposed by Gordon et al. [2]. Particle filter is a sequential Monte Carlo method based on Bayesian estimation principle and uses a series of weighted random samples (called particles) to approximate the posterior probability density, so that any statistical estimates, such as the mean and variance, can be computed easily, which makes it capable to deal with any nonlinear models. The particle filtering relies on importance sampling, so the design of that can approximate the posterior distribution reasonably well is required. The most common proposal distributions uses transition prior, which could fail if new measurements appear in the tail of the prior or if the likelihood is too peaked in comparison to the prior probability [3]. To overcome this problem, several techniques based on linearization have been proposed. For example, De Freitas et al. [4] used the EKF Gaussian approximation as the proposal distribution. Rudolph et al. [3] proposed similar approach, but replaced the EKF proposal distribution by a UKF proposal distribution to get better performance. Besides, standard PF has a major disadvantage particle impoverishment due to the resampling procedure. Kotecha and Djuric [5] proposed the Gaussian particle filter (GPF), which approximates the posterior probability density by Gaussian densities, and resampling is not required. Ng et al. [6] studied the performance of carrier signal tracking particle filter, which consistently outperformed EKF and were less sensitive to SNR levels than EKF.

Particle filter has not been applied to high dynamic scenarios since the resampling procedure almost fails to curb the degradation with the increase of epoch time. In this paper, a high dynamic carrier tracking algorithm based on the GPF is proposed. The remainder of this paper is organized as follows. In Sect. 52.2, we first introduce the Gaussian particle filter. Section 52.3 introduces a carrier tracking algorithm based on Gaussian partial filter for high dynamic GNSS receiver. In Sect. 52.4, two optimization methods are proposed to deal with the problem of divergence and obtain a better robustness. Section 52.5 provides an extensive simulation results to show the comparative tracking performance of the proposed GPF-based algorithms for different signal-to noise ratio (SNR) conditions. Finally, conclusions are drawn in Sect. 52.6.

52.2 Gaussian Particle Filter

Based on particle filter, the Gaussian particle filter approximates the posterior probability density by Gaussian densities, and resampling is not required.

The density of a Gaussian random variable X is as follows

$$N(x; \mu; \Sigma) = \frac{1}{(2\pi)^{n/2} \det|\Sigma|^{1/2}} \exp\left\{-\frac{1}{2}(x - \mu)^T \Sigma^{-1}(x - \mu)\right\} \quad (52.1)$$

where the m -dimensional vector μ is the mean, and Σ denotes the positive definite covariance matrix. Assuming that at the moment $k-1$, we have

$$p(x_{k-1}|z_{k-1}) \approx N(x_{k-1}, \bar{\mu}_{k-1}, \bar{\Sigma}_{k-1}) \quad (52.2)$$

from which samples can be drawn and denoted as $x_{k-1}(i)$. Then draw samples from $p(x_k|x_{k-1}^{(i)})$ and denote them as $x_{k|k-1}(i)$.

$$p(x_k|z_{k-1}) = \int p(x_k|x_{k-1})N(x_{k-1}, \bar{\mu}_{k-1}, \bar{\Sigma}_{k-1})dx_{k-1} \quad (52.3)$$

approximated by the Monte Carlo, we have

$$p(x_k|z_{k-1}) = \frac{1}{N} \sum_{i=1}^N p(x_k|x_{k-1}^{(i)}) \quad (52.4)$$

the mean and covariance of $p(x_k|z_{k-1})$ is computed as

$$\bar{\mu}_{k|k-1} = \frac{1}{N} \sum_{i=1}^N x_{k|k-1}^{(i)}, \quad \bar{\Sigma}_{k|k-1} = \frac{1}{N} \sum_{i=1}^N (x_{k|k-1}^{(i)} - \bar{\mu}_{k|k-1})(x_{k|k-1}^{(i)} - \bar{\mu}_{k|k-1})^T \quad (52.5)$$

the GPF approximates (52.3) as Gaussian, i.e.,

$$p(x_k|z_{k-1}) \approx N(x_k, \bar{\mu}_{k|k-1}, \bar{\Sigma}_{k|k-1}) \quad (52.6)$$

as new measurement z_k is received, the distribution is given by

$$p(x_k|z_k) = \frac{p(z_k|x_k)p(x_k|z_{k-1})}{p(z_k|z_{k-1})} \approx \frac{p(z_k|x_k)N(x_k, \bar{\mu}_{k|k-1}, \bar{\Sigma}_{k|k-1})}{p(z_k|z_{k-1})} \quad (52.7)$$

the GPF approximates the above density as a Gaussian, i.e.,

$$p(x_k|z_k) \approx N(x_k, \mu_k, \Sigma_k) \quad (52.8)$$

where the Monte Carlo estimates of μ_k and Σ_k are computed from the weighted samples $\{x_k(i)\}$ which obtained from the importance sampling function. As $N \rightarrow \infty$

and given the observations until time k , μ_k converges almost surely to the MMSE estimate of x_k [7].

52.3 Carrier Tracking Based on Improved Partial Filter for High Dynamic GNSS Receiver

Given the system state equation as follows,

$$X_k = \Phi X_{k-1} + BU_{k-1} + W_k \quad (52.9)$$

where $X_k = [\theta_e(k), f_c(k), f'_c(k), f''_c(k)]_k^T$ is the state vector, W_k is the process noise and Φ denotes the state transition matrix which is shown as

$$\Phi = \begin{bmatrix} 1 & 2\pi T & 2\pi T^2/2 & 2\pi T^3/6 \\ 0 & 1 & T & T^2/2 \\ 0 & 0 & 1 & T \\ 0 & 0 & 0 & 1 \end{bmatrix} \quad (52.10)$$

$$B = \begin{bmatrix} -2\pi T & -1 \\ 0 & 0 \\ 0 & 0 \\ 0 & 0 \end{bmatrix}, \quad U = \begin{bmatrix} f_{nco}(k) \\ \Delta\theta_{nco} \end{bmatrix} \quad (52.11)$$

and the process noise with covariance matrix as

$$Q_k = \begin{bmatrix} T^6/252 & T^5/72 & T^4/30 & T^3/24 \\ T^5/72 & T^4/20 & T^3/8 & T^2/6 \\ T^4/30 & T^3/8 & T^2/3 & T/2 \\ T^3/24 & T^2/6 & T/2 & 1 \end{bmatrix} N_y T \quad (52.12)$$

where N_y represents the third-order rate of change for frequency jitter.

The output signal with a phase and frequency deviation after local carrier stripping and spreading code despreading can be presented as follows

$$r(k) = \begin{bmatrix} r_I(k) \\ r_Q(k) \end{bmatrix} = \begin{bmatrix} AD_k R(\Delta\tau) \frac{\sin(\pi f_e T)}{\pi f_e T} \cos \theta(k) \\ AD_k R(\Delta\tau) \frac{\sin(\pi f_e T)}{\pi f_e T} \sin \theta(k) \end{bmatrix} + \begin{bmatrix} n_I \\ n_Q \end{bmatrix} \quad (52.13)$$

Denote the average residual phase within the coherent integration time interval as the phase of the observation vector, which is shown as follows,

$$\begin{aligned}
\bar{\theta}(k) &= \frac{1}{T} \int_{(k-1)T}^{kT} \left(\theta_c(k) + 2\pi f_c(k)T + 2\pi f'_c(k) \frac{T^2}{2} + 2\pi f''_c(k) \frac{T^3}{6} \right) d\tau \\
&\quad - \frac{1}{T} \int_{(k-1)T}^{kT} (\theta_{nco}(k) + 2\pi f_{nco}(k)T + \Delta\theta_{nco}) d\tau \\
&= \theta_c(k) + \pi f'_c(k)T + \pi f''_c(k) \frac{T^2}{3} + \pi f'''_c(k) \frac{T^3}{12} - \pi f_{nco}(k)T
\end{aligned} \tag{52.14}$$

the loop observation equation can be expressed as

$$Z_k = h(X_k) + n_k = \begin{bmatrix} I_Z \\ Q_Z \end{bmatrix} = \begin{bmatrix} A \cos[\bar{\theta}] \\ A \sin[\bar{\theta}] \end{bmatrix} + V_k \tag{52.15}$$

where the covariance matrix R_k of the observation noise matrix V_k is

$$R_k = E[V_k V_k^T] = \begin{bmatrix} \sigma_n^2 & 0 \\ 0 & \sigma_n^2 \end{bmatrix} \tag{52.16}$$

where $\sigma_n^2 = N_0/(2T)$.

The GPF algorithm is as follows,

1. Draw samples from $N(x_{k-1}, \mu_{k-1}, \Sigma_{k-1})$ and denote them as $\{x_{k-1}(i)\}, i = 1, \dots, N$
2. For $i = 1, \dots, N$, sample from $p(x_{k|k-1}|x_{k-1} = x_{k-1}^i)$ to obtain $\{x_{k|k-1}(i)\}, i = 1, \dots, N$
3. Compute the mean $\bar{\mu}_{k|k-1}$ and the covariance $\bar{\Sigma}_{k|k-1}$ as

$$\bar{\mu}_{k|k-1} = \frac{1}{N} \sum_{i=1}^N x_{k|k-1}^{(i)}, \quad \bar{\Sigma}_{k|k-1} = \frac{1}{N} \sum_{i=1}^N \left(x_{k|k-1}^{(i)} - \bar{x}_{k|k-1} \right) \left(x_{k|k-1}^{(i)} - \bar{x}_{k|k-1} \right)^T.$$

After receiving Z_k

4. Draw samples from the importance function $q(x_k(i)|z_k)$ and denote them as $\{x_k(i)\}, i = 1, \dots, N$
5. Obtain the respective weights by

$$w_k^i = \frac{p(z_k|x_k^i)N\left(x_k^{(i)}, \bar{\mu}_{k|k-1}, \bar{\Sigma}_{k|k-1}\right)}{q\left(x_k^i|z_k\right)} \tag{52.17}$$

normalized as

$$\tilde{w}_k(i) = \frac{w_k(i)}{\sum_{i=1}^N w_k(i)}. \quad (52.18)$$

6. Estimate the mean and covariance by

$$\mu_k = \sum_{i=1}^N \tilde{w}_k(i) x_k(i), \quad \Sigma_k = \sum_{i=1}^N \tilde{w}_k^i (\mu_k - x_k(i)) (\mu_k - x_k(i))^T \quad (52.19)$$

52.4 Optimization of the Gaussian Particle Filter

The Gaussian particle filter provides pretty good performance in carrier tracking, since the system model, system initial conditions, and noise characteristics have already specified a priori. But in a number of practical situations, the availability of a precisely known model is unrealistic, the poor robustness against model mismatches can't be ignored. Besides, generally the GPF choose the system transition probability function as the importance function, which does not take the new observations into account, this fact inevitably resulting in deviation while approximating the real state pdf, and leading to performance degradation. To prevent the problems discussed above, two optimization methods are proposed in the following sections.

52.4.1 Strong Tracking Filter Optimization

To enhance robustness, a GPF tracking algorithm based upon strong tracking filter (STF-GPF) is proposed here. The strong tracking filter (STF) [8] is based on the adaptively fading mechanism, reducing the impact of old measurement on the current estimate by introducing fading factor. The STF-GPF replaces the procedure 1, 2 and 3 in the GPF algorithm with the linear transformation of state transition in STF as follows,

$$\bar{\mu}_{k|k-1} = \Phi \mu_{k-1}, \quad \bar{\Sigma}_{k|k-1} = \lambda_k \cdot \Phi \Sigma_{k-1} \Phi^T + Q_k \quad (52.20)$$

which significantly reduces the computational load. Due to the introduction of fading factors, the proposed algorithm adjusts Σ adaptively, which enables faster responsibility to signal mutation. To extract all useful information in the observations, the residual error, defined by $\gamma_k = Z_k - h(\hat{X}_{k,k-1})$, should be orthogonal at each step [9], which is

$$E(\gamma_{k+j}\gamma_k^T) = 0, \quad k = 0, 1, 2, \dots, j = 1, 2, \dots \quad (52.21)$$

so the fading factor can be derived as follows,

$$\lambda_k = \begin{cases} \lambda_{0,k}, & \lambda_{0,k} \geq 1 \\ 1, & \lambda_{0,k} < 1 \end{cases} \quad (52.22)$$

where $\lambda_{0,k} = \frac{tr(N_k)}{tr(M_k)}$, $M_k = H\Phi_{k,k-1}P_{k-1}\Phi_{k,k-1}^T H^T$, $N_k = C_{0,k} - HQH^T - l_k R$,

$$C_{0,k} = \begin{cases} \gamma_k \gamma_k^T, & k = 0 \\ \frac{\rho V_{0,k-1} + \gamma_k \gamma_k^T}{1 + \rho}, & k \geq 1 \end{cases}.$$

$tr(\cdot)$ denotes trace of a matrix, ρ is the forgetting factor which is set as 0.95. $l_k \geq 1$ is the softening factor. $H_k = \left. \frac{dh(X_k, V_k)}{dX} \right|_{X=\hat{X}_{k,k-1}}$ denotes the Jacobian of the measurements model.

Moreover, the algorithm improves tracking accuracy greatly by denoting the Gaussian distribution obtained by linear transformation as the importance function.

52.4.2 Unscented Kalman Filter Optimization

Although the STF-GPF provides improved performance than the GPF to a certain extent, there are still some problems. One is that the EKF only uses the first order terms of the Taylor series expansion, which inevitably introduces large errors in the true posterior mean and covariance. The other is the difficulty in differential operation of the Jacobian. The UKF addresses these problems by applying a deterministic sampling approach, which approximates the probability distribution rather than an arbitrary nonlinear function. The UKF is capable to scale the approximation errors in the higher order moments of the posterior distribution. Moreover, due to the fact that the UKF calculates the posterior covariance accurately to the 2nd order while EKF relies on a 1st order biased approximation, distributions generated by the UKF generally have a bigger support overlap with the true posterior distribution than the overlap obtained by EKF [3]. This means that the UKF is a better choice for more accurate proposal distribution generation. Using UKF to generate proposal distribution within a GPF framework is shown as follows,

$$N(\bar{\mu}_{k|k-1}, \bar{\Sigma}_{k|k-1}) = \text{UKF}[N(\mu_{k-1}, \Sigma_{k-1})] \quad (52.23)$$

Replacing the procedure 1, 2 and 3 in the GPF algorithm with the equation above, the new filter is called the Unscented Gaussian Particle Filter (UGPF). To

enhance robustness, the adaptively fading mechanism mentioned above is also introduced.

52.5 Simulation and Results

The proposed algorithms are tested by simulation. The signal power P_r and noise power N_0 are determined by the carrier to noise ratio (CNR), which is obtained by $CNR = SNR \times B_n = P_r/N_0 \times B_n$. Where B_n denotes the signal bandwidth, i.e. 2.046 MHz. Coherent integration time T is 1 ms and the number of particles N is set as 500. The initial frequency offset is 125 Hz, the initial phase is 0° . This paper uses the high dynamic model proposed by Jet Propulsion Laboratory (JPL). Figure 52.1 shows the Doppler root mean square error (RMSE) under different CNR conditions with $N = 500$ particles. As shown in Fig. 52.1 that the tracking accuracy of STF is no much different from that of UKF with tracking threshold 29 dB-Hz while the proposed GPF-based algorithms, whose tracking threshold is 24 dB-Hz, significantly outperform STF and UKF. Furthermore, the optimization methods improve the tracking accuracy due to a more appropriate choice for proposal distribution while the UGPF outperforms the STF-GPF for the same reason. In Fig. 52.2, the average RMSE of the GPF is plotted for different particle numbers. It can be seen that the tracking accuracy has a limited (mainly due to the particle degeneracy and loss of diversity) improvement with the increase of particle numbers.

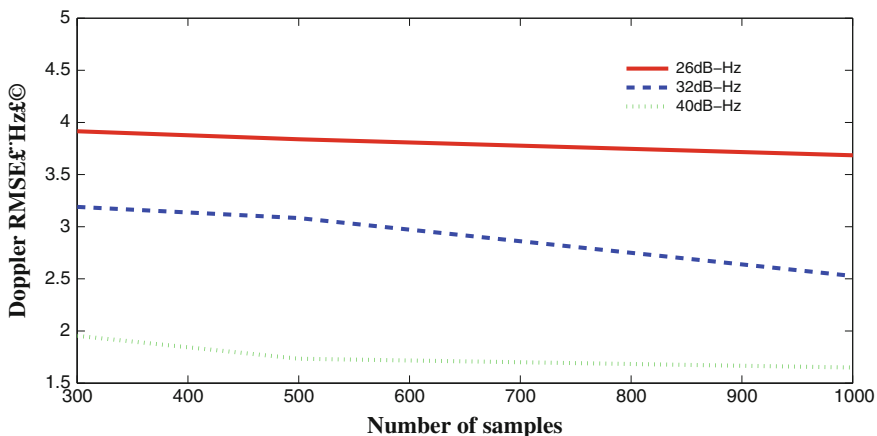


Fig. 52.1 Doppler RMSE under different CNR conditions with $N = 500$ particles

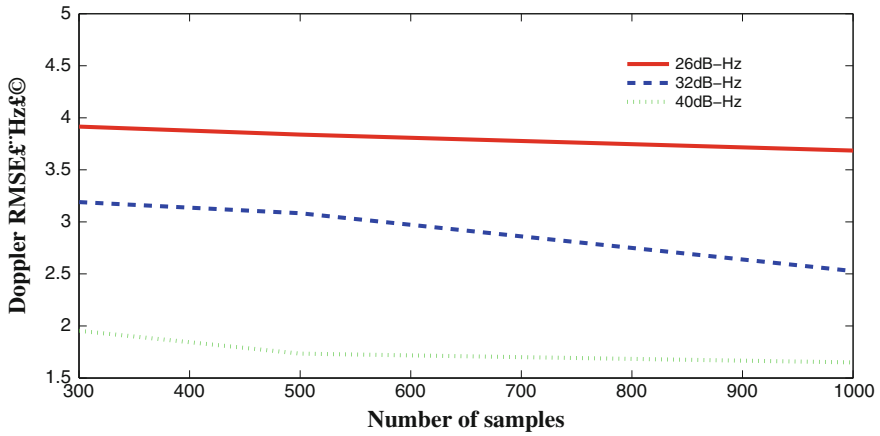


Fig. 52.2 Average RMSE of the GPF for different particle numbers

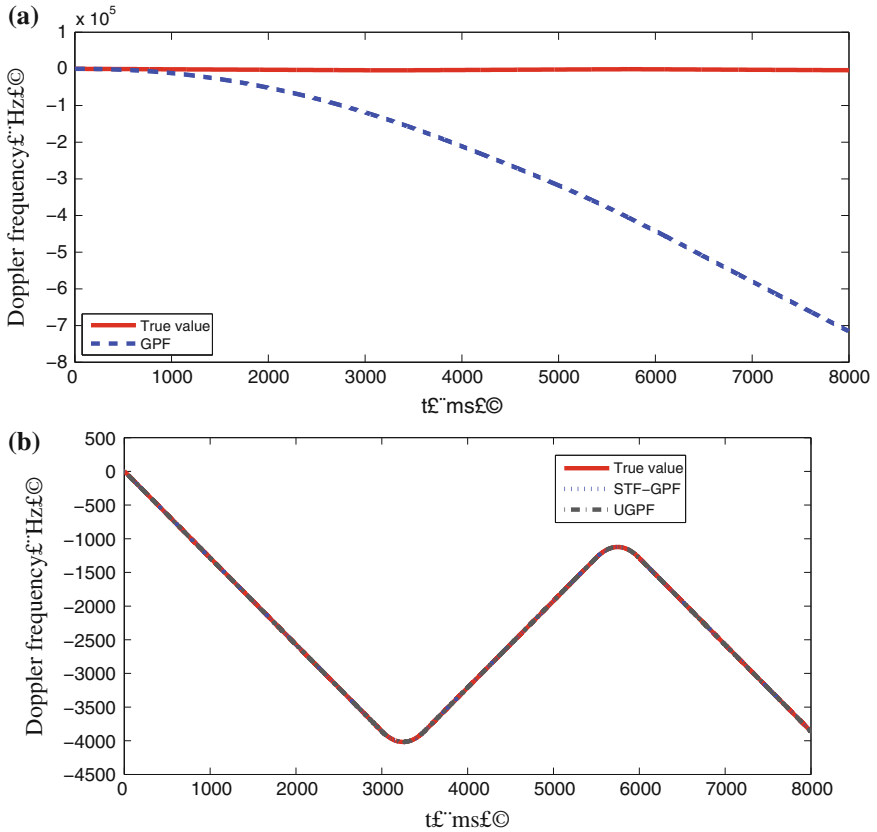


Fig. 52.3 Tracking information for GPF, STF-GPF, UGPF without accurate P_0

Table 52.1 Improvements in computational complexity over the GPF for different N

ϕ	N = 200	N = 300	N = 500	N = 1000	N = 2000
STF-GPF	1.2708	1.2909	1.3080	1.3852	1.5749
UGPF	1.1824	1.2334	1.3118	1.4228	1.6291

As shown in Fig. 52.3, when acceleration and jerk are unknown in the system initial conditions, the GPF fails to track the signal while the STF-GPF and UGPF are not affected.

The STF-GPF and UGPF have improvements in computational complexity over the GPF, which becomes even more prominent with the increase of particle numbers. Define a computational efficiency parameter to show the improvement in performance.

$$\phi = \frac{t_{GPF}}{t_{STF-GPF/UGPF}} \quad (52.24)$$

the results are shown in the following Table 52.1.

It can be seen that as the number of particles increase, the two optimization methods efficiently reduce calculation load. The efficiency of the deterministic sampling approach used in UGPF is better than linear transformation used in STF-GPF.

52.6 Conclusion

This paper presents novel carrier tracking algorithms for GNSS receivers, using Gaussian particle filter based approaches to carry out robust signal tracking under high dynamic conditions. The STF-GPF is proposed to obtain better robustness by combining STF and GPF, and the UGPF is further proposed to improve tracking accuracy by using UKF to generate proposal distribution within a GPF framework. Numerical simulation results show that the proposed GPF tracking loop and two optimization methods significantly outperform the conventional approaches, as well as achieving lower SNR sensitivity in comparison with EKF and UKF. Both optimization methods provide improved performance over GPF, in terms of dynamic performance robustness, tracking accuracy and computational load, while the efficiency of the deterministic sampling approach used in UGPF is better than linear transformation used in STF-GPF.

Acknowledgments This work was supported by Xiamen Satellite Navigation R&D Test Base, funding number 3502Z20121010.

References

1. Hinedi S, Statman JI (1988) High-dynamic GPS tracking. NASA Publication
2. Gordon NJ, Salmond DJ, Smith AF (1993) Novel approach to nonlinear/non-gaussian bayesian state estimation. In: IEEE Proceedings F (Radar and signal processing)
3. Rudolph van der M, Arnaud D, Nando de F, Eric W The unscented particle filter. Technical report CUED/F-INFENG/TR 380, Cambridge University Engineering Department
4. De Freitas JFG, Niranjan M, Gee AH, Doucet a sequential Monte Carlo methods to train neural network models. *Neural Comput* 12(4):955–933
5. Kotecha JH, Djuric PM (2001) Gaussian sum particle filtering for dynamic state space models. In: Proceedings of the international conference acoustic, speech, signal process, Salt Lake City, UT, May 2001
6. Ng W, Ji C, Ma W et al (2009) A study on particle filters for single-tone frequency tracking. *IEEE Trans Aerosp Electron Syst* 45(3):1111–1125
7. Gordon N, Salmond D (1995) Bayesian state estimation for tracking and guidance using the bootstrap filter. *J Guidance Control Dyn* 18(6):1434–1443
8. Zhou DH, Xi YG, Zhang ZJ (1992) A suboptimal multiple fading extended Kalman filter. *Chin J Autom* 4(2):145–152
9. Xie XQ, Zhou DH, Jin YH (1999) Strong tracking filter based adaptive generic model control. *J Proc Control* 9(4):1283–1294

Chapter 53

Research on the Mast Antenna System for Communications Compounds Satellite Navigation

Haiguang Zhang, Ximing Liang and Jia Zhang

Abstract In this paper, a mast antenna for communications consists of satellite navigation and UHF/VHF antenna is proposed. On the top of the mast system includes a satellite navigation antenna which is fed by the L-probe with its phase difference of 90° . Under the antenna a broadband omni-directional antenna utilize dual-parasitic structures with a metal pole through the radiator for UHF/VHF operation is designed. The radiator includes biconical-structure and thick dipole in order to reducing the size, by use of this structure to improve the impedance. The working frequency of the satellite navigation antenna can cover BD, GPS, Glonass satellite navigation system. The working frequency band of the VHF/UHF antenna is 120–550 MHz. In the whole band the VSWR is less than 2.5. The measured and simulated results show that the antenna has good radiation pattern properties over high and low frequency. All the efficient results show that the UHF/VHF antenna can combine satellite navigation antenna well to form a new mast antenna system that has important utility values in multi-functional satellite navigation communication.

Keywords Satellite navigation · Metal pole through the antenna · Mast antenna

H. Zhang (✉) · X. Liang (✉) · J. Zhang (✉)
Xi'an Research Institute of Navigation Technology, Xi'an 710068, China
e-mail: zhg54321@163.com

X. Liang
e-mail: Mysun896@sina.com

J. Zhang
e-mail: 51800071@qq.com

53.1 Introduction

With the development of navigation communication technology, requires the antenna on mobile communication platform cover more broad band and implement multi-band receiving and transmitting. This demand leads the platform has a great many of antennas cause the EMC of the platform become much more complex. In order to solve this problem, overseas had developed several novel mast antenna system in mobile platform. The system utilize advanced design concept can compound multi-band, multifunction active or passive antenna efficiency.

A triple-system microstrip satellite navigation antenna is proposed in this paper which is fed by the L-probe with its phase difference of 90° [1–3]. Then proposed a VHF/UHF broadband omni-direction antenna utilize biconical-structure and thick dipole in order to reducing the size [4–7].

The satellite navigation antenna locates on the top of the UHF/VHF antenna and the feed line through the underneath radiator. A metal pole through the UHF/VHF antenna is designed in order to uphold the navigation antenna and shield the electromagnetic energy leak from the feed line. The simulation result shows that the VSWR of the VHF/UHF antenna become worsen after the metal pole through the radiator. Use dual-parasitic sleeve structures to improve the impedance, the inner sleeve is a cylinder copper sheet that combines the metal pole and the radiator. Utilize this structure realize a multi-functional mast antenna system.

53.2 Antenna Design

53.2.1 Analysis of the Theory of the Mast Antenna

The proposed mast antenna utilize integration of antenna, RF, and DSP theory that combines satellite navigation antenna, DF antenna of S wave band, UHF/VHF communication antenna, HF antenna and various RF network. The feed line of the upper antenna through the underneath radiator needs an inner metal cylinder not only shield the electromagnetic energy leak from the feed line but also uphold the upper antenna. The bottom of the mast antenna combines with active circuit module and radiator to achieve the mast system reconstruction in order to realize the LF navigation (Fig. 53.1).

53.2.2 Satellite Navigation Antenna Design

The proposed microstrip satellite navigation antenna use a cascade of 3 dB Wilkinson power divider and a broadband 90° phase shifter to achieve circularly polarized. The structure is shown in Fig. 53.2. The substrate thickness is 1 mm with

Fig. 53.1 The schematic diagram of the mast antenna

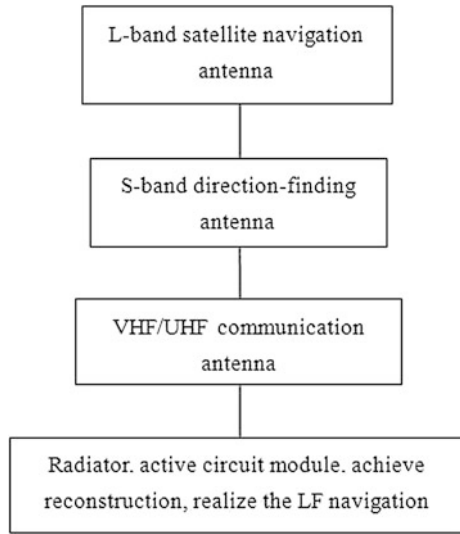


Fig. 53.2 Geometry of the feeding network

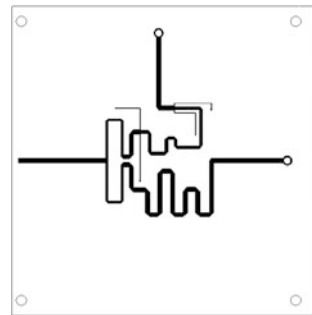
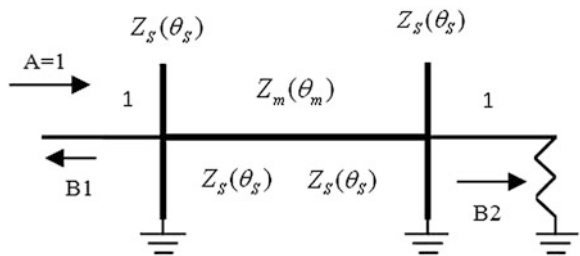


Fig. 53.3 Normalized 90° phase shifter



the dimension 100×97 mm, the dielectric constant is 6.3. The 90° phase shifter has two branches, one has two pairs of $\lambda_g/8$ terminal short and open transmission line to realize the broadband of 90° phase difference. The patch is fed by two L-probe in order to broaden impedance bandwidth (Fig. 53.3).

Use odd-even analysis theory to solve the input admittance of the circuit.

The even-mode equation as follows

$$Y_{in} = jY_m \tan \frac{\theta_m}{2} + jY_s \tan \theta_s \cot \theta_s \quad (53.1)$$

The odd-mode equation as follows

$$Y_{in} = -jY_m \cot \frac{\theta_m}{2} - jY_s \cot \theta_s + jY_s \tan \theta_s \quad (53.2)$$

The S parameter of the circuit as follows

$$S_{11} = \frac{1}{2} \left(\frac{1 - jK_1}{1 + jK_1} + \frac{1 + jK_2}{1 - jK_2} \right) \quad (53.3)$$

$$S_{21} = \frac{1}{2} \left(\frac{1 - jK_1}{1 + jK_1} - \frac{1 + jK_2}{1 - jK_2} \right) \quad (53.4)$$

where

$$K_i = Y_m \left(\tan \frac{\theta_m}{2} \right)^{(-1)^{i+1}} + (-1)^i 2Y_s \cot 2\theta_s, \quad i = 1, 2 \quad (53.5)$$

We can conclude that under the parameter VSWR of 1.2, $Y_s = 0.4$, $Y_m = 0.81$.

$$Z_s = 2.5Z_0, \quad Z_m = 1.24Z_0, \quad \text{where } Z_0 = 50 \Omega.$$

The patch had a resonant frequency of f , the encourage mode is TM₁₁. The square side length of the patch set as a .

$$\begin{cases} f = \frac{1.84118C}{2\pi a \sqrt{\epsilon_r}} \\ \epsilon_r = \frac{t+H}{\frac{t}{\epsilon_{r1}} + \frac{H}{\epsilon_{r2}}} \end{cases} \quad (53.6)$$

The thickness of the substrate generally choose thick in order to broaden the bandwidth, with the thickness increase simultaneity creates surface wave, summing up the above as follows $H = 16$ mm, the patch length can be calculated via the Eq. 53.6, the length $a = 50$ mm, the dielectric constant of the patch substrate is 2.55. The length of the two L-probes are set to 10 mm. The width of the coupling rectangle patches are set to 2 mm, the length of the patches are 32.5 mm. The antenna structure is shown in Fig. 53.4.

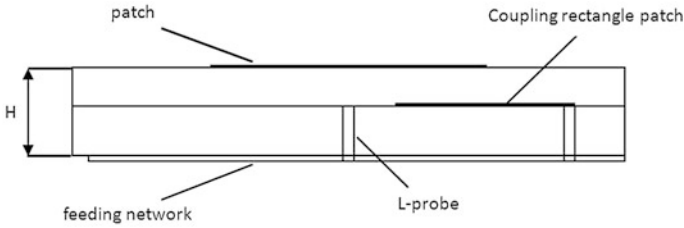


Fig. 53.4 Geometry of the proposed antenna

53.2.3 VHF/UHF Antenna Design

The characteristic impedance of the biconical-structure antenna with infinite length in vacuum is given by

$$Z_c = \frac{Z_w}{\pi} \ln \cot \frac{\theta}{2} = \frac{1}{\pi} \sqrt{\frac{\mu_0}{\epsilon_0}} \ln \cot \frac{\theta}{2} = 120 \ln \cot \frac{\theta}{2} \tag{53.7}$$

where Z_w denotes the wave impedance in vacuum, θ denotes half cone deg of the biconical antenna. The impedance characteristic of the biconical antenna with small θ is given by

$$Z_c = 120 \ln \left(\frac{\theta}{2} \right) \tag{53.8}$$

The simulation results of the biconical antenna with the cone angel of 20°, 30°, 40°, 45°, 50°, 60°, 70° are shown in Fig. 53.5. Figure 53.5 depicts the VSWR characteristic of the biconical antenna with different cone angel. The VSWR is less than 3 in the whole band when the cone angel is larger than 30°. Considered the impedance characteristic and the antenna dimension, the θ is given by 35°.

Figure 53.6 shows the structure of the biconical antenna. The radiator includes biconical-structure and thick dipole that is fed by a 50Ω coaxial line. Use cone angel and dipole length optimization to improve the VSWR characteristic. A metal pole with diameter of 3 cm through the UHF/VHF antenna is designed in order to uphold the navigation antenna and shield the electromagnetic energy from the feed line. The simulation VSWR results of the antenna with a metal pole through or not is shown in Fig. 53.7. From the Fig. 53.7 we can see that the impedance characteristic became worsen at about 420 MHz when the proposed metal pole through the radiator.

In order to improve the impedance characteristic use the structure that is proposed in this paper. The structure is shown in Fig. 53.8. The proposed radiator is composed of two inner sleeves and one outer sleeve. The two inner sleeves are

Fig. 53.5 VSWR of the antenna with different cone angle

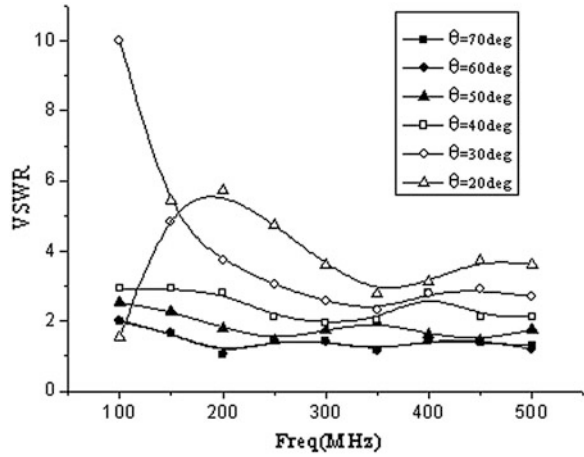
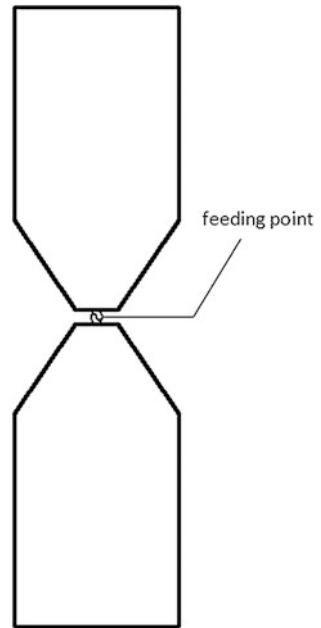


Fig. 53.6 The structure of the biconical antenna



cylinder copper sheet with diameter of D_2 and length of $H_3/2$. One side connected with the bottom of the biconical structure the other side connected with the center metal pole. Use this structure to obtain parallel inductance. Measure the length of H_3 to obtain the agreement inductance value. The outer sleeve structure is added to the feeding point for adjusting the input impedance. The optimized dimension parameters is given by

Fig. 53.7 VSWR of the antenna with a metal pole through or not

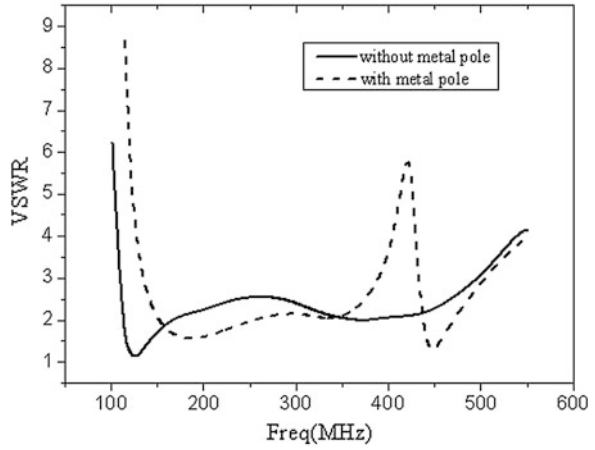
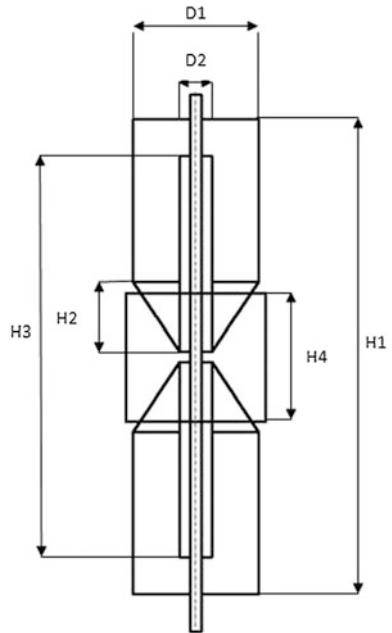


Fig. 53.8 The structure of the proposed antenna



H1 = 90 cm, D1 = 24 cm, H2 = 12 cm, D2 = 8 cm, H3 = 76 cm, H4 = 22 cm, D3 = 26 cm.

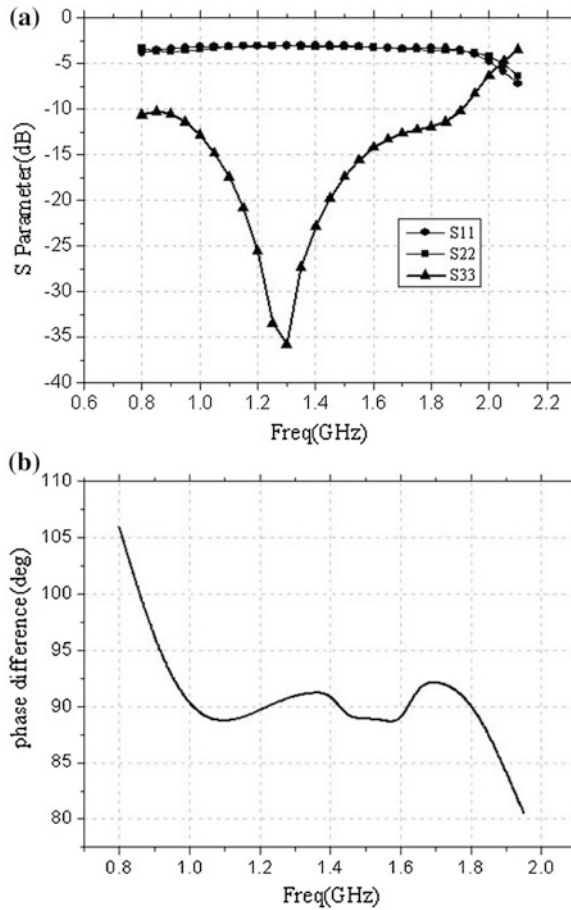


Fig. 53.9 Simulated the phase and amplitude results of the network

53.3 Results and Discussion

Figure 53.9 shows the simulated S parameter of the feeding network. From the Fig. 53.9, we can see the working frequency for $S_{11} < -10$ dB from 0.8 to 1.9 GHz. From Fig. 53.9a, S_{21} and S_{31} are almost equal from 1.1 to 1.8 GHz. From Fig. 53.9b, the phase difference between the two port is almost 90° in the whole band.

Figure 53.10 shows the photograph of the proposed triple-system microstrip satellite navigation antenna. Figure 53.11 shows the VSWR of the antenna, the solid and dashed lines in Fig. 53.11 represent the simulated and measured VSWR. The bandwidth (VSWR < 2) from 1.05 to 1.9 GHz is achieved. Simulated and measured axial ratio are shown in Fig. 53.12. We can see the bandwidth (AR < 3)



Fig. 53.10 Photograph of the satellite navigation antenna

Fig. 53.11 Simulated and measured VSWR results of the antenna

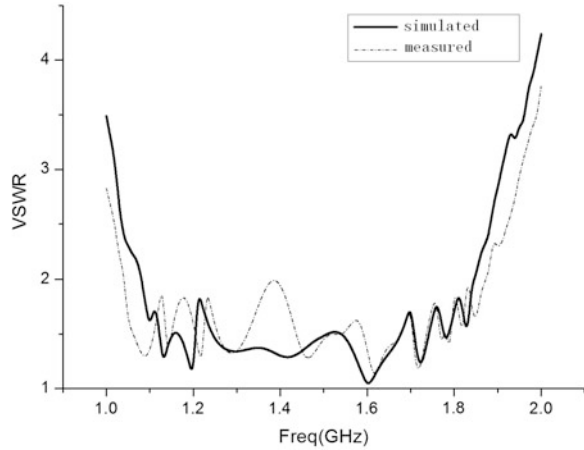


Fig. 53.12 Simulated and measured AR results of the antenna

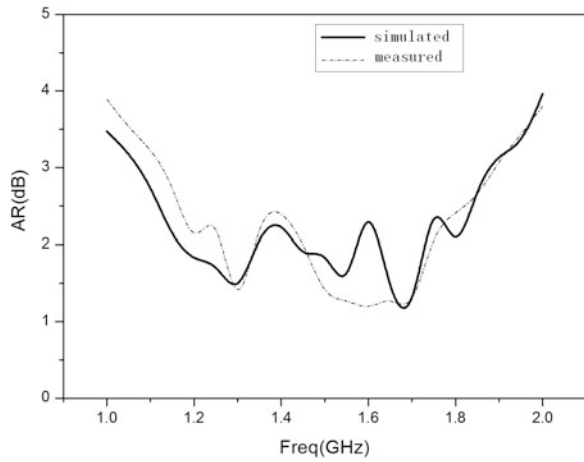
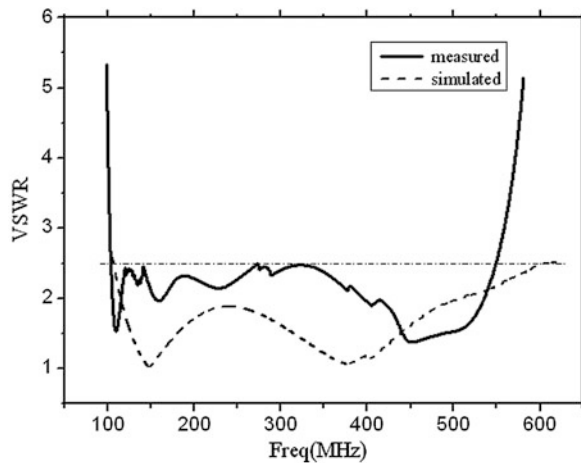


Fig. 53.13 Photograph of the proposed antenna



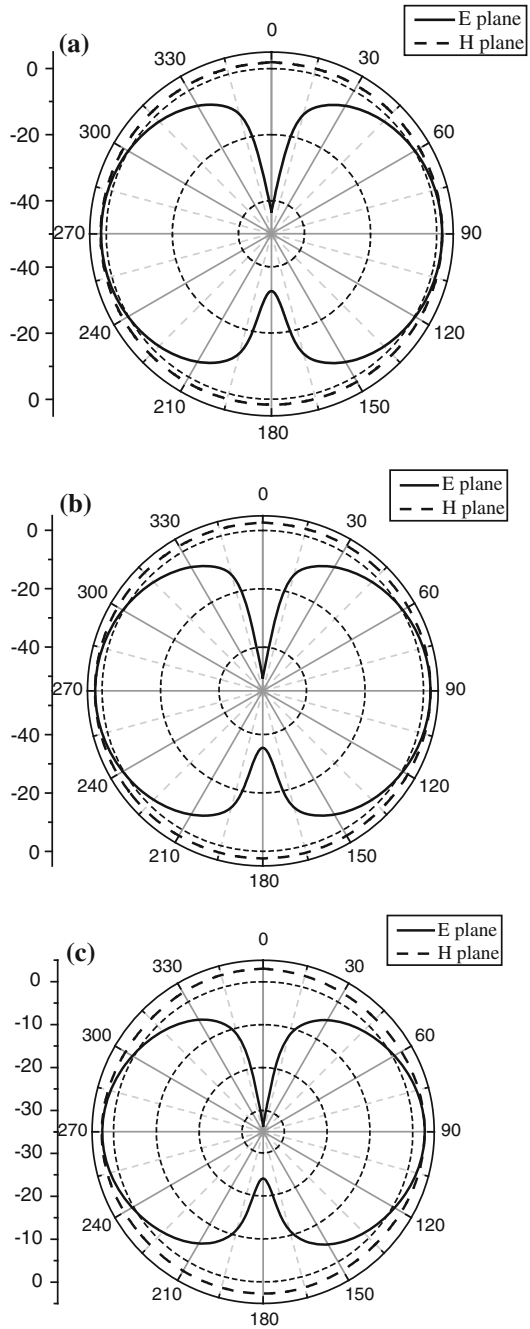
Fig. 53.14 Simulated and measured VSWR results of the antenna



from 1.1 to 1.8 GHz. In both figures, good agreement can be seen between simulated and measured results.

Figure 53.13 shows the photograph of the proposed VHF/UHF antenna. Figure 53.14 shows the simulated and measured VSWR of the antenna. The working frequency band of the VHF/UHF antenna is 120–550 MHz. In the whole band the VSWR is less than 2.5. Figure 53.15 presented the measured radiation pattern in E and H planes at the operating frequency 120, 350, 550 MHz, the gain of the proposed antenna in H planes are 1.5, 1.9 and 2.2 dBi. It can be seen that the all the peak beam are in horizontal plane, the radiation pattern of H plane is omnidirectional. All the efficiency results shows that the proposed antenna has good performance in impedance and radiation characteristic.

Fig. 53.15 Measured radiation pattern of the antenna **a** 120 MHz **b** 350 MHz **c** 550 MHz



53.4 Conclusion

In this paper, a mast antenna for communications consists of satellite navigation and UHF/VHF antenna is proposed. Utilize dual-parasitic structures with a metal pole through the radiator for UHF/VHF operation in order to improve the impedance. The simulated and measured results show that the mast antenna have good performance in the working band that has important utility values in multi-functional satellite navigation communication.

References

1. Lo WK, Chan CH, Luk KM (2004) Bandwidth enhancement of circularly polarized microstrip patch antenna using multiple L-shaped probe feeds. *Microwave Opt Technol Lett* 4:263–265
2. Lau KL, Luk KM (2005) A novel wide-band circularly polarized patch antenna based L-probe and aperture-coupling techniques. *IEEE Trans Antennas Propag* 1:577–580
3. Qing XM (2004) Broadband aperture-coupled circularly polarized microstrip antenna fed by a three-stub hybrid coupler. *Microwave Opt Technol Lett* 1:38–41
4. Schel Kunoff SA (1951) General theory of symmetric biconical antennas. *J Appl Phys* 22 (11):1330–1332
5. Brown GH, Wood Ward OM (1952) Experimentally determined radiation characteristics of conical and triangular antennas. *RCA Rev* 13(4):425–452
6. Sandler SS, King RWP (1994) Compact conical antenna for wide-band coverage. *IEEE Trans Antennas Propag* 13(3):436–439
7. Shigang Z, Baohua S (2009) Analysis and design of a novel omni-directional broadband biconical antenna for mobile communication. *Chin J Radio Sci* 24(2):224–227

Chapter 54

Research on the Satellite Navigation Independent Compound Receiving and Transmitting Array Concept

Ximing Liang, Haiguang Zhang and Jia Zhang

Abstract In this paper, the theory of satellite navigation independent compound receiving and transmitting array is proposed. Analyze the feasibility of satellite navigation receiving array, microwave energy transmitting array, RF rectification array and energy independent network. Explore the possibility framework of MEMS multifunction skin array. The concept of possibility application mode of array system in outer space, heaven and ground is proposed based on the simulation, analysis and experiment results. The elementary ideas in this paper have some reference value in development of BD system.

Keywords Satellite navigation · Multifunction skin · Rectification array · MEMS · Transmitting and receiving array

54.1 Introduction

Satellite navigation system and Internet, mobile communication has become the three pillar for information technology development in this century, and became an important national infrastructure, is an important symbol to measure a country's comprehensive national strength.

China's Beidou navigation system with all-weather, all-time, high precision, large range characteristics, can provide position, velocity, time coordinate, and message communication function for a variety of user platform, has become the essential infrastructure of our country modernization military activities and

X. Liang (✉) · H. Zhang (✉) · J. Zhang (✉)
Xi'an Research Institute of Navigation Technology, Xi'an 710068, China
e-mail: Mysun896@sina.com

H. Zhang
e-mail: zhg54321@163.com

J. Zhang
e-mail: 51800071@qq.com

equipment, related to the national economy and security. Figure 54.1 is a satellite navigation application framework.

Array antenna used in the satellite navigation field long-standing. As the use of a receiving array, can increase the received signal strength, the two can improve the anti-interference ability of the receiving equipment. The augmented pseudo satellite launch array used as a micro satellite or area, can be shaped beam, in order to achieve narrow beam or multiple beam applications. Array antenna and satellite navigation array depth integration, will be able to achieve flexibility in the use of autonomous navigation of confrontation, detection and many other functional perception. This common aperture array surface can achieve unit reconstruction and beam fitting. Array antenna in the used as microwave energy transmission emission, may use a particular algorithm for fitting out of flatten beam broadening, weakening the power density of Gauss beam the extreme uneven phenomenon.

In recent years, the development and application of many empty days, satellite navigation system, make the solar array and satellite navigation receiving equipment appears more and more tightly coupled state, study on antenna and solar cell integration has been frequently reported. But for the small satellite or regional enhanced small pseudo satellite transmitting array energy volume, size of contradiction. Especially for energy self-sufficiency, night conditions cannot meet the normal use of task platform. These are more restricted depth of Beidou navigation application in many fields. Active exploration and innovation research, the microwave energy transmission array, RF rectification array, energy self-sufficiency network and satellite navigation receiving array are integrated, the research will be

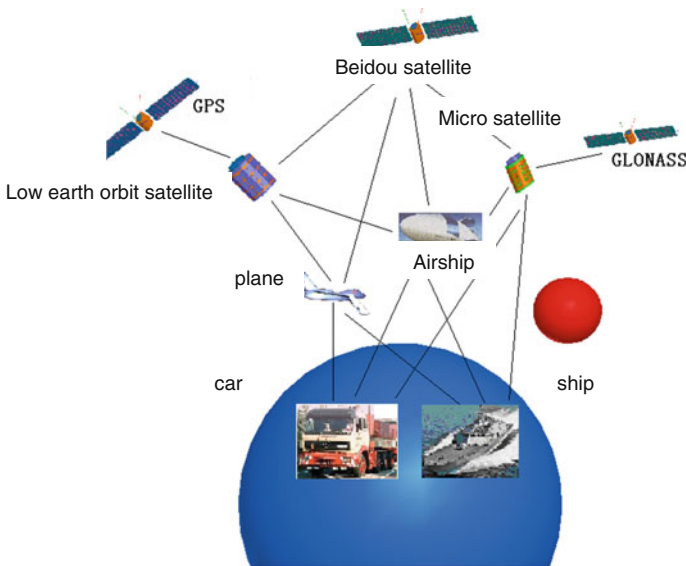


Fig. 54.1 The application frame diagram of satellite navigation

solar array and array integrated technical content will become very meaningful, and very challenging.

This paper analyzes the microwave energy transmission, satellite navigation anti-interference feasibility of receive and transmit beam forming in theory. In a dielectric constant of sheet metal on the simulation analysis of three system satellite navigation receiving unit and antenna array; gives two kinds of microwave energy receiving unit and a rectifier of RF network model, and developed the microwave energy transmission array, RF rectification array, energy self-sufficiency network integration framework. This paper constructs apart of solar cell array gives the satellite navigation of autonomous composite transceiver array concept, the simulation of the array of skin micro system the possibility of architecture.

Via the experimental study, this paper gives part of the research model and test data. Test data verified the rationality of satellite autonomous navigation part composite transceiver array concept.

54.2 Theoretical Analysis

54.2.1 Analysis of Microwave Energy Transmission

Usually navigation receiving device is using a transmitting antenna far field radiation zone, the transmitted energy is very low, usually orders of magnitude from 10^{-10} to 10^{-12} . In the microwave energy transmission, receiving the energy requirement is between 0.1 and 1, the use of radiation far field region will make most of the energy is wasted, so we need to use the antenna near field radiation [1–3].

Antenna area can be divided into: reactance near field and radiation in the near field region (namely Fresnel zone), far field radiation zone (the Fraunhofer region).

The dividing line between near field radiation reactance and the near field region is:

$$h = D^{4/3} / 2\lambda^{1/3} \quad (54.1)$$

the dividing line of radiation near field region and far field radiation area as:

$$h = 2D^2 / \lambda \quad (54.2)$$

the above D is the largest line of antenna aperture size, λ is the working wavelength.

In the microwave directional energy transmission, we need to be placed in the Final region of the target array receiving transmitting beam energy transport within the receiving antenna to transmit antenna, which is greater than $D^{4/3} / 2\lambda^{1/3}$, and less than $2D^2 / \lambda$.

If the representative of h microwave transmission in free space distance, T1, R1 respectively represent the transmitting antenna and the receiving antenna area, λ is

Table 54.1 The frequency, antenna caliber, distance number form

Serial number	Transmit frequency (GHz)	Antenna aperture (m)	Array spacing should be less than (km)
1	F = 10	200	2600
	F = 10	500	16,600
2	F = 35	200	9300
	F = 35	500	58,300
3	F = 200	100	6600
	F = 200	200	53,300

the working wavelength, η is microwave transmission efficiency in free space is the function of parameters $\sqrt{T1 * R1}(\lambda h)^{-1}$. Assuming the emission aperture field distribution for Gauss.

The transmission efficiency is determined by $\sqrt{T1 * R1}(\lambda h)^{-1}$, and not directly related to the transmission distance. Distance h increases by T1 and R1 increase or decrease to compensate the λ .

Non focused port surface decreased significantly at the power density of the far zone, the energy transfer efficiency is low. In the application of microwave energy transmission to realize the transmission of high power density and long distance, should improve the working frequency antenna aperture and system, and uses the focusing mouth surface emitting signal. Table 54.1 reference value calculation for several typical frequency, mouth face, spacing results.

54.2.2 Analysis of Anti Jamming Receiver

Satellite navigation receiver (L band) in the practical application environment, interference is inevitable. Array antenna can effectively enhance the signal, can more adaptive anti jamming. The anti jamming receiver array and microwave can be integrated array design transmission array, RF rectification array component will be effective anti except a plurality of interference, and improve the dynamic range of active radio frequency receiving channel, weaken the microwave energy (C.X band) may bring about the impact.

Using the power inversion algorithm directly to the array output as an error signal, the pursuit of the minimum mean square error, signal to interference ratio is greatly improved. The method is availability for the satellite signal receiving.

By introducing integral time constant, RC, then the iteration formula is as follows:

$$RC \frac{d\bar{w}}{dt} + 2\mu \bar{x}^* \bar{x}^T \bar{w} + \bar{w} = \bar{w}_b \tag{54.3}$$

the algorithm can be implemented by hardware circuit, weight calculation relationship:

$$w(n + 1) = w(n) + 2\mu y(n)x(n) \tag{54.4}$$

selection of N units in the composite antenna array, n - 1 array element is uniformly distributed on the radius of the circle of half wavelength. Through analysis the gain of the formed beam upward in the satellite, and the interference to the formation of null. Beam and null amplitude difference exceeds the expected target.

54.2.3 Beam Forming Emission Analysis

Research on integrated antenna array, the array beam broadening can be applied to microwave energy transmission. Beam broadening can avoid energy is too concentrated, the receiving array of non energy receiving device to cause additional load. Reasonable optimization makes the energy requirements within the region in the ideal distribution, so that the efficiency of receiving equipment optimization [4, 5].

Setting a rectangular planar array according to the unit rectangular grid arrangement in the XOY plane. As is shown in Fig. 54.2:

According to the principle of superposition of the electromagnetic wave, can give the planar array factor:

$$s(\theta, \phi) = \sum_{m=-M_x}^{M_x} \sum_{n=-M_y}^{M_y} \left(\frac{i'_{mn}}{i'_{00}} \right) \exp[jk \sin \theta (md_x \cos \phi + nd_y \sin \phi)] \tag{54.5}$$

Each unit of current i'_{mn} were normalized to the center of the current i'_{00} :

$$i_{mn} = i'_{mn} / i'_{00} \tag{54.6}$$

Fig. 54.2 The grid pareto diagram of rectangle surface array

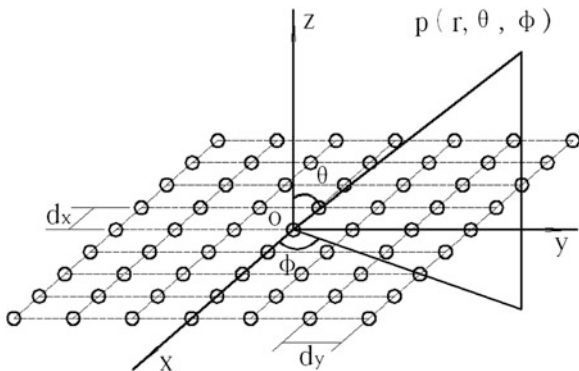
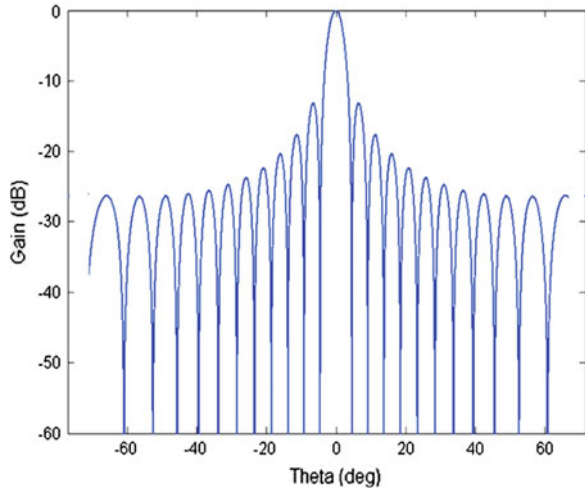


Fig. 54.3 The shaped beam of array antennas



were normalized to the center of the current i_{mn} . And the center of the current i'_{oo} . The phase difference is a, then the:

$$i_{mn} = I_{mn} \exp(ja_{mn}) \tag{54.7}$$

accordingly:

$$s(\theta, \phi) = \sum_{m=-M_x}^{M_x} \sum_{n=-M_y}^{M_y} (I_{mn}) \exp[jk \sin \theta (md_x \cos \phi + nd_y \sin \phi) + ja_{mn}] \tag{54.8}$$

for the transmitting array microwave energy transmitter unit structure, specific, the researchers used the Fu Li ye series transform and differential evolution algorithm combining beam forming, obtained better. Figure 54.3 beam array antenna shaped figure, Fig. 54.4 for array antenna beam broadening map.

54.3 Simulation Analysis

54.3.1 Focusing Field Energy Transmission Simulation

Based on the theory of different aperture focusing antenna, transmitting array is constructed in the special electromagnetic simulation tool. Using HFSS to simulate the antenna with different frequency, power, focal length and other parameters. Figure 54.5 is the focus emission mouth surface axial power density simulation diagram; Fig. 54.6 for longitudinal focal power density simulation diagram; Fig. 54.7 focusing port surface axial power density curve.

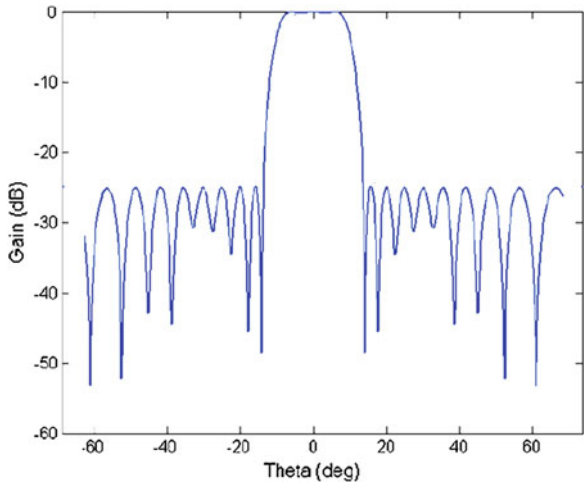


Fig. 54.4 Beam widen of array antennas

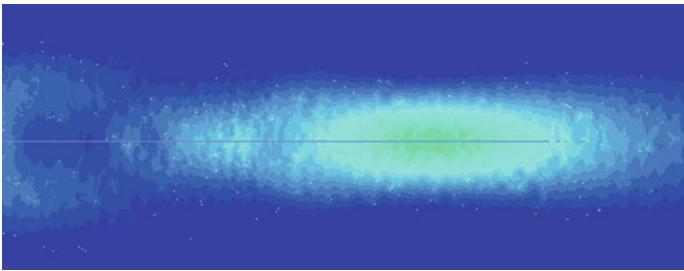


Fig. 54.5 The simulation of power density of focused aperture

Fig. 54.6 The simulation of power density of lengthways focal spot

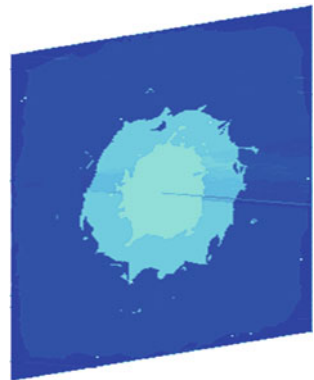
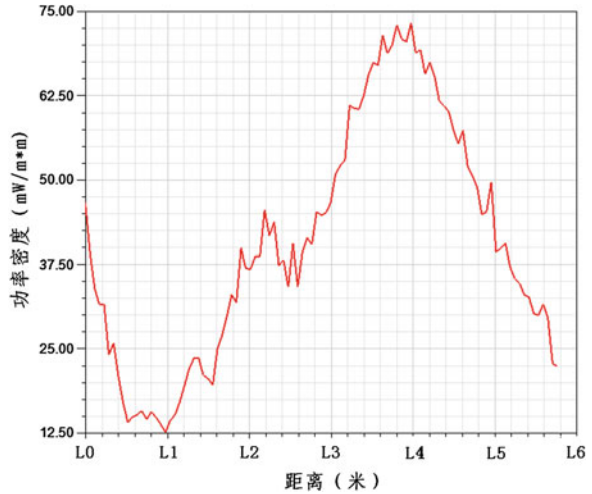


Fig. 54.7 The simulation of lengthways power density of focused aperture



From the simulation results, in the relatively distant areas can be effectively transmitted to the distal focused microwave. The simulation results of focal spot, theoretically in line with array energy receiving expected. And it can make the maximum power density array controlled by effective construction of transmitting array.

54.3.2 Unit Simulation of Triple Receiving Satellite Navigation System

Based on microstrip antenna theory design three system navigation antenna concludes GPS, Beidou System and GLONASS system. The upper layer is the patch, the second layer is coupled line, the third layer is the feeding network. The radiation patch selection of a dielectric constant of 2.55. The third layer is arranged at the lower end of active RF micro circuit. Figure 54.8 is a satellite navigation receiver

Fig. 54.8 The model of satellite navigation antenna

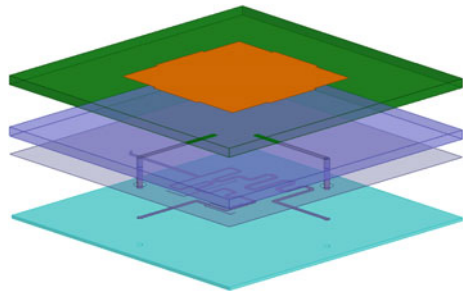


Fig. 54.9 VSWR simulation result

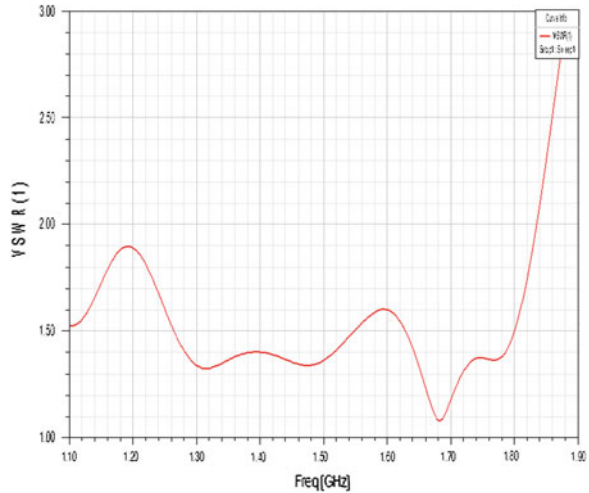
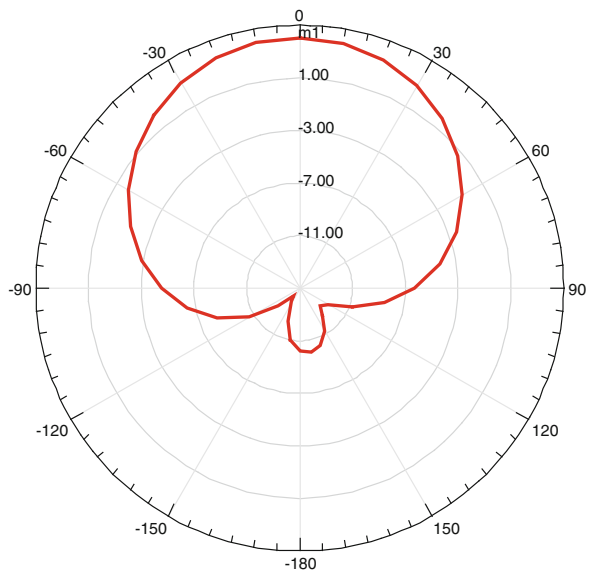


Fig. 54.10 BD radiation pattern



antenna model, Fig. 54.9 Simulation of standing wave curve, 10 Beidou antenna pattern in Fig. 54.11 GPS antenna pattern in Fig. 54.12 is a GLONASS antenna pattern (Fig. 54.10).

From the simulation results, the three receiving unit antenna model to construct the effective system. Each frequency point of standing wave is good, Big Dipper, GPS, GLONASS direction of the antenna can meet the expected. Units ample test results according to the design and the simulation results are consistent.

Fig. 54.11 GPS radiation pattern

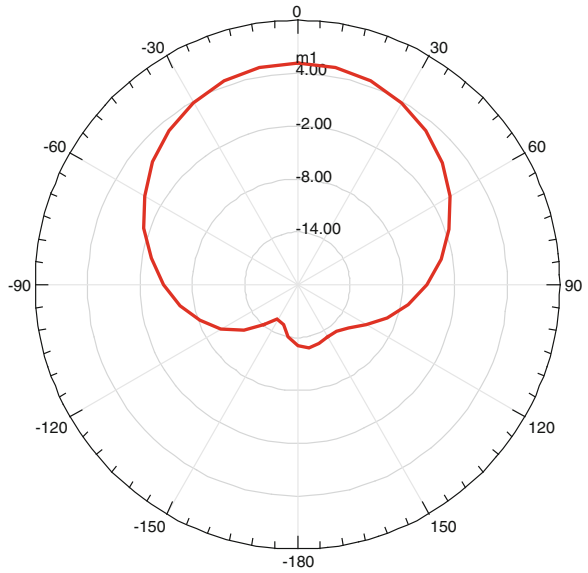
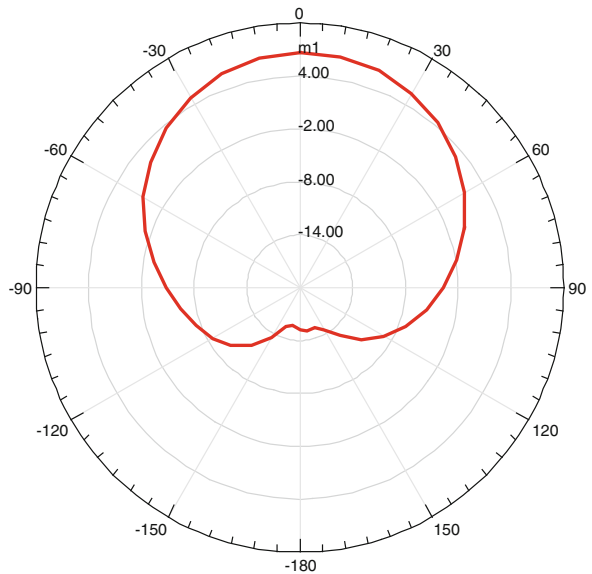


Fig. 54.12 GLONASS radiation pattern



54.3.3 Satellite Navigation Receiving Array Concept

Figure 54.13 is a satellite navigation receiver array top local view. The figure didn't show the RF circuit, signal processing circuit.

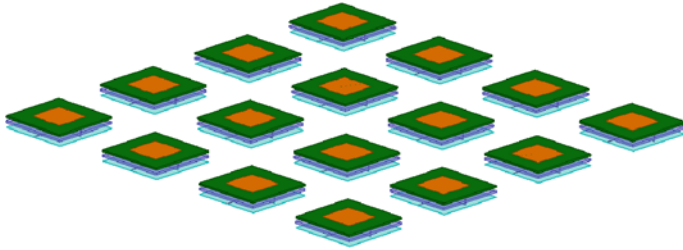
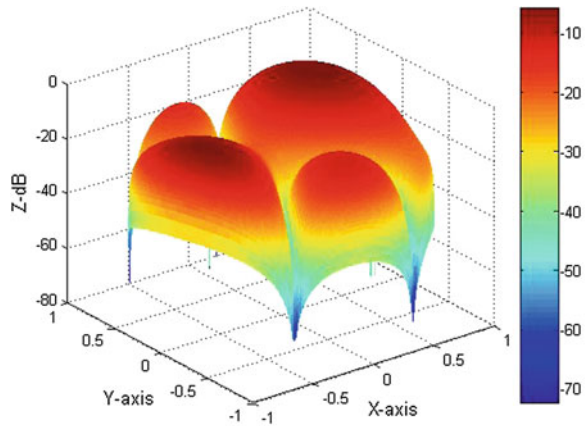


Fig. 54.13 The part view of satellite navigation receiving array

Fig. 54.14 The simulation of anti-jamming for GPS



According to certain tasks is expected to receive anti interference receiving appropriate unit selection in the array in the above. Figure 54.14 is the anti jamming receiver array simulation example, enhanced from the figure we can see the received signal, interference signal suppression.

54.3.4 Energy Antenna Unit

54.3.4.1 The Energy Receiving Integrated Unit

Build the following energy receiving integrated unit based on the theory of microstrip antenna. The top using narrowband structure, the second layer Nonlinear Rectification for radio frequency circuit, the third layer is the network cascade structure. Model construction are based on the study of S, C, X, Ka band. Figure 54.15 is a narrow energy receiver structure [6, 7].

Fig. 54.15 The structure of narrow-bandwidth energy receiving

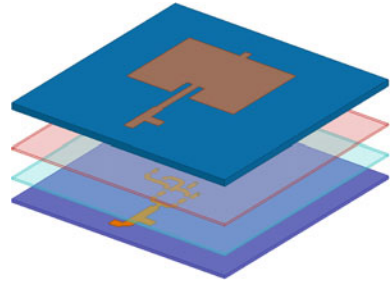
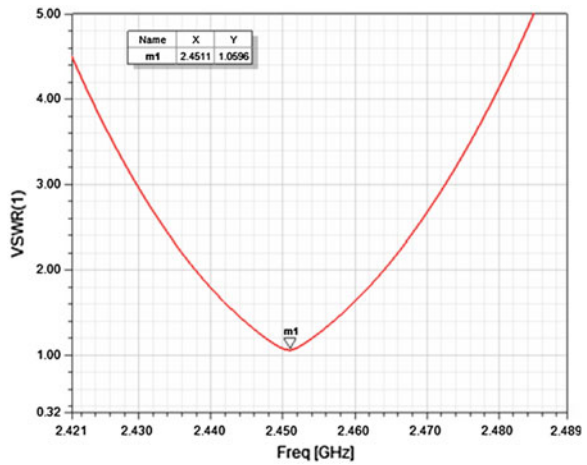


Fig. 54.16 The VSWR of S band receiving structure



Above board respectively using microwave substrate dielectric constant, the thickness of 4.5 1.524 mm and a dielectric constant of 3.2, thickness 0.762 mm. Tangent of the loss angle are respectively 0.002 and 0.0032. Figure 54.16 is the S band receiver structure standing wave curve, Fig. 54.17 for S band receiver structure gain curve.

Figure 54.18 is a S band receiver structure of 3D pattern. Look at the structure satisfy the narrowband microwave energy expected from the results of the analysis.

54.3.4.2 The Energy Receiving Integrated Unit Two

Build the following energy receiving antenna broadband integrated unit based on the theory of. The top using wideband planar Archimedes spiral structure as the radiation unit, the second layer Nonlinear Rectification for radio frequency circuit, the third layer is the network cascade structure. Model constructed respectively based on the study of S–C and X–Ka frequency. Figure 54.19 is a wideband energy receiving structure.

Fig. 54.17 The gain of S band receiving structure

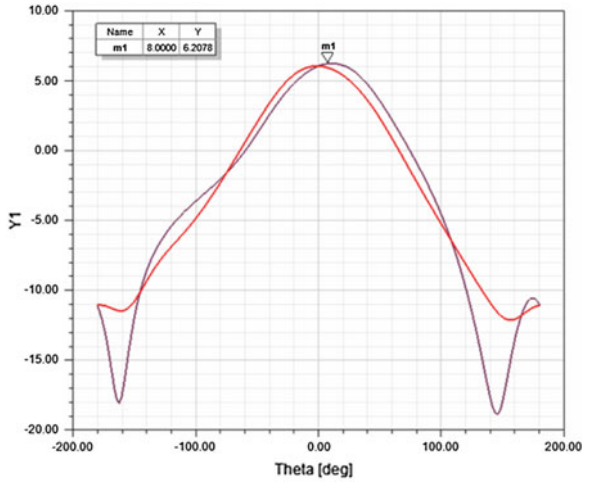


Fig. 54.18 The 3D radiation pattern of S band receiving structure

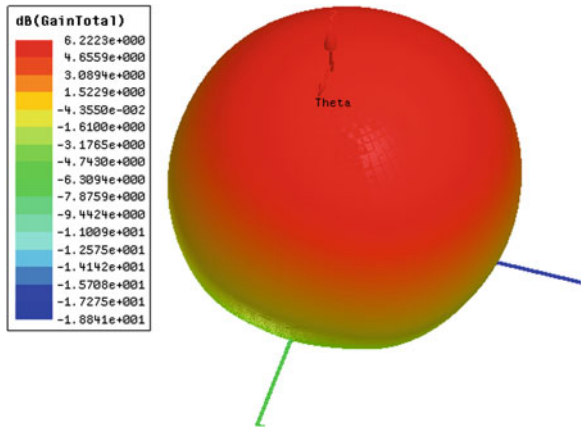


Fig. 54.19 The structure of wideband energy receiving

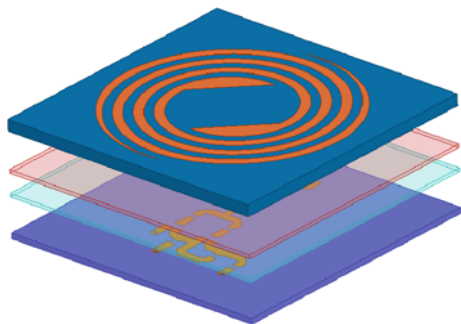


Fig. 54.20 The VSWR of wideband receiving

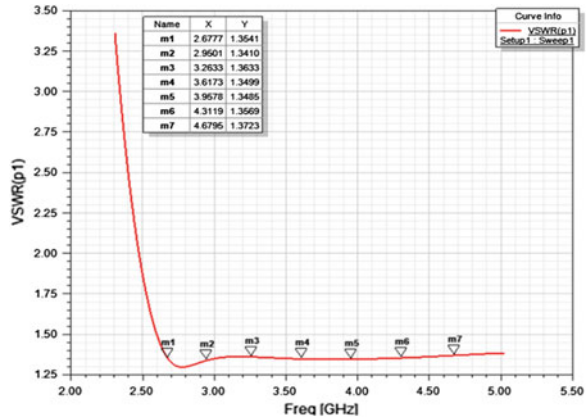
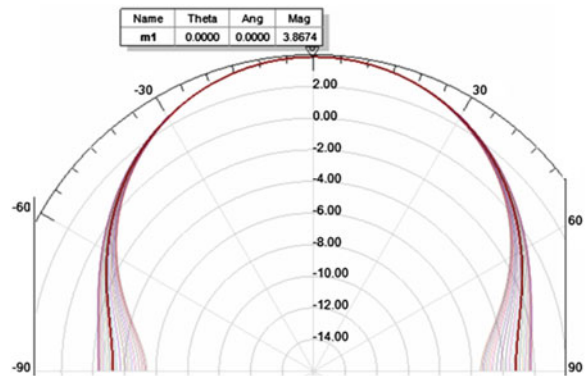


Fig. 54.21 The gain of wideband receiving



Map sheet can choose rigid or flexible microwave plate. Figure 54.20 is the structure of wideband receiving VSWR curve, Fig. 54.21 is the gain curve of the structure. From the analysis results of the structure to meet certain broadband microwave can receive the expected.

54.3.5 Rectifier Unit

The researchers constructed a multiple frequency RF rectification unit, a variety of circuit topology, a variety of dynamic range, and achieved good results. Figure 54.22 is a multi tube rectifier circuit unit structure. Figure 54.23 is a rectifier structure power S11 curve.

RF structure shown in Fig. 54.22 in the analysis showed the expected efficiency and power voltage than the ideal. Figure 54.24 is a unit under different loads of



Fig. 54.22 The structure of multi-diode rectifier circuit

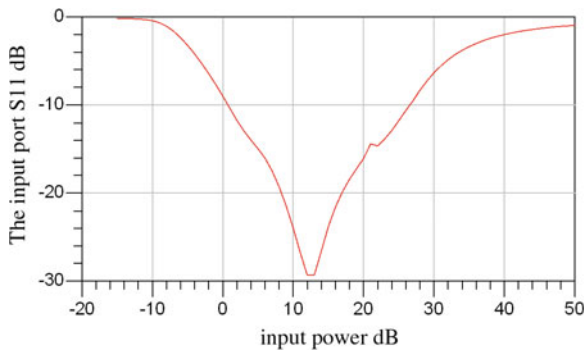


Fig. 54.23 The S parameter of rectifier circuit

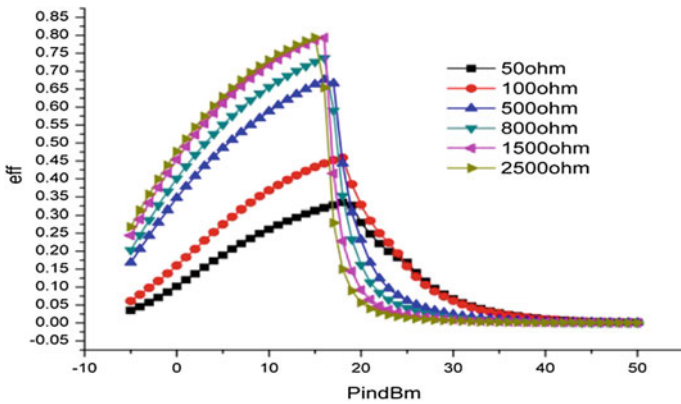
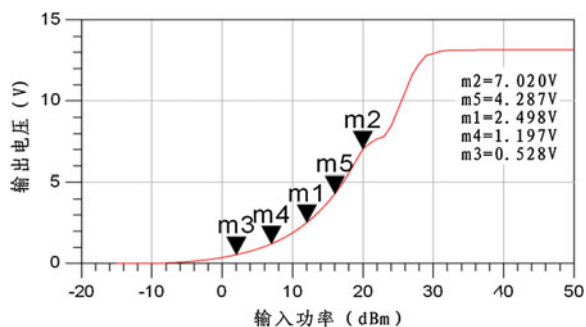


Fig. 54.24 The diagram of receiving efficiency and input power with different load

Fig. 54.25 The curve of ratio of power and voltage by RF unit



receiving efficiency and input power. Figure 54.25 is a radio frequency rectifier unit actual power voltage ratio curve.

54.3.6 The Energy Receiving Array Concept

Basis of progress made in the early stage of the unit structure, the researchers were constructed. Some band narrow band and wide band energy receiving skin concept array. In the flexible or semi flexible substrate material are respectively constructed as shown in Figs. 54.26, 54.27, and 54.28 shows the receiving array concept model [8–10].

Fig. 54.26 Concept model of a narrow-bandwidth receiving structure

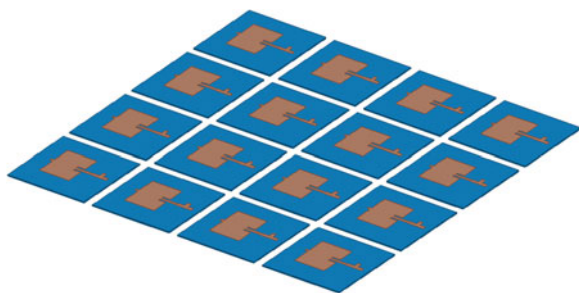


Fig. 54.27 Concept model of rectifier receiving array

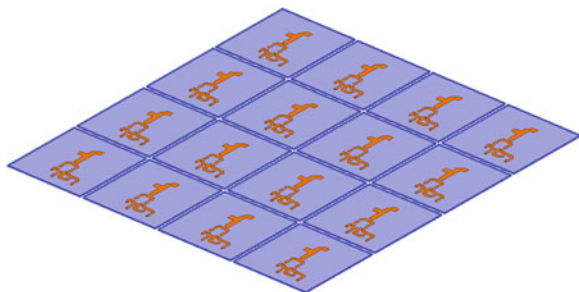
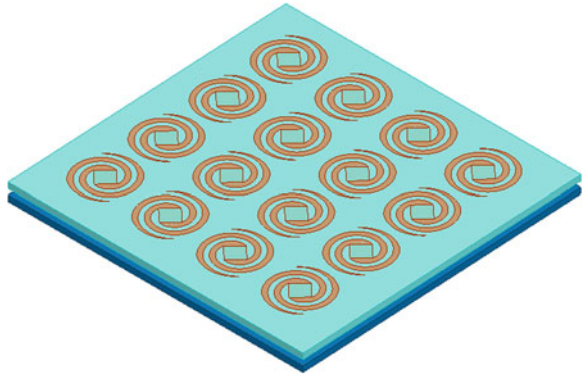


Fig. 54.28 Concept model of a wideband width receive structure



54.3.7 Satellite Autonomous Navigation of Composite Transceiver Array Concept

Because of the silicon solar cell is generally P+/N structure or N+/P structure, in the modeling analysis consider solar panels as satellite navigation antenna part back-plane array and energy receiving antenna array layer composite integrated system.

Figure 54.29 is a satellite navigation receiving integrated conceptual model matrix and solar array.

The microwave energy receiving array, the satellite navigation receiving array and the solar array of integrated modeling, the researchers constructed a satellite autonomous navigation of composite transceiver array concept model as shown in Fig. 54.30. The model has been verified in some frequency points. It should be noted that, to realize the model need more in-depth study materials, MEMS and RF integrated areas such as technical problems, but this work has already started.

Fig. 54.29 Navigation receiving and solar cell on the concept of system integration

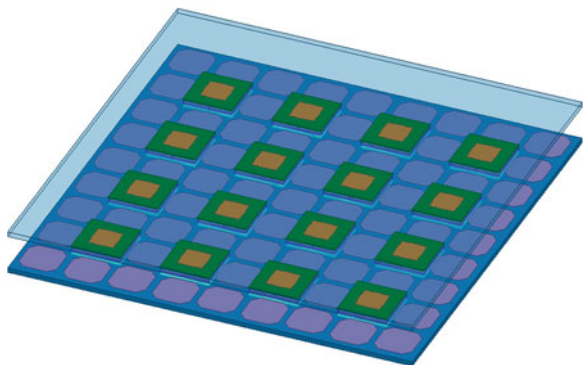
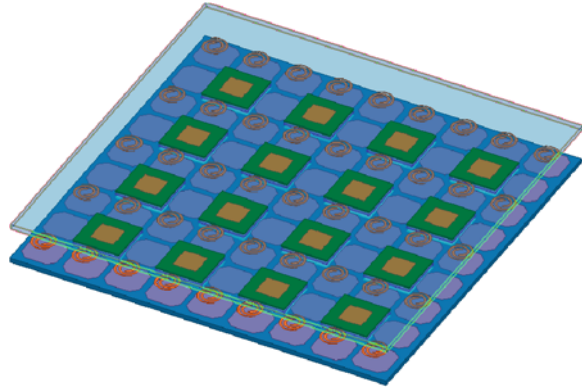


Fig. 54.30 Satellite autonomous navigation of composite transceiver array concept model



54.4 Experimental Study

54.4.1 The VSWR of the Antenna Array

Experimental design of microwave three groups of different 56 unit can transmit array, RF rectification array, energy self-sufficiency network (integrated in one). For one group of microwave energy transmission unit standing wave test results are as follows (Table 54.2 and Fig. 54.31):

54.4.2 The Voltage of the Array

Using the standard power source and standard antenna on a test matrix of each unit with a fixed power level in microwave anechoic chamber, the test results of unit actual rectifier voltage as follows (Table 54.3):

Table 54.2 VSWR receive datas

	1.06	1.05	1.37	1.32	
1.05	1.15	1.17	1.13	1.08	1.33
1.21	1.15	1.17	1.12	1.12	1.32
1.31	1.18	1.17	1.21	1.15	1.12
1.16	1.1	1.25	1.13	1.17	1.26
1.0-5	1.08	1.12	1.28	1.2	1.43
1.15	1.08	1.22	1.1	1.15	1.18
1.15	1.17	1.25	1.25	1.13	1.16
1.08	1.07	1.2	1.1	1.09	1.26
	1.03	1.22	1.05	1.15	

Fig. 54.31 The experimental antenna array of 56 cells

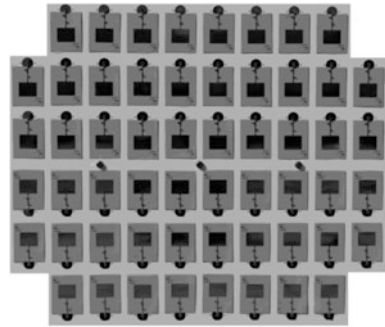


Table 54.3 Voltage receive datas

	0.989	1.006	0.857	0.979	
1.064	1.043	1.054	0.904	0.886	0.988
0.916	0.910	1.057	0.969	0.913	1.035
1.052	0.901	1.024	1.048	0.885	1.030
0.886	1.067	0.876	0.990	0.957	1.026
1.072	0.944	0.902	0.964	1.001	0.973
0.937	0.986	0.954	0.863	1.046	1.040
1.043	1.039	1.028	1.151	1.027	0.985
1.028	1.040	0.868	1.018	1.063	0.893
	1.032	0.979	1.052	0.889	

54.4.3 The Transmission Experiment of the Array

According to the theoretical study and simulation results of the model [11, 12], the construction of launch system, communication channel, for all types of rectifier array testing completed transmission can extract test. Signal level from -60 to 0 dBm, power amplifier level from 30 to 50 dBm. In accordance with the connection test way below, the measured array should be increased with the increase of signal level gradually produce voltage, and the voltage increases gradually changes. Test integrated array output energy obviously. Output voltage is directly driven by the load of goal setting (Table 54.4 and Fig. 54.32).

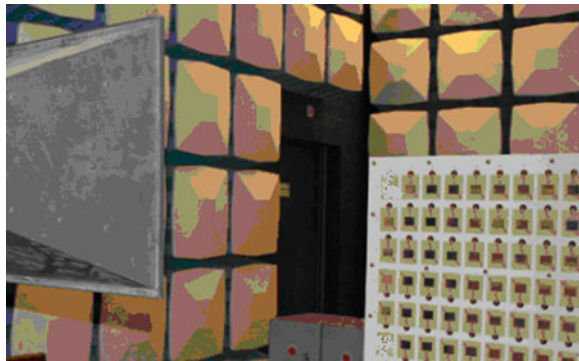
54.4.4 The Solar Energy Receiving Experiment

Test the design of a solar panel composite antenna receiving array, the array can test in sunlight to achieve power conversion reception. The output end of the 12 V could end the effective storage energy in storage. The 12 V power supply can effectively drive the low noise amplifier integrated unit of work.

Table 54.4 Voltage receiving datas

Number	Transmitting power (X + 30) dBm	Output (V)
1	-23	28.56
2	-22	33.14
3	-21	38.3
4	-19	50.9
5	-18	58.6
6	-17	67.7
7	-16	77.7
8	-15	89.4
9	-14	102.3

Fig. 54.32 56 experimental array unit test chart



54.4.5 Satellite Navigation Receiving Test

Test the design of a satellite navigation system three anti-interference receiving array composite solar panel test device, from battery array and microwave rectifier array energy can provide satellite navigation receiving system using. Through observation and experiment, obtained the Big Dipper, GPS, stable GLONASS receive data (Tables 54.5, 54.6 and 54.7, Fig. 54.33).

Table 54.5 Receive datas of BD

1 Group	Satellite number	3	1	2	4	5	7	8	10
	S/N	44	43	43	45	43	46	46	45
	<i>Result</i> E108°50'31.05" N33°14'19.57"								
2 Group	Satellite number	3	1	2	4	5	7	8	10
	S/N	44	43	42	46	45	46	48	46
	<i>Result</i> E108°50'30.97" N33°14'19.74"								

Table 54.6 Receive datas of GPS

1 Group	Satellite number	7	16	27	13	31	3	21	23
	S/N	46	47	52	49	39	49	40	50
	<i>Result</i> E108°50'30.70" N33°14'19.72"								
2 Group	Satellite number	7	16	27	13	8	3	21	23
	S/N	46	46	50	50	42	51	36	51
	<i>Result</i> E108°50'30.69" N33°14'19.75"								

Table 54.7 Receive datas of GLONASS

1 group	Satellite number	9	1	10	11	14	8	6	7
	S/N	48	42	52	51	47	42	48	42
	<i>Result</i> E108°50'30.94" N33°14'19.77"								
2 group	Satellite number	9	1	10	11	14	8	6	7
	S/N	49	43	52	50	45	43	47	43
	<i>Result</i> E108°50'31.11" N33°14'19.69"								

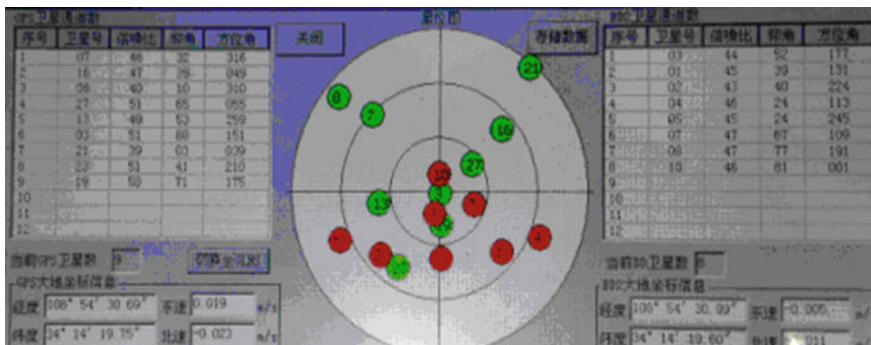


Fig. 54.33 Screenshot of the satellite navigation receiver data

54.5 Summary

The conceptual model of this study can be applied to a variety of platform of the future of microsatellite, pseudo satellite, airship, aircraft, ships, robots and other empty, day, multi field, which can achieve the power enhancement, energy self-sufficiency, interference and anti interference, multi system navigation receiver, detection network, land sea state monitoring and other functions. Figure 54.34 gives independent integrated transceiver array architecture graph and its application.

Microwave energy in space exploration for the shadow of the sun to the task where the platform will play a decisive role. For many small platform, if the

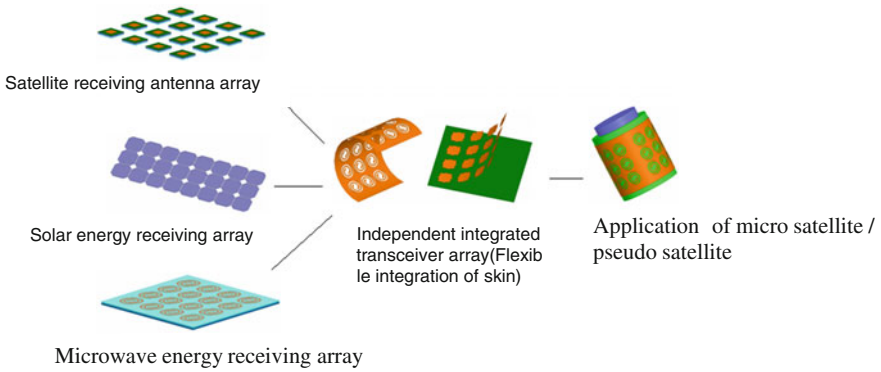


Fig. 54.34 Independent integrated transceiver array architecture and application

independent integrated transceiver array concept into practice, combined with the small super capacitor (or flywheel), and assisted by means of autonomous navigation, so many miracles will be born.

Conceptual model of the technology will realize with the further development of device, material, process integration, and RF and microwave technology and deepening.

The conceptual model using the left-handed materials, nano antenna technology, micro system technology will enable mentioned in this article to become real. Using light wave two like sex can be efficiently receiving light energy, which in the Internet of things and navigation data will revolutionize the development background.

The basic idea in this paper can expect further development and application of Beidou system to play a certain reference role.

Acknowledgments Thanks to research funded by the China Electronic Technology Group Corporation innovation fund; thank you for experts and technical staff of hard work and creative contributions paid in the study of.

References

1. Kawasaki S, Kido Y, Takano T (1999) Laminated active integrated amplifier antenna arrays for a space solar power satellite. *IEEE Trans Microwave Theory Tech* 47:1901–1909
2. Kawasaki S, Seita H, Suda T, Takei K, Nakajima K (2008) 32-Element high power active integrated phased array antennas operating at 5.8 GHz. In: *IEEE-AP-S digest*, 435.7, San Diego, July 2008
3. Antreich F, Denks H, Konovaltsev A, Hornbostel A (2008) Simulation of multi-element antenna systems for navigation applications. *IEEE Syst J*, March 2008
4. Yan B, Joseph K, Nicholas A, Minya G, Eric A (2002) Ultra flat tri-band high-power satellite array antenna for ground navigation. In: *20th AIAA International communications satellite systems conference and exhibit*, Montreal, Canada. American Institute of Aeronautics and Astronautics, Inc., Reston, VA, 7 pp, 2002–2029, 12–15 May 2002

5. Brown A, Silva R (2000) A GPS digital phased array antenna and receiver. In: Proceedings of 2000 IEEE international conference on, pp 153–156, 21–25 May 2000
6. Shailesh R, Aldo P (2009) GPS wideband circularly polarized microstrip antenna array. *Antennas Propag* 42:2990–2993
7. Manimegalai B, Periyasamy V, Vishwanathan L, Raju S, Abhaikumar V (2005) A novel MEMS based fractal antenna for multiband wireless applications. In: Microwave conference proceeding, 04–07 Dec 2005
8. Vaccaro S, Mosig JR, Maagt PD (2003) Two advanced solar antenna “SOLANT” designs for satellite and terrestrial communications. *IEEE Trans Antennas Propag* 51(8):2028–2034
9. Xie H, Li C, Yang B (2014) Application of differential evolution algorithm combined fourier transform on array beam broadening. *Mod Navig* 3:131–135
10. Yoshiharu F, Takashi S, Shoichiro M, Koichi I, Koji N, Yukihiro H, Takuro S, Yuichiro O, Eiichiro F, Teruo F (2011) Microwave energy transmission program for SSPS. In: General assembly and scientific symposium, 30th URSI. 20110813, pp 1–4
11. Mitra R (2007) Performance enhancement of small antennas using metamaterials—challenges and future directions, Applied electromagnetics and communications. In: ICECom 2007. 19th International conference on Sept 2007
12. Sabaawi AMA Infra-red nano-antennas for solar energy collection. In: Antennas and propagation conference, LAPC, Loughborough, 20111229, pp 1–4

Chapter 55

A Framework of Mathematic Model and Performance Evaluation for Conjunct GNSS Spoofing Detection

Dingbo Yuan, Hong Li and Mingquan Lu

Abstract GNSS spoofing is extremely deceitful and destructive for receivers. To guarantee safe access to GNSS, reliable spoofing detection is very important, especially for some critical GNSS applications and services. A great many spoofing detection techniques have been proposed in the last decade, they may be demonstrated to be effective for a special spoofing attack scenario. Nevertheless, there are few studies on generic and formal analysis on GNSS spoofing detection. In addition, there is no consolidated performance evaluation system for spoofing detection, which results in ambiguous interpretations. Therefore, a generalized mathematical model for conjunct GNSS spoofing detection based on Dempster-Shafer theory is proposed in this paper, and a performance evaluation framework for the proposed mathematical model is provided as well. To the authors' knowledge, the research is not only helpful for the researchers to propose new methods for spoofing detection and corresponding performance analysis, but also helpful for spoofing detection system construction. At last, simulation results are provided to demonstrate the theoretical derivations.

Keywords Spoofing detection model · Performance evaluation framework · Dempster-Shafer

55.1 Introduction

As more and more applications and services depend on precise time synchronization and position information such as financial transactions and communications networks [1], Global Navigation Satellite System (GNSS) is becoming more predominant than ever before. However, GNSS signals are vulnerable to intentional and unintentional interference, such as jamming and spoofing [2]. Among them,

D. Yuan (✉) · H. Li · M. Lu
Department of Electronic Engineering, Tsinghua University, 100084 Beijing, China
e-mail: ydb12@mails.tsinghua.edu.cn

spoofing attacks are extremely deceitful and destructive for GNSS receivers, whereas spoofing attack can force GNSS receivers to generate misleading time and position information while they are very difficult to be discovered by victim receivers [3, 4]. Therefore, to guarantee safe access to GNSS, researches on reliable spoofing detection techniques are of great importance, especially for some critical GNSS applications and services.

A lot of methods and techniques for spoofing detection and anti-spoofing have been proposed in the past few years [5–9], such as signal power detection [10], time of arrival (TOA) detection [11], and joint Dopplers consistency detection [12], et al. They may be demonstrated to be effective for a special spoofing attack scenario. For instance, signal power detection may be effective for repeater spoofing attack, in which the spoofing signal is supposed to be stronger than the authentic one. However, it may not be applicable for intermediate spoofing attack, since the spoofing signal power may be similarly the same with the authentic one [13], or even weaker. Hence, a great many literatures are focused on classify spoofing and authentic signal based on some certain attribute. But there are few studies on generalized and formal mathematic model and framework analysis on GNSS spoofing detection. Moreover, as lack of scientific experiments, there is no consolidated performance evaluation framework for spoofing detection, which results in ambiguous interpretations.

Dempster-Shafer theory [14] has turned out to be effective for evidence combination in many fields. Therefore, a generalized mathematic model for conjunct GNSS spoofing detection based on Dempster-Shafer theory is proposed in this paper. And a generalized performance evaluation framework corresponding to the proposed model is provided as well. To the authors' knowledge, the proposed mathematic model and performance evaluation framework is not focused on some certain spoofing detection technique, but focused on providing a generic framework that can make conjunction of all existing spoofing detection methods. The theoretical derivations and simulation results show that the proposed model and framework can enhance the spoofing detection performance and it is universally valid.

The rest of the paper is organized as follows: in Sect. 55.2, the proposed mathematic model is described. Performance evaluation framework is presented in Sect. 55.3. Numerical results and discussions are provided in Sect. 55.4 while conclusions are drawn in Sect. 55.5.

55.2 Mathematic Model

55.2.1 Mathematic Model for Single Spoofing Detection

As the receiver has no idea whether there is spoofing signal or not, there would be actually three states for the receiver. If there is no signal present, i.e., the received signal is noise, we denote it as state N ; if the received signal is authentic, we denote it

as state A ; if the received signal is counterfeit, we denote it as state C . Generally, there could be a lot of propositions for the state of the receiver. For example, we may declare that the received signal is noise; or we may declare that the received signal is absolutely not noise, but it is either authentic signal or spoofing signal, et al.

In order to introduce the mathematic model, some new notions would be defined in this paper. We denote the frame of signal discernment Θ as all possible mutually exclusive declared propositions of the receivers, and the frame Θ could be expressed as follows.

$$\Theta = \{N, A, C, \{N, A\}, \{N, C\}, \{A, C\}, \{N, A, C\}\} \tag{55.1}$$

Every part of Eq. (55.1) in due order means the received signal is “noise”, “authentic signal”, “counterfeit signal”, “either noise or authentic signal”, “either noise or counterfeit signal”, “either authentic or counterfeit signal”, and “either noise, authentic or counterfeit signal”, respectively.

For a single spoofing detection method T_i , it has its own propositions by assigning its beliefs over the frame Θ . And the assignment could be expressed as the basic probability function, which could be denoted as $m_i(\cdot)$. It has the following properties,

$$m_i(\emptyset) = 0 \tag{55.2}$$

$$m_i(N) + m_i(A) + m_i(C) + m_i(\{N, A\}) + m_i(\{N, C\}) + m_i(\{A, C\}) + m_i(\{N, A, C\}) = 1 \tag{55.3}$$

here \emptyset represents an empty set, $m_i\{N\}$ means the i -th spoofing detection method’s basic belief probability of the proposition that the received signal must be noise. Similarly, $m_i(\{N, A\})$ means the i -th spoofing detection method’s basic belief probability of the proposition that the received signal must be either noise or authentic signal. So is the same with other parts in Eq. (55.3).

As is illustrated in Fig. 55.1, based on the i -th spoofing detection method, the whole signal discernment Θ can be divided into seven different zones and each zone can be assessed with corresponding basic probability.

Since we have to know the probability of the fact that the received signal is whether noise, authentic signal, or counterfeit signal, we actually only care about the probability of the proposition N , A , and C , despite there are seven propositions



Fig. 55.1 Basic detection probability assessment for a single spoofing detection method

in the frame of discernment Θ . So, according to the i -th spoofing detection method's assignment, the actual belief probability is indicated by a confidence interval expressed as,

$$[L_i(N), U_i(N)] \quad (55.4)$$

$$[L_i(A), U_i(A)] \quad (55.5)$$

$$[L_i(C), U_i(C)] \quad (55.6)$$

the lower bound $L_i(N)$ is the actual belief probability that accounts for all evidence E that supports “the received signal is noise”, while the upper bound $U_i(N)$ is the actual belief probability that accounts for all evidence E that does not rule out “the received signal is noise”. They could be expressed as follows.

$$L_i(N) = \sum_{E \subseteq N} m_i(E) = m_i(N) \quad (55.7)$$

$$\begin{aligned} U_i(N) &= \sum_{E \cap N \neq \emptyset} m_i(E) = m_i(N) + m_i(\{N, A\}) \\ &\quad + m_i(\{N, C\}) + m_i(\{N, A, C\}) \end{aligned} \quad (55.8)$$

Similarly, the lower bound $L_i(A)$ is the actual belief probability that accounts for all evidence E that supports “the received signal is authentic”, while the upper bound $U_i(A)$ is the actual belief probability that accounts for all evidence E that does not rule out “the received signal is authentic”. They could be expressed as follows.

$$L_i(A) = \sum_{E \subseteq A} m_i(E) = m_i(A) \quad (55.9)$$

$$\begin{aligned} U_i(A) &= \sum_{E \cap A \neq \emptyset} m_i(E) = m_i(A) + m_i(\{N, A\}) \\ &\quad + m_i(\{A, C\}) + m_i(\{N, A, C\}) \end{aligned} \quad (55.10)$$

The lower bound $L_i(C)$ is the actual belief probability that accounts for all evidence E that supports “the received signal is counterfeit”, while the upper bound $U_i(C)$ is the actual belief probability that accounts for all evidence E that does not rule out “the received signal is counterfeit”. They could be expressed as follows.

$$L_i(C) = \sum_{E \subseteq C} m_i(E) = m_i(C) \quad (55.11)$$

$$\begin{aligned} U_i(C) &= \sum_{E \cap C \neq \emptyset} m_i(E) = m_i(C) + m_i(\{N, C\}) + \\ &\quad m_i(\{A, C\}) + m_i(\{N, A, C\}) \end{aligned} \quad (55.12)$$

55.2.2 Mathematic Model for Conjunct Spoofing Detection

The above part has introduced the mathematic model for a single spoofing detection method. In fact, if we want to construct a spoofing detection system, there would be a lot of spoofing detection methods and anti-spoofing techniques that should be taken into account. In this section, we will introduce the mathematic model for conjunct spoofing detection.

Consider I different spoofing detection methods taken into account, which can be denoted as $\{T_1, \dots, T_i, \dots, T_I\}$. The basic belief probability and confidence interval of each spoofing detection method is described in Sect. 55.2.1. Note that different spoofing detection method has different historical spoofing detection correctness rate. For instance, for a repeater spoofing attack, signal power detection and multi-modal detection would be more reliable than Doppler consistency detection, because the power of spoofing signal would be usually stronger than that of the authentic one while their Doppler consistency would be similarly the same. Herein, the spoofing detection correctness of i -th spoofing detection method T_i in history can be expressed as w_i .

Dempster-Shafer theory combination rule [15] is flexible and intuitive, and it can make information fusion by managing their imprecision and uncertainty. Herein, we choose it as our baseline for conjunct spoofing detection. Generally, we consider the case with I spoofing detection methods denoted as $\{T_1, \dots, T_I\}$. The conjunct basic probability function can be denoted as $m_{1\dots I}(S)$, where $S \in \Theta$, i.e., S could be $N, A, C, \{N, A\}, \{N, C\}, \{A, C\}, \{N, A, C\}$. And it could be expressed as follows.

$$m_{1\dots I}(S) = \frac{\sum_{\cap E_i=S} \prod_{1 \leq i \leq I} w_i m_i(E_i)}{\sum_{\cap E_i \neq \emptyset} \prod_{1 \leq i \leq I} w_i m_i(E_i)} \quad (55.13)$$

Then we can get the confidence interval of the conjunct detection probability of noise, authentic signal, and spoofing signal. And they can be expressed as $[L_{1\dots I(N)}, U_{1\dots I(N)}]$, $[L_{1\dots I(A)}, U_{1\dots I(A)}]$, and $[L_{1\dots I(C)}, U_{1\dots I(C)}]$, respectively. The lower bound and upper bound of the conjunct detection probability of noise, the authentic signal, and the spoofing signal can be expressed as follows, respectively. Similarly, the lower bound is the probability that accounts for the evidences that supports the corresponding proposition while the upper bound is the probability that accounts for the evidences that does not rule out the corresponding proposition.

$$L_{1\dots I}(N) = \frac{\sum_{\cap E_i=N} \prod_{1 \leq i \leq I} w_i m_i(E_i)}{\sum_{\cap E_i \neq \emptyset} \prod_{1 \leq i \leq I} w_i m_i(E_i)} \quad (55.14)$$

$$\begin{aligned}
U_{1\dots I}(N) &= \frac{\sum_{\cap E_i=N} \prod_{1 \leq i \leq I} w_i m_i(E_i)}{\sum_{\cap E_i \neq \emptyset} \prod_{1 \leq i \leq I} w_i m_i(E_i)} + \frac{\sum_{\cap E_i=\{N,A\}} \prod_{1 \leq i \leq I} w_i m_i(E_i)}{\sum_{\cap E_i \neq \emptyset} \prod_{1 \leq i \leq I} w_i m_i(E_i)} \\
&+ \frac{\sum_{\cap E_i=\{N,C\}} \prod_{1 \leq i \leq I} w_i m_i(E_i)}{\sum_{\cap E_i \neq \emptyset} \prod_{1 \leq i \leq I} w_i m_i(E_i)} + \frac{\sum_{\cap E_i=\{N,A,C\}} \prod_{1 \leq i \leq I} w_i m_i(E_i)}{\sum_{\cap E_i \neq \emptyset} \prod_{1 \leq i \leq I} w_i m_i(E_i)} \quad (55.15)
\end{aligned}$$

$$L_{1\dots I}(A) = \frac{\sum_{\cap E_i=A} \prod_{1 \leq i \leq I} w_i m_i(E_i)}{\sum_{\cap E_i \neq \emptyset} \prod_{1 \leq i \leq I} w_i m_i(E_i)} \quad (55.16)$$

$$\begin{aligned}
U_{1\dots I}(A) &= \frac{\sum_{\cap E_i=A} \prod_{1 \leq i \leq I} w_i m_i(E_i)}{\sum_{\cap E_i \neq \emptyset} \prod_{1 \leq i \leq I} w_i m_i(E_i)} + \frac{\sum_{\cap E_i=\{N,A\}} \prod_{1 \leq i \leq I} w_i m_i(E_i)}{\sum_{\cap E_i \neq \emptyset} \prod_{1 \leq i \leq I} w_i m_i(E_i)} \\
&+ \frac{\sum_{\cap E_i=\{A,C\}} \prod_{1 \leq i \leq I} w_i m_i(E_i)}{\sum_{\cap E_i \neq \emptyset} \prod_{1 \leq i \leq I} w_i m_i(E_i)} + \frac{\sum_{\cap E_i=\{N,A,C\}} \prod_{1 \leq i \leq I} w_i m_i(E_i)}{\sum_{\cap E_i \neq \emptyset} \prod_{1 \leq i \leq I} w_i m_i(E_i)} \quad (55.17)
\end{aligned}$$

$$L_{1\dots C} = \frac{\sum_{\cap E_i=C} \prod_{1 \leq i \leq I} w_i m_i(E_i)}{\sum_{\cap E_i \neq \emptyset} \prod_{1 \leq i \leq I} w_i m_i(E_i)} \quad (55.18)$$

$$\begin{aligned}
U_{1\dots I}(C) &= \frac{\sum_{\cap E_i=C} \prod_{1 \leq i \leq I} w_i m_i(E_i)}{\sum_{\cap E_i \neq \emptyset} \prod_{1 \leq i \leq I} w_i m_i(E_i)} + \frac{\sum_{\cap E_i=\{N,C\}} \prod_{1 \leq i \leq I} w_i m_i(E_i)}{\sum_{\cap E_i \neq \emptyset} \prod_{1 \leq i \leq I} w_i m_i(E_i)} \\
&+ \frac{\sum_{\cap E_i=\{A,C\}} \prod_{1 \leq i \leq I} w_i m_i(E_i)}{\sum_{\cap E_i \neq \emptyset} \prod_{1 \leq i \leq I} w_i m_i(E_i)} + \frac{\sum_{\cap E_i=\{N,A,C\}} \prod_{1 \leq i \leq I} w_i m_i(E_i)}{\sum_{\cap E_i \neq \emptyset} \prod_{1 \leq i \leq I} w_i m_i(E_i)} \quad (55.19)
\end{aligned}$$

Note that the reason why there are confidential intervals of the conjunct spoofing detection probability is because there are uncertain items for each spoofing detection method, as is illustrated in Fig. 55.1. If there is no uncertain item for each spoofing detection method, the frame of signal discernment Θ in Eq. (55.1) would be $\Theta = \{N, A, C\}$. Consequently, the lower bound and upper bound of corresponding detection probability would be the same. That is to say,

$$L_{1\dots I}(N) = U_{1\dots I}(N), L_{1\dots I}(A) = U_{1\dots I}(A), L_{1\dots I}(C) = U_{1\dots I}(C) \quad (55.20)$$

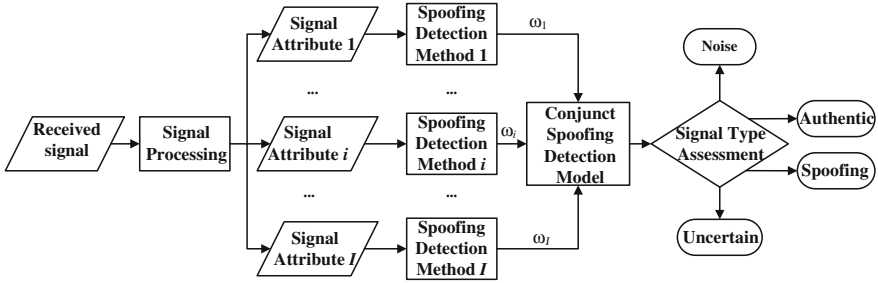


Fig. 55.2 Architecture of the proposed mathematic model for conjunct GNSS spoofing detection

The architecture of the proposed mathematic model for conjunct GNSS spoofing detection is illustrated in Fig. 55.2. Firstly, for the received GNSS signal, we can get its signal attributes (signal power, code phase, Dopplers, et al.) after digital signal processing. Then, we can perform different spoofing detection based on corresponding signal attributes. Then we can make joint usage of the spoofing detection results based on the proposed conjunct spoofing detection model. At last, we will make signal type assessment based on the above derivations to decide whether the received signal is noise, authentic signal, spoofing signal, or we are uncertain about it.

55.3 Performance Evaluation

In order to evaluate the performance of the proposed mathematic model for conjunct GNSS spoofing detection, a performance evaluation framework will be proposed in this section. Since we are performing conjunct spoofing detection based on different spoofing detection methods, we should consider the additional benefits we can get if we make conjunct spoofing detection based on more different spoofing detection methods. Herein, a performance evaluation framework is described in the following part.

As expressed in Eq. (55.1), the frame of signal discernment Θ contains seven mutually exclusive declared propositions of the receivers. Then, we denote Ω as the performance evaluation space of the proposed mathematic model. The base vector of the space can be expressed in Eq. (55.21). Herein, Ω is a Cartesian space \mathbb{R}^7 .

$$\vec{m}_i = [m_i(N), m_i(A), m_i(C), m_i(\{N, A\}), m_i(\{N, C\}), m_i(\{A, C\}), m_i(\{N, A, C\})] \tag{55.21}$$

Define the difference metric [15] between two different spoofing detection methods T_i and T_j in the performance evaluation space as in Eq. (55.22), where $E_p, E_q \in \Theta$ and $|E_p \cap E_q|$ denotes the cardinality of $E_p \cap E_q$. And W is a 7×7

weight matrix, with the element $W_{pq} = \frac{|E_p \cap E_q|}{|E_p \cup E_q|}$. Therefore, if the detection results of T_i and T_j are the same, then the difference metric $d(T_i, T_j)$ would be zero. And the greater the difference metric $d(T_i, T_j)$ is, the more additional benefits we will get in the conjunct spoofing detection. For I spoofing detection methods, the difference metric matrix can be denoted as $D_{I \times I}$, where the element $d_{ij} = d(T_i, T_j)$. We can easily find that the matrix is symmetrical, since the difference metrics between T_i and T_j , T_j and T_i are the same.

$$\begin{aligned}
 d(T_i, T_j) &= \sqrt{\frac{1}{2} (\vec{m}_i - \vec{m}_j)^T \mathbf{W} (\vec{m}_i - \vec{m}_j)} \\
 &= \sqrt{\frac{1}{2} \sum_{p=1}^7 m_i^2(E_p) + \frac{1}{2} \sum_{q=1}^7 m_j^2(E_q) - \sum_{p=1}^7 \sum_{q=1}^7 m_i(E_p) \frac{|E_p \cap E_q|}{|E_p \cup E_q|} m_j(E_q)} \quad (55.22)
 \end{aligned}$$

Herein, we define the benefit function of the proposed mathematic model as Ben , and it can be defined as follows.

$$Ben = \sum_{i=1}^I \sum_{j=i+1}^I d(T_i, T_j) \quad (55.23)$$

We can regard the benefit function Ben as an indicator to evaluate the performance of the proposed model. As the benefit function increases, we will get more information when adding into a new spoofing detection technique. Consequently, we will get a higher spoofing detection performance. In other words, if the benefit function does not increase after introducing a new spoofing detection technique, then it indicates that the new spoofing detection technique is not necessary, which is consistent with the information theory.

55.4 Simulation Results and Discussions

To demonstrate the validity of the proposed conjunct spoofing detection model and performance evaluation framework, this section provides some spoofing scenes and numerical results. Here we take GPS L1 C/A signal as an example. Consider an intermediate spoofing attack, the corresponding constellation is illustrated in Fig. 55.3. There are six authentic signals and one spoofing signal. And the authentic signals are illustrated in green while the spoofing signal is in red. The authentic signal-to-noise ratio (SNR) is -18 dB while the spoofing-to-authentic ratio (SAR) is 1 dB. We consider three different spoofing detection methods: Signal Power Detection (SPD) [10], Multi-Peak Detection (MPD), and DCD (Dopplers Consistency Detection) [12]. And the corresponding detection probabilities are illustrated in Table 55.1.

Fig. 55.3 The constellation of a spoofing attack scenario, with six authentic (green) signals and one spoofing (red) signal

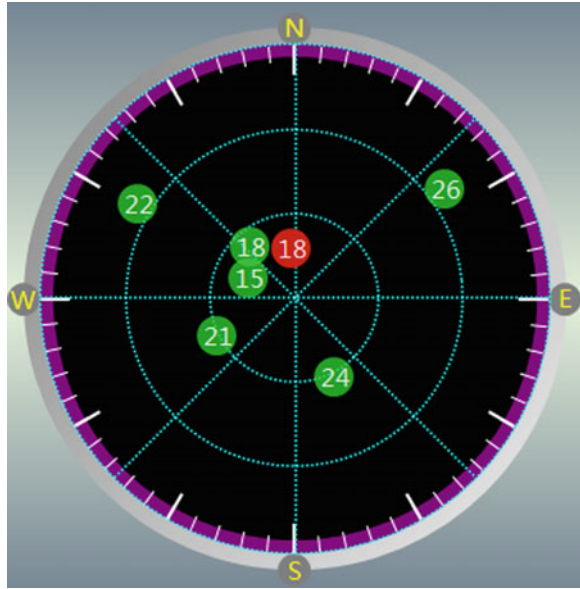


Table 55.1 Three different spoofing detection methods and the corresponding detection probabilities

	N	A	C	$\{N, A\}$	$\{N, C\}$	$\{A, C\}$	$\{N, A, C\}$
SPD	0	0.15	0.37	0	0	0.48	0
MPD	0	0.26	0.24	0	0	0.6	0
DCD	0	0.04	0.87	0	0	0.09	0
CSDM	0	0.0532	0.8884	0	0	0.0585	0

Since the signal power of the authentic and spoofing signals are almost the same, for SPD, there is a great probability that the present signal is not noise, but actually not quite sure which one is spoofing [10]. Similarly, as C/A pseudo-noise code is short-cycle code, we are not quite sure which one is spoofing based on MPD, either. Therefore, we will enhance the spoofing detection performance by the proposed conjunct spoofing detection model (CSDM). Since DCD is more effective for the intermediate spoofing detection, here the spoofing detection correctness of each spoofing detection method in history can be designated as 0.2, 0.2, 0.6, respectively.

Based on the Eqs. (55.14)–(55.19), we can get the corresponding conjunct spoofing detection probability, which is illustrated in the last line in Table 55.1. We can find that the spoofing detection performance has been enhanced based on the proposed conjunct spoofing detection model. The uncertain between the authentic

and spoofing signals has been reduced, since we can make use of more information about the different signal attributes based on the CSDM.

Here we also try to evaluate the performance of the CSDM. Firstly, we calculate the difference metric matrix of the above three spoofing detection method, and it can be denoted as follows.

$$D = \begin{bmatrix} 0 & 0.1832 & 0.5435 \\ 0.1832 & 0 & 0.6831 \\ 0.5435 & 0.6831 & 0 \end{bmatrix} \quad (55.24)$$

From the difference metric matrix, we find that the difference between SPD and MPD is not apparent, since both of them have a great uncertain on identifying the authentic and spoofing signals. Nevertheless, the difference metric between SPD (or MPD) and DCD is apparent enough, since DCD has a great spoofing detection probability. Therefore, considering the tradeoff between computation resources and performances, we can just take SPD and DCD into account to perform CSDM.

55.5 Conclusions

This paper has proposed a generalized mathematic model for conjunct GNSS spoofing detection based on Dempster-Shafer theory. The principle and the architecture of the conjunct spoofing detection model are analyzed. It shows how to combine different spoofing detection techniques to achieve more reliable spoofing detection results. Meanwhile, a generalized performance evaluation framework corresponding to the proposed model is provided as well. The difference metric matrix is introduced to measure the differences between different spoofing detection methods. And the benefit function is also introduced to evaluate the performance of the proposed model. The derivations indicate that the higher the benefit function is, the more reliable spoofing detection results we will get. The proposed mathematic model and corresponding performance evaluation framework is not only helpful for the researchers to propose new methods for spoofing detection and corresponding performance analysis, but also helpful for spoofing detection system construction. And simulation results have shown that the proposed model and framework is valid.

References

1. U. S. GOVERNMENT (2010) Global positioning system. <http://www.gps.gov>
2. Humphreys TE et al (2008) Assessing the spoofing threat: development of a portable GPS civilian spoofer. In: Proceedings of the ION GNSS international technical meeting of the satellite division, vol 55
3. Warner JS, Johnston RG (2002) A simple demonstration that the global positioning system (GPS) is vulnerable to spoofing. *J Secur Adm* 25:19–28

4. Ledvina BM et al (2010) An In-Line anti-spoofing device for legacy civil GPS receivers. In: The proceedings of national technical meeting - ION NTM 2010, San Diego, CA, 25–27 January 2010
5. O'Hanlon, Brady W et al (2012) Real-time spoofing detection using correlation between two civil GPS receiver. In: Proceedings of the ION GNSS Meeting, Institute of Navigation, Nashville, TN, 2012
6. Broumandan A, Jafarnia-Jahromi A, Lachapelle G (2014) Spoofing detection, classification and cancellation (SDCC) receiver architecture for a moving GNSS receiver. *GPS Solutions*, 1–13. doi: [10.1007/s10291-014-0407-3](https://doi.org/10.1007/s10291-014-0407-3)
7. Chen X, Lenzini G, Martins M, Mauw S, Pang J (2013) A trust framework for evaluating GNSS signal integrity. In: Computer security foundations symposium (CSF), 26th IEEE, June 2013, pp 179–192
8. Khanafseh S et al (2014) GPS spoofing detection using RAIM with INS coupling. In: Position, location and navigation symposium-PLANS 2014, IEEE/ION, 2014
9. Daneshmand S et al (2014) A GNSS structural interference mitigation technique using antenna array processing. In: Sensor array and multichannel signal processing workshop (SAM), 8th IEEE, 2014
10. Yuan D, Li H, Lu M. (2014) A method for GNSS spoofing detection based on sequential probability ratio test. In: Position, Location and Navigation Symposium-PLANS 2014, IEEE/ION, May 2014, pp 351–358
11. Nicola M, Musumeci L, Pini M, Fantino M, Mulassano P (2010) Design of a GNSS Spoofing Device Based on a GPS/Galileo Software Receiver for the Development of Robust Countermeasures, ENC GNSS 2010, Braunschweig, Germany, 19–21 October 2010
12. Yuan D, Li H, Lu M (2014). GNSS spoofing mitigation based on joint detection of code doppler and carrier doppler in acquisition. In: Proceedings of China satellite navigation conference (CSNC), vol 1, Springer Berlin, Heidelberg, pp 763–774, January 2014
13. Cavaleri A, Motella B, Pini B, Fantino M (2010) Detection of spoofed GPS signals at code and carrier tracking level, In: Proceedings of the 5th ESA Workshop on Satellite Navigation Technologies and European Workshop on GNSS Signals and Signal Processing (NAVITEC '10), pp 1–6, December 2010
14. Dempster Arthur P (2008) The Dempster-Shafer calculus for statisticians. *Int J Approximate Reasoning* 48(2):365–377
15. Zadeh LA (1986) A simple view of the Dempster-Shafer theory of evidence and its implication for the rule of combination, *AI magazine* 7(2), p 85
16. Jousselme AL, Grenier D, Bossé É (2001) A new distance between two bodies of evidence. *Inform fus* 2(2):91–101

Chapter 56

A Near-Far Effect Mitigation Method of Pseudolites Based on Array Signal

Libin Shen, Lixin Li, Huisheng Zhang and Tao Bao

Abstract This paper proposes a new near-far effect mitigation method based on array signal to resolve the near-far problem in pseudolites. It can adjust the power intensity of the pseudolite by constraining the beam direction to make it accord with the real navigational signal. Meanwhile, this method achieves maximum interference signal filtering, thus the navigation receiver can work properly under the concurrence of pseudolites, strong interferences and navigation signals. The effectiveness of the proposed method is proved through simulations and performance analysis.

Keywords Pseudolite · Near-far effect · Array signal processing · Beamforming

56.1 Introduction

Initially proposed by Beser and Parkinson in 1982 [1], pseudolite technology is mainly used to verify the performances of receivers on the ground before GPS satellite was launched. However, pseudolites can increase the number of visible satellites, and improve the geometric factors greatly with suitable arrangements. It [1] can enhance the positioning accuracy of the navigation system significantly [2, 3]. Therefore, pseudolite technology has received extensive attention and widespread application in various fields since it was put forward. Using pseudolites to position separately or in combination with navigation satellites has become one of the effective ways to improve the performance of navigation system. However, the near-far effect is still one of the urgent problems in pseudolites [4].

L. Shen (✉) · L. Li · H. Zhang · T. Bao
School of Electronics and Information, Northwestern Polytechnical University, Xi'an, China
e-mail: shenlibin1003@126.com

Various possible methods have been proposed to overcome the near-far effect in recent years. TDMA, FDMA and CDMA were the earliest three possible approaches [5]. The TDMA technique adopts pulses with a certain duty cycle to transmit pseudolite signals. While the FDMA method enables transmitting frequency of pseudolites and GPS to have a certain frequency offset, but maintains it in the same waveband. Unlike TDMA and FDMA, the CDMA technique uses a longer code sequence than the GPS code. The detailed studies on these methods are performed in [6–8], and the results show that the radio frequency module and correlators of the receiver need great changes with the latter two methods. When it comes to the TDMA, despite of its easy implementation, it is limited due to its scant improvement in SNR and higher requirements for the AGC performance of the receiver.

An “interference cancellation” method mentioned in [9, 10] conducts peak detection of pseudolite signals which produces strong interference by adding relevant channels of the GPS receiver. After subtracting the reconstructed pseudolite signal from the total received signals, the received signals are sent back to the correlator of each channel for despreading. However, this method has much delay and relatively great changes are made in the correlator of the receiver. To achieve the purpose of suppressing interference, a new method named “multi-user detection” is proposed in [11], which obtains information of interference signals by increasing the number of receiving channels, and subtracts the interference signal from the received signal. However, this process is too complicated for engineering realization [12]. The anti-interference technology with adaptive nulling antenna mentioned in [4], conducts adaptive zero interference suppression processing while regarding the pseudolite signal as a wideband interference signal. Navigation signals can be better captured and tracked in this way, but pseudolite signal is completely inhibited.

In this paper, a new near-far effect mitigation method based on array signal processing is proposed to resolve the near-far problem in pseudolites. It can adjust the power intensity of the pseudolite by constraining the beam direction to make it accord with the real navigation signal. At the same time, this method achieves maximum interference signal filtering, thus the navigation receiver works properly under the concurrence of pseudolites, strong interferences and navigation satellite signals.

56.2 Linear Constrained Minimum Variance (LCMV) Algorithm

Taking uniform linear array(ULA) consisting of M sensor elements as an example, let us assume that there is one desired signal $d(t)$ and J narrowband interferences $i_j(t), j = 1, \dots, J$ in the far field, with the Directions-Of-Arrival (DOA) θ_d and θ_j respectively. Additive white noise on each array element is $n_k(t)$, and noise variance is σ_n^2 . Therefore, the received signal on the array element k can be modeled as

$$x_k(t) = a_k(\theta_d)d(t) + \sum_{j=1}^J a_k(\theta_{ij})i_j(t) + n_k(t) \quad (56.1)$$

where $a_k(\theta_d)$, $a_k(\theta_{ij})$ are steering vectors for desired signal and interference signals, and the three terms on right side of the equation represent signal, interference and noise respectively. A matrix representation is as (56.2) and the covariance matrix of received signal array is given by (56.3)

$$\begin{bmatrix} x_1(t) \\ x_2(t) \\ \vdots \\ x_M(t) \end{bmatrix} = [a(\theta_d), a(\theta_{i_1}), \dots, a(\theta_{i_J})] \begin{bmatrix} d(t) \\ i_2(t) \\ \vdots \\ i_J(t) \end{bmatrix} + \begin{bmatrix} n_1(t) \\ n_2(t) \\ \vdots \\ n_M(t) \end{bmatrix} \quad (56.2)$$

$$R_x = E(X(t)X^H(t)) \quad (56.3)$$

where $X(t) = [x_1(t) \ x_2(t) \ \dots \ x_M(t)]^T$ is the sampling matrix of received signals. According to linear constraint criteria, LCMV algorithm should meet the following linear constrained conditions

$$\begin{cases} w^H a(\theta_d) = 1 \\ w^H a(\theta_{ij}) = 0 \ (j = 1, 2, \dots, J) \end{cases} \quad (56.4)$$

where w is the complex weight vector, and the matrix representation can be expressed as

$$C^H W = f \quad (56.5)$$

where $C = [a(\theta_d), a(\theta_{i_1}), \dots, a(\theta_{i_J})]$ represents the constrained matrix, f is constrained vector, and $W(\theta) = [w_1(\theta) \ w_2(\theta) \ \dots \ w_M(\theta)]^T$ is the complex weight vector. Since θ_d is the direction of desired signal, and $i_j(t), j = 1, \dots, J$ are interference signals, we can set the constrained vector f to be $f = [1, 0, 0, \dots, 0]^T$, which ensures the desired signal is received free of distortion and interference signals are completely inhibited [13].

LCMV algorithm can be expressed as the following constrained optimization problem

$$\begin{cases} \text{Min}_W P_{out} = \text{Min}_W E\{|y_s(n)|^2\} = \text{Min}_W E\{w^H R_{xx} w\} \\ C^H W = f \end{cases} \quad (56.6)$$

Thus, the optimal weight vector is calculated as

$$w_{opt} = R_x^{-1} C (C^H R_x^{-1} C)^{-1} f \quad (56.7)$$

56.3 A Near-Far Effect Mitigation Beamforming Method of Pseudolites

According to the constraint condition of (56.5), when the array receives $P + 1$ signals (one desired signal, P interference signals), the beam pattern forms a fixed gain in the direction of desired signal, and a deep null in the interference directions. Thus, the greatest degree of interference suppression and the maximum output SINR can be achieved. That is because values of the constraint vector f are set to be “0” in directions of interference signals while they are “1” in the direction of the desired signal. Considering that the values are constrained to a value between “0” and “1” in the interference directions, thus, the null in the beam pattern is shallower than that under the condition of constraint value “0”, whereas it becomes deeper than that in presence of constraint value “1”. Hence, the suppression of interference signals is crippled. Suppression degree of interference signals can be achieved by adjusting the constraint vector values. When a pseudolite is close to a receiver, the receiver will be blocked due to overlarge power intensity of the pseudolite signal. In this case, the pseudolite signal will serve as an interference instead. Thus, an appropriate suppression for pseudolite signals is required to make its power intensity coincident with that of the navigation signal. Accordingly, the method is to adjust the constraint values of pseudolite signals between “0” and “1”, so that pseudolite signals can be received effectively, and the reception of navigation signals won't be affected by pseudolite signals.

56.3.1 An Improved LCMV Algorithm for Pseudolites

According to the previous analysis, let us assume that M navigation signals and P pseudolite signals impinge on an array with an arbitrary geometry. The improved LCMV algorithm can be described as

$$\begin{cases} \underset{W}{\text{Min}} P_{out} = \underset{W}{\text{Min}} W^H R_x W \\ W^H C_d = f_d^H \\ W^H C_q = f_q^H \end{cases} \quad (56.8)$$

Among them, $C_d = [a(\theta_{d_1}), a(\theta_{d_2}), \dots, a(\theta_{d_M})]$ consists of the steering vectors $a(\theta_{d_k}), k = 1, \dots, M$, $f_d = [1, 1, \dots, 1]^T$ represents for the constraint vector of M navigation signals, $C_q = [a(\theta_{q_1}), a(\theta_{q_2}), \dots, a(\theta_{q_P})]$ consists of the steering vectors $a(\theta_{q_k}), k = 1, \dots, P$, $f_q = [\lambda_1, \lambda_1, \dots, \lambda_P]$ is the constraint vector of P pseudolite signals, and the values of $\lambda_1, \lambda_1, \dots, \lambda_P$ are between 0 and 1. The signal power of pseudolites can be consistent with the navigation signal by making real-time adjustment to the value of $\lambda_1, \lambda_1, \dots, \lambda_P$.

Thus, the key improvement in (56.8) is the selection of constraint values $\lambda_1, \lambda_1, \dots, \lambda_P$ for P pseudolite signals. According to Capon algorithm, the spatial spectrum estimation can be written as

$$P_{Capon}(\theta) = \frac{1}{a(\theta)^H \times R_x^{-1} \times a(\theta)} \quad (56.9)$$

Let us assume the spatial spectrum of M navigation signals are $P_d(\theta_1), P_d(\theta_2) \dots P_d(\theta_M)$, and the spatial spectrum of M pseudolite signals are $P_q(\theta_1), P_q(\theta_2) \dots P_q(\theta_P)$. It is well known that the navigation satellite is about 20,000 km far away from the earth's surface, and the signal power in the receiver is quite weak due to its spread spectrum signal format [14]. Therefore, the signal power of different navigation satellites becomes nearly identical in the receiver. For the convenience of calculating constraint values $\lambda_1, \lambda_1, \dots, \lambda_P$, we make a rule as follows

$$P_d = \frac{1}{M} \sum_{i=1}^M |P_d(\theta_i)| \quad (56.10)$$

where $|\cdot|$ donates modulus. Provided that the ratio of the j th pseudolite signal power $P_q(\theta_j)$ to navigation signal P_d is $\xi_j (j = 1, 2, \dots, P)$

$$\tilde{\xi}_j = \frac{|P_q(\theta_j)|}{P_d}, (j = 1, 2, \dots, P) \quad (56.11)$$

To make the power intensity of the pseudolite accord with the real navigational satellite, the constraint values $\lambda_1, \lambda_1, \dots, \lambda_P$ can be calculated as

$$\lambda_j = \sqrt{\frac{1}{\tilde{\xi}_j}}, (j = 1, 2, \dots, P) \quad (56.12)$$

Plugging (56.11) into (56.12), the constraint values $\lambda_1, \lambda_1, \dots, \lambda_P$ can be written as

$$\lambda_j = \sqrt{\frac{|P(\theta_j)|}{P_d}}, (j = 1, 2, \dots, P) \quad (56.13)$$

Hence, the optimal weight vector can be written as

$$w_{opt} = R_x^{-1} C (C^H R_x^{-1} C)^{-1} \begin{pmatrix} f_d \\ f_q \end{pmatrix} \quad (56.14)$$

where $C = [C_d, C_q]$.

56.3.2 An Improved LCMV Algorithm for Pseudolite and Interference Signals

According to the principle of LCMV algorithm and contents in Sect. 3.1, when the receiver is under the concurrence of pseudolites, strong interferences and navigation signals, the proposed algorithm can be modified by just adding the interference signal constraints to achieve maximum interference signal filtering, and the optimum solution w_{opt} can be given by

$$w_{opt} = R_x^{-1} C (C^H R_x^{-1} C)^{-1} \begin{pmatrix} f_d \\ f_q \\ f_g \end{pmatrix} \quad (56.15)$$

where $f_d = [1, 1, \dots, 1]^T$, $f_q = [\lambda_1, \lambda_1, \dots, \lambda_p]$ and $f_g = [0, 0, \dots, 0]^T$ are the constraint vectors of navigation signals, pseudolite signals and interference signals respectively, $C = [C_d, C_q, C_g]$, and C_d, C_q, C_g represent for epidemic array Matrix of navigation signals, pseudolite signals, and interference signals separately.

56.4 Simulation and Analysis

To confirm the analysis and gain more insight into the achievable performance, we provide numerical simulation results in this section. In our simulations, a uniform linear array (ULA) with $M=10$ elements spaced a half wavelength is considered. The additive noise is modeled as a complex Gaussian zero-mean spatially and temporally white process. Let's assume that 4 narrowband signals (one navigation signal, three pseudolite signals) impinge on the antenna array. The navigation signal is assumed to be coming from $\theta_d = 0^\circ$ and the medium frequency is 65 MHz, with $\text{SNR} = -10$ dB. Three pseudolite signals are assumed to have DOAs of $20^\circ, -40^\circ, -20^\circ$, and the corresponding frequency are supposed to be 66 MHz, 67 MHz, and 65.5 MHz, with fixed SNR of 45 dB, 50 dB, 40 dB respectively. In the following experiments, we employ $L = 1000$ snapshots, and the beam pattern is shown in Fig. 56.1(a).

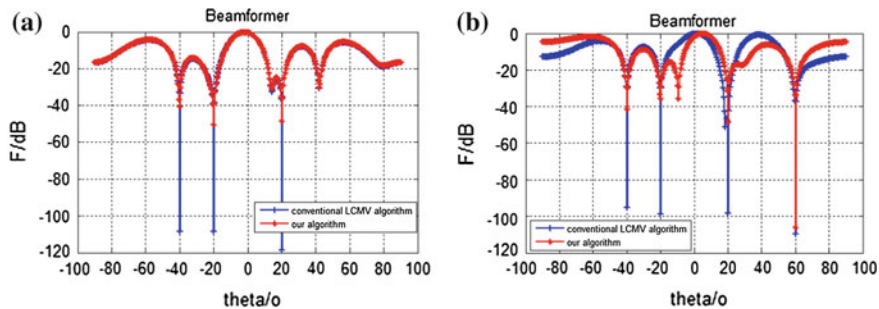


Fig. 56.1 Results of beam pattern experiment

In Fig. 56.1(a), the blue curve is the simulation result of conventional LCMV algorithm, and the red curve represents the proposed algorithm. We can observe that a deep nulling is formed in the direction of 20° , -40° , -20° with conventional LCMV algorithm, while that is much shallower in the same directions with the proposed algorithm. Thus the suppression of the pseudolite signals is crippled. Then, the curve of signal power spectrum is given in Fig. 56.2.

The curve shown in Fig. 56.2a is the received signal power spectrum without adopting near-far effect mitigation method. In the figure, the navigation signal power is more than 50 dB lower compared with pseudolite signals. While the signal power of pseudolites with the proposed algorithm is approximately consistent with the navigation signal, and the value is about 20 dB shown in Fig. 56.2b.

To further demonstrate the robustness of the proposed algorithm against strong interference signal, under above experimental conditions, we take account of a narrowband interference signal impinging on the antenna array from direction $\theta = 60^\circ$, and the corresponding frequency is assumed to be 66.5 MHz, with a SNR of 75 dB. The beam pattern is shown in Fig. 56.1b. both conventional LCMV algorithm and the proposed method form a deep nulling of -110 dB in the direction

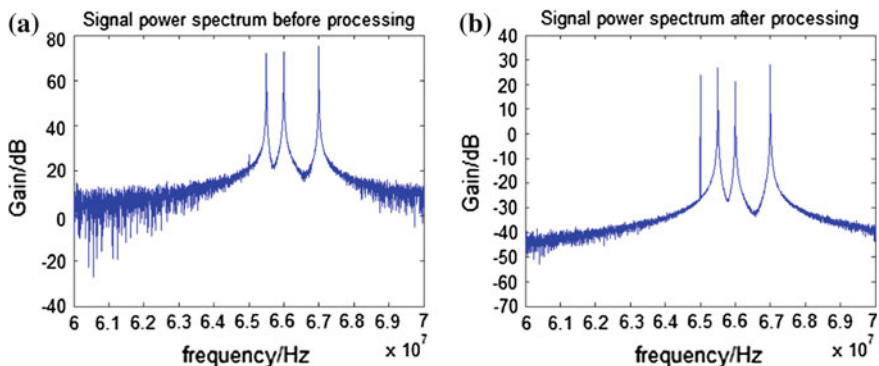


Fig. 56.2 Results of signal power spectrum experiment

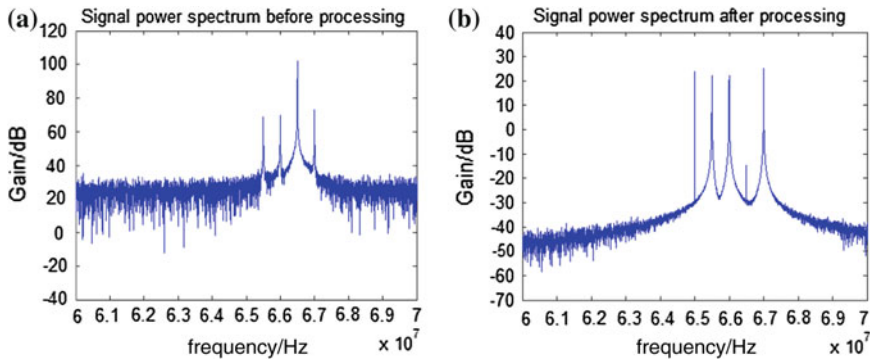


Fig. 56.3 Results of signal power spectrum experiment

of $\theta = 60^\circ$, while that is much shallower in 20° , -40° , -20° directions of pseudolite signals with the proposed algorithm. And the value is about -40 dB shown in Fig. 56.1b.

The curve shown in Fig. 56.3 is the received signal power spectrum. As is shown in Fig. 56.3a, the signal power of 66, 67, 65.5 MHz pseudolite signals and 66.5 MHz interference signal is much greater compared with the navigation signal which is buried into the strong interference and noise. After processing, the signal power of pseudolites is approximately coincident with the navigation signal, and the value is about 20 dB shown in Fig. 56.3b. At the same time, maximum interference signal filtering is achieved, with a value less than -20 dB, which is far less than the navigation signal.

In order to verify the navigation signals and pseudolite signals can be received normally with the proposed algorithm, the capture results are given in Figs. 56.4 and 56.5. According to Figs. 56.4a and 56.5a, navigation signals and pseudolite signals are suppressed by interference signals, and the receiver is blocked under the concurrence of interference signals. Thus, the relevant peak of the capture result

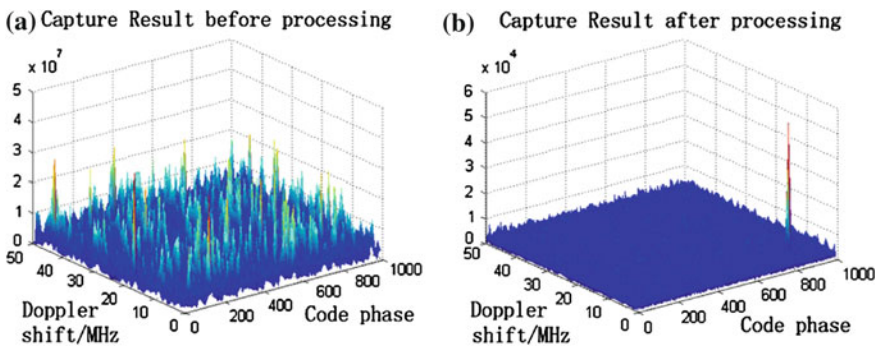


Fig. 56.4 Results of navigation satellite capture experiment

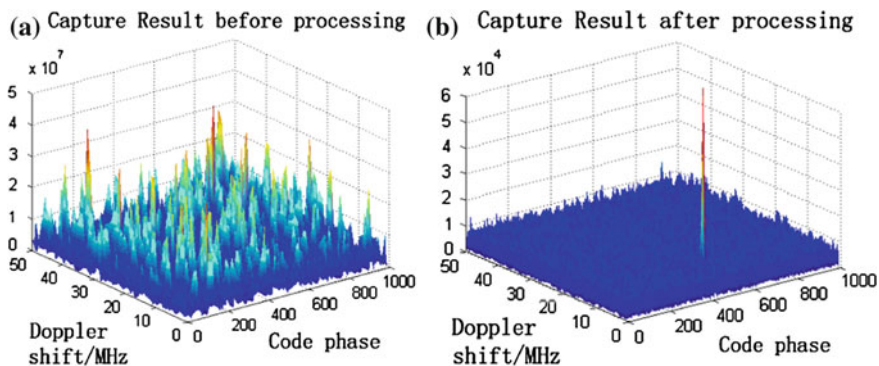


Fig. 56.5 Results of pseudolite capture experiment

does not appear. With our method, the suppression of interference signals is crippled, approximately coincident with the navigation signal, and maximum interference signal filtering is achieved. Therefore, the navigation signal and pseudolite signals can be received normally, with a strong correlation peak as shown in Fig. 56.4b and 56.5b.

Simulation results and analysis show that the new near-far effect mitigation method is effective to resolve the near-far problem in pseudolites, which makes the power intensity of the pseudolite accord with the real navigation satellite. At the same time, this method achieves maximum interference signal filtering, thus the navigation receiver works normally under the concurrence of pseudolite signals, strong interference signals and satellite navigation signals, which enhances the robustness of the receiver greatly.

56.5 Conclusions

Near-far problem in pseudolites has a serious effect on the regional positioning performance of navigation satellite system, as well as restricts the development of pseudolite technology. In this work, we propose a novel near-far effect mitigation method based on array signal. The simulations and performance analysis demonstrate that the proposed method is effective to resolve the near-far problem in pseudolites, and robust to strong interference signals.

Acknowledgments This study is funded by the “the Fundamental Research Funds for the Central Universities” (No. 3102014JCQ01052), by the Project funded by China Postdoctoral Science Foundation (No.2014M552489), by Scientific Research Program Funded by Shaanxi Provincial Education Department (Program No.14JK2152), by the Shaanxi Province Postdoctoral Research Project, by the Graduate Starting Seed Fund of Northwestern Polytechnical University.

References

1. Beser J, Parkinson B (1982) The application of NAVSTAR differential GPS in the civilian community. *J Inst Navig* 29(2):107–136
2. Liu C, Wang J, Xu C (2010) Integration of GPS/Pseudolites baseline solution based on empirical mode decomposition. *Geomatics Inf Sci Wuhan Univ* 35(8):996–1000
3. Matsuoka M, Rock SM, Bualat MG (2004) Autonomous deployment of a self-calibrating pseudolite array for mars rover navigation. In: Position location and navigation symposium, Stanford University, USA
4. Han T, Cao J, Lu M (2011) Anti-interference antenna based near-far effect mitigation method. *Geomatics Inf Sci Wuhan Univ* 36(10):1223–1225
5. Klein D, Parkinson BW (1986) The use of pseudo-satellites for improving GPS performance. *Glob Positioning Syst* 3:135–146
6. Van Dierendonck AJ, Elrod DB (1993) Testing and evaluation of GPS augmented with pseudolites for precision approach applications. In: Presented at DSNS conference, Amsterdam
7. Stansell T Jr (1986) RTCM SC104 recommended pseudolite signal specifications. *Navigation* 33:42–59
8. Martin S (1999) Antenna diagram shaping for pseudolite transmitter antennas—a solution to the near-far problem. In: Proceedings of ION GPS-99. Nashville, Sept pp 1473–1482
9. Wang J, Wang LB, Zhang Z (2008) Research on near far resistance method based on interference cancellation to GPS pseudolite. *Measur Control Technol* 27(3):43–48
10. Premal HM, Penina A, Kent K et al (2012) Application of successive interference cancellation to the CPS pseudolite near-far problem. *IEEE Trans Aerosp Electron Syst* 39(2):481–488
11. Varanasi MK, Aazhang B (1990) Multistage detection in asynchronous code-division multiple-access communications. *IEEE Trans Commun* 38(4):509–519
12. Liang M, Qin H, Li F (2010) Solving the near far problem for positioning the high earth orbital satellite with GPS. *Chin J Space Sci* 30(3):255–262
13. Wang Y, Ding QJ, Li R (2006) Adaptive array processing. Tsinghua University Press, Beijing
14. Xie G (2009) Principles and design of GPS Receiver. Electronic Industry Press, Beijing

Chapter 57

A Fast Positioning Method for Hot Start in GNSS Receiver

Xiaohui Ba, Shidong Luo, Haiyang Liu, Qing Yuan, Yun Wang and Jie Chen

Abstract Time to First Fix (TTFF) is an important parameter used for the evaluation of the performance of a GNSS receiver. For most mass market applications, it is attractive that the GNSS receiver has a first position fix within few seconds, while providing a relatively accurate first fix output. A short TTFF can be obtained by using Akopian's iterative estimation of satellite time of transmissions with a least-square method. The position computation needs at least five satellites in Akopian's method. However, several factors (such as 1-ms fuzziness and mis-acquisition, etc.) limit the usage of Akopian's method. This paper proposes the corresponding schemes to solve these problems and give a reliable and feasible fast positioning method considering both TTFF and the accuracy.

Keywords GNSS · Fast position · TTFF · Hot start

57.1 Introduction

The TTFF defines the time span of a receiver to output the first position fix, after the receiver has been switched on, which includes the time required for a GNSS receiver to start up, acquire satellite signals, demodulate ephemeris data and calculate its current position. Typically, TTFF is classified into three different start types (cold, warm and hot) based on the how much information the receiver has already known [1].

In a cold start, the previous position or time is unknown, and the receiver has no valid ephemeris or almanac data in memory. The primary limiting factor is the collection time of the ephemeris. For GPS signal, the transmission rate is 50 bps and the ephemeris data is 900 bit [2]. Thus, the absolute minimum time of a cold start is

X. Ba (✉) · S. Luo · H. Liu · Q. Yuan · Y. Wang · J. Chen
The Institute of Microelectronics of Chinese Academy of Sciences (IMECAS),
Beijing, China
e-mail: baxiaohui@ime.ac.cn

18 s. The TTFF of mass-market GPS receiver is usually no more than 30 s. For example, the cold start TTFF of u-Blox M8 is about 26 s [3]. There are some schemes that can shorten the TTFF of cold start efficiently. For example, the GNSS orbit prediction algorithm [4, 5] can provide predicted long-term high precision satellite position (i.e., achieving median accuracies of 58 m in satellite position for prediction up to four days ahead).

In a warm start mode, the valid almanac and time are required and the current location is usually within 60 miles of the last fix location [6]. Almanac data allows the receiver to predict which satellites are overhead, and thereby, the receiver can acquire signals faster than in a cold start [7]. But it still needs to download current Ephemeris data from at least three satellites. Thus, the primary limiting factor is also the collection time of the ephemeris.

In a hot start mode, a fix has been established within the last 2 h and the receiver has the valid ephemeris data and time. In this mode the receiver rapidly tracks the overhead satellites and there is no need to wait for the slow ephemeris broadcast. Manufacturers generally claim the hot start time is within one second. Thus, the primary limiting factor is the time of bit synchronization and frame synchronization, which is so-called time stamps (time-of-week, TOW). A Fast Positioning Method has been presented by Akopian without TOW information from navigation message [8, 9]. Instead, pseudorange values are reconstructed from partially available measurements, and five or more satellites are used for position computation. The technique is based on iterative estimation of satellite times of transmissions (TOT), receiver time, and position using a least-squares method [9].

However, there are still some factors that limit the utility of Akopian's method. The inaccuracy of the time and the initial position maybe cause the problem of the one-millisecond-fuzziness, which results in the wrong fix. In this paper, the phenomena of one-millisecond-fuzziness is analyzed and solved. A reliable and feasible fast positioning method considering both TTFF and the accuracy is also presented.

The paper is organized as follows. The Akopian's method is briefly described in Sect. 2. The problem of one-millisecond-fuzziness is analyzed in Sect. 3. Section 4 details the proposed fast positioning algorithm. Section 5 shows experimental results and Sect. 6 draws the conclusions.

57.2 The Akopian's Method

In this section, we briefly introduce the Akopian's method. The Akopian's method can reconstruct the satellite times of transmissions without the TOW.

Let T_{TOR} denote the time of receiver based on the reading of the receiver clock and T_{TOR_a} the accurate receiver time. Assume τ is the difference between T_{TOR} and T_{TOR_a} .

The estimated TOT is defined as \hat{T}_{TOT} . We let

$$\hat{T}_{TOT} = T_{TOR} \quad (57.1)$$

The estimated satellite position $s(\hat{T}_{TOT})$ is computed by the ephemeris and \hat{T}_{TOT} . The receiver position of switch-off (the initial position) is defined as \vec{u} . The estimated pseudorange ρ_1 is calculated as

$$\rho_1 = \|s(\hat{T}_{TOT}) - \vec{u}\| \quad (57.2)$$

The reconstructed TOT T_{TOT_rec} is calculated according to

$$T_{TOT_rec} = \lfloor T_{TOR} - \rho_1/c \rfloor_{ms} + T_{chip}, \quad (57.3)$$

where T_{chip} is called the tracking component of the TOT as it is typically obtained from tracking loops, $\lfloor x \rfloor_{ms}$ means the largest integer less than or equal to x millisecond.

The reconstructed pseudorange ρ_{rec} is calculated according to

$$\rho_{rec} = (T_{TOR} - T_{TOT_rec}) \cdot c, \quad (57.4)$$

The new equation is given as below.

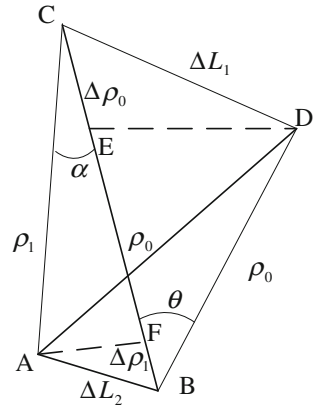
$$\rho_{rec} = (T_{TOR} - T_{TOT_rec}) \cdot c = \|s(T_{TOT_rec}) + \mathbf{v}(T_{TOT_rec}) \cdot \tau - \vec{u}_c\| + \Delta t_u \cdot c, \quad (57.5)$$

where \vec{u}_c , τ and Δt_u are unknown, and \vec{u}_c is the receiver's current position, Δt_u is the offset of the receiver clock, and \mathbf{v} is the speed of the satellite at the moment T_{TOT_rec} . Since there are five unknown variables, we need five or more satellites for position computation. The least-squares method or extended Kalman filter solution can be used to solve Eq. (57.5).

57.3 The Problem of the One-Millisecond-Fuzziness

The Akopian's algorithm is used to shorten the hot start TTFF. Although the ephemeris, the time and the receiver position are known in advance, the time is approximately accurate (not truly accurate), and the position of switch-on maybe is different with the position of switch-off. We must analyze that how much the error of the time and the position effect on the Akopian's algorithm.

Fig. 57.1 The effect of the receiver's time and position used in the first fix of the hot start



57.3.1 The Static Receiver

Assume the receiver is static and located at the position B. When the receiver is switched on, position C is the accurate satellite position. Because we can not obtain the accurate time without TOW, we can compute the satellite position by the inaccurate TOT (\hat{T}_{TOT} in Eq. (57.1)), denoted by D in Fig. 57.1.

As shown in Fig. 57.1, BC is the accurate range between the receiver and the satellite, and BD is the computed range between the receiver and the satellite. We define $BD = \rho_0$, $BC = BE + CE = \rho_0 + \Delta\rho_0 = \rho_2$, $CD = \Delta L_1$. From the basic knowledge of plane geometry, we have

$$\begin{aligned} \Delta L_1^2 &= \rho_0^2 + (\rho_0 + \Delta\rho_0)^2 - 2(\rho_0 + \Delta\rho_0)\rho_0 \cos \theta \\ &= \Delta\rho_0^2 + (2\rho_0^2 + 2\rho_0\Delta\rho_0)(1 - \cos \theta) \geq \Delta\rho_0^2 \end{aligned} \tag{57.6}$$

According to Eq. (57.6), we have

$$|\rho_2 - \rho_0| = |\Delta\rho_0| \leq |\Delta L_1| \tag{57.7}$$

57.3.2 The Kinematic Receiver

If the receiver is kinematic, we assume the receiver is switched off at the position B and switched on when it is moved to the position A. The position C is the accurate satellite position and the position D is the estimated satellite position. This means that AC is the accurate range between the receiver and the satellite and BD is the computed range between the receiver and the satellite. We define

$$AC = CF = \rho_1, \quad BC = CF + FB = \rho_1 + \Delta\rho_1, \quad AB = \Delta L_2$$

According to Eq. (57.7), we have

$$|\Delta\rho_1| \leq |\Delta L_2| \quad (57.8)$$

According to $BC = \rho_1 + \Delta\rho_1 = \rho_0 + \Delta\rho_0$, Eq. (57.7) and (57.8), it can be obtained as

$$|\rho_1 - \rho_0| = |\Delta\rho_0 - \Delta\rho_1| \leq |\Delta\rho_0| + |\Delta\rho_1| \leq |\Delta L_1| + |\Delta L_2| \quad (57.9)$$

57.3.3 The One-Millisecond-Fuzziness

Since Eq. (57.7) is the special case of Eq. (57.9), we only need to analyze Eq. (57.9).

The restriction condition of the Akopian's algorithm is

$$|\Delta L_1| + |\Delta L_2| < c \times 1 \text{ ms} \approx 300 \text{ km} \quad (57.10)$$

According to Eqs. (57.9) and (57.10), we have

$$|\rho_1 - \rho_0|/c < 1 \text{ ms} \quad (57.11)$$

According to Eqs. (57.3) (57.4) and (57.11), we have

$$(\rho_{rec} - \rho_0)/c = 0, \pm 1 \text{ ms} \quad (57.12)$$

If $(\rho_{rec} - \rho_0)/c = 0$, it means the pseudorange reconstruction is perfect and the receiver position calculated by Eq. (57.5) is correct. If $(\rho_{rec} - \rho_0)/c = \pm 1 \text{ ms}$, the problem of one-millisecond-fuzziness emerges and produces the wrong fix.

57.4 The Proposed Algorithm

In this section, we provide the corresponding schemes to solve the above-mentioned problems in the Akopian's original method. As a result, a reliable and feasible fast positioning method is proposed considering both TTFF and the accuracy.

57.4.1 The Solution for One-Millisecond-Fuzziness

The main steps of the method presented in this paper are listed as below.

- (1) Define a new variable ψ

$$\psi = \|\mathbf{s}(T_{TOT_rec}) - \vec{u}_c\| - (T_{TOR} - T_{TOT_rec}) \cdot c \quad (57.13)$$

We need at least five satellite to obtain the position solution, thus we need to compute $\psi_i, i \in [1, N], N \geq 5$.

- (2) Construct a variable

$$\gamma = \max(\psi_i) - \min(\psi_i) \quad (57.14)$$

If $\gamma < th$, all the reconstructed pseudoranges are correct; If $\gamma \geq th$, the variable j is defined that $\psi_j = \min(\psi_i), T_{TOT_rec,j} = T_{TOT_rec} + 1 \text{ ms}$ The variable th denotes the decision threshold.

- (3) Repeat the step (2) until $\gamma < th$.
 (4) Calculate the receiver position by Eq. (57.5).

57.4.2 The Accuracy Requirement

According to the analysis in Sect. 57.3 and 57.4.1, it is easy to see that TTFF is less than one second without TOW under the strong signal condition. This means the raw measurements are used immediately after the signals are acquired or in pull-in state. Under the strong signal conditions, the pull-in process is rapid and the local PRN code can align with the received PRN code promptly. Under the weak signal conditions, the pull-in process becomes slow, even may be wrong. If the coarse raw measurements are used to position, the accuracy of the fix may become bad. Thus, we need to find a method to detect the quality of the raw measurements (the pseudorange and the Doppler frequency).

The method of carrier phase smoothing pseudorange is utilized to construct a decision. We define

$$\rho_k = \rho_{k-1} - \lambda\Phi_k, \quad (57.15)$$

where ρ_k is the pseudorange at moment k , Φ_k is the carrier cycles between the moment $k-1$ and the moment k , λ is the carrier wave length. Then we have

$$\rho_k = c(t_{r,k} - (t_{s,k} - \Delta t_k^s)), \quad (57.16)$$

where $t_{r,k}$ denote the TOR, $t_{s,k}$ denote the TOT, Δt_k^s denote the satellite clock correction term. Usually, we have $\Delta t_k^s \approx \Delta t_{k-1}^s$.

According to Eqs. (57.15) and (57.16), we obtain

$$\lambda\Phi_k \approx c(t_{s,k} - t_{s,k-1}) - c(t_{r,k} - t_{r,k-1}) \quad (57.17)$$

A new decision variable is defined as

$$\eta = \left| \lambda\Phi_k - c(t_{s,k} - t_{s,k-1}) + c(t_{r,k} - t_{r,k-1}) \right| \quad (57.18)$$

If $\eta < th_2$, the quality of the raw measurements is acceptable and can be used to compute the receiver's position. Otherwise, the raw measurements can not be used. th_2 is a empirical threshold. If the small value of th_2 is selected, the tracking errors of the carrier loop and code loop will decrease, which cause a good fix accuracy. However, the cost is that TTFF may become long. Thus, a trade-off is considered for the selection of th_2 .

57.5 Experimental Results

The algorithm presented in this paper is tested in a multi-mode baseband GNSS receiver developed by our Lab, supporting GPS/BDS/QZSS/SBAS. The Spirent 6700 GNSS simulator is used to provide the GNSS signal. In the experiment, th is 150 km and th_2 is 30 m. A static scenario of Spirent is used and the x, y, z of ECEF coordinate is -2423428, 4968767 and 3170375 respectively.

We need to test the effect caused by the inaccuracy of receiver's time and position. In hot start, the receiver is powered down only for a short time (4 h or less). When the receiver is switched on, the time information is obtained from the Real Time Clock (RTC). RTC is used to provide an incremental time indicator. Usually it is based on a 32768 Hz crystal oscillator with 200 ppm (part per million). After 4 h, the difference between the local time from RTC and the real time is not more than $200 \times 10^{-6} \times 4 \times 3600 = 2.88$ s. The speed of GPS satellite is about 3874 m/s. According to Fig. 57.1 and the analysis in Sect. 3.1, we obtain

$$|\Delta L_1| < 3874 \times 2.88 = 11157.12 \text{ m}$$

Several different initial positions are selected to test the presented algorithm, including $|\Delta L_2| = 10$ km, $|\Delta L_2| = 30$ km, $|\Delta L_2| = 100$ km, $|\Delta L_2| = 130$ km. The selection of $|\Delta L_2|$ needs to meet the conditions in Eq. (57.10). One hundred hot starts have been tested by the GNSS receiver for every initial position. The experimental results are list in Table 57.1. Table 57.1 is obtained under the condition that the power level of the signal output from the Spirent simulator is -130 dBm.

It is known from Table 57.1 that the proposed algorithm in this paper can give the correct fix under the condition of $|\Delta L_2| \leq 100$ km and $|\Delta L_1| \approx 11$ km. If the bias of the initial position and the accurate position become larger, the hot start will fail.

Table 57.1 The hot start tests under the condition of $|\Delta L_1| \approx 11$ km and different $|\Delta L_2|$

The ECEF coordinate of the receiver computed by hot start (unit: meter)		$ \Delta L_2 = 10$ km	$ \Delta L_2 = 30$ km	$ \Delta L_2 = 100$ km	$ \Delta L_2 = 130$ km
x	Average value	-2,423,436	-2,423,435	-2,423,431	NA
	Standard deviation	0.9592	0.6496	1.4320	NA
y	Average value	4,968,784	4,968,771	4,968,775	NA
	Standard deviation	1.8967	2.8288	2.200	NA
z	Average value	3,170,387	3,170,378	3,170,372	NA
	Standard deviation	1.7870	1.3322	3.3262	NA

The reason is that γ in Eq. (57.14) is more and more difficult to satisfy the condition of $\gamma < th$ with the increasing position bias. The step (2) in Sect. 4.2 is repeated frequently and maybe the condition of $\gamma < th$ is always unsatisfied.

When the GNSS signals become weak, the mis-acquisition or the wrong pull-in may appear. If the wrong measurements are excluded by Eq. (57.18), a good first fix accuracy can be obtained.

57.6 Conclusions

In this paper, a new fast positioning method is proposed to improve the Akopian's method and solve the problem of one-millisecond-fuzziness. Under the condition that the position bias is 100 km, the hot start still succeed. The accuracy of hot start is also guaranteed. If the receiver can fast acquire the GNSS signal and quickly finish the correct pull-in, the receiver can right away give the correct and accurate position for hot start..

Acknowledgments This study is supported by National Natural Science Foundation of China 61221004.

References

1. Paonni M, Anghileri M, Wallner S, Ávila-Rodríguez JA, Eissfeller B (2010) Performance assessment of GNSS signals in terms of time to first fix for cold, warm and hot start. In: Proceedings of the international technical meeting of the institute of navigation ION-ITM 2010, 25–27 Jan 2010, San Diego, CA, USA, pp 1051–1066
2. JB Tsui (2005) Fundamentals of global positioning receivers: a software approach, 2nd edn. Wiley, Newyork
3. UBX-M8030 datasheet (2015) http://www.u-blox.com/images/downloads/Product_Docs/UBX-M8030_ProductSummary_%28UBX-13002862%29.pdf. Accessed 25 Jan 2015

4. Seppänen M, Ala-Luhtala J, Piché R, Martikainen S, Ali-Löytty S (2012) Autonomous prediction of GPS and GLONASS satellite orbits. *Naviga-J Inst Navig* 59(2):119–134
5. Hsu T-A, Chang F-R, Wang L-S, Tseng Y-F (2010) Long-term prediction of GPS satellite orbit. In: *Proceedings of SICE annual conference 2010, Taipei*, pp 2906–2909, 18–21 Aug 2010
6. <http://www.measys.com/docs/TTFStartup.pdf>. Accessed 25 Jan 2015
7. Lehtinen M, Happonen A, Ikonen J (2008) Accuracy and time to first fix using consumer-grade GPS receivers. In: *16th International conference software, telecommunications and computer networks. SoftCOM 2008*, pp 334–340, 25–27 Sept 2008
8. Akopian D, Syrjärinne J (2009) A fast positioning method without navigation data decoding for assisted GPS receivers. *IEEE Trans Veh Technol* 58(8):4640–4645
9. Akopian D, Syrjärinne J (2002) A network aided iterated LS method for GPS positioning and time recovery without navigation message decoding. In: *Position location and navigation symposium, 2002 IEEE*, pp 77–84

Chapter 58

A New Iterative Method for Multipath Mitigation

Yan Gao, Wei Li, Jinli Li, Hongliang Qu and Xiang Shi

Abstract Multipath is the dominant source of positioning error in modern GNSS receiver. Maximum likelihood (ML) parameter estimation is an optimal method to mitigate the multipath effects while ML involves nonlinear optimization and requires iterative algorithms. Iterative methods usually lack of global convergence when the paths are closely spaced, if the initial value is arbitrarily assigned. In this paper, however, we first employ a grid search method to choose the initial value before iteration. Most computation of the grid search can be done offline. After that, an iterative method with simple forms is used to improve the parameter accuracy and global convergence can be achieved with just a few iterations. The simulations results show the estimator of time delay is almost unbiased when the time relative delay of two paths is larger than 0.20 chips.

Keywords GNSS receiver · Multipath mitigation · Maximum likelihood · Grid search · Iteration

58.1 Introduction

The presence of multipath greatly affects the localization performance of GNSS system. In GNSS receivers, due to multipath, the correlation between the local PN sequence and received signal no longer has an ideal triangular shape but is superimposed by many delayed versions of auto correlation function (ACF). Conventional methods such as Early-Late (EL) delay locked loop (DLL) which are easily trapped into the wrong equilibrium point, cannot tackle this problem, thus resulting great ranging error, especially when the LOS path is not dominant. In the past years, various methods have been proposed to reduce the multipath errors,

Y. Gao (✉) · W. Li · J. Li · H. Qu · X. Shi
Hwa Create Corporation Ltd, Yi.18, No. 8 Dongbeiwang West Road,
Haidian District, Beijing 100094, People's Republic of China
e-mail: yan.gao1989@hotmail.com

which can be categorized into two groups: modified DLL method and multipath parameters (complex amplitude, time delay) estimation methods. The first group of methods try to simply modify the traditional DLL and make it capable of mitigating multipath, typical methods including narrow spacing correlator, strobe correlator, double delta correlator [1–3]. The latter group of methods employ parameter estimation methods to resolve the multipath [4–11].

The multipath parameter estimation is generally based on the principle of maximum likelihood (ML). Note that the output of the correlator is linear with amplitude while nonlinear with time delay, thus that ML is a nonlinear optimization problem. It's well known that solving the nonlinear optimization problems needs iterative algorithms while the solution is very sensitive to the initial value. In other words, the iterative methods may converge to local minima rather than the global minima, if the initial value is poorly set [5–7]. In [8], the author proposed a grid search algorithm instead of iterative method to avoid the local convergence phenomenon. Compared to iterative algorithms, the grid search requires more computational overhead but the most calculation can be undertaken offline. One disadvantage of this method is that the estimation accuracy is limited by the size of the grid. Although the author used an interpolation method to further improve the estimation accuracy, the interpolation was just an approximation operation and will cause modeling error.

In this paper, we propose a combination of offline grid search and online iteration method to improve the estimation performance. ML estimation of multipath parameter can be reduced to minimize the object function only with respect to time delay. Therefore, grid search is possible because we can confine the search range in a chip and large online computation can also avoided because the most computation extensive part can be completed offline. The results of the grid search are taken as the initial value of iterative algorithms. In fact, for a given set of amplitudes, the time delay can also be seen linearly with output of correlation due to the piece-wise linear property of ACF [6] and then ML estimation of time delay can be obtained. The time delay can be used to update the ML estimation of amplitude. Repeat the above process and we can derive a new iterative method. The combined method almost always converges to the global minima with just a few iterations, if the sampling interval is appropriately chosen, which is very computational acceptable. Most importantly, the proposed method greatly improves the accuracy of estimation when the path separation is less than half a chip.

58.2 System Model

Due to multipath propagation, the receiver will receive multiple replicas of PN sequence $c(t)$ transmitted by the satellite. Suppose the received signal has been stripped of navigation data and the Doppler shift is perfectly compensated before correlation, then it can be written as follows

$$r(t) = \sum_{k=1}^L a_k e^{j\theta_k} c(t - \tau_k) + w(t) \tag{58.1}$$

where $A_k = a_k e^{j\theta_k}$, τ_k is the complex amplitude and time delay of k th path respectively and L is number of paths. $w(t)$ is the zero-mean additive white Gaussian noise (AWGN) with double-side power density N_0 . For simplicity, the ACF of PN sequence is ideally considered as a triangular shape i.e. $R(\tau) = 1 - \frac{|\tau|}{T_c}$ for $|\tau| < T_c$ and $R(\tau) = 0$ otherwise, where T_c is chip duration. The received signal is correlated by a local generated PN sequence and the cross correlation function $R_c(\tau)$ is

$$R_c(\tau) = \frac{1}{T} \int_0^T r(t)c^*(t - \tau)dt = \sum_{k=1}^L A_k R(\tau - \tau_k) + w_c(\tau) \tag{58.2}$$

where $T = 1023T_c$ is the integration time and $w_c(\tau) = \frac{1}{T} \int_0^T w(t)c^*(t - \tau)dt$ is the correlation between noise and the local PN sequence. It can be seen that $R_c(\tau)$ is the superposition of L attenuated versions of ACF and additive noise, as illustrated in Fig. 58.1. $R_c(\tau)$ is the continuous form of the output of the correlation while we can

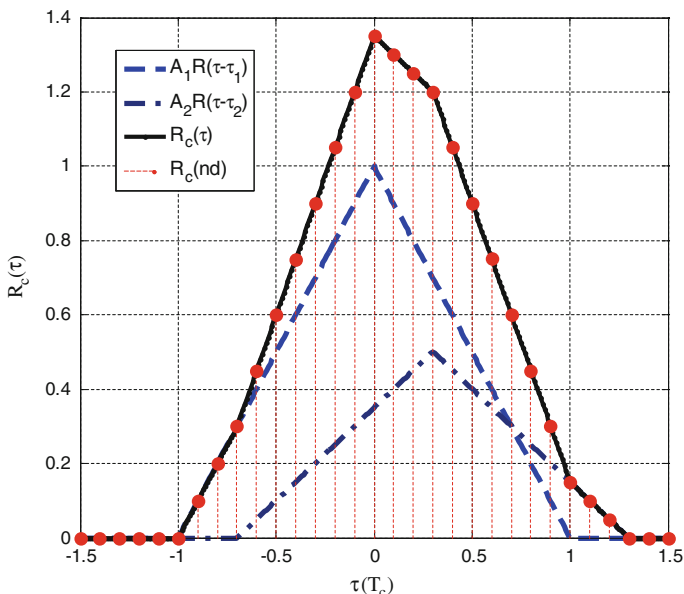


Fig. 58.1 An illustration of cross correlation function

only get some sampling points of $R_c(\tau)$ through multicorrelator or sliding correlator. Suppose $R_c(\tau)$ is uniformly sampled, the sampling point can be expressed as

$$R_c(nd) = \sum_{k=1}^L A_k R(nd - \tau_k) + w_c(nd), n \in [-M, M] \quad (58.3)$$

where d is the sampling interval and $(2M + 1)$ is the number of sampling points. The covariance of noise denotes \mathbf{C} and has entry $C_{m,n} = E[w_c(md)w_c^*(nd)] = \frac{2N_0}{T} R((m - n)d)$ [8].

Stacking all the points into a column vector and denoting $\mathbf{R}_c = [R_c(-Md), R_c(-(M - 1)d), \dots, R_c(nd), \dots, R_c(Md)]^T$, then (3) can be rewritten as a more compact form as

$$\mathbf{R}_c = \mathbf{R}\mathbf{A} + \mathbf{w}_c \quad (58.4)$$

where $\mathbf{A} = [A_1, A_2, \dots, A_k, \dots, A_L]^T$, $\mathbf{w}_c = [w_c(-Md), w_c(-(M - 1)d), \dots, w_c(nd), \dots, w_c(Md)]^T$ and \mathbf{R} is a $(2M + 1) \times L$ dimension matrix related to $\boldsymbol{\tau} = [\tau_1, \tau_2, \dots, \tau_k, \dots, \tau_L]^T$ and has the element $R_{c(n,k)} = R(nd - \tau_k)$.

Obviously, \mathbf{R}_c is linear with respect to \mathbf{A} regardless of the value of $\boldsymbol{\tau}$ while nonlinear with $\boldsymbol{\tau}$ because of the nonlinearity of ACF.

58.3 ML Estimation

Consider the covariance matrix \mathbf{C} is known, the joint probability density function (pdf) is

$$p(\mathbf{R}_c; \boldsymbol{\tau}, \mathbf{A}) = \frac{1}{(2\pi)^{(2M+1)/2} \det^{1/2}(\mathbf{C})} \exp\left[-\frac{1}{2}(\mathbf{R}_c - \mathbf{R}\mathbf{A})^H \mathbf{C}^{-1}(\mathbf{R}_c - \mathbf{R}\mathbf{A})\right]$$

ML estimation indicates minimize the following object function

$$(\hat{\boldsymbol{\tau}}, \hat{\mathbf{A}}) = \arg \min_{(\boldsymbol{\tau}, \mathbf{A})} \Gamma(\mathbf{A}, \boldsymbol{\tau}) = (\mathbf{R}_c - \mathbf{R}\mathbf{A})^H \mathbf{C}^{-1}(\mathbf{R}_c - \mathbf{R}\mathbf{A}) \quad (58.5)$$

Taking the partial derivative of the object function and setting it to zero, we can obtain the ML estimator with respect to \mathbf{A} .

$$\hat{\mathbf{A}} = (\mathbf{R}^H \mathbf{C}^{-1} \mathbf{R})^{-1} \mathbf{R}^H \mathbf{C}^{-1} \mathbf{R}_c \quad (58.6)$$

Substituting \mathbf{A} in (58.5) by $\hat{\mathbf{A}}$ and ignoring the terms independent of $\boldsymbol{\tau}$, we can obtain a new object function only with respect to $\boldsymbol{\tau}$.

$$\begin{aligned}\hat{\tau} &= \arg \max_{\tau} \Gamma'(\tau) = \mathbf{R}_c^H \mathbf{C}^{-1} \mathbf{R} (\mathbf{R}^H \mathbf{C}^{-1} \mathbf{R})^{-1} \mathbf{R}^H \mathbf{C}^{-1} \mathbf{R}_c \\ &= \mathbf{R}_c^H \mathbf{\Omega}(\tau) \mathbf{R}_c\end{aligned}\quad (58.7)$$

where $\mathbf{\Omega}(\tau)$ is a matrix only depending on τ . It can be seen that a closed form solution is impossible because of the nonlinear characteristic of the optimization problem.

58.3.1 Offline Grid Search

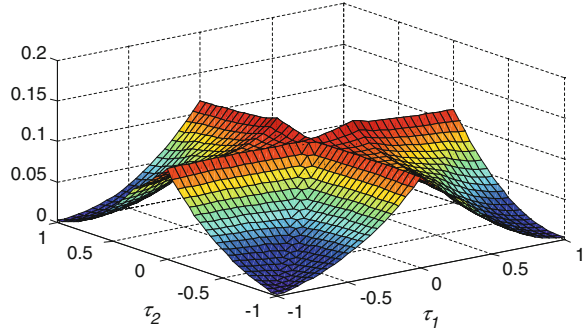
As we have mentioned, ML estimation of time delay is a nonlinear optimization problem. Direct use of iterative method suffers from local convergence without prior knowledge of initial value. And local convergence becomes more severe when the paths get closer. So it's significant to properly initialize the time delay before iteration. A straightforward approach to implement the initialization is by grid search which can exclude many local minima through comparison of the object function. Grid search means to consider all the possible cases of τ and select the case which maximizes the object function. The size of grid δ determines the complexity of the search procedure and the choice of δ depends on the resolution that the users want to acquire. For example, if $\tau_1 = 0.13T_c$, $\tau_2 = 0.64T_c$, $\sigma = 0.2T_c$ is enough to obtain an appropriate initial value while if $\tau_1 = 0.13T_c$, $\tau_2 = 0.24T_c$, $\sigma = 0.1T_c$ is needed. Here, we emphasize that grid search is just a coarse search to initialize the parameter and the refining parameter operation will be done in the iteration step in 58.3.2.

Moreover, the most exhaustive part of grid search is the computation of $\mathbf{\Omega}(\tau)$ for all the grid points in the L dimensional time delay space. In fact, $\mathbf{\Omega}(\tau)$ can be computed offline, stored in the memory and loaded for online computation of object function.

If $N\delta = T_c$, where N is the grid points along one dimension, considering that the search range of delay is within a chip. thus that we should compare $\binom{L}{2N+1}$ grid points, The offline work of grid search is to calculate $\mathbf{\Omega}(\tau)$ of each grid point of τ . The procedure of online grid search is : (1) Choose one grid point τ and compute the corresponding object function $\Gamma'(\tau)$. (2) Repeat (1) until the object function of all grid points are obtained. (3) Choose the grid point τ_0 which maximizes the object function, i.e., $\hat{\tau}_0 = \arg \min_{\tau \in \text{grid points}} \Gamma'(\tau)$.

As an illustration, Fig. 58.2 shows the grid search result when $L = 2$, $\mathbf{A} = [1e^{j\frac{\pi}{4}}, 0.5e^{j\frac{3\pi}{4}}]^T$, $\tau = [0.0, 0.35]^T$, $d = \delta = 0.05T_c$. The peak found which corresponds to the global minima is at grid point $\hat{\tau}_0 = [0.01T_c, 0.30T_c]^T$.

Fig. 58.2 The surface of $\Gamma'(\boldsymbol{\tau})$ versus τ_1 and τ_2



58.3.2 Online Iteration

The accuracy is limited by the grid search because we only consider that τ_k only takes integer grids, which is impractical in real cases. In [8], the author used a polynomial interpolation based to alleviate the accuracy limitation, which is simple but not accurate enough. The correlation between the LOS path and the local PN sequence is estimated by subtracting the contribution of other paths from the sampling points. Because the obtained parameters of each path is very rough, this estimator would contain the error of every paths.

However, for a fixed $\boldsymbol{\tau}$, if we use the piece-wise linearity property of ACF, (4) can also be represented by a linear relationship with respect to $\boldsymbol{\tau}$ [6], that is

$$\mathbf{R}_c = \mathbf{F}\boldsymbol{\tau} + \mathbf{g} + \mathbf{w}_c \tag{58.8}$$

$$\text{where } F_{n,k} = \begin{cases} \frac{A_k}{T_c}, -T_c + \tau_k < nd < \tau_k \\ \frac{-A_k}{T_c}, \tau_k < nd < T_c + \tau_k \\ 0, \text{otherwise} \end{cases} \text{ and}$$

$$g_n = \begin{cases} \sum_{k=1}^L A_k \left(1 + \frac{nd}{T_c}\right), -T_c + \tau_k < nd < \tau_k \\ \sum_{k=1}^L A_k \left(1 - \frac{nd}{T_c}\right), \tau_k \leq nd < T_c + \tau_k \\ 0, \text{otherwise} \end{cases}.$$

The object function can also be represented as

$$\min \Gamma(\mathbf{A}, \boldsymbol{\tau}) = (\mathbf{R}_c - \mathbf{F}\boldsymbol{\tau} - \mathbf{g})^H \mathbf{C}^{-1} (\mathbf{R}_c - \mathbf{F}\boldsymbol{\tau} - \mathbf{g}) \tag{58.9}$$

Similarly, the ML estimator of time delay is

$$\hat{\tau} = (\mathbf{F}^H \mathbf{C}^{-1} \mathbf{F})^{-1} \mathbf{F}^H \mathbf{C}^{-1} (\mathbf{R}_c - \mathbf{g}) \quad (58.10)$$

Note that each of the entries of \mathbf{F} depends on the old τ and the above estimator gives a new estimation of τ . Thus the estimator is iterative in nature. We can use this idea to derive an iterative method to estimate the time delay. Because the initial value obtained via grid search is very close to global minima, usually less than a grid interval, it's not hard to predict the iteration will converge to global minima with just a few iterations.

During the iteration, the amplitude and time delay are estimated in a successively way. Specially, for i iteration, if we have an old time delay estimation $\hat{\tau}_{i-1}$, the current ML estimator of amplitude $\hat{\mathbf{A}}_i$ is

$$\hat{\mathbf{A}}_i = (\mathbf{R}_{i-1}^H \mathbf{C}^{-1} \mathbf{R}_{i-1})^{-1} \mathbf{R}_{i-1}^H \mathbf{C}^{-1} \mathbf{R}_c \quad (58.11)$$

After obtaining $\hat{\mathbf{A}}_i$, it can be used to update $\mathbf{F}_i^H, \mathbf{g}_i$ and ML estimator of time delay can be updated by

$$\hat{\tau}_i = (\mathbf{F}_i^H \mathbf{C}^{-1} \mathbf{F}_i)^{-1} \mathbf{F}_i^H \mathbf{C}^{-1} (\mathbf{R}_c - \mathbf{g}_i) \quad (58.12)$$

$\hat{\tau}_i$ can also be used to obtain a new estimation $\hat{\mathbf{A}}_{i+1}$. Repeat the iteration until $\hat{\tau}$ converges.

In some cases, the matrix $\mathbf{R}_{i-1}^H \mathbf{C}^{-1} \mathbf{R}_{i-1}$ and $\mathbf{F}_i^H \mathbf{C}^{-1} \mathbf{F}_i$ might be singular because of rounding error during computation, which would lead to the occurrence of unstable solution. Adding a regularization term can avoid the unstable situation and then the iteration can be rewritten as

$$\begin{aligned} \hat{\mathbf{A}}_i &= (\mathbf{R}_{i-1}^H \mathbf{C}^{-1} \mathbf{R}_{i-1} + \lambda_A \mathbf{I})^{-1} \mathbf{R}_{i-1}^H \mathbf{C}^{-1} \mathbf{R}_c \\ \hat{\tau}_i &= (\mathbf{F}_i^H \mathbf{C}^{-1} \mathbf{F}_i + \lambda_\tau \mathbf{I})^{-1} \mathbf{F}_i^H \mathbf{C}^{-1} (\mathbf{R}_c - \mathbf{g}_i) \end{aligned} \quad (58.13)$$

where λ_A and λ_τ are the regularization parameters and are chosen empirically in this paper. Actually, the above estimators can also be explained from the Bayesian perspective [12].

58.4 Simulation Results

The performance of the proposed algorithm is investigated by simulation. In the simulation, without loss of generality, we consider a simple case when the received signal composes of the LOS path and a reflected path, i.e. $L = 2$. We define the signal-to-multipath ratio (SMR) is $SMR = 20 \log \left(\frac{|A_1|}{|A_2|} \right)$ signal-to-noise ratio is

$SNR = 10 \log \frac{|A_1|^2}{2N_0} T$, where B is the bandwidth of RF front end. The relative time delay of the two paths defines $\Delta\tau = \tau_2 - \tau_1$. The phases of both paths are uniformly distributed over $u(0, 2\pi)$ in each realization of simulation. Root mean square error (RMSE) of time delay τ_1 in T_c is used to compare the performance of the methods. The number of iteration is kept fixed as 10 and the regularization parameters are $\lambda_A = \lambda_\tau = 10^{-3}$.

58.4.1 RMSE Versus Relative Time Delay $\Delta\tau$

In this simulation, τ_1 is randomly distributed over the interval $[-d/2, d/2]$ and τ_2 is equal to $\tau_1 + \Delta\tau$. The SMR and SNR were assumed to be 6 and -20 dB respectively. For each $\Delta\tau$, the result is averaged by 1000 times Monte Carol simulations. Figure 58.3 shows the performance comparison between the proposed method and the normalized narrow E-L correlator [1] for both $d = 0.1T_c$ and $d = 0.2T_c$. For the sampling interval $d = 0.1T_c$, the proposed method always outperforms than narrow E-L correlator when $\Delta\tau > 0.1T_c$. In particular, when $\Delta\tau > 0.2T_c$, the RMSE of τ_1 of proposed method is nearly $0.003T_c$ while that of the narrow correlator is $0.035T_c$ which is over 10 times of proposed method. The performs gap still holds for sampling interval $d = 0.2T_c$ when $\Delta\tau > 0.3T_c$. For $\Delta\tau > 0.1T_c$, the performance of narrow correlator is better than proposed method, although both are biased, because as the two paths get closer, narrower d and δ are required to resolve the two paths and guarantee the global convergence.

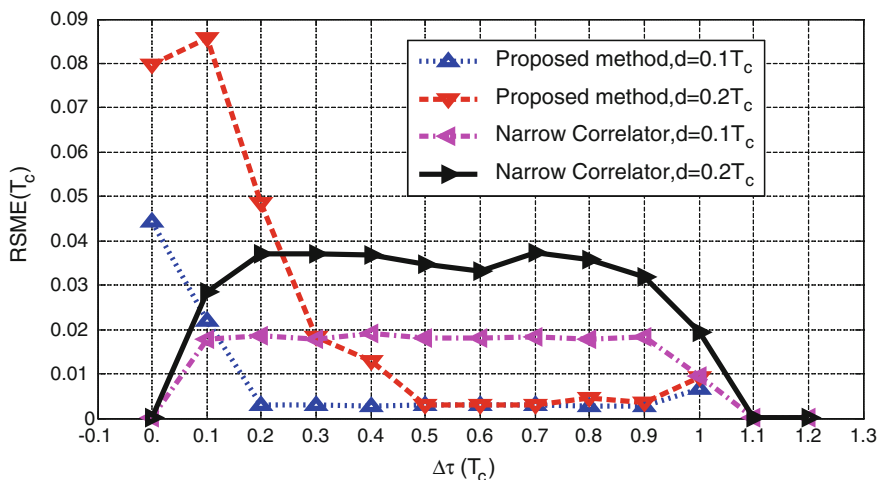


Fig. 58.3 RMSE of τ_1 versus $\Delta\tau$ for both proposed method and narrow correlator for different sampling interval d

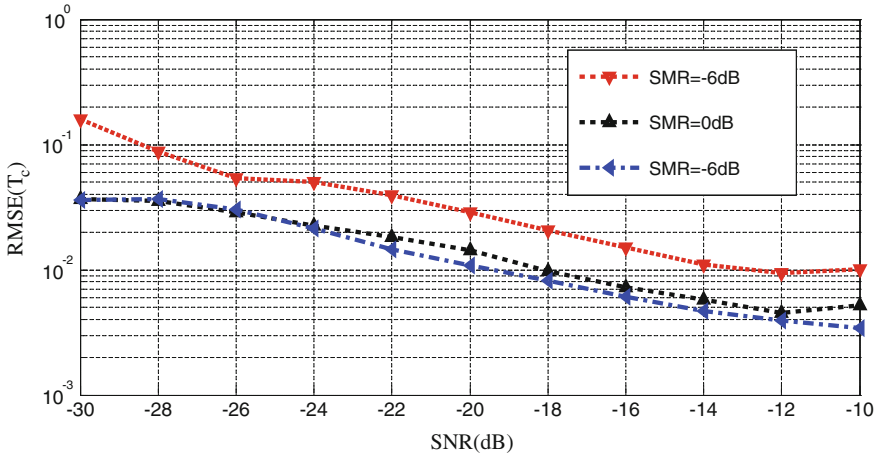


Fig. 58.4 RMSE of τ_1 versus SNR for different SMR

58.4.2 RMSE Versus SMR and SNR

In previous simulation, we have observed that the estimator is almost unbiased when $\Delta\tau > 0.2T_c$. Now we take into account the SMR and SNR. Both SMR and SNR affect the performance of the proposed method. If SMR is too low, the LOS path would be very weak and low SNR means the received signal will severely corrupted by noise. In this simulation, we consider three cases when the amplitude of LOS path is double of, equal to and half of the amplitude of reflection path, i.e. $SMR = -6, 0.6$ dB, respectively. Figure 58.4 shows the RMSE performance versus SNR and SMR with $d = 0.1T_c$, $\Delta\tau = 0.3T_c$. We can observe the RMSE degrades a little as SNR and SMR decreases but it is still in the acceptable range.

58.5 Conclusion

In this paper, we proposed a combination approach of grid search and iteration to closely spaced multipath mitigation in GNSS receiver based on the ML principle. Because of nonlinearity of ML estimation, the solution is very sensitive to the initial value of the time delay. The problem is solved by initialization via the grid search before iteration. The computational complexity of grid search seems to be very high, but the online burden is small because most of the computation can be done offline. Iteration algorithm derived from the piece-wise linearity of ACF has a simple form and converges to global maximum of ML function with a few number of iteration. The simulation results show that the time delay estimator almost unbiased and performs well when the LOS path is not dominant.

References

1. Van Dierendonck AJ, Fenton P, Ford T (1993) Theory and performance of narrow correlator spacing in a GPS receiver. *J Institut Navig* 39(3):265–283
2. Garin L, van Diggelen F, Rousseau JM (1996) Strobe and edge correlator multipath mitigation for code. In: Proceedings of the 9th international technical meeting of the satellite division of the institute of navigation, pp 657–664
3. Irsigler M, Eissfeller B (2003) Comparison of multipath mitigation techniques with consideration of future signal structures. In: Proceedings of ION GPS/GNSS 2003, Portland, OR, Sept 2003
4. Townsend BR, van Nee DJR (1995) Performance evaluation of the multipath estimating delay lock loop. In: Proceedings of ION national technical meeting
5. Sahnoudi M, Amin MG (2008) Fast iterative maximum-likelihood algorithm (FIMLA) for multipath mitigation in the next generation of gnss receivers. *IEEE Trans Wireless Commun* 7:4362–4372
6. Nam W, Kong SH (2013) Least-square-based iterative multipath super-resolution techniques. *IEEE Trans Signal Process* 61:519–529
7. Closas P, Prades CF (2007) Maximum likelihood estimation of position in GNSS. *IEEE Signal Process Lett* 14:359–362
8. Blanco-Delgado N, Nunes FD (2012) Multipath estimation in multicorrelator GNSS receivers using the maximum likelihood principle. *IEEE Trans Aerosp Electron Syst* 48:3222–3233
9. Soubielle J, Fijalkow I et al (2002) GPS positioning in a Multipath Environment. *IEEE Trans Signal Process* 50:141–149
10. Closas P, Prades CF et al (2009) A Bayesian approach to multipath mitigation in GNSS receivers. *IEEE J Sel Topic Signal Process* 3:695–706
11. Closas P, Prades CF (2007) Maximum likelihood estimation of position in GNSS. *IEEE Signal Process Lett* 14:359–362
12. Kay SM (1993) Fundamentals of statistical signal processing, vol 1. In: Estimation theory. Prentice Hall, Englewood Cliffs

Chapter 59

An Improved Practical Anti-jamming Technique for GNSS Receivers Based ADP in Frequency Domain

Tianqiao Zhang, Yao Wang, Yang Gao and Hongbing Wang

Abstract Anti-jamming techniques have been widely researched to enhance the reliability and effectivity of Global Navigation Satellite System (GNSS). Amplitude Domain Processing (ADP) is an anti-jamming method base on Locally Most Powerful (LMP) detection theory. While it works efficiently when dealing with some relatively simple interferences, such as one or two continuous wave interferences, it has a limitation when submitted to multiple interference scenarios. Then, some later researches prove that using ADP in frequency domain (FADP) would give a more superior performance, and put forward a simple global framework of this method. However, there are still several important specific problems needing to be solved before FADP's being brought into practice, as the spectrum leakage and malignant distribution of the frequency domain statistical data would surely degrade the performance of the method or even invalidate it. In this paper, an improved anti-jamming technique based on FADP is proposed, which is more robust for practical consideration. Firstly, a windowed FFT is used to inhibit the spectrum leakage and signal distortion, as well as the pattern of overlap-adding is chosen to minimize the degradation of the SNR. Then, along with the analysis of the differences between statistical characteristics of the time-domain waveform and spectrum data, a specialized mathematical function of ADP is designed, responding to the wide range and malignant distribution of spectrum data. Meanwhile, a simplification of the procedures also eliminates the need of mutual transformation between Cartesian coordinates and polar coordinates, saving the computation and storage resources in some way. Simulation results demonstrate that the proposed improved FADP method performs more efficaciously in realistic situation than the original one.

Keywords GNSS · Anti-jamming · ADP · FADP · Practical consideration

T. Zhang (✉) · Y. Gao · H. Wang
Beijing Satellite Navigation Center, Beijing 100094, China
e-mail: gary_85@163.com

Y. Wang
Department Electronic Engineering, Tsinghua University, Beijing 100084, China

59.1 Introduction

The global navigation satellite system (GNSS)—taking GPS, GLONASS, COMPASS and Galileo as representatives—has a certain capability of immunity from interference, since direct sequence spread system (DSSS) is utilized in the communication. However, the receiver would significantly perform unsatisfactorily or even lose efficacy when the interference surpasses the jamming margin. For this reason, the anti-jamming technology is extensively studied.

References [1, 2] introduced an anti-jamming solution to narrowband interference problem named amplitude domain processing (ADP), which is based upon Capon works [3] and Neyman-Pearson theory [4]. As an application of the locally most powerful (LMP) detection, this technique is fully adaptive and completely digital. And the relatively simple structure enables it easily to get implemented. However, while it works effectively when dealing with some relatively simple interference, such as one or two continuous wave interference (CWI); it has a limitation when submitted to multiple interference scenarios, when there are more simultaneous jammers. Then, as a further development, reference [5] puts forward an new method named FADP. By the means of adding a couple of FFT and IFFT blocks, FADP applies the amplitude domain processing to the spectrum instead of the time domain samples. Through series simulation, [5] proves that FADP filter shows to be significantly more efficient than the ADP one in the presence of complex interference.

However, current FADP method still has several problems to deal with before it could really get used. Firstly, the FFT in current framework pays no attention to the picket fence effect, which may cause a spectrum leakage and signal distortion. This will surely degrade the behavior of the later procedures, making the method fail at worst. And the effect varies according to the selected sequence length of FFT and the intensity of the interference. Though simulation in [5] coincidentally avoid this problem, as will mention in 59.2.4, it can't be ignored in practice. Secondly, the differences between the statistical characteristics of the time-domain waveform and spectrum data also need us to pay enough attention to. The original ADP function isn't very suitable to be used in the FADP method directly because of the wide range and malignant distribution of the frequency domain statistical data. So, there is a need to improve this method systematically for further usage.

Thereupon, an improved anti-jamming technique based on FADP is proposed in this paper, which is more robust for practical consideration. Firstly, a windowed FFT is used instead to inhibit the spectrum leakage and signal distortion. While windowing would bring inevitable loss of the signal-to-noise ratio (SNR) as well, the pattern of overlap-adding is chosen. Blackman window for instance, as shown in [6], a directly windowing would bring a SNR loss of 2.28 dB, while making a 1/2 delay overlap-adding would decrease it to 0.08 dB. Overlap-add-windowing ensures the utmost accuracy of the frequency spectrum, which is also a prerequisite of FADP technique. Then, having noticed the wide range and malignant distribution of the frequency domain statistical data, the general approaches to procure the probability density function (PDF) are not applicable to frequency samples. Thus,

by taking logarithms of the frequency samples, we compress the data in amplitude domain. Correspondingly, a specialized mathematical function of ADP is designed, which possesses the validity in theory as well as the practicability. Lastly, a simplification of the procedures also eliminates the need of mutual transformation between Cartesian coordinates and polar coordinates, saving the computation and storage resources in some way.

Chapter 2 briefly reviews the theoretical basis of ADP and FADP, and then analyzes the potential problems of current FADP framework for practical use. Chapter 3 elaborates the improvement methods. At last, simulation results in Chap. 4, based on a MATLAB platform of GPS L1 receiver, demonstrate that the proposed improved FADP method performs more efficaciously in realistic situation than the original one.

59.2 Theoretical Basis of ADP and FADP

The ADP technique, as well as FADP, is essentially an application of the Locally Most Powerful (LMP) detection in the spread spectrum communication. LMP detection has the maximum probability of detection under weak signal conditions, as shown in [7]. In this chapter, LMP theory is briefly introduced to the readers firstly. Then, a review of ADP and FADP techniques will show us how this theory works. For more details, the reader could refer to [1, 2, 5]. In the end, several potential problems of the present FADP method are analyzed, indicating the direction of improvement.

59.2.1 Introduction of LMP Theory

Consider the one-sided parameter test

$$\begin{aligned} H_0 : \theta &= \theta_0 \\ H_1 : \theta &> \theta_0 \end{aligned}$$

with no nuisance parameters. The probability density function (PDF) under H_0 and H_1 is parameterized by θ and is given by $p(x; \theta)$. Let the region for which we choose H_1 be denoted by R_1 . Then the probability of false alarm and detection would be

$$\begin{aligned} P_{FA} &= \int_{R_1} p(x; \theta_0) dx \\ P_D(\theta) &= \int_{R_1} p(x; \theta) dx. \end{aligned} \tag{59.1}$$

It shows that $P_D(\theta)$ depends on θ . On condition $\theta > \theta_0$ and $\theta - \theta_0$ is small, we can expand $P_D(\theta)$ in a first-order Taylor expansion about $\theta = \theta_0$ and get

$$P_D(\theta) \approx P_D(\theta_0) + \left. \frac{dP_D(\theta)}{d\theta} \right|_{\theta=\theta_0} \cdot (\theta - \theta_0) = P_{FA} + \left. \frac{dP_D(\theta)}{d\theta} \right|_{\theta=\theta_0} \cdot (\theta - \theta_0). \tag{59.2}$$

Since P_{FA} is fixed, we maximize $P_D(\theta)$ for any θ by maximizing the slope of $P_D(\theta)$ at $\theta = \theta_0$. With equivalence transformation, we have

$$\frac{dP_D(\theta)}{d\theta} = \frac{d}{d\theta} \int_{R_1} p(x; \theta) dx = \int_{R_1} \frac{dp(x; \theta)}{d\theta} dx = \int_{R_1} \frac{d \ln p(x; \theta)}{d\theta} p(x; \theta) dx \tag{59.3}$$

As P_{FA} is a constant, by using the Lagrangian multiplier method, referring to [7], we can finally obtain the new decision criterion

$$\left. \frac{d \ln p(x; \theta)}{d\theta} \right|_{\theta=\theta_0} > \gamma. \tag{59.4}$$

This is the LMP test. And it has a maximum probability of detection around θ_0 , following from the equivalence to the NP test under weak signal conditions.

59.2.2 Theory of Amplitude Domain Processing (ADP)

In spread spectrum communication systems, LMP theory is specially suitable, since the desired signal is always significantly weaker than the noises and interference—consistent with the condition in LMP theory. GPS for instance, The signal captured by the receiver can be written as

$$\begin{aligned} z(t) &= r(t, \theta) + w(t) \\ r(t, \theta) &= s(t) \cos(\omega t + \theta) \end{aligned}$$

where $z(t)$ is the received signal, $w(t)$ is the white Gaussian noise as well as potential interference, $r(t, \theta)$ is the modulated information. The detection problem is to decide whether the desired signal exists or not, viz. $z(t) = r(t, \theta) + w(t)$ or $z(t) = w(t)$. After extraction of the base band quadrature components, the problem is to decide between $x_i = s_i \cos \theta + n_{xi}$; $y_i = s_i \sin \theta + n_{yi}$ and $x_i = n_{xi}$; $y_i = n_{yi}$.

Generally, after the sequences being correlated to a local code C_i , we get the quadrature data $I = \frac{1}{N} \sum_{i=1}^N (x_i \cdot C_i)$; $Q = \frac{1}{N} \sum_{i=1}^N (y_i \cdot C_i)$ for a N -sampled complex signal. Then $I^2 + Q^2$ is compared to a decision threshold to make the detection decision. However, using the LMP theory, the optimal decision variable changes into

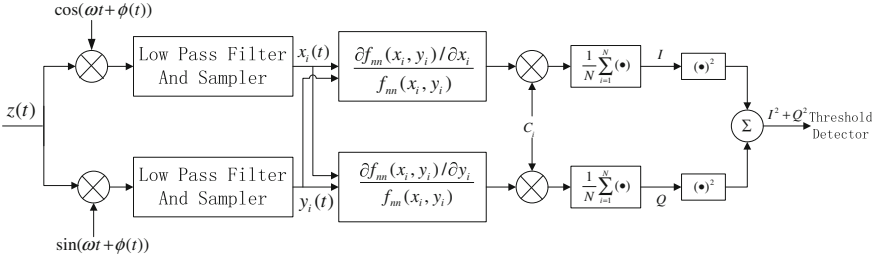


Fig. 59.1 Structure of locally most powerful detection in Cartesian coordinates

$$I^2 + Q^2 = \left[\frac{1}{N} \sum_{i=1}^N \left(C_i \cdot \frac{\partial f_{nn}(x_i, y_i) / \partial x_i}{f_{nn}(x_i, y_i)} \right) \right]^2 + \left[\frac{1}{N} \sum_{i=1}^N \left(C_i \cdot \frac{\partial f_{nn}(x_i, y_i) / \partial y_i}{f_{nn}(x_i, y_i)} \right) \right]^2, \tag{59.5}$$

where $f_{nn}(x, y)$ is the PDF of $z(t)$, x and y represent the real and imaginary parts of the signal. The structure of the LMP detection is shown in Fig. 59.1. And the key of this method is the non-linear function, which needs the estimation of the signals' PDF as a precondition. Discrete histogram statistics method can help us achieve it conveniently.

The above structure need us to deal with two roads simultaneous. However, according to [8], it is possible to save half of them by working in the polar coordinates, because noise and signal carrier are not synchronized. In this condition, decision variable is

$$I^2 + Q^2 = \frac{1}{N^2} \sum_{i=1}^N [C_i g_r(r_i)]^2 \left[\frac{(x_i^2 + y_i^2)}{r_i^2} \right]^2 = \left[\frac{1}{N} \sum_{i=1}^N C_i g_r(r_i) \right]^2, \tag{59.6}$$

where

$$g_r(r_i) = - \frac{\partial / \partial r_i (f_n(r_i) / r_i)}{f_n(r_i) / r_i} = - \frac{\partial}{\partial r_i} \ln \frac{f_n(r_i)}{r_i}, \tag{59.7}$$

and $f_n(r)$ is the ADP of the amplitude r . As to avoid the potential calculation errors, such as caused by r 's being too close to 0, Refs. [2, 3] give a modified version of $g_r(r)$, that

$$g_r(r) = - \frac{\partial}{\partial r} \ln \frac{f_n(r) + k}{\alpha r + \beta}, \tag{59.8}$$

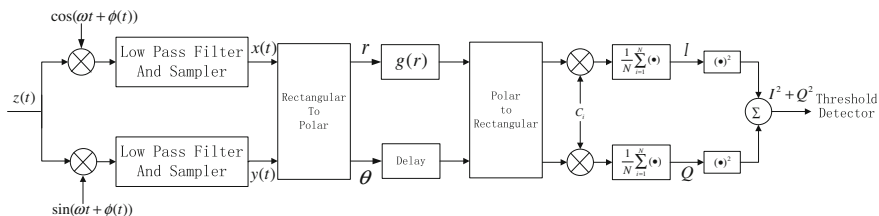


Fig. 59.2 Structure of locally most powerful detection in polar coordinates

and possible values of the parameters maybe like $\alpha = 0.08$, $\beta = 110$, $k = 0.001$. This is called amplitude domain processing (ADP) method, with the structure shown in Fig. 59.2.

As shown in [1, 2], ADP works effectively when dealing with some relatively simple interference, such as one or two continuous wave (CW) interference.

59.2.3 ADP in Frequency Domain (FADP)

As the performance of ADP would decline, when there is more simultaneous interference. Reference [5] proposes an idea of using ADP in the frequency domain and names this method FADP. The general framework of FADP, as shown in Fig. 59.3, is similar with that of the ADP's, except for a couple of additional FFT and IFFT blocks as well as some relevant processing. Compared with working in the time domain, frequency domain processing has a superior discrimination for interference, narrowband especially. Contrast experiments in [5] shows that FADP filter performs significantly better than ADP in the presence of complex interference, and can deal with various narrowband interference efficaciously.

59.2.4 Potential Problems of Current FADP Method

Simulations in Ref. [5] display considerable progress from ADP to FADP. However, there is still some sand in the wheels of FADP's coming into practical use.

Firstly, current FADP pays no attention to the picket fence effect, which may cause a spectrum leakage and signal distortion. This will surely degrade the behavior of the later procedures, making the method fail at worst. For instance, with

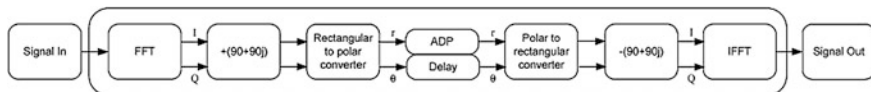


Fig. 59.3 General framework of FADP filter

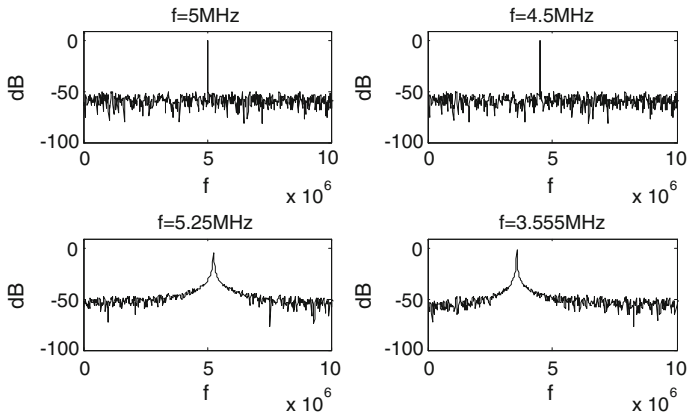


Fig. 59.4 Spectrum calculated directly through FFT (4 different CW frequency)

sample rate $F_s = 20$ MHz and FFT sequence length $N = 1024$, there won't be any spectrum leakage and signal distortion, when the frequency of the CW signal equals $i \cdot \frac{F_s}{N}$ (i is an integer)—that is $f_{CW} = i \cdot 0.02$ MHz. However, if this premise is untenable, the spectrum calculated directly through FFT would be distorted a lot near the corresponding frequency. A group of contrast result is shown in Fig. 59.4. When f_{CW} is set to 5.25 or 3.555 MHz (which just don't match $i \cdot 0.02$ MHz and are random selected), the spectrum leaked. And if N is set to 512 or 256, the no-leakage-condition would be stricter. Unfortunately, spectrum leakage is inevitable in practical problem, whatever FFT parameters you select, as the frequency wouldn't be so coincidental to agree with the no-leakage-condition. Spectrum leakage would degrade the accuracy of the statistical characteristics in frequency domain. As a result, the overall performance of FADP method would not be guaranteed. And as we'll see in Chap. 4, it does fail to work effectively, when spectrum leakage exists. Simulations in Ref. [5] happen to avoid meeting this problem, as no leakage exists.

Secondly, there are some differences between the statistical characteristics of the time-domain waveform and spectrum data. The amplitudes of the time-domain samples distribute in a relatively concentrated area, making the estimation of PDF convenient. However, in spectrum, amplitude values corresponding to the frequency points—where interference exists—are much higher than the others. In Fig. 59.5, amplitude data, as well as its distribution, is shown both in time domain and frequency domain, using an example signal in which narrowband interference exists. The wide range and malignant distribution bring notable difficulty to the estimation of PDF in practice. So the mathematical function of $g(r)$ used in time domain ADP isn't suitable to directly bring into frequency domain ADP.

Thus, there is a need to solve these problems for practical use of FADP method.

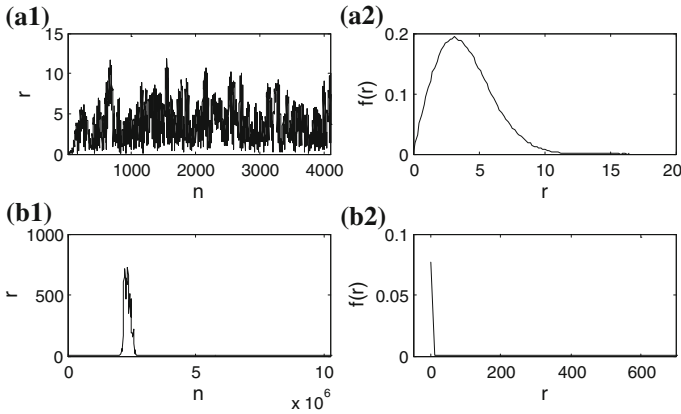


Fig. 59.5 Amplitude data and PDF in time and frequency domain. **a1** Time-domain amplitudes, **a2** PDF in time-domain, **b1** frequency-domain amplitudes, **b2** PDF in frequency-domain

59.3 Details of the Improvements on FADP Method

The improvements mainly aim at the two problems proposed in 59.2.4: Inhibiting the spectrum leakage and signal distortion to make sure the ADP in frequency domain work effectively; Designing a specialized mathematical function of $g(r)$ according to the statistical characteristics of spectrum amplitudes, that can be achieved conveniently in practice. Besides, a few adjustments of the framework are also made to save computation and storage resources.

59.3.1 1/2 Delayed Overlap-Add-Windowing Framework

To mitigate the effect of spectral leakage, frequency domain processing techniques typically use windowing. Windowing applies a weighting factor to the input signal

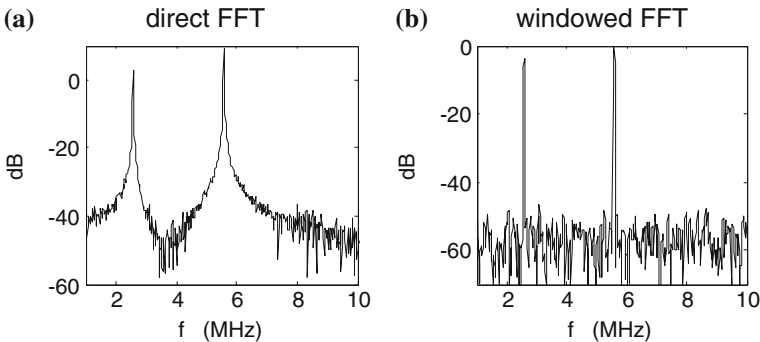


Fig. 59.6 FFT results without (a) and with (b) a Blackman windowing

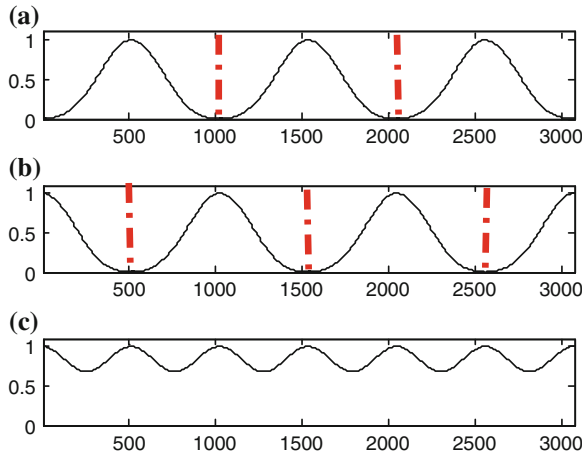


Fig. 59.7 The method of overlap-add windowing. **a** Window in standard path, **b** window in 1/2 block delayed path, **c** overlap-adding result

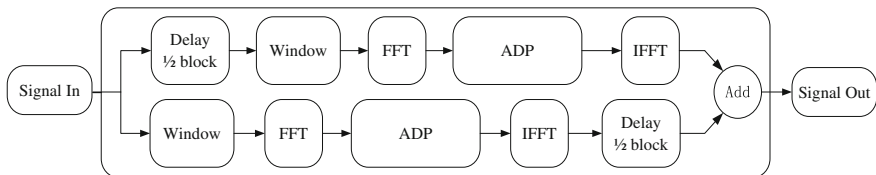


Fig. 59.8 The global diagram of the overlap-adding windowed FADP

prior to computing the FFT, and smoothes the discontinuities at the block boundary, and therefore lessens the effect of spectral leakage. There are a number of window functions described in [9], and here we choose Blackman window.

For instance, choose a 20 MHz sampled signal—with two CW interference in it, and $f_{CW1} = 2.555$ MHz; $f_{CW2} = 5.555$ MHz; $N = 1024$. The results of direct FFT and windowed FFT are shown in Fig. 59.6. The inhibition of spectral leakage, by windowing, is conspicuous.

Furthermore, directly windowing would cause a degradation of SNR, as high as 2.28 dB for Blackman window. By making a 1/2 delay overlap addition, as shown in Fig. 59.7, we could decrease it to 0.08 dB. Though this makes us to need to deal with two paths simultaneous, the improvement is appreciable. The global diagram of the overlap-adding windowed FADP is shown in Fig. 59.8. Processing results of the two paths are counted up correspondingly in the end, before getting correlated to the local code. Overlap add windowing ensures the utmost accuracy of the frequency spectrum, and decreases the SNR loss as possible at the same time.

59.3.2 Modified Mathematical Function of $g(r)$

The key of amplitude domain processing (ADP) is the nonlinear variation of r —function of

$$g_r(r) = -\frac{\partial}{\partial r} \ln \frac{f_n(r)}{r}.$$

As it is mentioned in 59.2.4 and showed in Fig. 59.5, Amplitudes of the signal’s spectrum malignantly distribute in a large region, when a narrowband interference exists. So it needs a more complicated histogram step solution to estimate the PDF of r , what is more important, it would easily get affected by the accident errors as well. To solve this problem, we take logarithms of r before the nonlinear variation, so as to compress the data in amplitude domain. Let $u = \ln(r + \tau)$, where τ is a modification factor, ensuring $r + \tau > 1$ so that $\ln(r + \tau) > 0$.

$\tau = 1$ for instance, the values and distribution of u , as well as r ’s for contrast, are shown in Fig. 59.9. Refer to b2 in Fig. 59.9, we can find the PDF curve line of u is significantly smoother than r . Area between 0 and 2 stands for the frequency bands related to the Gaussian noises and the weak useful signals, while area between 4 and 6 represents the narrowband interference. With a discrete histogram statistics of 20 steps or so, we can estimate the PDF function of u effectively. But for r , it needs much more steps, most of which are just corresponding to the nonsensical zero-periods.

Turning r to u surely makes it convenient and feasible to estimate the PDF function. Furthermore, an equivalent transformation of $g_r(r)$, $g_u(u)$, is required to make the result equally. As $u = \ln(r + \tau)$, $r = e^u - \tau$. Then according to the transfer function of the probability density, we get

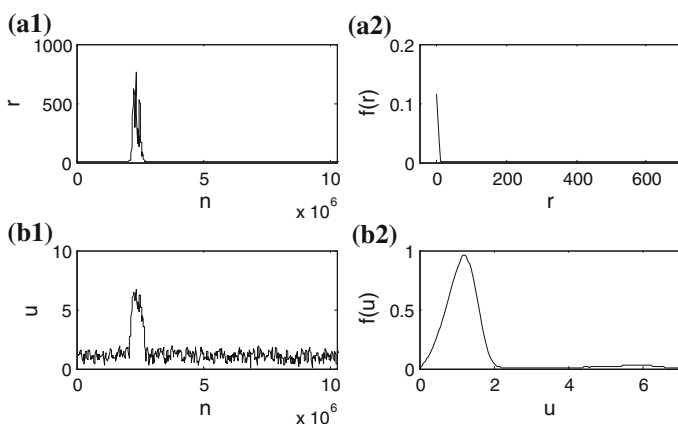


Fig. 59.9 Values and distribution of the amplitudes and their logarithms. **a1** Frequency-domain amplitudes- r , **a2** PDF of r , **b1** logarithms of the amplitudes- u , **b2** PDF of u

$$f_{n,u}(u) = f_{n,r}(r) \cdot \left| \frac{dr}{du} \right| = f_{n,r}(e^u - \tau) \cdot |(e^u - \tau)'| = f_{n,r}(e^u - \tau) \cdot e^u, \quad (59.9)$$

where $f_{n,u}()$ refers to PDF function of u , and $f_{n,r}()$ refers to PDF function of r . To make $g_u(u) = g_r(r)$, we have that

$$\begin{aligned} g_r(r) = g_r(e^u - \tau) &= -\frac{\partial}{\partial r} \left(\ln \frac{f_{n,r}(e^u - \tau)}{e^u - \tau} \right) = -\frac{\partial}{\partial r} \left(\ln \frac{f_{n,u}(u)}{e^u(e^u - \tau)} \right) \\ &= -\frac{\partial}{\partial u} \left(\ln \frac{f_{n,u}(u)}{e^u(e^u - \tau)} \right) \cdot \frac{\partial u}{\partial r}. \end{aligned} \quad (59.10)$$

Continuing to transform the equation, we get

$$g_u(u) = -\frac{f'_{n,u}(u)}{f_{n,u}(u)} \cdot \frac{1}{r} + \frac{2}{r} + \frac{\tau}{r^2} \quad (59.11)$$

at last. Though it theoretically equals to $g_r(r)$, it's more practical and meaningful. And for the same reason with (59.8) to avoid potential calculation errors, a modified version of the $g_u(u)$ definition is proposed as

$$g_u(u) = g_r(r) - \frac{f'_{n,u}(u)}{f_{n,u}(u)} \cdot \frac{\alpha}{\alpha r + \beta} + \frac{2\alpha}{\alpha r + \beta} + \frac{\tau \cdot \alpha^2}{(\alpha r + \beta)^2} \quad (59.12)$$

59.3.3 Framework of the Amplitude Domain Processing for Spectrum

As shown in Figs. 59.2 and 59.3, there are a couple of rectangular-to-polar and polar-to-rectangular blocks in the general ADP framework. However, the angle information isn't relevant to the nonlinear variation, and it costs a lot of computation and storage resources to do the transformations. So in the paper, we proposed a direct weighting method of carrying out ADP.

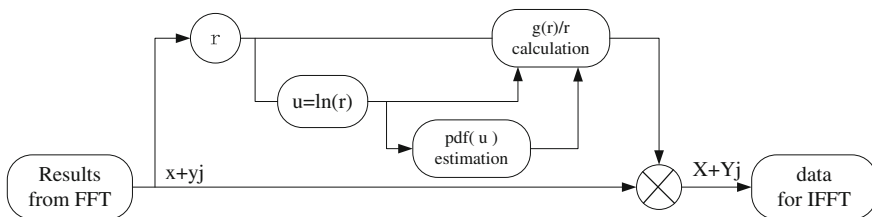


Fig. 59.10 Framework of the amplitude domain processing (for spectrum)

Let the weights be $\frac{g_r(r)}{r}$, the results of ADP would be $X + Yj = (x + yj) \cdot \frac{g_r(r)}{r}$. Meaning of $X + Yj$ and $x + yj$, as well as the framework of the amplitude domain processing of the spectrum, are shown in Fig. 59.10. Thus, concrete angle information isn't needed at all. And the results are absolutely equal with those gotten from the rectangular-to-polar-to-rectangular way.

59.4 Simulation of the Improved FADP Technique in MATLAB

Reference [5] has carried on a series of simulation to certify the effectiveness of the former FADP technique. In this paper, we mainly concern with the anti-jamming behaviors of the original and improved methods in more practical and factual experimental conditions.

59.4.1 Simulation Environment and Judgment Criteria

The input signal used in the simulator is a GPS L1 C/A code, with a rate of 1.023 Mchips/s and a period of 1023 chips, which lasts 1 ms. In the MATLAB platform, we could conveniently produce signals containing various noises and interference, so as to test the behaviors of the methods.

In Ref. [5], the changes of Signal-to-Noise ratio (SNR) and Jammer-to-Noise ratio (JNR) before and after the processing are set as the standard of comparison. And [5] also displays a way to calculate SNR_{in} and JNR_{in} , as well as SNR_{out} and JNR_{out} . However, it's hard to exactly define the SNR and JNR of the output signals, for the variation is nonlinear. And even if we can find relatively approximate estimations, it doesn't give a direct perception. So, here we use a criteria of coherent SNR [10], which is a utilitarian variable that closely related to the performance of subsequent acquisition and tracking.

Coherent SNR is calculated from the correlation result of $\sqrt{I^2 + Q^2}$. As shown in Fig. 59.11, s stands for the effective peak magnitude, from the peak to the mean value. And σ_n is the standard deviation. Then, we have

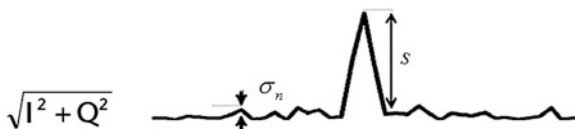


Fig. 59.11 Representation of the correlation response of the I and Q channels

$$\text{coherent SNR} = \frac{s}{\sigma_n} \tag{59.13}$$

Coherent SNR directly illustrates the result of correlation. A value up to 17 dB always suggests a good performance and being ready for acquisition and tracking [10].

59.4.2 Simulation Results and Analysis

All the simulations are with the condition of $F_s = 20$ MHz, FFT sequence length $N = 1024$ and a correlation time of 1 ms—the C/A code period. And the SNR is fix to -23 dB, while SIR is fix to -53 dB. A series of interference are considered.

- A. One Continuous-Wave-Interference (CWI) jammer ($f = 1.5$ MHz).
- B. One CWI jammer ($f = 1.5555$ MHz).
- C. three CWI jammers ($f = 1.5, 2.1, 2.5$ MHz).
- D. three CWI jammers ($f = 1.555, 2.111, 2.555$ MHz).
- E. narrowband suppression ($f = 2.2-3.2$ MHz).

These frequencies are randomly selected, except that A and C won't have a spectrum leakage, but B and D would, as it was analyzed in Chap. 2.4. There is a narrowband suppression in E, which contains a continuous frequency band, so it would surely be affected by spectrum leakage when taking a FFT processing. As we know, the parameter of interference would never be so coincident to meet the non-leakage condition in practical cases. B D and E have more practical significance.

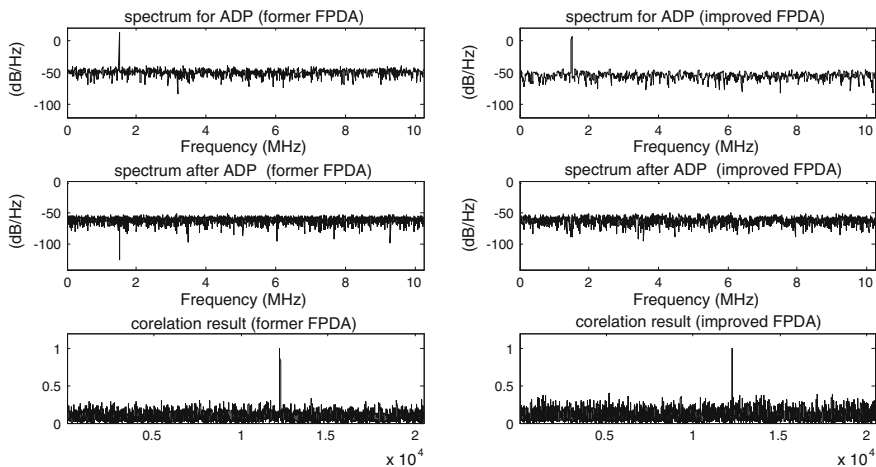


Fig. 59.12 Contrast results of the former and improved FADP (A: 1 CWI; 1.5 MHz)

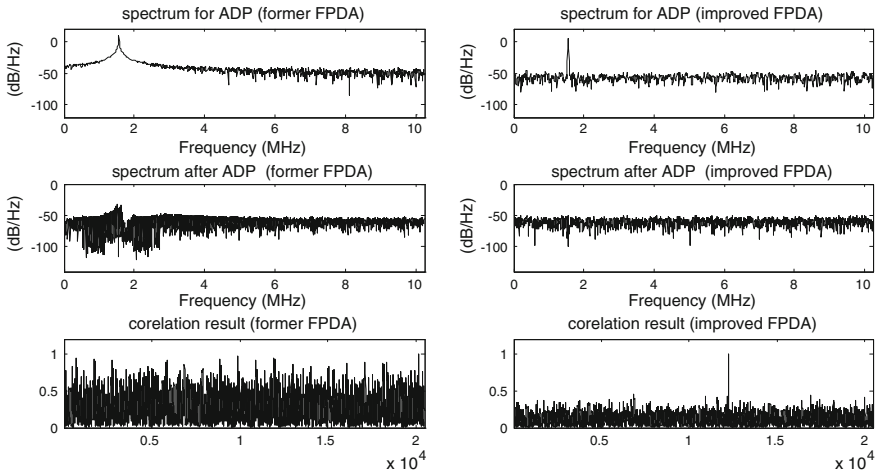


Fig. 59.13 Contrast results of the former and improved FADP (B: 1 CWI; 1.555 MHz)

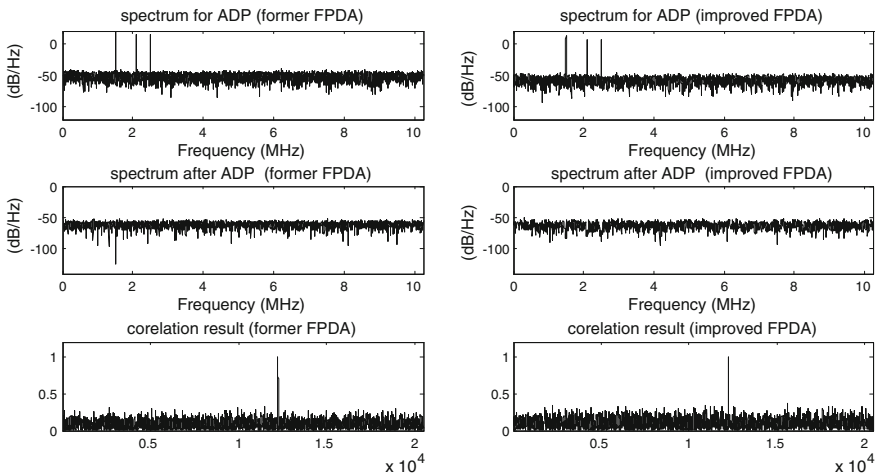


Fig. 59.14 Contrast results of the former and improved FADP (C: 3 CWI; 1.5, 2.1, 2.5 MHz)

However in the simulations, one would possibly ignore this and may give a less thoughtful decision of the parameters.

This simulation results are shown in Figs. 59.12, 59.13, 59.14, 59.15 and 59.16, corresponding to A–E. Each of them contain contrast of spectrum of the data for ADP and spectrum of the data dealt with APD, as well as the correlation result at last, which are most meaningful.

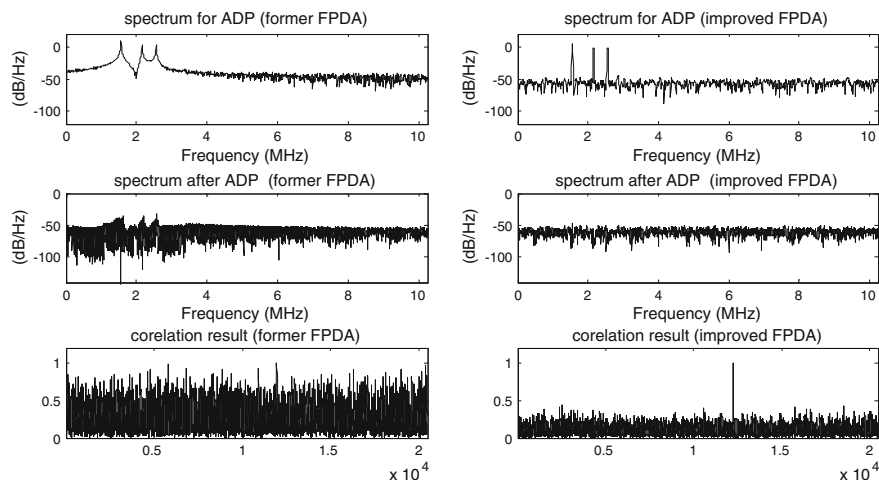


Fig. 59.15 Contrast results of the former and improved FADP (D: 3 CWI; 1.555, 2.111, 2.555 MHz)

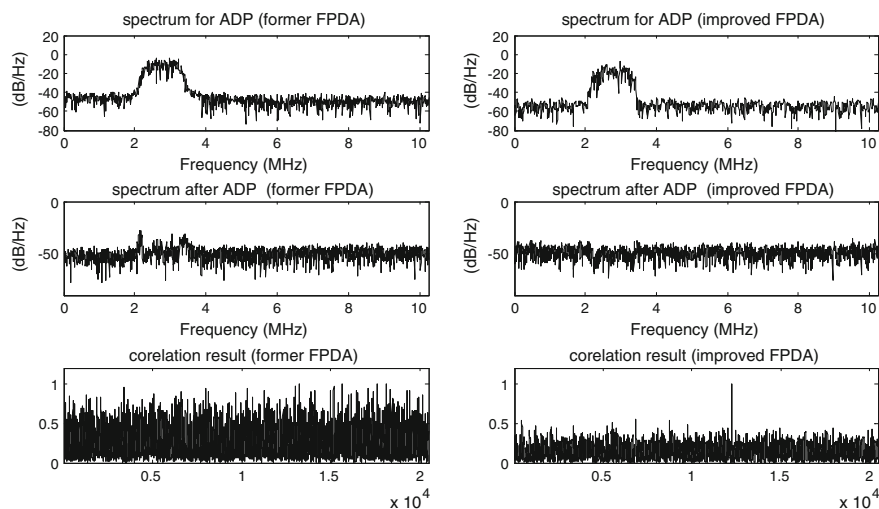


Fig. 59.16 Contrast results of the former and improved FADP (E: 2.2–3.2 MHz)

From these Figures, we can find that the successful inhibition of spectrum leakage ensures the effectivity of the FADP method. All of the narrowband interference is removed in the improved method, presenting a obvious peak in the correlation results. And without inhibition, the former method fails to work when leakage exists. This is essential for practical consideration.

The experiment also verify the usability of FADP in anti-narrowband-interference. Amelioration of correlation performance is significant.

59.5 Conclusions

The FADP technique is a development from the traditional ADP method. By working in the frequency domain, it has a significant superior performance of anti-narrowband-interference, when submitted to multiple interference scenarios. Spectral processing enables to eradicate precisely all sort of narrowband interference. However, because of the differences between processing in frequency domain and time domain, the existing simple framework of FADP is not suitable for practical use yet. In this paper, a more thoughtful anti-jamming technique based on FADP is proposed. Some important modifications are made to the global FADP framework and the key function of non-linear variation. The improved method successfully mitigate the effect of spectrum leakage, which couldn't be ignored in practice. The specialized mathematical function of ADP is designed for a consideration of convenient realization too, ensuring the effectivity of the technique as well.

Further investigations will be relevant to the effect of ADC to the FADP method, and evaluate this technique more comprehensively. Then, Implement this technique to software of hardware based GNSS receivers, helping to improve its ability to operate in all conditions and hostile environments.

Acknowledgments This research was supported by the National Natural Science Foundation of China (No.41304031).

References

1. AbiMoussa R, Landry RJ (2000) Anti-jamming solution to narrowband CDMA interference problem. In: Canadian conference on electrical and computer engineering, vol 2, pp 1057–1062
2. Shen F, Wang J, Wang J (2009) An Anti-interference method for spread spectrum system based on amplitude domain processing. In: ICMA 2009. International conference on mechatronics and automation, 9–12 Aug 2009
3. Capon J (1960) Optimum coincident procedures for detecting weak signals in noise. *IEEE Trans Inf Theory* IT-7:67–71
4. Algazi VR, Lerner RM (1964) Binary detection in white non-Gaussian noise. In: MIT Lincoln laboratory report, vol DS-2138
5. Landry RJ, Boutin P, Constantinescu A (2006) New anti-jamming technique for GPS and GALILEO receivers using adaptive FADP filter. *Digit Signal Process* 16(3):255–274
6. Zeng X, Li Z, Wang F (2004) Study on windowing degradation of frequency domain narrowband interference suppression algorithms in spread spectrum system. *J Electron Inf Technol* 26(8):1276–1281
7. Kay SM (1998) Fundamentals of statistical signal processing. In: Detection theory, vol II. Prentice Hall, Upper Saddle River, pp 217–221

8. Malicorne JM (1998) Approfondissement de la technique ADP. ENSAE, Toulouse
9. Harris F (1978) On the use of windows for harmonic analysis with the discrete Fourier transform. Proc IEEE 66:51–83
10. van Diggelen F (2009) A-GPS: assisted GPS, GNSS, and SBAS. Artech House, Boston, pp 171–175

Chapter 60

A Robust Dynamic Satellite-Searching Algorithm for Multi-constellation GNSS Receivers

Hengwei Zhou, Zheng Yao and Mingquan Lu

Abstract With the flourish development of GNSS community, the number of available navigation satellites is increasing rapidly. Benefiting from the super constellation consisting of satellites from various systems, the availability and reliability of positioning service are improved for multi-constellation GNSS receivers. Meanwhile, the complexity and uncertainty in satellite-searching process are multiplied as well, which significantly increases the receiver's time to first fix (TTFF) and decreases its performance. Dynamic satellite-searching algorithms can be employed to reduce TTFF. However, existing dynamic satellite-searching algorithm is not robust and efficient enough when masking problem exists. In this paper, a robust dynamic satellite-searching algorithm is proposed. Theoretical analysis and numeric simulations in masking situation are presented, and proves the efficiency and robustness of the new algorithm. In conclusion, the new dynamic satellite-searching algorithm provides an efficient and robust solution to practical multi-constellation GNSS receivers.

Keywords Robust dynamic satellite-searching · Multi-constellation GNSS receiver · Super constellation · Masking situation · TTFF

60.1 Introduction

Since global navigation satellite system (GNSS) plays a strategic role in modern society, new systems are emerging to replace or cooperate with the conventional GPS, which significantly increases the number of GNSS satellites in orbit [1, 2]. Multi-constellation GNSS receivers utilize a super constellation that consists of

H. Zhou · Z. Yao (✉) · M. Lu
Tsinghua University, Room 1103, Weiqing Building, Beijing 100084, China
e-mail: yaozheng@tsinghua.edu.cn

satellites from different GNSS. Benefiting from a larger number of satellites ever, multi-constellation GNSS receivers are able to provide positioning service with higher availability and reliability [3, 4].

Not only benefits but also challenges are brought to the promising multi-constellation receivers by increasing GNSS satellites. One of the challenges is the increasing time to first fix (TTFF). Before its first fix, the receiver has to implement the acquisition process and the tracking process. For a cold-started GNSS receiver, the acquisition process is actually a three-dimensional searching process that searches for visible satellites, Doppler frequency and PRN code phase [5]. The uncertain range of the three-dimensional searching process is quite large. It takes a lot of time for the receiver to finish the process and accounts for a long TTFF. Previous work including parallel frequency search and multi-dwell search detectors has been done to reduce the searching complexity in frequency and code phase domain [6, 7]. However, for the multi-constellation GNSS receivers, the challenge lies in the increasing complexity and uncertainty in satellite-searching domain, which asks for an efficient satellite-searching algorithm that helps the receiver to reduce the time spent searching visible satellites.

An efficient satellite-searching algorithm helps the receiver hit visible satellites and avoid invisible ones. The visibility of satellites is an important factor that accounts for TTFF. If the receiver picks an invisible satellite to search, it has to try every possible combination of Doppler frequency and code phase in the correlation process before eventually determine the searching procedure as unsuccessful, which is not contributing to the positioning process, yet quite time-consuming. Meanwhile, if the chosen satellite is actually visible, there is always a trial that gives a correlation result that exceeds the threshold value [8], which ends the searching procedure and return a successful searching result. To reduce TTFF, the receiver should always search the visible satellites and avoid invisible ones. However, for a cold-started GNSS receiver, little prior information could be used to determine the actual satellite visibility, hence an estimation of visibility must be made before the receiver chooses a satellite to search.

A dynamic satellite-searching algorithm was proposed to reduce TTFF for multi-constellation GNSS receivers, and its efficiency in ideal situation has been proven [9]. In this paper, the conventional algorithm is briefly reviewed in the first place, and its shortcoming of not working in practical applications with possible masking problem is thoroughly analysed. Then, we propose a robust dynamic satellite-searching algorithm that remains efficient and robust in masking situations. Numeric simulations are given to present the performance of the robust dynamic satellite-searching.

60.2 The Conventional Dynamic Satellite-Searching Algorithm

The algorithm in [9] has proposed a reasonable estimation of the satellite visibility by averaging the theoretical visibility on the time-space uncertain range, according to which the satellite-searching order is determined. The actual satellite-searching results helps cut the uncertain range in turn. Thus the algorithm is a dynamic scheduling. Also, conditional visibility is proposed to reduce the computational complexity. However, the conventional dynamic satellite-searching algorithm is not available in practical applications with existing masking problem. This section discusses the basic idea as well as the shortcoming of the conventional algorithm.

60.2.1 Review of the Conventional Algorithm

The conventional dynamic satellite-searching algorithm put forward an estimation of satellite visibility [9], the mean visibility, which could be calculated by (60.1).

$$\overline{Vis}(SV) = \frac{1}{|\{G\}|} \sum_{(t,L) \in \{G\}} Vis(SV, t, L) \quad (60.1)$$

$\overline{Vis}(SV)$ represents the mean visibility of satellite SV . The rough time span and space span in which the cold-started GNSS receiver might be located make a two-dimensioned uncertain range of time and space. Sampling point (t, L) discretely represents the time and space uncertainty, with t and L representing a sampling value of time and space respectively. $\{G\}$ is the set of all sampling points with $|\{G\}|$ representing the number of elements in $\{G\}$. $Vis(SV, t, L)$ is the visibility for satellite SV to a receiver at (t, L) computed using almanac, hence it's a theoretical value.

Averaging the theoretical satellite visibility on $\{G\}$ is the main idea of estimating a satellite visibility, based on which a dynamic satellite-searching algorithm is proposed. The satellite to be searched is chosen by sorting all unsearched satellites in a descending order of mean visibility and picking the one with the max mean visibility. After the correlation process gives the actual searching result $SrcRslt(SV)$ of the chosen satellite SV , the uncertain range of time and space is narrowed by excluding sampling points from $\{G\}$ of which the value of $Vis(SV, t, L)$ doesn't match $SrcRslt(SV)$. With the searching procedures going on, the uncertainty range is supposed to reduce and eventually get close to the sampling point at which the receiver is truly located.

60.2.2 Shortcoming of the Conventional Algorithm

The conventional dynamic satellite-searching algorithm has been proven efficient in ideal situation, but it cannot deal with masking problem in practical applications. For a practical GNSS receiver, the masking situation where satellite signals are randomly masked by objects like tall buildings or mountains happens a lot. In a masking situation, a theoretically visible satellite might become actually invisible because of being masked. For the conventional algorithm, a wrong update of $\{G\}$ might occur when a mismatch of the theoretical satellite visibility $Vis(SV, t, L)$ and the actual searching result $SrcRslt(SV)$ happens, because $\{G\}$ is updated right after comparing $Vis(SV, t, L)$ and $SrcRslt(SV)$ without considering the involved masking problem. If we use (t_{act}, L_{act}) to represent the sampling point that the receiver is truly located, (t_{act}, L_{act}) might be excluded when $Vis(SV, t_{act}, L_{act})$ mismatches $SrcRslt(SV)$. The excluding of (t_{act}, L_{act}) makes it impossible for $\{G\}$ to get close to (t_{act}, L_{act}) and all the following steps are based on a wrong $\{G\}$ and incorrect satellite visibility estimations, which leads to a lot of unsuccessful searching procedures and eventually increases TTFF. Because of the weakness of the conventional algorithm in practical applications, a robust dynamic satellite-searching algorithm that is able to avoid this problem and remains efficient in masking situation is needed for practical multi-constellation GNSS receivers.

60.3 The Robust Dynamic Satellite-Searching Algorithm

In this section, a robust dynamic satellite-searching algorithm is presented, which remains efficient in masking situation by using newly-introduced $Conf(t, L)$. Based on $Conf(t, L)$, a new estimation of satellite visibility is proposed. And the procedure of the robust algorithm is presented in the last part of this section.

60.3.1 Confidence of Sampling Points

The conventional algorithm updates $\{G\}$ right after comparing the theoretical $Vis(SV, t, L)$ and actual searching result $SrcRslt(SV)$ without considering the involved masking problem, which results in wrong updates of $\{G\}$. Therefore, we introduce $Conf(t, L)$ as an intermediate variable, and the update of $\{G\}$ is divided into two steps.

Suppose the probability for satellite SV to be masked is $\rho(0 < \rho < 1)$, $Conf(t, L)$ is updated first after the correlation process returns $SrcRslt(SV)$, as is shown in (60.2). According to the updated $Conf(t, L)$, $\{G\}$ is updated afterwards by excluding sampling points that satisfy $Conf(t, L) = 0$, as is shown in (60.3).

$$Conf_{new}(t, L) = \begin{cases} Conf_{old}(t, L) \cdot \rho, & \text{if } Vis(SV, t, L) = 1 \text{ and } SrcRslt(SV) = 0; \\ Conf_{old}(t, L), & \text{if } Vis(SV, t, L) = 0 \text{ and } SrcRslt(SV) = 0; \\ 0, & \text{if } Vis(SV, t, L) = 0 \text{ and } SrcRslt(SV) = 1; \\ Conf_{old}(t, L) \cdot (1 - \rho), & \text{if } Vis(SV, t, L) = 1 \text{ and } SrcRslt(SV) = 1; \end{cases} \quad (60.2)$$

$$\{G\}_{new} = \{(t, L) | (t, L) \in \{G\}_{old}, Conf(t, L) \neq 0\} \quad (60.3)$$

In (60.2), $SrcRslt(SV)$ represents the searching result of satellite SV , with 1 meaning the satellite is actually visible and 0 meaning the opposite.

Here $Conf(t, L)$ represents the confidence of the sampling point (t, L) , describing the degree to which it's believed that the GNSS receiver is located at (t, L) . Hence a new estimation of satellite visibility, named as the weighted mean visibility $Vis(SV)$, is defined to replace the mean visibility. Comparing to the mean visibility, the weighted mean visibility uses $Conf(t, L)$ as a weighting factor for $Vis(SV, t, L)$, as is shown in (60.4)

$$Vis(SV) = \frac{1}{|\{G\}|} \sum_{(t, L) \in \{G\}} Conf(t, L) \cdot Vis(SV, t, L) \quad (60.4)$$

Noticing the case where the masking problem might get involved and result in a mismatch of theoretical and actual satellite visibility, that is $Vis(SV, t, L) = 1$ while $SrcRslt(SV) = 0$, $Conf(t, L)$ decreases but still exceeds zero, thus the sampling points will not be excluded according to (60.3). As long as a sampling point, especially (t_{act}, L_{act}) , remains in $\{G\}$, its confidence can still increase in the following searching procedures. In this way, the wrong update of $\{G\}$ is successfully avoided and the algorithm remains robust.

60.3.2 Procedure of the Robust Algorithm

The flow chart of the robust dynamic satellite-searching algorithm is presented by Fig. 60.1. Comparing to the conventional algorithm, an update of $Conf(t, L)$ is added before updating $\{G\}$ and the weighted mean visibility is applied. The procedure is discussed step by step as follows:

1. Take samples in the two-dimensional time-space uncertain range and make the set of all sampling points, $\{G\}$.
2. Initial $Conf(t, L)$ with a uniform value.
3. Compute $Vis(SV)$ for all unsearched satellites using (60.4).
4. Sort the satellites in a descending order of $Vis(SV)$.
5. Choose the satellite with the max $Vis(SV)$.
6. Start the correlation process of the chosen satellite, and return the result of whether the chosen satellite is actually visible or not, represented by $SrcRslt(SV)$.

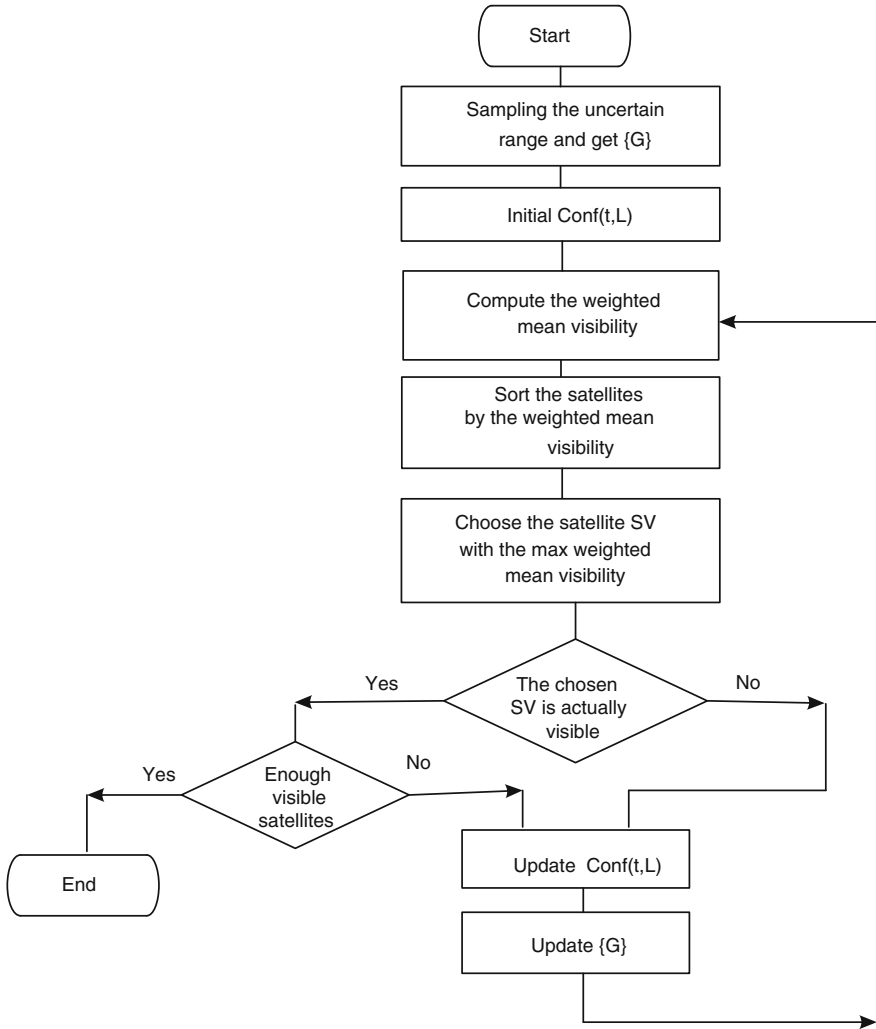


Fig. 60.1 The flow chart of the robust dynamic satellite-searching algorithm

7. If the chosen satellite is actually visible, compare the number of visible satellite to the threshold number that the GNSS receiver needs for its first fix. If the visible satellites are enough, the whole searching process ends, or go to step 9.
8. If the chosen satellite is invisible, go to step 9.
9. Update $Conf(t, L)$ using (60.2).
10. Update $\{G\}$ using (60.3).
11. Go to step 3 and start the next searching procedure.

The new robust algorithm inherits the dynamic feature by updating $Conf(t, L)$, $\{G\}$ and $Vis(SV)$ in each searching procedure. And it makes improvement by adjusting the intermediate variable $Conf(t, L)$, instead of directly updating $\{G\}$. The performance is numerically simulated in the next section.

60.4 Simulation

In this section, the robust dynamic satellite-searching algorithm is simulated in masking situation, of which the performance is discussed and compared to the conventional algorithm.

All the simulations are under assumptions or settings of:

- The constellation consists of 75 satellites including 31 GPS satellites, 29 GLONASS satellites and 15 Beidou satellites. Each satellite is assigned a new id number from 1 to 75.
- The almanac used was saved on June 3rd, 2014.
- The actual time is 12:00, June 7th, 2014(UTC).
- The uncertain range of time is 4 h with 30-min-long step length.
- The uncertain range of space is the whole surface of the earth with zero height value with 10° -long step length for both latitude and longitude.
- The receiver's actual position is (40°N, 116°E, 0), if not mentioned specially.
- The actual satellite positions are calculated using TLE files provided by <http://www.celestrak.com/>.

Figure 60.2 illustrates the performance of the conventional algorithm in the ideal situation without masking. In the upper subplot, the searching results are presented with green bars representing successful searching of actually visible satellites and red bars representing unsuccessful searching of invisible ones. The chosen satellites of each searching procedures are attached to the searching results. The conventional algorithm hits all 31 visible satellites after searching 35 times in the ideal situation. With a cold start, the lack of prior information accounts for the first three unsuccessful searching procedures. Afterwards, misses barely happen thanks to the dynamic programming and visibility estimation. The subplot below illustrates whether the sampling point (t_{act}, L_{act}) where the receiver is actually located at still remains in the uncertain range $\{G\}$. As we can see, the curve value remains 1 in Fig. 60.2, meaning no wrong update of $\{G\}$ occurs until the searching process ends. As is proved in [9], the conventional works well in the ideal situation without masking.

However, when several satellites are masked, as usually happens in practical applications, the performance of the conventional algorithm drops heavily, which is shown in Fig. 60.3. Three satellites are randomly masked and they are SV9, SV51 and SV70 in the following individual simulation. The upper subplot shows that the algorithm spends 75 searches to hit all 28 visible satellites, meaning the whole constellation is thoroughly searched. This is because a wrong update of $\{G\}$ occurs.

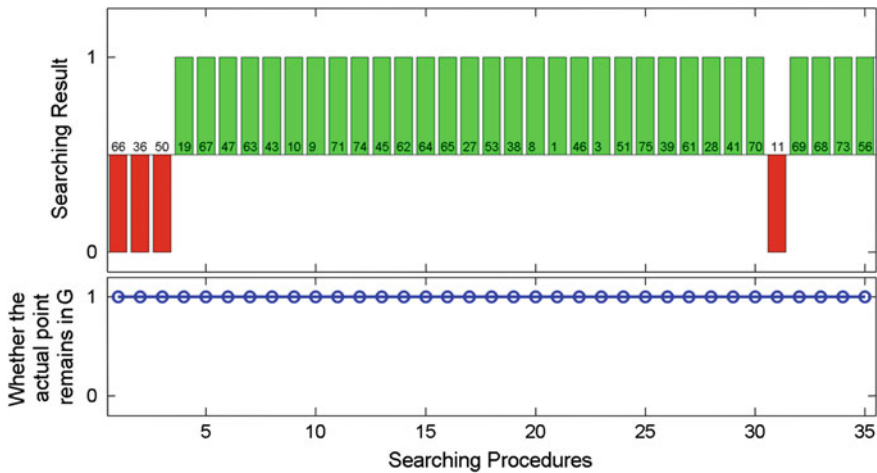


Fig. 60.2 The performance of the conventional algorithm without masking problem

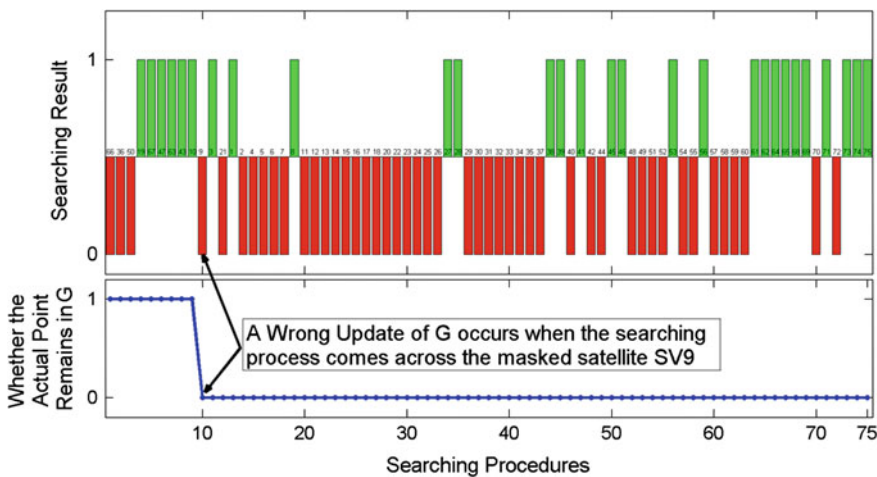


Fig. 60.3 The performance of the conventional algorithm with masking problem

As we can see in the subplot below in Fig. 60.3, (t_{act}, L_{act}) is excluded from $\{G\}$ in the 10th searching procedure. Therefore, the following visibility estimations are based on a wrong (t_{act}, L_{act}) , which results in lots of misses. Because masking problem is not avoidable for practical applications, the conventional dynamic satellite-searching algorithm is not an efficient solution to reducing TTFF for practical GNSS receivers.

The proposed algorithm is simulated in the same masking situation and its performance is illustrated in Fig. 60.4. It takes 37 searching times for the proposed

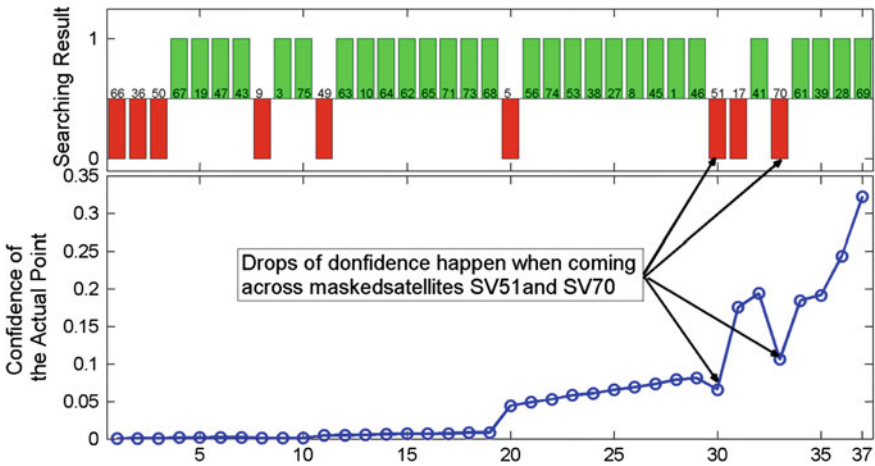


Fig. 60.4 The performance of the conventional algorithm with masking problem

algorithm to hit all 28 visible satellites, only half of time of the conventional algorithm. Unsuccessful searches happens when the searching process just starts or comes across the masked satellites.

The blue curve in the subplot below in Fig. 60.4 describes how $Conf(t_{act}, L_{act})$ changes with the searching process goes on. Generally, the value of $Conf(t_{act}, L_{act})$ increases in the process of searching. Clear drops could be seen when the masked satellites SV51, SV70 are searched. Despite of suffering from a value drop resulting from masking situation, $Conf(t_{act}, L_{act})$ continues to increase along with the searching time grows and reach its peak value when the searching process ends. This is how the newly-proposed algorithm remains robust in masking situation. Noted that the peak value of $Conf(t_{act}, L_{act})$ is not that close to 1, this is because sampling points around (t_{act}, L_{act}) may share the same satellite visibility and $\{G\}$ still contains more than one element till the searching ends, which won't affect the performance of the algorithm. Figure 60.4 has shown that the new algorithm we proposed in this paper works efficiently and robustly in masking situation, comparing to the conventional algorithm.

To prove the new algorithm universally performs better than the conventional one, a Monte Carlo method has been practiced. Both the conventional and robust algorithms are tested in 50 experiments. For each experiment, the actual position of the GNSS receiver is randomly selected on the earth and the masking probability remains 0.1 meaning 1/10 of the theoretically visible satellites are randomly masked. Figure 60.5 illustrates the results. In masking situation, the conventional algorithm averagely spends 74.88 searching times to get all the visible satellites (the average number of visible satellites is 28.04) in the constellation of 75 satellites, while the proposed robust algorithm only takes 36.4 times averagely. The robust

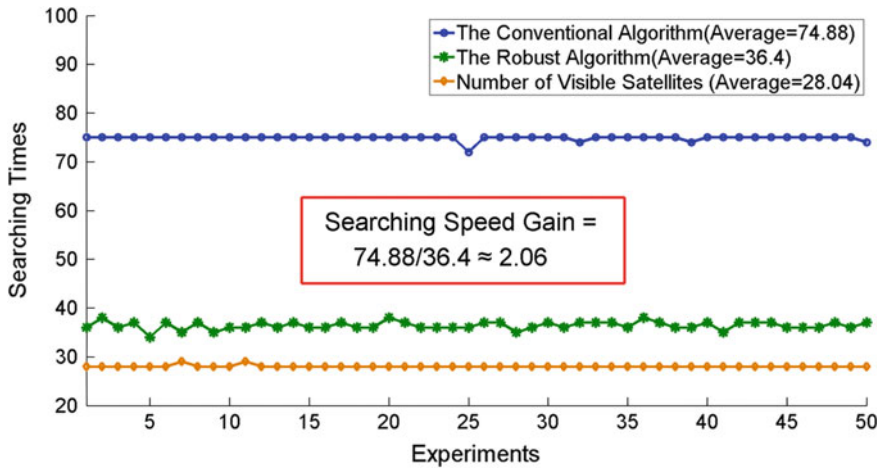


Fig. 60.5 50 searching performance experiments of the conventional and robust algorithms

dynamic satellite-searching algorithm proves to be universally faster than the conventional one by an average gain up to 2.06.

60.5 Conclusion

In this paper, aiming at reducing the complexity and uncertainty of satellite-searching process for the cold-started multi-constellation GNSS receivers that need to search visible satellites in a super constellation, an efficient and robust dynamic satellite-searching algorithm is proposed. Considering the uncertainty of time and space, the proposed algorithm makes a dynamic programming of the order that satellites are searched, which significantly reduces TTFF of cold-started receivers. Moreover, a new confidence updating strategy in which satellite masking probability is taken into account. Therefore this new algorithm is able to overcome the shortcoming of the conventional algorithm and remain efficient and robust in the masking situation where visible satellites may be masked. Simulations with practical GNSS receiver scenario have shown that, the conventional algorithm's performance decreases heavily in masking situation, while the proposed algorithm remains robust and gets a speed improvement by an average gain up to 2.06. The proposed dynamic satellite-searching algorithm is efficient and robust, providing an available solution to practical multi-constellation GNSS receivers.

Acknowledgments This paper is supported by the National Key Scientific Instrument and Equipment Development Project (2012YQ140026).

References

1. Chengqi R (ed) (2012) Development of the BeiDou navigation satellite system. Global navigation satellite systems report of the joint workshop of the national academy of engineering and the Chinese academy of engineering Washington, DC
2. Hofmann-Wellenhof B, Lichtenegger H, Wasle E (2007) GNSS—global navigation satellite systems: GPS, GLONASS, Galileo, and more. Springer, New York
3. Huang B, Yao Z, Guo F, Deng S, Cui X, Lu M (eds) (2013) STARx—A GPU based multi-system full-band real-time GNSS software receiver. In: ION GNSS, 2013
4. Joerger M, Neale J, Pervan B, Datta-Barua S (eds) (2010) Measurement error models and fault-detection algorithms for multi-constellation navigation systems. In: IEEE/ION position location and navigation symposium (PLANS)
5. Kaplan ED, Hegarty CJ (2005) Understanding GPS: principles and applications. Artech house, Boston
6. Lin D, Tsui J (eds) (1998) Acquisition schemes for software GPS receiver. In: Proceedings of Ion GPS, Institute of Navigation
7. Van Nee D, Coenen A (1991) New fast GPS code-acquisition technique using FFT. *Electron Lett* 27(2):158–160
8. Misra P, Enge P (2006) Global positioning system: signals, measurements and performance, 2nd edn. Ganga-Jamuna Press, Lincoln
9. Chen K-T (ed) (2008) A dynamic satellite search scheduling for GNSS super constellation. In: Proceedings of the 21st international technical meeting of the satellite division of the institute of navigation, ION GNSS 2008

Chapter 61

A High-Dynamic Null-Widen GNSS Anti-jamming Algorithm Based on Reduced-Dimension Space-Time Adaptive Processing

Lu Ge, Dan Lu, Wenyi Wang, Lu Wang, Qiongqiong Jia and Renbiao Wu

Abstract Space-Time Adaptive Processing (STAP) is an effective method to suppress interference in Global Navigation Satellite System (GNSS). But in high-dynamic environment, conventional adaptive anti-jamming algorithms are invalid since jammers may easily move out of the array pattern nulls. To solve this problem, a new null-widen method based on the Laplace distribution model is deduced in this paper, the method can get wider null at direction of jammers. However this method is computationally intensive by using STAP, thus a new null-widen method based on reduced-dimension multistage wiener filters (MWF) is deduced here. It has proved in simulation section that the new method can get better performance in few snapshots.

Keywords STAP · Null widening · MWF · High-dynamic · GNSS

61.1 Introduction

Space-Time Adaptive Processing (STAP) is an effective method to suppress the jammers in Global Navigation Satellite System (referred to as GNSS). While the jammers may easily move out of the nulls because jammer's rapidly moving. Nulling widen technique is an effective method to solve the above problems. Mailloux and Zatman respectively proposed the null-widen methods by adding virtual interference sources and expanding the bandwidth of interference signal only in spatial domain [1, 2]. A null-widen method was proposed by Li Rongfeng based

L. Ge (✉) · D. Lu · W. Wang · L. Wang · Q. Jia · R. Wu
Tianjin Key Lab for Advanced Signal Processing, Civil Aviation University of China,
Tianjin, China
e-mail: 13652070160@163.com

© Springer-Verlag Berlin Heidelberg 2015
J. Sun et al. (eds.), *China Satellite Navigation Conference (CSNC) 2015 Proceedings: Volume I*, Lecture Notes in Electrical Engineering 340,
DOI 10.1007/978-3-662-46638-4_61

707

on the assumption the changing interference DOA (Direction of arrival) is distributed normally [3]. Wu SiJun have discussed another null-widen method when the changing interference DOA is two-point distribution [4]. However, the changing interference DOA doesn't simply obey the uniform distribution mode in high-dynamic environment [5]. In this paper, a novel STAP null-widen method based on the supposed Laplace distribution model is deduced, which can suppress the jammers effectively in high-dynamic environment.

But just few snapshots can be obtained in high-dynamic environment, and STAP increase the computational complexity, so in this paper a null-widen algorithm based on reduced-dimension STAP is given. This method can decrease the computational complexity, be more robust with few snapshots.

61.2 Signal Model of the STAP Array

Consider a STAP uniform linear array with M elements, N taps, the space between adjacent elements is half of the wavelength. Suppose there are L satellite signals and Q interference signals, the data vector received by array can be written as

$$\mathbf{x}(t) = \sum_{l=1}^L \mathbf{a}(\varphi_l) \otimes \mathbf{s}_l(t) + \sum_{q=1}^Q \mathbf{a}(\varphi_q) \otimes \mathbf{j}_q(t) + \mathbf{n}(t) \quad (61.1)$$

where, $\mathbf{s}_l(t) = [s(t), s(t-T), \dots, s(t-(N-1)T)]^T$ and φ_l are the l -th satellite signal and its DOA; $\mathbf{j}_q(t) = [j(t), j(t-T), \dots, j(t-(N-1)T)]^T$ and φ_q represent the q -th interference signal and its DOA. $\mathbf{a}(\varphi_l)$, $\mathbf{a}(\varphi_q)$ are the steering vector of satellite and jammer signals. In the formula (61.1), \otimes is Kronecker product, $\mathbf{n}(t)$ represents the Gaussian white noise.

Compared to the interferences and the noise, the satellite signal is too weak. Thus the covariance matrix of data received by STAP array can be written as

$$\begin{aligned} R &= E[\mathbf{x}(t)\mathbf{x}^H(t)] \\ &\approx \sum_{q=1}^Q \left(\mathbf{a}(\varphi_q) \otimes \mathbf{a}(\varphi_q)^H \right) \otimes E[\mathbf{j}_q(t)\mathbf{j}_q^H(t)] + \sigma_n^2 \mathbf{I} = \mathbf{R}_q + \sigma_n^2 \mathbf{I} \end{aligned} \quad (61.2)$$

In actual anti-jamming system, we usually use batch mode. But in high-dynamic environment, the robustness of conventional algorithms is poor because the direction of interference is changing with time. Widen the null is an effective method to solve this problem. The general method of null-widen is to build a new covariance matrix $\bar{\mathbf{R}}$ which is the result of the covariance matrix dot product the taper matrix \mathbf{T} [6].

$$\bar{\mathbf{R}} = \mathbf{R} \odot \mathbf{T} \quad (61.3)$$

where, symbol \odot represents Hadamard product. \mathbf{T} is also called the extension matrix. A wider null can be get using the new covariance matrix $\bar{\mathbf{R}}$.

But in actual system, usually using the sample covariance matrix $\hat{\mathbf{R}}$ instead of the data covariance matrix.

$$\bar{\mathbf{R}} = \hat{\mathbf{R}} \odot \mathbf{T} \quad (61.4)$$

where, $\hat{\mathbf{R}} = \frac{1}{K} \sum_{k=1}^K \mathbf{x}_k \mathbf{x}_k^H$.

As previously described, null-widen methods have been discussed when the changing interference DOA is obey two distribution or normal distribution, but it doesn't simply obey this two kind of distribution mode in high-dynamic environment. In the next section, a new STAP null-widen method is proposed based on the change of interference DOA to be Laplace distribution [5].

61.3 STAP Null-Widen Method

In high-dynamic environment, the DOA of interference changes rapidly with time, $\varphi_q(t)$ can be described as an extension of the current direction φ_q .

$$\varphi_q(t) = \varphi_q + \Delta\varphi_q \quad (61.5)$$

Then the covariance matrix can be written as

$$\begin{aligned} \bar{\mathbf{R}} &= E[\mathbf{x}(t)\mathbf{x}^H(t)] \\ &\approx E\left[\sum_{q=1}^Q (\mathbf{a}(\varphi_q(t)) \otimes \mathbf{a}^H(\varphi_q(t)))\right] \otimes E[\mathbf{j}_q(t)\mathbf{j}_q^H(t)] + \sigma_n^2 \mathbf{I} \end{aligned} \quad (61.6)$$

where

$$\mathbf{a}[\varphi_q(t)] = \left[1, e^{-j\frac{2\pi}{\lambda}d \sin \varphi_q(t)}, \dots, e^{-j\frac{2\pi}{\lambda}d(M-1) \sin \varphi_q(t)}\right]^T \quad (61.7)$$

And $\Delta\varphi_q$ is very small, according to the First-Order Taylor expansion, it can be written as

$$\sin \varphi_q(t) = \sin(\varphi_q + \Delta\varphi_q) = \sin \varphi_q + \Delta\varphi_q \cos \varphi_q \quad (61.8)$$

Then, the steering vector of interference can be written as

$$\mathbf{a}[\varphi_q(t)] = \mathbf{a}_q \odot \mathbf{b} \quad (61.9)$$

where

$$\mathbf{a}_q = \left[1, e^{-j\frac{2\pi}{\lambda}d \sin \varphi_q}, \dots, e^{-j\frac{2\pi}{\lambda}d(M-1) \sin \varphi_q} \right]^T \quad (61.10)$$

$$\mathbf{b} = \left[1, e^{-j\frac{2\pi}{\lambda}d\Delta\varphi_q \cos \varphi_q}, \dots, e^{-j\frac{2\pi}{\lambda}d(M-1)\Delta\varphi_q \cos \varphi_q} \right]^T \quad (61.11)$$

The Laplace distribution model can be used to describe the change of interference DOA in high-dynamic environment. $f(\Delta\varphi_q)$ is the probability density function of $\Delta\varphi_q$.

$$f(\Delta\varphi_q) = \frac{1}{2\zeta_q} e^{-\frac{|\Delta\varphi_q|}{\zeta_q}} \quad (61.12)$$

where $2\zeta_q^2$ denotes variance, $\Delta\varphi_q$ is degree.

Then the covariance matrix can be written as

$$\begin{aligned} \bar{\mathbf{R}} &= E[\mathbf{x}(t)\mathbf{x}^H(t)] \\ &\approx \sum_{q=1}^Q \int f(\Delta\varphi_q) (\mathbf{a}(\varphi_q(t)) \otimes \mathbf{a}^H(\varphi_q(t))) \otimes E[\mathbf{j}_q(t)\mathbf{j}_q^H(t)] d\Delta\varphi_q + \sigma_n^2 \mathbf{I} \\ &= \sum_{q=1}^Q \int f(\Delta\varphi_q) \left((\mathbf{a}_q \otimes \mathbf{a}_q^H) \odot (\mathbf{b} \otimes \mathbf{b}^H) \right) \otimes E[\mathbf{j}_q(t)\mathbf{j}_q^H(t)] d\Delta\varphi_q + \sigma_n^2 \mathbf{I} \end{aligned} \quad (61.13)$$

Because only \mathbf{b} and $\Delta\varphi_q$ are related, the covariance matrix can be written as

$$\begin{aligned} \bar{\mathbf{R}} &= \int f(\Delta\varphi_q) \mathbf{B} \otimes \mathbf{I}_{N \times N} d\Delta\varphi_q \odot \sum_{q=1}^Q \left((\mathbf{a}_q \otimes \mathbf{a}_q^H) \otimes E[\mathbf{j}_q(t)\mathbf{j}_q^H(t)] \right) + \sigma_n^2 \mathbf{I} \\ &= \int f(\Delta\varphi_q) \mathbf{B} d\Delta\varphi_q \otimes \mathbf{I}_{N \times N} \odot R_q + \sigma_n^2 \mathbf{I} \end{aligned} \quad (61.14)$$

where, $\mathbf{B} = \mathbf{b} \otimes \mathbf{b}$, it can be gained by calculations that

$$\bar{\mathbf{R}} = (\mathbf{T}_L \otimes \mathbf{I}_{N \times N}) \odot \mathbf{R}_q + \sigma_n^2 \mathbf{I} = (\mathbf{T}_{STL} \odot \mathbf{R}_q) + \sigma_n^2 \mathbf{I} \tag{61.15}$$

where, $\mathbf{T}_{STL} = \mathbf{T}_L \otimes \mathbf{I}_{N \times N}$, and the elements of \mathbf{T}_L are

$$\mathbf{T}_L(k, l) = \frac{1}{1 + (\Lambda_{kl} \frac{\pi}{180})^2} \quad 1 \leq k, l \leq M \tag{61.16}$$

In formula (61.16), $\Lambda_{kl} = \frac{2\pi}{\lambda} \zeta_q d(l - k) \cos \varphi_q$.

And because that the diagonal elements of \mathbf{T}_{STL} and Unit Matrix are 1, other elements of the Unit Matrix are 0, it can be gained by calculations that

$$\bar{\mathbf{R}} = \mathbf{T}_{STL} \odot \mathbf{R} \tag{61.17}$$

where, $\mathbf{T}_{STL} = \mathbf{T}_L \otimes \mathbf{I}_{N \times N}$.

According to the high-dynamic movement model, it is can be known that when $\varphi_q = 90^\circ$, the interference DOA changes fastest. Therefore, we select the parameter ζ_{\max} which can generate the required maximum null width instead of $\zeta_q \cos \varphi_q$ to form the extension matrix.

But the STAP will increase the computational complexity, and only few snapshots can be caught in high-dynamic movement. In the next section, a new STAP null-widen method based on MWF is given.

61.4 The Null-Widen Model Based on Reduced-Dimension STAP

Correlation Subtraction Algorithms Multistage Wiener filter (CSA-MWF) is one kind of MWF, which decomposed the signal using a sequence of orthogonal projection, so that it can get the same performance as wiener filter. And it has low computational complexity because this method does not need compute the covariance matrix and the blocking matrix. And it can get better performance with few snapshots. The filter structure of the CSA-MWF is shown in Fig. 61.1.

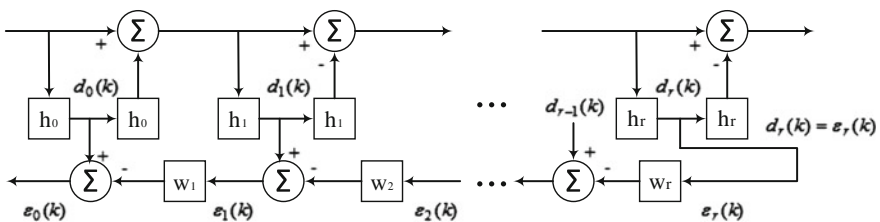


Fig. 61.1 The filter structure of the CSA-MWF

The covariance matrix is not needed to get CSA-MWF's weights [7], while the method proposed in above paragraphs widen nulls via rewriting covariance matrix. So the CSA-MWF can't using into the proposed method directly. In this paper it is settled by getting the equivalent weights [8].

For the power minimization approach, the weights of CSA-MWF can be expressed as

$$\mathbf{W}_{CSA-MWF} = \mathbf{h}_0 - \mathbf{T}_D \mathbf{W}_d \quad (61.18)$$

where

$$\mathbf{h}_0 = [1, 0, \dots, 0]^T \quad (61.19)$$

$$\mathbf{W}_d = \mathbf{R}_d^{-1} r_{dd_0} = (\mathbf{T}_D^H \mathbf{R}_{X_0} \mathbf{T}_D)^{-1} r_{dd_0} = (\mathbf{T}_D^H \mathbf{R}_{X_0} \mathbf{T}_D)^{-1} \mathbf{T}_D^H r_{X_0 d_0} \quad (61.20)$$

$$\mathbf{T}_D = [\mathbf{h}_1, \mathbf{h}_2, \dots, \mathbf{h}_D] \quad (61.21)$$

And because $\mathbf{X}_0 = (\mathbf{I} - \mathbf{h}_0 \mathbf{h}_0^H) \mathbf{X}(k)$, $d_0(k) = \mathbf{h}_0^H \mathbf{X}(k)$, then

$$\mathbf{r}_{X_0 d_0} = E(\mathbf{X}_0(k) d_0^*(k)) = (\mathbf{I} - \mathbf{h}_0 \mathbf{h}_0^H) \mathbf{R}_X \mathbf{h}_0 \quad (61.22)$$

$$\mathbf{R}_{X_0} = (\mathbf{I} - \mathbf{h}_0 \mathbf{h}_0^H) \mathbf{R}_X (\mathbf{I} - \mathbf{h}_0 \mathbf{h}_0^H) \quad (61.23)$$

And for $\mathbf{T}_D = [\mathbf{h}_1, \mathbf{h}_2, \dots, \mathbf{h}_D]$, each row can be expressed as

$\mathbf{h}_i = \frac{r_{X_{i-1} d_{i-1}}}{\|r_{X_{i-1} d_{i-1}}\|}$, and because that

$$\mathbf{X}_i = (\mathbf{I} - \mathbf{h}_i \mathbf{h}_i^H)^H \mathbf{X}_{i-1}(k) = (\mathbf{I} - \mathbf{h}_0 \mathbf{h}_0^H - \dots - \mathbf{h}_i \mathbf{h}_i^H) \mathbf{X}(k) \quad (61.24)$$

$$d_i = \mathbf{h}_i^H \mathbf{X}_{i-1}(k) = \mathbf{h}_i^H \mathbf{X}(k) \quad (61.25)$$

Then

$$\mathbf{r}_{X_{i-1} d_{i-1}} = \left(\mathbf{I} - \sum_{j=0}^{i-1} \mathbf{h}_j \mathbf{h}_j^H \right) \mathbf{R}_X \mathbf{h}_{i-1} \quad (61.26)$$

$$\mathbf{h}_i = \frac{\left(\mathbf{I} - \sum_{j=0}^i \mathbf{h}_j \mathbf{h}_j^H \right) \mathbf{R}_X \mathbf{h}_{i-1}}{\left\| \left(\mathbf{I} - \sum_{j=0}^i \mathbf{h}_j \mathbf{h}_j^H \right) \mathbf{R}_X \mathbf{h}_{i-1} \right\|} \quad (61.27)$$

So the weights of CSA-MWF can be expressed as

$$\mathbf{W}_{CSA-MWF} = \mathbf{h}_0 - \mathbf{T}_D (\mathbf{T}_D^H \mathbf{R}_X \mathbf{T}_D)^{-1} \mathbf{T}_D^H \mathbf{R}_X \mathbf{h}_0 \quad (61.28)$$

Table 61.1 Comparison of the computational complexity

	Number of multiplications
Null-widen method	$(8D + 2K)(MN)^2 + O(D^3) + (2D^2 + 4D)MN + D^3 - D^2 - D$
Method based on CSA-MWF	$(2K + 4)(MN)^2 + O((MN)^3) + MN - 1$

where

$$\mathbf{T}_D = [\mathbf{h}_1, \mathbf{h}_2, \dots, \mathbf{h}_D] \quad (61.29)$$

$$\mathbf{h}_i = \frac{\left(\mathbf{I} - \sum_{j=0}^i \mathbf{h}_j \mathbf{h}_j^H\right) \mathbf{R}_x \mathbf{h}_{i-1}}{\left\| \left(\mathbf{I} - \sum_{j=0}^i \mathbf{h}_j \mathbf{h}_j^H\right) \mathbf{R}_x \mathbf{h}_{i-1} \right\|} \quad (61.30)$$

From formulas (61.28), (61.29) and (61.30), it can be seen that the new weights is only relate to the covariance matrix, so that we can apply CSA-MWF to STAP null-widen method.

Assume that there are M elements, N taps, and D is the dimension. Computational complexity of the former proposed method and the new one are given in Table 61.1, which shows that the new method based on CSA-MWF has low computation.

61.5 Simulation Results

In simulation, a 5 elements and 4 taps STAP uniform linear array with uniform spacing of half wave length has been used. The sample frequency of the high dynamic GPS signals is 5.714 MHz, and IF is 4.309 MHz. The input SNR is -20 dB, and the input INR is 40 dB. As the satellites are very far away from the high dynamic receivers, the DOAs of GPS signals can be regard as constant. Assuming the DOA of GPS signals is 10° . The trajectory model of high dynamic GPS receiver carrier with rectilinear motion can be established according to the high dynamic definition presented by Hinedi S [9]. The initial velocity of the carrier is 1 km/s, the jamming is 10 km away from the receiver. And the DOA of interference changes from -20° to -17° . While the weights are obtained by the snapshots at -20° .

In order to verify the validity of the proposed algorithm, 100 snapshots are used by simulation. The beam patterns of widening nulling algorithm and minimum power algorithm are shown in Fig. 61.2. As Fig. 61.2 shows, the null at the direction of interference formed via the proposed algorithm is wider than the

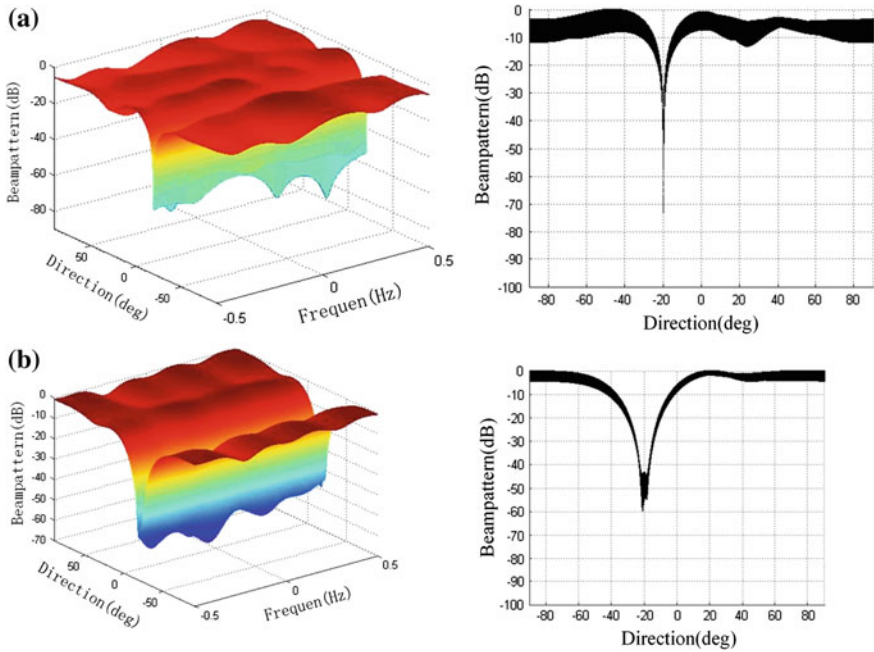


Fig. 61.2 Comparison of beam patterns obtained via the power minimization method and the null-widen method. **a** Conventional power minimization method; **b** Null-widen method

traditional minimum power algorithm. Figure 61.3 shows the acquisition results by two mentioned algorithms. As Fig. 61.3 shows, GPS satellites cannot be acquired from the signals processed by the minimum power algorithm in a high dynamic environment. However, it can be acquired via the proposed method.

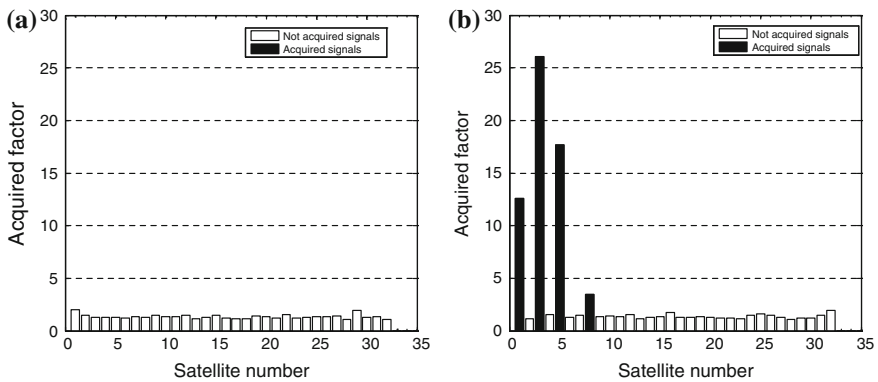


Fig. 61.3 Comparison of the acquisition performance between the power minimization method and the new method. **a** The power minimization method; **b** The new method

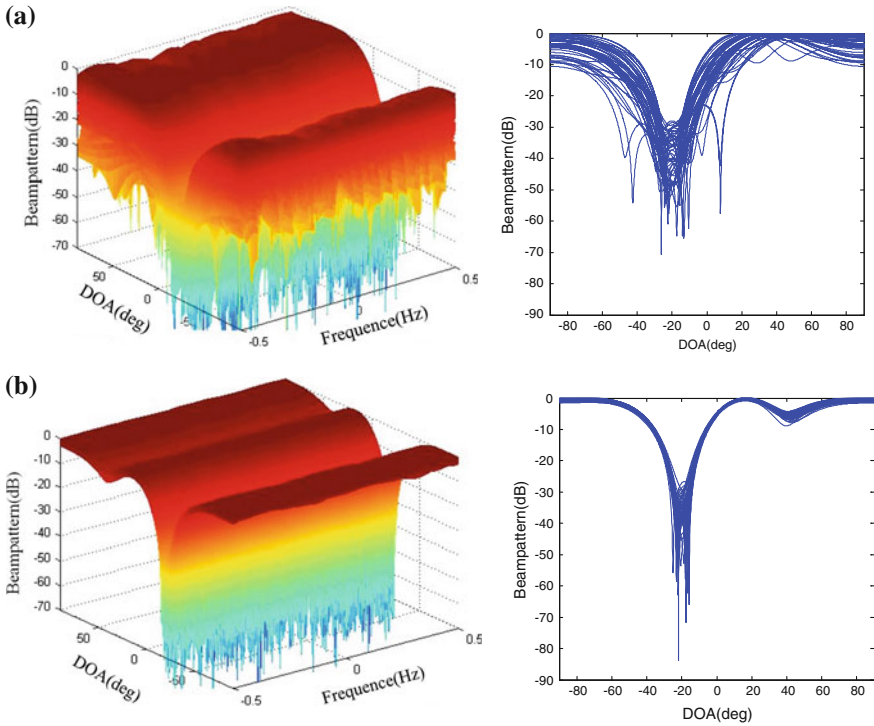


Fig. 61.4 Comparison of the robust between null-widen method and the method based on CSA-MWF in few snapshots. **a** The robust of null-widen method; **b** The robust of the method based on CSA-MWF

In order to verify the robustness of the new method based on CSA-MWF with few snapshots, 10 snapshots are used in simulation, through 50 times Monte Carlo experiments. From Fig. 61.4 it can be known that the proposed method obtains better performance with few snapshots.

61.6 Conclusion

A new STAP null-widen method based on the Laplace distribution model of the changing interference DOA is deduced, and then in order to reduce computational complexity a new method by applying the CSA-MWF to STAP null-widen method is adapted. The results in simulation show that the new method can provide correctly acquisition and accurately positioning, and it obtains better performance with few snapshots.

Acknowledgments The work of this paper is supported by the Projects of the National Natural Science Foundation of China (Grant No. 61172112, 61271404, 61471363), Fundamental Research Funds for the Central Universities (Grant No. 3122014D003).

References

1. Zatman M (1995) Production of adaptive array troughs by dispersion synthesis. *Electron Lett* 31 (25):2141–2142
2. Mailloux RJ (1995) Covariance matrix augmentation to produce adaptive array pattern troughs. *Electron Lett* 31(10):771–772
3. Li RF, Wang YL, Wan SH (2003) Research on adapted pattern null widening techniques. *Mod Radar* 25(2):42–45
4. Wu SJ, Zhang JZ, Zhang S (2005) Robust adaptive beamforming against pointing error. *J Harbin Eng Univ* 26(4):531–535
5. Ma Y, Lu D, Wang W, Wang L, Wu R (2014) A high-dynamic null-widen GPS anti-jamming algorithm based on statistical model of the changing interference DOA. In: *Proceedings of 2014 China Satellite Navigation Conference*, Springer, Heidelberg, pp 695–702
6. Guerci JR (2004) Theory and application of covariance matrix tapers for robust adaptive beamforming. *IEEE Trans. Signal Processing*, 47(4):977–985. In: Meng X, Gao Y (eds) *Electric systems analysis*, Higher Education Press, Beijing, pp 3–21
7. Rick DC, Goldstein JS (2000) Efficient architectures for implementing adaptive algorithms. *Proceedings of the 2000 antenna application symposium*, Monticello, pp 29–41
8. Wang M, Zhu JH (2011) A novel null broadening algorithm based on reduced-rank multistage wiener filter. *Aerosp Electron Warfare* 27(3):51–53
9. Hinedi S, Statman JI (1988) High-dynamic GPS tracking final report. JPL Publication, Pasadena, pp 88–35

Chapter 62

Interference Suppression with L1-Norm Constraint for Satellite Navigation Systems

Wenyi Wang, Qingrong Du, Renbiao Wu, Dan Lu, Lu Wang
and Qiongqiong Jia

Abstract Currently, there have been many studies of interference suppression for satellite navigation systems. Power minimization approach is an effective interference suppression algorithm. It forms automatically deep nulls in the DOAs (direction of arrival) of interferences without prior information about the DOAs of satellite signals and interferences. However, the power minimization approach can not provide flat gains in other directions. Thus there will be fluctuation in the beampattern, especially when the number of snapshots is not enough. It means that the desired satellite signal may be partly suppressed when they locate in the shallow nulls. In this paper, by combining eigenvalue thresholding method and l1-norm constraint, we propose a new interference suppression algorithm to suppress interferences and provide flat gains in all directions except that of interferences. The difference between the new algorithm and the conventional power minimization approach lies in the improvement of covariance matrix which is constituted based on the main eigenvalues and corresponding eigenvectors of covariance matrix. In addition, an explicit l1-norm constraint on the beam gains is exploited to provide flat gain in all directions except that of interferences. When there are interferences and spoofing, the spoofing is generally suppressed heavier than the authorized signal. It will decrease the power difference between the spoofing and authorized signals. Thus it will degrade the performance of subsequent spoofing detection. So the proposed algorithm also can be applied to the spoofing detection in satellite navigation systems. The simulations demonstrate the effectiveness of the proposed algorithm.

Keywords Satellite navigation · Flat gains · L1-norm constraint · Spoofing interferences

W. Wang (✉) · Q. Du · R. Wu · D. Lu · L. Wang · Q. Jia
Tianjin Key Laboratory for Advanced Signal Processing,
Civil Aviation University of China, Tianjin, China
e-mail: wenyi_wang@126.com

© Springer-Verlag Berlin Heidelberg 2015
J. Sun et al. (eds.), *China Satellite Navigation Conference (CSNC) 2015
Proceedings: Volume I*, Lecture Notes in Electrical Engineering 340,
DOI 10.1007/978-3-662-46638-4_62

717

62.1 Introduction

Satellite navigation system such as global positioning system (GPS) has been widely used in numerous applications in civil and military fields because it can provide accurate position and time information. Though the power of received satellite signal is generally 20–30 dB lower than that of noise [1], the receiver can still demodulate the signal by utilizing the spreading spectrum technology. Based on the same technology, it also gained a certain capability of interference suppression. But when the power of interferences is much higher than the receiver noise, the interferences will bring a significant degradation in the performance of satellite navigation systems.

There have been many studies of interference suppression for satellite navigation systems [1–8]. Time-domain filter is an effective way to suppress sinusoidal interference [2]. For other interferences, many interference suppression algorithms have been proposed in the framework of array signal processing. With an antenna array, the interferences can be suppressed by using spatial, time domain processing or a combination of them. When the direction of arrival (DOA) information is known, the minimum variance distortionless response (MVDR) beamforming [3] can be utilized to simultaneously suppress interferences and provide beamforming gain for desired signals. By utilizing the specific structure (such as self-coherence and period repetitive property) [4, 5], the blind adaptive beamforming algorithms are also proposed to suppress interferences. There are also some interference suppression algorithms which are proposed to suppress wideband interferences [6] or high-dynamic interferences [7].

Unlike the algorithms mentioned above, the power minimization approach [1, 8] can automatically form deep nulls in DOAs of the interferences without using DOAs and structure information of interferences and satellite signals. However, the power minimization approach can not provide flat gains in other directions. Thus there will be fluctuation in the beampattern, especially when the number of snapshots is not enough. It means that the desired satellite signal may be partly suppressed when they locate in the shallow nulls.

In this paper, by combining eigenvalue thresholding method [9] and l_1 -norm constraint, we propose a new interference suppression algorithm to suppress interferences and provide flat gains in all directions except that of interferences. Different with the conventional power minimization approach which minimize the total received power, the covariance matrix is replaced by a modified covariance matrix which is constituted based on the main eigenvalues and corresponding eigenvectors of covariance matrix. In addition, an explicit l_1 -norm constraint on the beam gains is exploited to provide flat gain which has been adopted in many fields, such as array signal processing [10, 11].

Another possible application of the proposed algorithm is the spoofing detection [12] in satellite navigation systems which is based on the fact that the power of satellite signals in the spoofing is higher than the authorized satellite signals. However, when there are interferences and spoofing, the minimization power

approach will partly suppress the spoofing. It decreases the power difference between the spoofing and real satellite signal. Thus it will degrade the performance of subsequent spoofing detection.

This paper is structured as follows. The signal model is introduced and the power minimization method is reviewed briefly in Sect. 62.2. The proposed method is provided in Sect. 62.3. Simulations results are given in Sect. 62.4 and conclusions are drawn in Sect. 62.5.

62.2 Signal Model

Consider a uniform linear array (ULA). Suppose the adjacent sensor spacing is one half of wavelength of the center frequency. Then the resulting steering vector can be expressed as follows

$$\mathbf{a}(\phi_k) = \left[1, e^{-j\pi \sin(\phi_k)}, \dots, e^{-j\pi(M-1) \sin(\phi_k)} \right]^T \quad (62.1)$$

where $\phi_k \in [-90^\circ, 90^\circ]$, $(*)^T$ denotes matrix transpose.

Assume that there are far field narrow band interferences impinging on the array. Then the array output snapshot is given by

$$\mathbf{x}_i = \mathbf{A}\mathbf{v}_i + \mathbf{s}_i + \mathbf{n}_i \quad (62.2)$$

where $\phi_k (k = 1, \dots, K)$ denotes the DOA of the interferences, \mathbf{x}_i is the received snapshot, $\mathbf{v}_i = [\mathbf{v}_{i1}, \dots, \mathbf{v}_{iK}]^T$ denotes the waveforms of far field narrow band interferences, \mathbf{s}_i is the vector due to satellite signals, \mathbf{n}_i is zero-mean Gaussian measurements noise, \mathbf{A} is the steering matrix as

$$\mathbf{A} = [\mathbf{a}(\phi_1), \dots, \mathbf{a}(\phi_K)] \quad (62.3)$$

Without loss of generality, we assume that the satellite signal, the interference and the noise are mutually independent. Thus the theoretical covariance matrix \mathbf{R} of the array output vector can be denoted as

$$\begin{aligned} \mathbf{R} &= E\{\mathbf{x}_i \mathbf{x}_i^H\} \\ &= \mathbf{A}E\{\mathbf{v}_i \mathbf{v}_i^H\} \mathbf{A}^H + E\{\mathbf{s}_i \mathbf{s}_i^H\} + E\{\mathbf{n}_i \mathbf{n}_i^H\} \\ &\approx \mathbf{A}E\{\mathbf{v}_i \mathbf{v}_i^H\} \mathbf{A}^H + \delta \mathbf{I} \end{aligned} \quad (62.4)$$

where $E(*)$ and $(*)^H$, respectively, denote the expectation operator and conjugate transpose. The approximation is because the power of satellite signal is much lower than that of interferences and noise.

When the interferences are much stronger than the desired signal, the power minimization approach is an effective algorithm to suppress the interferences. It is chosen as the optimal solution of

$$\begin{aligned} \min_{\mathbf{w}} \quad & \mathbf{w}^H \mathbf{R} \mathbf{w} \\ \text{subject to} \quad & \mathbf{w}^H \mathbf{c} = 1 \end{aligned} \quad (62.5)$$

where $\mathbf{c} = [1, 0, \dots, 0]^T$.

Using the method of Lagrange multipliers, it is easy to obtain the optimal solution as

$$\mathbf{w} = \frac{\mathbf{R}^{-1} \mathbf{c}}{\mathbf{c}^H \mathbf{R}^{-1} \mathbf{c}} \quad (62.6)$$

Once the desired weight vector is obtained, the output is $y_i = \mathbf{w}^H \mathbf{x}_i$.

In practical applications, as the theoretical covariance matrix is unknown, it will be replaced by its finite sample estimate $\hat{\mathbf{R}}$

$$\hat{\mathbf{R}} = \frac{1}{L} \sum_{i=1}^L \mathbf{x}_i \mathbf{x}_i^H \quad (62.7)$$

where L is the number of snapshots.

The power minimization approach automatically forms deep nulls in the DOAs of interferences to cancel the interferences. As it does not need prior information about the DOAs of interferences and satellite signals, the power minimization approach is utilized in many practical applications.

However, because there is no explicit constraint on the beam gains, the power minimization approach can not provide flat gains in other directions. Therefore, the desired satellite signals may be partly suppressed when they locate in the shallow nulls. In following section, an explicit 11-norm constraint is incorporated into the objective function to obtain approximately flat beamforming gain in other directions.

62.3 The Proposed Approach

As stated before, because there is no explicit constraint on the beamforming gains, there is fluctuation in beamforming gains of power minimization approach. The DOAs of desired satellite signal are generally unknown. Therefore, when the DOAs of satellite signals just locate in the nulls, they will be partly suppressed. This is particularly undesirable for spoofing detection where the spoofing detection is based on the fact that the power of spoofing is higher than authorized signal. As the

power of spoofing is higher than that of authorized signal, the spoofing is generally suppressed heavier than the authorized signal. It will decrease the power difference between the spoofing and authorized signals which makes the spoofing detection more difficult. In order to avoid this problem, a possible solution is to only form deep nulls in the DOAs of interferences and let beamforming gains in other directions as flat as possible.

The eigendecomposition of covariance matrix is given by

$$\mathbf{R} = \sum_{m=1}^M \lambda_m \mathbf{b}_m \mathbf{b}_m^H \quad (62.8)$$

where λ_m and \mathbf{b}_m are the eigenvalues and corresponding eigenvectors. Without loss of generality, it is assumed that

$$\lambda_1 \geq \lambda_2 \geq \dots \geq \lambda_M \quad (62.9)$$

It is well known that the interference subspace is spanned by the columns of the eigenvectors corresponding to the first K eigenvalues. Then we define a modified covariance matrix based on the eigenvalue thresholding method as

$$\mathbf{R}_I = \sum_{m=1}^K \lambda_m \mathbf{b}_m \mathbf{b}_m^H \quad (62.10)$$

It is noted that the modified covariance matrix only includes the first K eigenvectors and corresponding eigenvalues. Thus it can be seen as a rough approximation of the interference covariance matrix. Thus we can use the modified covariance matrix to replace the covariance matrix in the power minimization approach. It implies that the power of interferences instead of total received power is minimized.

However, the number of interference is generally unknown, then K can be chosen as following

$$K = \arg \max_m \{ \lambda_m > \eta \lambda_M \} \quad (62.11)$$

where η is a given parameter which can be set in advance, e.g., $\eta = 10$.

The l1-norm constraint has been used in many fields to achieve sparse solutions in various optimization problems. Here, in order to obtain flat beamforming gains in all directions except that of interferences, an explicit l1-norm constraint on beamforming gains is incorporated into the objective function. However, the DOA space is continuous and it is difficult to directly apply the l1-norm constraint to a continuous space. Therefore, the DOA space is sampled with a given DOA grid, e.g., 1° . Then the corresponding steering matrix is as following

$$\mathbf{A}' = [\mathbf{a}(-90^\circ), \mathbf{a}(-80^\circ), \dots, \mathbf{a}(89^\circ)] \quad (62.12)$$

Unlike the DOA grid in DOA estimation based on sparse representation, there is no off-grid problem in the present application. A 1° DOA grid is enough for the proposed algorithm.

Then the new optimization problem is defined as following

$$\min_{\mathbf{w}} \mathbf{w}^H \mathbf{R}_I \mathbf{w} + \gamma \|\mathbf{w}^H \mathbf{A}' - \mathbf{1}^T\|_1 \quad (62.13)$$

where $\mathbf{1} = [1, 1, \dots, 1]^T$. The first part of objective function is to roughly minimize the power of interferences which is different with the power minimization approach, the second part is an l1-norm constraint to let the beamforming gains for all directions be one, γ is a tradeoff parameter between the first part and the second part. γ is an empirical value. In our simulations, γ can be set as $\gamma = 2 \times 10^{-6} \times \|\mathbf{R}_I\|_2$ by comparing the performance of different simulation environment, as well, γ is effective for different simulation environment.

It is noted that the optimization problem above can be transformed as

$$\min_{\mathbf{w}} \mathbf{w}^H \mathbf{R}_I \mathbf{w} + \gamma \|\mathbf{A}'^H \mathbf{w} - \mathbf{1}\|_1 \quad (62.14)$$

The new optimization problem is a convex problem which can be easily solved using convex optimization software, such as CVX. Once the desired weight vector is obtained, the output is $y_i = \mathbf{w}^H \mathbf{x}_i$.

62.4 Simulations

In this section, several simulation results are provided to illustrate the performance of the proposed algorithm. A uniform linear array (ULA) is assumed with $M = 10$ in all simulations. The array element spacing is one half of the wavelength. All sources are modeled as a constant-modulus signal, and the additive noise is assumed as complex white Gaussian noise. The signal-to-noise ratio (SNR) is defined as $\text{SNR} = P_S/\delta$, where P_S is the power of one desired signal and δ is the power of the noise. Similarly, the interference-to-noise ratio (INR) is defined as $\text{INR} = P_I/\delta$, where P_I is the power of one interference. In addition, the grid spacing is 1° , $\eta = 10$ and $\gamma = 2 \times 10^{-6} \times \|\mathbf{R}_I\|_2$, where \mathbf{R}_I is the modified covariance matrix.

In the first simulation, one GPS satellite signal impinges on the array from 65° and one interference impinges on the array from -40° . The SNR and INR are $\text{SNR} = -20$ dB and $\text{INR} = 20$ dB. The numbers of snapshot are 200 and 1000 in the two experiments, respectively. Figure 62.1 is a comparison of the beampatterns formed by the proposed algorithm and the power minimization approach. In order

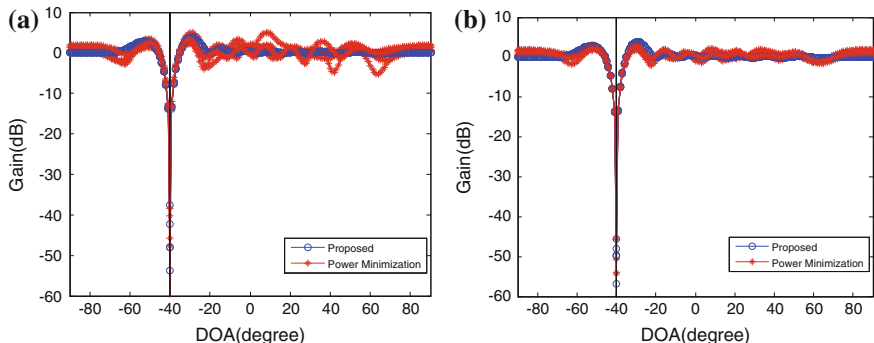


Fig. 62.1 Comparison of beampatterns of the proposed algorithm and power minimization approach. **a** 200 snapshots. **b** 1000 snapshots

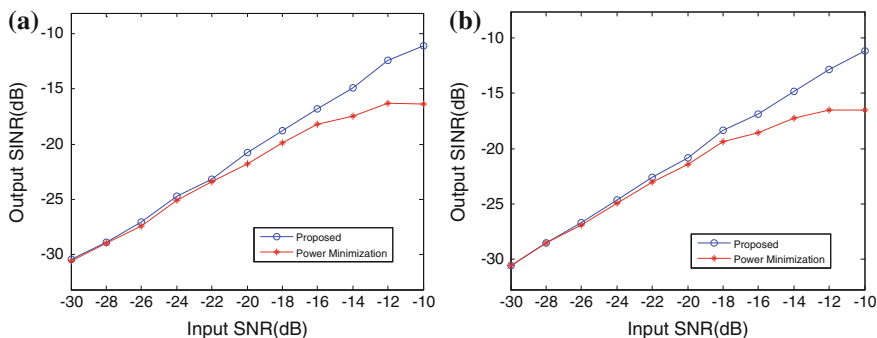


Fig. 62.2 Input SNR versus output SINR for the proposed algorithm and the power minimization approach. **a** 200 snapshots. **b** 1000 snapshots

to keep Fig. 62.1 clear, only 5 Monte-Carlo simulations are included. Figure 62.1a is the result with 200 snapshots and Fig. 62.1b is the result with 1000 snapshots. From Fig. 62.1, it can be seen that two algorithms form the deep null in the DOA of the interference, and the null formed by the proposed algorithm is deeper than the power minimization approach. For the power minimization approach, the beamforming gains in other directions have fluctuation, especially in Fig. 62.1a. Yet, the beampatterns formed by the proposed algorithm have approximately flat gains in all directions except that of interference in two experiments.

When the SNR varies from -30 to -10 dB, the curves of input SINR versus output SNR are shown in Fig. 62.2 which are calculated from 500 independent Monte-Carlo runs using the proposed algorithm and the power minimization approach. Figure 62.2a is the result with 200 snapshots and Fig. 62.2b is the result with 1000 snapshots. From Fig. 62.2, we can see that the proposed algorithm performs better than the power minimization approach. As it is expected, when the

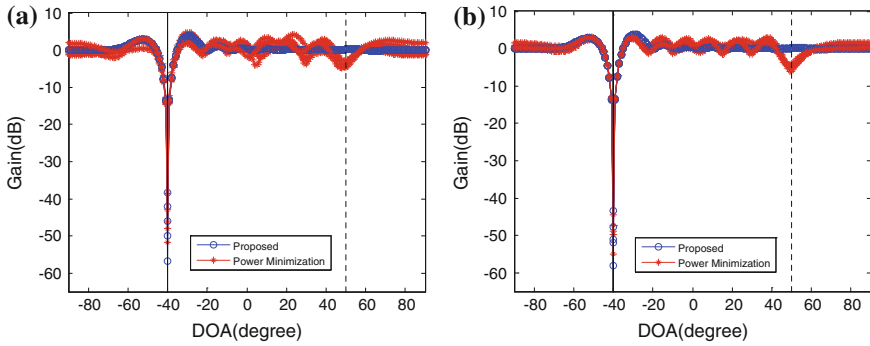


Fig. 62.3 Comparison of beam patterns of the proposed algorithm and power minimization approach including one spoofing. **a** 200 snapshots. **b** 1000 snapshots

SNR increases, the gap of curves between the proposed algorithm and the power minimization approach also increases.

In the second simulation, one GPS satellite signal impinges on the array from 65° , one repressive interference signal impinges on the array from -40° and one spoofing including six GPS satellite signals impinges on the array from -50° . The SNR and INR are same as that in the first simulation. To ensure the spoofing effective, the SNR of every satellite signal in the spoofing is $\text{SNR} = -18 \text{ dB}$ which is higher than the authorized satellite signal. The numbers of snapshot are also 200 and 1000 in the two experiments. Figure 62.3 is a comparison of the beam patterns formed by the proposed algorithm and the power minimization approach via 5 Monte-Carlo simulations. Figure 62.3a is the result with 200 snapshots and Fig. 62.3b is the result with 1000 snapshots. From Fig. 62.3, we can see that two algorithms form the deep null in the DOA of the interference. Besides, because the spoofing includes multiple GPS satellites signals, the power minimization approach forms a shallow null in the DOA of the spoofing. But the proposed algorithm has a unit gain in the DOA of spoofing which avoids the suppression of spoofing. Thus the spoofing can be detected based on the power difference between the spoofing and authorized satellite signal.

62.5 Conclusion

In this paper, a new interference suppression algorithm for satellite navigation systems is proposed which automatically forms deep nulls in the DOAs of interferences and provide approximately flat gains in other directions. The idea is to use a modified covariance matrix based on the eigenvalue thresholding methods to replace the covariance matrix in the minimized power approach, and an explicit l_1 -norm on the beam gains in all directions is incorporated. The simulations demonstrate the effectiveness of the proposed algorithm.

Acknowledgments The work of this paper is supported by the Projects of the National Natural Science Foundation of China (Grant No. 61172112, 61471363 and 61271404), Fundamental Research Fund for the Central Universities (3122014B001)

References

1. Sklar JR (2003) Interference mitigation approaches for the global positioning system. *Linc Lab J* 14(2):167–179
2. Borio D, Camoriano L, Presti LL (2008) Two-pole and multi-pole notch filters: a computationally effective solution for GNSS interference detection and mitigation. *Syst J IEEE* 2(1):38–47
3. Malmström J (2003) Robust navigation with GPS/INS and adaptive beamforming. Scientific report of Swedish Defence Research Agency
4. Sun W, Amin MG (2005) A self-coherence anti-jamming GPS receiver. *Sig Process IEEE Trans* 53(10):3910–3915
5. Amin MG, Sun W (2005) A novel interference suppression scheme for global navigation satellite systems using antenna array. *IEEE J Sel Areas Commun* 23(5):999–1012
6. Fante R, Vaccaro JJ (2000) Wideband cancellation of interference in a GPS receive array. *IEEE Trans Aerosp Electron Syst* 36(2):549–564
7. Wu RB, Li C, Lu D (2012) Power minimization with derivative constraints for high dynamic GPS interference suppression. *Sci China Inf Sci* 55(4):857–866
8. Zoltowski MD, Gecan AS (1995) Advanced adaptive null steering concepts for GPS. In: Military communications conference, 1995, MILCOM'95, Conference record, IEEE, vol 3, pp 1214–1218
9. Harmanci K, Tabrikian J, Krolik JL (2000) Relationships between adaptive minimum variance beamforming and optimal source localization. *IEEE Trans Sig Process* 48(1):1–12
10. Candès EJ, Romberg J, Tao T (2006) Robust uncertainty principles: exact signal reconstruction from highly incomplete frequency information. *IEEE Trans Inf Theory* 52(2):489–509
11. Malioutov D, Çetin M, Willsky AS (2005) A sparse signal reconstruction perspective for source localization with sensor arrays. *IEEE Trans Sig Process* 53(8):3010–3022
12. Meurer M, Konovaltsev A, Cuntz M et al (2012) Robust joint multi-antenna spoofing detection and attitude estimation using direction assisted multiple hypotheses RAIM. In: Proceedings of the 25th international technical meeting of The Satellite Division of the Institute of Navigation (ION GNSS 2012), Nashville, TN, pp 3007–3016

Chapter 63

A Spoofing Mitigation Algorithm Based on Subspace Projection for GNSS Receiver

Lei Chen, Shuai Han, Weixiao Meng and Zijun Gong

Abstract Spoofing attack can intentionally mislead the receiver to obtain the fake position or time by utilizing the counterfeit satellite signals. Although several anti-spoofing techniques have been reported to detect and suppress spoofing attack, most of the published researches are based on antenna array. In this paper, we present a spoofing mitigation algorithm based on subspace projection which is independent with antenna and even can be utilized in single-antenna GNSS receiver. With the acquired code phases, data-bit modulation, carrier frequencies and phase of all spoofing signals, the spoofing signals' subspace matrix can be constructed. The projection of input signals onto the spoofing signals' subspace is the sum of the spoofing signals and the projection of the noise. Then we can use the projection as an estimate of the spoofing signals. After subtracting the estimate from the input signals, the result consists of desired authorized signals, noises and the residue error resulted from the projection operation. We also prove that the performance of this method is independent of the carrier phases and data-bit modulation of the spoofing signals under special processing constraints. Besides, the BeiDou B1I signal has been tested to verify the validity of the subspace projection method.

Keywords Subspace projection · Spoofing attack

63.1 Introduction

By regenerating counterfeit satellite signals, spoofing attack is able to intentionally mislead the receiver to obtain fake location results or wrong time information. In comparison with blanketing jamming, spoofing attack is more invisible and

L. Chen (✉) · S. Han · W. Meng · Z. Gong
Communication Research Center, Harbin Institute of Technology, No. 2 Yikuang Street,
Nangang District, Harbin 150080, China
e-mail: leichen@hit.edu.cn

dangerous, thus has been one of major potential threat for Global Navigation Satellite System (GNSS). With the technique development of chip and software defined radio, the cost of spoofing attack is reducing whereas the flexibility is increasing. Consequently, the effective spoofing detection and mitigation techniques are indispensable to guarantee the receiver working normally.

So far, some kinds of spoofing detection and mitigation method have been reported. To avoid spoofing attack, literature [1] proposes a navigation message authorization (MEA) scheme by using the spread spectrum security codes (SSSC), although this scheme afford spoofing protection to GNSS signal, the location performance also deteriorate. Besides, a cryptographic method is investigated in literature [2] to detect spoofing attack. Literature [3, 4] suggest that spoofing attack is also able to be detected by using the carrier and code delay characteristics of the spoofing signals and the cross-correlation of the P(Y) codes received by two geographic separated receiver, respectively. With the variation of pseudorange, an anti-spoofing algorithm based on particle filter is presented in literature [5]. Generally, when spoofing attack is detected, the corresponding authorized satellite signal will be abandoned which will result in the decrease of available satellites. To receive the spoofed authorized satellite signals normally, several spoofing mitigation methods are investigated. Literature [6] evaluates an antenna array processing method based on AOA (Angle of Arrival) estimation to mitigate the spoofing attack. Although antenna array is also used in literature [7], it proposes a null steering process to successfully mitigate the spoofing signals.

Since most effective spoofing mitigation methods are based on antenna array and are not able to be expanded to single antenna receiver, this paper proposes a spoofing mitigation algorithm based on subspace projection which is independent with antenna number and also can be realized in typical single antenna receiver. Subspace projection is a classic signal processing method [8] and it has been used to mitigate the cross-correlation interference for GPS signal in our early research [9]. In this paper, we will develop the subspace projection method to mitigate the spoofing attack. With the acquired code phases, data-bit modulation, carrier frequencies and phase of all spoofing signals, the spoofing signals' subspace matrix can be constructed. The projection of input signals onto the spoofing signals' subspace is the sum of the spoofing signals and the projection of the noise. Then we can use the projection as an estimate of the spoofing signals. After subtracting the estimate from the input signals, the result approximately consists of desired authorized signals and noise. We also prove that the performance of the proposed spoofing mitigation method is independent of the carrier phases and data-bit modulation of the spoofing signals under special receiver structure constraints. Besides, the acquisition of BeiDou B1I signals has been tested to verify the validity of the subspace projection method.

63.2 Algorithm Model

In this section, we first introduce the mathematical model of the spoofing mitigation algorithm based in subspace projection. Assuming that there are N authorized signals and M spoofing signals, after down converting, the model of GNSS IF signal can be expressed as

$$\mathbf{r}_{IF} = \mathbf{r}_{Auth} + \mathbf{r}_{Spoof} + \mathbf{n}, \quad (63.1)$$

where $\mathbf{r}_{IF} = [r(t_1), r(t_2), \dots, r(t_L)]^T$ denotes the IF signal, $\mathbf{n} = [n(t_1), \dots, n(t_L)]^T$ is the additive white Gaussian noise and L is the length of the received signal.

In Eq. (63.1), the N authorized signals are given by

$$\mathbf{r}_{Auth} = \sum_{i=1}^N \mathbf{r}_{Auth}^i = \mathbf{S}_{Auth} \mathbf{a}_{Auth}, \quad (63.2)$$

where \mathbf{a}_{Auth} is the amplitude vector of N authorized signals and is defined as

$$\mathbf{a}_{Auth} = [a_{Auth}^1, a_{Auth}^2, \dots, a_{Auth}^N]^T, \quad (63.3)$$

and \mathbf{S}_{Auth} is the information matrix of N authorized signals, we have

$$\mathbf{S}_{Auth} = [\mathbf{s}_{Auth}^1, \mathbf{s}_{Auth}^2, \dots, \mathbf{s}_{Auth}^N]_{L \times N}$$

$$\mathbf{s}_{Auth}^i = \begin{bmatrix} d_{Auth}^i(t_1) C_{Auth}^i(t_1) e^{j(2\pi f_{Auth}^i t_1 + \theta_{Auth}^i)} \\ d_{Auth}^i(t_2) C_{Auth}^i(t_2) e^{j(2\pi f_{Auth}^i t_2 + \theta_{Auth}^i)} \\ \vdots \\ d_{Auth}^i(t_L) C_{Auth}^i(t_L) e^{j(2\pi f_{Auth}^i t_L + \theta_{Auth}^i)} \end{bmatrix}_{L \times 1}, \quad (63.4)$$

where $d_{Auth}^i(t_l)$, $C_{Auth}^i(t_l)$, f_{Auth}^i and θ_{Auth}^i respectively denote the navigation data, the PRN code, the carrier frequency and the carrier phase of i th authorized signal.

Similarly, the M spoofing signals are also given by

$$\mathbf{r}_{Spoof} = \sum_{i=1}^M \mathbf{r}_{Spoof}^i = \mathbf{S}_{Spoof} \mathbf{a}_{Spoof}, \quad (63.5)$$

where \mathbf{a}_{Spoof} is the amplitude vector of M spoofing signals and is defined as

$$\mathbf{a}_{Spoof} = [a_{Spoof}^1, a_{Spoof}^2, \dots, a_{Spoof}^M]^T, \quad (63.6)$$

matrix \mathbf{S}_{Spoof} is the information matrix of M spoofing signals and also can be expressed as

$$\mathbf{S}_{Spoof} = [\mathbf{s}_{Spoof}^1, \mathbf{s}_{Spoof}^2, \dots, \mathbf{s}_{Spoof}^M]_{L \times M}$$

$$\mathbf{s}_{Spoof}^i = \begin{bmatrix} d_{Spoof}^i(t_1) C_{Spoof}^i(t_1) e^{j(2\pi f_{Spoof}^i t_1 + \theta_{Spoof}^i)} \\ d_{Spoof}^i(t_2) C_{Spoof}^i(t_2) e^{j(2\pi f_{Spoof}^i t_2 + \theta_{Spoof}^i)} \\ \vdots \\ d_{Spoof}^i(t_L) C_{Spoof}^i(t_L) e^{j(2\pi f_{Spoof}^i t_L + \theta_{Spoof}^i)} \end{bmatrix}_{L \times 1}, \quad (63.7)$$

where $d_{Spoof}^i(t_l)$, $C_{Spoof}^i(t_l)$, f_{Spoof}^i and θ_{Spoof}^i respectively denote the navigation data, the PRN code, the carrier frequency and the carrier phase of i th spoofing signal.

If the spoofing signals have been successfully detected, by completing decoding and track process, the PRN code delays, navigation data, carrier frequencies and carrier phases of spoofing signals can be totally obtained. Then, the information matrix of spoofing signals can be reconstructed as Eq. (63.7). We finally obtain the subspace projection matrix of spoofing signals which is followed as

$$\mathbf{H} = \mathbf{S}_{Spoof} \left(\mathbf{S}_{Spoof}^H \mathbf{S}_{Spoof} \right)^{-1} \mathbf{S}_{Spoof}^H. \quad (63.8)$$

Next, the complementary space of the subspace projection matrix is obtained as

$$\mathbf{H}_C = \mathbf{I} - \mathbf{H}. \quad (63.9)$$

Since the projection of spoofing signals \mathbf{r}_{Spoof} onto the complementary space \mathbf{H}_C is $\mathbf{0}$:

$$\begin{aligned} \mathbf{H}_C \mathbf{r}_{Spoof} &= (\mathbf{I} - \mathbf{H}) \mathbf{r}_{Spoof} = (\mathbf{I} - \mathbf{H}) \mathbf{S}_{Spoof} \mathbf{a}_{Spoof} \\ &= \mathbf{r}_{Spoof} - \mathbf{S}_{Spoof} \left(\mathbf{S}_{Spoof}^H \mathbf{S}_{Spoof} \right)^{-1} \mathbf{S}_{Spoof}^H \mathbf{S}_{Spoof} \mathbf{a}_{Spoof} \\ &= \mathbf{r}_{Spoof} - \mathbf{S}_{Spoof} \left[\left(\mathbf{S}_{Spoof}^H \mathbf{S}_{Spoof} \right)^{-1} \mathbf{S}_{Spoof}^H \mathbf{S}_{Spoof} \right] \mathbf{a}_{Spoof}, \quad (63.10) \\ &= \mathbf{r}_{Spoof} - \mathbf{S}_{Spoof} \mathbf{a}_{Spoof} \\ &= \mathbf{S}_{Spoof} \mathbf{a}_{Spoof} - \mathbf{S}_{Spoof} \mathbf{a}_{Spoof} \\ &= \mathbf{0} \end{aligned}$$

by projecting the received signal \mathbf{r}_{IF} onto the complementary space \mathbf{H}_C , we have

$$\begin{aligned}
 \mathbf{r} &= \mathbf{H}_C \mathbf{r}_{IF} = (\mathbf{I} - \mathbf{H}) \mathbf{r}_{IF} \\
 &= (\mathbf{I} - \mathbf{H}) \mathbf{r}_{Auth} + (\mathbf{I} - \mathbf{H}) \mathbf{r}_{Spoof} + (\mathbf{I} - \mathbf{H}) \mathbf{n}. \\
 &= (\mathbf{I} - \mathbf{H}) \mathbf{r}_{Auth} + \mathbf{0} + (\mathbf{I} - \mathbf{H}) \mathbf{n} \\
 &= (\mathbf{I} - \mathbf{H}) \mathbf{r}_{Auth} + (\mathbf{I} - \mathbf{H}) \mathbf{n}
 \end{aligned}
 \tag{63.11}$$

Because the cross-correlation of the PRN codes between different satellite is very small and the self-correlation of the PRN code is also very small when the code delay does not match, the above projection result approximatively equals as

$$\begin{aligned}
 \mathbf{r} &= (\mathbf{I} - \mathbf{H}) \mathbf{r}_{Auth} + (\mathbf{I} - \mathbf{H}) \mathbf{n} \\
 &\approx \mathbf{r}_{Auth} + \mathbf{n},
 \end{aligned}
 \tag{63.12}$$

which means the spoofing signals have been successfully mitigated after the projection operation.

Figure 63.1 shows the structure of the receiver in detail and the following five steps present the processing procedure for the GNSS receiver to eliminate spoofing attack from the received signals:

- Step 1 Achieve spoofing detection, evaluate which satellites are under spoofing attack;
- Step 2 Acquire, track and decode the spoofing signals; obtain the PRN code delays, navigation data, carrier frequencies and carrier phases of spoofing signals;
- Step 3 Make the received signals through the spoofing mitigator which is shown as Fig. 63.2; construct the information matrix with the acquired parameters of spoofing signals;
- Step 4 Build the spoofing subspace projection matrix;
- Step 5 Project the received signal onto the spoofing subspace; subtract the projection result from the received signal.

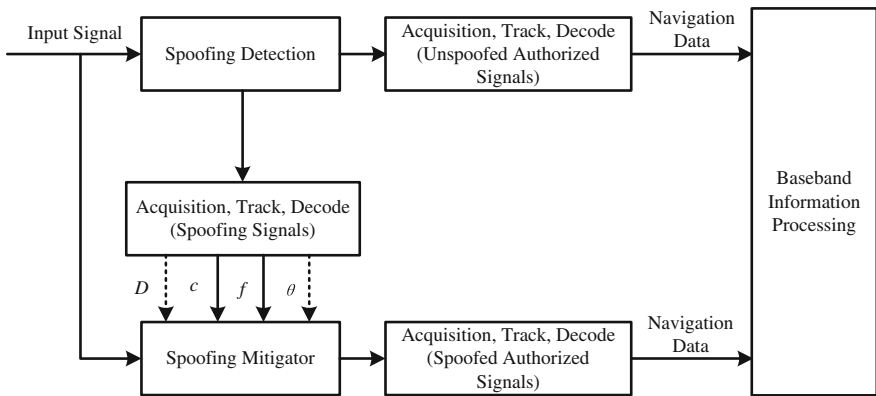


Fig. 63.1 The structure of the GNSS receiver

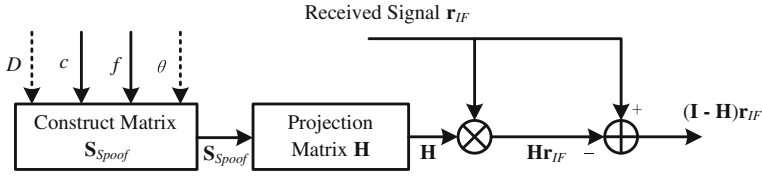


Fig. 63.2 The structure of the spoofing signal mitigator

When all the five steps are achieved, the spoofing signals will be mitigated, moreover, the receiver can observe the spoofed authorized signals.

63.3 Performance Analysis

In this section, we will present the relation between the performance of the spoofing mitigation algorithm and the estimated parameters of spoofing signals.

63.3.1 Carrier Phase

According the construction of the information matrix, Eq. (63.7) also can be re-written as

$$\begin{aligned}
 \mathbf{S}_{Spoof} &= [\hat{\mathbf{s}}_{Spoof}^1, \hat{\mathbf{s}}_{Spoof}^2, \dots, \hat{\mathbf{s}}_{Spoof}^M] \Theta = \hat{\mathbf{S}} \Theta \\
 \hat{\mathbf{s}}_{Spoof}^i &= \begin{bmatrix} d_{Spoof}^i(t_1) C_{Spoof}^i(t_1) e^{j(2\pi f_{Spoof}^i t_1)} \\ d_{Spoof}^i(t_2) C_{Spoof}^i(t_2) e^{j(2\pi f_{Spoof}^i t_2)} \\ \vdots \\ d_{Spoof}^i(t_L) C_{Spoof}^i(t_L) e^{j(2\pi f_{Spoof}^i t_L)} \end{bmatrix}_{L \times 1}, \quad (63.13)
 \end{aligned}$$

where Θ is the carrier phase matrix which denotes the initial carrier phases of spoofing signals and is given by

$$\Theta = \text{diag}\{e^{j\theta_{Spoof}^1}, e^{j\theta_{Spoof}^2}, \dots, e^{j\theta_{Spoof}^M}\}. \quad (63.14)$$

Thus, the spoofing space projection matrix \mathbf{H} is re-written as

$$\begin{aligned}
\mathbf{H} &= \mathbf{S}_{Spoof} \left(\mathbf{S}_{Spoof}^H \mathbf{S}_{Spoof} \right)^{-1} \mathbf{S}_{Spoof}^H \\
&= \left(\hat{\mathbf{S}} \Theta \right) \left\{ \left(\hat{\mathbf{S}} \Theta \right)^H \left(\hat{\mathbf{S}} \Theta \right) \right\}^{-1} \left(\hat{\mathbf{S}} \Theta \right)^H \\
&= \left(\hat{\mathbf{S}} \Theta \right) \left\{ \Theta^H \hat{\mathbf{S}}^H \hat{\mathbf{S}} \Theta \right\}^{-1} \left(\Theta^H \hat{\mathbf{S}}^H \right) \\
&= \left(\hat{\mathbf{S}} \Theta \right) \left\{ \Theta^H \left(\hat{\mathbf{S}}^H \hat{\mathbf{S}} \right) \Theta \right\}^{-1} \left(\Theta^H \hat{\mathbf{S}}^H \right). \tag{63.15} \\
&= \left(\hat{\mathbf{S}} \Theta \right) \left\{ \Theta^{-1} \left(\hat{\mathbf{S}}^H \hat{\mathbf{S}} \right)^{-1} \left(\Theta^H \right)^{-1} \right\} \left(\Theta^H \hat{\mathbf{S}}^H \right) \\
&= \hat{\mathbf{S}} \left(\Theta \Theta^{-1} \right) \left(\hat{\mathbf{S}}^H \hat{\mathbf{S}} \right)^{-1} \left\{ \left(\Theta^H \right)^{-1} \Theta^H \right\} \hat{\mathbf{S}}^H \\
&= \hat{\mathbf{S}} \left(\hat{\mathbf{S}}^H \hat{\mathbf{S}} \right)^{-1} \hat{\mathbf{S}}^H
\end{aligned}$$

The above equation shows that the carrier phase matrix Θ is independent with the spoofing space projection matrix \mathbf{H} . Therefore, the carrier phases of spoofing signals can be neglected when acquiring the parameters of spoofing signals. However, the precondition for the validity of Eq. (63.13) is that the complex signal processing is applied in GNSS receiver. So, when I/Q down-conversion mixer is utilized in GNSS receiver, the carrier phases of spoofing signals are needless, whereas, when only single channel down-conversion mixer is equipped, complex signal processing can not be realized and the carrier phases of spoofing signals are essential.

63.3.2 Navigation Data

Choose the proper data length L to keep the navigation data of the spoofing signals in constant in per projection operation:

$$d_{Spoof}^i(t_1) = d_{Spoof}^i(t_2) = \dots = d_{Spoof}^i(t_L) = D_{Spoof}^i, \tag{63.16}$$

then, the information matrix can be constructed as

$$\begin{aligned}
\mathbf{S}_{Spoof} &= \left[\hat{\mathbf{S}}_{Spoof}^1, \hat{\mathbf{S}}_{Spoof}^2, \dots, \hat{\mathbf{S}}_{Spoof}^M \right] \mathbf{D} = \hat{\mathbf{S}} \mathbf{D} \\
\hat{\mathbf{S}}_{Spoof}^i &= \begin{bmatrix} C_{Spoof}^i(t_1) e^{j(2\pi f_{Spoof}^i t_1)} \\ C_{Spoof}^i(t_2) e^{j(2\pi f_{Spoof}^i t_2)} \\ \vdots \\ C_{Spoof}^i(t_L) e^{j(2\pi f_{Spoof}^i t_L)} \end{bmatrix}_{L \times 1}, \tag{63.17}
\end{aligned}$$

where \mathbf{D} is the navigation data matrix which represents the navigation data of spoofing signals and is given by

$$\mathbf{D} = \text{diag}\{D_{Spoof}^1, D_{Spoof}^2, \dots, D_{Spoof}^M\}. \quad (63.18)$$

Thus, the spoofing space projection matrix \mathbf{H} is presented as

$$\begin{aligned} \mathbf{H} &= \mathbf{S}_{Spoof} \left(\mathbf{S}_{Spoof}^H \mathbf{S}_{Spoof} \right)^{-1} \mathbf{S}_{Spoof}^H \\ &= (\hat{\mathbf{S}}\mathbf{D}) \left\{ (\hat{\mathbf{S}}\mathbf{D})^H (\hat{\mathbf{S}}\mathbf{D}) \right\}^{-1} (\hat{\mathbf{S}}\mathbf{D})^H \\ &= (\hat{\mathbf{S}}\mathbf{D}) \left\{ \mathbf{D}^H \hat{\mathbf{S}}^H \hat{\mathbf{S}} \mathbf{D} \right\}^{-1} (\mathbf{D}^H \hat{\mathbf{S}}^H) \\ &= (\hat{\mathbf{S}}\mathbf{D}) \left\{ \mathbf{D}^H (\hat{\mathbf{S}}^H \hat{\mathbf{S}}) \mathbf{D} \right\}^{-1} (\mathbf{D}^H \hat{\mathbf{S}}^H) \\ &= (\hat{\mathbf{S}}\mathbf{D}) \left\{ \mathbf{D}^{-1} (\hat{\mathbf{S}}^H \hat{\mathbf{S}})^{-1} (\mathbf{D}^H)^{-1} \right\} (\mathbf{D}^H \hat{\mathbf{S}}^H). \\ &= \hat{\mathbf{S}} (\mathbf{D}\mathbf{D}^{-1}) (\hat{\mathbf{S}}^H \hat{\mathbf{S}})^{-1} \left\{ (\mathbf{D}^H)^{-1} \mathbf{D}^H \right\} \hat{\mathbf{S}}^H \\ &= \hat{\mathbf{S}} (\hat{\mathbf{S}}^H \hat{\mathbf{S}})^{-1} \hat{\mathbf{S}}^H \end{aligned} \quad (63.19)$$

So, we prove that the navigation data matrix \mathbf{D} is independent with the spoofing space projection matrix \mathbf{H} when choosing the proper L to keep the navigation data of the spoofing signals in constant in per projection operation. Under this condition, the navigation data of spoofing signals are needless for the subspace projection algorithm. However, if the navigation data for some spoofing signals are changing in once projection operation, Eq. (63.17) is false, so the navigation data is essential to construct the information matrix of spoofing signals.

In conclusion, by taking the complex signal processing and keeping the navigation data in constant in per projection operation, the carrier phases and navigation data of spoofing signals are needless to construct the information matrix \mathbf{S}_{Spoof} which is shown as the dash line in Figs. 63.1 and 63.2.

63.4 Numerical Analysis and Simulation

We have investigated the spoofing mitigation algorithm based on subspace projection in theory. In this section, the acquisition of BeiDou B1I signal will be tested to verify the validity of the proposed algorithm. Simulation parameters are set in Table 63.1, and the acquisition is 1 ms. In the simulation, PRN 4 is chosen as the spoofed satellite, so the received signals consist of one spoofing signal and one authorized signal.

Table 63.1 Simulation parameters

Parameter	Value
PRN	4
IF	3.25 MHz
Sample frequency	8 MHz
C/N_0 for authorized signal	44 dB-Hz
C/N_0 for spoofing signal	50 dB-Hz
Length of projection operation	500 Samples
Total data length	200 ms

The acquisition results before spoofing mitigation and after spoofing mitigation for PRN 4 are respectively shown in Figs. 63.3 and 63.4. In the simulation, for spoofing signal, the Doppler frequency bias and the code delay are 1 kHz and 5120 samples, whereas, the Doppler frequency bias and the code delay of authorized signal are 0 Hz and 2354 samples. Before the spoofing mitigation, as shown in Fig. 63.3, the results consist of two correlation peaks. Since the spoofing signal is 6 dB stronger than the authorized signal, the receiver will generally judge the correlation peak of spoofing signal as the final acquisition result. However, after mitigating the spoofing signal, only the correlation peak of authorized signal exists which verify the validity of the spoofing mitigation algorithm based on subspace projection.

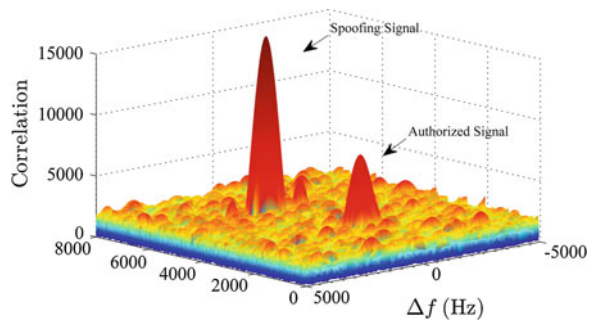
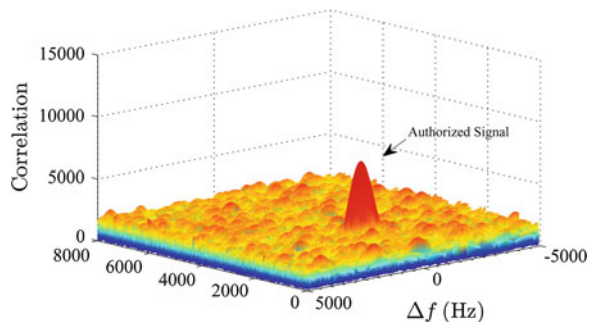
Fig. 63.3 The acquisition for PRN 4 before spoofing mitigation**Fig. 63.4** The acquisition for PRN 4 after spoofing mitigation

Fig. 63.5 The acquisition before spoofing mitigation (Same code delay)

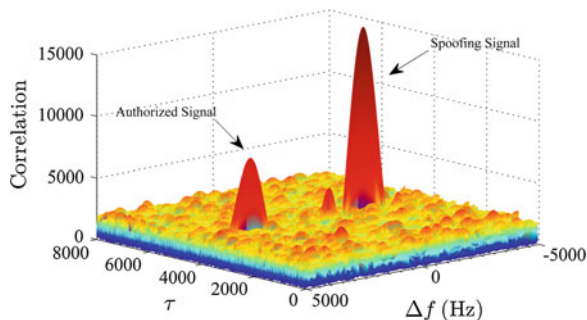
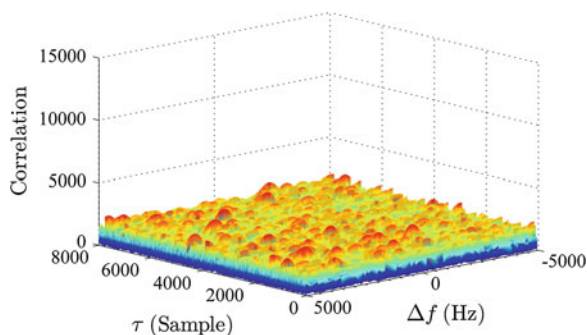


Fig. 63.6 The acquisition after spoofing mitigation (Same code delay)



For the PRN codes, the maximum self-correlation when the code delays are matching is much larger than the self-correlation when the code delays are mismatching, and this is the essence of the spoofing mitigation algorithm based on subspace projection. Consequently, when the spoofing signal and the authorized signal have same code delays, after mitigating the spoofing by the proposed algorithm, the authorized signal will be eliminated too. The simulation in Figs. 63.5 and 63.6 verify this deduction. In the simulation, for spoofing signal, the Doppler frequency bias and the code delay are -2 kHz and 4032 samples, whereas, for authorized signal, the Doppler frequency bias and the code delay are 3 kHz and 4032 samples. With the comparison between the acquisition results in Figs. 63.5 and 63.6, after processed by the proposed method, both spoofing signal and authorized signal are eliminated together. However, as the length of GNSS PRN code is very large and the code delay for the signal accessing receiver are independent, the probability that spoofing signal and authorized signal share the same code delay is negligible, for BeiDou B1I, the probability is $1/2046$.

63.5 Conclusion

In this study, we have proposed a spoofing mitigation algorithm based on subspace projection. The spoofing attack can be eliminated effectively with few estimated parameters. By taking the complex signal processing and keeping the navigation data in constant in per projection operation, the carrier phases and navigation data of spoofing signals are also unnecessary for the proposed algorithm. Moreover, this algorithm is independent with the number of antenna and also can be utilized in typical single antenna receiver.

Acknowledgments This research is sponsored by National High-technology Research and Development Program (863 Program) of China (project no. 2012AA120802) and National Natural Science Foundation of China (Grant No. 61401119), also sponsored by Harbin Distinguished Academic Leader Program (Grant No. 2014RFXXJ002).

References

1. Scott L (2003) Anti-spoofing and authenticated signal architectures for civil navigation systems. In: ION GPS/GNSS 2003, Portland, OR, USA, pp 1543–1552, Sept 2003
2. Humphreys TE (2013) Detection strategy for cryptographic GNSS anti-spoofing. *IEEE Trans Aerosp Electron Syst* 49(2):1073–1090
3. Wullems C (2012) A spoofing detection method for civilian L1 GPS and the E1-B Galileo safety of life service. *IEEE Trans Aerosp Electron Syst* 48(4):2849–2864
4. O’Hanlon BW, Psiaki ML (2012) Real-time spoofing detection using correlation between two civil GPS receivers. In: ION GNSS 2012, Nashville, TN, USA, pp 3584–3590, Sept 2012
5. Han S, Luo D, Meng W, Li C (2014) A novel anti-spoofing method based on particle filter for GNSS. In: ICC 2014. IEEE, Sydney, AUS, pp 5413–5418, June 2014
6. McDowell CE (2007) GPS spoofer and repeater mitigation system using digital spatial nulling. US Patent 7250903 B1
7. Daneshmand S, Jafamia-Jahromi A, Broumandon A, Lachapelle G (2012) A low-complexity GPS anti-spoofing method using a multi-antenna array. In: ION GNSS 2012, Nashville, TN, USA, pp 1233–1243, Sept 2012
8. Scharf LL, Friedlander B (1994) Matched subspace detectors. *IEEE Trans Sig Process* 42(8):2146–2157
9. Chen L, Meng W, Han S, Liu E (2012) A cross-correlation mitigation method based on subspace projection for GPS receiver. In: ION GNSS 2012, Nashville, TN, USA, pp 1428–1434, Sept 2012

Chapter 64

A Quick A-BDS Location Method Based on Characteristics of GEO Satellite and Ridge Estimate

Shourang Jing, Wenxiang Liu, Ling Yong and Guangfu Sun

Abstract The calculation of traditional A-GPS time-free positioning method will be very complex without the approximate position. But hybrid constellation was adopted by BeiDou Navigation Satellite System (BDS). And the GEO satellite of BDS has high speed of NAV data rate. So a fast positioning method for BDS receiver based on characteristics of GEO satellite and ridge estimate was proposed in this paper. First, an approximate position was got by using ridge estimate with GEO constellation. The ridge estimation can solve problem of coefficient matrix ill-conditioned. Then the signal transmission time of MEO/IGSO satellite was restored with the approximate position. A simulation environment was built by using BDS broadcast ephemeris information. The white noise with 6 m standard deviation was added to pseudoranges. The success rate of the quick location method is big than 99.65 % in China surrounding area. And about 80 % of China surrounding area can 100 % guarantee to restore a complete satellite signal emission time and obtain an accurate position.

Keywords BeiDou navigation satellite system (BDS) · GEO constellation · Signal transmission time recovery · Ridge estimate

64.1 Introduction

TTF (Time to First Fix, TTF) is an important performance indicator of navigation receiver. And the factors which affecting the TTF include satellite ephemeris acquisition time and pseudoranges acquisition time. The broadcast ephemeris or extended ephemeris can be stored in the receivers. Or the receiver autonomous forecast the extended ephemeris [1–3]. The pseudoranges are different of the

S. Jing (✉) · W. Liu · L. Yong · G. Sun
College of Electronic Science and Engineering, National University of Defense Technology,
Changsha 410073, China
e-mail: hanchongjsr@163.com

© Springer-Verlag Berlin Heidelberg 2015
J. Sun et al. (eds.), *China Satellite Navigation Conference (CSNC) 2015 Proceedings: Volume I*, Lecture Notes in Electrical Engineering 340,
DOI 10.1007/978-3-662-46638-4_64

739

receiver time and the satellite signal transmission time. And The pseudoranges is generally constructed from two parts, one part was called millisecond pseudoranges which is got through frame synchronization and bit synchronization, the other part was called sub-millisecond pseudoranges which is obtained by pseudo code phase measurements [4]. In the traditional positioning method, the receiver calculates the position until got the full pseudoranges by code phase measurements and frame synchronization. Therefore, restriction TTFF is the time to get full pseudoranges when the ephemeris information is known.

Generally speaking, there four steps to complete frame synchronization [5]. First, Search for either upright or inverted preamble. Second, check the parity bits are right or not. Third, if parity passes, it verifies the handover word (HOW). At the end, a final check on the next telemetry (TLM) word and HOW solidifies the frame synchronization. So it is generally spend 6–12 s to complete the frame synchronization for GPS receiver. To improve the TTFF performance, time-free positioning technique was proposed. The position can be estimated in a receiver using only code phase measurements [6, 7]. However, the a priori receiver position requirement to accuracy of approximately half a GNSS code chip (approximately 150 km for GPS C/A code). Otherwise, the calculation will increase sharply and difficult to use [8, 9]. A fast position search method from the signal transmission time dimension was proposed in literature [10]. But it requires high-precision receiver clock auxiliary. A new quick A-BDS location method based on characteristics of Geostationary Earth Orbit (GEO) satellite and ridge estimate was proposed in this paper. It used the characteristic of GEO satellites in BeiDou Navigation Satellite System (BDS) which has high NAV message rate. And the method does not require additional approximate position or receive clock assistance. The approximate position can be estimated using GEO constellation. It can be directly applied BDS receiver implementations, can effectively improve the performance of TTFF.

64.2 Quick Location Method for BDS Receiver

The BDS formally provide regional service in December 2012. Compared to the GPS, the constellation of BDS was design as a hybrid system. As of today, there are five GEO satellites, four Medium Earth Orbit (MEO) satellites and five Inclined Geosynchronous Satellite Orbit (IGSO) satellites in orbit [11]. The NAV message rate of GEO is 500 bps. The duration of one message frame is only 0.6 s. While NAV message rate of the MEO/IGSO is 50 bps. And the duration of one message frame is 6 s. Therefore, after the signal acquisition, the GEO satellite can quickly complete message frame synchronization. At the same time, there are five GEO satellites BeiDou navigation system. And generally realize positioning at least need four satellites. So it is possible to positioning by using GEO constellation. Therefore, this paper attempts to propose a quick location method for BDS receiver with

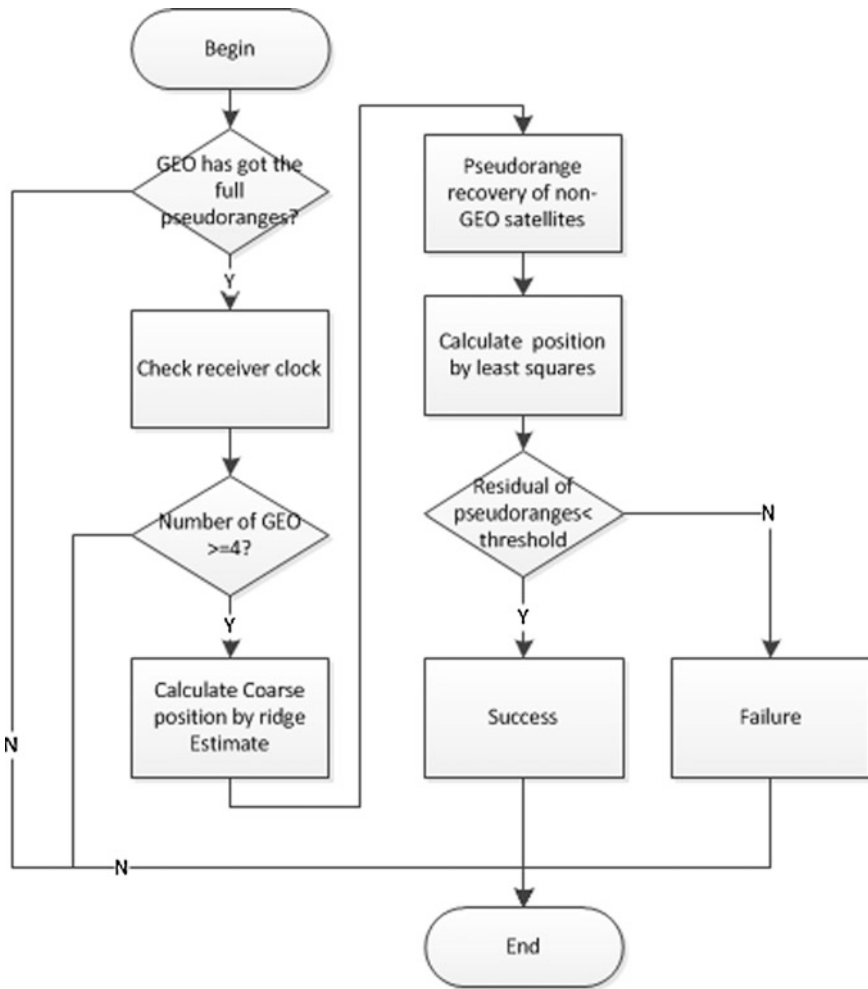


Fig. 64.1 Flow chart of the quick location method based on coarse positioning by GEO constellation

this characteristic. First the approximate position was got by ridge estimate using only GEO constellation after frame synchronization. Then the signal transmission time of MEO/IGSO satellite was recovered according to the approximate position and their code phase measurements. Finally, the precise position was calculated by using all visible satellites. In addition, it easy to point out the satellite pseudorange recovery is correct or not through posteriori residuals. The specific flow chart of the quick location method based on coarse positioning by GEO constellation is shown in below Fig. 64.1.

64.2.1 Coarse Positioning with Ridge Estimate

The offset Δx in the user's position and time bias relative to the linearization point is related to the offset in the error-free pseudorange values $\Delta \rho$ by the relation:

$$\Delta \rho = H \Delta x + \varepsilon \quad (64.1)$$

The vector Δx has four components. The first three are the position offset of the user from the linearization point; the fourth is the offset of the user time bias from the bias assumed in the linearization point. $\Delta \rho$ is the vector offset of the error-free pseudorange value corresponding to the user's actual position and the pseudorange values that correspond to the linearization point. ε is normally distributed error vector with zero mean and variance $\sigma^2 I$. Typically if there are more than four satellites, the method of least squares can be used to solve formula (64.1) for Δx . But if the satellites are all GEO, the normal equation coefficients may be ill-conditioned. Then minimizing the sum of residual squares may not guarantee that the variances of the parameter estimates are small. The ridge estimate is an estimated decrease of the mean square error method biased estimate. The basic idea is to use the original least squares estimation of mathematical models, but plus a small positive number in the diagonal of equation coefficient matrix. That ridge estimate of Δx can be expressed as

$$\Delta \hat{x}(k) = (H^T H + kI)^{-1} H^T \Delta \rho \quad (64.2)$$

wherein, k is the ridge parameter, I is identity matrix.

By the formula (64.2), we can get the following formula (64.3).

$$\begin{aligned} \Delta \hat{x}(k) &= (H^T H + kI)^{-1} (H^T H) (H^T H)^{-1} H^T \Delta \rho \\ &= (H^T H + kI)^{-1} (H^T H) \Delta \hat{x} \\ &= (I - k(H^T H + kI)^{-1}) \Delta \hat{x} \end{aligned} \quad (64.3)$$

where the $\Delta \hat{x}$ is the result of least squares. The mean and variance of ridge estimate can be expressed as

$$E(\Delta \hat{x}(k)) = (I - k(H^T H + kI)^{-1}) \Delta x \quad (64.4)$$

$$Var(\Delta \hat{x}(k)) = \sigma^2 (H^T H + kI)^{-1} (H^T H) (H^T H + kI)^{-1} \quad (64.5)$$

The desired distance between ridge estimate and true value can be expressed as

Table 64.1 Longitude of BDS GEO satellites

Satellite ID	G1	G2	G3	G4	G5
Longitude	140°E	80°E	110.5°E	160°E	58.75°E

$$\begin{aligned}
 E(S_k^2) &= E[(\Delta\hat{x}(k) - \Delta x)^T (\Delta\hat{x}(k) - \Delta x)] \\
 &= \sigma^2 \sum_{i=1}^4 \lambda_i / (\lambda_i + k)^2 + k^2 \Delta x^T (H^T H + kI)^{-2} \Delta x
 \end{aligned}
 \tag{64.6}$$

where in, λ_i is the eigenvalues of $H^T H$ matrix. Because $\lambda_i / (\lambda_i + k)^2 \leq 1 / (4 \times k)$ and the Δx of k -th estimate is difference between $(k-1)$ -th estimate and true value. If the iterative is convergence, even the eigenvalues are small, the position error will be less than 150 km if select an appropriate ridge parameter.

Although the ridge estimate can effectively solve the problem of matrix ill-conditional in least squares estimate, but its application still need enough observation information. The visibility of GEO constellation was analysed as follow.

The BDS contains five GEO satellites. The GEO satellite orbit altitude is about 35,786 km. And the longitude of the five GEO satellites are 58.75°, 80°, 110.5°, 140° and 160°, as showing in the following Table 64.1.

The GEO constellation visibility in China surrounding area (latitude 5°–55°, longitude 70°–140°) was traversed with 1°. When elevation cut-off angle is 0°, the visual satellite number of GEO is shown in Fig. 64.2. The figure shows that in China and the surrounding areas, most of the region can observe five GEO

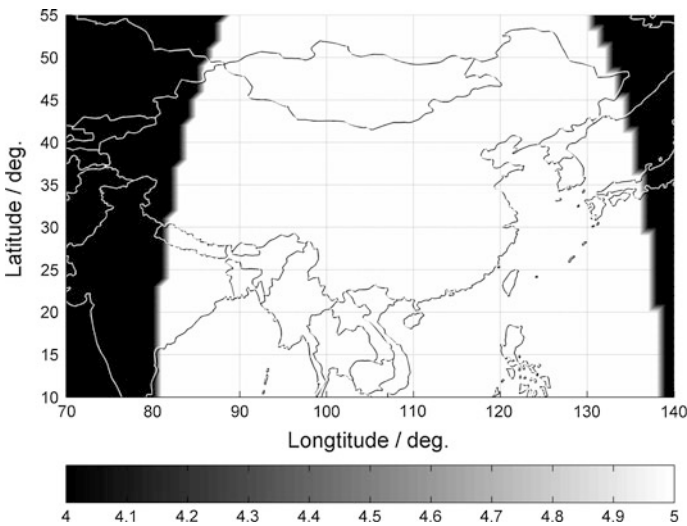


Fig. 64.2 The visual satellite number of GEO in China area

satellites. Part of the border region can just observe four GEO satellites. So it possible calculates coarse position with the GEO constellation by ridge estimate.

64.2.2 Full-Pseudorange Recovery

The i th satellite’s pseudorange can be expressed as

$$\begin{aligned}
 \rho_i &= c(t^r - t_i^s) = c(t^r - t_i^{ms,s} - t_i^{chip,s}) \\
 &= r_i(t_i^s, t^r) + ct_d^r + \varepsilon_i(t^r) \\
 &= N_i \cdot c/1e3 + \rho_i^{frca}
 \end{aligned}
 \tag{64.7}$$

wherein, t_i^s is signal transmission time, t^r is receiver time, c is the speed of light, $t_i^{ms,s}$ is the integer millisecond part of signal transmission time, $t_i^{chip,s}$ is fractional milliseconds part of the signal transmission time, $r_i(t_i^s, t^r)$ is the range from satellite to receiver, t_d^r is the user time bias, $\varepsilon_i(t^r)$ contains the measurement errors, including un-modeled atmospheric delays and so on, N_i represents an integer number of milliseconds pseudorange and ρ_i^{frca} representing sub-milliseconds pseudorange. We can get the sub-milliseconds pseudorange by formula $\rho_i^{frca} = c \times \text{mod}\left((t^r - t_i^{chip,s}), 1e - 3\right)$ with pseudo-code phase measurements. Wherein, the mod is modulus operation. Therefore, the pseudorange (full pseudoranges and sub-millisecond pseudoranges) can be written as follows:

$$\begin{cases}
 \rho_i = r_i(t_i^s, t^r) + ct_d^r + \varepsilon_i(t^r) \\
 N_j \cdot c/1e3 + \rho_j^{frca} = r_j(t_j^s, t^r) + ct_d^r + \varepsilon_j(t^r)
 \end{cases}
 \tag{64.8}$$

So the N_j can be calculated by formula as follows:

$$N_j \approx \left(\rho_i - r_i(t_i^s, t^r) + r_j(t_j^s, t^r) - \rho_j^{frca}\right) \cdot 1e3/c
 \tag{64.9}$$

Following the van Diggelen technique described in [6]. The method of pseudorange recovery of non-GEO satellites is shown below if the coarse position was known (Fig. 64.3).

64.3 Simulation and Analysis

By using BDS broadcast ephemeris data (March 17, 2014–March 24, 2014), we build a simulation environment to check the validity of the quick location method. The noise with zero mean and 6 m standard deviation was added to pseudoranges.

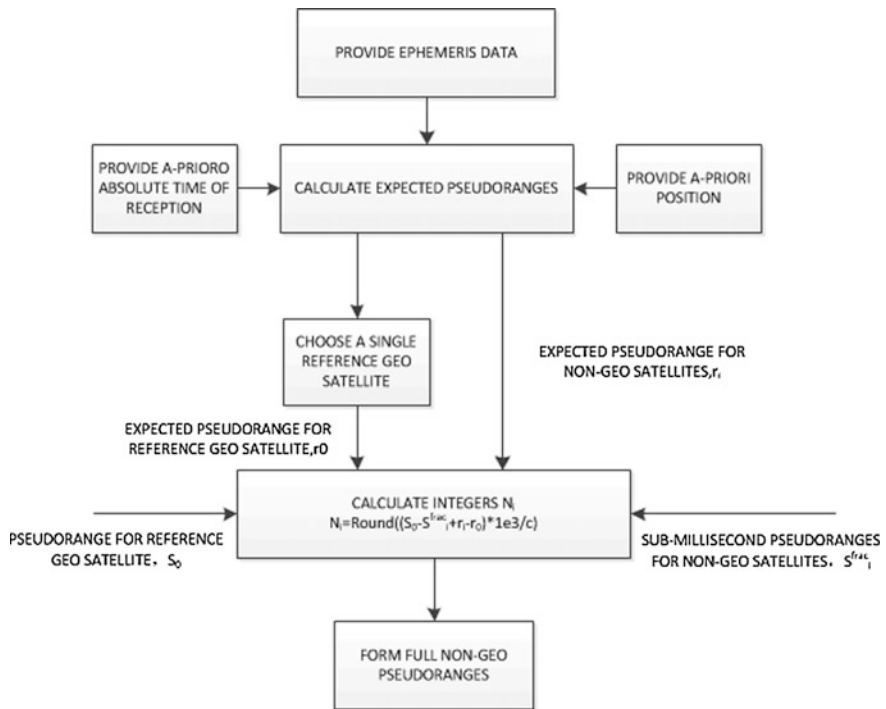


Fig. 64.3 Pseudorange recovery of non-GEO satellites

The Table 64.2 shows the success rate of rapid positioning method with least squares and ridge estimate coarse positioning with GEO constellations in some city of China. The ridge parameter was set as $1e-7$. The geometric dilution of precision (GDOP) of visible GEO constellation in Taxkorgan is too bad to estimate a fine approximate position which was used to restore pseudorange of non-GEO satellites. So the success rate of Taxkorgan cannot achieve 100 %.

Table 64.2 Success rate for least squares and ridge estimate

Station position	Success rate	
	Least squares (%)	Ridge estimate (%)
Suiyang (53°N,122°E)	100.0	100.0
Beijing (40°N,116°E)	100.0	100.0
Xiamen (24°N,118°E)	100.0	100.0
Qiongzong (19°N,110°E)	100.0	100.0
Urumqi (43°N,87°E)	100.0	100.0
Taxkorgan (38°N,75°E)	99.23	99.86

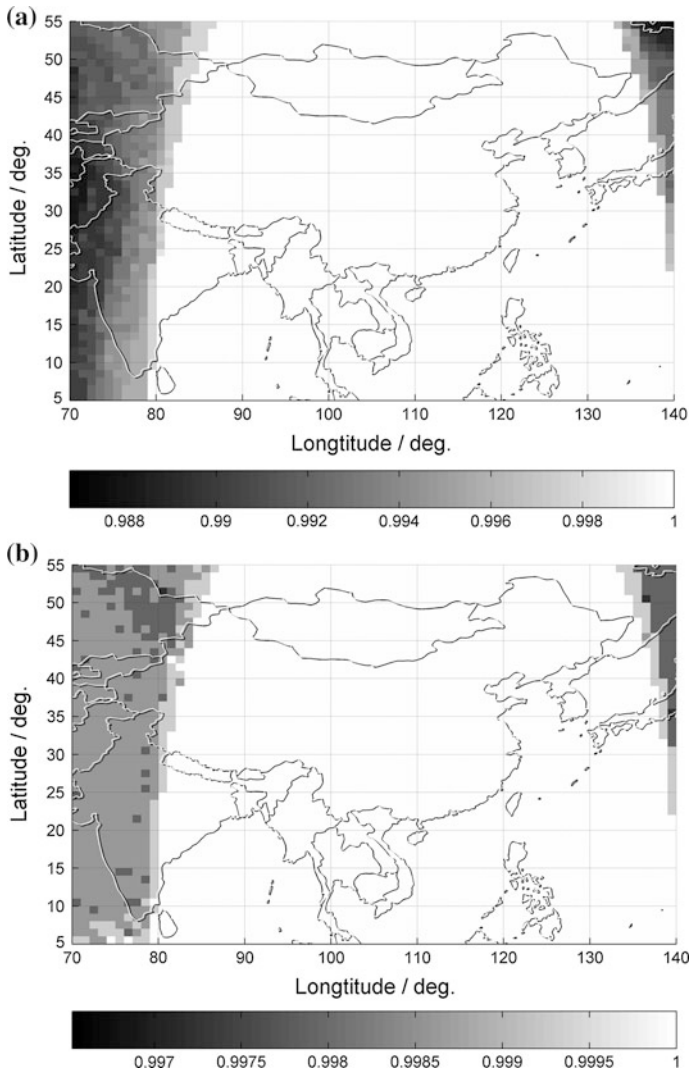


Fig. 64.4 Success rate in China area. **a** Least square. **b** Ridge estimate

In the case of 1° intervals traverses user position in China, the success rate rapid positioning method with least squares and ridge estimate coarse positioning are shown in Fig. 64.4.

From the simulation we can got the results:

1. the success rate of fast positioning method with ridge estimate is more than 99.65 % in China surrounding area. This is a little better than fast positioning with least-squares estimate.

2. 79.23 % of China surrounding area can 100 % guarantee to recovery full-pseudoranges of non-GEO and success obtain the accurate position.

64.4 Conclusions

In this paper, a new quick location method for BDS receiver with ridge estimate based on characteristics of GEO satellite was proposed. It used the high NAV data rate of GEO satellites in BDS to improve receiver's TTFF. The method can calculate receiver's position after message frame synchronization of GEO and code phase measurement of non-GEO. The simulation shows the success rate of the quick location method is big than 99.65 % in China area. And about 80 % of China surrounding area can 100 % guarantee to recovery full-pseudorange of non-GEO and obtain an accurate position.

References

1. Lundgren D, Van Diggelen F (2005) Assistance when there's no assistance: long-term orbit technology for cell phones, PDAs. *GPS world*
2. Mattos P (2008) Self-assisted GPS: no server, no connection requirement. *GPS World*
3. Ahn J, Song HY, Sung S et al (2010) An efficient GPS parameter prediction method using GPS ephemeris patterns for Self-Assisted GPS. In: *International conference on control, automation and systems 2010*, Gyeonggi-do, Korea
4. Kaplan ED, Hegarty CJ (2006) *Understanding GPS: principles and applications*, 2nd edn. Artech House, Norwood
5. Gang Xie (2009) *Principles of GPS and receiver design*. Publishing House of Electronics Industry, Beijing
6. Van Diggelen F (2002) Method and apparatus for time-free processing of GPS signals. US patent 6,417,801, 9 July 2002
7. Sirola N, Syrjärinne J (2002) GPS position can be computed without the navigation data. In: *Proceedings of ION GPS 2002*, pp 1613–1619
8. Sirola N (2006) Exhaustive global grid search in computing receiver position from modular satellite range measurements. *J Phys Conf Series IOP Publishing* 52(1):73–82
9. Hui CAO, Hong YUAN (2012) Method for time-of-transmission recovery based on assisted-GPS positioning. *Chin J Space Sci* 32(4):585–591
10. Wu P, Jing S, Liu W, Wang F (2013) A quick location method for high dynamic GNSS receiver based on time assistance. *Int J Comput Commun Control* 8(5):754–759
11. BeiDou Navigation Satellite System (2013) Signal in space interface control document open service signal (Version 2.0). China Satellite Navigation Office 2013.12

Chapter 65

Feasibility Analysis of GNSS Multi-constellation Positioning for Lunar Spacecraft

Lei Chen, Yangbo Huang, Wenxiang Liu and Gang Ou

Abstract With the development of deep space exploration technology, as the representative project of the Chinese lunar exploration, the possibility of using global navigation satellite system (GNSS) for deep space exploration spacecraft positioning has become a hot issue. Based on the existing GNSS research on high orbital spacecraft positioning, the feasibility of using GNSS multi-constellation for lunar orbit spacecraft positioning is deep analyzed. On condition of signal acquisition's lowest carrier to noise ratio (CNR) threshold, 21 dB Hz, two cases of signal receiving are analyzed from which GNSS satellite transmitting antenna beam's main lobe and side lobe. Simulation results show that when only receiving the beam main lobe signal of GNSS transmitting antenna, any single constellation or multi-constellation combination of GNSS cannot satisfy positioning of lunar spacecraft on the lunar revolution orbit for whole period (about 27 days). When signals from the main lobe and side lobe of the GNSS received, three constellations combination or more can satisfy positioning for the whole lunar orbit period. Conclusion is that GNSS multi-constellation combination method is possible to complete the mission of deep space exploration project for lunar spacecraft positioning on the simulated conditions.

Keywords Lunar spacecraft · Multi-constellation combined positioning · Carrier to noise ratio threshold · Main lobe · Side lobe

L. Chen · Y. Huang · W. Liu · G. Ou (✉)
College of Electronic Science and Engineering, National University
of Defense Technology, Changsha 410073, People's Republic of China
e-mail: ougang_nnc@163.com

L. Chen
e-mail: chenlei1025@nudt.edu.cn

65.1 Introduction

With the modernization of GPS (Global Position System), the establishment of the European Galileo Navigation System, the recovery of Russian GLONASS and the propulsion of Chinese BeiDou 2nd Generation Navigation System (BDS-2), Global Navigation Satellite Systems (GNSS) have been widely used on the field of land, sea, air and space.

In recent years, on-board experiments show that satellite navigation and positioning technology has been widely used in the Low Earth Orbit (LEO), Medium Earth Orbit (MEO) for satellite and spacecraft. The orbit determination precision has reach centimetre level (see [1–3]).

For Geostationary Earth Orbital (GEO) Satellite, Highly Eccentric Earth Orbital (HEEO) Satellite and High Earth Orbit (HEO) Satellite, the application of GNSS study also gradually going deeper.

Compared with the LEO orbit determination, the difficulties of HEO GNSS orbit determination [4] is less visible satellite number, weaker signal strength and different atmosphere transmission error. Reference [5] considered that GPS navigation satellite visibility for the users will be significantly less when the altitude of spacecraft is above 3000 km. Reference [6] took the satellite “Feng Yun II” as example to analyse the visibility of GEO orbit of GNSS satellites. Assuming that satellite visible represents signal available, the quantity of GEO orbit satellites can meet the demand of the orbit determination without considering the clock difference between different constellations. Reference [7] calculates carrier to noise ratio (CNR) of GPS receiver on HEO. On the condition of general CNR threshold of 33–35 dB Hz, 48 h’ simulation results indicate that GPS constellation is unable to meet the demand of real-time positioning. Reference [8] showed that GPS signal has stronger strength, batter visibility, higher dynamic and higher positioning accuracy on the spacecraft orbit perigee while has weaker signal strength, poorer visibility, lower dynamic and poorer positioning accuracy on spacecraft apogee. Improving receiver sensitivity can improve visibility on the condition of a determined spacecraft orbit. Improved receiver can acquire high dynamic GPS signals which has only 21 dB Hz CNR. Reference [9] verifies that multi-constellation integration navigation system can improve the positioning precision for GEO and HEO satellites. In recent years, a series of researching achievements [10–12] showed that the application of high sensitivity GNSS receiver on the GEO and HEO is feasible. The feasibility of the GNSS application in deep space orbit determination will be analysed below, especially for feasibility of lunar spacecraft orbit determination by considering the indicators below: single and multiple GNSS constellation visibility, CNR, etc.

65.2 Deep Space Orbit Simulation Platform Design

On October 24th, 2014, the Chinese lunar exploration project period III re-entry return flight succeeds, marked China has mastered the key technology of lunar spacecraft re-entry returns [13]. Chinese “Chang-e I” and “Chang-e II” missions use the speed and distance measure combined with VLBI (Very Long Baseline Interferometry) for determination of the lunar spacecraft orbits [14]. The existing system for lunar explorer navigating task used very large antenna (several meters to tens of meters in diameter), very complex and expensive ground radio system which must ensure to have reliable radio communication ability over hundreds of thousands of kilometres distances [15]. And lunar spacecraft based on GPS measurements limited to nearly area (below 10,000 km), can achieve the real-time navigation and high precision [16]. When the distance from detector to the centre of the earth is less than 12,000 km, positional deviation is less than 60 m, while more than 12,000 km, the position deviation is less than 300 m and speed deviation is less than 0.3 m/s [17]. The distance of the luna and the earth is about 385,000 km that published literatures haven’t involved the application of GNSS on the lunar orbit.

Since the lunar orbit influenced by the disturbing force of the earth and the sun, the parameters of the orbit are not fixed. We use the parameters from Ref. [18] which are averaged over a certain period of time for the simulation and calculation.

65.2.1 GNSS Constellation Characteristics

Table 65.1 indicates that GPS, Galileo and GLONASS constellation are all composed of MEO constellation while BDS is a hybrid constellation which consists of GEO, MEO and IGSO. Unlike the low orbit, the GNSS signal for spacecraft on the high orbit is “sparse” [19]. Especially for the orbit height of spacecraft is above the MEO constellation, the current researches show that, in high orbit, visible satellites quantity is rarely reach four or above, and the received signal is very weak. In this condition, receiver’s acquisition and tracking ability drops and cannot provide a stable positioning accuracy. The domestic and external technique is still in exploring [20]. Doctor Xie has done some researches in his doctoral thesis [8] about HEC autonomous orbit determination by GPS. In this paper, the problem of high

Table 65.1 Characteristic of GNSS constellation

GNSS	Constellation type	Orbital altitude (km)
GPS	MEO	20,200
BDS	GEO, MEO, IGSO	21,528(MEO)/35,786(IGSO)/35,786(GEO)
Galileo	MEO	23,222
GLONASS	MEO	19,100

orbit satellite positioning will expand to the deep space applications, attempts to prove the feasibility of positioning for the lunar spacecraft using the GNSS in the Chinese lunar exploration project.

65.2.2 Analysis of Geometric Visibility Boundary Parameter

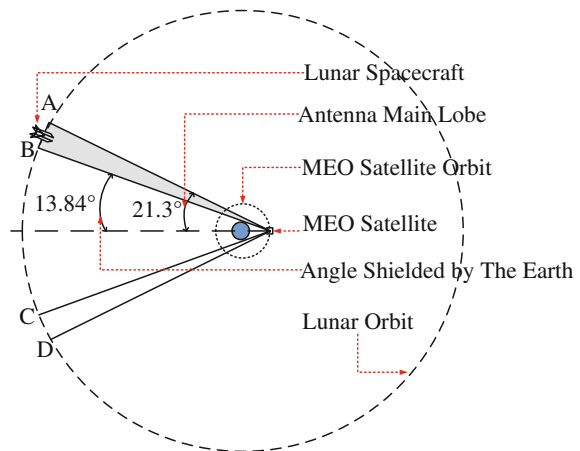
Currently, even the Galileo system construction is not complete that cannot reflect the actual performance of the system, available in orbit satellite less, with the quickening, financial support and construction progress in recent years, the completion of each construction is coming soon. Therefore, for BDS, Galileo and GLONASS simulations are processed with standard constellation design.

The revolve cycle of the luna around the earth (Sidereal month) is about 27.32166 days. The revolves cycle of the luna (synodic month) which considering the earth's revolves is 29.530488 days [21]. The research object in this paper is the lunar orbit and the GNSS constellation simulation; therefore simulations only need to be processed under the period of the sidereal month (27.32166 days). Simulation start time: 2008/07/01 12:00:00.000, simulation stop time: 2008/07/28 19:43:11.424.

The spacecraft in deep space is far away from the earth, can only receive the signal of the satellite antenna from the other side of the earth. The geometric relationship is shown in Fig. 65.1. So the lunar explorer should apply down-looking antenna.

Figure 65.1 shows position relation of lunar spacecraft and MEO satellite, in this chapter and the next chapter, the visibility in simulation is based on the GNSS main lobe signal received and assuming the main lobe signal is to point to the centre of the earth. When the lunar spacecraft running to highlighted region, whose angle is greater than the earth shade angle and less than signal radiation angle. In AB and CD segment, lunar spacecraft can receive the GNSS constellation satellites' signal;

Fig. 65.1 Sketch position relation of lunar spacecraft and GNSS



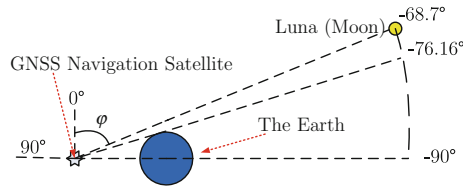


Fig. 65.2 Sketch elevation of the navigation satellite to the lunar spacecraft

In BC segment, signal under shade cannot reach the earth. And on the other segment, due to the angle of navigation satellite antenna beam forming limit, lunar spacecraft cannot receive navigation signals.

According to the antenna pattern of GPS [22], the main lobe range of GPS signal is $0^\circ \pm 13.84^\circ$ and the side lobe ranges are $21.3^\circ\text{--}47^\circ$ and -21.3° to -47° .

Therefore, no account of side lobe signal, lunar spacecraft’s GPS MEO satellites observable segment are $+13.84^\circ \leq \theta \leq +21.3^\circ$ and $-21.3^\circ \leq \theta \leq -13.84^\circ$ corresponding to antenna beam region. In STK software, the GPS satellite elevation angle takes centre of the earth as the centre of the radial direction (at this point to satellite observation point). Therefore, we have the conversion relationship:

$$\varphi = |\theta| - 90^\circ \tag{65.1}$$

The corresponding elevation is $-76.16^\circ < \varphi < -68.7^\circ$, shown in Fig. 65.2.

65.2.3 Analysis of CNR Boundary Parameters

This chapter focus on the impact of the lunar spacecraft received signal CNR on the feasibility of GNSS positioning.

Literature [23] indicates outdoor GPS received signal CNR generally in 35–55 dB Hz range. The signal greater than 40 dB Hz is generally considered as strong signal, and less than 28 dB Hz is regarded as weak signal. General GPS receiver can process signal CNR is higher than that of 35 dB Hz. When the CNR is lower than 28 dB Hz, receivers will be unable to effectively process the received signals. Previous analysis [20] of the GPS signal coverage does not take into account the effect of the sensitivity of the receiver, only from the geometric point of view that will be discussed below.

The existing experiment verify that [19], when the spacecraft located at an altitude of 60,000 km, the receiver can still receive GPS side lobe signal. Literature [8] simulation results show that the Doppler frequency shift aided pretreatment algorithm, BAP (Block Averaging Pre-Processing), can effectively track the signal whose CNR is low to 21 dB Hz. Moreover, literature [23] declares that using the extended Kalman filter, weak signal receiver can acquire and keep tracking signal whose CNR is 15 dB Hz.

GNSS signal's CNR of spacecraft received relate to the following factors: Equivalent isotropically radiated power (EIRP): P_{EIRP} ; Free space loss: L_d ; Receiving antenna gain: G_r .

Among them, P_{EIRP} is the product of send power and antenna gain, shows the joint effect of sending power and the antenna gain. Expressed below:

$$P_{EIRP}(\text{dBW}) = P_t(\text{dBW}) + G_t(\text{dB}) \quad (65.2)$$

L_d is related to the propagation distance. The greater the distance is, the more loss the signal has, which expressed below:

$$L_d(\text{dB}) = 20 \log \left(\frac{\lambda}{4\pi R} \right) (\text{dB}) \quad (65.3)$$

For the general ground GPS receiver, the average of antenna gain is 3.0 dB. While for space receiver and deep spacecraft, receiver antenna gain is key factor to decide received signal CNR. The received power of the receiver (P_r) can be represented as:

$$P_r(\text{dBW}) = P_{EIRP}(\text{dBW}) - L_d(\text{dB}) + G_r(\text{dB}) \quad (65.4)$$

In addition to the above factors, there are some other factors, including atmospheric loss, polarization mismatch and antenna phase center. From the existing literatures, EIRP of GPS L1 frequency point satellite is $P_{EIRP} = 26.8$ dBW.

In GPS L1, take L2 frequency point as an example, the frequencies of the transmitted signal are $f_{L1} = 1575.42$ MHz, $f_{L2} = 1227.6$ MHz and $c = 299,792,458$ m/s. At 2008/07/01 12:00:00, distance from GPS No. 2 satellite to spacecraft is $R = 345319.600831$ km. By equation (65.3), $L_d = -207.16$ dB. GPS receiver general for omnidirectional antenna gain is $G_r = 3$ dB. For deep space receiver, antenna gain needs to be improved.

Therefore, from Eq. (65.4), the general omnidirectional antenna receiver signal receiving power is $P_r = -177.36$ dBW = -147.36 dBm. Receiving signal CNR is (relative spatial noise background):

$$\text{CNR} = -147.36 - (-174) = 26.64 \text{ dB Hz} \quad (65.5)$$

Present research showed that [8] the signal CNR of 26.64 dB Hz can be acquired.

65.3 GNSS Signals Beam Main Lobe Receiving Performance Analysis for Lunar Spacecraft

Lunar spacecraft, from launch to revolution the luna, need to experience three stages: the earth phase modulation orbit, the earth-luna transfer orbit and lunar acquisition. For GNSS orbit determination, the most important part is the luna

phase synchronous orbit far away from the earth. Since the distance of the earth and the luna is about 60 times the radius of the earth, the luna can be treated as a point for analyzing. Therefore, in order to verify the feasibility of lunar spacecraft orbit determine with GNSS constellation, this paper will take lunar mass center as the reference point to complete geometric visibility analysis. In the process of simulation calculation, with the help of the AGI company STK (Satellite Tool Kit) software for lunar spacecraft orbit modeling [24]. The STK software is used directly for estimating the lunar orbit. Planets in STK, often used to represent the heliocentric orbit objects, such as: planets, planets, asteroids and comets. In order to use convenient, STK including the luna and the sun in planet in class. The software takes into account the influence, the gravity of the luna and some quality using compression ephemeris book of the U.S. naval observatory to predict the position of the luna and satellite.

65.3.1 Visibility and CNR Analysis of Single GNSS Constellation

For a single MEO satellite, taking GPS satellite MEO_SVN02 as an example, during mid-month, there are continuous multi-day that satellite cannot be observed by the spacecraft on the lunar orbit.

Satellite visible time of GPS is shown in Fig. 65.3. Satellites covered all the simulation time. But solving positioning functions need at least 4 satellites. By calculation, during the simulation time, we found that only a few time can receive signals from 4 satellites synchronously. Therefore, it is not feasible for lunar spacecraft positioning by single constellation of GPS.

Beside geometry visible, we also analyse the signal CNR change. Calculate the CNR change trend of visible GPS satellites, shown in Fig. 65.4. During satellite

Fig. 65.3 Sketch satellites visible time of GPS

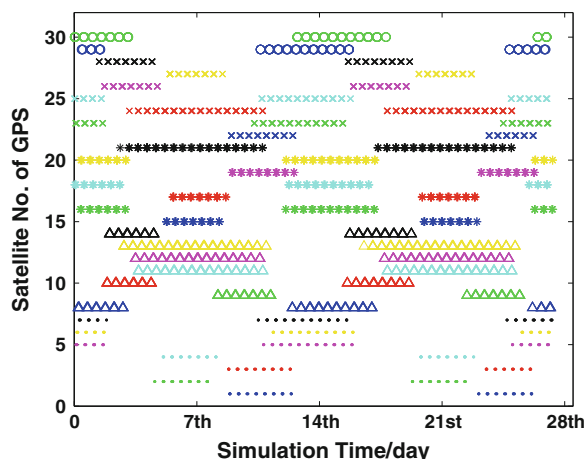
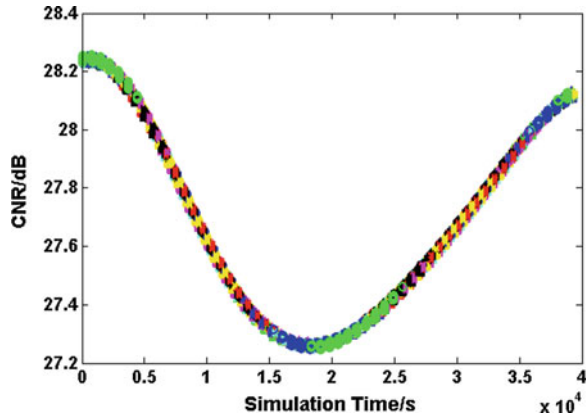


Fig. 65.4 Sketch GPS satellites CNR changing tendency on the lowest CNR threshold



visible period, CNR of all satellite is greater than 21 dB Hz, higher than the minimum signal acquisition CNR threshold. So the key limitation of positioning is not CNR but visible quantity in this situation.

Visibility of BDS's MEO satellite is similar to GPS. Besides, the BDS constellation contains IGSO and GEO satellites. According to the simulation result, there are also several days cannot observe any satellite for spacecraft on the lunar revolution orbit. IGSO visibility is also not perfect. Due to words limitation, the details are omitted here. Whole constellation visibility is shown in Fig. 65.5, during the period, the BDS constellation has too less visible satellites to satisfy the positioning demand of lunar spacecraft in lunar orbit. Therefore, rely on the single BDS is not feasible to complete lunar orbit revolution determination.

Visibility of Galileo's satellites is shown in Fig. 65.6. Signals from all Galileo satellites also exist a few days that no satellites visible. CNR calculating results

Fig. 65.5 Sketch satellites visible time of BDS

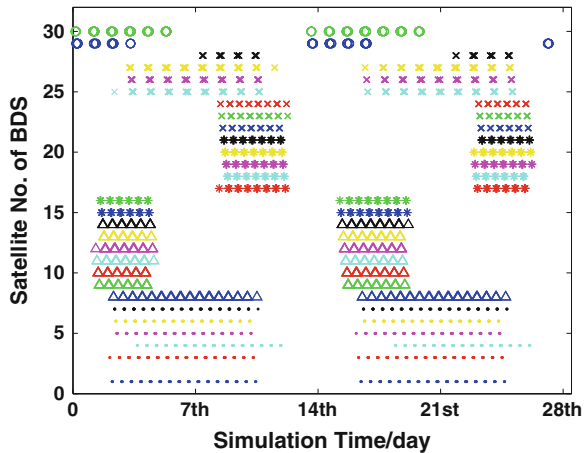
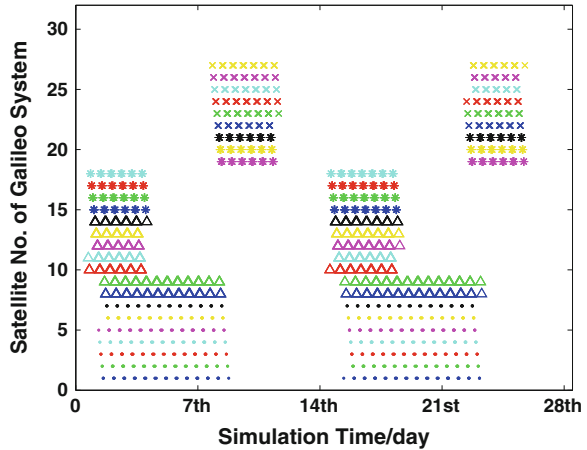


Fig. 65.6 Sketch satellites visible time of Galileo



show that Galileo satellites' CNR is all above 21 dB Hz during the visible period. Therefore, rely on Galileo to positioning lunar spacecraft is not feasible.

GLONASS MEO satellites visibility is similar to Galileo that also has a few days that all the satellites are not visible. Rely on the single GLONASS to complete lunar spacecraft positioning is not feasible.

Summary, each one constellation of GPS, BDS, Galileo and GLONASS is unable to satisfy positioning demand for spacecraft on lunar orbit.

65.3.2 Visibility and CNR Analysis of Dual GNSS Constellations Combination

Using the same CNR threshold to analysis the visible satellites quantity of dual GNSS constellations combined. Since the clock difference is different, when using the dual constellation satellite positioning algorithm, at least 5 satellites are needed for solving the equations. Table 65.2 shows the visibility of each dual constellations combination when 5 satellites of dual constellations (or 4 satellites of single constellation) are visible and above CNR threshold for lunar spacecraft.

65.3.3 Visibility and CNR Analysis of Multiple GNSS Constellations Combination

Continue to analyses 4 cases of 3 constellations combination and one case of 4 constellations combination above the CNR threshold. Calculate different visible satellites quantity distribution. For 3 constellations combination, there are 6 unknowns, therefore requires at least 6 equations. And at least 7 satellites are

Table 65.2 The percentage of available time of dual constellations combination

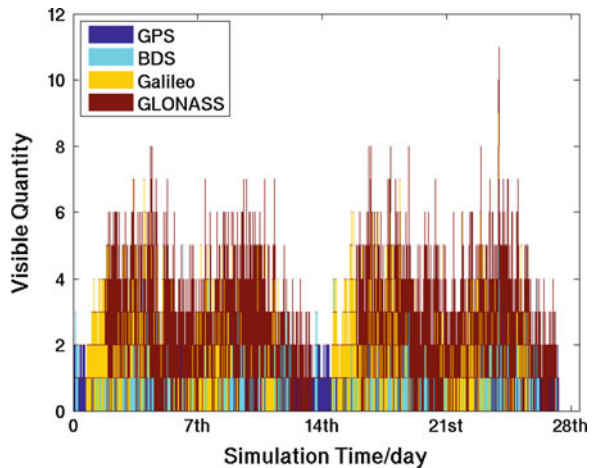
GNSS	Available time (%)
GPS/BDS	0.05
GPS/Galileo	0.04
GPS/GLONASS	0.04
BDS/Galileo	0.13
BDS/GLONASS	0.02
Galileo/GLONASS	0

Table 65.3 The percentage of available time of multiple constellations combination

GNSS	Available time (%)
GPS/BDS/Galileo	0.63
GPS/BDS/GLONASS	0.45
GPS/Galileo/GLONASS	0.11
BDS/Galileo/GLONASS	0.20
GPS/BDS/Galileo/GLONASS	0.69

needed when 4 constellations combined, for solving positioning equations. Table 65.3 shows the visibility of each 3 constellations combination when 6 satellites of 3 constellations (or 5 satellites of dual constellation or 4 satellites of single constellation) are visible and above CNR threshold for lunar spacecraft. Figure 65.7 shows visible satellites quantity for 4 constellations combined. Conclusion is that only a very little part of time can meet the demand of positioning solution.

Fig. 65.7 Sketch visible satellites quantity for 4 constellations combined



65.3.4 Summary of Beam Main Lobe Signal Received Analysis

This chapter refers to the existing results and public literature, takes antenna beam radiation main lobe angle and the lowest acquisition CNR as a threshold of simulation, analysis 15 cases of combination. By calculating the time distribution, it can be concluded that the existing main lobe signal receiving above CNR threshold cannot satisfy the demand of lunar spacecraft positioning.

65.4 GNSS Signals Beam Side Lobe Receiving Performance Analysis for Lunar Spacecraft

According to the conclusions in the previous chapter, this chapter expands ideas of side lobe signal acquisition for lunar spacecraft on the lunar orbit.

According to literature [7], PiVoT receiver can acquire GPS's main lobe signal and side lobe signal on HEO where receivers can receive signals from both the same side and the opposite side of the earth.

The experimental results by foreign scholars show that the side lobe signal receiving is feasible for the GPS receiver on HEO [25] which can improve the visible satellite quantity.

65.4.1 CNR of Side Lobe Signal

The lunar spacecraft GNSS side lobe signal receiving research should consider the impact power loss of side lobe signal and then take methods to keep the CNR still above acquisition threshold. Take GPS as example, side lobe signals are lower than the main lobe about 15 dB. So $L_s = -15$ dB. According to expression (65.4), the CNR of side lobe signal is 11.64 dB Hz. Therefore, on one hand, the transmitting power of satellites should be improved. On the other hand, higher gain receiving antenna should be used in order to improve the signal CNR in receiver.

65.4.2 Multiple Constellation Visibility Analysis of Side Lobe Signal Receiving

Since some methods can be adopted to improve the received signal CNR, assume acquisition threshold is still 21 dB Hz. Analyses single constellation, dual constellations and multiple constellations combination with side lobe signal receives.

Take GPS as example, Fig. 65.8 shows the visible satellites of GPS by histogram. Figure 65.9 shows satellite visible time of GPS combined BDS with side lobe

Fig. 65.8 Histogram: satellites visible time interval of GPS with side lobe signal received

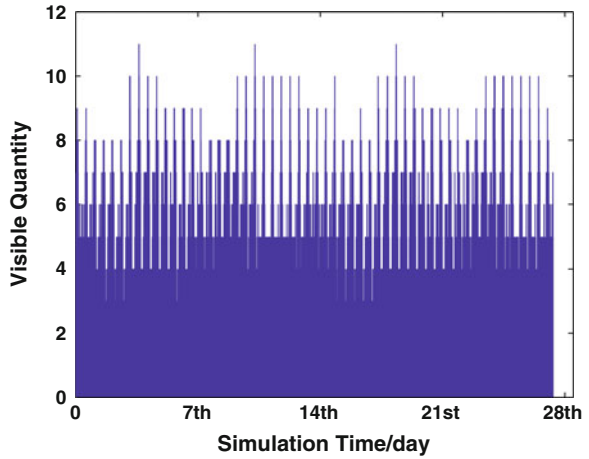
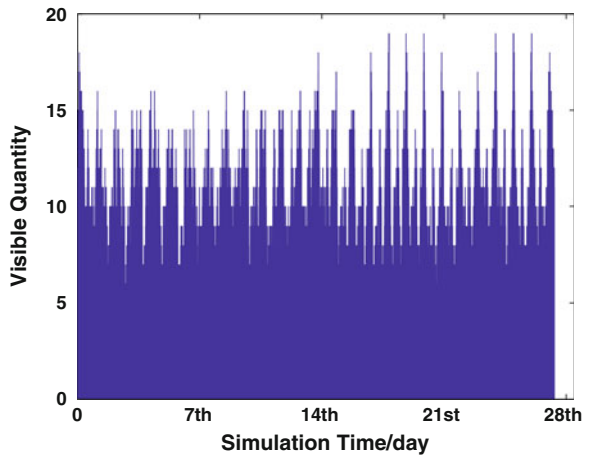


Fig. 65.9 Histogram: satellites visible time of GPS combined BDS with side lobe signal received



signal received by histogram. Figure 65.10 shows satellite visible time of GPS combined BDS and Galileo with side lobe signal received by histogram. Figure 65.11 shows visible satellites quantity when four constellations combined. Others combinations omitted here since the words limited. Calculate the percentage of visible time and list in Table 65.4.

Thus, when considering side lobe signal receiving, combination of the three constellations can satisfy the demand of spacecraft lunar orbit positioning for the 100 % of the simulation time. When 4 constellations combined, the demand of 7 satellites (or 6 satellites of three constellations, or 5 satellites of dual constellations) received also met for 100 % of the simulation time.

Fig. 65.10 Histogram: satellites visible time of GPS, BDS and Galileo with side lobe signal received

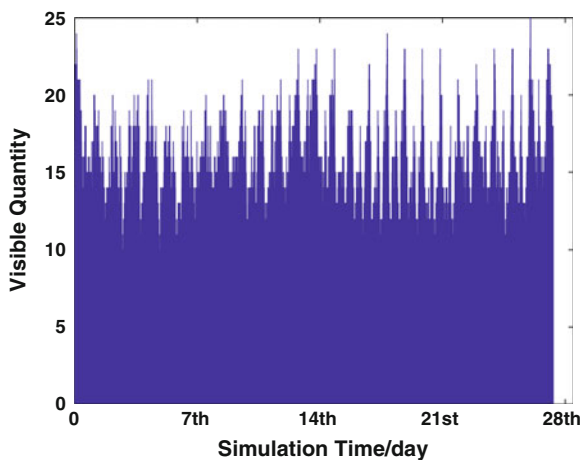


Fig. 65.11 Histogram: satellites visible time interval when four GNSS constellations combines with side lobe signal received

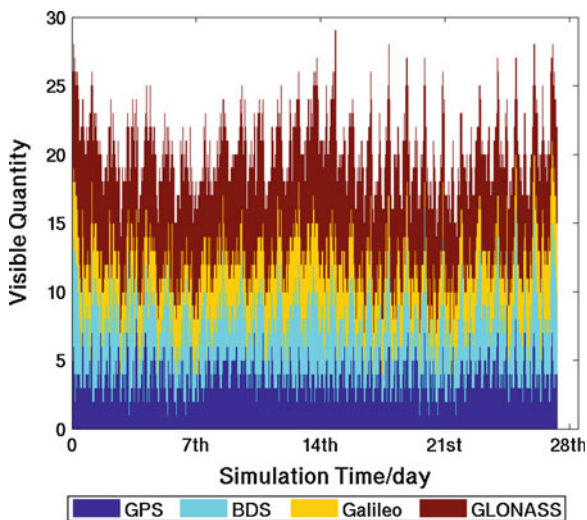


Table 65.4 The percentage of available time with side lobe signal received

Single GNSS	Available time (%)	Dual GNSS	Available time (%)	Multiple GNSS	Available time (%)
GPS	59.7	GPS/BDS	99.961	GPS/BDS/Galileo	100
BDS	45.2	GPS/Galileo	99.954	GPS/BDS/GLONASS	100
Galileo	34.7	GPS/GLONASS	99.189	GPS/Galileo/GLONASS	100
GLONASS	10.3	BDS/GLONASS	98.614	BDS/Galileo/GLONASS	100
-	-	Galileo/GLONASS	99.992	GPS/BDS/Galileo/GLONASS	100

65.4.3 *The Analysis Summary*

This chapter calculates the antenna beam radiation range including main lobe and side lobe. By taking lowest acquisition CNR threshold as a condition for simulation, we analysed positioning feasibility of single constellation, dual constellations combination, three constellations combination and four constellations combination. Fifteen cases are analysed here and a conclusion is drawn: by considering the side lobe signal receiving, in the simulation time, three or more constellations combined can meet the demand of least quantity of satellites for function solving. And the demand of the lunar spacecraft positioning tasks can be satisfied.

65.5 Conclusion

The simulation analysis shows that when only receive antenna pattern main lobe signals from the GNSS constellation whatever kinds of combination cannot satisfy the basic conditions for spacecraft positioning on the lunar orbit. By increasing the antenna gain or other methods to make up the space transmission loss, the receivers' signal CNR for lunar spacecraft is acceptable. When side lobe signals are received, any three or more GNSS constellations combination can satisfy the demand of full time lunar orbit positioning. Lunar spacecraft positioning tasks by using GNSS multiple constellations navigation is feasible.

Acknowledgments Financial aid information: Natural Science Foundation of China, Fund Code: 41304026.

References

1. Zhao Q, Liu J, Ge M et al (2006) Precision orbit determination of champ satellite with cm-level accuracy. *Geomat Inf Sci Wuhan Univ* 31(10):879–882
2. Gold K, Brown A (2004) Architecture and performance testing of a software GPS receiver for space-based applications. In: 2004 IEEE aerospace conference proceedings
3. Bai J, Zhang H, Yang C (2004) New generation spaceborne GPS receiver at Tsinghua Space Center. In: Proceedings of the 6th Asia-Pacific conference on control and measurement, Chengdu, China
4. Li C, Gao X, Sun M et al (2006) GPS application in deep space. In: The twelfth national space and moving body control technology conference, pp 167–170
5. Yu S, Gao Y (2006) High orbit GPS satellite autonomous orbit technique based on analysis of feasibility study. *Control Eng* (1):38–42
6. Liu L, Dong X, Zheng K, Wang W (2011) Load GNSS determine the integral filter method of the orbit of GEO satellite. *Chin Space Sci Technol* 01:70–75
7. Moreau MC (2001) Test results of the PiVoT receiver in high earth orbits using a GSS GPS simulator. In: ION GNSS 2001 meeting, Salt Lake City, UT, 11–14 Sept 2001

8. Xie Y (2011) Rail technology and independent set in high orbit spacecraft GPS weak signal processing. Harbin Engineering University. doi:[10.7666/d.y2054058](https://doi.org/10.7666/d.y2054058)
9. Zhan P (2012) Study on high orbit satellite orbit determination technology based on GNSS. Nanjing University of Aeronautics & Astronautics
10. Qin H, Liang M (2008) Research on positioning of high earth orbital satellite using GNSS. *Chin Space Sci Technol* 04:316–325
11. Yu J, Liu D (2000) The feasibility of orbit determination of geostationary satellites using GPS. *Chin Space Sci Technol* (4):36–40
12. Yu S, Gao Y (2005) GPS based autonomous orbit determination research for geostationary satellites. *Aerosp Control* 23(4):35–40. doi:[10.3969/j.issn.1006-3242.2005.04.009](https://doi.org/10.3969/j.issn.1006-3242.2005.04.009)
13. Xinhua (2015) Phase three reentry lunar exploration project launched successfully return flight tester. http://news.xinhuanet.com/tech/2014-10/24/c_127134550.htm. Accessed 25 Jan 2015
14. Dong G, Chen S, Li H (2013) Research on high precision ground-based navigation of lunar orbiter rendezvous and docking. *J Spacecr TT&C Technol* 32(1)
15. Wen Y, Wang W, Zeng G et al (2001) Navigation for the lunar probe based on ground tracking sites. *J Natl Univ Def Technol* 23(6):33–37. doi:[10.3969/j.issn.1001-2486.2001.06.009](https://doi.org/10.3969/j.issn.1001-2486.2001.06.009)
16. Wang W, Wen Y-l, Zeng G, Xi X (2001) GPS navigation of the lunar probe in the close earth orbit phase. *J Natl Univ Def Technol* 23(2):1–5. doi:[10.3969/j.issn.1001-2486.2001.02.001](https://doi.org/10.3969/j.issn.1001-2486.2001.02.001)
17. Xi X, Ceng G (2001) Lunar trajectories design. National Defence Industry Press, Beijing
18. Orbit Parameters (2015) Chinese encyclopedia net. <http://www.chinabaik.com>. Accessed 25 Jan 2015
19. Moreau MC (2001) GPS receiver architecture for autonomous navigation in high earth orbits. Department of Aerospace Engineering Sciences, University of Colorado at Boulder
20. Wen J, Diao H, Dong Z (2009) Modeling and simulation of coverage performance of 32 GPS satellites constellation. *Aerosp Control* 27(6):52–55
21. Shao Y (2012) A simple deduction of the luna revolves around the earth cycle. *Phys Teach* (6):42–42. doi:[10.3969/j.issn.1002-042X.2012.06.020](https://doi.org/10.3969/j.issn.1002-042X.2012.06.020)
22. Parkinson BW, Spilker JJ (1996) Global positioning system: theory and applications, vol I. American Institute of Aeronautics and Astronautics, Washington, pp 234–242
23. Mark L (2002) Psiaki-extended Kalman filter methods for tracking weak GPS signals. In: ION GPS 2002, 24–27 Sept 2002. Portland, OR
24. STK User Manual. Section 5, p 97
25. Kronman JD (2000) Experience using GPS for orbit determination of a geosynchronous satellite. In: Proceedings of the institute of navigation GPS 2000 conference, Salt Lake City, pp 1622–1626

Chapter 66

Spoofing Interference Suppression for GNSS Based on Estimating Steering Vectors

Yaotian Zhang, Lu Wang, Wenyi Wang, Dan Lu, Qiongqiong Jia
and Renbiao Wu

Abstract The paper proposes a spoofing interference suppression algorithm for multiple spoofing interferences existing simultaneously. First, the signals which received from the reference antenna array are captured. The information about visible satellite signals' Doppler frequency and code delay are acquired. Using these information, we can reconstruct the visible satellite signals. Then, the visible satellite signals' steering vectors are estimated by calculating cross-correlation between the estimated visible satellite signals and the antenna array received signals. Utilizing the normalized cross-correlation coefficients of the visible satellite signals' steering vectors to detect spoofing interference and its steering vectors. Final, the proposed algorithm constructs an orthogonal projection matrix based on spoofing interference' steering vectors. Spoofing interference are suppressed by utilizing the constructed orthogonal projection matrix. The proposed novel spoofing interference suppression algorithm can simultaneously suppress multiple spoofing interference, which does not need to know the array manifold in advance and the DOAs (Direction of Arrival) of satellite signals and spoofing interference.

Keywords Spoofing interference · Spoofing suppression · Steering vector · GNSS

66.1 Introduction

Currently, satellite navigation interference suppression research focuses on oppressive interference suppression. Power inversion algorithm utilizes the fact that oppressive interference power is much greater than satellite signal power and noise power. Then, power inversion algorithm forms antenna nulling on the direction of oppressive interference. However, spoofing interference power is lower than noise

Y. Zhang (✉) · L. Wang · W. Wang · D. Lu · Q. Jia · R. Wu
Tianjin Key Lab for Advanced Signal Processing,
Civil Aviation University of China, Tianjin, China
e-mail: 595297514@qq.com

© Springer-Verlag Berlin Heidelberg 2015
J. Sun et al. (eds.), *China Satellite Navigation Conference (CSNC) 2015
Proceedings: Volume I*, Lecture Notes in Electrical Engineering 340,
DOI 10.1007/978-3-662-46638-4_66

765

power, power inversion algorithm can't suppress spoofing interference. By forwarding or mimicking authentic satellite signals, spoofing interference can achieve the purpose of misleading or even controlling the satellite navigation receiver. Therefore, spoofing interference is a huge security threat of satellite navigation system, especially in safety-related applications.

How to detect and suppress spoofing interference has become a main problem in the Global Navigation Satellite Systems (GNSS) community. Existing anti-spoofing interference techniques can be roughly classified into two main categories, namely spoofing interference detection and spoofing interference mitigation. Currently, the majority of anti-spoofing interference techniques belong to spoofing interference detection. Spoofing interference detection is mainly based on monitoring abnormal changes of some signal characteristics, such as CNR (Carrier to Noise Ratio) [1], absolute power, relative delay of L1/L2 signals [2], code and phase rate, TOA (Time of Arrival) [3], correlation output peak and AGC (Automatic Generation Control) parameter in the tracking loop [4], etc. Spoofing interference detection only focuses on discriminating the existing of spoofing interference. However, these detection techniques can't suppress spoofing interference directly.

The existing spoofing interference mitigation techniques suppress spoofing interference from aspects of interference' DOA, capturing part, tracking part, positioning results, as well as navigation message. Daneshmand proposed a spoofing mitigation technology based on dual antennas [5]. It estimated the angle of spoofing by calculating cross-correlation between two antennas. But this technology is sensitive to array manifold errors and need to know the array manifold. Besides, this technology is only suitable for single forwarding spoofing interference existing and the power of spoofing interference must be higher. Shi proposed a spoofing mitigation technology by estimating satellites' DOAs and calculating position of receiver [6]. However, this technology has high computational complexity because it need to demodulate the navigation message. This paper proposed a novel spoofing interference suppression algorithm using antenna array can simultaneously suppress multiple spoofing interference, which does not need to know the array manifold in advance and the DOAs of satellites and spoofing interference.

66.2 Data Model

Spoofing interference is consisted by multiple satellite signals (referred to pseudo signals) and transmitted in the same direction. When multiple spoofing interference sources incident on the antenna array, the received IF signals can be written as

$$\mathbf{y}(nT_s) = \sum_{m=1}^M \mathbf{a}_m s_m^a(nT_s) + \sum_{p=1}^P \mathbf{b}_p s_p^{sp}(nT_s) + \mathbf{n}(nT_s) \quad (66.1)$$

where, M and P are the number of authentic satellites and spoofing interference sources respectively. $s_m^a(nT_s)$ is the m th authentic satellites' navigation signals, $s_p^{sp}(nT_s)$ represents the p th spoofing interference sources signals, a and sp refer to authentic satellite signals and spoofing interference respectively.

$$s_m^a(nT_s) = \sqrt{p_m^a} D_m^a(nT_s - \tau_m^a) c_m^a(nT_s - \tau_m^a) e^{j\phi_m^a + j2\pi f_m^a nT_s} \quad (66.2)$$

$$s_p^{sp}(nT_s) = \sum_{l=1}^{L_p} \sqrt{p_l^{sp}} D_l^{sp}(nT_s - \tau_l^{sp}) c_l^{sp}(nT_s - \tau_l^{sp}) e^{j\phi_l^{sp} + j2\pi f_l^{sp} nT_s} \quad (66.3)$$

ϕ , f' and τ are the phase, Doppler frequency and code delay of the received signals respectively. $D(nT_s)$ and $c(nT_s)$ are navigation data and C/A code respectively. In (66.3), L_p represents the number of pseudo signals in p th spoofing interference sources. $\mathbf{n}(nT_s)$ is the complex additive white Gaussian noise vector, T_s is the sampling interval. \mathbf{a}_m and \mathbf{b}_p represent array manifold of authentic signals and spoofing interference respectively.

66.3 Estimating the Visible Satellites' Steering Vectors

The signals which received from the reference antenna array are captured. The information about visible satellites' Doppler frequency and code delay are acquired. When spoofing interference existing, the correlation function matrix for each PRN usually has more than one peak. Using the ratio of the peak value and average noise as conditions of capture judgment can guarantee to capture all authentic signal and pseudo-satellite signal for each PRN. Thus, we can estimate Doppler frequency and code delay of all authentic signal and pseudo-satellite signal and reconstruct them. Assuming $\hat{\tau}_l$ and \hat{f}_l are the l th satellite' code delay and Doppler frequency respectively, the l th satellite' reconstruct signal can be written as

$$\hat{s}_l = [c_l(1 - \hat{\tau}_l)e^{j2\pi\hat{f}_l(1-\hat{\tau}_l)}, \dots, c_l(K - \hat{\tau}_l)e^{j2\pi\hat{f}_l(K-\hat{\tau}_l)}]^T \quad (66.4)$$

where, K is the length of the data block, namely the number of samples within one spreading code period. Making the l th satellite signal's reconstruct signal correlate with the antenna array received IF signals,

$$\mathbf{r}_l = \mathbf{Y}\hat{s}_l^* = R_l\mathbf{a}(\theta_l) \quad (66.5)$$

where, $\mathbf{Y} = [\mathbf{y}_1 \dots \mathbf{y}_K]$, R_l represents spreading code correlating gain which is a constant. $\mathbf{a}(\theta_l)$ represents steering vectors of the l th satellite signal. Obviously, we can use \mathbf{r}_l as the estimation vectors of the l th satellite signal's steering vector.

66.4 Detect the Number of Spoofing Interference and Its Steering Vector

Assuming \mathbf{r}_i and \mathbf{r}_j respectively represent steering vectors of satellites signal s_i and s_j . ρ_{ij} represents the normalized cross-correlation coefficients of \mathbf{r}_i and \mathbf{r}_j ,

$$\rho_{ij} = \left| \left(\frac{\mathbf{r}_i}{\|\mathbf{r}_i\|} \right)^H \left(\frac{\mathbf{r}_j}{\|\mathbf{r}_j\|} \right) \right| \quad (66.6)$$

Considered that authentic satellite signals come from different directions, however, spoofing interference which contains multiple pseudo signals and transmitted in the same direction. Therefore, the steering vectors of pseudo signals have much high normalized cross-correlation coefficients. But the normalized cross-correlation coefficients of steering vectors between pseudo signals and authentic satellite signals are very small. Making all the steering vectors which estimated from Eq. (66.5) correlate each other. When normalized cross-correlation coefficients of two steering vectors larger than the decision threshold D_Δ . Then, the two signals which the two steering vectors corresponding to can be considered from the same direction. Namely,

$$\rho_{ij} \geq D_\Delta \quad (66.7)$$

We can concluded that once normalized cross-correlation coefficients of steering vectors larger than D_Δ , the steering vectors corresponding to satellite signals are pseudo signals, others steering vectors corresponding to satellite signals are authentic satellite signals.

According to the judgment result of spoofing interference, constructing an spoofing interference subspace based on spoofing interference' steering vectors,

$$\mathbf{U} = \text{span}\{\mathbf{r}_1, \dots, \mathbf{r}_p\} \quad (66.8)$$

The orthogonal complement space of \mathbf{U} is

$$\mathbf{U}_\perp = \mathbf{I} - \mathbf{U}(\mathbf{U}^H \mathbf{U})^{-1} \mathbf{U}^H \quad (66.9)$$

The orthogonal projection matrix of spoofing interference is

$$\mathbf{P}_\perp = \mathbf{U}_\perp (\mathbf{U}_\perp)^H \quad (66.10)$$

The spoofing interference is suppressed by utilizing the constructed orthogonal projection matrix.

$$\mathbf{z}(nT_s) = \mathbf{P}_\perp \mathbf{y}(nT_s) \quad (66.11)$$

Eventually, putting any way output of $\mathbf{z}(nT_s)$ into satellite navigation receiver for tracking and positioning.

66.5 Numerical Results

An antenna array with ten elements is used and the antenna configuration is chosen a uniform linear array with a half GPS L1 wavelength spacing. Four authentic satellite signals are PRN1, PRN2, PRN3 and PRN25, transmitted from the direction at azimuth of -5° , 10° , -25° and 25° , $\text{SNR} = -20$ dB. There are two spoofing interference sources. One spoofing interference source composed by SP1-PRN1, SP1-PRN3, SP1-PRN25 from the direction at azimuth of -50° . The other spoofing interference source composed by SP2-PRN1, SP2-PRN2 and SP2-PRN3 and SP2-PRN25 from the direction at azimuth of 40° . The PRN's power of each spoofing interference source is $\text{INR} = -18$ dB.

In Fig. 66.1, black dashed line represents the authentic satellite signals' DOAs, black solid line represents the pseudo signals' DOAs. From the Fig. 66.1, we can obviously see that the estimated steering vectors' spatial domain response aim to the direction of all authentic satellite signals and spoofing interference.

Figure 66.2 is array pattern obtained by the proposed algorithm. It's obviously observe that the proposed algorithm can form two antenna nulling on the direction of spoofing interference sources, while on the direction of authentic satellite signals the array pattern has relatively flat gain.

Figure 66.3 is the PRN2's correlation function matrix before spoofing interference suppression. It is clearly to observe that the correlation function matrix existing two obviously correlation peaks. One peak is belong to authentic satellite signal, the other peak is belong to spoofing interference. Figure 66.4 is the PRN2's correlation function matrix after spoofing interference suppression. After spoofing interference suppression, the correlation function matrix only existing authentic satellite signal's correlation peak, the spoofing interference's correlation peak has been suppressed totally.

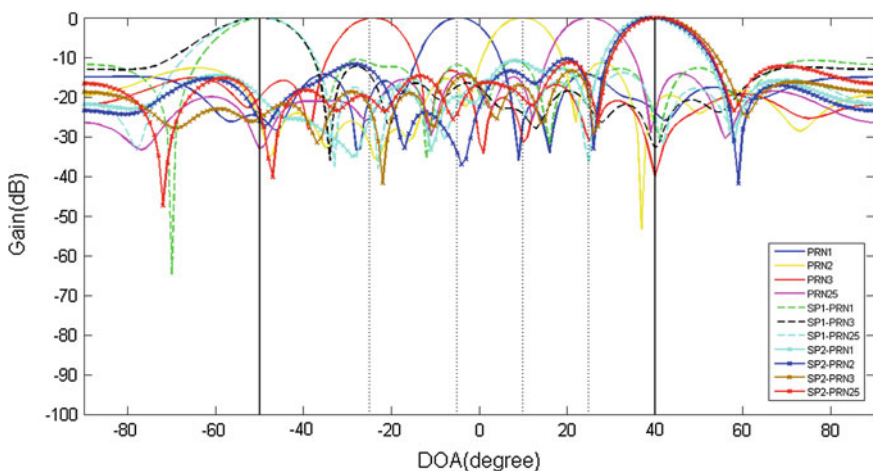


Fig. 66.1 Spatial domain response of estimated steering vectors

Fig. 66.2 Array pattern

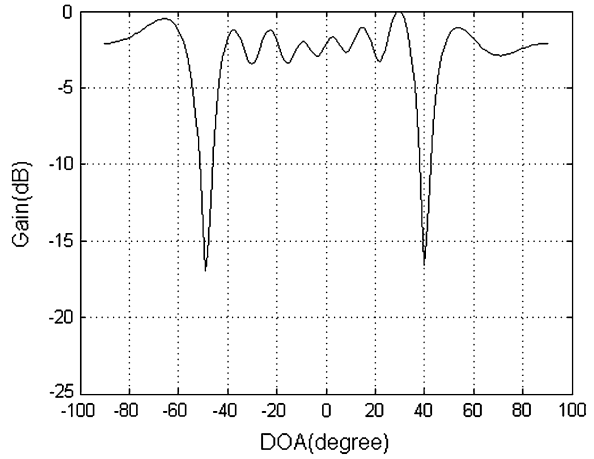


Fig. 66.3 The PRN2's correlation function matrix before spoofing interference suppression

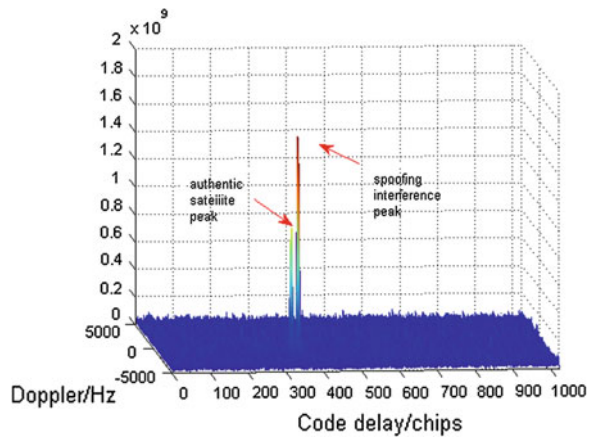
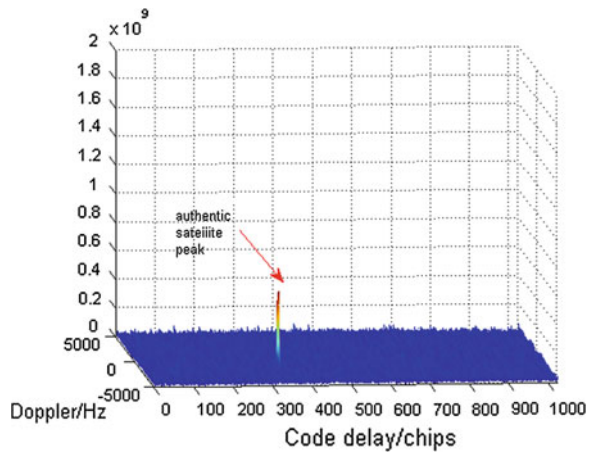


Fig. 66.4 The PRN2's correlation function matrix after spoofing interference suppression



66.6 Conclusion

This paper proposed a novel suppression algorithm for multiple spoofing interference existing. By reconstructing visible satellite signals and correlating with antenna received signals estimate steering vectors of visible satellite signals can be estimated. Finally, use steering vectors of spoofing interference, an orthogonal projection matrix can be obtained. The spoofing interference is suppressed by utilizing the constructed orthogonal projection matrix. The proposed novel spoofing interference suppression algorithm can simultaneously suppress multiple spoofing interference, without prior information of the array manifold in advance and the DOAs of satellites and interference.

Acknowledgments The work of this paper is supported by the Project of the National Natural Science Foundation of China (Grant No. 61172112, 61271404 and 61471363) and the Fundamental Research Funds for the Central Universities (Grant No. ZXH2009A003, 3122014B001 and 3122014D003).

References

1. Jafarnia-Jahromi A, Broumandan A, Nielsen J, Lachapelle G (2012) GPS spoofer countermeasure effectiveness based on signal strength, noise power and C/N_0 observables. *Int J Satell Commun Netw* 30(4):181–191
2. Wen H, Huang PYR, Dyer J, Archinal A, Fagan J (2005) Countermeasures for GPS signal spoofing. In: Proceedings of the 18th international technical meeting of the satellite division of the institute of navigation (ION GNSS'2005), pp 1285–1290
3. Dovic F, Chen X, Cavaleri A, Ali K, Pini M (2011) Detection of spoofing threats by means of signal parameters estimation. In: Proceedings of the 24th international technical meeting of the satellite division of the institute of navigation (ION GNSS' 2011), pp 416–421
4. Akos DM (2012) Who's afraid of the spoofer? GPS/GNSS spoofing detection via automatic gain control (AGC). *Navigation* 59(4):281–290
5. Daneshmand S, Jafarnia-Jahromi A, Broumandan A, Lachapelle G (2012) Low-complexity spoofing mitigation. *GPS World* 22(12):44–46
6. Shi W, Zhu H, Cai P (2013) The GPS deception jamming identification technology of based on the DOA of received signal. *Ship Sci Technol* 35(4):111–116

Chapter 67

Satellite Navigation Anti-jamming Algorithm Based on Extended Array

Fusheng Li, Wenyi Wang, Dan Lu, Lu Wang, Qionqiong Jia
and Renbiao Wu

Abstract In the complex electromagnetic environment, the Global Navigation Satellite System (GNSS) was seriously influenced by the interference. The anti-jamming algorithm based on the uniform array have been widely used in GNSS interference suppression technology, but the number of the interference is limited by the number of the antenna sensor. This paper proposed an interference suppression algorithm based on the extended array, the algorithm could suppress more interference than the number of antenna sensor. Firstly, the covariance matrix of the non-uniform array is vectorized. After that, the spatial smoothing is used to build up the rank of the covariance matrix. With the smoothed covariance matrix, power inversion algorithm is used to estimate the directions of the interference. Then, forming an overdetermined equation based on the interference subspace and an arbitrary signal's steering vector, whose direction is different from the interference. Finally, solving its least-squares solution to get the optimal weight, which can form nulls in the direction of interference without affecting the useful signal. The simulation results verify the effectiveness of the proposed algorithm.

Keywords Satellite navigation · Extended array · Spatial smoothing · Least squares solution

67.1 Introduction

The Global Navigation Satellite System (GNSS) has many characteristics such as all-weather, global coverage, high accuracy in three dimensional timing and positioning, rapid time-saving and high-efficiency, multi-functional, which making it widely used in military and civilian fields. However, the satellite is usually far away

F. Li (✉) · W. Wang · D. Lu · L. Wang · Q. Jia · R. Wu
Tianjin Key Lab for Advanced Signal Processing,
Civil Aviation University of China, Tianjin, China
e-mail: 353087268@qq.com

from earth, which makes the power of the received satellite signal very weak (about -160 dBW). And it is drowned in the noise, also the structure of the GNSS signal is known as public, so it is vulnerable to be interferenced. If the power of interference exceeds the processing gain of the system, the GNSS receiver will not be able to acquire and track the useful signal, and it cannot achieve the goal of navigation. Therefore, it is necessary to suppress the interference.

The existed anti-jamming algorithms, mainly from the time domain, frequency domain, spatial domain or the joint domain to suppress the interference. The methods in time/frequency domain can only suppress narrowband interference, and do not have the ability to distinguish the spatial characteristics between the useful signal and interference, thus it is unable to deal with a large number of narrowband interference and broadband interference. In these cases, anti-jamming algorithm based on adaptive antenna array attracts more and more scholars' attention. The literatures have proposed many algorithms, such as the power minimization algorithm [1], the interference subspace algorithm [2] and the blind adaptive beamforming algorithm base on the GNSS signal characteristic [3, 4]. However, these algorithms are usually based on uniform linear array, and the number of the suppressed interference is strictly limited by the number of antenna array element.

In the complex electromagnetic environment, the receiver is seriously influenced by the interference. The traditional anti-jamming algorithm based on uniform linear arrays can not suppress more number of interference than the number of physical antenna element. In order to deal with more number of signal, Pillai proposed a spectrum estimation method based on the minimum redundancy array (MRA) [5], Pal proposed a direction-of-arrival (DOA) estimation method based on the nested arrays [6]. Although these methods can handle more signals than the actual number of array element, but they only estimate the direction-of-arrival (DOA) of the signal.

This paper proposed an interference suppression algorithm based on extend array, the algorithm can suppress more number of interference than the number of the physical array element. Firstly, using the received covariance matrix of the physical array to obtain the received covariance matrix of the extend array, which can be used to estimate the DOA of interference with the power inversion algorithm. Then, forming null in the direction of interference and gain in the direction of arbitrary signal. It is an overdetermined equation when the number of interference exceeds the actual array element. Finally, by solving the overdetermined equation to obtain the optimal weight, this weight is used to suppress more number of interference than the number of the actual array element. Experimental results demonstrate the effectiveness of the algorithm.

The remainder of this paper will be organized as follows. The signal model is introduced in the Sect. 67.2. In Sect. 67.3 the DOA estimated method of the interference is proposed. The optimal weight is calculated in the Sect. 67.4, and simulation results are presented in Sect. 67.5.

67.2 Signal Model

We consider K uncorrelated narrowband jammers and L satellite signals impinging on an M -antenna nonuniform linear array ($K > M$), which are spatially distributed in angle ϕ_k , $k = 1, \dots, K$, and ϕ_l^s , $l = 1, \dots, L$, respectively. Then, the received signal vector at time t can be written as,

$$\begin{aligned} \mathbf{x}(t) &= \sum_{l=1}^L s_l(t) \mathbf{v}_l^s + \sum_{k=1}^K q_k(t) \mathbf{v}_k + \mathbf{n}(t) \\ &= \mathbf{V}\mathbf{s}(t) + \mathbf{n}(t) \end{aligned} \quad (67.1)$$

where $s_l(t)$ and $q_k(t)$ are the complex amplitudes of the l th satellite and the k th jammer, respectively. $\mathbf{n}(t)$ is additive white Gaussian noise with zero mean and the variance is $\sigma^2 \cdot \mathbf{V} = [\mathbf{v}_1^s, \mathbf{v}_2^s, \dots, \mathbf{v}_L^s, \mathbf{v}_1, \mathbf{v}_2, \dots, \mathbf{v}_K]$ is the steering vector matrix of useful signal and interference, and $\mathbf{s}(t)$ is the signal vector. The steering vectors $\mathbf{v}_l^s, l = 1, \dots, L$ and $\mathbf{v}_k, k = 1, \dots, K$ are defined as,

$$\mathbf{v}_l^s = \left[e^{-jk_0 d_1 \sin(\phi_l^s)}, \dots, e^{-jk_0 d_M \sin(\phi_l^s)} \right]^T \quad (67.2)$$

and

$$\mathbf{v}_k = \left[e^{-jk_0 d_1 \sin(\phi_k)}, \dots, e^{-jk_0 d_M \sin(\phi_k)} \right]^T \quad (67.3)$$

where $k_0 = 2\pi/\lambda$ and d_m is the position of the m th antenna, which is typically an integer multiple of half-wavelengths.

67.3 Estimating DOA of Interference

Power inversion algorithm can form nulls in the direction of strong interference without knowing any priori information, so it is widely used in the GNSS interference suppression. In this section the paper use the power inversion algorithm's feature forming null in the direction of strong interference to estimate the DOA of interference.

In order to explain briefly, this paper take the four-antenna minimum redundancy array (MRA) [7] as an example, as shown in the upper plot of Fig. 67.1. In the Fig. 67.1 denotes a half-wavelength. When estimate the DOA of interference, the covariance matrix of the original four-antenna MRA is instead by the covariance matrix of the extended seven-antenna ULA, thereby increasing the degree of freedom of the array. The following explains how to obtain the covariance matrix of the extend array.

represented by \mathbf{p} and the noise becomes a deterministic vector given by $\sigma^2 \vec{\mathbf{1}}_n$. The distinct rows of $\mathbf{V}_i^* \odot \mathbf{V}_i$ behave like the manifold of a (longer) array whose sensor locations are given by the distinct values in the set $\{\vec{\mathbf{d}}_i - \vec{\mathbf{d}}_j, 1 \leq i, j \leq M\}$, where $\vec{\mathbf{d}}_i$ denotes the position vector of the i th sensor of the original array. But after the previous processing, the original random number is instead by the signal power, the interference become correlated sources, so we need spatial smoothing to build up the rank of the covariance matrix. To apply the spatial smoothing we construct a new \mathbf{V}_1 form $\mathbf{V}_i^* \odot \mathbf{V}_i$. In (67.7) remove the repeated rows (after their first occurrence), and also sort the steering vector like a ULA (exponentially from negative to positive), get a vector as,

$$\mathbf{z}_1 = \mathbf{V}_1 \mathbf{p} + \sigma^2 \vec{\mathbf{e}} \quad (67.8)$$

After processing, $\vec{\mathbf{e}}$ becomes a vector whose L th element is 1, and the remained elements are zero. We now divide this array into L overlapping subarrays, every subarray has L elements, the received data of the subarray can be written as:

$$\mathbf{z}_{1j} = \mathbf{V}_{1j} \mathbf{p} + \sigma^2 \vec{\mathbf{e}}_j, j = 1, 2, \dots, L \quad (67.9)$$

Resulting the covariance matrix of each subarray as,

$$\mathbf{R}_j \triangleq \mathbf{z}_{1j} \mathbf{z}_{1j}^H, j = 1, 2, \dots, L \quad (67.10)$$

The smoothed covariance matrix is,

$$\mathbf{R}_{ss} = \frac{1}{L} \sum_{j=1}^L \mathbf{R}_j \quad (67.11)$$

The smoothed covariance matrix behave like the extend array's covariance matrix. On the smoothed covariance matrix, we can estimate the DOA of the interference with the power inversion algorithm [9]. Getting the weight of power inversion algorithm,

$$\mathbf{w}_{PI} = \mu \mathbf{R}_{ss}^{-1} \mathbf{f} \quad (67.12)$$

where μ is a scaling factor, the constraint vector is $\mathbf{f} = [1, 0, 0, \dots, 0]^T$, so as to avoid all the weights becoming zero.

67.4 Calculate the Anti-jamming Weight

We have estimated the DOA of interference previously, so we can get the spanning space of the interference steering vector $\tilde{\mathbf{V}}_i = [\tilde{\mathbf{v}}_1, \tilde{\mathbf{v}}_2, \dots, \tilde{\mathbf{v}}_K]$. With the arbitrary signal (the DOA is known), whose direction is different from the interference, and the steering vector of this signal can be written as \mathbf{a}_s . We only need to find a weight to satisfy the following formula,

$$\begin{cases} \mathbf{w}^H \tilde{\mathbf{V}}_i \simeq \mathbf{0}^T \\ \mathbf{w}^H \mathbf{a}_s \simeq 1 \end{cases} \quad (67.13)$$

Because of the number of estimated interference signal exceeds the actual number of array elements. The above problem is to solve an overdetermined equation. It can be written as,

$$\mathbf{A}\mathbf{x} \simeq \mathbf{b} \quad (67.14)$$

where $\mathbf{A} = [\tilde{\mathbf{V}}_i \ \mathbf{a}_s]^T$ (\mathbf{A} is a $(K+L) \times M$ matrix), $\mathbf{x} = (\mathbf{w}^H)^T$ (\mathbf{x} is a $M \times 1$ vector) $\mathbf{b} = [1, 0, \dots, 0]^T$. Overdetermined equation is generally has no exact solution, so we can only get its least squares solution. It can be got from minimize the following question:

$$\min \|\mathbf{A}\mathbf{x} - \mathbf{b}\|^2 \quad (67.15)$$

Now we solve the minimize question, because \mathbf{A} is a full rank matrix, then there has a unitary matrix \mathbf{Q} and a nonsingular upper triangular matrix \mathbf{R} ,

$$\mathbf{A} = \mathbf{Q} \begin{bmatrix} \mathbf{R} \\ \mathbf{0} \end{bmatrix} \triangleq \begin{bmatrix} \underbrace{\mathbf{Q}_1}_{(K+L) \times M} & \underbrace{\mathbf{Q}_2}_{(K+L) \times (K+L-M)} \end{bmatrix} \begin{bmatrix} \mathbf{R} \\ \mathbf{0} \end{bmatrix} \quad (67.16)$$

The least squares solution can be written as,

$$\mathbf{x}_{LS} = \mathbf{R}^{-1} \mathbf{Q}_1^H \mathbf{b} \quad (67.17)$$

Therefore,

$$\mathbf{w}^H = \mathbf{x}_{LS}^T \quad (67.18)$$

After suppressing the interference the received data can be expressed as,

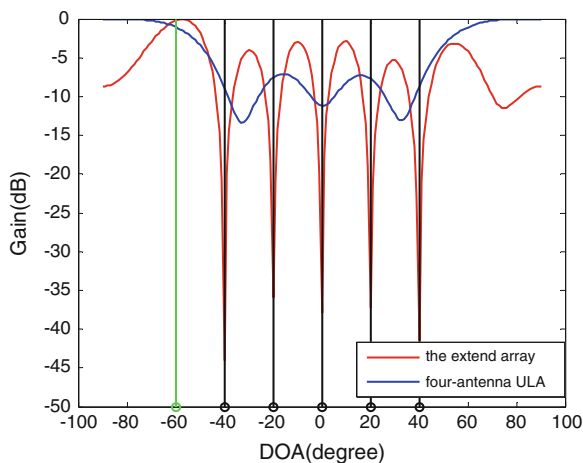
$$y(t) = \mathbf{w}^H \mathbf{x}(t) = \mathbf{x}_{LS}^T \mathbf{x}(t) \quad (67.19)$$

67.5 Simulation Results

The simulation using a four-antenna minimum redundancy array (MRA) to do experiment. The experimental data used in the simulation is produced by a high-fidelity GPS simulation software, whose sampling frequency is 5.714 MHz. The validity of the data has been verified by the software and hardware receiver. The interference is Gaussian white noise. Assuming the received signal contains only one satellite signal and five jammers, the DOA of satellite signal is -60° , and the DOA of the interference are $[-40^\circ, -20^\circ, 0^\circ, 20^\circ, 40^\circ]$. The signal-to-noise ratio (SNR) value is -20 dB and the interference-to-noise ratio (INR) is 15 dB. Figure 67.2 shows the beampattern of the extended array of the four-antenna MRA and the four-antenna ULA base on the power inversion algorithm. As can be seen from Fig. 67.2, when the number of the interference exceeds the number of the array element, the four-antenna ULA cannot form nulls in all directions of the interference, but the extended array can form nulls in all directions, which can be accurately used to estimate the DOA of the interference.

The beampattern is generated using the weight computed from (67.17) and plotted in Fig. 67.3, from the figure we can see, it can form nulls in all directions of the interference, and does not affect the useful signal's passing. To illustrate the performance of this algorithm further, we do experiment with the data before and after interference suppression. Figure 67.4a, b shows the results of the experiment. In the figure, the factor of acquisition means the ratio of the maximum peak to the second largest peak of the cross-correlation function, which is the function between the code of intermediate frequency signal and the local code. When the value exceeds 2 means the satellite signal can be acquired. It can be seen from the figure we cannot acquire the useful signal without interference suppression, but after the suppression we can get the useful signal.

Fig. 67.2 PI beampattern based on four-antenna ULA and the extended array



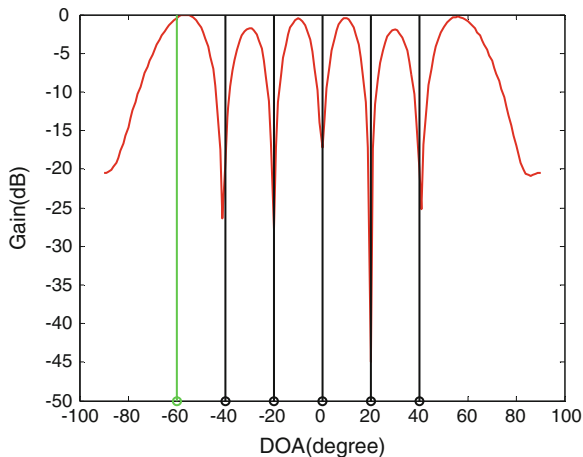


Fig. 67.3 Beampattern based on the proposed method

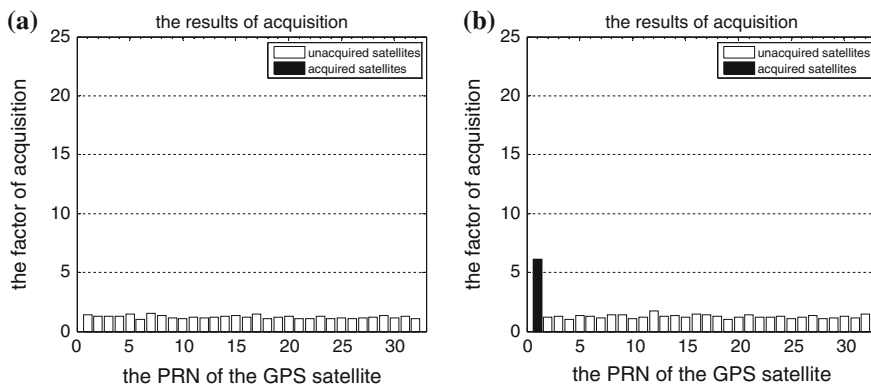


Fig. 67.4 The comparison between the acquire results before the interference suppression (a) and after the interference suppression (b)

67.6 Conclusion

In this paper, we proposed an anti-jamming algorithm based on extended array, when the number of the interference exceeds the actual number of the antenna element. The algorithm estimates the DOA of the interference with the power inversion algorithm based on the extended array. Then forming an overdetermined equation based on the interference subspace and a known arbitrary signal's steering vector, whose direction is different from the interference. Solving its least-squares solution to get the optimal weight of the interference suppression. Weighted to the

receiving data to suppress the interference. The experiment verified, after the interference suppression, we can acquire the satellite signal. It illustrates the effectiveness of the algorithm.

Acknowledgments The work of this paper is supported by the Projects of the National Natural Science Foundation of China (Grant No. 61172112, 61471363 and 61271404) and Fundamental Research Fund for the Central Universities (Grant No. 3122014B001).

References

1. Gecan A, Zoltowski M (1995) Power minimization technique for GPS null steering antennas. In: Institute of navigation conference, vol 12, issue no 1, Palm Springs, CA, pp 13–15
2. Sun W, Amin M (2005) Maximum signal-to-noise ratio GPS anti-jamming receiver with subspace tracking. In: IEEE international conference on acoustics, speech, and signal processing (ICASSP), Philadelphia, PA, March 2005, pp 1085–1088
3. Sun W, Amin M (2005) A self-coherence anti-jamming GPS receiver. *IEEE Trans Signal Process* 53(10):3910–3915
4. Suk SH (2006) Multicomponent receiver architectures for GPS interference suppression. *IEEE Trans Aerosp Electron Syst* 42(2):489–502
5. Pillai S, Bar-Ness Y, Haber F (1985) A new approach to array geometry for improved spatial spectrum estimation. *Proc IEEE* 73(3):1522–1524
6. Pal P, Vaidyanathan PP (2010) Nested arrays: a novel approach to array processing with enhanced degrees of freedom. *IEEE Trans Signal Process* 58(8):4167–4181
7. Moffet A (1968) Minimum-redundancy linear arrays. *IEEE Trans Antennas Propag* 16 (2):172–175
8. Ma WK, Hsieh TH, Chi CY (2009) DOA estimation of quasistationary signals via Khatri-Rao Subspace. In: Proceeding of International Conference on acoustics, Speech Signal Process (ICASSP), vol 34, issue no 2, pp 2165–2168
9. Amin M, Wang X, Ahmad F et al (2014) Minimum output power anti-jam with fully augmentable arrays. *IEEE BenMAS* 12(1):1335–1350

Chapter 68

Performance Assessment of Signal Quality Monitoring Based GNSS Spoofing Detection Techniques

Yichen Yang, Hong Li and Mingquan Lu

Abstract People are putting a great concern on Global Navigation Satellite System (GNSS) security while enjoying its convenience. GNSS is vulnerable and easily interfered by jamming or spoofing because of its opening signal structure, low signal power and complicated transmission environment, and this may lead potential security accidents or losses. Intermediate spoofing is an efficient spoofing attack method which is able to implement spoofing attacks without interrupting the regular functioning of user receivers and being noticed. This paper applies signal quality monitoring (SQM) techniques to GNSS intermediate spoofing detection and assesses the performance. The basic principle of intermediate spoofing attacking process and its detection are explained at first, which shows its effects on tracking loop status. Then, the techniques of SQM based on single correlator and multi-correlator are discussed respectively and the factors affecting the performance are analyzed and evaluated in detail, such as the number of correlators, SNR and so on. At last the paper summarizes the performances of SQM for GNSS spoofing detection.

Keywords Intermediate spoofing detection · Signal quality monitoring (SQM) · Multicorrelator techniques · Performance assessment

68.1 Introduction

Nowadays, Global Navigation Satellite System (GNSS) is playing an extreme significant role in everyday life and these wide utilizations gradually develop into dependency. But tremendous danger is hiding behind these precise, convenient systems all the time. As early as 2001, the U. S. Department of Transportation gave the report on vulnerability assessment of the transportation infrastructure relying on

Y. Yang (✉) · H. Li · M. Lu
Department of Electronic Engineering, Tsinghua University, Beijing, China
e-mail: 15210581169@163.com

© Springer-Verlag Berlin Heidelberg 2015
J. Sun et al. (eds.), *China Satellite Navigation Conference (CSNC) 2015 Proceedings: Volume I*, Lecture Notes in Electrical Engineering 340,
DOI 10.1007/978-3-662-46638-4_68

783

GPS and a great concern was raised on GPS interferences and spoofing attacks [1]. As we know, the signal power of GPS is extremely low, ordinary receivers cannot work at all when high power disturbs occur. What is worse, counterfeit signal can be easily reproduced by a GPS signal generator due to the open structure of GPS civil signals so that receivers may be spoofed without perceiving it and the position or timing results will be wrong or even manipulated. The other navigation systems are facing the same problems either.

In Ref. [2], the author categorized common spoofing attacks into three types: simplistic attack, intermediate attack and sophisticated attack. Simplistic attack can be performed simply by generating and broadcasting GPS signals with a simple GPS generator. Intermediate attack synchronizes spoofing signals to the real received signals and then increases its power to take the control of tracking loops. Sophisticated attack needs multiple spoofers and antennas to generate counterfeit signals which are deceptive and difficult to prevent. Among these three kinds of spoofing attacks, intermediate spoofing is the most practical because it's implemented much more easily than sophisticated spoofing and it can mislead the receivers surreptitiously with higher success probabilities than simplistic spoofing.

Considering the vulnerability of GNSS, plenty of interference mitigation and anti-spoofing methods have been proposed in recent years. In Ref. [3], the author addressed a method as signal quality monitoring (SQM), which is used to detect the "evil waveform" caused by signal generation failures of GNSS satellites or multipath interferences at first. SQM techniques monitor the status of tracking loops and raise alarms as soon as parameter anomalies are detected [3, 4]. Since spoofing attacks will cause the status of tracking loops changing abnormally, it's quite appropriate to apply SQM to spoofing detection [5, 6].

This paper focuses on the detection of intermediate spoofing and methods based on SQM techniques are proposed. After this introduction, the effect of intermediate spoofing on signal tracking is explained in Sect. 68.2. The fundamental of SQM techniques based spoofing detection and its performance are discussed in Sect. 68.3. Then in Sect. 68.4, this paper analyzes the multicorrelator based SQM techniques for spoofing detection and two different application situations are discussed to show the advantages of this method. Section 68.5 summarizes the conclusions and presents some ideas about the future researches.

68.2 Effect of Intermediate Spoofing on Signal Tracking

Taking the GPS C/A signal as an example, the ideal correlation peak is perfectly symmetric, and the values of early and late correlator are the same and the half of the prompt one when signals are tracked normally. In practical situation, the correlation peak is affected by the quality of received signals but still nearly symmetric.

As mentioned above, an intermediate spoofing can achieve attack without forcing the receiver to lose lock. This process can be explained as follows. First, the tracking loops lock to the authentic signal before an intermediate spoofing attack comes. Then

an intermediate spoofer generates counterfeit signal and adjust its frequency and code phase to that of real signal. After correlation peak of the counterfeit signal aligns the genuine one, the counterfeit signal power increases gradually. The tracking loops will finally lock to the spoofing signal and be totally controlled. Then the counterfeit signal may continue to change its code phase, navigation data or others to lead the receiver to get incorrect time or location. Figure 68.1 shows the process that how intermediate spoofing attack controls the tracking loops.

Though intermediate spoofing attacks seem to be elusive, the status of tracking loops reacts anomalously during an attack, such as the correlation peak distortion showed in Fig. 68.1. The values of early, prompt and late correlator during an intermediate spoofing attack are shown in Fig. 68.2. These three values fluctuate tempestuously when the counterfeit signal is taking the tracking loops, and they return to “normal situation” after the spoofing attack succeeds. This shows that a distorted correlation peak or other abnormal phenomena can help us to detect intermediate spoofing attacks.

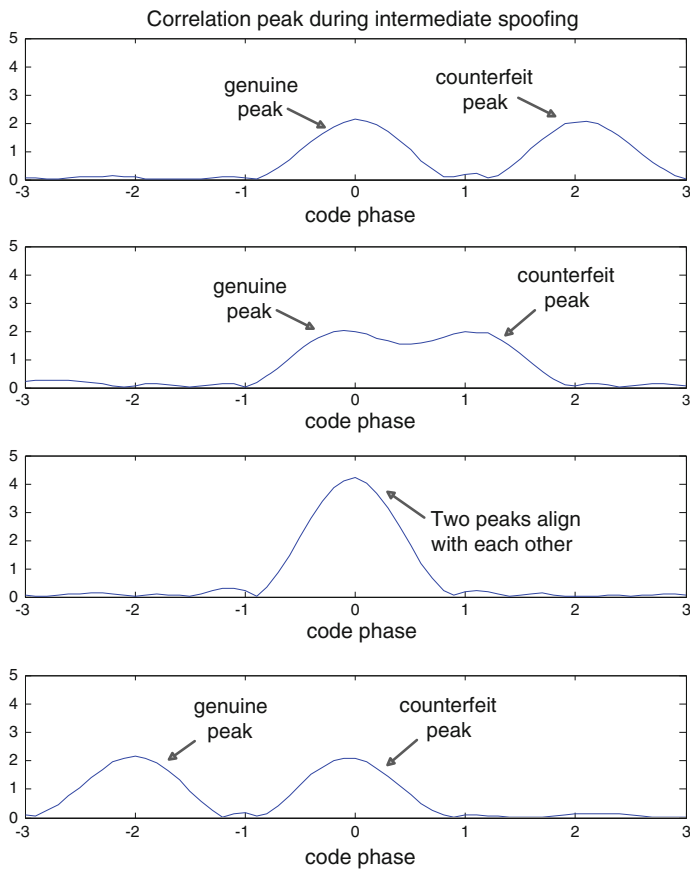
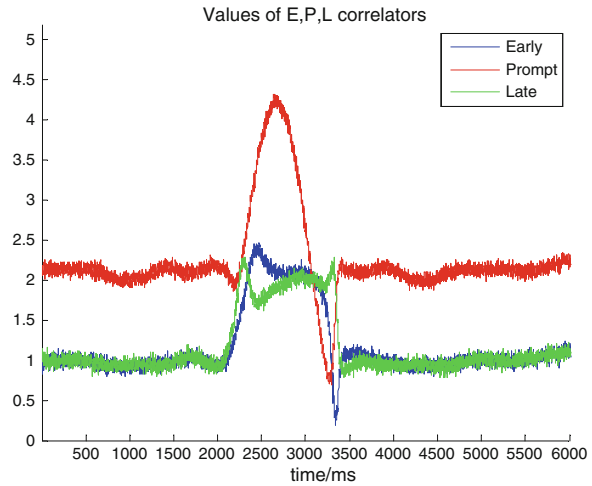


Fig. 68.1 The process that how intermediate spoofing attack controls the tracking loops

Fig. 68.2 Values of early, prompt and late correlator during an intermediate spoofing attack



68.3 Assessment of SQM Based Spoofing Detection

The distortion of correlation peak can be seen as an evidence of the existence of an intermediate spoofing attack. So it is appropriate to apply SQM techniques to spoofing detection by monitoring the correlation values and other tracking loops parameters in real time.

68.3.1 Symmetry Tests

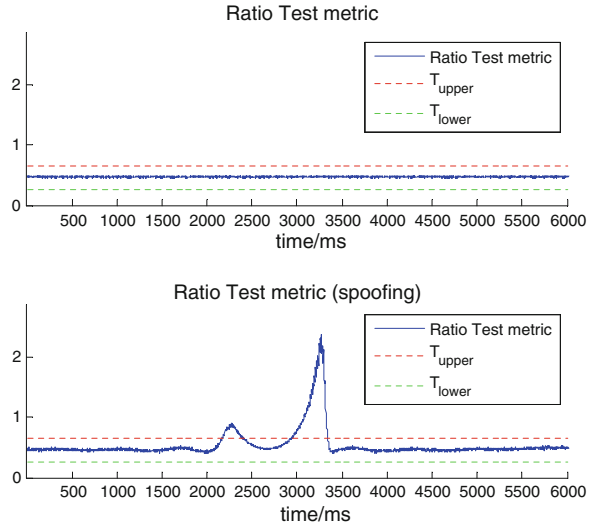
Symmetry tests are the main methods in SQM techniques and they are useful to detect the distortion of correlation peak. Symmetry tests can be performed just using the values of early, prompt and late correlator, which means low cost and complexity. There are several metrics that can evaluate the correlation peak symmetry quantitatively, such as ratio tests, delta tests and so on [3]. In this section, ratio tests metric is used to discuss the ability of spoofing detection.

The most common ratio tests metric is described as follows [3]

$$R = \frac{I_E + I_L}{2I_P} \quad (68.1)$$

where I_E , I_P and I_L are the values of early, prompt and late correlator respectively and the correlator spacing between early and late correlator is half of code chip as Fig. 68.1 represents.

Fig. 68.3 Ratio test metric values with and without an intermediate spoofing (SNR = 0 dB)



The first figure in Fig. 68.3 shows the ratio test metric value when tracking loops lock to the authentic signal for a period of 6 s, which keeps almost stable around a constant and doesn't exceed the two thresholds. The other figure shows the metric value that an intermediate spoofing is added. We can see that the ratio value increases promptly over the upper threshold when the fake signal is adjusting its code phase to align to the real one. If the metric value exceeds the thresholds sometime, an alarm should be raised to warn that the received signal is not reliable.

68.3.2 Performance Analysis and Evaluation

According to Ref. [7], the ratio test metric R can be approximated as a Gaussian distributed variable in some conditions. Under this hypothesis, the mean value μ_R and variance σ_R^2 of R can be derived according to Ref. [7, 8] and reported in the following

$$\mu_R = \frac{R_c(\tau - \frac{1}{2}) + R_c(\tau + \frac{1}{2})}{2R_c(\tau)} \tag{68.2}$$

$$\sigma_R^2 = \frac{1}{N \cdot SNR} \cdot \left\{ \frac{R_c(\tau) + R_c(\tau + 1)}{2R_c^2(\tau)} - \frac{R_c^2(\tau + \frac{1}{2})}{R_c^3(\tau)} \right\} \tag{68.3}$$

where $R_c(\tau)$ is the correlation function estimated by the tracking loops and N is number of integrated samples.

Then two thresholds can be set with a certain false alarm probability. In non-spoofing situation, this false alarm probability P_{fa} is the sum of probability that ratio test metric R is larger than upper threshold T_u and smaller than lower threshold T_l , described in Eq. (68.4)

$$P_{fa} = P_R(R > T_u) + P_R(R < T_l) \quad (68.4)$$

As $R \sim N(\mu_R, \sigma_R^2)$, Eq. (68.4) can be denoted as follows

$$P_{fa} = \text{erfc} \left(\frac{T_u - \mu_R}{\sqrt{2\sigma_R^2}} \right) = \text{erfc} \left(\frac{\mu_R - T_l}{\sqrt{2\sigma_R^2}} \right) \quad (68.5)$$

Then we can get the expressions of two thresholds as Eqs. (68.6) and (68.7)

$$T_u = \mu_R + \sqrt{2\sigma_R^2} \text{erfc}^{-1}(P_{fa}) \quad (68.6)$$

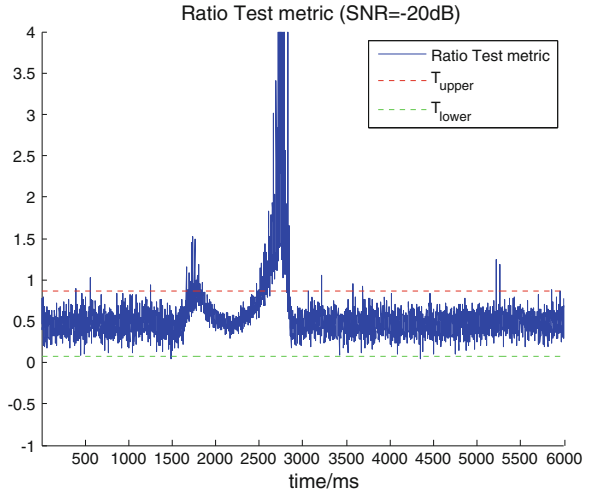
$$T_l = \mu_R - \sqrt{2\sigma_R^2} \text{erfc}^{-1}(P_{fa}) \quad (68.7)$$

Equation (68.2), (68.3), (68.6) and (68.7) can also be found in Ref. [7]. We can find that the thresholds are related to SNR closely. If the SNR gets higher, then the variance σ_R^2 is smaller so that these two thresholds become closer to the mean value μ_R . This result accords to common sense. Higher SNR means navigation signal is less interfered and tracking loops can work better and get measurements in higher accuracy. The ratio test values R calculated in real time are more likely to gather around a certain constant μ_R , which means that these values have smaller variance. And the probability that R get too far away from μ_R becomes really low unless an intermediate spoofing or other interferences occur.

68.4 Assessment of Multicorrelator Based SQM for Spoofing Detection

As discussed in last section, symmetry tests can be performed well on the detection of intermediate spoofing in some situations, but there are still several weaknesses that limit their performances. For examples, an alarm is given when the metric value is beyond the thresholds and this spoofing detection is successful, but this also denotes that the counterfeit signals have been already trying to take the tracking loops and causing negative effects on normal working condition. The detection alarm had better to be raised as early as possible for receivers to take appropriate measures against spoofing signals. And the thresholds are affected seriously by SNR. The variance σ_R^2 gets larger and the number of false alarm increases, so as to the false alarm probability. Figure 68.4 illustrates the ratio test value when SNR is -20 dB. The false alarm probability is 2.83 %, which is high and unaccepted in some cases.

Fig. 68.4 Ratio test value when SNR is -20 dB



So it is inaccurate to perform spoofing detection with only one single set of correlators or detection criterion to some extent. Considering the problems mentioned above, multicorrelator techniques give enlightenment and show great advantages. The tracking situation can be much more exhaustively obtained by using multicorrelator techniques with different strategies, so that the spoofing detection accuracy will enhance.

The detection performance based on multicorrelator techniques is affected by the detection strategies, in other words it is decided by several factors, such as metrics, correlator location, correlator spacing and so on, and by how to combine them. Take the choice of metrics as an example. Multicorrelators suggest that different kind of metrics can be calculated with multicorrelator values. Just like the ratio test metric talked before, metrics such as delta test metrics can be used as a detection criterion. These three metrics are presented as follows [3]

- Ratio test metric

$$R_i = \frac{I_{E_i} + I_{L_i}}{2I_{P_i}} \tag{68.8}$$

- Delta test metric

$$\Delta_i = \frac{I_{E_i} - I_{L_i}}{2I_{P_i}} \tag{68.9}$$

where I_{E_i} , I_{P_i} and I_{L_i} are the values of the i th early, prompt and late correlator. Then the detection criterion is the combination of the metrics above, as expressed below

$$\gamma = \{R_i, \Delta_j, \dots\} \quad (68.10)$$

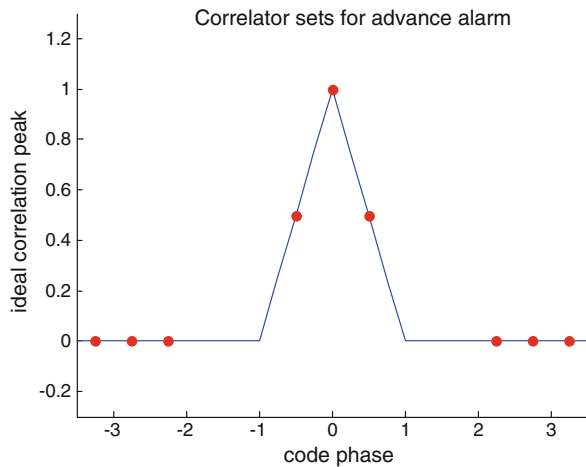
It is quite complicated to choose appropriate the combination criterion to deal with different spoofing cases and user needs. This section gives two situations as examples below to show how multicorrelator detections are performed.

68.4.1 Situation I: Advance Alarm

In situation I, an advance alarm is needed before the counterfeit signals affect the tracking loops. As to intermediate spoofing, the code phase or other parameters have to adjust towards the real ones and the fake correlation peak also must move gradually to the correlation peak of the genuine signal, just as the scene illustrated in Fig. 68.1. So two sets of correlators are placed beside the real correlation peak, which is shown in Fig. 68.5, so that they can detect spoofing signals before fake correlation peaks align with the real one.

Figure 68.6 shows the detection results by ratio test metric using the first correlator set located right at the correlation peak and the second set beside it. We can see that the false alarm is raised by first correlator set at 2.170 s, while the second set gives result at 1.822 s, which is early and leave extra time for further anti-spoofing measurements.

Fig. 68.5 Correlator sets for advance alarm



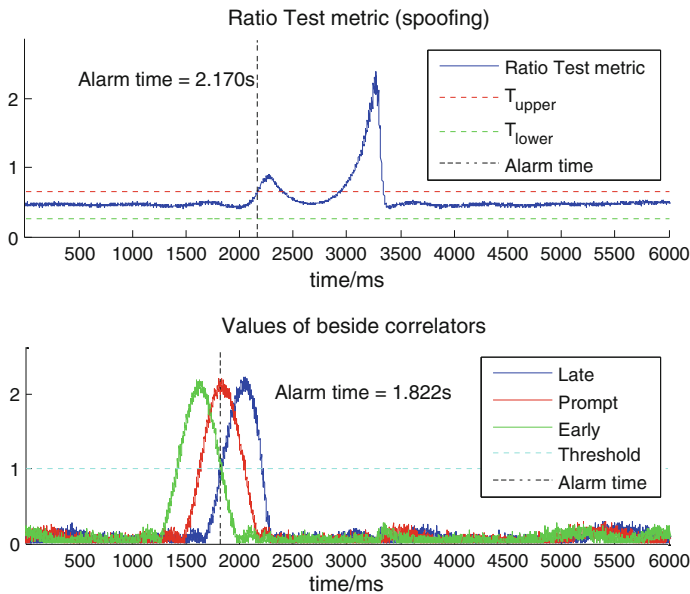


Fig. 68.6 Detection results by ratio test metric using beside correlator set and the comparison of alarm times

68.4.2 Situation II: Joint Detection of Ratio and Delta Metric

In situation II, SNR is low and probability of false alarm using only ratio test metric is high. So a detection criterion that combines ratio test metric and delta test metric is established. This criterion can be denoted as Eq. (68.11).

$$\gamma_{II} = \{R_1, \Delta_2\} \tag{68.11}$$

where R_1 is the same meaning with Eq. (68.1) and Δ_2 chooses the same prompt correlator with R_1 but another early and late correlator set. This criterion indicates that a detection alarm will not be raised unless both the values of R_1 and Δ_2 go beyond their respective thresholds at the same time, which can give results in higher accuracy.

Figure 68.7 shows simulation results of criterion γ_{II} under -20 dB SNR for a period of 6 s. Their thresholds can be derived with the same method in Sect. 68.3. Table 68.1 shows the detail information of using metric R_1 , Δ_2 and γ_{II} respectively. We can see that metric γ_{II} has the lower false alarm probability and better performance.

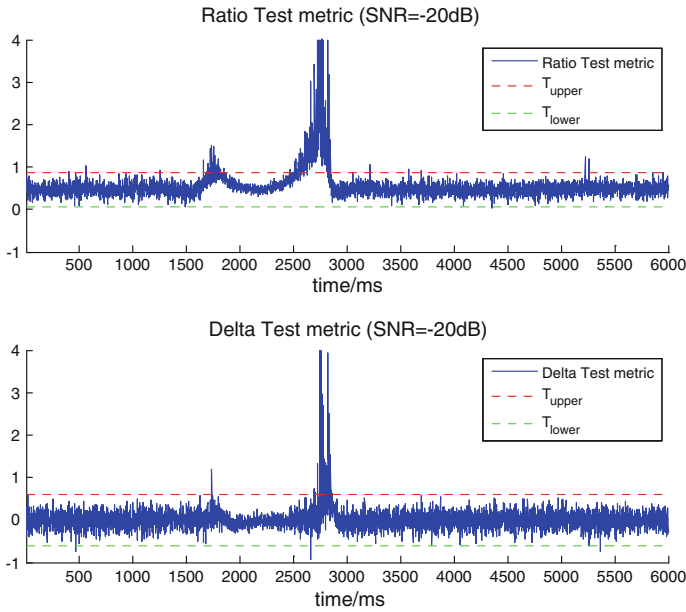


Fig. 68.7 Simulation results of criterion γ_{II} under -20 dB SNR for a period of 6 s

Table 68.1 Detail information of using metric R_1 , Δ_2 and γ_{II}

Criterion	Number of alarms	Number of false alarms	False alarm probability (%)
R_1	354	10	2.83
Δ_2	56	4	7.14
$\gamma_{II} = \{R_1, \Delta_2\}$	47	0	0.00

68.5 Conclusion

The security of GNSS is being threatened seriously by spoofing attacks. This paper has focused on the fundamental of intermediate spoofing attack and its influence on the tracking loops. Since this spoofing attack causes the tracking status to change unusually, this paper proposes a detection mechanism based on signal quality monitoring techniques, which were originally designed to detect “evil waveform” or interferences. The simulation results of single correlator set based SQM techniques and multicorrelator based SQM techniques for spoofing detection are presented respectively, then their performances are evaluated and compared with each other. We can get conclusions that: (1) the methods of single correlator set based SQM techniques and multicorrelator based SQM techniques are both effective to intermediate spoofing detection overall. (2) SNR is one of the most important factors that affect the performance of SQM based spoofing detection. Single

correlator set based SQM techniques will give higher false alarm probability when SNR is low, while the performance of the multicorrelator ones is better and more robust. (3) Considering different spoofing situations and user needs, the strategy choice of anti-spoofing criterion is decisive when using the multicorrelator based SQM techniques. Only appropriate strategy can bring correct and reliable detection results.

The next step of the research will be focused on the choice of detection strategies based on multicorrelator techniques and a more detailed performance analysis should be given.

References

1. Volpe J (2001) Vulnerability assessment of the transportation infrastructure relying on the global positioning system
2. Humphreys TE, Ledvina BM, Psiaki ML, O'Hanlon BW, Kintner Jr PM (2008) Assessing the spoofing threat: development of a portable GPS civilian spoofer. In: Proceedings of the ION GNSS international technical meeting of the satellite division, vol 55, p 56
3. Phelts RE (2001) Multicorrelator techniques for robust mitigation of threats to GPS signal quality. Doctoral dissertation, Stanford University
4. Mitelman AM (2004) Signal quality monitoring for GPS augmentation systems. Doctoral dissertation, Stanford University
5. Wesson K, Shepard D, Bhatti J, Humphreys TE (2011) An evaluation of the vestigial signal defense for civil GPS anti-spoofing. In: Proceedings of the ION GNSS meeting
6. Ledvina BM, Bencze WJ, Galusha B, Miller I (2001) An in-line anti-spoofing device for legacy civil GPS receivers. In: Proceedings of the 2010 international technical meeting of the Institute of Navigation, pp 698–712
7. Fantino M, Molino A, Mulassano P, Nicola M, Rao M (2009) Signal quality monitoring: Correlation mask based on ratio test metrics for multipath detection. In: Proceedings of the international global navigation satellite systems society (IGNSS) symposium, Gold Coast, Australia, December, pp 1–3
8. Fantino M (2006) Study of architectures and algorithms for software Galileo receivers. Doctoral dissertation, PhD thesis, Politecnico di Torino

Chapter 69

Robust SFAP Anti-jamming Algorithm Based on Generalized Sidelobe Cancellation

Long Liu, Zhaolin Zhang and Ling Wang

Abstract With the rapid development and the wide application of Global Navigation Satellite System (GNSS), anti-jamming technology has been widely studied and applied for anti-jamming satellite navigation receivers in recent years. The robust space-frequency adaptive processing (SFAP), combining array signal processing theory, adaptive filtering algorithm and Fast Fourier Transform (FFT), based on segmentation of the frequency-domain is proposed in this paper. And the method for calculating the anti-jamming weight of the frequency-domain based on Generalized Sidelobe Cancellers (GSC) is also presented, which reduces the dimension of the matrix during the process of the covariance matrix inversion. Consequently, it makes the system much easier to implement. In addition, the algorithm is improved further, combined with robust beamforming technology. Through notch widen against frequency-domain, the error that exist in the actual system, influencing the performance of algorithm, will be effectively reduced, and the adaptability for high dramatic environment will also be enhanced.

Keywords Satellite navigation · SFAP · GSC · Robust beamform · Notch widen

69.1 Introduction

Adaptive array processing is a spatial sampling technology, i.e. the spatial signals are sampled by a certain arrangement of the array element, and then get the desired output result by the weighting processing (see [1]). Since the beam of the adaptive antenna array can be easily controlled, and so it's widely being used with digital

L. Liu · Z. Zhang (✉) · L. Wang

The Key Lab. of Aerospace Information Perception and Photoelectric Control, Ministry of Education, School of Electronics and Information, Northwestern Polytechnical University, Xi'an, China
e-mail: z184@sina.com

L. Liu

e-mail: liulongnwp@126.com

© Springer-Verlag Berlin Heidelberg 2015

J. Sun et al. (eds.), *China Satellite Navigation Conference (CSNC) 2015*

Proceedings: Volume I, Lecture Notes in Electrical Engineering 340,

DOI 10.1007/978-3-662-46638-4_69

spread-spectrum signal receivers in order to suppress radio frequency interference (RFI) and noise. As the interference signal can be wideband and may have strong multipath, space-time adaptive processing (STAP) is being proposed for interference suppression generally. In STAP, the filter coefficients (anti-jamming weights), in general, are adjusted to minimize the mean power of the output signal, which subject to the look direction constraints. And this solution always requires manipulation of $LN \times LN$ size matrices, where L is the number of elements in the antenna array and N is the number of taps behind each antenna element. However, in environments with severe RFI, especially with coherent RFI, STAP is known to distort the desired signal which would lead to pseudorange and carrier phase errors [2].

Space-Frequency adaptive processing (SFAP) is an approach where the time domain signals received by antenna array are transformed to the frequency domain using the fast discrete Fourier transform (FFT). The constrained minimization algorithm is also be applied to suppress the jamming signals in the frequency domain. In SFAP, one can process each frequency bin independently and enhance the performance by increasing the number of frequency bins. In general, the adaptive weights of the single frequency bin need to manipulate only $L \times L$ size matrix.

In this paper, the performance of a space-frequency adaptive processing is studied under strong jamming environment. The SFAP based on segmented FFT technique where the time domain multi-sampling signals are segmented to perform FFT, has been proposed by Gupta and Moore [2]. But as the real system snap-sampling signals and the weights calculating need some time, a huge amount of computation will weaken the real-time performance of system and lead to the mismatch of adaptive weights, this which will bring errors to the satellite navigation system. In order to improve the real-time performance of the real system, the SFAP based on Generalized Sidelobe Cancellation (GSC) is proposed in this paper. This will make the computation of the single frequency bin weights, where one only need to deal with $(L - 1) \times L$ size matrix, rather than usual size $L \times L$. And the lower of dimension will enhance the real-time performance of the satellite navigation system. Simultaneously, when the vibration exists in the satellite navigation system, or the jammer moves rapidly relative to the satellite navigation system, the nulling mismatch of the pattern can lead to a huge drop of anti-jamming performance. To deal with this problem, the notch widen technique [3, 4], based on convex optimization is put forward by He [5] and Vandenberghe [6], etc. But the direction and moving range of jamming need to be measured in advance, it's difficult to carry out in project. In this paper, a modified approach based on covariance matrix taper [3, 7], is proposed in frequency domain, the notch widen can be achieved directly without the previous measurement of the direction and the moving range of jamming.

The rest of the paper is organized as follows. The robust SFAP mathematical model is presented in Sect. 69.2. Section 69.3 discusses the antenna array and the signal scenarios in this study. The simulation and analysis results of this study are given in Sect. 69.4. And finally, Sect. 69.5 contains the conclusion and the prospective of this work.

69.2 Robust SFAP Mathematical Model

69.2.1 Input Signal Model

Let the antenna array contains L elements. The signals received by antenna array are down converted to midband and digitized. A block of $M \times N$ is sampled from each antenna element, where M is the number of the segment and N represents the number of frequency bins for FFT in each segment. Assume θ_0 is the direction of the desired signal. The frequency domain samples for the m th segment are given by:

$$\tilde{\mathbf{X}}(m) = \tilde{\mathbf{S}}(m) + \tilde{\mathbf{J}}(m) + \tilde{\mathbf{N}}(m) \quad m = 1, 2, \dots, M \quad (69.1)$$

where $\tilde{\mathbf{S}}(m)$ is the $L \times N$ matrix of desire signal corresponding to the m th segment in time domain. Similarly, $\tilde{\mathbf{J}}$ and $\tilde{\mathbf{N}}$ respectively corresponding to the jamming matrix and noise matrix. Covert $\tilde{\mathbf{X}}(m)$ to frequency domain through N points FFT, and then get the frequency domain form, $F(m)$, $m = 1, 2, \dots, M$. Extract the k th frequency bins from $F(m)$, and subsequently make up the $L \times M$ matrix, $\mathbf{X}(k)$, $k = 1, 2, \dots, N$, which is the k th same frequency bin matrix among the M segments.

69.2.2 Generalized Sidelobe Cancellation Model

Generalized Sidelobe Cancellation (GSC) transforms the signal that the antenna array receiving into two branches by using the directional information of desired signal, as shown in Fig. 69.1. Where the upper branch signal, $d_0(k)$, is the reference signal after process of spatial match filter, which contains the desired signal and the jamming, and the desired signal after processing satisfies the distortionless constraint. On the lower branch, the desired signal is blocked by the blocked matrix, B_0 , therefore, the lower branch only consists of jamming and noise. Obviously, the jamming signals form two branches are associated. The signal-converted after Wiener filtering make the jamming adaptive cancelling, and then the desired signal without distortion is obtained [1].

$X(k)$ is a $L \times 1$ -dimensional vector, which denotes the input signal, and k denotes the frequency bin. \mathbf{B}_0 is full rank blocked matrix and the dimension is

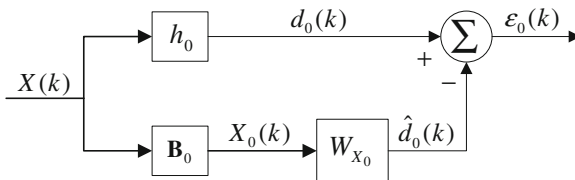


Fig. 69.1 The Structure of generalized sidelobe cancellation (GSC)

$(L - 1) \times L$. The normalized steering vector for direction of the desired signal, h_0 , is then given by

$$h_0 = \frac{a(\theta_0)}{\|a(\theta_0)\|} \quad (69.2)$$

where θ_0 denotes the direction of the desired signal. In Fig. 69.1, where

$$d_0(k) = h_0^H X(k) \quad (69.3)$$

and

$$X_0(k) = B_0 X(k) \quad (69.4)$$

in (69.3), superscript “ H ” denotes conjugate transpose, and there are two such relationships that $h_0^H h_0 = 1$, $B_0 h_0 = 0$. In (69.4), $X_0(k)$ is a $(L - 1) \times 1$ -dimensional vector. The $L \times L$ -dimensional transformation matrix, \mathbf{T} , is given by h_0 and B_0

$$\mathbf{T} = \begin{bmatrix} h_0^H \\ B_0 \end{bmatrix} \quad (69.5)$$

where \mathbf{T} is a non-singular matrix. Combining (69.3), (69.4) and (69.5), one obtains

$$\begin{bmatrix} d_0(k) \\ X_0(k) \end{bmatrix} = \mathbf{T}X(k) = \begin{bmatrix} h_0^H \\ B_0 \end{bmatrix} X(k) \quad (69.6)$$

in Fig. 69.1, the output signal of GSC can be given by

$$\begin{aligned} y(k) &= \varepsilon_0(k) = h_0^H X(k) - W_{X_0}^H B_0 X(k) \\ &= \left(h_0^H - W_{X_0}^H B_0 \right) X(k) \end{aligned} \quad (69.7)$$

where

$$W_{GSC} = h_0 - B_0^H W_{X_0} \quad (69.8)$$

the following form can be derived according to the minimum variance distortionless response (MVDR) beamformer.

$$W_{Quasi-MVDR} = \frac{\mathbf{T}^H (\mathbf{T} \mathbf{R}_X \mathbf{T}^H)^{-1} \mathbf{T} h_0}{h_0^H \mathbf{T}^H (\mathbf{T} \mathbf{R}_X \mathbf{T}^H)^{-1} \mathbf{T} h_0} \quad (69.9)$$

where the $W_{Quasi-MVDR}$ is named as weight vector of MVDR. According to the formula (69.6), one obtains

$$\begin{aligned} \mathbf{TR}_X\mathbf{T}^H &= E \left[\begin{bmatrix} d_0(k) \\ X_0(k) \end{bmatrix} \begin{bmatrix} d_0^*(k) & X_0^H(k) \end{bmatrix} \right] \\ &= \begin{bmatrix} \sigma_{d_0}^2 & r_{X_0d_0}^H \\ r_{X_0d_0} & \mathbf{R}_{X_0} \end{bmatrix} \end{aligned} \quad (69.10)$$

where $\sigma_{d_0}^2 = E[d_0d_0^*]$, $r_{X_0d_0} = E[X_0(k)d_0^*(k)]$, $\mathbf{R}_{X_0} = E[X_0(k)X_0^H(k)]$. Substitute (69.10) in (69.9), one obtains

$$W_{Quasi-MVDR} = h_0 - \mathbf{B}_0^H \mathbf{R}_{X_0}^{-1} r_{X_0d_0} = h_0 - \mathbf{B}_0^H W_{X_0} \quad (69.11)$$

where $W_{X_0} = \mathbf{R}_{X_0}^{-1} r_{X_0d_0}$. As $W_{GSC} = W_{Quasi-MVDR}$, the formula (69.11) can be rewritten as

$$W_{GSC} = h_0 - \mathbf{B}_0^H \mathbf{R}_{X_0}^{-1} r_{X_0d_0} = h_0 - \mathbf{B}_0^H W_{X_0} \quad (69.12)$$

69.2.3 Covariance Matrix Taper Model

The capon beamforming technique based on conventional GSC model analyzed in Sect. 69.2.1, has poor robust performance. In order to enhance the robust performance of real system, a improved technique of covariance matrix taper is proposed in this paper, to widen notch of the pattern the widen matrix, \mathbf{G} , is given by

$$[\mathbf{G}]_{mn} = \text{sinc}(l_{mn} \cdot \Delta / \pi) \quad (69.13)$$

where l_{mn} is the distance between the m th and the n th antenna elements, Δ is a parameter denoting the spread width. And the Δ for uniform linear array (ULA), is the normalized bandwidth of jamming. One can rewrite (69.12) as

$$W_{GSC} = h_0 - \mathbf{B}_0^H \mathbf{R}_{X_0}^{-1}(k) \mathbf{B}_0 \mathbf{R}_X(k) h_0 \quad (69.14)$$

where

$$\begin{aligned} \mathbf{R}_{X_0}(k) &= E[\mathbf{B}_0 X(k) X^H(k) \mathbf{B}_0^H] \\ &= \mathbf{B}_0 \mathbf{R}_X(k) \mathbf{B}_0^H \end{aligned} \quad (69.15)$$

where $\mathbf{R}_{X_0}(k)$ is the covariance matrix of $X_0(k)$, and $\mathbf{R}_X(k)$ is the covariance matrix of $X(k)$. $\mathbf{R}_X(k)$ can be tapered through Hadamard multiplying (represented by “ \circ ” in formula) with the widen matrix, one obtains

$$\widehat{\mathbf{R}}_X(k) = \mathbf{R}_X(k) \circ \mathbf{G} \tag{69.16}$$

$$\widehat{\mathbf{R}}_{X_0}(k) = \mathbf{B}_0 \widehat{\mathbf{R}}_X(k) \mathbf{B}_0^H \tag{69.17}$$

where $\widehat{\mathbf{R}}_{X_0}(k)$ and $\mathbf{R}_X(k)$ respectively denotes the covariance matrix after taper. And then the form of weights after covariance matrix taper can be given by

$$\widehat{W}_{GSC} = h_0 - \mathbf{B}_0^H \widehat{\mathbf{R}}_{X_0}^{-1}(k) \mathbf{B}_0 \widehat{\mathbf{R}}_X(k) h_0 \tag{69.18}$$

formula (69.18) is the representation of anti-jamming weights based on the robust GSC in frequency domain. The weights are obtained by limited space snap-sampling, therefore the signal model with statistical significance, $\mathbf{X}(k)$, is used as the input of the system in this paper. And then the adaptive weights, $\widetilde{W}_{GSC}(k)$, according with the k th frequency bin, can be obtained.

69.3 Antenna Array and Signal Scenarios

To facilitate the analysis, the radiation sources are assumed to be located in the far-field array, and the signal received by antenna array is plane wave, and the geometric aperture of antenna array is much smaller than the distance to radiation source. What’s more, the desired signal is a narrowband signal, and the propagation medium is isotropic, homogeneous. Also, the random noise regarded as stationary and zero-mean, is uncorrelated with the desired signal.

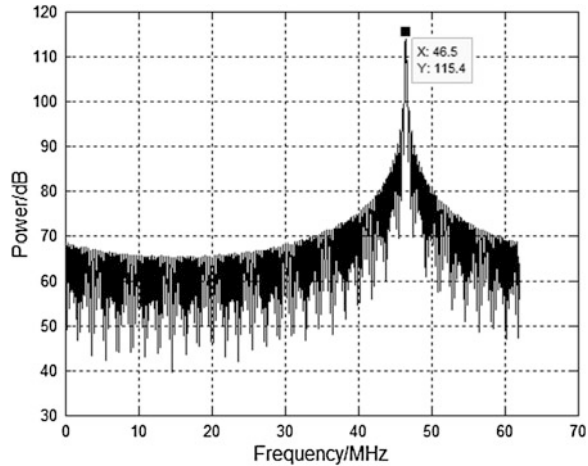
A linear uniform antenna array consisting of seven elements is used in this study. The interval of elements is selected to be $\lambda/2$, λ is the wavelength of the desired signal. These antenna elements receive RFI signals centered at 1.575 GHz. The signals are down-converted to midband 46.5 MHz, and sampled at a rate of 62 MHz. The value of M is set as 30, and the N is set as 1024, i.e. 1024×30 points are segmented into 30 segments, and then transformed to frequency domain by 1024-bin FFT.

The signals received by antenna elements consist of desired signal, jamming and noise. Table 69.1 shows the center frequency, bandwidth, power and angular location of various signals.

Table 69.1 Signal scenario of antenna array

Form	Frequency (MHz)	Bandwidth (MHz)	Power (dB)	θ (°)
Desired signal	1575.42	20	-13	0
Jamming 1	1575.42	Narrow-band	60	45
Jamming 2	1575.42	Narrow-band	90	-60

Fig. 69.2 The spectrum of synthesized signal



According to the signal scenario shown in Table 69.1, the frequency spectrum of the synthesized signal received by antenna elements that contains the desired signal, jamming 1, jamming 2, and noise, as shown in Fig. 69.2.

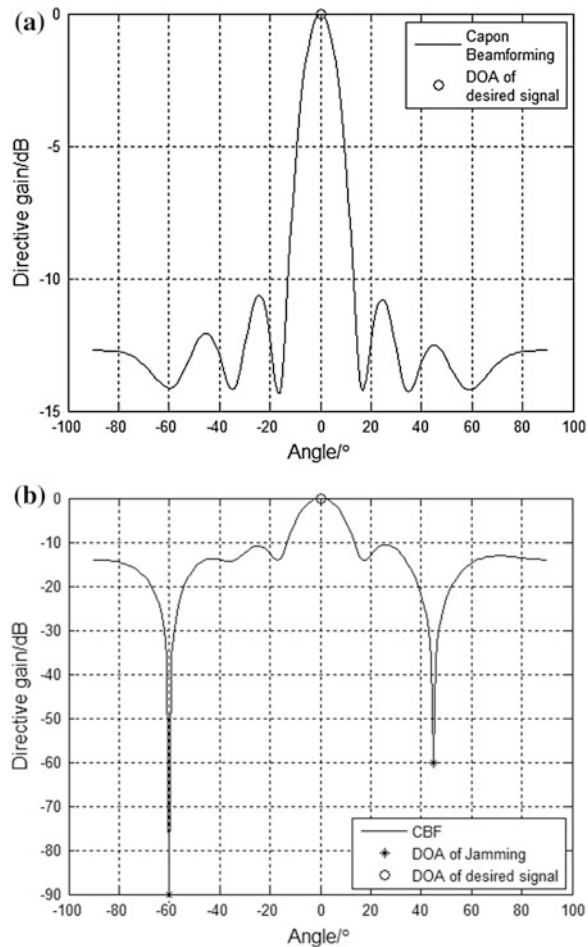
69.4 Simulation and Analysis

As shown in Fig. 69.2, due to the impact of the jamming, the amplitude of the spectrum reaches its maximum at 46.5 MHz. This will make the navigation system unable to calculate the orientation information correctly. In this section, the signals received by antenna elements are processed by the mathematical model of SFAP, which is established in Sect. 69.2, and then the performance of the model is also analyzed.

When the synthesized signal has no jamming, the conventional Capon beamforming (CBF) pattern is given in Fig. 69.3a, and the pattern sidelobe of SFAP is relatively flat, with no significant fluctuation. In Fig. 69.3b, the CBF of the synthesized signal which contains jamming 1 and jamming 2 is given. In the directions of jamming 1 and jamming 2, 60 and 90 dB attenuations are respectively formed. This shows that the SFAP based on GSC can effectively filter out the space jamming.

In Fig. 69.3, the anti-jamming performance of SFAP based on GSC is obvious in the ideal static environment without relative movement. However, the nulling mismatch of the pattern will occur when the random vibration and the rapid relative movement between the jammer and the antenna array are present in a real system, and which can lead to a huge drop in anti-jamming performance. Thus, a wide notch for jamming is required in a satellite navigation system, in order to suppress jamming.

Fig. 69.3 The pattern of SFAP based on GSC. **a** Contains signal. **b** Contains signal, jamming 1 and jamming 2



effectively in a realistic environment. In this paper, it will come true by covariance matrix taper mentioned in the Sect. 69.2.3. Just as shown in Fig. 69.4, the robust capon beamforming (RCB) is given.

In Fig. 69.4, the notch widen can be realized effectively by RCB, and make the navigation system able to bear the random vibration and relative movement of some extent. As the random vibration and the relative movement bring the angular deflection, the output SINR is obviously affected. In Fig. 69.5, the influences for CBF and RCB are shown.

In Fig. 69.5, the output SINR performance of RCB is superior to CBF. Since the input SNR of the system model is -13 dB, the error caused by angular deflection within 2° can be borne to RCB system, but for the CBF system, the satellite navigation receiver unable to calculate the orientation information normally when the angular deflection just reaches 0.5° .

Fig. 69.4 The pattern of CBF and RCB

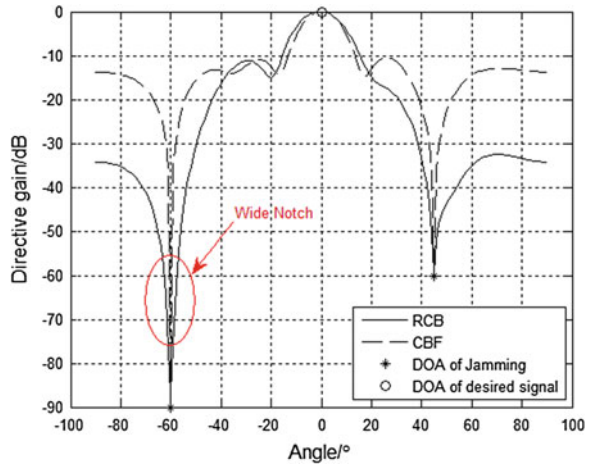
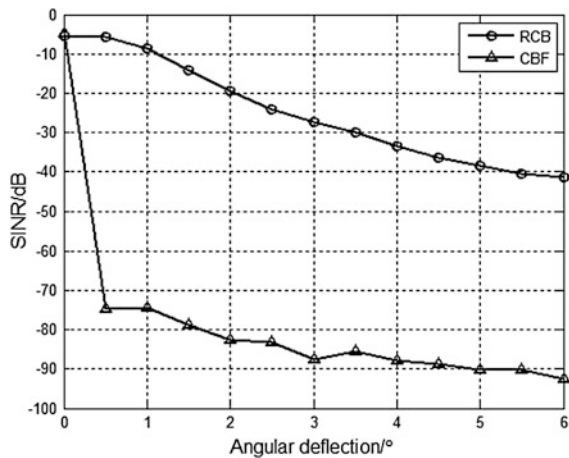


Fig. 69.5 The relation between angular deflection and output SINR



69.5 Conclusion

The performance of robust SFAP based on GSC has been studied in this paper. It is shown that when the random vibration and the relative movement exist in the system, RCB based on covariance matrix tapers leads to improved performance. And the calculated amount can be reduced effectively due to the implication of GSC in SFAP; the real-time performance is then enhanced.

The robust SFAP algorithm analyzed in this paper has been realized in embedded system based on FPGA and DSP, and the update time of adaptive weights is about 200 ms. If the satellite navigation system is flying in the 10,000 m high, and the jammer is located on the ground, in case that the angular deflection reaches 2°, speed of the satellite navigation system need to achieve five times speed

of sound. Therefore the environment adaptability of this system is very strong. Moreover, the less amount calculation of this method and the advantage of SFAP, make it possible to achieve an anti-jamming system based on single FPGA. This will reduce the complexity of the anti-jamming system, and the robust performance of the system will be enhanced simultaneously.

Acknowledgments This work was supported in part by the National Natural Science Foundation of China (No. 61271416 and No. 61301093) and the Fundamental Research Funds for the Central Universities (No. 3102014KYJD027).

References

1. Wang YL, Ding QJ, Li RF (2009) Adaptive array processing technique. Tsinghua University Press, Beijing, pp 13–84
2. Gupta IJ, Moore TD (2004) Space-frequency adaptive processing (SFAP) for radio frequency interference mitigation in spread-spectrum receivers. *IEEE*
3. Guerci JR (1999) Theory and application of covariance matrix tapers for robust adaptive beamforming. *IEEE Trans SP* 47(4):P977–P985
4. Li J, Stoica P (eds) (2006) Robust adaptive beamforming. Wiley, New York, pp 1–254
5. He XH (2010) Synthesis algorithm of radar waveform design and array pattern based on convex optimization. Xidian University, Shanxi pp 3–8, 16–19
6. Boyd S, Vandenberghe L (2004) Convex optimization. Cambridge University Press, Cambridge
7. Zatman M (1995) Production of adaptive array troughs by dispersion synthesis. *Electron Lett* 31 (25):P2141–P2142

Chapter 70

Research on the BDS Inter-Satellite-Type Carrier Phase Bias Introduced by Different NH Code Sign Conventions

Zuohu Li, Hailing Wu, Liduan Wang and Hui Liu

Abstract As for D1 NAV message broadcast by BDS MEO/IGSO satellites, a secondary code of Neumann-Hoffman (NH) code with length of 20 bits is modulated on ranging code. However, the secondary coding are not implemented on D2 NAV message from BDS GEO satellites. While different GNSS receivers from different manufactures were used for carrier phase difference applications, a bias of 180° (half a cycle) may be induced between those carrier phases obtained from two different sign conventions A and B. The bias would result in that RTK activities failed. For the issue mentioned in former content, this paper presents an intensive research on the rationale of the BDS inter-satellite-type carrier phase bias introduced by different NH code sign conventions. We select three kinds of most popular GNSS OEM boards for testing and verification. A serial of crossover trails and long-term stability tests are executed to identify the half-cycle carrier phase bias between the BDS signals which two different OEM boards output. In addition, we change the sign convention of NH code in the OEM board K508 of ComNav Technology for further validation. Based on our test results, the paper proposes a recommended solution as all GNSS device manufactures should take Convention B for dealing with NH code between different BDS signals, to avoid the inter-satellite-type carrier phase bias in RTK application.

Keywords BDS · NH code · Sign convention · Real-time kinematic

Z. Li (✉) · H. Wu
Beijing Institute of Tracking and Telecommunication Technology, Beijing, China
e-mail: ahu_1981@126.com

L. Wang
ComNav Technology, Ltd, Shanghai, China

H. Liu
Wuhan University, Wuhan, China

70.1 Introduction

BeiDou Navigation Satellite System (BDS) MEO/IGSO satellites broadcast D1 navigation message which is modulated with a secondary code, i.e. a 20-bit length Neumann-Hoffman (NH) code (0, 0, 0, 0, 0, 1, 0, 0, 1, 1, 0, 1, 0, 1, 0, 0, 1, 1, 1, 0). However, the secondary coding is not implemented on D2 navigation message from BDS GEO satellites [1]. In case of BDS RTK (Real-time kinematic) activities, GNSS receivers from different manufactures may take use of different NH code sign conventions for BDS signals acquisition and tracking. A bias of 180° (half a cycle) might be induced into double differences (DD) between those carrier phases obtained from two different sign conventions A and B of two different manufacturers' GNSS receivers. The bias would result that RTK activities failed, or that two GNSS receivers/devices from different manufactures could not work together for GNSS difference application.

70.2 NH Code Sign Conventions and 1/2-Cycle Ambiguity

70.2.1 Two Sign Conventions

There are two sign convention options for mapping the logic levels of NH code onto signal levels: sign convention A and sign convention B, as listed in Table 70.1. Sign convention A maps logic levels “0s” and “1s” of NH code onto signal levels -1 and +1, respectively. This option is adapted by Grace Xinxin Gao from Stanford University in her first publication on BDS signal structure in 2007 [2]. On the contrary, sign convention B maps the logic levels “0s” and “1s” onto signal levels +1 and -1, respectively. It's prescribed in GPS and Galileo ICDs. On the surface, these two sign conventions have different mapping results of signal levels. Actually, this would result in a 180° carrier phase ambiguity for BDS MEO/IGSO signal.

70.2.2 Half-cycle Carrier Phase Ambiguity

BDS signal is composed of the carrier frequency, ranging code and navigation message. Signals on BDS B1 and B2 are the sum of channel I and Q which are in phase quadrature with each other. The ranging code and navigation message are

Table 70.1 Two sign conventions for NH code

Logic level of NH code	Sign convention for signal level	
	Sign convention A	Sign convention B
0	-1	+1
1	+1	-1

modulated on carrier. For convenience, we just take channel I of BDS signal for following analysis of half-cycle carrier phase ambiguity. Figure 70.1 depicts a typical process for GNSS receiver signal processing. In the process, NH code elimination for non-GEO satellite (MEO or IGSO) is the only different section as compared to that for GEO satellite.

BDS B1I signal or B2I signal can be expressed as follows:

$$s_I(t) = AC(t)D(t) \cos(2\pi ft + \varphi_0) \tag{70.1}$$

where, A is the signal amplitude of B1I or B2I, $C(t)$ is the ranging code of B1I or B2I, $D(t)$ is the data modulated on ranging code of B1I or B2I, f is the carrier frequencies of them, and φ represents their carrier initial phases [1]. Taking account of the 20-bit NH code modulated on D1 navigation message broadcasted by BDS MEO and IGSO satellites, the digital intermediate frequency (IF) signals of channel I of all BDS satellites, i.e. GEO, MEO and IGSO, can be written as:

$$\begin{aligned} s_{IF,I}^{MEO}(n) &= AC(n)D(n)NH(n) \cos(\varphi(n)) \\ s_{IF,I}^{GEO}(n) &= AC(n)D(n) \cos(\varphi(n)) \end{aligned} \tag{70.2}$$

In the former equation, for clarity and easy expression only a ‘MEO’ is used to identify those IF signals from MEO and IGSO satellites. And $NH(n)$ denotes the NH code modulated on MEO/IGSO satellites’ D1 navigation message.

As for IF signals expressed in Eq. (70.2), if signal carrier was eliminated in carrier tracking loop, the basic carrier information of received signal is stored in local carrier NCO (numerically controlled oscillator), and we can have [3]:

$$\begin{aligned} I^{MEO}(n) &= AD(n)NH(n) \cos(\Delta\varphi(n)) \\ I^{GEO}(n) &= AD(n) \cos(\Delta\varphi(n)) \end{aligned} \tag{70.3}$$

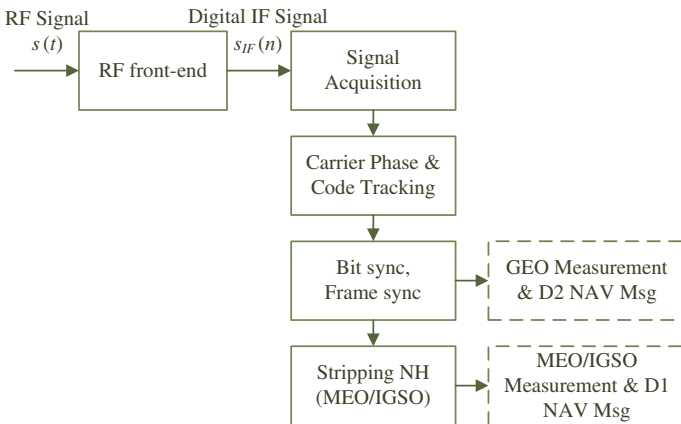


Fig. 70.1 Signal processing of BDS satellites

where $\Delta\varphi(n)$ is the carrier phase difference between received signal carrier and a replica of carrier phase produced by GNSS receiver's NCO circuits, in which a 180° phase ambiguity (half a cycle) is incurred during the process of carrier elimination from received signal. Fortunately, the half-cycle ambiguity can be easily confirmed while the ranging code is eliminated from the input signal and frame synchronization of navigation message is achieved.

According to Eq. (70.3), after code synchronization manipulation is finished, the carrier phase measurement of GEO satellite can be obtained as follows:

$$\phi_{obs}^{GEO} = N^{GEO} + \phi_{frac}^{GEO} \quad (70.4)$$

In the equation, N^{GEO} is the integral part of GEO satellite carrier phase measurement, i.e. integer ambiguity, and ϕ_{frac}^{GEO} is the fraction part of the measurement.

But as for MEO or IGSO satellites, if only NH code was removed before code synchronization from the received signal, their carrier phase measurement could be obtained. NH code modulated on received signal can be eliminated using an operation of modulo-2 addition, and it appears that for polarized NRZ (non-return to zero code) the modulo-2 addition operation can be replaced by using +1, -1 multiplication [4]. Because signal level of NH code is uncertain, it's just like that eliminating manipulation for NH code using two sign conventions as listed in Table 1 would introduce a half-cycle (180°) ambiguity into carrier phase measurement of MEO/IGSO satellites, as compared with that of GEO satellites. Then, the carrier measurement of MEO/IGSO satellites can be formulated as:

$$\phi_{obs}^{MEO} = N^{MEO} + \phi_{frac}^{MEO} + \phi_{NH}^{MEO} \quad (70.5)$$

where the half-cycle carrier phase ambiguity ϕ_{NH}^{MEO} has values of:

$$\phi_{NH}^{MEO} = \begin{cases} 0 \\ \pm 0.5 \end{cases}, \quad (unit : cycle) \quad (70.6)$$

70.3 BDS 1/2-Cycle Carrier Phase Biases Analysis on RTK

70.3.1 Double Differences (DD)

Generally, a difference positioning system would like to make use of DD for RTK (real-time kinematic) computation. Herein, a short baseline RTK with DD will be taken as an example for analyzing the impact of different options of NH code sign conventions on high precise positioning algorithms.

Each DD measurement is relevant to two satellites' measurement of the same time from two GNSS receivers, which is derived from the results of two different satellites' single difference (SD), that is, twice differences are executed between two

stations (rover and reference) and between two satellites respectively. DD diagram is shown in the following Fig. 70.2

Given rover receiver u and reference station receiver r tracked BDS satellites i and j at the same time, SD observation $\phi_{obs,ur}^{(i)}$ regarding BDS satellite i of these two receivers could be expressed as follows, temporarily in spite of the half-cycle carrier phase ambiguity ϕ_{NH}^{MEO} probably induced by the elimination manipulation for MEO/IGSO satellites' NH code using different sign conventions [5].

$$\phi_{obs,ur}^{(i)} = \phi_{obs,u}^{(i)} - \phi_{obs,r}^{(i)} = N_{ur}^{(i)} + \phi_{ur,frac}^{(i)} \tag{70.7}$$

in which cycle integer difference $N_{ur}^{(i)}$ and carrier phase measurement fraction difference $\phi_{ur,frac}^{(i)}$ are defined as:

$$N_{ur}^{(i)} = N_u^{(i)} - N_r^{(i)} \tag{70.8}$$

$$\phi_{ur,frac}^{(i)} = \phi_{u,frac}^{(i)} - \phi_{r,frac}^{(i)} \tag{70.9}$$

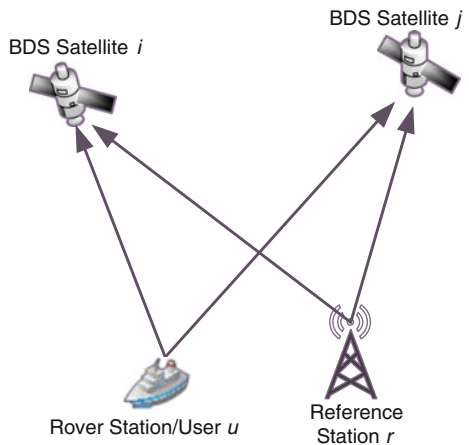
Similarly, SD observation $\phi_{obs,ur}^{(j)}$ regarding BDS satellite j of rover receiver and reference station receiver can be expressed as:

$$\phi_{obs,ur}^{(j)} = N_{ur}^{(j)} + \phi_{ur,frac}^{(j)} \tag{70.10}$$

Based on Eqs. (70.7) and (70.10), DD carrier phase observation is defined as:

$$\phi_{obs,ur}^{(ij)} = \phi_{obs,ur}^{(i)} - \phi_{obs,ur}^{(j)} = N_{ur}^{(ij)} + \phi_{ur,frac}^{(ij)} \tag{70.11}$$

Fig. 70.2 Double differences diagram



where

$$\begin{aligned}
 N_{ur}^{(ij)} &= N_{ur}^{(i)} - N_{ur}^{(j)} \\
 \phi_{ur,frac}^{(ij)} &= \phi_{ur,frac}^{(i)} - \phi_{ur,frac}^{(j)}
 \end{aligned}
 \tag{70.12}$$

Here, DD cycle integer ambiguity $N_{ur}^{(ij)}$ is a redefined unknown integer. The fraction part of DD carrier phase $\phi_{ur,frac}^{(ij)}$ mainly includes two items: a negligible DD measurement noise and a carrier phase component which could be determined by a result of baseline vector divided by signal wave length [3].

70.3.2 BDS Inter-Satellite-Type 1/2-Cycle Carrier Phase Biases

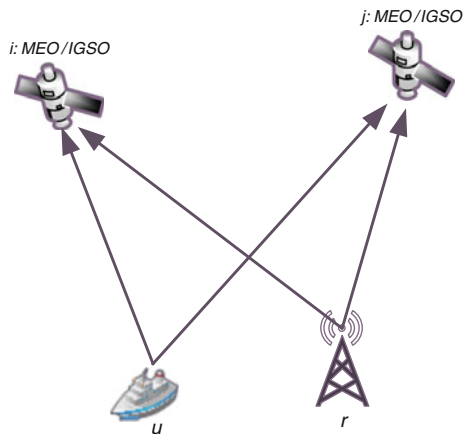
In this section, three kinds of DD combinations among BDS MEO/IGSO satellite and GEO satellite are present for analyzing 1/2-cycle carrier phase biases and impact of NH sign convention on RTK computation related to different DD combination with BDS satellites.

70.3.2.1 DD Between Two BDS MEO/IGSO Satellites

Case 1 Two MEO or IGSO satellites are involved in rover receiver’s DD RTK computation, as shown in Fig. 70.3.

Substituting Eq. (70.5) into Eqs. (70.7) and (70.10), and then their results into Eq. (70.11), and considering the half-cycle carrier phase ambiguity ϕ_{NH}^{MEO} at the same time, one can get:

Fig. 70.3 Double difference diagram of BDS MEO/IGSO



$$\phi_{obs,ur}^{MEO(ij)} = N_{ur}^{MEO(ij)} + \phi_{ur,frac}^{MEO(ij)} + \phi_{ur,NH}^{MEO(ij)} \quad (70.13)$$

where

$$\begin{aligned} \phi_{ur,NH}^{MEO(ij)} &= \phi_{ur,NH}^{MEO(i)} - \phi_{ur,NH}^{MEO(j)} \\ &= \phi_{u,NH}^{MEO(i)} - \phi_{r,NH}^{MEO(i)} - \left(\phi_{u,NH}^{MEO(j)} - \phi_{r,NH}^{MEO(j)} \right) \\ &= \left(\phi_{u,NH}^{MEO(i)} - \phi_{u,NH}^{MEO(j)} \right) + \left(-\phi_{r,NH}^{MEO(i)} + \phi_{r,NH}^{MEO(j)} \right) \end{aligned} \quad (70.14)$$

In Eq. (70.14), the first item $\left(\phi_{u,NH}^{MEO(i)} - \phi_{u,NH}^{MEO(j)} \right)$ on the right side is the difference of carrier phase ambiguities generated by NH code elimination manipulation while two MEO or IGSO satellites are observed for DD by rover receiver. At that time, no matter which NH sign convention was adopted, these two carrier phase ambiguities $\phi_{u,NH}^{MEO(i)}$ and $\phi_{u,NH}^{MEO(j)}$ are always equal or have one cycle difference. Similarly, the second item on the right side of the equation also has the value of 0 or 1.

Such that, the item $\phi_{ur,NH}^{MEO(ij)}$ in Eq. (70.13) equals to 0 or 1, which means that the 1/2-cycle carrier phase ambiguities will not have any impact on the RTK computation involving two non-GEO (MEO or IGSO) satellites' DD.

70.3.2.2 DD Between Two BDS GEO Satellites

Case 2 Two GEO satellites are involved in rover receiver's DD RTK computation, as shown in Fig. 70.4. Since there's no NH code modulated on D2 navigation message of GEO satellite, i.e. no NH carrier phase ambiguity item is included in Eq. (70.4), NH sign conventions will not affect DD RTK computation.

70.3.2.3 DD Between Two BDS GEO Satellites

Case 3 One GEO satellite and one non-GEO satellite (MEO/IGSO) are involved in rover receiver's DD RTK computation, as shown in Fig. 70.5.

Substituting Eqs. (70.5) and (70.4) into Eqs. (70.7) and (70.10) respectively, and then their results into Eq. (70.11), and considering the half-cycle carrier phase ambiguity ϕ_{NH}^{MEO} at the same time, one can get:

Fig. 70.4 Double difference diagram of BDS GEO

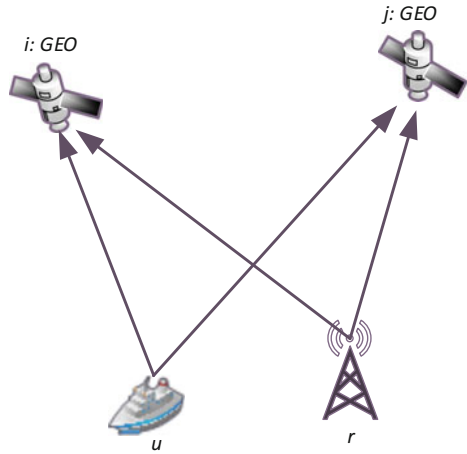
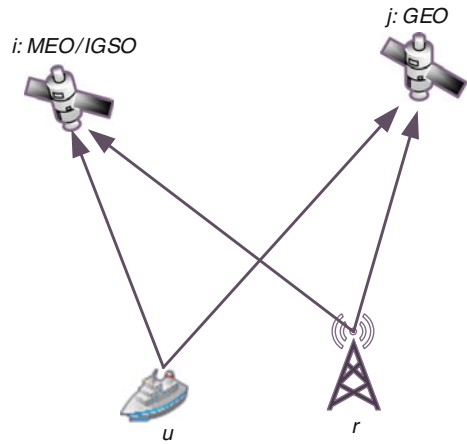


Fig. 70.5 Double difference diagram of BDS GEO and MEO/IGSO



$$\begin{aligned} \phi_{obs,ur}^{MEO(i)-GEO(j)} &= N_{ur}^{MEO(i)-GEO(j)} + \phi_{ur,frac}^{MEO(i)-GEO(j)} \\ &\quad + \phi_{ur,NH}^{MEO(i)-GEO(j)} \end{aligned} \tag{70.15}$$

in which

$$\phi_{ur,NH}^{MEO(i)-GEO(j)} = \phi_{ur,NH}^{MEO(i)} = \phi_{u,NH}^{MEO(i)} - \phi_{r,NH}^{MEO(i)} \tag{70.16}$$

In Eq. (70.15), the item $\phi_{ur,NH}^{MEO(i)}$ is the difference of carrier phase ambiguities generated by NH code elimination manipulation while two MEO or IGSO satellites are observed for DD by rover receiver u and by reference station receiver r , respectively. As for this item, we need to identify two situations to determine its specific value:

1. 1st situation: while both rover receiver u and reference station receiver r adopt the same sign convention (A or B) for removing NH code, values of $\phi_{u,\text{NH}}^{\text{MEO}(i)}$ and $\phi_{r,\text{NH}}^{\text{MEO}(i)}$ will be equal or have one cycle difference.

$$\phi_{ur,\text{NH}}^{\text{MEO}(i)} = \begin{cases} (\pm 0.5) - (\pm 0.5) & = 0 \\ (\pm 0.5) - (\mp 0.5) & = \pm 1 \\ 0 - 0 & = 0 \end{cases} \quad (70.17)$$

In this case, NH code eliminating manipulations will not bring a 1/2-cycle carrier phase bias and have no impact on DD RTK computation.

2. 2nd situation: while rover receiver u and reference station receiver r adopt different sign conventions for removing NH code, A or B respectively, $\phi_{u,\text{NH}}^{\text{MEO}(i)}$ and $\phi_{r,\text{NH}}^{\text{MEO}(i)}$ will not be equal. NH code eliminating manipulations of two receivers will bring a 1/2-cycle carrier phase bias and make DD RTK computation failed.

$$\phi_{ur,\text{NH}}^{\text{MEO}(i)} = \begin{cases} (\pm 0.5) - 0 & = \pm 0.5 \\ 0 - (\mp 0.5) & = \mp 0.5 \end{cases} \quad (70.18)$$

70.4 Evaluation Results

70.4.1 Testing

At the end of 2013, researchers from ComNav Tech's found that ComNav Tech's K505 OEM board could not have a RTK computation with Trimble BD970 as BDS satellites were involved in. In April 2014, after a series of experiments and data analysis in depth, we revealed that if a BDS MEO/IGSO satellite was taken as the reference satellite of DD, GEO satellites' carrier phase measurement from ComNav Tech's K508 would have a 1/2-cycle bias as compared to those from Trimble BD970, and vice versa. In addition, the 1/2-cycle bias also exist between NovAtel OEM628 board and Trimble BD970, while there's no such a bias between NovAtel's and ComNav Tech's boards. The testing results are listed in Table 70.2 as Item (1)–(3). And the testing equipment are shown in Fig. 70.6

On Jun 9–13 and Dec 1–5 2014, two further experiments were undertaken by ComNav Tech and SOUTH Surveying and Mapping Instrument CO., for validating former analysis results. Corresponding conclusions are as follows, and specific results are also presented in Table 70.2:

- As we added a 1/2-cycle carrier phase to the carrier phase measurement output of GEO BII from Trimble BD970 OEM board using a firmware of before Dec 2014, these corrected measurement could have a successful DD RTK computation with ComNav Tech's OEM boards.

Table 70.2 Comparative results of BDS 0.5-cycle carrier phase biases between different receivers

Testing cases	Receiver pairs	Freq.	IGSO	IGSO	GEO
			— GEO	— MEO	— MEO
(1) April 2014, Trimble BD970 (before firmware is updated) vs. ComNav Tech K508	BD970—K508	B1	-0.5	0.0	0.5
		B2	0.0	0.0	0.0
(2) April 2014, NovAtel OEM628 vs. ComNav Tech K508	OEM628—K508	B1	0.0	0.0	0.0
		B2	0.0	0.0	0.0
(3) April 2014, Trimble BD970 (before firmware is updated) vs. NovAtel OEM628	BD970—OEM628	B1	-0.5	0.0	0.5
		B2	0.0	0.0	0.0
(4) June 9–13 2014, Trimble BD970 (before firmware is updated) vs. ComNav Tech K508 (<i>a temporary firmware for testing</i>)	BD970—K508	B1	0.0	0.0	0.0
		B2	0.0	0.0	0.0
(5) Dec 1–5 2014, ComNav Tech K508 vs. Trimble BD970 (<i>after firmware is updated with sign convention B for B1</i>)	K508—BD970 (<i>latest firmware</i>)	B1	0.0	0.0	0.0
		B2	0.0	0.0	0.0



Fig. 70.6 Tests on 0.5-cycle biases of carrier phase between different GNSS OEM boards

- Moreover, we changed the NH sign convention of ComNav Tech’s boards from B to A for BDS B1I. A dedicated temporary firmware was released for updating ComNav Tech’s K508. As expected, the board had a very successful DD RTK computation with Trimble BD970 with the firmware of before Dec 2014.
- By Dec 2014, ComNav Tech’s K508 can work together with Trimble BD970 for RTK computation after BD970 is updated by a new released firmware.

Table 70.3 Summary of NH code sign conventions used by GNSS receiver manufacturers

Manufacturers	Sign conventions	
	B1I	B2I
Trimble (before Nov 2014)	<i>Convention A</i>	Convention B
Trimble (nowadays)	<i>Convention B</i>	Convention B
Javad [6]	Convention B	Convention B
Septentrio (before the end of 2013) [6]	Convention A	Convention A
Septentrio (nowadays) [6]	<i>Convention B</i>	<i>Convention B</i>
ComNav Tech, Ltd	Convention B	Convention B
NovAtel	Convention B	Convention B
Unicore Communications, Inc.	Convention B	Convention B

70.4.2 Current Situation of NH Code Sign Conventions

In accordance with those results listed in Table 70.2, and also combining Jean-Marie Sleewaegen (Septentrio) and his team's research conclusions [6], we specified those NH sign conventions used by several major GNSS receiver manufacturers in Table 70.3.

From Sleewaegen's research and testing results [6], after Septentrio changed their NH sign conventions (from A to B for both B1I and B2I), a 1/2-cycle bias of B2I between receivers of Trimble and Septentrio vanished, and a new 1/2-cycle bias of B1I between two of them comes up. Furthermore, the 1/2-cycle bias between receivers of Javad and Septentrio also vanished. Such results just provide a proof for those summaries in Table 70.3.

Before Nov 2014, among several major GNSS receiver and OEM board manufacturers, there's only Trimble GNSS board using NH sign convention A for BDS B1I signal, which is different from all the other manufacturers. In the RTCM SC104 annual meeting of Sep 2014, SC104 BDS work group addresses this issue about Trimble's choice of NH sign convention for BDS B1I. By the beginning of Dec 2014, Trimble releases a new firmware to update the sign convention for BDS B1I from A to B. Such a updating is also to fulfill his promise of announcing he would make a change of what he used in the RTCM SC104 annual meeting of Sep 2014.

70.5 Conclusion and Advice

From the former analysis and evaluation results, we can see that BDS inter-satellite carrier phase biases are not a system level drawback as what the research team from Septentrio has thought [7, 8]. It just comes from different choices regarding the two NH code sign conventions for BDS MEO/IGSO signal processing.

In conclusion, to avoid 1/2-cycle carrier phase biases arising again and also to improve the compatibility of different GNSS receivers as using BDS signals for

RTK activities, sign convention B should be taken as the only choice handling NH code modulated on MEO/IGSO D1 navigation message. The research and related results delivered in this paper could provide a reference and instructive suggestions for RTCM SC104 standards while their contents are related to BDS NH code.

References

1. China Satellite Navigation Office (2013) BeiDou navigation satellite system signal in space—interface control document. CSNO (ed)
2. Gao GX, Chen A, Lo S et al (2007) GNSS over China, the compass MEO satellite codes. *Inside GNSS*
3. Zuohu L (2008) Study on simulation of GPS software receiver technology. Master thesis, PLA Information Engineering University, 52–54
4. Borre Kai, Akos Dennis M (2007) A software-defined GPS and GALILEO receiver: a single-frequency approach. Boston, Basel, Berlin
5. Kaplan E (1990) Understanding GPS: principles and applications. Artech House Publishers, Massachusetts, pp 82–130
6. Nadarajah N, Teunissen PG, Sleewaegen J-M et al (2014) The mixed-receiver BeiDou inter-satellite-type bias and its impact on RTK positioning. *GPS Solution*, 1–12
7. Nadarajah N, Teunissen P, Raziq N (2013) BeiDou Inter-satellite-type bias evaluation and calibration for mixed receiver attitude determination. *Sens* 13:9435–9463
8. Sleewaegen J-M (2014) BeiDou Inter-satellite-type biases. RTCM Annual Meeting. RTCM SC-104 (3), Darmstadt, Germany

Chapter 71

A Position Calibration Algorithm of Antenna Arrays

Jiachi Wang and Zhongjun Chen

Abstract The paper presents an adaptive position calibration algorithm of antenna arrays basing on the FW algorithm, in which the alternative iteration method is used. Simulation and theory analysis in Matlab shows that the proposed algorithm work well with good resolution.

Keywords Position calibration · FW algorithm · Alternative iteration

71.1 Introduction

In order to solve the problem of position deviation in phase center from geometric center of antenna arrays, which is caused in the process of producing and installation of the antenna arrays. The main approaches of position calibration are active-calibration and passive-calibration. The active-calibration needs a signal source, which direction is known, then using the error model to calibrate the position. But this approach is very difficult in implementing process. One reason is the signal source which has precise position is hard to get. The other reason is the old data may no longer adapt to the new environment when the antenna array's working environment is changed.

The passive-calibration, also known as adaptive-calibration, which is no longer need a signal source which has precise position. Firstly, this approach uses Least Squares (LS) algorithm to approximate the ideal array model. Secondly, creating and minimizing a cost function. In other words, the passive-calibration converts the position calibration question into the optimization problem. The adaptive-calibration algorithm is based on software properties, which is easy to implement. This approach can compensate for baffling hardware.

J. Wang (✉) · Z. Chen
Guangzhou Haige Communications Group Incorporated Company, Guangzhou, China
e-mail: jc.wang@haige.com

In nowadays, there are few articles studying about self-adaptive error calibration questions. The most successful self-adaptive algorithms are based on the algorithm proposed by Friedlander and Weiss in 1991. This algorithm uses Music algorithm to estimate the DOA and errors online. It has high precision, but the convergence is not very well, which maybe convergence to local optimal point.

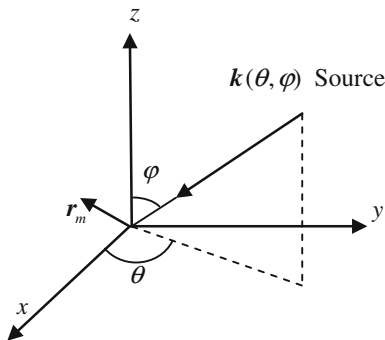
Looking at the results of existing researches, the position error correction is mostly used active-calibration algorithm. The self-adaptive position error calibration algorithm is seldom studied. In this paper, we proposed a new active-calibration algorithm which can exactly estimate the error of antenna array's position. The framework of this algorithm is based on FW adaptive calibration algorithm. This algorithm has many advantages. For example, it has software properties, which is not depend on the signal source that has precise position. But the main drawback of this algorithm is the heavy computation. It has the common problem of converging to local optimal value and also depend on the initial value. While, in consideration of the characteristics of one-time, the algorithm does not require real-time processing, so the heavy computation is acceptable. If the ideal antenna array's position is accurate, and the processing is not rough, this algorithm can finally converge to the actual location.

71.2 Antenna Array Oriented Vector

The space rectangular coordinate system established as shown in Fig. 71.1, Assuming that the antenna array is composed of M array element, the ordinal numbers is $1, 2, \dots, M$. Note that the position vector of array element m as r_m . The incident plane wave signal to the array reference point with angle (θ, φ) , the signal received by array reference point can be written as

$$x_0(t) = s(t)e^{j\omega t} \tag{71.1}$$

Fig. 71.1 Array geometry model



where $s(t)$ is the amplitude of the signals, ω represents angular frequency of the signal, then the signal received by array element M can be expressed as

$$x_m(t) = s[t - \tau_m(\theta, \varphi)]e^{j\omega[t - \tau_m(\theta, \varphi)]} \quad (71.2)$$

where $\tau_m(\theta, \varphi)$ is the relative time delay of array element M relative to reference point when receive the incoming signal, then

$$\omega\tau_m(\theta, \varphi) = r_m^T k(\theta, \varphi) \quad (71.3)$$

where $k(\theta, \varphi)$ the vector of incoming signals, whose amplitude is $2\pi/\lambda$, define the orientation vector matrix as

$$e(\theta, \varphi) = [\sin(\varphi) \cos(\theta), \sin(\varphi) \sin(\theta), \cos(\varphi)] \quad (71.4)$$

If the received signal is a narrow-band signal, then

$$s[t - \tau_m(\theta, \varphi)] \approx s(t) \quad (71.5)$$

Further, assuming that

$$\phi_m(\theta, \varphi) = -\omega\tau_m(\theta, \varphi) = \frac{2\pi}{\lambda} r_m^T e(\theta, \varphi) \quad (71.6)$$

The signal received by array M has the expression

$$x_m(t) = s(t)e^{j\omega t} e^{j\phi_m} \quad (71.7)$$

Considering the baseband signal, that is, through the spectrum shift and sampling, assuming that

$$x_m[n] = s[n]e^{j\phi_m} \quad (71.8)$$

Then the baseband digital signal can be written as

$$x[n] = (x_1[n], x_2[n], \dots, x_M[n])^T = s[n]\alpha \quad (71.9)$$

With

$$\alpha(\theta, \varphi) = (e^{j\phi_1}, e^{j\phi_2}, \dots, e^{j\phi_M})^T \quad (71.10)$$

where α is the matrix of steering vector, which depends on the directions of arrival (DOAs).

71.3 Oriented Vector Model with Position Error

At the time of antenna array disposal, due to machining accuracy and antenna array element itself is not the ideal points, there is the position disturbance of antenna array element. If we set position disturbance error of array M as Δr_m , then the corresponding error correction model can be revised as

$$\begin{cases} \tilde{\phi}_m(\theta, \varphi) = \phi_m(\theta, \varphi) + \Delta\phi_m(\theta, \varphi) \\ \Delta\phi_m(\theta, \varphi) = \frac{2\pi}{\lambda} \Delta r_m^T e(\theta, \varphi) \end{cases} \quad (71.11)$$

Accordingly, steering vector can be revised as

$$\gamma(\theta, \varphi) = \text{diag}[W(\theta, \varphi)]\alpha(\theta, \varphi) \quad (71.12)$$

where $\gamma(\theta, \varphi)$ represents the steering vector which determined by the actual arrays geometry location

$$W(\theta, \varphi) = (e^{j\Delta\phi_1}, \dots, e^{j\Delta\phi_M})^T \quad (71.13)$$

If we consider the amplitude-phase error and mutual coupling of the array, then the final math model of array steering vector can be expressed as

$$\rho(\theta, \varphi) = TZ\gamma(\theta, \varphi) \quad (71.14)$$

where T is the diagonal matrix of amplitude-phase error, Z is the mutual coupling matrix.

71.4 The Framework of FW Algorithm

The self-adaptive algorithm proposed by Friedlander and Weiss [1] in 1991 is discussed below.

Suppose the number of signal source is L . They inject on the array in different directions $(\theta_1, \varphi_1), \dots, (\theta_L, \varphi_L)$. The FW self-adaptive algorithm's cost function which can estimate the direction of arrival, amplitude and phase errors, mutual coupling and position error online is below:

$$\text{Min}J = \sum_{i=1}^L \|\rho^H(\theta_i, \varphi_i)U_n\|^2 = \sum_{i=1}^L \|\gamma^H(\theta_i, \varphi_i)Z^H T^H U_n\|^2 \quad (71.15)$$

If we only use Lagrange multiply or steepest descent method to find optimal solution, then the convergence performance is not satisfied and the computation is complex, while many variables are involved.

FW algorithm uses alternating iterative to find optimum solution, as described below:

- Step 1 Parameter setting: k is number of iterations, $(\theta_i^k, \varphi_i^k)$, γ_k , Z_k and T_k is the k th iteration.
- Step 2 According to the autocorrelation matrix \hat{R}_{xx} , obtain the noise subspace U_n [2].
- Step 3 Set $k = 0$, $\gamma_0 = \alpha$, $Z_0 = T_0 = I$. Also set $\rho_0(\theta, \varphi) = \alpha(\theta, \varphi)$, according to spatial spectrum function $P_0 = \|\rho_0(\theta, \varphi)U_n\|^{-2}$ to search peak-peak of L , and find $DOA(\theta_i^0, \varphi_i^0)$.
- Step 4 The parameter alternate iteration ($k \geq 1$). $Z = Z_k$, $\gamma = \gamma_k$, $(\theta_i, \varphi_i) = (\theta_i^{k-1}, \varphi_i^{k-1})$, T is a variable parameter. We minimize the cost function of J , then obtain T_k which is the k iteration of T .
Then set $T = T_k$, $\gamma = \gamma_k$, $(\theta_i, \varphi_i) = (\theta_i^{k-1}, \varphi_i^{k-1})$, Z is a variable parameter. We minimize the cost function of J , then obtain Z_k which is the k th iteration of Z .
Then set $Z = Z_k$, $\gamma = \gamma_k$, $(\theta_i, \varphi_i) = (\theta_i^{k-1}, \varphi_i^{k-1})$, r_m is a variable parameter. We minimize the cost function of J , then obtain γ_k which is the k th iteration of γ .
Finally set $\rho_k(\theta, \varphi) = T_k Z_k \gamma_k(\theta, \varphi)$, We use spatial spectrum function $P_k = \|\rho_k(\theta, \varphi)U_n\|^{-2}$ to search peak-peak of L , and find DOA's k th iteration $(\theta_i^k, \varphi_i^k)$ where

$$J_k = \sum_{l=1}^L \|\rho_k^H(\theta_i^k, \varphi_i^k)U_n\|^2 \quad (71.16)$$

- Step 5 if $J_k - J_{k-1} < \varepsilon$ (threshold), stop the iteration process.

71.5 The Calibration Algorithm of Position Errors

71.5.1 Framework of Algorithm

In order to use alternating iterative method to calibrate the error of position, we overwrite the cost function:

$$J = \sum_{l=1}^L \gamma(\theta_i^{k-1}, \varphi_i^{k-1})^H \Omega_r \gamma(\theta_i^{k-1}, \varphi_i^{k-1}) \quad (71.17)$$

where,

$$\Omega_r = Z_k^H T_k^H U_n U_n^H T_k Z_k \quad (71.18)$$

We obtain

$$\begin{cases} J_0 = \gamma(\theta, \varphi)^H \mathbf{\Omega}_r \gamma(\theta, \varphi) \\ J_i = J_0(\theta_i^{k-1}, \varphi_i^{k-1}) \end{cases} \quad (71.19)$$

Then, the cost function J is

$$J = \sum_{i=1}^L J_i \quad (71.20)$$

Suppose the m array antenna element's geometrical position is: $r_m = (x_m, y_m, 0)$, $m = 2, 3, \dots, M$, we obtain $x = (x_2, x_3, \dots, x_M)^T$, $y = (y_2, y_3, \dots, y_M)^T$. We also obtain $\frac{\partial}{\partial x} = \left[\frac{\partial}{\partial x_2}, \frac{\partial}{\partial x_3}, \dots, \frac{\partial}{\partial x_M} \right]^T$, $\frac{\partial}{\partial y} = \left[\frac{\partial}{\partial y_2}, \frac{\partial}{\partial y_3}, \dots, \frac{\partial}{\partial y_M} \right]^T$. Then

$$\begin{cases} \frac{\partial J_0}{\partial x} = 2\text{Re} \left\{ \frac{\partial \gamma(\theta, \varphi)^H}{\partial x} \mathbf{\Omega}_r \gamma(\theta, \varphi) \right\} \\ \frac{\partial J_0}{\partial y} = 2\text{Re} \left\{ \frac{\partial \gamma(\theta, \varphi)^H}{\partial y} \mathbf{\Omega}_r \gamma(\theta, \varphi) \right\} \\ \frac{\partial J}{\partial x} = \sum_{i=1}^L \frac{\partial J_0(\theta_i^{k-1}, \varphi_i^{k-1})}{\partial x} \\ \frac{\partial J}{\partial y} = \sum_{i=1}^L \frac{\partial J_0(\theta_i^{k-1}, \varphi_i^{k-1})}{\partial y} \end{cases} \quad (71.21)$$

Suppose the m array antenna element's geometrical position is $x = x_k$, $y = y_k$, then:

$$x_k = x_{k-1} - \lambda_k \frac{\partial J}{\partial x}(x_{k-1}, y_{k-1}) \quad (71.22)$$

We obtain

$$y_k = y_{k-1} - \mu_k \frac{\partial J}{\partial y}(x_{k-1}, y_{k-1}) \quad (23)$$

where λ_k and μ_k are step-length coefficient.

71.5.2 Choice of Step-Length Coefficient

We use steepest descent method to determine the step length coefficient λ_k and μ_k . Firstly, we introduce the steepest descent theorem.

Theorem 4.1 *If there exists the constant $C, \rho > 0$, and $|x_1 - x_2| < \rho$,*

$$\left| \frac{\partial J}{\partial x}(x_1) - \frac{\partial J}{\partial x}(x_2) \right| \leq C|x_1 - x_2| \tag{71.24}$$

Then,

$$J(x_k) < J(x_{k-1}) \tag{71.25}$$

where, x_k is created below:

$$\begin{cases} x_k = x_{k-1} - \lambda_k \frac{\partial J}{\partial x}(x_{k-1}) \\ \lambda_k < \min(1/C, \rho/d) \\ d = \left| \frac{\partial J}{\partial x}(x_{k-1}) \right| \end{cases} \tag{71.26}$$

71.6 Simulation

We calibrate the position errors of arrays which is a five-sensor array-antenna, as shown in Fig. 71.2. We suppose there is no other error exists except position error. The ideal array position is calculated based on the frequency of receive signal 1268.52 MHz and the geometric position of five-sensor array-antenna. After adding the error of agitation, we can finally calculate the actual position of antenna array. The location coordinates of ideal position and actual position is shown in Table 71.1.

After we simulate 150 alternate iterations, the comparison of spatial spectrum is shown in Fig. 71.3, and the before-and-after calibration of position errors is shown in Table 71.2.

Fig. 71.2 A five-sensor array-antenna

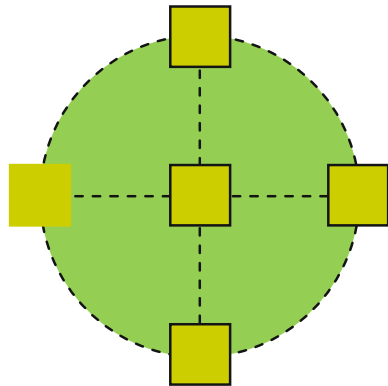


Table 71.1 The location coordinates of ideal position and actual position (units: m)

	Ideal position	Actual position
Sensor 1	(0, 0)	(0, 0)
Sensor 2	(0.1182, 0)	(0.1382, -0.018)
Sensor 3	(0, 0.1182)	(-0.025, 0.1392)
Sensor 4	(-0.1182, 0)	(-0.1032, -0.017)
Sensor 5	(0, -0.1182)	(-0.019, -0.1022)

Fig. 71.3 The comparison of spatial spectrum, before and after calibration, DOA = (60°, 45°) and (130°, 45°)

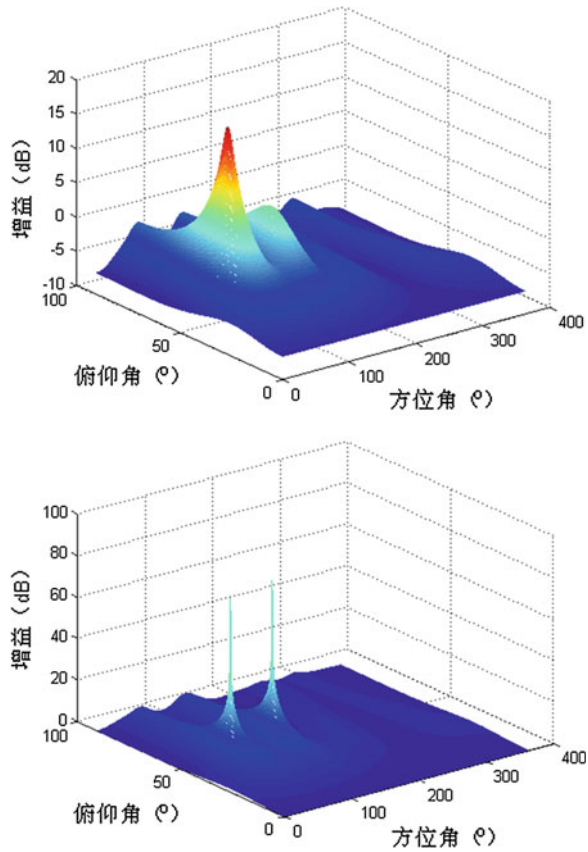


Table 71.2 The before-and-after calibration of position errors, DOAs = (60°, 45°) 和 (130°, 45°), (units: m)

	Actual position	Calibration position	Position error
Sensor 1	(0, 0)	(0, 0)	(0, 0)
Sensor 2	(0.1382, -0.018)	(0.1340, -0.0161)	(0.0043, 0.0019)
Sensor 3	(-0.025, 0.1392)	(-0.0197, 0.1351)	(-0.0053, 0.0041)
Sensor 4	(-0.1032, -0.017)	(-0.1012, -0.0176)	(-0.0021, -0.0006)
Sensor 5	(-0.0190, -0.1022)	(-0.0220, -0.0996)	(-0.0029, -0.0027)

71.7 Conclusion

In this paper, we give a new position calibration algorithm combined with FW algorithm that can calibrate the position of antenna arrays in online estimation. Experiments have confirmed that the algorithm is effective in the position calibration of antenna arrays, which can meet the requirements of position calibration in beam direction of antenna arrays.

References

1. Friedlander B, Weiss AJ (1991) Direction finding in the presence of mutual coupling. *IEEE Trans Antennas Propag* 39(3):273–284
2. Gong Y (2003) Adaptive filter. House of Electronics Industry, Beijing

Chapter 72

Performance Analysis of a Dual-Frequency Software-Defined BeiDou Receiver with B1 and B2 Signals

M. Zahidul H. Bhuiyan, Stefan Söderholm, Sarang Thombre, Laura Ruotsalainen and Heidi Kuusniemi

Abstract The Chinese BeiDou Navigation Satellite System (BDS) is one of the fastest emerging Global Navigation Satellite Systems (GNSS) that offers two civilian navigation signals through its 14 operational satellites as of November 2014. The release of the 2nd version of the BeiDou Interface Control Document (ICD) in December 2013 makes it possible for the researchers worldwide to investigate the performance of the 2nd civilian BeiDou B2 signal along with the legacy BeiDou B1 signal. In this paper, the researchers at the Finnish Geospatial Research Institute (FGI) make an effort to analyze the performance of BeiDou B1 and B2 signals in Finland considering the similarities and differences between the signals that affect the final positioning result. The performance analysis is carried out in a software-defined multi-frequency multi-GNSS research receiver developed at FGI. The data collection and the result analysis are carried out in two steps. In the first step, a hardware multi-frequency multi-GNSS simulator is utilized to verify the performance of the developed software-defined receiver. Afterwards, in the second step, the performance evaluation of BeiDou B1 and B2 signals is carried out with live data sets.

Keywords BeiDou navigation satellite system · Software-defined dual-frequency receiver

72.1 Introduction

The Chinese BeiDou Navigation Satellite System (BDS) has a mixed space constellation that has, when fully deployed, five Geostationary Earth Orbit (GEO) satellites, twenty-seven MEO satellites and three Inclined Geosynchronous Satellite

M.Z.H. Bhuiyan (✉) · S. Söderholm · S. Thombre · L. Ruotsalainen · H. Kuusniemi
Finnish Geospatial Research Institute, National Land Survey, Geodeetinrinne 2,
FI-02430 Masala, Finland
e-mail: zahidul.bhuiyan@nls.fi

Orbit (IGSO) satellites. The BeiDou system has been under development for more than a decade, and it is estimated to be operational with global coverage at the latest in 2020 [1, 2]. At present, the BDS has 14 operational satellites transmitting both B1 and B2 civilian signals in two frequency bands: BeiDou B1 at 1561.098 MHz and BeiDou B2 at 1207.140 MHz [3]. Unlike the US GPS and the European Galileo navigation satellite systems, each BDS satellite transmits the same unique PRN ranging code in both the frequencies. Generally speaking, both the BeiDou signals (i.e., B1 and B2) exhibit similar signal characteristics, though they might have different impact on the perceived performance of a receiver.

BeiDou B1 and B2 signals have different satellite transmission bandwidth. The 1-dB signal transmission bandwidth for BeiDou B1 is 4.092 MHz, whereas for B2, it is 20 MHz [3]. Therefore, a dual-frequency BeiDou receiver having the same front-end bandwidth for both the frequency bands will end up receiving signals with different signal strengths from the same satellite, even though the user-satellite geometry being the same for both the signals. Apart from that, the ionosphere is the other differentiating factor between BeiDou B1 and B2 signals due to its frequency dependent nature. In general, the B2 signal should experience more code-phase delay than that of B1 signal, since B2 has a carrier frequency that is 353.958 MHz less than B1 carrier frequency. In view of these differences between the two signals, the authors carry out a comparative study on the perceived performance of BeiDou B1 and B2 receiver, assuming each signal as a single system.

The rest of this paper is organized as follows. In Sect. 72.2, three different ionospheric error correction methods are discussed. Section 72.3 briefly addresses the main features of the implemented multi-frequency multi-GNSS software-defined receiver. The data collection and the result analysis are carried out in two steps. In the first step, a hardware multi-frequency multi-GNSS simulator is utilized to verify the performance of the dual-frequency receiver. Afterwards, in the second step, the performance of the dual frequency receiver is analyzed via live data collection. Section 72.4 outlines the hardware simulation setup and the corresponding result analysis for a dual-frequency software-defined receiver. In Sect. 72.5, live data-collection scenarios are presented along with a detail analysis of the positioning performance of B1 and B2 receiver. Finally, conclusions and the future work directions are presented in Sect. 72.6.

72.2 Ionospheric Error Correction

Different methods can be utilized to minimize the ionospheric effect on the final positioning solution. Three of these techniques are adopted in this research, and therefore, these techniques are briefly addressed in the following.

- Use of broadcast ionospheric model,
- Use of global ionospheric maps, and
- Use of dual-frequency code phase-based iono-free combination.

72.2.1 Use of Broadcast Ionospheric Model

The navigation message broadcast by the satellites contains a predicted ionospheric model (four α and four β parameters) that can be used with the predefined ionospheric model to correct single frequency observations [4]. GPS and BeiDou both utilize Klobuchar model as the broadcast ionosphere correction model. In case of GPS, the Klobuchar correction parameters are broadcasted in sub-frame 4 for which the GPS receiver might need to wait for a maximum of 12.5 min to obtain the required coefficients. But, in case of BeiDou, the Klobuchar correction parameters are included already in the first sub-frame requiring only a maximum of 30 s in case of IGSO and MEO satellites and a maximum of 3 s in case of GEO satellites.

The inputs to the Klobuchar model are the user geodetic latitude, the longitude, the time of the day at the intersection between the mean ionospheric layer and the receiver to satellite line-of-sight, the relative azimuth and the elevation angle of the satellite. In general, it is believed that in a normal ionospheric condition, Klobuchar model can provide a correction for about 50 % of the ionospheric range delay in terms of Root-Mean-Square Error (RMSE) [5].

72.2.2 Use of Global Ionospheric Maps

The International GNSS Service (IGS) produces ionospheric Vertical Total Electron Content (VTEC) maps as one of the IGS products for the GNSS community. The IGS offers their ionosphere products as two-dimensional Global Ionosphere Maps (GIMs) in IONosphere map EXchange format (IONEX) [6]. The final IGS products are uploaded with a delay of about 12–18 days for public downloading. Meanwhile, a rapid version of GIMs is made available to the public with a latency of about 1–2 days. Both the final and the rapid GIMs have a temporal resolution of 2 h and a spatial resolution of 2.5° in latitude and 5° in longitude. The ultimate accuracy varies from the level of 2 TECU to about 8–9 TECU [7].

The inputs for the GIMs Ionex model are the geocentric latitude and longitude of the ionospheric point. For this position, the VTEC values are computed at each observation epoch. The TEC maps are rotated around the Z-axis in the temporal interpolation process in order to compensate the strong correlation between the ionosphere and the Sun's position. Finally, the interpolated VTEC values are then converted to Slant TEC (STEC) in order to compute the estimated ionospheric correction for a given frequency. In this work, either the final or the rapid IGS ionospheric products are utilized depending on their availability at the time of position computation.

72.2.3 Use of Dual-Frequency Code Phase-Based Ionosphere-Free Combination

No ionosphere modelling is required when measurements from more than one carrier frequencies are available. For example, a dual-frequency receiver measures the pseudorange for each of the two received signals, both of which are contaminated by the same ionospheric effect. Theoretically, in an ideal error-free scenario, a proper combination of the available measurements allows the receiver to completely remove the ionospheric delay caused by the first order effects [8] and this is one of the main advantages of dual-frequency receivers over single frequency ones.

In a code phase-based GNSS receiver, the measured pseudorange can be written as:

$$c\hat{\tau}_{f_i} = \rho + I_{f_i} + c\tau_{Other} + c\tau_{\epsilon_i} \quad (72.1)$$

where c is the speed of light, $\hat{\tau}_{f_i}$ is the measured pseudorange in seconds for a given frequency f_i (for $i = 1, 2$), ρ is true geometric range in meters (which is the same for both signals), I_{f_i} is the frequency-dependent ionospheric delay given in meters, τ_{Other} contains all other delays which are independent of the carrier frequency such as tropospheric delay, multipath, clock bias and τ_{ϵ_i} is the delay measurement error ($\tau_{\epsilon_i} = \hat{\tau}_{f_i} - \tau_{f_i}$) produced at the code tracking stage. By following the derivations in [9], the ionosphere-free combinations can be written as:

$$\hat{\rho}_{IF} = \frac{f_1^2}{f_1^2 - f_2^2} \hat{\rho}_1 - \frac{f_2^2}{f_1^2 - f_2^2} \hat{\rho}_2 \quad (72.2)$$

where $\hat{\rho}_{IF}$ is the estimated ionosphere-free pseudorange in meters, $\hat{\rho}_1$ and $\hat{\rho}_2$ are the pseudoranges in meters for frequencies f_1 and f_2 , respectively. The ionosphere-free pseudorange is usually significantly noisier than the pseudoranges measured at f_1 and f_2 . The ability of code phase-based dual-frequency receiver to remove ionospheric delay resides solely on the assumption of zero measurement error [10]. In reality, the potential presence of measurement errors (i.e., multipath, clock bias, etc.) cannot be ignored completely, which at the end degrade significantly the accuracy of ionospheric delay estimation. Therefore, sufficient level of confidence regarding the accuracy of the pseudorange measurements (i.e., the level of noise, and the possible inherent bias) is needed before targeting a dual-frequency ionosphere-free position solution.

72.3 Multi-frequency Multi-GNSS Software-Defined GNSS Receiver

A multi-frequency multi-GNSS software-defined receiver, known as FGI-GSRx, has been developed in Finnish Geodetic Institute for analyzing and validating the research findings in the context of multi-frequency multi-GNSS systems. At present

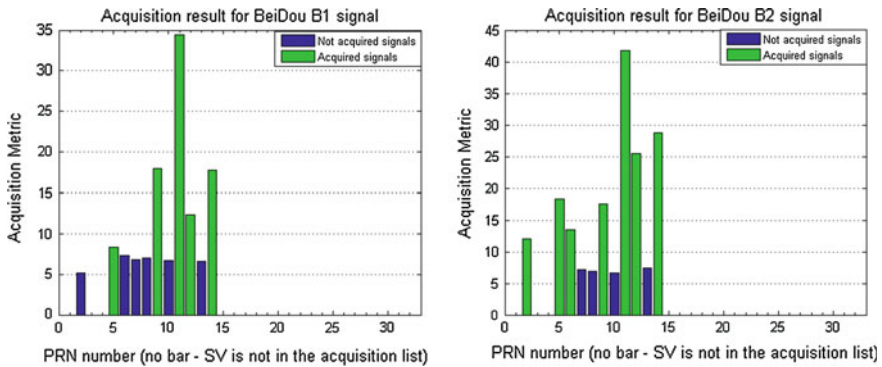


Fig. 72.1 The acquisition metric for the December 03, 2014 data set at 10:40 o'clock local time

the FGI-GSRx is capable of processing signals from five different systems, namely GPS, GLONASS, Galileo, BeiDou and IRNSS. The FGI-GSRx can process signals from GPS L1, Galileo E1, GLONASS L1, IRNSS L5 and BeiDou B1 and B2 frequencies. However, in this work, a comparative analysis will be carried out in the developed FGI-GSRx software-defined receiver between BeiDou B1 and B2 signals highlighting the differences in their positioning performances due to the effect of ionosphere and also due to the received signal strengths.

As mentioned in the BeiDou ICD [3], BeiDou B1 and B2 have identical signal structure with the same set of PRN codes used for both the signals. The signal acquisition for BeiDou B1 and B2 is carried out according to the scheme presented before in [11] and [12]. With the use of same acquisition algorithm for the same data set (collected at 10:40 o'clock on December 03, 2014), the FGI-GSRx successfully acquires 5 B1 satellites and 7 B2 satellites as seen from Fig. 72.1.

The signal tracking is carried out according to the procedure mentioned in [11, 12]. The Signal-to-Noise Power Ratio (SNPR) based C/N_0 estimation technique is used for both B1 and B2 signals, which is claimed to be one of the best C/N_0 estimators for BeiDou signals [13]. All the necessary implementation details about the BeiDou software-defined receiver can be found in [11, 12].

72.4 Data Collection and Result Analysis with Hardware Simulator

72.4.1 Data Collection with Hardware Simulator

A multi-frequency multi-GNSS hardware signal simulator from Spectracom (GSG 6 series [14]) was used to simulate BeiDou B1 and B2 signals in two different cases:

Case I: An ideal scenario with excellent signal strength and with no other external source of errors (i.e., no environmental error, no multipath, etc.): the

Table 72.1 Simulation profile for case I: BeiDou signals with no ionosphere and troposphere error

Parameters	Value	Details
C/N_0	~ 50 dB-Hz	Signal strength
BeiDou B1	Maxim 2769B, Bandwidth: 4.2 MHz	
BeiDou B2	Maxim 2112, Bandwidth: 10 MHz	
Ionosphere error	No	No ionospheric error
Troposphere error	No	No tropospheric error
Multipath	No	Multipath is not present

objective here is to verify the performance of the developed BeiDou B1 and B2 receivers in an ideal no noise environment.

Case II: A moderate scenario with signal strength around 45 dB-Hz in the presence of ionospheric and tropospheric error sources: the objective here is to verify the performance of a code phase-based dual-frequency ionosphere-free combination in a moderate environment in the presence of ionosphere and troposphere.

The key simulation configuration parameters are mentioned in Table 72.1. The BeiDou signals from Spectracom simulator is captured via a dual-frequency front-end from Nottingham Scientific Limited (NSL) [15]. Among the two on-board front-ends, the maxim 2769B front-end was configured to receive BeiDou B1 signal at 1561.098 MHz with a bandwidth of 4.2 MHz, whereas the maxim 2112 front-end was configured to receive BeiDou B2 signal at 1207.140 MHz with a bandwidth of 10 MHz. The received samples were complex for Beidou B2 signal and were real for BeiDou B1 signal. Both the signals were sampled at 26 MHz sampling frequency, and were synchronized with an internal onboard clock. The simulation profile for case II is presented in Table 72.2.

72.4.2 Result Analysis with Hardware Simulator Data

The ENU plots for BeiDou B1 and B2 signals are shown in Fig. 72.2, and the positioning result is presented in Table 72.3. It can be observed from Table 72.3

Table 72.2 Simulation profile for case II: BeiDou signals with ionosphere, troposphere and noise

Parameters	Value	Details
C/N_0	~ 45 dB-Hz	Signal strength
BeiDou B1	Maxim 2769B, Bandwidth: 4.2 MHz	
BeiDou B2	Maxim 2112, Bandwidth: 10 MHz	
Ionosphere error	Yes	Klobuchar model
Troposphere error	Yes	Saastamoinen model

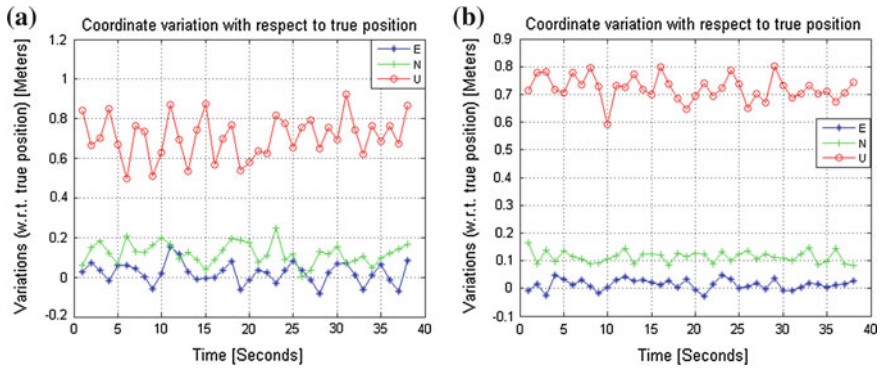


Fig. 72.2 ENU plots for BeiDou B1 (a) and B2 signal (b)

Table 72.3 Simulation result for case I: BeiDou signals with no ionosphere and troposphere error

Parameters (m)	PDOP	BeiDou B1	BeiDou B2	BeiDou B1-B2
RMSE _E	1.47 (11 satellites) for both B1 and B2	0.06	0.02	0.14
RMSE _N		0.13	0.12	0.19
RMSE _U		0.72	0.72	0.74
RMSE _{3D}		0.73	0.73	0.78
σ_{Hor}		0.05	0.02	0.11
σ_{Ver}		0.11	0.05	0.28
HPE (95 %)		0.22	0.16	0.4

that both the B1 and B2 signals offer a nice positioning fix with a 3D RMS less than a meter (i.e., ~0.73 m). The slight biases (mostly in Up component) may come from many different reasons including the non-idealities between the simulator and the front-end, PDOP, front-end noise, etc.

Table 72.4 compares the performance of a dual-frequency ionosphere-free code phase-based positioning solution against a single-frequency ionospheric correction based positioning solution assuming an average 50 % error correction with

Table 72.4 Simulation result for case II: BeiDou signals with ionosphere, troposphere and noise

Parameters (m)	BeiDou B1		BeiDou B2		B1-B2
	No Iono. corr.	50 % iono. corr. via Klobuchar Model	No Iono. corr.	50 % iono. corr. via Klobuchar Model	Dual Frequency code phase-based iono-free combination
RMSE _{3D}	4.37	2.19	6.44	3.22	1.96
σ_{Hor}	0.17	–	0.11	–	0.36
σ_{Ver}	0.53	–	0.22	–	1.02

broadcast Klobuchar model. The performance improvement is clearly visible in case of dual-frequency ionosphere-free code phase-based solution. It is important to note here that the simulation model does not include any multipath, clock bias or any other errors than ionosphere, troposphere, and receiver noise.

72.5 Data Collection and Result Analysis with Live Data

72.5.1 Live Data Collection

Two dual-frequency front-ends from NSL were used to capture the live BeiDou B1 and B2 signal. The first NSL front-end with Maxim 2112 chip [15] is configured to receive BeiDou B1 signal, whereas the second NSL front-end with Maxim 2112 chip is configured to receiver BeiDou B2 signal. The key configuration parameters are presented in Table 72.5. The idea here is to compare the performance of BeiDou B1 and B2 signals keeping all the front-end configuration parameters and acquisition and tracking algorithms unchanged for both the systems.

Unfortunately, the two front-ends were not time synchronized due to the lack of an external clock source. For that reason, it was not possible to have a dual-frequency ionospheric-free solution for the first data set collected on December 03, 2014. The sky plot for December 03, 2014 data set is shown in Fig. 72.3.

For the other two data sets on November 05 and September 02, 2014, one single NSL front-end was used with Maxim 2112 and Maxim 2769B onboard chips configured to receive BeiDou B2 and B1 signals respectively, as mentioned in Table 72.6. These two chips were time synchronized by a 10 MHz onboard clock.

72.5.2 Result Analysis with Live Data

72.5.2.1 Signal Strength Comparison

One traditional way of measuring the GNSS signal strength is by estimating the carrier-to-noise density ratio of the signal. The Signal-to-Noise Power Ratio

Table 72.5 Two NSL stereo v2 front-Ends configuration for BeiDou B1 and B2 signal reception for December 03, 2014 data set

Signal	BeiDou B1	BeiDou B2
Front-end chipset	Maxim 2112	Maxim 2112
Intermediate frequency (MHz)	0	0
Front-end bandwidth (MHz)	10	10
Sampling frequency (MHz)	26	26
Number of quantization bits	3 bits	3 bits
Signal type	I&Q, complex	I&Q, complex

Fig. 72.3 Sky-plot for BDS at 10:40 local time at Helsinki, Finland on December 03, 2014 with elevation cut off angle 5°

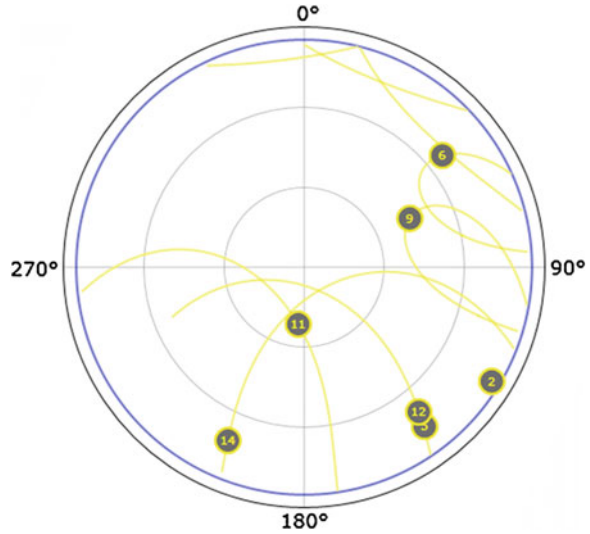


Table 72.6 NSL stereo v2 front-End configuration for BeiDou B1 and B2 signal reception for November 05, 2014 and September 02, 2014 data sets

Signal	BeiDou B1	BeiDou B2
Front-end chipset	Maxim 2769B	Maxim 2112
Intermediate frequency (MHz)	6.39	0
Front-end bandwidth (MHz)	4.2	10
Sampling frequency (MHz)	26	26
Number of quantization bits	2 bits	3 bits
Signal type	Real	Complex

(SNPR) based C/N_0 estimation technique, as mentioned in [13], was used for both B1 and B2 signals. The estimated C/N_0 plots for BeiDou B1 and B2 signals, and the differences in the estimated C/N_0 for the same tracked satellites are shown in Fig. 72.4a–c respectively for December 03, 2014 data set. It can be observed from Fig. 72.4c and 72.3 that the C/N_0 differences are quite significant especially for low-elevated satellites (satellites which have elevation angle below 30°). It is important to note here that the same acquisition algorithm with similar acquisition parameters (like B2) failed to acquire PRNs 2 and 6 for BeiDou B1.

72.5.2.2 Positioning Performance Comparison

A comparative analysis was carried out to measure the performance of BeiDou B1 and B2 signals in three different cases:

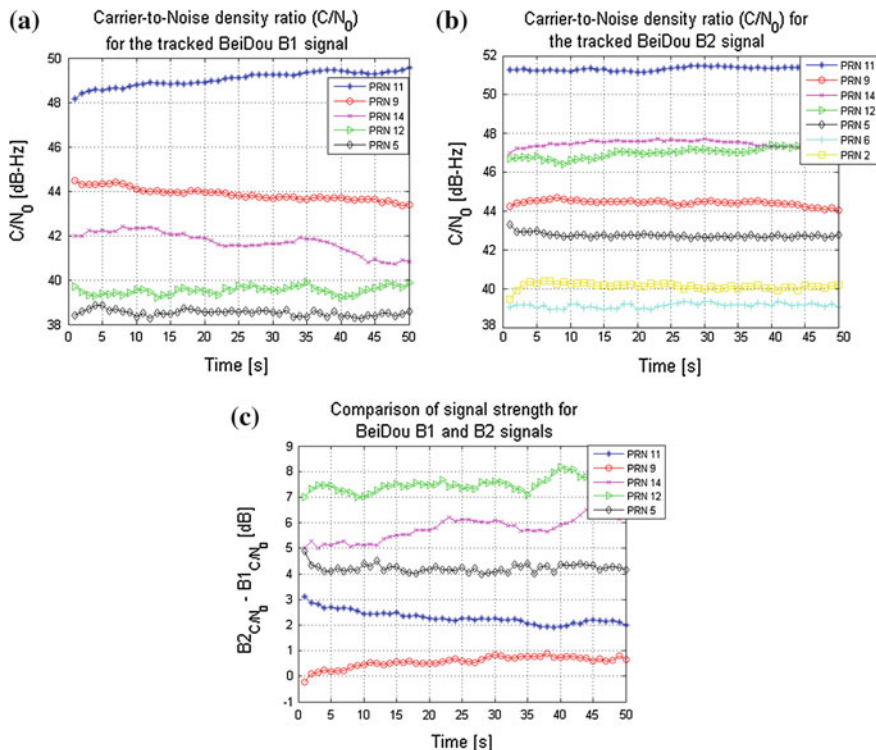


Fig. 72.4 **a** C/N₀ for BeiDou B1 signal; **b** C/N₀ for BeiDou B2 signal; **c** C/N₀ differences for BeiDou B2 and B1 signals in dB

- Case I: Use of broadcast ionospheric model,
- Case II: Use of global ionospheric maps, and
- Case III. Use of dual-frequency code phase-based ionosphere-free combination

It can be observed from Table 72.7 that the use of environmental correction models improves the overall positioning performance for both B1 and B2 signals for all the data sets. The positioning performance of B1 with broadcast ionospheric correction parameters is much better than the positioning performance of B2 with the same broadcast ionospheric correction parameters. The coefficient, $k = \left(\frac{f_{B1}}{f_{B2}}\right)^2$ is utilized while computing the ionospheric delay for BeiDou B2 signal as mentioned in [3], where f_{B1} is the B1 carrier frequency, and f_{B2} is the B2 carrier frequency. The poor positioning performance of BeiDou B2 as compared to BeiDou B1 is due to the fact that the effect of ionosphere is much higher in lower frequencies (i.e., B2 signal got affected much more than B1 as carrier frequency for B2 is about 353.958 MHz less than B1 carrier frequency). Therefore, it is expected that the average 50 % error corrections with broadcast Klobuchar model parameters are less

Table 72.7 Positioning results with the use of broadcast ionospheric model

Data sets	Parameters (m)	BeiDou B1			BeiDou B2		
		Before Iono. and Tropo. corr.	After Iono. and Tropo. corr.	Improvement (%)	Before Iono. and Tropo. corr.	After Iono. and Tropo. corr.	Improvement (%)
Dec 03, 2014	RMSE _{3D}	23.15	11.84	48.86	27.68	18.96	31.50
Nov 05, 2014	RMSE _{3D}	17.44	10.57	39.39	29.14	14.81	49.18
Sep 02, 2014	RMSE _{3D}	18.55	8.54	53.96	20.15	15.14	24.86
Overall improvement for B1				47.40	Overall improvement for B2		35.18

for B2 than for B1, meaning that the remaining left over ionospheric error will be higher for B2 than for B1.

It can be observed from Table 72.8 that the use of Ionex files improves the positioning performance in all the cases for both B1 and B2 signals. On the contrary, with the use of Ionex files, BeiDou B2 eventually offers better positioning performance than B1 mainly for the following reasons:

- I. B2 has higher signal strength leading to more satellites that are being tracked for positioning solution than B1 with the same set of acquisition and tracking algorithms,
- II. B2 has better noise mitigation than B1 due to higher C/N_0 (as can be seen from the horizontal and the vertical standard deviation measurements from Table 72.8), and
- III. B2 ionospheric corrections are compensated more accurately with Ionex files as compared to broadcast Klobuchar correction parameters.

It can also be observed from Table 72.8 that the use of dual-frequency code phase-based ionosphere-free combination performs relatively poorly as compared to broadcast correction-based positioning solution. This is mainly because of the fact that the potential presence of measurement errors (i.e., multipath, receiver noise, etc.) cannot be completely ignored, which at the end degrade significantly the accuracy of ionospheric delay estimation. More specifically, most of the BeiDou satellites when visible are most of the time poorly elevated while viewed from a high-latitude country like Finland ($>60^\circ$ North). The low-elevated satellite usually suffers from greater noise than a moderate-to-high-elevated satellite. Therefore, it is

Table 72.8 Comparison of BeiDou B1 and B2 positioning performance with three different ionospheric correction methods

Data sets	PDOP	Parameters (m)	BeiDou B1		BeiDou B2		B1–B2
			After Iono. corr.	After Ionex corr.	After Iono. corr.	After Ionex corr.	
Dec 03, 2014	4.06 for B1 (5 sat.) and 2.74 for B2 (7 sat.)	RMSE _{3D}	11.84	7.57	18.96	1.51	N/A (Two unsynchronized front-ends were used)
		σ_{Hor}	2.10	0.69	0.51	0.32	
		σ_{Ver}	2.08	2.09	0.6	0.59	
		HPE (95 %)	7.70	4.14	19.40	1.07	
Nov 05, 2014	4.06 for B1 (4 sat.) and 2.66 for B2 (7 sat.)	RMSE _{3D}	10.57	9.14	14.81	6.07	16.17
		σ_{Hor}	3.11	2.94	0.56	0.46	3.78
		σ_{Ver}	3.44	3.49	0.87	0.85	7.62
		HPE (95 %)	13.32	9.14	15.39	5.90	14.23
Sep 02, 2014	4.03 for B1 (5 sat.) and 3.68 for B2 (6 sat.)	RMSE _{3D}	8.54	9.61	15.14	8.85	29.25
		σ_{Hor}	2.09	1.31	1.23	1.32	4.69
		σ_{Ver}	3.10	4.14	2.43	2.45	13.77
		HPE (95 %)	8.50	6.36	15.20	5.10	19.23

worthwhile to investigate the performance of a dual-frequency ionosphere-free position solution in a location (i.e., Asia-pacific region) where there is a sufficient number of BeiDou satellites with elevation angle greater than 20°.

72.6 Conclusions

This paper presents a comparative performance analysis of BeiDou B1 and B2 signal, as a single system receiver and as a dual-frequency receiver. It is concluded that a dual-frequency BeiDou receiver receives B2 signal with higher signal energy than B1 due to the higher transmission bandwidth used to transmit B2 signal. Therefore, a B2-only receiver can offer higher sensitivity acquisition and tracking as compared to a B1-only receiver. On the contrary, B2 has greater ionospheric residual error than B1, if broadcast ionospheric model correction parameters are utilized. It was shown that B2 offered better positioning performance than that of B1 when global ionospheric map-based correction (i.e., Ionex) model was utilized. It was also concluded that a dual-frequency code phase-based ionosphere-free

technique was not very effective in the presence of noise, multipath and other possible error sources. The authors plan to investigate further the benefits of having a dual-frequency receiver over a single-frequency receiver in terms of accuracy, integrity, implementation complexity and so on.

References

1. Li M, Qu L, Zhao Q, Guo J, Su X, Li X (2014) Precise point positioning with the BeiDou navigation satellite system. In: *Sensors* 2014, vol 14, pp 927–943
2. Xu A, Xu Z, Ge M, Xu X, Zhu H, Sui X (2013) Estimating zenith tropospheric delays from BeiDou navigation satellite system observations. In: *Sensors* 2013, vol 13, pp 4514–4526
3. BeiDou Navigation Satellite System Signal In Space Interface Control Document (2013) Open service signal (Version 2.0), China Satellite Navigation Office
4. Klobuchar JA (1996) Ionospheric effects on GPS. In: Spilker JJ, Parkinson BW (eds) *Global positioning system: theory and applications*, vol 1. AIAA, pp 485–515
5. Klobuchar JA, Kunches JM (2000) Eye on ionosphere. *GPS Solutions* 5(1):68–69
6. Schaer S, Gunter W, Feltens S (1998) IONEX: the IONosphere map exchange format version 1. In: *Proceedings of the IGS AC workshop*, Darmstadt, Germany, 9–11 Feb 1998. ESA/ESOC, pp 233–237
7. IGS (2014) International GNSS service. <http://igs.org/products>. Accessed 05 Dec 2014
8. Engel U (2008) A theoretical performance analysis of the modernized GPS signals. In: *Position, location and navigation symposium, IEEE/ION*, pp 1067–1078
9. Misra P, Enge P (2011) *Global positioning system: signals, measurements and performance*, 2nd edn. Ganga-Jamuna Press, Lincoln. ISBN 0-9709544-1-7
10. Skourmetou D (2012) Mitigation of dominant channel propagation effects in GNSS-based positioning. Ph.D. thesis, Tampere University of Technology, Publication No. 1007
11. Bhuiyan MZH, Söderholm S, Thombre S, Ruotsalainen L, Kuusniemi H (2014) Overcoming the challenges of BeiDou receiver implementation. In: *Sensors* 2014, vol 14, pp 22082–22098
12. Bhuiyan MZH, Söderholm S, Thombre S, Ruotsalainen L, Kuusniemi, H (2014) Implementation of a software-defined BeiDou receiver. In: *Chinese satellite navigation conference proceedings*. Volume I, *Lecture notes in electrical engineering*, vol 303, pp 751–762. Springer, ISSN 1876-1100
13. Bhuiyan MZH, Söderholm S, Thombre S, Ruotsalainen L, Kirkko-Jaakkola M, Kuusniemi H (2014) Performance evaluation of carrier-to-noise density ratio (C/N_0) estimation techniques for BeiDou B1 signal. In: *UPINLBS'2014*, Texas, USA, 20–21 Nov 2014
14. Spectracom (2014) GSG-6 series multi-channel, multi-frequency advanced GNSS simulator. <http://www.spectracomcorp.com>. Accessed 05 Oct 2014
15. Nottingham Scientific Limited (2014) Delivering reliable and robust GNSS. <http://www.nsl.eu.com/datasheets/stereo.pdf>. Accessed 05 Nov 2014